Transactions of the ASME®

HEAT TRANSFER DIVISION
Chairman, R. GREIF
Secretary, G. P. PETERSON
Technical Editor, R. VISKANTA (1995)
Associate Technical Editors,
Y. BAYAZITOGLU (1995)
S. H. CHAN (1997)
V. K. DHIR (1996)
A. FAGHRI (1996)
W. L. GROSSHANDLER (1995)
C. E. HICKOX, JR. (1995)
Y. JALURIA (1996)
J. R. LLOYD (1995)
M. F. MODEST (1996)
R. A. NELSON, JR. (1996)
T. J. RABAS (1997)
T. W. SIMON (1995)
K. VAFAI (1997)
B. W. WEBB (1997)

BOARD ON COMMUNICATIONS
Chairman and Vice President
R. D. ROCKE

Members-at-Large
T. BARLOW, N. H. CHAO, A. ERDMAN,
G. JOHNSON, L. KEER, W. MORGAN,
E. M. PATTON, S. PATULSKI, R. E. REDER,
S. ROHDE, R. SHAH, F. WHITE,
J. WHITEHEAD

OFFICERS OF THE ASME
President, P. J. TORPEY
Executive Director,
D. L. BELDEN
Treasurer,
R. A. BENNETT

PUBLISHING STAFF
Mng. Dir., Publ.,
CHARLES W. BEARDSLEY
Managing Editor,
CORNELIA MONAHAN
Sr. Production Editor,
VALERIE WINTERS
Production Assistant,
MARISOL ANDINO

**Transactions of the ASME, Journal of Heat Transfer** (ISSN 0022-1481) is published quarterly (Feb., May, Aug., Nov.) for $185.00 per year by The American Society of Mechanical Engineers, 345 East 47th Street, New York, NY 10017. Second class postage paid at New York, NY and additional mailing offices. POSTMASTER: Send address changes to Transactions of the ASME, Journal of Heat Transfer, c/o THE AMERICAN SOCIETY OF MECHANICAL ENGINEERS, 22 Law Drive, Box 2300, Fairfield, NJ 07007-2300.
**CHANGES OF ADDRESS** must be received at Society headquarters seven weeks before they are to be effective. Please send old label and new address.
**PRICES:** To members, $40.00, annually: to nonmembers, $185.00. Add $30.00 for postage to countries outside the United States and Canada.
**STATEMENT from By-Laws.** The Society shall not be responsible for statements or opinions advanced in papers or . . . printed in its publications (B7.1, para. 3).
**COPYRIGHT © 1995** by The American Society of Mechanical Engineers. Authorization to photocopy material for internal or personal use under circumstances not falling within the fair use provisions of the Copyright Act is granted by ASME to libraries and other users registered with the Copyright Clearance Center (CCC) Transactional Reporting Service provided that the base fee of $3.00 per article is paid directly to CCC, 222 Rosewood Dr., Danvers, MA 01923. Request for special permission or bulk copying should be addressed to Reprints/Permission Department. **INDEXED** by Applied Mechanics Reviews and Engineering Information, Inc. Canadian Goods & Services Tax Registration #126148048.

# Journal of Heat Transfer

Published Quarterly by The American Society of Mechanical Engineers

VOLUME 117 • NUMBER 2 • MAY 1995

## TECHNICAL PAPERS

### *Heat Conduction*

256 On Hyperbolic Heat Conduction and the Second Law of Thermodynamics
C. Bai and A. S. Lavine

264 A Lumped-Parameter Model for Stagnant Thermal Conductivity of Spatially Periodic Porous Media
C. T. Hsu, P. Cheng, and K. W. Wong

270 The Thermal Contact Conductance of Hard and Soft Coat Anodized Aluminum
M. A. Lambert, E. E. Marotta, and L. S. Fletcher

### *Forced Convection*

276 Prandtl Number Influence on Heat Transfer Enhancement in Turbulent Flow of Water at Low Temperatures
T. S. Ravigururajan and A. E. Bergles

283 Local Friction and Heat Transfer Behavior of Water in a Turbulent Pipe Flow With a Large Heat Flux at the Wall
E. Choi and Y. I. Cho

289 Pressure Drop and Heat Transfer in Turbulent Duct Flow: A Two-Parameter Variational Method
N. Ghariban, A. Haji-Sheikh, and S. M. You

296 Combined Effect of Free-Stream Turbulence and Unsteady Wake on Heat Transfer Coefficients From a Gas Turbine Blade
L. Zhang and J.-C. Han

303 Augmented Heat Transfer in a Recovery Passage Downstream From a Grooved Section: An Example of Uncoupled Heat/Momentum Transport
M. Greiner, R.-F. Chen, and R. A. Wirtz

309 Experimental Investigation of Corona Wind Heat Transfer Enhancement With a Heated Horizontal Flat Plate
B. L. Owsenek, J. Seyed-Yagoobi, and R. H. Page

316 Heat Transfer and Flow Characteristics of an Oblique Turbulent Impinging Jet Within Confined Walls
K. Ichimiya

323 Effect of Ferric Chloride on Silica Fouling
S. H. Chan, Z. J. Chen, and P. He

### *Natural Convection*

329 Stabilization of the No-Motion State of a Horizontal Fluid Layer Heated From Below With Joule Heating
J. Tang and H. H. Bau

334 Direct Simulation of Double-Diffusive Layered Convection
M. T. Hyun and T. L. Bergman

### *Radiative Transfer*

340 Characteristics of Radiation Absorption in Metallic Particles
T. Q. Qiu, J. P. Longtin, and C. L. Tien

346 Nonisothermal Nongray Absorbing-Emitting-Scattering Suspension of $Fe_3O_4$ Particles Under Concentrated Solar Irradiation
D. Mischler and A. Steinfeld

355 Pigments to Reflect the Infrared Radiation From Fire
P. Berdahl

359 The Spectral Line-Based Weighted-Sum-of-Gray-Gases Model in Nonisothermal Nonhomogeneous Media
M. K. Denison and B. W. Webb

366 Bolometric Response of High-$T_c$ Superconducting Detectors to Optical Pulses and Continuous Waves
Rong-Chang Chen, Jhy-Ping Wu, and Hsin-Sen Chu

373 Two Approaches to Optimal Sensor Locations
T. D. Fadale, A. V. Nenarokomov, and A. F. Emery

Downloaded 04 Feb 2011 to 194.85.80.107. Redistribution subject to ASME license or copyright; see http://www.asme.org/terms/Terms_Use.cfm

### *Boiling and Condensation*

380 Low-Velocity Subcooled Nucleate Flow Boiling at Various Orientations
K. M. Kirk, H. Merte, Jr., and R. Keller

387 A Painting Technique to Enhance Pool Boiling Heat Transfer in Saturated FC-72
J. P. O'Connor and S. M. You

394 Shape of a Vapor Stem During Nucleate Boiling of Saturated Liquids
J. H. Lay and V. K. Dhir

402 Interfacial Heat Transfer Between Steam Bubbles and Subcooled Water in Vertical Upward Flow
O. Zeitoun, M. Shoukri, and V. Chatoorgoon

408 Pool Boiling of *n*-Pentane, CFC-113, and Water Under Reduced Gravity: Parabolic Flight Experiments With a Transparent Heater
T. Oka, Y. Abe, Y. H. Mori, and A. Nagashima

418 Condensation of a Vapor Flowing Inside a Horizontal Rectangular Duct
Q. Lu and N. V. Suryanarayana

### *Phase-Change Heat Transfer*

425 Exact Solution to the One-Dimensional Inverse-Stefan Problem in Nonideal Biological Tissues
Y. Rabin and A. Shitzer

432 Stochastic Modeling of Molecular Transport to an Evaporating Microdroplet in a Superheated Gas
V. P. Carey and N. E. Hawks

440 Flow and Cold Heat-Storage Characteristics of Phase-Change Emulsion in a Coiled Double-Tube Heat Exchanger
H. Inaba and S. Morita

### *Porous Media and Fluidized Beds*

447 Non-Darcian Forced Convection in Porous Media With Anisotropic Dispersion
P. Adnani, I. Catton, and M. A. Abdou

452 Direct Contact Melting of a Packed Bed
D. A. Kearns and O. A. Plumb

458 Finite Difference Modeling of Anisotropic Flows
M. Keyhani and R. A. Polehn

465 Deterministic Chaotic Behavior of Heat Transfer in Gas Fluidized Beds
D. V. Pence, D. E. Beasley, and J. B. Riester

### *Heat Transfer in Manufacturing*

473 A Variable Heat Flux Model of Heat Transfer in Grinding: Model Development
T.-C. Jen and A. S. Lavine

479 Predicting the Impact of Quenching on Mechanical Properties of Complex-Shaped Aluminum Alloy Parts
D. D. Hall and I. Mudawar

489 Assessing Halon Alternatives for Aircraft Engine Nacelle Fire Suppression
W. Grosshandler, C. Presser, D. Lowe, and W. Rinkinen

495 Modeling of Nitrogen and Oxygen Recombination on Partial Catalytic Surfaces
O. Deutschmann, U. Riedel, and J. Warnatz

502 Fog Inerting Effects on Hydrogen Combustion in a PWR Ice Condenser Containment
W. Luangdilok and R. B. Bennett

## TECHNICAL NOTES

508 Thermal Contact Conductance of Ceramic Substrate Junctions
K. C. Chung, H. K. Benson, and J. W. Sheffield

510 Analytical Solution for Balanced Symmetric Counterflow Regenerator
J. J. Saastamoinen

512 On the Effective Driving Force for Transport in Cooling Towers
M. Sadasivam and A. R. Balakrishnan

515 Unsteady Buoyancy Exchange Flow Through a Horizontal Partition
M. Singhal and R. Kumar

520 Generalized Zoning Method in One-Dimensional Participating Media
A. K. Ma

524 Smoothing Monte Carlo Exchange Factors
R. I. Loehrke, J. S. Dolaghan, and P. J. Burns

(Contents continued on page 263)



Downloaded 04 Feb 2011 to 194.85.80.107. Redistribution subject to ASME license or copyright; see http://www.asme.org/terms/Terms_Use.cfm

(Contents continued from page 255)

526 Enhancement of Nucleate Boiling Heat Transfer and Depression of Surface Tension by Surfactant Additives
Wuu-Tsann Wu, Yu-Min Yang, and Jer-Ru Maa

529 Forced Convection Film Condensation on a Horizontal Tube—Influence of Vapor Boundary-Layer Separation
S. B. Memory and J. W. Rose

533 "Wrinkled" Film Boiling
S. M. Lu and D. J. Lee

536 The Effect of Inlet Subcooling on the Critical Heat Flux for Downward Flow With Upstream Compressibility
X. C. Huang, S. W. Ruan, and G. Bartsch

538 Condensation of Nonazeotropic Binary Refrigerant Mixtures Including R22 as a More Volatile Component Inside a Horizontal Tube
M. Shizuya, M. Itoh, and K. Hijikata

543 Onset of Natural Convection in a Horizontal Porous Medium With Mixed Thermal Boundary Conditions
K. E. Wilkes

547 Free Convection Induced by a Vertical Wavy Surface With Uniform Heat Flux in a Porous Medium
D. A. S. Rees and I. Pop

550 Simulation of the Cyclic Injection Mold-Cooling Process Using Dual Reciprocity Element Method
Shia Chung Chen and Yung Chien Chung

## ANNOUNCEMENTS

275 Address for submission of papers to the ASME JOURNAL OF HEAT TRANSFER

302 Errata to the list of journal referees

339 Change of address form for subscribers

488 Announcement: Third KSME–JSME Thermal Engineering Conference

507 Errata on a previously published paper by H. R. B. Orlande and M. N. Özişik

554 Discussion on two previously published papers by K. Vafai and P. C. Huang

556 Call for papers: ISTP-9

Inside back cover Information for authors



Downloaded 04 Feb 2011 to 194.85.80.107. Redistribution subject to ASME license or copyright; see http://www.asme.org/terms/Terms_Use.cfm

# On Hyperbolic Heat Conduction and the Second Law of Thermodynamics

**C. Bai**
Department of Mechanical Engineering,
Yeungnam University,
Keungsan, Korea

**A. S. Lavine**
Mechanical, Aerospace, and Nuclear
Engineering Department,
University of California, Los Angeles,
Los Angeles, CA 90095-1597

*For situations in which the speed of thermal propagation cannot be considered infinite, a hyperbolic heat conduction equation is typically used to analyze the heat transfer. The conventional hyperbolic heat conduction equation is not consistent with the second law of thermodynamics, in the context of nonequilibrium rational thermodynamics. A modified hyperbolic type heat conduction equation, which is consistent with the second law of thermodynamics, is investigated in this paper. To solve this equation, we introduce a numerical scheme from the field of computational compressible flow. This scheme uses the characteristic properties of a hyperbolic equation and has no oscillation. By solving a model problem, we show that the conventional hyperbolic heat conduction equation can give physically wrong solutions (temperature less than absolute zero) under some conditions. The modified equation does not display these erroneous results. However, the difference between results of these two models is negligible except under extreme conditions.*

## Introduction

The usual parabolic heat conduction equation assumes an infinite thermal propagation speed. It is known that this assumption can be inaccurate for short times, especially at cryogenic temperatures due to the corresponding low thermal propagation speed. Cattaneo's equation (1948) can be used in place of Fourier's Law to consider the effect of the finite speed of thermal propagation. When combined with the first law of thermodynamics, this results in the "conventional" hyperbolic heat conduction equation, which we will refer to as the CHE. Coleman et al. (1982, 1986) showed (in the context of nonequilibrium rational thermodynamics) that the CHE is not consistent with the second law of thermodynamics, and presented a modified system of equations that is. We call this modified system of equations the "modified hyperbolic type heat conduction equation" or MHE. To the present authors' knowledge, the MHE has never been solved, even though it was proposed more than ten years ago. Thus, we are faced with a model of heat transfer, the CHE, that has been solved extensively in the heat transfer literature, but that does not satisfy the second law. An alternative model of heat transfer, the MHE, has been proposed, but never solved. The question is clear, "Do the solutions to these two equations differ significantly?" If so, the CHE should not be used. If not, the CHE can be used without significant error.

We investigate this question by solving both equations (and the parabolic heat conduction equation, PE) for a model problem. We will show that under certain conditions the CHE gives temperatures below absolute zero, which is obviously wrong. The MHE remedies these physically wrong solutions. As a practical matter, we note that the disagreement between the CHE and the MHE is only significant for very thin domains (on the order of a carrier mean free path) exposed to very high heat transfer rates, and it may be that neither equation is valid in this case due to the breakdown of the continuum hypothesis. Thus, the results of the model problem suggest (without proving conclusively) that the CHE can be used whenever the continuum hypothesis is valid, even though in theory it violates the second law.

Contributed by the Heat Transfer Division and presented at the National Heat Transfer Conference, San Diego, California, August 9–12, 1992. Manuscript received by the Heat Transfer Division September 1992; revision received May 1994. Keywords: Conduction, Thermodynamics and Second Law, Transient and Unsteady Heat Transfer. Associate Technical Editor: L. S. Fletcher.

## Background

**Conventional Hyperbolic Heat Conduction Equation.** The hyperbolic heat conduction equation has been derived or postulated by many researchers. Joseph and Preziosi (1989, 1990) give an excellent review.

The thermal energy balance for an incompressible solid can be written

$$\frac{\partial e}{\partial t^*} + \nabla \cdot \mathbf{q} = g \tag{1}$$

where $e$ is the internal energy per unit volume, $\mathbf{q}$ is the heat flux, and $g$ is the heat source per unit volume. In Eq. (1),

$$e = e_0(T), \quad \text{i.e.,} \frac{\partial e}{\partial t^*} = \rho c(T) \frac{\partial T}{\partial t^*} \quad \text{with} \quad \rho c(T) = \frac{de_0}{dT} \tag{2}$$

We call $e_0$ and $c$ the equilibrium internal energy per unit volume and specific heat (as functions of temperature).

Fourier's classical heat conduction equation takes the form

$$\mathbf{q} = -k\nabla T \tag{3}$$

where $k$ is the thermal conductivity. Equations (1), (2), and (3) are combined to give the parabolic heat conduction equation. The basic assumption underlying this parabolic heat conduction equation is an infinite thermal propagation speed (Eq. (3)) and it is known that this assumption can be inaccurate for short times, especially at low temperature due to the corresponding low thermal propagation speed.

The finite thermal propagation speed can be accounted for by using the generalized Fourier's Law, or Cattaneo's equation (Cattaneo, 1948)

$$\mathbf{q} = -\left[k\nabla T + \tau \frac{\partial \mathbf{q}}{\partial t^*}\right] \tag{4}$$

where $\tau$ is thermal relaxation time. Substituting Eq. (4) for the heat flux $\mathbf{q}$ into Eq. (1) with Eq. (2), interchanging the order of differentiation of the resulting $\nabla \cdot (\partial \mathbf{q}/\partial t^*)$ term, and then using Eq. (1) once more for $\nabla \cdot \mathbf{q}$ yields (assuming constant properties)

$$\frac{1}{C^2}\frac{\partial^2 T}{\partial t^{*2}} + \frac{1}{\alpha}\frac{\partial T}{\partial t^*} = \nabla^2 T + \frac{g}{k} + \frac{1}{C^2 \rho c}\frac{\partial g}{\partial t^*} \tag{5}$$

where $C$ is the thermal propagation speed, defined as $\sqrt{\alpha/\tau}$. This is the conventional hyperbolic heat conduction equation (CHE).



Copyright © 1995 by ASME

Downloaded 12 Dec 2010 to 193.140.21.150. Redistribution subject to ASME license or copyright; see http://www.asme.org/terms/Terms_Use.cfm

Note that typical values of $\tau$ and $C$ for dielectric materials at cryogenic temperatures (the interest of the present authors) are order of magnitude $10^{-11}$ s and $10^3$ m/s, respectively.

**Second Law Considerations.** There has been some confusion over whether or not the CHE is compatible with the second law of thermodynamics (2nd Law). There are two schools of thought, based on extended irreversible thermodynamics and rational thermodynamics (which are both forms of nonequilibrium thermodynamics). Both schools allow that under nonequilibrium conditions, entropy may depend on heat flux. Then, using Cattaneo's equation for the heat flux in the expression for entropy production rate, it can be shown that there are a variety of expressions for entropy that yield a nonnegative entropy production rate (Jou et al., 1988). Thus, Cattaneo's equation itself is compatible with the 2nd Law. The extended irreversible thermodynamics argument essentially ends there, with the conclusion that the CHE is consistent with the 2nd Law (Jou et al., 1988). The rational thermodynamics approach (Coleman et al., 1982, 1986) goes further, to show that if entropy depends on heat flux, so must internal energy, and to derive unique expressions for entropy and internal energy which allow the 2nd Law to be satisfied. Since internal energy must depend on heat flux (in a particular way), equation (2) does not hold. Therefore, the CHE, which assumes $e = e_0$, is inconsistent with the 2nd Law, even though Cattaneo's equation itself is not.

In particular, Coleman et al. (1982, 1986) show that the following relationships must hold between internal energy and entropy (in the one-dimensional case, for notational simplicity)

$$\frac{\partial e}{\partial T} = T\frac{\partial s}{\partial T} \tag{6}$$

$$\frac{\partial e}{\partial q} = T\frac{\partial s}{\partial q} + \frac{zq}{T} \tag{7}$$

where

$$z(T) = \frac{\tau(T)}{k(T)} \tag{8}$$

From this, it is easily derived that the nonequilibrium internal energy and entropy are given by

$$e = \tilde{e}(T, q) = e_0(T) + a(T)q^2 \tag{9}$$

$$s = \tilde{s}(T, q) = s_0(T) + b(T)q^2 \tag{10}$$

with

$$a(T) = -\frac{T^2}{2}\frac{d}{dT}\left(\frac{z(T)}{T^2}\right) \tag{11}$$

$$b(T) = -\frac{1}{2}\frac{d}{dT}\left(\frac{z(T)}{T}\right) \tag{12}$$

where $e_0$ and $s_0$ are the equilibrium internal energy and entropy, that is, the values when $q = 0$. These equations contain nonequilibrium terms that are quadratic in heat flux $q$, where the classical equations of state are only functions of temperature.

It can be shown that there is one special case for which the formulation of Jou et al. (1988) is in agreement with Coleman et al. (1982, 1986). If the parameter $z(T)$ happens to have the form $z(T) = DT^2$ (where $D$ is a constant), then the general result of Coleman et al. (1982, 1986) reduces to $\tilde{e}(T, q) = e_0(T)$ and $\tilde{s}(T, q) = s_0(T) - zq^2/2T^2$, which is the relationship given by Jou et al. (1988). However, if one uses the CHE with thermophysical properties $\tau(T)$ and $k(T)$, which do not yield this form for $z(T)$, then there is an inconsistency and the 2nd Law is not satisfied.

It appears to the present authors that the issue of whether the CHE satisfies the 2nd Law (within the context of nonequilibrium thermodynamics) is unresolved within the thermodynamics community. However, the present authors find the arguments of Coleman et al. (1982, 1986) convincing, particularly in light of the fact that the CHE predicts temperatures below absolute zero in certain situations.

Kaliski (1965) proposed a formulation similar to that of Coleman et al. (1982, 1986). He introduced the thermal inertia concept in the heat conduction process and generalized the thermodynamics of stationary processes to rapidly varying nonstationary ones. In his nonstationary heat flow process the first law of

## Nomenclature

$A$ = nondimensional change in surface temperature = $(T_w - T_0)/T_0$
$a$ = parameter defined by Eq. (11)
$[B]$ = matrix defined by Eq. (38)
$[\tilde{B}]$ = matrix defined by Eq. (36)
$b$ = parameter defined by Eq. (12)
$C$ = thermal propagation speed = $\sqrt{\alpha/\tau}$
$[C]$ = matrix defined by Eq. (39)
$[\tilde{C}]$ = matrix defined by Eq. (37)
$c$ = specific heat (for an incompressible substance)
$e$ = internal energy per unit volume
$\tilde{e}$ = nonequilibrium internal energy per unit volume
$\mathbf{f}$ = flux vector
$\hat{\mathbf{f}}$ = numerical flux vector
$g$ = volumetric heat source
$H$ = Heaviside unit step function
$I_1$ = first-order modified Bessel function
$k$ = thermal conductivity
$L$ = nondimensional length = $Cl/(2\alpha)$
$l$ = domain length
$l_{mfp}$ = carrier mean free path
$Q$ = nondimensional heat flux = $\alpha q/(CkT_0)$
$\mathbf{q}$ = heat flux vector
$q$ = heat flux
$\mathbf{s}$ = numerical source vector
$s$ = entropy per unit volume
$\tilde{s}$ = nonequilibrium entropy per unit volume
$T$ = temperature
$t^*$ = time
$t$ = nondimensional time = $C^2t^*/(2\alpha)$
$\mathbf{u}$ = dependent variable vector
$\bar{\mathbf{u}}$ = averaged dependent variable vector
$V$ = temperature rate wave speed
$\mathbf{v}$ = characteristic variable vector
$v$ = characteristic variables
$\mathbf{w}$ = parameter vector
$x^*$ = spatial coordinate
$x$ = nondimensional spatial coordinate = $Cx^*/(2\alpha)$
$z$ = parameter defined by Eq. (8)
$\alpha$ = thermal diffusivity
$\beta$ = constant defined by Eq. (45)
$\gamma$ = constant defined by Eq. (45)
$\Delta t$ = time step
$\Delta x$ = space step
$\epsilon$ = convergence criterion for iterations
$\theta$ = nondimensional temperature = $T/T_0$
$\lambda$ = eigenvalue
$\nu$ = Courant number = $\Delta t/\Delta x$
$\rho$ = density
$\dot{\sigma}$ = volumetric entropy production rate
$\tau$ = thermal relaxation time
$\varphi$ = defined by Eq. (47)

### Subscripts

0 = initial value, equilibrium value
$i$ = grid index
$w$ = surface

### Superscripts

$n$ = time step
$\pm$ = positive/negative direction
$*$ = nondimensional variable, iterative step



Downloaded 12 Dec 2010 to 193.140.21.150. Redistribution subject to ASME license or copyright; see http://www.asme.org/terms/Terms_Use.cfm

thermodynamics is generalized by the addition of thermal kinetic energy to the usual equilibrium internal energy. With this additional term he showed that the entropy production rate is positive during the process and finally derived the wave-type heat conduction equation.

**Modified Hyperbolic Type Heat Conduction Equation.** Based on the expression for internal energy derived by Coleman et al. (1982, 1986) (Eq. (9)), it follows that $\partial e/\partial t^*$ is not given by the classical formula $\partial e/\partial t^* = \rho c(T)\partial T/\partial t^*$, but is given by

$$\frac{\partial e}{\partial t^*} = \left[\rho c(T) + q^2 \frac{d}{dT} a(T)\right] \frac{\partial T}{\partial t^*} + 2a(T) q \frac{\partial q}{\partial t^*} \quad (13)$$

Therefore, the system of equations for the evolution of $T$ and $q$ is (in one-dimensional heat flow with $x^*$ axis chosen for space):

*Cattaneo's Equation:*

$$\tau(T) \frac{\partial q}{\partial t^*} + q + k(T) \frac{\partial T}{\partial x^*} = 0 \quad (14)$$

*First Law:*

$$\frac{\partial q}{\partial x^*} + \left[\rho c(T) + q^2 \frac{d}{dT} a(T)\right] \frac{\partial T}{\partial t^*} + 2a(T) q \frac{\partial q}{\partial t^*} = g \quad (15)$$

Here $k(T)$, $\tau(T)$, and $c(T)$ always have positive values. We call this system of equations the modified hyperbolic type heat conduction equation (MHE). It may be hyperbolic or parabolic depending on the parameter values (Coleman and Owen, 1983).

**Entropy Production Rate.** The entropy production rate $\dot{\sigma}$ in a one-dimensional system is given by

$$\dot{\sigma} = \frac{\partial s}{\partial t^*} + \frac{\partial}{\partial x^*}\left(\frac{q}{T}\right) - \frac{g}{T} \quad (16)$$

By the second law of thermodynamics, this quantity must always be positive and in the reversible limit equals zero. We use Eq. (10) to express $\partial s/\partial t^*$, and then use the classical relationship $\partial s_0/\partial t^* = (\rho c/T)(\partial T/\partial t)$. Then, dividing Eq. (15) by $T$ and subtracting (and making use of Eqs. (8), (11), and (12)) yields

$$\dot{\sigma} = -\frac{q}{T^2}\left(\frac{\tau}{k}\frac{\partial q}{\partial t^*} + \frac{\partial T}{\partial x^*}\right) \quad (17)$$

This reveals that if Cattaneo's Eq. (14) holds, then

$$\dot{\sigma} = \frac{q^2}{kT^2} \quad (18)$$

This is not only nonnegative but also positive if $q$ is not zero, therefore satisfying the second law of thermodynamics. It is interesting to note that if $q$ is varying with time, it is possible to have heat flowing from cold to hot without violating the second law. That is, Cattaneo's Eq. (14) allows $\partial T/\partial x^*$ and $q$ to have the same sign, provided that $\partial q/\partial t^*$ is sufficiently large (in absolute value), but the entropy production rate is positive nonetheless, as given by Eq. (18).

The formulation of Jou et al. (1988) also yields the same nonnegative entropy production rate as in Eq. (18), but it violates the additional requirements derived by Coleman et al. (1982, 1986), Eqs. (6) and (7). For the parabolic heat conduction Eq. (1) and (3), the entropy production rate is also the same. In fact, the parabolic heat conduction equation is just a special case of the MHE, with $\tau = 0$, and so Eqs. (6) and (7) are satisfied.

## Problem Statement

A model problem has been defined to compare the behavior of the CHE and MHE solutions. It is one-dimensional heat conduction in a layer subjected to a step change of temperature on both sides. Initially the layer is at temperature $T_0$, and for $t^* > 0$, the temperature of both boundary surfaces ($x^* = 0$, $l$) is dropped to $T_w (T_w < T_0)$. It should be noted that, since the MHE is nonlinear in temperature, dropping the surface temperature is fundamentally different from raising it. There is no heat source for this model problem and constant properties have been assumed. The analytical solution of the CHE for the case of raising the surface temperatures has been obtained by Taitel (1972). (Since the CHE is linear, this is essentially the same as dropping the surface temperatures.) The choice of dropping the surface temperatures rather than raising them was made here to illustrate that the CHE can predict temperatures below absolute zero.

The thermal behavior of the model problem will be investigated for parabolic, conventional hyperbolic, and modified hyperbolic type heat conduction equations.

The governing equations in nondimensional form are then (see Nomenclature for variable definitions)

*PE:*

$$2\frac{\partial \theta}{\partial t} = \frac{\partial^2 \theta}{\partial x^2} \quad (19)$$

*CHE (nondimensional form of Eq. (5)):*

$$\frac{\partial^2 \theta}{\partial t^2} + 2\frac{\partial \theta}{\partial t} = \frac{\partial^2 \theta}{\partial x^2} \quad (20)$$

*MHE (nondimensional form of Eqs. (14) and (15)):*

$$\frac{\partial Q}{\partial t} + \frac{\partial \theta}{\partial x} = -2Q \quad (21)$$

$$\frac{\partial}{\partial t}\left[\theta + \frac{Q^2}{\theta}\right] + \frac{\partial Q}{\partial x} = 0 \quad (22)$$

or in vector form as

$$\frac{\partial \mathbf{u}}{\partial t} + \frac{\partial \mathbf{f}}{\partial x} = \mathbf{s} \quad (23)$$

where

$$\mathbf{u} = \begin{bmatrix} Q \\ \theta + Q^2/\theta \end{bmatrix}, \quad \mathbf{f} = \begin{bmatrix} \theta \\ Q \end{bmatrix}, \quad \mathbf{s} = \begin{bmatrix} -2Q \\ 0 \end{bmatrix} \quad (24)$$

The initial and boundary conditions for the problem in which the surface temperatures are lowered are as follows:

*Initial Conditions:*

$$\theta(x, 0) = 1, \quad \frac{\partial \theta}{\partial t}(x, 0) = 0 \quad (25)$$

*Boundary Conditions:*

$$\theta(0, t) = \theta(L, t) = 1 + A \quad \text{for} \quad t > 0 \quad (26)$$

where $A = (T_w - T_0)/T_0$ and $L = Cl/2\alpha$. The second initial condition is not needed for the PE, and for the MHE it is replaced by $Q(x, 0) = 0$.

## Solutions

**Analytical Solutions.** The analytical solutions for the PE and CHE are

*PE:*

$$\theta(x, t) = 1 + A\left[1 + \sum_{m=1}^{\infty} \frac{2}{m\pi}[(-1)^m - 1] \sin \lambda_m x \, e^{(-\lambda_m^2/2)t}\right] \quad (27)$$

where $\lambda_m = m\pi/L$.



Downloaded 12 Dec 2010 to 193.140.21.150. Redistribution subject to ASME license or copyright; see http://www.asme.org/terms/Terms_Use.cfm

*CHE:*

$$\theta(x,t) = 1 + A\sum_{m=1}^{\infty}\{F[L(2m-2)+x,t] + F[L(2m-1)-x,t] - F[L(2m-1)+x,t] - F[L(2m)-x,t]\} \quad (28)$$

Here

$$F(x,t) = H(t-x)\left[e^{-x} + x\int_x^t e^{-\xi}\frac{I_1(\sqrt{\xi^2-x^2})}{\sqrt{\xi^2-x^2}}d\xi\right] \quad (29)$$

where $I_1$ is the first-order modified Bessel function and $H(t)$ is the Heaviside unit step function.

**Numerical Solution of MHE.** Since the analytical solution for the MHE is not available, the solution will be obtained by numerical calculation. Both types of hyperbolic heat conduction equation display the sharp discontinuity of a moving thermal front, and it is difficult to capture this discontinuity with conventional finite difference schemes. The solutions from these schemes show spurious oscillations near the discontinuity. For our solution method, the relatively well developed TVD (total variation diminishing) scheme from the field of computational compressible flow is used. This numerical method is based on the integral form of the system of conservation laws and can permit weak (piecewise continuous) solutions. We follow the Roe scheme (Roe, 1981) with modifications described later, and use Roe's superbee flux limiter (Roe, 1985) for second-order spatial accuracy.

Beginning with Eq. (23) and integrating with respect to $x$ and $t$ over space and time steps $\Delta x$ and $\Delta t$, we obtain

$$(\bar{\mathbf{u}}_i^{n+1} - \bar{\mathbf{u}}_i^{n})\Delta x + (\hat{\mathbf{f}}_{i+1/2}^{n} - \hat{\mathbf{f}}_{i-1/2}^{n})\Delta t = \mathbf{s}_i\Delta x\Delta t \quad (30)$$

where $t^n$, $t^{n+1}$ and $x_{i+1/2}$, $x_{i-1/2}$ define the limits of integration,

$$\bar{\mathbf{u}}_i = \frac{1}{\Delta x}\int_{x_{i-1/2}}^{x_{i+1/2}}\mathbf{u}\,dx \quad (31)$$

is the cell average of the dependent variables, and

$$\hat{\mathbf{f}}_{i\pm1/2} = \frac{1}{\Delta t}\int_{t^n}^{t^{n+1}}\mathbf{f}_{i\pm1/2}dt \quad (32)$$

is the flux at the cell boundaries over an interval of time. Equation (30) can be written in the fully discrete form for the system of conservative equations as

$$\frac{\bar{\mathbf{u}}_i^{n+1} - \bar{\mathbf{u}}_i^{n}}{\Delta t} + \frac{\hat{\mathbf{f}}_{i+1/2}^{n} - \hat{\mathbf{f}}_{i-1/2}^{n}}{\Delta x} = \mathbf{s}_i \quad (33)$$

It should be noted that Eq. (33) is the integral form and does not require the existence of derivatives. It only requires the weaker conditions and therefore the solutions of Eq. (33) can include piecewise continuous solutions.

In Eq. (33), we can obtain the solution to the next time level if we know the numerical flux at the cell interface. Assuming piecewise polynomial behavior of the dependent variables within each cell, this results in local Riemann problems at each cell interface. By using an appropriate Riemann solver, we can obtain the flux $\hat{\mathbf{f}}$ at the cell interfaces. We use the Roe scheme (Roe, 1981) for the Riemann solver. In the Roe scheme, the numerical flux is obtained from exact solution to an approximate Riemann problem. In Roe's approach, specially averaged cell interface values are used. In Eq. (33), the numerical flux for the Roe scheme can be obtained from the locally linearized form of Eq. (23) via the parameter vector $\mathbf{w}$,

$$[\tilde{B}]\frac{\partial\mathbf{w}}{\partial t} + [\tilde{C}]\frac{\partial\mathbf{w}}{\partial x} = 0 \quad (34)$$

Here the parameter vector $\mathbf{w}$ is

$$\mathbf{w} = \begin{bmatrix} w_1 \\ w_2 \end{bmatrix} = \begin{bmatrix} \theta \\ Q \end{bmatrix} \quad (35)$$

The Roe scheme gives the algorithm for linearizing Eq. (23). That is, it gives the expressions for $[\tilde{B}]$ and $[\tilde{C}]$ in Eq. (34),

$$[\tilde{B}] = \int_0^1 [B(p)]dp \quad (36)$$

$$[\tilde{C}] = \int_0^1 [C(p)]dp \quad (37)$$

where $[B]$ and $[C]$ are

$$[B] = \frac{\partial\mathbf{u}}{\partial\mathbf{w}} = \begin{bmatrix} 0 & 1 \\ 1 - \dfrac{w_2^2}{w_1^2} & \dfrac{2w_2}{w_1} \end{bmatrix} \quad (38)$$

$$[C] = \frac{\partial\mathbf{f}}{\partial\mathbf{w}} = \begin{bmatrix} 1 & 0 \\ 0 & 1 \end{bmatrix} \quad (39)$$

Here

$$\mathbf{w}(p) = \mathbf{w}_L + p(\mathbf{w}_R - \mathbf{w}_L) \quad (40)$$

where $p$ is a parameter varying between 0 and 1 (Roe, 1981). Equation (34) can be solved for $\mathbf{w}$, and in this case $\mathbf{f} = \mathbf{w}$.

Since it is expensive to get the specially averaged values of $[\tilde{B}]$ for the MHE, we have developed an iterative modification of the Roe scheme as follows. In Eq. (23), we move the nonlinear term $\partial/\partial t(Q^2/\theta)$ to the right-hand side and redefine the vectors $\mathbf{u}$ and $\mathbf{s}$

$$\frac{\partial\mathbf{u}}{\partial t} + \frac{\partial\mathbf{f}}{\partial x} = \mathbf{s} \quad (41)$$

where

$$\mathbf{u} = \begin{bmatrix} Q \\ \theta \end{bmatrix}, \quad \mathbf{f} = \begin{bmatrix} \theta \\ Q \end{bmatrix}, \quad \mathbf{s} = \begin{bmatrix} -2Q \\ -\dfrac{\partial}{\partial t}\left(\dfrac{Q^2}{\theta}\right) \end{bmatrix} \quad (42)$$

Integrating Eq. (41) with respect to $x$ and $t$, and using the definition of $\bar{\mathbf{u}}_i$ and $\hat{\mathbf{f}}_{i\pm1/2}$ in Eqs. (31) and (32), we can get the fully discrete form for the system of conservative Eqs. (33) with a different numerical source term

$$\mathbf{s}_i = \begin{bmatrix} -2Q_i^n \\ -((Q^2/\theta)^* - (Q^2/\theta)^n)/\Delta t \end{bmatrix} \quad (43)$$

where the superscript * means the iterative stage for the next time level. For the convergence check in the calculations, the maximum change from * values to newly calculated values is required to be less than a convergence criterion number $\epsilon$, which depends on the problem. Since the scheme used is second order in space (strictly speaking, second order in the smooth region and first order near a discontinuity), $\epsilon$ is at least less than $(\Delta x)^2$. In the numerical calculations, $\epsilon$ is taken to be $10^{-5}$ or less.

A second-order accuracy scheme is obtained by defining a second-order accurate numerical flux. Roe's superbee flux limiter (Roe, 1985) is used. The flux difference is compared with the corresponding values in a neighboring interval and limited by the superbee flux limiter.

In the numerical calculation, two boundary conditions (one each for $\theta$ and $Q$) are required at each boundary. However for the model problem, only $\theta$ is specified at each boundary. To determine $Q$ at the boundaries, we use the locally linearized MHE with Roe's averaging. Since the equation is linearized, we can



Downloaded 12 Dec 2010 to 193.140.21.150. Redistribution subject to ASME license or copyright; see http://www.asme.org/terms/Terms_Use.cfm

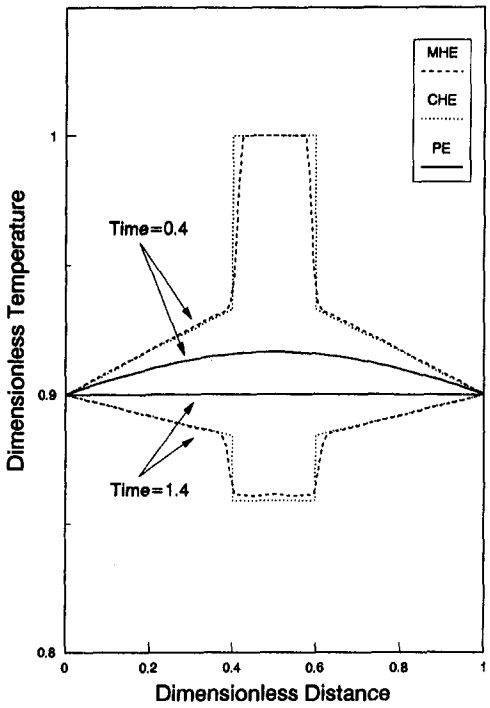



**Fig. 1 Temperature distribution for $A = -0.1$, $L = 1.0$**

get the decoupled characteristic forms of Eqs. (21) and (22) by defining the characteristic variables. This locally linearized equation has two characteristic variables, one propagating in the positive $x$ direction ($v^+$) and the other propagating in the negative $x$ direction ($v^-$). A new vector v of characteristic variables is

$$\mathbf{v} = \begin{bmatrix} v^- \\ v^+ \end{bmatrix} = \frac{1}{\sqrt{\gamma^2 + 4(1-\beta)}} \begin{bmatrix} \dfrac{\gamma + \sqrt{\gamma^2 + 4(1-\beta)}}{2}\theta - Q \\ \dfrac{-\gamma + \sqrt{\gamma^2 + 4(1-\beta)}}{2}\theta + Q \end{bmatrix} \tag{44}$$

where $\beta$ and $\gamma$ are defined by their relationship to the components of the matrix $[\tilde{B}]$ (Eq. (36))

$$[\tilde{B}] = \begin{bmatrix} 0 & 1 \\ 1-\beta & \gamma \end{bmatrix} \tag{45}$$

At the left boundary, the $v^-$ equation is integrated by the upwind difference scheme, and then heat flux $Q$ can be found from Eq. (44). The same procedure is performed for $v^+$ at the right boundary.

This iterative numerical scheme has been tested in a variety of ways. First, it has been seen to agree with the parabolic solution in the steady-state limit (as will later be shown in Figs. 4 and 5). Second, the solution has been tested in the small $|A|$ limit. When $|A|$ is small, the nonequilibrium term in the internal energy ($Q^2/\theta$) is negligible, because the nondimensional temperature is order of 1 and the nondimensional heat flux is order of $|A|$ (see also Results and Discussion section). Therefore the solution of the MHE should approach that of the CHE. For the case of small $|A|$, the numerical solution of the MHE has been compared to the exact solution of the CHE (Eq. (28)) and the solutions agree to within the error of $\epsilon$. Thus our numerical solution of the MHE is seen to be correct in the limit of small $|A|$. For the case of large $|A|$, the numerical method has been tested and validated by doing convergence tests for different grid sizes. When $A$ is $-0.5$, for instance, the grid points for nondimensional length $L$ of 1.0 are taken from 10 to 1000. With the convergence criterion $\epsilon$ of $10^{-6}$, the numerical results of the different grid sizes are compared at several grid points for various time steps. The results show that the solutions converge to that of the finest grid size. The solutions for 100 and 1000 grid points agree to three significant digits. The effect of the convergence criterion, $\epsilon$, was also tested. For 100 grid points, the solutions with the convergence criterion $\epsilon$ of $10^{-5}$ and $10^{-6}$ agree to four significant digits.

For the numerical scheme for linear hyperbolic equations, the Courant number $\nu = \Delta t/\Delta x$ has to be less than 1.0 for stability and to preserve monotonicity. With the nonlinearity in the equation, this stability bound is reduced. As $|A|$ increases, the nonlinearity in the MHE becomes strong. Since results with a large Courant number revealed spurious oscillations, $\nu$ of 0.2, 0.1, and 0.1 is used in the calculation of the MHE for $A = -0.1$, $-0.5$, and $-0.8$.

## Results and Discussion

Before presenting the results, the parameter $A$ will be discussed. For the case of dropping the surface temperature, as is considered in this paper, $A$ is negative (recall $A = (T_w - T_0)/T_0$). A small drop in surface temperature ($T_w$ near $T_0$) corresponds to a small value of $|A|$. In this case, it will be shown that the nonlinear term in the MHE is unimportant. A large drop in surface temperature ($T_w$ approaching absolute zero) corresponds to a value of $A$ near $-1$. In this case, the nonlinear term will be shown to be important. It should also be noted that since the PE and CHE are linear, a change in $A$ does not change the shape of the solution (see Eqs. (27) and (28)).

The results for the model problem of lowering the surface temperatures are given in Figs. 1, 2, and 3. The results for the PE (solid line), CHE (dotted line) and MHE (dashed line) are shown together in the figures for nondimensional times of 0.4 and 1.4. The nondimensional length $L$ is taken to be 1. This value was chosen because the solutions clearly illustrate the differences

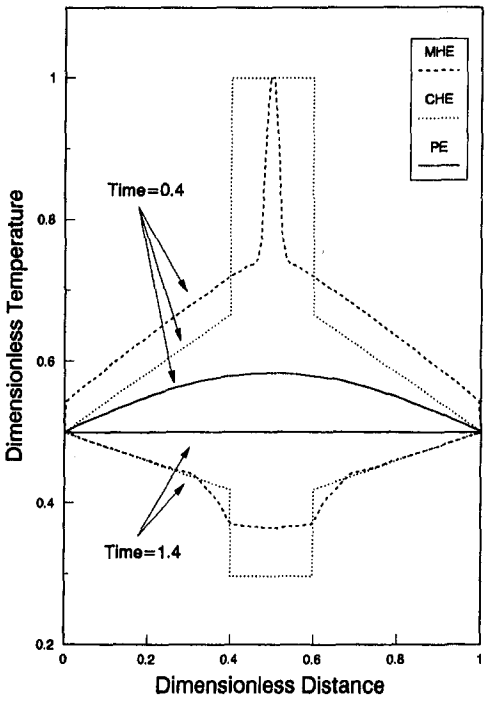



**Fig. 2 Temperature distribution for $A = -0.5$, $L = 1.0$**



Downloaded 12 Dec 2010 to 193.140.21.150. Redistribution subject to ASME license or copyright; see http://www.asme.org/terms/Terms_Use.cfm

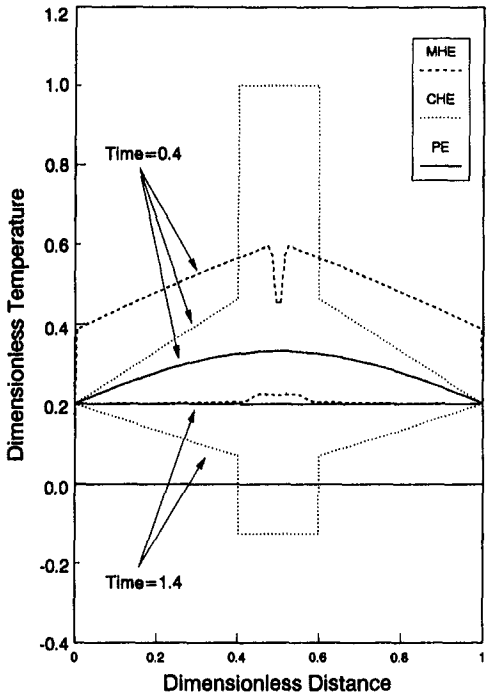



**Fig. 3 Temperature distribution for $A = -0.8$, $L = 1.0$**

between the three equations. A larger value of $L$ will be considered later.

Figure 1 is the nondimensional temperature distribution for $A = -0.1$. The results show that there is not much difference between the CHE and MHE solutions but the PE solution is significantly different. In this problem, the calculated nondimensional heat flux is on the order of $A$ and the temperature is around 1. In Eq. (22), we can consider $\theta$ as the nondimensional equilibrium internal energy and $Q^2/\theta$ as the nonequilibrium term for internal energy. The nonequilibrium term $Q^2/\theta$ is not important compared to the equilibrium internal energy $\theta$ for such values of temperature and heat flux, which explains the close agreement between the CHE and MHE solutions. Both of these solutions show wave-type characteristics and sharp discontinuities in the temperature distribution. There also is an undisturbed region beyond the thermal front for time less than 0.5. After the wave fronts meet from the left and right, a superposition occurs and results in a lower temperature in the middle region than the surface temperature (see curve for $t = 1.4$). This counterintuitive temperature undershoot behavior does not violate the second law of thermodynamics, since the entropy production rate remains positive as shown by Eq. (18), and Eqs. (6) and (7) are satisfied by the MHE. This does not, however, mean that this behavior is physically real, as will be discussed later. For time 1.4, the parabolic solution is already in the steady state and shows a uniform temperature distribution.

Figure 2 shows the temperature distribution for $A = -0.5$. Although the temperature distributions for the MHE and CHE show wave-type behavior as for the case of $A = -0.1$, they are significantly different from each other when $A = -0.5$. Here the magnitudes of nondimensional temperature and heat flux are not much different, so the nonequilibrium term in the internal energy is as important as the equilibrium internal energy. From the results of the MHE, we can see the thermal front propagating faster than for the CHE. Also, the MHE results show dissipation effects like the parabolic equation (that is, smooth thermal front instead of sharp discontinuity as in the CHE). Coleman et al. (1982, 1986) derived the temperature rate wave velocity for the MHE. When the time derivative of the temperature experiences a jump across a curve, this curve is called a temperature rate wave. The speed $V$ of the temperature rate wave for the MHE in the dimensional form is

$$V = V(T, q) = C[\sqrt{1 + \varphi^2} - \varphi] \tag{46}$$

with

$$\varphi = \frac{1}{C}\cdot\frac{q}{T}\cdot\frac{1}{\rho c - \dfrac{\tau}{k}\dfrac{q^2}{T^2}} \tag{47}$$

where $C$ is the speed of the temperature rate wave for $q = 0$ ($C = \sqrt{\alpha/\tau}$). By Eqs. (46) and (47)

$$\text{when} \quad q > 0, \quad V(T, q) < V(T, -q) \tag{48}$$

Equation (46) is the speed of the temperature rate wave propagating in the direction of increasing $x$, faster than $C$. Equation (48) says that if heat flux $q$ is negative, the temperature rate wave travels faster than it would for positive $q$. When we lower the surface temperature, the heat flux is negative in the region between 0 and 0.5 before the thermal fronts meet at the middle. Therefore, the thermal front is moving faster than that of the CHE. Similarly, it can be shown that in the region between 0.5 and 1, the thermal front moves faster in the negative $x$ direction. For the dimensionless time of 0.4, the undisturbed region for the CHE is between 0.4 and 0.6 (the nondimensional speed of the thermal front is 1). However, at this same time the thermal fronts of the MHE have almost arrived at the middle of the layer. For the time of 1.4, we can see a large difference in the temperature profile between the CHE and MHE. Since the CHE is linear (for constant properties), the shape of the temperature profile is always the same regardless of the value of $A$. The temperature from the MHE at the time of 1.4 is not as low as that from the CHE. This is a very important feature for the MHE. We can see the importance of this trend in Fig. 3.

Figure 3 shows the temperature distribution for the case of $A = -0.8$. For the MHE, the speed of the temperature rate wave is faster than for $A = -0.5$ and the thermal fronts have already met in the middle at the time of 0.4. At the time of 1.4, the temperature for the MHE is almost at steady state (see also Fig. 4), where the parabolic temperature is already at steady state. The CHE

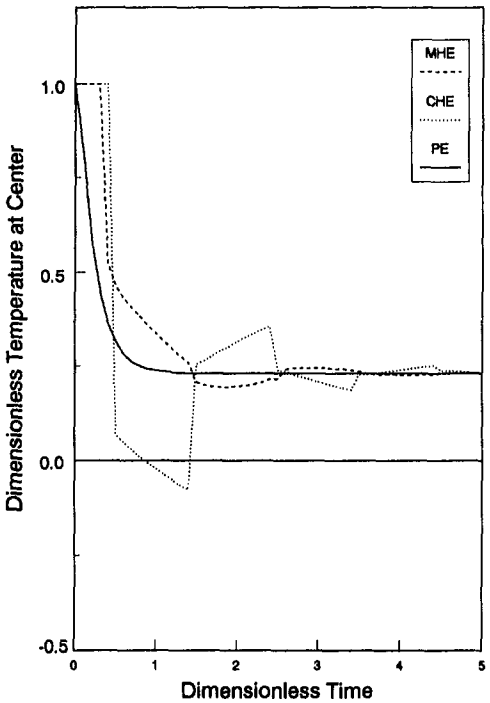



**Fig. 4 Temperature at the center of layer for $A = -0.8$, $L = 1.0$**



Downloaded 12 Dec 2010 to 193.140.21.150. Redistribution subject to ASME license or copyright; see http://www.asme.org/terms/Terms_Use.cfm

gives temperatures below absolute zero at time of 1.4, which is clearly physically impossible. The MHE remedies this unphysical result.

Figures 4 and 5 show the temperature at the center of the layer as time elapses for different values of $L = 1.0$ and 5.0 with $A = -0.8$. When $L = 1.0$, the temperatures from the MHE and the CHE are significantly different as discussed before and the MHE remedies the physically wrong situation which occurs for the CHE (temperature less than absolute zero). The MHE temperature reaches steady state somewhat faster than the CHE temperature.

Figure 5 shows the temperatures for $L = 5.0$. In this case, the results of the three equations are not very different except for the early time transient even though $A$ is near $-1$. Although both hyperbolic temperatures exhibit wave type behavior, the effect of reflection is not significant for large $L$ because by the time the wave fronts superpose, diffusive effects have become dominant. Therefore, all the analyses predict a monotonically decreasing temperature.

From the results of the calculations we can conclude the following: For large $L$, all three solutions agree regardless of the value of $A$ (except that for very small times the parabolic solution is in error). For $L$ near one, reflections of thermal waves from the boundaries are important. Therefore the parabolic solution is in error for all values of $A$ (except in the steady state limit). The agreement between the two hyperbolic solutions depends on the value of $A$. For small $|A|$, they agree, but as $A$ approaches $-1$, the nonequilibrium term becomes important and the two solutions disagree. The CHE displays temperatures below absolute zero, whereas the MHE does not.

Since the CHE disagrees significantly with the MHE only for $L$ of order one (or less), it is important to examine the meaning of this parameter. Since the mean free path for phonons (from a kinetic model) is $l_{mfp} = 3\alpha/C$, the parameter $L$ can be rewritten as $L = 1.5l/l_{mfp}$. Thus, the CHE is only in error when the domain thickness is on the order of the carrier mean free path or less. In this case, the continuum hypothesis upon which Cattaneo's equation depends is probably not valid. Thus, provided that the continuum hypothesis *is* clearly valid ($L$ greater than order one), the CHE agrees well with the MHE and can be used, even though in theory it violates the second law. It should also be noted that the temperature undershoot behavior observed for both the CHE and the MHE occurs only for $L$ of order one or less, and we therefore cannot say from a continuum model whether or not it is physically real.

## Conclusion

To consider the effect of the finite thermal propagation speed, Cattaneo's equation (generalized Fourier's Law) has been used. This results in the conventional hyperbolic heat conduction equation. However, the CHE may give physically wrong solutions under certain conditions. The modified, nonlinear hyperbolic type heat conduction equation, which is consistent with the second law of thermodynamics, remedies this. By investigating a model problem, we show under what conditions the solutions agree or disagree. When the heat flux is the same order as the temperature (in the nondimensional form), the nonequilibrium term in the internal energy is important and the solutions of the MHE and CHE are different. In dimensional form, the nonequilibrium term is important if $q$ is not small compared to the quantity $\rho cTC$, which can be thought of as the rate at which energy is carried at the thermal propagation speed.

The MHE and CHE temperatures show wave type behavior, and after the thermal fronts meet the temperature becomes lower than the surface temperature. When $A$ is near $-1$ (i.e., the surface temperature drops nearly to absolute zero), the CHE gives temperatures below absolute zero, which is physically impossible. Although the MHE also shows wave type behavior for $A$ near $-1$, it remedies the error in the CHE. The differences in the temperatures of the three equations become negligible as $L$ increases.

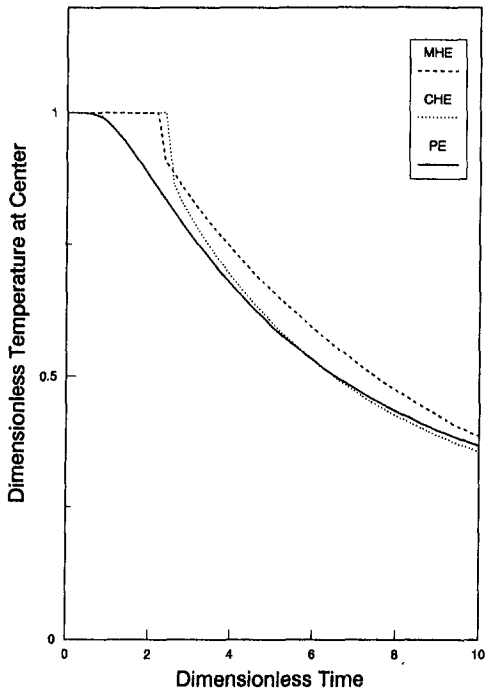



**Fig. 5 Temperature at the center of layer for $A = -0.8$, $L = 5.0$**

The nondimensional thickness $L$ is a measure of the domain length relative to the carrier mean free path. For $L$ near one or less, the macroscopic equations (PE, CHE, and MHE) may not be valid due to the breakdown of the continuum hypothesis. For moderate (and large) values of $L$, it may be feasible to analyze the interior region using these macroscopic equations (PE, CHE, or MHE) with matching boundary conditions to perform a transition from the kinetic boundary condition at the wall to the macroscopic description of the interior region. Some preliminary work (Bai and Lavine, 1993) shows that the boundary condition treatment has a significant effect on the behavior of thermal waves. In fact, when boundary conditions are used such that the surface temperature varies gradually rather than instantaneously, the temperature undershoot behavior observed here disappears and solutions of the CHE and the MHE become more similar. This further supports the idea that the CHE is a useful model of heat transfer.

To conclude, we can say that the CHE is a simplified form of the MHE, in which the nonequilibrium internal energy term has been neglected. In the present model problem, the CHE is inaccurate for $A$ near $-1$ and small $L$. Physically, this corresponds to surface temperatures near absolute zero and domain thickness on the order of a carrier mean free path. In this situation, the nonequilibrium internal energy is not negligible and the conventional hyperbolic heat conduction equation is inaccurate. As a practical matter, however, the results of the model problem suggest that the CHE agrees well with the MHE as long as the continuum hypothesis is valid; the CHE can therefore be used even though in theory it violates the second law of thermodynamics. The present authors suspect that there are few realistic situations in which it would be necessary to solve the MHE rather than the CHE. However, this has not been absolutely proved here, since only one model problem was considered, physical properties were held constant, etc.

## Acknowledgments

The authors would like to thank the National Science Foundation and Tektronix, Inc., for their support.



Downloaded 12 Dec 2010 to 193.140.21.150. Redistribution subject to ASME license or copyright; see http://www.asme.org/terms/Terms_Use.cfm

## References


Bai, C., and Lavine, A. S., 1993, "Thermal Boundary Conditions for Hyperbolic Heat Conduction," *Heat Transfer on the Microscale—1993*, ASME HTD-Vol. 253, pp. 37–44.

Cattaneo, C., 1948, "Sulla Conduzione de Calore," *Atti del Semin. Mat. e Fis. Univ. Modena*, No. 3, pp. 83–101.

Coleman, B. D., Fabrizio, M., and Owen, D. R., 1982, "On the Thermodynamics of Second Sound in Dielectric Crystals," *Arch. Rat. Mech. Anal.*, Vol. 80, No. 2, pp. 135–158.

Coleman, B. D., and Owen, D. R., 1983, "On the Nonequilibrium Behavior of Solids That Transport Heat by Second Sound," *Comp. and Math. With Appls.*, Vol. 9, No. 3, pp. 527–546.

Coleman, B. D., Fabrizio, M., and Owen, D. R., 1986, "Thermodynamics and the Constitutive Relations for Second Sound in Crystals," in: *New Perspectives in Thermodynamics*, J. Serrin, ed., pp. 171–185.

Joseph, D. D., and Preziosi, L., 1989, "Heat Waves," *Rev. Modern Phys.*, Vol. 61, pp. 41–73.

Joseph, D. D., and Preziosi, L., 1990, "Addendum to the Paper 'Heat Waves'," *Rev. Modern Phys.*, Vol. 62, pp. 375–391.

Jou, D., Casas-Vazquez, J., and Lebon, G., 1988, "Extended Irreversible Thermodynamics," *Reports on Progress in Physics*, Vol. 51, pp. 1105–1179.

Kaliski, S., 1965, "Wave Equation for Heat Conduction," *Bull. Acad. Pol. Sci. VIII*, No. 4, pp. 211–219.

Roe, P. L., 1981, "Approximate Riemann Solvers, Parameter Vectors, and Difference Schemes," *J. Comp. Phys.*, Vol. 43, pp. 357–372.

Roe, P. L., 1985, "Some Contributions to the Modeling of Discontinuous Flows," *Lectures in Applied Mathematics*, Vol. 22, pp. 163–193.

Taitel, Y., 1972, "On the Parabolic, Hyperbolic and Discrete Formulation of the Heat Conduction Equation," *Int. J. Heat Mass Transfer*, Vol. 15, pp. 369–371.





Downloaded 12 Dec 2010 to 193.140.21.150. Redistribution subject to ASME license or copyright; see http://www.asme.org/terms/Terms_Use.cfm

**C. T. Hsu**
Department of Mechanical Engineering,
The Hong Kong University of
Science & Technology,
Clear Water Bay, Kowloon, Hong Kong

**P. Cheng**
Department of Mechanical Engineering,
University of Hawaii,
Honolulu, HI 96822
Fellow ASME

**K. W. Wong**
Department of Mechanical Engineering,
The Hong Kong University of
Science & Technology,
Clear Water Bay, Kowloon, Hong Kong

# A Lumped-Parameter Model for Stagnant Thermal Conductivity of Spatially Periodic Porous Media

*Based on a lumped-parameter method, algebraic expressions for the stagnant thermal conductivity of some two-dimensional and three-dimensional spatially periodic media are obtained. The geometries under consideration include arrays of touching and nontouching in-line square and circular cylinders (two-dimensional), as well as touching and nontouching in-line cubes (three-dimensional). A comparison of results based on these algebraic expressions with existing numerical solutions and experimental data shows that they are in excellent agreement.*

## Introduction

The problem of determining the effective stagnant thermal conductivity of a porous medium has been of great interest to chemical engineers and geophysicists for more than one hundred years [see Kaviany (1991) for a review of literature]. Deisser and Boegli (1958) were among the first to point out that thermal conductivity of a saturated porous medium can be calculated based on a two-layer model analogous to electric resistances in an electric circuit. They show that the value of the stagnant thermal conductivity is maximum if the two layers are in parallel in the direction of the temperature gradient. On the other hand, if the two layers are in series in the direction of the temperature gradient, the effective stagnant thermal conductivity of the medium is minimum.

To derive an expression for the stagnant thermal conductivity of a packed-sphere bed, Kunii and Smith (1960) consider a unit cell model consisting of two contacting spheres. They assume that the temperature gradient is applied along the direction connecting the centers of the spheres. While heat conduction near the outer region of the unit cell is mostly through the void space occupying by the fluid phase, heat in the central region near the contact point has to pass from the solid phase through the fluid phase before re-entering to the solid phase. Kunii and Smith (1960) assume that the thermal resistances of these two heat transfer mechanisms can be represented by a fluid layer in parallel with a composite layer consisting of both fluid and solid phases. The equivalent thermal resistance of the composite layer is obtained by assuming the thermal resistance of the fluid phase is in series with the solid phase.

An analytical expression for the effective stagnant thermal conductivity of a packed bed was obtained by Zehner and Schlunder (1970) who chose a cylindrical unit cell that contains a spherical particle. They considered heat transfer by conduction through two parallel paths: conduction through the gas-filled voids in the outer cylinder and conduction through the solid and gas phases in the inner cylinder. Based on a semi-analytical approach, they obtained the following expression for the effective stagnant thermal conductivity of a packed bed:

$$\frac{k_e}{k_f} = [1 - \sqrt{1-\phi}] + \frac{2\sqrt{1-\phi}}{1-\lambda B} \times \left[\frac{(1-\lambda)B}{(1-\lambda B)^2}\ln\frac{1}{\lambda B} - \frac{B+1}{2} - \frac{B-1}{1-\lambda B}\right] \quad (1a)$$

where the shape factor $B$ is approximated by

$$B = 1.25\left(\frac{1-\phi}{\phi}\right)^{10/9} \quad (1b)$$

It is pertinent to note that the first term on the right-hand side of Eq. (1$a$) represents heat conduction through the outer cylinder consisting of the fluid phase while the second term represents heat conduction through the inner composite cylinder consisting of both solid and fluid phases. Comparing Eq. (1) with experimental results of Nozad et al. (1985) for a packed-sphere bed, Kaviany (1991) concluded that Eq. (1) is accurate for moderate values of the solid/fluid thermal conductivity ratio, but it underpredicts the stagnant thermal conductivity when the thermal conductivity ratio is high.

Based on closure schemes of the macroscopic heat conduction equations in the solid and the fluid phases and assuming local thermal equilibrium, Nozad et al. (1985) obtained numerical solutions for the stagnant thermal conductivities of arrays of touching and nontouching square cylinders. They found that the numerical instabilities occurred at high thermal conductivity ratios (with $k_s/k_f > 100$), and a perturbation method was used to overcome these difficulties. Their numerical results for the touching square cylinders with the touching parameter $c/a = 0.02$ are shown in excellent agreement with their experimental data. Subsequently, Shonnard and Whitaker (1989) pointed out that there is an error in the computations of Nozad et al. and that their numerical solutions with $c/a = 0.01$ would be more appropriate to represent the experimental data. Using the same approach, Sabraoui and Kaviany (1993) obtained a numerical solution for the stagnant thermal conductivities of arrays of in-line and staggered nontouching circular cylinders in addition to those of in-line square cylinders. They pointed out that their numerical results with $c/a = 0.01$ are much higher than the experimental data of Nozad et al. and found that their numerical results with $c/a = 0.002$ agree the best with experimental data. In a recent paper, Saez et al. (1991) obtained a numerical solution for the stagnant thermal conductivity of nontouching cubes. At a given porosity and thermal conductivity ratio, they found that their model gives a slightly higher value than those based on a two-dimensional model.

Contributed by the Heat Transfer Division for publication in the JOURNAL OF HEAT TRANSFER. Manuscript received by the Heat Transfer Division July 1993; revision received April 1994. Keywords: Packed and Fluidized Beds. Associate Technical Editor: L. S. Fletcher.



Copyright © 1995 by ASME

Downloaded 12 Dec 2010 to 193.140.21.150. Redistribution subject to ASME license or copyright; see http://www.asme.org/terms/Terms_Use.cfm

In this paper we shall show that a judicious application of the electric resistance analogy (henceforth called a lumped parameter model) will lead to algebraic expressions for the stagnant thermal conductivity of a number of two-dimensional and three-dimensional spatially periodic porous media. The essence of the method is to assume one-dimensional heat conduction in a unit cell. The cell is then divided into parallel layers (which may consist of fluid, solid, or composite layers) in the direction of the macroscopic temperature gradient. The stagnant thermal conductivity of the composite layer is then obtained based on a series model. The two-dimensional geometries under consideration in this paper include touching and nontouching in-line square and circular cylinders. Results based on the algebraic expressions obtained in the present paper for these two-dimensional porous media are found in excellent agreement with numerical solutions obtained previously by Nozad et al. (1985) as well as by Sabraoui and Kaviany (1993). In addition, we shall obtain algebraic expressions for the stagnant thermal conductivity of arrays of touching and nontouching cubes (a three-dimensional periodic medium), the former of which has never been considered. It is found that results based on the touching cubes model (three-dimensional) agree the best with experimental data of a packed-sphere bed obtained by Nozad et al. (1985) and Prasad et al. (1989).

## Square Cylinders

Consider first the stagnant thermal conductivities of two-dimensional arrays of square cylinders (having a square cross section of $a \times a$) with connecting plates (having a width of $c$) as shown in Fig. 1($a$). The stagnant thermal conductivity of this periodic medium was considered previously by Nozad et al. (1985) who modeled the finite contact between spheres by connecting plates with $c/a$ denoting the contact parameter. It is pertinent to note that flattening of spheres in the vicinity of contact points may occur due to some external mechanical loads or to the weight of the bed itself. Under this situation, the value of $c/a$ can be estimated from the well-known Hertz relation for elastic contacts between spheres as discussed by Chan and Tien (1973) and Ogniewicz and Yovanovich (1978).

Because of the symmetry of thermal paths, we choose a unit cell as shown in Fig. 1($b$), which is one quadrant of the unit cell chosen by Nozad et al. (1985). The unit cell shown in Fig. 1($b$) can be considered to be consisting of three layers: a rectangular solid layer and two rectangular composite layers consisting of both solid and fluid phases. The dimensions of these layers are $(c/2 \times l/2)$ for the solid layer, and $l/2$ by $(a - c)/2$ and $l/2$ by $(l - a)/2$ for the composite layers. From Fig. 1($b$), it is apparent that the area solid fraction of the unit cell is

$$1 - \phi = \gamma_a^2 + 2\gamma_c\gamma_a(1 - \gamma_a) \tag{2}$$

where

$$\gamma_a = a/l, \quad \gamma_c = c/a \tag{3}$$

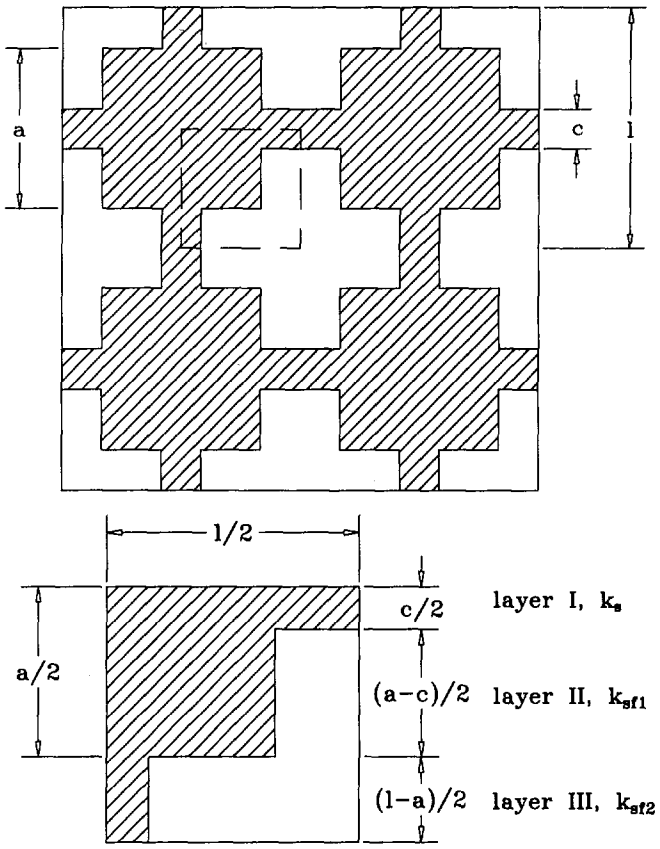



**Fig. 1 (a) An array of touching square cylinders (above) and (b) its unit cell (below)**

The effective thermal conductivity of the three parallel layers is

$$k_e = \gamma_a\gamma_c k_s + \gamma_a(1 - \gamma_k)k_{sf1} + (1 - \gamma_a)k_{sf2} \tag{4}$$

where $k_{sf1}$ and $k_{sf2}$ are the thermal conductivities of the composite layers. The values of $k_{sf1}$ and $k_{sf2}$ can be obtained based on a series-layer model. For example, the value of $k_{sf1}$ is given by

$$\frac{1}{k_{sf1}} = \frac{a/l}{k_s} + \frac{(l - a)/l}{k_f} \tag{5a}$$

which can be rewritten as

$$\frac{k_{sf1}}{k_f} = \frac{1}{1 + (\lambda - 1)\gamma_a} \tag{5b}$$

Similarly, the value of $k_{sf2}$ is

$$\frac{k_{sf2}}{k_f} = \frac{1}{1 + (\lambda - 1)\gamma_a\gamma_c} \tag{6}$$

## Nomenclature

$a$ = length of one side of the solid square cylinder shown in Fig. 1($b$); diameter of the circular cylinder shown in Fig. 5($b$); length of one side of a cube shown in Fig. 8($a$)
$B$ = shape factor of the solid particle defined in Eq. (1$b$)
$c$ = width of a connecting plate shown in Fig. 1($a$), and width of a square connecting column shown in Fig. 8($a$)
$h$ = height of a connecting plate between circular cylinders shown in Fig. 5($b$)
$k_e$ = effective stagnant thermal conductivity of the saturated porous medium
$k_f$ = thermal conductivity of the fluid phase
$k_s$ = thermal conductivity of the solid phase
$k_{sf}$ = equivalent thermal conductivity of a composite layer
$l$ = length of a unit cell shown in Figs. 1($a$) and 8($a$)
$\gamma_a, \gamma_c$ = quantities defined in Eq. (3)
$\theta_c$ = angle defined in Eq. (11) and Fig. 5($b$)
$\lambda$ = fluid/solid thermal conductivity ratio
$\phi$ = porosity



Downloaded 12 Dec 2010 to 193.140.21.150. Redistribution subject to ASME license or copyright; see http://www.asme.org/terms/Terms_Use.cfm

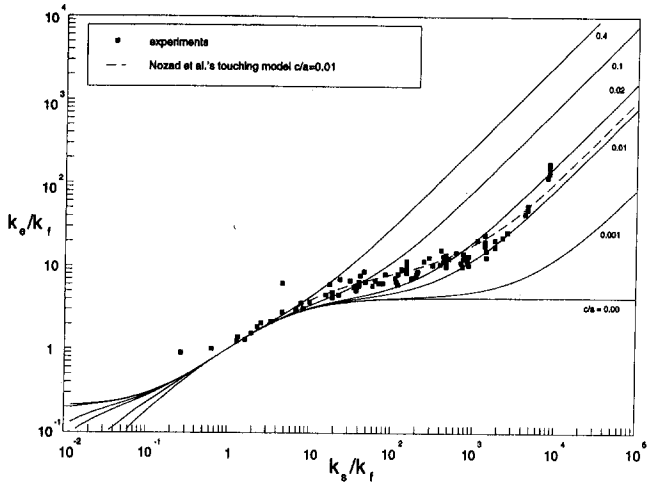



**Fig. 2 Comparison of stagnant thermal conductivity of touching square cylinders based on the lumped-parameter model with experimental data**

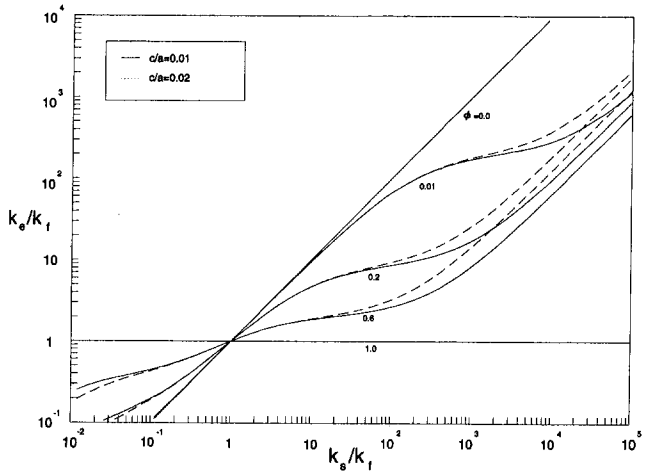



**Fig. 3 Effects of porosity and touching parameter on the stagnant thermal conductivity of square cylinders (two-dimensional model)**

Substituting Eqs. (5*b*) and (6) into Eq. (4) yields

$$\frac{k_e}{k_f} = \frac{\gamma_a\gamma_c}{\lambda} + \frac{\gamma_a(1-\gamma_c)}{1+(\lambda-1)\gamma_a} + \frac{(1-\gamma_a)}{1+(\lambda-1)\gamma_a\gamma_c} \tag{7}$$

where $\gamma_a$ and $\gamma_c$ are related by Eq. (2). Equation (7) is presented in Fig. 2 for $\phi = 0.36$ with different values of the touching parameter $c/a$. The results show that the effect of the touching parameter $c/a$ is important when the solid/fluid thermal conductivity ratio is high. For comparison, the experimental data of Nozad et al. (1985) and Prasad et al. (1989) as well as the numerical results of Nozad et al. (1985) for $c/a = 0.01$ (indicated as dashed lines) are also presented in the same graph. It is shown that results computed from Eq. (7) for $c/a = 0.01$ are in excellent agreement with experimental data. Figure 3 shows the stagnant thermal conductivity of touching square cylinders as a function of porosity for touching parameters of 0.01 (solid lines) and 0.02 (dashed lines). The straight solid lines are for pure solid ($\phi = 0$) and for pure fluid ($\phi = 1$), respectively. All other curves converge asymptotically at large value of $k_s/k_f$. It can be concluded from Fig. 3 that the touching parameter $c/a$ is deterministic when $k_s/k_f$ is high while the porosity $\phi$ becomes deterministic when $k_s/k_f$ is near one.

Since the nontouching square cylinders are a special case of the touching square cylinders, we can obtain the thermal conductivity of the latter case by letting $c = 0$. Consequently, $\gamma_c = 0$ and $\gamma_a = (1-\phi)^{1/2}$. Under this condition Eq. (7) becomes

$$\frac{k_e}{k_f} = (1-\sqrt{1-\phi}) + \frac{\sqrt{1-\phi}}{1+(\lambda-1)\sqrt{1-\phi}} \tag{8}$$

Equation (8) for $\phi = 0.2$, 0.4, and 0.7 is presented in Fig. 4. For comparison, the numerical results of Nozad et al. (1985) for $\phi = 0.19$, 0.36, 0.437 and 0.64 are also presented in the same graph. It is shown that they are in excellent agreement.

## Circular Cylinders

We now consider the stagnant thermal conductivity of arrays of in-line circular cylinders (of diameter $a$) with connecting plates (of thickness $c$ and height $h$) as shown in Fig. 5(*a*). A unit cell of this two-dimensional spatially periodic medium is depicted in Fig. 5(*b*). From a geometric consideration, we note that

$$\frac{h}{l} = 1 - \gamma_a\sqrt{1-\gamma_c^2} \tag{9}$$

where $\gamma_a$ and $\gamma_c$ are also given by Eq. (3). The effective stagnant thermal conductivity of the three parallel layers shown in Fig. 5(*b*) is given by

$$k_e = \frac{c}{l}k_s + \left(1 - \frac{c}{l} - \frac{h}{l}\right)k_{sf1} + \frac{h}{l}k_{sf2} \tag{10}$$

where $k_{sf2}$ is given by Eq. (6) while the value of $k_{sf1}$ is given by

$$\left(1 - \frac{c}{l} - \frac{h}{l}\right)\frac{k_{sf1}}{k_f} = \frac{\frac{\pi}{2} - 2\theta_c}{\lambda - 1} - \frac{1}{(\lambda-1)} \times \int_{\theta_c}^{\pi/2-\theta_c} \frac{d\theta}{(\lambda-1)\gamma_a \sin\theta + 1} \tag{11}$$

where $\theta_c = \sin^{-1}(\gamma_c)$. The last integral in Eq. (11) can be integrated depending on whether $(\lambda-1)\gamma_a$ is less than, equal to, or larger than one.

Substituting Eqs. (6) and (11) into Eq. (10) gives the following expressions of the stagnant thermal conductivity for in-line circular cylinders:

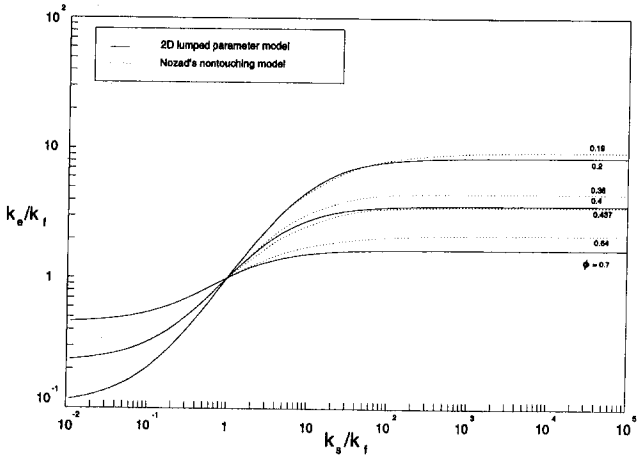



**Fig. 4 Comparison of stagnant thermal conductivity of nontouching square cylinders based on the lumped-parameter model with the numerical results of Nozad et al. (1985)**



Downloaded 12 Dec 2010 to 193.140.21.150. Redistribution subject to ASME license or copyright; see http://www.asme.org/terms/Terms_Use.cfm

*(i) For* $(\lambda - 1)\gamma_a < 1$

$$\frac{k_e}{k_f} = \frac{\gamma_c\gamma_a}{\lambda} + \frac{1 - \gamma_a\sqrt{1 - \gamma_c^2}}{\gamma_a\gamma_c(\lambda - 1) + 1} + \frac{\pi/2 - 2\theta_c}{(\lambda - 1)} - \frac{2}{(\lambda - 1)\sqrt{1 - (\lambda - 1)^2\gamma_a^2}} \times \left\{ \tan^{-1}\left[ \frac{\tan(\pi/4 - \theta_c/2) + (\lambda - 1)\gamma_a}{\sqrt{1 - (\lambda - 1)^2\gamma_a^2}} \right] - \tan^{-1}\left[ \frac{\tan(\theta_c/2) + (\lambda - 1)\gamma_a}{\sqrt{1 - (\lambda - 1)^2\gamma_a^2}} \right] \right\} \quad (12a)$$

*(ii) For* $(\lambda - 1)\gamma_a > 1$

$$\frac{k_e}{k_f} = \frac{\gamma_c\gamma_a}{\lambda} + \frac{1 - \gamma_a\sqrt{1 - \gamma_c^2}}{\gamma_a\gamma_c(\lambda - 1) + 1} + \frac{\pi/2 - 2\theta_c}{(\lambda - 1)} - \frac{1}{(\lambda - 1)\sqrt{(\lambda - 1)^2\gamma_a^2 - 1}} \times \left\{ \ln\left[ \frac{\tan(\pi/4 - \theta_c/2) + (\lambda - 1)\gamma_a - \sqrt{(\lambda - 1)^2\gamma_a^2 - 1}}{\tan(\pi/4 - \theta_c/2) + (\lambda - 1)\gamma_a + \sqrt{(\lambda - 1)^2\gamma_a^2 - 1}} \right] - \ln\left[ \frac{\tan(\theta_c/2) + (\lambda - 1)\gamma_a - \sqrt{(\lambda - 1)^2\gamma_a^2 - 1}}{\tan(\theta_c/2) + (\lambda - 1)\gamma_a + \sqrt{(\lambda - 1)^2\gamma_a^2 - 1}} \right] \right\} \quad (12b)$$

*(iii) For* $(\lambda - 1)\gamma_a = 1$

$$\frac{k_e}{k_f} = \frac{\gamma_c\gamma_a^2}{\gamma_a + 1} + \frac{1 - \gamma_a\sqrt{1 - \gamma_c^2}}{\gamma_c + 1} + \gamma_a\left(\frac{\pi}{2} - 2\theta_c\right) - \left[ \tan\left(\frac{\pi}{4} - \frac{\theta_c}{2}\right) - \tan\left(\frac{\theta_c}{2}\right) \right] \quad (12c)$$

The corresponding expressions for nontouching in-line circular cylinders can be obtained by setting $\gamma_c = \theta_c = 0$ in Eq. (12). It is relevant to note that the stagnant thermal conductivity of an array of in-line point-contact circular cylinders can be obtained by setting $\gamma_c = \theta_c = 0$ and $\gamma_a = 1$ in Eq. (12). A similar expression for the stagnant thermal conductivity of this geometry was obtained by Hall and Martin (1981).

Figure 6 is a comparison of experimental data with results based on touching square cylinders (with $c/a = 0.01$) and touching circular cylinders (with $c/a = 0.01$). It is shown that the results based on the circular cylinders are slightly higher than that of square cylinders for $k_s/k_f > 1$ and the behavior reverses itself when $k_s/k_f < 1$. Similar characteristics are observed in Fig. 7 for nontouching circular cylinders and nontouching square cylinders with $\phi = 0.4$, 0.5, and 0.6. It is shown that the stagnant thermal conductivity decreases as the porosity is increased for $k_s/k_f > 1$. In the same graph, Sabraoui and Kaviany's numerical results (1993) for nontouching square and circular cylinders are also plotted for comparison. It is shown that Sabraoui and Kaviany's results are higher than those obtained based on the present model.

## Cubes

We now consider the stagnant thermal conductivity of an array of in-line cubes with smaller connecting bars as shown in Fig. 8(*a*). A unit cell of this three-dimensional periodic medium is shown in Fig. 8(*b*). From a geometric consideration, it can be shown that the volume fraction of the solid is

$$1 - \phi = (1 - 3\gamma_c^2)\gamma_a^3 + 3\gamma_c^2\gamma_a^2 \quad (13)$$

where $\gamma_a = a/l$ and $\gamma_c = c/a$. The effective stagnant thermal conductivity can be considered as the sum of four columns in parallel that gives

$$k_e/k_f = (1 - \gamma_a^2 - 2\gamma_c\gamma_a + 2\gamma_c\gamma_a^2) + \frac{\gamma_c^2\gamma_a^2}{\lambda} + \frac{\gamma_a^2 - \gamma_c^2\gamma_a^2}{(1 - \gamma_a + \gamma_a\lambda)} + \frac{2(\gamma_c\gamma_a - \gamma_c\gamma_a^2)}{(1 - \gamma_c\gamma_a + \gamma_c\gamma_a\lambda)} \quad (14)$$

For nontouching cubes where $\gamma_c \to 0$ and $\gamma_a = (1 - \phi)^{1/3}$, the equation above reduces to

$$\frac{k_e}{k_f} = [1 - (1 - \phi)^{2/3}] + \frac{(1 - \phi)^{2/3}}{1 + (\lambda - 1)(1 - \phi)^{1/3}} \quad (15)$$

The effect of the touching parameter $c/a$ on the stagnant thermal conductivity of cubes given by Eq. (14) is presented in Fig. 9. It is shown that the behaviors of the curves for $k_s/k_f > 1$ are qualitatively similar to those of the two-dimensional case as shown in Fig. 2. The magnitude of effective stagnant thermal conductivity of the cubes for the touching parameter of $c/a = 0.1$ is almost the same as the effective stagnant thermal conductivity of square cylinders with a touching parameter of $c/a = 0.01$. In fact, they represent roughly the same touching area ratio. This is because the touching area ratio for cubes is equal to $(c/a)^2$ while that for the square cylinders is equal to $c/a$. Note that in Fig. 9 the value of the stagnant thermal conductivity based on the three-dimensional model in the range of $k_s/k_f < 1$ is insen-

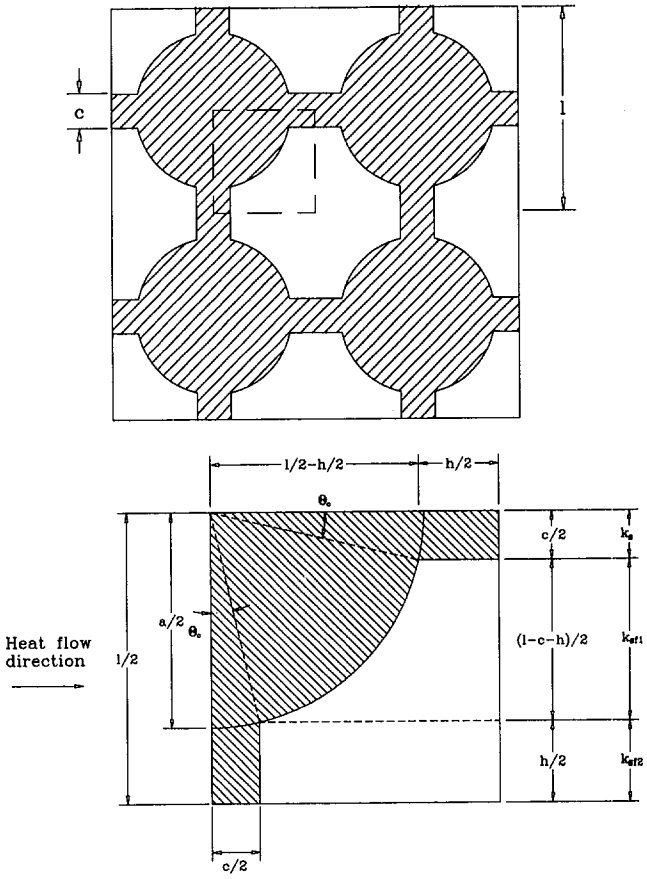



**Fig. 5 (a) An array of touching circular cylinders (above) and (b) its unit cell (below)**



Downloaded 12 Dec 2010 to 193.140.21.150. Redistribution subject to ASME license or copyright; see http://www.asme.org/terms/Terms_Use.cfm

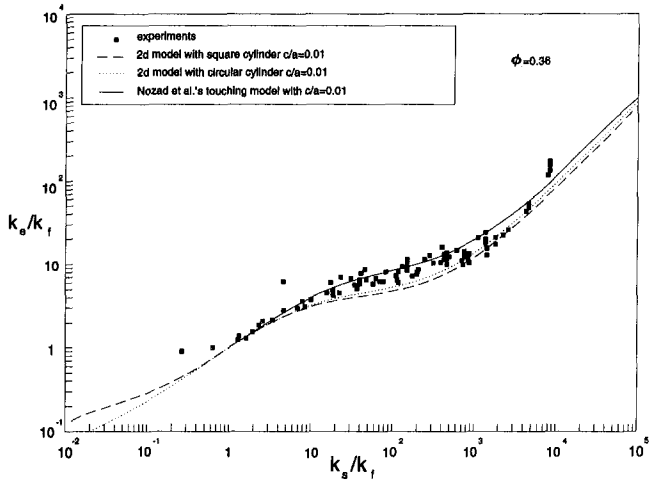
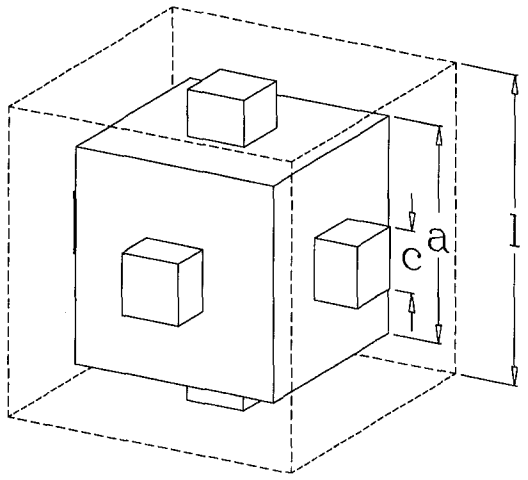



**Fig. 6 Comparison of stagnant thermal conductivity of touching square and touching circular cylinders based on the lumped-parameter model with the numerical results of Nozad et al. (1985)**



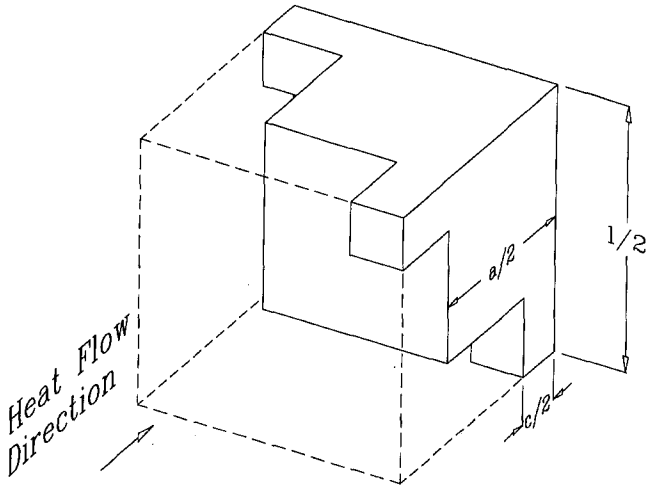




**Fig. 8 (a) In-line touching cubes (above) and (b) their unit cell**

sitive to the touching parameter, a result quite different from the two-dimensional model (square cylinders) shown in Fig. 2.

Figure 10 is a comparison of experimental data with its best fit of models based on touching cubes (with $c/a = 0.13$) and touching square cylinders with two values of the touching parameters ($c/a = 0.01$ and 0.02). It is shown that the results based on touching cubes model (three-dimensional) agree better with experimental data than touching square cylinders model (two-dimensional). It should be noted that there is important difference in the behavior of the effective thermal conductivity given by the two-dimensional and three-dimensional model in the limit of $k_s/k_f \to 0$. At this limit, the third dimension in the three-dimensional model provides an added parallel path for fluid thermal conduction; the effective stagnant thermal conductivity given by the three-dimensional model is proportional to $k_f$ while that given by the two-dimensional model is proportional to $k_s$ because the fluid is isolated. This reflects the physics that the solid barrier with lower conductivity prevails in a series layer model. For comparison purposes, the results for nontouching square cylinders and nontouching cubes are also plotted in Fig. 10. It is shown that the stagnant thermal conductivity of nontouching cubes (three-dimensional model) is higher than that of nontouching square cylinders (two-dimensional model), which is consistent with the findings of Saez et al. (1991). The effect of porosity on the stagnant thermal conductivity of cubes having $c/a = 0.13$ is presented in Fig. 11, which is similar to those of square cylinders with touching parameter $c/a = 0.01$ presented in Fig. 3.

Figure 12 is a comparison of experimental data with predicted results based on Zehner and Schlunder's model (1970), the two-dimensional (square cylinders with $c/a = 0.01$) and three-di-

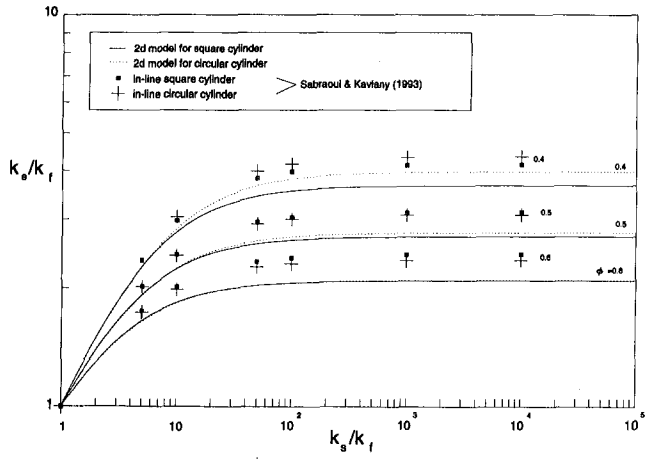



**Fig. 7 Comparison of stagnant thermal conductivity of nontouching square and circular cylinders based on the lumped-parameter model with Sabraoui and Kaviany's numerical results (1993)**

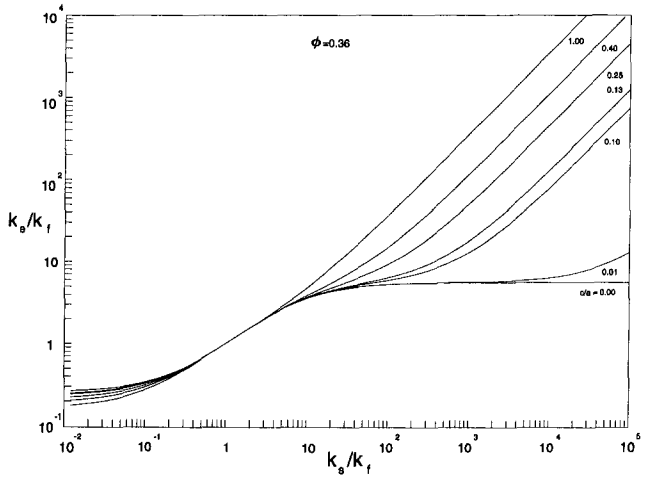



**Fig. 9 Effects of the touching parameter on the stagnant thermal conductivity of arrays of cubes based on three-dimensional lumped-parameter model**



Downloaded 12 Dec 2010 to 193.140.21.150. Redistribution subject to ASME license or copyright; see http://www.asme.org/terms/Terms_Use.cfm

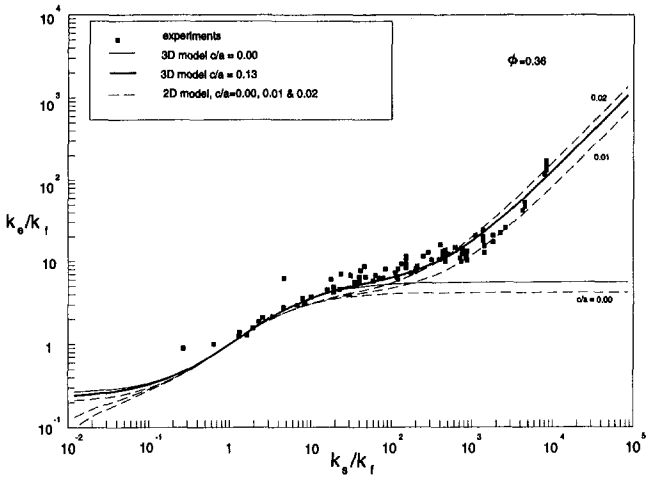



**Fig. 10 Comparison of two-dimensional (touching square cylinders) and three-dimensional (touching cubes) lumped-parameter models with experimental data**

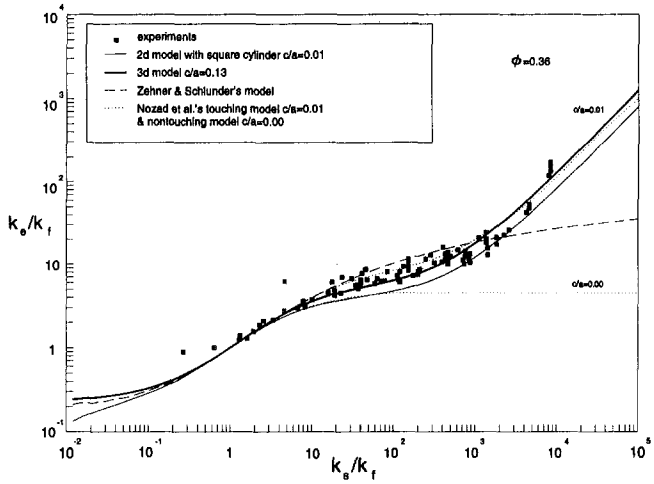



**Fig. 12 Comparison of lumped-parameter models with Zehner–Schlunder's model (1970)**

mensional (cubes with $c/a = 0.13$) lumped parameter models, as well as the numerical results of Nozad et al. (with $c/a = 0.01$). As mentioned earlier, Zehner and Schlunder's model (1970) underpredicts the effective stagnant thermal conductivity when the solid/fluid thermal conductivity ratio is high. The results based on the three-dimensional lumped parameter model with $c/a = 0.13$ compared the best with experimental data for the whole range of the thermal conductivity ratio.

## Concluding Remarks

The lumped parameter model used in this paper is inspired by the earlier work of Kunii and Smith (1960) and Zehner and Schlunder (1970). The method consists of choosing a unit cell, dividing the geometry under consideration into solid, fluid, or composite layers (consisting of both fluid and solid), and assuming one-dimensional conduction in the unit cell. The thermal resistance of the medium is obtained by assuming these layers are in parallel with one another while the thermal resistance of the composite layers is obtained by assuming the layers are in series. The concept of a cell model for a periodic medium has been widely used in a host of other physical problems, including micromechanics, electrical conductivity, permeability, etc. The significance of selecting a unit cell lies not only in its simplified representation of a global average, but also in the condition of no heat flux at the boundaries parallel to the macroscopic temperature gradient direction. In other words, the surfaces of the unit cell parallel to the macroscopic heat flux behave as insulated surfaces. As a result, the problem becomes macroscopically one dimensional. Although heat conduction near the solid/fluid interface is multidimensional at the microscopic level, its overall effect on the effective thermal conductivity after integration is expected to be canceled at least to the first-order approximation. This is confirmed by the small differences in results based on the present model and existing numerical solutions. Based on the present model, we have obtained algebraic expressions for the thermal conductivity of touching and nontouching in-line cylinders (two-dimensional) as well as cubes (three-dimensional). It is found that the stagnant thermal conductivity based on the in-line touching cubes model (with a touching parameter of 0.13) agrees best with experimental data of a packed-sphere bed.

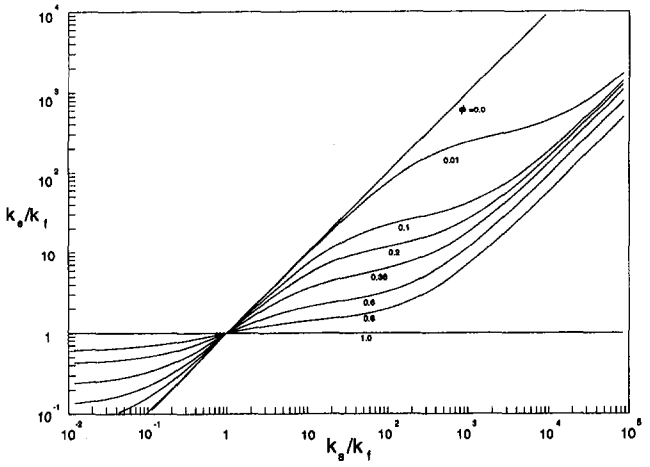



**Fig. 11 Effect of porosity on the stagnant thermal conductivity of touching cubes (three-dimensional) for $c/a = 0.13$**

## References


Chan, C. K., and Tien, C. L., 1973, "Conductance of Packed Spheres in Vacuum," ASME JOURNAL OF HEAT TRANSFER, Vol. 95, pp. 302–308.

Deisser, R. G., and Boegli, J. S., 1958, "An Investigation of Effective Thermal Conductivities of Powders in Various Gases," *ASME Transactions,* Vol. 80, pp. 1417–1425.

Hall, R. O. A., and Martin, D. G., 1981, "The Thermal Conductivity of Power Beds. A Model, Some Measurements on $UO_2$ Vibro-Compacted Microspheres, and Their Correlation," *J. of Nuclear Materials,* Vol. 101, pp. 172–183.

Kaviany, M., 1991, *Principles of Heat Transfer in Porous Media,* Springer-Verlag, New York.

Kunii, D., and Smith, J. M., 1960, "Heat Transfer Characteristics of Porous Rocks," *AIChE J.,* Vol. 6, pp. 71–78.

Nozad, S., Carbonell, R. G., and Whitaker, S., 1985, "Heat Conduction in Multiphase Systems. I: Theory and Experiments for Two-Phase Systems," *Chem. Engg. Sci.,* Vol. 40, pp. 843–855.

Ogniewicz, Y., and Yovanovich, M. M., 1978, "Effective Conductivity of Regularly Packed Spheres: Basic Cell Model With Constriction, Heat Transfer and Thermal Control Systems," *Progress in Astronautics and Aeronautics,* L. S. Fletcher, ed., Vol. 60, pp. 209–228.

Prasad, V., Kladias, B. A., and Tian, Q., 1989, "Evaluation of Correlations for Stagnant Thermal Conductivity of Liquid-Saturated Porous Beds of Spheres," *Int. J. Heat Mass Transfer,* Vol. 32, pp. 1793–1796.

Sabraoui, M., and Kaviany, M., 1993, "Slip and No-Slip Temperature Boundary Conditions at Interface of Porous, Plain Media: Conduction," *Int. J. Heat Mass Transfer,* Vol. 36, pp. 1019–1033.

Saez, A. E., Perfetto, J. C., and Rusinek, I., 1991, "Prediction of Effective Diffusivities in Porous Media Using Spatially Periodic Models," *Transp. Porous Media,* Vol. 6, pp. 143–157.

Shonnard, D. R., and Whitaker, S., 1989, "The Effective Thermal Conductivity for a Point-Contact Porous Medium: An Experimental Study," *Int. J. Heat Mass Transfer,* Vol. 32, pp. 503–512.

Zehner, P., and Schlunder, E. U., 1970, "Thermal Conductivity of Granular Materials at Moderate Temperatures" [in German], *Chemie. Ingr.-Tech.,* Vol. 42, pp. 933–941.




Downloaded 12 Dec 2010 to 193.140.21.150. Redistribution subject to ASME license or copyright; see http://www.asme.org/terms/Terms_Use.cfm

# The Thermal Contact Conductance of Hard and Soft Coat Anodized Aluminum

**M. A. Lambert**
Graduate Research Assistant.
Student Mem. ASME

**E. E. Marotta**
Graduate Research Assistant.
Student Mem. ASME

**L. S. Fletcher**
Thomas A. Dietz Professor.
Fellow ASME

Mechanical Engineering Department,
Texas A&M University,
College Station, TX 77843-3123

*An experimental investigation of the thermal contact conductance of anodized coatings, synthesized at different bath temperatures and in different electrolyte solutions, was performed, and the results were compared with previously published information. Electrolyte solutions of sulfuric acid at bath temperatures of 7°C (Type III) and 25°C (Type II) and chromic acid at a bath temperature of 54°C (Type I) were used to grow coating thicknesses ranging from 3.2 to 61 μm (0.11 to 2.4 mil). Experimental thermal contact conductance data were obtained for a junction between anodized aluminum 6101-T6 and uncoated aluminum A356-T61 as a function of apparent contact pressure and anodized coating thickness. Apparent contact pressure ranged from 172 to 2760 kPa (25 to 400 psi) and the mean interface temperature was maintained at 40°C (104°F). The thermal contact conductance for the low-temperature sulfuric acid anodized (Type III) coatings varied from 300 to 13,000 W/m² K, while the conductance of the room temperature sulfuric anodized (Type II) coatings varied between 100 to 3000 W/m² K. The chromic acid (Type I) coatings yielded conductance values of 60 to 3000 W/m² K. In general, the use of elevated temperatures for the anodizing bath will lead to lower surface microhardness and lower thermal contact conductance. The greatest conductance measurements were obtained for coatings grown in low-temperature sulfuric acid.*

## Introduction

The thermal performance of microelectronic components has become increasingly important as systems are miniaturized. The dense packaging on standard electronic modules (SEM), widely used in military applications, often leads to thermally induced failures because of the thermal resistance occurring between the module guide ribs and the chassis card rails. This thermal resistance results from the limited contact area at the interface, the uneven contact pressure, surface characteristics, and the bulk resistance of the coatings on the card rails and guide ribs.

As circuit densities have increased, cooling schemes have been developed to maintain device temperatures within their optimum design specification. However, other techniques that help reduce the temperature change across component interfaces must also be investigated. Many electronic systems incorporate anodized surfaces, which contribute to the thermal resistance at component interfaces. This paper reports the results of an experimental investigation of anodized films grown at different temperatures and in different electrolyte solutions, and compares these results with previously published information.

Tsao and Heimburg (1970) observed that very thin oxide films on aluminum 7075-T5 resulted in only small reductions in the thermal contact conductance, while thicker oxide coatings significantly reduced the thermal conductance. Mikic and Carnasciali (1970) developed an analytical technique for predicting the thermal behavior of oxide layers. Assuming constant heat flux conditions over the contact area, the maximum discrepancy between predicted and experimental results was about 20 percent, which occurred at low layer thicknesses. Therefore, their experimental results indicated a slight increase in conductance due to thin layers. Kharitonov et al. (1974) considered the effects of oxide layers with thickness not exceeding 1 μm on the surface of metals. They concluded that the contact resistance has a weak dependence on the thermal conductivity of the oxide layer for the contact of wavy or rough surfaces.

Contributed by the Heat Transfer Division for publication in the JOURNAL OF HEAT TRANSFER. Manuscript received by the Heat Transfer Division November 1993; revision received May 1994. Keywords: Conduction, Electronic Equipment, Thermal Packaging. Associate Technical Editor: R. Viskanta.

Yip (1975) developed a prediction expression for the contact resistance of oxidized metal surfaces. His expression for estimating contact resistance includes as variables: surface roughness, asperity slope, nondimensional oxide thickness, the ratio of apparent pressure to substrate metal hardness, and the thermal conductivities of both the metal and its oxide. The theory predicts a 100-fold increase in contact resistance for aluminum with an oxide thickness approximately equal to the surface roughness.

Mian et al. (1979) examined the contact resistance of oxide films on samples of mild steel. The test specimens were lapped flat, then sandblasted to a roughness of 0.08 μm (3.2 μin.). Their data indicated that the thermal contact resistance decreased with increasing load and surface roughness. They stated that film thickness, rather than surface roughness, was the dominant variable affecting the resistance. They also demonstrated that their experimental data were in reasonably good agreement with Yip's theory.

Khan et al. (1969) conducted an experimental investigation of the thermal contact resistance of thick oxide layers synthesized on two steel alloys. The oxide films produced were light gray in color and varied in thickness from 242 to 1940 μm (0.0095 to 0.0764 in.) and exhibited a porosity in the range of 20 to 25 percent. The data indicate that break-up of the oxide layer leads to lower contact resistance only after sufficient deformation has occurred for the base metal to flow through the cracks in the oxide layer. Correlation of the data shows that at high loads the thermal contact resistance depends primarily on the oxide layer thermal conductivity and thickness, while at low pressure the oxide layer surface roughness is also important.

Al-Astrabadi et al. (1980) developed a theoretical prediction for the thermal resistance of a contact between two nominally flat randomly rough oxidized metallic surfaces. They concluded that formation of oxides tends to reduce the true metal-to-metal contact for freshly assembled joints, especially at high temperatures, thus increasing the thermal contact resistance.

Their experimental measurements consisted of six contact assemblies formed between the flat faces of 12 cylindrical specimens of EN3B mild steel. The flat faces were ground, lapped, and polished to optical flatness, and then cleaned with both acetone and isopropyl alcohol. Uniform thicknesses of oxide film, which ranged from 0.055 to 0.118 μm (2.2 to 4.6 μin.), were



Copyright © 1995 by ASME

Downloaded 12 Dec 2010 to 193.140.21.150. Redistribution subject to ASME license or copyright; see http://www.asme.org/terms/Terms_Use.cfm

grown in a high-temperature furnace and surface roughnesses varied from approximately 0.12 to 2.0 $\mu$m (4.7 to 79 $\mu$in.).

The authors assume that when the oxide layer thickness exceeds the surface roughness, the thermal contact resistance will be greater than that for the bare surfaces at all load conditions. However, if the layer thickness is of the order of or less than the surface roughness, then the thermal contact resistance would decrease only if the oxide layer hardness is less than the substrate hardness or if the oxide layer fractures. The latter mechanism would lead to greater metal-to-metal contact and lower thermal contact resistance.

Peterson and Fletcher (1990) conducted an experimental investigation to determine the thermal contact conductance and effective thermal conductivity of anodized coatings. The authors tested seven anodized aluminum 6061-T6 specimens with coating thicknesses between 60.9 and 163.8 $\mu$m (2.5 to 6.8 mils) in contact with a single bare aluminum surface. They estimated the effective thermal conductivity of the anodized coatings as the reciprocal of the slope of the overall thermal resistance as a function of coating thickness.

Keller et al. (1953) conducted an experimental investigation, using an electron microscope, of the structural features of the porous type of anodic oxide coating as synthesized on aluminum. Their investigation revealed that anodic oxide coatings consist of close-packed cells, predominantly hexagonal in shape, with each cell containing a single pore above a fully dense "barrier layer." They concluded that pore size was directly influenced by the solution electrolyte used and independent of forming voltage, while wall and barrier layer thickness are primarily functions of forming voltage.

## Experimental Program

The experimental program involved the evaluation of the thermal conductance for selected anodized coatings. The test facility, test specimen characteristics, anodization process, and test procedure are all described.

**Test Facility.** The experimental test facility used in this investigation consists of a vertical stack consisting of a frame with sliding plates for supporting two combination heat source/sink specimen holder assemblies, the heat flux meters (specimens), a load cell, and pneumatic bellows as shown in Fig. 1. The axial force on the test column is applied by pressurizing the bellows and the contact load is monitored by a BLH load cell and signal amplifier. Uniform contact pressure over the test interfaces is assured by the use of hardened steel ball bearings to transfer load from the frame to the source-sink-holder assemblies and in turn to the specimens. Flexible neoprene hoses are used to supply coolant to the holder assemblies in order to essentially eliminate lateral loads that would skew the pressure distribution over the interfaces.

The experimental facility is housed in a vacuum chamber. A pressure of $10^{-5}$ torr is attained by a Varian VHS-6 oil diffusion pump backed by an Alcatel 2300 two-stage rotary pump. The vacuum pressure is monitored by thermocouple and filament gages connected to a Perkin Elmer Monitorr 300 indicator.

**Test Specimens.** The thermal contact conductance heat flux meters are all 2.54 cm (1.0 in.) in diameter. The upper and lower

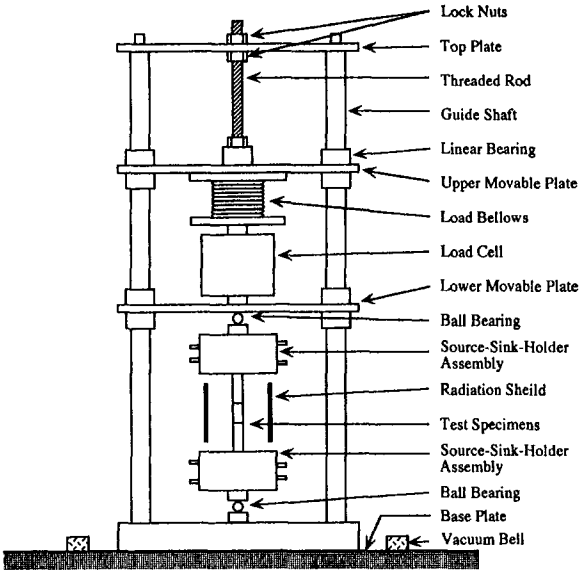



**Fig. 1 Schematic of the thermal contact conductance test facility**

heat flux meters are 10.16 cm (4 in.) long and are fabricated from aluminum alloy A356-T61, while the middle heat flux meter is 3.81 cm (1.5 in.) long and is machined from aluminum alloy 6101-T6. This particular alloy is used for standard electronic module frames due to its relatively high thermal conductivity (approximately 208 W/m K at 25°C as compared to 167 W/m K for the more common aluminum alloy 6061-T6). The surfaces of the aluminum 6101-T6 heat flux meters were anodized using the electrolytes and procedures described below.

Each heat flux meter was instrumented with five special limit of error (1.1°C) K type thermocouples (AWG 30) inserted into 0.12 cm (0.0465 in.) diameter holes drilled radially to their axes at 0.635 cm (0.25 in.) intervals. Aluminum powder was then tamped into the holes to ensure good thermal contact of the thermocouple beads to the peripheries of the holes. The thermocouples are connected to a Hewlett Packard 3497A data acquisition unit, which communicates with a personal computer.

**Anodization Process.** Three types of anodic coating were synthesized. These entailed sulfuric acid electrolyte processing at temperatures of 7°C and 25°C, and chromic acid electrolyte processing at 54°C.

The sulfuric acid process of anodization produces coatings that are colorless and transparent on aluminum. The thickness of the coating is limited, due to its relatively high solubility in the electrolyte, and thicknesses above 38.10 $\mu$m (1.5 mils) require specific techniques. The anodization conditions greatly influence the properties of this coating. The use of dilute solutions and lower temperatures favors harder, thicker coatings, while more concentrated solutions and increased temperatures and operating times produce coatings that are softer at the surface and harder throughout the rest of the film. In general, the properties of these coatings are closely tied to the rate of growth and the solvent action of the electrolyte, which not only determines the thickness of the

## Nomenclature

$F$ = flatness deviation
$h$ = thermal contact conductance
$H$ = hardness
$k$ = thermal conductivity
$P$ = apparent contact pressure
$q$ = heat flux through interface
$R$ = roughness
$S$ = asperity slope
$t$ = coating thickness
$\Delta T$ = temperature discontinuity across interface
$x$ = distance from contact interface
$W$ = waviness

**Subscripts and Superscripts**

$a$ = average
$q$ = root mean square (rms)
$'$ = effective



Downloaded 12 Dec 2010 to 193.140.21.150. Redistribution subject to ASME license or copyright; see http://www.asme.org/terms/Terms_Use.cfm

coating, but also its porosity, mechanical properties, and chemical composition.

The chromic acid anodization process provides a comparatively thin but corrosion-resistant coating and is particularly suitable when rigid structures or parts with laps, joints, or crevices are to be treated. Films produced by chromic acid anodization are generally softer than sulfuric acid coatings and the traces of electrolyte remaining in crevices are noncorrosive. Some coatings produced at higher chromic acid electrolyte compositions have been shown to comply with the military salt fog specifications.

In order to determine precisely the anodic coating thickness on the aluminum 6101 specimens, a number of coating-rate trials were performed. These trials involved coating several samples for varying lengths of time in the selected electrolytes and subsequently measuring the coating thickness by microscopic examination of the cross-sections according to ASTM Test Method B487.

**Surface Characteristics.** Because the profiles of the contacting surfaces have a profound effect on the measured contact conductance values, all surfaces were characterized utilizing a Federal Products Surfanalyzer 4000/5000 profilometer. The surface measurements are listed in Table 1.

Surface microhardness also substantially influences contact conductance. Consequently, a number of aluminum 6101-T6 coupons were anodized by each of the three processes to thicknesses similar to those applied to the heat flux meters employed in contact conductance tests. The Vickers microhardness (VHN) of the coupons was measured for an indentor load range of 25 to 500 grams force. The range of Vickers microhardness for each coating thickness is listed in Table 1.

**Test Procedure.** Each test began with insertion of the selected middle anodized aluminum 6101-T6 heat flux meter between the upper and lower aluminum A356-T61 flux meters. A special alignment fixture was clamped around the column, comprised of the three heat flux meters, to ensure exact coaxial mating of the surfaces. A light load was applied, the alignment fixture then removed, and a preload pressure of 2760 kPa (400 psi) applied. This preloading, equal to the maximum contact pressure applied during subsequent conductance tests, was performed to simulate the practice of applying maximum rated torque to wedge clamps in accordance with military specifications. The bell jar was sealed over the apparatus and evacuated. Power was supplied to the heater on one source-sink-holder assembly, and coolant was pumped through the opposite assembly.

The reported contact conductance data are for the case of heat flux passing from the anodized aluminum 6101-T6 heat flux meter to one of the bare aluminum A356-T61 heat flux meters. Conductance measurements were obtained during reloading at pressures increasing from 172 to 2760 kPa (25–400 psi). All tests were performed at a mean interface temperature of 40°C (104°F).

**Data Analysis.** Once the test stack temperature profile achieved a quasi-steady-state condition, which was assumed to have occurred when the mean interface temperature changed by no more than 0.3°C per hour, a data acquisition and analysis program was executed. The temperature gradients in all three heat flux meters were computed from linear least-squares regressions of their individual thermocouple readings. Their temperature-dependent conductivities were obtained from prior calibrations. The gradients and conductivities were used to calculate the heat flux through each flux meter from Fourier's law. The temperature profiles in the three heat flux meters were extrapolated to the interfaces to obtain the temperature discontinuities across the interfaces. The thermal contact conductance was computed as the quotient of the mean heat flux across the junction and the temperature discontinuity, as follows:

$$h = \frac{q}{\Delta T} \tag{1}$$

**Uncertainty Analysis.** Experimental uncertainties in contact conductance data arise from a number of sources, the most dominant of which is the randomness in thermocouple readings due to slight variations in their compositions. This randomness in readings exerts its greatest influence on the computed temperature gradients, which are known to an accuracy of ±7.9 percent. The uncertainty in the interfacial temperature discontinuities is ±1.0 percent. Uncertainties in the metal thermal conductivities are ±2.38 percent for the aluminum A356-T61 and ±3.14 percent for the aluminum 6101-T6. The analysis method of Kline and McClintock (1953) yields an average overall uncertainty of ±8.9 percent.

## Results and Discussion

The basic properties of these anodic coatings are closely tied to the rate of growth and the solvent action of the electrolyte,

**Table 1 Surface metrological data for test specimens**

| Specimen Number-Surface* | Anodizing Electrolyte/Temperature/Type | t (um) | Ra (um) | Rq (um) | Wa (um) | Wq (um) | F (um) | Sq | VHN (kg/mm^2) |
|---|---|---|---|---|---|---|---|---|---|
| A356-F1 | Bare | 0.0 | 0.64 | 0.83 | 0.31 | 0.43 | 7.15 | 0.155 | 100 - 128 |
| A356-F2 | " | 0.0 | 0.65 | 0.84 | 0.43 | 0.52 | 8.15 | 0.160 | 100 - 128 |
| A356-F4 | " | 0.0 | 0.65 | 0.86 | 0.63 | 0.82 | 10.35 | 0.218 | 100 - 128 |
| 6101-S23T | Sulfuric Acid, 15wt% | 12.2 | 0.77 | 1.02 | 0.84 | 1.03 | 11.25 | 0.202 | --------- |
| 6101-S24T | 7 C | 24.7 | 1.37 | 1.89 | 1.41 | 1.70 | 22.40 | 0.226 | 143 - 259 |
| 6101-S21T | Type III, Class 2 | 36.5 | 1.14 | 1.47 | 0.85 | 1.04 | 14.65 | 0.232 | 158 - 290 |
| 6101-S20T | | 48.6 | 1.20 | 1.60 | 1.35 | 1.59 | 16.75 | 0.212 | 217 - 379 |
| 6101-S19T | | 60.8 | 1.09 | 1.49 | 1.66 | 2.11 | 17.05 | 0.219 | 217 - 315 |
| 6101-S23B | Sulfuric Acid, 15wt% | 7.0 | 0.94 | 1.25 | 1.38 | 1.64 | 14.20 | 0.218 | 76 - 299 |
| 6101-S24B | 25 C | 13.5 | 3.74 | 4.74 | 2.42 | 2.87 | 37.00 | 0.273 | 78 - 168 |
| 6101-S21B | Type II, Class 2 | 20.2 | 0.91 | 1.23 | 0.99 | 1.17 | 13.55 | 0.172 | 102 - 200 |
| 6101-S19B | | 27.7 | 0.63 | 0.82 | 1.63 | 1.94 | 13.00 | 0.100 | 78 - 140 |
| 6101-S20B | | 33.7 | 1.15 | 1.56 | 0.88 | 1.10 | 21.20 | 0.122 | 58 - 126 |
| 6101-S12T | Chromic Acid, 10wt% | 3.2 | 0.73 | 0.96 | 1.30 | 1.59 | 12.55 | 0.175 | 84 - 211 |
| 6101-S11T | 54 C | 5.3 | 0.62 | 0.81 | 0.83 | 0.96 | 8.60 | 0.154 | 81 - 243 |
| 6101-S8T | Type I, Class 2 | 7.5 | 1.00 | 1.37 | 1.50 | 1.90 | 17.80 | 0.233 | 69 - 220 |
| 6101-S10T | | 10.2 | 1.18 | 1.53 | 1.43 | 1.72 | 16.20 | 0.214 | 70 - 106 |
| 6101-S9T | | 13.2 | 0.91 | 1.18 | 1.37 | 1.62 | 11.90 | 0.165 | 69 - 104 |

*Note: Type III coatings in contact with specimen A356-F2
Type II coatings in contact with specimen A356-F1
Type I coatings in contact with specimen A356-F4



Downloaded 12 Dec 2010 to 193.140.21.150. Redistribution subject to ASME license or copyright; see http://www.asme.org/terms/Terms_Use.cfm

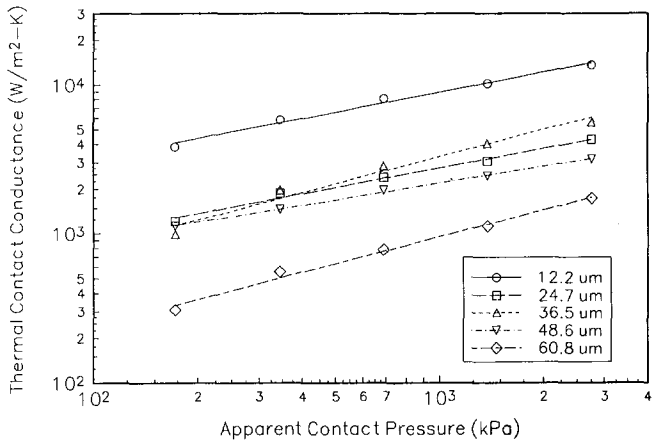



**Fig. 2 Thermal contact conductance of low-temperature (7°C) sulfuric acid anodized aluminum 6101-T6 (Type III) in contact with uncoated aluminum A356 as a function of contact pressure and anodized coating thickness**

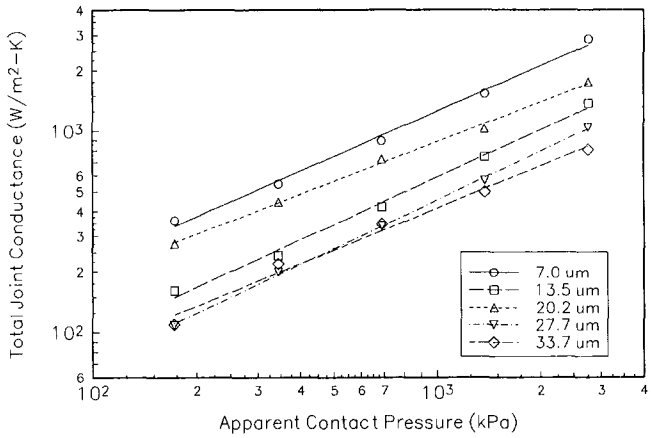



**Fig. 3 Thermal contact conductance of room temperature (25°C) sulfuric acid anodized aluminum 6101-T6 (Type II) in contact with uncoated aluminum A356 as a function of contact pressure and anodized coating thickness**

which not only determines the thickness of the coating, but also its porosity, mechanical properties, and chemical composition.

The thermal contact conductance data for low-temperature (7°C) sulfuric anodized (Type III) aluminum 6101-T6 to bare aluminum A356-T61 are shown in Fig. 2. The thermal contact conductance varied from 300 to 13,000 W/m$^2$ K for the range of interface pressures and coating thicknesses employed. The thermal contact conductance generally decreases with increasing anodized coating thickness, and increases with increasing interface pressure.

The same trends were observed for anodized coatings synthesized using room temperature (25°C) sulfuric acid (Type II) and elevated temperature (54°C) chromic acid (Type I). The thermal contact conductance data for both 25°C sulfuric acid and chromic acid anodized coatings are shown in Figs. 3 and 4, respectively. The thermal contact conductance of the room temperature sulfuric anodized (Type II) coatings varied from 110 to 3000 W/m$^2$ K, while the conductance of the chromic acid anodized (Type I) coatings varied from 63 to 3000 W/m$^2$ K for the interface pressures and coating thicknesses tested.

The coatings processed at low temperature, although considerably harder than those processed at room and elevated temperature (see Table 1 for listings of Vickers microhardness), afford the greatest contact conductance, possibly because the coatings processed at low temperature are much denser, thus probably possessing higher thermal conductivity. Increasing sulfuric acid bath temperature increases electrolyte attack of the coating during growth, resulting in greater coating porosity, lower overall coating thermal conductivity, and reduced microhardness.

The Vickers microhardness (VHN) for chromic acid anodized (Type I) coatings decreases with increasing coating thickness for light indentor loads. The lower microhardness measured for thicker coatings can be attributed to enlargement of the pores as the coatings grow, due to increased electrolyte attack of the coatings with the longer processing times required to achieve greater thicknesses. The harder barrier layer, adjacent to the metallic substrate, provides higher microhardness readings for the thinner coatings. For high indentor loads the VHN for all coating thicknesses shows little variance and approximates the hardness of the aluminum 6101 substrate because the hardness of the metal dominates behavior.

The VHN for room temperature sulfuric acid anodized (Type II) coatings also showed the same general trends observed for the chromic acid anodized coatings with the highest microhardness obtained for the thinner coatings and low indentor loads.

The Vickers microhardness of low-temperature sulfuric anodized (Type III) coatings exhibits trends quite different from coating Types I and II. The microhardness of the Type III anodized coatings generally increases with increasing coating thickness and shows little dependence on load. The increase in microhardness with increasing coating thickness is due to the more uniform higher density of the coatings and the decreased influence of the aluminum substrate.

Peterson and Fletcher (1990) investigated the thermal contact conductance and thermal conductivity of several different anodized coating thicknesses. The experimental thermal conductance values of the present investigation are compared with those of Peterson and Fletcher (1990) and Lambert and Fletcher (1992) in Fig. 5. The anodizing process used by Lambert and Fletcher is the same as the 7°C sulfuric acid process used for the present investigation, while the process employed by Peterson and Fletcher was not reported. The mean junction temperature of the Lambert and Fletcher data also was the same, however, the mean junction temperature of the Peterson and Fletcher data was slightly lower (25°C). The general trend reflected by the data in Fig. 5 is that contact conductance decreases by two orders of magnitude with a factor of seven increase in coating thickness. The combined rms roughness of the contact pairs used in the present investigation and by Lambert and Fletcher (1992) is less than 2 $\mu$m, whereas the combined rms roughness reported by Peterson and Fletcher (1990) was on the order of 6 $\mu$m. All coatings were thicker than the rms surface roughness.

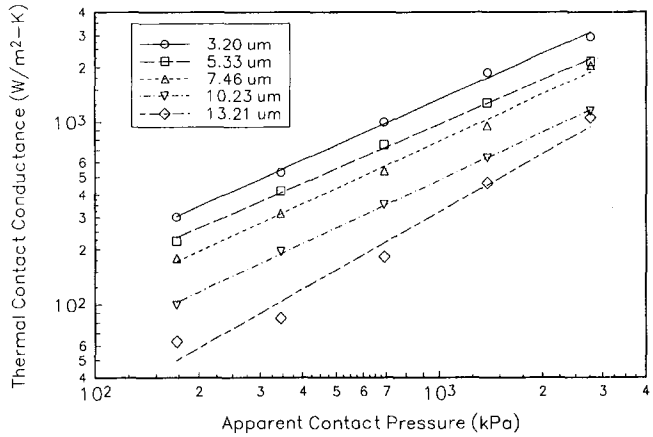



**Fig. 4 Thermal contact conductance of elevated temperature (54°C) chromic acid anodized aluminum 6101-T6 (Type I) in contact with uncoated aluminum A356 as a function of contact pressure and anodized coating thickness**



Downloaded 12 Dec 2010 to 193.140.21.150. Redistribution subject to ASME license or copyright; see http://www.asme.org/terms/Terms_Use.cfm

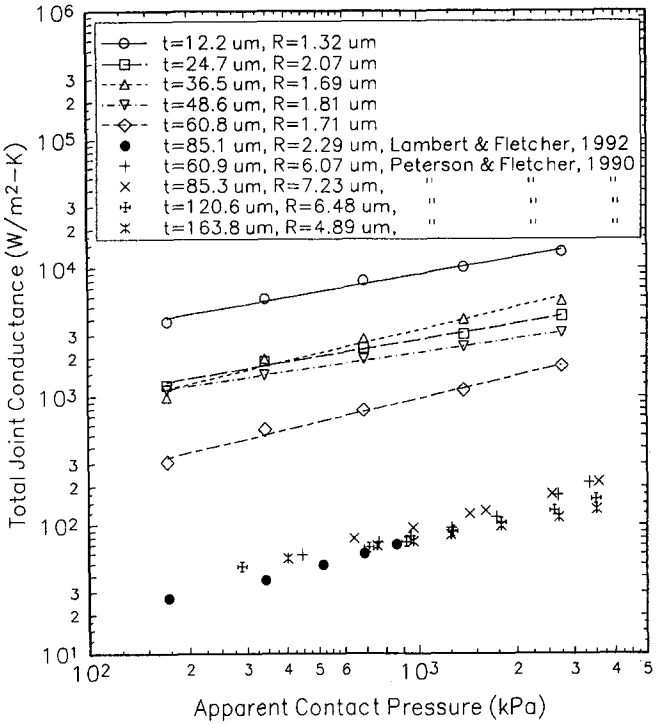



**Fig. 5 Thermal contact conductance as a function of pressure and temperature for low-temperature (7°C) sulfuric acid anodized aluminum 6101-T6 (Type III) to uncoated aluminum A356-T61 with a comparison to published data**

Yip (1975) and Al-Astrabadi et al. (1980) both present theories for predicting the thermal contact conductance of oxidized or anodized metals. The experimental data obtained in the present investigation, as well as data reported by Peterson and Fletcher (1990) and Lambert and Fletcher (1992), are compared to the theories of Yip (1974) and Al-Astrabadi et al. (1980) in Fig. 6. An additional theory for predicting the contact conductance of metallic coated metals, developed by Antonetti and Yovanovich (1985), is also included in Fig. 6. The dimensionless conductance and relative pressure values used in Fig. 6 were calculated using the theory of Antonetti and Yovanovich (1985), since this theory is most easily employed. The justification for using this theory for oxidized and anodized metals, originally intended for metallic coated metals, is as follows.

The theory of Al-Astrabadi et al. (1980) is analogous to a theory for metallic-coated metals developed by their colleagues, O'Callaghan et al. (1981), except that metallic coating properties in the latter theory are replaced by oxide or anodic coating properties in the theory of Al-Astrabadi et al. (1980). Lambert and Fletcher (1991) demonstrated that the theories of O'Callaghan et al. (1981) and Antonetti and Yovanovich (1985) are essentially equivalent. Therefore, the theory of Al-Astrabadi et al. (1980) closely approximates that of Antonetti and Yovanovich (1985).

As shown in Fig. 6, the dimensionless conductance values for the thick anodic coatings utilized by Peterson and Fletcher (1990) lie considerably above the theories. The results reported by Lambert and Fletcher (1992) exhibit scatter of an order of magnitude and generally fall between the uppermost theory of Al-Astrabadi et al. (1980) and the lowermost theory of Yip (1974). The conductance measurements of the present investigation are also widely scattered and somewhat evenly distributed above and below the theory of Al-Astrabadi et al. (1980).

The very high dimensionless conductance measurements for the results of Peterson and Fletcher (1990) may be due to the very low value of thermal conductivity they measured for their anodic coatings (0.0292 W/m K), in comparison to the average thermal conductivity of six types of commercially prepared sulfuric acid anodized coatings (0.73 W/m K) as measured by Ogden et al. (1987). The conductivity value reported by Ogden et al. (1987) was used to calculate dimensionless conductance values for the results of Lambert and Fletcher (1992) and those of the present investigation. Yip (1974) assumed the thermal conductivity of the aluminum oxide films to be that of bulk aluminum oxide (32 W/m K), and Al-Astrabadi et al. (1980) assumed the conductivity of iron oxide films to be 0.875 W/m K.

## Conclusions and Recommendations

This investigation presents experimental thermal contact conductance measurements for anodized coatings, synthesized at different temperatures and in different electrolyte solutions, and compares these results with previously published information and predictive theories.

The experimental data were obtained for a junction between anodized aluminum 6101-T6 and uncoated aluminum A356-T61 as a function of interface contact pressure and anodized coating thickness. The thermal contact conductance for low temperature sulfuric acid (Type III) anodized coatings varied from 300 to 13,000 W/m$^2$ K for the range of parameters tested. The lower bath temperature lowers the activity of the electrolyte as the film grows, which results in anodized coatings having higher density, higher microhardness, and higher thermal contact conductance than coating Types I and II.

The thermal contact conductance for room temperature sulfuric acid (Type II) anodized coatings varied from 110 to 3000 W/m$^2$ K, and for elevated temperature chromic acid (Type I) anodized coatings, the conductance varied from 63 to 3000 W/m$^2$ K for the range of parameters tested. Generally, the use of elevated temperatures for the anodizing bath will lead to greater electrolyte attack of the growing film during processing, resulting in greater film porosity and lower microhardness.

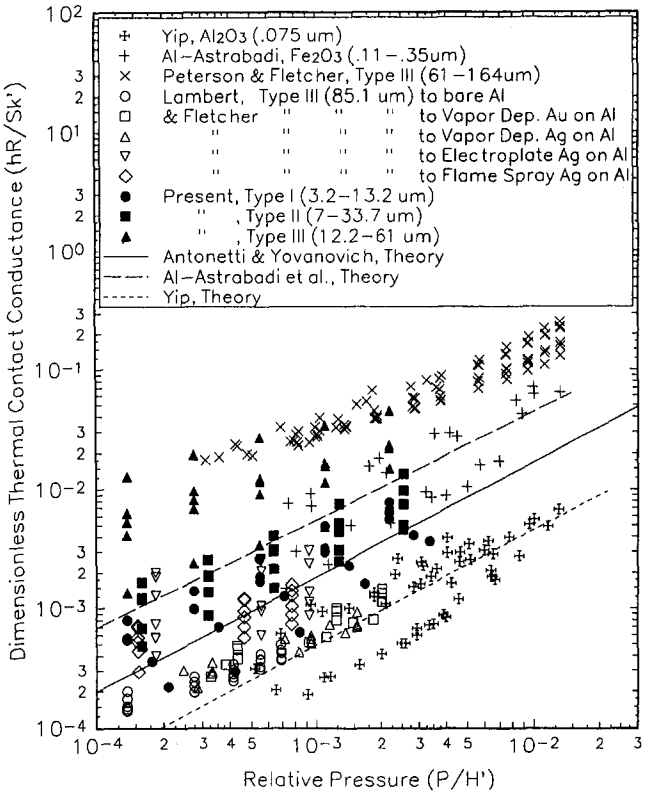



**Fig. 6 Dimensionless thermal contact conductance as a function of relative pressure for oxidized steel and oxidized and anodized aluminum**



Downloaded 12 Dec 2010 to 193.140.21.150. Redistribution subject to ASME license or copyright; see http://www.asme.org/terms/Terms_Use.cfm

The overall conductance of anodic coatings is greatly affected by coating thickness. The conductance of low-temperature (7°C) sulfuric acid anodized (Type III) coatings decreases approximately two orders of magnitude from 4000 to 13,000 $W/m^2$ K at an anodic coating thickness of 12.2 $\mu$m to 30 to 120 $W/m^2$ K at a thickness of 163.8 $\mu$m over the pressure range of 172 to 2758 kPa. The thicknesses of all coatings are greater than the average surface roughnesses of the underlying metallic substrates prior to anodization.

The theory of Al-Astrabadi et al. (1980) may overpredict or underpredict the dimensionless conductances derived from the experimental measurements of Peterson and Fletcher (1990), Lambert and Fletcher (1992), and the present investigation by as much as an order of magnitude, while the theory of Yip (1974) describes a lower bound to these data.

## Acknowledgments

Support for this study was provided by NSWC Contract No. N00164-91-C-0043 and the Center for Space Power at Texas A&M University.

## References

Al-Astrabadi, F. R., O'Callaghan, P. W., and Probert, S. D., 1980, "Thermal Resistance of Contacts: Influence of Oxide Films," AIAA Paper No. 80-1467.

Antonetti, V. W., and Yovanovich, M. M., 1985, "Enhancement of Thermal Contact Conductance by Metallic Coatings: Theory and Experiment," ASME JOURNAL OF HEAT TRANSFER, Vol. 107, pp. 513–519.

Keller, F., Hunter, M. S., and Robinson, D. L., 1953, "Structural Features of Oxide Coatings on Aluminum," *Journal of the Electrochemical Society,* Sept., pp. 411–419.

Khan, E. U., Dix, R. C., and Kalpakjian, S., 1969, "Thermal Contact Resistance of Thick Oxide Layers on Steel," *Journal of the Iron and Steel Institute,* Apr., pp. 457–460.

Kharitonov, V. V., Kokorev, L. S., and Tyurin, Y. A., 1974, "Effect of Thermal Resistance," *Soviet Atomic Energy,* Vol. 36, Apr., pp. 385–387.

Kline, S. J., and McClintock, F. A., 1953, "Describing Uncertainties in Single-Sample Experiments," *Mechanical Engineering,* Vol. 75, No. 1, Jan., pp. 3–8.

Lambert, M. A., and Fletcher, L. S., 1991, "A Review of the Thermal Contact Conductance of Junctions With Metallic Coatings and Films," AIAA Paper No. 92-0709.

Lambert, M. A., and Fletcher, L. S., 1992, "Metallic Coatings for Enhancing the Thermal Contact Conductance of Electronic Modules," AIAA Paper 92-2849.

Mian, M. N., Al-Astrabadi, F. R., O'Callaghan, P. W., and Probert, S. D., 1979, "Thermal Resistance of Pressed Contacts Between Steel Surfaces: Influence of Oxide Films," *Journal of Mechanical Engineering Science,* Vol. 21, pp. 159–166.

Mikic, B., and Carnasciali, G., 1970, "The Effect of Thermal Conductivity of Plating Material on Thermal Contact Resistance," ASME JOURNAL OF HEAT TRANSFER, Vol. 92, pp. 475–482.

O'Callaghan, W., Snaith, B., Probert, S. D., and Al-Astrabadi, F. R., 1981, "Prediction of Optimal Interfacial Filler Thickness for Minimum Thermal Contact Resistance," AIAA Paper No. 81-1166.

Ogden, T. R., Rathsam, A. D., and Gilchrist, J. T., 1987, "Thermal Conductivity of Thick Anodic Oxide Coatings on Aluminum," *Materials Letters,* Vol. 5, No. 3, Elsevier Science Publishers, pp. 84–87.

Peterson, G. P., and Fletcher, L. S., 1990, "Measurement of the Thermal Contact Conductance and Thermal Conductivity of Anodized Aluminum Coatings," ASME JOURNAL OF HEAT TRANSFER, Vol. 112, pp. 579–585.

Tsao, Y. H., and Heimburg, R. W., 1970, "Effect of Surface Films on Thermal Contact Conductance: Part 2—Macroscopic Experiments," ASME Paper No. 70-HT-SpT-27.

Yip, F. C., 1975, "Effects of Oxide Films on Thermal Contact Resistance," *AIAA Progress in Astronautics and Aeronautics: Heat Transfer With Thermal Control Applications,* Vol. 39, M. M. Yovanovich, ed., MIT Press, Cambridge, MA, pp. 45–46.



Downloaded 12 Dec 2010 to 193.140.21.150. Redistribution subject to ASME license or copyright; see http://www.asme.org/terms/Terms_Use.cfm

# Prandtl Number Influence on Heat Transfer Enhancement in Turbulent Flow of Water at Low Temperatures

**T. S. Ravigururajan**
Department of Mechanical Engineering,
Wichita State University,
Wichita, KS 67260

**A. E. Bergles**
Department of Mechanical and
Aerospace Engineering and Mechanics,
Rensselaer Polytechnic Institute,
Troy, NY 12180

*The paper presents the results of an experimental study that was carried out to determine the Prandtl number influence on the thermal-hydraulic performance of enhanced tubes. The enhanced tubes were identical in all aspects, except the roughness height. Emphasis was placed on turbulent flow, with water as the working fluid. Experiments were performed for Prandtl numbers from 10.2 to 5.8. Data for friction factor were obtained under both isothermal and heating conditions. The study confirmed the strong influence of rib roughness on heat transfer and pressure drop increase. In addition, the results of the investigation strongly suggest that the optimum roughness is application specific, because it is dependent on Reynolds and Prandtl numbers. The results show that the presence of entrance effects and the influence of temperature on the friction factor of enhanced tubes may be significant. The experiments show that a rib height-to-diameter ratio of 0.02 provides the best overall performance for water at Pr = 10; while at Pr = 6.0, the optimum e/d depends on the Reynolds number.*

## Introduction

Heat transfer enhancement through surface modification has become a common method of increasing the efficiency of medium-to-large-size heat exchangers, and thereby, reducing their size and cost. A typical example is a heat exchanger employed in Ocean Thermal Energy Conversion (OTEC) power plants (Ravigururajan and Bergles, 1986). A popular and successful technique is to introduce surface roughness to disturb the flow boundary layer. During the past decade numerous studies on flow in enhanced tubes (Bergles, 1988) have resulted in a variety of correlations. For instance, Withers (1980a, b), Li et al. (1982), and Nakayama et al. (1983) developed analogy-based correlations, extending the work of Webb et al. (1971). Other studies (Yorkshire, 1982; Kalinin, 1974; Ravigururajan and Bergles, 1985, 1986) presented statistical correlations that can be used independently to evaluate friction factor and heat transfer coefficient. Webb (1969) recognized the importance of Prandtl number on the effectiveness of repeated ribs. The problem of low-temperature water (close to the freezing point) inside enhanced tubes has not been specifically discussed in the open literature, however, Chillers and industrial condensers, where cold water flows inside tubes, are important applications. The study of Ravigururajan and Bergles (1986) indicated that the optimum disruption height/inside diameter ratio ($e/d$) for spirally indented tubes is around 0.02. By extension of Webb's (1969) suggestion on the Prandtl number influence, one might conclude that the optimum design of disruption height could well vary for different heat exchanger applications. For example, even in the same application, optimum designs would be different for evaporators and for condensers because of different operating temperatures.

The objectives of this study are to obtain experimental data for in-tube flow of low temperature water, to understand the characteristics of internally enhanced tubes for small $e/d$ ratios of 0.02 and less, and to establish the optimum disruption design parameters for different Prandtl numbers.

Contributed by the Heat Transfer Division for publication in the JOURNAL OF HEAT TRANSFER. Manuscript received by the Heat Transfer Division December 1992; revision received March 1994. Keywords: Augmentation and Enhancement, Heat Exchangers, Refrigeration. Associate Technical Editor: T. W. Simon.

## Background

During the past decade, several correlations have been proposed that are applicable to indented tubes. Equations (1) and (2) represent analogy-based, general correlations for friction and heat transfer developed by Withers (1980a) specifically for spirally fluted tubes with water as the working fluid.

$$(f/2)^{0.5} = -1/\{2.46 \ln [r + (7/\mathrm{Re})^m]\} \quad (1)$$

where

$$m = 0.9 - 12.5e/d_i; \quad m_{\min} = 0.44$$

$$r = 0, \quad \text{for} \quad e/d_i \le 0.02$$

The heat transfer function is given by

$$\mathrm{St} = (f/2)^{0.5}/[W_1 \mathrm{Pr}^{0.5}\{\mathrm{Re}(f/2)^{0.5}\}^{0.127} + W_2$$

$$W_1 = 7.22(p/d_i) - 0.33(e/d_i)^{0.127}$$

$$W_2 = -\{2.5 \ln (2e/d_i) + 3.5\} \quad (2)$$

Statistical correlations for friction factor and heat transfer coefficient, as developed by Ravigururajan (1986), are given in Eqs. (3) and (4):

$$f_a/f_s = [1 + 29.1\{\mathrm{Re}^{Y1}(e/d)^{Y2}(p/d)^{Y3}(\alpha/90)^{Y4} \times (1 + 2.94/n) \sin \beta\}^{15/16}]^{16/15} \quad (3)$$

where

$$Y1 = 0.67 - 0.06(p/d) - 0.49(\alpha/90)$$

$$Y2 = 1.37 - 0.157(p/d)$$

$$Y3 = -1.66\ \mathrm{Re}/10^{-6} - 0.33(\alpha/90)$$

$$Y4 = 4.59 + 4.11\ \mathrm{Re}/10^{-6} - 0.15(p/d)$$

The heat transfer correlation for enhanced tube flow is presented as

$$\mathrm{Nu}_a/\mathrm{Nu}_s = \{1 + '[2.64\ \mathrm{Re}^{0.036}(e/d)^{0.212}(p/d)^{-0.21} \times (\alpha/90)^{0.29} \times \mathrm{Pr}^{-0.024}]^7\}^{1/7} \quad (4)$$


Copyright © 1995 by ASME


Downloaded 12 Dec 2010 to 193.140.21.150. Redistribution subject to ASME license or copyright; see http://www.asme.org/terms/Terms_Use.cfm

The following smooth tube friction and heat transfer correlations (Petukhov and Popov, 1963) were used in conjunction with Eqs. (3) and (4):

$$f_s = (1.58 \ln \mathrm{Re} - 3.28)^{-2} \quad (5)$$

$$\mathrm{Nu}_s = (f/2)\,\mathrm{Re}\,\mathrm{Pr}/\{1 + 12.7(f/2)^{0.5}(\mathrm{Pr}^{2/3} - 1)\} \quad (6)$$

Mehta and Rao (1979) proposed correlations based on a severity index, $\phi = e^2/(pd_i)$, which is a function of the rope-tube roughness parameters. Their correlations are friction factor:

$$f = A/\mathrm{Re}^B \quad (7)$$

where

$$A = 0.079 \exp(-92\phi)$$

$$B = 0.25 \exp(-215\phi)$$

and Nusselt number:

$$\mathrm{Nu} = C\,\mathrm{Re}^n\,\mathrm{Pr}^{0.4} \quad (8)$$

where

$$C = 0.029 \exp(-16\phi)$$

$$n = 0.8 \exp(25\phi)$$

Rabas et al. (1988) developed empirical correlations for spirally fluted tubes that are applicable just for water. The correlations are expressed in terms of the severity index, $\phi$, first proposed by Mehta and Rao (1979). The friction factor is given by

$$f_a = 0.005586\, A/\mathrm{Re}^B, \quad (9)$$

where $A$ and $B$ are functions of the severity index, $\phi = e^2/pd_i$.

$A = \exp(675.8)\, B = 0.25$: $\phi \le 0.0002$

$= 27.45^{0.373}\, B = 0.25$: $0.0002 < \phi \le 0.00035$

$= 27.45^{0.373} B = 0.2616 - 32.7\phi$: $0.00035 < \phi \le 0.001$

$= 170.0^{0.637}\, B = 0.2616 - 32.7\phi$: $0.001 < \phi \le 0.08$

$= 170.0^{0.673}\, B = 0.0$: $0.08 \le \phi$

The heat transfer correlation is presented as

$$\mathrm{Nu}_a = 0.027 E_1\,\mathrm{Re}^{0.8}\,\mathrm{Pr}^{0.4} \quad (10)$$

where

$$E_1 = 1.0 + 1.182 E_2 E_3/(p/d)^{0.406}$$

$$E_2 = \cos(\alpha^*); \quad \alpha^* = \tan^{-1}(p/\pi d)$$

$$-\ln E_3 = 4.4224 \ln(e/d) + 1.124 \ln(e/d)^2 + 0.067 \ln(e/d)^3$$

The statistically developed correlations may seem somewhat involved but they are simple to use and friction factors and heat transfer coefficients can be explicitly evaluated. Also, unlike the analogy-based correlations, these two correlations are decoupled. Therefore, correlations from different studies may be used separately for these two factors.

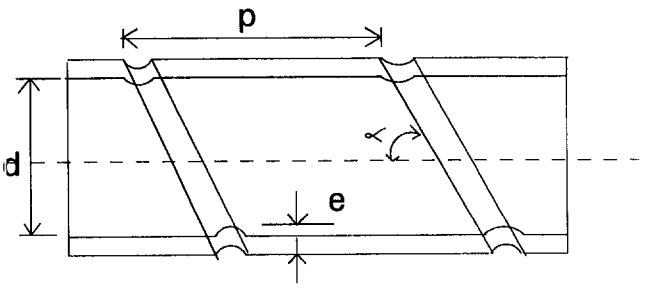


**Fig. 1 Sketch of a spirally indented tube**

By no means are these correlations universally applicable, although some of them are applicable to a wider range of parameters than are others. A condition under which enhanced tubes have not been tested vigorously is the flow of water at high Prandtl number. This has application to condensers, industrial heat exchangers, and chillers. The current study was conducted to obtain new data on heat transfer–friction factor increases due to different roughness heights at high Prandtl numbers.

## Experimental Procedure

In order to achieve the stated objectives, commercially available ribbed tubes were investigated. Dimensions of these tubes, for which a sketch is shown in Fig. 1, can vary widely. The normalized roughness heights of tubes used in the current investigation varied from 0.006 to 0.0387, and the normalized pitches ranged from 0.206 to 1.05. Table 1 shows the important dimensions of these tubes. They were made by the traditional method of indenting a seamless tube (Withers, 1973). It should be noted that diameter of an enhanced tube can be expressed in many ways. In this paper the inside diameter of an enhanced tube is taken to be the envelope diameter as suggested by Marner et al. (1983).

The experiments were conducted under constant-heat-flux conditions. Energy is added to the working fluid electrically by direct-current Joule heating. The temperatures were measured at three circumferential positions each at five stations along the length of the tube. A sketch of the experimental apparatus is shown in Fig. 2. Water from a positive displacement pump flowed through calibrated flowmeters and into the test section. The test section was electrically heated by direct current. The warm water was then cooled by a countercurrent flow heat exchanger before being returned to the pump. A deionizing unit, a surge/degassing tank, filter, and accumulators were included in

## Nomenclature

$d$ = envelope (maximum inside) diameter, mm
$e$ = rib roughness or disruption height, mm
$e^+$ = roughness Reynolds number
$F$ = Prandtl number function
$f$ = Fanning friction factor
$h$ = heat transfer coefficient, kW/m$^2$-°C
$L$ = test-section length, mm
$m$ = mass flow rate, kg/h
$N$ = number of starts
Nu = Nusselt number
$n$ = number of sharp corners in the roughness that face the flow
$p$ = pitch of roughness, mm
$P$ = pressure drop, N/m$^2$
Pr = Prandtl number
$q$ = heat transfer rate, kW
Re = Reynolds number
Sh = rib profile shape function
St = Stanton number
$T$ = temperature, °C
$T_b$ = fluid bulk temperature, °C
$T$ = average temperature difference, °C
$z$ = effectiveness
$\alpha$ = helix angle of rib, deg
$\beta$ = rib profile contact angle with base surface, deg
$\phi$ = severity index
$\mu$ = fluid dynamic viscosity, Pa·s
$\rho$ = fluid density, kg/m$^3$

### Subscripts

$a$ = augmented tube
$in$ = inlet
$s$ = smooth tube
$x$ = local



Downloaded 12 Dec 2010 to 193.140.21.150. Redistribution subject to ASME license or copyright; see http://www.asme.org/terms/Terms_Use.cfm

Table 1 Specification of test tubes

| Tube | $e$, mm | $p$, mm | $\alpha$, deg | $d$, mm | $L$, mm |
|---|---|---|---|---|---|
| 1 | 0.152 | 19.1 | 75.5 | 23.6 | 1829 |
| 2 | 0.305 | 19.1 | 75.5 | 23.6 | 1829 |
| 3 | 0.508 | 19.1 | 75.5 | 23.6 | 1829 |

the experimental loop, as shown for purification and degassing purposes. The reader is referred to other literature for a more detailed description of the experimental loop (Ravigururajan and Bergles, 1986). For tests where the water inlet temperature was less than 10°C, this experimental apparatus was modified slightly. Water from the laboratory chiller facility was used as the working fluid. The pressure in the chiller line was high enough and constant, that the pump was taken out of the experimental loop. No other modification was made to the rig: this included the flow, temperature, and pressure measurement sections.

The necessary data reduction was performed based on a segmental energy balance. The circumferential average linear wall temperature was calculated at each station and the fluid temperature at each station was found as

$$T_{out} = q_{in}L_{seg}/(L_{total}m) + T_{in}.$$

Estimating the fluid properties at the film temperature, the local heat transfer coefficient at any location, $x$, in the tube is given by the expression

$$q_{in}/L_x = h_x\pi d\Delta T_x.$$

The Nusselt number and Reynolds number were deduced from the expressions

$$\mathrm{Nu}_x = h_x d/k_x$$

and

$$\mathrm{Re}_x = 4m/\pi d\mu_x.$$

Finally the Fanning friction factor was found from the equation

$$f = \Delta P d\rho A^2/(2Lm^2)$$

where $r$ was taken to be the density at the mean bulk temperature. It may be noted that the envelope diameter as defined by Bergles et al. (1974) was used as the length scale for Re, Nu, and $f$. The envelope diameter is the maximum inside diameter (Fig. 1) for the tubes that are considered in this study. The increase in surface area due to surface disruptions is insignificant (less than 2 percent), especially for small roughness height and large $p/e$. This approach enables one to compare performances of an enhanced tube and a smooth tube of the same inside diameter and length.

The experimental uncertainty was calculated as recommended by Kline and McClintock (1953). Based on a 95 percent confidence uncertainty, the relative error for important quantities such as heat transfer coefficient, pressure drop, Reynolds number, and Prandtl number were determined. The measurement uncertainties used in the method were as follows: water temperature and wall temperatures ± 0.6°C, water flow rate ± 0.35 kg/h, voltmeter accuracy ± 0.5 percent, and fluid properties ± 1 percent. The error analysis showed uncertainties of 5.1 percent for Reynolds number, 3.5 percent for Prandtl number, 5 percent for pressure drop, 7.1 percent for friction factor, and 3.65 percent for Nusselt number. In all experiments, the energy balances were attained within ±5 percent (most were achieved well within ±2 percent), and steady-state conditions were ensured when no significant variation in temperature or flow rate was noticed for ten minutes or more.

## Results and Discussion

**Smooth Tube.** The experiments were conducted over a Re range of approximately 2500 to 35,000, a range normally encountered in chillers and other heat exchangers. The apparatus, instrumentation, and procedure were checked by comparing pressure drop and heat transfer data on a smooth tube (Ravigururajan and Bergles, 1986) to data from the literature. The turbulent flow friction correlation by Petukhov and Popov (1963) agrees well with the data (Fig. 3); therefore, the apparatus and the instrumentation are ratified.

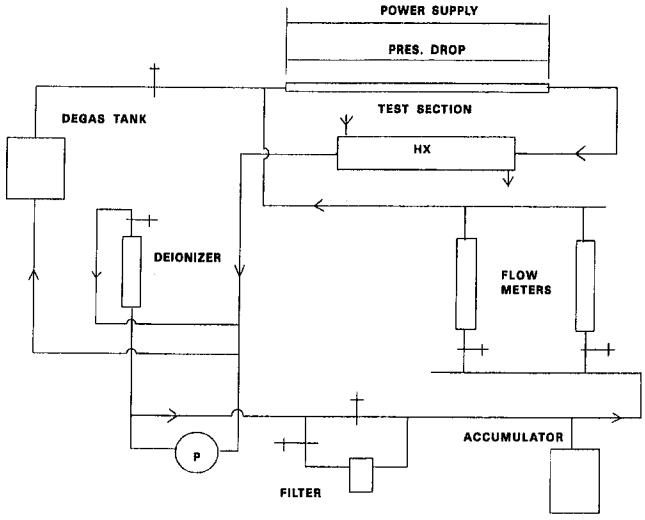



Fig. 2 A schematic diagram of the experimental rig

The heat transfer data (Fig. 3) were found to be in good agreement with the Petukhov and Popov (1963) correlation. The wall and the fluid bulk temperatures were such that the temperature dependency factor $(\mu_o/\mu_b)^{-0.11}$ as recommended by Kays and Crawford (1982), was very close to unity, and hence, not represented in the plot.

**Pressure Drop for Enhanced Tubes.** The pressure drop data for the three ribbed tubes were plotted as Fanning friction factors

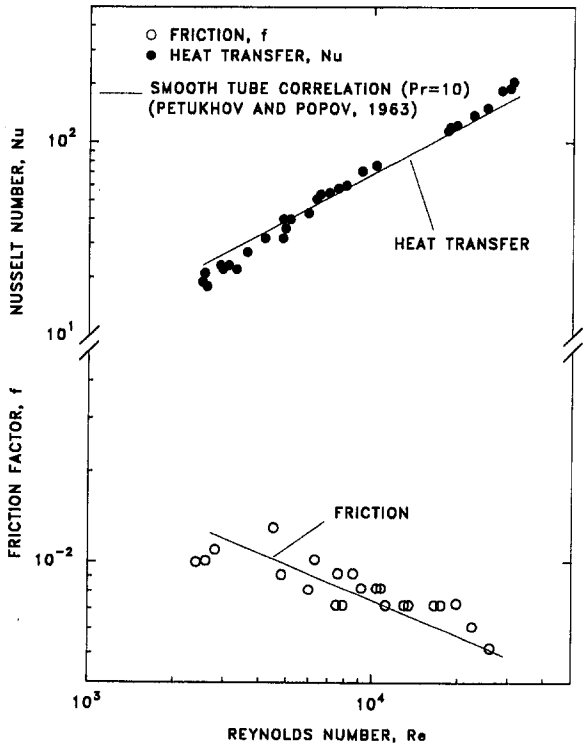



Fig. 3 Smooth tube friction and heat transfer results



Downloaded 12 Dec 2010 to 193.140.21.150. Redistribution subject to ASME license or copyright; see http://www.asme.org/terms/Terms_Use.cfm

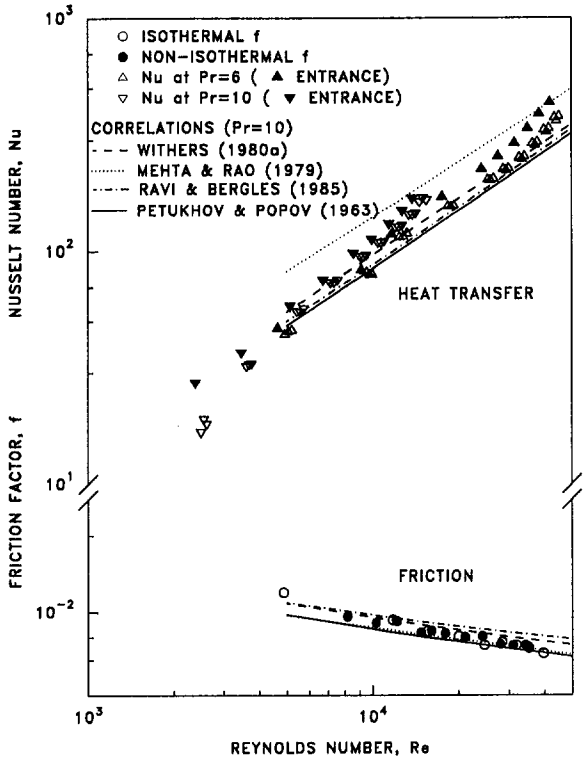



**Fig. 4 Friction and heat transfer results for Tube 1**

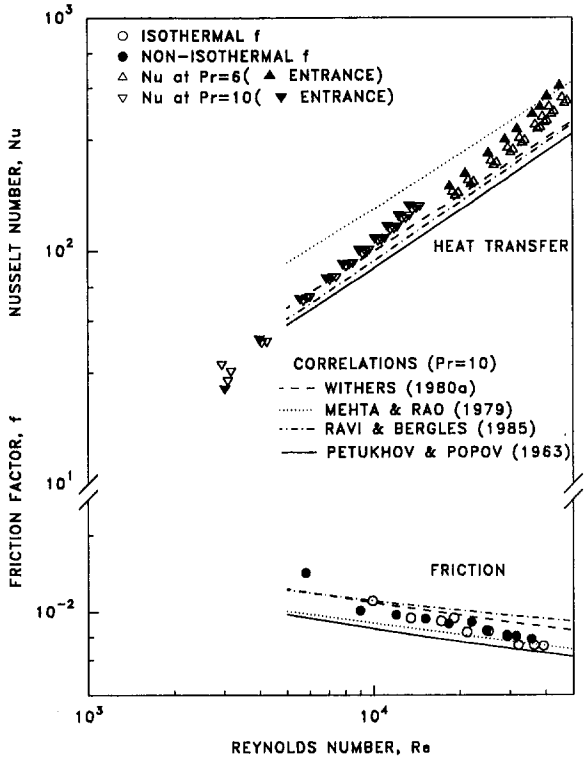



**Fig. 5 Friction and heat transfer results for Tube 2**

in Figs. 4–6. The Re range covered by the experiments depended on the temperature of the water. In this case also, as the viscosity of water decreased during heating, higher Reynolds numbers were attained for heated runs than for the isothermal tests. Flows up to or greater than 30,000 were tested, which were well into the turbulent region and of greatest significance to heat exchanger applications.

Figure 4 corresponds to data for Tube 1 ($e/d = 0.006$) and Fig. 5 for Tube 2 ($e/d = 0.012$). Comparing both sets of data indicates only marginal increase in friction factor for Tube 2 over Tube 1, despite the doubling of roughness height. On the other hand the data for Tube 3 ($e/d = 0.02$) show a marked increase in friction factor coefficient over the same Re range (Fig. 6). This figure shows that the friction factor decreases with Re, especially for Re greater than 10,000. While an increase in friction factor is to be anticipated, the plots seem to suggest that this increase depends not only on the increase in roughness height, but also the size of the roughness height itself. In other words, for the same percentage increase in roughness height, a greater pressure drop increase can be expected at large roughness height. Although the heat addition seems to have a slight influence on the friction factor, the difference can still be attributed to the experimental uncertainty.

The correlation of Ravigururajan and Bergles (1985) agrees well with the experimental data, with the deviation falling within 15 percent for the most part. Of the various correlations available in the literature, the well-known correlation of Withers (1980a) overpredicted the data for these tubes by a wider margin, particularly for Reynolds number less than 35,000. The prediction according to the correlation of Mehta and Rao (1979) is also higher than the data, by about 30 percent. In any case, caution must be exercised in interpreting the effectiveness of these correlations, since the geometries of the tubes tested in the various studies are slightly different and are fabricated by different manufacturers.

The increases in enhanced tube friction factor above smooth tube values, for spirally fluted tubes, have been found to be less than about 200 percent. This is a rather modest pressure drop penalty compared to other types of enhanced surfaces (e.g., repeated ribs) in the turbulent flow regime.

**Heat Transfer for Enhanced Tubes.** The heat transfer experimental data have been plotted, again, in Figs. 4–6. The tubes were especially selected to study the effects of roughness height,

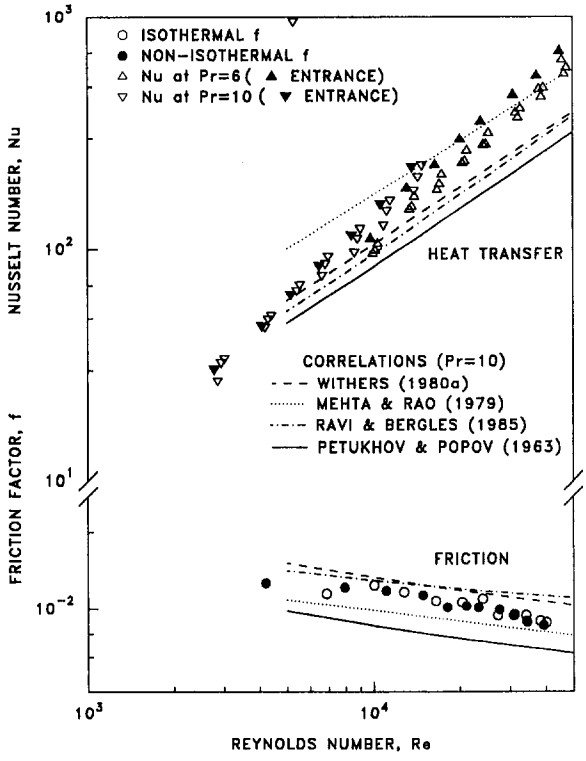



**Fig. 6 Friction and heat transfer results for Tube 3**



Downloaded 12 Dec 2010 to 193.140.21.150. Redistribution subject to ASME license or copyright; see http://www.asme.org/terms/Terms_Use.cfm

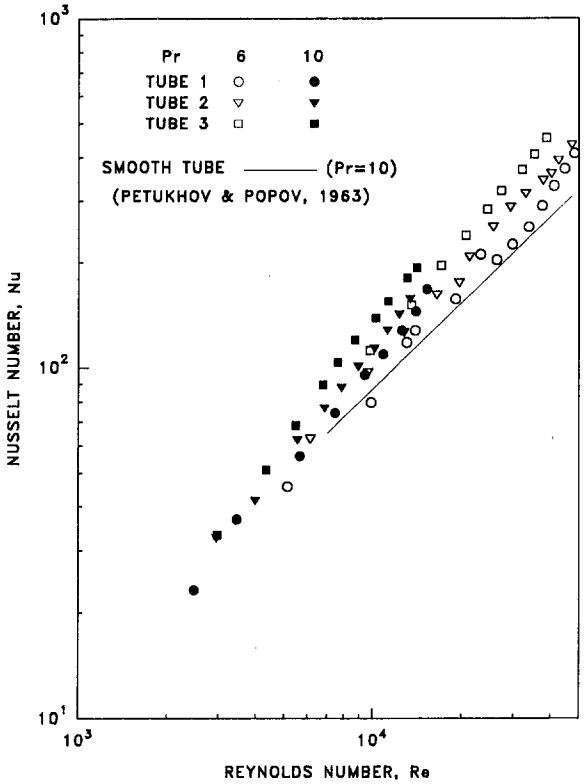



**Fig. 7 Average Nusselt number versus Reynolds number for Tubes 1, 2, and 3**

the single most important design parameter in the enhancement. Also, the bulk fluid temperature at inlet was maintained at about 22.5°C (72°F). The heat input to the test section was controlled such that the average bulk fluid temperature in the test section was 25°C. To simulate a condenser, the average fluid bulk temperature in the test section was maintained at 8°C (47°F).

The data are represented simply in terms of Nu and Re, for a specific Pr. This method was chosen because the correlations developed do not involve Pr in a traditional log-linear way. The various points refer to the local heat transfer coefficients, as measured at each axial station of the test section. Moreover, the heat transfer plots include two sets of data for the two temperature levels (25°C and 8°C), denoting the evaporator and condenser sections, respectively.

The positive influence of the Prandtl number on enhancement can be clearly seen in all three plots. The correlation of Withers (1980a) overpredicts the data for Re less than 30,000 and underpredicts the data for Re greater than 30,000. The correlation of Ravigururajan and Bergles (1986), on the other hand, predicts the values much more closely, even though the prediction is lower for Re less than 20,000. This heat transfer correlation (Eq. (4)) is able to predict data within 20 percent for the whole range of Re. The correlation of Rabas et al. (1988) (not shown in the plot) overpredicts the data by 30 percent at Re = 10,000 and underpredicts them by more than 50 percent for Re greater than 50,000.

An important inference that could be drawn from these plots is that there is a clear presence of entrance length effects on enhancement. The data points are grouped according to flow rate, with the initial data point being near the tube entrance. This is indicated by the increasing Nu along the axial stations for each experimental run. These entrance points exhibit a higher Nu for each flow rate. A more pronounced entrance effect can be noticed in Tube 3 ($e/d = 0.02$) than in Tube 1 ($e/d = 0.006$), indicating a possible relationship between the entrance length and the roughness height, and perhaps the pitch and the helix angle. The impact of Pr on the Nu in the entrance region is noticeable for all three tubes. Its influence is much more pronounced at lower values. The difference in Nu between the entrance region and the developed region is greater at Pr = 6 (solid triangles). At Pr = 10 this difference is minimal especially as the roughness height increases. An interesting observation is that the Nusselt number drops off below Re = 10,000. Figure 7 present the average Nusselt numbers for the last two axial positions, which can be considered to represent fully developed flow. They indicate a rather well-defined dependence of Nusselt number on roughness height, with the data for the roughest tube (Tube 3) lying farthest from the smooth tube curve.

The heat transfer enhancements with these three tubes were not as large as the friction factor increases, nor did they vary as widely. The values of Nu ranging from 70 to 80 at Re = 5000, increased to 350 to 400 at Re = 30,000, thus yielding an enhancement over the smooth tube of about 550 percent at lower Re flows and slightly more than 80 percent at the higher Reynolds numbers. The increase in heat transfer is much greater at a Pr of 6 than at Pr = 10 (data not shown). Several correlations were found to predict the experimental data with reasonable accuracy for the enhanced tubes; Eq. (4) was consistently able to estimate the friction factors and heat transfer coefficients quite accurately for all of the tubes. However, it may be pointed out that none of these established correlation is strictly valid for Tube 1 ($e/d = 0.006$). Although the tested Pr is within the range covered by these correlations, their applicability to a fluid that is close to the freezing point is not tested rigorously.

In comparing the performance of enhanced tubes with those of smooth tubes, it is necessary to take into account both the heat transfer increase and the corresponding pressure drop increase. Figure 8 shows the performance data of the three enhanced tubes in the form of an effectiveness parameter, $z$, which is defined as

$$z = h_a \cdot f_s / h_s / f_a.$$

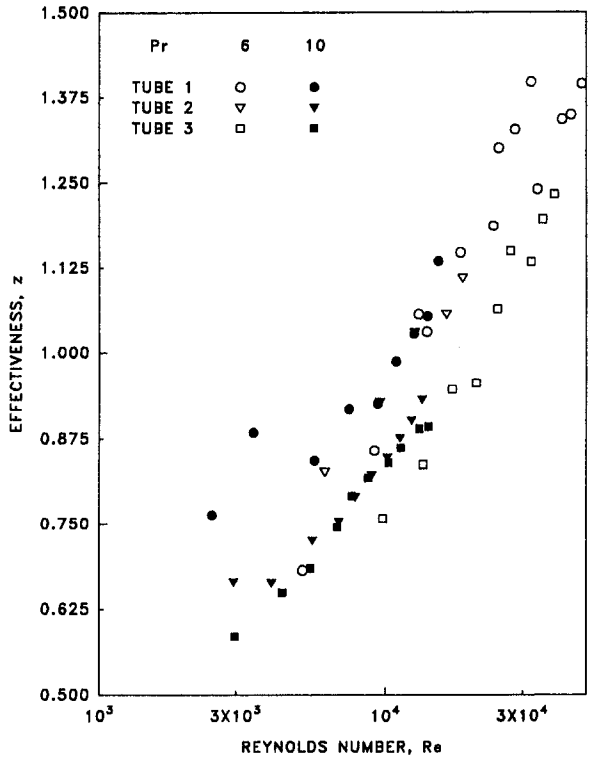



**Fig. 8 Effectiveness versus Reynolds number for Tubes 1, 2, and 3**



Downloaded 12 Dec 2010 to 193.140.21.150. Redistribution subject to ASME license or copyright; see http://www.asme.org/terms/Terms_Use.cfm

Physically, $z$ gives the ratio of the heat transfer to pressure drop increase of an enhanced tube over that of a smooth tube at the same Reynolds number. The data indicate that Tube 1, with the smallest roughness height, shows the greatest effectiveness. This is followed by less efficient performances of Tubes 2 and 3. This trend reinforces the belief that the smaller the roughness, the greater the overall efficiency. However, in actual systems, the operating conditions are governed by a variety of constraints. Various comparison methods have been proposed (Webb et al., 1971; Bergles et al., 1974). For example, a commonly employed criterion maximizes the heat transfer capacity of a tube with the associated constraints of constant pressure drop and surface area. This criterion, termed R-3 (Bergles et al., 1974) was evaluated for the three enhanced tubes at 25°C and 8°C. Figure 9 shows the reduced experimental data for the three enhanced tubes. The R-3 factor provides a common measure of the tube efficiency, with the assumption that the pumping power and the total heat exchanger area remain the same. The data in both the figures refer to the smooth-tube-equivalent Reynolds numbers.

It is interesting to note that the performances of Tubes 1 and 2 are inferior to that of Tube 3, even though the disruption is much smaller in Tubes 1 and 2. A possible explanation is that the very small $e/d$ used in Tube 1 may not be contributing to the separation and reattachment mechanism, but merely increasing the turbulence. This will increase the friction factor coefficient much more than the heat transfer coefficient, which is increased primarily by the reattachment of the viscous layers. One may notice that the performance of Tube 2 is closer to that of Tube 1 for Re of less than 15,000 and close to that of Tube 3 as flow Re increases further. This strongly suggests the influence of both Re and Pr on the optimum design parameters for the disruption.

This study deals with the enhanced tube performance for Pr = 10, a valuable extension to the existing data base. Industrial and commercial chillers use water at 5 to 10°C (Pr = 11.13 to 9.45). Also, it is well known that enhanced tubes are being used increasingly. The study shows that the existing correlation can indeed be employed in estimating the performance with reasonable accuracy (±20 percent). Of course, it is easy to develop yet another correlation based on the data, but such an exercise will be of limited use as the intended correlation may not be applicable for the wide varieties of other enhanced tubes. Hence, the focus on the suitability of some of the commonly employed correlations.

The paper shows that a distinct difference in performance exists in the entrance region. The prevailing notion is that the entrance length in enhanced tube flows is too short to affect the overall performance. The study seems to confirm this notion, but only under certain circumstances. When the roughness height is reduced as in tube 1, the entrance length may become significant. Since preferred optimum roughness height is around 0.02 × envelope diameter, the higher performance in the entrance region could prove to be beneficial. While the increase in performance is to be anticipated in the entrance region, the length of this region (15 to 18 × diameter) is significant. Consequently, the results suggest that the performance in the entrance region may warrant a closer look due to the more pronounced difference that is exhibited as Pr is decreased. Finally, the study once again provides data for very small roughness height ($e/d$ = 0.006), data for which are nonexistent in the open literature. The paper scrutinizes the performance of such a tube and compares it with tubes with higher roughness.

## Conclusion

Experiments were conducted for low-temperature water flows in enhanced tubes. The study offered data for a set of enhanced tubes for water flow at relatively low temperature and for very small $e/d$, that are unavailable in the open literature. The applicability of the correlations to chillers and other heat exchangers involving low temperature water has been shown to be very good. Although there is no study in the open literature that could be used for comparison, application of the most appropriate rope tube correlations indicate the suitability of these correlations for these flows, with Eqs. (3) and (4) performing better than other correlations.

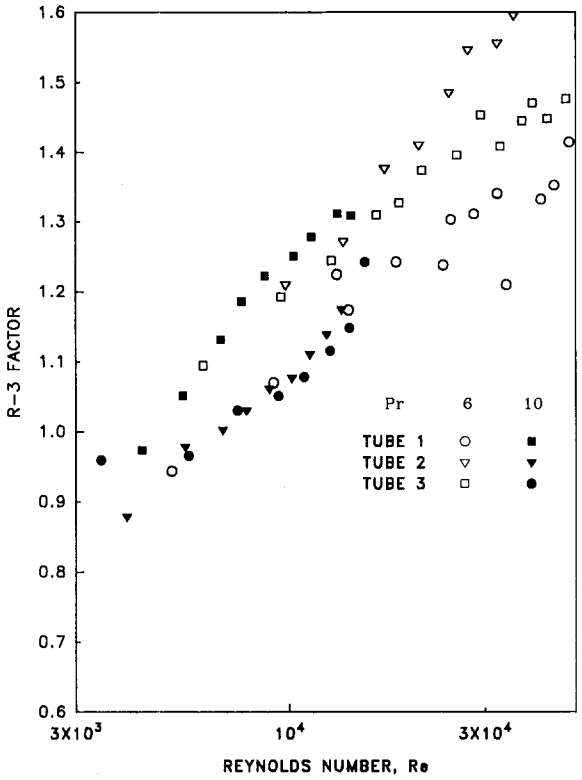



**Fig. 9 R-3 factor versus Reynolds number for Tubes 1, 2, and 3**

## Acknowledgments

The investigation was carried out at Iowa State University under a contract from the Department of Energy through Argonne National Laboratory. The authors wish to thank Dr. C. B. Panchal and Dr. T. Rabas for their comments during and after the execution of the project. Thanks are also due to Mr. A. Thomas, Program Manager for his support of this project.

## References

Bergles, A. E., 1988, "Some Perspectives on Enhanced Heat Transfer-Second-Generation Heat Transfer Technology," ASME JOURNAL OF HEAT TRANSFER, Vol. 110, pp. 1082–1096.

Bergles, A. E., Blumenkrantz, A. R., and Taborek, J., 1974, "Performance Evaluation Criteria for Enhanced Heat Transfer Surfaces," *Heat Transfer 1974*, JSME, Tokyo, Vol. II, pp. 239–243.

Kalinin, E. K., 1974, "Tubular Heat Exchangers With Bilateral Heat Transfer Augmentation and Calculation of a Heat Exchanger Under Unsteady Operating Conditions," *Heat Exchangers: Design and Theory Source Book*, N. Afgan and E. U. Schlunder, eds., Chap. 8, pp. 177–206.

Kays, X. X., and Crawford, Y. Y., 1982, *Convective Heat Transfer*, 2nd ed., McGraw-Hill, New York.

Kline, S. J., and McClintock, F. A., 1953, "Describing Uncertainties in Single-Sample Experiments," *Mechanical Engineering*, Vol. 75, Jan., pp. 3–8.

Li, H. M., Ye, K. S., Tan, Y. K., and Deng, S. J., 1982, "Investigation on Tube-Side Flow Visualization, Friction Factors and Heat Transfer Characteristics of Helical-Ridging Tubes," *Heat Transfer 1982, Proc. 7th Int. Heat Transfer Conf.*, Vol. 3, Hemisphere Publishing Corp., Washington, DC, pp. 75–80.

Marner, W. J., Bergles, A. E., and Chenoweth, J. M., 1983, "On the Presentation of Performance Data for Enhanced Tubes in Shell-and-Tube Heat Exchangers," ASME JOURNAL OF HEAT TRANSFER, Vol. 105, pp. 358–365.

Mehta, M. H., and Raja, Rao, M., 1979, "Heat Transfer and friction Characteristics of Spirally Enhanced Tubes for Horizontal Condensers," *Advances in Enhanced Heat Transfer*, San Diego, CA, pp. 11–22.



Downloaded 12 Dec 2010 to 193.140.21.150. Redistribution subject to ASME license or copyright; see http://www.asme.org/terms/Terms_Use.cfm

Nakayama, M., Takahashi, K., and Daikoku, T., 1983, "Spiral Ribbing to Enhance Single-Phase Heat Transfer Inside Tubes," *Proc. ASME–JSME Thermal Engineering Joint Conf.*, Honolulu, HI, pp. 365–372.

Petukhov, B. S., and Popov, V. N., 1963, "Theoretical Calculation of Heat Exchange and Frictional Resistance in Turbulent Flow in Tubes of an Incompressible Fluid With Variable Physical Properties," *High Temperature 1*, pp. 69–83.

Rabas, T. J., Bergles, A. E., and Moen, D. L., 1988, "Heat Transfer and Pressure Drop Correlations for Spirally Grooved (Rope) Tubes Used in Surface Condensers and Multistage Flash Evaporators," *Proc. National Heat Transfer Conference*, ASME HTD-Vol. 96; pp. 693–704.

Ravigururajan, T. S., and Bergles, A. E., 1985, "General Correlations for Pressure Drop and Heat Transfer for Single-Phase Turbulent Flow in Internally Ribbed Tubes," *Augmentation of Heat Transfer in Energy Systems*, ASME HTD-Vol. 52, pp. 9–20.

Ravigururajan, T. S., and Bergles, A. E., 1986, "An Experimental Verification of General Correlations for Single Phase Turbulent Flow in Ribbed Tubes," *Advances in Heat Exchanger Design*, ASME HTD-Vol. 66, pp. 1–11.

Thomas, L. C., 1992, *Heat Transfer*, Prentice-Hall, Inc., New Jersey.

Webb, R. L., 1969, "Turbulent Heat Transfer in Tubes Having Two-Dimensional Roughness, Including the Effect of Prandtl Number," Ph.D Thesis, University of Minnesota.

Webb, R. L., Eckert, E. R. G., and Goldstein, R. J., 1971, "Heat Transfer and Friction in Tubes With Repeated-Rib Roughness," *Int. J. Heat Mass Transfer*, Vol. 14, pp. 601–617.

Withers, J. G., 1973, "Heat Transfer Tube Having Multiple Internal Ridges," U.S. Patent 3,779,312.

Withers, J. G., 1980a, "Tube-Side Heat Transfer and Pressure Drop for Tubes Having Helical Internal Ridging With Turbulent/Transitional Flow of Single-Phase Fluid. Part 1. Single-Helix Ridging," *Heat Transfer Engineering 2*, No. 1, pp. 48–58.

Withers, J. G., 1980b, "Tube-Side Heat Transfer and Pressure Drop for Tubes Having Helical Internal Ridging With Turbulent/Transitional Flow of Single-Phase Fluid. Part 2. Multiple-Helix Ridging," *Heat Transfer Engineering 2*, No. 2, pp. 43–50.

Yorkshire Imperial Metals, 1982, "YIM Heat Exchanger Tubes: Design Data for Horizontal Rope Tubes in Steam Condensers," Technical Memorandum 3, Yorkshire Imperial Metals, Ltd., Leeds, United Kingdom.



Downloaded 12 Dec 2010 to 193.140.21.150. Redistribution subject to ASME license or copyright; see http://www.asme.org/terms/Terms_Use.cfm

# Local Friction and Heat Transfer Behavior of Water in a Turbulent Pipe Flow With a Large Heat Flux at the Wall

E. Choi

Y. I. Cho

Department of Mechanical Engineering and Mechanics, Drexel University, Philadelphia, PA 19104

*The present study investigated the behavior of friction and heat transfer coefficients of water flowing turbulently in a relatively long (i.e., 950 diameter long) circular pipe. When a large heat flux was applied at the wall, the viscosity of water significantly decreased along the axial direction due to the increasing temperature of water. A concept of a "redeveloping region" was introduced, where the local heat transfer coefficient increased while the local friction coefficient decreased due to the above-mentioned viscosity change. The present study proposed the use of local bulk-mean temperature to determine local Nusselt numbers by using local Reynolds ($Re_{LB}$) and Prandtl numbers ($Pr_{LB}$), a method that automatically took into account the effect of axial viscosity change on the evaluation of local heat transfer coefficients. A new turbulent heat transfer correlation for the prediction of the local Nusselt number is given as* $Nu_x = 0.00425\, Re_{LB}^{0.979}\, Pr_{LB}^{0.4} (\mu_w/\mu_b)^{-0.11}$.

## Introduction

The behavior of turbulent heat transfer in a circular pipe has been studied for the last 80 years. Researchers have usually concentrated on obtaining pressure drops and heat transfer coefficients in the so-called "fully developed region." They assumed that there was a thermally fully developed region at some distance from the starting point of heating. Clearly, when the amount of heat transfer at the wall is relatively small, the assumption of the fully developed flow is valid.

The present study questions whether the thermally fully developed region exists in a relatively long circular pipe for a large heat flux case. For example, in electronic packaging that uses liquid-cooling modules made of microchannels to remove heat from chips, the understanding of the local heat transfer behavior becomes extremely important in order to maintain chip temperatures at a safe level. Generally, the viscosity of liquid decreases with increasing temperature. When there is a significant decrease in the viscosity along the heating test section, the local Reynolds numbers vary significantly, i.e., by 30–50 percent. In this case, the concept of the fully developed flow may be no longer valid. Further, if one wants to predict local wall temperature as in the above chip cooling example, there is a need for a new correlation, which includes the effect of viscosity variation along the axial direction in order to determine local heat transfer behavior more accurately.

There are a number of well-known correlations for turbulent friction and heat transfer coefficients in both the developing and fully developed flow regions. When there is a large temperature difference between bulk fluid and wall, the effect of viscosity change along the radial direction on friction and heat transfer behavior was accommodated by introducing a dimensionless group, $\mu_w/\mu_b$, which is the ratio of fluid viscosities at average wall and fluid temperatures. However, to the best of our knowledge, the effect of viscosity variation along the axial direction on the local friction and heat transfer performance of a fluid in a relatively long pipe has not been reported by any previous investigators. The objective of the present study was to investigate the axial-viscosity-change effect on the determination of local friction and heat transfer coefficients when there is a large temperature variation of fluid along the axial direction.

## Background

The turbulent heat transfer behavior of a constant-property fluid in a fully developed region has been studied analytically and experimentally by a number of investigators. The Fanning friction coefficient, $f$, can be predicted by the Blasius equation (Kays and Crawford, 1980), which assumes the one-seventh power-law velocity profile:

$$f = 0.079\, \mathrm{Re}^{-0.25}. \tag{1}$$

The Nusselt number of a fully developed turbulent flow was reported by Petukhov (1970), who used an analogy between friction and heat transfer behavior, as follows:

$$\mathrm{Nu} = \frac{\mathrm{RePr}(f/8)}{1.07 + 12.7(\mathrm{Pr}^{2/3} - 1)\sqrt{f/8}} \tag{2}$$

where

$$f = (1.82 \log_{10} \mathrm{Re} - 1.64)^{-2}. \tag{3}$$

This Petukhov correlation was modified by Gnielinski (1976), who used experimental data in a Reynolds number range between 2300 and 10,000, as follows:

$$\mathrm{Nu} = \frac{(f/8)(\mathrm{Re} - 1000)\,\mathrm{Pr}}{1 + 12.7\sqrt{f/8}\,(\mathrm{Pr}^{2/3} - 1)}. \tag{4}$$

The Dittus–Boelter correlation (Dittus and Boelter, 1930) is one of the most widely used experimental correlations to predict the Nusselt number. Dittus and Boelter summarized all the available data in 1930, and averaged them to get their correlation, which was primarily based on the data from McAdams and Frost (1922, 1924), and from Morris and Whitman (1928). For a heating case, the Dittus–Boelter correlation becomes

$$\mathrm{Nu} = 0.023\, \mathrm{Re}^{0.8}\mathrm{Pr}^{0.4}. \tag{5}$$

Hartnett (1955) performed experiments with water and oil to obtain turbulent heat transfer coefficients in the thermally developing region of a circular pipe flow. He found that the heat trans-

Contributed by the Heat Transfer Division for publication in the JOURNAL OF HEAT TRANSFER. Manuscript received by the Heat Transfer Division July 1993; revision received July 1994. Keywords: Forced Convection, Measurement Techniques. Associate Technical Editor: R. Viskanta.



Copyright © 1995 by ASME

Downloaded 12 Dec 2010 to 193.140.21.150. Redistribution subject to ASME license or copyright; see http://www.asme.org/terms/Terms_Use.cfm

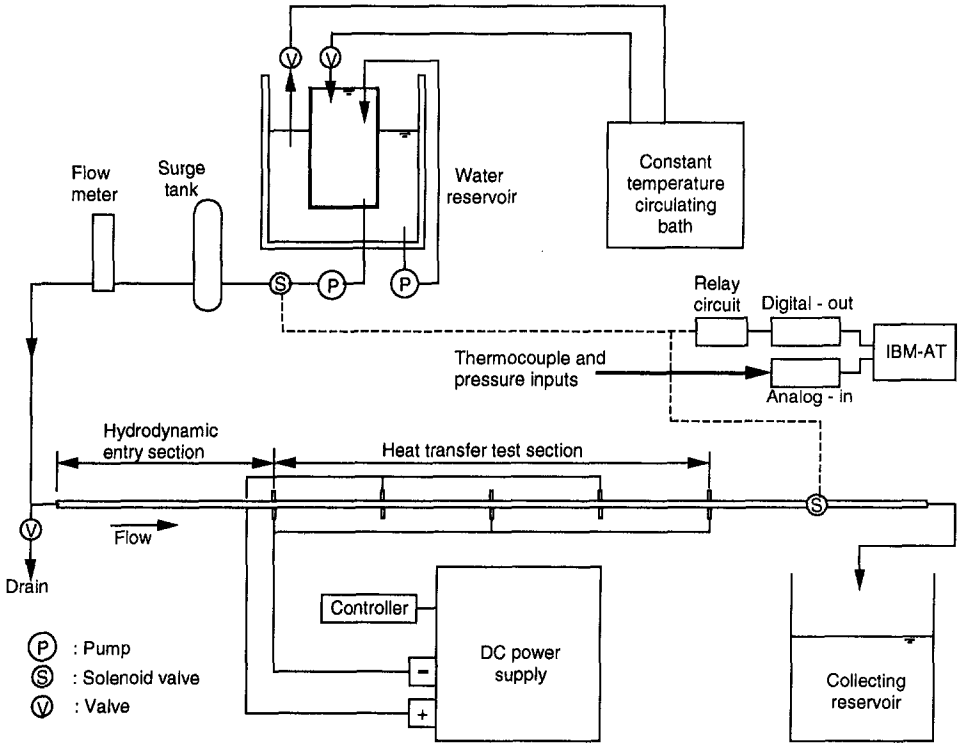



**Fig. 1 Schematic diagram of the experimental apparatus**

fer coefficient sharply decreased at the starting point of heating, reaching an asymptotic value at $x/D = 10-15$, and then gradually increased. He suggested that the asymptotic heat transfer coefficient, $h_s$, could be used as the thermally fully developed heat transfer coefficient. Because Hartnett used relatively small heat fluxes at the wall, he did not consider the viscosity change along the axial and radial directions.

Two methods have been used to consider the effect of the radial viscosity change on the Fanning friction coefficient and the Nusselt number: the reference temperature method and the property ratio method. Deissler (1951, 1954) reported that if all the properties were calculated at a reference temperature, the effect of the radial viscosity change could be neglected. Sieder and Tate (1936) reported that a property ratio of $(\mu_w/\mu_b)^{-0.14}$ could correct the effect of the radial viscosity change on heat transfer.

Allen (1959) and Allen and Eckert (1964) performed a systematic experiment in a thermally developing flow region to find the effect of the temperature difference between wall and bulk-mean fluid on the Nusselt number (and friction coefficients). They obtained the so-called "zero-heating-rate" heat transfer coefficients by extrapolating the values with various heating rates, and good agreements were found when compared with available analytical solutions. They reported that the effect of the radial viscosity change on the friction coefficient could be represented by $(\mu_w/\mu_b)^{0.25}$. For the heat transfer coefficient, they found that the exponent in the property ratio depended on the Reynolds number. Subsequently, Petukhov (1970) proposed a new exponent of $-0.11$ for the heat transfer coefficient instead of Sieder and Tate's $-0.14$. However, a method to include the effect of axial viscosity change on heat transfer correlations has not been fully developed.

## Experimental Apparatus

Figure 1 shows the schematic diagram of the present experimental apparatus, which consisted of a reservoir tank, a surge tank, a pump, a flow meter, a static mixer, a constant-temperature circulating bath, a hydrodynamic entry section, a main heat transfer test section, a collecting reservoir, and a DC power supply. The test section was made up of stainless steel tubing of 1.016

## Nomenclature

$D$ = inside diameter
$f$ = friction coefficient
$h$ = convection heat transfer coefficient
$h_s$ = asymptotic convection heat transfer coefficient
$k$ = thermal conductivity
Nu = average Nusselt number
$\mathrm{Nu}_{xc}$ = corrected local Nusselt number defined in Eq. (8)
$\Delta P$ = pressure drop
$\Delta P_{50}$ = pressure drop over every 50 diameter distance along test section
Pr = Prandtl number
$q''$ = heat flux from wall
Re = Reynolds number
$T_b$ = local bulk-mean temperature
$T_{iw}$ = inner wall temperature
$V$ = mean fluid velocity
$x$ = axial distance
$\mu_b$ = viscosity at bulk-mean temperature
$\mu_w$ = viscosity at wall temperature
$\tau_w$ = wall shear stress
$\rho$ = density

**Subscripts**

$c$ = corrected for radial viscosity change
$LB$ = based on local bulk-mean temperature
$x$ = local



Downloaded 12 Dec 2010 to 193.140.21.150. Redistribution subject to ASME license or copyright; see http://www.asme.org/terms/Terms_Use.cfm

cm ID. In order to use the maximum power of 24 kW in the DC power supply, the heat transfer tube was electrically (not physically) divided into four zones connected in a parallel circuit as shown in Fig. 1.

Nineteen pressure taps were installed every 50 diameters along the test section. Local pressures were measured differentially between every two adjacent pressure taps by using two Scanivalve switch wafers and a Validyne DP103-18 pressure transducer with a 0.5 psi diaphragm; this method allowed for all the pressure measurements to fall in a similar range and thus significantly increased the measuring accuracy.

Twenty-six thermocouples were cemented on the outside surface of the tube along the heating test section. All the temperature and pressure data were recorded directly into an IBM PC through a 16-channel, 16-bit high-resolution Omega data acquisition system. Calibration results of the pressure transducer, thermocouples, and others such as flowmeter and DC power supply are given elsewhere (Choi, 1993).

## Results and Discussion

The accuracy of the pressure measuring system was checked by measuring the local pressure drop over every 50 diameters, $\Delta P_{50}$, along the test section when heating was not applied at the wall. Fanning friction coefficients were calculated from the pressure drop data and compared with analytical predictions. The Fanning friction coefficients obtained from the present experiments gave excellent agreement with the predicted values using the Blasius equation, confirming the validity of the present experimental test and data reduction procedure (Choi, 1993).

Figure 2 shows the results of pressure drop measurements for the case of constant heat fluxes supplied in the heating test section. For the case of zero heating rate, the local pressure drop was uniform over the entire test section (see square symbols in Fig. 2). With heating, the pressure drop abruptly decreased at the starting point of heating, i.e., $x/D = 0$, and gradually decreased along the axial direction. This phenomenon can be attributed mainly to the local bulk-mean-temperature increase along the test section (i.e., axial-viscosity-change effect).

Figure 3($a$) presents local friction coefficients as a function of local bulk-mean Reynolds number, $\mathrm{Re}_{LB}$, which is defined at the local bulk-mean temperature of water for four different heating rates (i.e., from 3.086 kW to 12.56 kW). As the heating rate increased, the local friction coefficient decreased, indicating the effect of the radial viscosity change on the friction coefficient. Following Allen and Eckert's approach, i.e., using $(\mu_w/\mu_b)^{0.25}$, the effect of the radial viscosity change was corrected in the calculation of the friction coefficient; the corrected friction coefficient result is plotted in Fig. 3($b$). All the data fell on one

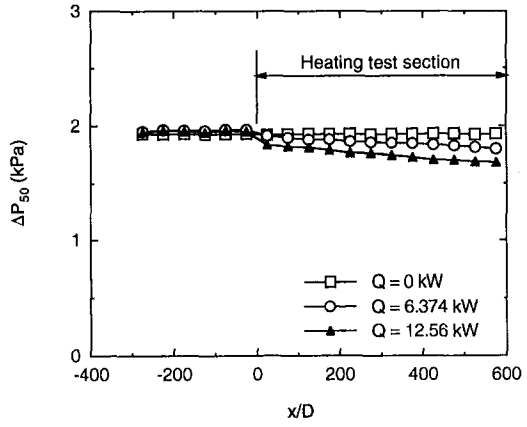



**Fig. 2 Local pressure drop profiles measured over every 50 diameters along the test section**

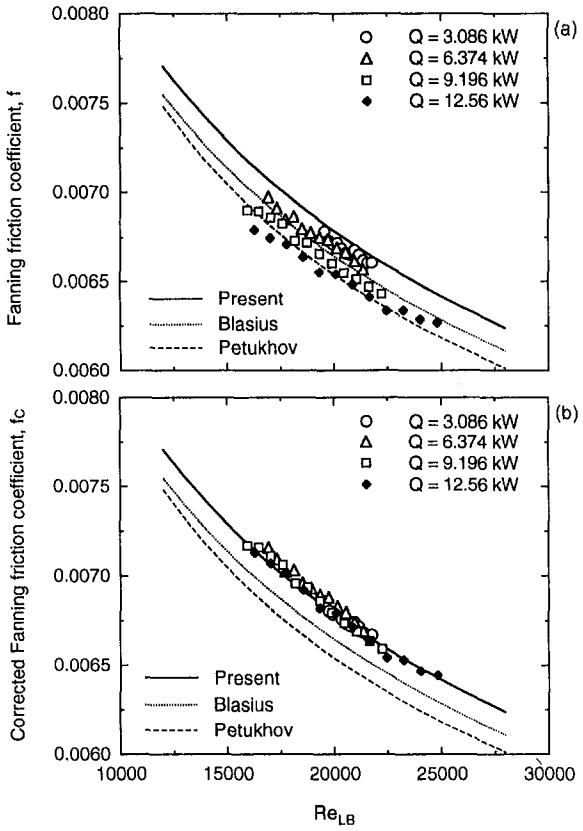



**Fig. 3 (*a*) Local friction coefficients in redeveloping region along the heating test section; (*b*) local friction coefficients corrected for radial viscosity change**

curve (i.e., solid line) that was consistently 2.1 percent higher than the Blasius correlation. Thus, in the redeveloping region, the local friction coefficients can be predicted by using the correlation obtained from the experiments without heating if the Reynolds number is calculated at the local bulk-mean temperature.

Figure 4($a$) shows the local Nusselt numbers in the redeveloping region of $37.5 < x/D < 587.5$ for two different heating rates. The local Nusselt number, $\mathrm{Nu}_x$, is defined as follows:

$$\mathrm{Nu}_x = \frac{h_x D}{k} \tag{7}$$

where

$$h_x = \frac{q''}{(T_{iw} - T_b)}.$$

The local inner wall temperature, $T_{iw}$, was calculated from the measured local outer wall temperature, $T_{ow}$, by a heat conduction equation with uniform heat generation in the tube wall. The local bulk-mean temperature, $T_b$, was calculated from the measured bulk-mean temperature of water at the inlet and outlet of the test section.

The average Prandtl and Reynolds numbers in the redeveloping region were 6.12 and 19,220 for a heating rate of 9.196 kW; 5.74 and 20,740 for a heating rate of 12.56 kW, respectively. The measured local Nusselt numbers increased along the test section. The rate of increase in the Nusselt number was greater for the higher heating rate case (i.e., $Q = 12.56$ kW), a phenomenon that can be attributed to the large local bulk-mean-temperature increase. If an average Nusselt number based on average wall and fluid temperatures had been used for each heating rate, the corresponding Nusselt number would have been overestimated



Downloaded 12 Dec 2010 to 193.140.21.150. Redistribution subject to ASME license or copyright; see http://www.asme.org/terms/Terms_Use.cfm

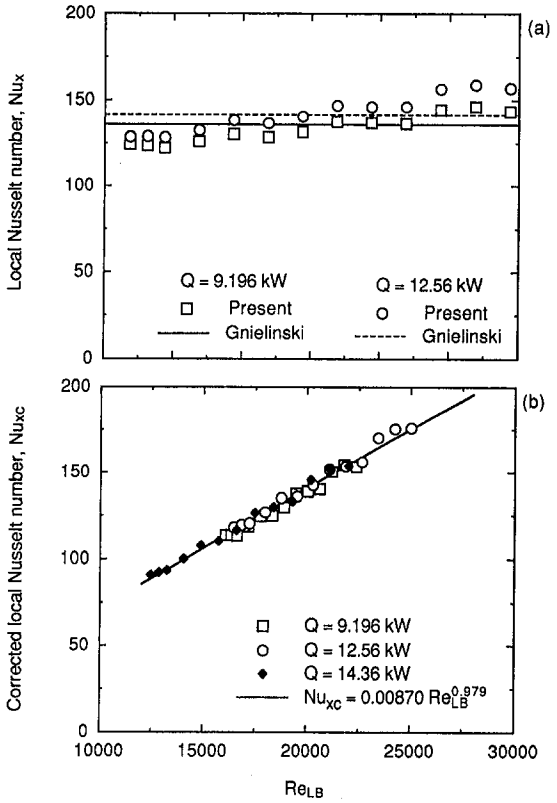



**Fig. 4 (*a*) Local Nusselt numbers in redeveloping region. Average Prandtl and Reynolds numbers were 6.12 and 19,220 for a heating rate of 9.196 kW; 5.74 and 20,740 for 12.56 kW. (*b*) Local Nusselt numbers corrected for radial and axial viscosity changes versus local Reynolds numbers.**

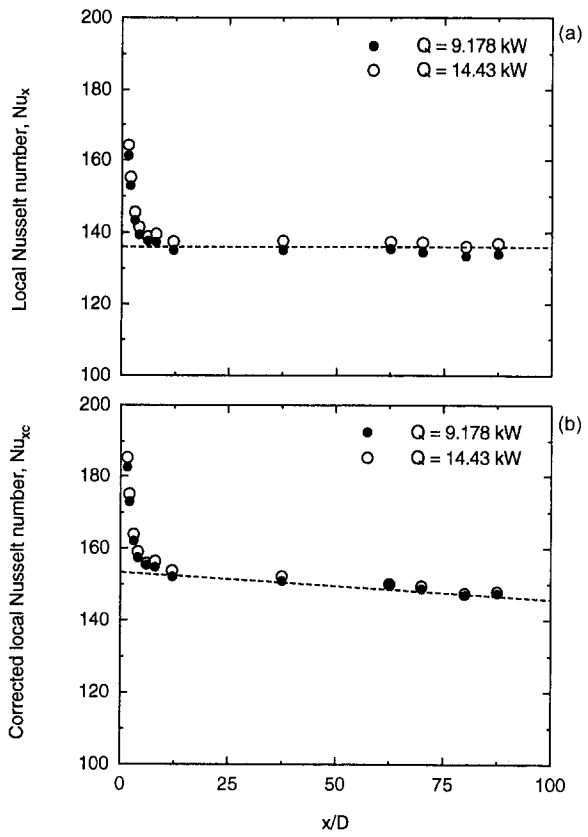



**Fig. 5 (*a*) Local Nusselt numbers in thermally developing region. Average Prandtl and Reynolds numbers were 5.868 and 19,020 for heating rate of 9.18 kW; 5.819 and 19,190 for 14.43 kW. (*b*) Local Nusselt numbers corrected for radial viscosity change.**

upstream and underestimated downstream as demonstrated by solid and dashed lines (see Gnielinski, Fig. 4*a*).

Figure 4(*b*) shows the corrected local Nusselt numbers, $Nu_{xc}$, as a function of the local Reynolds number, $Re_{LB}$, calculated based on local bulk-mean fluid temperatures. It is of note that the effects of the radial viscosity change and Prandtl number were eliminated in this figure in order to show the effect of the Reynolds number on the local Nusselt number.

$$Nu = Nu_x(\mu_w/\mu_b)^{0.11}\left(\frac{6}{Pr_{LB}}\right)^{0.4} = 0.0087\ Re_{LB}^{0.979} \qquad (8)$$

In order to predict the local Nusselt number in the thermally redeveloping region, a new turbulent heat transfer correlation that agreed with the present experimental data was obtained through linear regression analysis as follows:

$$Nu_x = 0.00425\ Re_{LB}^{0.979} Pr_{LB}^{0.4}(\mu_w/\mu_b)^{-0.11} \qquad (9)$$

Figure 5(*a*) presents the local Nusselt numbers for two different heating rates of 9.178 and 14.43 kW. The Nusselt number profile in the region of $12 < x/D < 87.5$ appears to be almost horizontal (i.e., see the dashed line in Fig. 5*a*), a phenomenon that led many researchers to believe that they had a thermally fully developed flow. We speculate that the constant Nusselt number was the combined result of the three following effects: the thermally developing effect, the radial-viscosity-change effect, and the axial-viscosity-change effect. In order to verify this speculation, the radial-viscosity-change effect was corrected and the results are given in Fig. 5(*b*), which shows a gradual decrease in the local Nusselt numbers (i.e., see the dashed line in Fig. 5*b*), indicating that the flow is still developing in this region (i.e., $25 < x/D < 85$). In other words, the horizontal Nusselt number profile in Fig. 5(*a*) does not indicate a thermally fully developed flow, but rather shows the net result of the decreasing Nusselt number caused by the thermally developing flow and the increasing Nusselt number caused by the viscosity change along the radial and axial directions.

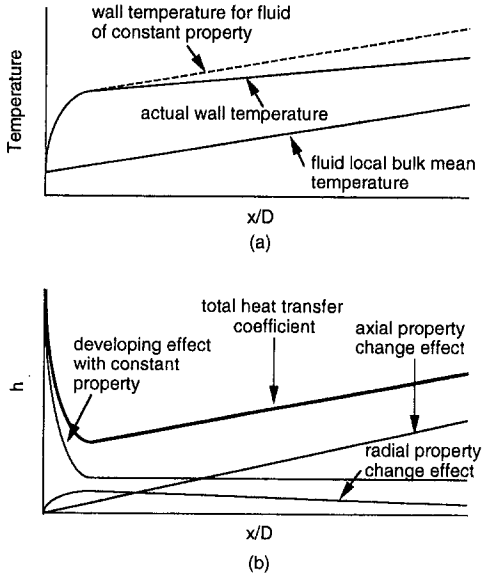



**Fig. 6 (*a*) Qualitative sketch of wall and bulk-mean fluid temperature profiles along the axial direction. Dashed line represents wall temperature with a constant property fluid. (*b*) Corresponding convective heat transfer coefficient along the axial direction.**



Downloaded 12 Dec 2010 to 193.140.21.150. Redistribution subject to ASME license or copyright; see http://www.asme.org/terms/Terms_Use.cfm

Figure 6 shows qualitatively the wall and bulk-mean fluid temperatures and the corresponding local heat transfer coefficient for a fluid flowing turbulently in a circular tube with a constant heat flux boundary condition. The local bulk-mean temperature of the fluid increases linearly, and its slope is determined by the heating rate at the wall. The local wall temperature is determined by the combined result of three effects: the developing effect, the radial-viscosity-change effect, and the axial-viscosity-change effect.

The developing flow effect is predominant in a thermal entrance region, where the local heat transfer coefficient decreases rapidly. Beyond the thermal entrance region, the local heat transfer coefficient could have remained constant if there had not been any changes in the viscosity of a test fluid. However, the viscosity of water in the present heating experiment can decrease significantly along both the radial and axial directions. The former causes a high velocity gradient at the wall, thereby increasing the local heat transfer coefficient. The latter increases the local Reynolds number, thus increasing the local heat transfer coefficient. In summary, the total heat transfer coefficient gradually decreases in the thermally developing region, reaching an asymptotic value, and then increases afterward in the "redeveloping region."

It is of note that Wolf (1959) conducted similar experiments with air and carbon dioxide in a thermal entrance region of a circular duct with large gas to wall temperature differences. In Wolf's cooling experiments with gas, gas temperature decreased significantly along the axial direction, thereby increasing local Reynolds numbers. Similarly, in the present heating experiment with water, water temperature increased, thus increasing local Reynolds number along the axial direction also. It is of note that gas viscosity increases with temperature, whereas liquid viscosity decreases.

Wolf found that the local Nusselt number decreased very rapidly in the thermal entrance region. Beyond $x/D$ equal to approximately 15–20, the local Nusselt numbers increased along the axial direction for cooling cases and decreased for heating cases. Wolf attributed these axial variations of the local Nusselt numbers solely to thermal-conductivity changes of gas. Although the thermal conductivity of gas decreased, the local heat transfer coefficient and thus the Nusselt number can also be affected by the variation of gas viscosity axially. For example, when air cools from 700 to 500°C as in a typical cooling experiment in Wolf, the thermal conductivity of air decreases from 0.0524 to 0.0407 W/mK, whereas the dynamic viscosity of air decreases from 0.0339 to 0.027 mPas. Hence, the Prandtl number changes very little, i.e., from 0.695 to 0.684.

When one considers local Nusselt numbers as a function of local Reynolds and Prandtl numbers, the effect of the latter must be very small in Wolf's experiments because the Prandtl number did not change much. In the present experiment, the increase in the thermal conductivity of water along the axial direction is much smaller than the decrease in the dynamic viscosity of water. Therefore, the present study concludes that the changes in the local Nusselt number should be attributed to "redeveloping flow" or an increase in the local Reynolds numbers.

## Uncertainty Analysis

The accuracy of temperature readings in the present study was ±0.1°C, which could cause a maximum ±0.3 percent error in the calculation of the viscosity of water. The error in the measurement of the inner diameter of the test section was 0.1 percent. The mean velocity of water was calculated from a measured volume flow rate, which had approximately 0.4 percent error. The maximum error in the measurement of the pressure drop over every 50 diameters was less than 0.5 percent. The corresponding uncertainties for the Reynolds number and the friction coefficient were 0.8 and 1.3 percent, respectively.

The error for heat flux measurement usually depends on the heat loss from the test section to the environment. The total heat supplied by a DC power supply was compared with $\dot{m}C_p\Delta T$ and the difference was less than ±2 percent. As the heating rate decreased, the error in the temperature difference measurement between the wall and water increased to ±2 percent in the smallest heating rate in the present study. The corresponding uncertainty for the Nusselt number was ±4 percent. More detailed descriptions on the uncertainty analysis are given elsewhere (Choi, 1993).

## Conclusions

A long heating test section (627 diameter length) heated electrically with a uniform heat flux boundary condition was constructed in order to observe the behavior of friction and heat transfer coefficients of water flowing turbulently beyond a thermally developing region. For large heat flux cases, the viscosity of water significantly decreased, thereby increasing the local Reynolds number along the axial direction. By defining the local Reynolds and Prandtl numbers at the local bulk-mean temperature, the effect of viscosity changes due to temperature changes along both the radial and axial directions could be automatically taken into account in the correlation of local friction and heat transfer coefficients. More specifically, the following conclusions may be drawn:

1 The conventional thought on the thermally fully developed flow was examined by carefully studying the effect of both the radial and axial viscosity changes on the local heat transfer coefficient. Asymptotic heat transfer results for the thermally fully developed flow case reported in the literature represent the combined result of three effects: the developing effect, the radial-viscosity-change effect, and the axial-viscosity-change effect.
2 For the case of large heat flux at the wall, the axial viscosity of water could significantly decrease, increasing the local Reynolds number (i.e., by 30–40 percent in the present study) along the axial direction. In this case, the heat transfer section is mostly dominated by a so-called "redeveloping region," where the local Nusselt number gradually increases. Well-known turbulent heat transfer correlations for the thermally fully developed flow proposed by Dittus and Boelter, Petukhov, and Gnielinski cannot predict the local Nusselt numbers.
3 The present study proposes the use of local bulk-mean temperature to determine local Nusselt numbers by using local Reynolds and Prandtl numbers. A new turbulent heat transfer correlation for the prediction of the local Nusselt number is given as $\mathrm{Nu}_x = 0.0045\ \mathrm{Re}_{LB}^{0.979}\ \mathrm{Pr}_{LB}^{0.4}(\mu_w/\mu_b)^{-0.11}$.

## Acknowledgments

The support of this work by the U.S. Department of Energy, Office of Conservation and Renewable Energy is gratefully acknowledged.

## References

Allen, R. W., 1959, "Measurements of Friction and Local Heat Transfer for Turbulent Flow of a Variable Property Fluid (Water) in a Uniformly Heated Tube," Ph.D thesis, University of Minnesota.

Allen, R. W., and Eckert, E. R. G., 1964, "Friction and Heat-Transfer Measurements to Turbulent Pipe Flow of Water (Pr = 7 and 8) at Uniform Wall Heat Flux," ASME JOURNAL OF HEAT TRANSFER, Vol. 86, pp. 301–310.

Choi, E., 1993, "Forced Convection Heat Transfer With Water and Phase-Change-Material Slurries: Turbulent Flow in a Circular Tube," Ph.D thesis, Drexel University, Philadelphia, PA.

Deissler, R. C., 1951, "Investigation of Turbulent Flow and Heat Transfer in Smooth Tubes, Including the Effects of Variable Fluid Properties," ASME JOURNAL OF HEAT TRANSFER, Vol. 73, pp. 101–107.

Deissler, R. C., 1954, "Heat Transfer and Fluid Friction for Fully Developed Turbulent Flow of Air and Supercritical Water With Variable Fluid Properties," ASME JOURNAL OF HEAT TRANSFER, Vol. 76, pp. 73–85.



Downloaded 12 Dec 2010 to 193.140.21.150. Redistribution subject to ASME license or copyright; see http://www.asme.org/terms/Terms_Use.cfm

Dittus, F. W., and Boelter, L. M. K., 1930, "Heat Transfer in Automobile Radiators of the Tubular Type," *Univ. Calif. (Berkeley) Pub. Eng.*, Vol. 2, pp. 443–461.

Gnielinski, V., 1976, "New Equations for Heat and Mass Transfer in Turbulent Pipe and Channel Flow," *International Chemical Engineering*, Vol. 16, No. 2, pp. 359–368.

Hartnett, J. P., 1955, "Experimental Determination of the Thermal-Entrance Length for the Flow of Water and of Oil in Circular Pipes," ASME JOURNAL OF HEAT TRANSFER, Vol. 77, pp. 1211–1220.

Kays, W. M., and Crawford, M. E., 1980, *Convective Heat Transfer*, 2nd ed., McGraw-Hill, New York.

McAdams, W. H., and Frost, T. H., 1922, "Heat Transfer," *The Journal of Industrial and Engineering Chemistry*, Vol. 14, No. 1, pp. 13–18.

McAdams, W. H., and Frost, T. H., 1922, "Heat Transfer by Conduction and Convection. II—Liquids Flowing Through Pipes," *The Journal of Industrial and Engineering Chemistry*, Vol. 14, No. 12, pp. 1101–1105.

McAdams, W. H., and Frost, T. H., 1924, "Heat Transfer for Water Flowing Inside Pipes," *Refrigerating Engineering*, Vol. 10, No. 9, pp. 323–334.

Morris, F. H., and Whitman, W. G., 1928, "Heat Transfer for Oils and Water in Pipes," *The Journal of Industrial and Engineering Chemistry*, Vol. 20, No. 3, pp. 234–240.

Petukhov, B. S., 1970, "Heat Transfer and Friction in Turbulent Pipe Flow With Variable Physical Properties," *Advances in Heat Transfer*, Vol. 6, pp. 503–564.

Sieder, E. N., and Tate, G. E., 1936, "Heat Transfer and Pressure Drop of Liquids in Tubes," *The Journal of Industrial and Engineering Chemistry*, Vol. 28, No. 12, pp. 1429–1435.

Wolf, H., 1959, "Heating and Cooling Air and Carbon Dioxide in the Thermal Entrance Region of a Circular Duct With Large Gas to Wall Temperature Differences," ASME JOURNAL OF HEAT TRANSFER, Vol. 81, pp. 267–279.



Downloaded 12 Dec 2010 to 193.140.21.150. Redistribution subject to ASME license or copyright; see http://www.asme.org/terms/Terms_Use.cfm

# Pressure Drop and Heat Transfer in Turbulent Duct Flow: A Two-Parameter Variational Method

N. Ghariban

A. Haji-Sheikh

S. M. You

Department of Mechanical Engineering,
The University of Texas at Arlington,
Arlington, TX 76019-0023

*A two-parameter variational method is introduced to calculate pressure drop and heat transfer for turbulent flow in ducts. The variational method leads to a Galerkin-type solution for the momentum and energy equations. The method uses the Prandtl mixing length theory to describe turbulent shear stress. The Van Driest model is compared with experimental data and incorporated in the numerical calculations. The computed velocity profiles, pressure drop, and heat transfer coefficient are compared with the experimental data of various investigators for fully developed turbulent flow in parallel plate ducts and pipes. This analysis leads to development of a Green's function useful for solving a variety of conjugate heat transfer problems.*

## Introduction

This paper introduces a method to calculate pressure drop and heat transfer for incompressible turbulent flow in ducts with different cross sections. A simple mathematical model is sought that is capable of producing relatively accurate results with minimum computational effort. The Galerkin-based solution method described in Haji-Sheikh et al. (1983) and Beck et al. (1992) for laminar flow in ducts is modified for the study of turbulent flow. This method has proved to be simple and effective for calculating heat transfer for laminar flow in ducts of various shapes. It is shown that a Galerkin-type solution method can be used for turbulent flow; however, major modifications are needed. The Galerkin-type solution leads to development of a Green's function solution method for various conjugate heat transfer problems in turbulent flow.

Classical methods that describe velocity profiles for turbulent flow in pipes use a power-law profile to describe the local velocity as a function of the distance from the wall to a power of a number less than one. The deficiency of this method is twofold: There is no systematic method of evaluating the exponent, and the slope of the velocity profile at the wall is infinite. In this paper, a method is sought that will produce an accurate velocity profile for turbulent flow, and a velocity gradient that will provide shear stress. To satisfy these requirements, a two-parameter, variational method is introduced to compute the velocity profile and shear stress in turbulent flow. Although the essentials of this method are described for flow between two parallel plates and pipe flow, the same method can be extended to ducts with other cross sections. The mathematical procedure for the two-parameter variational method is described in a separate section. It is shown that this method reduces to a Galerkin-based solution as discussed in Haji-Sheikh et al. (1983) and Beck et al. (1992).

Modifications are necessary to accommodate the dependence of effective viscosity on the shear stress. A set of basis functions that are markedly different from the basis functions for laminar flow must be selected. Improved accuracy and rapid convergence are achieved when the basis functions include the dependence of turbulent viscosity on the velocity gradient. For this solution method, the Van Driest model was chosen from among several different turbulent viscosity models. The two-parameter variational method introduced here provides computed data that agree well with the experimental data.

The analytical velocity solutions for turbulent flow between parallel plates are compared with the experimental data of Laufer (1950). The pressure drop is compared with the experimental data of Dean (1978) and Beavers et al. (1971). Experimental data for flow in pipes are available from many sources. Here, the computed velocity data are compared with the experimental data of Laufer (1954) and Nikuradse (1966). The computed pressure drop is compared with data from Filonenko (1954), and the computed heat transfer data for pipe flow are compared with the experimental data of Gnielinski (1976). Finally, a Green's function is presented and a numerical example is used to show the formulation and procedural steps.

## Analysis

The objective of this paper is to develop a simple and computationally efficient method for finding pressure drop and heat transfer in ducts. A variational method that leads to a Galerkin-type solution for the velocity field and temperature profile is used. A description of the solution method follows the presentation of the governing equation.

**Governing Equations.** The Galerkin-based method is a simple technique for finding the velocity field in ducts with arbitrary cross section areas. For convenience, Cartesian coordinates are used to describe the method of solution, and cylindrical coordinates are used to study pipe flow. The momentum equation for fully developed channel flow is

$$-\frac{\partial P}{\partial z}+\frac{\partial}{\partial x}\left(\mu_e\frac{\partial w}{\partial x}\right)+\frac{\partial}{\partial y}\left(\mu_e\frac{\partial w}{\partial y}\right)=0 \qquad (1)$$

where $\mu_e = \mu + \mu_t$. The Boussinesq's eddy-diffusivity coefficients for momentum are defined as $-\rho\overline{u'w'} = \mu_t\partial w/\partial x$ and $-\rho\overline{v'w'} = \mu_t\partial w/\partial y$. This momentum equation can be written in nondimensional form as

$$1+\nabla_1\cdot(\mu_e^*\nabla_1 W)=0 \qquad (2)$$

where $\mu_e^* = 1 + (\mu_t/\mu) = 1 + \mu_t^*$, $W = -(\mu w/a^2)/(\partial P/\partial z)$, $X = x/a$, $Y = y/a$; $a$ is the characteristic length, and operator $\nabla_1$ stands for $\nabla_1 = \vec{i}\partial/\partial X + \vec{j}\partial/\partial Y$. The energy equation in dimensional form is

$$\nabla\cdot(k\mu_h^*\nabla T)-\rho c_p w\frac{\partial T}{\partial z}=0 \qquad (3)$$

Contributed by the Heat Transfer Division and presented at the ASME Winter Annual Meeting, New Orleans, Louisiana, November 28–December 3, 1993. Manuscript received by the Heat Transfer Division September 1993; revision received May 1994. Keywords: Forced Convection, Heat Exchangers, Turbulence. Associate Technical Editor: A. Faghri.



Copyright © 1995 by ASME

Downloaded 12 Dec 2010 to 193.140.21.150. Redistribution subject to ASME license or copyright; see http://www.asme.org/terms/Terms_Use.cfm

where $\mu_h^* = 1 + \mu_t^* \, \mathrm{Pr}/\mathrm{Pr}_t$ and $\mu_t^*$ is $\mu_t/\mu$. The turbulent flux quantities $c_p\rho\overline{u'T'}$ and $c_p\rho\overline{v'T'}$ are related to turbulent viscosity by the relations

$$c_p\rho\overline{u'T'} = -k\frac{\mathrm{Pr}}{\mathrm{Pr}_t}\mu_t^*\frac{\partial T}{\partial x} \quad \text{and} \quad c_p\rho\overline{v'T'} = -k\frac{\mathrm{Pr}}{\mathrm{Pr}_t}\mu_t^*\frac{\partial T}{\partial y}$$

**Variational Steps.** Variational calculus is employed to develop a solution for Eq. (1). It was noted that the basis functions commonly used to calculate the velocity profile for laminar flow are too stiff and will not produce fast converging solutions. To circumvent this difficulty, Ghariban (1994) used a flexibility parameter $\beta = \beta(\bar{\tau}_w)$ to allow the solution functions to change with the changing turbulence level. The dependence of $\beta$ on the average shear stress, $\bar{\tau}_w$, greatly improves the convergence characteristics of the solution. The variational integral (Kantorovich and Krylov, 1960), using $\beta$ as an additional parameter,

$$I = \int_A F\left(W, \frac{\partial W}{\partial x}, \frac{\partial W}{\partial y}, \beta\right) dA \tag{4}$$

will be minimized. The integrand in this integral is set to depend on $W$, $\partial W/\partial x$, $\partial W/\partial y$, and $\beta$. The two-parameter variational procedure refers to the presentation of the variation of functions $W$ and $\beta$ as

$$\bar{W}(x, y) = W(x, y) + \epsilon\eta(x, y)$$

$$\bar{\beta} = \beta + \epsilon\eta_0$$

where $\eta$ and $\eta_0$ are the two parameters. It is a standard procedure in variational calculus to replace $W$ and $\beta$ in Eq. (4) by $\bar{W}$ and $\bar{\beta}$. The minimization process requires that $\partial I/\partial\epsilon$ be equal to zero as $\epsilon \to 0$. The differentiation of $I$ with respect to $\epsilon$ yields

$$\frac{\partial I}{\partial \epsilon} = \int_A \frac{\partial F}{\partial \epsilon} dA$$

$$= \int_A \left(\frac{\partial F}{\partial \bar{W}}\frac{\partial \bar{W}}{\partial \epsilon} + \frac{\partial F}{\partial \bar{W}_x}\frac{\partial \bar{W}_x}{\partial \epsilon} + \frac{\partial F}{\partial \bar{W}_y}\frac{\partial \bar{W}_y}{\partial \epsilon} + \frac{\partial F}{\partial \bar{\beta}}\frac{\partial \bar{\beta}}{\partial \epsilon}\right) dA$$

where $\bar{W}_x = \partial\bar{W}/\partial x$ and $\bar{W}_y = \partial\bar{W}/\partial y$. After replacing $\partial\bar{W}/\partial\epsilon$, $\partial\bar{W}_x/\partial\epsilon$, $\partial\bar{W}_y/\partial\epsilon$, and $\partial\bar{\beta}/\partial\epsilon$ by $\eta$, $\partial\eta/\partial x$, $\partial\eta/\partial y$, and $\eta_0$, respectively, the value of $\partial I/\partial\epsilon$ after using the divergence theorem reduces to

$$\frac{\partial I}{\partial \epsilon} = \int_A \eta\left(\frac{\partial F}{\partial \bar{W}} - \nabla\cdot\vec{\Omega}\right) dA + \int_A \eta_0 \frac{\partial F}{\partial \bar{\beta}} dA + \int_C \eta\vec{\Omega}\cdot\vec{n} ds \tag{5}$$

where $\vec{\Omega} = \vec{i}\partial F/\partial\bar{W}_x + \vec{j}\partial F/\partial\bar{W}_y$, and $\vec{i}$ and $\vec{j}$ are unit vectors along the $x$ and $y$ axes. The last term on the right side of Eq. (5) vanishes since it is assumed that $W = \bar{W} = 0$ at the solid walls, hence $\eta = 0$ along the contour $C$. According to the minimization principle, the integral $I$ is minimum when $(\partial I/\partial\epsilon)_{\epsilon\to 0} = 0$, or

$$\int_A \eta\left(\frac{\partial F}{\partial W} - \nabla\cdot\vec{\Omega}\right) dA = 0 \tag{6a}$$

and

$$\int_A \eta_0 \frac{\partial F}{\partial \beta} dA = 0 \tag{6b}$$

because the parameters $\eta$ and $\eta_0$ are independent and chosen arbitrarily. Furthermore, the arbitrary nature of $\eta$ and $\eta_0$ in Eqs. (6$a$) and (6$b$) suggests the two conditions

$$\frac{\partial F}{\partial W} - \nabla\cdot\vec{\Omega} = \frac{\partial F}{\partial W} - \frac{\partial}{\partial x}\left(\frac{\partial F}{\partial W_x}\right) - \frac{\partial}{\partial y}\left(\frac{\partial F}{\partial W_y}\right) = 0$$

$$\text{and} \quad \frac{\partial F}{\partial \beta} = 0$$

The first condition represents the standard Euler–Lagrange equation that, upon comparison with Eq. (2), yields $\partial F/\partial W = -1$, $\partial F/\partial W_x = \mu_e^* W_x$, and $\partial F/\partial W_y = \mu_e^* W_y$, and, following integration, one obtains the function $F$;

$$F = \frac{1}{2}\mu_e^*[(W_x)^2 + (W_y)^2] - W + c \tag{7}$$

The constant of integration $c$ has no effect on the solution; hence, it is omitted in subsequent calculations.

The second condition following differentiation of $F$ with respect to $\beta$ produces

## Nomenclature

$a$ = characteristic length, m
$a_{ij}, b_{ij}, c_{ij}$ = element of matrices **A**, **B**, **C**
$A$ = flow area of duct, m$^2$
$A^+$ = damping constant
**A, B, C** = matrices
$C_f$ = friction factor
$c_p$ = specific heat, J/kg·K
$D_e$ = hydraulic diameter, m
$d_i$ = element of the array **d**
**d** = array of velocity coefficient
$d_{nj}$ = element of $\mathbf{d}_n$ vector
$\mathbf{d}_n$ = eigenvectors
$f_i$ = basis function
$g_i$ = element of the array **g**
**g** = auxiliary array, Eq. (17)
G = Green's function
$h$ = heat transfer coefficient, W/m$^2$·K
$i, j$ = indices
$k$ = thermal conductivity, W/m·K
$L$ = half-distance between parallel plates
$\vec{n}$ = unit vector normal to surface
$N$ = number of terms in series
Nu = Nusselt number = $hD_e/k$
$p_{ni}$ = element of $[(\mathbf{D}\cdot\mathbf{B})^T]^{-1}$
$P$ = static pressure, kPa
Pr = molecular Prandtl number
$\mathrm{Pr}_t$ = turbulent Prandtl number
$q$ = heat flux, W/m$^2$
$r$ = cylindrical coordinate, m
$R$ = cylindrical coordinate
Re = Reynolds number = $w_{\mathrm{avg}}D_e/\nu$
$\mathrm{Re}_x$ = Reynolds number = $u_\infty x/\nu$
$R_0$ = pipe radius, m
$T$ = local temperature, K
$T'$ = fluctuating temperature, K
$u', v', w'$ = fluctuating velocity components, m/s
$u^+$ = $u/\sqrt{\tau_w/\rho}$
$w$ = axial velocity, m/s
$W$ = axial velocity
$x, y, z$ = coordinates, m
$X, Y$ = $x/a$ and $y/a$
$y^+$ = $y\sqrt{\tau_w/\rho}/\nu$
$Z$ = $(z/a)/(\mathrm{Re}\,\mathrm{Pr})$
$\alpha$ = thermal diffusivity, m$^2$/s
$\beta$ = flexibility parameter
$\kappa$ = von Kármán constant
$\lambda_n$ = eigenvalue, m$^{-1}$
$\bar{\lambda}_n$ = $w_{\mathrm{avg}}\lambda_n/\alpha$, m$^{-2}$
$\mu$ = molecular viscosity, N·s/m$^2$
$\mu_e$ = effective viscosity, N·s/m$^2$
$\mu_e^*$ = effective viscosity
$\mu_h^*$ = thermal eddy diffusivity
$\mu_t$ = turbulent viscosity, N·s/m$^2$
$\mu_t^*$ = turbulent viscosity
$\nu$ = kinematic viscosity, m$^2$/s
$\rho$ = fluid density, kg/m$^3$
$\tau_w$ = wall shear stress, N/m$^2$

### Subscripts

avg = average
$e$ = entrance
$w$ = wall



Downloaded 12 Dec 2010 to 193.140.21.150. Redistribution subject to ASME license or copyright; see http://www.asme.org/terms/Terms_Use.cfm

$$\frac{\partial F}{\partial \beta} = \frac{1}{2}\frac{\partial \mu_e^*}{\partial \beta}[(W_x)^2 + (W_y)^2] = 0$$

Since $(W_x)^2 + (W_y)^2 > 0$, then

$$\frac{\partial \mu_e^*}{\partial \beta} = \frac{\partial \mu_e^*}{\partial \bar{\tau}_w}\frac{\partial \bar{\tau}_w}{\partial \beta} = 0$$

The relationship between shear stress and rate of deformation in the flow suggests that $\partial \mu_e^*/\partial \bar{\tau}_w \neq 0$; then, $\partial \bar{\tau}_w/\partial \beta = 0$. Accordingly, the velocity profile may include a flexibility parameter, $\beta$; for best results, this parameter must have a value that minimizes the shear stress. The existence of a flexibility parameter is the major difference between this solution method and the standard Galerkin method when calculating pressure drop for laminar flow in ducts. The existence of a flexibility parameter that makes the shear stress at the wall minimum is studied numerically in a later section.

The standard Galerkin method is an application of the variational method described earlier. Equation (6*a*) with $F$ from Eq. (7) becomes

$$\int_A \eta(x, y)\left[1 + \frac{\partial}{\partial x}\left(\mu_e^*\frac{\partial W}{\partial x}\right) + \frac{\partial}{\partial y}\left(\mu_e^*\frac{\partial W}{\partial y}\right)\right]dA = 0 \quad (8)$$

Replacing velocity, $W$, in Eq. (8) by

$$W = \sum_{j=1}^{N} d_j f_j(x, y) \quad (9)$$

and the arbitrary function $\eta(x, y)$ by $f_i(x, y)$ yields the Galerkin solution method,

$$\int_A f_i(x, y)\left\{1 + \sum_{j=1}^{N} d_j\left[\frac{\partial}{\partial x}\left(\mu_e^*\frac{\partial f_j}{\partial x}\right) + \frac{\partial}{\partial y}\left(\mu_e^*\frac{\partial f_j}{\partial y}\right)\right]\right\}dA = 0$$

$$\text{for} \quad i = 1, 2, \ldots, N. \quad (10)$$

This equation represents $N$ equations to be solved simultaneously. The application of Eq. (10) will be amplified later. The Galerkin finite element is a special case of the standard Galerkin method. For example, if coefficients $d_1$ through $d_N$, Eq. (9), are written in terms of the velocity at $N$ discrete nodes, the procedure will be referred to as the finite element method. For ducts with simple shapes, the discretization is not necessary and one can directly calculate the coefficients in Eq. (9).

**Turbulent Viscosity and Turbulent Prandtl Number.** Equations (2) and (3) indicate that the momentum equations contain turbulent viscosity and the energy equation contains the turbulent Prandtl number. A turbulence model is necessary to determine the turbulent diffusivity terms before attempting to solve these equations. The mixing-length model is selected for this study because it has a convenient form for this study.

A wind-tunnel experiment was set up to compare the experimental velocity data with selected turbulence models. The Van Driest (1956), Reichardt, Spalding, and Prandtl–Taylor models (Bhatti and Shah, 1987) are chosen for comparison; except for the Prandtl–Taylor model, a single equation describes the velocity field over the entire boundary layer. A hot-wire anemometer was used to obtain experimental data for boundary-layer flow over a flat plate in the $x$ direction. Figure 1 shows the measured velocity from the wall (in the $y$ direction) with the nondimensional parameters $u^+ = u/\sqrt{\tau_w/\rho}$ and $y^+ = y\sqrt{\tau_w/\rho}/\nu$ where $\tau_w$ is the wall shear stress. The local velocity in the boundary layer was measured using a boundary layer probe at two Reynolds numbers, $u_\infty x/\nu = 1.0 \times 10^6$ and $1.5 \times 10^6$. Figure 1 compares the measured velocity with the turbulence models mentioned earlier. All of these models are satisfactory; however, a continuous model is sought that provides good agreement with the experimental data at the near-wall region. The Van Driest model was selected because of good prediction of turbulence near the wall.

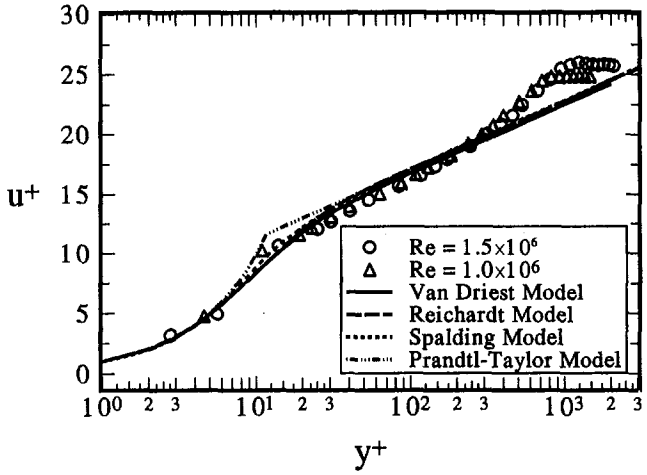



**Fig. 1 A comparison of measured $u^+(y^+)$ in turbulent boundary layer flow with different models**

The Van Driest model is solely a function of $y^+$; therefore, it considerably simplifies the numerical calculations and enhances the accuracy of the results. According to the Van Driest model, the turbulent viscosity is given as

$$\mu_t = \rho\kappa^2 y^2[1 - \exp(y^+/A^+)]\left|\frac{\partial u}{\partial y}\right| \quad (11)$$

where $\kappa$ is the von Kármán constant that is defined later and $A^+ = 28$. Rearranging the above equation, the effective viscosity can be written as

$$\mu_e = \frac{1}{2}\mu\{1 + \{1 + 4\kappa^2(y^+)^2[1 - \exp(-y^+/A^+)]^2\}^{1/2}\} \quad (12)$$

Malhotra and Kang (1984) used Eq. (11) with an additional correction factor that emerged as a result of studies on a two-equation model of turbulence for pipe flow. The turbulence viscosity then becomes

$$\mu_t = \frac{\rho\kappa^2 y^2[1 - \exp(y^+/A^+)]}{1 + 3y/R_0 + 3y^2/R_0^2}\left|\frac{\partial u}{\partial y}\right| \quad (13)$$

where $R_0$ is the radius of the pipe and $y$ is the distance from the wall. Richman and Azad (1973) assumed a turbulent viscosity as

$$\mu_t = \frac{1}{2}\mu\{\{1 + 4\kappa^2(y^+)^2[1 - \exp(-y^+/A^+)]^2\}^{1/2} - 1\}$$

$$\text{for} \quad 0 \le y/R_0 \le 0.158 \quad (14a)$$

and a constant

$$\mu_t = (\mu_t)_{y/R_0=0.158} \quad \text{for} \quad 0.158 \le y/R_0 \le 1. \quad (14b)$$

In this study, the Richman and Azad (1973) modification yields a closer agreement with the experimental data.

The turbulent Prandtl number is another term that should be defined before solving the energy equations. Expressions that relate the turbulent Prandtl number to the molecular Prandtl number are given by Graber (Reynolds, 1975)

$$\mathrm{Pr}_t^{-1} = 0.91 + 0.13\,\mathrm{Pr}^{0.545}; \quad 0.7 < \mathrm{Pr} < 100 \quad (15)$$

and by Malhotra and Kang (1984) for a larger range of the Prandtl numbers,

$$\begin{cases} \mathrm{Pr}_t = 1.01 - 0.09\,\mathrm{Pr}^{0.36}; & 1 < \mathrm{Pr} < 145 \\ \mathrm{Pr}_t = 1.01 - 0.25\log \mathrm{Pr}; & 145 < \mathrm{Pr} < 1800 \\ \mathrm{Pr}_t = 0.99 - 0.44\,(\log \mathrm{Pr})^{1/2}; & 1800 < \mathrm{Pr} < 12{,}500 \end{cases} \quad (16)$$

for the Reynolds number ($10^4 < \mathrm{Re} < 10^6$).



Downloaded 12 Dec 2010 to 193.140.21.150. Redistribution subject to ASME license or copyright; see http://www.asme.org/terms/Terms_Use.cfm

**Calculation of Pressure Drop and Heat Transfer.** A Galerkin-based integral (GBI) method (Beck et al., 1992) is used to solve momentum and energy equations. This method converts the momentum equation to a linear algebraic system and the energy equation to an eigenvalue problem.

**Solution of the Momentum Equation.** Equation (2) is the momentum equation in nondimensional space with the boundary condition $W = 0$ on the wall. According to the Galerkin-based integral method, the solution is approximated as a linear combination of a set of basis functions, Eq. (9). The basis functions, $f_i$, in Eq. (9) must be linearly independent and satisfy the same homogeneous boundary conditions as $W$. Equation (10) in the matrix notation is

$$\mathbf{A}\cdot\mathbf{d} = \mathbf{g} \tag{17}$$

where $\mathbf{d}$ is the vector of coefficients that has the elements $d_1, d_2, \ldots, d_N$ and it is the solution of the above system of $N$ linear equations. The vector $\mathbf{g}$ has the elements

$$g_i = -\int_A f_i\, dA \tag{18a}$$

and matrix $\mathbf{A}$ has the elements

$$a_{ij} = \int_A f_i \nabla_1\cdot(\mu_e^*\nabla_1 f_j)dA \tag{18b}$$

The solution of Eq. (17) results in the evaluation of the coefficients, $d_1, d_2, \ldots, d_N$, and subsequently Eq. (9) yields the solution for $W$.

Haji-Sheikh et al. (1983) derived the following equations for skin friction and dimensionless velocity by this method.

$$C_f \mathrm{Re} = \frac{2(D_e/a)^2}{W_{\mathrm{avg}}} \tag{19}$$

$$\frac{W}{W_{\mathrm{avg}}} = \frac{w}{w_{\mathrm{avg}}} = \frac{C_f \mathrm{Re}}{2(D_e/a)^2}\sum_{i=1}^{N} d_i f_i \tag{20}$$

where $C_f = -(\partial P/\partial z)D_e/(\rho w_{\mathrm{avg}}^2/2)$, $\mathrm{Re} = \rho D_e w_{\mathrm{avg}}/\mu$, and $a = R_0$ for pipe flow and $a = L$ for parallel channel flow.

**Solution of the Energy Equation.** After calculating $w$ (or $W$), the energy equation can be solved. The energy equation for fully developed turbulent flow inside a duct is given by Eq. (3) subject to boundary conditions of the first, second, or third kind. For laminar flow, $\mu_h^* = 1$, the solution for arbitrary-shaped ducts is discussed in Lakshminarayanan and Haji-Sheikh (1986). For turbulent flow, the term $k\mu_h^*$ depends on $x$ and $y$ coordinates and can be viewed as a variable thermal conductivity. Equation (3) has the same form as an equation for transient conduction in a two-dimensional body whose thermal conductivity is $k\mu_h^*$ and volumetric specific heat is $\rho c_p w$, while time is replaced by $z$. Therefore, the Green's function solution method in Beck et al. (1992, Chap. 10) applies to Eq. (3). The Green's function is

$$G(x, y, z|x', y', z') = \sum_{n=1}^{N} \Psi_n(x, y)\bar{\Psi}_n(x', y')\exp[-\lambda_n(z - z')] \tag{21}$$

where the eigenfunction, $\Psi_n(x, y)$, and the ratio of eigenfunction to the norm, $\bar{\Psi}_n(x', y')$, are

$$\Psi_n(x, y) = \sum_{j=1}^{N} d_{nj} f_j(x, y) \quad \text{and} \quad \bar{\Psi}_n(x', y') = \sum_{i=1}^{N} p_{ni} f_i(x', y')$$

where $\lambda_n$ is the $n$th eigenvalue. The basis functions, $f_j(x, y)$, are selected so that they are linearly independent and they satisfy the homogenous boundary conditions. The parameters $d_{nj}$ represent the components of eigenvector $\mathbf{d}_n$ of the equation

$$(\mathbf{C} + \bar{\lambda}_n\mathbf{B})\mathbf{d}_n = 0 \tag{22}$$

where $\bar{\lambda}_n = w_{\mathrm{avg}}\lambda_n/\alpha$, and $B$ and $C$ are square matrices of size $N$ with elements

$$c_{ij} = \int_A f_i \nabla\cdot(\mu_h^*\nabla f_j)dA \tag{23}$$

and

$$b_{ij} = \int_A \frac{w}{w_{\mathrm{avg}}} f_i f_j dA \tag{24}$$

The parameters $p_{ni}$ are elements of the matrix $\mathbf{D}\cdot\mathbf{B}$ after it is transposed and then inverted; details are available in Beck et al. (1992). Lakshminarayanan and Haji-Sheikh (1986) also showed that the Nusselt number for fully developed flow is related to the first eigenvalue as

$$\mathrm{Nu} = \frac{1}{4} D_e^2 \bar{\lambda}_1 \tag{25}$$

The heat transfer in turbulent flow is reduced to a form that can be solved by established mathematical techniques. The Green's function solution method described in Beck et al. (1992) can be used to calculate heat transfer in turbulent flow in ducts.

## Numerical Calculations and Results

Channel flow between two parallel plates is a direct application of the turbulence models usually obtained using flow over a flat plate. In dimensionless coordinates, the basis functions for a parallel plate channel are

$$f_i = \{1 - \exp[-\beta Y(2 - Y)]\}(1 - Y)^{2(i-1)};$$
$$\text{for} \quad 0 < L < 2, \quad \text{and} \quad i = 1, 2, \ldots, N \tag{26}$$

The turbulent flow inside a circular duct is studied to extend this solution method to pipe flow. By replacing $1 - Y$ in Eq. (26) by $R$, the basis functions describe the turbulent flow velocity profile in a pipe. The factor $\beta$ in Eq. (26) is the flexibility parameter. The flexibility parameter depends on the average shear stress; hence, it depends on the Reynolds number.

To verify the existence of the minimum shear stress hypothesis in the variational principles, the computed friction factor for different values of $\beta$ are plotted in Fig. 2. Figure 2 illustrates that the calculated skin friction for a parallel plate duct decreases by increasing the coefficient $\beta$, then begins to increase as $\beta$ increases. According to the variational procedure, a value of $\beta$ that minimizes the skin friction is the proper choice and the calculated skin friction at the optimum $\beta$ provides the best agreement with the experimental values. For higher Reynolds numbers, the changes in the skin friction become more pronounced as $\beta$

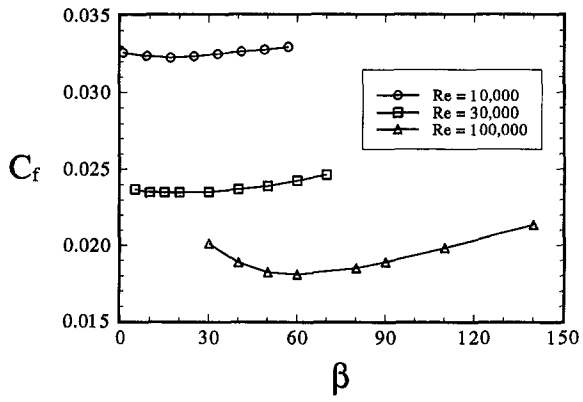



**Fig. 2 Calculated skin friction for different values of $\beta$**



Downloaded 12 Dec 2010 to 193.140.21.150. Redistribution subject to ASME license or copyright; see http://www.asme.org/terms/Terms_Use.cfm

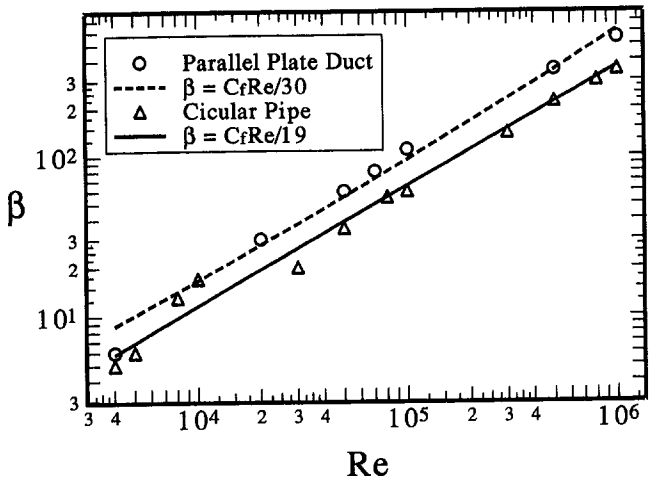



**Fig. 3 Optimum $\beta$ for parallel plate ducts and circular pipes versus the Reynolds numbers**

changes whereas, when the Reynolds number is small, the skin friction assumes a flatter profile.

As the Reynolds number increases, the basis functions assume steeper slopes at the wall. When the Reynolds number is small, the minimum shear stress corresponds to a small value of $\beta$. In this case, the quantity $1 - \exp[-\beta Y(2 - Y)] \approx \beta Y(2 - Y)$ and the constant $\beta$ has no effect on the solution.

As mentioned earlier, the optimum value of $\beta$ depends on the Reynolds number. A relation between $\beta$ and Re simplifies the numerical steps. For this reason, the optimum values of $\beta$ at different Reynolds numbers are computed and the results are given in Fig. 3. Correlations for optimum $\beta$ are prepared as $\beta = C_f\,\mathrm{Re}/30$ for flow in a parallel plate channel, and $\beta = C_f\,\mathrm{Re}/19$ for flow in a pipe. Once a correlation for $\beta$ is available, one can proceed to solve for the velocity profile, skin friction, and heat transfer coefficient at any Reynolds number.

**Skin Friction.** The convergence of the solution is the same for flow in a parallel plate duct and a pipe. The convergence of skin friction for flow in a pipe, using three different Reynolds numbers, was examined by Ghariban et al. (1993). Their data show, when the Reynolds number is small (Re = 50,000), a series solution with two terms gives the skin friction that has a satisfactory agreement with the experimental values. However, the data with eight terms produced excellent results for all Reynolds numbers examined; up to $10^6$. Figure 4($a$) shows the results of computed skin friction as a function of the Reynolds number for a parallel plate duct. The skin friction is calculated for a wide range of Reynolds numbers ($4 \times 10^3$ to $10^6$) using $N = 8$. The value of $\kappa = 0.4$ is used for calculation of the "circular" symbols in the figure. However, the "plus" symbols are for $\kappa = 0.4$ when $\mathrm{Re} \le 10^5$ and $\kappa = 0.41 - (4/9) \times 10^{-7}$ Re when $10^5 < \mathrm{Re} \le 10^6$. Also, the skin friction data of Dean (1978) and Beavers et al. (1971) are plotted in Fig. 4($a$). The calculated skin friction shows better agreement with the experimental data using a variable $\kappa$ value for the Reynolds number near $10^6$.

Similar calculations are carried out for pipe flow and the results are given in Fig. 4($b$). The skin friction data are compared with the correlation,

$$\frac{1}{\sqrt{C_f}} = 0.79 \ln (\mathrm{Re}) - 1.64 \qquad (27)$$

given by Filonenko (1954). According to Filonenko (1954), this correlation agrees with extensive experimental measurements from different investigators for turbulent flow in a smooth pipe to within ±2 percent. Figure 4($b$) illustrates a remarkably close agreement between analytically obtained data and Eq. (27).

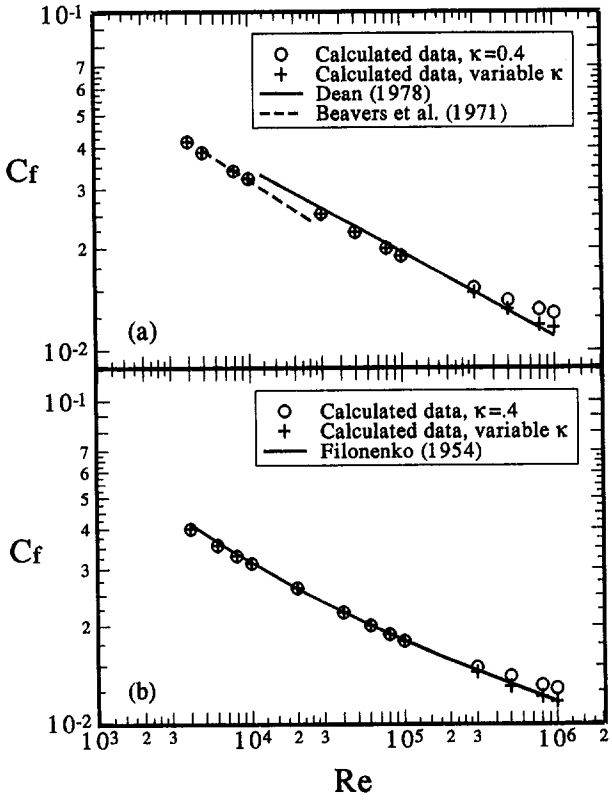



**Fig. 4 Skin frictions: (*a*) for smooth parallel plate ducts, (*b*) for smooth circular ducts**

The velocity data show excellent convergence, especially, at the lower range of Reynolds numbers. To demonstrate this, analytical data from this study for $N = 2$ and 4 and Re = 50,000 are presented in Fig. 5. The calculated velocity profiles show good agreement with the experimental velocity profile given by Laufer (1954); the agreement is within 6 percent using as few as two terms in the series, $N = 2$. All subsequent calculations will use $N = 8$ terms. The calculated velocity profiles, for $\mathrm{Re} = 5 \times 10^4$ and $5 \times 10^5$, are shown in Fig. 6 and compared with the experimental data of Laufer (1954). Also, in Fig. 6, the calculated velocity profiles, using Reynolds numbers $10^5$ and $10^6$, are compared with the experimental data of Nikuradse (1966). The comparison shows there is close agreement between the calculated velocity data and the velocity profiles from Laufer (1954)

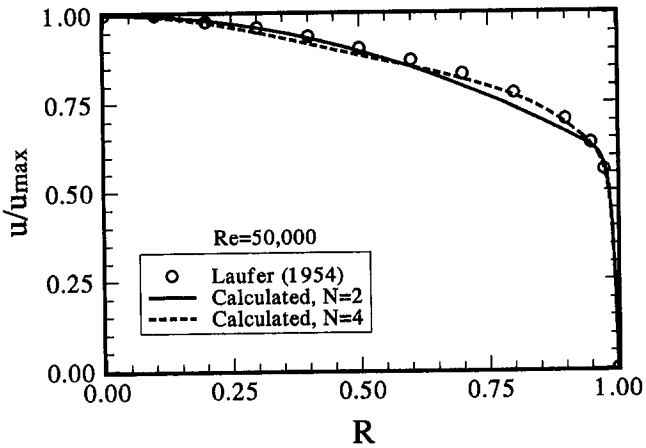



**Fig. 5 Convergence of the series solution for velocity profile when $N$ = 2 and $N$ = 4**



Downloaded 12 Dec 2010 to 193.140.21.150. Redistribution subject to ASME license or copyright; see http://www.asme.org/terms/Terms_Use.cfm

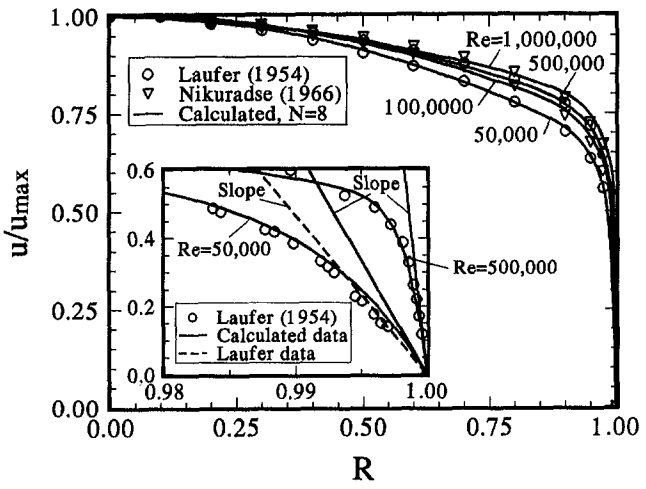



**Fig. 6 Comparison of the calculated velocity profile with experimental data of Laufer (1954) and Nikuradse (1966)**

and Nikuradse (1966). All analytical velocity profiles agree with the experimental measurements to within 3 percent. For more than $N = 8$ terms, no significant improvement was observed. To study the behavior of the solution near the wall, the Laufer (1954) data from Fig. 6 are used to plot the velocity profiles close to the wall and the results are shown in the inset of Fig. 6. Generally, accurate skin friction data can be obtained indirectly from the measured pressure drop; however, velocity measurement next to a wall is difficult and is susceptible to various types of errors. The analytically computed velocity gradient at the wall yields the skin friction more accurately than the experimentally obtained velocity gradients. For this reason, the velocity gradient using the experimental data of Laufer, inset of Fig. 6, underestimates the velocity gradient at the wall.

**Heat Transfer Coefficient.** Following the computation of velocity field and skin friction, the temperature distribution is calculated using the Green's function solution method. The method of calculation is available in Beck et al. (1992). The Malhotra and Kang (1984) correlation is used to define the turbulent Prandtl number for use in calculating elements of matrix **C**. For the case of constant wall temperature, the basis functions given by Eq. (26) are used for the calculation of temperature. The eigenvalues are calculated for Eq. (22) following numerical integration of matrices **C** and **B**; Eqs. (23) and (24). The first eigenvalue is related through Eq. (25) to the Nusselt number for thermally, fully developed flow. Table 1 contains a sample of the calculated eigenvalues for a Reynolds number of 50,000 and a Prandtl number of one. The entries in Table 1 are for $N = 2$, 4, 6, and 8. When $N$ is larger than 8, no significant change in the first eigenvalue is observed.

The Nusselt number for a range of Reynolds numbers and Prandtl numbers of 1, 10, 100, and 1000 are computed and the results are shown in Fig. 7; the circular symbols are for the turbulent pipe flow and the triangular symbols are for flow between two parallel plates. Figure 7 also includes a comparison with the correlation of Gnielinski (1976). The Gnielinski correlation is based on experimental data for $2300 < \mathrm{Re} < 5 \times 10^6$ and $0.5 < \mathrm{Pr} < 2000$,

$$\mathrm{Nu} = \frac{(C_f/8)(\mathrm{Re} - 1000)\,\mathrm{Pr}}{1 + 12.7(C_f/8)^{1/2}(\mathrm{Pr}^{2/3} - 1)} \qquad (28)$$

The data show good agreement between the calculated and measured values of the heat transfer coefficient. It can be seen from the figure that the difference between the heat transfer coefficients for a parallel plate duct and a circular pipe is quite small.

**Table 1 Calculated eigenvalues for turbulent flow in pipes**

| Calculated eigenvalues for different N, $a^2\bar{\lambda}_n$ | | | |
|---|---|---|---|
| N=2 | N=4 | N=6 | N=8 |
| 126.65 | 123.58 | 122.51 | 122.21 |
| 2032.6 | 1216.5 | 1214.2 | 1211.8 |
| | 4122.5 | 3644.2 | 3637.2 |
| | 13011 | 7591.8 | 7283.7 |
| | | 15412 | 12080 |
| | | 32446 | 19551 |
| | | | 34780 |
| | | | 63577 |

## Conclusions and Remarks

A simple Galerkin-based solution has been presented that predicts the heat transfer coefficient, as well as the skin friction and velocity flow field, in fully developed duct flow. The analytical steps, described in this study, apply to turbulent flow in ducts with various cross-sectional shapes. A comparison of the calculated values with the experimental data shows satisfactory agreement leading to the following major conclusions.

The solution for turbulent flow shows that special care must be taken in selecting basis functions. A suitable set of basis functions reduces the number of terms in the series, $N$, and consequently decreases computing time and increases the accuracy of the results. The computing time for matrix algebra is negligible; it depends on the size of matrices and the precision of numerical integration. The value of $N = 8$ provides data with good accuracy over a rather large range of the Reynolds number, $4 \times 10^3 < \mathrm{Re} < 10^6$, and $1 < \mathrm{Pr} < 1000$.

It is shown that the modified Van Driest model for effective viscosity given by Richman and Azad (1973) is a sufficiently accurate model for predicting turbulence. The calculated Nusselt numbers based on this model show good agreement with the pipe flow correlation of Gnielinski (1976) for Prandtl numbers up to 1000.

This method is useful for solving various heat transfer problems. Once the Green's function is in hand, thermally developing flow and various conjugate heat transfer problems, e.g., volumetric heat sources, can be accommodated. To demonstrate the capability of this method, Fig. 8 shows the wall temperature along a heated wall of a parallel plate channel. The upper plate is insulated. The lower plate is also insulated except at two sections, $0 < Z < 0.001$ and $0.002 < Z < 0.003$, where the heat

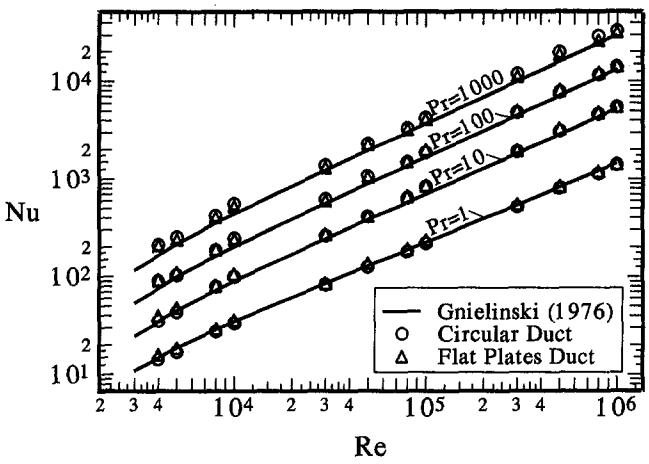



**Fig. 7 Predicted Nusselt number for turbulent flow in smooth parallel plate ducts and pipes, and comparison with experimental data for pipe flow**



Downloaded 12 Dec 2010 to 193.140.21.150. Redistribution subject to ASME license or copyright; see http://www.asme.org/terms/Terms_Use.cfm

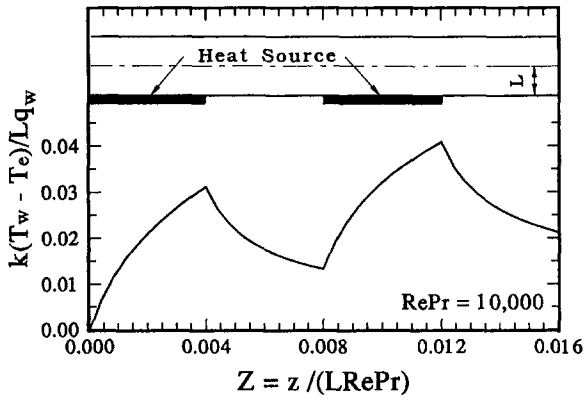



**Fig. 8 Wall temperature of a sectionally heated flat wall**

flux is $q_0$, see the inset in Fig. 8. The Green's function solution method (Beck et al., 1992) was used for the calculation of temperature distribution. The basis functions satisfying the homogeneous boundary conditions of the second kind are given in Beck et al. (1992).

The primary contributor to the errors is the inexact nature of the turbulent viscosity and turbulent Prandtl number. Table 1 illustrates a measure of numerical accuracy for heat transfer in fully developed turbulent flow. For example, the deviation of the first eigenvalue between $N = 6$ and $N = 8$ is only 0.25 percent. Since the solution uses a finite series, the convergence becomes poor as $Z$ is extremely small. Additional steps are needed to improve the convergence when there are small heat sources along a wall; e.g., electronic cooling applications. The application of this method to electronic cooling will be presented in subsequent publications. Additionally, the solution presented for temperature field is independent of velocity calculations; velocity and turbulence diffusivity computed using other numerical methods are acceptable.

## References


Beavers, G. S., Sparrow, E. M., and Lloyd, J. R., 1971, "Low Reynolds Number Flow in Large Aspect Ratio Rectangular Ducts," *ASME Journal of Basic Engineering*, Vol. 93, pp. 296–299.

Beck, J. V., Cole, K. D., Haji-Sheikh, A., and Litkouhi, B., 1992, *Heat Conduction Using Green's Functions*, Hemisphere Publishing Corp., Washington, DC, Chaps. 10 and 11.

Bhatti, M. S., and Shah, R. K., 1987, "Turbulent and Transition Flow Convective Heat Transfer in Ducts," in: *Handbook of Single Phase Convective Heat Transfer*, S. Kakac, R. K. Shah, and W. Aung, eds., Wiley, New York, Chap. 4.

Dean, R. B., 1978, "Reynolds Number Dependence of Skin Friction and Other Bulk Flow Variables in Two-Dimensional Rectangular Duct Flow," *ASME Journal of Fluids Engineering*, Vol. 100, pp. 215–223.

Filonenko, G. K., 1954, "Hydraulic Resistance in Pipes," *Teploenergetika*, Vol. 1, No. 4, pp. 40–44.

Ghariban, N., 1994, "Turbulent Flow and Heat Transfer in Ducts," Ph.D. Thesis, Department of Mechanical Engineering, The University of Texas at Arlington.

Ghariban, N., Haji-Sheikh, A., and You, S. M., 1993, "A Galerkin-Based Solution for Pressure Drop and Heat Transfer for Turbulent Flow in Pipes," ASME HTD-Vol. 256, pp. 49–56.

Gnielinski, V., 1976, "New Equations for Heat and Mass Transfer in Turbulent Pipe and Channel Flow," *Int. Chem. Eng.*, Vol. 16, pp. 359–468.

Haji-Sheikh, A., Mashena, M., and Haji-Sheikh, M. J., 1983, "Heat Transfer Coefficient in Ducts With Constant Wall Temperature," ASME JOURNAL OF HEAT TRANSFER, Vol. 105, pp. 878–883.

Kantorovich, L. V., and Krylov, V. I., 1964, *Approximate Methods of Higher Analysis*, Wiley, New York.

Lakshminarayanan, R., and Haji-Sheikh, A., 1986, "A Generalized Closed Form Solution to Thermal Entrance Problem," *Heat Transfer 86*, C. L. Tien, V. P. Carey, and J. K. Ferrel, eds., Hemisphere Publishing Corp., pp. 871–876.

Laufer, J., 1950, "Some Recent Measurements in a Two-Dimensional Turbulent Channel," *J. Aerosp. Sci.*, Vol. 17, pp. 277–287.

Laufer, J., 1954, "The Structure of Turbulence in Fully Developed Pipe Flow," NACA Rept. 1174.

Malhotra, A., and Kang, S. S., 1984, "Turbulent Prandtl Number in Circular Pipes," *Int. J. Heat and Mass Transfer*, Vol. 27, No. 11, pp. 2158–2161.

Nikuradse, J., 1966, "Gesetzmabigkiten der turbulenten stromung in glatten Rohen," *Forsch. Arb. Ing.-Wes.*, No. 356, 1932; English transl., NASA TT F-10,359.

Reynolds, A. J., 1975, "The Prediction of Turbulent Prandtl and Schmidt Numbers," *Int. J. Heat Mass Transfer*, Vol. 18, pp. 1055–1069.

Richman, J. W., and Azad, R. S., 1973, "Developing Turbulent Flow in Smooth Pipes," *Appl. Sci. Res.*, Vol. 28, pp. 419–440.

Van Driest, E. R., 1956, "On Turbulent Flow Near a Wall," *J. Aeronautical Sciences*, Vol. 23, pp. 1007–1012.




Downloaded 12 Dec 2010 to 193.140.21.150. Redistribution subject to ASME license or copyright; see http://www.asme.org/terms/Terms_Use.cfm

# Combined Effect of Free-Stream Turbulence and Unsteady Wake on Heat Transfer Coefficients From a Gas Turbine Blade

**L. Zhang**
Senior Design Engineer,
Solar Turbines Inc.,
San Diego, CA 92186-5376

**J.-C. Han**
HTRI Professor,
Turbine Heat Transfer Laboratory,
Department of Mechanical Engineering,
Texas A&M University,
College Station, TX 77843-3123
Fellow ASME

*The combined effect of free-stream turbulence and unsteady wakes on turbine blade surface heat transfer was studied. The experiments used a five-blade linear cascade in a low-speed wind tunnel facility. A turbulence grid and spoked-wheel type wake generator produced the free-stream turbulence and unsteady wakes. The mainstream Reynolds numbers based on the cascade inlet mean velocity and blade chord length were 100,000, 200,000, and 300,000. Results show that the blade time-averaged heat transfer coefficient depends on the mean turbulence intensity, regardless of whether this mean turbulence intensity is from unsteady wake only, turbulence grid only, or a wake and grid combination. The higher mean turbulence promotes earlier boundary layer transition and causes much higher heat transfer coefficients on the suction surface. It also significantly enhances the heat transfer coefficients on the pressure surface. The unsteady wake greatly affects blade heat transfer for low oncoming free-stream turbulence; however, the wake effect diminishes for high oncoming turbulence. The free-stream turbulence also strongly affects blade heat transfer for a low wake passing frequency, but the oncoming turbulence effect diminishes for a high unsteady wake condition.*

## Introduction

The effect of free-stream turbulence and unsteady wakes generated by the combustor and the upstream blade row on the airfoil heat transfer is a crucial problem in gas turbine airfoil design. The effect of free-stream turbulence on increasing surface heat transfer coefficients has been reported for flow over a flat plate (Blair, 1983; Maciejewski and Moffat, 1992; Young et al., 1992), flow across a leading edge cylindrical model (Lowery and Vachon, 1975; Traci and Wilcox, 1975; Mehendale et al., 1991), and flow in a turbine blade model (Brown and Martin, 1979, 1982; Zhang and Han, 1994).

Many studies have focused on the effects of unsteady wake caused by the upstream blade row on the downstream airfoil heat transfer. Experiments have been conducted in turbines (Dunn, 1986; Dunn et al., 1986, 1989, 1994; Blair et al., 1989; Blair, 1994; Abhari et al., 1992) or in laboratory simulations (Pfeil et al., 1983; Wittig et al., 1987, 1988; O'Brien and Capp, 1989; O'Brien, 1990; Liu and Rodi, 1992; Dullenkopf et al., 1991; Han et al., 1993). Results show that unsteady wake promotes earlier and longer boundary layer transition on a suction surface and causes a much higher heat transfer coefficient on both the suction and pressure surfaces. Theoretical work, using a time-averaged intermittency factor, has also been reported (Mayle and Dullenkopf, 1990, 1991; Mayle, 1991; Dullenkopf and Mayle, 1994).

For the combined effect of free-stream turbulence and unsteady wake on turbine heat transfer, Ashworth et al. (1985) reported that with the existence of unsteady wake, the effect of increasing the free-stream turbulence level from low value (less than 1 percent) to approximately 4 percent moved transition on both the pressure and suction surfaces from 50–60 percent to about 10–30 percent of X/C. Doorly and Oldfield (1985) and Doorly (1988) studied the unsteady suction surface boundary layer in the presence of combined wake passing and free-stream turbulence. They reported the effect of wake passing on an already turbulent boundary layer is fairly small. The additional turbulence imposed by the wakes did not affect the heat flux associated with a turbulent boundary layer.

This study is a continuation of Han et al. (1993) and Zhang and Han (1994), and focuses on the combined effect of unsteady wake and free-stream turbulence on the turbine blade heat transfer (Zhang, 1993). The main objectives of this study were to: (1) determine the combined effect of free-stream turbulence and unsteady wake ($\bar{T}u$ = 12.2–21.2 percent) on the blade heat transfer coefficients at a given mainstream flow Reynolds number; (2) determine the effect of free-stream turbulence ($Tu$ = 2.8–17.1 percent) on the blade heat transfer coefficients for a given unsteady wake condition; (3) determine the effect of unsteady wake ($S$ = 0.1–0.3) on the blade heat transfer coefficients for a given free-stream turbulence; (4) determine the effect of mainstream flow Reynolds number on the blade heat transfer coefficients at a given free-stream turbulence level and a given unsteady wake condition; and (5) identify the similarity of the effects of free-stream turbulence, unsteady wake, and combined unsteady wake and free-stream turbulence on the blade time-averaged heat transfer.

## Test Apparatus and Instrumentation

**Test Apparatus.** Figure 1 shows the low-speed, open-loop wind tunnel designed for this study; see Han et al. (1993) for a detailed description. The center part of Fig. 1 shows the linear cascade, which accommodates the low-speed wind tunnel facility with an inlet velocity of 7, 14, and 21 m/s. The flow has a 107 deg turn in the cascade and the mean velocity increases 2.5 times from the inlet to the outlet. The airfoil configuration, scaled up by a factor of 5, produces a velocity ratio distribution similar to that inside a typical advanced high pressure turbine blade row. The cascade, made of high-quality model wood, has a chord length ($C$) of 22.68 cm, a radial span of 25.4 cm, and a blade spacing of 17.01 cm. The middle blade can be an instrumented pressure tap blade or an instrumented heat transfer blade.

Contributed by the Heat Transfer Division for publication in the JOURNAL OF HEAT TRANSFER. Manuscript received by the Heat Transfer Division June 1993; revision received July 1994. Keywords: Flow Transition, Turbines, Wakes. Associate Technical Editor: R. Viskanta.



Copyright © 1995 by ASME

Downloaded 12 Dec 2010 to 193.140.21.150. Redistribution subject to ASME license or copyright; see http://www.asme.org/terms/Terms_Use.cfm

A rotating spoked-wheel wake generator simulates unsteady moving wake as discussed by Han et al. (1993). The wake generator was located 8.89 cm upstream of the cascade inlet. The wake Strouhal number (St) simulates the unsteady wake flow characteristics of modern gas turbines (the estimated Strouhal numbers in real gas turbines range from 0.1 to 0.5). This paper's Strouhal number can range from 0 to 0.9 by varying the rod rotating speed ($N$ = 0 to 384 rpm) and flow inlet velocity ($V_1$ = 7, 14, 21 m/s), for a fixed rod number ($n$ = 32) and rod diameter ($d$ = 0.63 cm). The Reynolds number (Re) varies from 100,000, 200,000, to 300,000.

This study used two different turbulence grids designed to generate different levels of turbulence intensity, as described by Zhang and Han (1994). The coarse square bar grid (grid #1) or the fine square bar grid (grid #2) can be at different upstream locations from the cascade inlet. Each of the grids has an open area of 54 percent and could be 21 cm, 30 cm, and 60 cm, respectively, upstream from the inlet plane of the cascade. From now on we will use locations #1, #2, and #3 to refer to these grid locations.

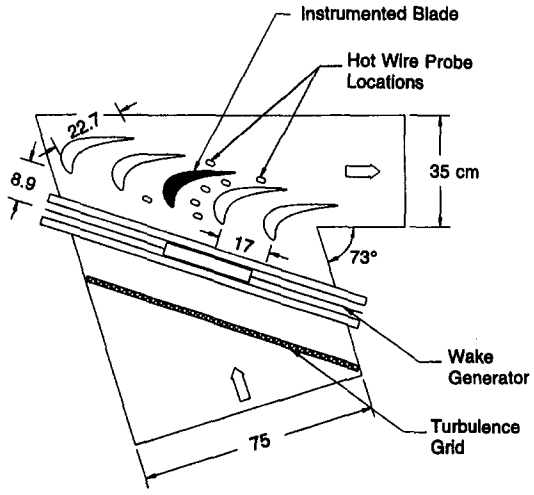



**Fig. 1 Schematic of the linear turbine blade cascade**

**Instrumentation.** A calibrated single hot-wire probe can be located in any slot around the middle blade as shown in Fig. 1. The phase-averaged (or ensemble-averaged) method was used to get the time-dependent periodic velocity and time dependent turbulence intensity. The phase-averaged velocity is obtained by dividing the instantaneous velocity signal into a rod-passing period and phase averaging them with the following equation:

$$\tilde{V}(m) = \frac{1}{N}\sum_{1}^{N} V(m) \tag{1}$$

where $N$ is the number of periods for each data set and $m$ is the serial number (bin number) in each period. In this paper, digital sampling rates of up to 100 kHz are obtained, depending on the rod-passing frequency, so that approximately 100 rod-passing periods ($N$ = 100) and 150 samples per period ($m$ = 1, 2, . . . , 150) are included in each digital record. The phase-averaged turbulence intensity is obtained based on the phase-averaged velocity by the following equation:

$$\tilde{Tu}(m) = \sqrt{\frac{\sum_{n=1}^{N} (V(m\cdot dt + n\cdot\tau) - \tilde{V}(m))^2}{N}} \Bigg/ \tilde{V}(m) \tag{2}$$

where $m$ is the serial number in each period, $dt$ is the time duration between each data signal, and $\tau$ is the time duration of one period. Mean turbulence intensity ($\bar{Tu}$) is defined to help find the turbulence level of the combined free-stream turbulence and unsteady wake flow. The mean turbulence intensity is the mean value of the phase-averaged turbulence intensity over one period as in the following equation:

$$\bar{Tu} = \frac{1}{M}\sum_{1}^{M} \tilde{Tu}(m) \tag{3}$$

where $M$ is the number of bins in a wake passing period ($M$ = 150 in this study). Note that the Strouhal number (S) characterized the turbulence level of the unsteady wake flow only (Han et al., 1993) while the turbulence intensity ($Tu$) characterized the turbulence level of the free-stream turbulence flow only (Zhang and Han, 1994).

**Heat Transfer Instrumented Blade.** Seventy-eight calibrated, 36 gage, copper-constantan thermocouples, located on the middle span of the blade, measured the time-averaged temperatures on the blade surface (Han et al., 1993). The local heat transfer coefficient $h$ can be calculated as

$$h = \frac{q''}{T_w - T_\infty} = \frac{q''_{\text{gen}} - q''_{\text{loss}}}{T_w - T_{aw}} \tag{4}$$

Since the Mach number $\ll 1$, $T_\infty \approx T_{aw} \approx 25$°C. Heat loss tests (for no-flow condition) and heat loss predictions using conduction and radiation heat transfer estimations were carried out at several temperatures ($T_w$ = 40 ~ 50°C). The overall heat losses for the entire blade surface are about 10 percent of the heat input

## Nomenclature

$C$ = airfoil chord length, straight distance between leading and trailing
$d$ = wake simulator rod diameter
$h$ = heat transfer coefficient
$k$ = thermal conductivity of air
$K$ = acceleration parameter = $\nu/V^2 \cdot dV/dX$
$n$ = wake simulator rod number
$N$ = wake simulator rod rotating speed, rpm
Nu = Nusselt number based on blade chord length = $hC/k$
$q''$ = net local convective heat flux from foil surface
$q''_{\text{gen}}$ = foil-generated surface heat flux from voltage-current measurements
$q''_{\text{loss}}$ = local heat flux loss
Re = Reynolds number based on chord length and cascade inlet velocity = $V_1C/\nu$
$\text{Re}_\theta$ = momentum thickness Reynolds number = $V\theta/\nu$
$Tu$ = local turbulence intensity
$V$ = local velocity
$V_1$ = cascade inlet velocity
$V_2$ = cascade exit velocity
$X$ = blade surface coordinate in streamwise direction
S = wake passing Strouhal number = $2\pi Ndn/(60V_1)$
$T_{aw}$ = local adiabatic wall temperature
$T_w$ = local wall temperature
$T_\infty$ = mainstream air temperature at the inlet of the cascade
$\tilde{V}$ = phase-averaged velocity
$\tilde{Tu}$ = phase-averaged turbulence intensity
$\bar{Tu}$ = mean turbulence intensity
$\theta$ = local momentum thickness
$\nu$ = kinematic viscosity of air



Downloaded 12 Dec 2010 to 193.140.21.150. Redistribution subject to ASME license or copyright; see http://www.asme.org/terms/Terms_Use.cfm

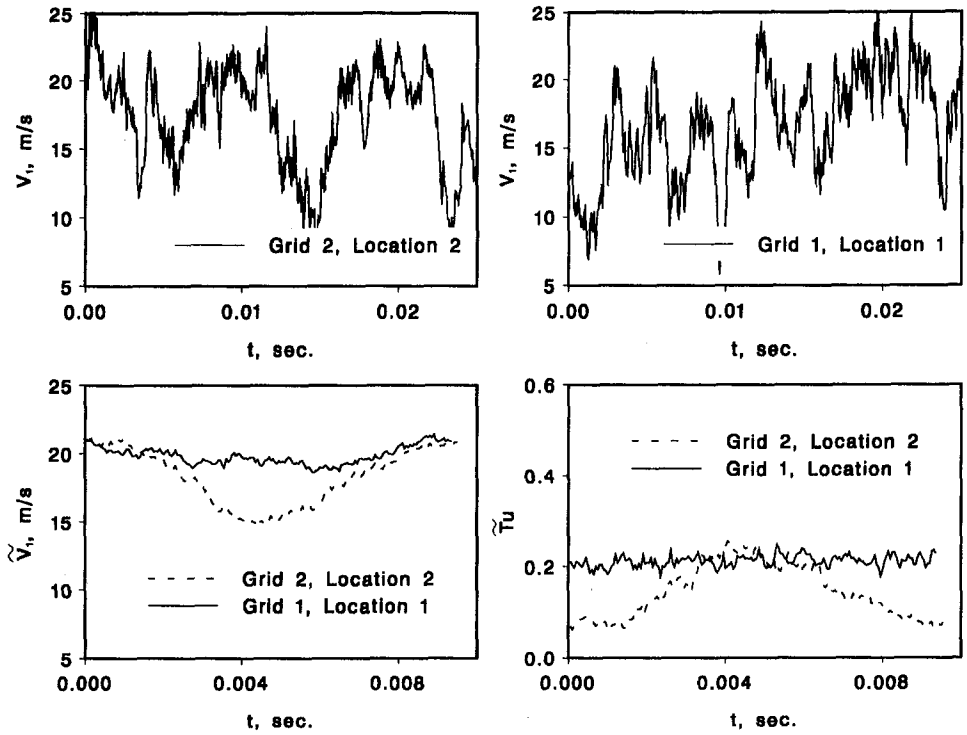



**Fig. 2 Cascade inlet instantaneous velocities, phase-averaged velocity, and turbulence intensities under unsteady wake (S = 0.2) and different turbulence grid conditions**

(4 percent due to conduction and 6 percent due to radiation) while the local heat losses vary from 6 to 11 percent depending on location and surface temperature. Uncertainty analysis was carried out based on Kline and McClintock (1953). The uncertainties due to $q''_{gen}$, $q''_{loss}$, and $(T_w - T_{aw})$ is 2, 4, and 4.1 percent, respectively. The results showed that the uncertainties in $h$ and Nu are below 7 percent while the uncertainties in phase-averaged turbulence intensity and mean turbulence intensity are below 10 percent for all three Reynolds number cases.

## Flow Measurement

Figure 2 shows the instantaneous velocity profiles for flow with a wake Strouhal number S = 0.2 superimposed with a low free-stream turbulence (grid #2, location #2, $Tu$ = 5.7 percent) and a high free-stream turbulence (grid #1, location #1, $Tu$ = 17.1 percent). The mean turbulence intensities ($\bar{T}u$) are 14.42 and 21.16 percent, respectively, after the free-stream flow is superimposed with the unsteady wake. The results show that the wake profile can be located for the low-turbulence grid, while the wake cannot be distinguished in a high-turbulence grid. The phase-averaged velocity profile becomes wider and shallower for the same given Strouhal number as the superimposed free-stream turbulence intensity increases. Figure 2 also shows the phase-averaged turbulence intensity increases by increasing the superimposed free-stream turbulence intensity. All Fig. 2 results show that an increase in superimposed free-stream turbulence intensity causes a decrease in the unsteadiness of the flow, an increase in randomness and phase-averaged turbulence intensity for a given wake Strouhal number (S = 0.2).

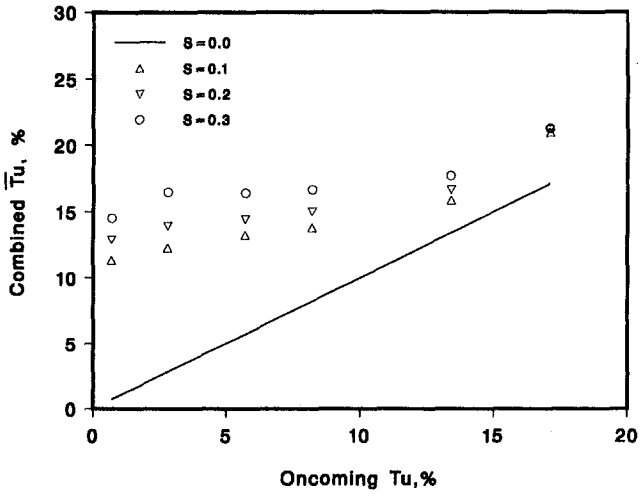



**Fig. 3 Mean turbulence intensities induced by unsteady wake and turbulence grid conditions**

Figure 3 shows the combined mean turbulence intensities ($\bar{T}u$) at the cascade inlet for flow with various oncoming free-stream turbulence for Reynolds number 300,000 ($Tu$ = 2.8, 5.0, 5.7, 8.2, 13.4, 17.1 percent, solid line in Fig. 3) superimposed with unsteady wake (S = 0.1, 0.2, and 0.3). Note that the free-stream turbulence intensity at the cascade inlet without grid or wake generator is about 0.7 percent. The corresponding length scales are about 1.3 cm, 1.4 cm, and 1.5 cm, respectively, for $Tu$ = 17.1, 13.4, and 5 percent. The results show that the combined mean turbulence intensity ($\bar{T}u$, vertical coordinate) for a given oncoming free-stream turbulence intensity (solid line in Fig. 3), increases with the increase of the superimposed wake Strouhal number (S = 0.1, 0.2, and 0.3). This wake effect diminishes at a higher oncoming free-stream turbulence intensity. The combined mean turbulence intensity is identical ($\bar{T}u$ = 21 percent) at a high oncoming free-stream turbulence intensity ($Tu$ = 17.1 percent) for all three Strouhal number cases.

Figure 4 shows the velocity ratio ($V/V_2$, local to the exit velocity) for Reynolds number 300,000 measured from time-averaged static pressure distributions for flow without grid or wake condition ($Tu$ = 0.7 percent), flow with grid only ($Tu$ = 17.1 percent), flow with unsteady wake only (S = 0.3), and flow with combined grid ($Tu$ = 17.1 percent) and unsteady wake (S =



Downloaded 12 Dec 2010 to 193.140.21.150. Redistribution subject to ASME license or copyright; see http://www.asme.org/terms/Terms_Use.cfm

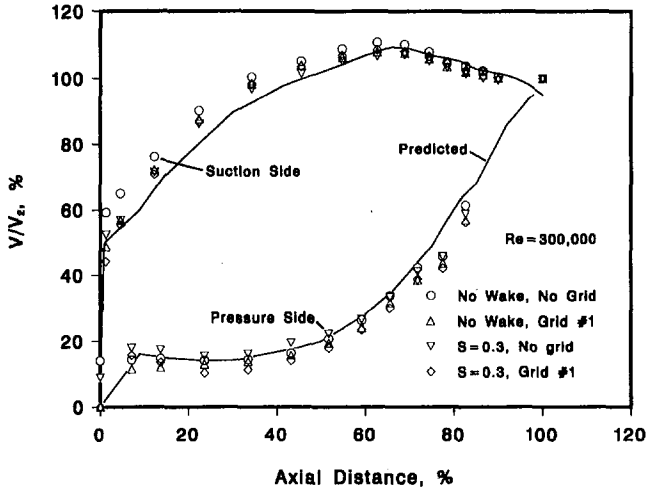



Fig. 4 Velocity distribution on the pressure tap blade model under unsteady wake and turbulence grid conditions

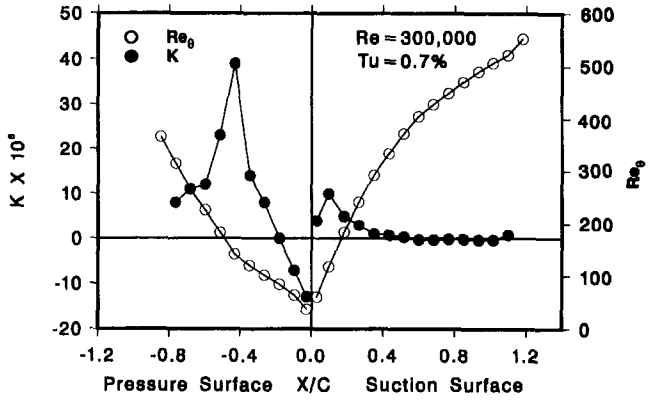



Fig. 5 Calculated acceleration parameter and momentum thickness Reynolds number for $Tu$ = 0.7 percent

0.3). The results suggest that the velocity distributions around the blade surface are similar to the flow under the various conditions listed above. This implies that the unsteady wake or free-stream turbulence may not change the mean (time-averaged) velocity near the blade surface. The solid line in Fig. 4 is the pretest prediction of the computer code "BLADING." The measured velocity on the pressure side surface is close to the prediction. However, the measured velocity on the suction side surface is higher than the predicted value. The velocity on the suction side accelerates to about $X/C = 0.6$ then decelerates until the exit. The velocity decelerates to about $X/C = -0.2$ on the pressure side and then accelerates. Figure 5 shows the calculated acceleration parameter and momentum thickness Reynolds number for $Tu = 0.7$ percent. These pressure gradients strongly affect the boundary layer transition and blade heat transfer.

## Heat Transfer Results

Figure 6 shows the effect of unsteady wake on local Nusselt number distributions on the blade's pressure and suction surfaces for Reynolds number 300,000, and for a given low oncoming free-stream turbulence (grid #2, location #2, $Tu = 5.7$ percent). The superimposed wake Strouhal numbers are 0.1, 0.2, and 0.3, which result in a mean turbulence intensity ($\bar{T}u$) at the cascade inlet of 13.2, 14.2, and 16.4 percent, respectively. The Nusselt number distributions on the blade for the flow without wake or grid ($Tu = 0.7$ percent) follow the predicted results from the modified version of the STAN 5 program (Gaugler, 1981). For low oncoming free-stream turbulence (5.7 percent), the local Nusselt number over the entire blade surface increases by increasing the Strouhal number. For flow with a Strouhal number 0.3 ($\bar{T}u = 16.4$ percent), the leading edge Nusselt number is about 15 percent higher than that for flow without turbulence grid or unsteady wake ($Tu = 0.7$ percent). This is a significant increase in leading edge heat transfer. The increase in the local Nusselt number for the blade suction surface is even more significant due to the increase of the superimposed Strouhal number. The corresponding mean turbulence intensity at the cascade inlet is as high as 16.4 percent, for flow with Strouhal number 0.3. The maximum local Nusselt number (at $X/C = 0.8$) is about 3.4 times that for flow without turbulence grid or unsteady wake. Figure 6 also shows that the increase of superimposed wake Strouhal number induces an earlier boundary layer transition from laminar to turbulent flow. As the wake Strouhal number increases, the transition point moves forward and the transition zone becomes longer. This is because the higher unsteady wake flow induces earlier transition while the flow acceleration (see Figs. 4 and 5) suppresses the production of turbulence spots and elongates the transition zone. The solid lines in Fig. 6 are predictions based on the time-averaged intermittency factor method proposed by Mayle (1991). The values of $X_{tw}$, the onset location of wake-induced transition, are $0.25C$, $0.2C$, and $0.15C$, respectively, for S = 0.1, 0.2, and 0.4. The results show a good match on the suction side Nusselt number distributions, except that the theory underpredicts the data before flow transition. Figure 6 also shows that the pressure surface Nusselt number increases considerably, with an increasing Strouhal number, for this given low oncoming free-stream turbulence. The Nusselt number increases slightly over the main portion of the pressure surface at each Strouhal number. No transition point can be clearly located by examining the pressure side Nusselt number distributions (see Fig. 5). The maximum local Nusselt number increment on the pressure surface (at $X/C = -0.2$) for Strouhal number 0.3 case is about 1.8 times that for flow without turbulence grid or unsteady wake.

Figure 7 shows the effect of unsteady wake on local Nusselt number distributions on the pressure and suction surfaces of the blade for a given high oncoming free-stream turbulence (grid #1, location #1, $Tu = 17.1$ percent). The superimposed wake Strouhal numbers are 0.1, 0.2, and 0.3, which result in a mean turbulence intensity ($\bar{T}u$) at the cascade inlet of 20.9, 21.1, and 21.2 percent, respectively. The results show that the local Nusselt number does not increase with increasing the Strouhal number for a given high free-stream turbulence. This might be explained

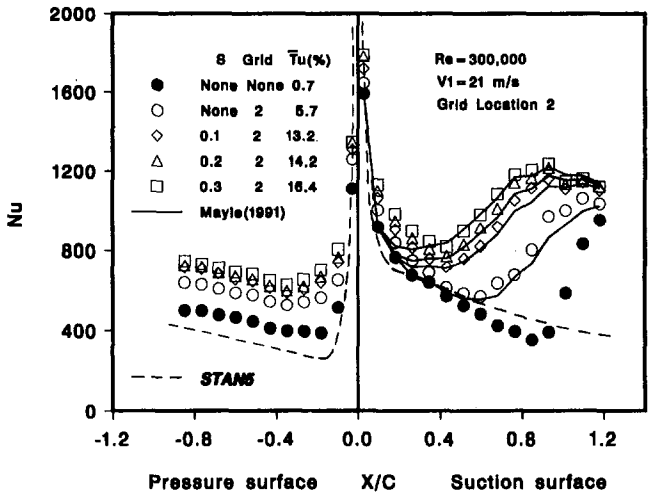



Fig. 6 Effect of unsteady wake on local heat transfer coefficient distributions for a given low oncoming free-stream turbulence condition



Downloaded 12 Dec 2010 to 193.140.21.150. Redistribution subject to ASME license or copyright; see http://www.asme.org/terms/Terms_Use.cfm

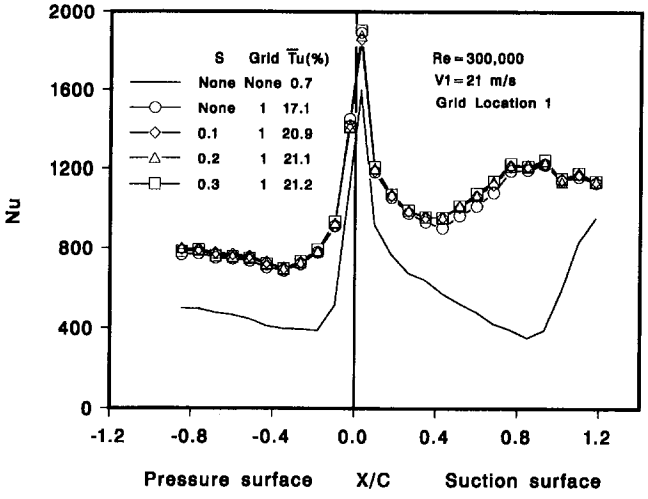



Fig. 7 Effect of unsteady wake on local heat transfer coefficient distributions for a given high oncoming free-stream turbulence condition

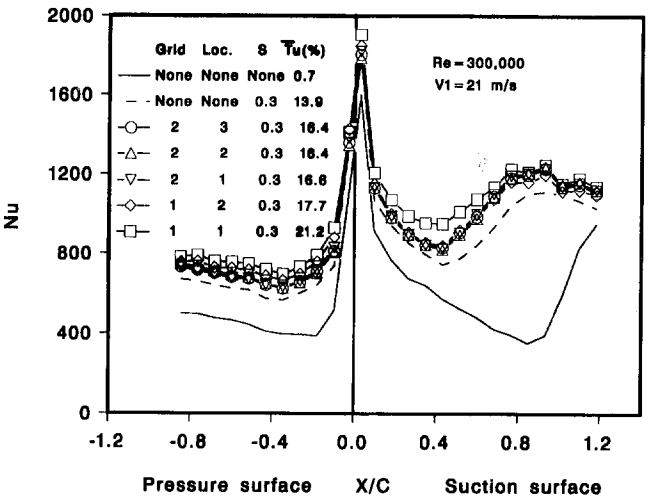



Fig. 9 Effect of oncoming free-stream turbulence on local heat transfer coefficient distributions for a given high unsteady wake condition

by the fact that their mean turbulence intensities (20.93, 21.16, and 21.24 percent) are almost identical, which suggests that further increase in mean turbulence intensity (by unsteady wake) at a high oncoming free-stream turbulence intensity may not cause a significant increase in heat transfer.

Figure 8 shows the effect of oncoming free-stream turbulence ($Tu$ = 2.8, 5.7, 8.2, 13.4, 17.1 percent) on local Nusselt number distributions on the blade's pressure and suction surfaces for Reynolds number 300,000 and for a given medium unsteady wake (S = 0.1, $\bar{T}u$ = 10.3 percent). For a medium Strouhal number (S = 0.1, $\bar{T}u$ = 10.3 percent), the local Nusselt number over the entire blade surface increases incrementally by increasing the oncoming free-stream turbulence level ($\bar{T}u$ = 12.2–20.9 percent). Figure 9 gives the effect of oncoming free-stream turbulence on local Nusselt number distributions on pressure and suction surfaces of the turbine blade for a given stronger unsteady wake (S = 0.3, $\bar{T}u$ = 13.9 percent). The increase in the local Nusselt number, for a stronger Strouhal number (S = 0.3 with $\bar{T}u$ = 13.9 percent), becomes less obvious due to the increase of the oncoming free-stream turbulence ($\bar{T}u$ = 16.4–17.7 percent), except for the high free-stream turbulence case ($\bar{T}u$ = 21.2 percent).

This discussion makes an effort to relate the Nusselt number distribution with the mean (combined) turbulence intensity. Figure 10 further demonstrates this by showing the effects of unsteady wake only (S = 0.3, $\bar{T}u$ = 13.9 percent), free-stream turbulence only ($Tu$ = 13.4 percent), and combined unsteady wake with free-stream turbulence (S = 0.1, free-stream $Tu$ = 5.7 percent, combined $\bar{T}u$ = 13.2 percent) on the Nusselt number distributions for Reynolds number 300,000. The results show that the three Nusselt number distributions are about the same for the same level of mean turbulence intensity. It seems that for a given Reynolds number, the mean (combined) turbulence intensity ($\bar{T}u$) is an important parameter in determining the effects of unsteady wake, free-stream turbulence, and the combination of both on turbine blade time-averaged heat transfer. In reality, however, the blade surface temperature (and heat transfer) under the unsteady wake condition is time dependent due to the periodic time-dependent nature of the unsteady wake passing, while the blade surface temperature (and heat transfer), under the condition of free-stream turbulence only, is random with time and not periodic time dependent. Thermocouples measure the "time-averaged" blade surface temperature and are not able to distinguish the time-dependent effect (due to unsteady wake) and the time-averaged effect (due to oncoming grid-generated free-stream turbulence) as long as their mean turbulence intensities are the same.

Figure 11 shows the effect of Reynolds number on the local Nusselt number augmentations for a wake Strouhal number S

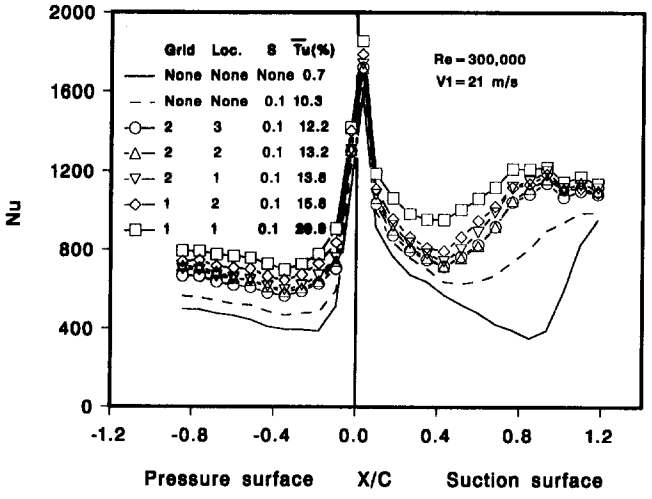



Fig. 8 Effect of oncoming free-stream turbulence on local heat transfer coefficient distributions for a given medium unsteady wake condition

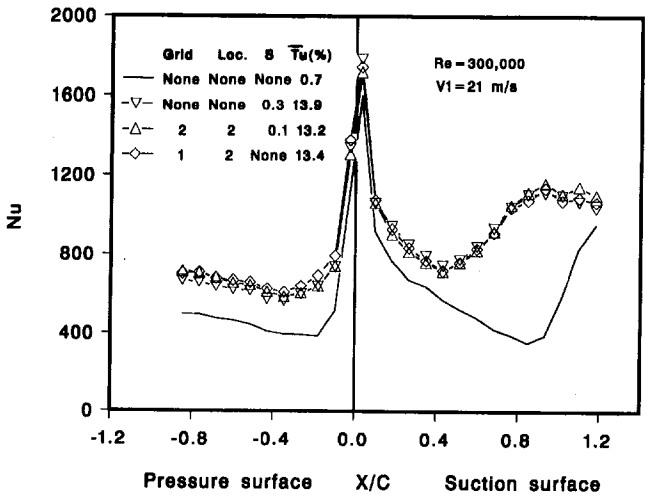



Fig. 10 Effect of oncoming free-stream, unsteady wake, and combined conditions on local heat transfer coefficient distributions



Downloaded 12 Dec 2010 to 193.140.21.150. Redistribution subject to ASME license or copyright; see http://www.asme.org/terms/Terms_Use.cfm

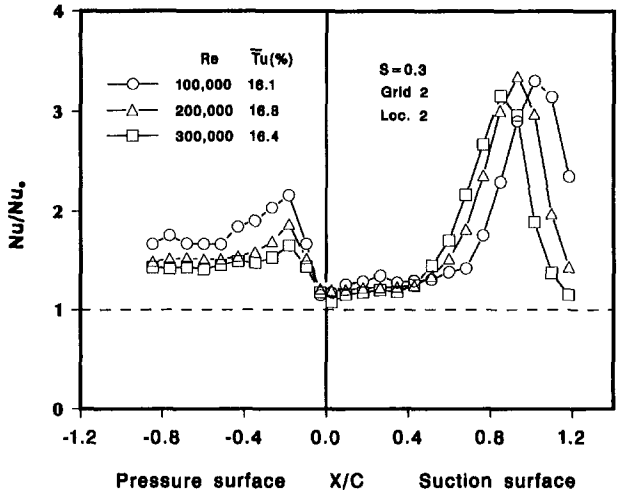



**Fig. 11 Effect of Reynolds number on local heat transfer coefficient augmentations for a combined wake and grid turbulence condition**

= 0.3 superimposed with a low free-stream turbulence (grid #2, location #2, $Tu$ = 5.7 percent). The local Nusselt number augmentation is the ratio of local heat transfer coefficient for flow under the combined free-stream turbulence and unsteady wake conditions ($\bar{T}u$ = 16.1–16.8 percent) to that for flow without turbulence grid or unsteady wake ($Tu$ = 0.7 percent). Results show that the maximum Nusselt number augmentations at the suction surface are about the same but the location of the maximum Nusselt number augmentation moves forward with an increase of the Reynolds number. The Nusselt number augmentation and its maximum value decrease at the pressure surface with the increase of the Reynolds number. However, the location of the maximum Nusselt number augmentation remains the same for the three Reynolds numbers studied.

## Conclusions

The influence of free-stream turbulence and unsteady wake on turbine airfoil surface heat transfer has been investigated. Local Nusselt number distributions are obtained under various combinations of free-stream turbulence level superimposed with unsteady wake for three Reynolds numbers. The main conclusions are:

1 The mean turbulence intensity (mean value of phase-averaged turbulence intensity), for a given flow Reynolds number, may be an important parameter in determining the flow condition (unsteady wake, free-stream turbulence, or combined) and its effect on the blade "time-averaged" heat transfer distribution.

2 The unsteady wake or grid-generated turbulence significantly augments the turbine blade heat transfer. In some cases, the unsteady wake, the grid-generated turbulence, and the combination of both may create a similar effect on the blade "time-averaged" heat transfer, when they produce the same level of mean turbulence intensity.

3 The superimposed unsteady wake causes an increase of turbine blade heat transfer for a given low or medium oncoming free-stream turbulence. However, the superimposed unsteady wake effect diminishes for a high oncoming free-stream turbulence.

4 The superimposed free-stream turbulence causes an increase of turbine blade heat transfer for a wake Strouhal number. However, the superimposed free-stream turbulence effect diminishes for a high wake Strouhal number.

5 The peak values of heat transfer coefficient augmentation on the suction surface for oncoming free-stream turbulence and wake Strouhal number remains constant (about 3.4) for the three studied Reynolds numbers. However, the location of the peak heat transfer augmentation moves forward for a higher Reynolds number.

6 The present results are based on a spoked-wheel type wake generator and the grid-generated turbulence level for Reynolds numbers between 100,000 and 300,000. Readers should be cautious in extrapolating the results from this study to gas turbine applications.

## Acknowledgments

The Texas Higher Education Coordinating Board—Advanced Technology Program supported this project under Grant Number 999903-104(TEES7090). Special thanks go to Ms. H. Wanda Jiang and Dr. M. T. Schobeiri of Texas A&M University for preparing the STAN 5 prediction in Fig. 6.

## References

Abhari, R. S., Guenette, G. R., Epstein, A. H., and Giles, M. B., 1992, "Comparison of Time-Resolved Measurements and Numerical Calculations," ASME *Journal of Turbomachinery*, Vol. 114, pp. 818–827.

Ashworth, D. A., LaGraff, J. E., Schultz, D. L., and Grindrod, K. J., 1985, "Unsteady Aerodynamic and Heat Transfer Processes in a Transonic Turbine Stage," ASME *Journal of Engineering for Gas Turbines and Power*, Vol. 107, pp. 1022–1030.

Blair, M. F., 1983, "Influence of Free-Stream Turbulence on Turbulence Boundary Layer Heat Transfer and Mean Profile Development: Part I—Experimental Data; Part II—Analysis of Results," ASME JOURNAL OF HEAT TRANSFER, Vol. 105, pp. 33–47.

Blair, M. F., Dring, R. P., and Joslyn, H. D., 1989, "The Effects of Turbulence and Stator/Rotor Interactions on Turbine Heat Transfer: Part I—Design Operating Conditions; Part II—Effects of Reynolds Number and Incidence," ASME *Journal of Turbomachinery*, Vol. 111, pp. 87–103.

Blair, M. F., 1994, "An Experimental Study of Heat Transfer in a Large-Scale Turbine Rotor Passage," ASME *Journal of Turbomachinery*, Vol. 116, pp. 1–13.

Brown, A., and Martin, B. W., 1979, "Heat Transfer to Turbine Blades, With Special Reference to the Effects of Mainstream Turbulence," ASME Paper No. 79-GT-26.

Brown, A., and Martin, B. W., 1982, "Flow Transition Phenomena and Heat Transfer Over the Pressure Surface of Gas Turbine Blades," ASME *Journal of Engineering for Power*, Vol. 104, pp. 360–367.

Doorly, D. J., and Oldfield, M. L. G., 1985, "Simulation of the Effects of Shock-Waves Passing on a Turbine Rotor Blade," ASME *Journal of Engineering for Gas Turbines and Power*, Vol. 107, pp. 998–1006.

Doorly, D. J., 1988, "Modeling the Unsteady Flow in a Turbine Rotor Passage," ASME *Journal of Turbomachinery*, Vol. 110, pp. 27–37.

Dullenkopf, K., Schulz, A., and Wittig, S., 1991, "The Effect of Incident Wake Conditions on the Mean Heat Transfer of an Airfoil," ASME *Journal of Turbomachinery*, Vol. 113, pp. 412–418.

Dullenkopf, K., and Mayle, R. E., 1994, "The Effects of Incident Turbulence and Moving Wakes on Laminar Heat Transfer in Gas Turbines," ASME *Journal of Turbomachinery*, Vol. 116, pp. 23–28.

Dunn, M. G., 1986, "Heat Flux Measurements for the Rotor of a Full-Stage Turbine: Part I—Time-Averaged Results," ASME *Journal of Turbomachinery*, Vol. 108, pp. 90–97.

Dunn, M. G., George, W. K., Rae, W. J., Woodward, S. H., Moller, J. C., and Seymour, J. P., 1986, "Heat Flux Measurements for the Rotor of a Full-State Turbine: Part II—Description of Analysis Technique and Typical Time-Resolved Measurements," ASME *Journal of Turbomachinery*, Vol. 108, pp. 98–107.

Dunn, M. G., Seymour, P. J., Woodward, S. H., George, W. K., and Chupp, R. E., 1989, "Phase-Resolved Heat Flux Measurements on the Blade of a Full-Scale Rotating Turbine," ASME *Journal of Turbomachinery*, Vol. 111, pp. 8–19.

Dunn, M. G., Kim, J., Civinskas, K. C., and Boyle, R. J., 1994, "Time-Averaged Heat Transfer and Pressure Measurements and Comparison With Prediction for a Two-Stage Turbine," ASME *Journal of Turbomachinery*, Vol. 116, pp. 14–22.

Gaugler, R. E., 1981, "Some Modifications to, and Operational Experiments With, the Two-Dimensional, Finite-Difference Boundary-Layer Code, STAN 5," NASA TM-81631.

Han, J. C., Zhang, L., and Ou, S., 1993, "Influence of Unsteady Wake on Heat Transfer Coefficients From a Gas Turbine Blade," ASME JOURNAL OF HEAT TRANSFER, Vol. 115, pp. 904–911.

Kline, S. J., and McClintock, F. A., 1953, "Describing Uncertainties in Single Sample Experiments," *Mechanical Engineering*, Vol. 75, Jan., pp. 3–8.

Liu, X., and Rodi, W., 1992, "Measurements of Unsteady Flow and Heat Transfer in a Linear Turbine Cascade," ASME Paper No. 92-GT-323.

Lowery, G. W., and Vachon, R. I., 1975, "The Effect of Turbulence on Heat Transfer From Heated Cylinders," *International Journal of Heat and Mass Transfer*, Vol. 18, pp. 1229–1242.



Downloaded 12 Dec 2010 to 193.140.21.150. Redistribution subject to ASME license or copyright; see http://www.asme.org/terms/Terms_Use.cfm

Maciejewski, P. K., and Moffat, R. J., 1992, "Heat Transfer With Very High Free-Stream Turbulence: Part I—Experimental Data; Part II—Analysis of Results," ASME JOURNAL OF HEAT TRANSFER, Vol. 114, pp. 827–839.

Mayle, R. E., and Dullenkopf, K., 1990, "A Theory for Wake Induced Transition," ASME *Journal of Turbomachinery,* Vol. 112, pp. 188–195.

Mayle, R. E., and Dullenkopf, K., 1991, "More on the Turbulent-Strip Theory for Wake-Induced Transition," ASME *Journal of Turbomachinery,* Vol. 113, pp. 428–432.

Mayle, R. E., 1991, "The Role of Laminar-Turbulent Transition in Gas Turbine Engines," ASME *Journal of Turbomachinery,* Vol. 113, pp. 509–537.

Mehendale, A. B., Han, J. C., and Ou, S., 1991, "Influence of High Mainstream Turbulence on Leading Edge Heat Transfer," ASME JOURNAL OF HEAT TRANSFER, Vol. 113, pp. 843–850.

O'Brien, J. E., and Capp, S. P., 1989, "Two-Component Phase-Averaged Turbulence Statistics Downstream of a Rotating Spoked-Wheel Wake Generator," ASME *Journal of Turbomachinery,* Vol. 111, pp. 475–482.

O'Brien, J. E., 1990, "Effect of Wake Passing on Stagnation Region Heat Transfer," ASME *Journal of Turbomachinery,* Vol. 112, pp. 522–530.

Pfeil, H., Herbst, R., and Schroeder, T., 1983, "Investigation of the Laminar-Turbulent Transition of Boundary Layers Disturbed by Wakes," ASME *Journal of Engineering for Power,* Vol. 105, pp. 130–137.

Traci, R. M., and Wilcox, D. C., 1975, "Free-Stream Turbulence Effects on Stagnation Point Heat Transfer," *AIAA Journal,* Vol. 13, No. 7, pp. 890–896.

Wittig, S., Dullenkopf, K., Schulz, A., and Hestermann, R., 1987, "Laser-Doppler Studies of the Wake-Effected Flow Field in a Turbine Cascade," ASME *Journal of Turbomachinery,* Vol. 109, pp. 170–176.

Wittig, S., Schulz, A., Dullenkopf, K., and Fairbanks, J., 1988, "Effects of Free-Stream Turbulence and Wake Characteristics on The Heat Transfer Along a Cooled Gas Turbine Blade," ASME Paper No. 88-GT-179.

Young, C. D., Han, J. C., Huang, Y., and Rivir, R. B., 1992, "Influence of Jet-Grid Turbulence on Flat Plate Turbulent Boundary Layer Flow and Heat Transfer," ASME JOURNAL OF HEAT TRANSFER, Vol. 114, pp. 65–72.

Zhang, L., 1993, "Influence of Mainstream Turbulence and Unsteady Wake on Turbine Blade Heat Transfer," Ph.D. Dissertation, Texas A&M University, May.

Zhang, L., and Han, J. C., 1994, "Influence of Mainstream Turbulence on Heat Transfer Coefficients From a Gas Turbine Blade," ASME JOURNAL OF HEAT TRANSFER, Vol. 116, pp. 896–903.



Downloaded 12 Dec 2010 to 193.140.21.150. Redistribution subject to ASME license or copyright; see http://www.asme.org/terms/Terms_Use.cfm

# Augmented Heat Transfer in a Recovery Passage Downstream From a Grooved Section: An Example of Uncoupled Heat/Momentum Transport

**M. Greiner**
Associate Professor.
Mem. ASME

**R.-F. Chen**
Research Assistant.
Student Mem. ASME

**R. A. Wirtz**
Professor.
Fellow ASME

Mechanical Engineering Department,
University of Nevada,
Reno, NV 89557

*Earlier experiments have shown that cutting transverse grooves into one surface of a rectangular cross-sectional passage stimulates flow instabilities that greatly enhance heat transfer/pumping power performance of air flows in the Reynolds number range $1000 < Re < 5000$. In the current work, heat transfer, pressure, and velocity measurements in a flat passage downstream from a grooved region are used to study how the flow recovers once it is disturbed. The time-averaged and unsteady velocity profiles, as well as the heat transfer coefficient, are dramatically affected for up to 20 hydraulic diameters past the end of the grooved section. The recovery lengths for shear stress and pressure gradient are significantly shorter and decrease rapidly for Reynolds numbers greater than Re = 3000. As a result, a 5.4-hydraulic-diameter-long recovery region requires 44 percent less pumping power for a given heat transfer level than if grooving continued.*

## Introduction

Transport augmentation schemes are regularly used to reduce the size and operating costs of heat exchangers. Typical methods involve fins to extend the transport surface area, or offset strips that promote thin boundary layers (Kays and London, 1984). Nevertheless, heat transfer in these passages is generally limited by an absence of convective mixing since small geometric dimensions limit the Reynolds number.

Augmentation techniques have been developed that promote mixing in channels by intentionally stimulating normally damped Tollmien–Schlichting waves through the use of continuous arrays of spatially periodic disturbances such as transverse-cylinder eddy promoters (Greiner et al., 1988; Majumdar and Amon, 1992) or transverse grooves cut into the channel walls (Kozlu et al., 1988; Greiner et al., 1990, 1991a, 1991b). Deep grooves promote inflection points in the axial-velocity profile. Kelvin-Helmholtz instabilities of these points destabilize two-dimensional Tollmien–Schlichting waves in the channel mainstream for Reynolds numbers greater than $Re > 350$. Significant heat transfer augmentation coincides with the early onset of *three*-dimensional mixing at $Re = 800$, and this flow develops rapidly after the first groove. A significant result for air heat exchange devices is that fully developed heat transfer is enhanced relative to laminar flow in a flat channel by as much as a factor of 4.6 at equal Reynolds numbers and 3.5 at equal pumping powers. Furthermore, significant augmentation extends into the transitional flow regime, $1000 < Re < 5000$.

Investigations of heat transfer on flat surfaces *downstream* from disturbances have also shown favorable performance characteristics. For example, measurements made on a flat plate downstream from different turbulence-generating grids show that the ratio of heat transfer to friction factor increases linearly with increasing turbulence intensity (Blair, 1983). Maciejewski and Moffat (1992) measure heat transfer from a flat plate subject to very high levels of free-stream turbulence. Their measured heat transfer coefficients, along with that of Blair, increase linearly with the maximum turbulence intensity of the flow.

In the current work, a flat recovery region in a rectangular cross-sectional channel downstream from a grooved section is considered to determine what effect axially decaying unsteady flows and pressure gradients have on uncoupling heat and momentum transport. This paper reports measured axial variations of heat transfer, pressure gradient, and center-span velocity profiles for a range of Reynolds number, $1500 \leq Re \leq 5000$. A method for determining axial-profiles of *wall shear stress* from pressure drop and velocity measurements is developed. These profiles are compared directly to heat transfer measurements to determine whether the decay rates are significantly different, implying that heat/momentum transport mechanisms are uncoupled. As a practical measure of performance augmentation, the heat transfer/pumping power characteristics of the downstream recovery region are compared to the performance of a fully grooved channel.

## Test Configuration

We consider the *partially* grooved channel shown in Fig. 1. A fully developed air flow from a 20:1 aspect ratio rectangular channel enters a section with thirteen right-triangular grooves cut into the lower wall (length $a$, depth $b$), and then passes into another flat-walled duct. Starting at the beginning of the grooved section, $x = 0$, the lower wall temperature is held constant at the inlet value $T_0$, while the upper wall develops a thermal boundary layer by dissipating a uniform heat flux, $q''$.

This geometry is a modification of a "fully grooved" passage studied by Greiner et al. (1991a, 1991b). In that work, a passage with forty-six cavities is examined. Flow visualizations and pressure measurement from the previous work show that the flow is essentially fully developed by the fifth groove for Reynolds numbers greater than $Re = 1000$, indicating that the flow conditions at the exit of the grooved section of the current experiment are fully developed in a groove-periodic sense. Dimensionless temperature difference measurements are not fully developed, however. Our general experimental protocol is to measure local heat transfer and pressure drop from the upper, flat surface along with profiles of time-averaged and root-mean-squared (rms) axial velocity at the center span in the grooved and flat sections of the

Contributed by the Heat Transfer Division for publication in the JOURNAL OF HEAT TRANSFER. Manuscript received by the Heat Transfer Division September 1993; revision received July 1994. Keywords: Augmentation and Enhancement, Forced Convection, Heat Exchangers. Associate Technical Editor: R. Viskanta.


Copyright © 1995 by ASME


Downloaded 12 Dec 2010 to 193.140.21.150. Redistribution subject to ASME license or copyright; see http://www.asme.org/terms/Terms_Use.cfm

channel for a range of Reynolds numbers. These results are compared to local measurements in the same passage with fully grooved and fully flat lower surfaces.

An open-loop wind tunnel is used in this investigation. Laboratory air at approximately 26°C and $8.7 \times 10^4$ Pa (elevation 1300 m) is drawn through a filter/screen box, an entrance nozzle, and then into a flat Plexiglas flow development section. The channel height is $H = 10$ mm, width (normal to the plane of the Fig. 1) is $W = 203$ mm, and length is 1.34 m. For the Reynolds numbers considered in this work, the flow is fully developed by the time it exits this section. The air then flows through the test section described below. Upon leaving that section, the fluid enters a large, baffled exit-plenum, flows through calibrated rotameters (whose three standard deviation flow rate uncertainty is always less than 4 percent), and is drawn into a variable speed blower.

The test section is 1.10 m long. Its chassis consists of a 12-mm-thick aluminum lower surface and two Plexiglas side walls. The lower aluminum plate is backed by a water jacket for temperature control, and has provisions for mounting a set of right triangular ribs, to form a thirteen-cavity grooved surface ($a = 24$ mm, $b = 12$ mm, Fig. 1), followed by a flat 12-mm-thick aluminum plate downstream. The minimum channel spacing is $H = 10$ mm, making the dimensionless grooved-section length $L_g/D_h = 16.4$, and flat recovery section length $L_r/D_h = 40.3$. The chassis is designed so that two different Plexiglas upper surfaces may be installed; one is for pressure drop and velocity profile measurements; the other is for heat transfer experiments.

The upper plate used for heat transfer measurements has six custom heater/thermocouple/heat-flux-gage plates bonded to its surface. The heaters are standard electrical resistive foil elements. Each of the six heaters is wired in series with a trimming rheostat, and these subcircuits are wired in parallel to a regulated DC power supply. The heat flux passing to the fluid from each plate is monitored with an accuracy of ±1 percent (99 percent confidence level) by a 102 mm square thermopile heat-flux gage located at its center. During an experimental run, trimming rheostats are adjusted until the gage-indicated heat flux is the same for each heater plate. The axial variation of the centerspan heat flux is therefore less than 2 percent.

The six plate assemblies contain copper-constantan thermocouple junctions located 0.28 mm beneath the wetted surface at 18 points along the channel centerline. These thermocouples are referenced to a rake of three junctions located in the flow development section, at

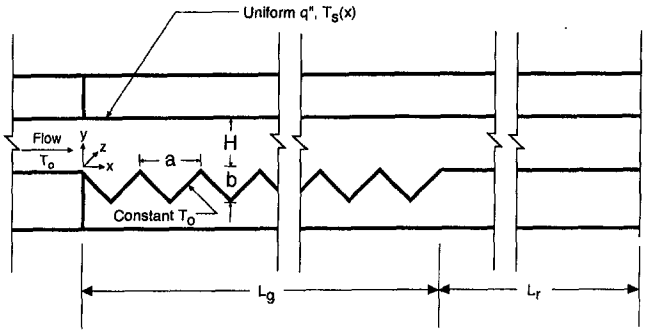



**Fig. 1 The partially grooved, rectangular cross-sectional channel. The channel has width $W$ normal to the page. The $z$-coordinate origin ($z = 0$) is at the center span.**

$x = -150$ mm. The local difference between the surface and inlet temperatures is determined by measuring the thermocouple voltage difference. A small correction is made for the conduction temperature drop between the local thermocouple and the wetted surface. Temperature measurements are made for a range of heat flux and indicate that natural convection effects are unimportant (Greiner et al., 1991a, 1991b). The uncertainty (one standard deviation) in dimensionless temperature difference (inverse Nusselt number) $\theta(x)$ is always less than 7 percent (Greiner et al., 1991a). The correction for radiation heat flux is found to be very small (less than 1 percent) since the aluminum grooved wall is maintained at a high gloss (emmisivity 0.09).

Pressure measurements are made to determine how the pressure and its gradient, $dp/dx$, depend on location and Reynolds number. In this experiment, the upper plate used to measure pressure has 24 2-mm-diam taps along its center span ($z = 0$) starting at $x = 0$. The tap spacing is 24 mm in the grooved section and the region just downstream ($0 \le x/D_h \le 21.4$) and 102 mm apart further downstream. The pressure difference between the first and the other 23 taps is measured with an electronic pressure transducer with a ±2.5 Pa accuracy (99 percent confidence) and plumbed using a switching valve.

Profiles of the streamwise velocity component are measured using a single component laser velocimeter in conjunction with a counter processor and frequency shifter. Transmitting optics

## Nomenclature

$a$ = groove length (Fig. 1)
$A$ = channel cross-sectional area = $HW$
$b$ = groove depth (Fig. 1)
$D_h$ = minimum channel hydraulic-diameter = $2HW/(H + W)$
$f$ = Fanning friction factor = $\tau/(\frac{1}{2}\rho V^2)$
$f_f, f_g$ = Fanning friction factor, in fully developed flat and grooved channels, respectively
$H$ = minimum channel height (Fig. 1)
$k$ = fluid thermal conductivity
$L$ = recovery-region zone length
$L_g$ = grooved-section length, Fig. 1
$L_r$ = recovery-section length, Fig. 1
$M$ = dimensionless momentum-flux gradient, Eq. (3$b$)
Nu = zone-average Nusselt number, Eq. (9)
$p$ = pressure
$P$ = dimensionless pressure gradient, Eq. (3$a$)
Pr = fluid Prandtl number
$q''$ = heat flux
Re = Reynolds number = $VD_h/\nu$
$R_\tau$ = wall shear stress recovery coefficient = $(f(x) - f_f)/(f_g - f_f)$
$R_\theta$ = dimensionless temperature recovery coefficient = $(\theta_f(x) - \theta(x))/(\theta_f(x) - \theta_g(x))$
$S$ = velocity profile shape factor, Eq. (4$a$)
$T_0$ = fluid entrance temperature
$T_s$ = local flat-surface temperature
$T$ = spatially averaged turbulence intensity, Eq. (4$b$)
$u$ = axial velocity
$\bar{U}_c$ = average center-span axial velocity = $(1/H)\int_0^H \bar{u}_c dy$.
$V$ = mass-averaged velocity based on minimum channel cross-sectional area
$W$ = channel width, Fig. 1
$x, y, z$ = coordinates, Fig. 1
$\theta$ = local, dimensionless, upper-wall temperature = $(T_s - T_0)k/q''D_h$
$\theta_f, \theta_g$ = local dimensionless temperature in fully flat and fully grooved ducts, respectively
$\nu$ = fluid kinematic viscosity
$\rho$ = fluid density
$\tau$ = effective wall shear stress
$\Phi$ = zone-average dimensionless pumping power, Eq. (10)

### Subscripts and Superscripts

$\overline{(\ )}$ = time-averaged steady component
$(\ )'$ = unsteady component
$(\ )_c$ = center-span value, $z = 0$
$(\ )_{rms}$ = root-mean-square deviation



Downloaded 12 Dec 2010 to 193.140.21.150. Redistribution subject to ASME license or copyright; see http://www.asme.org/terms/Terms_Use.cfm

with a beam crossing angle of 8.9 ± 0.2 deg (99 percent confidence) produce an ellipsoidal measurement volume with a 0.5-mm minor diameter and a 1.0-mm major diameter. The resulting velocity calibration uncertainty is less than 3 percent. Receiving optics are arranged in back-scatter mode. Particle seeding (propylene glycol) is introduced into the flow at the entrance nozzle of the wind tunnel. Variations in particle seeding rate show no effect on reported values.

The LDV is traverse mounted with a positioning accuracy of ±0.1 mm and measurements are made across the channel height, $0 < y/H < 1$, at center span, $z = 0$. At each location 1024 samples of the axial velocity are taken. Increasing the sample size shows that the time-averaged $\bar{u}$ and root-mean-square fluctuation $u_{\rm rms}$ components do not change. Sampling rates are typically 4–30 Hz with a validation rate of 15–20 percent, so that it takes approximately 0.5 to 4 minutes to acquire each data point. For each Reynolds number, profiles are measured at nine axial locations in the entrance, grooved, and recovery regions $-5.33 \le x/D_h \le 45.07$, well before end of the channel at $x/D_h = 56.7$. Further information on the experimental apparatus and procedures is described in Chen (1993).

## Wall Shear Stress

A method to determine the wall shear stress in the recovery region from pressure and velocity measurements is now developed. A force/momentum-flux balance on a recovery-region control volume of length $\Delta x$ with cross-sectional area $A$ gives

$$(p_x - p_{x+\Delta x})A - 2\tau(H + W)\Delta x = -\int_x \rho u^2 dA + \int_{x+\Delta x} \rho u^2 dA. \quad (1)$$

The pressure, wall shear stress, and velocity are now broken into time-averaged and unsteady components, for example, $u = \bar{u} + u'$. The resulting equation is then averaged over time and the limit is taken as $\Delta x \to 0$, giving

$$f = P + M, \quad (2)$$

where $f$ is the Fanning friction factor (dimensionless wall shear stress). In Eq. (2), the local, dimensionless pressure gradient, $P$, and the local, dimensionless momentum-flux gradient, $M$, are defined as

$$P = \frac{D_h}{2\rho V^2}\left(-\frac{d\bar{p}}{dx}\right) \quad (3a)$$

$$M = \frac{D_h}{2}\frac{d}{dx}(S^2 + T^2), \quad (3b)$$

respectively. In Eq. (3$b$), the velocity-profile shape factor, $S$, and the spatial-average of the streamwise turbulence intensity, $T$, are:

$$S = \sqrt{\frac{1}{A}\int_A \left(\frac{\bar{u}}{V}\right)^2 dA}, \quad (4a)$$

$$T = \sqrt{\frac{1}{A}\int_A \left(\frac{u_{\rm rms}}{V}\right)^2 dA}. \quad (4b)$$

The squares of these terms characterize the momentum-flux per unit mass of the steady and unsteady components of the axial velocity.

The term $P$ can be determined in a straightforward way from pressure measurements. The momentum-flux gradient $M$ is zero in fully developed flow, but must be evaluated in axially varying situations, such as the recovery region of the present test configuration. In order to evaluate $M$, we must calculate $S$ and $T$ at each axial location and then determine the axial gradient of the sum of their squares, Eq. (3$b$).

Evaluation of $S$ at a given axial location requires that the variation of the time-averaged velocity in the $y$,$z$-plane be known. To approximate $\bar{u}(y, z)$, we make convenient and *qualitatively* plausible assumptions that (1) the dependence of $\bar{u}$ on the spatial variables can be separated by factoring, and (2) the spanwise $z$ variation caused by boundary layers that develop along the channel side walls may be represented by a smooth, power-law profile, i.e.,

$$\bar{u}(y, z) = \bar{u}_c(y)\left(1 - \frac{|z|}{W/2}\right)^m. \quad (5)$$

In this expression, $\bar{u}_c(y)$ is the time-averaged velocity profile measured at the center span ($z = 0$). The power $m$ characterizes the side-wall boundary layer thickness. Its value is found by substituting the assumed velocity profile into the continuity equation, yielding the result, $m = \bar{U}_c/V - 1$, where $\bar{U}_c$ is the average center-span velocity. Measurements in the present test configuration show that the side-wall boundary layers causes the value of $\bar{U}_c/V$ to exceed unity by as much as 20 percent at lower Reynolds numbers (Chen, 1993). To approximate $S$, we substitute the assumed velocity profile into its definition, yielding:

$$S \approx \sqrt{\left[\frac{1}{2\left(\frac{\bar{U}_c}{V}\right) - 1}\right]\frac{1}{H}\int_0^H \left(\frac{\bar{u}_c(y)}{V}\right)^2 dy}. \quad (6)$$

To approximate $T$, we assume the spanwise variation of $u_{\rm rms}$ decreases as the side walls are approached in the same way that the time-mean velocity decreases. Similar to Eq. (5), we write,

$$u_{\rm rms}(y, z) = u_{{\rm rms},c}(y)\left(1 - \frac{|z|}{W/2}\right)^m, \quad (7)$$

where $u_{{\rm rms},c}(y)$ is measured at center span, and the power $m$ has the same value as that determined from the time-averaged velocity. The resulting approximation for $T$ is

$$T \approx \sqrt{\left[\frac{1}{2\left(\frac{\bar{U}_c}{V}\right) - 1}\right]\frac{1}{H}\int_0^H \left(\frac{u_{{\rm rms},c}(y)}{V}\right)^2 dy} \quad (8)$$

In summary, to evaluate the dimensionless momentum-flux gradient $M$, first center-span velocity profiles of $\bar{u}_c(y)$ and $u_{{\rm rms},c}(y)$ are measured at several axial locations. Equations (6) and (8) are evaluated at each axial location using numerical integration. Finite differencing is then used to evaluate the derivative in Eq. (3$b$). It is noted that a similar analysis using a trapezoid-shaped spanwise velocity profile (instead of the power-law contours of Eqs. (5) and (7)) produces essentially the same results as described in the following section (Chen, 1993).

## Results

**Velocity.** A series of center-span axial-velocity profiles for Re = 2000 and 4000 are shown in Figs. 2($a$) and 2($b$), respectively. Profiles are presented for six axial locations and are nondimensionalized by the channel mass-averaged velocity, $V$. Lines are used to connect the average values to show time-mean profiles, $\bar{u}_c/V$. Horizontal "error bars" show the magnitude of the local streamwise turbulence intensity, $u_{{\rm rms},c}/V$, on either side of the time-mean value. The two-standard-deviation uncertainty level (95 percent confidence) of the time-averaged velocity is six percent of $u_{{\rm rms},c}$.

We first consider the steady component of the velocity profiles. Upstream from the grooved section ($x/D_h = -5.33$), the mean profiles for both Reynolds numbers are smooth and symmetric about $y/H = 0.5$, and their shapes are representative of fully developed laminar and well-mixed transitional flat-channel flows. At $x/D_h = 13.85$, which is above the leading-edge peak of the last groove, the time-averaged velocity profiles are skewed away from the bottom grooved wall since enhanced mixing and



Downloaded 12 Dec 2010 to 193.140.21.150. Redistribution subject to ASME license or copyright; see http://www.asme.org/terms/Terms_Use.cfm

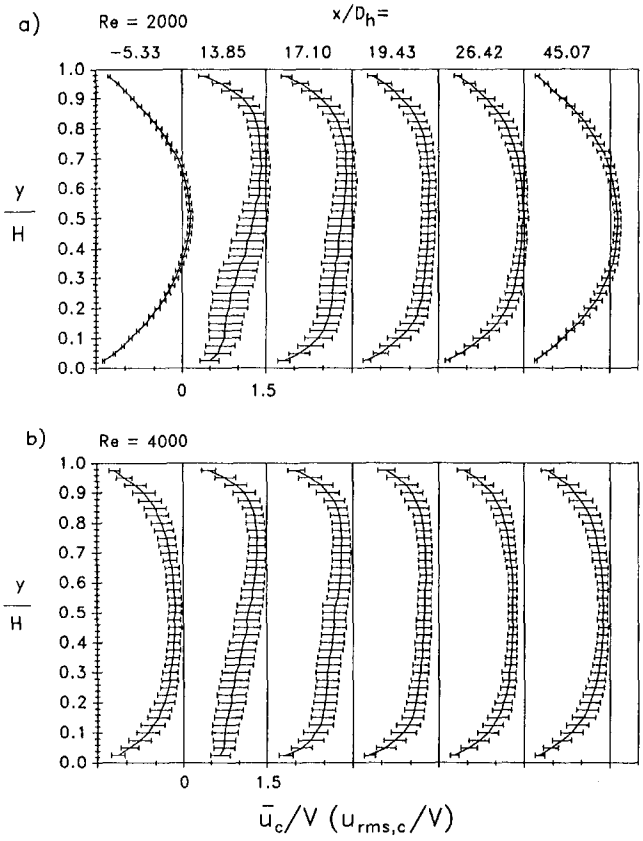



Fig. 2 Streamwise variation of dimensionless center span ($z = 0$), time-averaged (lines) and rms (error bars) axial-velocity profile measured from $x/D_h = -5.33$ to 45.07. The grooved section begins at $x/D_h = 0$ and ends at $x/D_h = 16.4$. The recovery region ends at $x/D_h = 56.7$. (*a*) Re = 2000. (*b*) Re = 4000.

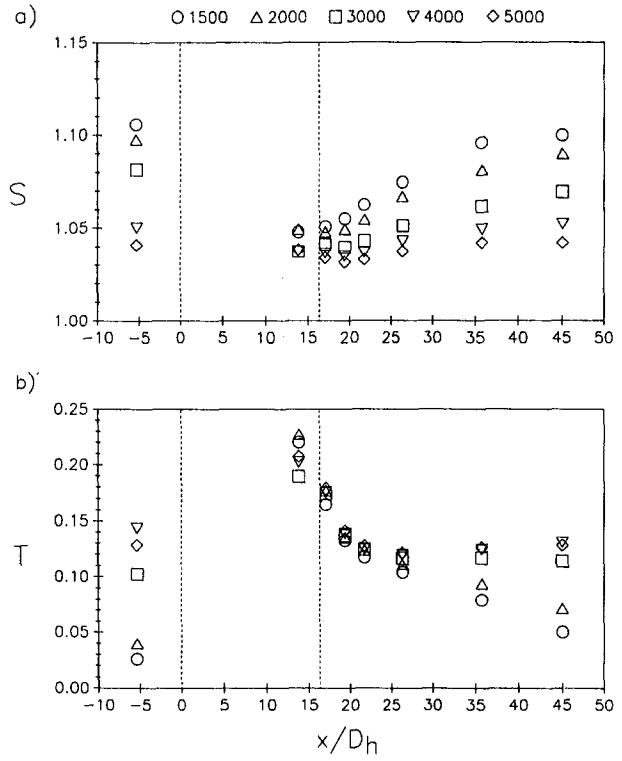



Fig. 3 Steady- and unsteady-velocity profiles parameters versus location for Re = 1500 to 5000. Vertical lines show the extent of the grooved section. (*a*) Time-averaged velocity profile shape factor. (*b*) Spatially averaged turbulence intensity.

momentum transport from the grooves retards the flow at the bottom of the channel. It is interesting to note that the velocity profiles in the grooved region are very similar for both Reynolds numbers. The profiles in the recovery region ($x/D_h > 16.4$) regain symmetry further downstream. For Re = 2000, the profile at the last measurement location exhibits center-channel flatness compared to $x/D_h = -5.33$, indicating it is still not fully recovered, while that for Re = 4000 appears to be fully recovered. This is the first of several indicators that show that the recovery lengths for this flow decreases with increasing Reynolds number.

The time-averaged velocity profile shape factor, $S$ (Eq. (4*a*)), is presented in Fig. 3(*a*) as a function of location and Reynolds numbers. Since this parameter is based on the square of the velocity, it is a measure of profile peaking in that it is larger for peaked contours, such as laminar, parabolic profiles, than for flatter shapes characteristic of well-mixed flows (we note that $S = 1$ for slug flow). This is shown in Fig. 3(*a*) where the entrance-region values are seen to decrease toward unity with increasing Reynolds number. In the grooved region, values of $S$ tend to collapse to the same low value, indicating the shape of the time-averaged velocity profiles are essentially independent of Reynolds number. In the recovery region downstream from the grooves, the values of $S$ eventually climb back to their flat channel levels. It is noted that this recovery is very rapid for Re > 3000.

We now return to Fig. 2 so we may consider the local streamwise-turbulence intensity, $u_{rms,c}/V$. Upstream from the grooves, the level of unsteadiness increases with Reynolds numbers, as expected. Instability in the grooved-section causes the level of mixing to be much larger than that at the entrance. In the downstream recovery region, unsteadiness diminishes rapidly at the channel center height, where the time-averaged velocity profiles are fairly flat. The fluctuations also decay quickly near the walls. In the intermediate, shear layer region, the decay of unsteadiness is much less rapid. A surprising observation may be made regarding unsteadiness in the grooved region. The dimensionless center-span turbulence intensity is actually larger at Re = 2000 than it is at Re = 4000, especially close to the lower wall.

The spatially averaged turbulence intensity, $T$ (Eq. (4*b*)), indicates the mean level of unsteadiness in the flow, and its variation with location and Reynolds number is shown in Fig. 3(*b*). As already mentioned, the entrance flow exhibits mixing, which increases with Reynolds number, with $T$ ranging from approximately 3 to 15 percent. The grooves serve to increase this level sharply and it appears that the Reynolds number dependence in

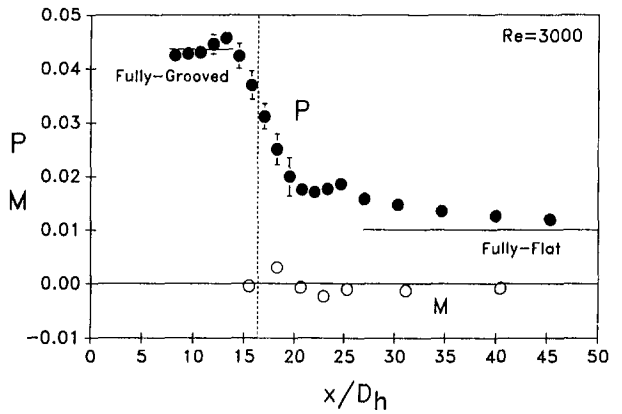



Fig. 4 Dimensionless pressure gradient (*P*, solid circles) and dimensionless momentum-flux gradient (*M*, open symbols) versus location at Re = 3000. A vertical line shows the end of the grooved section. Horizontal lines show the value of *P* measured in fully grooved and fully flat channels. Error bars show the uncertainty (95 percent confidence level) in *P* at representative locations.



Downloaded 12 Dec 2010 to 193.140.21.150. Redistribution subject to ASME license or copyright; see http://www.asme.org/terms/Terms_Use.cfm

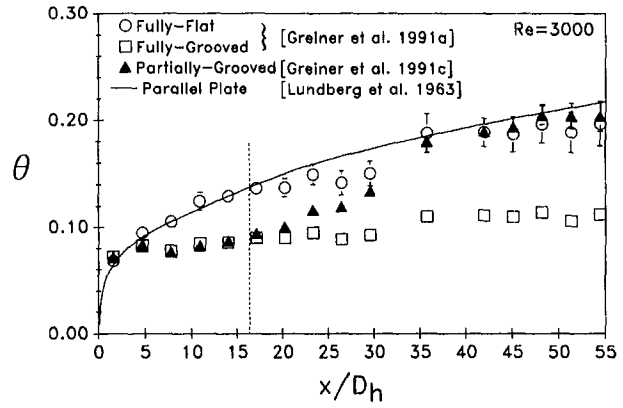



**Fig. 5 Dimensionless temperature difference measured on the flat surface versus location in partially grooved (solid triangles), fully grooved (open squares), and fully flat (open circles) channels at Re = 3000. Error bars show the uncertainty limits (95 percent confidence level) when they are larger than the symbols. The dashed vertical line shows the end of the grooved section.**

this region is much weaker than it is in the flat development section. Downstream from the grooves, the values of $T$ return to their entrance levels much more rapidly for Re $\geq$ 3000 than they do for lower Reynolds numbers, again indicating that the effect of the grooves is felt measurably further downstream when Re $<$ 3000 than for higher Reynolds numbers.

**Momentum and Heat Transfer.** Figure 4 shows the local dimensionless pressure-gradient, $P$, as a function of location for Re = 3000 (solid circles). These gradients are the slope of least-squared lines fit to consecutive sets of four pressure measurements. Vertical error bars indicate the two-standard-deviation uncertainty (95 percent confidence level) in $P$ at representative locations. A vertical dashed line indicates the end of the grooved section, and two horizontal lines show the fully developed gradients measured in fully grooved and fully flat test sections (Greiner et al., 1991a, 1991b). We see that the pressure gradient in the partially grooved test section is high in the grooved region. In the recovery section, its initial dropoff is very rapid, returning most of the way to the flat passage gradient within four hydraulic diameters, and then trailing off more slowly downstream. Examination of the other Reynolds numbers investigated shows a marked decrease in the initial rapid recovery length for Reynolds numbers above Re = 3000.

The local dimensionless momentum-flux gradient $M$, calculated from velocity measurements described in the preceding section (Eq. (3*b*)), is also shown in Fig. 4 (open circles). We see that the momentum-flux gradient is much smaller than the pressure gradient and thus may be effectively neglected in Eq. (2). This observation is true for all Reynolds numbers investigated (Chen, 1993). We therefore conclude that, for the present flow, the pressure gradient is an accurate reflection of the total shear stress, $f \approx P$.

Figure 5 shows a plot of dimensionless temperature difference, $\theta(x)$, versus location for Re = 3000 in fully flat, partially grooved, and fully grooved channels (Greiner et al., 1991c). The theoretical line for developing laminar-flow heat transfer between parallel plates with the same thermal boundary conditions (Lundberg et al., 1963) is included in this figure and confirms the measurement technique. The vertical line at $x/D_h$ = 16.4 indicates the end of the grooved region of the partially grooved channel.

The temperature differences in the fully and partially grooved channels are measurably less than those in the flat passage, indicating enhancement. At the end of the grooved region of the partially grooved channel, the temperature profile departs from that of the fully grooved duct and eventually rejoins the flat passage value after roughly 20 hydraulic diameters. This recovery length is typical for the Reynolds numbers below Re = 3000, but it decreases *mildly* at higher Reynolds numbers.

**Uncoupled Heat/Momentum Transport.** Comparing Figs. 4 and 5, we see that the shear stress (and pressure gradient) in the recovery region merges back to its flat channel value much more rapidly than the dimensionless temperature. Recovery coefficients are now defined to compare their recovery behaviors quantitatively. The recovery coefficient for shear stress at a given location, $R_\tau$, is defined as the difference between the Fanning friction factor at that location and the fully developed value in the fully flat channel $f_f$, divided by the maximum difference, $R_\tau = (f(x) - f_f)/(f_g - f_f)$. The recovery coefficient for dimensionless temperature is defined similarly, $R_\theta = (\theta_f(x) - \theta(x))/(\theta_f(x) - \theta_g(x))$.

The axial variations of the recovery coefficients for Re = 2000 and 4000 are shown in Figs. 6(*a*) and 6(*b*), respectively. Open diamonds represent $R_\theta$ while the filled circles indicate $R_\tau$. The shear stress drops back to its flat channel value more rapidly than the heat transfer for both Reynolds numbers. Furthermore, the decay lengths for pressure gradient and temperature difference both decrease as the Reynolds number increases. However, the decrease in the pressure gradient recovery length is much more dramatic than that for heat transfer. These results suggest that the heat/momentum transport mechanisms are *not* coupled in the recovery region. Moreover, over short recovery regions (i.e., five hydraulic diameters), the heat transfer is slightly less than that if the grooves continued, but the pressure drop is significantly lower, especially for Re $>$ 3000. This suggests that short flat regions, intermittently placed in a grooved channel, may be useful in reducing the overall pumping power requirement for a given heat transfer level.

**Heat Transfer/Pumping Power Performance.** We wish to assess practical performance gains from the use of recovery regions. Consider a recovery-region zone extending from $x/D_h$ = 16.4 to 21.8, corresponding to the first 5.4 hydraulic diameters of the recovery region (a dimensionless zone length of $L/D_h$ = 5.4). In Fig. 7 we plot the zone-average Nusselt number,

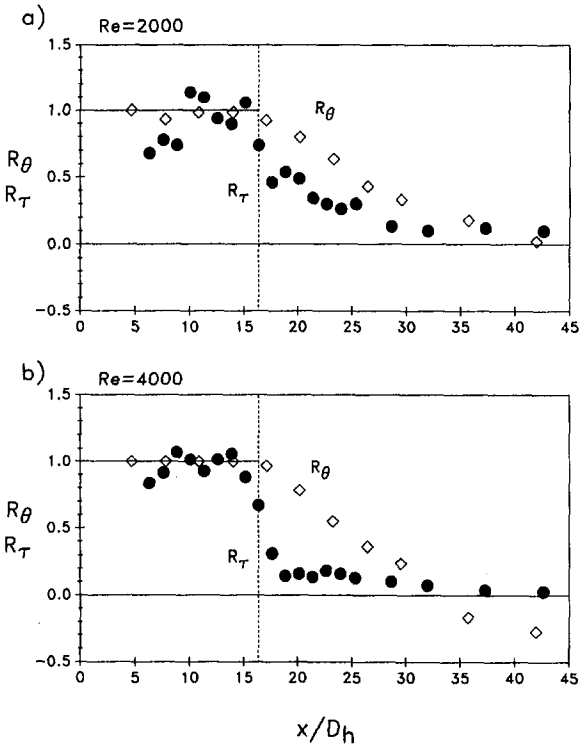



**Fig. 6 Recovery coefficients for shear stress (solid circles) and heat transfer (open diamonds) versus location. The vertical line shows the end of the grooved section. (*a*) Re = 2000. (*b*) Re = 4000.**



Downloaded 12 Dec 2010 to 193.140.21.150. Redistribution subject to ASME license or copyright; see http://www.asme.org/terms/Terms_Use.cfm

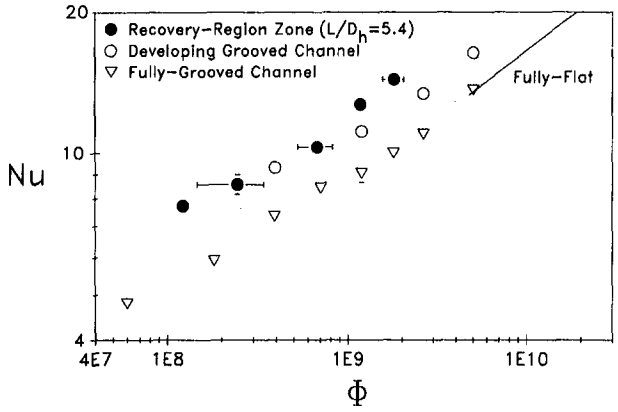



**Fig. 7 Average Nusselt number versus dimensionless pumping power in the recovery-region zone of the partially grooved channel and the same zone location in the developing-grooved passage. Experimental data for fully developed flow in fully grooved channels and theoretical results for turbulent fully flat passages are also included for comparison. Vertical and horizontal error bars indicate the 95 percent confidence level uncertainty limits in Nu and Φ, respectively, when they are larger than the symbols.**

$$\mathrm{Nu} = L \Big/ \left( \int_{L_g}^{L_g+L} \theta dx \right), \tag{9}$$

versus its dimensionless pumping power,

$$\Phi = \frac{\mathrm{Re}^3}{L} \int_{L_g}^{L_g+L} f dx, \tag{10}$$

using solid circles. We refer to this as the recovery-region zone performance. For comparison, open circles show the performance of the same zone location in the fully grooved channel ($x/D_h$ = 16.4 to 21.8). We call this the developing grooved channel data since Fig. 5 shows that the dimensionless temperature differences in 16.4 $\leq x/D_h \leq$ 21.8 of the fully grooved channel is measurably less than that in fully developed flow, $x/D_h > 40$. Data for fully developed flow in a fully grooved channel (Greiner et al., 1991a, 1991b) and turbulent flow in a fully flat passage are also shown, and these results are referred to as fully grooved and fully flat results, respectively. Two-standard-deviation uncertainty limits on Φ and Nu are included, but their corresponding horizontal and vertical error bars are smaller than the symbols for many of the points.

The data show that the fully grooved channel performance (open triangles) is little more than an extrapolation of turbulent fully flat passage characteristics into the transitional Reynolds number regime. We also see that performance in the developing grooved channel zone (open circles) exceeds that of the fully grooved (fully developed) flow by approximately 20 percent. Furthermore, at low pumping powers, $\Phi < 10^9$, the performance of the recovery-region zone is about the same as that in the developing grooved channel. However, as the pumping power (and Reynolds number) increases, the recovery-region heat transfer exceeds that in the developing grooved channel zone by 17 percent. Alternately stated, for a given Nusselt number, the pumping power may be reduced 44 percent due to the uncoupled heat/momentum transport of the decaying unsteady flow.

The onset of favorably uncoupled heat/momentum transport at higher Reynolds numbers is not surprising. The pressure gradient, which uncouples the heat and momentum transport mechanisms, increases with Reynolds number. As a result, the pressure gradient merges back to the flat channel value far more rapidly than the dimensionless temperature. It appears that a heat transfer/pumping power performance gain continues to higher pumping powers, but no recovery-region data are available beyond $\Phi = 3 \times 10^9$.

Data for a longer recovery regions show less augmentation since their behaviors tend to approach those of flat passages. However, a zone with length $L/D_h$ = 11.6 still has a heat transfer augmentation of 8 percent compared to the same zone location in a developing grooved channel at equal pumping power. This corresponds to a 30 percent pumping power reduction for a given Nusselt number (Chen, 1993).

## Conclusions

Earlier work shows that transverse grooves enhance the heat transfer/pumping power performance of exchange passages in the Reynolds number range 1000 < Re < 5000 by stimulating three-dimensional flow instabilities (Greiner et al., 1991a, 1991b). The current work demonstrates that the resulting unsteady flow persists for a considerable distance downstream from the grooved region in that the time-averaged and unsteady velocity profiles, as well as the heat transfer coefficient, are dramatically effected for up to 20 hydraulic diameters past the end of the grooved section. The recovery lengths for shear stress and pressure gradient drop off rapidly as the Reynolds number increases beyond Re = 3000, while the decrease in the heat transfer decay length is much less rapid, leading to a net heat transfer/pumping power performance advantage relative to flow in a fully grooved channel. The difference between the recovery lengths for shear stress and heat transfer indicate that heat/momentum transport mechanics in this region are *un*coupled.

The augmented performance observed in the recovery region of the present study suggests that intermittently grooved passages, in which unsteady flow alternately develops in grooved sections and decays in flat regions, would yield even higher heat transfer/pumping power performance than continuously grooved passages. However, further information on the development of destabilized flow in short grooved channels is necessary to determine an optimal design of these passages.

## Acknowledgments

This work was sponsored by National Science Foundation under grant number CBT-8708802 and Gas Research Institute under contract number 5087-260-1562.

## References

Blair, M. F., 1983, "Influence of Free-Stream Turbulence on Turbulent Boundary Layer Heat Transfer and Mean Profile Development: Part I—Experimental Data; Part II—Analysis of Results," ASME JOURNAL OF HEAT TRANSFER, Vol. 105, pp. 33–47.

Chen, R.-F., 1993, "Experimental Investigation of Passive Flow Destabilization and Heat Transfer Enhancement in Grooved Channels," Ph.D. Dissertation, University of Nevada, Reno, NV.

Greiner, M., Karniadakis, G. E., Mikic, B. B., and Patera, A. T., 1988, "Heat Transfer Augmentation and Hydrodynamic Stability Theory: Understanding and Exploitation," *Heat Transfer: Korea–US Seminar on Thermal Engineering and High Technology,* ed. J. H. Kim, T. R. Ro, and T. S. Lee, Hemisphere Publishing Corp., New York, pp. 31–50.

Greiner, M., Chen, R.-F., and Wirtz, R. A., 1990, "Heat Transfer Augmentation Through Wall-Shape-Induced Flow Destabilization," ASME JOURNAL OF HEAT TRANSFER, Vol. 112, pp. 336–341; also in: *Heat Transfer in Convective Flows,* ASME HTD-Vol. 107, 1989, pp. 337–342.

Greiner, M., Chen, R.-F., and Wirtz, R. A., 1991a, "Passive Heat Transfer Enhancement on a Flat Surface in a Grooved Channel," *Proceedings of the ASME/JSME Thermal Engineering Joint Conference,* Reno, NV, Vol. 3, pp. 97–101.

Greiner, M., Chen, R.-F., and Wirtz, R. A., 1991b, "Enhanced Heat Transfer/Pressure Drop Measured From a Flat Surface in a Grooved Channel," ASME JOURNAL OF HEAT TRANSFER, Vol. 113, pp. 498–501.

Greiner, M., Chen, R.-F., and Wirtz, R. A., 1991c, "Decay of Supercritical-Flow Heat Transfer Enhancement Downstream From a Grooved Surface," *Heat Transfer in Unsteady Flows,* ASME HTD-Vol. 158, pp. 35–39.

Kays, W. M., and London, A. L., 1984, *Compact Heat Exchangers,* McGraw-Hill, New York.

Kozlu, H., Mikic, B. B., and Patera, A. T., 1988, "Minimum-Dissipation Heat Removal by Scale-Matched Flow Destabilization," *Int. J. Heat Mass Trans.,* Vol. 31, pp. 2023–2032.

Lundberg, R. E., Reynolds, W. C., and Kays, W. M., 1963, NASA TN D-1972, Washington, Aug.

Maciejewski, P. K., and Moffat, R. J., 1992, "Heat Transfer With Very High Free-Stream Turbulence: Part I—Experimental Data; Part II—Analysis of Results," ASME JOURNAL OF HEAT TRANSFER, Vol. 114, pp. 827–839.

Majumdar, D., and Amon, C. H., 1992, "Heat and Momentum Transport in Self-Sustained Oscillatory Viscous Flows," ASME JOURNAL OF HEAT TRANSFER, Vol. 114, pp. 866–873.



Downloaded 12 Dec 2010 to 193.140.21.150. Redistribution subject to ASME license or copyright; see http://www.asme.org/terms/Terms_Use.cfm

# Experimental Investigation of Corona Wind Heat Transfer Enhancement With a Heated Horizontal Flat Plate

B. L. Owsenek

J. Seyed-Yagoobi

R. H. Page

Drying Research Center,
Department of Mechanical Engineering,
Texas A&M University,
College Station, TX 77843-3123

*Corona wind enhancement of free convection was investigated with the needle-plate geometry in air. High voltage was applied to a needle suspended above a heated plate, and heat transfer coefficients were computed by measuring the plate surface temperature distribution with an infrared camera. Local heat transfer coefficients greater than 65 W/m$^2$ K were measured, an enhancement of more than 25:1 over natural convection. The enhancement extended over a significant area, often reaching beyond the 30 cm measurement radius. At high power levels, Joule heating significantly reduced the effective impingement point heat transfer coefficient. The corona wind was found to be more efficient with positive potential than with negative. The heat transfer efficiency was optimized with respect to electrode height and applied voltage. The needle-plate heat transfer effectiveness improved rapidly with increasing height, and became relatively insensitive to height above a threshold value of about 5 cm.*

## Background

Heat and mass transfer coefficients between a surface and the surrounding air can be significantly enhanced through the application of an electric field. The electric field induces a fluid motion, or "corona wind," that is similar to a low-velocity impinging jet or plume. The jet, however, is unlike standard in-line jets in that it is driven by electrostatic body forces that can be unsteady and rotational. Due to the low velocities obtained (<10 m/s), the wall-jet portion of the flow can be considered laminar, although under some conditions the ion flux may promote irregular flow. The resulting heat and mass transport enhancement requires little power, causes virtually no sound or vibration, and can be rapidly controlled by simply changing the applied voltage. In addition, corona wind transfer enhancement may be applicable to certain complex geometries and curved passages where fans and blowers are cumbersome and ineffective. Finally, in the absence of gravity, the corona wind may be used to generate convection and thereby enhance heat transfer.

There are four possible ways in which an electric field may influence convection processes, including Joule heating of the fluid, and motion generated by the Coulomb, dielectric, and electrostriction forces. The three elemental body forces appear in the electrohydrodynamic equation (Stratton, 1941),

$$\mathbf{f}_e = Q\mathbf{E} - \tfrac{1}{2}|E|^2\nabla\epsilon + \tfrac{1}{2}\nabla\left(\rho\frac{\partial\epsilon}{\partial\rho}|E|^2\right) \qquad (1)$$

and arise, respectively, from the electrical force on free charges, permittivity gradients, and electric field gradients. Although permittivity is a function of temperature, the permittivity gradient term is negligible in most gases. In addition, Nelson and Shaughnessy (1986) have shown that the third term, electrostriction, cannot affect the flow field in the absence of a two-phase interface. Joule heating effects on fluid motion are negligible except at the highest power dissipation levels. The corona wind and resultant transfer enhancement arise solely from the Coulomb force term. Physically, the Coulomb term represents the distributed drag force that the ions impose on the neutral fluid.

A corona wind thus requires both an imposed electric field and a source of free charges. Both of these conditions can be satisfied by applying a high voltage to a small-diameter electrode. While the mechanisms involved in ion formation near the electrode are complex (Loeb, 1965), and differ for positive and negative voltages, it is sufficient to recognize that they are formed in the high electric field region as a result of partial electrical breakdown; no sparks are created. With a positive applied voltage in atmospheric air, the corona can take one of two distinct forms, glow or streamer discharge. Streamer discharge is characterized by current flow through partially ionized filamentary charge paths, and can exist at both low and high voltages. Glow discharge appears at midrange voltages and consists of homogeneous and relatively steady charge flow.

The flow field produced by the electrostatic force resembles that of a plume or a submerged jet. In a vertical submerged jet (e.g., air to air) impinging on a horizontal surface, within the impingement zone, the flow is influenced by the target surface and is rapidly decelerated and accelerated in the normal and transverse directions, respectively. However, since the flow continues to entrain zero momentum fluid from the ambient, the horizontal acceleration cannot continue indefinitely and the accelerating flow in the impingement region is transformed into a decelerating wall jet. In the case of a horizontal heated surface, the flow will develop a buoyancy effect, generating an upward motion due to the density difference between the heated fluid on the surface and the surrounding fluid. A toruslike recirculation zone can develop, especially when the jet height is relatively small. At small jet heights, the toruslike recirculation zone can play a significant role in the local heat transfer coefficients; however, the effect becomes negligible at larger heights. It should be noted that the corona wind flow characteristics are poorly understood, and may not precisely follow the submerged jet analogy.

## Literature Review

The corona wind was observed as early as 1719 (Hauksbee) and was first rigorously analyzed by Chattock (1899). Analysis by Steutzer (1959) and Robinson (1961) resulted in a basic understanding of the fluid mechanics of the phenomenon. Steutzer

Contributed by the Heat Transfer Division for publication in the JOURNAL OF HEAT TRANSFER. Manuscript received by the Heat Transfer Division January 1994; revision received August 1994. Keywords: Augmentation and Enhancement, Measurement Techniques, Natural Convection. Associate Technical Editor: Y. Bayazitoglu.


Copyright © 1995 by ASME


Downloaded 12 Dec 2010 to 193.140.21.150. Redistribution subject to ASME license or copyright; see http://www.asme.org/terms/Terms_Use.cfm

presented a theoretical analysis of ion-drag phenomena, and pointed out that one-dimensional pressure generation is proportional to the applied current. Robinson extended this result by applying Bernoulli's equation, and showed that the corona wind velocity is proportional to the square root of current. He verified this experimentally, and reported velocities in air of up to 4 m/s. He also showed that the electrokinetic conversion efficiency in air is on the order of 1–2 percent.

Marco and Velkoff (1963) were the first to examine the application of the corona wind to heat transfer enhancement. Using an apparatus in which a wire-generated corona wind impinged on the bottom of a horizontal plate, Marco and Velkoff were able to increase average heat transfer coefficients to as much as six times the free convection value. In addition, they presented a momentum-integral analysis that showed heat transfer to be proportional to the $\frac{1}{4}$ power of current. O'Brien and Shine (1967) followed with an investigation into the effects of pressure and gas type. They found that heat transfer enhancement cannot occur below a (electrode specific) threshold atmospheric pressure. A maximum local heat transfer enhancement, at atmospheric pressure and 5.9 $\mu$A, of 8.5 times the no-field value was reported.

Franke (1969) investigated vertical plate heat transfer in the presence of corona-generated vortices. He placed alternating high potential and grounded vertical wires on both sides of a heated, constant-temperature phenolic-covered aluminum plate and measured the resulting heat transfer through both an energy balance and interferometric photographs. Franke reported doubling the convective component of the total heat transfer with an applied corona power equivalent to only 5 percent of the increased heat transfer. More importantly, he demonstrated that the single-wire enhancement technique could be successfully extended to multiwire systems.

Windischmann (1974) investigated temperature profiles on a flat, upward-facing plate exposed to a needle-generated corona discharge in various gases and at various pressures, but did not attempt to compute heat transfer coefficients. However, he found that the corona wind was much more efficient in helium than in air, nitrogen, or argon. Mitchell and Williams (1978) used a thermal imaging system to measure the heat transfer coefficients in the needle-plate and wire-plate geometries. Their report presented Nusselt number correlations as a function of nondimensional parameters and reported the existence of a significant amount of Joule heating at high current levels. They also suggested that the Joule-heated corona wind heat transfer is similar to that of a turbulent impinging jet at temperatures above ambient.

Franke and Hogue (1991) considered the case of corona wind enhancement of free convection from a horizontal, heated cylinder. A corona source, consisting of a multipoint emitter or a fine wire, was oriented directly below the grounded cylinder. Results showed a heat transfer increase with reduced emitter-cylinder distance and the superiority of multipoint emitters with respect to both maximum heat transfer enhancement and power consumption. They also reported that heat transfer coefficients were predominantly a function of applied current and only weakly related to the distance between the electrode and ground.

Although corona wind transfer enhancement has been more widely studied than this survey of important and relevant papers may indicate (see Kulacki, 1982, or Owsenek, 1993), no work has been reported that investigates the phenomenon from the standpoint of optimization. This paper presents the results of extensive measurements with a high voltage needle suspended above a grounded and heated plane surface. The effects of varying the emitter–ground distance, corona polarities, and applied potential are investigated, and optimization surfaces are presented.

## Experimental Apparatus

Heat transfer tests were conducted using the Heat Transfer Jet Impingement Facility (HJIF) illustrated in Fig. 1. This apparatus was developed for the purpose of obtaining highly accurate local heat transfer coefficients with an impinging or radial jet flow (Page et al., 1992). The facility consists of a thin (0.0024 cm) resistance-heated inconel sheet, an insulating vacuum chamber, a Mikron infrared camera, an image processor, and a computer.

The inconel foil serves as the heat transfer surface and is electrically heated by a DC power supply. The 30 cm × 60 cm foil is situated on an insulating vacuum chamber, and held flat by the distributed vacuum pressure of 900 small holes in the top surface of the Plexiglas chamber. The vacuum pump reduced the chamber absolute pressure to approximately 5 kPa, which was sufficient to hold the foil in place and reduce gaseous conduction losses through the chamber. To enhance the accuracy of the infrared camera, the top surface of the foil was painted black to eliminate reflections and increase emissivity to nearly unity.

Foil surface temperatures were measured with a Mikron thermal vision system. This camera measures infrared radiation in the 8–13 $\mu$m range, and was utilized with a temperature sensitivity of ±0.06°C, and a pixel size of 2.75 mm. Each image consisted of 255 × 207 pixels, but only pixels along the horizontal centerline were used in the data reduction scheme. The image processor displayed the surface temperatures in false color and provided various image manipulation capabilities, such as zoom, image storage, and image subtraction. A 386 microcomputer was used to save the images for later data analysis and reduction.

The inconel foil surface was cooled by the corona wind in ambient laboratory air at approximately 22°C and 40 percent relative humidity. The corona wind was generated by an adjustable high-voltage power supply, which could supply up to 50 kV at 5 mA. This power source was connected to a needle suspended above the inconel foil. High voltage wires carried current from the power supply, through a microammeter, to the electrode. The current then bridged the air gap in the form of a corona discharge, traveled through the grounded foil, and completed the circuit back to the high voltage power supply. The supplied voltage was measured with a voltage-divider circuit and multimeter, and current loss to other grounded parts of the apparatus was shown to be negligible by measuring the current leaving the foil.

Although most investigators have preferred to investigate the corona wind with a hemispherical needle point, no attempt was made to control the electrode geometry in this study. The needle was, however, examined under a microscope to measure the geometry and assure the absence of irregularities. The stainless steel needle point was in the form of a frustum of a cone with a convergence angle of 25 deg and a minimum diameter of 0.1 mm.

## Nomenclature

$A$ = area on the heat transfer surface, m$^2$
$b$ = charge mobility, m$^2$/Vs
$E$ = electric field, V/m
$\mathbf{f}_e$ = body force on elemental volume, N/m$^3$
$H$ = distance between needle and plane, m
$h_{avg}$ = average heat transfer coefficient, W/m$^2$ K
$h_{loc}$ = local heat transfer coefficient, W/m$^2$
$i$ = current, $A$
$P$ = power flux, W/m$^2$
$Q$ = electrical charge, C/m$^3$
$T_{s,corona}$ = temperature of corona cooled surface, °C
$T_{s,ambient}$ = surface temperature under ambient conditions, °C
$V$ = voltage, V
$V_0$ = corona initiation voltage, V
$\epsilon$ = permittivity, C/Vm
$\rho$ = mass density, kg/m$^3$



Downloaded 12 Dec 2010 to 193.140.21.150. Redistribution subject to ASME license or copyright; see http://www.asme.org/terms/Terms_Use.cfm

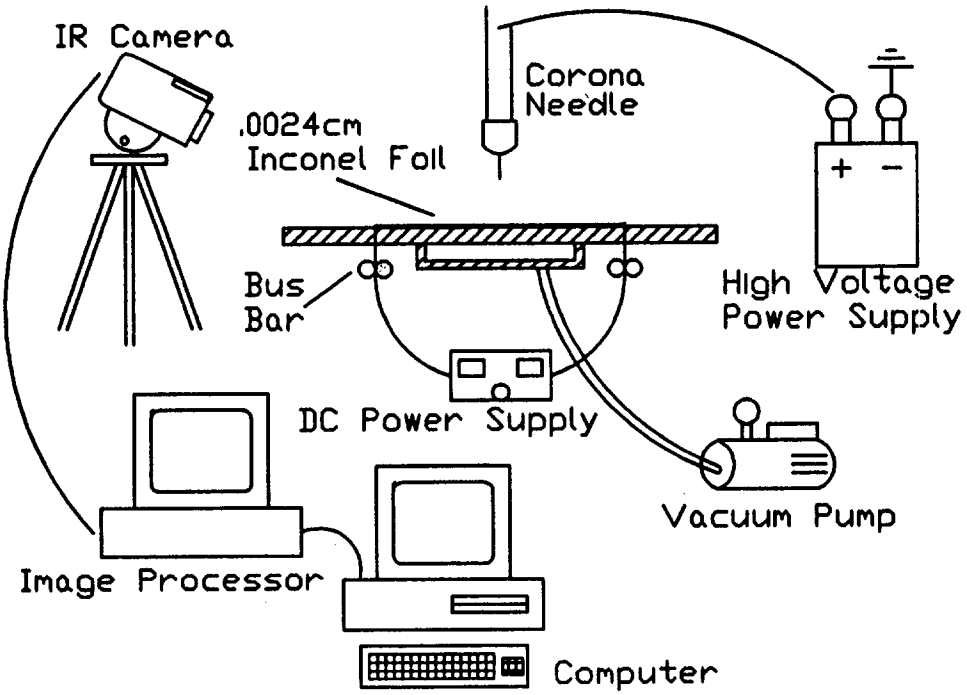



**Fig. 1 Heat Transfer Jet Impingement Facility (HJIF) with corona needle and high-voltage power supply**

Corona wind heat transfer coefficients were determined with a multistep data acquisition and reduction process. First, a cold infrared image was taken of the impingement surface at ambient temperature with no corona wind. The foil was then heated with the DC power supply set to 20 amps. This led to a voltage drop across the foil of approximately 2.15 V, and a consequent uniform power dissipation level of approximately 156 W/m$^2$. The needle was cleaned with alcohol and set to the appropriate polarity, height, and voltage, then energized. The plate was typically given between 30 minutes and an hour to reach equilibrium. Steady state was declared when the maximum temperature variation between measurements taken four minutes apart fell to less than 0.1°C.

Local convection heat transfer coefficients from the foil surface were determined along a horizontal line crossing through the center of the image. The energy loss to convection, on a unit area basis, was found by

$$q''_{\text{convection}} = q''_{\text{generation}} - q''_{\text{conduction}} - q''_{\text{radiation}} \qquad (2)$$

Conduction losses were calculated by assuming one-dimensional heat flow through the vacuum chamber. The overall thermal resistance to conduction through the bottom of the chamber was 2.7 m$^2$ K/W. Radiation losses were estimated by assuming the foil to be a small surface with an emissivity of 0.99 inside a room-sized cavity, where the wall temperature was assumed identical to the measured air temperature. The local heat transfer coefficients were then found from $q_{\text{convection}}$ and the local temperature difference between the hot and the cold images:

$$h_{\text{loc}} = \frac{q''_{\text{convection}}}{(T_{s,\text{corona}} - T_{s,\text{ambient}})}. \qquad (3)$$

The importance of correcting for heat loss to conduction and radiation can be appreciated with the help of a few typical values. The heat flux due to radiation and conduction was naturally greatest when the convection coefficient was small, resulting in a high surface temperature. At the usual applied heat flux of approximately 156 W/m$^2$, a local convection heat transfer coefficient of 10 W/m$^2$ K resulted in a radiation heat flux of 54 W/m$^2$, a conduction flux of only 3 W/m$^2$, and a surface temperature of 10°C above ambient. Therefore, even at this very low convection coefficient, the convection heat flux accounted for more than 60 percent of the total. The radiation and conduction losses dropped off rapidly with increasing convection, accounting for only 11 percent of the total heat transfer when the convection coefficient reached 50 W/m$^2$ K with a surface temperature of 2.8°C above ambient.

Throughout testing, heat transfer coefficient distributions were obtained that were nearly symmetric about the impingement point. Measurements were obtained along a horizontal line that passed through the point of maximum cooling. To improve accuracy and eliminate redundancy, symmetry was employed to average the local heat transfer coefficients on each side of the impingement point. This produced local heat transfer data that represented the convection coefficients along a radial line from the impingement point. These local heat transfer results were then integrated with respect to area to determine average heat transfer values. Note that dimensional heat transfer coefficients are reported, since the use of the Nusselt number would only obscure results by introducing an extraneous length parameter.

Heat transfer coefficients were obtained for needle heights ranging from 1 cm to 10 cm. The minimum height was selected on the basis of preliminary tests which showed an abrupt drop in heat transfer enhancement per unit power at heights below 1 cm. The maximum height examined was chosen on the basis of tests, which showed only a gradual drop in heat transfer effectiveness above 10 cm, and with the understanding that the plate may be considered "large" with respect to corona phenomenon when the needle height is less than the distance from the impingement point to the plate edge (Solomon, 1983).

## Current-Voltage Relationship

Heat transfer was investigated for positive voltages, which ranged from slightly above the apparent corona onset voltage up to the onset of pre-breakdown streamers. Measurements were therefore made mostly in the onset streamer and glow regimes. The onset of pre-breakdown streamers was identified by the characteristic audible corona hiss, and was avoided in the interest of preventing sparking. This method of identifying the pre-breakdown region is only approximate, but was sufficient for the pur-



Downloaded 12 Dec 2010 to 193.140.21.150. Redistribution subject to ASME license or copyright; see http://www.asme.org/terms/Terms_Use.cfm

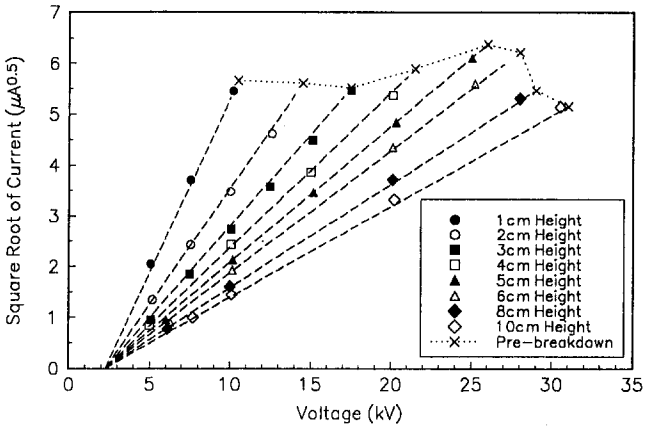



**Fig. 2 Needle-plate current–voltage relationship with positive applied potential**

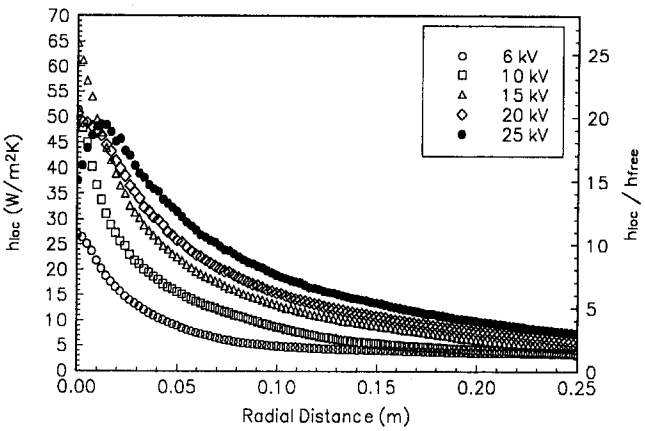



**Fig. 3 Local heat transfer coefficients with various voltages and needle height of 5 cm**

poses of this study. Note that the pre-breakdown region is both acoustically and electrically noisy and exhibits an unsteady current flow; consequently this region is best avoided in industrial applications. No attempts to identify the corona regimes better were made.

The experimental positive current–voltage relationship and the approximate onset of pre-breakdown streamers is illustrated in Fig. 2. Steutzer (1959) has shown that the current in a one-dimensional geometry is related to the applied voltage and needle height by the expression,

$$i = 1.125 b\epsilon \frac{A}{H^3} (V - V_0)^2 \qquad (4)$$

It is also well known that the current flux distribution on the plane surface may be represented by Warburg's law, $J = J_0 \cos^5 (x/H)$. It can easily be shown that Warburg's law implies that the area on the surface through which most of the current flows is proportional to $H^2$ in the needle-plane geometry (Owsenek, 1993). Theory would thus indicate that the current is proportional to the inverse of the needle height. Considering the highly approximate nature of Steutzer's one-dimensional assumption, it is somewhat surprising that the regression curve fit, Eq. (5), indicates a current dependence so close to the predicted relationship discussed above,

$$i = 1.56 \frac{b\epsilon}{H^{1.165}} (V - 2260)^2 \qquad (5)$$

The corona discharge generates ions of a number of different species, each of which can have a different mobility. The species distribution can vary substantially with the presence of water vapor and other impurities in the air. A representative positive ion mobility, *averaged across all charge-carrying species*, of $b = 1.6 \times 10^{-4}$ m²/Vs was used to calculate the proportionality constant in Eq. (5). The current, at a given voltage, is higher with negative potential than with positive. Since individual negative and positive ions have approximately the same mobility, this can be explained by the finite time required for (high mobility) electrons to attach to oxygen in the negative corona discharge (Böhm, 1982). Despite a slightly lower negative corona initiation voltage, Eq. (5) proved a good fit to the negative polarity current–voltage data with an *effective* negative average charge mobility of $b = 2.1 \times 10^{-4}$ m²/Vs.

## Heat Transfer Results

Local heat transfer coefficients of more than 65 W/m² K were observed with various voltage-height combinations. This is especially significant when compared to the approximately 2.5 W/m² K natural convection coefficient observed in the absence of a corona discharge. Figure 3 illustrates the effect of increasing the voltage at a fixed needle height of 5 cm. The ratios between the corona wind heat transfer coefficients and the free convection heat transfer coefficients are illustrated by the right $y$ axis. Free convection heat transfer is more sensitive to the applied heat flux than the corona wind heat transfer, so the ratios expressed here may drop significantly at higher heat fluxes.

Higher voltages lead to increased current, and thus, according to the theory developed by Steutzer and Robinson, to increased pressure generation and fluid velocity. Higher fluid velocity, of course, leads to greater heat transfer. However, Fig. 3 indicates that voltage increases improved the maximum local heat transfer only to a point. Beyond this point, further increases in voltage actually decreased the observed enhancement near the impingement point. A similar trend is evident in Fig. 4, which illustrates the variation in average heat transfer, as the needle height was changed, for a circular area under the needle. Note that heat transfer was optimized, despite greater power consumption with lower needle heights, at a needle height of 3 cm.

Two phenomena are responsible for this apparent violation of theory; Joule heating of the air and entrainment inefficiency. As Mitchell and Williams (1978) have noted, Joule heating of the air leads to a situation in which a jet at temperatures above ambient impinges on a heated surface. In the situation considered here, this leads to a decrease in the *effective* impingement point local heat transfer coefficient, since the heated corona wind simply cannot cool the surface as much as an unheated flow. The dissipated power resulted in an air temperature, measured at the impingement point (with no power applied to the inconel foil),

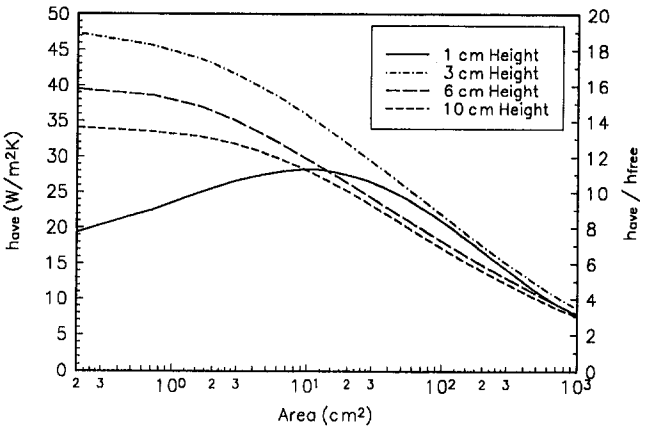



**Fig. 4 Average heat transfer coefficients at +10 kV with various needle heights**



Downloaded 12 Dec 2010 to 193.140.21.150. Redistribution subject to ASME license or copyright; see http://www.asme.org/terms/Terms_Use.cfm

of up to three degrees above the ambient temperature. This agrees with an approximate temperature rise calculation for the volume of air affected by Joule heating. Joule heating effects can therefore become very significant when the difference between the surface temperature and the ambient temperature is on the same order as the Joule heating.

Convection coefficients were computed that removed the effect of Joule heating by subtracting the hot plate temperatures from the temperatures on an unheated plate subjected to a corona wind. This produced *actual* heat transfer coefficients, which were uninfluenced by the Joule heating. Heat transfer coefficients obtained in this fashion exhibited virtually no drop in the impingement point local heat transfer. This indicates that Joule heating was the major cause of the decreased *impingement point* heat transfer.

Although the Joule heating had a large effect directly under the needle, it had only a small influence on the heat transfer coefficients when a relatively large area was considered. In fact, Figs. 3 and 4 seem to indicate that Joule heating effects were confined to the circular region directly under the needle with radius of about 3 cm, or an area of the order of 30 $cm^2$. Note that the influence of Joule heating on the effective heat transfer coefficient varies with the surface heat flux, and would actually be beneficial if the surface were being heated, instead of cooled, by the corona wind.

At very small needle heights, Joule heating continued to exert a strong influence on the effective heat transfer coefficients near the impingement point. However, when a corona needle is close to the grounded surface, a large body force is applied to a very small volume of air. The electric field is stronger, for a given current, when the interelectrode gap is small, leading to higher average ion velocities. Furthermore, the concentrated body force and the small interelectrode gap can be expected to strengthen the torus-shaped recirculation zone. Under these conditions, neutral, unheated air is not efficiently entrained, and the average heat transfer coefficients are severely reduced. This effect can be clearly seen in Fig. 5, which presents the average heat transfer over a 100 $cm^2$ area versus applied current. Since Joule heating cannot account for more than a small portion of the heat transfer reduction at heights of 1 cm and 2 cm, it must be due largely to entrainment inefficiencies.

## Optimization

It is generally desirable to achieve the highest possible heat transfer with the minimum power input. An optimization surface can therefore be defined to represent the heat transfer as a function of both applied power and needle height. Figure 6 presents heat transfer contour lines for the local heat transfer coefficient at the impingement point. There was a region of maximum heat transfer effectiveness when the needle was located at a height of approximately 5.5 cm and the voltage was adjusted to yield 0.3 W (≅18 kV, 17 $\mu$A). It is also interesting to note that over a broad range, increased power did not increase the impingement point heat transfer. Similarly, no significant change in heat transfer with height was evident above 4 cm and below 0.2 W. The small heat transfer coefficients at low needle heights was a result of both Joule heating and reduced entrainment efficiency.

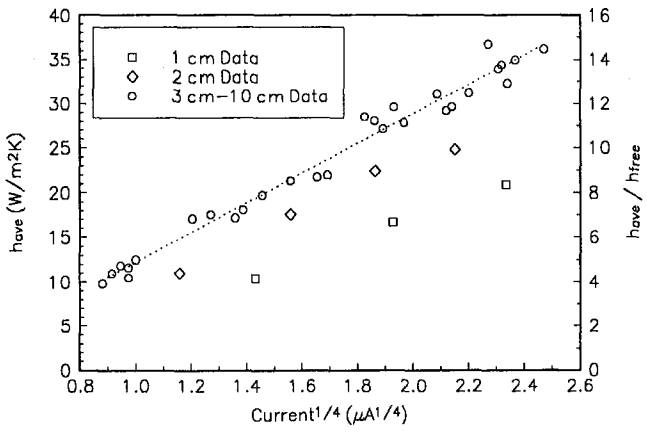



**Fig. 5 Relationship between applied current and heat transfer over a 100 $cm^2$ area**

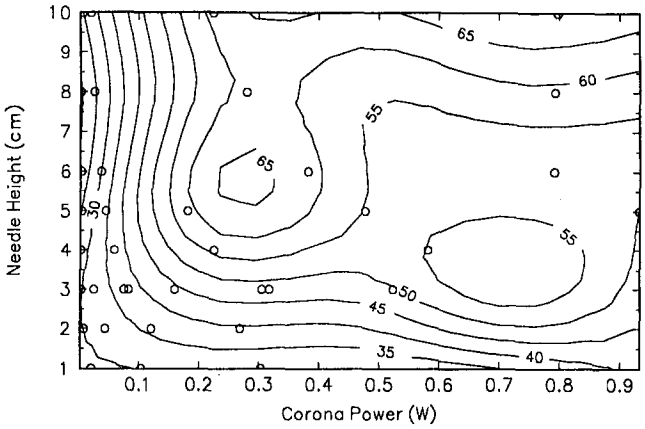



**Fig. 6 Impingement point local heat transfer coefficient (W/$m^2$ K) contours versus power and height**

Although it can be important to optimize the impingement point heat transfer coefficient, it is generally more useful to optimize the heat transfer over the surface area. Since the geometry considered here has no characteristic heat transfer surface area, heat transfer must be optimized over an arbitrary area. This study considers an area of 100 $cm^2$, as the average heat transfer coefficients over this area were relatively large, and exhibited reduced Joule heating effects.

A heat transfer enhancement parameter can be defined that presents the ratio of the average heat transfer coefficient to the applied power. The parameter thus presents a measure of the heat transfer efficiency. Since the average heat transfer is associated with a specific area, the parameter can be formulated as

$$\eta = \frac{\bar{h}A}{P} \tag{6}$$

The enhancement parameter has the units of 1/K, and may thus be interpreted as the approximate ratio of heat energy removed to electric power input, over the area considered, for a unit temperature difference. This interpretation is, of course, highly approximate, as the heat transfer coefficient can be expected to change significantly with the surface temperature and applied heat flux.

Nevertheless, the parameter can be a useful instrument for illustrating the corona wind heat transfer effectiveness at different voltages and needle heights. Figure 7 presents an optimization surface for the 100 $cm^2$ average heat transfer, with contours based on the $\log_{10}$ of the enhancement parameter. Note the rapid reduction of the parameter, at all needle heights, with increasing voltage. The parameter also increased with height at all voltages, as a result of reduced power consumption, and became less sensitive to height above about 4 cm. The needle height remained a factor above a height of 4 cm, since this figure presents voltage, rather than power, along the $x$ axis. At 10 kV, a parameter value of 5 can be obtained with a needle height of 6 cm; if the interpretation discussed above can be considered approximately valid, a surface temperature 10°C above ambient would lead to approximately 50 times more dissipated heat than input power.



Downloaded 12 Dec 2010 to 193.140.21.150. Redistribution subject to ASME license or copyright; see http://www.asme.org/terms/Terms_Use.cfm

The accuracy of the contours is very dependent upon distance from data points, so measurement locations are included to indicate regions where the contours may be unreliable. It should also be noted that these results are specific to the needle-plane geometry in air, and that the specific heat transfer coefficients may vary with electrode geometry, type of gas, pressure, temperature, and heat flux. However, the trends illustrated in these figures can be expected to be valid under these conditions, as well as extend to multipoint and wire electrode configurations.

## Polarity

A set of tests was conducted to study the effect of polarity on the heat transfer. Figure 8 shows the local heat transfer coefficients at both polarities. As implied by the theories of Steutzer and Robinson, constant voltage local heat transfer coefficients proved to be almost completely independent of polarity. However, at high voltages the negative ions proved to produce less of a drop in the impingement point local heat transfer coefficient. This implies that the negative polarity corona wind generated less Joule heating than the positive corona wind. This was verified by a test, performed at 20 kV with a needle 5 cm from the ground plane, which showed a maximum surface temperature rise of 1.5°C for the positive corona, and 1.1°C for the negative corona. This is both counterintuitive and unexpected, as the negative corona wind actually consumed nearly 30 percent more power. Electrochemical processes may be responsible for this apparent discrepancy, as excited molecules can carry energy away from the system that might otherwise have been released as measurable Joule heating.

To demonstrate the repeatability of the data presented in this paper, the heat transfer coefficient with a needle at a height of 3 cm and voltages of 10 and 15 kV was measured on three different occasions. The data proved highly reliable, with an average standard error (standard deviation/local heat transfer coefficient) of approximately 3 percent, and a maximum of nearly 9 percent. The standard error was not, however, constant, but varied substantially with radial distance. The impingement point local error was approximately 1 percent. The maximum error occurred at the outer edge of the transfer enhancement, and presumably represented fluctuation due to the interaction of the corona wind and natural convection.

## Conclusions

Heat transfer can be significantly enhanced by the application of a corona wind. Local heat transfer coefficients of up to 65 W/m$^2$ K were measured, an enhancement of more than 25:1 over natural convection. The heat transfer enhancement extended over a significant area, often reaching beyond the 30 cm measurement radius. At a given power, maximum enhancement was located at the impingement point for most measurements. At high power levels, however, a local drop in convection coefficient was observed at the impingement point, as a result of Joule heating effects. Furthermore, when the needle was placed too close to the surface, the entrainment efficiency was reduced, lowering the heat transfer effectiveness.

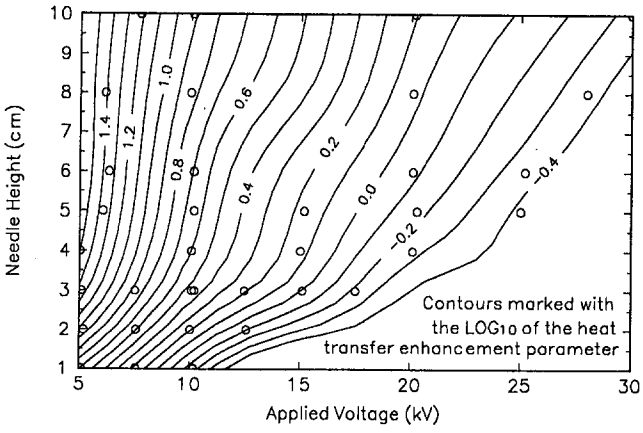



**Fig. 7 Optimization surface for the 100 cm$^2$ average heat transfer with the log of the enhancement ratio plotted against the needle height and the applied voltage**

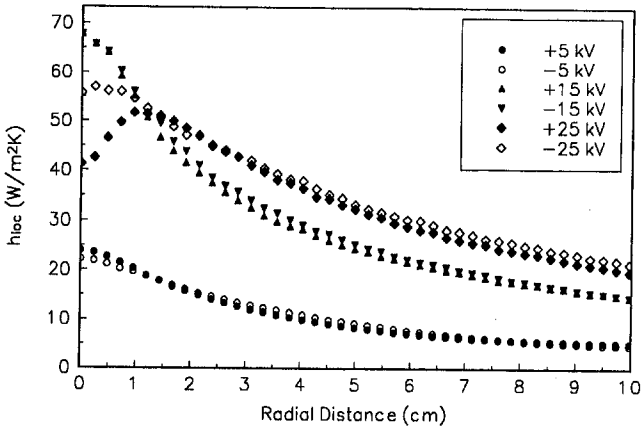



**Fig. 8 Local heat transfer coefficients at various voltages for both positive and negative corona wind at needle height of 5 cm**

Heat transfer enhancement can be optimized by proper selection of the needle-plate gap distance and applied potential. Efficiency is greatly reduced when the gap distance is too small, primarily as a result of inefficient entrainment of neutral air. However, efficiency does not change significantly with increasing height once the needle gap increases beyond a threshold. Under the specific conditions considered here, and with an applied power of at least 0.2 W, this threshold height was approximately 5 cm. It has also been shown that, within a broad range of conditions, increases in applied power do not appreciably affect the impingement point heat transfer when the gap spacing is less than about 5 cm.

Despite increased power consumption, the negative corona wind generated less Joule heating than the positive corona wind. Therefore, at a constant voltage, the negative corona wind generates a slightly higher impingement point heat transfer coefficient. However, as expected, the positive corona wind consumed less power, and thus proved more efficient than the negative corona wind.

## Acknowledgments

This work was supported in part by the Texas A&M University Drying Research Center.

## References

Böhm, J., 1982, *Electrostatic Precipitators,* Elsevier Publishing Company, New York, pp. 32–33, 78–79.

Chattock, A. P., 1899, "On the Velocity and Mass of Ions in the Electric Wind in Air," *Phil. Magazine,* Vol. 48, pp. 401–420.

Davidson, J. H., and Shaughnessy, E. J., 1986, "Turbulence Generation by Electric Body Forces," *Experiments in Fluids 4,* pp. 17–26.

Franke, M. E., 1969, "Effect of Vortices Induced by Corona Discharge on Free-Convection Heat Transfer From a Vertical Plate," ASME JOURNAL OF HEAT TRANSFER, Vol. 91, pp. 427–433.

Franke, M. E., and Hogue, L. E., 1991, "Electrostatic Cooling of a Horizontal Cylinder," ASME JOURNAL OF HEAT TRANSFER, Vol. 113, pp. 544–548.

Hauksbee, F., 1719, *Physico-Mechanical Experiments on Various Subjects,* 1st ed., London, pp. 46–47.

Hay, J. C., 1984, "The Electric Field and Vorticity Production in a Wire-Plate Precipitator With Uniform Discharge," Master's Thesis, Duke University, Durham, NC.

Kulacki, F. A., 1982, "Electrohydrodynamical Enhancement of Convective Heat Transfer," *Advances in Transport Processes,* Vol. II, A. S. Mujumdar and R. A. Mashelkar, eds., Halstead Press, New York.



Downloaded 12 Dec 2010 to 193.140.21.150. Redistribution subject to ASME license or copyright; see http://www.asme.org/terms/Terms_Use.cfm

Loeb, L. B., 1965, *Electrical Coronas: Their Basic Physical Mechanisms,* University of California Press, Los Angeles, CA.

Marco, S. M., and Velkoff, H. R., 1963, "Effect of Electrostatic Fields on Free Convection Heat Transfer From Flat Plates," ASME Paper No. 63-HT-9.

Mitchell, A. S., and Williams, L. E., 1978, "Heat Transfer by the Corona Wind Impinging on a Flat Surface," *Journal of Electrostatics,* Vol. 5, pp. 309–324.

Nelson, D. A., and Shaughnessy, E. J., 1986, "Electric Field Effects on Natural Convection in Enclosures," ASME JOURNAL OF HEAT TRANSFER, Vol. 108, pp. 749–754.

O'Brien, R. J., and Shine, A. J., 1967, "Effect of Electrostatic Fields on Free-Convection Heat Transfer From Flat Plates," ASME JOURNAL OF HEAT TRANSFER, Vol. 89, pp. 114–115.

Owsenek, B. L., 1993, "An Experimental, Theoretical and Numerical Investigation of Corona Wind Heat Transfer Enhancement," M.S. Thesis, Texas A&M University.

Page, R. H., Ostowari, C., and Seyed-Yagoobi, J., 1992, "Infrared Images of Jet Impingement," *Proc. 20th Int. Congress on High-Speed Photography and Photonics,* Vol. 1801, pp. 703–709.

Robinson, M., 1961, "Movement of Air in the Electric Wind of the Corona Discharge," *Transactions of the American Institute of Electrical Engineers,* Vol. 80, pp. 143–150.

Solomon, G., 1983, "Electrically Driven Flow in a Needle-Plate Electrode Geometry," M.S. Thesis, Duke University, Durham, NC.

Steutzer, O. M., 1959, "Ion Drag Pressure Generation," *J. Appl. Phys.,* Vol. 30, pp. 984–994.

Stratton, J. A., 1941, *Electromagnetic Theory,* McGraw-Hill, New York, Section 2.21.

Windischmann, H., 1974, "Investigation of Corona Discharge Cooling (CDC) of a Horizontal Plate Under Free Convection," *AIChE Symposium Series 138,* Vol. 70, pp. 23–30.



Downloaded 12 Dec 2010 to 193.140.21.150. Redistribution subject to ASME license or copyright; see http://www.asme.org/terms/Terms_Use.cfm

# Heat Transfer and Flow Characteristics of an Oblique Turbulent Impinging Jet Within Confined Walls

**K. Ichimiya**
Department of Mechanical System Engineering,
Yamanashi University,
Takeda-4, Kofu,
Yamanashi, 400 Japan

*Experiments were conducted to determine the turbulent heat transfer and flow characteristics of an oblique impinging circular jet within closely confined walls using air as a working fluid. The local temperature distribution on the impingement surface was obtained in detail by a thermocamera using a liquid crystal sheet. A correction to the heat flux was evaluated by using the detailed temperature distribution and solving numerically the three-dimensional equation of heat conduction in the heated section. Two-dimensional profiles of the local Nusselt numbers and temperatures changed with jet angle and Reynolds number. These showed a peak shift toward the minor flow region and a plateau of the local heat transfer coefficients in the major flow region. The local velocity and turbulent intensity in the gap between the confined insulated wall and impingement surface were also obtained in detail by a thermal anemometer.*

## Introduction

Impinging jets are used to improve the local heat transfer in various applications, including gas turbine cooling (Han et al., 1983), temperature equalization for a slab in continuous casting direct rolling process (Ichimiya et al., 1987), and cooling of electronics (Hollworth and Durbin, 1992). Martin (1977), Jambunathan et al. (1992), and Viskanta (1993) provided a comprehensive list of the available literature on impingement cooling. In practical applications, the orientation of the nozzle in relatively narrow spaces with confined walls is an important factor, together with the compactness of the facility. McMurray et al. (1966) experimented with an impinging jet flow for removing heat from a hot plate and, in so doing, configured the local heat transfer on the impingement surface by control of inclination angle. Sparrow and Lovell (1980) examined the shift of the position of maximum heat transfer coefficient for various inclination angles by using similarity between mass transfer and heat transfer. Goldstein and Franchett (1988) conducted experiments to determine the heat transfer to a jet impinging at different angles on a flat surface using a surface heater and liquid crystal. Contours of constant temperature (color: red) in the liquid crystal were obtained at different heat fluxes. The local Nusselt number was correlated by an exponential relationship, which included the local position and jet orientation. Stevens and Webb (1991) obtained an empirical equation for local heat transfer coefficient that includes the inclination angle. This research was performed on an impinging jet without confining walls. Ward et al. (1991) determined the local heat transfer associated with impinging air jets within a confined crossflow by using the mass transfer analogy technique.

With an oblique impinging jet, Foss and Kleis (1976) reported the mean flow characteristics, surface isobars, streamwise vorticity, and stagnation point location, for jet inclination angles less than 12 deg. Kamoi and Tanaka (1977) measured the static pressure distribution, velocity distribution, and shear stresses with various levels of turbulence at nozzle exit for inclination angles ranging from 30 to 90 deg. Foss (1979) measured the turbulence intensity values near the impingement surface, isopressure distribution on the surface and velocity vectors distribution for an inclination angle of 45 deg. Rubel (1981, 1982) analyzed the flow at the jet impingement zone. These previous studies were performed in a system without confined walls.

In the present paper, the impinging flow and turbulent heat transfer characteristics of an inclined circular jet within a channel with confining walls of comparatively narrow space ($h/D = 1.0$) are examined experimentally. The surface temperature was measured by the liquid crystal technique as recorded by an image processor. With this technique, isothermal lines on the impingement surface were determined without a large number of thermocouples or without changing heat flux level. In addition, the velocity distribution, the turbulence intensity, and the power spectrum of velocity fluctuation were examined experimentally for each case and correlations are made with heat transfer results.

## Experimental Apparatus and Procedure

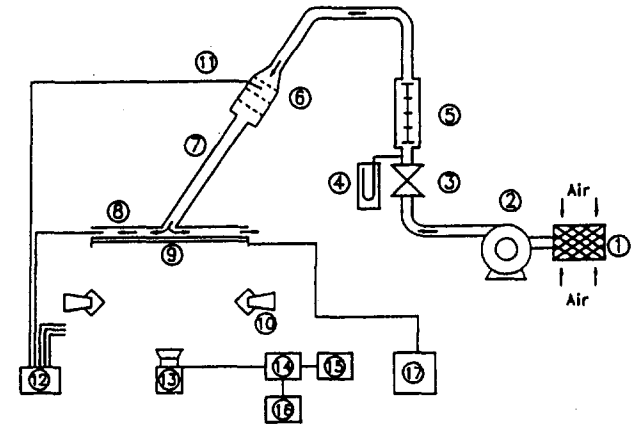
A schematic diagram of the experimental apparatus is shown in Fig. 1. The apparatus is composed of the flow delivery passage, the heated section including the surface upon which the flow impinges, and the measuring system. After the air impinges upon the heated surface from an inclined circular nozzle of 30 mm diameter, it is released to the atmosphere. The distance between the nozzle and the impingement surface is 30 mm. The upper wall, set at the same level the nozzle, is made of acrylic resin and is thermally insulated. The inclined angles, $\theta$ (refer to Fig. 2), are 45, 60, and 90 deg from horizontal. The shape of the nozzle exit is a circle in the case of $\theta = 90$ deg and an ellipse in the other cases. The impingement section is composed of an transparent acrylic plate, a thermosensitive liquid crystal sheet, and a stainless steel foil 20 $\mu$m thick. These were closely connected by binding tapes with transparency 99 percent. The foil was heated electrically. The impingement surface temperature was measured by transforming the color intensity of the liquid crystal sheet to the corresponding temperature (refer to the section "Temperature Measurement"). The back side of the impingement section was illuminated by four 100-W tungsten halogen lamps. Illumination was from a low angle so that light was not specularly reflected to the CCD (Charge-Coupled Device) camera. These lamps were equipped with infrared radiation absorbing filters to prevent radiative heating of the liquid crystal. Three kinds of optical filters were mounted, one after another, in

Contributed by the Heat Transfer Division and presented at the 29th National Heat Transfer Conference, Atlanta, Georgia, August 8–11, 1993. Manuscript received by the Heat Transfer Division October 1993; revision received April 1994. Keywords: Augmentation and Enhancement, Forced Convection, Measurement Techniques. Associate Technical Editor: T. Simon.



Copyright © 1995 by ASME

Downloaded 12 Dec 2010 to 193.140.21.150. Redistribution subject to ASME license or copyright; see http://www.asme.org/terms/Terms_Use.cfm




① Air filter
② Blower
③ Valve
④ Manometer
⑤ Flow Meter
⑥ Settling Chamber
⑦ Nozzle
⑧ Insulated Wall
⑨ Impingement Surface
⑩ Halogen Lamp
⑪ Thermocouple
⑫ Multirecorder
⑬ C.C.D. Camera
⑭ Image Processor
⑮ Host Computer
⑯ Color Monitor
⑰ A.C. Power Supply

**Fig. 1 Schematic diagram of experimental facility**

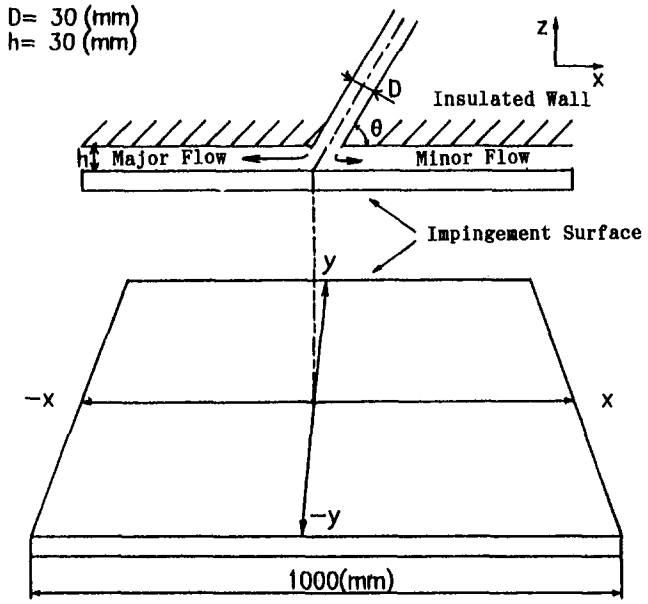



**Fig. 2 Coordinate system**

front of the camera lens. The color image was converted into an electrical signal by a CCD camera. The measuring region was divided into 128 × 128 pixels (the size of one pixel is 1 mm × 1.25 mm).

The local heat transfer coefficient, $\alpha$, and the local Nusselt number, Nu, on the impingement surface were calculated by the following equations, which use the net heat flux $q_{net}$ (refer to the section "Correction of Local Heat Flux") and the mixed mean temperature at the nozzle exit, $T_{in}$,

$$\alpha = q_{net}/(T_w - T_{in}) \tag{1}$$

$$\mathrm{Nu} = \alpha \cdot D/\lambda \tag{2}$$

where $\lambda$ is the thermal conductivity of the fluid.

Velocity and turbulence intensity across the section were measured in unheated condition by a thermal anemometer (single wire probe) to document the flow at Re = $2 \times 10^4$ ($u_0$ = 11 m/s). A probe was set to face the flow and be parallel to the impingement surface. The jet flow was classified into the major flow along the negative side of $X$ and the minor flow along the positive side of $X$ (refer to Fig. 2). Experimental conditions are as follows: The diameter of the nozzle is $D$ = 30 mm; the distance between the nozzle and the impingement surface, $h$, is 30 mm; the Reynolds numbers based upon the nozzle diameter, Re, are $2 \times 10^4$, $10^4$, 5000, and 2000; and the angles of inclination, $\theta$, are 90, 60, and 45 deg. The flow at nozzle exit was nearly fully developed and the exit turbulence intensity ranged from 2 to 6 percent for Re = $2 \times 10^4$. The temperature difference between the impingement surface and the fluid ranged from 10°C to 15°C.

## Temperature Measurement

The liquid crystal was a mixture of cholesteric nonanoate and cholesteric chloride. It was microencapsulized and bound between a transparent plate and a stainless steel foil. The relationship between light brightness from the liquid crystal and temperature was calibrated in advance (Akino et al., 1989). Calibration tests were carried out changing temperature gradients to determine accuracy and resolution. The scattered reflected light from the liquid crystal at a given temperature, $T$, was divided into three main color components—red, green, and blue—by optical filters, and the brightness of each component was obtained at each pixel as the image data. The temperature, $T$, was estimated by the regression equation including the relative brightness $(r, g, b)$,

$$T = \xi \cdot r + \eta \cdot g + \gamma \cdot b + \delta \tag{3}$$

The values of $r$, $g$, and $b$ were defined as follows:

$$r = R/S, \quad g = G/S, \quad b = B/S$$

where $R$, $G$, and $B$ were the brightness values and $S$ was the total $S = R + G + B$. The regression coefficients $\xi$, $\eta$, $\gamma$, and $\delta$ were

## Nomenclature

$B$ = brightness value
$D$ = nozzle diameter
$G_{aa}$ = power spectrum
$G$ = brightness value
$h$ = distance between nozzle and impingement surface
$H$ = dimensionless distance between nozzle and impingement surface = $h/D$
Nu = Nusselt number = $\alpha \cdot D/\lambda$
$q_{acr}$ = corrected heat flux in acrylic plate
$q_{cond}$ = corrected heat flux in the heated section = $q_{acr} + q_{sus}$
$q_{net}$ = net heat flux
$q_{rad}$ = radiative heat flux
$q_{sus}$ = corrected heat flux in stainless steel foil
$q_{unif}$ = uniform heat flux by Joule heating
$R$ = brightness value
Re = Reynolds number = $u_0 \cdot D/\nu$
$S$ = total brightness = $R + G + B$
$T$ = temperature
$T_{in}$ = fluid temperature at nozzle exit
$T_w$ = impingement surface temperature
$u$ = velocity
$u_{max}$ = maximum velocity at nozzle exit
$u_0$ = average velocity at nozzle exit
$x$ = $x$ coordinate (refer to Fig. 2)
$X$ = dimensionless $x$ coordinate = $x/D$
$y$ = $y$ coordinate (refer to Fig. 2)
$Y$ = dimensionless $y$ coordinate = $y/D$
$z$ = $z$ coordinate (refer to Fig. 2)
$Z$ = dimensionless $z$ coordinate = $z/D$
$\alpha$ = local heat transfer coefficient = $q_{net}/(T_w - T_{in})$
$\theta$ = inclination angle of nozzle
$\lambda$ = thermal conductivity of fluid
$\nu$ = kinetic viscosity of fluid



Downloaded 12 Dec 2010 to 193.140.21.150. Redistribution subject to ASME license or copyright; see http://www.asme.org/terms/Terms_Use.cfm

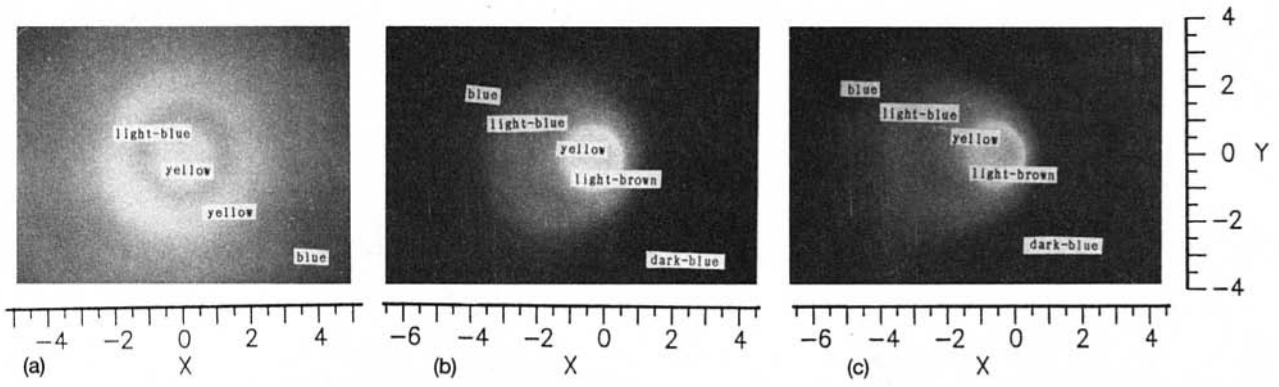



**Fig. 3 Color-temperature visualization (Re = $2 \times 10^4$): (*a*) $\theta$ = 90 deg, (*b*) $\theta$ = 60 deg, (*c*) $\theta$ = 45 deg**

determined using the groups of the temperature and brightness data for optical filters. In the present experiment, these constant values were $\xi = 2.29678$, $\eta = 5.78914$, $\gamma = 19.9525$, and $\delta = 30.4762$ and have the unit of temperature °C. The temperatures were measured in the range of 35 ~ 42°C and the accuracy was within 0.2°C. The colors were brown, orange, yellow, green, and blue ranging from low temperature to high temperature.

## Correction of Local Heat Flux

The local heat flux must be corrected locally using the detailed temperature distribution (Kunugi et al., 1991). The heat flow in the acrylic plate and the stainless steel foil was estimated as a steady thermal conduction problem. Thermal conduction without heat generation is expressed by the following equation:

$$\nabla^2 T = 0 \tag{4}$$

In the acrylic plate, the three-dimensional thermal conduction equation was solved numerically at all pixels. The temperature distribution on one side was given by the measured values and another five sides were insulated thermally. The distribution of heat flux $q_{acr}$ was estimated from the calculated temperature in the plate. In the stainless steel foil, the heat flux $q_{sus}$ was calculated in a two-dimensional system because the foil was thinner than the size of one pixel. Additionally, the radiation loss from the impingement surface was evaluated. Consequently, the net heat flux $q_{net}$ from the impingement surface to the fluid was obtained as the following equation:

$$q_{net} = q_{unif} + q_{aor} + q_{sus} - q_{rad} \tag{5}$$

where $q_{unif}$ is the uniform heat flux by Joule heating (power supply over unit surface to the stainless steel foil), $q_{aor}$ the corrected heat flux in the acrylic plate, $q_{sus}$ the corrected heat flux in the stainless steel foil, and $q_{rad}$ the radiative heat flux. The positive and negative values in each heat flux ($q_{aor}$ and $q_{sus}$) mean "inflow" to a pixel and "outflow" from a pixel, respectively.

## Experimental Uncertainties

All the uncertainties were estimated by the procedure described by ANSI/ASME, PTC 19-1 (1985) and Moffat (1988). The main sources of errors in Nusselt number were the evaluation of the temperature, the heat flux, the thermal conductivity of the fluid, and the size of nozzle diameter. Their bias limits were representatively 0.11°C for *Tw* from 35 to 42°C, 0.84 W/m$^2$ for $q_{net}$ = 206 W/m$^2$, $4.55 \times 10^{-6}$ W/(m·K) for $\lambda$ = 0.023 W/(m·K) and 0.05 mm for $D$ = 30 mm. Their precision limits were 0.018°C, 0.12 W/m$^2$, $1.28 \times 10^{-7}$ W/(m·K) and 0 mm, respectively. The partial derivatives of the Nusselt number with respect to the variables were determined numerically using finite difference method. Consequently, a 95 percent relative coverage of uncertainty for Nusselt number was from 1.62 to 6.01 percent depending on flow condition. On the other hand, a 95 percent relative coverage of uncertainty for flow velocity was 5.1 percent.

## Experimental Results and Discussions

*Impingement Surface Temperature.* Figures 3(*a, b, c*) and 4(*a, b, c*) show the temperature visualization and the isothermal distribution for various inclination angles ($\theta$ = 90, 60, and 45 deg) for Re = $2 \times 10^4$, respectively. The abscissa is dimensionless distance $X$ and the ordinate is the dimensionless distance $Y$. The origin (0, 0) is the geometric center, which means that a line extending from the nozzle center intersects the impingement surface. Image smoothing was used twice before the contour print was made. In the case of $\theta$ = 90 deg (Fig. 3*a*), the jet is normal

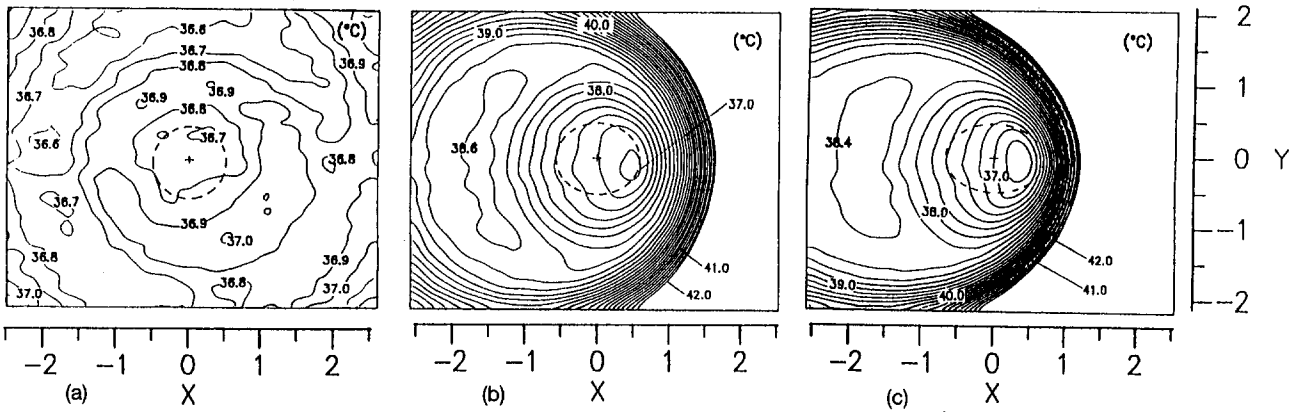



**Fig. 4 Isothermal line (Re = $2 \times 10^4$): (*a*) $\theta$ = 90 deg, (*b*) $\theta$ = 60 deg, (*c*) $\theta$ = 45 deg**



Downloaded 12 Dec 2010 to 193.140.21.150. Redistribution subject to ASME license or copyright; see http://www.asme.org/terms/Terms_Use.cfm

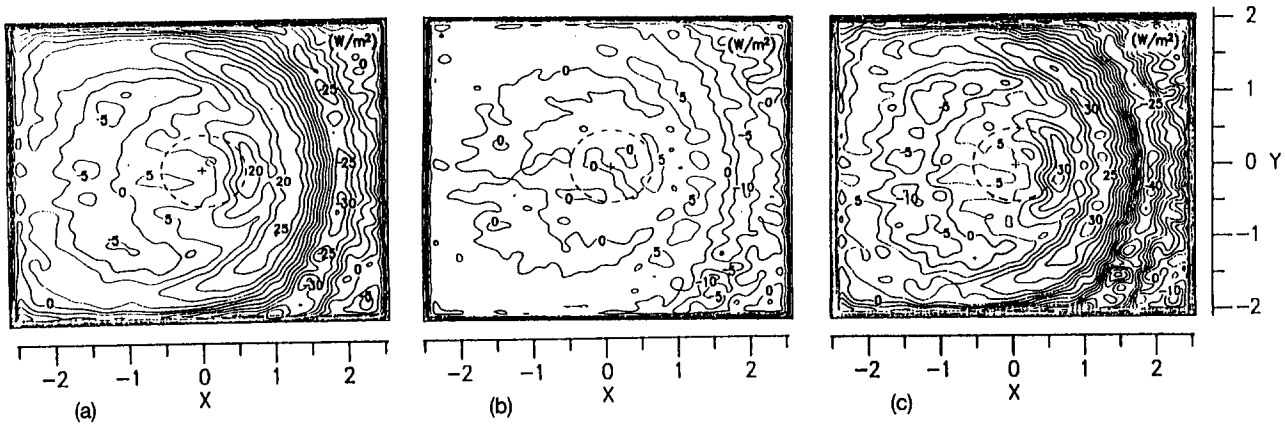



Fig. 5 Corrected heat flux (Re = $2 \times 10^4$, $\theta$ = 60 deg): (*a*) $q_{acr}$, (*b*) $q_{sus}$, (*c*) $q_{cond}$

to the impingement surface and a yellow and light blue annular pattern is shown on the impingement surface. The radius of the annular region ranges from dimensionless length 1 to 1.5. For $\theta$ = 60 deg (Fig. 3*b*), the high-temperature region moves to the downflow side of the low-temperature region (color: light brown) where the jet impinged directly. The distribution is symmetric for $Y = 0$ and is shaped like a horseshoe type. This tendency becomes marked for $\theta$ = 45 deg (Fig. 3*c*). That temperature step in Fig. 4 is 0.1 ~ 0.2°C. The dotted line shows the region at which the extension of the nozzle end intersected with the impingement surface. The inner circle of the annular temperature distribution moves to the right-hand side where the temperature gradient becomes high. Concretely, for $\theta$ = 60 deg (Fig. 4*b*) the temperature increase is about 5°C from $X \fallingdotseq 0.5$ to $X \fallingdotseq 1.6$ and on the other hand, it is about 1.6°C from $X \fallingdotseq 0.5$ to $X \fallingdotseq -1$. A plateau section appears from $X \fallingdotseq -1$ to $X \fallingdotseq -2$ for $\theta$ = 60 deg and from $X \fallingdotseq -1.2$ to $X \fallingdotseq -3$ for $\theta$ = 45 deg (Fig. 4*c*) at Re = $2 \times 10^4$. The plateau section appears generally at comparatively high Reynolds number (more than Re = 5000) and extends in the $Y$ direction with increase of Reynolds number. For $\theta$ = 45 deg, isothermal lines also extend to the negative region of $X$ because the ellipticity of the nozzle end becomes larger.

*Corrected Heat Flux.* The heat flow in the heated section was evaluated by using the detailed temperature distribution. Figures 5(*a, b, c*) show the corrected heat fluxes in the acrylic plate, the stainless steel foil, and the total corrected heat flux with heat flux step 5 W/m$^2$ for $\theta$ = 60 deg and Re = $2 \times 10^4$. The positive value means "inflow" and the negative value, "outflow." The lines 0 W/m$^2$ in $q_{acr}$ exist in the shape of a horseshoe near $X$ = +2.0 and $X = -0.5 \sim -2.0$. The heat of comparatively high absolute value (from +25 to −30 W/m$^2$) flows in or out at the positive side from the geometric center and on the other hand, the heat of lower absolute value (from −5 to +5 W/m$^2$) flows in or out at the negative side. Heat flows from the outside to the inside of the horseshoe region. In the stainless steel foil, the heat flow $q_{sus}$ is qualitatively the same as $q_{acr}$ in the acrylic plate. However, the absolute value is of a lower level. Consequently, the total corrected heat flux $q_{cond}$ has comparatively higher values at the positive side and lower values at the negative side. The ratios of the corrected heat flux in the heated section and the uniform heat flux by Joule heating, $q_{cond}/q_{unif}$, are +16.9 ~ −14.5 percent at Re = 2000, +12.7 ~ −10.6 percent at Re = 10,000 and +6.4 ~ −8.5 percent at Re = $2 \times 10^4$. The effect of thermal radiation is from 1 to 2.9 percent. The heat flow in the impingement section has not been considered precisely in previous studies.

*Local Heat Transfer.* Local Nusselt numbers are represented in Figs. 6(*a, b, c*) corresponding to Figs. 3 and 4. In the case of $\theta$ = 90 deg (Fig. 6*a*), the local Nusselt number assumes a peak near the stagnation point for laminar jet and two peaks (radius from the center $X \fallingdotseq 0.5$ and 1.5) in annular form for turbulent jet (Ichimiya and Nakamura, 1992). Local distribution is not symmetric because the perfect symmetric flow was not realized in practice and the space resolution of the present measurement was better than that of previous methods. In the case of $\theta$ = 60 deg (Fig. 6*b*), the peak changes to the right edge of the dashed ellipse and a plateau section exists in the major flow region (the negative direction of $X$). This section extends in the negative direction of $X$ with the decrease of the inclination angle and in the case of turbulent jet. This tendency is different from the behavior of the iso-Nusselt number that Goldstein and Franchett (1988) obtained. This depends on the confined walls and the

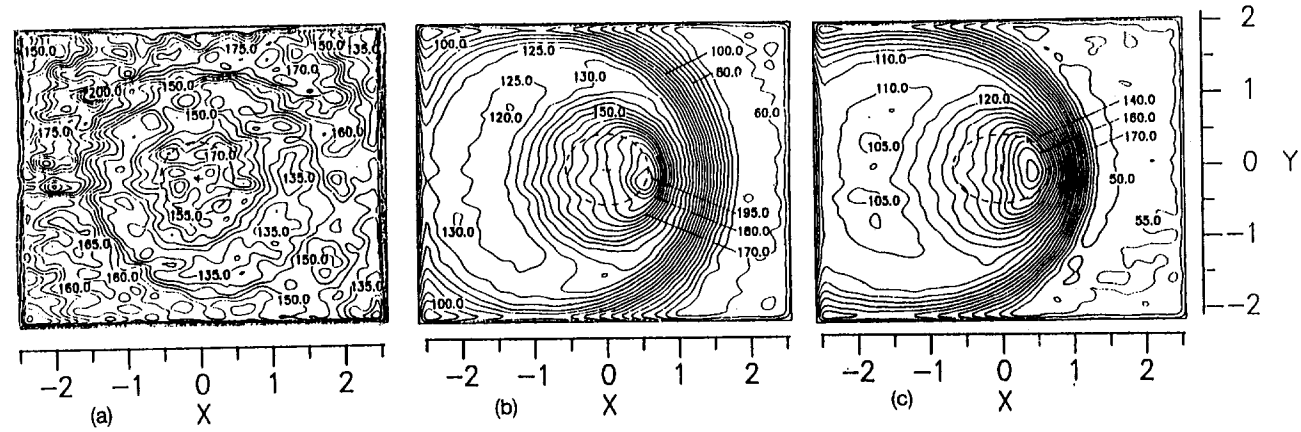



Fig. 6 Local Nusselt number (Re = $2 \times 10^4$): (*a*) $\theta$ = 90 deg, (*b*) $\theta$ = 60 deg, (*c*) $\theta$ = 45 deg



Downloaded 12 Dec 2010 to 193.140.21.150. Redistribution subject to ASME license or copyright; see http://www.asme.org/terms/Terms_Use.cfm

space resolution of temperature measurement. In the case of $\theta$ = 45 deg (Fig. 6*c*), the Nusselt number gradient becomes steeper and the position of the peak moves to the inside of the dashed ellipse. Figures 7(*a, b, c*) show the topography contours, which represent the entire behavior of the local Nusselt numbers. According to the figures, the local irregular distribution for $\theta$ = 90 deg is flattened by inclined jets ($\theta$ = 60 and 45 deg). Figures 8(*a, b, c*) show the local Nusselt numbers along the center line of the impingement surface with and without the correction of the local heat flux for Re = 2000 and $2 \times 10^4$. The solid line denotes the local Nusselt number for the net heat flux $q_{net}$ and the dashed line that for the uniform heat flux $q_{unif}$. The net heat flux improves the maximum and minimum of local Nusselt numbers. This effect is especially noticeable at low Reynolds numbers, which appears to justify the examination of local Nusselt number in detail by considering the correction of local heat flux.

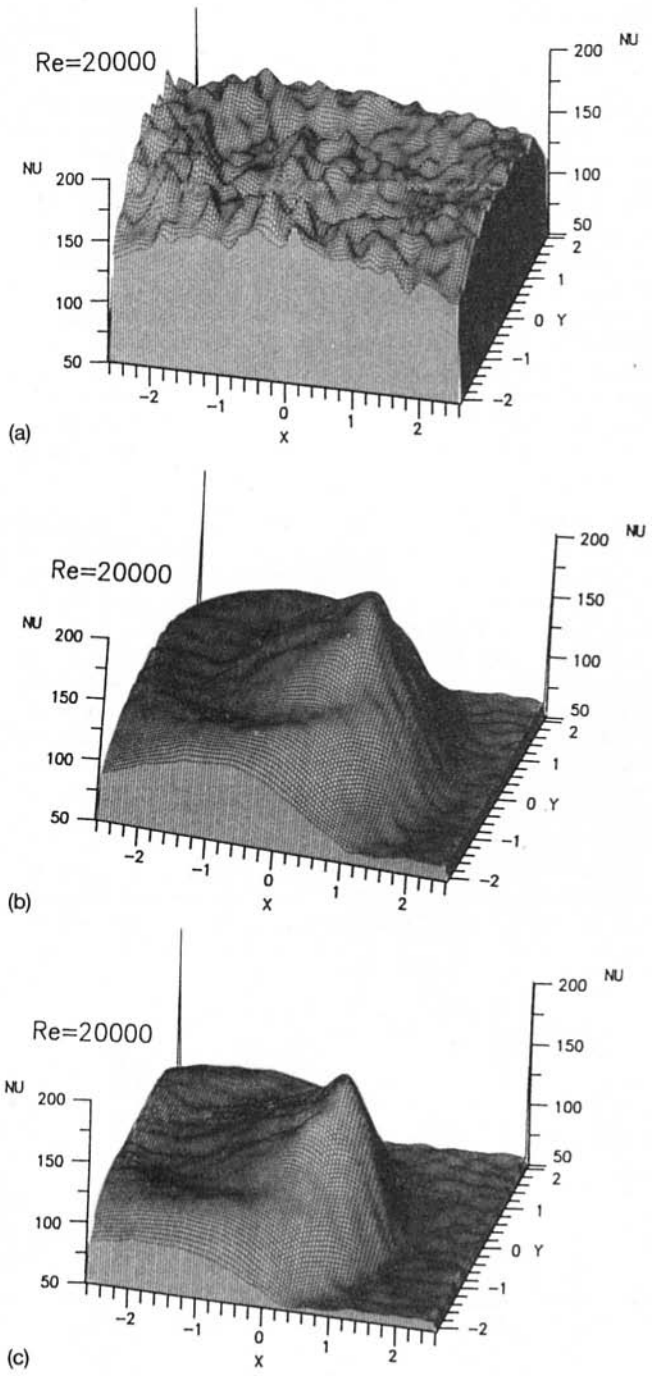



**Fig. 7 Topography contours of local Nusselt number (Re = $2 \times 10^4$): (*a*) $\theta$ = 90 deg, (*b*) $\theta$ = 60 deg, (c) $\theta$ = 45 deg**

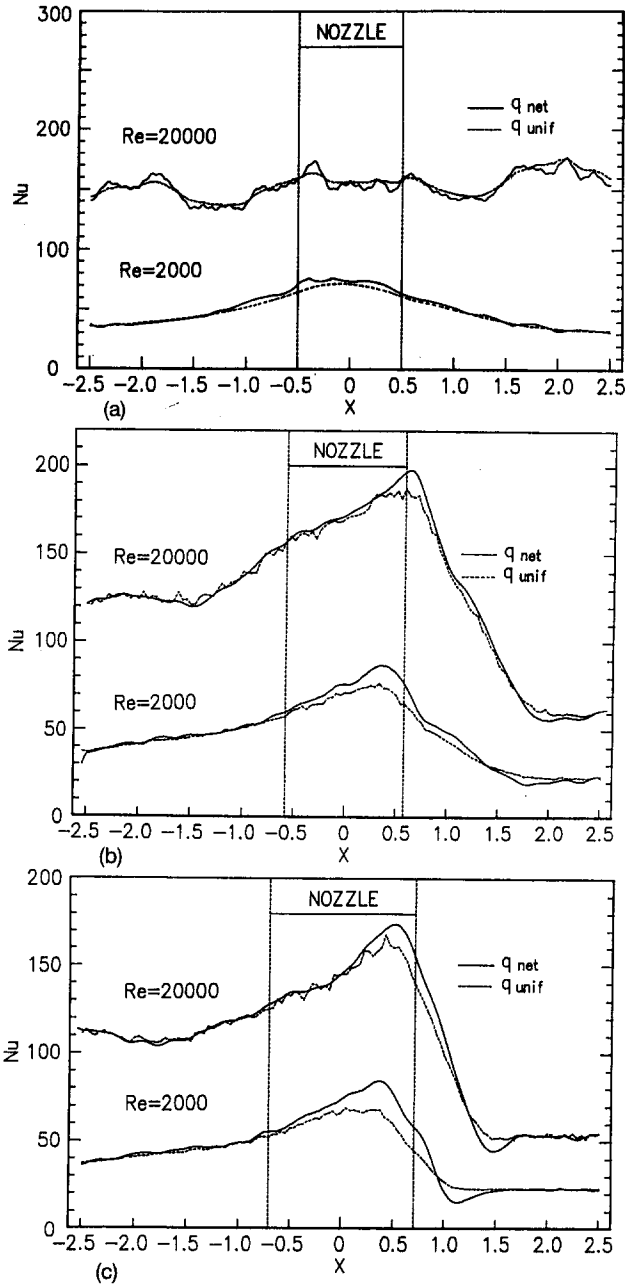
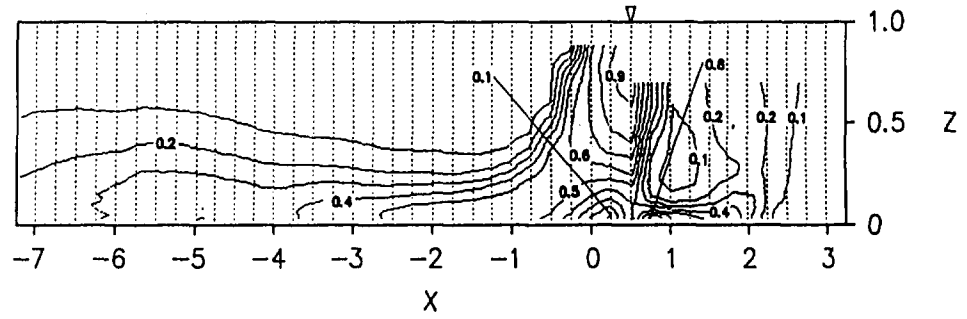



**Fig. 8 Effect of heat flux correction on Nusselt number: (*a*) $\theta$ = 90 deg, (*b*) $\theta$ = 60 deg, (c) $\theta$ = 45 deg**

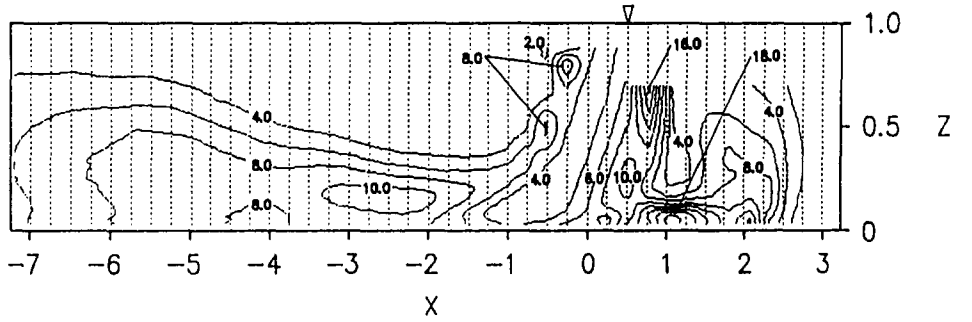
*Flow Field.* The flow was measured and found to be related to the local heat transfer. Figures 9(*a, b*) represent the dimensionless velocity and the turbulent intensity for $\theta$ = 60 deg and Re = $2 \times 10^4$, respectively. The dimensionless value is obtained in terms of the maximum velocity at the nozzle exit ($U_{max}$ = 13 m/s). The symbol $\nabla$ and $X = 0$ denote the center of nozzle and the geometric center, respectively. The jet from the nozzle crossed through the surrounding stationary fluid and impinged on the flat surface. The actual stagnation point existed between the geometric center and the nozzle edge. The rolling back of the flow (vortex) and the amplification of turbulence near the impingement surface in the region of the minor flow ($0 \leq X \leq 0.5$) peaked the local heat transfer, as noted in Fig. 8. Although the flow is decelerated from $X \fallingdotseq -1$ to $X \fallingdotseq -2.5$ at the major flow region and the absolute value of the turbulence intensity is com-



Downloaded 12 Dec 2010 to 193.140.21.150. Redistribution subject to ASME license or copyright; see http://www.asme.org/terms/Terms_Use.cfm




(a) Dimensionless velocity $u/u_{max}$




(b) Turbulence intensity $\sqrt{u'^2}/u_{max} \times 100$ percent

Fig. 9 Flow field (Re = $2 \times 10^4$, $\theta$ = 60 deg; $Y$ = 0)

paratively high, the gradient is mild. As a result, the heat transfer improvement at the major flow region is not as significant as that at the minor flow region. The gradients of these physical parameters seem to affect the local heat transfer augmentation as their absolute values do. The power spectrum of the velocity fluctuation at $X = -1$, $Y = 0$, $Z = 0.017$ for $\theta = 60$ deg and Re = $2 \times 10^4$ is presented in Fig. 10. The superior frequency (the spike in the power spectrum) that causes the local heat transfer augmentation is from 150 Hz to 250 Hz for Re = $2 \times 10^4$ and 150 Hz for Re = $10^4$, and consequently this depends on Reynolds number. These frequencies were also the same as those for $\theta = 45$ deg. However, in the present stage, it is not clear why this superior frequency affects heat transfer augmentation. These correlations should be examined in detail in the future.

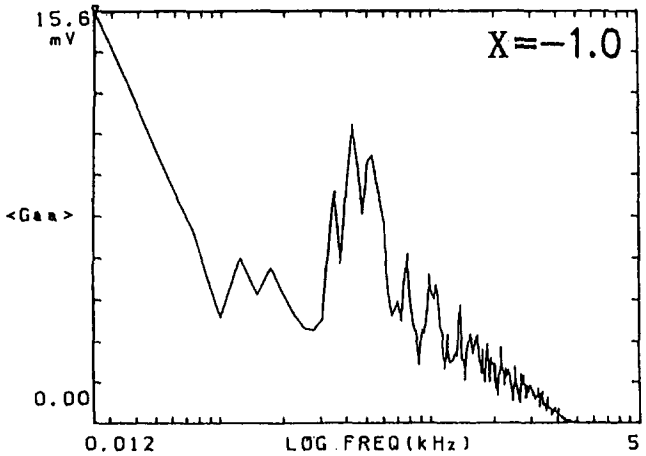



Fig. 10 Power spectrum (Re = $2 \times 10^4$, $\theta$ = 60 deg, $X = -1.0$, $Y = 0$, $Z = 0.017$)

## Conclusions

The heat transfer and flow characteristics of an oblique circular air jet with confined walls were investigated experimentally at $h/D = 1.0$ for $\theta$ = 90, 60, and 45 deg. The local temperature on the impingement surface was obtained in detail by a thermocamera using a liquid crystal sheet.

1 The local Nusselt number showed the characteristic peak shift in the minor flow region and the plateau in the major flow region. The local turbulent intensity and the acceleration near the impingement surface depending on the inclination angle and the Reynolds number corresponded to the behavior of the local heat transfer.
2 The effect of the correction of the local heat flux in the heated section is marked at low Reynolds number and amounts to about 6 ~ 17 percent of uniform heat flux.
3 Vortex generation and amplification of turbulence in the minor flow region cause the local heat transfer increase.
4 The superior frequency in power spectrum of velocity fluctuation affecting heat transfer enhancement ranges from 150 to 250 Hz and depends on Re within the present conditions.

## Acknowledgments

The author wishes to acknowledge the financial support by the Ministry of Education from the research project grant-in-aid for scientific research (c) and thanks to Mr. T. Nasu, Mitsubishi Heavy Industries Co. Ltd., who assisted the experiment.

## References

Akino, N., Kunugi, T., Ichimiya, K., Mitsushiro, K., and Ueda, M., 1989, "Improved Liquid-Crystal Thermometry Excluding Human Color Sensation," ASME JOURNAL OF HEAT TRANSFER, Vol. 111, pp. 558–565.

ANSI/ASME PTC 19-1, 1985, "Supplement to Performance Test Coded, Instrument and Apparatus. Part 1—Measurement Uncertainty," ASME, New York.



Downloaded 12 Dec 2010 to 193.140.21.150. Redistribution subject to ASME license or copyright; see http://www.asme.org/terms/Terms_Use.cfm

Foss, J. F., and Kleis, S. J., 1976, "Mean Flow Characteristics for the Oblique Impingement of an Axisymmetric Jet," *AIAA Journal,* Vol. 14, No. 6, pp. 705–706.

Foss, J. F., 1979, "Measurement in a Large-Angle Oblique Jet Impingement Flow," *AIAA Journal,* Vol. 17, No. 8, pp. 801–802.

Goldstein, R. J., and Franchett, M. E., 1988, "Heat Transfer From a Flat Surface to an Oblique Impinging Jet," ASME JOURNAL OF HEAT TRANSFER, Vol. 110, pp. 84–90.

Han, L. S., Kayansayan, N., and Dantzer, C. W., 1983, "Impingement Cooling of Turbine Airfoils by Multiple Two-Dimensional Jets," *Proc. Tokyo International Gas Turbine Congress,* pp. 75–82.

Hollworth, B. R., and Durbin, M., 1992, "Impingement Cooling of Electronics," ASME JOURNAL OF HEAT TRANSFER, Vol. 114, pp. 607–613.

Ichimiya, K., Kobayashi, K., and Echigo, R., 1987, "Basic Study on the Flattening of Temperature Distribution of Steel Slab for Direct Rolling (Unsteady-State Heat Transfer in Heat Conductive-Convective Field on the Flattening of Temperature Distribution)," *Proceedings of 2nd ASME/JSME Thermal Engineering Joint Conference,* Vol. 5, pp. 79–84.

Ichimiya, K., and Nakamura, Y., 1992, "Heat Transfer of a Single Circular Impinging Jet Considered on Heat Conduction in a Heated Plate," *Transactions of JSME(B),* Vol. 58, No. 550, pp. 2031–2035.

Jambunathan, K., Lai, E., Moss, M. A., and Button, B. L., 1992, "A Review of Heat Transfer Data for Single Circular Jet Impingement," *International Journal of Heat and Fluid Flow,* Vol. 13, No. 2, pp. 106–115.

Kamoi, A., and Tanaka, H., 1977, "Study on Two-Dimensional Impingement Jet Flow Considered Initial Turbulence (Part 2, Static Characteristics of Boundary Layer in Stagnation Region)," *Transactions of JSME,* Vol. 43, No. 372, pp. 2957–2969.

Kunugi, T., Akino, N., Ichimiya, K., and Takagi, I., 1991, "Evaluation of Heat Conduction and Visualization of Heat Flux in a Plate Making Use of Heat Transfer Experiments," *Experimental Thermal and Fluid Science,* Vol. 4, pp. 448–451.

Martin, H., 1977, "Heat and Mass Transfer Between Impinging Gas Jets and Solid Surface," *Advances in Heat Transfer,* Vol. 13, Academic Press, New York, pp. 1–60.

McMurray, D. C., Myers, P. S., and Uyehara, O. A., 1966, "Influence of Impingement Jet Variables on Local Heat Transfer Coefficients Along a Flat Surface With Constant Heat Flux," *Proceedings of 3rd International Heat Transfer Conference,* Vol. 2, pp. 292–299.

Moffat, R. J., 1988, "Describing the Uncertainties in Experimental Results," *Experimental Thermal and Fluid Science,* Vol. 1, pp. 3–17.

Rubel, A., 1981, "Computations of the Oblique Impingement of Round Jets Upon a Plane Wall," *AIAA Journal,* Vol. 19, No. 7, pp. 863–871.

Rubel, A., 1982, "Oblique Impingement of a Round Jet on a Plane Surface," *AIAA Journal,* Vol. 20, No. 12, pp. 1756–1758.

Sparrow, E. M., and Lovell, B. J., 1980, "Heat Transfer Characteristics of an Obliquely Impinging Circular Jet," ASME JOURNAL OF HEAT TRANSFER, Vol. 102, pp. 202–209.

Stevens, J., and Webb, B. W., 1991, "The Effect of Inclination on Local Heat Transfer Under an Axisymmetric, Free Liquid Jet," *International Journal of Heat and Mass Transfer,* Vol. 34, pp. 1227–1236.

Viskanta, R., 1993, "Heat Transfer to Impinging Isothermal Gas and Flame Jets," *Experimental Thermal and Fluid Science,* Vol. 6, No. 2, pp. 111–134.

Ward, J., Oladiran, M. T., and Hammond, G. P., 1991, "The Effect of Nozzle Inclination on Jet-Impingement Heat Transfer in a Confined Cross-Flow," *Fundamentals of Forced Convective Heat Transfer,* ASME HTD-Vol. 181, pp. 25–31.



Downloaded 12 Dec 2010 to 193.140.21.150. Redistribution subject to ASME license or copyright; see http://www.asme.org/terms/Terms_Use.cfm

**S. H. Chan**
Wisconsin Distinguished Professor.

**Z. J. Chen**
Graduate Research Assistant.

**P. He**
Graduate Research Assistant.

Department of Mechanical Engineering,
University of Wisconsin—Milwaukee,
Milwaukee, WI 53211

# Effect of Ferric Chloride on Silica Fouling

*This study presents the results of an experimental investigation of the effects of $Fe^{3+}$ ion in aqueous solution on silica fouling of heat exchanger and assesses the relative effect of $Fe^{3+}$, $Na^+$, and $K^+$ ions on silica fouling. Experiments were conducted at 165–125°C, 1.58 MPa, and under turbulent flow conditions. It was shown that adding a few ppm of $Fe^{3+}$ into silica solution was sufficient to formulate chemical coagulation and deposition of silica colloidal particles, which in turn caused a significant increase in the fouling rate. It was also observed that when $Fe^{3+}$ was added to the silica solutions containing either $Na^+$ or $K^+$ ions, the fouling behaviors were found to be similar. Thus $Fe^{3+}$ was found to be dominant over $Na^+$ and $K^+$ ions in its effects on silica fouling.*

## Introduction

Fouling, the accumulation of undesired solid material at phase interfaces, is a phenomenon that adversely affects a wide variety of industrial operations. It is by no means confined only to heat transfer surfaces but also to non-heat transfer surfaces like membrane processes (Hoyland and Carter, 1976; Gutman, 1977). In many instances, steps can be taken to significantly reduce and even virtually eliminate the fouling. However, these treatments are often expensive and are based on incomplete knowledge of actual cause and mechanism of fouling that occurs. The importance of the fouling problem in heat transfer has long been recognized (Taborek et al., 1972), but progress has been slow in the fundamental understanding and modeling of fouling phenomena because of the complexity of the physical and chemical fouling processes involved and the coupling with heat, mass, and momentum transport processes (Suitor et al., 1977; Somerscales and Knudsen, 1981; Bryers, 1982; Melo et al., 1988; Chan and Ghassemi, 1991).

Recently, an increased effort has been expanded toward the problems of silica and calcium carbonate scale depositions, including iron effects on calcium carbonate fouling. Herzog et al. (1989) investigated the effect of $Fe^{2+}$ on calcium carbonate nucleation and growth and found $Fe^{2+}$ to be a good inhibitor of calcite growth, although the precise mechanism whereby $Fe^{2+}$ inhibits calcite growth is not known. Also, they observed a similar effect with $Fe^{3+}$, but to a lesser degree. It is noted that the ferrous ion ($Fe^{2+}$) is relatively unstable as it rapidly oxidates to ferric ions ($Fe^{3+}$) at a rate proportional to $[O][OH]^2$, namely, the product of the concentrations of O and $(OH)^2$.

Silica fouling is commonly found in heat exchanger equipment utilizing geothermal brines or ground water. Since many different salts are commonly present, $Na^+$, $K^+$, ferric ions, etc., are often found in the brines. The individual and combined effect of two dominant salts, NaCl and KCl, on silica fouling have recently been reported (Chan et al., 1993). It is of interest to examine the effect of ferric ions in those brines. Specifically, the effect of $Fe^{3+}$, which is more stable than $Fe^{2+}$, on silica deposition is investigated experimentally. The theory of coagulation is applied to explain the experimental results.

## Fouling Experiments and Data

The fouling loop facility described previously (Chan et al., 1988) is used to investigate the effect of $Fe^{3+}$ on silica fouling in a heat exchanger. Briefly, in the primary loop a heated solution saturated with silica is fed through the titanium tube of a shell-and-tube heat exchanger, which is cooled by a secondary loop. Silica fouling is formed on the inner surface of a 2.82-m-long, 2.54-cm-diam titanium tube with a 0.165 cm wall thickness. Chemicals including silica gel, $FeCl_3$, etc., are fed into two saturation columns in the third loop, through which the solution in the brine tank of the primary loop is circulated to achieve a desirable chemical composition. A high-grade silica circulated gel (Fisher Scientific Co.) without aluminum or sodium impurities was placed in the columns of the saturators with 100 mesh size screens at both ends of the saturators. Ferric chloride ($FeCl_3$) with 6 $OH_2$, formula weight 270.30 (same as the molecular weight) was added inside the saturation column between the top and bottom screen cups for the experimental runs of T5-Na2 and T5-Fe1. But for later runs, T5-Fe2 and T5-Fe3, it was placed inside the top screen (100 mesh) cup such that $FeCl_3$ was directly discharged into the saturation tank without going through the saturation column to avoid coagulation with the silica gel in the column (see Table 2 footnotes). $FeCl_3$ was chosen in order to keep the anion (mainly $Cl^-$) consistent with the silica fouling experiments using silica-saturated solutions containing sodium chloride (NaCl) or potassium chloride (KCl) in order to assess the relative effect of $Fe^{3+}$, $Na^+$, and $K^+$ ions on silica fouling. Total iron concentration was measured by an atomic absorption (AA) spectroscopy, which yielded the total Fe (not $Fe^{3+}$ only) concentration. The experimental procedure, data reduction, and error analysis were given previously (Chan et al., 1988).

Five sets of experimental results, runs T5-Na11, T5-Na2, T5-Fe1, T5-Fe2, and T5-Fe3, using synthetic brine were recently obtained and are presented in Figs. 1(*a–e*). They show the transient thermal resistances (averaged over the length of heat exchanger) of the silica scale formed on the inner tube surface. The negative fouling resistance values are probably due to enhancement in heat transfer caused by roughing the laminar sublayer by fouling deposits. Also shown in the figures are the concentration levels, $C_{SiO_2}$, of silica monomer dissolved in the brine tank during the course of experiments. Table 1 lists the thermal hydraulic conditions of the fouling experiments and Table 2 lists their chemical compositions containing NaCl, KCl, and $FeCl_3$ salts. The comparisons of fouling behaviors among the runs with $Fe^{3+}$ are summarized in Table 3. As shown in Table 2, run T5-Na11 contained only silica and NaCl without any $Fe^{3+}$ and is used here as a reference (see Fig. 1*a*). In run T5-Na2, 27.5 ppm of $Fe^{3+}$ (0.0005 M) was added at the end of the run to test the effect of $Fe^{3+}$ in the brine (see Table 2 footnotes). This experiment was terminated 57 hours later, after 27.5 ppm $Fe^{3+}$ was added, since the thermal resistance curve (see Fig. 1*b*) jumped from $-0.55 \times 10^{-4}$ to $0.60 \times 10^{-4}$ m² K/W, then remained constant. The color of the brine became dark brown and the residual silica in two saturators was even darker. In runs T5-Fe1 (Fig. 1*c*) and T5-Fe2 (Fig. 1*d*), 1 ppm and 2 ppm of $Fe^{3+}$ were added, respectively, before the experiments started and several times dur-

Contributed by the Heat Transfer Division for publication in the JOURNAL OF HEAT TRANSFER. Manuscript received by the Heat Transfer Division November 1993, revision received April 1994. Keywords: Fouling, Heat Exchangers. Associate Technical Editor: W. A. Fiveland.



**Copyright © 1995 by ASME**

Downloaded 12 Dec 2010 to 193.140.21.150. Redistribution subject to ASME license or copyright; see http://www.asme.org/terms/Terms_Use.cfm

ing the course of the experiments. In these two runs, the brines saturated with silica contained dissolved NaCl salt. In run T5-Fe3 (Fig. 1*e*), NaCl salt was replaced by KCl and 2 ppm of $Fe^{3+}$ were also added before the experiments started and several times during the experiment.

In comparing run T5-Fe1 to the reference run T5-Na11, similar fouling resistance curve slopes were found. They revealed that adding 1 ppm $Fe^{3+}$ in run T5-Fe1 does not affect silica scale fouling rate. However, the measurement results showed that the total Fe concentration was only about 0.1 ppm, although 1 ppm was added at each time. The reason for such a drop in Fe concentration will be explained later. It can be concluded here that 1 ppm of $Fe^{3+}$ placed in the saturation column between the upper and lower screens does not affect silica scale fouling rate.

2 ppm $Fe^{3+}$ was then added and placed outside the fine screen, that is, inside the cup of the top screen at each time before and during the experiments in run T5-Fe2 that contained 0.1 M (5850 ppm) NaCl, and in T5-Fe3, which contained 0.1 M (7460 ppm) KCl. The results showed that 2 ppm of $Fe^{3+}$ placed outside of the fine screen did affect the fouling resistance. Whenever 2 ppm of $Fe^{3+}$ was added, the resistance curve jumped rather quickly. Later on, the curve dropped somewhat. The total Fe concentration measured was around 0.5 ppm for most samples taken directly from the brine tank at about 20–30 minutes after $FeCl_3$ addition.

The scale that formed on the heat exchanger containing iron appeared fundamentally different from the non-iron scale. In the experiments without iron addition, the scale was deposited in bands and had a very rough appearance. It was possible to see the bare heat exchanger surface between the bands of scale. Thus, silica preferentially deposited on the silica scale instead of the adjacent bare surfaces. However, in the experiments containing iron, the scale at the exit of the heat exchanger was relatively smooth and covered the entire surface. This indicates that the deposition was of a particulate deposition nature. The particles did not bond to the heat exchanger surface as strongly as the other scale.

A quantitative chemical analysis of the silica scale deposit removed from the surface of the heat exchanger was carried out by an X-ray spectrometry using a scanning electron microscope. It is noted that the X-ray spectrometry cannot measure any lighter elements listed ahead of Na in the Periodic Table of Elements without additional effort. Table 4 lists the main compositions of fouling scales on heat exchanger surfaces. The scales were removed from the heat exchanger surface by two methods. The first method was physically to scrape the scale off the fouling tube surface near the exit of the heat exchanger with a knife. The other method used a high-pressure water jet to wash the scale off the surface and a screen with a paper filter inside to catch the washed-off scale. The fouling scale collected by the first method is termed the unwashed scale, and that collected by the second, the washed scale. All scales were dehydrated and their compositions are given in Table 4, except for run T5-Fe2, in which only the washed scale composition is listed, since the scale at the exit could not be reached by a knife. In comparison among the runs (T5-Fe1, -Fe2, and -Fe3) that contain iron, the weight percent of Si element was found to increase slightly with the fouling rate in both the washed and unwashed scales. As for the iron element, it is interesting to note that, based on run T5-Fe3 in which significant $Fe^{3+}$ effect was observed, the Fe weight percent in the unwashed scale (the scale collected at the heat exchanger outlet) is 11.45 percent, higher than the 2.32 percent of the washed scale (the mixed scale collected from the entire length of heat exchanger). The nonuniform $Fe^{3+}$ distribution in the scale deposition is believed to be largely due to the coagulation of the colloidal silica by the iron hydrolysis product. This is because colloidal particles are known to exist when pH $< 9$ (Iler, 1979) and because the present experimental condition of pH $\simeq 7.2$ (see Table 2) does lie within this range favorable for silica coagulation. Furthermore, the coagulation theory seems to explain well the experimental results, as will be seen later, after the relevant coagulation theories are briefly described.

## Chemical Aspects of Coagulation

Coagulation is, essentially, the grouping or joining of colloidal particles to create larger particles (Hutchison and Healy, 1990). Colloids are particles of very small diameter that exist in water (or other liquids). These particles remain suspended in the solution due to a couple of reasons. First, these particles are electrostatically charged and their mutual repulsion keeps them from setting out. Also, the particles are usually so small that small motions of the water molecules (Brownian motion) serve to counteract the effects of gravity and to keep the particles from setting out (Stumm and Morgan, 1962).

Various investigators (Stumm and Morgan, 1962; Sheludko, 1966) have explained about the mechanisms of chemical coagulation. Stumm and Morgan (1962) introduced two leading theories, the older "chemical theory" and the newer "physical theory." The chemical theory states that coagulation occurs because of chemical interactions between the colloidal particles. These chemical interactions can create a series of chemical bridges that enmesh the colloidal particles in a three-dimensional network called a floc. The physical theory emphasizes the concept of the electrical double layer and significance of predominantly physical factors, such as counter ion adsorption, reduction of zeta potential, and ion pair formation in the destabilization of colloids. The electrical double layer at an interface between, say, a colloidal particle and an electrolytic solution, consists of an excess of ions or electrons on the particle surface, and an equivalent amount of oppositely charged ions in the solution, situated at a minimum distance, corresponding to the particular ionic radius, from the metal (Kortum, 1965). If counter ions (ions having a charge opposite that of the colloidal particle) are added to the solution, some of them may be adsorbed onto the surface of the colloid particle. If enough of the surface of the particle is covered with these counter ions, the electrostatic charge on the particle may be neutralized and the particle may begin to come together to create larger particles.

In the present application, since silica colloidal particles are negatively charged (Chan et al., 1993) the addition of $FeCl_3$ provides $Fe^{3+}$, which can act as the counter ion to neutralize the charge. Thus, it is reasonable to state that silica colloidal particles were coagulated into larger particles, which precipitated out and deposited onto the fouling layer on the heat exchanger surface in the present experiments.

## Nomenclature

$c$ = concentration in molality or ppm
$m$ = mass flow rate, kg/s
$M$ = molality, g mole of solute per 1 kg of solvent
$Re_b$ = Reynolds number of brine
$R$ = thermal fouling resistance, $m^2$ K/W
$t$ = time period, h
$T$ = temperature, K
$U$ = overall heat transfer coefficient, W/$m^2$ K
$V$ = fluid velocity, m/s

**Subscripts**

$b$ = brine
$c$ = coolant
$cl$ = clean
$f$ = fouling film
$in$ = inlet of heat exchanger
out = outlet of heat exchanger



Downloaded 12 Dec 2010 to 193.140.21.150. Redistribution subject to ASME license or copyright; see http://www.asme.org/terms/Terms_Use.cfm

Table 1 Thermal hydraulic conditions in ferric effect experiments

| Run No. | $Re_b$ | $T_{b1\ in}$ (°C) | $T_{b2\ in}$ (°C) | $T_{b1\ out}$ (°C) | $T_{b2\ out}$ (°C) | $T_{c1\ in}$ (°C) | $T_{c2\ in}$ (°C) | $T_{c1\ out}$ (°C) | $m_{b1}$ (kg/s) | $V_{b1}$ (m/s) | $m_{c1}$ (kg/s) | $U_{o\ c1}$ ($w/m^2$ °C) | Run Time (h) |
|---|---|---|---|---|---|---|---|---|---|---|---|---|---|
| T5-Na11 | 74392 | 166.0 | 165.6 | 125.6 | 121.4 | 71.8 | 71.8 | 72.9 | 0.265 | 0.691 | 9.46 | 2928 | 702 |
| T5-Na2 | 73749 | 162.9 | 165.1 | 125.3 | 122.6 | 70.3 | 71.7 | 71.3 | 0.265 | 0,691 | 9.46 | 2723 | 471 |
| T5-Fel | 74424 | 165.0 | 165.3 | 125.9 | 123.8 | 70.7 | 71.5 | 71.8 | 0.265 | 0.691 | 9.46 | 2783 | 323 |
| T5-Fe2 | 74873 | 165.9 | 165.8 | 129.1 | 126.2 | 71.5 | 71.7 | 72.5 | 0.265 | 0.691 | 9.46 | 2697 | 350 |
| T5-Fe3 | 74738 | 165.4 | --- | 128.8 | --- | 72.2 | --- | 73.2 | 0.265 | 0.691 | 9.46 | 2669 | 613 |

$T_b$ - brine temperature, $m_b$, $v_b$ - brine mass flow rate and brine velocity
$T_c$ - coolant temperature, $m_c$ - coolant mass flow rate
$U_{0\ c1}$ - heat transfer coefficient at starting time
subscript 1 - starting time value, subscript 2 - after induction time

One interesting feature of colloidal stability and coagulation is the ability of the counter ions to destabilize and restabilize the suspensions arises from the ionization of complex ionogenic groups (Stumm and Morgan, 1962) (i.e., to cause coagulation and redispersion of the colloidal particles). According to the physical theory, as the counter ions are adsorbed onto the surface of the particle, the net charge of the particle decreases (becomes closer to neutral). At a certain critical point, the surface of the particle will be covered with enough of the counter ion such that coagulation will begin. As more of the counter ion is adsorbed, the net charge of the particle will become zero and then actually start to reverse polarity (i.e., if the particle started with a negative charge, adsorption of counter ions will cause the charge to drop to zero and then become positive). At another critical point, the charges of the particles may start causing particles to repel themselves, and redisperse throughout the solution (Stumm and Morgan, 1962). The concentration of the counter ion that produces coagulation is called the critical coagulation concentration (c.c.c.), and that which produces restabilization of the solution is called the critical stabilization concentration (c.s.c.). Essentially, then, coagulation is enhanced by counter ion concentrations between the c.c.c. and c.s.c. (O'melia and Stumm, 1967; Hutchison and Healy, 1990).

The c.c.c. of the counter ion, $Fe^{3+}$, is unknown at the present operating condition (brine temperature of 125 ~ 166°C). However, its information is essential to determine the condition above which coagulation is enhanced and precipitation of larger particles occurs. This study in part aims to assess this critical coagulation concentration by varying ferric ion concentration in the experimental runs.

## The Role of Polyvalent Metal Ions

Numerous studies have shown that polyvalent metal ions such as $Fe^{3+}$ and $Al^{3+}$ can be used as coagulations aids, and that coagulation is enhanced by the hydrolysis products of $Fe^{3+}$ (Stumm and Morgan, 1962; Matijevic and Janauer 1966). In the present investigation, when a ferric salt, $FeCl_3$, was dissolved in silica–water solutions, hydrolysis reactions may proceed as follows:

$$Fe^{+++} + 6H_2O = [Fe(H_2O)_6]^{+++} \quad (1)$$

$$[Fe(H_2O)_6]^{+++} + H_2O = [Fe(H_2O)_5(OH)]^{++} + H_3O^+ \quad (2)$$

$$[Fe(H_2O)_5]^{++} + H_2O = [Fe(H_2O)_4(OH)_2]^{++} + H_3O^+ \quad (3)$$

This process may continue by successive decomposition of the coordinated water groups. In addition, these hydrolysis products may start to polymerize, namely

$$2[Fe(H_2O)_5(OH)]^{++} = [Fe(H_2O)_8(OH)_2]^{4+} + 2H_2O \quad (4)$$

Hydrolyzed iron species such as $[Fe(H_2O)_5(OH)]^{++}$ and $[Fe(H_2O)_4(OH)_2]^+$ have the ability to coagulate silica colloids (Stumm and Morgan, 1962; Matijevic and Janauer, 1966). O'melia and Stumm (1967) showed that $Fe^{3+}$ can be used to coagulate silica colloid particles with effective diameters of 1.1 $\mu$m. The coagulation phenomenon can occur across the pH range studied, pH = 1.5–10. The phenomenon is complicated by the fact that dilute silica solution can conversely coagulate iron colloids (a process that has been used to remove iron from water) and the iron containing colloid is formed immediately after addition of the silica (Browman et al., 1989).

Browman et al. (1989) showed that the presence of various cations can inhibit the coagulation-enhancing effect of some ions. In the case of silicates used to coagulate iron, more silicates were needed to do the same job when $Ca^{++}$ ion was present in the solution. It is not clear whether the presence of $Na^+$ and $K^+$ ions in the present silica solutions will have a similar effect.

## Application of Silica Coagulation Theory in Silica Fouling Experiments

According to the above-mentioned chemical and physical theories, pre-existing silica colloidal particles are a necessary condition for silica coagulation. Iler (1979) indicates that silica in supersaturated solutions exists mainly as colloidal particles in equilibrium with $Si(OH)_4$, if the pH value of the silica solution is below approximately 9.0. The pH values in all experimental runs are between 7.1 and 7.4 and the supersaturation ratio is about two based on the

Table 2 Chemical composition of brines in ferric effect experiments

| Run No. | $C_{SiO2}$ | $C_{NaCl}$ | $C_{KCl}$ | $C_{FeCl3}$ | pH |
|---|---|---|---|---|---|
| T5-Na11 | 0.0109 (660) | 0.1 (5850) | 0 | 0 | 7.30 |
| T5-Na2 | 0.0107 (650) | 0.1 (5850) | 0 | .0005 $(27.5)^{1,3}$ | 7.24 |
| T5-Fel | 0.0106 (645) | 0.1 (5850) | 0 | $1.8*10^{-5}$ $(1)^1$ | 7.25 |
| T5-Fe2 | 0.0108 (656) | 0.1 (5850) | 0 | $3.6*10^{-5}$ $(2)^2$ | 7.18 |
| T5-Fe3 | 0.0107 (648) | 0 | 0.1 (7460) | $3.6*10^{-5}$ $(2)^2$ | 7.20 |

$C_{SiO2}$ = saturation concentration; units in molality and (PPM)
1: $FeCl_3$ was added between screens
2: $FeCl_3$ was added inside the top screen cup
3: $FeCl_3$ was added near the end of experiment



Downloaded 12 Dec 2010 to 193.140.21.150. Redistribution subject to ASME license or copyright; see http://www.asme.org/terms/Terms_Use.cfm

**Table 3 Comparison of fouling behavior due to ferric effect**

| Run No. | $dR_f/dt$ ($m^2K/w.h.$)*$10^7$ | Asymptotic value of $R_f$ ($m^2K/w \cdot h$)*10 | Increase in $\Delta P$ (%)[2] |
|---|---|---|---|
| T5-Na11 | 0.51 (90-700 h) | | 326 |
| T5-Na2 | 93.0 (408-418h) | 5.9 | 256 |
| T5-Fe1 | 0.74 (50-320 h) | | 167 |
| T5-Fe2 | 81.0 (average)1 | | 113 |
| T5-Fe3 | 86.6 (average)1 | | 106 |

1. Slopes immediately after FeCl3 was added as shown by solid lines in Figs. 1d and 1e.
2. Across heat exchanger tube at end of experiments

inlet temperature of 165°C and the brine-tube interface temperature of 89°C. One can therefore assume the existence of silica colloidal particles in the brines for the experimental runs here.

The results of fouling experiments (runs T5-Na2, T5-Na11, T5-Fe1, T5-Fe2 and T5-Fe3) gave a good indication that iron-promoted coagulation was occurring. Due to the high pressure nature of the fouling heat transfer loop, continuously adding iron salts to the brine is difficult. Instead, periodically throughout the experiment, 4 g of $FeCl_3$ or so (enough to produce 2 ppm $Fe^{3+}$ ion) was added to one saturation column and allowed to dissolve in the brine tank. Two interesting things were observed after each addition. First, AA measurement of the iron concentration in the loop, 30 minutes after the addition of the iron salt, shows an iron concentration of 0.5 ppm. Also, when one looks at the resistance curve for the trials, the resistance suddenly increases after the iron salt addition, but then decreases somewhat or becomes constant. As mentioned earlier, the chemical interaction between the iron and silica colloids occurs almost immediately. The speed of this interaction explains the sudden increase in fouling resistance, which is caused by sudden coagulation and deposition of silica colloid due to the increased iron concentration. It also explains

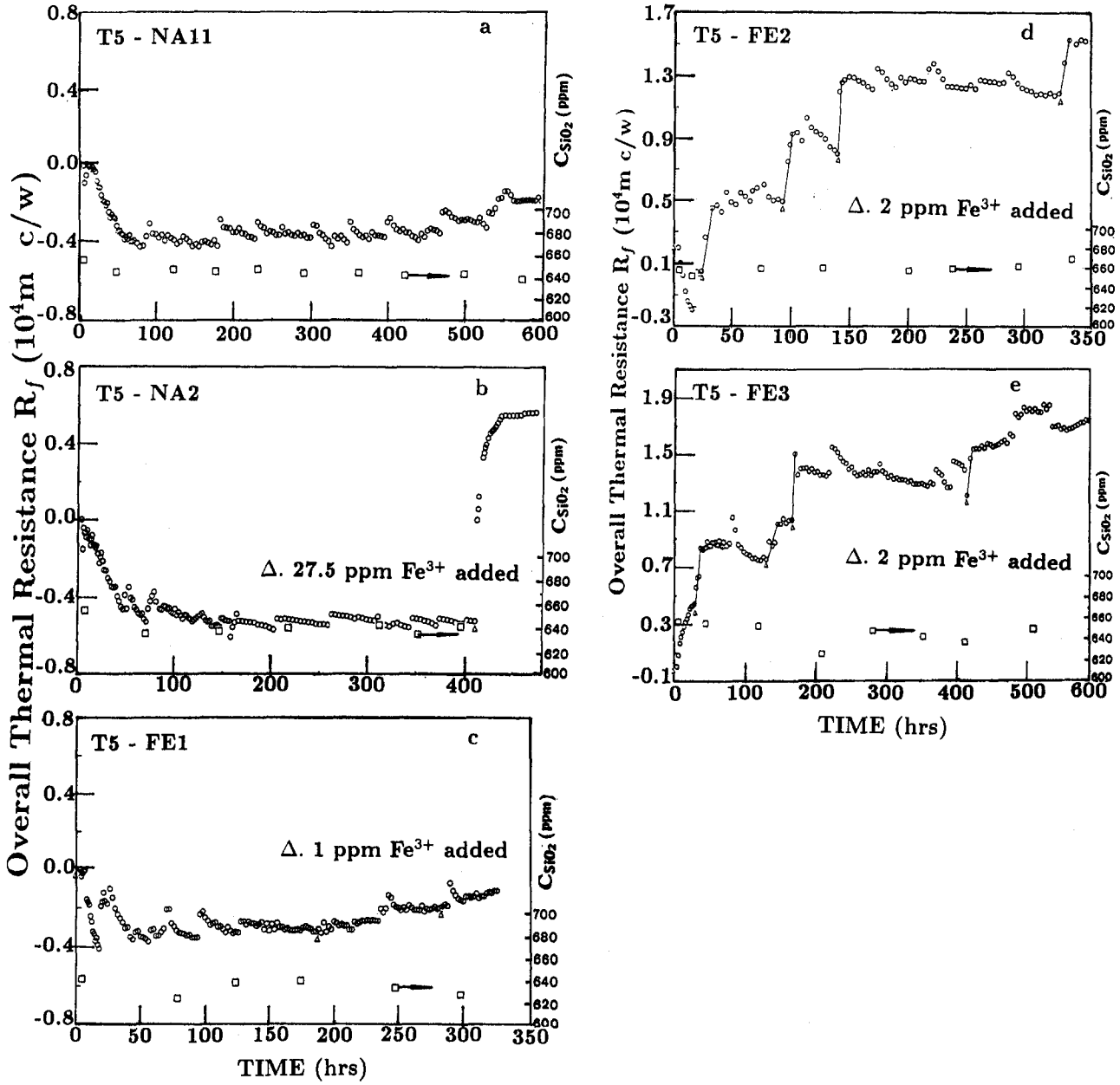



**Fig. 1 The transient curves of silica fouling resistance and silica monomer concentration in brines with NaCl, KCl, and FeCl3: (*a*) run T5-Na2 (0.1 NaCl); (*b*) run T5-Na2 (0.1 NaCl and 0.0005 M $FeCl_3$); (*c*) run T5-Fe1 (0.1 M NaCl and $1.8 \times 10^{-5}$ M $FeCl_3$); (*d*) run T5-Fe2 (0.1 M NaCl and $3.6 \times 10^{-5}$ M $FeCl_3$); (*e*) run T5-Fe3 (0.1 M KCl and $3.6 \times 10^{-6}$ M $FeCl_3$)**



Downloaded 12 Dec 2010 to 193.140.21.150. Redistribution subject to ASME license or copyright; see http://www.asme.org/terms/Terms_Use.cfm

Table 4 Composition of "washed" and "unwashed" scales

| | Run T5-Na 2 | | | | Run T5-Fe1 | | | | Run T5-Fe2 | | Run T5-Fe3 | | | |
|---|---|---|---|---|---|---|---|---|---|---|---|---|---|---|
| | unwashed | | washed | | unwashed | | washed | | washed | | unwashed | | washed | |
| Element | w% | A% | w% | A% | w% | A% | w% | A% | w% | A% | w% | A% | w% | A% |
| NA | 28.3 | 35.5 | 6.06 | 8.30 | 9.25 | 12.03 | 1.40 | 1.81 | | | | | | |
| AL | 1.61 | 1.76 | 3.66 | 4.27 | 2.79 | 2.98 | 2.96 | 3.25 | 1.14 | 1.79 | 3.34 | 3.77 | 1.72 | 1.81 |
| SI | 41.89 | 43.03 | 64.08 | 71.80 | 72.67 | 74.63 | 82.24 | 86.83 | 93.38 | 94.98 | 78.46 | 85.18 | 95.47 | 96.65 |
| S | 0.53 | 0.48 | 0.80 | 0.78 | 0.69 | 0.62 | 2.53 | 2.34 | | | 0.86 | 0.82 | | |
| CL | 16.74 | 13.62 | 1.44 | 1.28 | 8.10 | 6.59 | | | | | 0.37 | 0.32 | | |
| CA | | | 0.47 | 0.37 | | | | | 0.47 | 0.36 | 0.51 | 0.39 | | |
| TI | | | 0.20 | 0.13 | | | | | 0.38 | 0.28 | 3.17 | 2.02 | | |
| FE | 10.69 | 5.52 | 22.33 | 12.58 | 4.86 | 2.51 | 10.87 | 5.77 | 4.38 | 2.43 | 11.45 | 6.25 | 2.32 | 1.18 |
| NI | 0.23 | 0.11 | 0.35 | 0.19 | 1.30 | 0.64 | | | 0.25 | 0.16 | 0.38 | 0.20 | | |
| ZN | | | 0.61 | 0.29 | | | | | | | | | | |
| K | | | | | | | | | | | 1.03 | 0.80 | 0.49 | 0.36 |
| CR | | | | | | | | | | | 0.44 | 0.26 | | |

w% = weight %; A% = atomic %

the immediate drop in iron concentration, because iron is depleted by binding to silica colloids, which precipitate out as scale on heat exchanger surface.

It is further noted that 2 ppm of $Fe^{3+}$ was added periodically in runs T5-Fe2 and T5-Fe3, but only 0.5 ppm of Fe (total Fe) was detected in the solution. This may indicate that the c.c.c. value of iron is 0.5 ppm under the present high-temperature (165°C) loop conditions. Several simple chemistry experiments were then made to determine the c.c.c. value by AA machine. Since high-temperature (and therefore high-pressure) tests are more difficult to conduct, room temperature experiments were made. Standard silica solution (Aldrich Co.) and $Fe^{3+}$ solution made from $FeCl_3$ powder were used. Twenty-five ml of 1000 ppm standard silica solution was poured in a 50 ml container first and 25 ml of 2 ppm ferric solution was added later. The mixing procedure was repeated in reversed order, in case the dilute silica solution significantly coagulated iron colloids as described in the last section. Hours later, the undisturbed solutions were sampled and 0.2 ppm of Fe concentration was found in both cases. The same amount of Fe concentration was obtained when the standard silica solution was replaced by the silica gel used in the loop experiments. The measurement also showed little effects of pH in the range of 3 to 10. It can be concluded that the c.c.c. value of ferric ion in the present silica solution is 0.2 ppm or $1.4 \times 10^{-5}$ mole at room temperature, which is close to the value of $10^{-5}$ mole for $Fe^{3+}$ in silica (min-u-sil-5 suspensions) reported by O'melia and Stumm (1967). While there are no data reported at high temperatures, the c.c.c. value of 0.5 ppm at our experimental condition of 165°C appears to be reasonable.

The composition of fouling scale also confirms the presence of "coagulation deposition." From run T5-Fe3 in Table 4, iron content is 11.4 percent by weight in the unwashed scale sample taken from the exit section of the heat exchanger, higher than 6.25 percent in the washed scale or the proportion of all iron added in the solution. Near the exit section of the heat exchanger, it is believed that the coagulation deposition mechanism prevails. As the brine flowing in the heat exchanger was cooled down, the brine supersaturation ratio with respect to silica increased. Then, more polymers were formed from monomers and subsequently coagulated by $Fe^{3+}$. Thus more silica-coagulated particles were precipitated out as scale deposit at the exit section. Because Fe ions were adsorbed on these particles, the Fe content in the scale can exceed that in the brine solution. Near the inlet section, the dominant mechanism of silica deposition is believed to be "crystal growth" (instead of the "coagulation deposition"). The monomers were transported and deposited onto the polymeric scale that already formed on the tube surface. The scale formed by crystal growth contains considerably less $Fe^{3+}$. Thus, less iron content was found in the scale near the inlet and, consequently, in the washed scale (which was the mixed sample over the entire length of the tube) than in the unwashed scale (taken at the exit). Furthermore, since the bonding of the scale by coagulation deposition to the surface is relatively weak, it is easier for the shear force of the brine flow to wash away the newly deposited coagulated silica particles. This may account for the decrease in the fouling resistance curves (Figs. 1*d* and 1*e*) following the increases after iron was added. As for run T5-Fe2, no unwashed scales were collected since the scales were unreachable by knife. However, since the physical appearance of the scale formation was like that of run T5-Fe3, similar iron effects could be expected.

It is noted that even if the unwashed scale had been rinsed with water to dissolve some $K^+$ and $Cl^-$ residue (assuming they are dissolvable) out of the scale such that their weight percentages are reduced to the same percentage as that found in washed scale (see Table 4), a simple calculation shows that the iron weight percentage in the unwashed scale is still much higher than that in the washed scale. Thus the above-mentioned explanation regarding runs T5-Fe3 and T5-Fe2 remains true and so is the explanation given next regarding other runs (T5-Na2 and T5-Fe1).

In run T5-Na2, a large amount (27.5 ppm) of $Fe^{3+}$ was not added until the end of the experiment. Before the iron addition, more silica scale without iron had already formed in the exit than in the inlet section. When a large dose of $Fe^{3+}$ was later added, a somewhat uniform layer of Fe containing silica layer was deposited on the top of the original scale. Thus, the average iron concentration in the unwashed (exit) scale is expected to be less than the washed scale. In run T5-Fe1, a very low concentration (1 ppm) of $Fe^{3+}$ was added between the screens in the saturator (see Table 2 footnotes). A small amount of $Fe^{3+}$ was transported out of the saturation column and into the loop (only 0.1 ppm was detected in the loop), which then quickly depleted along the tube, resulting in less concentration of iron in the unwashed (exit) scale, as shown in Table 4.

Finally, the averaged slopes of fouling resistance curves (fouling resistance rate), immediately after $FeCl_3$ was added are summarized in Table 3. The slopes for run T5-Fe2, which contained 0.1 M NaCl, and for run T5-Fe3, which contained 0.1 M KCl, are close to each other. It is interesting to note that the individual effects of NaCl and KCl salts on silica fouling resistance rate were found to be different (Chan et al., 1993). However, with the addition of $FeCl_3$, the difference became much smaller (see runs T5-Fe2 and T5-Fe3 in Table 3). Thus, $Fe^{3+}$ has a dominant effect over $Na^+$ and $K^+$ ions in the brine solution. When iron



Downloaded 12 Dec 2010 to 193.140.21.150. Redistribution subject to ASME license or copyright; see http://www.asme.org/terms/Terms_Use.cfm

was added to the solution, it was adsorbed by silica to form larger particles by coagulation for deposition, causing an increase in the fouling resistance rate. As stated earlier, part of the weakly bonded scale by coagulation was washed away by the brine flow, such that the resistance curve dropped somewhat until more ions were added. Such an erratic fouling phenomenon apparently overrides the steady increase in fouling resistance caused by $Na^+$ and $K^+$.

## Conclusions

The fouling behavior of supersaturated silica solution in a heat exchanger tube at conditions (temperature, pressure, and solution composition) close to actual conditions in geothermal power plants has been investigated. The results of the study can be concluded as follows:

1 With the presence of $Fe^{3+}$ in the solution, the fouling deposition mechanism shifted from crystal growth to coagulation deposition mechanism.
2 The fouling layer of the scale with $Fe^{3+}$ was found to be much smoother than the scale without $Fe^{3+}$, especially near the exit of the heat exchanger.
3 In the presence of $Fe^{3+}$, $Na^+$, and $K^+$ ions in a solution, $Fe^{3+}$ ion was found to be a dominant ion, which governed the fouling resistance curve slope rather than $Na^+$ or K ions. Furthermore, $Na^+$ and $K^+$ ions appeared to exhibit a similar effect on silica deposition when $Fe^{3+}$ was present.
4 Adding a few ppm of $Fe^{3+}$ increased the fouling resistance rate immediately and significantly.

## Acknowledgments

This research was sponsored by the National Science Foundation under grant No. CTS-9117230.

## References

Browman, M. G., Robinson, R. B., and Reed, G. D., 1989, "Silica Polymerization and Other Factors in Iron Control by Sodium Hypochlorite Additions," *Envir. Sci. & Technol.*, Vol. 23, pp. 566–572.

Bryers, R. W., 1982, *Fouling of Heat Exchanger Surface,* United Engineering Trustees, Inc.

Chan, S. H., Rau, H., Debellis, C., and Neusen, K. F., 1988, "Silica Fouling of Heat Transfer—Experiments and Model," ASME JOURNAL OF HEAT TRANSFER, Vol. 110, pp. 841–849.

Chan, S. H., and Ghassemi, K. F., 1991, "Analytical Modeling of Calcium Carbonate Deposition for Laminar Falling Films and Turbulent Flow in Annuli: Part I—Formulation and Single-Species Model; Part II—Multispecies Model," ASME JOURNAL OF HEAT TRANSFER, Vol. 113, pp. 735–740, 741–746.

Chan, S. H., Chen, Z. J., and He, P., 1993, "Effects of Sodium and Potassium Chlorides on Silica Fouling," ASME JOURNAL OF HEAT TRANSFER, Vol. 115, pp. 82–90.

Gutman, R. G., 1977, *The Chemical Engineer,* p. 510.

Herzog, R. E., Shi, Q., Patil, J. N., and Katz, J. L., 1989, "Magnetic Water Treatment: The Effect of Iron on Calcium Carbonate Nucleation and Growth," *Langmuir,* Vol. 5, pp. 861–867.

Hoyland, G., and Carter, J. W., 1976, *Proc. 5th Int. Symp. on Fresh Water From the Sea,* p. 21.

Hutchison, P. R., and Healy, T., 1990, "Coagulation and Flocculation-Destabilizing Practices (With Particular Reference to Metal Ion Coagulants)," in: *Surface and Colloid Chemistry in Natural Waters and Water Treatment,* R. Bekett, ed., Plenum Press, New York.

Iler, R. K., 1979, *The Chemistry of Silica—Solubility, Polymerization, Colloid and Surface Properties, and Biochemistry,* Wiley, New York, p. 131.

Kortum, G., 1965, *Treatise on Electrochemistry,* Elsevier Publishing Co., New York, p. 390.

Matijevic, E., and Janauer, G. E., 1966, "Coagulation and Reversal of Charge of Lyophobic Colloids by Hydrolyzed Metal Ions II. Ferric Nitrate," *J. Colloid and Interface Sci.,* Vol. 21, pp. 197–223.

Melo, L. F., Bott, T. R., and Bernardo, C. A., 1988, *Fouling Science and Technology,* NATO ASI Series E, *Applied Sciences,* Vol. 145, Kluwer Academic Pub., Boston, MA.

O'melia, C. R., and Stumm, W., 1967, "Aggregation of Silica Dispersions by Iron (III)," *J. Colloid and Interface Sci.,* Vol. 23, pp. 437–447.

Sheludko, A., 1966, *Colloid Chemistry,* Elsevier Publishing Company, New York, pp. 210–235.

Somerscales, E. F. C., and Knudsen, J. G., 1981, *Fouling of Heat Transfer Equipment,* Hemisphere Pub. Corp., Washington, DC.

Stumm, W., and Morgan, J. J., 1962, "Chemical Aspects of Coagulation," *J. American Water Works Association,* pp. 971–990.

Suitor, J. W., Marner, W. J., and Ritter, R. B., 1977, "The History and Status of Research in Fouling of Heat Exchangers in Cooling Water Service," *Canadian J. of Chem. Eng.,* Vol. 55, pp. 374–380.

Taborek, J., Aoki, T., Ritter, R. B., Palen, J. W., and Knudsen, J. G., 1972, "Fouling: The Major Unresolved Problem in Heat Transfer (Parts I and II)," *Chemical Engineering Progress,* Vol. 68, No. 2, pp. 59–67; Vol. 68, No. 7, pp. 69–78.



Downloaded 12 Dec 2010 to 193.140.21.150. Redistribution subject to ASME license or copyright; see http://www.asme.org/terms/Terms_Use.cfm

# Stabilization of the No-Motion State of a Horizontal Fluid Layer Heated From Below With Joule Heating

J. Tang

H. H. Bau

Department of Mechanical Engineering and Applied Mechanics, University of Pennsylvania, Philadelphia, PA 19104-6315

*Using linear stability theory and numerical simulations, we demonstrate that the critical Rayleigh number for bifurcation from the no-motion (conduction) state to the motion state in the Rayleigh–Bénard problem of an infinite fluid layer heated from below with Joule heating and cooled from above can be significantly increased through the use of feedback control strategies effecting small perturbations in the boundary data. The bottom of the layer is heated by a network of heaters whose power supply is modulated in proportion to the deviations of the temperatures at various locations in the fluid from the conductive, no-motion temperatures. Similar control strategies can also be used to induce complicated, time-dependent flows at relatively low Rayleigh numbers.*

## 1 Introduction

We consider the Rayleigh–Bénard problem of a horizontal, infinite layer heated with Joule heating from below and cooled from above. As the heat input increases, the system undergoes a sequence of bifurcations from no motion to time-independent, cellular motion to time-dependent (possibly periodic) motion and finally to chaos and turbulence.

The Rayleigh–Bénard problem is a paradigm for convective processes occurring in material processing. In many applications, it may be desirable to operate under conditions in which convection normally occurs and yet have no convection. Current alternatives for suppressing convection include the use of magnetic fields to damp fluid motion in electrically conducting materials and processing at reduced gravity in space. A considerable amount of work also has been devoted to delaying the onset of Rayleigh–Bénard convection through active control consisting of time-periodic modulation of the temperature difference across the layer (for lucid reviews, see Davis, 1976; Donnelly, 1990; Meyer et al., 1992). Unfortunately, this technique provides only marginal stabilization (Meyer et al., 1992). Moreover, periodic modulation may lead to a subcritical bifurcation (Roppo et al., 1984), thereby causing the "stabilized" no-motion state to be stable only for small disturbances.

Alternatively, we have chosen to employ feedback control strategies to alter the flow patterns of convective flows. This paper builds on previous work in which we demonstrated both experimentally and theoretically (Singer et al., 1991; Singer and Bau, 1991; Wang et al., 1992) that a feedback controller can alter the bifurcation patterns of convective flows in a thermal convection loop heated from below and cooled from above. For example, with the aid of a controller, we were able to delay the transition from a no-motion to a motion state; laminarize the naturally occurring chaotic motion in the loop for Rayleigh numbers far exceeding the one at the onset of chaos in the uncontrolled system; stabilize otherwise unstable periodic orbits embedded in the chaotic attractor; and induce chaos under conditions in which the flow normally would be laminar. In subsequent work (Bau, 1993; Tang and Bau, 1993a, 1993b, 1994), we have demonstrated theoretically that with the aid of a feedback controller, one can significantly delay the onset of convection in a saturated porous layer (the Lapwood problem) and in a Newtonian fluid (the Rayleigh–Bénard problem) heated from below. In these prior studies, we controlled the temperature of the heated surface. In many applications, however, the controlled variable at the heated surface is the power input rather than the temperature. For this reason, we embarked in this paper on investigating the feasibility of delaying the transition from the no-motion to the motion state by controlling the power supply to the heated surface.

## 2 Problem Formulation

Consider a horizontal, homogeneous layer of a Boussinesq fluid confined between two horizontal, infinite parallel plates positioned a distance $d$ apart. The plates are normal to the Cartesian coordinate $z$ that is parallel to the gravity vector. Coordinates $(x, y)$ span a horizontal platform parallel to the confining plates. The origin of the coordinate system is located middistance between the plates. The bottom plate consists of a network of heaters whose power input can be individually controlled. In the absence of a controller, the power input is at a uniform magnitude $q$ (W/m$^2$). The top plate is kept at a uniform, fixed temperature $T_2 = 0$.

We use, respectively, the height $d$, the thermal diffusion time $d^2/\alpha$, and $qd/k$ as the length, time, and temperature scales. $\alpha$ and $k$ are the thermal diffusivity and the conductivity of the fluid. The motion of the fluid is described by the nondimensional, Oberbeck–Boussinesq (OB) equations, which are available in many references (e.g., Chandrasekhar, 1969; Joseph, 1976; Drazin and Reid, 1981). For brevity, we write these equations in symbolic form:

$$\frac{\partial \Xi}{\partial t} = F(\Xi; \mathrm{Ra}, \mathrm{Pr}), \tag{1}$$

where $\Xi(x, y, z, t)^T = \{\mathbf{u}, \theta\}$. $\mathbf{u}^T = \{u_x, u_y, u_z\}$ is the divergent free ($\nabla \cdot \mathbf{u} = 0$), nondimensional velocity vector, which is zero on all solid surfaces. $\theta(x, y, z, t) = T(x, y, z, t) - (\frac{1}{2} - z)$ is the deviation of the nondimensional temperature from the linear (conduction) profile, $\frac{1}{2} - z$. In the absence of a controller, the temperature satisfies the boundary conditions

$$\theta(x, y, \tfrac{1}{2}, t) = \frac{\partial \theta(x, y, -\frac{1}{2}, t)}{\partial z} = 0. \tag{2}$$

$F(\cdot)$ is a nonlinear, partial-differential operator. $t$ is time. $R = g\beta q d^4/k\alpha\nu$ is the Rayleigh number. Pr is the Prandtl number. $g$, $\beta$, and $\nu$ are, respectively, the gravitational acceleration, the thermal expansion coefficient, and the kinematic viscosity.

Contributed by the Heat Transfer Division for publication in the JOURNAL OF HEAT TRANSFER. Manuscript received by the Heat Transfer Division December 1993; revision received April 1994. Keywords: Materials Processing and Manufacturing Processes, Natural Convection. Associate Technical Editor: J. R. Lloyd.



Copyright © 1995 by ASME

Downloaded 12 Dec 2010 to 193.140.21.150. Redistribution subject to ASME license or copyright; see http://www.asme.org/terms/Terms_Use.cfm

The equations of motion (1) admit the no-motion (conduction) solution, $\mathbf{u}(x, y, z, t) = \theta(x, y, z, t) = 0$. Using linear stability theory, Sparrow et al. (1964) showed that the no-motion state of the infinite fluid layer is stable for $\mathrm{Ra} < \mathrm{Ra}_c \sim 1295.78$.

Our objective is to demonstrate theoretically that, with the aid of a feedback controller, the critical Rayleigh number for the onset of convection can be significantly increased. At various locations inside the fluid, the controller senses the deviation of the temperature from its conductive, no-motion value and directs the heaters to modify their power input in proportion to this deviation. Here, we assume that the sensors are placed at the layer's midheight. Preliminary calculations revealed that this sensor placement leads to more effective control than that achieved by placing the sensors on the heated surface. Mathematically, the control strategy can be expressed as:

$$\frac{\partial\theta(x, y, -\frac{1}{2}, t)}{\partial z} = K_p\theta(x, y, 0, t), \tag{3}$$

where $K_p$ is the proportional controller gain. In the equation above, for mathematical convenience, we assumed that the temperature distribution at the horizontal cross section ($z = 0$) is known or can be reconstructed and that the power input can be continuously varied across the bottom surface. Neither of these conditions is necessary for the practical application of the controller. Numerical experiments suggest that knowledge of the temperature at a few discrete locations in the fluid and the use of a few discrete heaters suffices for a successful operation of the controller.

To aid in understanding how the controller works, we briefly state the mechanisms responsible for the loss of stability of the no-motion state in the classical Rayleigh–Bénard problem. The no-motion state is an equilibrium state for all Rayleigh numbers. As a result of random disturbances, the temperature in the fluid may deviate from its conductive value. Such a deviation will provide a buoyant force, which, in turn, will induce fluid motion. For subcritical Rayleigh numbers, the induced motion is sufficiently slow to allow ample time for thermal conduction to dissipate any disturbances, remove the resulting buoyant forces, and restore the no-motion state. The controller acts to assist these dissipative mechanisms, thereby making it possible to maintain the no-motion state for higher Rayleigh numbers. To this end, the controller reduces/increases slightly the power input at locations where the fluid tends to ascend ($\theta(x, y, 0, t) > 0$)/descend ($\theta(x, y, 0, t) < 0$). These power alterations cause the bottom temperature to decrease/increase beneath ascending/descending columns of fluid, thereby reducing the buoyant force and causing a slowdown in the flow so as to allow ample time for the dissipating mechanisms to eliminate the disturbance. Once the disturbance has been suppressed, the power input is restored to its nominal value.

## 3 Linear Stability Theory

We use linear stability theory to assess the effect of the controller gain on the critical Rayleigh number for the onset of convection. In contrast to the classical, uncontrolled case, the eigenvalues that correspond to the growth rate are not guaranteed to be real. As we shall see, Hopf bifurcations into time-dependent (periodic) motion do, indeed, occur.

The stability analysis starts with the linearized version of Eqs. (1) and (3). Any perturbations (deviations from the conductive solution) are expanded into a Fourier series (normal modes). Below, we write only the expressions for the vertical velocity ($u_z$) and the temperature ($\theta$):

$$\begin{pmatrix} u_z(x, y, z, t) \\ \theta(x, y, z, t) \end{pmatrix} = \begin{pmatrix} W(z) \\ \Theta(z) \end{pmatrix} \exp(i(k_x x + k_y y) + \sigma t), \tag{4}$$

where $k_x$ and $k_y$ are wavenumbers of the periodic disturbances in the $x$ and $y$ directions, respectively, $\sigma = \sigma_R + i\sigma_I$ is the growth rate, and $i = \sqrt{-1}$.

Substituting Eq. (4) into the linearized OB equations, we obtain a sixth-order ODE for the temperature deviation,

$$(D^2 - a^2)(D^2 - a^2 - \sigma)\left(D^2 - a^2 - \frac{\sigma}{\mathrm{Pr}}\right)\Theta = -a^2R\Theta, \tag{5}$$

where $a = \sqrt{k_x^2 + k_y^2}$ is the horizontal wavenumber, $\sigma$ is the growth rate, and $D = d/dz$. The boundary conditions are zero normal and tangential velocities at the top and bottom. There is zero temperature disturbance at the top boundary. Thermal conditions on the bottom boundary are dictated by the controller.

$$(D^2 - a^2 - \sigma)\Theta(\pm\tfrac{1}{2}) = D(D^2 - a^2 - \sigma)\Theta(\pm\tfrac{1}{2})$$
$$= \Theta(\tfrac{1}{2}) = D\Theta(-\tfrac{1}{2}) - K_p\Theta(0) = 0. \tag{6}$$

Equation (5) admits the general solution:

$$\Theta(z) = \sum_{i=1}^{3} \{A_i \cosh(x_i z) + B_i \sinh(x_i z)\}, \tag{7}$$

where $x_i^2$ satisfies the cubic equation

$$(x_i^2 - a^2)(x_i^2 - a^2 - \sigma)\left(x_i^2 - a^2 - \frac{\sigma}{\mathrm{Pr}}\right) + a^2R = 0. \tag{8}$$

Upon substituting Eq. (7) into the boundary conditions (6), we obtain six linear algebraic equations for the coefficients $A_i$ and $B_i$. To assure that all these coefficients are not identically zero, the system matrix must be singular, i.e.,

$$M = \begin{vmatrix} \mathbf{M}_1 & \mathbf{M}_2 \\ \mathbf{M}_3 & \mathbf{M}_4 \end{vmatrix} = M_R(a, \mathrm{Ra}, \sigma) + iM_I(a, \mathrm{Ra}, \sigma) = 0, \tag{9}$$

## Nomenclature

$a = \sqrt{k_x^2 + k_y^2}$ = wavenumber
$d$ = height of fluid layer, $m$
$D$ = $d/dz$
$g$ = gravitational acceleration, m/s$^2$
$k$ = thermal conductivity, W/m-K
$k_x, k_y$ = wavenumbers in the $x$ and $y$ directions
$K_p$ = controller gain
Pr = Prandtl number
$q$ = heat flux, W/m$^2$
$r$ = reduced Rayleigh number = Ra/1295.78
Ra = Rayleigh number
$t$ = nondimensional time
$T$ = temperature, K
$\mathbf{u}$ = velocity vector
$W$ = amplitude of the vertical velocity
$x, y, z$ = Cartesian coordinates
$\alpha$ = thermal diffusivity, m$^2$/s
$\beta$ = thermal expansion coefficient, K$^{-1}$
$\theta$ = temperature deviation from its conductive value
$\Theta$ = temperature deviation amplitude
$\nu$ = kinematic viscosity, m$^2$/s
$\sigma$ = growth rate



Downloaded 12 Dec 2010 to 193.140.21.150. Redistribution subject to ASME license or copyright; see http://www.asme.org/terms/Terms_Use.cfm

where

$$\mathbf{M}_1 = \begin{bmatrix} \cosh\frac{x_1}{2} & \cosh\frac{x_2}{2} & \cosh\frac{x_3}{2} \\ (x_1^2 - a^2 - \sigma)\cosh\frac{x_1}{2} & (x_2^2 - a^2 - \sigma)\cosh\frac{x_2}{2} & (x_3^2 - a^2 - \sigma)\cosh\frac{x_3}{2} \\ x_1(x_1^2 - a^2 - \sigma)\sinh\frac{x_1}{2} & x_2(x_2^2 - a^2 - \sigma)\sinh\frac{x_2}{2} & x_3(x_3^2 - a^2 - \sigma)\sinh\frac{x_3}{2} \end{bmatrix},$$

$$\mathbf{M}_2 = \begin{bmatrix} \sinh\frac{x_1}{2} & \sinh\frac{x_2}{2} & \sinh\frac{x_3}{2} \\ 0 & 0 & 0 \\ 0 & 0 & 0 \end{bmatrix},$$

$$\mathbf{M}_3 = \begin{bmatrix} -x_1\sinh\frac{x_1}{2} - K_p & -x_2\sinh\frac{x_2}{2} - K_p & -x_3\sinh\frac{x_3}{2} - K_p \\ 0 & 0 & 0 \\ 0 & 0 & 0 \end{bmatrix},$$

and

$$\mathbf{M}_4 = \begin{bmatrix} x_1\cosh\frac{x_1}{2} & x_2\cosh\frac{x_2}{2} & x_3\cosh\frac{x_3}{2} \\ (x_1^2 - a^2 - \sigma)\sinh\frac{x_1}{2} & (x_2^2 - a^2 - \sigma)\sinh\frac{x_2}{2} & (x_3^2 - a^2 - \sigma)\sinh\frac{x_3}{2} \\ x_1(x_1^2 - a^2 - \sigma)\cosh\frac{x_1}{2} & x_2(x_2^2 - a^2 - \sigma)\cosh\frac{x_2}{2} & x_3(x_3^2 - a^2 - \sigma)\cosh\frac{x_3}{2} \end{bmatrix}.$$

At marginal stability, we set the real part of the growth rate $\sigma_R = 0$. Equation (9) is then a complex equation that allows one to compute Ra and $\sigma_I$ as functions of $K_p$, Pr and the wavenumber $a$. We performed these calculations with the aid of the bifurcation software package, AUTO (Doedel, 1986).

A representative example of our results is shown in Fig. 1, which depicts the reduced Rayleigh number (the ratio of the critical Rayleigh number for the onset of convection in the controlled system to that for the uncontrolled system, $r = \mathrm{Ra}/1295.78$), as a function of the wavenumber $a$ for $\{K_p, \mathrm{Pr}\} = \{14.5, 7.0\}$ and $\{23.49, 0.7\}$. The solid line represents loss of stability through a real growth rate ($\sigma_I = 0$, exchange of stability). Note that on the solid line $M_R(a, \mathrm{Ra}, 0) \equiv 0$ for all Ra and $a$. This branch is independent of the Prandtl number. The dashed line represents bifurcation into time-dependent motion ($\sigma_I \neq 0$, Hopf bifurcation). The location of the dashed line depends on the Prandtl number; it shifts upward as the Prandtl number decreases. Since, in the case of an infinite fluid layer, all wavenumbers $a$ are admissible, for $\{K_p, \mathrm{Pr}\} = \{14.5, 7.0\}$ and $\{23.49, 0.7\}$, the critical reduced Rayleigh numbers are ~2.6 and 3.9, respectively. Witness that the critical Rayleigh number for the controlled system is significantly larger than that for the uncontrolled one.

In Fig. 1, we illustrate the atypical case when the minima of the solid and dashed curves occur at the same $r$ value. When the minima of both curves coincide, the bifurcation occurs through a triple eigenvalue (two complex conjugates and one real). This type of bifurcation may give rise to complicated, time-dependent, supercritical behavior.

Point $C$ in Fig. 1 denotes the intersection of the solid (exchange of stability) and dashed (Hopf bifurcation) curves. The location of $C$ was determined using the implicit function theorem. Figure 2 depicts the wavenumber $a$ and the reduced Rayleigh number $r$ at $C$ as functions of Pr for $K_p = 20$ and 30. As Pr increases, the intersection point moves to higher $a$ and smaller $r$ values.

Of prime interest are the minima of the curves in Fig. 1. $r_c = \min_a(r)$. Figure 3 depicts $r_c$ (solid, dashed, and dot-dashed lines) and the corresponding normalized wavenumber, $a/2.55$ (dashed-dot line, exchange of stability only), as functions of the controller gain ($K_p$). The solid line and dashed-dot lines are independent of the Prandtl number and represent a bifurcation into time-independent flow. The dashed lines represent bifurcation into time-periodic flow at Pr = 0.7 and 7. As the controller's gain increases, so does the critical $r$ number. This increase terminates, however, once the Hopf bifurcation occurs. For example, in the case of a

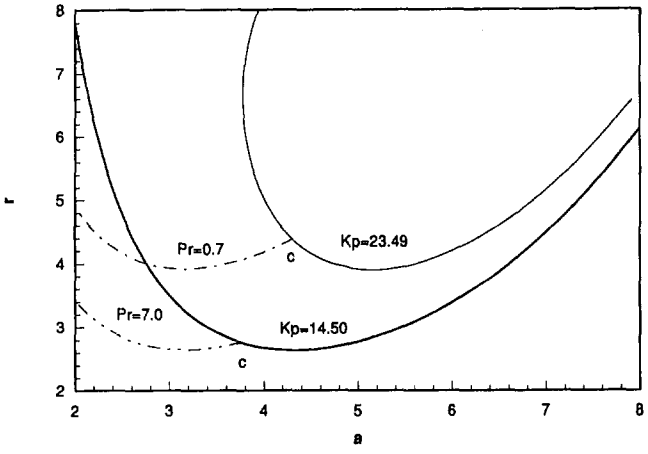



**Fig. 1 The reduced critical Rayleigh number ($r = \mathrm{Ra}/1295.78$) at the onset of convection is depicted as a function of the wavenumber ($a$) for a controller with gains and Prandtl numbers $\{K_p, \mathrm{Pr}\} = \{23.49, 0.7\}$ and $\{14.50, 7\}$. The solid and dot-dash curves describe, respectively, loss of stability through a simple eigenvalue (exchange of stability) and a Hopf bifurcation into time-periodic flow.**



Downloaded 12 Dec 2010 to 193.140.21.150. Redistribution subject to ASME license or copyright; see http://www.asme.org/terms/Terms_Use.cfm

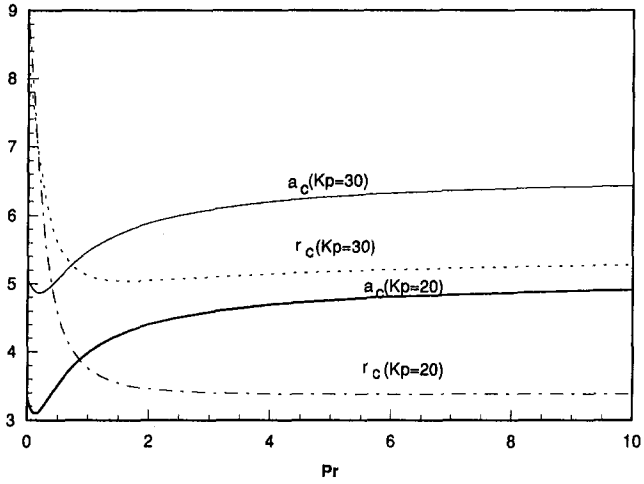



**Fig. 2 The reduced critical Rayleigh number ($r$ = Ra/1295.78) and wavenumber $a$ at the intersection of the solid and dashed lines in Fig. 1, depicted as functions of the Prandtl number for controller gains $K_p$ = 20 and 30**

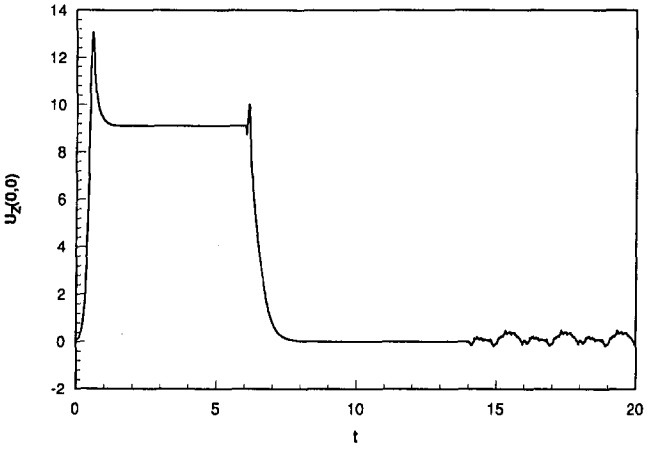



**Fig. 4 The vertical velocity $u_z(0, 0)$ is depicted as a function of time ($t$) for Ra = 4000 and Pr = 0.7. For $0 < t < 6$, the controller is off. For $6 < t < 14$, the controller with gain $K_p$ = 20.0 is active. For $t > 14$, the controller counteracts the action of random disturbances.**

Pr = 0.7 fluid, as the controller gain increases from 0 to 23.5, the critical Rayleigh number increases from 1 to 3.9 and the supercritical motion is time-independent. At $K_p \sim 23.5$ and $r \sim 3.9$, a bifurcation occurs through a triple eigenvalue (one real $\sigma$ and a complex conjugate pair). Once $K_p$ is increased beyond 23.5 and stability is dictated by the Hopf bifurcation curve, the critical $r$ number decreases as the controller gain increases and the corresponding supercritical motion is time-periodic. Clearly, in practice, for a Pr = 0.7 fluid, there is no point in increasing the controller gain beyond 23.5 unless the Hopf bifurcation curve can be shifted upwards. Tang and Bau (1993b) showed that this could be done by engaging a differential controller. As the Prandtl number decreases, the dashed-dot line moves upward to higher $r$ values.

## 4 Numerical Simulation

Using finite differences, we solved numerically the time-dependent, two-dimensional, nonlinear OB equations. The objectives of the numerical simulation were to demonstrate that the controlled system has a finite domain of attraction (i.e., the controller can suppress finite amplitude disturbances) and to examine the dynamics of the controlled system in the presence of stochastic disturbances.

Our numerical code employed primitive variables and Patankar's (1980) SIMPLER algorithm. The higher order upwind scheme, QUICK, was used to approximate convective terms. The numerical simulation was conducted on a single convective cell with periodic boundary conditions at the cell's lateral boundaries. The width of the convective cell was the one that linear theory predicted to render a minimum for the critical Rayleigh number at the onset of convection.

To verify the code, we computed the critical Rayleigh numbers for the controlled and uncontrolled systems and compared them with values predicted by linear stability analysis. We proceeded by selecting a Rayleigh number, starting the simulation with initial conditions corresponding to a perturbed no-motion state, and observing whether disturbances decayed or amplified. If the disturbances decayed with time, the chosen Rayleigh number was below the critical value, and the calculation was repeated for a larger Rayleigh number until the disturbance grew in time. For a $20 \times 20$ grid, which we used in most of our computations, the numerically obtained critical Ra for $K_p$ = 0.0 and 10.0 are, respectively, $1260 \pm 10$ and $2710 \pm 10$. This deviates less than 3 percent from the analytical value predicted by linear stability theory.

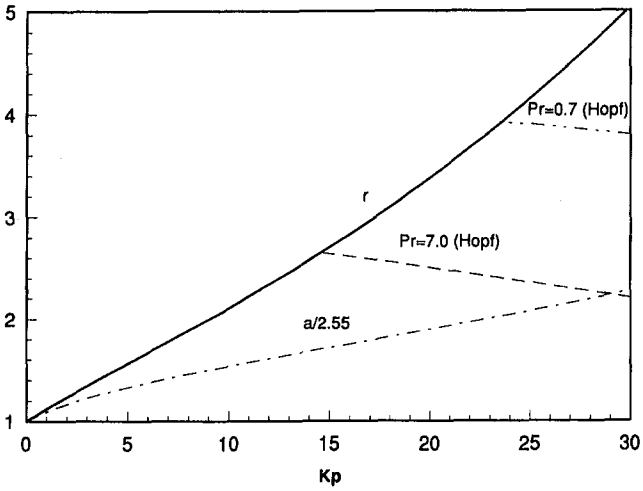



**Fig. 3 The normalized critical Rayleigh number ($r$ = Ra/1295.78) and wavenumber $a/2.55$ are depicted as functions of the controller's gain ($K_p$) for Prandtl numbers Pr = 0.7 and 7. The solid and dotted curves describe, respectively, loss of stability through a simple eigenvalue (exchange of stability) and a Hopf bifurcation.**

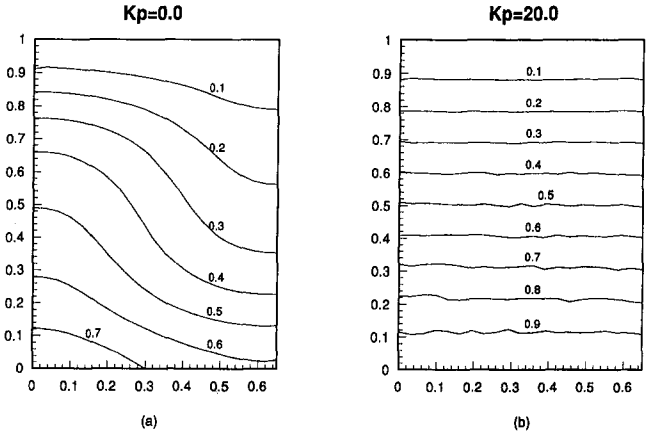



**Fig. 5 The temperature field (isotherms) for Ra = 4,000 and Pr = 0.7 in the absence (*a*) and the presence (*b*) of a controller with gain $K_p$ = 20.0 and random fluctuations in the temperature field**



Downloaded 12 Dec 2010 to 193.140.21.150. Redistribution subject to ASME license or copyright; see http://www.asme.org/terms/Terms_Use.cfm

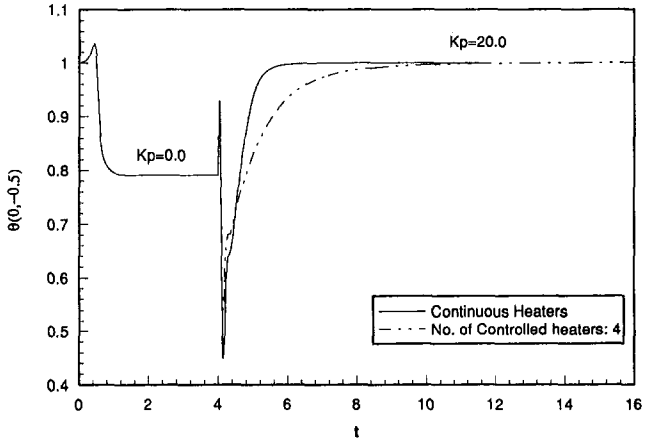



**Fig. 6 The temperature $\theta(0, -0.5)$ is depicted as a function of time ($t$) for Ra = 4000 and Pr = 0.7. For $0 < t < 4$, the controller is off. For $t > 4$, the controller with a gain $K_p = 20.0$ is active. The solid and dashed lines describe, respectively, the actions of a controller with a large number of heaters and one with only four controlled heaters.**

Next, we explored the controller's ability to cope with "large" disturbances. Figure 4 depicts the vertical velocity, $u_z$, at the layer's midheight and at the computational cell's left side, $(x, z) = (0, 0)$, as a function of time for Ra = 4000 ($r \sim 3.09$) and Pr = 0.7. For time $t < 6$, the controller was off. As a result of disturbances introduced in the vicinity of $(x, z) = (0, 0)$, time-independent, counterclockwise motion evolved. The temperature field (isotherms) corresponding to the steady motion is shown in Fig. 5($a$). The controller with gain, $K_p = 20.0$, was turned on at $t = 6$. The controller successfully suppressed the motion. At time $t = 7.5$, the system returned to a no-motion state and the bottom's heat flux assumed its nominal value of one. At $14 > t > 7.5$, the isotherms were perfectly horizontal and are not shown here. For $t > 14$, we explored how well the controller can cope with stochastic disturbances. We subjected the temperature field to random noise with a maximum magnitude of 1 percent of the undisturbed conductive temperature. Any motion induced by these disturbances was successfully suppressed by the controller and the magnitude of the vertical velocity remained very small. A snapshot of the temperature field (isotherms) at $t = 20$ is shown in Fig. 5($b$). Witness that the isotherms are almost horizontal, indicating a lack of significant convective currents. The temperature field in Fig. 5($b$) (with control) should be contrasted with the one depicted in Fig. 5($a$) (without control). Both cases are subjected to similar heating conditions. The controller successfully modified the system's stability without altering the no-motion state. Note also that in Fig. 4, the controller successfully suppressed fully established motion. In practical applications, it is likely that the controller will be active while the heating rate (or the Rayleigh number) is increased and fluid motion will never occur.

In the simulations described above, we assumed that the temperature profile at the fluid layer's midheight is known and that the bottom heat flux can be modified continuously as a function of surface coordinates. To approximate such conditions in practice, a large number of sensors and actuators would be needed. Below, we investigate whether the controller can operate successfully with a relatively small number of sensors and actuators. To this end, we divided the bottom surface into eight segments. Each segment was simulated as a separate heater. Four of the heaters were controlled, each by a single sensor installed directly above them at the layer's midheight. In the simulation, we used Ra = 4000 ($r = 3.09$) and Pr = 0.7. Figure 6 depicts the temperature on the left-hand side of the bottom plate $(x, z) = (0, -0.5)$ as a function of time. We started the simulation with the controller off. Once steady motion had been established, we engaged the controller at time $t = 4$. The solid and dashed lines depict, respectively, the results of the action of a continuous and a four-heater controller. The four-heater controller, although a bit less effective than the continuous one, was successful in suppressing the motion and maintaining the system in a no-motion state.

## 5 Conclusions

We have demonstrated that feedback control strategies can effectively stabilize the no-motion state of an infinite, horizontal fluid layer heated from below with uniform heat flux. With the aid of the controller, the critical Rayleigh number for the onset of convection can be significantly increased. Successful operation of the controller can be achieved with a finite number of sensors and actuators.

Without affecting the classical no-motion, equilibrium state, the controller modifies the system's dynamics and prolongs its stability by enhancing the disturbance-dissipating mechanisms in the fluid. In a system subject to finite amplitude noise, the controller will maintain the no-motion state through small modulations in the boundary's temperature or velocity.

The work also suggests another potential application of the controller that we have not explored here. The controller conceivably could be used to generate desired flow patterns and to induce complicated, time-dependent, supercritical motions at relatively low values of the Rayleigh number.

## Acknowledgments

This work was supported, in part, by the Department of Energy, Office of Basic Energy Sciences, through Grant No. DE-FG02-92ER14271. The numerical simulations were conducted, in part, using the Cornell National Supercomputer Facility. We are grateful to Prof. Doedel for providing us with the software package, AUTO.

## References

Bau, H. H., 1993, "Controlling Chaotic Convection," *Theoretical and Applied Mechanics 1992*, S. R. Bonder, J. Singer, A. Solan, and Z. Hashin, eds., Elsevier Science Publishers, pp. 187–203.

Chandrasekhar, S., 1969, *Hydrodynamic and Hydromagnetic Stability*, Oxford Press, United Kingdom.

Davis, S. H., 1976, "The Stability of Time Periodic Flows," *Ann. Reviews Fluid Mechanics*, Vol. 8, pp. 57–74.

Doedel, E., 1986, "AUTO: Software for Continuation and Bifurcation Problems in Ordinary Differential Equations," Applied Mathematics Report, California Institute of Technology.

Donnelly, R. J., 1990, "Externally Modulated Hydrodynamic Systems," in: *Nonlinear Evolution of Spatio-Temporal Structures in Dissipative Continuous Systems*, F. H. Busse and L. Kramer, eds., Plenum Press, New York, pp. 31–43.

Drazin, P. G., and Reid, W. H., 1981, *Hydrodynamic Stability*, Cambridge, United Kingdom.

Joseph, D. D., 1976, *Stability of Fluid Motions II*, Springer-Verlag, New York.

Meyer, C. W., Cannel, D. S., and Ahlers, G., 1992, "Hexagonal and Roll Flow Patterns in Temporally Modulated Rayleigh–Bénard Convection," *Physical Review A*, Vol. 45, pp. 8583–8604.

Patankar, S. V., 1980, *Numerical Heat Transfer and Fluid Flow*, McGraw-Hill, New York.

Roppo, M. N., Davis, S. H., and Rosenblat, S., 1984, "Bénard Convection With Time-Periodic Heating," *Physics Fluids*, Vol. 27, pp. 796–803.

Singer, J., Wang, Y.-Z., and Bau, H. H., 1991, "Controlling a Chaotic System," *Physical Review Letters*, Vol. 66, pp. 1123–1125.

Singer, J., and Bau, H. H., 1991, "Active Control of Convection," *Physics of Fluids A*, Vol. 3, pp. 2859–2865.

Sparrow, E. M., Goldstein, R. J., and Josson, V. K., 1964, "Thermal Instability in a Horizontal Fluid Layer: Effect of Boundary Conditions and Non-linear Temperature Profile," *J. Fluid Mechanics*, Vol. 18, pp. 513–528.

Tang, J., and Bau, H. H., 1993a, "Stabilization of the No-Motion State in Rayleigh–Bénard Convection Through the Use of Feedback Control," *Physical Review Letters*, Vol. 70, pp. 1795–1798.

Tang, J., and Bau, H. H., 1993b, "Feedback Control Stabilization of the No-Motion State of a Fluid Confined in a Horizontal, Porous Layer Heated From Below," *J. Fluid Mechanics*, Vol. 257, pp. 485–505.

Tang, J., and Bau, H. H., 1994, "Stabilization of the No-Motion State in the Rayleigh–Bénard Problem," *Proceedings Royal Society A*, Vol. 447, pp. 587–607.

Wang, Y.-Z., Singer, J., and Bau, H. H., 1992, "Controlling Chaos in a Thermal Convection Loop," *J. Fluid Mechanics*, Vol. 237, pp. 479–498.



Downloaded 12 Dec 2010 to 193.140.21.150. Redistribution subject to ASME license or copyright; see http://www.asme.org/terms/Terms_Use.cfm

**M. T. Hyun**
Assistant Professor,
Department of Mechanical Engineering,
Cheju National University,
Cheju-Do, 690-756 Korea

**T. L. Bergman**
Associate Professor,
Department of Mechanical Engineering,
The University of Texas at Austin,
Austin, TX 78712
Mem. ASME

# Direct Simulation of Double-Diffusive Layered Convection

*A two-layer, salt-stratified system destabilized and mixed by lateral heating and cooling is simulated numerically using a spectral methodology. As noted in previous studies, the mixing time is delayed as the stabilizing buoyancy ratio increases, and as the Rayleigh number decreases. Depending on the regime of operation, however, distinct physical mechanisms are responsible for interface erosion and system mixing. At low Ra, erosion is gradual with overlying (underlying) fluid sheared from the interface and mixed into the adjacent thermally convecting layer. At high Ra, an intermittent mechanism is predicted to occur with solutally distinct plumes bombarding the interface and ejecting fluid into the convecting layers. Predictions obtained with the spectral method are in relatively good agreement with experimental data.*

## Introduction

Double-diffusive natural convection occurs when simultaneous heat and species transfer establish temperature and concentration gradients that determine the density distribution within a Le $\neq$ 1 fluid. As pointed out by Ostrach (1980), various convection modes can exist, depending on how the temperature and concentration gradients are oriented relative to one another.

Initial double-diffusion research was performed to explain geophysical phenomena. Later investigations considered initially solute-stratified fluids that are heated (cooled) from vertical enclosure walls (Thorpe et al., 1969; Chen et al., 1971; Wirtz et al., 1972; Wirtz, 1977; Huppert et al., 1984; Bergman and Ungan, 1988; Lee et al., 1990; Kamakura and Ozoe, 1992). The formation, interaction, and merging of convective layers were observed. Recently, double diffusion induced by simultaneously imposed horizontal temperature and concentration differences has been considered (Lee and Hyun, 1988; Jiang et al., 1988; Hyun and Lee, 1990; Han and Kuehn, 1991; Jiang et al., 1991). Most recently, mechanisms responsible for high-frequency oscillatory double-diffusive convection have been discussed (Jiang et al., 1988, 1991; Beckermann et al., 1991; Chang and Lin, 1993; Alavyoon et al., 1994). The role of layered convection on determination of the macrostructure evolution during binary solidification is well known (Incropera and Viskanta, 1990), as is the importance of high-frequency convection on the evolution of microstructure in electronics materials grown from the melt (Ostrach, 1983; Langlois, 1985).

Here, double diffusion within an initially solute-stratified liquid, housed within a rectangular enclosure with heated and cooled vertical walls, is considered. The system's transient (low and high frequency) response is predicted by solving the descriptive equations of stream function, vorticity, energy, and species concentration conservation directly using a spectral methodology. Attention is paid to the predicted system response at large and small time scales. Physical mechanisms responsible for convective layer merging are elucidated, along with the origins of the system's high-frequency behavior.

## Mathematical Model

The two-dimensional computational domain is square with characteristic dimension of $2L$ (which eases use of Chebyshev polynomials). The top and bottom of the enclosure are adiabatic and impermeable, while isothermal (and impermeable) hot and cold walls are considered on the right and left, respectively. Initially, two isothermal salt water layers of equal depth, but different average concentration, are contained within the enclosure. At $t = 0$, side heating and cooling is imposed, with the wall temperatures being raised and lowered an equal amount from the initial uniform liquid temperature. Thermal buoyancy forces induce formation of convecting layers, while the species distribution delays mixing. Because all of the enclosure walls are impermeable, the solution eventually mixes to $C = 0.5$, resulting in pure thermal convection. The simulations mimic qualitatively the experiments reported by Bergman and Ungan (1988), and the simulations reported by Kamakura and Ozoe (1992). Of course, actual phenomena may be three dimensional, but three-dimensional simulation is impractical at this time.

For the Boussinesq fluid, the descriptive equations (with the origin at the cavity center, $x$ positive to the left and $y$ positive in the direction of gravity) are:

$$\partial^2\Psi/\partial x^2 + \partial^2\Psi/\partial y^2 = -\omega \tag{1}$$

$$\mathrm{Pr}\cdot((\partial\omega/\partial t + u\cdot\partial\omega/\partial x + v\cdot\partial\omega/\partial y) - (\partial^2\omega/\partial x^2 + \partial^2\omega/\partial y^2)) = -\mathrm{Ra}\cdot(\partial T/\partial x - N\cdot\partial C/\partial x)/8 \tag{2}$$

$$\mathrm{Pr}\cdot(\partial T/\partial t + u\cdot\partial T/\partial x + v\cdot\partial T/\partial y) = \partial^2 T/\partial x^2 + \partial^2 T/\partial y^2 \tag{3}$$

$$\mathrm{Sc}\cdot(\partial C/\partial t + u\cdot\partial C/\partial x + v\cdot\partial C/\partial y) = \partial^2 C/\partial x^2 + \partial^2 C/\partial y^2 \tag{4}$$

The boundary conditions are:

$$\Psi(t, \pm 1, y) = \Psi(t, x, \pm 1) = 0 \tag{5a}$$

$$\partial\Psi(t, \pm 1, y)/\partial y = \partial\Psi(t, x, \pm 1)/\partial x = 0 \tag{5b}$$

$$T(t, 1, y) = 0, \quad T(t, -1, y) = 1, \quad \partial T(t, x, \pm 1)/\partial y = 0 \tag{5c}$$

$$\partial C(t, \pm 1, y)/\partial x = \partial C(t, x, \pm 1)/\partial y = 0 \tag{5d}$$

Special consideration is given to the initial conditions since (*i*) a smooth variation from high to low concentration must exist experimentally and (*ii*) distinct species layers of uniform concentration cannot be described spectrally without suffering from significant Gibb's phenomena at early time. Here, the initial species distribution was determined by solving the one-dimensional species diffusion equation whose initial condition was a distinct two-layer salt-water system (yielding the semi-infinite solid type solutions). The assumed dimensionless diffusion time prior to application of the thermal boundary conditions is 12. This corresponds to a real time of about 2.5 h for a characteristic dimen-

Contributed by the Heat Transfer Division for publication in the JOURNAL OF HEAT TRANSFER. Manuscript received by the Heat Transfer Division March 1994; revision received June 1994. Keywords: Double-Diffusion Systems, Natural Convection, Stratified Flows. Associate Technical Editor: J. R. Lloyd.



Copyright © 1995 by ASME

Downloaded 12 Dec 2010 to 193.140.21.150. Redistribution subject to ASME license or copyright; see http://www.asme.org/terms/Terms_Use.cfm

sion of 50 mm in salt water, and was selected in order to be consistent with experiments (see the appendix). Predictions are relatively insensitive to the diffusion time.

The initial conditions are:

$$\partial\Psi(0, x, y)/\partial x = \partial\Psi(0, x, y)/\partial y = 0 \quad (6a)$$

$$T(0, x, y) = 0.5 \quad (6b)$$

$$C(0, x, 0 \le y \le 1) = 0.5 + 0.5 \text{ erf } (3.14y) \quad (6c)$$

$$C(0, x, -1 \le y \le 0) = 1 - C(0, x, -y) \quad (6d)$$

## Numerical Procedure

Simulation of double diffusion is difficult because of the high Sc ($\gg$100) associated with all liquids, making resolution of the concentration field difficult. To address this issue, a Chebyshev collocation (spectral) technique has been developed.

Spectral methods have been used to simulate double-diffusion (Ehrenstein and Peyret, 1989). The popularity of these methods is due to the accurate nature of spectral approximation, characterized by the rapid (exponential) decay of approximation errors as the spectral resolution is increased. Compared to the relatively slow (algebraic) convergence typical of finite-difference or finite-element methods, far more efficient numerical simulations can be achieved (Canuto et al., 1988). An additional benefit is the avoidance of issues involving numerical diffusion.

Equations (1)–(4) are solved using a Chebyshev-tau collocation technique. Utilization of Chebyshev polynomials resolves features most accurately near the boundaries of the domain, where, as will be seen, considerable activity takes place. Integration in time is accomplished by a finite-difference technique employing a semi-implicit Adams-Bashforth/second-order backward Euler procedure, which combines an implicit treatment of diffusive terms with explicit treatment of the advection terms. This procedure, when applied to Eqs. (2)–(4), results in two-dimensional Helmholtz equations at each time level. A full matrix diagonalization algorithm is used to solve the Helmholtz and Poisson equations. A key feature of the model is use of an influence matrix technique to enforce the vorticity boundary conditions. The technique allows arbitrary Dirichlet boundary conditions to be imposed at each time step, and provides a correction needed to enforce the actual boundary conditions. Nonlinear terms are evaluated *pseudo-spectrally* to minimize computational expense.

For all results presented here, 64 Chebyshev collocation points (in each direction) were used with time steps on the order of $10^{-4}$ to $10^{-5}$. The Ra = $10^6$, $N$ = 1 case was simulated using 48 and 80 Chebyshev points (in each direction) for $0 \le t \le 2.4$. Over this time period, the average difference between predicted Nu relative to the 80 × 80 simulation is 0.353 and 0.158 for the 48 and 64 point predictions, respectively. Resolution higher than 64 × 64 is needed for higher Ra (specifically $5 \times 10^6$), and these cases were not considered because of computational expense. Code validation is discussed in the appendix.

## Results

Simulations were performed for Pr = 6.5, $A$ = 1, and Le = 85. The Rayleigh numbers are $10^4$, $10^5$, and $10^6$ while $N$ = 0.5, 1.0 and 1.5. Overall (long time scale) results are discussed, heat transfer results are presented, and fluctuation (short time scale) phenomena are illustrated.

**Overall System Behavior.** Figures 1–3 show the stream function, concentration, and temperature contours at various times for different conditions. Here, 11 contours at evenly spaced values of the stream function and temperature are shown (except as noted). Concentration contours are shown at $C$ = 0.1 through 0.9 in increments of 0.1.

For Ra = $10^6$, $N$ = 0.5 (Fig. 1), two thermally driven convective layers form rapidly. The side wall boundary layers penetrate the initially horizontal salinity interface as soon as convective motion is established, and the interface is tilted (Fig. 1*a*). Strands of low (high) salinity fluid are pulled into the top (bottom) convective layer at the extreme top and bottom of the enclosure, as well as at two intermediate elevations. The salinity strands at intermediate heights are fragmented, while the salinity fingers at the extreme elevations are more slowly incorporated into the convective layers. As time proceeds, the interface becomes severely tilted as the stabilizing salinity gradients are reduced by mixing. The interface in the center region of the cell is almost vertical at $t$ = 0.70 (Fig. 1*b*) and, subsequently, a small vortex forms at the center of the enclosure (Fig. 1*c*, $t$ = 0.95). Establishment of the central vortex is a precursor to layer mixing (Bergman and Ungan, 1988), which is characterized by the formation of salt fingers and layer merging (Fig. 1*d*). Since the salt fingers are, in reality, highly three-dimensional structures, two-dimensional simulation of the final mixing process is not realistic. After layer merging, the system reaches steady state (Fig. 2*e*) characterized by pure thermal convection. The concentration (a single isopleth at $C$ = 0.5 is shown) is nearly uniformly distributed within the enclosure.

Phenomena for Ra = $10^6$, $N$ = 1.0 are shown in Fig. 2. Streamlines are shown as before, except at early times when $\Psi$ = −0.007 and −0.0007 are included for Fig. 2(*a*), and $\Psi$ = −0.015 and −0.004 are added in Fig. 2(*b*). Since solutal buoyancy forces are large relative to the $N$ = 0.5 case, thermal buoyancy

## Nomenclature

$A$ = enclosure aspect ratio = $H/L$
$C$ = dimensionless concentration = $(C' - C_l)/(C_h - C_l)$
$C_h$ = initial high concentration
$C_l$ = initial low concentration
$D$ = mass diffusivity
$g$ = gravitational acceleration
$H$ = half height of the enclosure
$L$ = half length of the enclosure
Le = Lewis number = $\alpha/D$
$N$ = buoyancy ratio = $\beta_C \cdot (C_h - C_l)/\beta_T \cdot (T_h - T_c)$
$\overline{\text{Nu}}$ = average Nusselt number = $\int_{-1}^{+1} (\partial T(t, -1, y)/\partial x)dy$
Pr = Prandtl number = $\nu/\alpha$
Ra = Rayleigh number = $g\beta_T(T_h - T_c)(2L)^3/\nu \cdot \alpha$
Sc = Schmidt number = $\nu/D$
$T$ = dimensionless temperature = $(T' - T_c)/(T_h - T_c)$
$T_c$ = temperature of cold wall
$T_h$ = temperature of hot wall
$t$ = dimensionless time = $t'\nu/L^2$
$t_m$ = dimensionless mixing time
$u$ = dimensionless $x$-direction velocity = $u'L/\nu$
$v$ = dimensionless $y$-direction velocity = $v'L/\nu$
$x$ = dimensionless horizontal coordinate = $x'/L$
$y$ = dimensionless vertical coordinate = $y'/L$
$\alpha$ = thermal diffusivity
$\beta_C$ = coefficient of solutal expansion
$\beta_T$ = coefficient of thermal expansion
$\nu$ = kinematic viscosity
$\rho$ = density
$\Psi$ = dimensionless stream function = $\Psi'/\nu$
$\omega$ = dimensionless vorticity = $\omega' L^2/\nu$

**Superscripts**

′ = dimensional value

**Subscripts**

max = maximum value
min = minimum value



Downloaded 12 Dec 2010 to 193.140.21.150. Redistribution subject to ASME license or copyright; see http://www.asme.org/terms/Terms_Use.cfm

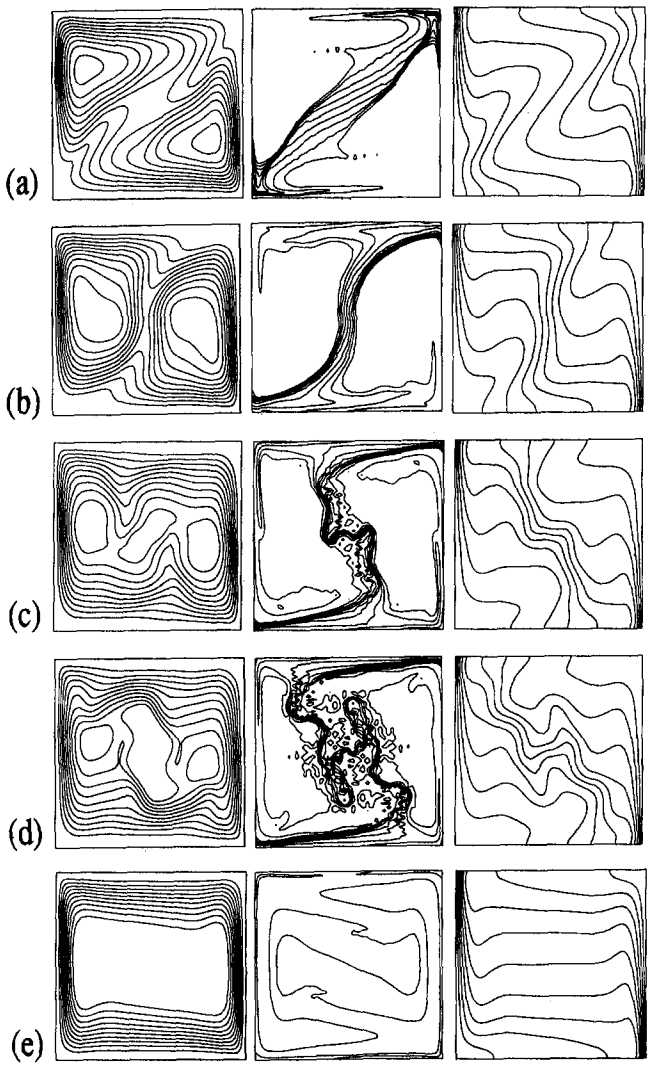



**Fig. 1 Stream function, concentration and temperature distributions for Ra = $10^6$ and $N$ = 0.5: (*a*) $t$ = 0.3 ($\Psi_{max}$ = 2.102, $C_{max}$ = 0.997), (*b*) $t$ = 0.7 ($\Psi_{max}$ = 2.145, $C_{max}$ = 0.983), (*c*) $t$ = 0.95 ($\Psi_{max}$ = 2.637, $C_{max}$ = 0.950), (*d*) $t$ = 1.05 ($\Psi_{max}$ = 2.935, $C_{max}$ = 0.923), (*e*) $t$ = 8.1 ($\Psi_{max}$ = 3.016, $C_{max}$ = 0.501)**

forces are not of sufficient strength to allow the vertical boundary layers able to puncture the salinity interface at early time and, in turn, induce layer mixing. Secondary convection cells appear within the interface (Fig. 2*a*), multiply and become pronounced at $t$ = 1.5 (Fig. 2*b*). The establishment of small recirculations within the interface was noted by Bergman and Ungan (1988), and the predictions of Fig. 2(*b*) bear remarkable resemblance to the experimental results of the reference.

As time proceeds, the overall stabilizing salinity difference decreases, resulting in a more radically tilted interface at $t$ = 3.95 (Fig. 2*c*). Solutal plumes appear along the vertical walls; they are entrained by the thermal main stream and recirculate along the walls of the enclosure. Finally, two-dimensional salt fingers are formed as in Fig. 1(*d*) and mixing proceeds yielding the same steady-state behavior as noted in the $N$ = 0.5 results.

Figure 3 shows results for Ra = $10^5$, $N$ = 1.0. Due to the decreased thermal buoyancy relative to the previous cases, layer motion is relatively slow, and the temperature distribution is weakly stratified. In contrast to the high-Ra case, the concentration distribution is characterized by relatively weak spatial gradients, and by a thick solutal interface (Figs. 3*a*, *b*). Weak salt fingers appear as shown in Fig. 3(*c*), and mix into the adjacent thermally driven layer. Similar behavior is observed for Ra = $10^4$.

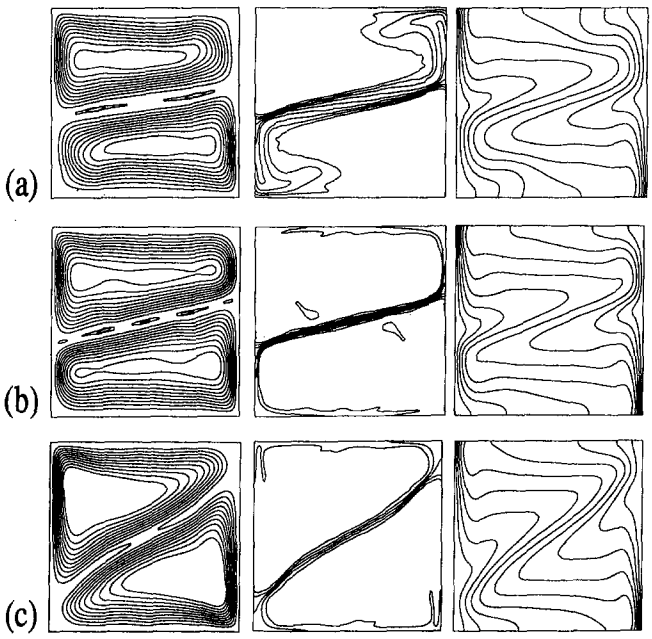



**Fig. 2 Stream function, concentration, and temperature distributions for Ra = $10^6$ and $N$ = 1.0: (*a*) $t$ = 0.4 ($\Psi_{max}$ = 1.985, $C_{max}$ = 0.997), (*b*) $t$ = 1.5 ($\Psi_{max}$ = 1.973, $C_{max}$ = 0.900), (*c*) $t$ = 3.95 ($\Psi_{max}$ = 1.965, $C_{max}$ = 0.794).**

**Heat Transfer Results.** Figures 4 and 5 show the spatially averaged Nusselt number variation with $N$ (for Ra = $10^6$) and with Ra (for $N$ = 1.0), respectively. As shown in Fig. 4, wall heat transfer rates are initially large but decrease with time as temperature gradients diffuse toward the core of the enclosure (the detailed heat transfer histories marked (*a*) through (*c*) will be discussed later). As time proceeds, thermal convection becomes established, increasing heat transfer rates. For $N$ = 1.0 and 1.5, heat transfer rates subsequently decrease, as the interface tilts toward the vertical position, and in turn poses an increasing thermal resistance to lateral heat transfer. Heat transfer rates increase suddenly as the salinity interface is destroyed (e.g., at $t$ = 4.9 for

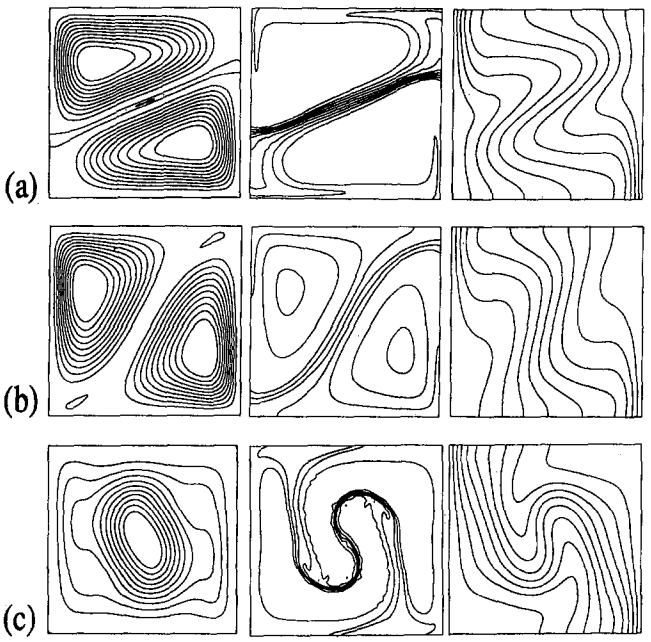



**Fig. 3 Stream function, concentration, and temperature distributions for Ra = $10^5$ and $N$ = 1.0: (*a*) $t$ = 3.15 ($\Psi_{max}$ = 0.942, $C_{max}$ = 0.982), (*b*) $t$ = 26.7 ($\Psi_{max}$ = 0.850, $C_{max}$ = 0.920), (*c*) $t$ = 32.7 ($\Psi_{max}$ = 2.373, $C_{max}$ = 0.780)**



Downloaded 12 Dec 2010 to 193.140.21.150. Redistribution subject to ASME license or copyright; see http://www.asme.org/terms/Terms_Use.cfm

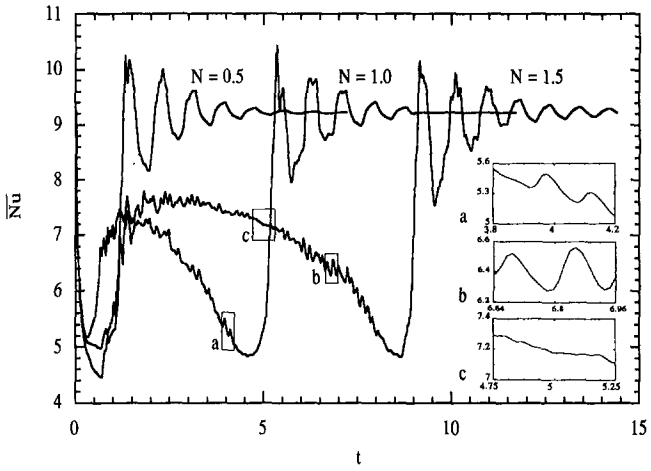



**Fig. 4 Transient averaged Nusselt number dependence upon $N$ for Ra = $10^6$**

$N = 1.0$). Heat transfer rates are maximized during mixing, and eventually become asymptotic to the pure thermal convection limit. For $N = 0.5$, similar trends are evident, but are truncated somewhat due to the early mixing illustrated in Fig. 1.

At Ra = $10^4$ (Fig. 5), the mixing time is delayed relative to those associated with Ra = $10^5$ and $10^6$. In addition, heat transfer oscillation does not occur prior to mixing for Ra = $10^5$ or $10^4$, except at early times for the Ra = $10^5$ case. For Ra = $10^4$, heat transfer rates are nearly equal to those of pure conduction prior to layer merging. Again, the peak-to-peak amplitudes of the heat transfer oscillations associated with mixing slowly decrease with time, until steady state is reached.

**Fluctuating Convection.** The preceding results show that temporal variations occur in the system hydrodynamics at both large and small time scale. Large time scale response depends upon Ra and $N$, but fluctuating behavior occurs in a more complicated fashion. Indeed, inspection of the details of Fig. 4 shows that, even in a particular simulation (e.g., $N = 1.5$), heat transfer rates can be characterized by times of vigorous fluctuation (Fig. 4*b* and early times) bracketing periods of intermediate, modest fluctuation (Fig. 4*c*).

Inspection of the concentration distributions associated with $N = 1$, Ra = $10^4$ and $10^5$ revealed uninteresting behavior. During most of the simulation, convection was quasi-steady, as implied by the heat transfer results of Fig. 5. In contrast, behavior at Ra = $10^6$ was highly transient, and Figs. 6 and 7 show the concentration isocontours for parts (*a*) and (*b*) of Fig. 4. Contour values are shown at $C = K(C_{max} - C_{min}) + C_{min}$, where $K$ is in increments of 0.2 from 0.1 through 0.9.

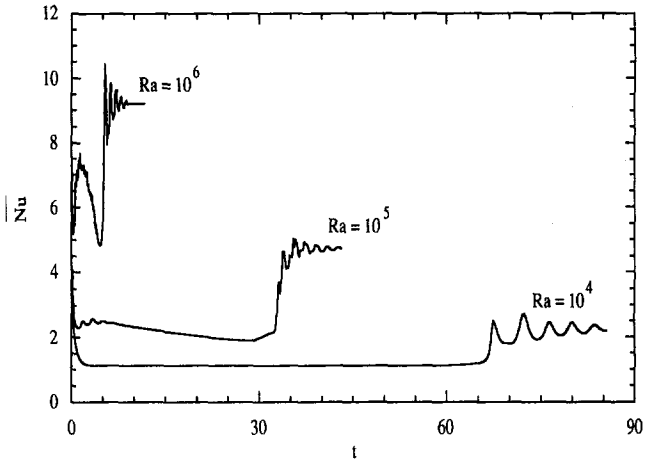



**Fig. 5 Transient averaged Nusselt number dependence upon Ra for $N$ = 1.0**

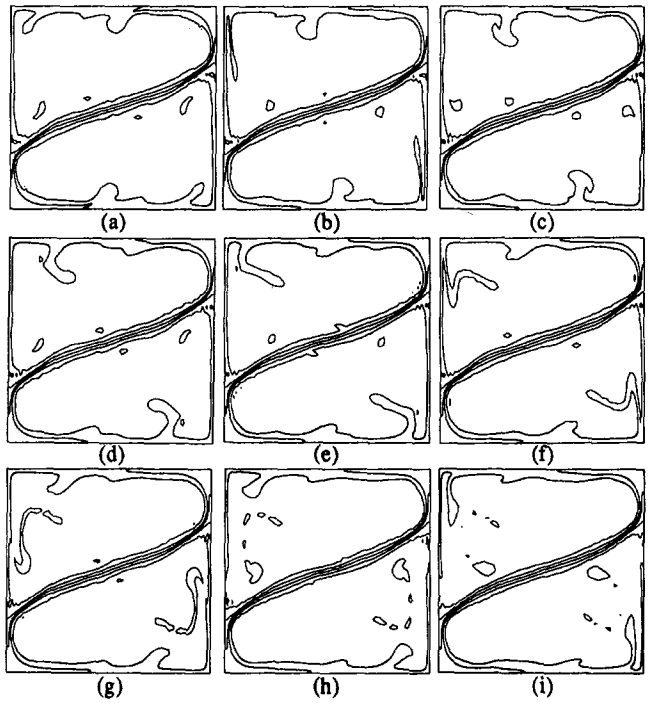



**Fig. 6 Concentration distributions for Ra = $10^6$, $N = 1.0$, and $3.8 \le t \le 4.2$: (*a*) $t = 3.8$ ($C_{max} = 0.8$), (*b*) $t = 3.85$ ($C_{max} = 0.798$), (*c*) $t = 3.9$ ($C_{max} = 0.796$), (*d*) $t = 3.95$ ($C_{max} = 0.794$), (*e*) $t = 4.0$ ($C_{max} = 0.791$), (*f*) $t = 4.05$ ($C_{max} = 0.789$), (*g*) $t = 4.1$ ($C_{max} = 0.787$), (*h*) $t = 4.15$ ($C_{max} = 0.785$), (*i*) $t = 4.2$ ($C_{max} = 0.783$)**

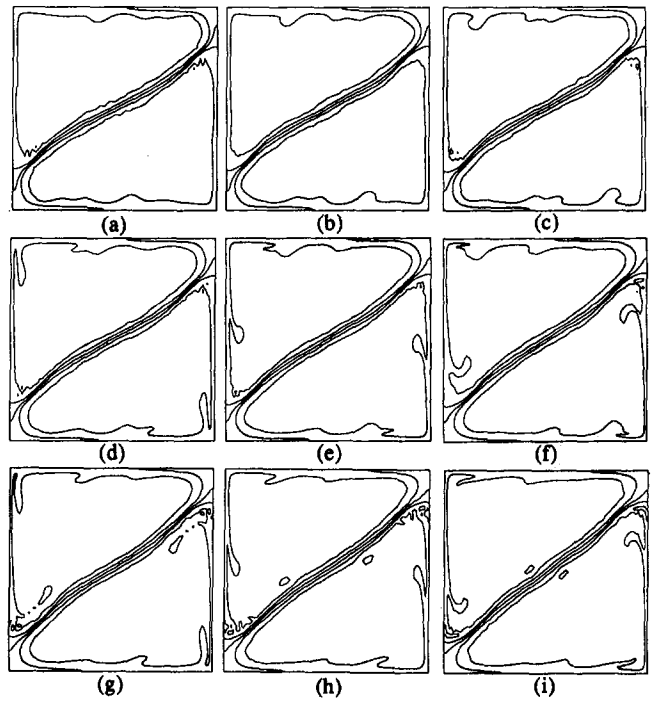



**Fig. 7 Concentration distributions for Ra = $10^6$, $N = 1.5$, and $6.64 \le t \le 6.96$: (*a*) $t = 6.64$ ($C_{max} = 0.732$), (*b*) $t = 6.68$ ($C_{max} = 0.731$), (*c*) $t = 6.72$ ($C_{max} = 0.730$), (*d*) $t = 6.76$ ($C_{max} = 0.728$), (*e*) $t = 6.8$ ($C_{max} = 0.727$), (*f*) $t = 6.84$ ($C_{max} = 0.727$), (*g*) $t = 6.88$ ($C_{max} = 0.725$), (*h*) $t = 6.92$ ($C_{max} = 0.723$), (*i*) $t = 6.96$ ($C_{max} = 0.722$)**



Downloaded 12 Dec 2010 to 193.140.21.150. Redistribution subject to ASME license or copyright; see http://www.asme.org/terms/Terms_Use.cfm

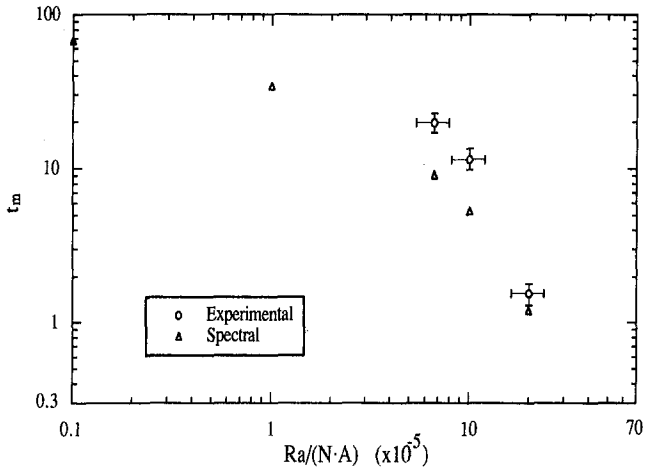



**Fig. 8 Comparison of the predicted and measured mixing times**

As shown in Fig. 6 (Ra = $10^6$, $N$ = 1.0, 3.8 $\leq t \leq$ 4.2), thermal buoyancy forces induce layer convection, which, in turn, drags relatively fresh (salty) fluid into the bottom (top) convecting layer (Fig. 6*c*). Subsequently, salt plumes are formed along the enclosure top and bottom, and are dragged by thermal convection to the opposite wall (Figs. 6*d*, *e*). As they propagate in wavelike fashion toward the opposing wall, they grow and are eventually shot toward the interface due to their (*i*) contact with the vertical enclosure surfaces and (*ii*) reinforcement by thermal buoyancy forces (Fig. 6*f*). As the fresh (salty) plume ascends (descends) back toward the interface, it breaks up and is partially mixed into the salty (fresh) layer (Fig. 6*g*, *h*). Upon close inspection of Figs. 4(*a*) and 6, it is evident that wall heat transfer rates reach local maxima when the salinity plumes scour the vertical isothermal walls.

Similar trends are observed in Fig. 7 (Fig. 4*b*, 6.64 $\leq t \leq$ 6.96). Instead of breaking up during propagation toward the interface, however, the plumes appear to retain their identity until they impinge upon the interface, resulting in a rather explosive fragmentation and, presumably, an efficient mixing process. Again, local maximum heat transfer rates (Fig. 4*b*) are associated with salt plumes wiping the vertical walls of the enclosure.

For Ra = $10^6$, $N$ = 1.5, 4.75 $\leq t \leq$ 5.25 (Fig. 4*c*), heat transfer rates are nearly steady and the concentration distribution changes only slightly with time. Weak salinity waves were observed on the bottom and top of the enclosure and after a short period of time, become of sufficient strength to again promote high-frequency system fluctuation.

Note that the type of fluctuating behavior of Figs. 6 and 7 is different from that described for systems with vertical boundaries held at unique temperatures and concentrations (Jiang et al., 1988).

## Conclusions

A two-layer, salt-stratified system destabilized by lateral heating and cooling has been investigated numerically. Simulations reveal long time scale system behavior such as (*i*) small geometric scale interfacial circulation, (*ii*) increased interface tilt with time, and (*iii*) eventual system mixing.

The mechanisms that lead to destruction of the salinity interface are also illustrated. At low Ra ($10^4$ and $10^5$), thermal convection gradually and smoothly peels the high (or low) saline water from the interface and folds it into the adjacent thermally driven layer. At high Ra ($10^6$), the simulations reveal the development of oscillatory convection, with salt plumes intermittently torn from the interface, carried in full circle by thermal convection, where they are reinforced by thermal buoyancy forces to subsequently bombard the interface.

For a particular Ra, mixing times increase as $N$ increases, as expected. For a particular $N$, mixing times are decreased as Ra is increased, due to (*i*) concentrated impingement of the vertical wall boundary layer upon the interface and (*ii*) the mechanical-like mixing effected by (*a*) the intermittent explosive impingement upon the interface or (*b*) salt plume breakup upon propagation up (down) the vertical heated (cooled) side wall.

## Acknowledgments

The first author would like to thank the Korea Science and Engineering Foundation for financial assistance. The authors are indebted to Mr. Dai-Chyi Kuo for help with the solution algorithms. The computations would not have been possible without the generosity of Prof. O. A. Ezekoye.

## References

Alavyoon, F., Masuda, Y., and Kimura, S., 1994, "On Natural Convection in Vertical Porous Enclosures Due to Opposing Fluxes of Heat and Mass Prescribed at the Vertical Walls," *International Journal of Heat and Mass Transfer*, Vol. 37, pp. 195–206.

Beckermann, C., Fan, C., and Mihailovic, J., 1991, "Numerical Simulations of Double-Diffusive Convection in a Hele-Shaw Cell," *International Video Journal of Engineering Research*, Vol. 1, pp. 71–82.

Bergman, T. L., and Ungan, A., 1988, "A Note on Lateral Heating in a Double-Diffusive System," *Journal of Fluid Mechanics*, Vol. 194, pp. 175–186.

Canuto, C., Hussaini, M. Y., Quarteroni, A., and Zang, T. A., 1988, *Spectral Methods in Fluid Dynamics*, Springer, New York.

Chang, J., and Lin, T. F., 1993, "Unsteady Thermosolutal Opposing Convection of Liquid–Water Mixture in a Square Cavity—II. Flow Structure and Fluctuation Analysis," *International Journal of Heat and Mass Transfer*, Vol. 36, pp. 1333–1345.

Chen, C. F., Briggs, D. G., and Wirtz, R. A., 1971, "Stability of Thermal Convection in a Salinity Gradient Due to Lateral Heating," *International Journal of Heat and Mass Transfer*, Vol. 14, pp. 57–65.

Ehrenstein, U., and Peyret, R., 1989, "A Chebyshev Collocation Method for the Navier–Stokes Equations With Application to Double-Diffusive Convection," *International Journal for Numerical Methods in Fluids*, Vol. 9, pp. 427–452.

Han, H., and Kuehn, T. H., 1991, "Double-Diffusive Natural Convection in a Vertical Rectangular Enclosure—I. Experimental Study," *International Journal of Heat and Mass Transfer*, Vol. 34, pp. 449–459.

Huppert, H. E., Kerr, R. C., and Hallworth, M. A., 1984, "Heating or Cooling a Stable Compositional Gradient From the Side," *International Journal of Heat and Mass Transfer*, Vol. 27, pp. 1395–1401.

Hyun, J. M., and Lee, J. W., 1990, "Double-Diffusive Convection in a Rectangle With Cooperating Gradients of Temperature and Concentration," *International Journal of Heat and Mass Transfer*, Vol. 33, pp. 1605–1617.

Incropera, F. P., and Viskanta, R., 1990, "Effects of Convection on the Solidification of Binary Mixtures," presented at the Oji International Seminar on Advanced Heat Transfer in Manufacturing and Processing of New Materials, Tomakomai, Hokkaido, Japan, Oct. 28–31.

Jiang, H. D., Ostrach, S., and Kamotani, Y., 1988, "Thermosolutal Convection Flow Regimes With Opposed Buoyancy Forces in Shallow Enclosures," *PhysicoChemical Hydrodynamics*, Vol. 10, pp. 599–613.

Jiang, H. D., Ostrach, S., and Kamotani, Y., 1991, "Unsteady Thermosolutal Transport Phenomena Due to Opposed Buoyancy Forces in Shallow Enclosures," ASME JOURNAL OF HEAT TRANSFER, Vol. 113, pp. 135–140.

Kamakura, K., and Ozoe, H., 1992, "Double-Diffusive Natural Convection in a Two-Layer System of Large Concentration Difference," in: *Proceedings of the First International Conference on Transport Phenomena in Processing*, S. I. Guceri, ed., Technomic, Lancaster, pp. 720–730.

Langlois, W. E., 1985, "Buoyancy-Driven Flow in Crystal-Growth From Melts," *Annual Reviews of Fluid Mechanics*, Vol. 55, pp. 614–646.

Lee, J., and Hyun, M. T., 1988, "Experiments on Thermosolutal Convection in a Shallow Rectangular Enclosure," *Experimental Thermal and Fluid Science*, Vol. 1, pp. 259–265.

Lee, J., Hyun, M. T., and Moh, J. H., 1990, "Numerical Experiments on Natural Convection in a Stably Stratified Fluid Due to Side-Wall Heating," *Numerical Heat Transfer*, Vol. 18, pp. 343–355.

Ostrach, S., 1980, "Natural Convection With Combined Driving Forces," *PhysicoChemical Hydrodynamics*, Vol. 1, pp. 233–247.

Ostrach, S., 1983, "Fluid Mechanics of Crystal Growth—The 1982 Freeman Scholar Lecture," *ASME Journal of Fluids Engineering*, Vol. 105, pp. 5–20.

Thorpe, S. A., Hutt, P. K., and Soulsby, R., 1969, "The Effect of Horizontal Gradients on Thermohaline Convection," *Journal of Fluid Mechanics*, Vol. 38, pp. 375–400.

Wirtz, R. A., Briggs, D. G., and Chen, C. F., 1972, "Physical and Numerical Experiments on Layered Convection in a Density Stratified Fluid," *Geophysical Fluid Dynamics*, Vol. 3, pp. 265–288.

Wirtz, R. A., 1977, "The Effect of Solute Layering on Lateral Heat Transfer in an Enclosure," *International Journal of Heat and Mass Transfer*, Vol. 20, pp. 841–846.



Downloaded 12 Dec 2010 to 193.140.21.150. Redistribution subject to ASME license or copyright; see http://www.asme.org/terms/Terms_Use.cfm

## APPENDIX

Experiments were performed using a nominally square (20 mm × 20 mm) test cell that was 62 mm deep. Ra values of $10^6$ were applied to the salt water solution, along with $N = 0.5$, 1.0, and 1.5. Experimental mixing times are defined as the moment when the interface was no longer visible with use of a shadowgraph. The predicted mixing time is defined as the time corresponding to the average of the maximum and minimum Nusselt numbers in the vicinity of mixing. Since only the integral mixing times are compared, the experiments cannot validate predicted details of the flow patterns.

Figure 8 shows predicted and measured mixing times. Each experiment was repeated seven times, and the uncertainty in the ordinate value is the range of mixing times for each experimental condition. The parameter listed in the abscissa collapses the data of Bergman and Ungan (1988), and so is used here (the referenced data are at much higher $\mathrm{Ra}/N \cdot A$, and so are not shown). The uncertainty in the abscissa value is based upon estimated uncertainties of (*i*) liquid layer dimensions of ±1 mm, (*ii*) the applied temperature difference of ±2 percent, (*iii*) property uncertainties of ±5 percent, and (*iv*) ±4 percent in the initial concentration difference. Discrepancies between the measured and predicted mixing times are attributed to three-dimensional effects, such as viscous damping by the front and back walls of the test cell.



Downloaded 12 Dec 2010 to 193.140.21.150. Redistribution subject to ASME license or copyright; see http://www.asme.org/terms/Terms_Use.cfm

# Characteristics of Radiation Absorption in Metallic Particles

T. Q. Qiu

J. P. Longtin

C. L. Tien

Department of Mechanical Engineering,
University of California,
Berkeley, CA 94720

*Thermal radiation absorption in metallic particles is an important phenomenon in many contemporary laser-processing techniques, including laser cladding of coating materials and laser cleaning of particulate contaminations. In this work, the Drude free-electron theory and electromagnetic wave theory are utilized to characterize the internal absorption of $CO_2$ laser radiation in aluminum, chromium, and nickel particles. The results show that metallic particles have unique radiation properties. Radiation absorption in large particles occurs only in a very narrow region of the front particle surface, which results in inefficient radiation absorption. On the other hand, micron and submicron particles can absorb radiation very efficiently, due to the strong diffraction effect at the particle surface. For extremely small particles (e.g., nanometer particles), radiation absorption becomes less efficient. The particle absorption efficiency is found to increase with temperature, and this temperature dependence can be determined from those of flat metal surfaces at the normal incidence.*

## Introduction

Laser cladding is a very promising surface modification technique that can dramatically increase surface hardness and surface resistance to wear and corrosion (Komvopoulos and Nagarathnam, 1990; Mazumder et al., 1992). It employs a high-power laser beam to fuse metallic cladding powders to a substrate surface forming a thin layer of novel material. If the cladding powder is well heated before it reaches the cladding surface, less laser energy is required to melt the cladding surface, which in turn improves the cladding quality (Atamert and Bhadeshia, 1989; Oberlander and Lugscheider, 1992) as well as the cladding speed. However, due to the lack of engineering information regarding radiation absorption in the cladding particles, accurate prediction and control of the particle temperature have been difficult (Hoadley and Rappaz, 1992; Pustovalov and Bobuchenko, 1993). The purpose of the present work is to characterize absorption of $CO_2$ laser radiation at the wavelength of 10.6 $\mu$m in aluminum, chromium, and nickel powders.

Radiation-particle interactions often involve strong refraction and diffraction phenomena at the particle surface, which can enhance radiation absorption. Tuntomo et al. (1991) showed that weakly reflecting and absorbing particles absorb radiation most efficiently in certain size regions. For metallic powders, due to their highly conducting nature, a very different size region for efficient radiation absorption is expected. Absorptivity of flat metal surfaces generally increases with temperature for infrared radiation (Prokhorov and Konov, 1990). The temperature dependence of radiation absorption in metallic particles, however, has not been studied. This work utilizes Drude's free-electron theory and classical electromagnetic wave theory to characterize radiation absorption in metallic cladding particles and its temperature dependence.

## Analysis

Aluminum, chromium, and nickel powders are commonly used as cladding materials, with the particle diameter ranging from 1 $\mu$m to about 100 $\mu$m. The powders are delivered into the cladding zone with the assistance of an argon gas flow at a typical particle density around $10^4$ cm$^{-3}$ (Komvopoulos and Nagarathnam, 1990; Pustovalov and Bobuchenko, 1993). The distance between individual particles is much larger than the $CO_2$ laser wavelength (10.6 $\mu$m); thus each particle interacts with the laser beam independently (Brewster and Tien, 1982). Multiple radiation scattering by the particles can be well accounted for by the radiation transfer equation once the radiation properties of individual particles are known (Brewster, 1992). Therefore, this study focuses on radiation properties of single particles.

The shape of cladding particles depends strongly on the powder production method and the powder material (Avner, 1964; Hausner and Mal, 1982). For example, powder particles prepared from atomization of liquid metals are typically spherical, while those particles produced from reduction of metal oxides often have irregular shapes, and are porous. Micron and submicron powders—which are commonly prepared from condensation of metal vapors in inert gases, precipitation from metal salt solutions, or decomposition of metal hydrides/carbonyls—are generally spherical (Hausner and Mal, 1982; Figlarz et al., 1992). The current work only considers spherical cladding particles.

All metals except gold tend to form oxides when exposed to oxygen. For many metals, such as aluminum, copper, chromium, and nickel, the oxide layer formed at relatively low temperatures, e.g., 200°C, is compact and pore-free, which effectively prevents further oxidation (Hauffe, 1965). As a result, the oxide layer is very thin. For example, at room temperature the oxide layer on aluminum grows very fast in the first few minutes, and then stops growing after one month, attaining a thickness of 45 Å (Kubaschewski and Hopkins, 1953). Furthermore, during laser cladding, argon gas is often used to prevent the cladding powder and cladding surface from oxidation. Therefore, this study neglects the effects of the thin metal oxide layer on radiation absorption.

**Drude's Free-Electron Theory.** For infrared radiation, optical properties of metals and their temperature dependence can be modeled by Drude's free-electron theory (Ujihara, 1972; Arnold, 1984; Bruckner et al., 1991). In Drude's theory, free electrons in metals behave like a gas, which has remarkable mobility within the closely packed atoms, that determines fundamental optical and transport properties of metals. The complex refractive index of metals, $m = n + ik$, is characterized by the plasma frequency of electrons, $\omega_p$, and the electron-lattice collision frequency, $\gamma$, as (Bohren and Huffman, 1983)

$$m = n + ik = \left[1 - \frac{\omega_p^2}{\omega(\omega + i\gamma)}\right]^{1/2} \quad (1)$$

where $\omega$ is the angular frequency of the incident radiation. The plasma frequency depends on temperature very weakly below the melting point, while the electron-lattice collision frequency is

Contributed by the Heat Transfer Division and presented at the AIAA/ASME Thermophysics and Heat Transfer Conference, Colorado Springs, Colorado, June 19–23, 1994. Manuscript received by the Heat Transfer Division September 1993; revision received May 1994. Keywords: Radiation, Radiation Interactions. Associate Technical Editor: M. F. Modest.



Copyright © 1995 by ASME

Downloaded 12 Dec 2010 to 193.140.21.150. Redistribution subject to ASME license or copyright; see http://www.asme.org/terms/Terms_Use.cfm

strongly temperature dependent, as indicated by its relationship with the direct-current resistivity, $R$, as (Kittel, 1986)

$$\gamma(T) = \frac{n_e e^2}{m_e} R(T) \tag{2}$$

where $n_e$ is the free-electron number density, $e$ the electron charge, and $m_e$ the effective mass of electrons. In the temperature range from 300 K to 900 K, the electrical resistivity of aluminum, chromium, and nickel increases linearly with temperature (Lide, 1992). Therefore the collision frequency is also linearly dependent on temperature. The evaluated temperature coefficients for aluminum, chromium, and nickel, $\alpha = d\gamma/\gamma_0 dT$, along with $\gamma_0$ and $\omega_p$ are listed in Table 1, where $\gamma_0$ is the collision frequency at 300 K. The temperature dependence of the collision frequency gives rise to the temperature dependence of infrared optical properties of metals.

**Electromagnetic Wave Theory.** Laser interactions with particles can be described by classical electromagnetic wave theory. When the beam diameter is large compared to the particle diameter, the laser beam can be treated as a monochromatic plane wave. Figure 1 shows a spherical polar coordinate system for a particle irradiated by a laser beam traveling along the $Z$ axis. The particle absorbs the incident radiation energy by Joule heating (Born and Wolf, 1989),

$$Q(r, \theta, \phi) = \tfrac{1}{2}\sigma |\mathbf{E}(r, \theta, \phi)|^2 \tag{3}$$

where $Q$ is the local radiation absorption, $\sigma$ the electrical conductivity of the particle at the incident radiation frequency, and $\mathbf{E}$ the local electric field strength. Equation (3) can be further expressed in terms of the incident radiation intensity, $I_0$, wavelength, $\lambda$, and refractive index, $n$ and $k$, as (Tuntomo et al., 1991)

$$Q(r, \theta, \phi) = \frac{4\pi n k I_0}{\lambda} S(r, \theta, \phi) \tag{4}$$

$$S(r, \theta, \phi) = |\mathbf{E}(r, \theta, \phi)/E_0|^2 \tag{5}$$

where $E_0$ is the incident electric field strength, and $S$ is the dimensionless distribution of radiation absorption. The electric field vector inside the particle can be obtained by solving the Maxwell equations. Its three components are (Bohren and Huffman, 1983)

$$E_r = \frac{E_0 \cos\phi}{m^2\rho^2} \sum_{n=1}^{\infty} i^{n-1}(2n+1) d_n \psi_n(m\rho) P_n^1(\cos\theta) \tag{6}$$

$$E_\theta = \frac{E_0 \cos\phi}{m\rho} \sum_{n=1}^{\infty} \frac{i^n(2n+1)}{n(n+1)} \times \left[ c_n \psi_n(m\rho) \frac{P_n^1(\cos\theta)}{\sin\theta} - i d_n \psi_n'(m\rho) \frac{dP_n^1(\cos\theta)}{d\theta} \right] \tag{7}$$

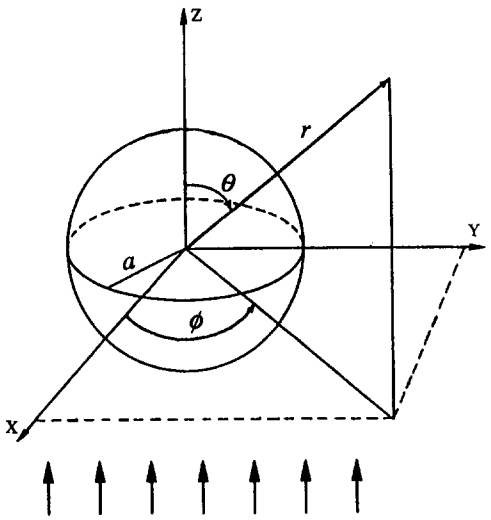



**Fig. 1 Spherical polar coordinate system for an irradiated particle**

$$E_\phi = \frac{E_0 \sin\phi}{m\rho} \sum_{n=1}^{\infty} \frac{i^{n+1}(2n+1)}{n(n+1)} \times \left[ i c_n \psi_n(m\rho) \frac{dP_n^1(\cos\theta)}{d\theta} + d_n \psi_n'(m\rho) \frac{P_n^1(\cos\theta)}{\sin\theta} \right] \tag{8}$$

where $\rho$ is the dimensionless radial coordinate given by

$$\rho = \frac{2\pi r}{\lambda} \tag{9}$$

The function $\psi_n$ is the Riccati–Bessel function of order $n$, the prime denotes differentiation with respect to the argument, $P_n^1(\cos\theta)$ is the associated Legendre polynomial, and $c_n$ and $d_n$ are the expansion coefficients,

$$c_n = \frac{m\psi_n(x)\xi_n'(x) - m\psi_n'(x)\xi_n(x)}{\psi_n(mx)\xi_n'(x) - m\psi_n'(mx)\xi_n(x)} \tag{10}$$

$$d_n = \frac{m\psi_n(x)\xi_n'(x) - m\psi_n'(x)\xi_n(x)}{m\psi_n(mx)\xi_n'(x) - \psi_n'(mx)\xi_n(x)} \tag{11}$$

where $x = \pi d/\lambda$ is the size parameter and $\xi_n$ is the Riccati–Bessel function of the third kind (Abramowitz and Stegun, 1970). For linearly polarized radiation, $\phi$ represents the angle between the polarization plane and the $X$–$Z$ plane. For unpolarized or circularly polarized radiation, the internal field can be obtained by setting $\phi = \pi/4$ (Macowski, 1989).

The radiation absorptivity of the particle can be represented by the absorption cross section, $C_a$, which is the ratio of the total

## Nomenclature

$A$ = absorptivity of a flat surface
$C_a$ = absorption cross section
$d$ = particle diameter
$\mathbf{E}$ = electric field vector
$i$ = $\sqrt{-1}$
$I_0$ = intensity of incidence radiation
$k$ = imaginary part of refractive index
$m$ = complex refractive index = $n + ik$
$n$ = real part of refractive index
$P$ = skin-depth parameter = $d/2\delta$
$P_n^1$ = associated Legendre polynomial
$Q$ = distribution of radiation absorption
$Q_a$ = absorption efficiency
$Q_{av}$ = volumetric absorption efficiency
$r$ = radial coordinate
$R$ = electrical resistivity
$S$ = normalized source function
$T$ = temperature
$x$ = size parameter = $\pi d/\lambda$
$\alpha$ = temperature coefficient of $\gamma$; $\alpha = d\gamma/\gamma dT$
$\gamma$ = electron-lattice collision frequency
$\delta$ = skin depth = $\lambda/4\pi k$
$\theta$ = polar coordinate
$\lambda$ = wavelength
$\xi_n$ = Riccati–Bessel function of the third kind
$\rho$ = dimensionless radial coordinate = $2\pi r/\lambda$
$\sigma$ = electrical conductivity
$\phi$ = azimuthal coordinate
$\psi_n$ = Riccati–Bessel function of the first kind
$\omega$ = angular frequency
$\omega_p$ = plasma frequency of free electrons



Downloaded 12 Dec 2010 to 193.140.21.150. Redistribution subject to ASME license or copyright; see http://www.asme.org/terms/Terms_Use.cfm

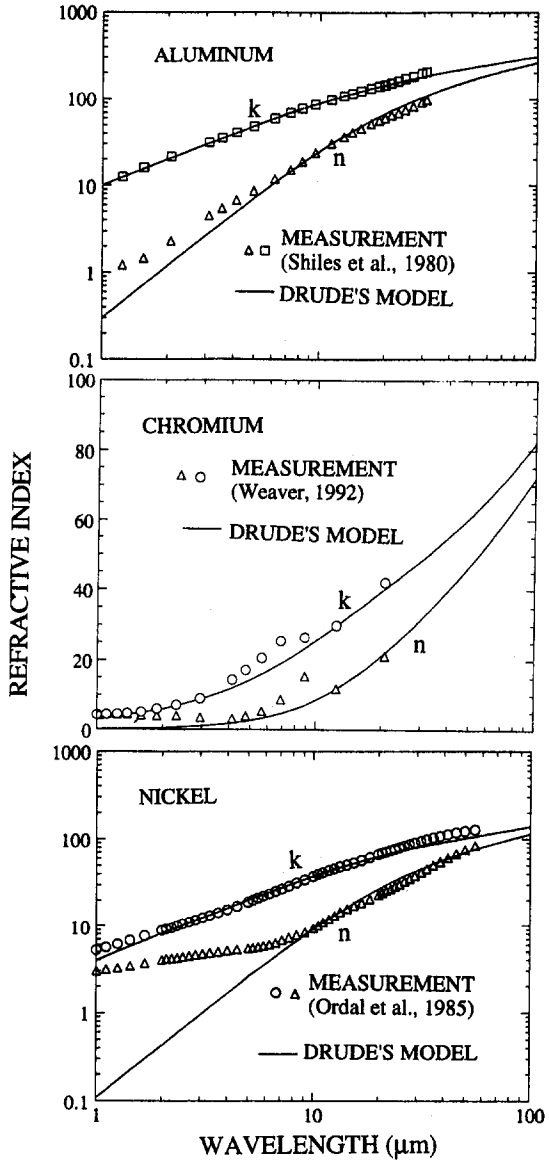



**Fig. 2 Comparison between prediction and measurements**

amount of absorbed energy to the incident radiation intensity. It can be evaluated either by integrating the absorbed radiation energy inside the particle or by subtracting the energy scattered by the particle from the total radiation extinction (Bohren and Huffman, 1983),

$$C_a = \frac{\lambda^2}{2\pi} \sum_{n=1}^{\infty} (2n+1)[\mathrm{Re}(a_n + b_n) - (|a_n|^2 + |b_n|^2)] \quad (12)$$

$$a_n = \frac{m\psi_n(mx)\psi_n'(x) - \psi_n(x)\psi_n'(mx)}{m\psi_n(mx)\xi_n'(x) - \psi_n'(mx)\xi_n(x)} \quad (13)$$

$$b_n = \frac{\psi_n(mx)\psi_n'(x) - m\psi_n(x)\psi_n'(mx)}{\psi_n(mx)\xi_n'(x) - m\psi_n'(mx)\xi_n(x)} \quad (14)$$

The efficiency for a particle to absorb radiation can be characterized by the *absorption efficiency* based on its cross-sectional area, $Q_a = C_a/(\pi d^2/4)$, and the *volumetric absorption efficiency* based on its volume, $Q_{av} = 6C_a/\pi d^3$.

**Numerical Scheme.** The optical properties were calculated from Eq. (1). The local radiation absorption and the total absorption in particles were obtained by solving Eqs. (4)–(8) and (12) numerically. The Riccati–Bessel function and its derivative in the expansion coefficients, $a_n$, $b_n$, $c_n$, and $d_n$, were computed from the Miev0 code (Wiscombe, 1979). The grid points in the $r$ and $\theta$ direction are 50 and 180, respectively. Results calculated with doubled grid points were virtually identical. The numerical accuracy was further checked by comparing the total absorbed energy by a particle evaluated from the *external-field* Mie calculation (Bohren and Huffman, 1983), Eq. (12), with that from the *internal-field* integration (Tuntomo et al., 1991). In all cases the difference was less than 2 percent.

## Results and Discussion

Figure 2 shows the comparison between predictions of Drude's free-electron theory and published measurement data for aluminum, chromium, and nickel in the wavelength range from 1 $\mu$m to 100 $\mu$m at 300 K. The parameters used in Drude's theory, $\omega_p$ and $\gamma_0$, are deduced by best fitting the experimental results in the wavelength region between 10 $\mu$m to 20 $\mu$m, and are listed in Table 1. For incident radiation with a relatively short wavelength, e.g., shorter than 5 $\mu$m, electrons experience relatively strong photon excitation and strong interactions with atoms. The electrons are not perfectly free, and thus predictions based on the free-electron assumption deviate from measured data. But for radiation with longer wavelengths, electrons behave like a free electron gas, and thus model predictions agree well with experimental data. The refractive index evaluated at 10.6 $\mu$m and 300 K for aluminum, chromium, and nickel is $27.3 + i93.8$, $9.4 + i26.7$, and $10.2 + i39.6$, respectively.

Figure 3 shows the local radiation absorption in nickel particles irradiated by an unpolarized $CO_2$ laser beam. The cross section of the particles lies in the $Y-Z$ plane, and the laser beam propagates along the $Z$ axis. The local absorption pattern has distinctive features that depend on the dimensionless *particle size parameter* and the *skin-depth parameter*. The size parameter, $x = \pi d/\lambda$, characterizes the importance of the diffraction effect. The skin-depth parameter, which is defined as the ratio of the particle radius to the radiation skin depth of the particle ($\delta = \lambda/4\pi k$), $p = d/2\delta$, characterizes the radiation absorption inside the particle.

For large particles ($x \gg 1$), the effect of diffraction is small, and the incident radiation is absorbed mostly at the front particle surface. When $x$ is of order one, diffraction becomes significant. The incident plane wave is bent around the particle surface, which in turn results in both front surface absorption and back surface absorption. In addition, the diffraction effect causes an oscillating pattern of radiation absorption around the particle surface. In the very small particle regime ($x \ll 1$), radiation absorption at the front and back surfaces approaches the same level. For large skin-depth parameters, the incident electromagnetic wave cannot penetrate deeply into the particle, thus radiation absorption is mainly a surface phenomenon. When the skin-depth parameter is comparable or smaller than one, the incident radiation can propagate inside the particle, resulting in more uniform internal radiation absorption.

Metals have extremely small skin depth, typically around 200 Å. As a result, the distribution of internal radiation absorption is still highly nonuniform for particles with a diameter as small as 0.5 $\mu$m ($x = 0.15$). This feature is very different from those in previous studies on radiation absorption in weakly absorbing particles (Tuntomo et al., 1991). In their case ($m = 1.5 + i0.1$),

**Table 1 Drude's theory parameters**

| Parameters | Al | Cr | Ni |
|---|---|---|---|
| Plasma frequency, $\omega_p$ ($s^{-1}$) | $1.89 \times 10^{16}$ | $5.69 \times 10^{15}$ | $7.76 \times 10^{15}$ |
| Collision frequency, $\gamma_0$ ($s^{-1}$) | $1.13 \times 10^{14}$ | $1.43 \times 10^{14}$ | $9.76 \times 10^{13}$ |
| Temperature coefficient, $\alpha$ ($K^{-1}$) | $4.5 \times 10^{-3}$ | $3.5 \times 10^{-3}$ | $7.7 \times 10^{-3}$ |



Downloaded 12 Dec 2010 to 193.140.21.150. Redistribution subject to ASME license or copyright; see http://www.asme.org/terms/Terms_Use.cfm

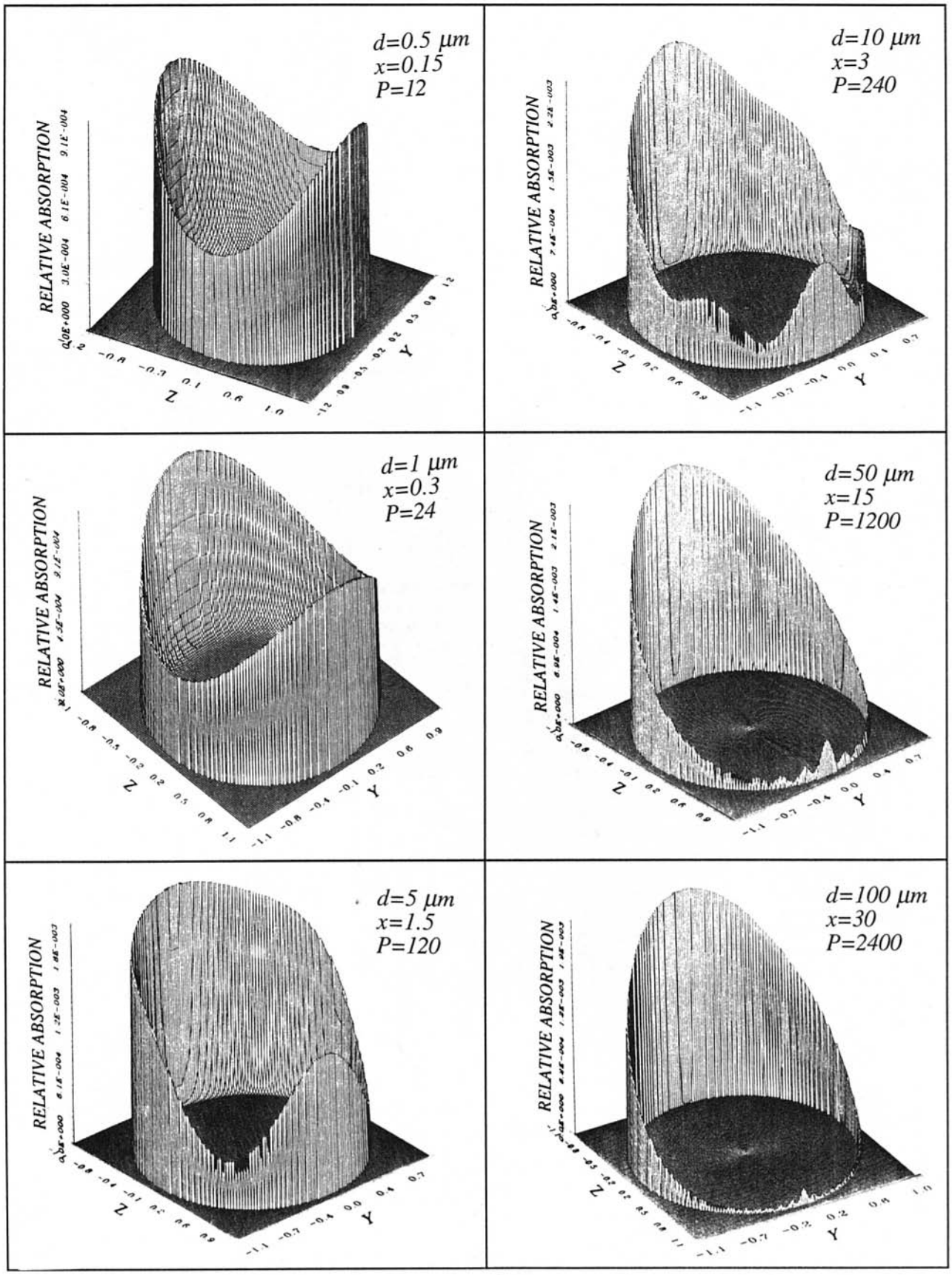



**Fig. 3 Distributions of internal radiation absorption in nickel particles**



Downloaded 12 Dec 2010 to 193.140.21.150. Redistribution subject to ASME license or copyright; see http://www.asme.org/terms/Terms_Use.cfm

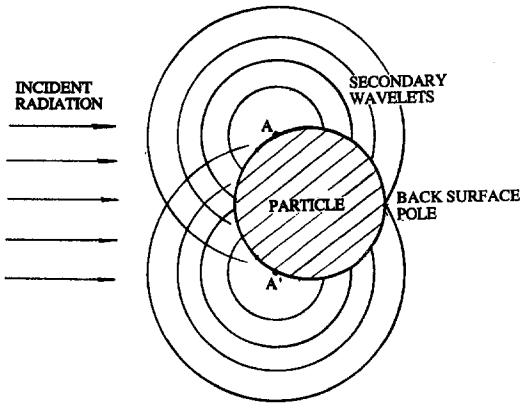



**Fig. 4 Constructive interference of secondary wavelets at back surface pole**

radiation absorption in particles becomes highly uniform for particle size parameters as large as $x = 0.5$.

An interesting phenomenon in the radiation absorption pattern is that the pole of the back particle surface always absorbs more radiation than its surrounding points, which is impossible under the geometric optics framework (Fig. 3). This phenomenon is due to the diffraction effect, which can be explained qualitatively by Huygens' principle (Fig. 4). Each element of a wave front can be regarded as the source of secondary spherical wavelets. The position of the wave front at a later time is the envelope of all such wavelets, and its intensity at a point results from interference of all the secondary wavelets at that point. For example, after the laser beam reaches the particle surface, each surface point starts to emit secondary wavelets. Due to the spherical symmetry, all surface points in a plane perpendicular to the incident beam emits secondary wavelets with the same intensity and phase, e.g., $A$ and $A'$ in Fig. 4. As the secondary wavelets from these points reach the back surface pole, they are all still in phase and thus form constructive interference. As a result, the back surface pole always receives the highest radiation relative to its neighboring points.

Figure 5 shows the volumetric absorption efficiency, $Q_{av}$, for aluminum, chromium, and nickel particles at 300 K and at the $CO_2$ laser wavelength. In the particle diameter region $d > 10$ $\mu$m, surface absorption dominates (Fig. 3). Therefore, $Q_{av}$ decreases rapidly as the particle diameter increases. In the region 0.1 $\mu$m $< d < 10$ $\mu$m, $Q_{av}$ has a maximum value for each metal, as a result of strong effects of light diffraction around the particle surface. Particles absorb radiation most efficiently in the region 0.1 $\mu$m $< d < 1$ $\mu$m. For vanishingly small particles (e.g., $d < 0.01$ $\mu$m), $Q_{av}$

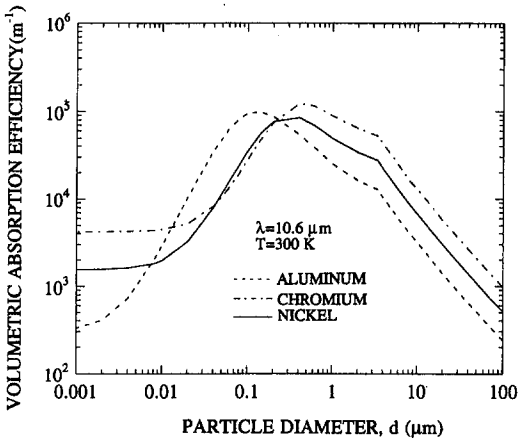



**Fig. 5 Volumetric absorption efficiency at room temperature**

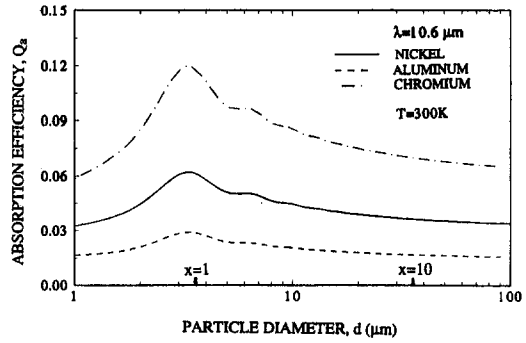



**Fig. 6 Absorption efficiency based on cross-sectional area at room temperature**

approaches a constant, which is the Rayleigh limit of light scattering by small particles (Bohren and Huffman, 1983),

$$Q_{av} = \frac{6\pi}{\lambda} \mathrm{Im}\left\{\frac{m^2 - 1}{m^2 + 2}\right\} \approx \frac{36\pi}{\lambda} \cdot \frac{nk}{(n^2 + k^2)^2} \qquad (15)$$

The Rayleigh region begins when particle diameters are comparable with the skin depth, which is 0.009 $\mu$m, 0.03 $\mu$m, and 0.02 $\mu$m for aluminum, chromium, and nickel, respectively. Therefore, metallic particles do not have the Rayleigh scattering behavior unless they are extremely small, e.g., approaching nanometers in diameters. For weakly absorbing particles, the Rayleigh solution provides an upper limit on $Q_{av}$ (e.g., Tuntomo et al., 1991). For metallic particles, however, the maximum $Q_{av}$ is about two orders of magnitude larger than the Rayleigh limiting value.

Figure 6 presents the cross-sectional area based particle absorption efficiency, $Q_a$, at room temperature. The absorption efficiency is very sensitive to the particle diameter for small par-

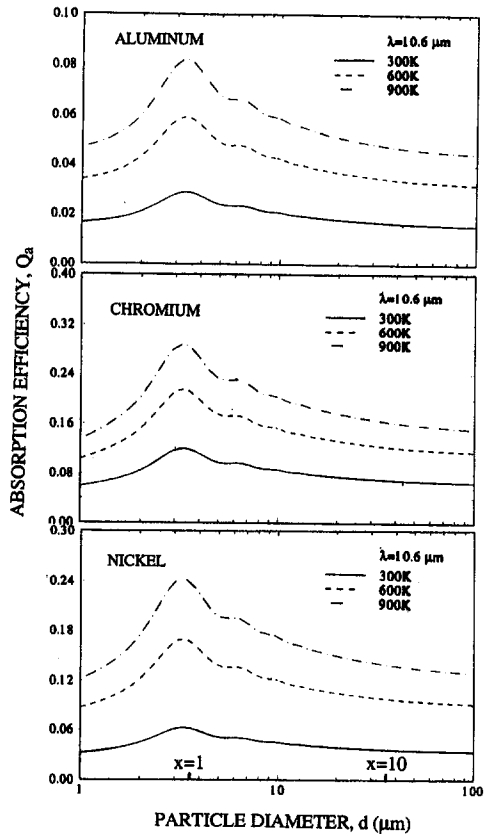



**Fig. 7 Absorption efficiency at different temperatures**



Downloaded 12 Dec 2010 to 193.140.21.150. Redistribution subject to ASME license or copyright; see http://www.asme.org/terms/Terms_Use.cfm

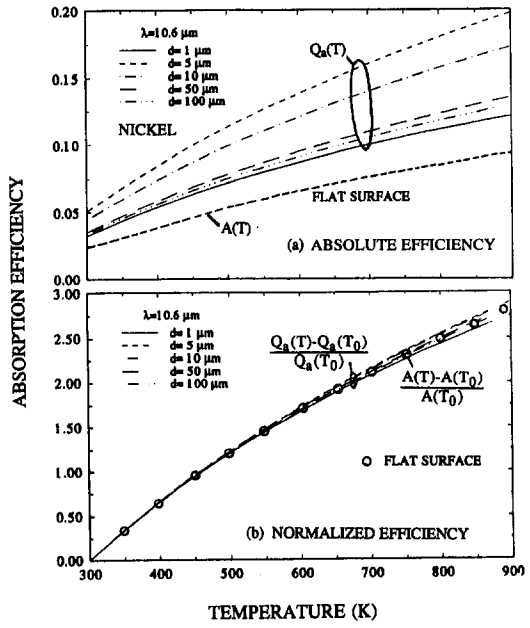



**Fig. 8 Temperature dependence of radiation absorption for particles and flat surfaces**

ticles and insensitive to the diameter for large particles. For size parameters around one, the absorption on the cross-sectional basis is most efficient due to the strong diffraction effect.

Figure 7 shows the absorption efficiency, $Q_a$, at 300 K, 600 K, and 900 K. The absorption efficiency increases with temperature uniformly for particles with diameters ranging from 1 $\mu$m to 100 $\mu$m. As the particle temperature increases from 300 K to 900 K, the absorption coefficient increases by about four, three, and two times, for nickel, aluminum, and chromium particles, respectively. Therefore, preheating of particles can effectively enhance radiation absorption in metallic particles.

Figure 8 shows the temperature dependence of radiation absorption for particles and flat surfaces. The normal-incident absorptivity of a flat surface is evaluated from the equation (Bohren and Huffman, 1983),

$$A(T) = \frac{4n}{(n+1)^2 + k^2} \tag{16}$$

The comparison between $Q_a(T)$ and $A(T)$ reveals two important features. First, due to the diffraction effect at the particle surface, particles can absorb more radiation energy than a flat surface with the same cross-sectional area. Second, spherical particles have the same temperature dependence of radiation absorption as a flat surface does at the normal incidence. Therefore, the effect of heating on the changes of $Q_a$ can be simply estimated as

$$\frac{Q_a(T) - Q_a(T_0)}{Q_a(T_0)} \approx \frac{A(T) - A(T_0)}{A(T_0)} \tag{17}$$

where $T_0$ is a reference temperature.

## Conclusions

The present work has applied the Drude free-electron theory and electromagnetic wave theory to characterizing internal absorption of $CO_2$ laser radiation in aluminum, chromium, and nickel powders. The results show that for large particles radiation absorption occurs only in a very narrow region of the front particle surface, which results in inefficient radiation absorption. On the other hand, for micron and submicron particles, the strong diffraction effect can bend the incident radiation around the particle surface, which in turn leads to very efficient radiation absorption on a volumetric basis compared to both large particles and vanishingly small particles. Furthermore, increasing the particle temperature from 300 K to 900 K can enhance radiation absorption in nickel, aluminum, and chromium particles by about four, three and two times, respectively. The particles have the same temperature dependence of radiation absorption as flat surfaces at the normal incidence.

## Acknowledgments

The authors acknowledge the financial support from the U.S. National Science Foundation, the U.S. Department of Energy, and the K. C. Wang Education Foundation in Hong Kong.

## References

Abramowitz, M., and Stegun, I. A., 1970, *Handbook of Mathematical Functions*, Dover, New York.

Arnold, G. S., 1984, "Absorptivity of Several Metals at 10.6 $\mu$m: Empirical Expressions for the Temperature Dependence Computed From Drude's Theory," *Applied Optics*, Vol. 23, pp. 1434–1436.

Atamert, S., and Bhadeshia, H. K. D. H., 1989, "Comparison of the Microstructures and Abrasive Wear Properties of Stellite Hardfacing Alloys Deposited by Arc Welding and Laser Cladding," *Metallurgical Transactions A*, Vol. 20, pp. 1037–1054.

Avner, A. H., 1964, *Introduction to Physical Metallurgy*, McGraw-Hill, New York.

Bohren, C. F., and Huffman, D. R., 1983, *Absorption and Scattering of Light by Small Particles*, Wiley, New York.

Born, M., and Wolf, E., 1989, *Principles of Optics*, 6th ed., Pergamon Press, New York.

Brewster, M. Q., 1992, *Thermal Radiative Transfer and Properties*, Wiley, New York.

Brewster, M. Q., and Tien, C. L., 1982, "Radiative Transfer in Packed and Fluidized Beds: Dependent vs. Independent Scattering," ASME JOURNAL OF HEAT TRANSFER, Vol. 104, pp. 573–579.

Bruckner, M., Schafer, J. H., Schiffer, C., and Uhlenbusch, J., 1991, "Measurements of the Optical Constants of Solid and Molten Gold and Tin at $\lambda = 10.6$ $\mu$m," *J. Applied Physics*, Vol. 70, pp. 1642–1647.

Figlarz, M., Ducamp-Sanguesa, C., Fievet, F., and Lagier, J-P., 1992, "Preparation and Characterization of Monodisperse Co, Ni, Cu, and Ag Metal Particles of Uniform Shape," in: *Advances in Powder Metallurgy and Particulate Materials*, Vol. 1, J. M. Capus and R. M. German, eds., American Powder Metallurgy Institute, Princeton, NJ.

Hauffe, K., 1965, *Oxidation of Metals*, Plenum Press, New York.

Hausner, H. H., and Mal, M. K., 1982, *Handbook of Powder Metallurgy*, Chemical Publishing Co., New York.

Hoadley, A. F. A., and Rappaz, M., 1992, "A Thermal Model of Laser Cladding by Powder Injection," *Metallurgical Transactions B*, Vol. 23, pp. 631–642.

Kittel, C., 1986, *Introduction to Solid State Physics*, 6th ed., Wiley, New York.

Komvopoulos, K., and Nagarathnam, K., 1990, "Processing and Characterization of Laser-Cladded Coating Materials," ASME *Journal of Engineering Materials and Technology*, Vol. 112, pp. 131–143.

Kubaschewski, O., and Hopkins, B. E., 1953, *Oxidation of Metals and Alloys*, Academic Press, New York.

Lide, D. R., ed., 1992, *CRC Handbook of Chemistry and Physics*, 73rd ed., CRC Press, Boca Raton, FL, Section 12, pp. 34–35.

Mackowski, D. W., 1989, "Photophoresis of Aerosol Particles in the Free Molecular and Slip-Flow Regimes," *Int. J. Heat Mass Transfer*, Vol. 32, pp. 843–854.

Mazumder, J., Sircar, S., Ribaudo, C., and Kar, A., 1992, "Laser Cladding of Nonequilibrium Metallic Alloys," in: *Thermomechanical Aspects of Manufacturing and Materials Processing*, R. K. Shah et al., eds., Hemisphere Publishing Corp., New York, pp. 319–335.

Oberlander, B. C., and Lugscheider, E., 1992, "Comparison of Properties of Coatings Produced by Laser Cladding and Conventional Methods," *Materials Science and Technology*, Vol. 8, pp. 657–665.

Ordal, M. A., Bell, R. J., Alexander, R. W., Long, L. L., Jr., and Querry, M. R., 1985, "Optical Properties of Fourteen Metals in the Infrared and Far Infrared: Al, Co, Cu, Au, Fe, Pb, Mo, Ni, Pd, Pt, Ag, Ti, V, and W," *Applied Optics*, Vol. 24, pp. 4493–4499.

Prokhorov, A. M., and Konov, V. I., 1990, *Laser Heating of Metals*, Adam Hilger, New York.

Pustovalov, V. K., and Bobuchenko, D. S., 1993, "Thermal Processes in Gas-Powder Laser Cladding of Metal Materials," *Int. J. Heat Mass Transfer*, Vol. 36, pp. 2449–2456.

Shiles, E., Sasaki, T., Inokuti, M., and Smith, D. Y., 1980, "Self-Consistency and Sum-Rule Tests in the Kramers-Kroning Analysis of Optical Data: Applications to Aluminum," *Physical Review B*, Vol. 22, pp. 1612–1628.

Tuntomo, A., Tien, C. L., and Park, S. H., 1991, "Internal Distribution of Radiant Absorption in a Spherical Particle," ASME JOURNAL OF HEAT TRANSFER, Vol. 113, pp. 407–412.

Ujihara, K., 1972, "Reflectivity of Metals at High Temperatures," *J. Applied Physics*, Vol. 43, pp. 2376–2383.

Weaver, J. H., 1992, "Optical Properties of Metals," in: *CRC Handbook of Chemistry and Physics*, 73rd ed., D. R. Lide, ed., CRC Press, Boca Raton, FL, Section 12, pp. 111–126.

Wiscombe, W. J., 1979, "Mie Scattering Calculations: Advances in Technique and Fast, Vector-Speed Computer Codes," NCAR Technical Report #NCAR/TN-140+STR, NCAR, Boulder, CO.



Downloaded 12 Dec 2010 to 193.140.21.150. Redistribution subject to ASME license or copyright; see http://www.asme.org/terms/Terms_Use.cfm

# Nonisothermal Nongray Absorbing-Emitting-Scattering Suspension of $Fe_3O_4$ Particles Under Concentrated Solar Irradiation

**D. Mischler**

**A. Steinfeld**

Laboratory for Energy and
Process Technology,
Paul Scherrer Institute,
CH-5232 Villigen-PSI, Switzerland

*Radiation transfer within a cloud of magnetite ($Fe_3O_4$) particles contained in an infinite slab is considered. The particulate cloud is modeled as a pseudo-continuous, nongray, nonisothermal, absorbing, emitting, and anisotropically scattering medium. The energy source is concentrated solar irradiation, which is assumed to be diffusely and uniformly distributed over a circular opening and has a 5780 K blackbody spectrum. Mie-scattering theory is applied to calculate the spectrally and directionally dependent optical properties of the particles. The Monte Carlo ray-tracing method is used to calculate the attenuation characteristics of the cloud and the temperature distribution under radiative equilibrium. The Monte Carlo simulation is optimized by incorporating the appropriate cumulative probability density functions via Bezier surfaces. The effect of spectral and directional dependency is investigated by comparing the results with those obtained for a gray and isotropic-scattering medium under diffuse or perpendicular incident radiation. It is found that a cloud of Mie-scattering $Fe_3O_4$ particles under perpendicular incident radiation requires approximately twice as much optical thickness to obtain the same attenuation (of radiation at all wavelengths and directions) as a cloud of isotropic-scattering particles under diffuse incident radiation. It is demonstrated that the gray approximation using Planck mean values can lead to considerable error in the temperature solution because the spectral absorption coefficient is higher in the region of longer wavelengths where the peak emission by $Fe_3O_4$ particles occurs.*

## 1 Introduction

In recent years there has been an increasing interest in volumetric receivers/reactors for solar thermochemical processes. Their design concept uses gas-particle suspensions or selective-absorbing gases to serve the functions of direct energy absorption of concentrated solar radiation, heat transfer, catalysis, and chemical reactants as well (Hunt et al., 1986). Volumetric, or direct-absorption particle receivers, have been experimentally demonstrated for heating air (Hunt and Brown, 1983; Rightley et al., 1992) and are presently being investigated for solar-driven chemistry at the Paul Scherrer Institute. In contrast to cavity-type receivers in which the incident radiation is mostly absorbed at the inner surfaces and from there indirectly transferred to the reactor, volumetric receivers provide instead efficient heat transfer directly to the reaction site, where the energy is needed. Moreover, the direct irradiation of the reactants may result, under proper conditions, in photochemical enhancement of the reaction kinetics.

Among energy-intensive reactions, which may be well adapted to direct-absorption processes, the thermal reduction of magnetite ($Fe_3O_4$) to form wustite (FeO) is of special interest. This reaction is part of a two-step water splitting cycle (Nakamura, 1977), according to:

*1st step:* $Fe_3O_4 = 3FeO + 0.5O_2$
*2nd step:* $3FeO + H_2O = Fe_3O_4 + H_2$

In the first step, iron oxide is thermally reduced using concentrated solar radiation as the energy source of high-temperature process heat. In the second step, the lower-valence oxide reacts with water to form hydrogen. The net reaction is $H_2O = H_2 + 0.5O_2$; hydrogen and oxygen are derived in different steps, eliminating the need for high-temperature gas separation. The first, solar, step proceeds endothermically at above about 2300 K and 1 atm. If we were to use cavity receivers at such high temperatures, one might encounter difficulties with suitable refractory materials of construction since the entire inner wall of the enclosure is at the highest temperature in the system. To the contrary, by directly illuminating a dense $Fe_3O_4$-particle cloud with the concentrated solar beam, a gradient of temperatures could be achieved between the reaction zone and the reactor inner walls. Such shielding effect would reduce the thermal load on the walls and temperature requirements of the containment. Radiative transport in a volumetric reactor is the dominant heat transfer mode at high temperatures (2000 K and above). The design of innovative reactor concepts requires a detailed and accurate radiation model.

The radiant interchange in particle clouds among gas, particles, and reactor walls is a complex mathematical problem. Simplifying assumptions in the geometry and optical properties are necessary in order to be able to solve approximations to real situations. For example, approximate solutions have been derived for a gray nonscattering gas and particles in a coal furnace (Canadas et al., 1990), for an isothermal nongray slab containing carbon particles and $CO_2$ (Yuen and Ma, 1992), for a free-falling particle-laden flow within a two-dimensional rectangular solar cavity-receiver (Evans et al., 1987; Houf and Greif, 1987), and for a box-type geometry with incident light coming along one coordinate axis (Miller and Koenigsdorff, 1991). The radiative transfer in a planar participating medium that scatters anisotropically has been considered in numerous previous investigations

Contributed by the Heat Transfer Division for publication in the JOURNAL OF HEAT TRANSFER. Manuscript received by the Heat Transfer Division October 1993; revision received June 1994. Keywords: Numerical Methods, Radiation, Solar Energy. Associate Technical Editor: Y. Bayazitoglu.



Copyright © 1995 by ASME

Downloaded 12 Dec 2010 to 193.140.21.150. Redistribution subject to ASME license or copyright; see http://www.asme.org/terms/Terms_Use.cfm

because it approximates well many physical problems without introducing geometric complexities (e.g., Hsia and Love, 1967; Modest and Azad, 1980; and literature cited therein).

Gray, isothermal, and isotropic scattering media are some of the assumptions commonly used in engineering calculations. The gray assumption can lead to considerable error when modeling solar particle receivers since particle clouds may exhibit strong selective properties for absorption in the solar spectrum and emission in the IR (Abdelrahman et al., 1979). It was already demonstrated that gray gas formulations cannot predict even qualitatively the experimental measurements of absorption and emission of nonisothermal $CO_2$ and $H_2O$ gases (Edwards et al., 1967). It would be reasonable to extend the same conclusions for selective particle suspensions. Nongray solutions for plane parallel media bounded by black walls have been obtained by Kim et al. (1991) using the discrete ordinates method and a statistical narrow-band model. The isotropic assumption, often justified in radiation heat transfer modeling of cavity receivers, may also result in discrepancies when applied to directly irradiated particle clouds because of the strong angular dependence of the scattering phase function. Sasse (1992) measured the scattering intensity as a function of the scattered angle for single carbon particles and oil droplets suspended in an electrodynamic levitator and observed significant deviation from isotropic scattering. Gupta et al. (1983) considered both isotropic and anisotropic scattering fly ash cloud using Mie theory and the Monte Carlo method. It was found that neglecting scattering overestimates radiative transfer to the sink of the furnace, while assuming isotropic scatter underestimates radiative transfer, both resulting in errors up to 30 percent. Finally, the isothermal assumption is obviously not valid for the temperature-gradient reactor under investigation.

In the present work we incorporate wavelength-dependent and directional-dependent optical properties of magnetite to simulate by Monte Carlo a nongray, nonisothermal, absorbing, emitting, and anisotropic-scattering particle suspension under concentrated solar irradiation. The focus of this study is to find out how much of the incident radiation is transmitted through the cloud, to obtain the temperature distribution within the cloud, and to present the effect of spectral and directional dependencies.

## 2 Analysis

The system configuration is depicted schematically in Fig. 1. The particle suspension is contained in a slab of constant thickness $D$. It is bounded between two infinite parallel planes assumed blackbodies at 0 K, i.e., the planes absorb all incident radiation coming from the medium but do not emit any radiation. The front plane contains a circular aperture of radius $r_{ap}$ through which concentrated solar irradiation enters. The incoming solar flux is assumed diffusely and uniformly distributed over the circular aperture since this is the power flux distribution likely to be obtained when nonimaging secondary elements, such as CPCs, are used in tandem with imaging primary reflectors for augmenting the concentration (Welford and Winston, 1989). The spectral distribution of the incoming solar intensity is approximated by the Planck distribution of a 5780 K blackbody source. Thus, the hemispherical spectral emissive power entering through the aperture is proportional to:

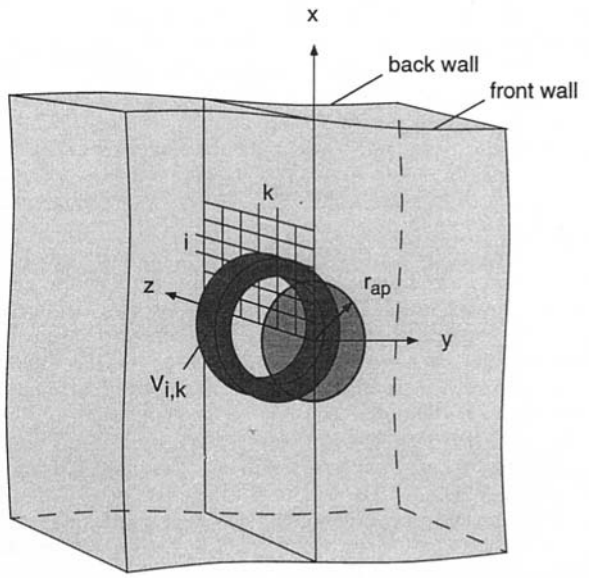



Fig. 1 Schematic diagram of the system

$$e_{\lambda b}(\lambda, T) = \frac{2\pi C_1}{\lambda^5(e^{C_2/\lambda T} - 1)} \tag{1}$$

for $T = 5780$ K.

## Nomenclature

$a_\lambda$ = spectral absorption coefficient
$C_1$ = constant in Planck spectral energy distribution = $0.59552 \times 10^8$ W $\mu$m$^2$
$C_2$ = constant in Planck spectral energy distribution = 14,388 $\mu$m K
$D$ = slab thickness
$d$ = particle diameter
$e_{\lambda b}(\lambda, T)$ = hemispherical spectral emissive power = $2\pi C_1/\lambda^5(e^{C_2/\lambda T} - 1)$
$f_v$ = volume fraction = $N\pi d^3/6$
**i, j, k** = unit vectors in Cartesian system
$K_\lambda$ = spectral extinction coefficient = $a_\lambda + s_\lambda$
$\tilde{K}$ = Planck mean extinction coefficient = $\int_0^\infty K_\lambda e_{\lambda b}(\lambda, T)d\lambda/\sigma T^4$
$l$ = probable mean free path
$N$ = number density, particles per unit volume
$P_i$ = generic point of ray
$Q_a$, $Q_s$, $Q_K$ = absorption, scattering, and extinction efficiency
$r_{ap}$ = aperture radius
$\mathcal{R}$ = random number between [0, 1]
$s_\lambda$ = spectral scattering coefficient
$T$ = absolute temperature, $K$
**u** = unit vector parallel to the direction of the incident ray
$V_{ik}$ = volume element in Fig. 1
$X$ = dimensionless normal coordinate = $x/D$
$\eta$ = azimuthal angle of scattered beam
$\theta$ = polar angle, measured from normal of surface
$\kappa_\lambda$ = spectral optical thickness
$\tilde{\kappa}$ = Planck mean optical thickness = $\tilde{K}D$
$\lambda$ = wavelength
$\xi$ = angle between scattered and incident direction
$\sigma$ = Stefan–Boltzmann constant = $5.6705 \times 10^{-8}$ W/(m$^2 \cdot$K$^4$)
$\tilde{\tau}$ = Planck mean directional total transmittance = $\int_0^\infty e^{-K_\lambda D} e_{\lambda b}(\lambda, T)d\lambda/\sigma T^4$
$\Phi_\lambda$ = scattering phase function, ratio of scattered intensity in the direction $(\xi, \eta)$ to the intensity of isotropic scattering
$\phi$ = dimensionless emissive power
$\varphi$ = circumferential angle
$\Omega_\lambda$ = albedo = $s_\lambda/K_\lambda$
$\tilde{\Omega}$ = Planck mean albedo = $\int_0^\infty \Omega_\lambda e_{\lambda b}(\lambda, T)d\lambda/\sigma T^4$



Downloaded 12 Dec 2010 to 193.140.21.150. Redistribution subject to ASME license or copyright; see http://www.asme.org/terms/Terms_Use.cfm

The particulate medium is modeled as a pseudo-continuous medium, i.e., a monodisperse distribution of particles, with some number density $N$, surrounded by a nonparticipating gas with a refractive index of 1. The optical characteristics of the discrete particles are used to determine the extinction properties of the whole medium (Tien and Drolen, 1987). Each particle is assumed opaque (no transmission), with infinite thermal conductivity (isothermal), spherical (a generally good assumption for most irregularly shaped, randomly oriented particles) and having independent scattering (a condition whereby the scattering from a single particle in the assembly is not influenced by the proximity of its neighbors). The independent scattering assumption is justified by referring to the independent/dependent scattering regime map, as given by Yamada et al. (1986), for the range of particle volume fractions ($f_v$) and size parameters ($\pi d/\lambda$) used in this study. Particle diameter has been taken equal to 5 $\mu$m because it is the average diameter we have been using in our experimental studies. The monodispersity assumption will permit a better detection and understanding of the effect of spectral and directional dependency of the cloud optical properties.

Special attention is devoted to the realistic case of nongray and anisotropically scattering particles. The Mie-anisotropic scattering theory is applied. The Mie theory adequately describes the range $0.6 < \pi d/\lambda < 5$, but it can also be practically applied for spherical particles of arbitrary size (Siegel and Howell, 1992; Bohren and Huffman, 1983). We have performed our Monte Carlo computations over a wider range of size parameters. However, because incident and emitted radiation are confined mostly in the visible and infrared spectra, the statistically active range of particle size parameters falls within $0.5 < \pi d/\lambda < 30$. Scattering characteristics depend also on the optical properties of the particles under consideration. The complex refractive index of $Fe_3O_4$, expressed in terms of the complex dielectric constant as a function of wavelength, has been taken from Hellwege (1982).

Given the size parameter and the complex refractive index, we have used Mie theory (BHMIE subroutine by Bohren and Huffman, 1983) to calculate the scattering phase function $\Phi_\lambda(\xi, \eta)$. For spherical or randomly oriented particles, $\Phi_\lambda$ is independent of $\eta$. For isotropic scattering, $\Phi_\lambda = 1$. The diagram of Fig. 2 illustrates how far away from isotropic scatterers the $Fe_3O_4$ particles are. $\Phi_\lambda$ is plotted as a function of $\xi$ for three representative wavelengths: 0.5, 1.5, and 10 $\mu$m. These are the corresponding wavelengths for maximum spectral intensity, given by Wien's displacement law, of a 5780 K, 2000 K, and 300 K blackbody, respectively. For all three wavelengths, and for all wavelengths in the range 0.158–10 $\mu$m (not displayed in the graph), the $Fe_3O_4$ particles exhibit significant preference for forward scattering, becoming more pronounced as the wavelength decreases. For $\lambda \approx 0.5$ $\mu$m, scattering is exclusively forward. Thus, solar rays perpendicularly incident on the external layer of a particle cloud are most likely to be either absorbed or scattered more into the heart of cloud rather than back-scattered.

Additional output from the Mie theory are the spectral efficiencies $Q_a$, $Q_s$, and $Q_K$ ($Q_K = Q_a + Q_s$), i.e., the ratio of the absorption, scattering, and extinction cross-sectional areas to the physical particle cross-sectional area. These efficiencies are plotted in Fig. 3 as a function of wavelength. They reveal an increasing trend with wavelength up to about 20 $\mu$m. Peak attenuation occurs for radiation at 17 $\mu$m, giving an apparent particle area up to 3.25 times bigger than the actual physical area. Therefore, from a standpoint of maximizing the attenuation of radiation through a particle cloud, it would be better to have this radiation coming from an infrared source in the 10–20 $\mu$m range rather than from a visible source. However, for $\lambda > 20$ $\mu$m, the efficiencies decrease dramatically to the extent that for $\lambda > 50$ $\mu$m the medium is practically transparent. It is seen that a cloud of magnetite particles behaves differently than, for example, a fly ash cloud. In a pulverized-coal-fired furnace, a fly ash cloud has instead an absorption efficiency that monotonically decreases with wavelength in the 1–10 $\mu$m range (Gupta et al., 1983).

Given the amount of particles per unit volume of the medium, the spectral absorption and scattering coefficients can be calculated as:

$$a_\lambda = 1.5 Q_a f_v / d$$

$$s_\lambda = 1.5 Q_s f_v / d$$

respectively. These are usually combined in the extinction coefficient $K_\lambda$, which, when constant over the whole domain, becomes the reciprocal of the so-called mean penetration distance, i.e., the average distance radiation propagates through the medium before absorption or scattering occurs. Since the incident radiation has a Planck spectral distribution of a 5780 K blackbody, it is convenient to define the Planck mean extinction coefficient, $\tilde{K}$, as:

$$\tilde{K} = \frac{\int_0^\infty K_\lambda e_{\lambda b}(\lambda, T) d\lambda}{\int_0^\infty e_{\lambda b}(\lambda, T) d\lambda} = \frac{1}{\sigma T^4} \int_0^\infty K_\lambda e_{\lambda b}(\lambda, T) d\lambda \qquad (2)$$

for $T = 5780$ K. $\tilde{K}$ is the mean of the spectral extinction coefficient when weighted by a 5780 K blackbody emission spectrum. A dimensionless parameter that describes radiation attenuation by a uniform medium depth $x$ of constant $K_\lambda$ is the optical thick-

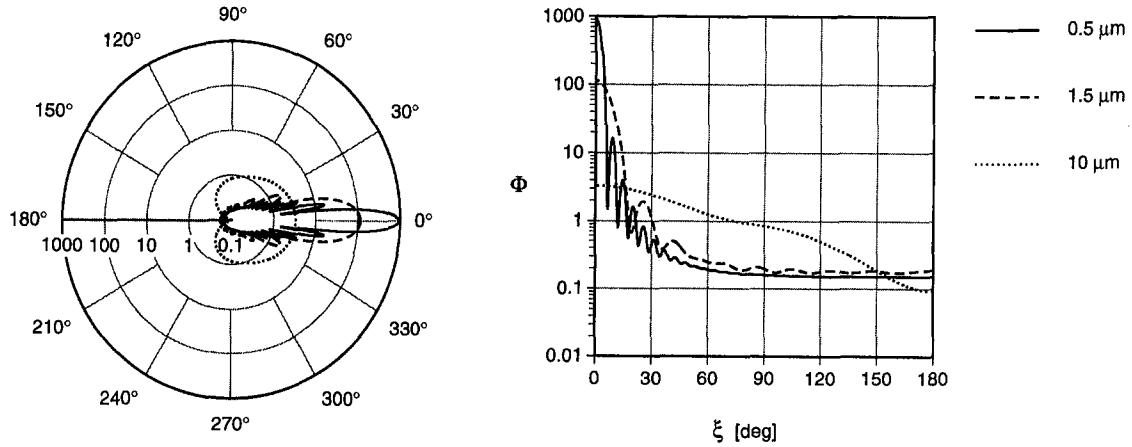



**Fig. 2 The scattering phase function for $Fe_3O_4$ particles (spherical, $d = 5$ $\mu$m), as a function of the angle $\xi$ between the scattered and incident direction, calculated using Mie theory for three representative wavelengths: 0.5, 1.5, and 10 $\mu$m**



Downloaded 12 Dec 2010 to 193.140.21.150. Redistribution subject to ASME license or copyright; see http://www.asme.org/terms/Terms_Use.cfm

ness $\kappa_\lambda$, defined as: $\kappa_\lambda = K_\lambda x$. Similarly, the Planck mean optical thickness over a slab of thickness $D$, is defined as the spectrally averaged optical thickness when weighted by a 5780 K blackbody emission spectrum: $\tilde{\kappa} = \tilde{K}D$. Results of this study are presented in terms of $\tilde{\kappa}$.

The relative importance of scattering to absorption is measured by the albedo $\Omega_\lambda$, $\Omega_\lambda = s_\lambda/K_\lambda$. The albedo for $Fe_3O_4$ particles, obtained via the BHMIE subroutine, is shown in Fig. 3 as a function of wavelength. Statistically, it indicates the probability of an incident ray being scattered. For $\lambda < 15$ $\mu$m, the incident rays have about 60 percent chance of being scattered, 40 percent chance of being absorbed. As the wavelength of the incident ray increases, so does the probability of absorption. At $\lambda = 100$ $\mu$m an incident ray is more likely to be absorbed rather than scattered. However, we have already seen in Fig. 3 that at such a long wavelength there would be practically no rays interacting with particles. A representative mean value of the albedo for the incident radiation is obtained by integrating, over all wavelengths, the spectral albedo weighted by a 5780 K blackbody emission spectrum. Thus, the Planck mean albedo is defined as:

$$\tilde{\Omega} = \frac{1}{\sigma T^4}\int_0^\infty \Omega_\lambda e_{\lambda b}(\lambda, T)d\lambda \tag{3}$$

For $T = 5780$ K and $\Omega_\lambda$ given by Fig. 3, $\tilde{\Omega} = 0.5894$.

The Monte Carlo ray-tracing method was used. This technique, widely employed for the analysis of radiative transport (Siegel and Howell, 1992; Howell and Perlmutter, 1964), enables the treatment of problems beyond the reach of analytical techniques, and is flexible enough to remove any or all of the diffuse-gray-isotropic simplifying assumptions. The methodology will be briefly outlined in the following paragraphs. It consists of following stochastic paths of a large number of discrete bundles of energy as they travel through the interacting medium. Each energy bundle carries the same amount of energy (equal to the incident power divided by number of bundles), and has a certain direction and a certain associated wavelength, which are determined from the appropriate probability density functions.

Our generic incident ray, or energy bundle path, enters the slab through the opening at point $P_1$ and has a direction parallel to the unit vector $\mathbf{u}$. The equation that gives the coordinates of a generic point $P_i$ on the ray is, in vectorial notation, $(P_i - P_1) \times \mathbf{u} = 0$. Since incoming irradiation is diffuse and uniformly distributed over the aperture, the number of energy bundles through a certain ring of radius $r$ on the aperture is proportional to its area $2\pi r dr$, and their direction is chosen randomly from a set that is weighted according to Lambert's cosine law. Thus, the direction of the ray should satisfy $\mathbf{u}\cdot\mathbf{k} = \cos(\sin^{-1}\sqrt{\mathcal{R}_1})$, where $\mathcal{R}_1$ is a random number drawn from a uniformly distributed set between zero and one. Incoming intensity has a Planck spectral distribution of a 5780 K blackbody source. Thus, a wavelength of radiation assigned to the incident ray is given implicitly by:

$$\mathcal{R}_2 = \frac{1}{\sigma T^4}\int_0^\lambda e_{\lambda b}(\lambda, T)d\lambda \tag{4}$$

$\lambda$ is numerically calculated using Eq. (4) for $T = 5780$ K. The incident bundle will intercept a particle after traveling a distance $l$ (path length to probable point of absorption/scattering), given by $l = -(1/K_\lambda)\ln \mathcal{R}_3$. The point of intersection, $P_2$, is simply $P_2 = P_1 + l\cdot\mathbf{u}$. Here, another random choice, depending on the albedo, determines whether the bundle is absorbed or scattered. The probability of absorption is equal to $1 - \Omega_\lambda$, evaluated at the bundle wavelength. If the bundle is scattered by the particle, the direction of scattering forms an angle $\xi$ with the incident direction, obtained by numerically solving:

$$\mathcal{R}_4 = \tfrac{1}{2}\int_0^\xi \Phi_\lambda(\xi, \eta)\sin\xi d\xi \tag{5}$$

where the scattering phase function $\Phi_\lambda(\xi, \eta)$ gives, in statistical terms, the probability of scattering in a certain direction. The azimuthal angle of the scattered beam, $\eta$, is randomly chosen between 0 and $2\pi$ because, for spherical particles, $\Phi_\lambda$ is independent of $\eta$. The wavelength of the scattered bundle is unchanged (elastic scattering). If the bundle is absorbed by the particle, a count is recorded and its history is terminated. However, to ensure no energy accumulation in radiative equilibrium, a new bundle must be emitted from the same particle. The direction of isotropic emission is randomly determined by the polar and circumferential angles, $(\theta, \varphi)$, given by: $\theta = \cos^{-1}(1 - 2\mathcal{R}_5)$ and $\varphi = 2\pi\mathcal{R}_6$. The new bundle is emitted by a nongray particle at a wavelength corresponding to the temperature of the particle. This new wavelength assigned to the new bundle is found by solving:

$$\mathcal{R}_7 = \frac{\int_0^\lambda a_\lambda e_{\lambda b}(\lambda, T)d\lambda}{\int_0^\infty a_\lambda e_{\lambda b}(\lambda, T)d\lambda} \tag{6}$$

evaluated at the particle temperature. Once we know the direction and wavelength of the *new* emitted bundle or of the *old* scattered bundle, we can again track the ray to determine the new point of interception with a particle and repeat the algorithm until the bundle reaches a blackbody boundary. Eventually, each bundle of energy would undergo either scattering, absorption (and subsequent emission), or would leave through the plane boundaries. The history of a bundle is then a complete random sequence, which terminates when a boundary is encountered. This procedure is repeated for a large enough sample of bundles so that the results are statistically meaningful.

Since the complex refractive index is spectrally dependent, the Mie subroutine BHMIE for calculating $\Phi_\lambda$ and $\Omega_\lambda$ would need to be executed for each incident energy bundle in each Monte Carlo iterative run. For the large number of bundles used in this study, the computing time consumed would be prohibitive. Instead, external to the Monte Carlo simulation code, we have used the Mie subroutine to compute the monochromatic scattering phase function $\Phi_\lambda$ as a function of the cone angle $\xi$, for a set of wavelengths in the 0.158–100 $\mu$m range. Next, we have numerically integrated the probability density phase functions over $\xi$ to obtain a set of cumulative distribution functions according to Eq. (5). Finally, after exchanging axes, we have produced a three-dimensional interpolation to surface-fit the angle $\xi$ as a function of the independent variables $\mathcal{R}_4$ and $\lambda$. The technique used to produce this surface fitting is based on the bicubic Bezier-Spline algorithm (Engeln-Muellges and Reutter, 1987). The function $\xi = \xi(\mathcal{R}_4, \lambda)$ is plotted in Fig. 4. This surface, stored as a matrix, can

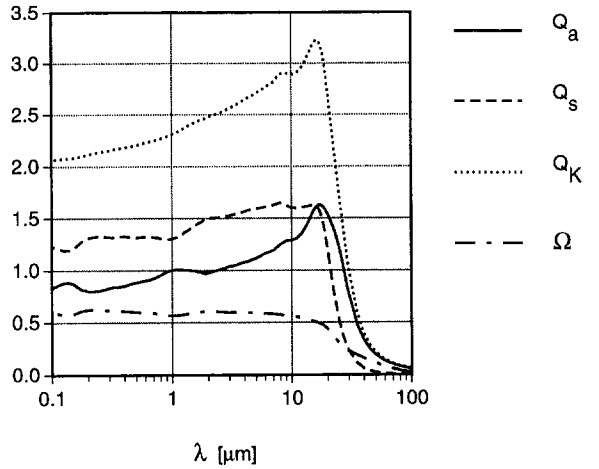



**Fig. 3 The absorption, scattering, and extinction efficiencies, and the albedo, as a function of wavelength, calculated for $Fe_3O_4$ particles using Mie-scattering theory**



Downloaded 12 Dec 2010 to 193.140.21.150. Redistribution subject to ASME license or copyright; see http://www.asme.org/terms/Terms_Use.cfm

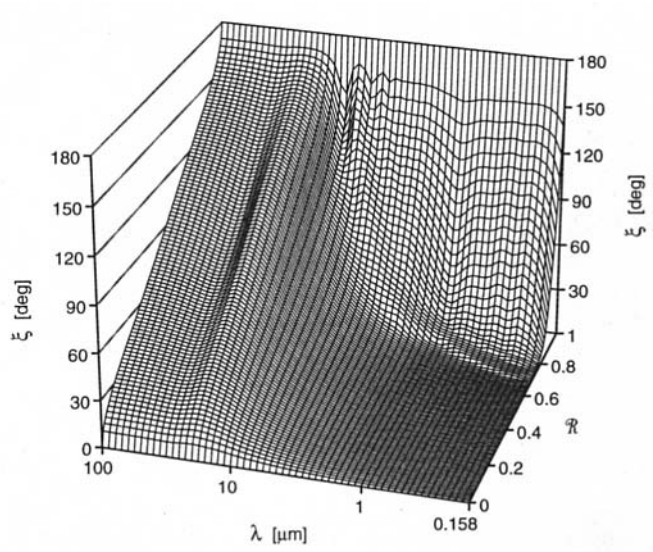



**Fig. 4 The angle between the scattered and incident direction as a function of the radiation wavelength and a given random number. This Bezier surface, stored as a matrix, is incorporated in the Monte Carlo simulation for direct determination of the direction of scattering.**

readily be incorporated in a Monte Carlo simulation to calculate the direction of scattering for a given random number and wavelength.

Similarly, the integrals of Eq. (6) were numerically carried out over $\lambda$ to obtain the cumulative distribution functions of the probability of emission of an energy bundle at a certain wavelength from a particle at a given temperature. Again, after exchanging axes, we have used the bicubic Bezier-Spline interpolation to surface-fit the wavelength as a function of the independent variables $\mathcal{R}_7$ and $T$. The surface $\lambda = \lambda(\mathcal{R}_7, T)$ can be directly used in a Monte Carlo simulation to calculate the wavelength of emission for a given random number and particle temperature.

In Eq. (6), the particle temperature is a priori unknown. A temperature distribution within the medium is assumed for a first Monte Carlo run. Then, a new temperature is obtained by solving the radiative equilibrium equation for a volume element $dV$:

$$\text{Energy absorbed} = \text{Energy emitted} = 4dV\int_0^\infty a_\lambda e_{\lambda b}(\lambda, T)d\lambda \qquad (7)$$

where the energy absorbed by $dV$ is simply the number of bundles absorbed in that volume element times the energy carried by each bundle. The new temperatures obtained is used for the next Monte Carlo iteration until convergency. Because of the axial symmetry of the geometry and power distribution, it was found convenient to divide the slab into a fine grid of ring cells $V_{ik}$, as depicted schematically in Fig. 1, and assume isothermal conditions for particles belonging to the same unit volume cell. Since particles are uniformly dispersed in the slab, each volume cell contains $N \times V_{ik}$ particles. We have counted the number of absorptions taking place at each cell and used Eq. (7) to calculate the *average* temperature of particles for each cell.

## 3 Results

A sample of 5 million energy bundles was employed for each Monte Carlo run. The accuracy of the Monte Carlo computation was checked against the exact analytical solutions available for the case of a nonisothermal absorbing-emitting-nonscattering gray medium between infinite parallel black walls. This specific idealized problem has been previously solved by Usiskin and Sparrow (1960) using numerical integration, by Howell and Perlmutter (1964) using Monte Carlo, and by Heaslet and Warming (1965) by means of tabulated functions. Heaslet and Warming (1965) present the results to a considerable degree of precision and may be considered exact. The governing integral equation for the gas temperature distribution is given in dimensionless form by:

$$\int_0^{X_0}\phi(X)\left[\int_{\kappa(X_0-X)}^\infty \frac{e^{-\lambda}}{\lambda}d\lambda\right]dX + \int_{X_0}^1 \phi(X)\left[\int_{\kappa(X-X_0)}^\infty \frac{e^{-\lambda}}{\lambda}d\lambda\right]dX + \frac{\exp[-\kappa(1-X_0)]}{\kappa} = (1-X_0)\left[\int_{\kappa(1-X_0)}^\infty \frac{e^{-\lambda}}{\lambda}d\lambda\right] + \frac{2}{\kappa}\phi(X_0) \qquad (8)$$

where $\phi$ is the dimensionless emissive power, $\phi = (T^4 - T_1^4)/(T_2^4 - T_1^4)$, $X$ is the dimensionless normal coordinate $x/D$, and $T_1$, $T_2$ are the wall temperatures. Equation (8) was solved for $\phi$ by numerical computation using the *Mathematica* software package. The dimensionless emissive power at the boundaries, $\phi(0)$ and $\phi(1)$, are within 0.3 percent of the numerical values reported by Heaslet and Warming (1965). Note that in contrast to the analytical solution, the Monte Carlo simulation needs to consider specific values for the wall temperatures. Our Monte Carlo program was run for the following parameters: front wall was taken at 5780 K, the back wall at 0 K, the albedo equal zero (no scattering), and the optical thickness equal 0.1 and 1 for every wavelength. Table 1 presents the accuracy of the Monte Carlo solution when $T^4/5780^4$ is compared against the "exact" values.

Obviously, the accuracy increases with the number of bundles taken in the sample. The computational costs of increasing these numbers is high, and sample sizes of 5 million bundles were found to be adequate for this study. The accuracy also increases for larger $\kappa_\lambda$ because, in a thicker cloud, bundles undergo more absorption-emission processes that give a statistically more accurate value for $\phi$. The repeatability of the Monte Carlo simulation is, for $\kappa_\lambda = 1$ and a sample of 5 million bundles, within 0.8 percent.

We now proceed to study the system configuration of Fig. 1 for a nonisothermal nongray absorbing-emitting-scattering suspension of $Fe_3O_4$ particles under concentrated solar irradiation. The boundary conditions and computational procedure have been described in the "Analysis" section. The ability of such a cloud to attenuate incident radiation by absorption and scattering is described in Fig. 5. Attenuation, reflectance, and absorptance through the slab are defined in this study as:

$$\text{Attenuation} = 1 - \left(\frac{\text{Energy bundles arriving at the back wall}}{\text{Total number of energy bundles entering through the aperture}}\right) \qquad (9)$$

$$\text{Reflectance} = \left(\frac{\text{Energy bundles scattered back to the front wall}}{\text{Total number of energy bundles entering through the aperture}}\right) \qquad (10)$$

$$\text{Absorptance} = \text{Attenuation} - \text{Reflectance} \qquad (11)$$

**Table 1 Error = maximum$|1 - \phi_{\text{Monte Carlo}}/\phi_{\text{exact}}|$**

| $\kappa_\lambda$ | 1 million | 5 million | 10 million |
|---|---|---|---|
| 0.1 | 0.090 | 0.033 | 0.020 |
| 1 | 0.027 | 0.016 | 0.010 |



Downloaded 12 Dec 2010 to 193.140.21.150. Redistribution subject to ASME license or copyright; see http://www.asme.org/terms/Terms_Use.cfm

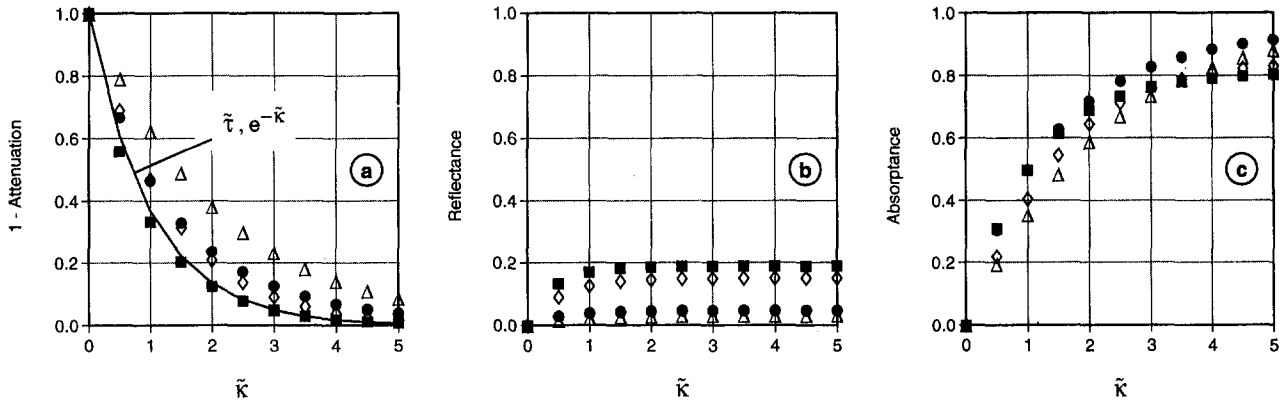



**Fig. 5 Figures 5(*a*), 5(*b*), and 5(*c*) show the 1 − attenuation, reflectance, and absorptance through the slab, respectively, as a function of the Planck mean optical thickness (see definitions in Eqs. (9), (10), and (11)). Only absorption/scattering processes are considered in these figures. Four cases are being investigated: (1) Mie-scattering particles under diffuse incident radiation (with symbol ●); (2) Mie-scattering particles under perpendicular incident radiation (with symbol △); (3) isotropic-scattering particles under diffuse incident radiation (with symbol ■); (4) isotropic-scattering particles under perpendicular incident radiation (with symbol ◇). In all four cases, the cloud consists of nongray $Fe_3O_4$ particles and the incident radiation has a 5780 K Planck spectral distribution.**

Note that this definition of attenuation considers radiation at all wavelengths traversing through the slab and exiting in any direction. 1 − attenuation, reflectance, and absorptance are plotted in Figs. 5(*a*), 5(*b*), and 5(*c*), respectively, as a function of the Planck mean optical thickness $\tilde{\kappa}$. Four cases are being investigated: (1) Mie-scattering particles under diffuse incident radiation; (2) Mie-scattering particles under perpendicular incident radiation; (3) isotropic-scattering particles under diffuse incident radiation; (4) isotropic-scattering particles under perpendicular incident radiation. In all four cases, the incident radiation has a 5780 K Planck spectral distribution, and the cloud consists of nongray $Fe_3O_4$ particles with $Q_K$ and $\Omega_\lambda$ given by Fig. 3. The comparison between these four cases presents the influence of the directional dependency of the incident radiation and the scattering phase function. As expected, perpendicular incident radiation, impinging normally on the front wall, is able to penetrate the cloud more efficiently than diffuse incident radiation having a directional distribution following Lambert's cosine law. Also, a cloud of Mie-scattering $Fe_3O_4$ particles permits radiation to penetrate deeper than a cloud of isotropic-scattering particles because, as seen in Fig. 2, $Fe_3O_4$ particles exhibit significant preference for forward scattering. Thus, case (2) (a cloud of Mie-scattering $Fe_3O_4$ particles under perpendicular incident radiation) gives the least attenuation, while case (3) (a cloud of isotropic-scattering particles under diffuse incident radiation) gives the largest attenuation. The difference is significant: case (3) needs a 2.25 optically thick slab in order to attenuate 90 percent of the incident radiation, while case (2) needs twice as much optical thickness to obtain the same result. For $\tilde{\kappa} = 1$, about 35 percent of the incident radiation is transmitted for case (3), 65 percent is transmitted for case (2), and 50 percent is transmitted for cases (1) and (4). The isotropic-scattering assumption leads to an error in the calculation of attenuation of up to 79 percent for diffuse incident radiation and $\tilde{\kappa} = 5$, and up to 80 percent for perpendicular incident radiation and $\tilde{\kappa} = 5$. For $\tilde{\kappa} = 1$, the error is 28 percent for diffuse incident radiation and 25 percent for perpendicular incident radiation.

When the objective is to utilize a cloud of particles as a means of shielding a surface from incident radiation, then case (3) is preferred. The optical thickness of the cloud could be optimized to meet the specific requirements of the reactor by changing either the volume fraction or the thickness of the cloud. The directional nature of the incident radiation could be modified by nonimaging optical elements. For example, in solar concentrators, the use of compound parabolic concentrators (CPCs) can boost concentration at the expense of making the incident radiation more diffuse, and vice versa (Welford and Winston, 1989).

The reflectance, i.e., radiation reflected back to its source after single or multiple scattering, could considerably hinder the transport of radiation into the heart of a cloud. All four cases show back-scattering increasing with the optical thickness of the cloud and approaching a constant value after $\tilde{\kappa} = 2.5$. Evidently, isotropic-scattering particles reflect more radiation than Mie-scattering $Fe_3O_4$ particles do. Quantitatively, this effect is about 4.2 times larger for diffuse incident radiation, and 5.6 times larger for perpendicular incident radiation. A bundle scattered by a Mie-scattering particle at the front layer of the cloud is most likely to penetrate further into the cloud. In contrast, a bundle scattered by an isotropic-scattering particle at the front layer has 50 percent chance of being reflected back and eventually lost. The percentage of bundles absorbed in the cloud, shown in Fig. 5(*c*), is determined by subtracting Figs. 5(*a*) and 5(*b*) from unity. This third figure becomes important when the objective is to maximize energy transfer to the cloud, as it is the case in volumetric solar receivers. It is observed, for example, that although Fig. 5(*a*) shows more radiation being attenuated for case (3) than for case (1), it does not necessarily imply more radiation being absorbed for case (3). Adversely, Fig. 5(*b*) shows more radiation being reflected for case (3) than for case (1). Examination of Fig. 5(*c*) shows, however, that there is no substantial difference on the net absorption capacity between cases (1) and (3) for $\tilde{\kappa} = 1$.

The intensity of monochromatic radiation incident normally on an absorbing-scattering slab of thickness $D$ is attenuated along its path according to Bouguer's law by a factor $e^{-K_\lambda D}$, for $K_\lambda$ independent of position in the medium. However, Bouguer's law is a particular case of the general equation of transfer when emission and scattering along the optical path are not included. By integrating Bouguer's law over the entire spectrum, a directional total transmittance for incident blackbody radiation can be defined as:

$$\tilde{\tau} = \frac{1}{\sigma T^4} \int_0^\infty e^{-K_\lambda D} e_{\lambda b}(\lambda, T) d\lambda \qquad (12)$$

Strictly, $1 - \tilde{\tau}$ gives the portion of Planck radiation lost by being absorbed or scattered away along the normal direction. The transmittance $\tilde{\tau}$, as defined by Eq. (12), is plotted in Fig. 5(*a*). A different approximation to calculate the mean attenuation of incident blackbody radiation over all wavelengths is to use Bouguer's law form with the Planck mean optical thickness, i.e., incident radiation being attenuated by a factor $e^{-\tilde{\kappa}}$. The $e^{-\tilde{\kappa}}$-approximation, as well as $\tilde{\tau}$, cannot predict the effect of the angular dependency of $\Phi_\lambda$, nor of the incident radiation. Nevertheless, their use is justified when compared with the complexity



Downloaded 12 Dec 2010 to 193.140.21.150. Redistribution subject to ASME license or copyright; see http://www.asme.org/terms/Terms_Use.cfm

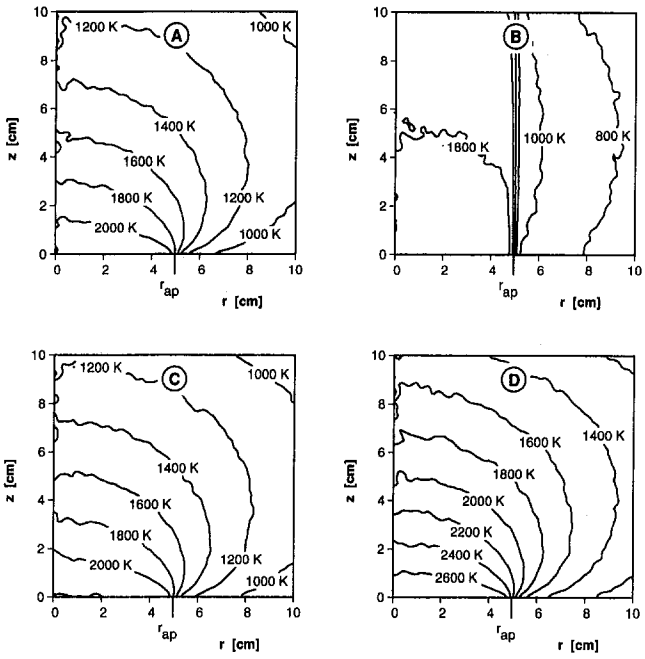



**Fig. 6 Figures 6(A), 6(B), 6(C), and 6(D) are the temperature distribution under radiative equilibrium for cases (A), (B), (C), and (D), respectively, and for $\tilde{\kappa} = 1$. Case (A) is the baseline; case (B) is the baseline with perpendicular incident radiation; case (C) is the baseline with isotropic-scattering particles ($\Phi_\lambda = 1$); case (D) is the baseline with a gray-isotropic medium having $\kappa_\lambda = \tilde{\kappa} = 1$, $\Omega_\lambda = \tilde{\Omega} = 0.58942$, and $\Phi_\lambda = 1$.**

of handling detailed spectral calculations. They give practically the same results and their curves lie close to the Monte Carlo solution obtained for isotropic scattering under diffuse incident radiation. However, a large error (up to 82 percent at $\tilde{\kappa} = 5$) is committed when either $\tilde{\tau}$ or the $e^{-\tilde{\kappa}}$ approximation are employed for treating Mie-scattering particles under perpendicular incident radiation.

Under radiative equilibrium, the temperature distribution within the cloud is calculated iteratively using Eq. (7). As the baseline we take a slab thickness $D = 0.1$ m, and a volume fraction $f_v = 1.4641 \times 10^{-5}$ (0.075841 kg of $Fe_3O_4$ particles per $m^3$ of slab space), so that the Planck mean optical thickness $\tilde{\kappa} = 1$. The aperture radius, $r_{ap} = D/2$. The power flux through this aperture is taken equal to 2500 kW/$m^2$, which is a solar flux intensity achievable with typical concentrating systems (Grasse et al., 1987). Thus, the total power entering the slab is 19.6 kW and each of the 5 million bundles carries $3.92 \times 10^{-6}$ kW. In addition, the baseline uses diffuse radiation with a 5780 K Planck distribution, incident upon a cloud of nongray Mie-scattering particles described by Figs. 2 and 3. Four new cases are analyzed: (A) the baseline; (B) the baseline with perpendicular incident radiation; (C) the baseline with isotropic-scattering particles ($\Phi_\lambda = 1$); (D) the baseline for a gray-isotropic medium having $\kappa_\lambda = \tilde{\kappa} = 1$, $\Omega_\lambda = \tilde{\Omega} = 0.5894$, and $\Phi_\lambda = 1$. Figures 6A, 6B, 6C, and 6D present the temperature distribution within the slab obtained for cases (A), (B), (C), and (D), respectively. Comparison between Figs. 6(A) and 6(B) shows a remarkable effect of the directional nature of the incident radiation. Radiation impinging normally to the slab is not absorbed efficiently by the cloud. This effect is explained by referring to Figs. 5(*b*) and 5(*c*), which show the least attenuation and the least absorptance for perpendicular incident radiation. A relatively small number of absorptions implies a small number of emissions as well, and consequently the improbability of radiation being distributed isotropically. Since forward scattering is favored for Mie-scattering $Fe_3O_4$ particles, a bundle entering perpendicularly through the aperture is likely to travel a short distance in the cloud before exiting through the back wall. This reduces considerably the probability of intercepting a particle and being absorbed. In contrast, a bundle entering in a diffuse manner has evidently a longer path length to the back wall and, therefore, a higher probability of intercepting a particle, of being absorbed, and of being emitted isotropically. Comparison between Figs. 6(A) and 6(C) presents the effect of $\Phi_\lambda$ by taking either Mie-scattering or isotropic-scattering particles. The difference is practically negligible for $\tilde{\kappa} = 1$. The number of absorptions for cases (A) and (C) are nearly the same for $\tilde{\kappa} = 1$, as already indicated in Fig. 5(*c*). Since emission is isotropic for both cases, radiation transfer within the medium becomes less dependent on the directional properties of $\Phi_\lambda$. Figures 5(*b*) and 5(*c*) show a larger reflectance and a smaller absorptance for case (C), compared to case (A), when $\tilde{\kappa} > 1$. Therefore, it is expected that temperatures will be underestimated by taking the isotropic approximation for $\tilde{\kappa} > 1$. This was corroborated for $\tilde{\kappa} = 5$.

The gray approximation, case (D), does not yield a sufficiently accurate solution, when compared to the baseline case (A). Temperatures are overestimated by about 27 percent. The reason is that, by definition, $\tilde{\kappa}$ and $\tilde{\Omega}$ are the mean of the spectral $\kappa_\lambda$ and $\Omega_\lambda$ when weighted by a 5780 K blackbody emission spectrum, Eqs. (2) and (3). However, the spectral distribution of the incident radiation does not remain unchanged as it travels through the cloud. Instead, it is shifted to longer wavelengths due to the emission of radiation by particles at temperatures much lower than 5780 K. The magnitude of this wavelength shift is illustrated in Fig. 7. It shows the probability density function of wavelengths assigned to all energy bundles entering through the aperture and emitted by particles in radiative equilibrium. Included for comparison is the probability density function of wavelengths assigned only to bundles entering through the aperture. The shift in the wavelength distribution from the one obtained for incident blackbody radiation to the one obtained for the baseline case (A) is the cause for the error in the gray approximation (case (D)). Longer wavelengths of emission result in higher absorption efficiencies $Q_a$ (see Fig. 3), and consequently in higher values for $a_\lambda$, which according to Kirchhoff's law is equal to the emission coefficient. Therefore, the nongray cloud is absorbing radiation mostly in the spectral region around 0.5 $\mu$m, but emits radiation in the spectral region around 3 $\mu$m, where $a_\lambda$ is somewhat higher. The gray cloud instead uses a constant absorption coefficient for both absorption and emission, independent of wavelength. This constant value is the Planck mean of the spectral $a_\lambda$, equal to $\tilde{\kappa}(1 - \tilde{\Omega})/D$. By applying Eq. (7), the equilibrium temperatures obtained for the gray approximation are higher than those obtained for the nongray cloud. For purposes of solar energy collection, it would be desirable to have a cloud of particles with a high $a_\lambda$ in the visible spectrum where the solar energy peaks, but

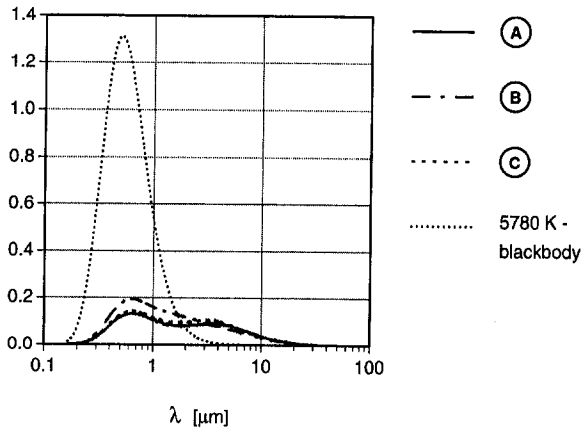



**Fig. 7 Probability density functions of wavelengths assigned to energy bundles for incident blackbody radiation at 5780 K, and for cases (A), (B), and (C) under radiative equilibrium**



Downloaded 12 Dec 2010 to 193.140.21.150. Redistribution subject to ASME license or copyright; see http://www.asme.org/terms/Terms_Use.cfm

with a low $a_\lambda$ in the IR spectrum where emission peaks. Unfortunately, a cloud of $Fe_3O_4$ particles features just the opposite spectral behavior.

Cases (B) and (C) are also included in Fig. 7. The difference between the curves obtained for cases (A) and (B) is due to the fact that more absorption-emission processes occur for case (A), resulting in more wavelengths assigned to bundles at the particle temperature. No significant difference is observed between cases (A) and (C), as seen already in the temperature distribution maps of Figs. 6(A) and 6(C).

Finally, Fig. 8 presents the temperature distribution within the slab obtained for the baseline case with $\tilde{\kappa} = 5$. A cloud 5 times more dense or 5 times thicker achieves temperatures that are about 10 percent higher. For the given conditions, temperatures of the order of 2250 K are being attained in the proximity of the aperture, which are about the level of temperatures required to conduct the thermal reduction of $Fe_3O_4$ to FeO. Temperatures become moderate as we approach the back wall or as we go farther away from the $z$ axis, as a result of the shielding effect of the cloud. The temperature gradient between front and back layers is about 1000 K. A reactor design based on these results would require materials of construction able to withstand about 1200 K.

Although not considered in this study, polydispersions can be treated by integration of the phase function and attenuation efficiencies over the particle size distribution (see, for example, Mengüc and Viskanta, 1986; Gupta et al., 1983). These integrations are executed external to the Monte Carlo simulation and therefore have no influence on its computational time or accuracy. The mean properties obtained for coarse size distributions of polydispersions will most probably exhibit a lesser (or smoother) dependency on $\lambda$ and $\xi$, and, as opposed to monodispersions, the cloud selectivity might become unimportant. Also not included in this study, reflections from nongray and directional-dependent reflective boundary surfaces can be easily implemented in the Monte Carlo simulation. Reacting clouds undergoing exothermal/endothermal chemical transformations may be simulated by introducing a source/sink of energy in each particle equal to the enthalpy change of the reaction at the particle temperature. Particles or boundary walls subjected to convection heat losses could be treated in a similar manner, where the sink of energy is calculated from the heat transfer coefficient and the temperature difference between solids and flow. However, if the flow velocity and temperature fields are not prescribed, the equation of radiative transfer and the flow equations (continuity, momentum, and energy) are coupled, and their solution requires an iterative process. Simplified analysis of combined radiation and convection in a particulate-laden flow has been presented by Kumar and Tien (1990). Insofar as the transient behavior is concerned, convective transfer rates have been found to be comparable to radiative ones for small particles ($d < 1$ $\mu$m), while for particles larger than 1 mm in diameter, the gas temperature stays unchanged during rapid heating of the particles (Wang and Yuen, 1987).

## 4 Conclusions

A cloud of $Fe_3O_4$ particles under concentrated solar irradiation has been investigated by the Monte Carlo method. Special attention was devoted to the realistic case of a nongray, nonisothermal, absorbing, emitting, and anisotropically scattering medium. The spectrally and directionally dependent optical properties of the particles were calculated using Mie theory. The appropriate cumulative distribution functions were incorporated in the Monte Carlo simulation via Bezier surfaces, which permitted the use of large samples of energy bundles (within a reasonable computational time) and consequently better accuracy and repeatability.

The effect of directional dependency of the incident radiation and the scattering phase function was shown to be significant when calculating the attenuation of radiation at all wavelengths and directions. The transmittance $\tilde{\tau}$, defined by Eq. (12), or the $e^{-\tilde{\kappa}}$ approximation, can predict the attenuation by an isotropic-scattering medium under diffuse radiation, but is not suitable for treating a cloud of Mie-scattering particles under perpendicular incident radiation. The isotropic-scattering assumption leads to an error in the calculation of attenuation of up to 79 percent for diffuse incident radiation, and up to 80 percent for perpendicular incident radiation. Temperature distributions within the cloud were calculated under radiative equilibrium. The directional nature of the incident radiation was found to have a remarkable effect on the temperature solution. It was demonstrated that the gray approximation does not yield accurate results because it ignores the shift in the spectral distribution to longer wavelengths where the spectral absorption coefficient is higher. When the gray approximation with Planck mean values is used, temperatures are overestimated by about 27 percent.

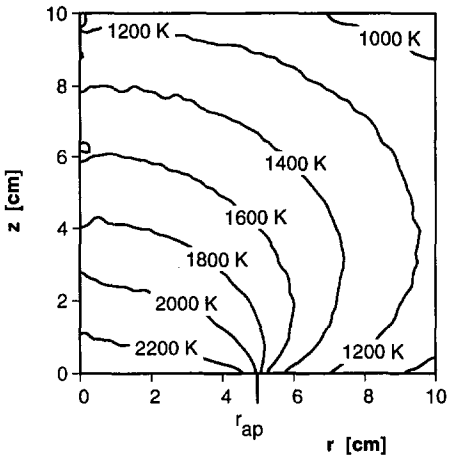



**Fig. 8 Temperature distribution under radiative equilibrium for the baseline case and $\tilde{\kappa} = 5$**


## Acknowledgments

This work has been funded by the Swiss Federal Office of Energy, BEW Contract EF-REN(92)033.


## References


Abdelrahman, M., Fumeaux, P., and Suter, P., 1979, "Study of Solid-Gas-Suspensions Used for Direct Absorption of Concentrated Solar Radiation," *Solar Energy*, Vol. 22, pp. 45–48.

Bohren, F. C., and Huffman, D. R., 1983, *Absorption and Scattering of Light by Small Particles*, Wiley, New York, Appendix A: BHMIE subroutine, pp. 477–482.

Canadas, L., Salvador, L., and Ollero, P., 1990, "Radiative Heat-Transfer Model in the Interior of a Pulverized Coal Furnace," *Ind. Eng. Chem. Res.*, Vol. 29, pp. 669–675.

Edwards, D. K., Glassen, L. K., Hauser, W. C., and Tuchscher, J. S., 1967, "Radiation Heat Transfer in Nonisothermal Nongray Gases," ASME JOURNAL HEAT TRANSFER, Vol. 89, pp. 219–229.

Engeln-Muellges, G., and Reutter, F., 1987, *Numerische Mathematik fuer Ingenieure*, B. I. Wissenschaftsverlag, Zurich, pp. 339–347.

Evans, G., Houf, W., Greif, R., and Crowe, C., 1987, "Gas-Particle Flow Within a High Temperature Solar Cavity Receiver Including Radiation Heat Transfer," *ASME Journal of Solar Energy Engineering*, Vol. 109, pp. 134–142.

Grasse, W., Becker, M., and Finnstroem, B., 1987, "Solar Energy for High Temperature Technology and Applications," DFVLR, Cologne, Germany.

Gupta, R. P., Wall, T. F., and Truelove, J. S., 1983, "Radiative Scatter by Fly Ash in Pulverized-Coal-Fired Furnaces: Application of the Monte Carlo Method to Anisotropic Scatter," *Int. J. Heat Mass Transfer*, Vol. 26, pp. 1649–1660.

Heaslet, M. A., and Warming, R. F., 1965, "Radiative Transport and Wall Temperature Slip in an Planar Medium," *Int. J. Heat Mass Transfer*, Vol. 8, pp. 979–994.

Hellwege, K. H., ed., 1982, *Landolt-Boernstein Numerical Data and Functional Relationships in Science and Technology*, New Series, Springer-Verlag, Berlin, Vol. 17g, p. 543.

Houf, W. G., and Greif, R., 1987, "Radiant Transfer in a Solar Absorbing Particle Laden Flow," *Chemical Engineering Communications*, Vol. 51, pp. 153–165.

Howell, J. R., and Perlmutter, M., 1964, "Monte Carlo Solution of Thermal Transfer Through Radiant Media Between Gray Walls," ASME JOURNAL OF HEAT TRANSFER, Vol. 86C, pp. 116–122.





Downloaded 12 Dec 2010 to 193.140.21.150. Redistribution subject to ASME license or copyright; see http://www.asme.org/terms/Terms_Use.cfm

Hsia, H. M., and Love, T. J., 1967, "Radiative Heat Transfer Between Parallel Plates Separated by a Nonisothermal Medium With Anisotropic Scattering," ASME JOURNAL OF HEAT TRANSFER, Vol. 89C, pp. 197–204.

Hunt, A. J., and Brown, C. T., 1983, "Solar Test Results of an Advanced Direct Absorption High Temperature Gas Receiver (SPHER)," *Proc. ISES Solar World Congress,* Perth, Australia, Aug. 15–19, Vol. 2, pp. 959–962.

Hunt, A. J., Ayer, J., Hull, P., Miller, F., Noring, J. E., and Worth, D., 1986, "Solar Radiant Heating of Gas-Particle Mixtures," Lawrence Berkeley Laboratory, University of California LBL-22743, Berkeley, CA 94720.

Kim, T. K., Menart, J. A., and Lee, H. S., 1991, "Nongray Radiative Gas Analysis Using the S-N Discrete Ordinates Method," ASME JOURNAL OF HEAT TRANSFER, Vol. 113, pp. 946–952.

Kumar, S., and Tien, C. L., 1990, "Analysis of Combined Radiation and Convection in a Particulate-Laden Liquid Film," *ASME Journal Solar Energy Engineering,* Vol. 112, pp. 293–300.

Mengüc, M. P., and Viskanta, R., 1986, "An Assessment of Spectral Radiative Heat Transfer Predictions for a Pulverized Coal-Fired Furnace," *Heat Transfer—1986,* Vol. 2, pp. 815–820.

Miller, F., and Koenigsdorff, R., 1991, "Theoretical Analysis of a High-Temperature Small-Particle Solar Receiver," *Solar Energy Materials,* Vol. 24, pp. 210–221.

Modest, M., and Azad, F., 1980, "The Influence and Treatment of Mie-Anisotropic Scattering in Radiative Heat Transfer," ASME JOURNAL OF HEAT TRANSFER, Vol. 102, pp. 92–98.

Nakamura, T., 1977, "Hydrogen Production From Water Utilizing Solar Heat at High Temperatures," *Solar Energy,* Vol. 19, pp. 467–475.

Rightley, M. J., Matthews, L., and Mulholland, G. P., 1992, "Experimental Characterization of the Heat Transfer in a Free-Falling-Particle Receiver," *Solar Energy,* Vol. 48, pp. 363–374.

Sasse, C., 1992, Ph.D. Thesis, University of Karlsruhe, Germany.

Siegel, R., and Howell, J. R., 1992, *Thermal Radiation Heat Transfer,* 3rd ed., Hemisphere Publishing Corp., Washington DC.

Sparrow, E. M., and Cess, R. D., 1966, *Radiation Heat Transfer,* Wadsworth Publishing Company, Belmont, CA.

Tien, C. L., and Drolen, B. L., 1987, "Thermal Radiation in Particulate Media With Dependent and Independent Scattering," *A. Rev. Numer. Fluid Mech. Heat Transfer,* Vol. 1, pp. 1–32.

Usiskin, C. M., and Sparrow, E. M., 1960, "Thermal Radiation Between Parallel Plates Separated by an Absorbing-Emitting Nonisothermal Gas," *Int. J. Heat Mass Transfer,* Vol. 1, pp. 28–36.

Wang, K. Y., and Yuen, W. W., 1987, "Rapid Heating of Gas/Small Particle Mixture," *ASME Journal Solar Energy Engineering,* Vol. 109, pp. 143–149.

Welford, W. T., and Winston, R., 1989, *High Collection Nonimaging Optics,* Academic Press, Inc., San Diego, CA.

Yamada, Y., Cartigny, J. D., and Tien, C. L., 1986, "Radiative Transfer With Dependent Scattering by Particles: Part 2—Experimental Investigation," ASME JOURNAL OF HEAT TRANSFER, Vol. 108, pp. 614–618.

Yuen, W. W., and Ma, A., 1992, "Evaluation of Total Emittance of an Isothermal Nongray Absorbing, Scattering Gas-Particle Mixture Based on the Concept of Absorption Mean Beam Length," ASME JOURNAL OF HEAT TRANSFER, Vol. 114, pp. 653–658.



Downloaded 12 Dec 2010 to 193.140.21.150. Redistribution subject to ASME license or copyright; see http://www.asme.org/terms/Terms_Use.cfm

# Pigments to Reflect the Infrared Radiation From Fire

**P. Berdahl**
Energy & Environment Division,
Lawrence Berkeley Laboratory,
Berkeley, CA 94720

*Conventional paints transmit or absorb most of the intense infrared radiation emitted by fire, a fact that contributes to the spread of fire. Techniques used for design of coatings with high visible reflectivity are here adapted to the design of coatings that have high reflectivity in the 1 to 8 μm wavelength range important in fires. Promising materials for pigments include titanium dioxide, iron oxide, chromium oxide, and silicon, with particle diameters in the 1 to 2 μm range. Aluminum flake pigments are also effective. Pigment synthesis by the deposition of coatings on mica flakes is briefly discussed.*

## Introduction

It is well known that infrared radiation emitted by fire contributes to its spread. Convection is important as well, including the advection of burning embers. The relative importance of radiative transfer differs from case to case, but it is usually quite important. In the United Kingdom, minimum building separation distances are determined by consideration of the condition that the radiant flux on the building must not exceed 12 kW $m^{-2}$ if the neighboring structure is fully involved in fire (Law, 1963; Drysdale, 1990). The value 12 kW $m^{-2}$ (about 12 times the radiant flux of sunlight) is used because it is an estimate of the minimum radiant flux that can cause the ignition of wood (Drysdale, 1990; Lawson and Simms, 1952). Further evidence for the importance of infrared radiative transfer comes from tests measuring the rate of flame spread along walls and floors. These measurements demonstrate that the rate increases dramatically when the burning surface is irradiated with thermal radiation (Quintiere, 1981; Drysdale, 1990).

In view of the key role played by the absorption of infrared radiation by materials in the spread of fire, it seems reasonable, and in fact overdue, to consider coating the surfaces of combustible materials such as wood, polymers, fabrics, paper, etc., to provide an infrared reflective barrier, which could reduce the fire hazards associated with these materials. No coating can provide complete protection, because hot gas in direct contact with a combustible material can always ignite it. Rather, the benefits to be obtained are the absence of ignition despite the proximity of a heat source and, if ignition occurs, a delay in the ignition time and a decrease in the rate of flame spread.

A knowledge of the spectrum of the radiation from fire is necessary to determine the spectral range in which a fire-reflective coating should perform. Data from a burning wooden crib (Hagglund and Persson, 1976) show a smooth, blackbody-like spectrum extending from 1 to beyond 5 μm in wavelength, with superimposed emission peaks (at 1.8, 2.8, and 4.4 μm) due to $H_2O$ and $CO_2$. In contrast, data taken from airborne observation of a forest fire (Stearns et al., 1986) show dips at the same spectral locations due to absorption (by $H_2O$ and $CO_2$) in the cool air between emission and observation. The crossover from peaks to dips should occur at path lengths on the order of 1 m, since this is roughly the mean free path for propagation at the wavelengths of strong absorption (LaRocca, 1978). Soot in a fire leads to a more continuous broadband emission; that is, it obscures the emission peaks that would otherwise be observed. Considering the complexity of thermal emission from fire, it is particularly attractive to utilize a simple blackbody spectrum to represent the radiation. This approximation is qualitatively correct, and a more accurate treatment would require a rather detailed model of the radiative transport. The best blackbody temperature to employ, of course, depends upon the particular fire. The 1500 K used in what follows is about as high a temperature as an ordinary fire is likely to have (e.g., Drysdale (1990) suggests a maximum temperature of 1373 K). Gas-fired radiant panels used to test flammability of materials are often operated at temperatures near 1000 K (Becker et al., 1990). The 12 kW $m^{-2}$ criterion for ignition of wood translates, for full field of view of the radiator, to 650 K radiant temperature. Thus 650 K is a rough estimate of the minimum significant radiant temperature, although even lower radiant fluxes can contribute significantly to the rate of flame spread. For 1500 K radiation, the important wavelength range is roughly 1 to 8 μm. This range shifts inversely with absolute temperature. For example, it is 2 to 16 μm for cooler 750 K radiation. While 1500 K radiation is visible as an orange color, there is virtually no overlap with the visible spectrum. In particular, the visible appearance of a coating need have no relation to the reflectance for the radiation from fire.

The physical fact that the reflectivity for fire radiation can be quite low even for visibly reflective (white) coatings has clearly impeded progress in the development of reflective coatings. For example, two papers on fire-resistant coating technology (Ensminger, 1988; Ellis, 1992) refer approvingly to the use of $TiO_2$ pigments to achieve high infrared reflectivity. However, it will become clear that the infrared reflectivity is too small at longer wavelengths to provide much benefit.

The near-infrared reflectance (0.7–2.5 μm) is an important attribute of camouflage coatings useful in military applications and also for coatings to control the absorption of the solar infrared spectrum. This spectral range overlaps with the 1–8 μm range of primary interest here, and similar coatings are considered. An important contribution to this work has been presented recently by Brady and Wake (1992).

For the sake of simplicity, the emphasis in this paper is on polymeric coatings with $TiO_2$ (rutile) pigment. The effect of particle size on the spectral reflectance will be computed, to show explicitly how the reflectance of fire radiation can be greatly increased by the use of suitable pigment particles. These particles are 5 to 10 times the conventional 200 nm size used for visual opacity. The paper concludes with a discussion of alternative materials and approaches for formulating coatings to reflect fire radiation.

## Numerical Model

The pigment particles are assumed to be nonabsorbing spheres, which are imbedded in a transparent layer over an absorbing substrate. Thus Mie theory can be used to determine the exact scattering cross sections. The numerical model is based on the model employed by Palmer et al. (1989). In this one-dimensional, two-stream model the radiant energy flows are simply

Contributed by the Heat Transfer Division for publication in the JOURNAL OF HEAT TRANSFER. Manuscript received by the Heat Transfer Division April 1994; revision received August 1994. Keywords: Fire/Flames, Radiation, Transient and Unsteady Heat Transfer. Associate Technical Editor: W. L. Grosshandler.



**Copyright © 1995 by ASME**

Downloaded 12 Dec 2010 to 193.140.21.150. Redistribution subject to ASME license or copyright; see http://www.asme.org/terms/Terms_Use.cfm

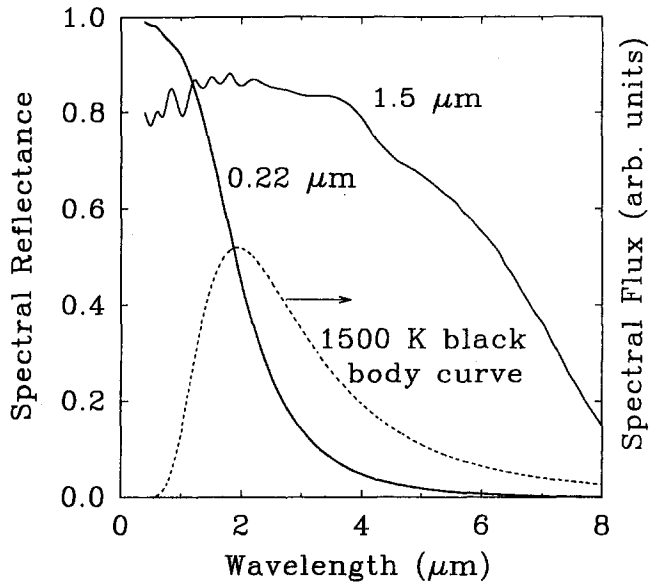



**Fig. 1 Spectral reflectance computed for 100-μm-thick layers with 0.1 volume fraction of rutile pigment, for particle diameters of 0.22 and 1.5 μm. The dashed curve shows the spectral distribution of 1500 K blackbody radiation, which simulates emission from a fire. The decline of the 1.5 μm curve at long wavelengths is in part due to dispersion; the refractive index of $TiO_2$ declines to 2.0 at 8 μm (Cronemeyer, 1952).**

divided into upward and downward flows. Each particle is assumed to scatter independently. A scattering coefficient $s$ characterizes the probability that an upward-directed photon is scattered downward or a downward-directed photon is scattered upward. The effects of multiple scattering, essential for simulation of pigmented coatings, are straightforward to handle in such a model. The spectral reflectivity of the coating is given by

$$R = sfh/(2 + sfh), \tag{1}$$

where $f$ is the volume fraction of the pigment in the film, $h$ is the film thickness, and the scattering coefficient $s$ is determined from the differential scattering cross section per unit particle volume, $\sigma(\theta, \phi)$:

$$s = \int d\Omega\, \sigma(\theta, \phi)\, [1 - \cos(\theta)]. \tag{2}$$

Thus $s$ is not the simple sum over scattering angles of the differential cross section, but includes the weighting function $[1 - \cos(\theta)]$. This weighting function imposes the physically important constraint that scattering at small angles does not contribute to the film reflectivity $R$. The nonlinear dependence of $R$ on $s$ in Eq. (1) is a multiple scattering effect.

For purposes of computation, Eq. (2) is rewritten in the form

$$s = Q_{sca} - gQ_{sca}, \tag{3}$$

where the first term is the total cross section, $Q_{sca} = \int d\Omega\, \sigma(\theta, \phi)$, and the second term defines $g$, the asymmetry parameter, as the average of the cosine of the scattering angle. The total cross section was computed using the subroutine BHMIE listed in Appendix A of the monograph by Bohren and Huffman (1983); the product $gQ_{sca}$ was computed in analogous fashion from the formula in Sec. 4.5 of this reference.

The refractive index values for $TiO_2$ were taken initially from the work of Devore (1951) as compiled by Ribarsky (1985), to compare with the results of Palmer et al. (1989). The $TiO_2$ (rutile) crystals are anisotropic, but refractive index values averaged over orientation are sufficiently accurate for the present work. For example, taking the average refractive index as $\frac{1}{3}$ of that for electric field parallel to the $c$-axis plus $\frac{2}{3}$ of that for field perpendicular, with wavelength of 546.1 nm, with refractive index of the medium of 1.0, it was possible to reproduce the scattering results for $Q_{sca}$ and $g$ shown in Figs. 1 and 3 of Palmer et al. (1989), which were computed for the same conditions. However, slightly different refractive index values published by Cronemeyer (1952), as compiled by Ribarsky (1985), were used for the remainder of this work because they extend further into the infrared, to 8 μm wavelength. The mean value is 2.7 in the visible, 2.5 at 3 μm, and declines to 2 at 8 μm. The imaginary (absorptive) part of the refractive index of $TiO_2$ is quite small (and dependent on impurity concentration) from 0.4 μm to 11 μm. At longer wavelengths the absorption becomes quite significant due to optical phonon absorption. In what follows, the refractive index of the medium is taken as 1.55 to simulate a typical transparent binder.

## Results

The computed spectral reflectance is shown as a function of wavelength in Fig. 1, for pigment particle diameters of 0.22 μm, optimized for visible light scattering, and for 1.5 μm, optimized for scattering of 1500 K blackbody radiation. Experimental measurements (Touloukian et al., 1972) on white coatings are in good qualitative agreement with the computations for 0.22 μm particles, and also in agreement with the trend that larger particle sizes lead to larger infrared reflectances. The dashed curve shows the spectral distribution of 1500 K radiation. It is clear that the conventional white coating becomes transparent with increase in wavelength, and that therefore it is ineffective for reflection of fire radiation. Physically, the particle size is much smaller than the wavelength, so that the scattering decreases in proportion to the inverse fourth power of the wavelength (Rayleigh's law). The visible reflectance of the conventional coating is about 0.98; the reflectance for 1500 K radiation is only 0.30. (The reflectance for 1500 K radiation is defined as the ratio of reflected to incident energy, with a 1500 K incident spectrum.) Furthermore, if a smaller particle size were to be used, or if a lower radiation temperature were employed, the reflectance is even smaller. In contrast, the "fire" reflectance of a layer with optimized particle size is 0.80. In this example, the 1500 K absorptance is reduced by a factor of 3.5. For this reason, the rate of temperature rise of a surface exposed to radiant heating will be reduced by this factor.

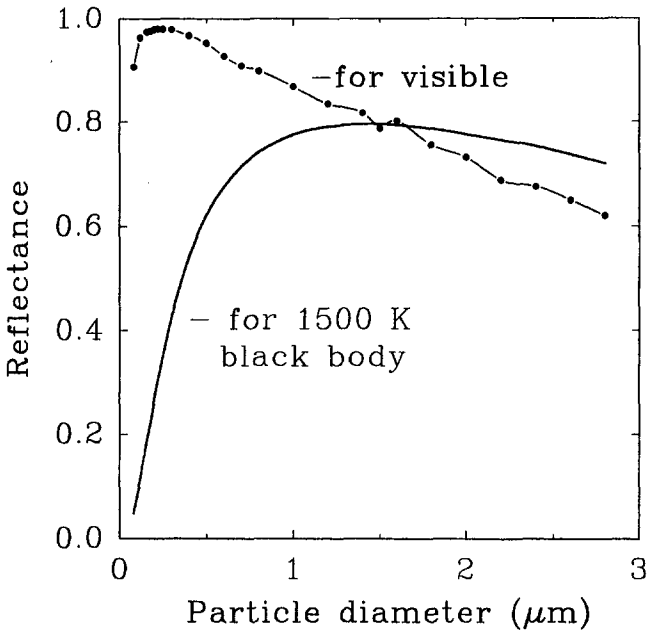



**Fig. 2 Visible and 1500 K reflectances for 100 μm layer with 0.1 volume fraction of rutile pigment, as a function of particle diameter**



Downloaded 12 Dec 2010 to 193.140.21.150. Redistribution subject to ASME license or copyright; see http://www.asme.org/terms/Terms_Use.cfm

The increase in infrared reflectance is accompanied by a decrease in visible reflectance, from 0.98 to 0.80.

Figure 2 summarizes how the visible and 1500 K reflectances vary with particle size. The 1500 K reflectance is very sensitive to particle size for small particles. The near-infrared reflectance (at 2.5 $\mu$m), can in fact be used to monitor particle flocculation (Rutherford and Simpson, 1985), with higher infrared reflectance indicative of the clumping of pigment particles. The optimum particle diameter for high 1500 K radiation reflectance is 1 to 2 $\mu$m. The relatively broad maximum in the curve is due to the wide spectral range of the heat radiation.

The 80 percent reflectance for fire radiation can in principle be increased further, by the use of thicker films or the use of higher pigment volume concentrations. Figure 3 shows the computed results for three different particle sizes, for a film which is 4 times thicker (400 $\mu$m). The 1500 K reflectances corresponding to these results are 0.80, 0.91, and 0.93 for particle diameters of 0.5, 1.0, and 1.5 $\mu$m, respectively. However, reflectances as high as 90 percent may be difficult to achieve, due to absorption in the binder.

Another pigment of potential interest is elemental silicon, which has absorption in the visible range, but which is transparent at wavelengths beyond 1.1 $\mu$m. The refractive index is very large, namely 3.45. Figure 4 shows the spectral reflectance of a 100 $\mu$m layer containing silicon spheres. Comparison with Fig. 1 shows that higher infrared reflectance can be obtained than with a similar film containing $TiO_2$. Due to the higher refractive index, the optimum particle size is a bit smaller, about 0.75 to 1.5 $\mu$m. The integrated 1500 K reflectance is roughly 0.9.

Of course, any material that is transparent to infrared radiation in the required spectral range and also has a refractive index substantially different from its binder's refractive index (e.g., 1.5) may be used as an infrared reflecting pigment. Examples of additional materials and their approximate refractive indices are: $Fe_2O_3$ (3.1), a red pigment, the anatase phase of $TiO_2$ (2.5), $Cr_2O_3$ (2.5), a green pigment, ZnS (2.4), $Sb_2O_3$ (2.2), $ZrO_2$ (2.1), and ZnO (2.0).

While the above-mentioned materials are substantially nonabsorbing in much of the infrared, they typically have optical phonon absorption, which limits the longest wavelength they can reflect. Thus $TiO_2$ starts absorbing strongly at about 12 $\mu$m, $Sb_2O_3$ at about 12.5 $\mu$m, $Fe_2O_3$ at about 14 $\mu$m, $Cr_2O_3$ at greater than about 14 $\mu$m, and ZnO at about 17 $\mu$m. Elemental silicon is nonabsorbing from about 1.1 to about 30 $\mu$m, because its phonon modes are not infrared active. Likewise aluminum and other metal flakes (see below) are reflective throughout the infrared region. Thus, if relatively cool 750 K radiation is to be reflected (2 to 16 $\mu$m range), then Si, $Cr_2O_3$, metal flakes, and ZnO may be preferred over $TiO_2$.

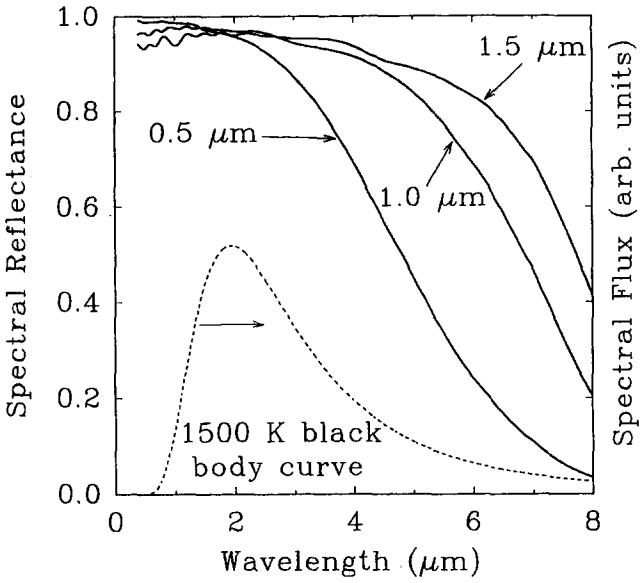



**Fig. 3 Spectral reflectance computed for 400-$\mu$m-thick layers with 0.1 volume fraction of rutile pigment, for particle diameters of 0.5, 1.0, and 1.5 $\mu$m**

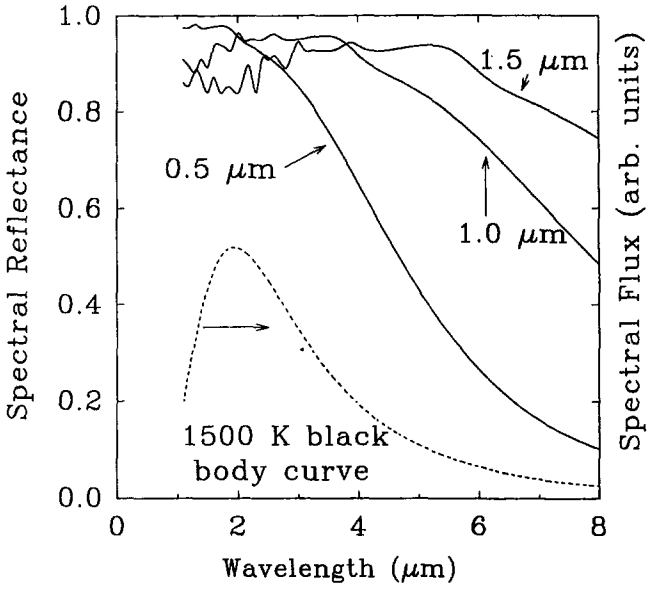



**Fig. 4 Spectral reflectance for a 100-$\mu$m-thick layers with 0.1 volume fraction of silicon spheres, for particle diameters of 0.5, 1.0, and 1.5 $\mu$m. Below 1.1 $\mu$m silicon becomes absorptive (not shown).**

Coatings of high-index materials such as $TiO_2$ and $Fe_2O_3$ on mica flakes are presently used to fabricate pigments that display color due to optical interference (Greenstein, 1988). Presumably the same techniques can be employed to reflect infrared radiation, by the use of thicker mica flakes and thicker high-index coatings. For this purpose it may prove desirable to employ synthetic fluorophlogopite micas in which the (infrared absorbing) OH groups have been eliminated by the use of fluorine substitution (Hawley, 1988). To achieve high reflectance over a wide spectral range, it may be necessary to use more than one type of coated flake.

Another important pigment for coatings that reflect infrared radiation is aluminum metal in the form of thin flakes. (Flakes of other metals could be used as well.) Aluminum is reflective in the infrared due to the high concentration of mobile electrons. The infrared absorption of Al-pigmented paint may be expected to be due primarily to absorption in the binder and coatings on the Al flakes. "Leafing" aluminum paints should be particularly reflective. These coatings contain overlapping pigment flakes, which are parallel to and concentrated near the surface of the binder (Hare, 1992). One set of measurements (Touloukian et al., 1972) shows Al paint reflectance values of 0.75 to 0.8 for the key spectral range of 1 to 8 $\mu$m.

A further type of infrared reflective pigment, one which is *transparent* in the visual range, can be formulated based on the technology of low emittance coatings for windows (Granqvist, 1990; Stjerna and Granqvist, 1990). These coatings are composed of transparent semiconductors, which are doped to provide a high concentration of free charge carriers. At low frequencies (i.e., in the infrared) the free carriers cause reflection, but above the plasma frequency the coating becomes transparent. The concentration of free carriers may be adjusted to provide the desired plasma frequency. Examples are ZnO:Al, $In_2O_3$:Sn, and $SnO_2$:F. These and similar materials can be used to coat mica flakes to produce an infrared reflecting pigment. The advantage of transparency or translucency in the visual range is that the visual appearance of a surface (e.g., wood) need not be determined by the infrared reflective coating.



Downloaded 12 Dec 2010 to 193.140.21.150. Redistribution subject to ASME license or copyright; see http://www.asme.org/terms/Terms_Use.cfm

Yet another option, used in the low-emittance window coating industry, is the use of very thin (~10 nm) noble metal coatings (Smith et al., 1986). Like the semiconductor coatings, they are transparent in the visible and reflective in the infrared, and could be employed in a similar way on mica flakes.

Finally, it seems worthwhile to point out explicitly that since many coatings now in use are not strongly absorptive in the infrared, but are transparent, it is possible to use a reflective undercoat to provide enhanced infrared reflectivity.

## Effects of the Binder

So far the absorption of infrared radiation by the binder supporting the pigment has been neglected. However, most materials exhibit some absorption in the 1 to 8 $\mu$m wavelength range, due to vibrational modes of the molecules in the material. This section contains a qualitative discussion of this issue.

Organic polymers exhibit strong absorption near 3.4 $\mu$m due to C–H stretching vibrations (Conley, 1972). The precise spectral location and width of the absorption depend on the particular polymer, but the width is often only 0.1–0.2 $\mu$m, so that the resulting 1500 K radiation absorption need not exceed a few percent. Other, weaker, C–H absorption features occur at 2.0–2.4, 1.6–1.8, and 1.1–1.2 $\mu$m. The carbonyl group (C=O) has absorption at 5.75 $\mu$m; carbon–carbon bonds are associated with absorption near 6.1 $\mu$m. In addition to this absorption at discrete wavelengths, organic polymers also exhibit a poorly understood "continuous" or background absorption, which has no marked spectral structure. This absorption could be due to the continuum distribution of vibrational modes in amorphous polymer regions (Zallen, 1983). As a specific example, consider a polyethylene film of 50 $\mu$m thickness with a normal spectral transmittance of about 0.78 at 5 $\mu$m wavelength (Berdahl et al., 1983). Its reflectance is 0.08, so that the absorptance is 0.14. This level of absorptance is large enough to have a significant effect on a pigment-filled film. Additional data on background absorption in polyethylene are given by Nilsson et al. (1992) who suggest that it may be due to impurities. Clearly, more work is needed to characterize the infrared absorption of polymers quantitatively, in order to clarify the potential performance of infrared reflective paints. Qualitatively, it appears that overall 1500 K reflectances of 0.8 are achievable with $TiO_2$ pigment, but it is not clear to what extent polymer absorption will hinder the achievement of much higher values.

Inorganic silicate binders (Brady and Wake, 1992; Brady, 1987) may prove advantageous in the formulation of infrared reflective coatings. Silicon–oxygen bonds cause absorption near 9 $\mu$m, and other vibrational modes are not likely to be situated at shorter wavelengths if the involved atoms are heavy (e.g., K, Na, Al).

In general, objectionable absorption in the 1 to 8 $\mu$m wavelength range is likely to be due to the presence of strongly bonded light atoms, especially hydrogen, which can vibrate at sufficiently high frequencies. (The vibrational frequency is inversely proportional to the square root of the atomic mass.) The presence of OH groups, in either pigments or binder, leads to broad absorption in the 2.9 $\mu$m region, with an overtone at 1.4 $\mu$m. The water molecule absorbs strongly at 1.4, 1.9, 2.7, 5.9, and 6.6 $\mu$m (LaRocca, 1978). Thus, in particular, pigments with water of hydration should be avoided.

## Conclusions

It has been shown that suitable pigments can be synthesized that can greatly enhance the reflectance of coated surfaces for the radiation emitted by fire. Research is now needed to advance the development of coatings with high reflectance for fire radiation, and to determine the best applications of these coatings to enhance fire safety.


## Acknowledgments

A. Rosenfeld and A. Young catalyzed the initiation of this work. E. Raicu assisted with a literature search and emphasized the importance of aluminum pigment. J. Cole pointed out the need for visually transparent coatings. R. B. Williamson provided valuable advice on the subject of fire protection engineering. Valuable conversations with R. Brady, B. Palmer, and C. Bohren are also acknowledged.

The work reported here was funded by the California Institute for Energy Efficiency (CIEE), a research unit of the University of California. Publication of research results does not imply CIEE endorsement of or agreement with these findings, nor that of any CIEE sponsor. Lawrence Berkeley Laboratory is operated by the University of California for the U.S. Department of Energy under Contract No. DE-AC03-76SF00098.


## References


Becker, W., Rupprecht, H., and Troitzsch, J., 1990, "National and International Fire Protection Regulations and Test Procedures," in: *International Plastics Flammability Handbook,* J. Troitzsch, ed., Oxford University Press, New York.

Berdahl, P., Martin, M., and Sakkal, F., 1983, "Thermal Performance of Radiative Cooling Panels," *Int. J. Heat Mass Transfer,* Vol. 26, p. 871.

Bohren, C. F., and Huffman, D. R., 1983, *Absorption and Scattering of Light by Small Particles,* Wiley, New York.

Brady, R. F., Jr., 1987, *J. Prot. Coat. Linings,* Vol. 4, No. 7, p. 42.

Brady, R. F., Jr., and Wake, L. V., 1992, "Principles and Formulations for Organic Coatings With Tailored Infrared Properties," *Prog. in Organic Coatings,* Vol. 20, p. 1.

Conley, R. T., 1972, *Infrared Spectroscopy,* Allyn and Bacon, Inc., Boston.

Cronemeyer, D. C., 1952, *Phys. Rev.,* Vol. 87, p. 876.

Devore, J. R., 1951, *J. Opt. Soc. Amer.,* Vol. 41, p. 416.

Drysdale, D., 1990, *An Introduction to Fire Dynamics,* Wiley, New York.

Ellis, H., 1992, "Fire Barrier Coating and Fire Barrier Plywood," U.S. Patent No. 5,130,184.

Ensminger, R. I., 1988, "Pigmentation of Flame-Resistant and Intumescent Paints," in: *Pigment Handbook,* Vol. 2, P. A. Lewis, ed., Wiley, New York, 123.

Granqvist, C. G., 1990, "Window Coatings for the Future," *Thin Solid Films,* Vol. 193/194, p. 730.

Greenstein, L. M., 1988, "Nacreous (Pearlescent) Pigments and Interference Pigments," in: *Pigment Handbook, Vol. 1, Properties and Economics,* P. A. Lewis, ed., Wiley, New York.

Hagglund, B., and Persson, L. E., 1976, "An Experimental Study of the Radiation From Wood Flames," *FoU-Brand,* Vol. 1, p. 2; see also Drysdale (1990), Sec. 2.4.

Hare, C. H., 1992, "Aluminum Pigments—Radiant Energy Reflection, Barrier Protection, and Improved Film Durability," *J. Prot. Coat. Linings,* Aug., p. 63.

Hawley, G. C., 1988, "Aluminum Potassium Silicate," in: *Pigment Handbook, Vol. 1, Properties and Economics,* P. A. Lewis, ed., Wiley, New York, p. 227.

LaRocca, A. J., 1978, "Atmospheric Absorption," in: *The Infrared Handbook,* W. L. Wolfe and G. J. Zisis, eds., Environmental Research Institute of Michigan, Ann Arbor, Fig. 5-14.

Law, M., 1963, "Heat Radiation From Fires, and Building Separation," *Fire Research Technical Paper No. 5,* HMSO, London.

Lawson, D. I., and Simms, D. L., 1952, "The Ignition of Wood by Radiation," *British J. Appl. Phys.,* Vol. 3, p. 288.

Nilsson, T. M. J., Niklasson, G. A., and Granqvist, C. G., 1992, "A Solar Reflecting Material for Radiative Cooling Applications: ZnS Pigmented Polyethylene," *Solar Energy Materials and Solar Cells,* Vol. 28, p. 175.

Palmer, B. R., Stamatakis, P., Bohren, C. F., and Salzman, G. C., 1989, "A Multiple-Scattering Model for Opacifying Particles in Polymer Films," *J. Coatings Technol.,* Vol. 61, No. 779, p. 41.

Quintiere, J. G., 1981, "A Simplified Theory for Generalizing Results From a Radiant Panel Rate of Flame Spread Apparatus," *Fire and Materials,* Vol. 5, p. 52.

Ribarsky, M. W., 1985, "Titanium Dioxide ($TiO_2$) (Rutile)," in: *Handbook of Optical Constants of Solids,* Academic Press, Orlando, FL, p. 795.

Rutherford, D. J., and Simpson, L. A., 1985, "Use of a Flocculation Gradient Monitor for Quantifying Titanium Dioxide Pigment Dispersion in Dry and Wet Paint Films," *J. Coatings Technol.,* Vol. 57, No. 724, p. 75.

Smith, G. B., Niklasson, G. A., Svensson, J. S. E. M., and Granqvist, C. G., 1986, *J. Appl. Phys.,* Vol. 59, p. 571.

Stearns, J. R., Zahniser, M. S., Kolb, C. E., and Sandford, B. P., 1986, "Airborne Infrared Observations and Analyses of a Large Forest Fire," *Appl. Optics,* Vol. 25, p. 2554.

Stjerna, B., and Granqvist, C. G., 1990, "Optical and Electrical Properties of $SnO_x$ Thin Films Made by Reactive R. F. Magnetron Sputtering," *Thin Solid Films,* Vol. 193/194, p. 704.

Touloukian, Y. S., DeWitt, D. P., and Hernicz, R. S., 1972, *Thermal Radiative Properties, Coatings, Thermophysical Properties of Matter,* Vol. 9, IFI/Plenum, New York.

Zallen, R., 1983, *The Physics of Amorphous Solids,* Sec. 6.2, Wiley, New York.





Downloaded 12 Dec 2010 to 193.140.21.150. Redistribution subject to ASME license or copyright; see http://www.asme.org/terms/Terms_Use.cfm

# The Spectral Line-Based Weighted-Sum-of-Gray-Gases Model in Nonisothermal Nonhomogeneous Media

M. K. Denison

B. W. Webb

Brigham Young University,
Provo, UT 84602

*An approach is developed to extend the previously developed spectral-line weighted-sum-of-gray-gases (SLW) model to nonisothermal, nonhomogeneous media. The distinguishing feature of the SLW gas property model is that it has been developed for use in arbitrary solution methods of the radiative transfer equation (RTE). A spatial dependence of the gray gas absorption cross sections on local temperature, pressure, and mole fraction is introduced through the absorption-line blackbody distribution function. Incorporating this spatial dependence results in significant improvement over the use of spatially uniform gray gas absorption cross sections in comparisons with line-by-line benchmarks.*

## Introduction

The weighted-sum-of-gray-gases model (Hottel and Sarofim, 1967; Smith et al., 1982), which has been used for expressing total emissivities of gases and in the zone method of radiative transfer, has recently been extended to the general radiative transfer equation (RTE) (Modest, 1991; Denison and Webb; 1993a). The spectral-line-based weighted-sum-of-gray-gases (SLW) model of Denison and Webb (1993a) is based on detailed spectral line data in lieu of total emissivity data from previous engineering models such as the wide-band model (Edwards, 1976). These developments have allowed the total radiative transfer in gases to be efficiently calculated using arbitrary solution methods of the RTE. In the absence of scattering the weighted-sum-of-gray-gases form of the RTE is written:

$$\frac{dI_j}{ds} = \kappa_j\left(a_j \frac{\sigma T^4}{\pi} - I_j\right) \tag{1}$$

Here, $I_j$, $\kappa_j$, and $a_j$ are the intensity, absorption coefficient, and corresponding blackbody weight, respectively, associated with the $j$th gray gas. $s$ is the distance along the given line of sight. The blackbody weights $a_j$ may be interpreted as the fraction of blackbody energy in the portions of the spectrum where the effective absorption coefficient is $\kappa_j$ (Hottel and Sarofim, 1967). The total heat transfer rates are found by simply summing the solutions of Eq. (1) over all gray gases:

$$I = \sum_j I_j \tag{2}$$

Denison and Webb (1993b) have recently introduced a novel absorption-line blackbody distribution function, which easily allows the determination of the weighted-sum-of-gray-gases weights for any desired number of gray gases via differencing. This model has been shown to yield predictions in excellent agreement with computationally expensive line-by-line solutions in isothermal, homogeneous media. However, due to the complex dependence of high-resolution gas spectra on temperature, total pressure, and mole fraction of broadening species, the weighted-sum-of-gray-gases model yields only approximate results in nonisothermal and/or nonhomogeneous media. Denison and Webb (1993a) made the approximation in nonisothermal, nonhomogeneous media that a single absorption cross-sectional spectrum prevails over the entire spatial domain. The reason for this assumption was a need to fix throughout the spatial domain the spectral location of the many subline segments associated with a given value of the absorption cross section. In general, a band in the spectrum of a gas becomes more absorbing with increasing temperature due to the growth of hot lines. The assumption of a single spectrum leads to an overprediction in net volumetric radiative heat gain in cooler spatial regions and an underprediction of radiative heat loss in hotter regions (Denison and Webb, 1993a). The neglect of line half-width variations due to self-broadening of $H_2O$ also leads to errors in the divergence field of the net radiative flux vector. These errors are expected to increase with increasing spatial variation in temperature and/or mole fraction.

Although in the SLW model spectral locations of subline segments associated with a single gray gas are to remain spatially fixed, this does not preclude a spatial variation in the individual gray gas absorption cross sections used to calculate the local gray gas absorption coefficients. In this paper an approach is developed to allow spatial dependence of the gray gas absorption cross sections on temperature, pressure, and species concentration. $H_2O$ is the gas in the development of this work but the concepts can be applied to any radiating gas. This approach is tested by comparison with computationally intensive line-by-line calculations. The line-by-line data come from the Air Force Geophysics Laboratory's high-resolution transmission molecular absorption (HITRAN) data base (Rothman et al., 1991) and from high-temperature line estimates (Denison and Webb, 1993b). Although validation of the proposed model is based on comparison using the same reference line-by-line data, earlier comparisons with Hottel's total emissivity data (Denison and Webb, 1993b) provide a level of confidence in the spectral-line data used.

## Model Formulation

**The Absorption-Line Blackbody Distribution Function.** The absorption-line blackbody distribution function (Denison and Webb, 1993b) provides the means for incorporating a spatial dependence of the gray gas absorption cross sections on the local temperature, pressure, and mole fraction. The absorption-line blackbody distribution function is defined as that fraction of the blackbody energy in the portions of the spectrum where the high-resolution spectral absorption cross section of the gas, $C_{\text{abs},\eta}$, is less than a prescribed value $C_{\text{abs}}$. This is illustrated in Fig. 1 for

Contributed by the Heat Transfer Division for publication in the JOURNAL OF HEAT TRANSFER. Manuscript received by the Heat Transfer Division November 1993; revision received May 1994. Keywords: Combustion, High-Temperature Phenomena, Radiation. Associate Technical Editor: W. L. Grosshandler.



Copyright © 1995 by ASME

Downloaded 12 Dec 2010 to 193.140.21.150. Redistribution subject to ASME license or copyright; see http://www.asme.org/terms/Terms_Use.cfm

a few absorption lines at high resolution. The portions of the spectrum over which Planck's function is integrated are represented by the shaded segments in the graph. The distribution function is then expressed for species $s$ as

$$F_s(C_{\text{abs}}, T_b, T_g, P_T, Y_s) = \frac{1}{\sigma T_b^4} \sum_i \int_{\Delta\eta_i(C_{\text{abs}}, T_g, P_T, Y_s)} E_{b\eta}(\eta, T_b) d\eta, \quad (3)$$

where $\sigma$ is the Stefan–Boltzmann constant and $E_{b\eta}$ is Planck's function evaluated at the wave number $\eta$ and blackbody (source) temperature $T_b$. The subscript $i$ refers to the $i$th spectral segment and the summation is performed over all segments covering the entire spectrum. The dependence of the function on the spectrum is through the spectral interval of integration of each segment $\Delta\eta_i$, which is dependent on the absorption cross section, gas temperature $T_g$, the total pressure $P_T$, and species concentration, which affect line broadening. The absorption-line blackbody distribution function of Eq. (3) monotonically increases from zero to unity with increasing absorption cross section. A mathematical correlation for the distribution function has been given by Denison and Webb (1993b, 1995) for $H_2O$ and $CO_2$.

The fraction of the blackbody energy for a given source temperature in the spectral segments where the absorption cross section is between arbitrary absorption cross sections $\tilde{C}_{\text{abs},j}$ and $\tilde{C}_{\text{abs},j+1}$ may be found simply as the difference of the distribution function evaluated at these two absorption cross sections. These absorption cross sections are called *supplemental* absorption cross sections since they are used to determine the blackbody weight but do not appear directly in the corresponding gray gas absorption coefficient $\kappa_j$. Note that $\kappa_j = NC_{\text{abs},j}$ where $N$ is the molar density. The difference of the distribution function evaluated at the these supplemental cross sections is the blackbody weight in the weighted-sum-of-gray-gases RTE [Eq. (1)]:

$$a_j = F_s(\tilde{C}_{\text{abs},j+1}, T_b, T_g, P_T, Y_s) - F_s(\tilde{C}_{\text{abs},j}, T_b, T_g, P_T, Y_s). \quad (4)$$

In a numerical calculation, the absorption cross-sectional domain is divided into discrete increments and a solution is carried out for each increment using any arbitrary solution method for the RTE. Denison and Webb (1993a) have shown for $H_2O$ that good accuracy can be achieved with as few as three gray gases (three discrete values of $C_{\text{abs}}$) when the absorption cross sections and supplemental absorption cross sections are determined from an optimization involving total emissivities.

**The Implicit Dependence of $C_{\text{abs},j}$.** Narrow- and wide-band gas property models are extended to nonisothermal and/or nonhomogeneous media through scaling approximations wherein a nonisothermal and/or nonhomogeneous gas along a given path length is replaced with an equivalently absorbing isothermal homogeneous gas. Goody and Yung (1989) summarize these scaling approximations. Perhaps the best known is the Curtis–Godson approximation (Godson, 1953). Goody and Yung (1989) show that the scaling approximations are exact if the high-resolution absorption cross section can be expressed as the product of two functions:

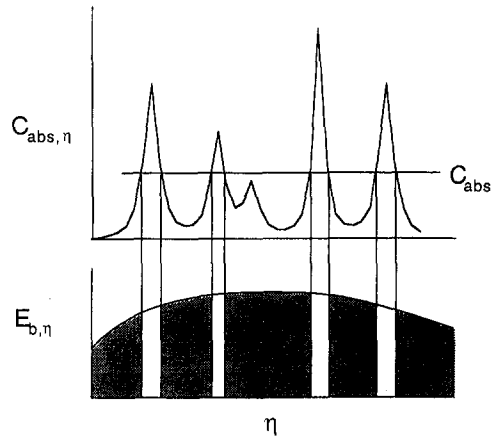



**Fig. 1 Portions of the spectrum for a few representative absorption lines where the fraction of blackbody energy is calculated**

$$C_{\text{abs},\eta}(\eta, T_g, P_T, Y_s) = \phi(T_g, P_T, Y_s)\psi(\eta) \quad (5)$$

Note that the function $\psi(\eta)$ only defines the spectral dependence. Equation (5) along with the definition of the absorption-line blackbody distribution function provides the basis of the present SLW approach for modeling nongray gas radiative transfer in nonisothermal nonhomogeneous media. Figure 2 shows a high-resolution portion of an ideal spectrum of a gas as described by Eq. (5) at two different states. Consider the spectrum at state 1 with temperature $T_1$, total pressure $P_{T1}$, and mole fraction $Y_{s1}$. The absorption-line blackbody distribution function may be calculated at this state by integrating Planck's function over all spectral segments where $C_{\text{abs},\eta}(T_1, P_{T1}, Y_{s1})$ is less than the prescribed value $C_{\text{abs},j}(T_1, P_{T1}, Y_{s1})$. Next consider the spectrum at state 2 $(T_2, P_{T2}, Y_{s2})$. If Eq. (5) is valid, then the specified absorption cross section $C_{\text{abs},j}(T_2, P_{T2}, Y_{s2}) = C_{\text{abs},j}(T_1, P_{T1}, Y_{s1})\phi(T_2, P_{T2}, Y_{s2})/\phi(T_1, P_{T1}, Y_{s1})$ will yield the same value of the absorption-line blackbody distribution function for a given reference blackbody source temperature. This is because the function $\psi(\eta)$, which describes the spectral dependence of $C_{\text{abs},\eta}$, is assumed to be independent of the gas state according to Eq. (5). In other words, the spectral segments defined where $C_{\text{abs},\eta}(T_1, P_{T1}, Y_{s1})$ is less than the prescribed value $C_{\text{abs},j}(T_1, P_{T1}, Y_{s1})$ are identically those spectral segments where $C_{\text{abs},\eta}(T_2, P_{T2}, Y_{s2})$ is less than $C_{\text{abs},j}(T_2, P_{T2}, Y_{s2})$. The following equality in the absorption-line blackbody distribution function of species $s$ results from these observations:

## Nomenclature

$a$ = blackbody weight of the weighted-sum-of-gray-gases model
$\tilde{C}_{\text{abs},j}$ = supplemental absorption cross section
$C_{\text{abs}}$ = absorption cross section
$E_{b,\eta}$ = Planck's function of blackbody emitted flux
$F_s$ = absorption-line blackbody distribution function of species $s$
$I$ = radiation intensity
$L$ = path length
$P_T$ = total pressure
$q$ = radiative heat flux
$s$ = distance along line of sight
$T$ = temperature
$Y_s$ = mole fraction of species $s$
$\epsilon$ = total emissivity
$\eta$ = wave number
$\kappa$ = absorption coefficient
$\sigma$ = Stefan–Boltzmann constant

**Subscripts**

$b$ = blackbody or blackbody source
$g$ = gas
$j$ = $j$th gray gas
loc = local
ref = reference
$s$ = general species
$w$ = wall
$\eta$ = spectral



Downloaded 12 Dec 2010 to 193.140.21.150. Redistribution subject to ASME license or copyright; see http://www.asme.org/terms/Terms_Use.cfm

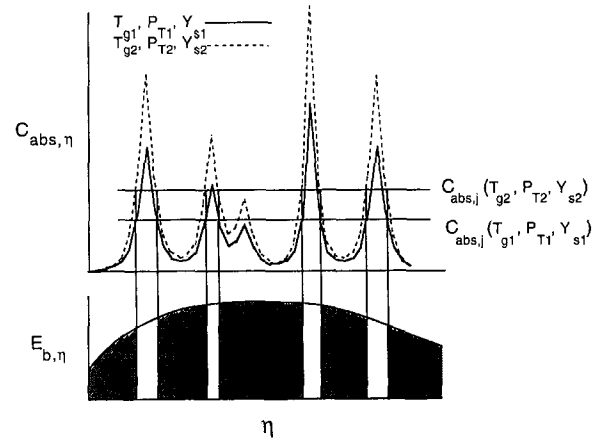



**Fig. 2 Idealized dependence of high resolution spectrum on $T_g$, $P_T$, and $Y_s$ resulting in equivalent blackbody fractions**

$$F_s[C_{\text{abs},j}(T_2, P_{T2}, Y_{s2}); T_b = T_{\text{ref}}; T_g = T_2; Y_s = Y_{s2}; P_T = P_{T2}] = F_s[C_{\text{abs},j}(T_1, P_{T1}, Y_{s1}); T_b = T_{\text{ref}}; T_g = T_1; Y_s = Y_{s1}; P_T = P_{T1}] \quad (6)$$

Equation (6) provides an implicit dependence of $C_{\text{abs},j}$ on the local gas state. In practice a reference state is selected associated with a set of reference absorption cross-sections for the various gray gases. The local absorption cross section, $C_{\text{abs},j}$, is then determined from the following implicit equation, which is Eq. (6) written for equivalent absorption-line blackbody functions at the reference and the local states:

$$F_s[C_{\text{abs},j}; T_b = T_{\text{ref}}; T_g = T_{\text{loc}}; Y_s = Y_{s,\text{loc}}; P_T = P_{T,\text{loc}}] = F_s[C_{\text{abs},j,\text{ref}}; T_b = T_{\text{ref}}; T_g = T_{\text{ref}}; Y_s = Y_{s,\text{ref}}; P_T = P_{T,\text{ref}}] \quad (7)$$

In this work it was found that the reference state determined as the spatial average of the temperature, total pressure, and composition fields yielded good results. This same reference state is used to calculate the blackbody weights as discussed below.

The reference absorption cross section, $C_{\text{abs},j,\text{ref}}$ is an appropriate value between the supplemental absorption cross-sectional areas $\tilde{C}_{\text{abs},j}$ and $\tilde{C}_{\text{abs},j+1}$. If a sufficient number of gray gases are used $C_{\text{abs},j,\text{ref}}$ may be determined as the logarithmic mean of $\tilde{C}_{\text{abs},j}$ and $\tilde{C}_{\text{abs},j+1}$:

$$C_{\text{abs},j,\text{ref}} = \exp\left[\frac{\ln(\tilde{C}_{\text{abs},j}) + \ln(\tilde{C}_{\text{abs},j+1})}{2}\right] \quad (8)$$

where the supplemental absorption cross-sections are logarithmically spaced. If relatively few gray gases (less than 10) are used such that an optimization as outlined by Denison and Webb (1993a) is required, $C_{\text{abs},j,\text{ref}}$ is determined from the optimization. The optimization involves minimizing the relative deviation in emissivities evaluated at the reference state predicted by the SLW model from emissivities at the same reference state determined from a relatively large number of gray gases (typically 20 or more). The emissivities are evaluated over the path-length range of the problem of interest.

The local $j$th gray gas absorption coefficient is found as the product of the local molar density $N$ determined from an appropriate equation of state and the local gray gas absorption cross section:

$$\kappa_j = N(T_{\text{loc}}, P_{T,\text{loc}}, Y_{s,\text{loc}}) C_{\text{abs},j}(T_{\text{loc}}, P_{T,\text{loc}}, Y_{s,\text{loc}}) \quad (9)$$

It should be stated that this approach is similar to the correlated $k$-distribution ($c$-$k$) method used to extend $k$-distributions to nonisothermal nonhomogeneous media (Goody and Yung, 1989; Goody et al., 1989; Lacis and Oinas, 1991). In the $c$-$k$ method, the absorption cross sections of each band are also dependent on the local temperature, pressure, and mole fraction implicit in the cumulative $k$-distribution. The $c$-$k$ method however, is a band model, and does not incorporate the variation of the Planck distribution over wave number *a priori* as does the present model. This *a priori* accounting of Planck's distribution significantly reduces the required number of solutions of the RTE to obtain total heat transfer rates as compared to the $c$-$k$ method. However, it necessitates fixing the source temperature, $T_b$, at a reference value in calculating the local absorption cross section as stated in Eq. (6). Therefore, the present model is approximate in predicting the emission as a local phenomenon. If this temperature were not fixed, the fraction of blackbody energy at the two states would no longer be equivalent under the assumption of Eq. (5).

**Determination of the Blackbody Weights.** The blackbody weights for the $j$th gray gas calculation are determined as described previously [Eq. (4)]. However, the question arises as to what values the gas temperature, total pressure, and mole fraction should take in evaluating the blackbody weights. The source temperature, $T_b$, is obviously set to the local temperature to account properly for Planck's distribution locally since $a_j$ is the fraction of blackbody energy in the portions of the spectrum where the effective absorption coefficient is $\kappa_j$. One may also be inclined to set $T_g$, $P_T$, and $Y_s$ to the local values since changes in line and band structure modify $a_j$. Denison and Webb (1993a) give a derivation of the weighted-sum-of-gray-gases RTE and discuss the issue of additional Leibnitz terms that arise in the weighted-sum-of-gray-gases RTE due to the floating spectral segments associated with a gas absorption spectrum, which is changing with spatial position. One must either invoke the approximation of blackbody weights determined from a single spectrum over the entire spatial domain, thereby fixing the spectral segments associated with a given gray gas, or incur the error of allowing the spectral segments to float. In the proposed approach the spectral segments are to be fixed and the weights are determined as:

$$a_j = F_s(\tilde{C}_{\text{abs},j+1}; T_b = T_{\text{loc}}; T_g = T_{\text{ref}}; Y_s = Y_{s,\text{ref}}; P_T = P_{T,\text{ref}}) - F_s(\tilde{C}_{\text{abs},j}; T_b = T_{\text{loc}}; T_g = T_{\text{ref}}; Y_s = Y_{s,\text{ref}}; P_T = P_{T,\text{ref}}) \quad (10)$$

For a wall boundary condition the blackbody emission weights are found similarly by setting the blackbody source temperature to the wall temperature:

$$a_j = F_s(\tilde{C}_{\text{abs},j+1}; T_b = T_{\text{wall}}; T_g = T_{\text{ref}}; Y_s = Y_{s,\text{ref}}; P_T = P_{T,\text{ref}}) - F_s(\tilde{C}_{\text{abs},j}; T_b = T_{\text{wall}}; T_g = T_{\text{ref}}; Y_s = Y_{s,\text{ref}}; P_T = P_{T,\text{ref}}) \quad (11)$$

Comparisons of predictions with weights determined from setting $T_g$ to the reference value versus local values are made in the next section.

**Summary of the Procedure.** The procedure of the present SLW approach may be outlined as follows: (1) The reference state is calculated as the spatial average of the temperature, total pressure, and mole fraction. The temperature, pressure, and compositions fields are assumed known. (2) The absorption cross-sectional domain is divided into increments bounded by the supplemental absorption cross sections, $\tilde{C}_{\text{abs},j}$, and each increment is represented by an absorption cross section representative of the average value in the increment, for example Eq. (8). This division is logarithmic if a sufficient number of gray gases are used, otherwise the absorption cross sections and supplemental absorption cross sections are determined from the optimization of emissivities at the reference state previously outlined. (3) At each spatial location the local absorption coefficient is calculated from Eqs. (7) and (9), and the associated blackbody weight is calculated from Eq. (10). The blackbody weights for wall emission in the boundary conditions are determined from Eq. (11). (4) The weighted-sum-of-gray-gases RTE is solved for the current



Downloaded 12 Dec 2010 to 193.140.21.150. Redistribution subject to ASME license or copyright; see http://www.asme.org/terms/Terms_Use.cfm

$j$th gray gas. Steps 3 and 4 are repeated for each gray gas and a running sum of the resulting heat transfer rates is kept.

Since Eq. (7) is implicit, $C_{\text{abs},j}$ must be determined at each spatial location from an iterative technique such as bisection or Newton–Raphson. Bisection was used for the problems presented in the next section. In large multidimensional comprehensive modeling applications, evaluation of local absorption cross sections and weights may be accelerated by generating look-up tables.

## Benchmark Predictions

Benchmark predictions for validation of the present approach were generated by solving for the intensity field line-by-line using detailed spectral line data from the Air Force Geophysics Laboratory's high-resolution transmission molecular absorption (HITRAN) data base (Rothman et al., 1992) and from high-temperature line estimates (Denison and Webb, 1993b). These same spectral line data were also used for the generation of the absorption-line blackbody distribution function correlation given by Denison and Webb (1993b), which was used in the model predictions presented. The spectral-line database is considered here as a reference and the intrinsic accuracy of the proposed SLW model is evaluated by a comparison of the results issued from the model and from the line-by-line calculations. Nevertheless, earlier comparisons with Hottel's total emissivity data (Denison and Webb, 1993b) provide confidence in the spectral line data used. Each of the line-by-line benchmark predictions involved between 80,000 and 500,000 spectral calculations. For each benchmark the actual high resolution gas absorption spectrum was divided into 10 spectral regions between each pair of adjacent local maxima (perceptible lines), and a solution was carried out using the average absorption coefficient in each subline region. An increase in spectral resolution to 50 spectral calculations between adjacent local maxima showed no appreciable difference in the solution. The spectrum at the highest temperature of the spatial domain and with the least amount of line-broadening, which therefore had the greatest number of local maxima, was used as the basis for the spectral division just outlined. Each subline spectral interval was held fixed throughout the spatial domain and the absorption coefficient was allowed to vary by determining the average absorption coefficient over the same subline interval but from the spectrum at the local temperature and species concentration. The spatial grid was sufficiently refined with model predictions before a computationally intensive benchmark calculation was begun using the same grid resolution.

**Solution of the RTE.** In this work the discrete ordinates method is used applicable to a gray analysis described by Carlson and Lathrop (1968) for solving a similar governing equation for neutron transport. The one-dimensional problems were solved using an even-order Gauss quadrature set for the discrete ordinates. A quadrature order of 20 was chosen. This is the quadrature order used by Kim et al. (1991) who reported no significant improvement with higher order solutions. The discrete ordinates solution method was used in both spectral line-by-line benchmark and SLW model predictions.

## Results and Discussion

Problems involving radiative transfer from nonisothermal and/or nonhomogeneous $H_2O$ gas between infinite parallel walls are considered with comparison against the line-by-line benchmarks. A range of problems has been studied in an attempt to draw general conclusions on the errors of the present approach. The total pressure in all problems considered is one atmosphere. Spatial variations in the local mole fraction considerably stronger than what would normally be encountered in engineering situations were deliberately imposed in the test problems studied in order to evaluate the present model under the most rigorous conditions. The local radiative flux divergence is used as the figure-of-merit in evaluating model accuracy; evaluations based on predicted wall flux are usually more forgiving. Although the problems considered are one-dimensional to facilitate line-by-line benchmark solutions, the model presented may be easily extended without additional assumption to multidimensional situations using arbitrary solution methods of the RTE. Some of the problems are taken from Denison and Webb (1993a), who presented solutions of the SLW model under the assumption of spatially constant absorption cross-sections.

**Nonisothermal Homogeneous Medium.** A nonisothermal medium between parallel infinite walls is first considered with the following cosine temperature variation:

$$T = T_{\text{avg}} + \frac{\Delta T}{2} \cos(\pi x/L). \tag{12}$$

This temperature profile provides a systematic departure from an isothermal medium by increasing the temperature variation, $\Delta T$. $T_{\text{avg}}$ is taken as 1000 K and the $H_2O$ mole fraction is spatially uniform at 0.1 (90 percent air). The walls are spaced 2 m apart and are black at the temperatures of $T_{\text{avg}} + \Delta T/2$ and $T_{\text{avg}} - \Delta T/2$, respectively. Predictions were generated for a $\Delta T$ of 500 K and 1000 K. The predicted variation in local radiative flux divergence is shown in Figs. 3($a$) and 3($b$) for a $\Delta T$ of 500 K and 1000 K, respectively. For comparison, the previous predictions of Denison and Webb (1993a), which assume spatially constant absorption cross sections, are also shown. The model predictions have used three optimized gray gases. Although the approach used here is still approximate, significant reduction in local error is noted. The maximum errors in the radiative flux divergence for a $\Delta T$ of 500 K are 3 and 4 percent in the hot and cold regions, respectively. This is a significant improvement over the maximum errors of 9 and 20 percent in the predictions of Denison and Webb (1993a) for a $\Delta T$ of 500 K. At a $\Delta T$ of 1000

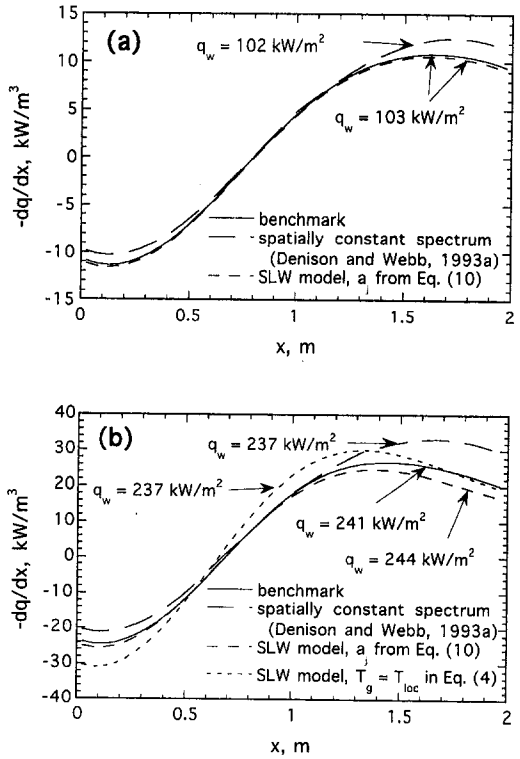



**Fig. 3 Radiative source and net cold wall flux for uniform 10 percent $H_2O$ and the cosine temperature distribution [Eq. (12)] with ($a$) $\Delta T$ = 500 K and ($b$) $\Delta T$ = 1000 K. $T_{\text{avg}}$ = 1000 K. $\epsilon_w$ = 1. The SLW predictions are with three optimized gray gases.**



Downloaded 12 Dec 2010 to 193.140.21.150. Redistribution subject to ASME license or copyright; see http://www.asme.org/terms/Terms_Use.cfm

K (Fig. 3($b$)) the maximum errors in the radiative flux divergence for the corrected predictions with the weights determined from Eq. (10) are 5 and 17 percent in the hot and cold regions, respectively, compared to 15 and 40 percent for the uniform spectrum predictions. Even in the previous approach (Denison and Webb, 1993a) $\kappa_j$ was allowed to vary through $N$, but $C_{\text{abs},j}$ was fixed spatially at the spectral value for average state conditions.

Also shown in Fig. 3($b$) is the prediction with the weights determined from the gas temperature, $T_g$, set to the local temperature in Eq. (4) as opposed to the reference value as indicated in Eq. (10). Allowing the spectral segments to float results in a general overprediction of the radiative flux divergence. Fixing the spectral segments by setting $T_g$, $P_T$, and $Y_s$ to the reference values yields much more accurate predictions.

The error trends of Denison and Webb (1993a) are reversed with less absolute error using the present approach with weights determined from Eq. (10). Whereas assuming spatially constant absorption cross sections resulted in an overprediction in radiative heat gain in cold regions, the present approach results in a slight underprediction. A similar reversal in trends is noted in the hot region. As expected, the error is seen to increase with greater spatial temperature variations in the domain.

The error in the present approach is due to the deviation of the real dependence of the spectrum on temperature (or more generally, gas state) from the idealized dependence described by the spectrum approximation of Eq. (5). In a real gas, the absorption cross sections at many spectral locations that are identical at one temperature diverge at a different temperature. Greater accuracy than that demonstrated here requires much greater computational effort such as line-by-line solutions or some other scheme. Rivière et al. (1992) have developed an extension of the $c$-$k$ method where the absorption lines of a given narrow band are divided into groups of similar lower energy level so that the line intensities of a given group have similar dependence on temperature. However, this approach requires a quadrature in $k$-space (over the absorption cross section) for each group of each narrow band, and there are typically on the order of 50 narrow bands that encompass the entire spectrum.

The next problem considered consists of the boundary layer profile studied by Kim et al. (1991) and Menart et al. (1993). Their discrete ordinates approach, which uses narrow-band transmissivities or wide-band absorptances, modifies the form of the RTE to be written in terms of the transmissivity (or band absorptance) differentiated along the line of sight of each ordinate. Menart et al. (1993) extended the approach to reflective boundaries via a closure approach where the narrow-band averaged product of the wall intensity and transmissivity is treated in a correlated manner. These approaches are fairly complicated and have only been applied in relatively simple geometries. The boundary layer temperature profile studied involves a much larger temperature gradient than the problem of Fig. 3. The temperature varies from 1500 K at the hot wall and falls rapidly close to the hot wall and then more gradually to 300 K at the other wall. The walls are at 1500 K and 300 K. The $H_2O$ mole fraction is unity. Comparison between the line-by-line benchmark, the present SLW model, and the narrow-band results of Kim et al. (1991) is given in Fig. 4($a$) where the walls are black and spaced 0.2 m apart. In Fig. 4($b$) a comparison of the present SLW model with the narrow-band results of Menart et al. (1993) is presented where the hot wall has a gray diffuse reflectivity of 0.9 and the cold wall is black. All SLW predictions in Fig. 4 are with three optimized gray gases. The figures show good agreement between the proposed SLW model, the benchmark (Fig. 4($a$)), and the narrow-band results of Kim et al. (1991) and Menart et al. (1993). Objective comparison of the present model with the narrow-band results of Kim et al. (1991) and Menart et al. (1993) is difficult due to different spectroscopic data and numerical methods used. Nevertheless, the figures demonstrate that comparable results are achieved with the present approach, which lends itself to more complex multidimensional geometry since

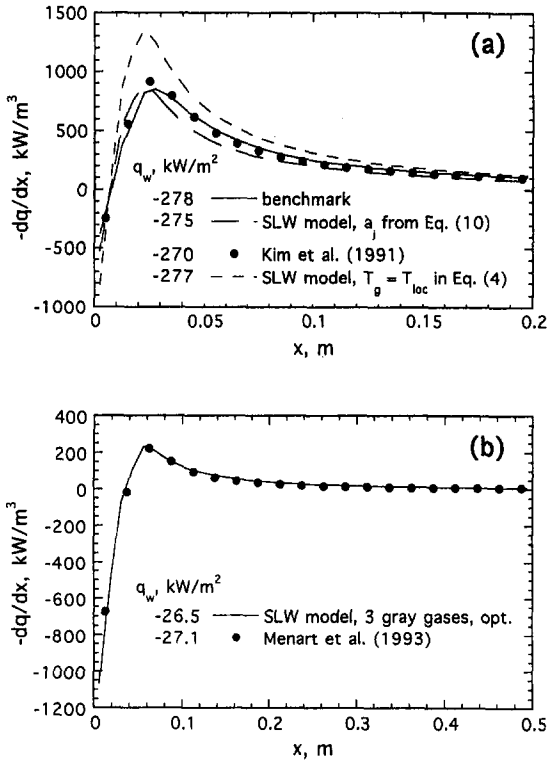



**Fig. 4 Radiative source and net hot wall flux for uniform 100 percent $H_2O$ and the boundary layer temperature profile studied by (*a*) Kim et al. (1991) ($\epsilon_w$ = 1) and (*b*) Menart et al. (1993) ($\epsilon_{w,x=0}$ = 0.1, $\epsilon_{w,x=L}$ = 1). The SLW predictions are with three optimized gray gases.**

the basic radiative property is the absorption coefficient in lieu of a transmissivity. In addition, reflective boundaries (Fig. 4($b$)) require no additional effort in implementing the solution with the present model in contrast to the closure approach developed by Menart et al. (1993).

Figure 4($a$) also shows a model prediction with the weights determined from the gas temperature, $T_g$, set to the local temperature in Eq. (4). The resulting overprediction of the radiative flux divergence is much more severe in this boundary layer than the cosine distribution of Fig. 3. Again, the use of a constant reference condition through Eq. (10) to calculate the weights yields much better results.

**Isothermal Medium With Parabolic Mole Fraction Profile.** The present approach is next tested in a problem of significant spatial variation of the absorption-line half-width. The problem studied is that of Kim et al. (1991), also analyzed by Denison and Webb (1993a). The gas temperature is held uniform at 1000 K, while the $H_2O$ mole fraction is given by a parabolic profile where the mole fraction is zero at the walls and peaks at the center. $H_2O$ is known to be a strong self-broadener due to its permanent electric dipole moment. Figures 5($a$) and 5($b$) are predictions for a peak $H_2O$ concentration of 45 and 100 percent, respectively. The results of the present approach are compared to those of Denison and Webb (1993a) where $C_{\text{abs},j}$ was spatially constant. The five-gray-gas predictions were obtained with absorption cross sections optimized using the procedure outlined previously while the cross sections of the ten-gray-gas predictions were logarithmically spaced [Eq. (8)]. Greater accuracy is again demonstrated using the present approach instead of assuming a single spectrum (at the average concentration) is spatially invariant. The present approach more correctly predicts the location of the peak radiative heat loss. The predicted wall fluxes have error of less than 4 percent.

**Nonisothermal Nonhomogeneous Medium.** The model is finally tested in a medium where there is simultaneous spatial vari-



Downloaded 12 Dec 2010 to 193.140.21.150. Redistribution subject to ASME license or copyright; see http://www.asme.org/terms/Terms_Use.cfm

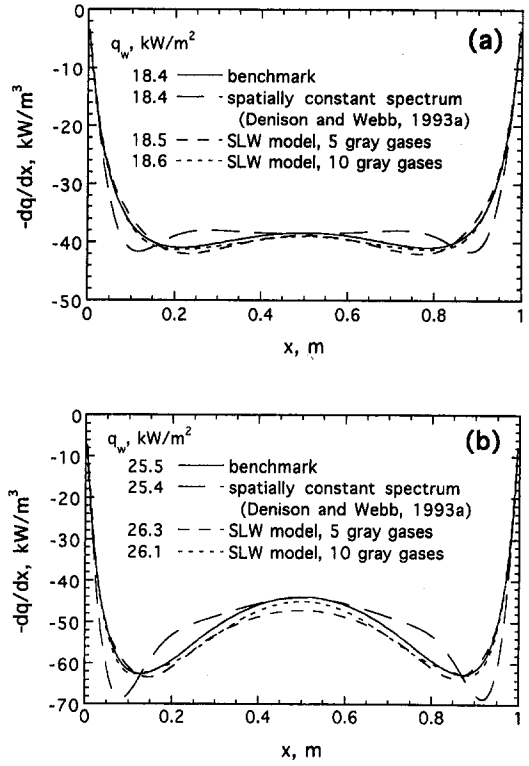



**Fig. 5 Radiative source and net wall flux for the parabolic $H_2O$ concentration profile and uniform temperature profile for a peak $H_2O$ concentration of (*a*) 45 percent, and (*b*) 100 percent. $\epsilon_w = 1$.**

ation in both temperature and concentration. The problems consider $H_2O$ between infinite parallel black walls. The temperature and mole fraction profiles within the media are given by the following sine distributions:

$$T = T_w + (T_c - T_w) \sin(\pi x/L) \tag{13}$$

$$Y_w = \sin(\pi x/L) \tag{14}$$

$T_w$ and $T_c$ are the temperatures at the wall and center, respectively. In this case the implicit dependence of $C_{\text{abs},j}$ includes variation in both $T_g$ and $Y_s$. Figure 6 shows the resulting predictions of the SLW model compared against the line-by-line benchmark for $T_w$ = 500 K and $T_c$ = 1500 K. The mole fraction varies between zero at the walls and unity at the center. The walls are spaced 10 m apart. The three-gray-gas prediction is optimized and the ten-gray-gas prediction is not. The maximum error is in the center

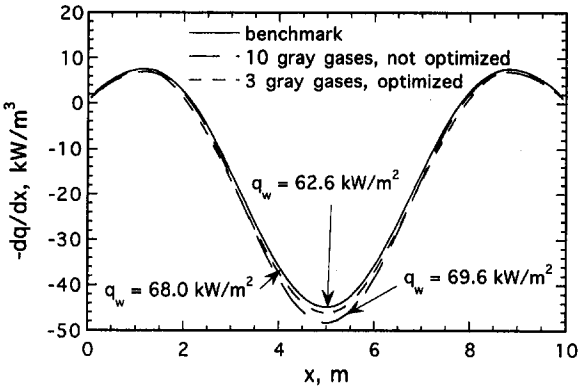



**Fig. 6 Radiative source and net wall flux for the sine temperature and mole fraction profiles of $H_2O$ [Eqs. (13) and (14)]. $T_w$ = 500 K. $T_c$ = 1500 K. $\epsilon_w = 1$.**

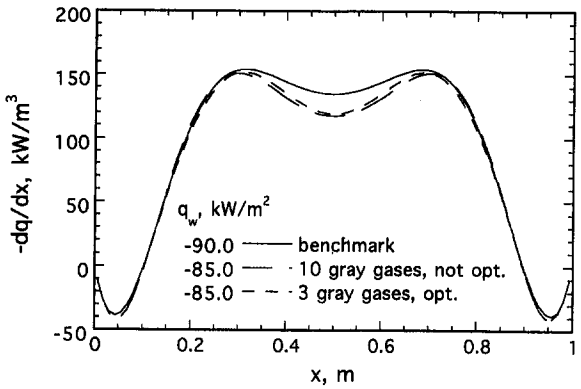



**Fig. 7 Radiative source and net wall flux for the sine temperature and mole fraction profiles of $H_2O$ [Eqs. (13) and (14)]. $T_w$ = 1500 K. $T_c$ = 500 K. $\epsilon_w = 1$.**

where the ten-gray-gas prediction is within 8 percent of the benchmark. Surprisingly, the optimized three-gray-gas prediction is within only 3 percent at the center. The net wall flux predicted by the ten-gray-gas model is 11 percent higher than the benchmark while that of the three-gray-gas model is 9 percent.

Figure 7 shows the results of hot walls at 1500 K radiating to a cold medium with $T_c$ = 500 K. This reversal in the emission/absorption roles of the walls and medium relative to the problem shown in Fig. 6 can yield quite different error characteristics, since the spectrum is so radically different. The temperature and mole fraction profiles are again given by Eqs. (13) and (14). The domain length is 1 m. Similar to the problem of Fig. 5 with a parabolic mole fraction profile, Fig. 7 shows two local maxima in the flux divergence profile. The largest errors in the flux divergence are 13 and 11 percent at the center for the ten and three-gray gas predictions, respectively. The models both underpredict slightly the local minimum of radiative source at the center. The net wall flux predictions are both within 6 percent of the benchmark.

**Computation Requirements.** The model presented here for nonisothermal/nonhomogeneous medium features considerable computational economy over the line-by-line predictions. The required computation times on an HP 750 workstation for the model predictions were about two and five seconds for a three- and ten-gray-gas model, respectively. This is in sharp contrast to computation times of the order of 25 hours required by the line-by-line benchmark solutions.

## Conclusions

An approach for extending the SLW model to problems of nonisothermal nonhomogeneous media has been developed. The absorption-line blackbody distribution function provides the means of modeling the dependence of the gray gas absorption cross sections on temperature, pressure, and species concentration. The SLW model allows arbitrary solution methods of the RTE without specification of a path length *a priori* as required by narrow- and wide-band models. Although the approach is still approximate, significantly improved accuracy compared with the previous SLW approach has been demonstrated when the weights are calculated by setting $T_g$, $P_T$, and $Y_s$ to fixed reference values.

## Acknowledgments

This work was supported by the Advanced Combustion Engineering Research Center (ACERC) at Brigham Young University. ACERC is sponsored by the National Science Foundation, the State of Utah, the U.S. Department of Energy, and a number of industrial participants. One of the authors (MKD) also



Downloaded 12 Dec 2010 to 193.140.21.150. Redistribution subject to ASME license or copyright; see http://www.asme.org/terms/Terms_Use.cfm

wishes to acknowledge the financial support of the NASA Rocky Mountain Grant Consortium.

## References

Carlson, B. G., and Lathrop, K. D., 1968, "Transport Theory—The Method of Discrete Ordinates," *Computing Methods in Reactor Physics,* H. Greenspan, C. N. Kelber, and D. Okrent, eds., Gordon and Breach, New York, pp. 171–266.

Denison, M. K., and Webb, B. W., 1993a, "A Spectral Line-Based Weighted-Sum-of-Gray-Gases Model for Arbitrary RTE Solvers," ASME JOURNAL OF HEAT TRANSFER, Vol. 115, pp. 1004–1012.

Denison, M. K., and Webb, B. W., 1993b, "An Absorption-Line Blackbody Distribution Function for Efficient Calculation of Total Gas Radiative Transfer," *Journal of Quantitative Spectroscopy and Radiative Transfer,* Vol. 50, pp. 499–510.

Denison, M. K., and Webb, B. W., 1995, "Development and Application of an Absorption-Line Blackbody Distribution Function for $CO_2$," *International Journal of Heat and Mass Transfer,* in press.

Edwards, D. K., 1976, "Molecular Gas Band Radiation," *Advances in Heat Transfer,* Vol. 12, pp. 115–193, Academic Press, New York.

Godson, W. L., 1953, "The Evaluation of Infrared Radiation Fluxes Due to Atmospheric Water Vapor," *Quarterly Journal of Royal Meteorological Society,* Vol. 79, pp. 367–379.

Goody, R. M., West, R., Chen, L., and Chrisp, D., 1989, "The Correlated-*k* Method for Radiation Calculations in Nonhomogeneous Atmospheres," *Journal of Quantitative Spectroscopy and Radiative Transfer,* Vol. 42, pp. 539–550.

Goody, R. M., and Yung, Y. L., 1989, *Atmospheric Radiation,* Clarendon Press, Oxford, United Kingdom.

Hottel, H. C., and Sarofim, A. F., 1967, *Radiative Transfer,* McGraw-Hill, New York.

Kim, T. K., Menart, J. A., and Lee, H. S., 1991, "Nongray Radiative Gas Analyses Using the S-N Discrete Ordinates Method," ASME JOURNAL OF HEAT TRANSFER, Vol. 113, pp. 946–952.

Lacis, A. A., and Oinas, V., 1991, "A Description of the Correlated *k*-Distribution Method for Modeling Nongray Gaseous Absorption, Thermal Emission, and Multiple Scattering in Vertically Inhomogeneous Atmospheres," *Journal of Geophysical Research,* Vol. 96, pp. 9027–9063.

Menart, J. A., Lee, H. S., and Kim, T. K., 1993, "Discrete Ordinates Solutions of Nongray Radiative Transfer With Diffusely Reflecting Walls," ASME JOURNAL OF HEAT TRANSFER, Vol. 115, pp. 184–193.

Modest, M. F., 1991, "The Weighted-Sum-of-Gray-Gases Model for Arbitrary Solution Methods in Radiative Transfer," ASME JOURNAL OF HEAT TRANSFER, Vol. 113, pp. 650–656.

Rivière, Ph., Soufiani, A., and Taine, J., 1992, "Correlated-*k* and Fictitious Gas Methods for $H_2O$ Near 2.7 $\mu$m," *Journal of Quantitative Spectroscopy and Radiative Transfer,* Vol. 48, No. 2, pp. 187–203.

Rothman, L. S., Gamache, R. R., Tipping, R. H., Rinsland, C. P., Smith, M. A. H., Chris Benner, D., Malathy Devi, V., Flaud, J. M., Camy-Peyret, C., Perrin, A., Goldman, A., Massie, S. T., and Brown, L. R., 1992, "The HITRAN Molecular Database: Editions of 1991 and 1992," *Journal of Quantitative Spectroscopy and Radiative Transfer,* Vol. 48, No. 5/6, pp. 469–507.

Smith, T. F., Shen, Z. F., and Friedman, J. N., 1982, "Evaluation of Coefficients for the Weighted Sum of Gray Gases Model," ASME JOURNAL OF HEAT TRANSFER, Vol. 104, pp. 602–608.



Downloaded 12 Dec 2010 to 193.140.21.150. Redistribution subject to ASME license or copyright; see http://www.asme.org/terms/Terms_Use.cfm

# Bolometric Response of High-$T_c$ Superconducting Detectors to Optical Pulses and Continuous Waves

**Rong-Chang Chen**
Research Assistant.

**Jhy-Ping Wu**
Research Assistant.

**Hsin-Sen Chu**
Professor.
Mem. ASME

Department of Mechanical Engineering,
National Chiao Tung University,
Hsinchu, Taiwan 300

*This work presents a thermal analysis on predicting the temperature increase and the voltage response of high-$T_c$ superconducting bolometers. Two heat transfer models, that is, the surface heating model and the heat generation model considering the skin depth, are introduced and compared. The surface heating model is found to be valid only for situations where the skin depth is much smaller than the film thickness. To consider the thermal boundary resistance between film and substrate, a radiation-boundary-condition model based on acoustic mismatch model (AMM) and an interfacial-layer model (ILM) are employed. The thermal boundary resistance significantly influences the voltage response. Additionally, several common substrates are examined. $SrTiO_3$ (100) or $LaAlO_3$ (100) is a better substrate for high-$T_c$ superconducting bolometers. One interesting finding was that when compared with experimental data, all the theoretical values from the present study as well as the other previously theoretical treatment overestimate the voltage response near the transition temperature.*

## Introduction

One potential applications of high-temperature (high-$T_c$) superconducting thin films is a superconducting bolometer. Since the discovery of high-$T_c$ superconductors, much effort has been focused on investigating the superconducting detectors (Biter et al., 1989; Brocklesby et al., 1989; Carr et al., 1990; Forrester et al., 1988; Frenkel et al., 1990; Kwok et al., 1989; Oppenheim et al., 1991; Talvacchio et al., 1989; Tanabe et al., 1991; Zeldov et al., 1989; Zheng et al., 1990), and several prototype bolometers have been designed and constructed (Brasunas et al., 1989; Hu and Richards, 1989; Richards et al., 1989; Verghese et al., 1991).

Besides the radiation absorption, the film energy will also increase through the imposition of bias current. When current flows through a conductor with resistance, the energy is dissipated. The heat energy, as a whole, can be transmitted through a crystal via the motion of phonons, photons, free electrons, electron-hole pairs, or excitons. In most situations the heat conduction is carried mainly by the free electrons for metals but almost carried by the lattice vibrations (phonons) for nonmetals. The high-$T_c$ superconductors exhibit a surprisingly large phonon contribution to the heat flow that, in single crystal, amounts to some 60 percent and, in sintered samples, up to 90 percent of the total heat conduction (Uher, 1990). On the other hand, the energy propagation through the substrate is only by phonons since most substrates are dielectric (insulating) materials. In brief, the energy propagation in the composite materials of the film and substrate is mainly by phonons.

In modeling the heat transfer behavior of a superconducting bolometer subjected to incident radiation, two models have generally been utilized. The first is the surface heating model, which assumes that all of the energy is absorbed by the front surface of the superconducting bolometer and that there is no absorption of the incident energy within the film. The second is the heat generation model, in which the front surface is assumed to be adiabatic due to its small energy loss to the surroundings. The incident energy is absorbed within the whole film or part of the film. To our knowledge, previous investigators with these two models did not discuss the effect of skin depth, $\delta$, on the heat transfer. The skin depth, $\delta$, is a measure of the exponential penetration of plane electromagnetic waves into normal conductors. The influence of the skin depth on the voltage response will be presented in this work.

In addition to the incident energy, the thermal boundary resistance between the superconducting film and the substrate also greatly affects the voltage response. Streiffer et al. (1991) indicated that a significant thermal barrier exists at the Y–Ba–Cu–O/substrate interface. Marshall et al. (1992) stated that the rate of flow through the Y–Ba–Cu–O/MgO interface is about 100 times less than the rate of flow in the Y–Ba–Cu–O film. Moreover, the barrier to thermal flow at the MgO substrate interface has a thickness of the order of the unit-cell size of ~11 Å. At present, there are at least two different models used for predicting the thermal boundary resistance. The first model is assumed with a radiation boundary condition, where the thermal flow across the interface is proportional to the difference of the fourth power of the temperature on each side of the interface (Little, 1959). This approximation is based on the acoustic mismatch model (AMM). However, the AMM is found to be in agreement with measurements only for temperatures below ~30 K (Swartz and Pohl, 1989). The second model (the interfacial layer model, ILM) assumes an interfacial layer of a variable thickness inside the superconducting film, where the diffusivity is significantly lower (~10–100 times) than that of bulk Y–Ba–Cu–O (Marshall et al., 1992).

Another important influencing factor is the substrate properties. The most common substrates used to fabricate high-$T_c$ superconducting bolometers are MgO, $SrTiO_3$, $LaAlO_3$, sapphire ($Al_2O_3$), and $ZrO_2$. The effect of these substrates on the temperature increase is considered in this study.

Two previously theoretical investigations did give fair analysis. Kumar and Joshi (1990) presented a parametric study of examining the effects of incoming radiation flux and bias current on the sensitivity and response of a bolometer. Flik et al. (1990) presented a rigorous thermal analysis of superconducting bolometers. They considered a conjugate radiation/conduction problem. They also considered the effects of variable properties of the film and the substrate as well as thermal boundary resistance based on the AMM.

Contributed by the Heat Transfer Division for publication in the JOURNAL OF HEAT TRANSFER. Manuscript received by the Heat Transfer Division September 1993; revision received May 1994. Keywords: Conduction, Electronic Equipment, Transient and Unsteady Heat Transfer. Associate Technical Editor: M. F. Modest.



Copyright © 1995 by ASME

Downloaded 12 Dec 2010 to 193.140.21.150. Redistribution subject to ASME license or copyright; see http://www.asme.org/terms/Terms_Use.cfm

This paper presents a new heat transfer model considering the skin depth to investigate the voltage response of the superconducting bolometers. The AMM and the ILM are both employed. The analysis is applied to short pulses, long pulses, and continuous waves. Our results show that the thermal boundary resistance has a great influence on the temperature increase and the voltage response of a high-$T_c$ superconducting bolometer.

## Analysis

A superconducting bolometer can be simply described as that a superconducting film is deposited on a substrate, as shown in Fig. 1.

**Joule Heating.** The film temperature at the $x$ direction is not constant during the conduction transient. Therefore by considering the film to be composed of infinitely many filaments and each filament in the film to be in parallel, the voltage change per unit length $v$ is given as (Kumar and Joshi, 1990)

$$v = Jd\left[\int_0^d \frac{dx}{\gamma(T(x))}\right]^{-1} \tag{1}$$

where $\gamma$ is the resistivity and is equal to resistance times unit cross-sectional area normal to the current per unit length, and $J$ is the current density. The local Joule heat per unit volume $g_j$ is equal to the square of the voltage changes per unit length divided by the resistivity, and can be represented as follows:

$$g_j = \frac{(Jd)^2}{\gamma(I, T_f)}\left[\int_0^d \frac{dx}{\gamma(I, T_f)}\right]^{-2} \tag{2}$$

**Heat Transfer Models.** The skin depth, $\delta$, is given as (Van Duzer and Turner, 1981)

$$\delta = \sqrt{\frac{2}{\omega\mu\sigma}} \tag{3}$$

where $\omega$ is the angular frequency, $\mu$ the permeability, and $\sigma$ the electrical conductivity. A typical skin depth for an infrared source is about 0.1 $\mu$m–1 $\mu$m. This skin depth, in fact, determines the validity of the surface heating model. Only when the skin depth $\delta$ is much smaller than the film thickness is the surface heating model valid.

*1 Surface Heating Model.* This model assumes that all incident energy is exerted on the front surface of the film and there is no absorption inside the film. The energy equations, initial conditions, and boundary conditions are as follows:

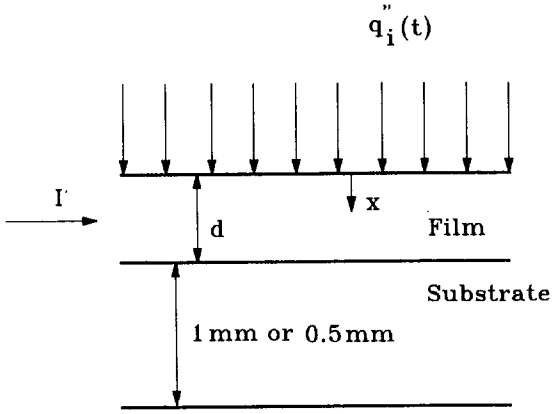



**Fig. 1 Schematic diagram of the physical system**

$$\rho_f c_f \frac{\partial T_f}{\partial t} = \frac{\partial}{\partial x}\left(k_f \frac{\partial T_f}{\partial x}\right) + \frac{(Jd)^2}{\gamma(I, T_f)}\left[\int_0^d \frac{dx}{\gamma(I, T_f)}\right]^{-2} \tag{4a}$$

$$\rho_s c_s \frac{\partial T_s}{\partial t} = \frac{\partial}{\partial x}\left(k_s \frac{\partial T_s}{\partial x}\right) \tag{4b}$$

$$T_f(x, t = 0) = T_s(x, t = 0) = T_0 \tag{5}$$

$$-k_f \frac{\partial T_f}{\partial x}(x = 0, t) = q_i''(t), \tag{6a}$$

$$-k_f \frac{\partial T_f}{\partial x}(x = d, t) = -k_s \frac{\partial T_s}{\partial x}(x = d, t) \tag{6b}$$

$$-k_f \frac{\partial T_f}{\partial x}(x = d, t) = q_b(t), \tag{6c}$$

$$T_s(x \to \infty, t) \to T_o \tag{6d}$$

where $T$ is the temperature, $\rho$ the density, $c$ the specific heat, and $k$ the thermal conductivity. Subscripts $f$ and $s$ stand for the film and the substrate, respectively. If the radiation-boundary condition model is employed, Eq. (6c) becomes

## Nomenclature

Bi = Biot number
$B_s$ = elastic bulk modulus
$c$ = specific heat
$d$ = thickness of superconducting film
$g, g_0$ = heat generation by absorption; see Eq. (10)
$g_j$ = heat generation by Joule heating
$h$ = Planck's constant = $6.6262 \times 10^{-34}$ J s
$h_b$ = solid–solid thermal boundary conductance
$h_l$ = heat conductance across the interfacial layer
$I$ = bias current
$J$ = current density
$k$ = thermal conductivity
$k_B$ = Boltzmann constant = $1.38062 \times 10^{-23}$ J K$^{-1}$
$p$ = period
$q, q_0$ = heat flux
$q_b$ = boundary heat flux
$q_i''$ = incident heat flux
$R$ = electrical resistance
$r_d$ = thickness ratio of interfacial layer to film
$r_k$ = thermal conductivity ratio of interfacial layer to film
$T$ = temperature
$T_{avg}$ = average film temperature
$T_0$ = initial temperature
$T_t$ = transition temperature
$t$ = time
$t_c$ = time scale for heat conduction across thin film
$t_p$ = pulse length
$V$ = voltage
$v$ = voltage per unit volume
$\bar{v}$ = sound velocity
$x$ = distance from film front surface
$\alpha$ = thermal diffusivity
$\Gamma$ = constant; see Eq. (7)
$\gamma$ = electrical resistivity
$\Delta$ = nondimensional skin depth, $\delta/d$
$\delta$ = skin depth
$\kappa$ = constant; see Eq. (7)
$\mu$ = permeability
$\sigma$ = electrical conductivity
$\rho$ = mass density

**Subscripts**

avg = average
$f$ = film properties
$l$ = interfacial layer properties
max = maximum
$s$ = substrate properties



Downloaded 12 Dec 2010 to 193.140.21.150. Redistribution subject to ASME license or copyright; see http://www.asme.org/terms/Terms_Use.cfm

$$-k_f \frac{\partial T_f}{\partial x}(x = d, t)$$

$$= \kappa\{[T_f(x = d, t)]^4 - [T_s(x = d, t)]^4\} \quad (6c')$$

$$\kappa = \frac{2\pi k_B^4 \Gamma}{h^3 \bar{v}^2}\left(\frac{\pi^4}{15}\right) \quad (7)$$

*2 Heat Generation Model.* Only the film energy equation and the boundary condition at the front surface are different from those of the surface heating model:

$$\rho_f c_f \frac{\partial T_f}{\partial t} = \frac{\partial}{\partial x}\left(k_f \frac{\partial T_f}{\partial x}\right) + g(x, t) + \frac{(Jd)^2}{\gamma(I, T_f)}\left[\int_0^d \frac{dx}{\gamma(I, T_f)}\right]^{-2} \quad (8)$$

$$\frac{\partial T(x = 0, t)}{\partial x} = 0 \quad (9)$$

where $g(x, t)$ represents volumetric heat generation. Uniform or constant heat generation is usually assumed. In this work, however, we consider the effect of the skin depth $\delta$, and thus the volumetric heat generation is expressed as

$$g(x, t) = g_0(t) \exp(-x/\delta) \quad (10)$$

To enable comparison between these two models, the energy incident on the film must be the same. This yields

$$q_i''(t) = \int_0^d g(x, t)dx \quad (11)$$

### Thermal Boundary Resistance

*1 Radiation-Boundary-Condition Model.* This approximation is based on the AMM (Little, 1959). Predictions based on the AMM are found to be in agreement with measurements below 30 K. The expression for this boundary condition is given in Eqs. (6c') and (7). The most important constant is $\Gamma$, a function of the material properties of the two contacting media. Using the figure provided by Little (1959), $\Gamma$ can be obtained if the density ratio and the sound velocity ratio of two media are known. To the authors' knowledge, no direct measurements have been made for the average sound velocities of some typical substrates. However, there are at least two ways to find the sound velocity. The first way is from the elastic bulk modulus, $B_s$ (Blakemore, 1985):

$$\bar{v} = \sqrt{B_s/\rho} \quad (12)$$

For solids, Eq. (12) gives the correct order of magnitude for the longitudinal sound velocity. Comparison with direct measurements shows that sound velocities calculated from the elastic bulk modulus give tolerably favorable values for some typical solids and demonstrates that sound velocities are of the order of 5000 m/s in typical metallic, covalent, and ionic solids. The second method is from the Debye temperature, $\theta_D$ (Blakemore, 1985; Kittel, 1991):

$$\bar{v} = \frac{k_B \theta_D}{\hbar}\left(6\pi^2 \frac{N}{\bar{V}}\right)^{-1/3} \quad (13)$$

where $\hbar = h/(2\pi)$, $\bar{V}$ is the volume of the specimen, and $N$ is the number of atoms of the specimen. For MgO, $\bar{V}/N = 9.35$ Å. Substituting this value and $\theta_D = 946$ K (AIP, 1972) into Eq. (13), we obtain $\bar{v} \sim 6700$ m/s, about 4 percent lower than the value reported by Slack (1962).

*2 Interfacial-Layer Model.* The thermal boundary resistance between solids is often actually higher than that calculated from the AMM. Thus, it is important to find a model that can predict the thermal boundary resistance more accurately. The other model for calculating thermal boundary resistance is the interfacial-layer model (ILM) (Marshall et al., 1992). This model assumes a layer of a variable thickness (~1–10 percent of the total sample thickness) inside the Y–Ba–Cu–O film, where the diffusivity is significantly lower (~10–100 times) than that of bulk Y–Ba–Cu–O.

## Method of Solution

Since the Joule heating is a complicated function of film temperature, the film energy equation is highly nonlinear. We will use a fully implicit, finite-difference scheme with an underrelaxation technique to solve this highly nonlinear conjugate film/substrate conduction problem. Harmonic mean is employed to model the nonuniform thermal conductivities. Iterations between the Joule heating, thermal properties, and energy equation at each time step continue until the criterion of convergence, $|T - T_{\text{iter}}|/|T_{\max}|$, is within $10^{-4}$.

## Results and Discussion

To enable comparison of our results with those of other previous investigations, the configuration of the bolometer is chosen to be the same as those from the experimental work of Frenkel et al. (1990) and a theoretical analysis in Flik et al. (1990). The film thickness is 40 nm. The substrate is MgO. The incident heat flux for the 200 ns long pulse is represented as (Flik et al., 1990).

$$q_i'' = (3.81 \times 10^7) \exp\left[\frac{-(t/t_p - 1)^2}{0.36067}\right] \quad (14)$$

The conductivity ratio $r_k$ of interfacial layer to film is 0.01 and the thickness ratio $r_d$ is 0.025.

**Heat Transfer Models.** Figure 2 shows the effect of the skin depth on the temperature increase. Since the purpose of this figure is to demonstrate the influence of the skin depth, only the film is considered. A constant-properties film energy equation that neglects Joule heating is sufficient. The back surface of the film is kept at initial temperature $T_0$. A long pulse of 200 ns, as represented in Eq. (14), is incident onto the front surface of the film. The nondimensional skin depth, $\Delta$, defined as $\delta/d$, is an important parameter governing the validity of the heat transfer models. The surface heating model gives a constant temperature increase independent of the skin depth. When $\Delta$ approaches 0, the result of the heat generation model approaches asymptotically that of the surface heating model. As $\Delta$ increases, the difference between the average film temperatures from the two models increases. The front surface temperatures from these two different models show an even greater difference. The surface heating model overestimates the temperature increase. Since superconducting bolometers are generally operated at the transition tem-

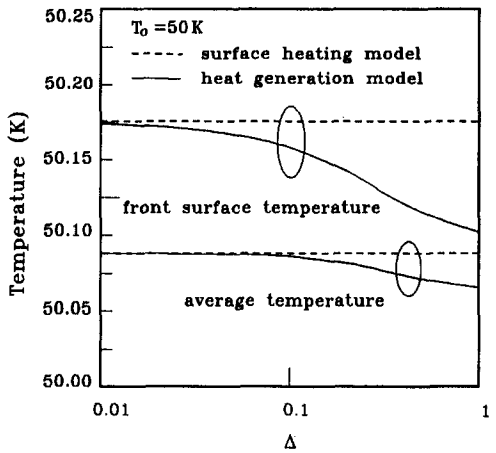



**Fig. 2 Effect of skin depth on the temperature increase**



Downloaded 12 Dec 2010 to 193.140.21.150. Redistribution subject to ASME license or copyright; see http://www.asme.org/terms/Terms_Use.cfm

perature, a slight temperature increase will cause a large voltage response. To predict the voltage response correctly, we suggest that the effect of the skin depth should be considered in a heat transfer analysis of superconducting bolometers.

**Long Pulse.** Since the surface heating model neglects the effect of the skin depth, the following results were all obtained by employing the heat generation model.

Figure 3($a$) shows the temperature profiles across the film and the interfacial layer and partially into the substrate. Incident heat flux $q_i''$ reaches a maximum at 200 ns. The temperature profiles, however, do not reach their maximum $T_{avg}$, average film temperature, until $t$ = 222 ns. The temperature decreases with distance into the substrate. At the interfacial layer, there is a great temperature difference. The Biot number, Bi, defined as $h_l d/k_f$, is ~0.4, indicating that heat conductance across the film is larger than the heat conductance across the interfacial layer, and thus the temperature difference across the interfacial layer is larger than that across the film.

Figure 3($b$) compares the results of different models for thermal boundary resistance. The value of $\Gamma$ for the AMM is 0.2. $R_{bd}$ = 0 represents the case for no thermal boundary resistance. The profile for $R_{bd}$ = 0 can be obtained in three different ways. The limiting case where $k \to \infty$, the prescribed condition $T_f = T_s$ at the film/substrate interface for the AMM, and the case where $r_k$ = 1, $r_d \to 0$ for the ILM give the same result, further illustrating the correctness of the numerical solution. The temperature differences across the interfacial layer calculated from the ILM are greater than those from the AMM. The Biot number for the AMM is ~0.6, and this causes a smaller temperature difference than in the ILM solutions. Marshall et al. (1992) stated that the rate of flow across the Y–Ba–Cu–O/MgO interface is ~100 times lower than the rate of flow across the Y–Ba–Cu–O film. This corresponds to the case where $r_k$ = 0.01. The maximum average temperature increase for $r_k$ = 0.01 is ~2 times larger than that for $R_{bd}$ = 0. This implies that neglecting the thermal boundary resistance causes the average film temperature to be greatly underestimated.

A plot of the voltage response is given in Fig. 3($c$). The results of our work are compared with the theoretical results of Flik et al. (1990) and the experimental analysis from Frenkel et al. (1990). The present result is from the ILM, while the results of Flik et al. are from the AMM. A noteworthy phenomenon is that at temperatures near the transition temperature, $T_t$, both theoretical papers overestimate the experimental value, while at temperatures below $T_t$, both underestimate the value. At temperatures below $T_t$, the underestimation is reasonable, since both thermal models can predict only the bolometric, i.e., the voltage change caused by absorption of radiation. However, there is a nonbolometric effect in the work of Frenkel et al. Only when the nonbolometric part is considered, do the theoretical results and experimental results match. To the authors' knowledge, this nonbolometric mechanism is still not well understood. A flux creep model has been employed to study the nonlinear characteristics in the low resistivity region, but the results of this model are questionable. Unlike the underestimation below $T_t$, the theoretical results overestimate the experimental voltage response at temperatures near $T_t$. There are several possible reasons for this overestimation. One is overestimation of the incident heat flux: A higher incident heat flux causes a higher temperature increase and voltage response. Another possible reason is that the energy loss from the front surface is large. A final possible reason is the hot-electron transport (Donaldson, 1989). The initial effect of radiation is to create a number of highly excited electrons and holes at the top of the film. Then the heat rapidly spreads an additional distance of ~1 $\mu$m via nonequilibrium hot electrons. The hot electrons then thermalize with the lattice, producing an essentially bolometric response.

There are two explanations for why the voltage response at temperatures near $T_t$ in the present study is higher than that predicted by Flik et al. One is that the thermal boundary resistance from the ILM is higher than that from the AMM. The other is that the present study considers Joule heating. Flik et al. neglected the effect of Joule heating, so they underestimated the temperature increase. At temperatures below ~40 K, however, the voltage response found in the present study is lower than that reported in Flik et al. This is because the thermal boundary re-

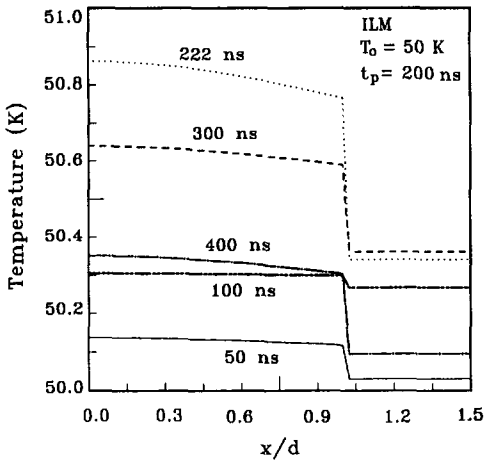



**Fig. 3(a) Temperature profiles across the film and the interfacial layer and partially into the substrate**

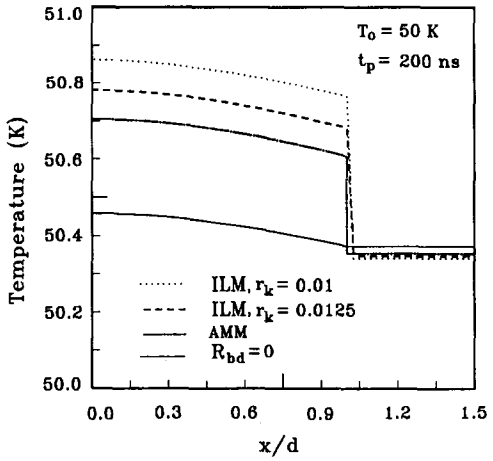



**Fig. 3(b) Effect of thermal boundary resistance on the temperature profiles. $R_{bd}$ = 0 represents the case of no thermal boundary resistance.**

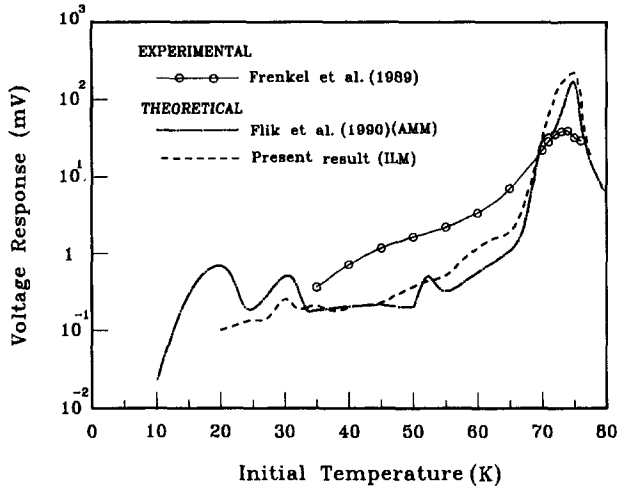



**Fig. 3(c) Comparison between the calculated voltage responses with experimental data**



Downloaded 12 Dec 2010 to 193.140.21.150. Redistribution subject to ASME license or copyright; see http://www.asme.org/terms/Terms_Use.cfm

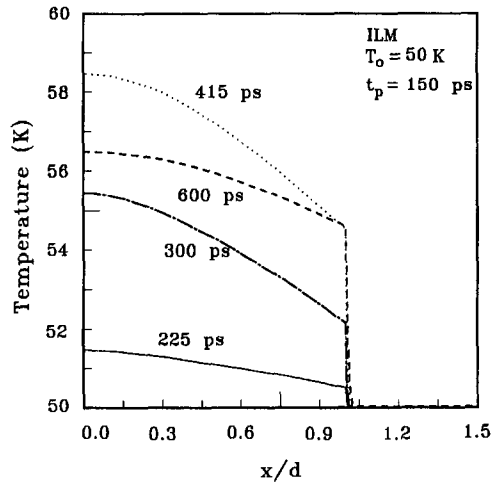



Fig. 4 Variation of maximum voltage response with pulse duration

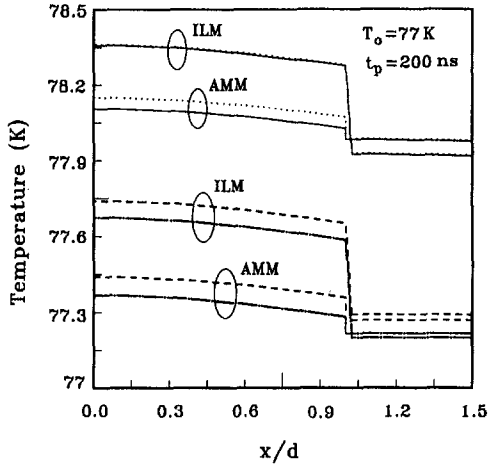



Fig. 5 Effects of different substrates on the temperature increase: ···, $SrTiO_3$; ——, $LaAlO_3$; – – –, MgO; – · – · –, sapphire

sistance predicted from the AMM is greater than ILM below $T \sim 40$ K. At $T \sim 40$ K, the Biot number, Bi, defined as $h_b d/k_f$, is ~0.36 for the AMM, lower than the value of 0.4, a constant value independent of temperature from the ILM.

**Pulse Duration.** The influence of pulse duration on the voltage response is shown in Fig. 4. The initial temperature is 50 K, and the energy flux and bias current are fixed at 1.02 J $m^{-2}$ and 5 mA, respectively. The voltage response increase with a decreasing pulse duration. The maximum average film temperature $T_{avg}$ shows the same trend. A shorter pulse gives a greater average incident heat flux, leading to a greater average temperature increase and voltage response. Note that the voltage response for $T_o = 50$ K is larger than that for $T_o = 25$ K for all the pulse durations. In the work of Flik et al., however, the voltage response for $T_o = 50$ K is lower than that for $T_o = 20$ K at about $t_p > 2$ ps. One important factor leading to this result is the thermal boundary resistance based on the AMM depends on temperature. The thermal boundary resistance at $T_o = 20$ K is greater than that at $T_o = 50$ K for the AMM. When this factor overwhelms the others, the voltage response will exceed that of $T_o = 50$ K.

**Substrate.** For Y–Ba–Cu–O films, the most common substrates used for fabricating superconducting bolometers are MgO, $SrTiO_3$, sapphire, and $LaAlO_3$. To examine the effects of these different substrates, we employed both the AMM and the ILM. Figure 5 displays the effect of different substrates on the temperature increase. The properties of substrates are listed in Table 1. For the ILM, $r_k$ and $r_d$ are assumed to be 0.01 and 0.025, respectively. Although measured data of $r_k$ and $r_d$ for $SrTiO_3$ (100), $LaAlO_3$ (100), and sapphire are unavailable, the results from the ILM also show some trends. Both the ILM and the AMM give the same result: The temperature increase for $SrTiO_3$ is the highest, that for $LaAlO_3$ is the second, that for MgO is the third highest, and that for sapphire is the lowest. Several factors lead to this result. A high thermal conductivity conducts heat more rapidly to the coolant and thus reduces the temperature increase of the film. A substrate with a higher heat capacity reduces the temperature increase of the substrate, leading to a higher temperature difference between the film and the substrate, so that heat is conducted easily from the film to the substrate. The heat capacity of $SrTiO_3$ is a little larger than that of $LaAlO_3$, negatively influencing the temperature increase of the film. In contrast, the thermal conductivity of $SrTiO_3$ is lower than that of $LaAlO_3$; this lower thermal conductivity magnifies the temperature increase of the film. The influence of thermal conductivity overwhelms that of the heat capacity, and thus the temperature increase of $SrTiO_3$ is greater than that of the $LaAlO_3$. From the AMM, the temperature increase of $SrTiO_3$ is apparently greater than that of $LaAlO_3$. This is because the thermal boundary resistance of $SrTiO_3$ predicted by the AMM is higher than that of $LaAlO_3$. The temperature increase of the film is lowest for sapphire, due to its very high thermal conductivity. Note that the temperature increase predicted by ILM is higher than that predicted by the AMM, as explained in Fig. 3(*c*). Another potential substrate is $ZrO_2$. Because data on the thermal conductivity of $ZrO_2$ at low temperatures are unavailable, the temperature increase cannot be predicted. A value of 1.5 W/mK is reported in Zheng et al. (1990). This low thermal conductivity is very favorable for the temperature increase. However, this value is questionable. Since the voltage response is approximately proportional to the temperature increase, the substrate that better enhances the responsivity of the bolometer seems to be $SrTiO_3$.

**Continuous Waves.** In addition to work focusing on the long pulses and short pulses, many experimental papers have been concerned with continuous waves. To investigate the dynamic response of a bolometer, a periodic light signal with 50 percent duty cycle controlled by a function generator is usually employed. In this study, we used a previous experimental configuration by Oppenheim et al. (1991) to investigate the response of the bolometer. The thickness of the $YBa_2Cu_3O_7$ film was 1 $\mu$m, the substrate was $SrTiO_3$, with a thickness of 0.5 mm. The irradiance at the plane of the bolometer was ~0.2 W/$cm^2$. A CW-$CO_2$ laser operating at 10.6 $\mu$m was mechanically chopped at 130 Hz. The skin depth $\delta$ in this case was ~0.2 $\mu$m. The incident heat flux is expressed as

$$q_i'' = \begin{cases} (4010.8) \exp\left[\dfrac{-18 \times \left(\dfrac{t}{p} - 0.25\right)^2}{0.36067}\right] & \\ & np < t \le (n + \tfrac{1}{2})p \\ 0 & (n + \tfrac{1}{2})p < t \le (n + 1)p \end{cases} \quad (15)$$

Table 1 Properties of substrates at $T_0 = 77$ K

| $T_0 = 77$ K | $\rho_s$, g/cm$^3$ | $k_s$, W/m K | $c_s$, J/kg K | $\bar{v}$, m/s | $\Gamma^a$ |
|---|---|---|---|---|---|
| $LaAlO_3$ | 6.52[b] | 18.6[b] | 14.1[b] | 5400[b] | 0.3 |
| $SrTiO_3$ | 5.12[d] | 18.3[c] | 181.6[c] | 7200[d] | 0.15 |
| Sapphire | 3.99[e] | 1131[c] | 60.7[c] | 6600[e] | 0.2 |
| MgO | 3.58[e] | 485.7[c] | 88.7[c] | 7000[e] | 0.2 |

[a] From figure provided by Little (1959); [b]Michael et al. (1992); [c]Touloukian and Dewitt (1981); [d]calculated from Young's modulus, Nassau and Miller (1988); [e]Slack (1962).



Downloaded 12 Dec 2010 to 193.140.21.150. Redistribution subject to ASME license or copyright; see http://www.asme.org/terms/Terms_Use.cfm

Calculated voltage responses from the present study are compared with that of experiment in Oppenheim et al. Figure 6 shows the voltage response of the bolometer as a function of initial temperature. The AMM is employed to investigate the responses, in the belief that it should give a lower thermal boundary resistance, and thus it will reduce the overestimation of the voltage response near $T_t$ that occurred in previous case. Three cases were investigated in this work. Cases 1 and 2 did not consider the effect of Joule heating, and the incident heat fluxes for these two cases were 750 W/m$^2$ and 2000 W/m$^2$, respectively. Case 3 considered Joule heating, with an incident heat flux of 2000 W/m$^2$. Case 1 was not chosen arbitrarily. The measured peak response is 9 $\mu$V. The peak responsivity (peak voltage response per unit incident power) reported from the work of Oppenheim et al. is 0.5 V/W. If this peak responsivity is correct, the corresponding incident heat flux should be 750 W/m$^2$. The predicted voltage responses from our study are found to agree with the measurement: There is only a bolometric effect, in contrast to the result of Frenkel et al. (1989). The peak voltage response in our study occurs at $T_o \sim 90.3$ K, giving the same trend as observed in the experimental data. However, it should be noted that the voltage response in the present study is higher than that found by experiment. Even in the cases where Joule heating is neglected, the calculated voltage responses are still higher than those observed experimentally. The possible reasons have been presented in the discussion of Fig. 3($c$).

**Frequency Dependence.** The voltage response of a continuous wave depends on the modulation frequency. Figure 7 depicts this dependence. The voltage response decreases with an increase in frequency. At very low frequencies, the voltage response is actually independent of frequency. This is because at low frequencies the instantaneous carrier density can follow the rise and decay of the radiation upon the bolometer surface. To obtain maximum responsivity, the modulation frequency should be made as low as possible. However, a very low frequency may cause a very large temperature increase, which will encourage thermal instability. Thus, an optimal frequency is needed in order to obtain maximum responsivity without thermal runaway. One guideline is that the ratio of the modulation frequency to the thermal response frequency of the system should be $(2\pi)^{-1}$ (Newhouse, 1964).

## Conclusions

A thermal analysis of high-$T_c$ superconducting bolometers has been carried out. One-dimensional, variable-properties, conjugate film/substrate heat conduction equations with complicated Joule heating have been solved. Two models, the interfacial-layer model (ILM), and the acoustic mismatch model (AMM) were used to examine the thermal boundary resistance.

The skin depth is a crucial parameter for heat transfer models. The surface heating model is only valid when the skin depth is very small compared to the film thickness. To predict the temperature increase and the voltage response of bolometers correctly, the skin depth should be taken into consideration.

At higher temperatures, the ILM gives a higher thermal boundary resistance, which improves the disagreement of thermal boundary resistance with measurement and leads to a higher predicted temperature increase for the bolometer. In contrast, the AMM predicts a higher thermal boundary resistance at lower temperatures. In brief, the ILM should be employed to model the thermal boundary resistance at temperatures higher than ~50 K, and the AMM should be employed at temperatures lower than 30 K.

A short pulse is favorable for a higher voltage response. From the viewpoint of heat transfer, $SrTiO_3$ (100) or $LaAlO_3$ (100) is a better substrate for fabricating high-$T_c$ superconducting bolometers. As far as CW is concerned, a lower frequency is favorable for better responsivity.

The voltage responses predicted from this work reach their maximum at temperatures near the transition temperature, indicating that a bolometric response does occur. However, at temperatures near the transition temperature, the calculated voltage responses in this study as well as the previously rigorous thermal analysis in Flik et al. are higher than those obtained by experimental measurements. The exact reason for this result is unclear. Possible reasons include neglect of the energy loss from the front surface to surroundings, overestimation of incident heat flux, unsuitable substrate properties, or mechanisms other than phonon conduction. Note that all the calculated responses in this work are based on experimentally obtained resistance-temperature curves and "estimated" incident heat fluxes reported by the previously experimental papers. It is assumed that these curves and incident heat flux values are exact. However, some error due to uncertainty of measurements is probably unavoidable. Thus, a possible reason for the disagreement between experimental results and theoretical values at temperatures near the transition temperature is the uncertainty of experiments. Further investigations are encouraged to remedy the disagreement between theoretical and experimental results.

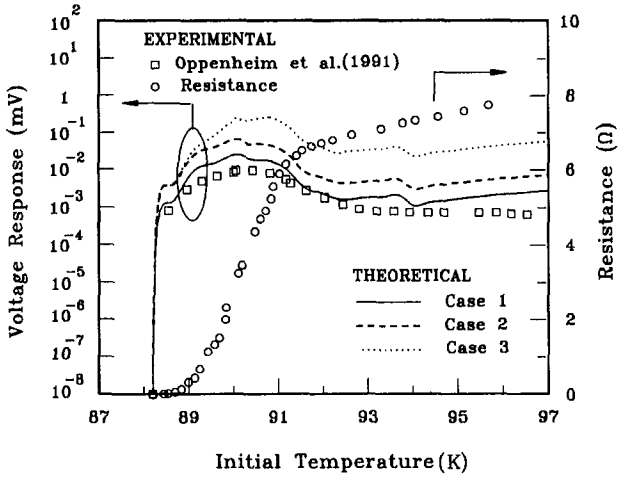



**Fig. 6 Comparison between the calculated voltage responses with experimental data of a typical continuous wave. The resistance is also shown. $T_t$ = 90.3 K.**

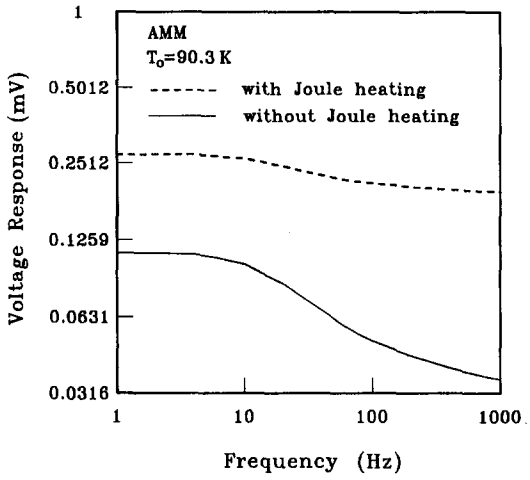



**Fig. 7 Influence of frequency on the voltage response**

## Acknowledgments

The authors wish to express their sincere appreciation to Professors Y.S. Gou, W.Y. Guan, and Dr. H.C. Lin for their inval-



Downloaded 12 Dec 2010 to 193.140.21.150. Redistribution subject to ASME license or copyright; see http://www.asme.org/terms/Terms_Use.cfm

uable advice and suggestions during the course of this paper. This research was supported by the National Science Council of the R.O.C. through grant NSC 81-0401-E-009-585.

## References

AIP, 1972, *American Institute of Physics Handbook,* McGraw-Hill Book Company, New York.

Biter, W., Rothwarf, A., and Scoles, K., 1989, "High $T_c$ Superconductor Infrared Detectors," *Proc. SPIE Conference,* p. 1106.

Blakemore, J. S., 1985, *Solid State Physics,* Cambridge University Press, United Kingdom.

Brasunas, J. C., Moseley, S. H., Lakew, B., Ono, R. H., Mcdonald, D. G., Beall, J. A., and Sauvageau, J. E., 1989, "Construction and Performance of a High-Temperature-Superconductor Composite Bolometer," *J. Appl. Phys.,* Vol. 66, No. 9, pp. 4551–4554.

Brocklesby, W. S., Monroe, D., Levi, A. F. J., Hong, M., Liou, S. H., Kwo, J., Rice, C. E., Mankiewich, P. M., and Howard, R. E., 1989, "Electrical Response of Superconducting $YBa_2Cu_3O_{7-\delta}$ to Light," *Appl. Phys. Lett.,* Vol. 54, No. 12, pp. 1175–1177.

Carr, G. L., Quijada, M., Tanner, D. B., Hirschmugl, C. J., Williams, G. P., Etemad, S., Dutta, B., DeRosa, F., Inam, A., Venkatesan, T., and Xi, X., 1990, "Fast Bolometric Response by High $T_c$ Detectors Measured With Subnanosecond Synchrotron Radiation," *Appl. Phys. Lett.,* Vol. 57, No. 25, pp. 2725–2727.

Donaldson, W. R., Kadin, A. M., Ballentine, P. H., and Sobolewski, R., 1989, "Interaction of Picosecond Optical Pulses With High $T_c$ Superconducting Films," *Appl. Phys. Lett.,* Vol. 54, No. 24, pp. 2470–2472.

Flik, M. I., Phelan, P. E., and Tien, C. L., 1990, "Thermal Model for the Bolometric Response of High-$T_c$ Superconducting Films to Optical Pulses," *Cryogenics,* Vol. 30, pp. 1118–1128.

Forrester, M. G., Gottlieb, M., Gavaler, J. R., and Braginski, A. I., 1988, "Optical Response of Epitaxial Films of $YBa_2Cu_{3-}\ O_{7-\delta}$," *Appl. Phys. Lett.,* Vol. 53, No. 14, pp. 1332–1334.

Frenkel, A., Saifi, M. A., Venkatesan, T., England, P., Wu, X. D., and Inam, A., 1990, "Optical Response of Non-granular High-$T_c$ $YBa_2Cu_3O_{7-x}$ Superconducting Thin Films," *J. Appl. Phys.,* Vol. 67, pp. 3054–3068.

Hu, Q., and Richards, P. L., 1989, "Design Analysis of a High $T_c$ Superconducting Microbolometer," *Appl. Phys. Lett.,* Vol. 55, No. 23, pp. 2444–2446.

Kittel, C., 1991, *Introduction to Solid State Physics,* Wiley, New York.

Kumar, S., and Joshi, A., 1990, "Thermal Assessment of a Transition-Edge High-$T_c$ Superconductor Infrared Detector," *Proc. AIAA/ASME Thermophysics and Heat Transfer Conference,* Seattle, WA.

Kwok, H. S., Zheng, J. P., Ying, Q. Y., and Rao, R., 1989, "Nonthermal Optical Response of Y-Ba-Cu-O Thin Films," *Appl. Phys. Lett.,* Vol. 54, No. 24, pp. 2473–2475.

Little, W. A., 1959, "The Transport of Heat Between Dissimilar Solids at Low Temperatures," *Can. J. Phys.,* Vol. 37, pp. 334–349.

Marshall, C. D., Fishman, I. M., Dorfman, R. C., Eom, C. B., and Fayer, M. D., 1992, "Thermal Diffusion, Interfacial Thermal Barrier, and Ultrasonic Propagation in $YBa_2Cu_3O_7$ Thin Films: Surface-Selective Transient-Grating Experiments," *Phys. Rev. B,* Vol. 45, No. 17, pp. 10009–10021.

Michael, P. C., Trefny, J. U., and Yarar, B., 1992, "Thermal Transport Properties of Single Crystal Lanthanum Aluminate," *J. Appl. Phys.,* Vol. 72, No. 1, pp. 107–109.

Nassau, K., and Miller, A. E., 1988, "Strontium Titanate: an Index to the Literature on Properties and the Growth of Single Crystals," *J. Crystal Growth,* No. 91, pp. 373–381.

Newhouse, V. L., 1964, *Applied Superconductivity,* Wiley, New York.

Oppenheim, U. P., Katz, M., Koren, G., Polturak, E., and Fishman, M. R., 1991, "High Temperature Superconducting Bolometer," *Physics C,* No. 178, pp. 26–28.

Richards, P. L., Verghese, S., Geballe, T. H., and Spielman, S. R., 1989, "The High $T_c$ Superconducting Bolometer," *IEEE Trans. Magn.,* Vol. 25, No. 2, pp. 1335–1338.

Slack, G. L., 1962, "Thermal Conductivity of MgO, $Al_2O_3$, $MgAl_2O_4$, and $Fe_3O_4$ Crystals from 3 to 300 K," *Phys. Rev.,* Vol. 126, No. 2, pp. 427–441.

Streiffer, S. K., Lairson, B. M., Eom, C. B., Clemens, B. M., Bravman, J. C., and Geballe, T. H., 1991, "Microstructure of Ultrathin Films of $YBa_2Cu_3O_{7-\delta}$ on MgO," *Phys. Rev. B,* Vol. 43, No. 16, pp. 13007–13018.

Swartz, E. T., and Pohl, R. O., 1989, "Thermal Boundary Resistance," *Rev. Mod. Phys.,* Vol. 61, pp. 605–668.

Talvacchio, J., Forrester, M. G., and Braginski, A. I., 1989, "Photodetection With High-$T_c$ Superconducting Films of $YBa_{2-}\ Cu_3O_{7-\delta}$," *Science and Technology of Thin—Film Superconductors,* Plenum, New York.

Tanabe, K., Kubo, S., Enomoto, Y., Asano, H., and Yamaji, A., 1991, "Coexistence of Bolometric and Nonbolometric Optical Responses in High-$T_c$ $LnBa_2Cu_3O_y$ (Ln = Y, Eu) Thin Films," *Jap. J. Appl. Phys.,* Vol. 30, No. 1B, pp. L110–L113.

Touloukian, Y. S., and Dewitt, D. P., 1981, *Thermophysical Properties of Matter,* IFI/Plenum, New York.

Uher, C., 1990, "Thermal Conductivity of High-$T_c$ Superconductors," *J. Superconductivity,* Vol. 3, No. 4, pp. 337–389.

Van Duzer, T., and Turner, C. W., 1981, *Principles of Superconductive Devices and Circuits,* Elsevier Press, New York.

Verghese, S., Richards, P. L., Char, K., and Sachtjen, S. A., 1991, "Fabrication of an Infrared Bolometer With a High $T_c$ Superconducting Thermometer," *IEEE Trans. Magn.,* Vol. 27, No. 2, pp. 3077–3080.

Zeldov, E., Amer, N. M., Koren, G., and Gupta, A., 1989, "Nonbolometric Optical Response of $YBa_2Cu_3O_{7-\delta}$ Epitaxial Films," *Phys. Rev. B,* Vol. 39, No. 13, pp. 9712–9714.

Zheng, J. P., Ying, Q. Y., and Kwok, H. S., 1990, "Y-Ba-Cu-O Thin Film Infrared Detectors," *Physica C,* Vol. 168, pp. 322–326.



Downloaded 12 Dec 2010 to 193.140.21.150. Redistribution subject to ASME license or copyright; see http://www.asme.org/terms/Terms_Use.cfm

**T. D. Fadale**[1]
Department of Aeronautics and Astronautics,
University of Washington,
Seattle, WA 98185

**A. V. Nenarokomov**
Department of Space System Engineering,
Moscow Aviation Institute,
Moscow, Russia

**A. F. Emery**
Department of Mechanical Engineering,
University of Washington,
Seattle, WA 98185

# Two Approaches to Optimal Sensor Locations

*Accurate modeling of thermal systems depends upon the determination of the material properties and the surface heat transfer coefficients. These parameters are frequently estimated from temperatures measured within the system or on the surface or from measured surface heat fluxes. Because of sensor errors or lack of sensitivity, the measurements may lead to erroneous estimates of the parameters. These errors can be ameliorated if the sensors are placed at points of maximum sensitivity. This paper describes two methods to optimize sensor locations: one to account for signal error, the other to consider interacting parameters. The methods are based upon variants of the normalized Fisher information matrix and are shown to be equivalent in some cases, but to predict differing sensor locations under other conditions, usually transient.*

## Introduction

Mathematical modeling of systems or processes relies upon accurate estimates of parameters or properties. Frequently these parameters are determined by an inverse method in which measured responses are compared with direct simulation. A sequence of simulations is performed and the parameter values are adjusted until the predicted response matches the measured response. The premise is that if agreement can be attained for a large number of responses, the parameters are uniquely and accurately determined. It is not uncommon that errors or nonrepeatable measured temperatures lead to conflicting conclusions about inferred property values.

This approach yields approximate values of the parameters (the degree of approximation is related to the heterogeneity of the material, the accuracy of the measurements, the spatial gradients existing in the neighborhood of the sensor, and the refinement of the discretization of the model). In addition, the results are subject to uncertainty in that the response upon which the estimation is based may not be sensitive to the parameter sought. One solution to a possible lack of sensitivity is to locate the sensors at the points of maximal sensitivity. Unfortunately, in most transient problems the point of maximal sensitivity is a function of time and the ideal location of a single sensor is not unequivocally defined. A prime example of such a behavior is given by Emery and Fadale (1990) in the analysis of the temperature response of a high-temperature test of a thermal protection system (Gorton and Shideler, 1988). The temperatures, which were measured at several different locations in the structure, were affected by radiation from an internal surface whose emissivity was unknown. Consequently it was important to determine the effect of the radiation (as characterized by the surface emissivity) on the measured temperatures. It was shown that the different locations had different sensitivity histories. Clearly, one cannot in general move sensors during an experiment. Thus the choice is twofold: (*a*) employ a large number of sensors and use the response from a given sensor while it possesses the greatest sensitivity; (*b*) employ only a few sensors, locating them at positions that will give the best integrated sensitivity over the entire experiment.

Mathematical modeling data also show that the error of determination of the parameters of the mathematical model from the solution of the inverse problem may depend significantly on the spatial placement of the temperature sensors (Beck et al., 1992). The proper setup of the thermophysical experiment requires the solution of an optimal experimental design problem, viz., to place a fixed number of sensors in the sample in such a way as to minimize the error of identification of the required characteristics. The stated problem can be solved on the basis of the fundamental principles of experimental design theory for a distributed-parameter system, although the precise criterion is not unique. It is also clear that in multiparameter systems, the response of a sensor will be affected by more than one parameter. The question naturally arises as to where to place a sensor to best determine the parameters sought without other parameters confounding the issue.

The general problem is to locate the sensors such that the estimation of the parameter ($B_l$) is not adversely affected by error in the responses, that is, $\partial B_l/\partial\phi$ is small. Another way of expressing this is that the sensitivity of the temperature to the parameter, $\partial\phi/\partial B_l$, should be as large as possible. At the same time it must be recognized that all measurements are subject to noise and that the sensors should be located to minimize the noise effects. It is not obvious that maximizing sensitivity to parameter variations and minimizing effects due to noise lead to the same sensor locations. This paper compares the use of sensitivity analysis and of the Fisher information matrix to define optimal sensor locations to gather the most statistical information about a parameter. Before discussing these two approaches, the various criteria used in the Inverse problems have been summarized. Although the methods are applicable to any system, we restrict our study to transient and steady-state, one and two-dimensional thermal systems. The time duration and the time intervals of the experimental measurements may also influence the optimal sensor locations; this effect has not been considered in the present study. A good discussion for optimal time intervals and the duration of the experiment can be found in the book by Beck and Arnold (1977).

## Analysis

Consider a thermal system with $P$ unknown parameters to be estimated. Let $\mathbf{B}$ represent a $P$-dimensional vector of these unknown parameters. In order to estimate the parameters, experimental observations of the responses of system are obtained at various locations $(x_i, y_i)$ and times $(t_k)$. Let $N$ be the number of sensors used in the experiment and $K$ the number of readings in time at these sensor locations. Then the experimental observations can be represented by $\mathbf{z}_k$, where

$$\mathbf{z}_k^T = \{z_i(t_k),\ i = 1, 2, \ldots, N\} \quad k = 1, 2, \ldots, K \qquad (1)$$

[1] Current address: Applied Graphics Simulations, 1009 N.E. Boat Street, Seattle, WA 98105.

Contributed by the Heat Transfer Division for publication in the JOURNAL OF HEAT TRANSFER. Manuscript received by the Heat Transfer Division August 1993; revision received August 1994. Keywords: Measurement Techniques, Numerical Methods, Thermophysical Properties. Associate Technical Editor: C. E. Hickox, Jr.



Copyright © 1995 by ASME

Downloaded 12 Dec 2010 to 193.140.21.150. Redistribution subject to ASME license or copyright; see http://www.asme.org/terms/Terms_Use.cfm

In practice, the unknown parameters are estimated by minimizing a criterion expressed in terms of the *residuals,* where the residuals are the differences between the predicted responses of the system using assumed parameters and the experimentally observed responses at the sensor locations and the sample times. Broadly speaking, there are two approaches to define this criterion, the Generalized Least Squares (GLS) approach and the Maximum Likelihood (ML) approach. A good description of the various criteria and their properties is given by Sorenson (1980).

In the Generalized Least Squares approach to the Inverse problem, the unknown parameters, $\mathbf{B}$, are estimated by minimizing the sum of the squares of the residuals, i.e., minimize $\Gamma(\mathbf{B})$, where $\Gamma$ is given as

$$\Gamma(\mathbf{B}) = \sum_{k=1}^{K} \{\Phi_k - \mathbf{z}_k\}^T \mathbf{W}_k \{\Phi_k - \mathbf{z}_k\} \tag{2}$$

where $\mathbf{W}_k$ is the weighting matrix and $\Phi_k$ is a vector of the predicted responses of the system at all the sensor locations based on the mathematical model such that,

$$\Phi_k^T = \{\phi(x_i, y_i, t_k), i = 1, 2, \ldots, N\} \quad k = 1, 2, \ldots, K \tag{3}$$

where $x_i$, $y_i$ is the location of the $i$th sensor and $t_k$ is the $k$th sample time. For distributed parameter systems this involves the solution of the field equations.

In the Maximum Likelihood approach, the problem is considered from a probabilistic point of view. The measurement noise of the sensors is considered to be additive, spatially and temporally independent, and normally distributed with a zero mean and a variance of $\sigma_n^2$. The best estimates of the unknown parameters are those that maximize the likelihood of the occurrence of the measurements relative to the predictions. In other words, the best estimate is that which maximizes the probability density function of the measurements $f(\mathbf{z}|\mathbf{B})$. This estimate of $\mathbf{B}$ makes the measurement *most likely* and therefore the probability density function $f(\mathbf{z}|\mathbf{B})$ is called the likelihood function, given by

$$f(\mathbf{z}|\mathbf{B}) = [(2\pi)^{NK} \prod_{k=1}^{K} \text{Det}\,(\mathbf{S}_k)]^{-1/2} \times \exp\left[\sum_{k=1}^{K} -\frac{1}{2}\{\Phi_k(\mathbf{B}) - \mathbf{z}_k\}^T \mathbf{S}_k^{-1} \{\Phi_k(\mathbf{B}) - \mathbf{z}_k\}\right] \tag{4}$$

where $\mathbf{S}_k$ is the covariance matrix of the measurements at time $t_k$ and is defined as,

$$\mathbf{S}_k = E[\delta\mathbf{z}_k \quad \delta\mathbf{z}_k^T], \quad \delta\mathbf{z}_k = \mathbf{z}_k - E[\mathbf{z}_k] \tag{5}$$

where $E[\mathbf{z}_k]$ is the expected value based on the assumed parameters. Because of the exponential character of the density function, it is convenient to deal with the logarithm of the likelihood function. The criterion for the estimation of the unknown parameters $\mathbf{B}$ is therefore defined by the likelihood functional $L^*$,

$$L^* = -2 \ln f(\mathbf{z}|\mathbf{B}) = NK \ln (2\pi) + \sum_{k=1}^{K} \ln (\text{Det}\,(\mathbf{S}_k)) + \sum_{k=1}^{K} \{\Phi_k(\mathbf{B}) - \mathbf{z}_k\}^T \mathbf{S}_k^{-1} \{\Phi_k(\mathbf{B}) - \mathbf{z}_k\} \tag{6}$$

where the best estimates of $\mathbf{B}$ will minimize the likelihood functional, $L^*$. Assuming that the experimental noise is independent of the unknown parameters, the first two terms are constants and the minimization of $L^*$ is equivalent to the minimization of $L$,

$$L = \sum_{k=1}^{K} \{\Phi_k(\mathbf{B}) - \mathbf{z}_k\}^T \mathbf{S}_k^{-1} \{\Phi_k(\mathbf{B}) - \mathbf{z}_k\} \tag{7}$$

It can be seen that, under these restrictions on the noise of the measurements, the maximum likelihood approach reduces to the least-squares approach with $\mathbf{S}_k^{-1} = \mathbf{W}_k$. If the variance of the measurement $\sigma_n^2$, is the same for all locations and readings, then the covariance matrix can be expressed as

$$\mathbf{S} = \sigma_n^2 \mathbf{I} \tag{8}$$

and,

$$L = \sigma_n^{-2} \sum_{k=1}^{K} \{\Phi_k - \mathbf{z}_k\}^T \{\Phi_k - \mathbf{z}_k\} \tag{9}$$

It must be emphasized that the minimum required number of temperature sensors and the limits on their placement are completely determined by an analysis of the conditions for the existence and uniqueness of the solution of the corresponding inverse problem. Fedorov (1972) has shown that, although in general the number of sensors must be equal to the number of parameters, there are circumstances in which a smaller number can be employed. For example, in order to determine either the conductivity $k$ or the specific heat capacity $c$ as a function of temperature, Musylev (1980) has shown that it is necessary to measure the transient temperature at at least one point. This point must be situated in the interior if Dirichlet boundary conditions are spec-

## Nomenclature

$B_l$ = specific outcome of $\mathbf{B}$
$B(\vec{x})$ = continuous random field
$\mathbf{B}$ = unknown parameter vector
$c$ = specific heat capacity
Cond [ ] = condition number
Cov [ ] = covariance operator
$D$ = domain
$D_i$ = $i$th elemental domain
Det [ ] = determinant
$E$[ ] = expected value operator
$f$ = probability density function
$\mathbf{G}$ = covariance matrix of parameters
$h$ = heat transfer coefficient
$H$ = width of the slab
$\mathbf{I}$ = identity matrix
$k$ = thermal conductivity
$K$ = number of measurements in time
$l$ = length of the slab
$L$ = likelihood
$\mathbf{M}$ = fisher information matrix
$N$ = number of sensor locations
$P$ = number of unknown parameters
$s$ = length parameter
$\mathbf{S}$ = covariance matrix of measured temperatures
$t$ = time
$T_0$ = prescribed temperature
$T_\infty$ = ambient temperature
Tr [ ] = trace of the matrix
Var [ ] = variance operator
$\mathbf{V}$ = covariance matrix of temperature related to parameters
$x, y$ = position
$\mathbf{X}$ = vector of sensor positions
$\mathbf{z}$ = measured temperatures
$\Gamma$ = mean square deviation functional
$\Theta$ = sensitivity matrix
$\sigma_B$ = standard deviation of $\mathbf{B}$
$\sigma_{\text{noise}}$ = standard deviation of measurement
$\sigma_T$ = standard deviation of temperature $\phi$
$\phi$ = temperature field
$\Phi$ = temperature vector

### Subscripts

$i, j$ = sensor location at $(x_i, y_i)$ or $(x_j, y_j)$
$k$ = time
$l, m$ = parameters



Downloaded 12 Dec 2010 to 193.140.21.150. Redistribution subject to ASME license or copyright; see http://www.asme.org/terms/Terms_Use.cfm

ified or on the boundary for a Neumann-type boundary condition. However, if the problem is to identify both $k$ and $c$ as functions of temperature, the unique solution of such an inverse problem requires measuring the temperature at two different points and specifying a Neumann boundary condition on at least one of the boundaries, in which case the heat flux must be nonvanishing. On the other hand, if both $k$ and $c$ are known to be constants, then a unique solution can be obtained with only one measurement point, since $k$ and $c$ appear only in the thermal diffusivity. If $k$ and $c$, not the thermal diffusivity, are to be estimated, then at least one nonzero heat flux boundary condition is necessary. Requirements of this type on the measurements dictate the minimum experimental information that is required, in principle, for the solution of a specific inverse problem.

**Fisher Information Matrix (FIM).** Even after the goal of the experiment has been decided upon, e.g., the estimation of unknown parameters, there are a number of variables that can be adjusted, subject to certain constraints, so that the information provided by the experiment is maximized. All experimental design must take account of the constraints on the allowable experimental conditions. To form a basis for the comparison of different experiments, a measure of the *goodness* of the experiment is required. Almost all approaches used to define an optimal criterion are based upon minimizing the estimation errors. By the Cramer–Rao inequality the estimation error has a lower bound of $\mathbf{M}^{-1}$, where $\mathbf{M}$ is the Fisher Information matrix (Fedorov, 1972; Goodwin and Payne, 1977). This matrix can be expressed in terms of the probability distribution function $f(\mathbf{z}|\mathbf{B})$ by

$$\mathbf{M}(\mathbf{z}, \mathbf{B}) = E_{\mathbf{z}|\mathbf{B}}\left\{\left[\frac{\partial \log f(\mathbf{z}|\mathbf{B})}{\partial \mathbf{B}}\right]\left[\frac{\partial \log f(\mathbf{z}|\mathbf{B})}{\partial \mathbf{B}}\right]^T\right\} \quad (10)$$

Substituting Eq. (4) in Eq. (10), gives the Fisher Information matrix as (Goodwin et al., 1974),

$$\mathbf{M}(\mathbf{z}, \mathbf{B}) = \sum_{k=1}^{K} [\mathbf{\Theta}_k^T \mathbf{S}_k^{-1} \mathbf{\Theta}_k + \mathbf{\Psi}_k] \quad (11)$$

where $\mathbf{\Psi}_k$ is defined as

$$(\mathbf{\Psi}_k)_{lm} = \tfrac{1}{2}\mathrm{Tr}\left[\mathbf{S}_k^{-1}\frac{\partial \mathbf{S}_k}{\partial B_l}\mathbf{S}_k^{-1}\frac{\partial \mathbf{S}_k}{\partial B_m}\right] \quad l, m = 1, 2, \ldots, P$$

The sensitivity matrix $\mathbf{\Theta}_k$, which is defined as

$$(\mathbf{\Theta}_k)_{il} = \frac{\partial \phi(x_i, y_i, t_k)}{\partial B_l}, \quad i = 1, \ldots, N, \quad l = 1, \ldots, P, \quad k = 1, \ldots, K \quad (12)$$

can be obtained by solving for $\partial \phi_{ki}/\partial B_l$ from the differentiated energy equation. The formulation with a detailed implementation of the algorithm for finite element application can be found in the paper by Fadale and Emery (1994). The matrix $\mathbf{S}_k$ is the covariance of the measured temperatures. It is usual to simplify the form of $\mathbf{M}$ by assuming that

$$\mathbf{S}_k = \sigma^2_{\text{noise}}\mathbf{I} \quad \text{and} \quad \frac{\partial \mathbf{S}_k}{\partial B_l} = 0 \quad (13)$$

That is: All sensors are exposed to the same noise; the sensor noise is uncorrelated; and the covariance of the noise is independent of the parameters. Thus $\mathbf{M}$ reduces to the usual form,

$$\mathbf{M} = \sigma^{-2}_{\text{noise}} \sum_{k=1}^{K} \mathbf{\Theta}_k^T \mathbf{\Theta}_k \quad (14)$$

The information matrix, $\mathbf{M}$, characterizes the total sensitivity of the entire set of measurements to the variation of all the unknown parameters. The optimal measurement design problem entails finding a design $\mathbf{X}^*$ for which the total sensitivity of the system (expressed as some scalar function of $\mathbf{M}$) in some sense will be a maximum or the estimation error (expressed as some scalar function of $\mathbf{M}^{-1}$) in some sense will be minimum.

Various criteria (D-, L-, E-, A-, C- Optimality) are used for the optimization of the experimental conditions (Walter and Pronzato, 1990; Seber and Wild, 1989; Kubrusly and Malebranche, 1982; Polis, 1982) to ensure the minimum error of estimation of the unknown parameters. In these cases, the optimal experiment design can be determined by requiring that some measure of the information matrix be a maximum, i.e.,

$$\max_{\mathbf{X} \in D} \{\text{Measure } \mathbf{M}(\mathbf{X})\} \Rightarrow \mathbf{X}^* \quad (15)$$

where the locations of the temperature sensors are defined in the form of a vector of spatial coordinates $\mathbf{X} = \{x_i, y_i, i = 1, 2, \ldots, N\ \mathbf{X} \in \mathbf{D}\}$. Artyukhin (1985) has shown that the best criterion is found by maximizing Cond$(\mathbf{M})$, but that maximizing Det $(\mathbf{M})$ is a nearly equivalent criterion. This approach is commonly referred to as the D-Optimal criterion. It is important to note that the use of $\mathbf{M}$ requires some knowledge about the noise of the readings, but requires no knowledge about the range of values of the parameters. It must be emphasized that the elements of the information matrix $\mathbf{M}$ and, hence, the optimal sensor positions $\mathbf{X}^*$, depend on the a priori estimates of the unknown parameters $\mathbf{B}$. This is because of the strongly nonlinear dependence of the temperature on the unknown parameters and is typical of measurement designs for the solution of inverse problem in thermal-structural problems. Accordingly, it is only meaningful to speak of locally optimal designs, which are formulated with the use of a priori information about the unknown parameters.

**Sensitivity Analysis.** In the sensitivity analysis approach, the unknown parameters are treated as random variables, which are characterized by probability distribution functions. An analysis can be carried out by using either a statistical or a nonstatistical approach. The statistical approach uses either experiments or Monte Carlo simulations. In both, repetitive tests are conducted in which one or more parameters are varied and the resulting response of interest is statistically analyzed. The nonstatistical approach, unlike sampling, is based upon an analytical treatment of the random variable. This approach involves procedures like numerical integrations, finite differencing, and perturbation methods (Lin, 1967; Ghanem and Spanos, 1988). The nonstatistical approach is not only an elegant way to handle uncertainties in systems but also has an advantage over the statistical approach in terms of computer time and in ease of interpretation.

Perturbation methods have been commonly used for nonlinear analysis, e.g., turbulence, nonlinear vibrations. One such perturbation method, which can be used for sensitivity analysis, is the first-order/second-order–second moment analysis (Haftka and Kamat, 1985; Ditlevesen, 1981). This technique consists of expressing the response in terms of a Taylor series expanded about the mean value of the unknown parameter and truncating the series at the first or second-order terms. The system is then solved for the mean value and the standard deviation of the response. The first-order and second-order derivatives of the responses with respect to the unknown parameters are, in effect, the sensitivities of the responses with respect to the unknown parameters.

The unknown parameters whose effects on the response are being studied are modeled as either random variables or as random fields defined in the interior or on the boundary of the system. For the finite element implementation, the continuous random field $B(\vec{x})$, which represents any of the variable parameters (e.g., material properties, heat transfer coefficient), is discretized over the domain of application. Thus if we consider the discretized random field as an elemental quantity, then the average of the continuous random field over a finite element can be treated as an elemental quantity (Vanmarcke, 1977). The local integral over a finite element of the random field is itself a random variable, referred to as $B_i$ for the $i$th element.



Downloaded 12 Dec 2010 to 193.140.21.150. Redistribution subject to ASME license or copyright; see http://www.asme.org/terms/Terms_Use.cfm

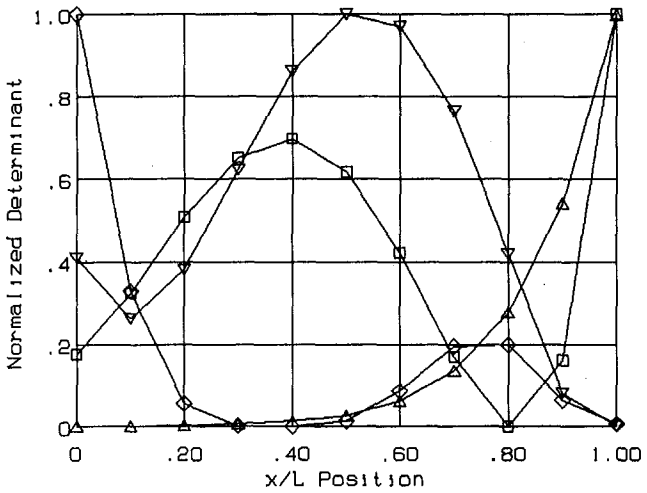



**Fig. 1(a) FIM determinant for $k$ (case a) and $k$, $h_b$, $h_f$ (case b) ($t_{max}$ = 500, $h_f$ = 50): □ sensor for case (a); ◇ first sensor for case (b); △ second sensor for case (b); ▽ third sensor for case (b)**

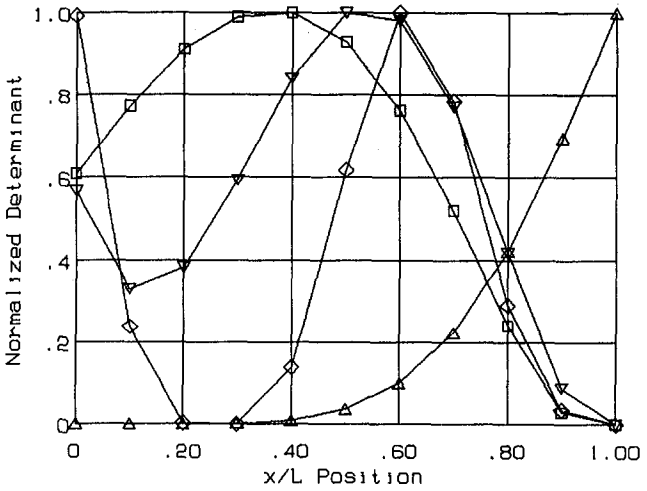



**Fig. 1(b) FIM determinant for $k$ (case a) and $k$, $h_b$, $h_f$ (case b) ($t_{max}$ = 500, $h_f$ = 500): □ sensor for case (a); ◇ first sensor for case (b); △ second sensor for case (b); ▽ third sensor for case (b)**

$$B_i = \frac{1}{D_i}\int_{D_i} B(\vec{x})d\vec{x} \tag{16}$$

Due to the discretization of the random field over the finite elements it is possible to account for the correlation between the discretized random variables and it is also convenient to evaluate their stochastic properties. It also makes it easier to develop the matrices of the first and second-order equations. These advantages of using the finite element to define a localized random variable are not present for a finite difference method, where point values are used and averaging over finite region is not done. Since a two-dimensional finite element code is being used, the random field, if present on the boundary (surface) of the system, will be defined in a one-dimensional space, i.e., $\vec{x} = (s)$, where $s$ is a length parameter along the surface, and if present in the interior (volume) of the system, will be defined in a two-dimensional space, i.e., $\vec{x} = (x_1, x_2)$. Such a finite element method, which accounts for the random variables and performs a sensitivity analysis, is commonly referred to as the stochastic finite element method. A large range of applications of stochastic finite element methods can be found in the field of structural mechanics (Ghanem and Spanos, 1988; Liu et al., 1988; Cruse, 1989).

The finite element formulation of the first-order, second-moment technique for a transient heat conduction problem is given in the paper by Fadale and Emery (1992). The formulation leads to the evaluation of derivatives of nodal temperature $\phi$ with respect to the random variables $B_l$. These derivatives indicate the sensitivities of nodal temperatures to the random variables $\mathbf{B}$ at various locations. This large amount of data on temperature sensitivities can be concisely represented by the statistical property of the covariance of the temperatures at the various sensor locations. For a first-order method, the first-order estimate of the covariance matrix is given as (Fadale, 1993),

$$E[(\mathbf{\Phi}_k - \overline{\mathbf{\Phi}_k})(\mathbf{\Phi}_k - \overline{\mathbf{\Phi}_k})^T] = \mathbf{\Theta}_k\mathbf{G}\mathbf{\Theta}_k^T \quad k = 1, \ldots, K \tag{17}$$

where $\overline{\mathbf{\Phi}_k}$ represents the predicted response at $\overline{\mathbf{B}_k}$; $G_{lm}$ = Cov $[B_l, B_m]$; $l, m = 1, \ldots, P$; $B_l$ represents the random variable associated with the $l$th parameter; and Cov $(B_l, B_m)$ represents the interaction between the parameters, with the diagonal terms being the variances of the random parameters. In the sensitivity analysis this matrix must be known prior to the analysis.

As discussed earlier, the D-optimal criterion for the optimizing sensor locations in the presence of noise deals with maximizing the determinant of the Fisher information matrix $\mathbf{M}$. This idea can be extended for parameter effects to the maximization of the determinant of the $\mathbf{V}$ matrix, which is given as

$$\mathbf{V} = \sum_{k=1}^{K} \mathbf{\Theta}_k\mathbf{G}\mathbf{\Theta}_k^T \tag{18}$$

where $\mathbf{V}$ is the sum, in time, of the covariance matrix of temperature obtained from the sensitivity analysis.

Note that there is an intrinsic difference between the two methods. The Fisher information matrix is a measure of the sensitivity of the signals to noise, but with no prescription of the statistical properties of the parameters. Optimizing $\mathbf{M}$ leads to the determination of the optimal sensor location but reveals nothing about the individual parameters. The sensitivity approach assumes that the signals are well defined (i.e., not noisy) but that they vary because of variations in the parameters. Thus sensitivity analysis can lead to conclusions about the effect of parameters, but not about noise. The first method requires a knowledge of $\mathbf{S}_k$ while the second requires a knowledge of $\mathbf{G}$. Naturally there are intrinsic difficulties in specifying either and neither are easy to come by unless much is already known about the system being studied. This point will be illustrated in the discussion of the steady-state example in the following section.

Under certain circumstances these two approaches will be equivalent. In the case of one measurement, when $K = 1$, or for steady-state measurement, the Fisher information matrix is nonsingular when the number of unknown parameters to be estimated, $P$, is less than or equal to the number of sensors $N$, and singular if $P > N$. On the other hand, the covariance matrix $\mathbf{V}$ is nonsingular for $P \geq N$ and singular when $P < N$. For the case when $N = P$, i.e., the number of sensors is equal to the number of unknown parameters to be estimated and the noise is *white* and independent of the parameters to be estimated, i.e., relations in Eq. (7) hold true, it can be shown that,

$$\frac{\text{Det }(\mathbf{M})}{(\sigma^2_{\text{noise}})^P} = \frac{\text{Det }(\mathbf{V})}{\text{Det }(\mathbf{G})} \tag{19}$$

For a transient case, when $K > 1$ the two approaches are related if, in addition to the restriction on $\mathbf{S}$, the parameters are uncorrelated and have equal deviation, i.e., $\mathbf{G} = \sigma_B^2\mathbf{I}$ and $N = P$. Under these conditions, the relation between $\mathbf{M}$ and $\mathbf{V}$ reduces to

$$\frac{\text{Det }(\mathbf{M})}{(\sigma^2_{\text{noise}})^P} = \frac{\text{Det }(\mathbf{V})}{(\sigma_B^2)^M} \tag{20}$$

Therefore, the results obtained from these two approaches for these special conditions will be the same. This will be demonstrated through the examples discussed below.

## Examples and Discussion

**(A) Transient Slab.** Consider a slab of thickness $L$ with an initial temperature of 0°C and with a boundary condition of the



Downloaded 12 Dec 2010 to 193.140.21.150. Redistribution subject to ASME license or copyright; see http://www.asme.org/terms/Terms_Use.cfm

third kind on both the back ($x/L = 0$) and the front ($x/L = 1$) surfaces. The plate is convectively heated with an ambient temperature of 100°C on both surfaces but with different heat transfer coefficients ($h_b$ on the back surface and $h_f$ on the front surface). At steady state, the temperature will be uniform throughout the plate, equal to the ambient temperature. Therefore an experiment carried out at steady state will not furnish any information that can lead to the estimation of the thermal diffusivity of the plate or the heat transfer coefficients on the boundaries. On the other hand, the transient temperatures of the plate depend upon the thermal properties of the plate and the nature of the convective boundary conditions and so can be used for the estimation of these parameters. A transient analysis was carried out using the Fisher information matrix and the sensitivity analysis to determine the optimal locations of sensors for the estimation of ($a$) thermal conductivity only and ($b$) the thermal conductivity along with the heat transfer coefficients $h_b$ and $h_f$ from a single experiment. Since, for the optimal placement of sensor locations *a priori* information of the parameters to be estimated is necessary, the effect of gross changes in the estimated value of one of the parameters on the sensor location for both the above-mentioned cases was investigated. The heat transfer coefficient on the front surface ($h_f$) was considered to be badly misjudged while the thermal conductivity ($k$) and the heat transfer coefficient on the back surface ($h_b$) were considered to be close to the true value estimates, viz., $k = 1$ W/(m-K) and $h_b = 10$ W/(m$^2$-K). The value of $\rho c$ was taken to be $1 \times 10^6$ J/(m$^3$-K).

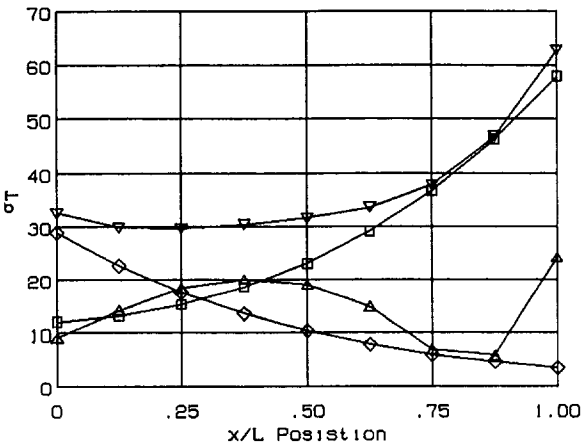



**Fig. 2(*a*) Sensitivity to $k$ (case *a*) and to $k$, $h_b$, $h_f$ (case *b*) ($t_{max} = 500$, $h_f = 50$); □ sensitivity to $h_f$; ◇ sensitivity to $h_b$; △ sensitivity to $k$; ▽ sensitivity to $h_b$, $h_f$, and $k$**

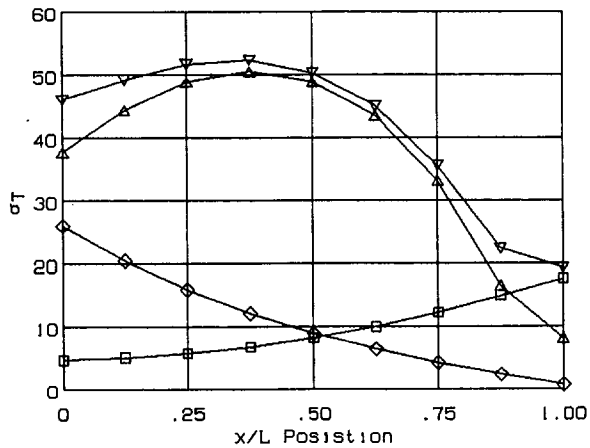



**Fig. 2(*b*) Sensitivity to $k$ (case *a*) and to $k$, $h_b$, $h_f$ (case *b*) ($t_{max} = 500$, $h_f = 500$): □ sensitivity to $h_f$; ◇ sensitivity to $h_b$; △ sensitivity to $k$; ▽ sensitivity to $h_b$, $h_f$, and $k$**

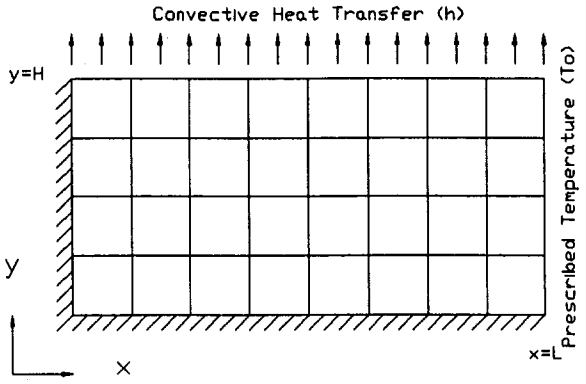



**Fig. 3 Two-dimensional test case**

Figures 1($a$) and 1($b$) present the variation of Det (**M**) over the thickness of the slab for $h_f = 50$, and 500 W/(m$^2$-K), respectively. The magnitude of Det (**M**) when using more than one sensor will indicate the relative value of the different sensors in estimating the parameters and thus the magnitude is of great interest for the inverse problem. However, when the goal is to optimize the location of sensors, given a specific number of sensors, it is the location of the local maximum that specifies the location. Thus plots with the normalized value of the Det (**M**) will suffice. For case ($a$) where only the thermal conductivity is to be estimated, the optimal sensor location when $h_f = 50$ W/(m$^2$-K) is at $x/L = 1$ but a nearly equivalent sensitivity exists near $x/L = 0.5$, while for $h_f = 500$ W/(m$^2$-K) the optimal sensor location is in the neighborhood of $x/L = 0.375$. This implies that for high values of $h_f$, the sensor location is going to be very close to the optimal location if placed in the region $x/L = 0.375$ while for low values of $h_f$ ($h_f < 62$ W/(m$^2$-K)),[1] the sensor location should be at $x/L = 1$.

In case ($b$) when estimating three parameters, viz., $k$, $h_b$, and $h_f$, one can use either one, two, or three sensors in the experiment. If four sensors are used to estimate these three parameters, the optimal location for the fourth sensor is found to coincide with one of the first three sensor locations, implying that nothing more will be gained by using the fourth sensor. When only one sensor is used for estimation of all three parameters, the optimal location for $h_f < 500$ W/(m$^2$-K) will always be at $x/L = 0$. With the use of two sensors, Figs. 1($a$) and 1($b$) show the variation of Det (**M**) when the first sensor is fixed at $x/L = 0$. It is seen that for all values of $h_f$ the second sensor should be placed at $x/L = 1$. For the use of three sensors, Figs. 1($a$) and 1($b$) represent the Det (**M**) with the first two sensors fixed at $x/L = 0$ and $x/L = 1$, respectively. Again the optimal location of the third sensor is not affected by the magnitude of $h_f$ and remains fixed near $x/L = 0.5$.

Figures 2($a$) and 2($b$) show the results of the time integral sensitivity of temperature expressed as the standard deviation $\sigma_T$ in $\phi$ (sensitivity analysis approach) to the desired parameters corresponding to results of Det (**M**) from Figs. 1($a$) and 2($b$), respectively (FIM approach). For the case of a single desired parameter $k$ (case ($a$)), the results obtained from sensitivity for the optimal locations are identical to the results obtained from FIM. Figures 2($a$) and 2($b$) also show results of temperature sensitivity to $h_b$ and $h_f$ indicating that the optimal sensor locations are at $x/L = 0$ and $x/L = 1$ for estimation of $h_b$ and $h_f$, respectively. These sensor locations are not affected by the magnitude of $h_f$ and so the locations are optimal for a wide range of $h_f$ values. For case ($b$) the temperature sensitivity shows a summing effect of the sensitivity of the individual parameters ($k$, $h_b$, and $h_f$, respectively), thus the maximum sensitivity indicates the effect of the most influential parameter on temperature compared to the rest of the parameters, for example when $h_f = 50$ W/(m$^2$-K), the temperature

[1] To estimate this value, the optimal sensor locations were determined for various values of $h_f$ between 50 and 500 W/(m$^2$-K).



Downloaded 12 Dec 2010 to 193.140.21.150. Redistribution subject to ASME license or copyright; see http://www.asme.org/terms/Terms_Use.cfm

in the region with highest sensitivity ($x/L = 1$) is most influenced by $h_f$ and only slightly affected by $k$ or $h_b$, while when $h_f = 500$ W/(m$^2$-K) the temperature in the region with highest sensitivity ($x/L = 0.375$) is most influenced by $k$, not $h_b$ or $h_f$.

**(B) Two D Problem.** Consider the slab shown in Fig. 3 with $k = 1$ W/(m-°C), $h = 10$ W/(m$^2$-°C), $\rho c = 10^6$ J/(m$^3$ °C), $T_0 = 100$°C $= T_\infty$. At steady state the temperature distribution is a function only of $h/k$ and the sensitivities $\partial\phi/\partial k$ and $\partial\phi/\partial h$ are related and have the same spatial distribution. In this case, as shown in Fig. 4, the optimal location for the sensor is at $x/L = 0$, $y/H = 1$, but the surface is relatively flat and nearly any point along the convective boundary near $x/L = 0$ will suffice. This result is identical to the results obtained from the sensitivity analysis if $\sigma_k = \sigma_h$ and Cov $(h, k) = 0$, (because of steady state, in this case, **V** and **M** have identical contours).

The transient problem yields much different results as indicated in Fig. 5($a$, $b$) and 6($a$, $b$). The optimal location for $h$ is on the convective boundary near $x/L = 0.8$, while for $k$ it is at about $x/L = 0.65$ and is quite insensitive to the value of $y$—at least for a total measurement time of 200 s. For a total measurement time of 400 s, the contours for sensitivity to $h$ do not change much, while the field for $k$ becomes even flatter near $x/L = 0$. This relative flatness of the $k$ surface is fortunate because it means that while the $h$ sensor must be accurately placed, that for $k$ is free to be located somewhat arbitrarily. If both $h$ and $k$ are to be determined, two sensors must be used. Figure 6($a$, $b$) compares the sensitivities associated with the second sensor. In Fig. 6($a$), one sensor is located at $x/L = y/H = 0$ and is used to estimate $k$. The second sensor should be located on the convective boundary and should be accurately placed—as shown by the steepness of the surface. On the other hand (Fig. 11$b$), if one sensor is located at $x/L = 0.75$ and $y/H = 1$, the second sensor can be located very approximately near $x/L = y/H = 0$. Thus some sensor locations are much more critical than others.

## Conclusions

Two different approaches have been described to determine the optimal location of sensors for thermal problems. The first, based upon the Fisher information matrix, requires a knowledge of the statistical properties of the sensor signal, but not of the parameters of the system. The second method, based upon sensitivity analysis, requires information about the statistical information of the parameters and their interactions. Although the methods are intrinsically different, if all signals have the same error characteristics, if the parameters are uncorrelated, and if the number of sensors equals the number of parameters, the results of the two approaches are identical. If these conditions are not met, the methods yield different results. Due to the nonlinear nature of the problem, both the methods require *a priori* estimates of the parameters. The Fisher information matrix approach predicts optimal locations of multiple sensors, without making use of the *a priori* statistical information about the parameters. On the other hand, the sensitivity approach allows one to understand how the different parameters interact (using the *a priori* statistical information about the parameters) and to choose locations such that the influence of parameters can be separated. This is particularly important for steady-state problems in which several independent parameters may affect the temperature in the form of a combined property (e.g., thermal diffusivity). In this case, the Fisher information matrix approach may be ineffec-

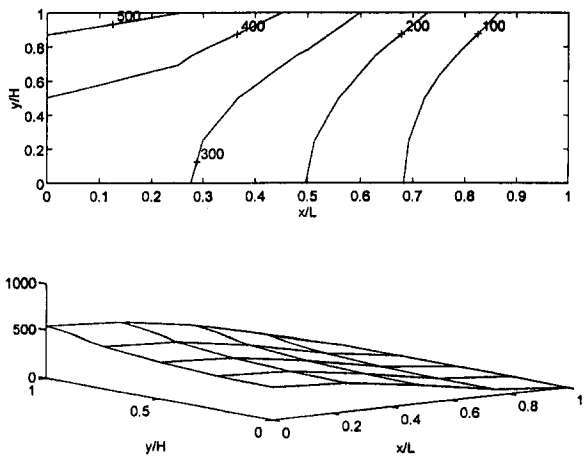



Fig. 4 FIM determinant contours at steady state while estimation of $k$

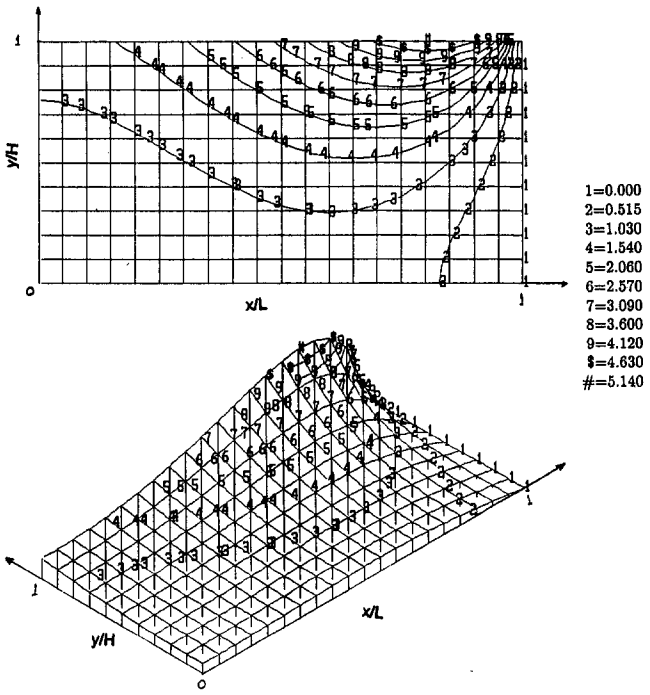



Fig. 5($a$) Temperature sensitivity to $h$ at $t = 200$ s

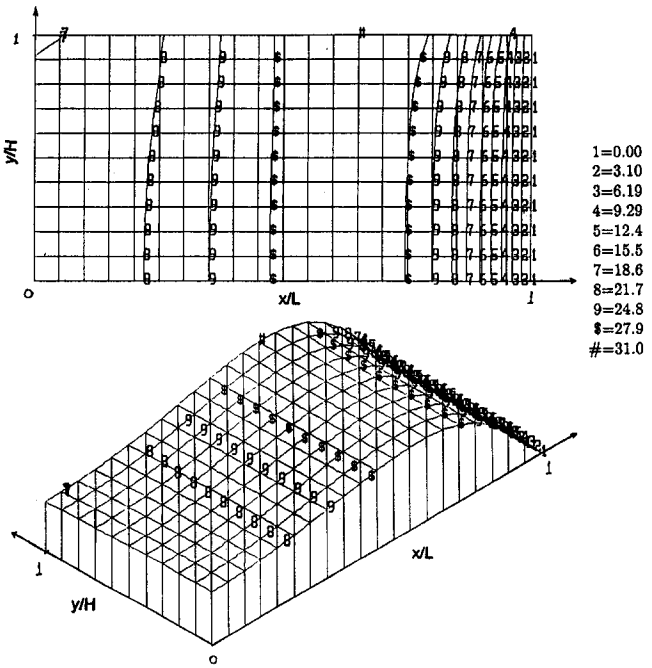



Fig. 5($b$) Temperature sensitivity to $k$ at $t = 200$ s



Downloaded 12 Dec 2010 to 193.140.21.150. Redistribution subject to ASME license or copyright; see http://www.asme.org/terms/Terms_Use.cfm

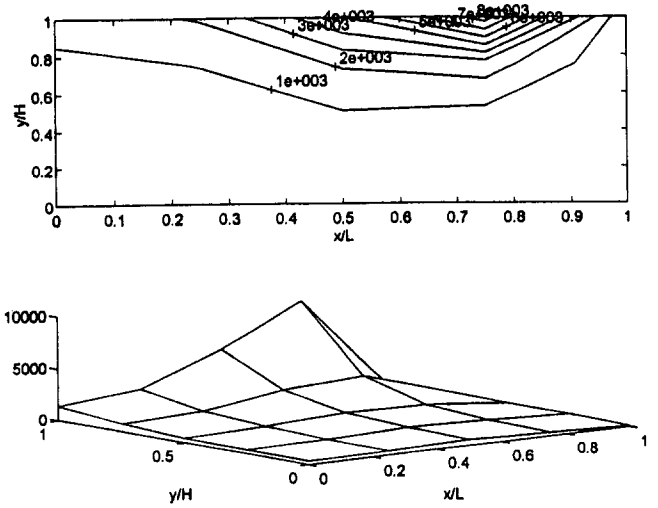
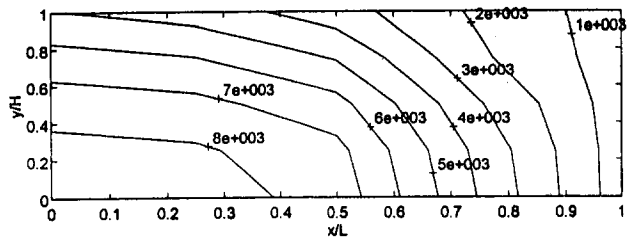






**Fig. 6(*a*) FIM determinant contours at $t$ = 400 s for estimation of $k$ and $h$ with one sensor fixed at $x$ = 0 and $y$ = 0**



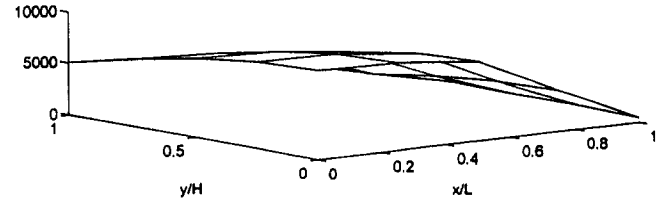




**Fig. 6(*b*) FIM determinant contours at $t$ = 400 s for estimation of $k$ and $h$ with one sensor fixed at $x$ = 0.03 and $y$ = 0.02**

tive. Because of the differing nature of the two approaches, both should be used and both may be included in numerical algorithms for optimal experiment design.

## Acknowledgments

A portion of this work was done while one of the authors (A. V. Nenarokomov) held a CAST grant from the National Academy of Sciences.

## References

Artyukhin, E. A., 1985, "Experimental Design of Measurement of the Solution of Coefficient-Type Inverse Heat Conduction Problem," *Journal of Engineering Physics,* Vol. 48, No. 3, pp. 372–376.

Artyukhin, E. A., and Nenarokomov, A. V., 1988, "Optimal Experimental Design for Determining the Total Emissivity of Materials," *High Temperatures,* Vol. 26, No. 5, pp. 761–767.

Beck, J. V., and Arnold, K. J., 1977, *Parameter Estimation in Engineering and Science,* Wiley, New York.

Beck, J. V., et al., 1992, "Joint American–Russian NSF Workshop on Inverse Problems in Heat Transfer," Michigan State University.

Cruse, T. A., 1989, "Probabilistic Structural Analysis Methods (PSAM) for Select Space Propulsion Components," manuscript prepared under SwRI Project No. 06-8338, NASA Contract NAS3-24389.

Ditlevesen, O., 1981, *Uncertainty Modeling—With Application to Multidimensional Civil Engineering Systems,* McGraw-Hill.

Emery, A., and Fadale, T. D., 1990, "The Sensitivity of the Temperature Histories in the Shuttle Thermal Protection System to Radiation Heat Transfer," ASME HTD-Vol 137, pp. 81–88.

Fadale, T. D., 1993, "Uncertainty Analysis Using Stochastic Finite Elements," Ph.D. Dissertation, University of Washington, Seattle, WA.

Fadale, T. D., and Emery, A. F., 1994, "Transient Effects of Uncertainties on the Sensitivities of Temperatures and Heat Fluxes Using Stochastic Finite Elements," ASME JOURNAL OF HEAT TRANSFER, Vol. 116, pp. 808–814.

Fedorov, V. V., 1972, *Theory of Optimal Experiment,* Academic Press, New York.

Ghanem, R. G., and Spanos, P. D., 1988, *Stochastic Finite Elements: A Spectral Approach,* Springer-Verlag, New York.

Gill, P. E., et al., 1986, "User's Guide for NPSOL—A Fortran Package for Nonlinear Programming," Department of Operations Research, Stanford University, Palo Alto, CA.

Goodwin, G. E., Zarrop, M. B., and Payne, R. L., 1974, "Coupled Design of Test Signals, Sampling Intervals and Filters for System Identification," *IEEE Transactions of Automatic Control,* Vol. AC-19, No. 6, pp. 784–752.

Goodwin, G. E., and Payne, R. L., 1977, *Dynamic System Identification. Experiment Design and Data Analysis,* Academic Press, New York.

Gorton, M. P., and Shideler, J. L., 1988, "Measured and Calculated Temperatures of a Superalloy Honeycomb Thermal Protection System Panel," *Proc. Workshop on Correlation of Hot Structures Test Data With Analysis,* NASA Ames Dryden Flight Research Center.

Haftka, R. T., and Kamat, M. P., 1985, *Elements of Structural Optimization,* Martinus Nijhoff Publishers.

Kubrusly, C. S., and Malebranche, H., 1982, "A Survey on Optimal Sensors and Controllers Locations in DPS," *IFAC 3rd Symposium, Control of Distributed Parameter Systems,* pp. 59–73.

Lin, Y. K., 1967, *Probabilistic Theory of Structural Dynamics,* McGraw-Hill, New York.

Liu, W. K., Besterfield, G., and Belytschko, T., 1988, "Transient Probabilistic Systems," *Computer Methods in Applied Mechanics and Engineering,* Vol. 67.

Musylev, N. V., 1980, "Uniqueness Theorems for Certain Inverse Heat Conduction Problems," *Zh. Vychisl. Mat. Fiz.,* Vol. 20, No. 2, pp. 388–400.

Polis, M. P., 1982, "The Distributed System Parameter Identification Problem: A Survey of Recent Results," *IFAC 3rd Symposium, Control of Distributed Parameter Systems,* pp. 45–58.

Seber, G. A. F., and Wild, C. J., 1989, *Nonlinear Regression,* Wiley-Interscience, New York.

Sorenson, H. W., 1980, *Parameter Estimation: Principles and Problems,* Marcel Dekker, Inc., New York.

Vanmarcke, E., 1977, "Probabilistic Modeling of Soil Profiles," *Journal of the Geotechnical Engineering Division,* Vol. 103, GT11.

Walter, E., and Pronzato, L., 1990, "Qualitative and Quantitative Experiment Design for Phenomenological Model—A Survey," *Automatica,* Vol. 26, No. 2, pp. 195–213.



Downloaded 12 Dec 2010 to 193.140.21.150. Redistribution subject to ASME license or copyright; see http://www.asme.org/terms/Terms_Use.cfm

**K. M. Kirk**
Research Analyst,
Center for Naval Analyses,
4401 Ford Ave.,
Alexandria, VA 22302

**H. Merte, Jr.**

**R. Keller**

Professor of Mechanical Engineering,
Department of Mechanical Engineering
and Applied Mechanics,
University of Michigan,
Ann Arbor, MI 48109

# Low-Velocity Subcooled Nucleate Flow Boiling at Various Orientations

*Subcooled forced convection nucleate boiling experiments with R-113 were conducted at low velocities using both thin film semitransparent gold-on-quartz and gold-coated copper substrate flat heaters at various orientations. The experiments demonstrate that if buoyancy is significant relative to bulk liquid momentum, then a decrease in the buoyant force normal to and away from the heater surface enhances the heat transfer, with the effect being greatest at low values of heat flux. Furthermore, the effect of the bulk liquid velocity is shown to be dependent on the surface orientation.*

## 1.0 Introduction

Forced convection or flow boiling is an attractive means of heat transfer in the microgravity environment of space owing to its ability to transport thermal energy with a small temperature difference. Potential applications in microgravity include Rankine cycle power generation and thermal energy management. The optimization of operating conditions and the ability to obviate potentially dangerous conditions requires the ability to predict accurately its behavior in such processes.

Notwithstanding the potential applications, the practical difficulties of obtaining or simulating a microgravity environment for experimentation have precluded significant research into flow boiling in microgravity or variable gravity. Nevertheless, earth-based flow boiling experiments performed at various heater surface orientations can contribute to a better understanding of the roles of buoyancy and bulk liquid momentum in flow boiling, and may improve predictions in variable gravity, including microgravity. Furthermore, although often neglected relative to the inertial forces, buoyancy will influence forced convection boiling at fluid velocities below some limiting value. Low velocity flow boiling experiments at various orientations may also help to identify this limiting velocity.

Distinct regimes of flow boiling have been identified in which the dominant heat transfer mechanism varies as the flowing two-phase mixture progresses through a heated duct. The initial regime, known as the bubbly flow regime, is characterized by very low quality and vapor bubbles, which form on the surface and are swept away by the bulk liquid motion. As the heating continues in the flow direction, the void fraction increases, and other flow regimes arise. Although these other flow regimes are certainly important in the overall study of flow boiling, the focus of the present study is on the bubbly flow regime.

To obtain a better understanding of the roles of buoyancy and bulk liquid momentum in forced convection boiling heat transfer, the processes of nucleation, growth, departure, and subsequent motion of the vapor bubble must each be examined and related to the observed heat transfer rates as the major parameters are varied. In the study described here, the independent parameters of heat flux, flow velocity, bulk liquid subcooling, heater surface character, and orientation relative to earth gravity are varied, and their influences on flow boiling over a flat heater surface are both quantitatively measured and qualitatively observed.

Although the level of gravity remains constant as the surface is rotated over 360 deg, the magnitudes of the components both normal and parallel to the heating surface are varied between $\pm 1$ $g$. By conducting experiments that bracket the zero gravity condition, the results may be useful in predicting gross behaviors in microgravity and assist in better defining the requirements for the study of flow boiling in the true microgravity environment of space.

## 2.0 Experimental Apparatus

**2.1 Forced Convection Boiling Loop.** A schematic of the forced convection boiling loop is given in Fig. 1. The loop is mounted on an axis near its center of gravity such that it can be rotated a full 360 deg while in operation in order to obtain the various heater surface orientations. The loop consists of five basic components: the test section, the condenser-cooler, the flow system, the pressure control system, and the preheater system. Degassed R-113 was employed as the test fluid for all the results given here. The sufficiency of the degassing process was demonstrated by comparing the measured vapor pressure curve with published saturation properties over the domain of interest. Agreement was within the accuracy of the pressure and temperature measurements.

Three aluminum test channels with heights of 0.318, 1.27, and 2.54 cm (0.125, 0.50, 1.0 in.) were used to obtain a wide range of flow velocities. Each test section provides a rectangular flow cross section 10.80 cm wide by 35.56 cm long (4.25 × 14.0 in.). Viewing windows made of optical grade quartz permit a transverse view of the flow boiling process on the flat heaters.

The condenser-cooler system condenses R-113 vapor leaving the test section, and subcools the liquid sufficiently to avoid cavitation at the pump inlet. Heat is transferred from the R-113 in the main flow loop to water circulating in the shell side of the primary heat exchanger, as illustrated in Fig. 1. A second heat exchanger (not shown) transfers heat from the recirculating water to building utility water.

The pressure control system actively maintains the pressure in the flow loop to within ±0.34 kPa (0.05 psi), and consists of four main components: a bellows, valves, electronic control circuits, and a pressure transducer. The 17.78 cm (7.0 in.) diameter stainless steel bellows separates the test fluid from the air in the chamber surrounding the bellows. Air is continuously admitted to the chamber through a manually adjustable needle valve, and is vented from the chamber through an electronically controlled proportional valve. Two additional pneumatic on-off solenoid valves compensate for large pressure deviations.

The two preheaters shown in Fig. 1 are used to raise the temperature of the R-113 to the desired level at the inlet to the test section. Upon exiting the pump, the R-113 enters the first preheater, a shell and tube counterflow heat exchanger, which provides the bulk of the energy input into the test loop. This first

Contributed by the Heat Transfer Division for publication in the JOURNAL OF HEAT TRANSFER. Manuscript received by the Heat Transfer Division October 1993; revision received April 1994. Keywords: Boiling, Microgravity Heat Transfer, Multiphase Flows. Associate Technical Editor: R. A. Nelson, Jr.

 Copyright © 1995 by ASME 

Downloaded 12 Dec 2010 to 193.140.21.150. Redistribution subject to ASME license or copyright; see http://www.asme.org/terms/Terms_Use.cfm

preheater raises the R-113 temperature to within 5°C of the set point temperature. The second preheater, also a counterflow heat exchanger but with approximately one third the capacity of the first, then heats the test fluid to the desired inlet temperature.

**2.2 Heater Surfaces.** Interest in the present study was in test heater surfaces of dimensions larger than the bubbles growing on them in order that they be more representative of boiling surfaces encountered in engineering applications. Two types of relatively large test surface, with dimensions of 1.905 × 3.81 cm (0.75 × 1.50 in.), were employed in this study: a thin gold film heater deposited on a quartz substrate, and a gold-coated copper substrate heater, referred to as the "metal" surface in the subsequent discussion.

The semitransparent thin film gold surface, illustrated in Fig. 2, functions simultaneously as a heater and as a resistance thermometer. The thin film surface consists of nominally 400 Å thick gold sputtered on a quartz substrate, which was presputtered with 20 Å of tantalum for improved gold adhesion. The quartz substrate was highly polished using a 1.4 $\mu$m pitch polish prior to deposition of the thin film. Measurement of the resistance of the thin film heater provides a spatially averaged mean surface temperature, which was deemed adequate for determining the macroscopic heat transfer behavior. The mean surface temperature measurement had an error of ±1.0°C. Details of the uncertainty calculations are given by Kirk (1992).

The metal heater consists of a copper block with a film heater on the underside and embedded in an electrical encapsulating potting compound, as shown in Fig. 3. A smooth copper foil 0.0254 mm (0.001 in.) thick was soldered to the copper block and to the stainless steel holder to eliminate the artificial boiling, which otherwise would result at the heater edge. The copper foil was sputtered with gold, approximately 1000 Å thick, to provide the identical surface-liquid energy combination as with the gold deposited on quartz. A chromel-constantan thermocouple with a bead of 0.64 mm (0.025 in.) diameter is inserted into a 0.76 mm (0.030 in.) diameter hole in the copper heater in order to estimate the temperature of the copper foil. The hole for the thermocouple was then filled with a thermally conducting copper compound. The tip of the thermocouple was about 0.76 mm (0.030 in.) from the gold-sputtered copper foil.

The metal heater surface temperature was determined from the chromel-constantan thermocouple embedded in the copper heating block and had an error of ±0.1°C. The error in assuming that the temperature of the thermocouple was equal to the surface temperature was estimated to be less than 0.002°C, by a simple one-dimensional conduction analysis, assuming a negligible contact resistance between the soldered copper foil and the copper block. This error is much less than the uncertainty of ±0.1°C associated with the thermocouple measurement.

## 3.0 Experimental Procedures

The steady flow experiments, which included both nonboiling and boiling tests, were conducted using both the thin film gold heaters and the solid metal heaters with the independent variables of heat flux, orientation, subcooling, and flow velocity, and the dependent variable being the heater surface temperature.

Once the desired steady-state operating conditions were achieved in the flow loop, the tests were initiated. The heat flux to the heater was set manually, and sufficient time was allowed for the surface to reach its steady-state operating temperature.

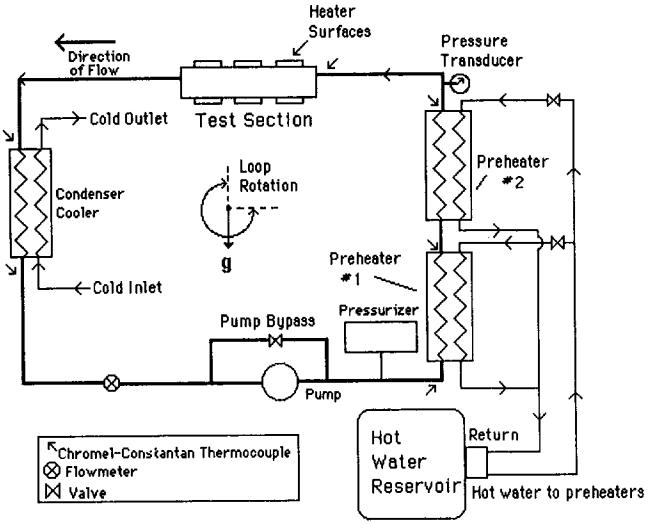



**Fig. 1 Forced convection boiling loop**

The heat loss, defined as that portion of the total power input that does not flow directly into the test fluid through the heating surface, was subtracted from the total power input, in order to determine the heat flux into the test fluid from the heating surface. As a result of the uncertainties associated with the voltage measurements and the heat loss, the uncertainty of the heat flux into the fluid via the heating surface was ±0.24 W/cm$^2$ for the thin film surface and ±0.29 W/cm$^2$ for the metal surface, as derived by Kirk (1992).

After recording the surface temperature, flow rate, heat flux, pressure, and bulk fluid temperature at the test section inlet, the heat flux would be increased incrementally by about 0.75 W/cm$^2$, and the procedure repeated up to a maximum heat flux of about 13 W/cm$^2$ to avoid a burnout condition.

The flow boiling experiments were performed at various orientations spanning 360 deg. All orientations are defined relative to the horizontal up position. Thus, vertical upflow corresponds to an angle of $\theta = 90$ deg and vertical downflow corresponds to an angle of $\theta = 270$ deg. The normal buoyant force is defined as positive when the force is directed away from the heating surface, and negative when the force is directed toward the surface. Thus, the normal component of earth gravity is $+1\ g$ at $\theta = 0$ deg and $-1\ g$ at $\theta = 180$ deg.

## 4.0 Results

The effect of orientation is first considered at very low velocities where the buoyancy is clearly dominant and comparable to pool boiling. It will be observed that the effect of orientation is most pronounced in this domain. The effect of orientation is then examined as the velocity is increased and transition occurs from the buoyancy-dominant regime to the flow boiling regimes in which the bulk flow inertia becomes significant. The effect of velocity will then be explored at several distinct orientations.

**4.1 Effect of Orientation.** Figure 4 shows the effect of orientation with the thin gold film on quartz heater surface at the lowest velocity, 4.1 cm/s, and the lowest subcooling, 2.2°C. As

## Nomenclature

$g$ = standard earth gravitational constant, m/s$^2$
$\Delta T$ = temperature difference, °C
$\theta$ = orientation angle, deg

**Subscripts**

sat = saturation
sub = subcooled
$w$ = wall



Downloaded 12 Dec 2010 to 193.140.21.150. Redistribution subject to ASME license or copyright; see http://www.asme.org/terms/Terms_Use.cfm

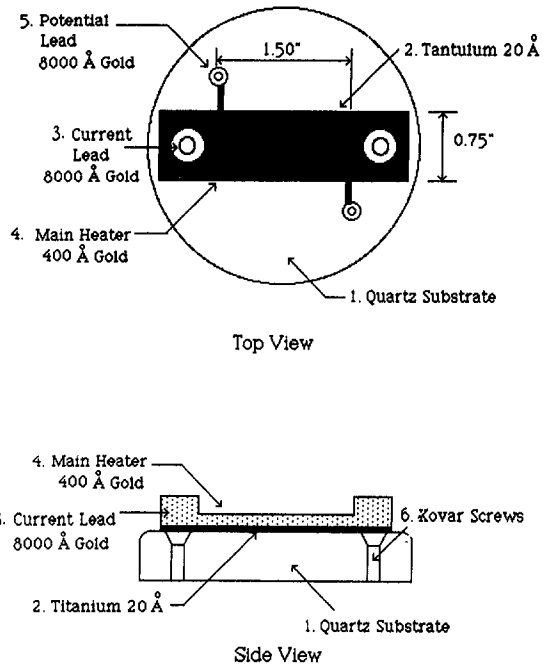



**Fig. 2 Thin film gold heater surface**

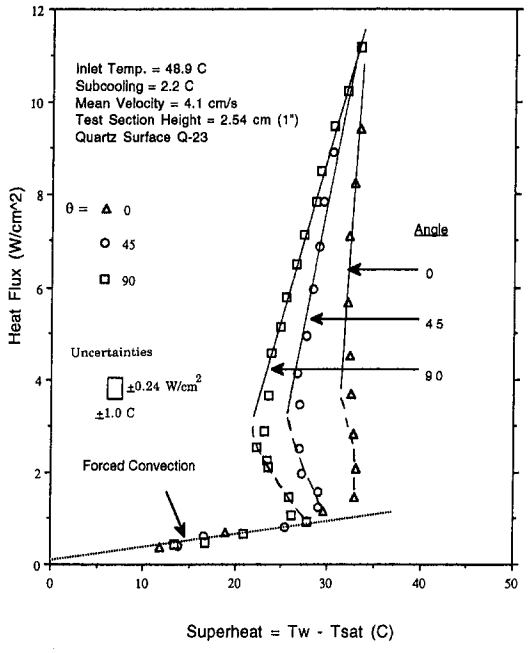



**Fig. 4 Heat flux versus surface superheat at various orientations. Inlet temperature = 48.9°C. $\Delta T_{sub}$ = 2.2°C. Velocity = 4.1 cm/s. Gold on quartz heating surface.**

the surface is rotated from the horizontal up position, $\theta = 0$ deg, to the vertical upflow position, $\theta = 90$ deg, a significant enhancement of heat transfer takes place at the lower levels of heat flux, with the enhancement diminishing as the heat flux is increased. At the horizontal down position, $\theta = 180$ deg, the low velocity was not sufficient to sweep the vapor away, and an immediate dryout occurred with the onset of boiling, necessitating the termination of the test. At other angles between 90 and 180 deg, dryout did not immediately occur upon nucleation; however, excessive accumulation of vapor in the flow loop inhibited the operation of the pressure controller.

Figure 5 shows the effect of orientation with both the thin gold film heater surface and the metal heater for a bulk liquid velocity of 8.1 cm/s, and a bulk inlet subcooling of 4.4°C. Similar to the behavior noted in Fig. 4, as the thin gold film heater surface is rotated from the horizontal up position, $\theta = 0$ deg, to $\theta = 90$ deg, the heater surface superheats decrease. However, as the surface is rotated past the vertical upflow orientation to $\theta = 135$ deg, the heater surface superheats now begin to shift back to higher values at the higher levels of heat flux.

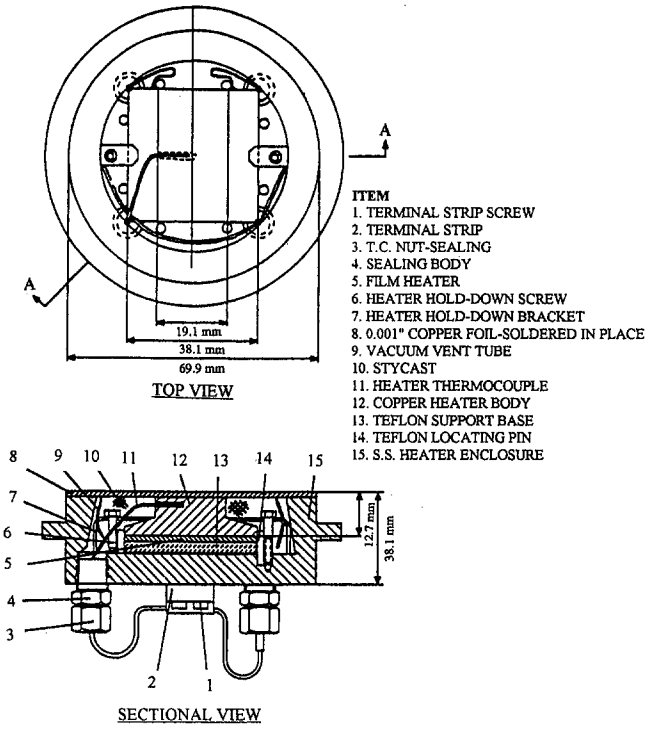



**Fig. 3 Gold-coated copper substrate heater**

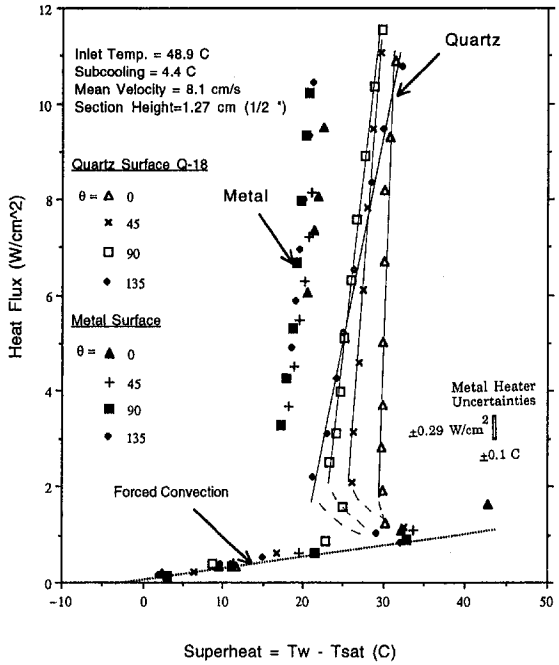



**Fig. 5 Heat flux versus surface superheat at various orientations. Inlet temperature = 48.9°C. $\Delta T_{sub}$ = 4.4°C. Velocity = 8.1 cm/s. Gold on quartz heating surface and gold-coated copper substrate heater.**



Downloaded 12 Dec 2010 to 193.140.21.150. Redistribution subject to ASME license or copyright; see http://www.asme.org/terms/Terms_Use.cfm

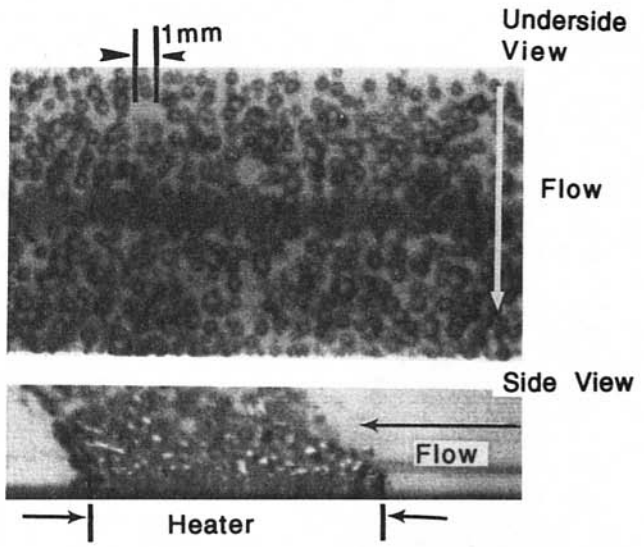



Fig. 6(a) Flow boiling. Horizontal flow. Velocity = 8.1 cm/s; $\theta$ = 0 deg; $q''$ = 4.5 W/cm$^2$; $\Delta T_{sub}$ = 4.4°C.

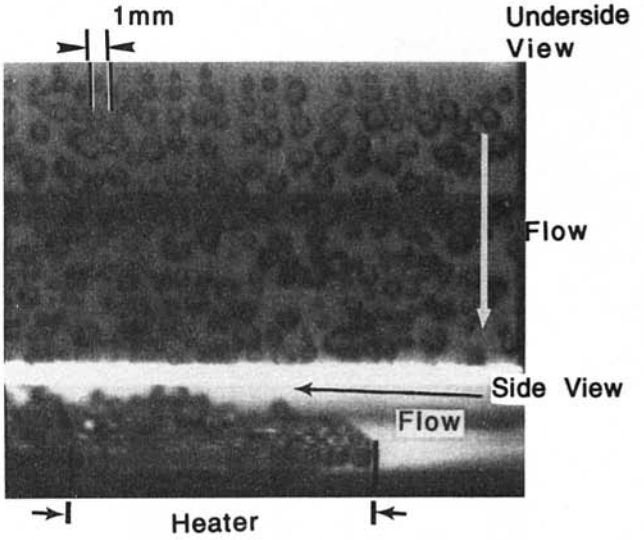



Fig. 6(b) Flow boiling. Vertical flow. $\theta$ = 90 deg.

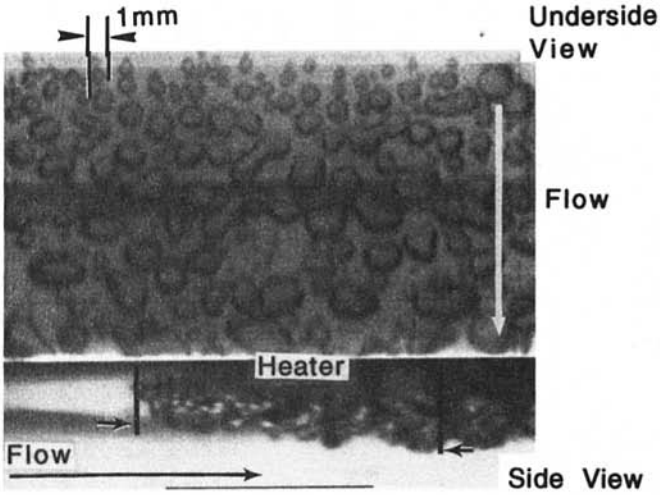



Fig. 6(c) Flow boiling. Surface inclined down $\theta$ = 135 deg.

The relative positions of the boiling curves at the various orientations with the metal heater surface are generally the same as those with the thin gold film surface. However, the curves now appear to remain nearly linear and parallel, with much less difference between the various orientations. Furthermore, the drops in the surface temperature upon nucleation appear much more dramatic with the metal heaters.

Selected photographs of the boiling on the thin film surface with a flow velocity of 8.1 cm/s, a heat flux of 4.5 W/cm$^2$, and at orientations of 0, 90, and 135 deg are shown in Figs. 6($a$–$c$), respectively, for the low subcooling case of 4.4°C. These conditions correspond to three points on the boiling curves in Fig. 5 at the specified angles of 0, 90, and 135 deg and a heat flux of 4.5 W/cm$^2$. In the side views of the boiling process in Fig. 6, the images were taken at a slight angle downward from being parallel to the heater surface, for purposes of clarity, and a portion of the unheated circular quartz substrate can be seen upstream from the heater surface. The horizontal up condition, shown in Fig. 6($a$), closely follows the behavior seen in pool boiling, with the vapor bubbles growing and departing the uniformly distributed nucleation sites. At the orientation, $\theta$ = 90 deg, in Fig. 6($b$), the majority of nucleation sites now appear at the leading edge of the heater, and the bubbles are observed to slide along the heating surface and grow to a size two to three times the average departure size observed in the horizontal up position. With the orientation $\theta$ = 135 deg, the bubbles also slide along the surface but grow to even larger sizes than with $\theta$ = 90 deg.

Above a heat flux of about 8 W/cm$^2$, the entire surface becomes covered by vapor bubbles at every orientation, with the bulk liquid flow no longer able to penetrate through the bubbly layer to the heater surface. It would appear from visual observations that fully developed boiling is present above this level of heat flux. Marked differences nevertheless exist in the bubble dynamics with different orientations. At the higher levels of heat flux, the bubbles coalesce, with departure from the heater surface occurring more as slugs of vapor rather than individual bubbles. With the surface in the horizontal up position, $\theta$ = 0 deg, the slugs of vapor appear to depart vertically from the heater surface, whereas at $\theta$ = 90 deg, the vapor slugs become elongated as they move across the heater surface. With surface inclined down at $\theta$ = 135 deg, the slugs of vapor grow to even larger sizes, with a corner of the heater experiencing dryout.

The data for both the metal and gold-on-quartz surfaces at the highest velocity of 32.4 cm/s used here are combined in Figs. 7 and 8 for the low and high subcoolings, respectively, and demonstrate that the orientation effect is now almost entirely eliminated, reflecting the dominance of bulk liquid inertial effects over buoyancy. Both figures also demonstrate that the wall superheats associated with the metal heater are less than those with the smooth polished heater surface, as is well known for nucleate boiling. It is also noted that all the heater surface superheats, including both surfaces, decrease slightly as subcooling increases. This observed decrease with subcooling contradicts with the findings of Bergles and Rohsenow (1964), but does agree with the observations of other researchers (e.g., Duke and Schrock, 1961). It may also be noted that the nonboiling data obtained with the quartz heater surface lie above those for the metal heater. This is attributed to the difference in single phase forced convection heat transfer between the uniform heat flux of the thin film heater, and the isothermal heating surface of the copper substrate heater. Further differences in heat transfer associated with these two boundary conditions are discussed by Kirk (1992).

**4.2 Effect of Velocity.** The effect of velocity on the nucleate boiling process varies with orientation. With the surface in the horizontal up position, $\theta$ = 0 deg, increasing the velocity enhances the heat transfer, as demonstrated in Fig. 9, although the effect is very slight with the metal surface.

On comparing photographs taken through the thin film surface in the horizontal up position at the low and high velocities, it was noted that although the heat transfer was enhanced with increasing flow velocity, the number of nucleating sites and the average bubble size markedly decreased. At the highest velocity, with



Downloaded 12 Dec 2010 to 193.140.21.150. Redistribution subject to ASME license or copyright; see http://www.asme.org/terms/Terms_Use.cfm

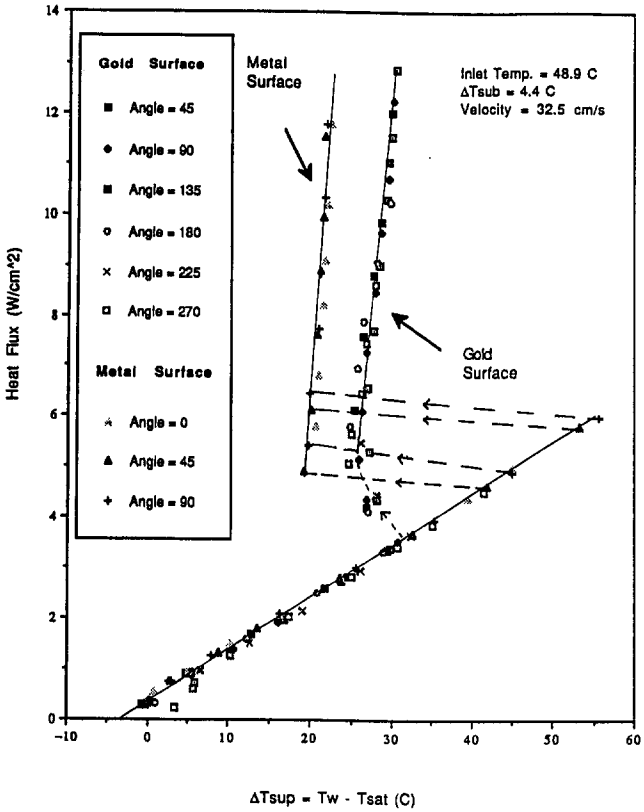



**Fig. 7 Heat flux versus surface superheat at various orientations. Inlet temperature = 48.9°C. $\Delta T_{sub}$ = 4.4°C. Velocity = 32.4 cm/s. Gold on quartz heating surface and gold-coated copper substrate heater.**

this orientation, the bulk liquid appears to move the bubbles along the heating surface as the bubbles grow, whereas in the low-velocity case the bubbles departed vertically.

When the orientation angle is increased to $\theta = 135$ deg, in Fig. 10, a degradation in the heat transfer takes place with the metal heater as the velocity is increased from 8.1 to 32.4 cm/s and remains nearly constant at all level of heat flux. The quartz heater at this orientation exhibits a distinct change with heat flux, ranging from a degradation in the heat transfer at the lower levels of heat flux to an enhancement at the higher levels.

## 5.0 Discussion of Results

Previous researchers have studied the influence of heater surface orientation in pool boiling and have observed trends similar to those observed for the low-velocity case in the present study. The interpretations of these pool boiling results have been the subject of much discussion.

Jung et al. (1987) considered the effect of orientation on nucleate pool boiling of R-11. At a relatively low heat flux, a noticeable increase in the heat transfer coefficient was observed as the heating surface was rotated from a horizontal up position of $\theta = 0$ deg to an orientation of $\theta = 165$ deg with the surface inclined facing downward. At a larger heat flux, the heat transfer coefficient was constant regardless of orientation, except for the horizontal downward inclined position. It was concluded that there are two heat transfer mechanisms associated with boiling on an inclined surface: (1) an evaporative mechanism, which is always present and is independent of orientation, and (2) a bubble agitation mechanism, which is a strong function of surface orientation. As the surface is inclined from the horizontal up position, the bubbles flow over the surface, causing the surrounding liquid to become more turbulent. Tong et al. (1988) also observed an enhancement of heat transfer in pool boiling on downward-facing inclined surfaces where the improved heat transfer behavior was attributed to the "stripping" of the superheated layer by the sliding vapor bubbles.

Contrary to the interpretation of Jung et al. (1987), evidence in the present study suggests that the evaporation mechanism is a strong function of orientation. At the lowest velocity with the heater in the horizontal up position, the bubble population density is the greatest with the sites evenly distributed across the surface, as seen in Fig. 6(*a*). As the orientation angle increases, the bubbles are observed to slide along the surface, effectively deactivating nucleation sites in their path, and continue to grow due to evaporation at the bubble base. As seen in Fig. 6(*c*), a bubble on a downward-facing surface grows to a size several times larger than one on a surface facing up, with all other parameters held constant. Visual evidence from the high-speed pictures suggests that boiling in the horizontal up position would produce the greatest bubble agitation, due to the large population density and the vigorous pumping action generated by the rapid succession of bubbles growing and departing vertically from the surface. However, despite the large population density, the surface in the horizontal up position is in fact the least effective for heat transport, suggesting that the enhancement of heat transfer at other orientations may not be attributed to increased agitation effects but rather to the evaporation of a thin liquid film beneath and in the path of the bubbles. An explanation that attributes the same orientation effect in pool boiling to microlayer evaporation beneath a sliding bubble is given by Nishikawa and Fujita (1990).

In their model for the heat transfer with a sliding bubble along a downward facing surface, two mechanisms are utilized: (1) transient heat conduction to the bulk liquid after the superheated liquid layer has been swept away by a preceding bubble and replaced by the bulk liquid and (2) latent heat transfer, which occurs once a moving bubble has swept the bulk liquid away so that the surface is covered by the vapor bubble but separated from it by a thin liquid film. The computations demonstrate that the

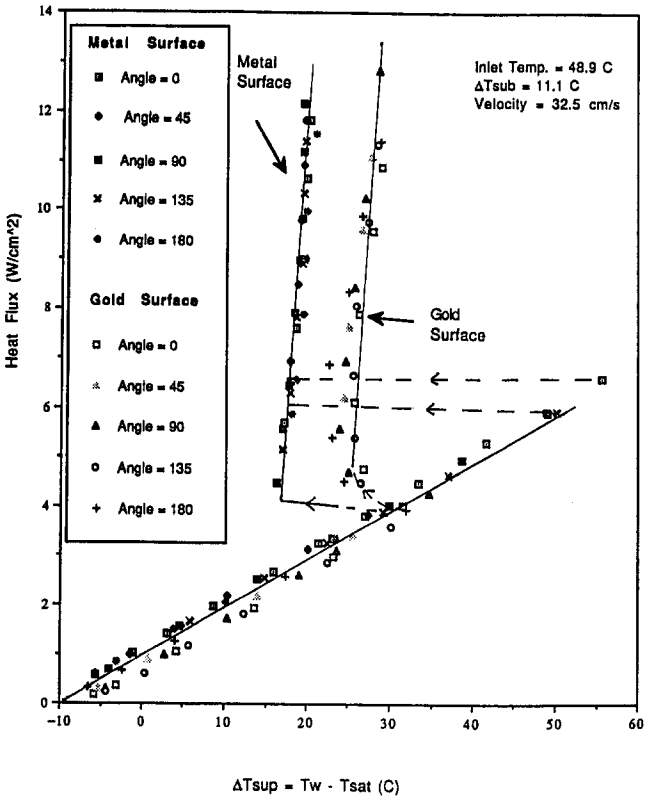



**Fig. 8 Heat flux versus surface superheat at various orientations. Inlet temperature = 48.9°C. $\Delta T_{sub}$ = 11.1°C. Velocity = 32.4 cm/s. Gold on quartz heating surface and gold-coated copper substrate heater.**



Downloaded 12 Dec 2010 to 193.140.21.150. Redistribution subject to ASME license or copyright; see http://www.asme.org/terms/Terms_Use.cfm

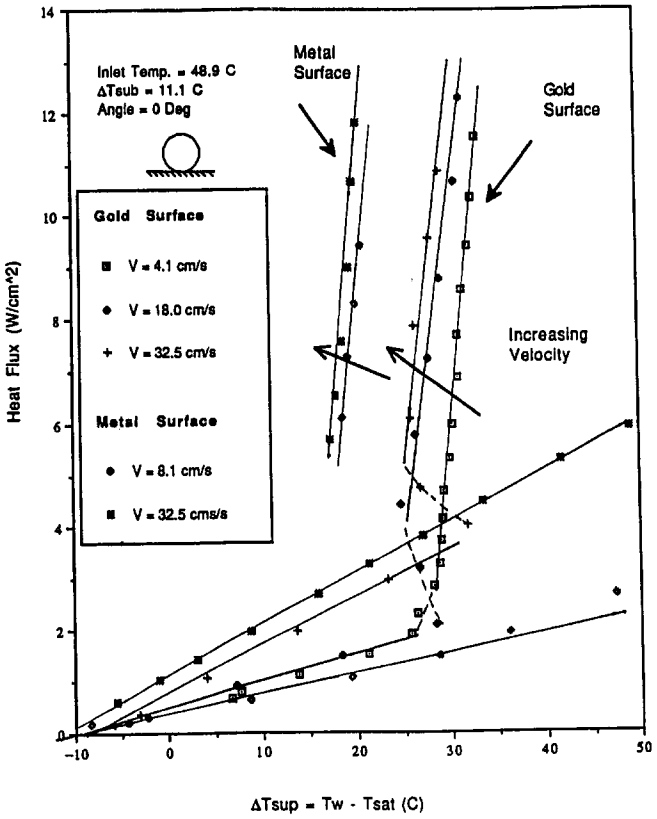



**Fig. 9 Heat flux versus surface superheat at different flow velocities. $\theta$ = 0 deg. Inlet temperature = 48.9°C. $\Delta T_{sub}$ = 11.1°C. Gold on quartz heating surface and gold-coated copper substrate heater.**

observed effect of orientation is almost completely due to the effect on the latent heat transport, which is a strong function of orientation.

Pool boiling experiments in variable gravity fields, including microgravity (Merte, 1988) indicate that increasing the body forces degrades heat transfer, while reducing gravity enhances heat transfer. This behavior is attributed to two different effects: (1) Reducing buoyancy keeps the heated fluid adjacent to the heating surface, and (2) negative buoyancy or its absence keeps the growing vapor bubbles closer to the superheated liquid and the heating surface, increasing the area of the microlayer and/or decreasing its thickness. Similarly, in the experiments here, as the heater surface is rotated and the normal component of gravity is reduced, the vapor bubbles elongate and slide along the heater surface with a noted enhancement in heat transfer.

Similar to the situation of bubbles sliding along a downward-facing surface under the action of gravity, the sliding effect attributed to the bulk liquid inertia in flow boiling may also contribute to the enhancement of heat transfer. In nucleate boiling with forced flow, Anderson and Minns (1970) suggested that immediately following nucleation the microlayer evaporation forms a dry spot. Then, as the bubble moves away from the site, sliding over a continuous film of liquid, the dry spot is re-wetted and the process is repeated. This argument is supported by the observations of Cooper et al. (1983), who noted that bubbles appeared to roll along the wall, forming a visible liquid film beneath it.

In a model of a sliding vapor bubble under high velocity forced convection, Tsung-Chang and Bankoff (1990) demonstrated, with the aid of a number of simplifying assumptions, that it is possible for a sliding bubble to augment the microlayer evaporation by at least a factor of two over that of a stationary bubble.

Previous studies on the influence of flow velocity on forced convection boiling have noted that although velocity may enhance heat transfer at relatively low values of heat flux, the surface superheat becomes essentially independent of velocity at sufficiently high levels of heat flux (e.g., Lemmert and Chawla, 1977). The results of the present study with the heater in a horizontal up position have demonstrated that increasing flow velocity enhances the heat transfer monotonically although the difference is slight with the metal heater. However, at orientations with the surface facing downward, increasing velocity actually tends to decrease the heat transfer, at least at the lower levels of heat flux, as seen in Fig. 10.

This curious behavior can be explained by a reduction in the latent heat transport as the bulk liquid velocity is increased. The total heat transfer in flow boiling is often considered to be a superposition of single-phase forced convection heat transfer and nucleate pool boiling heat transfer. Although increasing the bulk liquid velocity would increase the single-phase forced convection component of the total heat transfer for every orientation, increases in velocity also seem to decrease the latent heat transport for those orientations where buoyancy holds the sliding vapor bubbles to the surface. This results in a net degradation of heat transfer. The decreased contribution of latent heat transport with increasing velocity is supported by the sharp reduction in the average bubble size with vertical upflow and with the surface inclined down, $\theta$ = 135 deg, as the bulk liquid velocity increases. The decrease in the average bubble size may be due to the shorter times available for evaporation as the bubbles slide along the heater surface, the reduction in the liquid superheat energy near the heater surface, and the increased rate of condensation over the bubble cap.

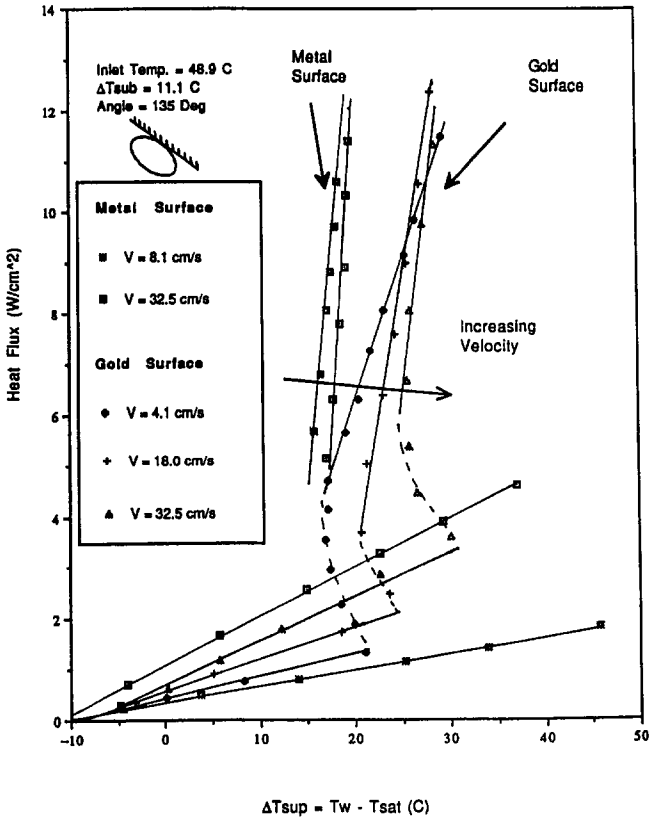



**Fig. 10 Heat flux versus surface superheat at different flow velocities. $\theta$ = 135 deg. Inlet temperature = 48.9°C. $\Delta T_{sub}$ = 11.1°C. Gold on quartz heating surface and gold-coated copper substrate heater.**



Downloaded 12 Dec 2010 to 193.140.21.150. Redistribution subject to ASME license or copyright; see http://www.asme.org/terms/Terms_Use.cfm

## 6.0 Conclusions

1 By changing the heater surface orientation from the horizontal up position such that the normal component of the buoyant force is reduced but remains positive, an enhancement of heat transfer occurs with subcooled, low-velocity, nucleate flow boiling. If this normal component is reduced further such that it becomes negative, an enhancement in the heat transfer takes place only at very low levels of heat flux, and as long as the flow velocity is sufficient to sweep away the bubbles. Similar behavior has been observed in pool boiling at various orientations and is most prominent at low values of heat flux.

2 Increasing the flow velocity reduces the effects of buoyancy induced by varying the orientation, and a limiting flow velocity exists beyond which the orientation, and hence gravity, can be completely neglected. Whether this limiting flow velocity is different in microgravity remains to be established.

3 The effect of flow velocity on heat transfer is dependent on the surface orientation. In horizontal flow boiling with the surface facing up, increasing the flow velocity increases the heat transfer through a combination of an increased single-phase forced convection component and an increased sliding effect of the vapor bubbles. By varying the orientation and decreasing the normal buoyant force, the effect of velocity will be reversed, and an orientation is eventually reached where increasing flow velocity acts to degrade the heat transfer, at least at the lower levels of heat flux. This effect may be attributed to a reduction in the latent heat transport.


## Acknowledgments

This work was supported in large part under NASA Grants NAG3-589 and NAG3-1310. The interest of Mr. J. McQuillan and Mr. J. Platt of the NASA Lewis Research Center are appreciated.


## References


Anderson, G. H., and Minns, D. E., 1970, "Nucleate Boiling in a Flow Liquid," *Proc. 4th Int. Heat Transfer Conference,* Paris, Paper B.4.1.

Bergles, A. E., and Rohsenow, W. M., 1964, "The Determination of Forced Convection Surface Boiling Heat Transfer," ASME JOURNAL OF HEAT TRANSFER, Vol. 86, pp. 365–372.

Cooper, M. G., Mori, K., and Stone, C. R., 1983, "Behavior of Bubbles Growing at a Wall With Forced Flow," *Int. J. Heat Mass Transfer,* Vol. 26, No. 10, pp. 1489–1507.

Duke, E. E., and Schock, V. E., 1961, "Void Volume, Site Density and Bubble Size for Subcooled Nucleate Pool Boiling," *Fluid Mechanics & Heat Transfer Institute,* pp. 138–145.

Jung, D. S., Venart, J. S., and Sousa, A. M., 1987, "Effects of Enhanced Surfaces and Surface Orientation on Nucleate and Film Boiling Heat Transfer in R11," *Int. J. Heat Mass Transfer,* Vol. 30, No. 12, pp. 2627–2639.

Kirk, K. M., 1992, "A Study of the Relative Effects of Buoyancy and Liquid Momentum in Forced Convection Nucleate Boiling," PhD Thesis, The University of Michigan, Ann Arbor, MI.

Lemmert, M., and Chawla, J. M., 1977, "Influence of Flow Velocity on Surface Boiling Heat Transfer Coefficient," *Heat Transfer in Boiling,* E. Hahne and U. Grigull, eds., Academic Press, pp. 237–247.

Merte, H., Jr., 1988, "Combined Roles of Buoyancy and Orientation in Nucleate Pool Boiling," *ASME Collected Papers in Heat Transfer 1988,* Vol. 2, ASME HTD-104, pp. 179–186.

Nishikawa, K., and Fujita, Y., 1990, "Nucleate Boiling Heat Transfer and Its Augmentation," *Advances in Heat Transfer,* J. P. Hartnett and T. F. Irvine, eds., Vol. 20, pp. 23–37.

Tong, W., Simon, J. W., and Bar-Cohen, A., 1988, "A Bubble Sweeping Heat Transfer Mechanism for Low Flux Boiling on Downward Facing Inclined Surfaces," *Collected Papers in Heat Transfer,* ASME HTD-Vol. 104, pp. 173–178.

Tsung-Chang, G., and Bankoff, S. G., 1990, "On the Mechanism of Forced Convection Subcooled Nucleate Boiling," ASME JOURNAL OF HEAT TRANSFER, Vol. 112, pp. 213–218.





Downloaded 12 Dec 2010 to 193.140.21.150. Redistribution subject to ASME license or copyright; see http://www.asme.org/terms/Terms_Use.cfm

# A Painting Technique to Enhance Pool Boiling Heat Transfer in Saturated FC-72

**J. P. O'Connor**
Graduate Research Assistant.

**S. M. You**
Assistant Professor.
Mem. ASME

Department of Mechanical Engineering,
University of Texas at Arlington,
Arlington, TX 76019-0023

*A benign method of generating a surface microstructure that provides pool boiling heat transfer enhancement is introduced. Pool boiling heat transfer results from an enhanced, horizontally oriented, rectangular surface immersed in saturated FC-72, indicate up to an 85 percent decrease in incipient superheat, a 70 to 80 percent reduction in nucleate boiling superheats, and a ~109 percent increase in the critical heat flux (CHF = 30 W/cm$^2$), beyond that of the nonpainted reference surface. For higher heat flux conditions (19 to 30 W/cm$^2$), localized dryout results in increased wall superheats (8 to 48°C). The enhanced surface heat transfer coefficients are four times higher than those from the reference surface and similar to those from the Union Carbide High Flux surface. Photographs that identify differences in bubble size and departure characteristics between the painted and reference surfaces are presented.*

## Introduction

Boiling heat transfer is one method of dissipating high amounts of thermal energy. When evaluating the nucleate boiling heat transfer performance of a surface, three parameters should be considered. The first is the wall superheat required to initiate boiling. The surface must reach the incipient wall superheat condition to initiate the nucleation process. Theoretical developments have indicated that the incipient wall superheat is inversely proportional to the volume of entrapped vapor/gas in a surface irregularity (Bar-Cohen and Simon, 1988). The second performance parameter to be considered is the heat transfer coefficient in the nucleate boiling regime. Increasing the boiling heat transfer coefficient from the surface leads to lower surface temperatures. Nucleate boiling heat transfer is enhanced as the active nucleation site density of the surface increases. The third boiling performance parameter to be considered is the Critical Heat Flux (CHF), which is the highest heat flux that can be removed without exposing the surface to film boiling.

The mechanism that causes CHF continues to be the focus of many investigations. Several theories exist that attempt to describe this mechanism. The most widely accepted theory was developed by Zuber (1959) for pool boiling on an infinite, upward-facing, horizontal flat plate. Zuber's theory emphasizes the collapse of vapor escape routes from the heated surface due to hydrodynamic instabilities and leads to the following correlation:

$$q_{maxz} = 0.131\rho_g^{1/2}h_{fg}[\sigma g(\rho_f - \rho_g)]^{1/4} \quad (1)$$

Equation (1) indicates that the CHF is independent of surface effects.

Studies focusing on boiling incipience and nucleation site distributions using partially wetting liquids (water, ether, methanol) (Griffith and Wallis, 1959; Hsu, 1962; Chowdhury and Winterton, 1985), verify that surface roughness significantly affects incipient superheat and nucleate boiling heat transfer. Many studies have been conducted concerning boiling incipience using highly wetting dielectric liquids. A summary of these investigations conducted prior to 1986 can be found in Bar-Cohen and Simon (1988). In general, wide variations in incipience superheats were reported and theories for this phenomenon were presented. Bar-Cohen and Simon concluded that commonly accepted incipience theories for nonhighly wetting liquids cannot be applied to highly wetting dielectric liquids. You et al. (1990a) observed wide variations (~20°C) in incipience superheats in highly wetting dielectric liquids and noted incipience superheat levels as high as 73°C for R-113. Further investigations by You et al. (1990b) showed similar results using FC-72 and a silicon surface.

Marto and Lepere (1982) investigated the heat transfer enhancement of three commercially available surfaces (Union Carbide High Flux, Hitachi Thermoexcel-E, and Wieland GEWA-T) on a cylindrical tube geometry immersed in highly wetting liquids (saturated FC-72 and R-113). Their data indicate up to a 60 percent decrease in nucleate boiling superheats and negligible increases in the CHF. Park and Bergles (1986) and Carvalho and Bergles (1990a) observed similar results in the nucleate boiling regime using the same commercially available heat sinks mounted on flat surfaces in saturated FC-72 and FC-87. Anderson and Mudawwar (1988) found that surface cavities of ~300 $\mu$m in diameter were ineffective in lowering incipience superheats, as well as enhancing nucleate boiling or the CHF in FC-72. They also showed that sanded (0.6–1.0 $\mu$m "scratches") and a vapor blasted (~15 $\mu$m cavity feature sizes) surfaces reduce incipient and nucleate boiling superheats by ~55 and 66 percent, respectively, compared to those from a polished surface. They did not observe, however, any increase in the CHF from these surfaces. Anderson and Mudawwar tested microfin, microstud, and microgroove structured surfaces. These surfaces produced up to a 250 percent increase in the CHF, which was primarily attributed to increases in heat transfer surface area. You et al. (1992) investigated a 0.3–3 $\mu$m alumina ($Al_2O_3$) particle treatment on a flat horizontal surface applied by a technique they termed "particle spraying." They reported significant reductions in incipient and nucleate boiling superheats (~50 percent), and an increase of ~32 percent in the CHF. This increase in CHF contradicts the CHF correlation presented in Eq. (1), possibly because of its failure to account for surface effects. From the previously mentioned investigations, it is apparent that surface microstructure of the correct size plays an important role in the enhancement of boiling incipience, nucleate boiling, and possibly CHF.

The current focus is to develop a surface treatment that will allow the boiling process to initiate at low superheat conditions, provide high heat transfer rates throughout the nucleate boiling region, and provide increased CHF levels without area enhancement, in FC-72. A complete understanding of the surface microstructure effect is needed, and the mechanisms through which boiling heat transfer improvements are made should be under-

Contributed by the Heat Transfer Division for publication in the JOURNAL OF HEAT TRANSFER. Manuscript received by the Heat Transfer Division January 1994; revision received November 1994. Keywords: Augmentation and Enhancement, Boiling, Phase-Change Phenomena. Associate Technical Editor: V. K. Dhir.



Copyright © 1995 by ASME

Downloaded 12 Dec 2010 to 193.140.21.150. Redistribution subject to ASME license or copyright; see http://www.asme.org/terms/Terms_Use.cfm

stood so further investigations can provide continued advancements.

## Experimental Apparatus, Heater, and Procedure

**Pool Boiling Test Facility.** The pool boiling test facility is illustrated in Fig. 1. It consists of two rectangular PYREX jars: One serves as a container for the test liquid (3.8 liter); the other is filled with water (22.7 liter) and serves as an isothermal bath. The immersion heater/circulator (1000 W) resides in the water bath and controls bulk liquid temperature. A magnetic stirrer reduces the time required to reach bulk liquid conditions and to degas the test liquid. Four copper-constantan thermocouples are employed, two for the test liquid and two for the water bath. The test liquid jar has a stainless steel cover plate with a heater support mounted to it. Two cover plate holes serve as a condenser and electronic harness port. One of the 3M Fluorinert liquids (FC-72) was selected for the experiment. It has a saturation temperature of 56°C at 1 atm, and is electrically nonconducting, having a volume resistivity of $10^{15}$ Ω-cm. It is thermally and chemically stable to temperatures in excess of 200°C.

A PC with a 486/33 MHz processor is used to control the National Instruments data acquisition system. The data acquisition system and all instrumentation are networked through the LabWindow Version 2.3 operating environment using Quick Basic as the primary programming language. A National Instruments AT-GPIB interface board provides communication with a direct current power supply (HP Model 6038-A) via IEEE-488 interface cables. A precision resistor (0.0999 Ω ± 0.05 percent) is used to determine the current going through the heater.

**Test Heater.** The test heater (top view) is illustrated in Fig. 2. It is rectangular in shape (0.51 cm × 1.65 cm) and flush mounted to a square block (5.08 cm × 5.08 cm) of LEXAN so that its projected surface area (~0.84 $cm^2$) is the only portion of the heater in direct contact with the test liquid. The LEXAN substrate is extended on one side of the heater for mounting purposes. Numerical analysis indicates the surrounding substrate is sufficiently thick to eliminate any nonsymmetric conduction edge effects. The test heater is mounted with the illustrated surface horizontally oriented and facing upward.

Two thin films, ~200 Å of nichrome base and ~900 Å of platinum, were bonded to a 1-mm-thick piece of aluminum nitride (AlN) using sputtering and evaporation deposition techniques, respectively. The resulting heating element resistance was ~14 Ω. Based on work by Bar-Cohen and McNeil (1992), and Carvalho and Bergles (1990b), the heater thickness (~1 mm) was designed to provide CHF data free of thermal conductance/capacitance effects. Four tin/silver leads were connected to each end of the heating element and provided voltage drop and measurement paths. Due to the low thermal resistance of platinum and aluminum nitride, the temperature gradient across the heater is negligible. Therefore, heater temperature is measured using a thin film (12.7 μm) thermocouple bonded directly to the center of the platinum heating element using an instant adhesive (3M CA4).

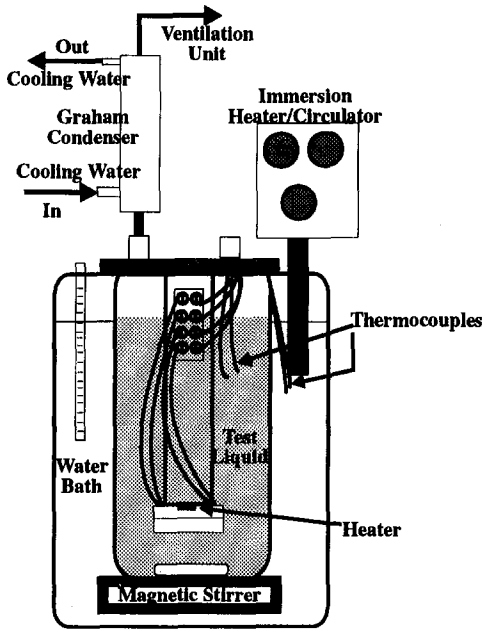



**Fig. 1 Pool boiling test facility**

To provide a reference surface to which the enhanced surface boiling performance could be compared, and also to allow a means of easy application of the surface treatment, aluminum foil (~20 μm) was bonded on top of the aluminum nitride surface using 3M CA4 instant adhesive (5 ± 2 μm). The total conductive thermal resistance ($R_{tcond}$) between the thermocouple and reference surface (aluminum foil) is ~31.15 × $10^{-6}$ $m^2$-°C/W. Using this resistance, the aluminum foil temperature ($T_{ref}$ – the temperature on top of the aluminum foil surface) was estimated to be ~3.1°C lower than that detected by the thermocouple ($T_{tc}$) at 10 W/$cm^2$.

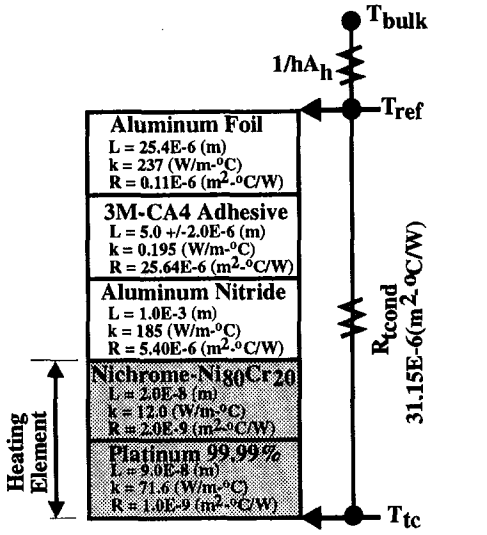
**Enhancement Paint and Its Application.** The boiling enhancement paint used for the present surface treatment is a mixture of 1.5 g of silver flakes (3–10 μm), 0.1 ml of Omegabond 101 thermal epoxy, and 10 ml of isopropyl alcohol. This paint composition was determined by conducting a study that systematically varied the silver flake content in the mixture, and was found to provide the highest level of enhancement throughout the boiling curve (O'Connor, 1994). The paint is applied to the reference (aluminum foil) surface using a "dripping" technique. When applying the paint, the smallest amount of solution that allows the entire reference surface to be covered with silver flakes is desired. The current geometry requires three drops from a small brush and results in a paint thickness of ~25 μm. After application, the paint is cured under a lamp at ~80°C for ~100 minutes. During cure, the alcohol evaporates and the mixture of flakes and epoxy adheres to the surface.

## Nomenclature

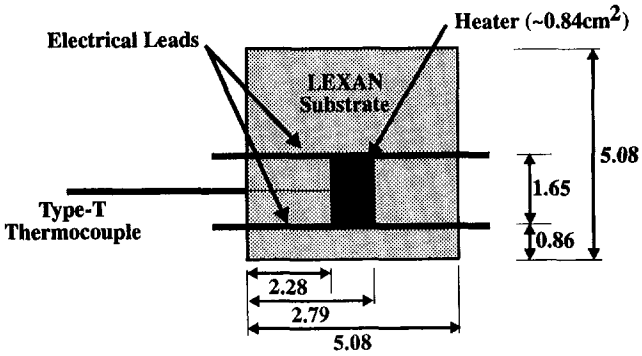
$A_h$ = projected heater surface area = 0.84 $cm^2$
$A_j$ = total vapor jet cross-sectional area, $cm^2$
$A_w$ = heater surface area feeding a single vapor jet, $cm^2$
CHF = Critical Heat Flux, W/$cm^2$
$g$ = gravitational acceleration, $m/s^2$
$h$ = heat transfer coefficient, W/$m^2$-°C
$h_{fg}$ = heat of vaporization, kJ/kg
$k$ = thermal conductivity, W/m-°C
$L$ = length, cm
$R$ = thermal resistance, $m^2$-°C/W
$R_{tcond}$ = total conductive thermal resistance, $m^2$-°C/W
$T_{bulk}$ = test liquid temperature, °C
$T_{ref}$ = reference surface (aluminum foil) temperature, °C
$T_{tc}$ = thermocouple temperature, °C
$T_w$ = paint surface temperature, °C
$\Delta T$ = wall superheat = $T_{ref} - T_{bulk}$, °C
$q$ = heat flux, W/$cm^2$
$q_{maxz}$ = Zuber critical heat flux, W/$cm^2$
$\lambda_T$ = Taylor one-dimensional wavelength, mm
$\rho_f$ = liquid density, $kg/m^3$
$\rho_g$ = vapor density, $kg/m^3$
$\sigma$ = surface tension, N/m



Downloaded 12 Dec 2010 to 193.140.21.150. Redistribution subject to ASME license or copyright; see http://www.asme.org/terms/Terms_Use.cfm




(a) - One Dimensional Heat Transfer Model




(b) - Heater and Substrate (cm - top view)

**Fig. 2 Heater geometry and dimensions**

Further development testing concerning the durability of the painted surface was conducted (O'Connor, 1994). Saturated pool boiling with the painted surface was maintained for time periods exceeding 80 hours. No degradation in boiling heat transfer enhancement was observed and the bonding strength of the paint was not weakened.

A Scanning Electron Microscope (SEM) image of the reference surface is illustrated in Fig. 3($a$). The reference surface (aluminum foil) has a sparse number of small cavities ($<1$ $\mu$m), a "smooth" surface in the boiling sense. Figures 3($b$, $c$) illustrate SEM images of the enhanced silver flake upper surface and cross section, respectively. The silver flake microstructures are multilayered with a total layer thickness of $\sim$25 $\mu$m and produce cavity feature sizes of $\sim$1 $\mu$m. The flake orientation is random, some lying horizontally, some vertically, and some in-between, and produces a thin porous layered structure. This thickness ($\sim$25 $\mu$m) is up to two orders of magnitude thinner, and the structure porosity appears significantly lower, than previously manufactured porous enhancement surfaces, a summary of which is given by Thome (1990).

**Test Procedure.** The heater is immersed in the test liquid, the magnetic stirrer and immersion heater/circulator are turned on, and the test liquid is heated to the desired temperature. These conditions are maintained for three hours, during which the dissolved gas concentration is reduced to approximately $0.2 \times 10^{-3}$ moles/mole (2 percent air by volume) according to You (1990). The magnetic stirrer is then turned off and data acquisition begins. Heat flux is increased in increments of less than 1.0 W/cm$^2$ (less than 0.5 W/cm$^2$ near incipience and CHF) by controlling power supply output voltage. At each power setting, the bulk liquid temperature is measured first.

For heat flux conditions less than $\sim$80 percent CHF, steady-state conditions are verified by assuring that the heater temperature is time invariant. For small heat flux increments ($q < 1.0$ W/cm$^2$) steady-state conditions are typically achieved within 30 seconds. After steady-state conditions prevail, a ten second delay is encountered and the parameters required to calculate the heat flux (heater current and resistance) and steady-state surface temperature are measured and averaged, 3000 samples at a rate of 600 samples/second.

For heat flux conditions greater than $\sim$80 percent CHF, after incrementing the heat flux, the heater surface temperature is immediately monitored for a 60 second time interval to prevent heater burnout. The CHF is defined as the highest nucleate boiling heat flux prior to the onset of film boiling. This condition is visually identifiable and can be detected by the data acquisition system through an excursion in heater temperature. If the temperature increase between two subsequent measurements for a 0.07 second time interval is larger than 12°C, CHF conditions are assumed to exist and the power supply is immediately disabled. At 0.5 W/cm$^2$ increments, the average increase in heater surface temperature is less than 1.5°C in the nucleate boiling regime. If CHF is not encountered, steady-state conditions are assumed to exist after 60 seconds, and the heat flux and surface temperature parameters are measured and averaged, 3000 samples at a sample rate of 6000 samples/second, and the power supply is then incremented to the next heat flux. The superheat is calculated by subtracting the bulk liquid temperature from the reference surface temperature ($\Delta T = T_{ref} - T_{bulk}$). The reference surface temperature represents the aluminum foil temperature calculated from the measured thermocouple temperature ($T_{ref} = T_{tc} - q*R_{tcond}$) as presented in Fig. 2. If CHF conditions are met, the process for one run is complete, after which there is a five minute delay before another run begins.

**Uncertainty Estimates.** Using the method of Kline and McClintock (1953), uncertainty estimates (20:1 odds—95 percent confidence level) were made for the heat flux and temperature measurements. The quoted uncertainties account for measurement resolution, instrumentation variance, geometric uncertainty, substrate conduction loss, and calibration error.

Substrate conduction losses were quantified at different heat flux conditions by solving three-dimensional conduction problems with a finite difference solver (FLUENT, 1991). The heater and substrate were modeled as a composite solid and natural convection heat transfer coefficients (Incropera and DeWitt, 1990) were specified for each respective surface immersed in saturated FC-72. Substrate and boiling surface heat transfer coefficients were initially specified from experimental data and reassigned through an iterative numerical process. Losses varied between 15 and 0.5 percent for heat flux conditions between 0.5 W/cm$^2$ (single-phase natural convection) and 19 W/cm$^2$ (nucleate boiling), respectively, and compare favorably to those reported by Mukutmoni et al. (1993) for similar conditions. Over the extended portion of the boiling curve (20–30 W/cm$^2$—to be discussed) losses increased to $\sim$1.8 percent. The other primary contributor to heat flux uncertainty was heater surface area. Combining these effects leads to overall uncertainty estimates in heat flux of 15.5 and 5.0 percent for single-phase (0.5 W/cm$^2$) and boiling ($q < 30$ W/cm$^2$) conditions, respectively.

Wall superheat uncertainty can be attributed primarily to thermocouple calibration (0.5°C) and the temperature correction from the thermocouple reading to the reference surface (primarily due to the 3M CA4 adhesive thickness; Fig. 2($a$)). At 10 W/cm$^2$ the overall wall superheat uncertainty was estimated to be 0.7°C.



Downloaded 12 Dec 2010 to 193.140.21.150. Redistribution subject to ASME license or copyright; see http://www.asme.org/terms/Terms_Use.cfm

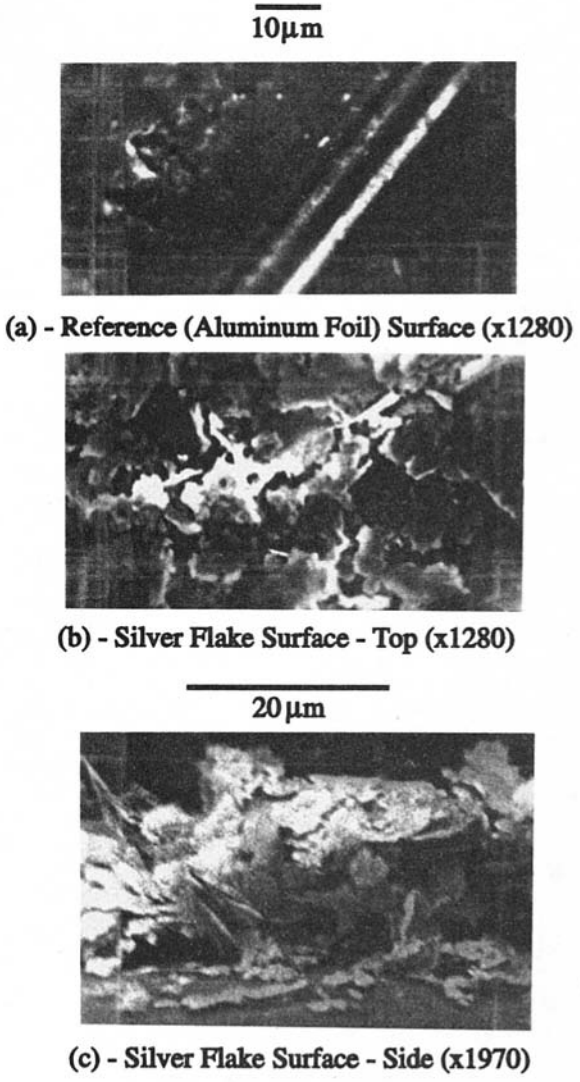



**Fig. 3 Surface microstructures**

## Discussion of Results

Figure 4 compares pool boiling data for the reference and enhanced surfaces at identical bulk liquid conditions. The observed differences in the boiling curves are an indication of variations in surface microstructures between the reference and enhanced surfaces. A comparison of the bubble behavior above the surfaces will aid in understanding these enhancement characteristics. Seven points are identified in Fig. 4, three along the reference surface curves, 5($a$), ($b$), and ($c$), corresponding to heat flux conditions of ~4, ~13, and ~14.3 W/cm$^2$ (CHF), respectively, and four along the enhanced surface curves, 6($a$), ($b$), ($c$), and ($d$), corresponding to heat flux conditions of 0.3, 4, 14, and 30 W/cm$^2$ (CHF), respectively. Photographs of the bubble behavior for the seven points are illustrated in Figs. 5 and 6 for the reference and enhanced surfaces, respectively. The bubble sizes were estimated by scaling them from the heater length (1.65 cm). Bubble size ranges are given for a qualitative comparison purpose.

Figure 5($a$) illustrates discrete bubble growth and departure behavior with departure diameters ranging between 0.6 and 1.0 mm, in good agreement with those predicted by the Cole and Rohsenow (1968) correlation (0.8 mm) applied to saturated FC-72. Bubble coalescence after departure produces bubble sizes as large as 3 mm. This behavior was observed from the reference surface between 4.0 and 9.0 W/cm$^2$, with the amount of bubble coalescence above the surface increasing with increasing heat flux conditions. Figure 5($b$) identifies two vapor columns departing from the reference surface. It is believed that the bubble departure frequency is sufficiently large so that the distance between departing bubbles is less than one bubble diameter causing bubble coalescence from an individual site as well as adjacent sites. The two vapor columns are separated by a distance approximately equivalent to the Taylor one-dimensional wavelength ($\lambda_T \sim 8$ mm for FC-72). Figure 5($c$) shows the bubble behavior just prior to CHF. Large vapor patches (~5 to 7 mm) are in contact with the surface, and the transition to film boiling is imminent. Figures 5($b$) and ($c$) identify bubble coalescence resulting in increased thermal resistance over the heated surface.

At low heat flux conditions near boiling incipience, discrete bubbles less than 0.3 mm in diameter departed from the entire enhanced surface as shown in Fig. 6($a$). This small bubble growth and departure behavior was observed up to a heat flux of ~1.2 W/cm$^2$. Referring to Fig. 4, the pool boiling data for the reference and enhanced 3–10 $\mu$m silver flake surfaces can be compared. The solid line represents the initial run and the dashed line runs 2 and 3 from the reference surface. The symbols represent enhanced surface boiling curve data for five runs (black symbols—initial run). The present enhancement paint does not increase the heat transfer surface area as seen by the initial run natural convection data in Fig. 4. Incipience superheat values for the reference surface range from ~20 to 27°C, whereas for the enhanced surface they range from ~3 to 8.5°C.

For saturated conditions, if it is assumed the noncondensable gas pressure inside an embryonic bubble is negligible, then mechanical equilibrium across the bubble interface is given by $[P_{sat}(T_w) - P_{sat}(T_{bulk}) = 2\sigma(T_w)/r_b]$. Using this relation and the measured incipient superheats, the calculated embryonic bubble radius for the reference surface ranged between 0.1 $\mu$m and 0.15 $\mu$m, and for the enhanced surface between 0.5 $\mu$m and 2.0 $\mu$m. This increase (three to twenty times) indicates the ability of the porous enhancement paint to trap vapor effectively. The computed embryonic bubble sizes for the enhanced surface are in good agreement with the apparent structure sizes existing among the 3–10 $\mu$m flakes (Fig. 3($b$) and ($c$)). Another mechanism that may play a role in reducing incipient superheats further is expediting the growth of and producing a more uniform superheated liquid layer. For the reference surface, the adjacent liquid layer becomes superheated via transient conduction through the liquid (Hsu, 1962). The porous silver flake microstructures locally expedite liquid heating and internal vaporization on a microscopic scale adjacent to the embryonic bubble.

Figure 6($b$) represents fully developed nucleate boiling (1.2 < $q$ < 10 W/cm$^2$) and indicates discrete bubble growth and

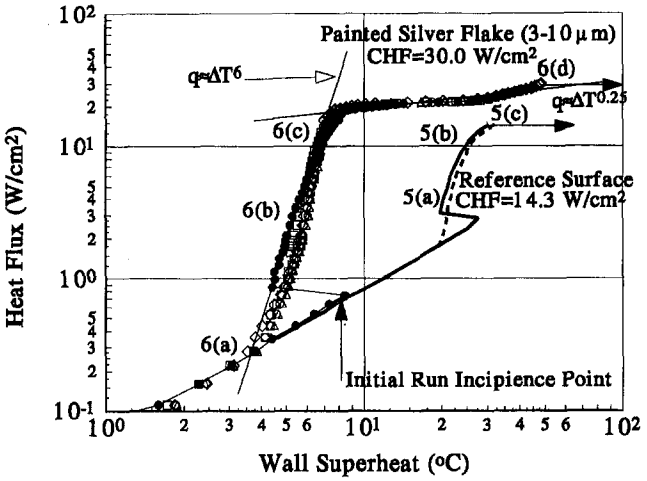



**Fig. 4 Boiling heat transfer enhancement**



Downloaded 12 Dec 2010 to 193.140.21.150. Redistribution subject to ASME license or copyright; see http://www.asme.org/terms/Terms_Use.cfm

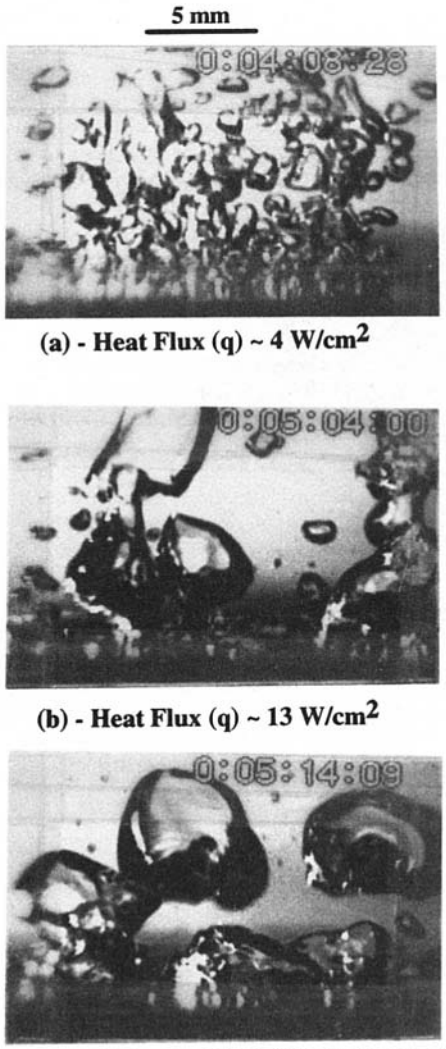



**Fig. 5 Reference surface bubble behavior**

departure behavior. Bubble departure sizes of ~0.4 to 0.8 mm are observed at 4 W/cm$^2$, noticeably smaller than those departing the reference surface at the same heat flux (Fig. 5($a$)). The photograph also identifies an increased nucleation site density compared to the reference surface, evident by the larger number of isolated bubbles over the surface. In this heat flux region bubble departure size increases but remains isolated, and the amount of bubble coalescence above the surface increases with increasing heat flux. Figure 6($c$) illustrates typical bubble behavior at heat flux values between 10 and 19 W/cm$^2$. Unlike the reference surface (Fig. 5($b$) and ($c$)), the enhanced surface produces many small bubbles (0.5–1.0 mm) adjacent to the surface, the majority of which coalesce into large vapor "mushrooms" above the surface.

Figure 6($d$) represents the bubble behavior just prior to CHF ($q \sim 30$ W/cm$^2$). Small bubbles (0.5–1.0 mm) are still observed adjacent to the enhanced surface, quite different from the bubble behavior just prior to CHF above the reference surface (Fig. 5($c$)). These bubbles appear to feed large vapor mushrooms hovering over the surface. As the heat flux was increased from ~19 W/cm$^2$ to the CHF condition, bubble coalescence into the vapor mushrooms was observed to occur closer to the heater surface (compare Fig. 6($c$) and ($d$)). A comparison of Figs. 5($a$–$c$) and Figs. 6($a$–$d$) indicates a significantly higher number of small bubbles existing above the enhanced surface at all heat flux conditions, including just prior to CHF. This difference in bubble departure characteristics leads to increased levels of heat transfer.

From the enhanced surface boiling curve shown in Fig. 4, two distinct boiling regions exist and are identifiable by the two boiling curve slopes. The lower nucleate boiling region ($q < \sim 19$ W/cm$^2$) has a log–log slope of ~6.0. The higher boiling region ($q > \sim 19$ W/cm$^2$) has a decreased slope (~0.25). This decreased slope region was also produced from a 450-$\mu$m-thick porous (30 percent) enhanced surface generated by sintering 60–100 $\mu$m spherical particles on a copper tube (Afgan et al., 1985).

This phenomenon is attributed to the formation of vapor patches at the base of the porous layer. Thome (1990) indicates the heat flux at which this "bend" in the boiling curve is initiated decreases with increasing porous layer thickness, and usually begins at heat flux conditions equal to or lower than the CHF from an untreated surface. From the current data it appears that these vapor patches began to form at ~19 W/cm$^2$, 5 W/cm$^2$ higher than the reference surface CHF. It is proposed that the "bend" heat flux is delayed (higher) for the current painted surface because of the reduced thickness of the porous paint layer. Bulk liquid can penetrate the thin porous layer and wet the heated surface.

With further increase in heat flux, these vapor patches spread slowly across the entire base of the porous surface increasing the

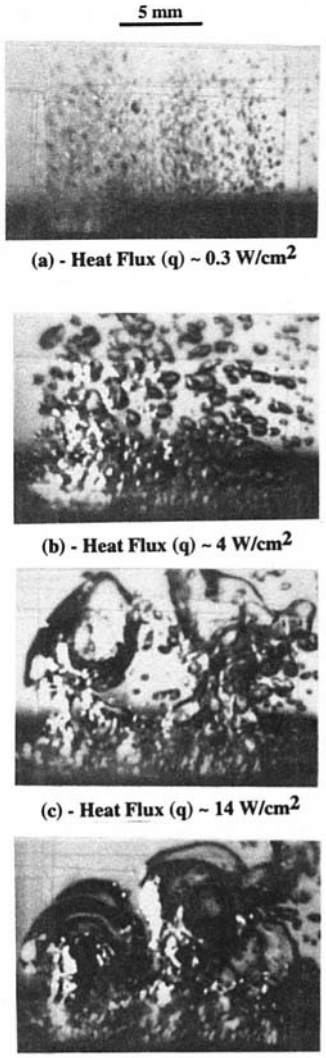



**Fig. 6 Painted surface bubble behavior**



Downloaded 12 Dec 2010 to 193.140.21.150. Redistribution subject to ASME license or copyright; see http://www.asme.org/terms/Terms_Use.cfm

thermal resistance across the structure until CHF occurs on the paint surface. When the CHF occurs, an instantaneous temperature increase (171°C/s) was measured. The local dryout in the paint structure prior to the CHF resulted in higher wall superheat values at the CHF compared to those from the reference surface—~45°C versus 29°C. The painted surface provides reductions of 70 to 80 percent in nucleate boiling superheats when $q < \sim 19$ W/cm$^2$. The nucleate boiling data illustrated in Fig. 4 are repeatable.

The enhanced surface CHF ($q \sim 30$ W/cm$^2$) is 109 percent higher than the reference surface CHF ($q \sim 14.3$ W/cm$^2$) for ostensibly identical test conditions. Therefore, it is evident that the microstructure provided by the 3–10 $\mu$m silver flakes plays a dominant role in increasing the CHF. The reference surface CHF compares favorably with the predicted CHF value from Zuber's correlation (13.98 W/cm$^2$). Based upon hydrodynamic theory, Zuber assumed the ratio of vapor jet area to heater surface area ($A_j/A_w$) was $\pi/16$. From Figs. 5($c$) and 6($d$), it appears that $A_j$ for the enhanced surface is larger than for the reference surface; however, the actual value is indeterminate. At a superheat of ~29°C (CHF of reference surface) a heat flux of ~23.5 W/cm$^2$ is provided by the enhanced surface. This is a 64 percent increase in heat flux at acceptable surface temperatures for electronic components (85°C).

Another CHF model developed by Haramura and Katto (1983) is based on bubble characteristics observed by Gaertner (1965). His observations closely resemble the phenomenon observed above the enhanced surface (Fig. 6($d$)), where large vapor mushrooms resting on top of a thin liquid film are nourished by columnar vapor stems. Haramura and Katto proposed that vapor blanketing results from Helmholtz instability of the vapor stems causing their collapse and the blanketing of the large vapor mushrooms onto the heated surface. Their correlation provides a CHF similar to that provided by Zuber (Eq. (1)). To the authors' knowledge, no CHF correlations exist that include surface effects. Existing CHF models have had formidable success in predicting CHF values from smooth surfaces and strongly indicate that hydrodynamic mechanisms dominate CHF, even from enhanced (nonsmooth) surfaces. Systematic investigations need to be conducted focusing on bubble behavior at the CHF point from different heater surface microstructures. Such investigations may lead to a means of introducing surface effects into existing hydrodynamic models.

**Heat Transfer Coefficient Determination and Comparison.** Figure 7 summarizes an investigation conducted to determine the minimum paint thickness that would provide the highest level of enhancement. A single paint mixture was fabricated (1.5 g silver flakes/10 ml alcohol/0.1 ml glue) and the enhancement paint thickness was systematically increased by applying successive layers on the reference surface. Pool boiling data between 5 and 19 W/cm$^2$ were generated for five enhanced surfaces, each having a different paint thickness; 25, 45, 61, 93, and 124 $\mu$m ($\pm 3$ $\mu$m). For a given heat flux, as the paint thickness increases the wall superheat increases due to additional thermal resistance.

If we assume that identical boiling surface conditions exist for all five paint thicknesses, the paint surface temperature ($T_w$) is fixed for a given heat flux. The thermal conductivity of the paint can be determined using any two data points at the same heat flux in Fig. 7. The thermal conductivity was estimated by averaging 20 values from randomly selected data in Fig. 7. The thermal conductivity was not a function of heat flux and varied randomly between 0.75 and 1.0 W/m-°C, with the average value being 0.95 W/m-°C. These calculations indicate between 5 and 19 W/cm$^2$, the increase in vapor layer thickness due to the localized dryout mechanism within the porous microstructure is negligible.

Knowing the paint thermal conductivity and thickness, the paint surface temperature ($T_w$) was determined using the expression $T_w = T_{ref} - q^*(L/k)_{paint}$. Superheats based on the paint surface temperature ($\Delta T = T_w - T_{bulk}$) were calculated for all five enhanced surfaces and are plotted in Fig. 7 (open symbols). These superheats represent enhanced conditions with zero paint thickness. The assumption of identical boiling surface conditions is appropriate as seen by convergence of the corrected data ($T_w - T_{bulk}$) to within a $\pm 1$°C band. Although the temperature on the bottom side of the paint ($T_{ref}$) increases with heat flux, the corrected data indicate the paint surface temperature decreases with heat flux ($q < 19$ W/cm$^2$).

Figure 8 compares boiling heat transfer coefficients generated from the reference and enhanced surfaces. The coefficients for the reference surface were calculated based upon the temperature difference between the reference surface and bulk liquid ($T_{ref} - T_{bulk}$). The reference surface heat transfer coefficient increases from ~1680 to 5200 W/m$^2$-°C. Heat transfer coefficients were generated using the enhanced surface data illustrated in Fig. 4 (25 $\mu$m thick) and are represented by the line made of short dashes (Fig. 8). The coefficients increase to 24,600 W/m$^2$-°C at a heat flux of ~19 W/cm$^2$, then decrease dramatically and level off at approximately 6000 W/m$^2$-°C near the CHF point. The dramatic decrease (in $h$) beyond 19 W/cm$^2$ is attributed to the gradual increase in the vapor layer thickness within the porous paint microstructure. The enhanced surface increases the heat transfer rate up to four times above that of the reference surface. For comparative purposes, High Flux and Thermoexcel-E data from Marto and Lepere (1982) are also illustrated in Fig. 8. The Union Carbide High Flux surface provides heat transfer coefficients comparable to those obtained from the current enhanced paint surface. Both the current enhanced surface and High Flux surface provide considerable heat transfer enhancement compared to the Hitachi Thermoexcel-E surface. The feature size of the High Flux surface is ~50 $\mu$m, smaller than any previously developed porous surface, and is closer to the feature size of the current paint structure (~1 $\mu$m).

## Conclusions

A boiling heat transfer enhancement paint was developed and tested. The current surface produces heat transfer enhancement primarily by increasing in the number of active nucleation sites. Photographic observations of the bubble departure pattern occurring at the surface showed significant differences between the painted and reference surfaces. These differences, along with SEM images, give insight into the mechanisms providing boiling heat transfer enhancement.

1 Repeatable and low incipience superheats (3 to 8.5°C) were observed for the painted surface. These superheats were ~70 to 85 percent lower than those for the reference surface.

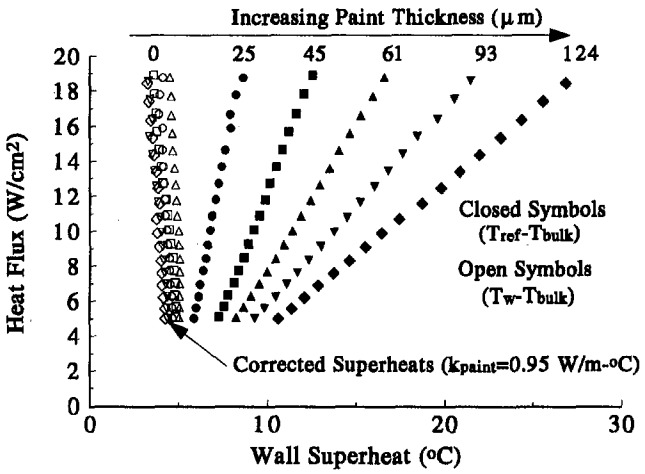



Fig. 7 Enhancement paint thickness study



Downloaded 12 Dec 2010 to 193.140.21.150. Redistribution subject to ASME license or copyright; see http://www.asme.org/terms/Terms_Use.cfm

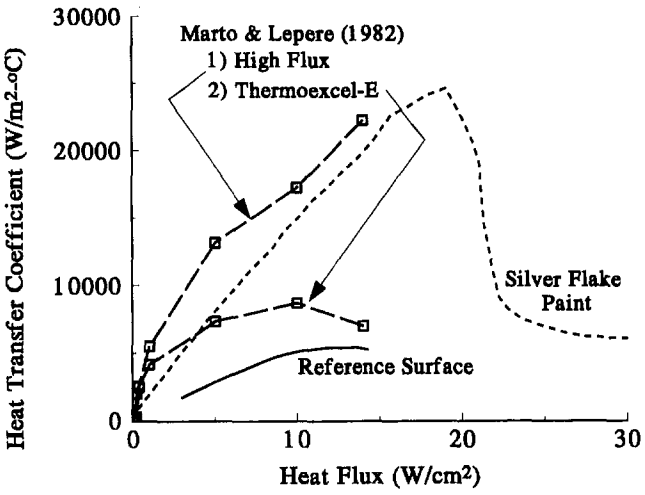



**Fig. 8 Heat transfer comparison**

2 The enhanced surface nucleate boiling superheats were 70 to 80 percent lower than those of the reference surface. This corresponds to an increase in boiling heat transfer, three (using $T_{ref}$) to nine (using $T_w$) times higher than the untreated reference surface.

3 A CHF increase of 109 percent (30 W/cm$^2$) was provided by the enhanced surface for identical bulk liquid conditions. Wall superheat at the CHF was ~45°C, 16°C higher than that of the reference surface CHF superheat. The CHF increase is due to surface microstructure and its influence on the boiling heat transfer characteristics. CHF correlations developed by Zuber (1959) and Haramura and Katto (1983) do not account for surface effects and appear to be applicable to smooth surfaces only.

4 Photographic observations revealed that the painted structure consistently produced many small bubbles throughout the entire boiling curve, including conditions just prior to CHF. This is unique and leads to enhanced boiling heat transfer mechanisms.

## Acknowledgments

This study was supported by the Texas Higher Education Coordinating Board: Advanced Research/Technology Program grant number 003656-001. In addition, donations of FC-72 from the 3M Industrial Chemical Products Division are appreciated.

## References

Afgan, N. H., Jovic, L. A., Kovalev, S. A., and Lenykov, V. A., 1985, "Boiling Heat Transfer From Surfaces With Porous Layers," *International Journal of Heat and Mass Transfer,* Vol. 28, No. 2, pp. 415–422.

Anderson, T. M., and Mudawwar, I., 1988, "Microelectronic Cooling by Enhanced Pool Boiling of a Dielectric Fluorocarbon Liquid," *Proc. of National Heat Transfer Conf.,* ASME HTD-Vol. 96, pp. 551–560.

Bar-Cohen, A., and Simon, T. W., 1988, "Wall Superheat Excursions in the Boiling Incipience of Dielectric Fluids," *Heat Transfer Eng.,* Vol. 9:1, pp. 19–31.

Bar-Cohen, A., and McNeil, A., 1992, "Parametric Effects on Pool Boiling Critical Heat Flux in Dielectric Liquids," *Proc. of Eng. Foundation Conference, Pool and External Flow Boiling,* Santa Barbara, CA, pp. 171–175.

Carvalho, R. D., and Bergles, A. E., 1990a, "The Influence of Subcooling on the Pool Nucleate Boiling and Critical Heat Flux of Simulated Electronic Chips," *Proc. of the 9th International Heat Transfer Conf.,* Jerusalem, Israel, pp. 289–294.

Carvalho, R. D., and Bergles, A. E., 1990b, "The Effect of Heater Thermal Properties on the Pool Boiling Critical Heat Flux," *Third Encontro Nacional de Ciencias Termicas,* Itaperna, Brazil.

Chowdhury, R. S. K., and Winterton, R. H. S., 1985, "Surface Effects in Pool Boiling," *International Journal of Heat and Mass Transfer,* Vol. 28, No. 10, pp. 1881–1889.

Cole, R., and Rohsenow, W. M., 1968, "Correlation of Bubble Departure Diameter for Boiling of Saturated Liquids," *Chemical Eng. Progress Symposium Series,* Vol. 65, No. 92, pp. 211–213.

FLUENT INC., 1991, "User's Manual," Version 4.1.

Gaertner, R. F., 1965, "Photographic Study of Nucleate Pool Boiling on a Horizontal Surface," ASME JOURNAL OF HEAT TRANSFER, Vol. 87:1, pp. 17–29.

Griffith, P., and Wallis, J. D., 1959, "The Role of Surface Conditions in Nucleate Boiling," *Chemical Eng. Progress Symposium Series,* Vol. 56, No. 30, pp. 49–63.

Haramura, Y., and Katto, Y., 1983, "A New Hydrodynamic Model of the Critical Heat Flux, Applicable to Both Pool and Forced Convective Boiling on Submerged Bodies in Saturated Liquids," *International Journal of Heat and Mass Transfer,* Vol. 26, pp. 389–399.

Hsu, Y. Y., 1962, "On the Size Range of Active Nucleation Cavities on a Heating Surface," ASME JOURNAL OF HEAT TRANSFER, Vol. 84, pp. 207–216.

Incropera, F. P., and Dewitt, D. P., 1990, *Fundamentals of Heat and Mass Transfer,* 3rd ed., Wiley, New York.

Kline, S. J., and McClintock, F. A., 1953, "Describing Uncertainties in Single-Sample Experiments," *Mechanical Engineering,* Vol. 75, Jan., pp. 3–8.

Marto, P. J., and Lepere, V. J., 1982, "Pool Boiling Heat Transfer From Enhanced Surfaces to Dielectric Fluids," ASME JOURNAL OF HEAT TRANSFER, Vol. 104, pp. 292–297.

Mukutmoni, D., Joshi, Y. K., and Kelleher, M. D., 1993, "Computations for a Three-By-Three Array of Protrusions Cooled by Liquid Immersion: Effect of Substrate Thermal Conductivity," *ASME Advances in Electronic Packaging,* ASME EEP-Vol. 4-2.

O'Connor, J. P., 1994, "Enhancement of Pool Boiling Heat Transfer in Highly-Wetting Dielectric Liquids," Ph.D. Thesis, University of Texas at Arlington, Arlington, TX.

Park, K. A., and Bergles, A. E., 1986, "Boiling Heat Transfer Characteristics of Simulated Microelectronic Chips With Fluorinert Liquids," HTL-40, Iowa State University, Ames, IA.

Thome, J. R., 1990, *Enhanced Boiling Heat Transfer,* Hemisphere Pub. Corp., New York.

You, S. M., Simon, T. W., Bar-Cohen, A., and Tong, W., 1990a, "Experimental Investigation of Nucleate Boiling Incipience With a Highly Wetting Dielectric Fluid (R-113)," *International Journal of Heat and Mass Transfer,* Vol. 33, No. 1, pp. 105–117.

You, S. M., Simon, T. W., and Bar-Cohen, A., 1990b, "Experiments on Boiling Incipience With a Highly-Wetted Dielectric Fluid: Effects of Pressure, Subcooling and Dissolved Gas," *Proc. of the 9th International Heat Transfer Conf.,* Jerusalem, Israel, Vol. 2, pp. 337–342, Hemisphere Publishing Co.

You, S. M., 1990, "Pool Boiling Heat Transfer With Highly-Wetting Dielectric Fluids," Ph.D. Thesis, University of Minnesota, Minneapolis, MN.

You, S. M., Simon, T. W., and Bar-Cohen, A., 1992, "A Technique for Enhancing Boiling Heat Transfer With Application to Cooling of Electronic Equipment," *IEEE Trans. CHMT,* Vol. 15, No. 5, pp. 823–831.

Zuber, N., 1959, "Hydrodynamic Aspects of Boiling Heat Transfer," AEC Report No. AECU-4439, Physics and Mathematics.



Downloaded 12 Dec 2010 to 193.140.21.150. Redistribution subject to ASME license or copyright; see http://www.asme.org/terms/Terms_Use.cfm

# Shape of a Vapor Stem During Nucleate Boiling of Saturated Liquids

J. H. Lay

V. K. Dhir

Mechanical, Aerospace and Nuclear Engineering Department, School of Engineering and Applied Science, University of California, Los Angeles, Los Angeles, CA 90024

*The transport processes occurring in an evaporating two-dimensional vapor stem formed during saturated nucleate boiling on a heated surface are modeled and analyzed numerically. From the heater surface heat is conducted into the liquid macro/microthermal layer surrounding the vapor stems and is utilized in evaporation at the stationary liquid–vapor interface. A balance between forces due to curvature of the interface, disjoining pressure, hydrostatic head, and liquid drag determines the shape of the interface. The kinetic theory and the extended Clausius–Clapeyron equation are used to calculate the evaporative heat flux across the liquid-vapor interface. The vapor stem shape calculated by solving a fourth-order nonlinear ordinary differential equation resembles a cup with a flat bottom. For a given wall superheat, several metastable states of the vapor stem between a minimum and maximum diameter are found to be possible. The effect of wall superheat on the shape of the vapor stem is parametrically analyzed and compared with limited data reported in the literature.*

## Introduction

Nucleate boiling is one of the most efficient and at the same time most complex modes of boiling. To understand this complex transport process, extensive studies have been performed in the past several decades. However, due to experimental difficulties, only a few studies have focused on the microphenomena of heat transport. In order to have a good understanding of the physics of the boiling process, the present study makes an effort to develop a model that describes the transport process occurring at the evaporating interface of a vapor stem formed during saturated nucleate boiling.

Gaertner (1965) conducted a series of experiments to study nucleate boiling on a horizontal surface. He identified the transition from isolated bubbles to fully developed nucleate boiling to occur when bubbles at a given site began to merge in the lateral and vertical directions. He described these merged bubbles as vapor mushrooms, which are attached to the heater surface via numerous vapor stems. From the heater surface, heat is conducted into the liquid macro/microthermal layer surrounding the vapor stems and is utilized in evaporation at the liquid–vapor interface. In Gaertner's photographic study, the thickness of the thermal layer was found to be about the same as the height of the vapor stems.

At high wall superheats, although most of the heat is utilized in evaporation through the liquid layer on the heater surface, the mechanism underlying this phenomenon is not yet fully understood. The liquid layer between the vapor mushroom and the heater surface has been termed as the macrolayer. It is distinguished from the microlayer, which is known as the thin liquid film, formed underneath vapor stems at high heat fluxes or underneath isolated bubbles at low heat fluxes.

Iida and Kobayasi (1969) used an electrical conductivity probe to make a direct quantitative determination of the void fraction profiles near the heater surface. The maximum void fraction in nucleate boiling was found to occur at 0.3 to 1 mm from the heater surface. A liquid-rich layer was identified near the heater surface. Bhat et al. (1983a), based on the assumption that the vapor stem diameter is zero at the heater surface and increases linearly with distance from the surface, developed a model to predict the thickness of the liquid layer between the heater surface and the vapor mushroom. Bhat et al. (1983b) also showed that at high heat fluxes, conduction across the liquid layer accounts for most of the heat transfer from the heater surface.

Recently, Dhir and Liaw (1989) proposed a time and area-averaged model for fully developed nucleate boiling. They conceptualized the boiling process on a vertical surface into three regions, i.e., thermal layer, intermediate region, and vapor flow dynamics-dominated region. The thermal layer containing vapor stems occupies the region immediately next to the wall. It was assumed that evaporation at the static vapor stems was the dominant mode of heat transfer. The vapor stems were located on the nucleation sites and the shape of the vapor stems was dictated by the contact angle. Heat from the wall was conducted into the macro/microlayer and was utilized in evaporation at the stationary liquid–vapor interface. The heat transfer rate into the thermal layer and the temperature distribution in the thermal layer were determined by solving a two-dimensional steady-state conduction equation in the liquid occupied region. Stem spacing and diameter were determined from their experimental values of wall void fractions and assumed functional dependence of active site density on wall superheat. Both stem diameter and stem spacing were found to decrease with wall superheat and increase with wettability.

Besides, numerous studies in the literature have focused on the physicochemical phenomena at the interface of evaporating thin films. For example, Potash and Wayner (1972) studied the transport processes occurring in an evaporating extended meniscus formed on a superheated flat glass plate immersed in a liquid pool. They noted that fluid flow in the evaporating meniscus resulted from disjoining pressure and a change in the meniscus curvature provided the necessary pressure gradient. In addition, the heat transfer across the meniscus was by conduction in a direction normal to the plate surface and was utilized for evaporation from the thin film. Subsequently, Wayner et al. (1976) and Wayner (1992) used an extended Clausius–Clapeyron equation to define an interline heat transfer coefficient and interfacial mass flux at the liquid–vapor interface. Mirzamoghadam and Catton (1988) extended this analysis to obtain the shape of an evaporating meniscus attached to an inclined heated plate partially submerged in a liquid pool. In a recent theoretical study, Schonberg et al. (1993) investigated the heat transport of a steady heptane meniscus in a 2 $\mu$m microchannel at high heat fluxes. They found that a stable evaporating meniscus that formed in the

Contributed by the Heat Transfer Division for publication in the JOURNAL OF HEAT TRANSFER. Manuscript received by the Heat Transfer Division May 1994; revision received August 1994. Keywords: Boiling, Evaporation, Thermocapillary Flows. Associate Technical Editor: R. Viskanta.



Copyright © 1995 by ASME

Downloaded 12 Dec 2010 to 193.140.21.150. Redistribution subject to ASME license or copyright; see http://www.asme.org/terms/Terms_Use.cfm

microchannel at a very high heat flux ($1.3-1.6 \times 10^6$ W/m$^2$) was theoretically possible.

Gaertner and Westwater (1960) have reported vapor stem diameters determined from the photographs. Dhir and Liaw (1989) and Wang and Dhir (1993a, b) have deduced the stem diameter from their measurement of void fraction. In this study the shape of the vapor stems and thickness of the liquid layer underneath is determined through theoretical and numerical analysis. The key objectives of the present study are:

(*i*) to develop a model that describes liquid flow in an evaporating two-dimensional interface of a vapor stem formed during saturated nucleate boiling, and

(*ii*) to delineate the static shape of vapor stems and evaporative heat flux profiles when the wall superheat is parametrically varied.

Furthermore, the effect of gravity on the shape of the vapor stems is also discussed. The model results can be used to predict the heat flux in fully developed nucleate boiling. If it is assumed that in fully developed nucleate boiling, evaporation is the dominant mode of heat transfer, the boiling heat flux is obtained by simply multiplying the heat removal rate from one stem with the number density of stems (active nucleation sites).

## Analysis

In fully developed nucleate boiling, bubbles at the neighboring sites begin to merge and appear as large mushroom-type bubbles. These mushroom-type bubbles are supported by several stems implanted in the thermal layer. Figure 1 shows the mushroom structure originally identified by Gaertner (1965) and subsequently used by Dhir and Liaw (1989) in their analysis. Figure 2 shows the vertical cross section of a vapor stem, which is formed on a single active cavity site. Heat from the wall is conducted into the thermal layer (macrolayer) surrounding the vapor stem and the liquid layer (microlayer) lying between the heater and the vapor stem interface and is utilized in evaporation at the liquid–vapor interface, which is assumed to be stationary. To compensate for the mass that is transferred as a result of evaporation, liquid flows in the space between the interface and the wall. The drag experienced by the liquid is overcome by the disjoining pressure and the capillary pressure that is available as a result of change in the radii of curvature of the stem in the plane of the paper and normal to it. The assumptions made in carrying out the analysis are as follows:

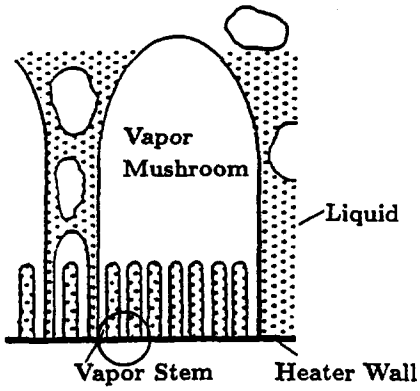



**Fig. 1 Conceptualization of the boiling process on a flat plate (Dhir and Liaw, 1989)**

1 The vapor stems are static. As such flow and thermal processes in the vicinity of the stems occur under steady-state conditions. This assumption is justified (see Lay, 1994) on the basis that times ($\simeq$3 ms) for a vapor stem to form and for steady-state temperature profile to develop in the thermal layer are found for water at one atmosphere pressure to be much smaller than the hovering period ($\simeq$60 ms) of a mushroom-type bubble.
2 The heater surface temperature does not vary temporally or spatially. This is true when a thick copper plate is used as test heater.
3 Lubrication theory is valid and the convective terms, radial conduction and viscous dissipation in the energy equation can be neglected.
4 The interfacial shear stress at the liquid–vapor interface can be neglected.
5 Ideal gas law is applicable to the vapor in the vapor stem.

## Nomenclature

$A$ = Hamaker constant
$a_1$ = evaporation coefficient
$d_w$ = stem diameter
$dp_A$ = pressure gradient resulting from disjoining pressure
$dp_g$ = pressure gradient resulting from liquid hydrostatic head
$dp_l$ = pressure gradient in the liquid layer
$dp_{q_e}$ = pressure gradient resulting from vapor recoil effect
$dp_{r_1}$ = pressure gradient resulting from the change of $r_1$
$dp_{r_2}$ = pressure gradient resulting from the change of $r_2$
$g$ = gravitational acceleration
$h_{fg}$ = latent heat of vaporization
$K$ = curvature
$k_l$ = liquid thermal conductivity
$\tilde{M}$ = molecular weight
$p_d$ = disjoining pressure
$p_l$ = liquid pressure
$p_{le}$ = liquid pressure at the vertical end of the vapor stem
$p_v$ = vapor pressure
$p_{ve}$ = vapor pressure at the vertical end of the vapor stem
$q$ = heat flux
$q_c$ = conductive heat flux
$q_e$ = evaporative heat flux
$q_0$ = conductive heat flux at $r_0$
$r_0$ = radial distance between the origin of the coordinates and cavity center
$r_1$ = stem radius in radial direction
$r_2$ = stem radius on the $r$–$z$ plane
$r$ = coordinate in the $r$ direction
$\bar{r}$ = liquid spreading distance
$R_1$ = $r_1$ at the vertical end of the vapor stem
$R_2$ = $r_2$ at the vertical end of the vapor stem
$\tilde{R}$ = universal gas constant
$T$ = temperature
$T_c$ = critical temperature
$T_i$ = liquid–vapor interface temperature
$T_{sat}$ = saturation temperature of liquid
$T_v$ = vapor temperature
$T_w$ = wall temperature
$\Delta T$ = wall superheat
$u_l$ = liquid velocity in the liquid layer
$\bar{u}_l$ = liquid local average velocity
$v_l$ = liquid velocity normal to the liquid–vapor interface
$v_v$ = vapor velocity normal to the liquid–vapor interface
$\tilde{v}_l$ = liquid molar volume
$z$ = coordinate in the $z$ direction
$\delta$ = film thickness
$\delta_0$ = minimum film thickness
$\delta_e$ = film thickness at the vertical end of the vapor stem
$\mu_l$ = viscosity of liquid
$\rho_l$ = density of liquid
$\rho_v$ = density of vapor
$\sigma$ = surface tension
$\sigma_{sat}$ = surface tension at saturation temperature
$\phi$ = contact angle



Downloaded 12 Dec 2010 to 193.140.21.150. Redistribution subject to ASME license or copyright; see http://www.asme.org/terms/Terms_Use.cfm

6 The value of the Hamaker constant is not affected by interfacial curvature, but its value changes with wettability.

As shown in Fig. 2, the interface has two radii of curvature, $r_1$ and $r_2$. The radius $r_1 = r_0 + r$ is the cylindrical radius in the liquid flow direction and measured from the cavity center, and $r_2$ describes the shape of the interface in the $r-z$ plane that relates to the thickness of the macro/microlayer, $\delta$, by

$$r_2 = \frac{(1 + \delta'^2)^{3/2}}{\delta''} \tag{1}$$

The superscripts (′) and (″) in Eq. (1) denote spatial derivatives in the $r$ direction. The minimum thickness of the liquid layer, $\delta_0$, which occurs at a certain radial distance $r_0$ from the cavity center, is used as a characteristic length to normalize all of the length variables. All parameters in the cylindrical coordinates are defined with respect to $r_0$. The spreading distance, $\bar{r}$, is the distance over which the interface shape changes from horizontal to totally vertical. The evaporative heat flux changes the curvature of the liquid–vapor interface. Most of the evaporation occurs along the curved interface of the vapor stem.

It is assumed that the interface becomes nearly normal to the surface at a certain height, $\delta = \delta_e$. At this location $r_1$ equals $R_1$, defined as the stem radius, and $r_2$ equals $R_2$ (with $R_2$ rapidly becoming very large). Pressure in the liquid at $\delta = \delta_e$ is assumed to be very close to the system pressure. The pressure in the vapor at the location ($\delta = \delta_e$) can be written as

$$p_{ve} = p_{le} + \sigma \cdot \left(\frac{1}{R_1} + \frac{1}{R_2}\right) \tag{2}$$

The vapor velocity in the stem is very small since the flow area of the stem is much larger than the curved interface area of the stem over which vapor is produced (see Fig. 2). As such, pressure at a given location on the vapor side of the curved interface can be approximated by using Bernoulli's equation, as

$$p_v = p_{ve} - \tfrac{1}{2}\rho_v v_v^2 + \rho_v g(\delta_e - \delta) \tag{3}$$

Combining Eqs. (2) and (3), we get

$$p_v = p_{le} + \sigma \cdot \left(\frac{1}{R_1} + \frac{1}{R_2}\right) - \tfrac{1}{2}\rho_v v_v^2 + \rho_v g(\delta_e - \delta) \tag{4}$$

The relationship between the pressure in the vapor and pressure in the liquid can be obtained by making a force balance at the interface. The force resulting from momentum change across the liquid–vapor interface is balanced by the resultant of the forces composed of liquid–vapor pressure difference, surface tension force, liquid hydrostatic head, and disjoining pressure. Thus,

$$\rho_v v_v^2 - \rho_l v_l^2 = p_l - p_v + \sigma \cdot \left(\frac{1}{r_1} + \frac{1}{r_2}\right) - \rho_l g(\delta - \delta_e) - p_d \tag{5}$$

The disjoining pressure, $p_d$ in Eq. (5), results from van der Waals forces. Derjaguin and Zorin (1957) defined the relationship between disjoining pressure and flat film thickness of nonpolar liquids. The disjoining pressure is expressed as

$$p_d = -\frac{A}{\delta^3} \tag{6}$$

where $A$ is the Hamaker constant, which accounts for the van der Waals forces. According to Sheludko (1966), for polar liquids simple dipole (Keesom) and induced dipole (Debye) interactions will occur, which vary inversely with the sixth power of the distance. However, the dipole interactions are not additive and the overall contribution is strongly reduced. Hence, in the present analysis, the forces due to this interaction have been neglected. The Hamaker constant has a positive or negative value depending on whether the liquid film completely wets the surface. The value of the Hamaker constant for a completely wetting case is generally about $10^{-20}$ J.

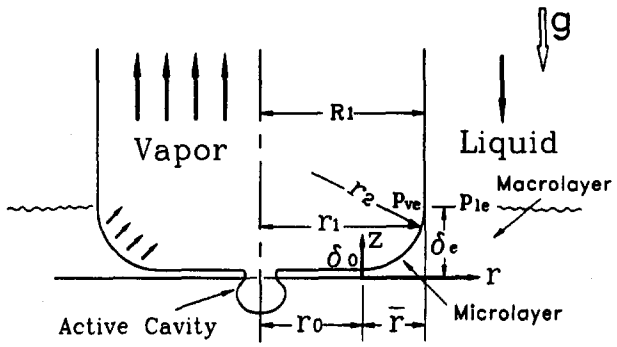



**Fig. 2 Vapor stem cross section**

In Eq. (5), the terms on the left-hand side represent the change of momentum as liquid evaporates at the interface. Since $\rho_v v_v = \rho_l v_l$ and at low pressures $\rho_v \ll \rho_l$, liquid inertia can be neglected in favor of vapor inertia. The mass rate of evaporation can be written in terms of the evaporative heat flux, $q_e$, as

$$\rho_v v_v = \frac{q_e}{h_{fg}} \tag{7}$$

Substituting for $p_v$, $p_d$ and $\rho_v v_v$ from Eqs. (4), (6), and (7), respectively, in Eq. (5) and differentiating with respect to $r$, an expression for the pressure gradient in the liquid is obtained as

$$\underbrace{\frac{dp_l}{dr}}_{dp_l} = \underbrace{-\frac{d}{dr}\left(\frac{\sigma}{r_1}\right)}_{dp_{r_1}} \underbrace{-\frac{d}{dr}\left(\frac{\sigma}{r_2}\right)}_{dp_{r_2}} \underbrace{+\frac{q_e\frac{dq_e}{dr}}{\rho_v h_{fg}^2}}_{dp_{q_e}} + \underbrace{\frac{3A\delta'}{\delta^4}}_{dp_A} + \underbrace{(\rho_l - \rho_v)g\delta'}_{dp_g} \tag{8}$$

As seen from Eq. (8), the pressure gradient in the liquid layer results from curvature change, surface tension gradient, vapor recoil effect, disjoining pressure, and hydrostatic head. The variation of surface tension with interface temperature is obtained by linearizing the relation given by Katayama-Guggenheim (Guggenheim, 1977) as

$$\sigma^* = \frac{\sigma}{\sigma_{\text{sat}}} = 1 - S_a T_i^* \tag{9}$$

where the dimensionless liquid–vapor interface temperature is defined as

$$T_i^* = \frac{T_i - T_{\text{sat}}}{T_w - T_{\text{sat}}} \tag{10}$$

and the parameter, $S_a$, accounts for the variation of surface tension with interface temperature. The parameter, $S_a$, is defined as

$$S_a = \frac{1.22(T_w - T_{\text{sat}})}{T_c} \tag{11}$$

where $T_{\text{sat}}$ is the saturation temperature corresponding to the pressure, $p_{le}$.

The heat flux, $q_c$, across the macro/microlayer can be determined by using the energy equation with the assumptions that convective terms, radial conduction, and viscous dissipation can be neglected. As such a linear temperature profile exists in the $z$ direction. Thus



Downloaded 12 Dec 2010 to 193.140.21.150. Redistribution subject to ASME license or copyright; see http://www.asme.org/terms/Terms_Use.cfm

$$q_c^* = \frac{q_c}{q_0} = \frac{1 - T_i^*}{\delta^*} \tag{12}$$

In Eq. (12), $q_0$, is the conductive heat flux at $r_0$ where film thickness is $\delta_0$, or

$$q_0 = \frac{k_l}{\delta_0} \cdot (T_w - T_{sat}) \tag{13}$$

By extending the Clausius–Clapeyron equation, Wayner (1992) developed an expression relating the liquid–vapor interface temperature and pressure to the mass flux crossing the interface. Using this approach, the resultant heat flux is expressed as

$$q_e = a_1 \left( \frac{\tilde{M}}{2\pi \tilde{R} T_{sat}} \right)^{1/2} \cdot \left\{ \frac{p_v \tilde{M} h_{fg}}{\tilde{R} T_v T_i} \cdot (T_i - T_v) + \frac{\tilde{v}_l p_v}{\tilde{R} T_i} \cdot (p_l - p_v) \right\} \cdot h_{fg} \tag{14}$$

It is assumed that the ideal gas law is applicable to the vapor in the stem and small variations of pressure within the stem can be neglected. If it is also assumed that the interface temperature is not too much different from the vapor temperature, Eq. (14) can be written as

$$q_e = a_1 \left( \frac{\tilde{M}}{2\pi \tilde{R} T_{sat}^3} \right)^{1/2} \cdot \left\{ \rho_v h_{fg} (T_i - T_v) + \frac{\tilde{v}_l p_v}{\tilde{R}} \cdot (p_l - p_v) \right\} \cdot h_{fg} \tag{15}$$

In Eq. (15), the first part is the same as the expression obtained from kinetic theory for evaporation rate and the second part accounts for the pressure effect. The value of $a_1$, the evaporation coefficient, has been reported in the literature (Hsu and Graham, 1976) to vary from 0.04 to 1. However, the studies of Hickman (1954) show that the value of 1 should be considered to be more appropriate for water. In the present study, a value of unity has been assumed for $a_1$. If the vapor and liquid momentum terms, $\rho_v v_v^2$, $\rho_l v_l^2$ and liquid hydrostatic head, $\rho_l g(\delta - \delta_e)$, are assumed to be small (only for the sake of evaluation of Eq. (15)), substitution of $p_l - p_v$ from Eq. (5) and $p_d$ from Eq. (6) in Eq. (15) yields

$$q_e = a_1 \left( \frac{\tilde{M}}{2\pi \tilde{R} T_{sat}^3} \right)^{1/2} \cdot \left\{ \rho_v h_{fg} (T_i - T_v) + \frac{\tilde{v}_l p_v}{\tilde{R}} \cdot \left[ -\sigma \cdot \left( \frac{1}{r_1} + \frac{1}{r_2} \right) - \frac{A}{\delta^3} \right] \right\} \cdot h_{fg} \tag{16}$$

It is assumed that the vapor temperature is close to the saturation temperature at $p_{le}$. The local interfacial superheat is the temperature difference between the liquid–vapor interface, $T_i$, and the vapor saturation temperature, $T_{sat}$. From Eq. (16), the tendency of the liquid to evaporate is promoted by interfacial superheat and hindered by capillary force and by disjoining pressure for a positive value of $A$. In dimensionless form, Eq. (16) can be expressed as

$$q_e^* = \frac{q_e}{q_0} = \Pi_1 T_i^* - \Pi_2 \sigma^* K^* - \frac{\Pi_3}{\delta^{*3}} \tag{17}$$

where three dimensionless groups, $\Pi_1$, $\Pi_2$, and $\Pi_3$, are defined as

$$\Pi_1 = \frac{a_1 \left( \frac{\tilde{M}}{2\pi \tilde{R} T_{sat}^3} \right)^{1/2} \rho_v h_{fg}^2 (T_w - T_{sat})}{q_0}$$

$$\Pi_2 = \frac{a_1 \left( \frac{\tilde{M}}{2\pi \tilde{R} T_{sat}^3} \right)^{1/2} \frac{\tilde{v}_l p_{le} h_{fg}}{\tilde{R}} \frac{\sigma_{sat}}{\delta_0}}{q_0}$$

$$\Pi_3 = \frac{a_1 \left( \frac{\tilde{M}}{2\pi \tilde{R} T_{sat}^3} \right)^{1/2} \frac{\tilde{v}_l p_{le} h_{fg}}{\tilde{R}} \frac{A}{\delta_0^3}}{q_0} \tag{18}$$

In the above, $\Pi_1$ is the ratio of the evaporative heat flux calculated from kinetic theory to the thermal conductive heat flux and $\Pi_2$ and $\Pi_3$ denote the effects of capillary force and disjoining pressure. The dimensionless curvature, $K^*$, is defined as

$$K^* = \frac{1}{r_1^*} + \frac{1}{r_2^*} = \frac{1}{r_0^* + r^*} + \frac{\delta^{*\prime\prime}}{(1 + \delta^{*\prime 2})^{3/2}} \tag{19}$$

In writing Eq. (19), $\delta_0$ has been chosen again as the scaling length. Equating the conductive and evaporative heat fluxes from Eqs. (12) and (17) respectively, the dimensionless interface temperature is determined as

$$T_i^* = \frac{1 + \Pi_2 \delta^* K^* + \frac{\Pi_3}{\delta^{*2}}}{1 + \Pi_1 \delta^* + \Pi_2 \delta^* K^* S_a} \equiv \frac{A_k}{B_k} \tag{20}$$

From Eq. (20), the interface temperature gradient in the $r$ direction is expressed as

$$\frac{dT_i^*}{dr^*} = \frac{A_k' B_k - A_k B_k'}{B_k^2} \tag{21}$$

Various parameters in Eq. (21) are defined as

$$A_k' = \Pi_2 \delta^{*\prime} K^* + \Pi_2 \delta^* K^{*\prime} - 2\Pi_3 \frac{\delta^{*\prime}}{\delta^{*3}}$$

$$B_k' = \Pi_1 \delta^{*\prime} + \Pi_2 \delta^{*\prime} K^* S_a + \Pi_2 \delta^* K^{*\prime} S_a$$

$$K^{*\prime} = -\left[ \frac{1}{(r_0^* + r^*)^2} + \frac{3\delta^{*\prime\prime 2} \delta^{*\prime}}{(1 + \delta^{*\prime 2})^{5/2}} - \frac{\delta^{*\prime\prime\prime}}{(1 + \delta^{*\prime 2})^{3/2}} \right] \tag{22}$$

The system pressure, $p_{le}$, is used to nondimensionalize the pressure. The liquid pressure gradient can be expressed from Eq. (8) as

$$\frac{dp_l^*}{dr^*} = -\Pi_4 \frac{d\sigma^*}{dr^*} K^* - \Pi_4 \sigma^* K^{*\prime} + \Pi_5 q_e^* \frac{dq_e^*}{dr^*} + 3\Pi_6 \frac{\delta^{*\prime}}{\delta^{*4}} + \Pi_7 \delta^{*\prime} \tag{23}$$

where four additional dimensionless groups in Eq. (23) are defined as

$$\Pi_4 = \frac{\sigma_{sat}}{p_{le} \delta_0}$$

$$\Pi_5 = \frac{q_0^2}{p_{le} \rho_v h_{fg}^2}$$

$$\Pi_6 = \frac{A}{p_{le} \delta_0^3}$$

$$\Pi_7 = \frac{\delta_0 (\rho_l - \rho_v) g}{p_{le}} \tag{24}$$

By neglecting the inertia terms, the momentum equation for liquid flow in the liquid layer is written as



Downloaded 12 Dec 2010 to 193.140.21.150. Redistribution subject to ASME license or copyright; see http://www.asme.org/terms/Terms_Use.cfm

$$\mu_l \frac{d^2 u_l}{dz^2} = \frac{dp_l}{dr} \tag{25}$$

Liquid velocity in the radial direction, $u_l$, is obtained by integrating Eq. (25) subject to the following boundary conditions:

$$z = 0, \quad u_l = 0$$

$$z = \delta, \quad \frac{du_l}{dz} = 0 \tag{26}$$

Here, a dynamic boundary condition is used at $z = \delta$ under the assumption that vapor drag will be very small. As such, an expression for liquid velocity is obtained as

$$u = -\frac{1}{\mu_l}\left(\frac{dp_l}{dr}\right)\cdot\left(\delta z - \frac{z^2}{2}\right) \tag{27}$$

Thus, the local average velocity for flow in the liquid layer is written as

$$\bar{u} = \frac{1}{\delta}\int_0^\delta u dz = -\frac{1}{3\mu_l}\left(\frac{dp_l}{dr}\right)\delta^2 \tag{28}$$

In dimensionless form, $\bar{u}^*$ can be expressed as

$$\bar{u}^* = \frac{\bar{u}}{\dfrac{\delta_0 p_{le}}{3\mu_l}} = -\delta^{*2}\left(\frac{dp_l^*}{dr^*}\right) \tag{29}$$

Using Eq. (23) for $dp_l^*/dr^*$ in Eq. (29), an expression for $\bar{u}^*$ can be written as

$$\bar{u}_l^* = \Pi_4\delta^{*2}\frac{d\sigma^*}{dr^*}K^* + \Pi_4\delta^{*2}\sigma^*K^{*\prime} - \Pi_5\delta^{*2}q_e^*\frac{dq_e^*}{dr^*} - 3\Pi_6\frac{\delta^{*\prime}}{\delta^{*2}} - \Pi_7\delta^{*2}\delta^{*\prime} \tag{30}$$

Flow of liquid in the film is in the negative $r$ direction. The first term in Eq. (30) accounts for the surface tension variation ($d\sigma^*/dT_i^*$) in the radial direction. Because the change in surface tension with temperature is negative, this term is positive and creates an adverse pressure gradient on the liquid flow.

Since evaporation occurs along the liquid–vapor interface, a mass and energy balance for the liquid layer results as

$$\rho_l h_{fg}\frac{d}{dr}(2\pi r_1 \bar{u}_l \delta) = -2\pi r_1 q_c \tag{31}$$

In dimensionless form, Eq. (31) can be written as

$$\frac{d}{dr^*}(r_1^*\bar{u}_l^*\delta^*) = -\Pi_8 r_1^* q_c^* \tag{32}$$

where another dimensionless group, $\Pi_8$, is defined as

$$\Pi_8 = \frac{3\mu_l q_0}{\rho_l h_{fg}\delta_0 p_{le}} \tag{33}$$

Combining Eqs. (20), (30), and (32), a fourth-order nonlinear ordinary differential equation is obtained for the liquid layer thickness, $\delta^*$. The final equation in dimensionless form is expressed as

$$\delta^{*\prime\prime\prime\prime} = \frac{1}{C_1 + C_2 + C_3}\cdot\sum_{i=4}^{16} C_i \tag{34}$$

Various parameters in Eq. (34) are complicated functions of the dimensionless groups, $\Pi_4$, $\Pi_5$, $\Pi_6$, and $\Pi_7$, and are given in the appendix.

## Results and Discussion

With the assumption that the vapor stem contacts the solid at a distance $r_0^*$ from the cavity center, the four boundary conditions that can be specified at $r^* = 0$ (see Fig. 2) are

$$\delta^* = 1$$

$$\delta^{*\prime} = 0$$

$$\delta^{*\prime\prime} = \delta_0^{*\prime\prime}$$

$$\delta^{*\prime\prime\prime} = 0 \tag{35}$$

The thickness $\delta_0$ at a distance $r_0$ from the cavity center (or at $r = 0$ in Fig. 2) is the interline thickness and represents the junction between the nonevaporating and the evaporating film. As discussed by Wayner et al. (1976) and Wayner (1992), if the film is sufficiently thin, it is kept from evaporating by van der Waals forces (because adhesion is stronger than cohesion). At the interline the thermal conductive resistance across the film is very small and the temperature drop across the film can be neglected. Now the interfacial superheat is approximately equal to the wall superheat. In an ideal case the thickness, $\delta_0$, is generally of the order of $10^{-9}$ m. However, the surface roughness can alter the value of $\delta_0$. In the present study saturated water at one atmosphere pressure is assumed to be the test liquid and a value of $2 \times 10^{-9}$ m is assigned to $\delta_0$. For a wall superheat of 10 K, the value of $\delta_0$ was varied from $9 \times 10^{-10}$ to $10^{-8}$ m and was found to have little effect on the maximum vapor stem size. The second and fourth boundary conditions correspond to a flat film at $r^* = 0$. Since $\delta_0^{*\prime\prime}$ and $r_0^*$ still need to be specified the problem is ill posed. A relation between $\delta_0^{*\prime\prime}$ and $r_0^*$ is obtained by requiring that at the outer edge of the stem where the interface nearly becomes normal to the surface, the flow into the liquid layer be sustained by the difference between the pressure gradients due to the change in the cylindrical radius, $r_1$, of the stem and that due to the vapor recoil effect. Still one more relation is needed. In the present work $\delta_0^{*\prime\prime}$ was parametrically varied to obtain a range of possible solutions or stem sizes. The fourth-order differential equation governing the film thickness under the stem was integrated by using an adaptive step size control fourth-order Runge–Kutta method.

Figure 3 shows the variation of radii of curvature $R_1$ ($=r_0 + \bar{r}$) and $R_2$ with $\delta_0''$ for a wall superheat of 10 K. The end points of the curves represent the range of values of $\delta_0''$ for which solutions of Eq. (34) are possible. These points also correspond to the maximum and minimum vapor stem radii for which steady-

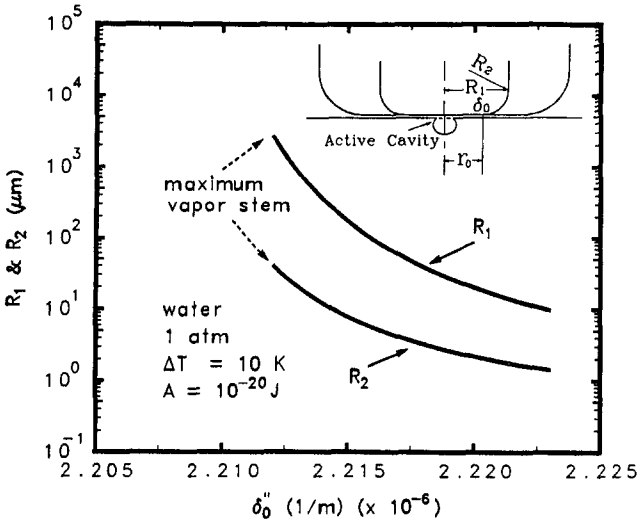



**Fig. 3 Solution domain as a function of radii and $\delta_0''$**



Downloaded 12 Dec 2010 to 193.140.21.150. Redistribution subject to ASME license or copyright; see http://www.asme.org/terms/Terms_Use.cfm

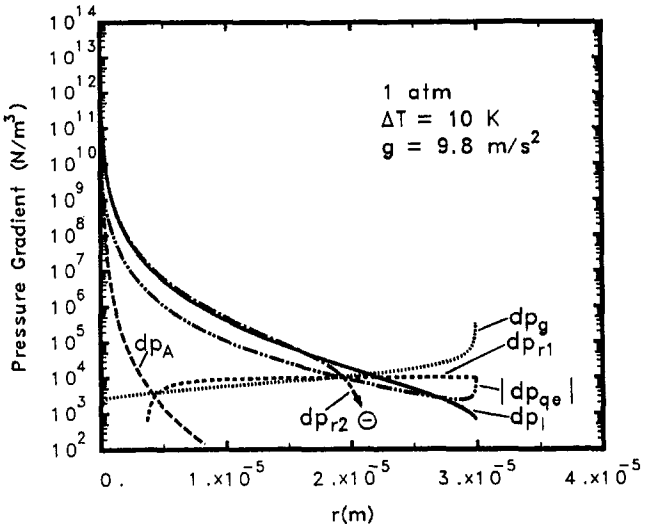



Fig. 4(*a*) Pressure gradient contribution

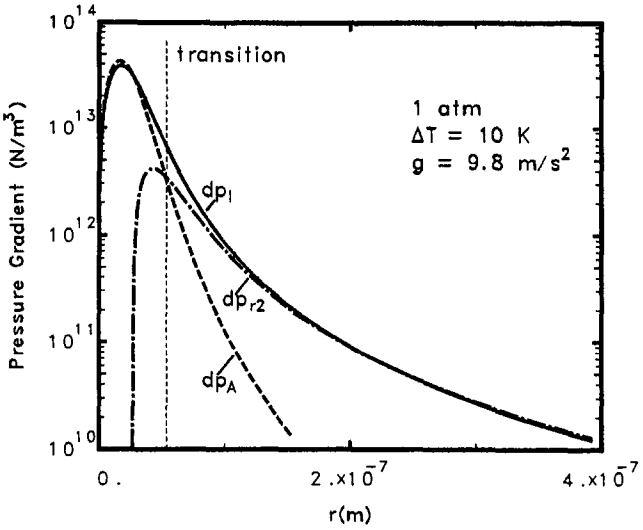



Fig. 4(*b*) Pressure gradient contribution (ultrathin film region)

state flow rates of liquid in the film can be sustained to match the evaporation rate. It is seen that both radii of curvature decrease with increase in $\delta_0''$. The maximum possible stem diameter is found to be about 200 times the minimum stem diameter. Any metastable stem diameter between the maximum and minimum is possible. Since a vapor stem is considered to initiate at a cavity as a bubble embryo and initial growth of the bubble embryo will be transient, it is envisioned that a static configuration of the stem will be achieved only after it attains its maximum diameter.

Figure 4($a$) shows the variation of pressure gradients resulting from various forces acting on the liquid film. The pressure gradient, $dp_{r_1}$, due to variation in the radius, $r_1$, of the stem changes slowly until the location where $\delta \to \delta_0$. Over most of the spreading distance, this pressure gradient supports the flow. The pressure gradient resulting from change in the radius of curvature, $r_2$, plays a dominant role and is in the direction of flow over most of the spreading portion of the stem. However, near the location where the interface starts to move away from the heater surface, the pressure gradient becomes negative and opposes the flow. The pressure gradient due to vapor recoil opposes the flow. The absolute value of the pressure gradient due to vapor recoil increases as film thickness decreases, except near the outer edge of the stem, where film thickness increases very rapidly. In the latter region lubrication theory starts to become invalid as two-dimensional effects become important. The gradient due to hydrostatic head continuously decreases as the liquid film becomes thinner. The disjoining pressure gradient becomes important only when the liquid film becomes very thin. The pressure gradients near the interline are shown in Fig. 4($b$). The transition from the dominance of capillary to disjoining pressure occurs at a distance of $5.4 \times 10^{-8}$ m from the interline. The magnitude of the total pressure gradient near the interline is several orders of magnitude greater than that near the outer edge of the stem.

To determine the effect of the absence of gravity on the pressure gradients and in turn on the vapor stem shape, calculations were performed by setting $g = 0$. Figure 5 shows the calculated pressure gradients for a wall superheat of 10 K with $g = 0$. A comparison of these pressure gradients with those plotted in Fig. 4 shows that all the pressure gradients except that due to change in radius of curvature, $r_2$, are essentially the same. The effect of absence of gravity is merely to extend the location at which the pressure gradient due to change in radius of curvature, $r_2$, becomes negative. The maximum value of the magnitude of the negative pressure gradient is also reduced. In the presence of gravity the magnitude of the negative pressure gradient is larger and it simply opposes the pressure gradient due to gravity. As such the effect of gravity on the total pressure gradient driving the flow of liquid in the film is negligible and the stems shape for the cases with and without gravity overlap.

Figure 6 shows the shapes of the vapor stems when the value of Hamaker constant, $A$, is parametrically changed while the wall superheat is fixed at 10 K. The value of the Hamaker constant changes from a negative value to a positive value as the surface changes from being partially wetted to completely wetted. At present, no quantitative basis exists for relating the contact angle with the magnitude of the Hamaker constant, although an attempt in this direction has been recently made by Wayner (1993). A key difficulty arises in making a distinction between micro and macro contact angles. The inset in Fig. 6 shows the enlarged shape of the interface near the location where the vapor stem contacts the surface. A small difference between the interface shape and the maximum stem diameter is observed for $A = 10^{-20}$ J and $A = 0$. With a decrease in the value of $A$, the stem radius and the spreading distance decrease. This in turn is manifested in a very rapid increase of the film thickness. Qualitatively, the interface shapes suggest an increase in contact angle as the magnitude of negative values of $A$ increases.

Table 1 lists for several wall superheats the spreading distance and the maximum stem diameter along with radius, $r_0$, and $\delta_0''$.

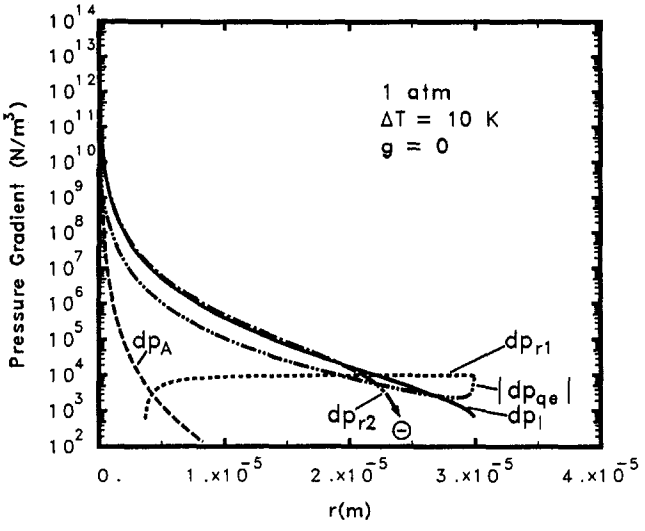



Fig. 5 Pressure gradient contribution (without gravity)



Downloaded 12 Dec 2010 to 193.140.21.150. Redistribution subject to ASME license or copyright; see http://www.asme.org/terms/Terms_Use.cfm

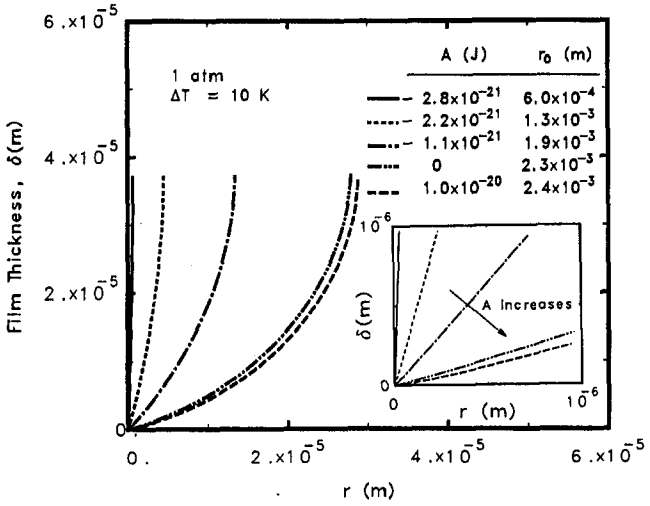



**Fig. 6 Effect of the magnitude of *A* on the shape of the maximum vapor stem**

The maximum stem diameter, $d_w$, and the spreading distance, $\bar{r}$, are seen to decrease with increase in wall superheat. It is physically realistic since with an increase in wall superheat the evaporation rate increases and the capillary forces can only maintain the required flow rate over a shorter distance.

Maximum vapor stem diameters predicted from the model for system pressure of one atmosphere are plotted in Fig. 7 as a function of wall superheat. In Fig. 7 the diameter of the stems deduced by Wang and Dhir (1993a, b) and Dhir and Liaw (1989) from their measurements of the void fraction and Gaertner and Westwater's (1960) data from their photographic study of boiling on a horizontal surface are also plotted. Dhir and Liaw (1989) used a correlation in the void fraction relationship for nucleation site density while Wang and Dhir (1993a, b) obtained the nucleation site density by exercising the model they developed. The contact angles shown in Fig. 7 are the macro contact angles. According to the present model, the stem diameter varies with wall superheat as approximately $\Delta T^{-1.7}$. It is interesting to note that functional dependence of the stem diameter on wall superheat and the magnitude of the stem diameter predicted from the present model compare quite favorably with the stem diameters deduced by Dhir and Liaw (1989) and Wang and Dhir (1993a, b). The deduction of Wang and Dhir (1993a, b) shows a slightly stronger dependence of stem diameter on wall superheat. Since in these two studies nucleation site density was used to determine the stem diameter, any uncertainty in the nucleation site density is reflected in the stem diameter. In Gaertner and Westwater's (1960) experiments, nickel salts were dissolved in water and boiling was observed on a 5-cm-dia horizontal copper surface. A value of contact angle was not given, but it is expected that the contact angle in their experiments was relatively small. The predictions from the vapor stem model compare favorably with the data except the two data points at wall superheat of about 30 K. It was pointed out by Dhir and Liaw (1989) that something is amiss in Gaertner and Westwater's data points at high wall superheats since the data show a reduction in wall void fraction with increase in wall superheat and heat flux. This is contrary to the trend reported in the literature by several other investigators. Nevertheless considering that no empirical adjustments have been made, the comparison between data and prediction is considered to be adequate.

In Fig. 7 the horizontal lines show the range of bubble diameters at departure reported by Gaertner and Westwater (1960). For superheats greater than about 12 K, the lower value of bubble diameter at departure is greater than the stem diameters, indicating that vapor stems can attain their predicted maximum diameters and can stay attached to the wall. For superheats less than about 12 K, the bubbles supported by the stems will detach before the stems can attain their maximum possible diameters. It is interesting to note that transition from partial to fully developed nucleate boiling was also observed to occur around 12–15 K superheat.

**Table 1 Maximum possible stem diameter corresponding to different wall superheats; 1 atm, $A = 10^{-20}$ J**

| $\Delta T$, K | $\delta_0''$, m$^{-1}$ | $r_0$, m | $\bar{r}$, m | $d_w$ (=$2R_1$), m |
|---|---|---|---|---|
| 10 | $2.21 \times 10^6$ | $2.40 \times 10^{-3}$ | $2.99 \times 10^{-5}$ | $4.86 \times 10^{-3}$ |
| 15 | $3.42 \times 10^6$ | $1.11 \times 10^{-3}$ | $2.45 \times 10^{-5}$ | $2.28 \times 10^{-3}$ |
| 20 | $4.61 \times 10^6$ | $7.20 \times 10^{-4}$ | $2.19 \times 10^{-5}$ | $1.48 \times 10^{-3}$ |
| 25 | $5.76 \times 10^6$ | $4.80 \times 10^{-4}$ | $1.96 \times 10^{-5}$ | $9.99 \times 10^{-4}$ |

Liquid velocity profiles showed the velocity to be very small at the outer edge of the vapor stem where the flow area is very large. The velocity increases as the film thickness decreases and reaches a maximum value near the location where transition from the dominance of capillary pressure to disjoining pressure occurs. Thereafter the velocity decreases again while the film thickness continues to decrease. The reduction is caused by increase in the interface temperature, which in turn reduces the conductive and evaporative heat fluxes. Eventually the liquid velocity approaches zero as interface superheat equals the wall superheat and evaporation ceases.

The variations of evaporative heat flux at the interface are plotted in Fig. 8. The heat flux increases with decrease in film thickness and attains a maximum value near the transition location. The evaporative heat flux is found to increase in proportion to the wall superheat. The maximum heat flux at a wall superheat of 20 K is found to be about 15 kW/cm$^2$. It should be noted that interfacial vapor velocity corresponding to this heat flux is less than the sonic velocity, indicating that local maximum heat flux can be increased further by increasing the wall superheat.

## Conclusions

1 A model for vapor stems formed during saturated nucleate boiling has been developed.
2 The model predicted shape of the vapor stem looks like a cup with a flat bottom. For a given wall superheat several metastable states of the vapor stem between a minimum and maximum diameter are possible.
3 The shape of the vapor stem is found to be independent of gravity.

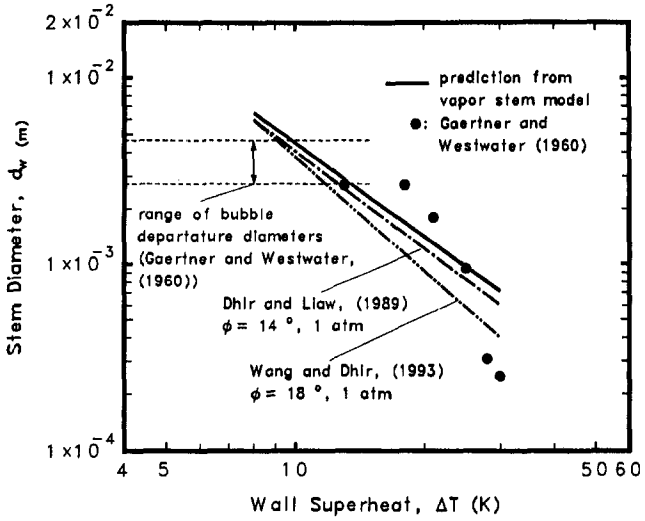



**Fig. 7 Variation of stem diameter with wall superheat**



Downloaded 12 Dec 2010 to 193.140.21.150. Redistribution subject to ASME license or copyright; see http://www.asme.org/terms/Terms_Use.cfm

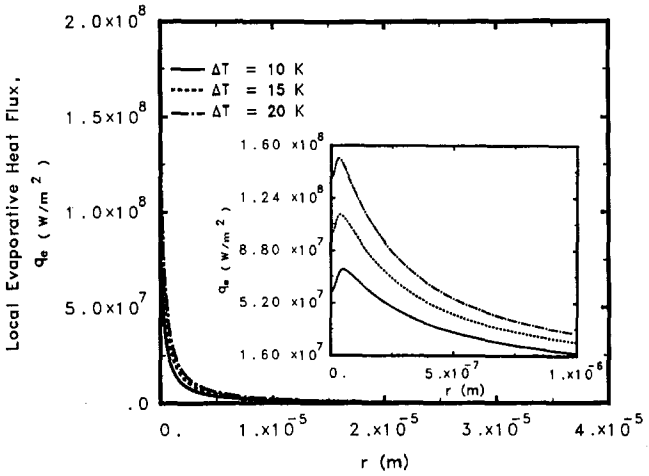



**Fig. 8 Variation of local evaporative heat flux with radial position for different wall superheats**

4 From the model vapor stem size is found to decrease with wall superheat. The predicted reduction in stem diameter with wall superheat is consistent with the observations reported in the literature.
5 The results suggest that a stable vapor stem with very high evaporative heat fluxes is possible.

## Acknowledgments

The authors would like to acknowledge the support from NASA through Flight System Laboratory at UCLA.

## References

Bhat, A. M., Prakash, R., and Saini, J. S., 1983a, "On the Mechanism of Macrolayer Formation in Nucleate Pool Boiling at High Heat Flux," *Int. J. Heat Mass Transfer,* Vol. 26, pp. 735–740.

Bhat, A. M., Prakash, R., and Saini, J. S., 1983b, "Heat Transfer in Nucleate Pool Boiling at High Heat Flux," *Int. J. Heat Mass Transfer,* Vol. 26, pp. 833–840.

Derjaguin, B. V., and Zorin, Z. M., 1957, "Optical Study of the Absorption and Surface Condensation of Vapors in the Vicinity of Saturation on a Smooth Surface," *Proc. 2nd International Congress on Surface Activity (London),* Vol. 2, pp. 145–152.

Dhir, V. K., and Liaw, S. P., 1989, "Framework for a Unified Model for Nucleate and Transition Pool Boiling," ASME JOURNAL OF HEAT TRANSFER, Vol. 111, pp. 739–746.

Gaertner, R. F., 1965, "Photographic Study of Nucleate Pool Boiling on a Horizontal Surface," ASME JOURNAL OF HEAT TRANSFER, Vol. 87, pp. 17–29.

Gaertner, R. F., and Westwater, J. W., 1960, "Population of Active Sites in Nucleate Boiling Heat Transfer," *Chem. Eng. Progr. Symposium Ser.,* Vol. 56, pp. 39–48.

Guggenheim, E. A., 1977, *Thermodynamics,* 6th ed., North Holland Publ. Co., New York, p. 164.

Hickman, K. C. D., 1954, "Maximum Evaporation Coefficient of Water," *Ind. Eng. Chem.,* Vol. 46, No. 7, pp. 1442–1446.

Hsu, Y. Y., and Graham, R. W., 1976, *Transport Processes in Boiling Two-Phase Systems,* McGraw-Hill, New York.

Iida, Y., and Kobayasi, K., 1969, "Distribution of Void Fraction Above a Horizontal Heating Surface in Pool Boiling," *Bulletin of JSME,* Vol. 12, pp. 283–290.

Lay, J. H., 1994, "Experimental Study in Enhanced Design of Boiling Surface Used in Jet Impingement Cooling and a Complementary Theoretical Analysis for Fully Developed Nucleate Boiling," Ph.D. dissertation, University of California, Los Angeles, CA.

Mirzamoghadam, A., and Catton, I., 1988, "A Physical Model of the Evaporating Meniscus," ASME JOURNAL OF HEAT TRANSFER, Vol. 110, pp. 201–207.

Potash, M., Jr., and Wayner, P. C., Jr., 1972, "Evaporation From a Two-Dimensional Extended Meniscus," *Int. J. Heat Mass Transfer,* Vol. 15, pp. 1851–1863.

Schonberg, J. A., DasGupta, S., and Wayner, P. C., 1993, "An Augmented Young–Laplace Model of an Evaporating Meniscus in a Micro-channel With High Heat Flux," *Aerospace Heat Exchanger Technology 1993,* R. K. Shah and A. Hashemi, eds., Elsevier Science Publishers B. V., pp. 239–254.

Sheludko, A., 1966, *Colloid Chemistry,* Elsevier Pub. Co., New York.

Wang, C. H., and Dhir, V. K., 1993a, "Effect of Surface Wettability on Active Nucleation Site Density During Pool Boiling of Water on a Vertical Surface," ASME JOURNAL OF HEAT TRANSFER, Vol. 115, pp. 659–669.

Wang, C. H., and Dhir, V. K., 1993b, "On the Gas Entrapment and Nucleation Site Density During Pool Boiling of Saturated Water," ASME JOURNAL OF HEAT TRANSFER, Vol. 115, pp. 670–679.

Wayner, P. C., Jr., Kao, Y. K., and LaCroix, L. V., 1976, "The Interline Heat Transfer Coefficient of an Evaporating Wetting Film," *Int. J. Heat Mass Transfer,* Vol. 19, pp. 487–492.

Wayner, P. C., Jr., 1992, "Evaporation and Stress in the Contact Line Region," *Engineering Foundation Conference on Pool and External Flow Boiling,* Santa Barbara, CA.

Wayner, P. C., Jr., 1993, "Thermal Effects in the Spreading of a Liquid Film Due to a Change in the Apparent Finite Contact Angle," *The 29th National Heat Transfer Conference,* Atlanta, GA.

## APPENDIX

The dimensionless parameters ($\{C_i\}$) generated during the formation of the Eq. (34) are:

$$C_1 = -\Pi_4 S_a K^* Ca_k \quad C_2 = \Pi_4 \sigma^* R_k$$

$$C_3 = -\Pi_5 q_c^* P_k \quad C_4 = -2\Pi_4 \delta^{*2}\delta^{*\prime}\frac{d\sigma^*}{dr^*}K^*$$

$$C_5 = \Pi_4 \delta^{*3} S_a K^* Cb_k \quad C_6 = -\Pi_4 \delta^{*3}\frac{d\sigma^*}{dr^*}K^{*\prime}$$

$$C_7 = -2\Pi_4 \delta^{*2}\delta^{*\prime}\sigma^* K^{*\prime} \quad C_8 = \Pi_4 \delta^{*3}\frac{d\sigma^*}{dr^*}K^{*\prime}$$

$$C_9 = -\Pi_4 \delta^{*3}\sigma^* K_1^{*\prime\prime} \quad C_{10} = 2\Pi_5 \delta^{*2}\delta^{*\prime} q_c^*\frac{dq_c^*}{dr^*}$$

$$C_{11} = \Pi_5 \delta^{*3}\left(\frac{dq_c^*}{dr^*}\right)^2 \quad C_{12} = \Pi_5 \delta^{*3} q_c^* Q_k$$

$$C_{13} = \Pi_7(2\delta^{*2}\delta^{*\prime 2} + \delta^{*3}\delta^{*\prime\prime}) \quad C_{14} = 3\Pi_6\frac{\delta^{*\prime\prime}\delta^* - 2\delta^{*\prime 2}}{\delta^{*2}}$$

$$C_{15} = -\bar{u}_l^*\left(\delta^{*\prime} + \frac{\delta^*}{r_1^*}\right) \quad C_{16} = -\Pi_8 q_c^*$$

and

$$Ca_k = \frac{G_k}{D_K} \quad Cb_k = \frac{H_k D_k - C_k D_K'}{D_K^2}$$

$$D_k = B_k^2 \quad D_k' = 2B_k B_k' \quad E_k = -\frac{dT_i^*}{dr^*}\delta^* - (1 - T_i^*)\delta^{*\prime}$$

$$F_k = \delta^{*2} \quad F_K' = 2\delta^*\delta^{*\prime}$$

$$G_k = \Pi_2 \delta^* \cdot \frac{B_k - S_a A_k}{(1 + \delta^{*\prime 2})^{3/2}}$$

$$H_k = K_1^{*\prime\prime}\Pi_2\delta^*(B_k - S_a A_k) + T_k B_k - A_k S_k \quad P_k = -\delta^*\frac{Ca_k}{F_k}$$

$$Q_k = -\frac{[Cb_k\delta^* + (1 - T_i^*)\delta^{*\prime\prime}]F_k + E_k F_k'}{F_k^2}$$

$$R_k = \frac{1}{(1 + \delta^{*\prime 2})^{3/2}} \quad S_k = \Pi_1\delta^{*\prime\prime} + \Pi_2 S_a(\delta^{*\prime\prime}K^* + 2\delta^{*\prime}K^{*\prime})$$

$$T_k = \Pi_2\delta^{*\prime\prime}K^* + 2\Pi_2\delta^{*\prime}K^{*\prime} - 2\Pi_3\frac{\delta^{*\prime\prime}\delta^* - 3\delta^{*\prime 2}}{\delta^{*4}}$$

$$\frac{d\sigma^*}{dr^*} = -S_a\frac{dT_i^*}{dr^*} \quad \frac{dq_c^*}{dr^*} = \frac{E_k}{F_k}$$

$$K_1^{*\prime\prime} = -\left[-\frac{2}{(r_0^* + r^*)^3} + \frac{(1 + \delta^{*\prime 2})(6\delta^{*\prime}\delta^{*\prime\prime}\delta^{*\prime\prime\prime} + 3\delta^{*\prime\prime 3}) - 15\delta^{*\prime 2}\delta^{*\prime\prime 3}}{(1 + \delta^{*\prime 2})^{7/2}} + \frac{3\delta^{*\prime}\delta^{*\prime\prime}\delta^{*\prime\prime\prime}}{(1 + \delta^{*\prime 2})^{5/2}}\right] \quad (36)$$



Downloaded 12 Dec 2010 to 193.140.21.150. Redistribution subject to ASME license or copyright; see http://www.asme.org/terms/Terms_Use.cfm

# Interfacial Heat Transfer Between Steam Bubbles and Subcooled Water in Vertical Upward Flow

**O. Zeitoun**
Graduate Student.

**M. Shoukri**
Professor.
Mem. ASME

Mechanical Engineering Department,
McMaster University,
Hamilton, Ontario, Canada, L8S 4L7

**V. Chatoorgoon**
Atomic Energy of Canada Ltd
Chalk River Nuclear Laboratories
Chalk River, Ontario, Canada, K0J 1J0

*In two-fluid modeling, accurate prediction of the interfacial transport of mass, momentum, and energy is required. Experiments were carried out to obtain a data base for the development of interfacial transport models, or correlations, for subcooled water–steam bubbly flow in vertical conduits. The experimental data of interest included the interfacial area concentration, interfacial condensation heat transfer, and bubble relative velocity. In the present investigation, bubble condensation in subcooled water–steam flow in a vertical annulus at low flow rate and low pressure is investigated experimentally. A high-speed video system (up to 1000 frame/s) was used to visualize two orthogonal views of the flow simultaneously. A digital image processing technique was used to track and measure the velocity and size of the collapsing bubbles. The axial void fraction distribution was also measured by a single beam gamma densitometer. The results were compared with existing correlations and a new correlation for bubble condensation Nusselt number was obtained based on the present data. In the proposed correlation, the bubble condensation Nusselt number is expressed in terms of the bubble Reynolds number, Jakob number, and void fraction. The latter term accounts for the multi-bubble effect. This correlation can predict the present data within ±20 percent with a correlation coefficient of 96 percent.*

## 1 Introduction

Vapor bubble condensation is an important physical phenomenon encountered in liquid–vapor two-phase flow when the liquid temperature is below saturation, i.e., subcooled liquid. The rate of vapor bubble condensation plays a major role in the stability of flows in which subcooled boiling and/or condensation occur. Among the various mathematical formulations of two-phase flow, the two-fluid model is considered the most accurate formulation. In this formulation, the two phases are described separately in terms of averaged phasic mass, momentum, and energy equations. Moreover, the interactions between the two phases are modeled by interfacial transfer terms to account for interfacial mass, momentum, and energy transport. A relationship for the interfacial heat transfer coefficient during condensation is needed as one of the constitutive equations required for closure. The present study was conducted to obtain experimental data on bubble condensation in a typical subcooled water–steam bubbly flow for comparison with existing correlations and models, which were developed based on data obtained for single bubbles.

## 2 Literature Review

Bubble collapse during condensation can be either inertia or heat transfer controlled. For high liquid subcooling, bubbles rapidly collapse, satisfying the so-called Rayleigh solution (1917) for the collapse of a spherical cavity in an infinite liquid in which the process is controlled by the inertia of the surrounding liquid. On the other hand, if the subcooling is relatively low, the bubble collapse period will be longer and the process will be controlled by the heat transfer at the interface. Chen and Mayinger (1992) showed that for a single bubble, the condensation is completely controlled by interfacial heat transfer for Jakob numbers Ja < 80, while for Ja > 100 the process is completely inertia controlled. The present work focuses on the heat transfer controlled bubble condensation in a typical liquid–vapor bubbly flow.

Most of the available studies on heat transfer controlled bubble condensation have been conducted for simple cases such as heat diffusion from a stagnant bubble and convection around a single bubble moving in an irrotational flow field. These studies were typically carried out to obtain the bubble history during condensation, from which the instantaneous interfacial condensation coefficient can be estimated using the simple energy balance,

$$h_c = \frac{\rho_g h_{fg}(-dv_b/d\tau)}{a_b(T_s - T_f)} \tag{1}$$

For a spherical bubble, the interfacial condensation coefficient is:

$$h_c = \frac{\rho_g h_{fg}}{2(T_s - T_f)}(-dD_b/d\tau) \tag{2}$$

Available models and correlations for bubble history and instantaneous condensation Nusselt number are listed in Table 1.

The condensation of stagnant bubbles was investigated experimentally and theoretically by a number of investigators: Zuber (1961), Florschuetz and Chao (1965) and Theofanous et al. (1970). The analysis of Zuber (1961) was based on the similarity between the well-known transient conduction with a moving boundary and heat transfer at a bubble surface. Florschuetz and Chao (1965) included the convection effect due to interfacial movement. Theofanous et al. (1970) pursued a two-fluid formulation but did not include the phasic momentum equations in the analysis, although thermal nonequilibrium at the interface was considered. Okhotsimskii (1988) investigated the effect of Jakob number on bubble collapse. Although his analysis covered the range of high Jakob number, where inertia effects are significant, the liquid momentum was ignored.

Many theoretical investigations have been carried out to study the condensation of moving bubbles in a stagnant liquid. The energy equations of the two phases were combined with the hy-

* Contributed by the Heat Transfer Division for publication in the JOURNAL OF HEAT TRANSFER. Manuscript received by the Heat Transfer Division December 1993; revision received July 1994. Keywords: Condensation, Multiphase Flows, Nonequilibrium Flows. Associate Technical Editor: R. A. Nelson, Jr.



Copyright © 1995 by ASME

Downloaded 12 Dec 2010 to 193.140.21.150. Redistribution subject to ASME license or copyright; see http://www.asme.org/terms/Terms_Use.cfm

drodynamic solution of irrotational flow around a solid sphere to solve for the thermal boundary layer around the condensing bubble. This procedure was followed by Ruckenstein (1959, 1967), Ruckenstein and Constantinescu (1969), and Ruckenstein and Davis (1971) to estimate the interfacial heat transfer coefficient. Using a similar analysis, Wittke and Chao (1967) showed that the rate of condensation increased with increasing bubble velocity and that the effect of bubble motion increased at lower Jakob numbers. Dimić (1977) introduced an analytical solution and investigated the effect of bubble size dependent velocity. Moalem and Sideman (1973) and Akiyama (1973) used standard relationships for modeling the interfacial condensation heat transfer coefficient, to determine the bubble collapse history. Experimental investigations of the condensation of moving bubbles in a stagnant liquid were carried out by Levenspiel (1959), Wittke and Chao (1967), Hewitt and Parker (1968), Isenberg and Sideman (1970), Akiyama (1973), Brucker and Sparrow (1977), Simpson et al. (1986), and Chen and Mayinger (1992). Hewitt and Parker (1968) reported that the model of Florschuetz and Chao (1965) for stagnant bubbles underpredicted their experimentally determined bubble condensation rate.

As shown in Table 1, the various models and correlations appear to disagree on the effect of subcooling, or Jakob number, on the condensation heat transfer coefficient. The models of Levenspiel (1959), Ruckenstein (1959), Akiyama (1973), and Isenberg and Sideman (1970) show that the Nusselt number is independent of subcooling, which is also supported by the high-pressure data of Brucker and Sparrow (1977). The effect of subcooling, however, appears in other correlations either explicitly or implicitly through the bubble history relationship of $\beta$. While the models of Dimić (1977) and Simpson et al. (1986) show that the Nusselt number is increased with increasing liquid subcooling, the model of Chen and Mayinger (1992) shows an opposite trend.

Single bubbles were considered in these investigations. Ruckenstein (1959), however, reported that multibubble effects should be included in the Nusselt number correlations through the effect of void fraction. Among the few investigations involving multiple bubbles are those of Abdelmessih et al. (1977) and Mayinger and Bucher (1977) who experimentally investigated the condensation of bubbles in subcooled flow boiling. The condensation coefficients used in the two-phase numerical codes TRAC-P1A and MINI-TRAC as given by Kelly and Kazimi (1982) and Hori and Toda (1991), respectively, are also listed in Table 1.

Based on this review, a number of difficulties exist in applying some of the existing correlations to predict the interfacial heat transfer in subcooled water–steam bubbly flow. The simple models developed for a single bubble in stagnant liquid are certainly not appropriate. Moreover, it is difficult to apply the Nusselt number correlations that contain the initial bubble diameter $D_0$ or $\beta$. In other correlations, e.g., Chen and Mayinger (1992), the initial bubble diameter was even based on the diameter of the nozzle from which the bubbles were introduced.

## 3 Experimental Arrangements

**3.1 Experimental Facility.** A schematic of the test loop is depicted in Fig. 1. The low-pressure circulating loop consists mainly of a holding tank in which the water temperature is controlled by an immersed electric heater and a cooling coil, a circulating pump, a preheater, and the test section. The test section contains a heated section, where vapor bubbles are formed, followed by an unheated section, where the vapor bubbles are condensed. The water at the test section outlet is pumped back to the holding tank where its temperature is regulated. A detailed description of the facility used in this study was reported in Shoukri et al. (1991) and Zeitoun et al. (1994).

The test section is a vertical concentric annular test section. The inner tube, which has an outer diameter of 12.7 mm, consists of three axial sections. The middle section of the inner tube is a 30.6 cm long, thin-walled stainless-steel tube (0.25 mm thickness) that is electrically heated. This heated section is preceded and followed by two thick-walled copper tubes, 34 and 50 cm long, respectively. The entire inner tube is connected to a 55 kW DC power supply. Accordingly, heat was generated uniformly in the middle section of the inner tube. The outer tube is a 25.4 mm inner diameter plexiglass tube that permits visual observation. The flow that enters the annulus develops through the first unheated section of the annular test section. Voids, which are generated in the heated section, collapse in the downstream unheated section. The present study was carried out in the unheated downstream section to investigate bubble condensation in subcooled water–steam condensing flow under typical bubbly flow conditions. A square cross-sectional plexiglass shield was put around the outer tube and filled with water during photography to reduce light reflection and refraction. Any minor change in the inlet temperature to the condensing region was compensated for by readjusting the preheater.

**3.2 Measurements and Instrumentation.** The measurements carried out during the present experiments include the test section inlet and exit fluid temperatures, subcooling temperature distribution along both the heated and unheated regions, flow

## Nomenclature

$A_b$ = average bubble surface area, m$^2$
$a$ = thermal diffusivity, m$^2$/s
$a_b$ = bubble surface area, m$^2$
$a_i$ = interfacial area concentration, m$^2$/m$^3$
$C_p$ = liquid specific heat, J/kg K
$D_b$ = Sauter bubble diameter, m
$D_0$ = initial bubble diameter, at $\tau$ = 0, m
$D_s$ = mean Sauter bubble diameter = 6 $V_b/A_b$, m
Fo = Fourier number = $aT/D_b^2$
$\text{Fo}_0$ = Fourier number based on initial bubble diameter = $aT/D_0^2$
$G$ = mass flux, kg/m$^2$ s
$g$ = gravitational acceleration, m/s$^2$
$h_c$ = condensation coefficient, W/m$^2$ K
$\bar{h}_c$ = average condensation coefficient at a given axial location, W/m$^2$ K
$h_{fg}$ = latent heat, J/kg
Ja = Jakob number = $\rho_f C_p(T_s - T_f)/\rho_g h_{fg}$
$k$ = liquid thermal conductivity, W/m K
$\text{Nu}_c$ = condensation Nusselt number = $\bar{h}_c D_s/k$
$\text{Pe}_b$ = bubble Peclet number = $\text{Re}_b$ Pr
Pr = liquid Prandtl number
$\text{Re}_b$ = bubble Reynolds number = $\rho_f U_b D_b/\mu$ or $\rho_f U_b D_s/\mu$
$\text{Re}_{b0}$ = Reynolds number based on the initial bubble diameter = $\rho_f U_b D_0/\mu$
$T_f$ = liquid temperature, K
$T_s$ = saturation temperature, K
$U_b$ = bubble relative velocity, m/s
$U_f$ = liquid velocity, m/s
$V_b$ = average bubble volume, m$^3$
$v_b$ = bubble volume, m$^3$
$\alpha$ = void fraction
$\beta$ = $D_b/D_0$
$\mu$ = liquid viscosity, Pa·s
$\rho_f$ = liquid density, kg/m$^3$
$\rho_g$ = vapor density, kg/m$^3$
$\sigma$ = surface tension, N/m
$\tau$ = time, s
$\tau_m$ = time of maximum bubble size, s

**Subscripts**

$f$ = liquid
$g$ = vapor
$s$ = saturation
0 = initial condition



Downloaded 12 Dec 2010 to 193.140.21.150. Redistribution subject to ASME license or copyright; see http://www.asme.org/terms/Terms_Use.cfm

**Table 1 Bubble condensation models**

| Author | Bubble History | Condensation Nusselt Number |
|---|---|---|
| Zuber (1961) | $\beta = (\tau/\tau_m)^{1/2}\left(2 - (\tau/\tau_m)^{1/2}\right)$ | ------ |
| Florschuetz & Chao (1965) | *a-* $\beta^2 + 2/\beta - 3 = 48/\pi\, Ja^2\, Fo_o$ | $Nu_c = 12/\pi\, Ja\, \beta^3/(1-\beta^3)$ |
| | *b-* $\beta = 1 - (16/\pi\, Ja^2\, Fo_o)^{1/2}$ | $Nu_c = 4/\pi\, Ja\, \beta/(1-\beta)$ |
| Levenspiel (1959) | $\beta = \exp(-3.933\,(T_s - T_p)\,\tau)$ | $Nu_c = 1.966\, D_b^2\, h_{fg}\, \rho_g/k$ |
| Ruckenstein (1959) | ------ | $Nu_c = \sqrt{4/\pi}\,(Re_b\, Pr)^{1/2}$ |
| Hewitt & Parker (1968) | $\beta = 1 - \left(\sqrt{4\pi/3}\, Ja^2\, Fo_o/\beta^2\,(1.3\, D_b/(T_s - T_p))^{3/2}\right)^{1/2}$ | $Nu_c = \dfrac{4\,\pi\,(1.3\, D_b/(T_s - T_p))^{3/2}\,\beta^{1/2}}{(\beta^{1/4} - \beta^{5/4})\,(\beta^{1/4} - 5\,\beta^{5/4})}$ |
| Isenberg & Sideman (1970) | $\beta = \left(1 - 3/\sqrt{\pi}\, Ja\, Re_{bo}^{1/2}\, Pr^{1/3}\, Fo_o\right)^{2/3}$ | $Nu_c = 1/\sqrt{\pi}\, Re_b^{1/2}\, Pr^{1/3}$ |
| Akiyama (1973) | $\beta = \left(1 - 2.8{*}0.37\, Re_{bo}^{0.6}\, Pr^{1/3}\, Ja\, Fo_o\right)^{1/1.4}$ | $Nu_c = 0.37\, Re_b^{0.6}\, Pr^{1/3}$ |
| Dimić (1977) | $\beta = \left(1 - 6/\sqrt{\pi}\, Ja\, Re_{bo}\, Pr\, Fo_o\right)^{2/3}$ | $Nu_c = 2/\sqrt{\pi}\, Re_b\, Pr\, \beta^{-1/2}$ |
| TRAC-PIA as in: Kelly & Kazimi (1982) | ------ | *The maximum of:* $Nu_c = 12/\pi\, Ja$ ; $Nu_c = 2 + 0.74\, Re_b^{1/2}$ |
| Simpson et al. (1986) | $\beta = \left(1 - 4.35\, Ja^{1.1}\, Pe_{bo}^{0.55}\, Fo_o^{1.11}\right)^{2/3}$ | ------ |
| MINI-TRAC as in Hori & Toda (1991) | ------ | $Nu_c = 0.02\, Re_b\, Pr$ |
| Chen & Mayinger (1992) | $\beta = \left(1 - 0.56\, Re_{bo}^{0.7}\, Pr^{0.5}\, Ja\, Fo_o\right)^{0.9}$ | $Nu_c = 0.6\, Re_b^{0.6}\, Pr^{1/2}\, \beta^{0.4}$ *Before detachment*; $Nu_c = 0.185\, Re_b^{0.7}\, Pr^{1/2}\, \beta^{0.3}$ *After detachment* |

rate, pressure at the test section inlet as well as the axial void fraction distribution in the unheated region downstream of the heated section. High-speed photography and digital image processing techniques were used to obtain data on bubble size history in the condensing region. The flow rate was measured using a calibrated rotameter, which had an estimated error of ±2 percent. The test section inlet and exit temperature, as well as the preheater inlet temperature, were measured using calibrated platinum resistance temperature detectors. The subcooling along the test section was measured at 10 cm intervals using *J*-type calibrated thermocouples with an estimated error ±0.2°C.

A single beam gamma densitometer was used for void fraction measurements. It consisted of a 75 mCi Cobalt 57 sealed line source and a cubic NaI (TI) scintillator. The gamma beam from the line source was collimated as a thin beam, which was wide enough to cover the entire cross section for measuring the area-averaged void fraction. The statistical error was reduced to less than 1 percent by counting for a long enough time. The densitometer was statically calibrated using an identical section where the liquid phase was simulated by a lucite plug, while the voids were generated by drilling holes into the plug. The static calibration tests showed that, for the range $0.02 < \alpha < 0.3$, the errors were in the range of ±4 percent of the calibrated range.

A high-speed video system, Kodak Ektapro EM Motion Analyzer was used to visualize the condensing bubbles. Three prism mirrors were used to obtain two orthogonal views simultaneously. The camera, mirrors, and light sources were mounted on the traversing table to enable the flow along the test section to be visualized at the same locations where the void fractions were measured. Digital image processing technology was used to measure bubble size from the two orthogonal images. Measured distances in the field of view were estimated to be accurate within ±0.1 mm. Additional details about the void fraction measurements as well as the photographic and digital image processing systems were reported by Zeitoun et al. (1994).

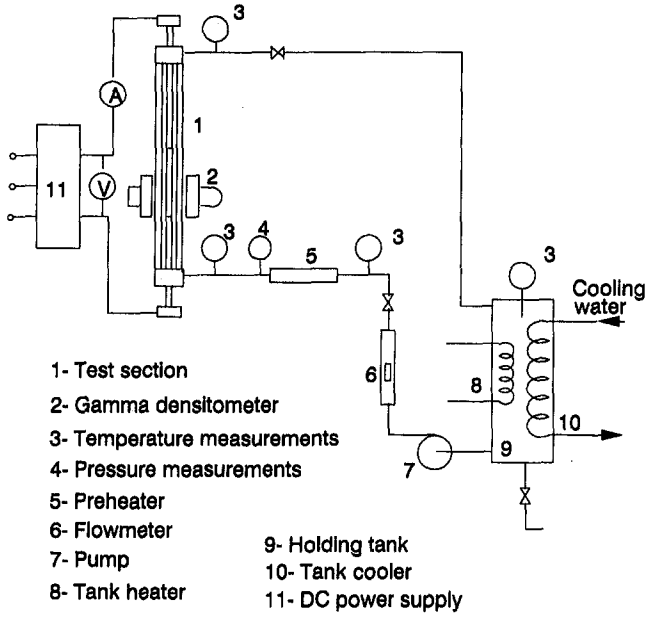



**Fig. 1 Test loop**

## 4 Experimental Results and Data Reduction

Tests were carried out at various levels of mass flow rate, power and subcooling. The test conditions are listed in Table 2.

**Table 2 Test conditions**

| Run No. | Mass flux kg/m² s | Pressure bar | Inlet subcooling °C | Inlet void fraction |
|---|---|---|---|---|
| 1 | 205.5 | 1.096 | 4.8 | 0.3 |
| 2 | 327.4 | 1.35 | 7.5 | 0.3 |
| 3 | 205.5 | 1.096 | 6.3 | 0.25 |
| 4 | 327.4 | 1.28 | 9.8 | 0.18 |
| 5 | 413.9 | 1.618 | 10.7 | 0.32 |
| 6 | 492.39 | 1.7 | 13.4 | 0.28 |
| 7 | 506.24 | 1.8 | 18.8 | 0.38 |
| 8 | 139.03 | 1.03 | 2.6 | 0.28 |



Downloaded 12 Dec 2010 to 193.140.21.150. Redistribution subject to ASME license or copyright; see http://www.asme.org/terms/Terms_Use.cfm

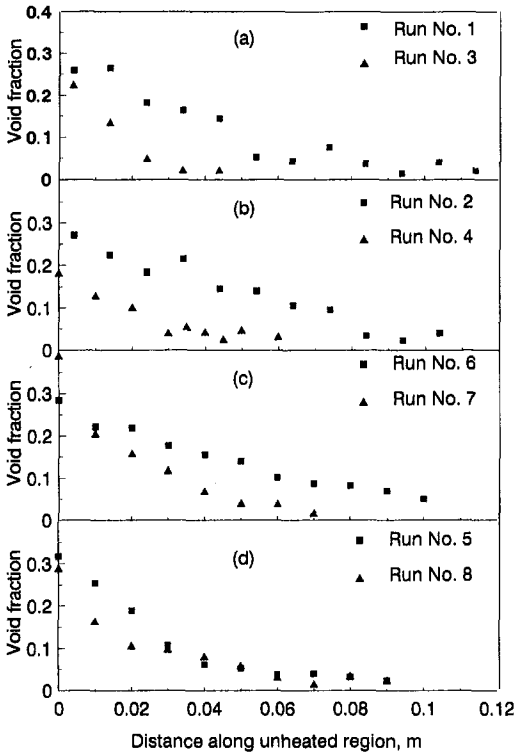



**Fig. 2 Void fraction distribution along condensing flow**

The void fraction measurements and the photography of the flow field were conducted at 1 cm intervals along the condensing region of the test section. The void fraction distributions along the condensing section are shown in Fig. 2. As shown in Figs. 2($a$–$c$), the rate of void collapse increased as the subcooling was increased for a given mass flux.

Using the two orthogonal views of a given bubble, an algorithm was developed for calculating the bubble surface area $a_b$ and volume $v_b$. The method used was described in detail by Zeitoun et al. (1994). The estimated error in measuring the bubble volume and surface area were ±4 and ±3.3 percent, respectively. The interfacial heat transfer rate was estimated by tracking the volume and surface area of individual bubbles through the field of view. For a typical bubble velocity and using a framing speed of 500 frames/s, it was possible to obtain 10–12 measurements of $v_b$ and $a_b$ versus time for each condensing bubble. The interfacial heat transfer coefficient was calculated based on the change of bubble volume between each two consecutive measurements using Eq. (1). The calculated values were averaged to obtain the average heat transfer coefficient $h_c$ for each bubble. The average interfacial heat transfer coefficient at a given axial location $\bar{h}_c$ was obtained by further averaging the calculated values for about 10–20 individual bubbles at that location. Using this procedure, the error in the calculated values of $\bar{h}_c$ was estimated to be less than ±9 percent.

The bubble condensation Nusselt number $\mathrm{Nu}_c$ was calculated using the local mean Sauter bubble diameter $D_s$ at the same location. The mean Sauter bubble diameter was calculated using the local average bubble surface area and volume. The local average bubble volume and surface area were obtained by sampling 200 bubbles at each location. The estimated error in the mean Sauter bubble diameter and bubble condensation Nusselt number were ±5 and ±10.5 percent, respectively.

The data were also used to obtain the relative bubble velocity, which is a parameter required for calculating the bubble Reynolds number. The absolute bubble velocity was determined by measuring the displacement of each bubble during a known time period. The average absolute bubble velocity at each axial location was obtained by averaging the measured individual absolute bubble velocities. The mean bubble relative velocity was calculated from the difference between the mean absolute bubble velocity and the mean liquid velocity at the same axial location. The mean liquid phase velocity was determined by solving the continuity equation using the known flow rate and the measured area-averaged void fraction at the same location. The estimated uncertainties in the liquid phase velocity and bubble relative velocity were in the range of ±2 and ±3.5 percent, respectively.

## 5 Analysis of the Results

**5.1 Interfacial Heat Transfer.** The calculated bubble condensation Nusselt number versus the bubble Reynolds number is shown in Fig. 3. The bubble Reynolds number was calculated using the measured mean bubble relative velocity and mean Sauter bubble diameter; the estimated uncertainty in the bubble Reynolds number was in the range of ±6 percent. The actual measured bubble velocities were used, rather than those predicted by existing correlations, to eliminate unnecessary smoothing of the data. As shown in the figure, the bubble condensation Nusselt number increases as the bubble Reynolds number is increased. Existing correlations in which the Nusselt number, for a given fluid, is a unique function of the bubble Reynolds number are superimposed on the experimental data in Fig. 3. In general, no correlation appears to be in good agreement with the present data. However, the data fall within the ranges predicted by these correlations, except for the MINI-TRAC correlation (Hori and Toda, 1991), which overpredicts the data significantly. As shown, the data are overpredicted by Ruckenstein's correlation and generally underpredicted by the model of Isenberg and Sideman (1970). The Isenberg–Sideman model is basically a modification of the irrotational flow model of Ruckenstein (1959) where a correction factor of $\frac{1}{2}\,\mathrm{Pr}^{-1/6}$ was used to account for viscous effects. It is also shown in Fig. 3 that TRAC-P1A (Kelly and Kazimi, 1982) may be capable of predicting the present data at low bubble Reynolds numbers, while the model of Akiyama (1973) predicts the data well at high bubble Reynolds numbers.

A stepwise regression analysis was used to correlate the present data on bubble condensation Nusselt number in terms of the local values of Jakob number, void fraction, and bubble Reynolds number. The resulting correlation was in the form:

$$\mathrm{Nu}_c = 2.04\,\mathrm{Re}_b^{0.61}\alpha^{0.328}\,\mathrm{Ja}^{-0.308} \qquad (3)$$

which is valid for steam–water flow at near atmospheric pressure and for void fraction up to 30 percent. This correlation predicts the present data within ±20 percent, as shown in Fig. 4, with a correlation coefficient of 96 percent.

It is interesting to note that in this correlation, the power index of the bubble Reynolds number is 0.61, which is in the range of

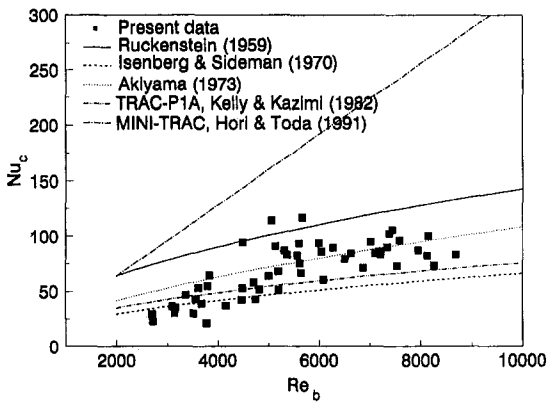



**Fig. 3 Comparison between present data of bubble condensation Nusselt number and existing models**



Downloaded 12 Dec 2010 to 193.140.21.150. Redistribution subject to ASME license or copyright; see http://www.asme.org/terms/Terms_Use.cfm

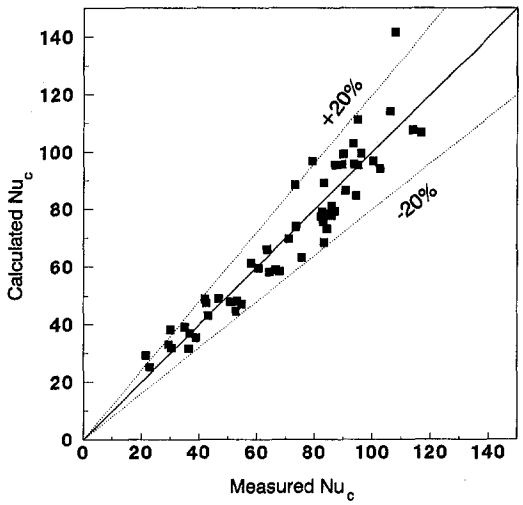



**Fig. 4 Comparison between present data and proposed correlation**

the existing correlations in which it tended to lie within the range of 0.5 to 1.0. The dependence of the Nusselt number on the concentration of the vapour phase $\alpha$ reflects the fluid mixing caused by the multibubble effect as suggested by Ruckenstein (1959). The present correlation also includes the effect of Jakob number, where the Nusselt number increases with decreasing Jakob number. This trend is consistent with the predictions of Chen and Mayinger correlation (1992) as given in Table 1.

By assuming that the mean Sauter bubble diameter represents the instantaneous bubble diameter, the bubble history was obtained by integrating Eq. (2) using Eq. (3),

$$\beta = (1 - 5.67\ \mathrm{Re}_{b0}^{0.61}\alpha^{0.328}\ \mathrm{Ja}^{0.692}\mathrm{Fo}_0)^{0.72} \qquad (4)$$

The predictions of Eq. (4) are compared with those of other correlations for fixed values of $\mathrm{Re}_{b0}$ and $\alpha$ at two values of Jakob number, Ja = 10 and 30. As shown in Fig. 5, the present correlation as well as the models of Akiyama (1973), Simpson et al. (1986), and Chen and Mayinger (1992) predict a much faster rate of condensation than the two models of Florschuetz and Chao (1965), which were based on pure thermal diffusion from single bubbles. This higher condensation rate is attributed to the effect of forced convection (bubble motion). At the beginning of the condensation process, the models of Florschuetz and Chao (1965) for pure thermal diffusion predict higher condensation rate than the others because of the initial condition used to obtain the transient temperature distribution in the thermal boundary layer around the vapor bubble. The interface, initially at saturation, was assumed to suddenly come in contact with the subcooled liquid at $\tau = 0$, i.e., infinite heat transfer rate. Zuber's diffusion model (1961), on the other hand (see Table 1), assumes that the bubble collapse follows a period of bubble growth in a nonuniform temperature field, i.e., $dD_b/d\tau = 0$ at $\tau = 0$, resulting in a zero condensation rate initially. The degree of agreement between Eq. (4) and the rest of the available correlations, on the other hand, is clearly dependent on the values of Jakob number and void fraction. It should be noted, however, that the present correlation is the only one that shows a dependence on void fraction.

**5.2 Bubble Rise Velocity and Diameter.** In recommending Eq. (3) for calculating the interfacial condensation Nusselt number as a function of the bubble Reynolds number $\mathrm{Re}_b$, it is important to recommend appropriate correlations for bubble relative velocity and bubble diameter. The present data for the measured mean relative bubble velocity versus the measured void fraction are shown in Fig. 6 together with predictions of the available correlations. It is shown that, within the range of the present test

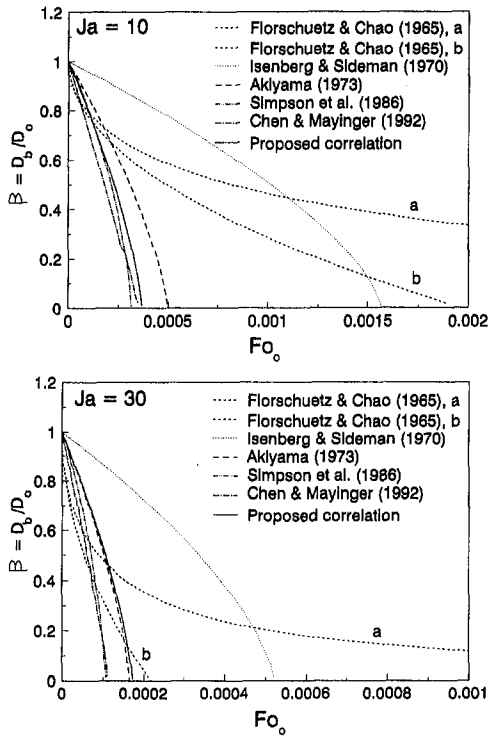



**Fig. 5 Comparison between the present model of bubble history and previous models ($\mathrm{Re}_{b0}$ = 5000, Pr = 1.6, and $\alpha$ = 0.15)**

conditions, the mean bubble relative velocity is in the range of $0.2 < U_b < 0.4$ m/s. The measured mean bubble relative velocity was compared with various bubble rise velocity models. Zuber and Findlay (1965) recommended the following relationship for bubble rise velocity:

$$U_b = \frac{C_z}{1-\alpha}\left(\frac{g\sigma(\rho_f - \rho_g)}{\rho_f^2}\right)^{1/4} \qquad (5)$$

This correlation was found to be generally capable of predicting the present data when the constant $C_z$ is 1.53 as recommended by Zuber and Findlay (1965) for churn-turbulent bubbly flow.

In order to use Eq. (3), the bubble diameter is also required. Using the present experimental arrangement, Zeitoun et al. (1994) carried out extensive measurements to obtain the interfacial area concentration in subcooled liquid–vapor bubbly flow. The range of conditions tested was similar to the conditions covered in the present work. The interfacial area concentration was correlated by Zeitoun et al. (1994) by:

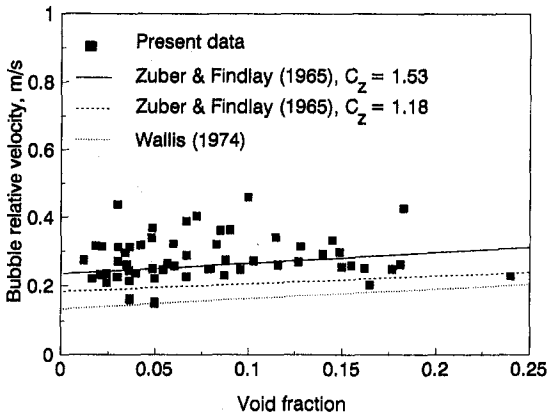



**Fig. 6 Bubble relative velocity**



Downloaded 12 Dec 2010 to 193.140.21.150. Redistribution subject to ASME license or copyright; see http://www.asme.org/terms/Terms_Use.cfm

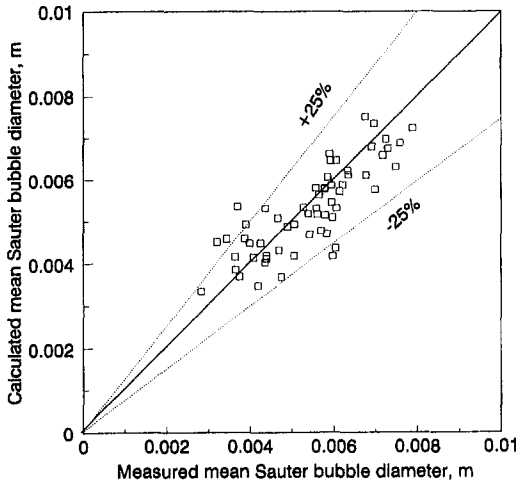



**Fig. 7 Comparison between the calculated and measured mean Sauter bubble diameter**

$$a_i = 3.24\alpha^{0.757}(g\Delta\rho/\sigma)^{0.55}(\mu/G)^{0.1} \quad (6)$$

The interfacial area concentration is related to the mean Sauter bubble diameter by:

$$a_i = 6\alpha/D_s \quad (7)$$

Therefore, the mean Sauter bubble diameter is:

$$D_s = 1.85\alpha^{0.243}\left(\frac{\sigma}{g\Delta\rho}\right)^{0.55}\left(\frac{G}{\mu}\right)^{0.1} \quad (8)$$

The predictions of Eq. (8) are compared with the mean Sauter bubble diameter measured in the present work in Fig. 7. The agreement is good and Eq. (8) is accordingly recommended for use in conjunction with Eqs. (3) and (5) for predicting the interfacial heat transfer coefficient in subcooled water–steam bubbly flow for void fractions up to 30 percent.

## 6 Conclusions

Experimental data on bubble condensation in low-pressure cocurrent upward subcooled liquid–vapor bubbly flow were obtained. Digital image processing techniques were used to obtain the rate of bubble condensation in terms of bubble size, local subcooling, void fraction, and bubble rise velocity. The data were used to develop a new empirical correlation for the interfacial condensation Nusselt numbers as a function of bubble Reynolds number, void fraction, and Jakob number. Since the proposed correlation requires knowledge of bubble diameter and relative velocity, the present data set was also used to recommend appropriate correlations for this purpose. The proposed correlation for interfacial heat transfer coefficient is also compared with those available in the literature, which were mostly developed on the basis of condensation of single bubbles.

## Acknowledgments

The authors acknowledge the financial support of Atomic Energy of Canada Ltd. and the Natural Science and Engineering Research Council of Canada. The fruitful discussion and support of Prof. R. L. Judd are greatly appreciated.

## References

Abdelmessih, A. H., Hooper, F. C., and Nangia, S., 1972, "Flow Effects on Bubble Growth and Collapse in Surface Boiling," *Int. J. Heat Mass Transfer,* Vol. 15, pp. 115–125.

Akiyama, M., 1973, "Bubble Collapse in Subcooled Boiling," *Bulletin of JSME,* Vol. 16, pp. 570–575.

Brucker, G. G., and Sparrow, E. M., 1977, "Direct Contact Condensation of Steam Bubbles in Water at High Pressure," *Int. J. Heat Mass Transfer,* Vol. 20, pp. 371–381.

Chen, Y. M., and Mayinger, F., 1992, "Measurement of Heat Transfer at Phase Interface of Condensing Bubble," *Int. J. Multiphase Flow,* Vol. 18, pp. 877–890.

Dimić, M., 1977, "Collapse of One-Component Vapour Bubble With Translatory Motion," *Int. J. Heat Mass Transfer,* Vol. 20, pp. 1325–1332.

Florschuetz, I. W., and Chao, B. T., 1965, "On the Mechanics of Bubble Collapse," ASME JOURNAL OF HEAT TRANSFER, Vol. 87, pp. 209–220.

Hewitt, H. C., and Parker, J. D., 1968, "Bubble Growth and Collapse in Liquid Nitrogen," ASME JOURNAL OF HEAT TRANSFER, Vol. 90, pp. 22–26.

Hori, Y., and Toda, S., 1991, "Condensation Rate of Vapour Bubbles in Subcooled Flow in a Vertical Tube," *Proceedings of the International Conference on Multiphase Flow '91,* Tuskuba, Japan, pp. 161–164.

Isenberg, J., and Sideman, S., 1970, "Direct Contact Heat Transfer With Change of Phase: Bubble Condensation in Immiscible Liquids," *Int. J. Heat Mass Transfer,* Vol. 13, pp. 997–1011.

Kelly, J. E., and Kazimi, M. S., 1982, "Interfacial Exchange Relations for Two-Fluid Vapour-Liquid Flow: A Simplified Regime-Map Approach," *Nuclear Science and Engineering,* Vol. 81, pp. 305–318.

Levenspiel, O., 1959, "Collapse of Steam Bubbles in Water," *Industrial and Engineering Chemistry,* Vol. 51.

Mayinger, F., and Bucher, B., 1977, "Subcooled Boiling," in: *Two-Phase Flows and Heat Transfer,* S. Kakac and T. N. Veziroglu, eds., Vol. II, Hemisphere Pub. Corp., Washington, pp. 581–621.

Moalem, D., and Sideman, S., 1973, "The Effect of Motion on Bubble Collapse," *Int. J. Heat Mass Transfer,* Vol. 16, pp. 2321–2329.

Okhotsimskii, A. D., 1988, "The Thermal Regime of Vapour Bubble Collapse at Different Jacob Numbers," *Int. J. Heat Mass Transfer,* Vol. 31, pp. 1569–1576.

Rayleigh, Lord, 1917, "On the Pressure Developed in a Liquid During Collapse of a Spherical Cavity," *Philosophy Magazine,* Vol. 34, pp. 94–98.

Ruckenstein, E., 1959, "On Heat Transfer Between Vapour Bubbles in Motion and the Boiling Liquid From Which They Are Generated," *Chemical Engineering Science,* Vol. 10, pp. 22–30.

Ruckenstein, E., 1967, "Mass Transfer Between a Single Drop and a Continuous Phase," *Int. J. Heat Mass Transfer,* Vol. 10, pp. 1785–1792.

Ruckenstein, E., and Constantinescu, D., 1969, "Mass or Heat Transfer With a Change in Interfacial Area," *Int. J. Heat Mass Transfer,* Vol. 12, pp. 1249–1255.

Ruckenstein, E., and Davis, E. J., 1971, "The Effect of Bubble Translation on Vapour Bubble Growth in a Superheated Liquid," *Int. J. Heat Mass Transfer,* Vol. 14, pp. 939–952.

Shoukri, M., Judd, R. L., Donevski, B., and Dimmick, G. R., 1991, "Experiments on Subcooled Flow Boiling and Condensation in Vertical Annular Channels," in: *Phase-Interface Phenomena in Multiphase Flow,* G. F. Hewitt, F. Mayinger, and J. R. Rizinic, eds., Hemisphere Pub. Corp., pp. 413–422.

Simpson, H. C., Beggs, G. C., and Isikan, O. M., 1986, "Collapse of Steam Bubbles in Sub-cooled Water," *Proceedings of the Eighth International Heat Transfer Conference,* San Francisco, CA, Vol. 4, pp. 1919–1924.

Theofanous, T. G., Biasi, L., Isbin, H. S., and Fauske, H. K., 1970, "Nonequalibrium Bubble Collapse: A Theoretical Study," *Chemical Engineering Progress Symposium Series,* No. 102, Vol. 66, pp. 37–47.

Wallis, G. B., 1974, "Terminal Speed of Single Drops or Bubbles in an Infinite Medium," *Int. J. Multiphase Flow,* Vol. 1, pp. 491.

Wittke, D. D., and Chao, B. T., 1967, "Collapse of Vapour Bubble With Translatory Motion," ASME JOURNAL OF HEAT TRANSFER, Vol. 89, pp. 17–24.

Zeitoun, O., Shoukri, M., and Chatoorgoon, V., 1994, "Measurements of Interfacial Area Concentration in Subcooled Liquid–Vapour Flow," *Nuclear Engineering and Design,* Vol. 152, pp. 243–255.

Zuber, N., 1961, "The Dynamics of Vapour Bubbles in Nonuniform Temperature Fields," *Int. J. Heat Mass Transfer,* Vol. 2, pp. 83–98.

Zuber, N., and Findlay, J., 1965, "Average Volumetric Concentration in Two-Phase Flow Systems," ASME JOURNAL OF HEAT TRANSFER, Vol. 87, pp. 453–462.



Downloaded 12 Dec 2010 to 193.140.21.150. Redistribution subject to ASME license or copyright; see http://www.asme.org/terms/Terms_Use.cfm

# Pool Boiling of *n*-Pentane, CFC-113, and Water Under Reduced Gravity: Parabolic Flight Experiments With a Transparent Heater

**T. Oka**[1]
Graduate Student,
Department of Mechanical Engineering,
Keio University,
Hiyoshi, Yokohama 223, Japan

**Y. Abe**
Senior Researcher,
Energy Materials Section,
Electrotechnical Laboratory,
Tsukuba, Ibaraki 305, Japan

**Y. H. Mori**
Professor.
Mem. ASME

**A. Nagashima**
Professor.
Mem. ASME

Department of Mechanical Engineering,
Keio University,
Hiyoshi, Yokohama 223, Japan

*A series of pool boiling experiments have been conducted under reduced gravity condition (the order of $10^{-2}$ times the terrestrial gravity) available in an aircraft taking parabolic flight. A transparent resistant heater, a transparent indium oxide film plated on a glass plate, was employed so that the vapor/liquid behavior interacting with the heater surface could be observed from the rear side of the heater simultaneously with the side view of vapor bubbles above the heater surface. The experiments were performed for three different fluids—n-pentane, CFC-113, and water—under subcooled conditions. The critical heat fluxes for both n-pentane and CFC-113 under the reduced gravity were lowered to about 40 percent of the corresponding terrestrial values. Although the heat transfer characteristics in a low heat flux nucleate boiling regime for both n-pentane and CFC-113 showed no more than a slight change with the reduction in gravity, a significant heat transfer deterioration was noted with water in the reduced gravity boiling. The observation from the rear side of the heater suggested that this particular difference in the gravity dependency of heat transfer was ascribed to a considerable difference, between the organic fluids and water, in the behavior of attachment to the heater surface of the bubbles grown up, while the behavior of attachment must depend on the surface tension of each fluid and the wettability of the heater surface with the fluid.*

## Introduction

Boiling heat transfer is one of the key technologies for future space thermal management systems because of its outstanding heat transfer performance in comparison with single-phase heat transfer in conventional space heat exchangers (for instance, Bland et al., 1984). Studies on microgravity pool boiling can provide fundamental information for the development of space boiling heat transfer devices. In addition, from the viewpoint of materials processing in space, the knowledge of boiling phenomena in microgravity is also indispensable for liquid materials handling, various thermal processes for materials processing like quenching, gas evolution control in solidification and electrolysis processes, and so on.

In the nearly 60-year history of boiling heat transfer research, a tremendous number of experimental results and correlations have been presented. As far as the effect of gravity on boiling is concerned, the question on the effectiveness of gravity in boiling heat transfer arose in the mid-1950s in the U.S.A., and the first pool boiling experiment with using a 0.7-second drop tower was reported in 1959 (Siegel and Usiskin, 1959). Since then, nearly 30 papers have reported experimental observations of boiling heat transfer in reduced, or sometimes elevated, gravity conditions. Early studies up to the mid-1960s were summarized by Siegel (1967). More recently Merte (1990) published comprehensive remarks on the effect of variable gravity.

The principal question in microgravity pool boiling studies is whether the nucleate boiling as an effective heat transfer mode is still available as gravity vanishes. Although most of the previous experimental data have suggested that the heat transfer characteristics in the nucleate boiling regime are nearly gravity independent, the present authors do agree that no definite answer to this question has been given yet. The answer must be based on experiments undertaken with a variety of fluids and heater geometries in a high-quality microgravity condition lasting for a sufficiently long period, and it is required to give a reasonable explanation on the microgravity boiling mechanism. Among the previous studies on microgravity boiling experiments, attempts at approaching the mechanism of microgravity boiling are extremely few (Straub and Vogel, 1991).

On the other hand, various boiling heat transfer models have been presented so far, some of which give gravity-dependent expressions for heat transfer coefficient, while the others give gravity-independent ones. Most of the gravity-dependent expressions predict the heat transfer coefficient being nearly proportional to the square root of gravity. It may also be possible to identify both gravity-dependent and gravity-independent regimes according to the variation of vapor/liquid dynamics with the imposed heat flux. Lienhard (1985) pointed out, based on the experimental results for the heater orientation effect by Nishikawa et al. (1984) and Moissis and Berenson's idea on hydrodynamic transitions (1963), that the nucleate boiling regime can be divided into two distinct regimes—a gravity-dependent regime, which is characterized by isolated bubbles, and a gravity-independent regime in which vapor slugs and columns dominate.

Another important question to be answered in microgravity pool boiling studies is how the CHF (critical heat flux) changes with gravity. Current theoretical CHF models assuming the Helmholtz instability on vapor stems to be the CHF-controlling mechanism all lead to the conclusion that the CHF is proportional to the one-fourth power of gravity. Recent sounding rocket experiments that provided a high-quality microgravity condition of

[1] Present address: Ishikawajima-Harima Heavy Industries Co., Ltd., Isogo, Yokohama 235, Japan.

Contributed by the Heat Transfer Division for publication in the JOURNAL OF HEAT TRANSFER. Manuscript received by the Heat Transfer Division October 1993; revision received May 1994. Keywords: Boiling, Microgravity Heat Transfer. Associate Technical Editor: V. K. Dhir.



Copyright © 1995 by ASME

Downloaded 12 Dec 2010 to 193.140.21.150. Redistribution subject to ASME license or copyright; see http://www.asme.org/terms/Terms_Use.cfm

the order of $10^{-4}g$ for about six minutes, however, have given obviously much higher CHFs than predicted by the one-fourth power relationship for a flat plate heater (Straub et al., 1992). On the other hand, it seems that the results of previous boiling experiments under gravities in the range $0.01 \sim 1\,g$ are generally inconsistent with the one-fourth power relationship (Siegel, 1967).

The present authors initiated pool boiling experiments under microgravity conditions to answer these old but as-yet unsolved questions through the efforts for illuminating the vapor/liquid mechanics underlying the microgravity boiling in addition to the acquisition of microgravity boiling heat transfer data. This approach may help our general understanding of the mechanisms of boiling and boiling heat transfer by removing, or subduing, the buoyancy effect that possibly makes some alternative mechanical effects at the terrestrial condition. The particular interest in the present study lies in the interactions between vapor bubbles and the heater surface, which may be presented in part by the behavior of the so-called microlayer and/or macrolayer of superheated liquid.

In advance of the present study, the authors conducted their first experimental study on reduced gravity pool boiling, in which a test cell containing $n$-pentane, the fluid to be boiled, and a flat plate heater (40 mm × 80 mm) was free-floated during parabolic flights (Oka et al., 1992). The heater consisted of a thin titanium foil to be Joule-heated and a transparent resin substrate sandwiching a thermochromatic liquid crystal layer, which was used to visualize the spatial temperature profile on the heater surface. The heat flux at the heater surface was necessarily limited to relatively low levels so that the heater surface temperature did not exceed the color-reflecting temperature range of the liquid crystal.

As far as a good quality of reduced gravity, say of the order of $10^{-3}g$, was maintained, $n$-pentane bubbles generated on the heater surface never detached from there, and hence a spatial temperature pattern on the heater surface gradually changing with time was clearly observed. Particularly in the region of isolated bubbles, the formation of a microlayer and its consumption were indicated by the development of a cold spot on the surface just under the isolated bubble, and with the subsequent development of a hot spot from the center of the cold spot, the cold spot turned out to be a cold ring. The bases of developed isolated bubbles, coalesced bubbles, and vapor slugs were characterized by cold contours, which suggested a preferential evaporation from the bubble/liquid/heater interline regions.

From the observation of boiling behavior, it was found that the transitions from the isolated bubble regime to the coalesced bubble regime and from the coalesced bubble regime to the vapor slug regime were strongly dependent on the gravity; the transitions took place at lower heat fluxes in reduced gravities, and this trend was even emphasized by a reduction in the subcooling of the liquid. Another experimental finding was that the effect of gravity on boiling heat transfer was very weak in the low heat flux (isolated bubbles) region, but more appreciable in the high heat flux (coalesced bubbles and vapor slugs) region. This finding was opposite to the inference of Lienhard (1985) mentioned above.

In the present study, parabolic flight was again employed; but this time three different fluids—$n$-pentane, CFC-113, and water—were employed for mutual comparison of their boiling behavior, and an alternative observation scheme was adopted that utilized a transparent glass heater for obtaining detailed information on the vapor/liquid mechanics on the heater surface. In the experiments with $n$-pentane and CFC-113, the heat flux was raised up to the respective CHFs, though the CHF was not reached with water.

**Table 1 Thermophysical properties of fluids used for experiments ***

| | | n-Pentane | CFC-113 | Water |
|---|---|---|---|---|
| $\sigma$, | mN/m | 15.5 | 14.7 | 58.9 |
| $\eta_l$, | μPa·s | 214 | 496 | 283 |
| $\Delta H$, | kJ/kg | 397 | 144 | 2,257 |
| $\rho_l$, | kg/m$^3$ | 610 | 1,507 | 958 |
| $\rho_v$, | kg/m$^3$ | 2.999 | 7.465 | 0.5777 |
| $Cp_l$, | kJ/kg·K | 2.34 | 0.98 | 4.21 |
| $\lambda_l$, | mW/m·K | 115 | 67.8 | 677 |

* Saturated states at 0.1013 MPa

It should be noted that the idea of using a transparent heater in boiling experiments was not new, but goes back to the mid-1960s when Torikai and Yamazaki first observed, with the aid of such a heater, a microlayer beneath a growing vapor bubble (Torikai and Yamazaki, 1965). The scheme of optical observation used in the present study essentially followed that devised by Torikai and Yamazaki. A slightly different version of the transparent glass heater technique with a semitransparent gold film was recently utilized by Ervin et al. (1992) in studying transient microgravity pool boiling.

## Experimental

The experiments were performed during a parabolic flight campaign with Caravelle 234 aircraft operated by CNES (Centre National d'Etudes Spatiales). A gravity level of the order of $10^{-2}g$ was available for 20 to 25 seconds during one parabola. The experiments lasted for three days, while 30 parabolic flights were provided each day. The flights taken in one day were wholly devoted to the experiments with one fluid. In any parabola, the experimental equipment was rigidly bolted onto the floor of the aircraft, and no free-floating experiment was attempted.

Table 1 compares the major thermophysical properties of the three fluids used as the boiling media. Among these fluids water is conspicuous with the large values of its thermal conductivity, latent heat of evaporation, and surface tension. CFC-113 has the highest viscosity among three fluids, which possibly contributes to the formation of a comparatively thick microlayer underneath growing bubbles. Each of the organic liquids was distilled before filling the boiling chamber, and further degassing was conducted before the parabolic experiments. The nominal purities for $n$-pentane and CFC-113 were >99.7 percent and >99.8 percent, respectively. The specific resistance of the deionized water in the experiments was 10 MΩ·m.

## Nomenclature

$C_p$ = isobaric specific heat
$F$ = fraction of heater surface area covered with bubbles
$g$ = gravitational acceleration at the terrestrial condition (positive sign directs normal to the heater surface)
$q$ = heat flux
$T_w$ = heater surface temperature
$\Delta H$ = latent heat of evaporation
$\Delta T_{sat}$ = heater surface superheat
$\Delta T_{sub}$ = subcooling of bulk liquid
$\eta$ = viscosity
$\lambda$ = thermal conductivity
$\rho$ = density
$\sigma$ = surface tension

**Subscripts**

$l$ = liquid state
$v$ = vapor state



Downloaded 12 Dec 2010 to 193.140.21.150. Redistribution subject to ASME license or copyright; see http://www.asme.org/terms/Terms_Use.cfm

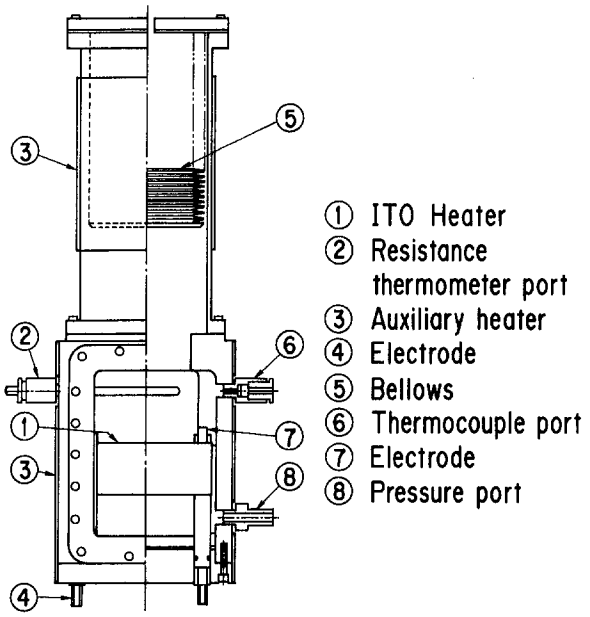



**Fig. 1 Boiling chamber**

Figure 1 illustrates the boiling chamber used in the experiments, which is basically the same as that used in the previous experiment (Oka et al., 1992). In short, it consisted of a rectangular chamber (inside dimensions 70 mm × 100 mm × 155 mm), in which a flat plate heater was installed, and of a cylinder holding a metallic bellows inside, which was to compensate the volume change of the fluid in the course of boiling. In advance of each series of parabola, the chamber was completely filled with a test fluid in the state of a subcooled liquid. Then the liquid was heated up by auxiliary heaters put on the outside chamber walls, to a prescribed temperature level, and was kept constant at the level throughout the series of parabolic flights (normally 30 parabolas a day).

The liquid temperature was monitored with two 0.5-mm-dia sheathed chromel-alumel thermocouples. The subcooling of the bulk liquid was controlled by manipulating the bellows to pressurize or depressurize the chamber, and the pressure was measured with a diaphragm pressure gage. Because of no cooling device for the boiling chamber and the above-mentioned pressurization and depressurization procedures, the temperature in the liquid bulk changed in the course of experiments. The liquid bulk temperatures and the pressures in the present experiments were 37.0 ~ 41.5°C and 81 ~ 119 kPa for CFC113, 29.2 ~ 36.9°C and 84 ~ 183 kPa for *n*-pentane, and 89.5 ~ 94.5°C and 84 ~ 139 kPa for water.

One of the points in the present experiments was the use of a transparent heater. ITO (indium oxide with a trace of tin oxide) was evaporated onto one side of BK-7 glass plate—50 mm wide, 100 mm long, and 30 mm thick—to form a uniform film 0.5 $\mu$m in thickness, over a 50 mm × 50 mm area. A chromium/gold double layer (0.3 $\mu$m thick and 0.5 $\mu$m thick, respectively) was prepared also by evaporation at both ends of the ITO film, and a voltage tap was soldered onto the double layer to measure the imposed voltage at the ITO film. The ITO film enjoyed a low electric resistance (about 3 ~ 4 $\Omega/cm^2$) and a high transparency of over 80 percent. In addition to this, the resistance versus temperature relation showed a good linearity, and thus the film could be well used as a resistance thermometer for the heater surface temperature. The uncertainty of the temperature reading with the ITO film was generally within ±0.5 K, but the possible maximum uncertainty was estimated to be ±1 K due to a weak aging effect on the resistance of the film. A SEM (scanning electron microscope) observation of the ITO film showed that the roughness of the surface was as small as 0.1 $\mu$m. This observation suggests that the ITO film may provide much fewer nucleation sites than common surfaces of solid metals, particularly at low heat fluxes. All the experimental data on the surface and bulk temperatures, the pressure, the voltage, and the electric current were acquired and stored in a hybrid recorder with 2 Hz interval.

The transparent heater was stepwise heated up after a stable reduced gravity condition was established in the aircraft during every parabola. The heater was then turned off when the gravity condition recovered from the reduced condition. The imposed voltage was kept constant during each heating period. Thus, one heat transfer data point was obtained in each parabola in the present experiments.

The boiling behavior was observed with the aid of two 8 mm video cameras at 30 frames/s, one from the side of the heater and the other from below at a proper angle. Figure 2 illustrates the principle of the optical observation system in this study. The liquid/vapor two-phase structure over the heater surface can be clearly identified through the camera at the lower position, by the structure-dependent reflection of a stroboscopic light flashed at the position opposite to the camera: The surface area on which bubbles are lying, either dried or with the microlayer of the order of $\mu$m, generally gives a bright reflection. In contrast to this, the other area in contact with the bulk liquid or thick liquid layer can be identified as a dark reflection. The stroboscope was synchronized with two video cameras and provided a 1.2 $\mu$s flash light.

The plots of three axis acceleration data recorded in the aircraft during the flights were supplied from CNES afterward. From the data in the axis normal to the heater surface, the acceleration levels at every 1.25 s during the parabolic flights have been read. The average acceleration levels and the standard deviations (in the parentheses) during the experiments for CFC-113, *n*-pentane, and water were $-0.015(\pm 0.035)g$, $-0.010(\pm 0.020)g$, and $-0.011(\pm 0.020)g$, respectively. The negative sign of the acceleration here denotes the residual acceleration depressing bubbles to the heater, and hence the bubbles lift off from the heater surface when the residual acceleration is positive. The acceleration data show that some negative acceleration was exerted, possibly forcing bubbles to be pressed against the heater surface over discrete periods. A relatively wide scatter of acceleration values is noted in the first-day flights devoted to the experiments with CFC-113, which is ascribed to an unfavorable climatic condition at that time.

## Results and Discussion

### 1 Boiling Behavior

*n-Pentane and CFC-113.* The observations revealed no essential difference in the boiling behavior between *n*-pentane and CFC-113. A slight difference in the effect of subcooling was noticed, but, as described later, it seems to be ascribable to a relatively large gravity jitter in the course of the experiments with CFC-113.

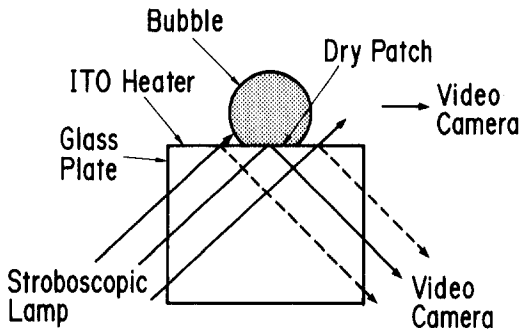
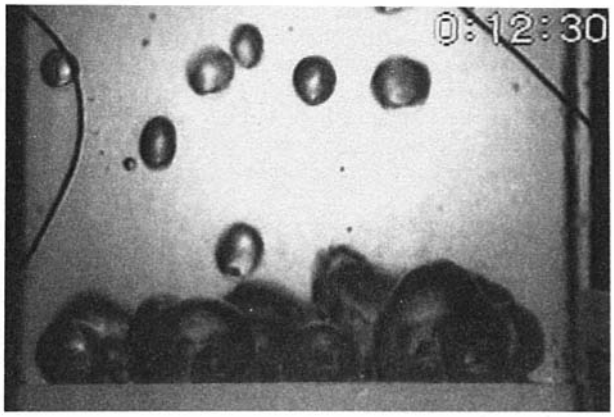



**Fig. 2 Principle of observation system**



Downloaded 12 Dec 2010 to 193.140.21.150. Redistribution subject to ASME license or copyright; see http://www.asme.org/terms/Terms_Use.cfm



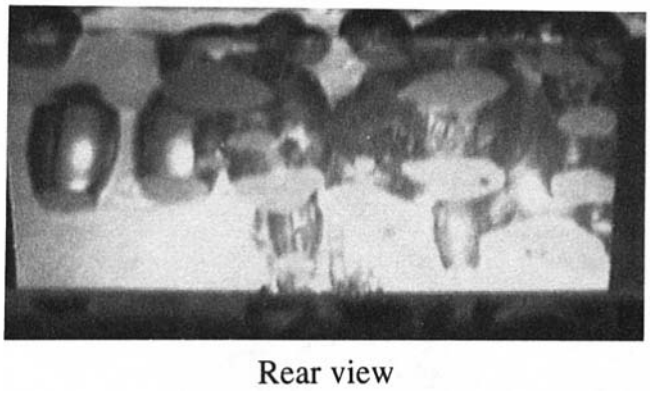



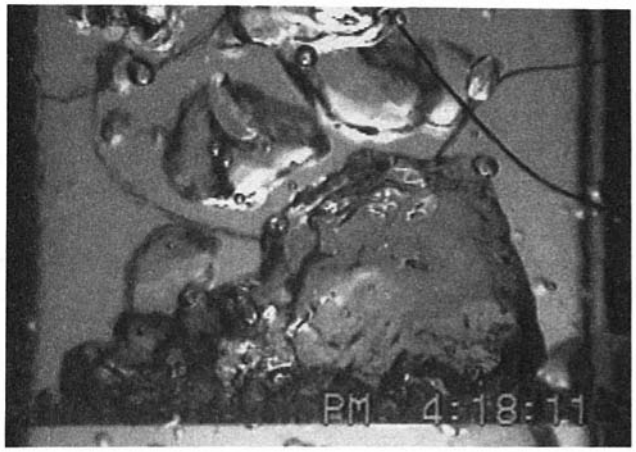

**Fig. 3 Boiling behavior of *n*-pentane in isolated bubble regime ($\Delta T_{sub}$ = 3 K, $q$ = 30 kW/m$^2$)**

Figure 3[2] gives both side and rear views simultaneously observed with *n*-pentane in the isolated bubble regime. Hemispherical bubbles kept attaching to the heater surface, each occupying a large circular contact area, as long as the instantaneous gravity did not exceed $+10^{-2}g$. Some of the bubbles slowly slid on the heater surface, sometimes resulting in coalescence with other stationary or sliding bubbles. Some Marangoni effect might arise from a trace of noncondensables confined in the bubbles (Straub et al., 1990b), and if this is the case, the effect should have contributed to some extent to attaching the bubbles to the surface.

Note that the base of each isolated bubble (the bubble/heater contact area) has a very circular shape with a smooth contour. Unfortunately we have no general means to discern whether the base is dried out or covered with a very thin liquid layer. Nevertheless, we can still suppose some mechanisms of supplying the liquid to a heater surface that is covered tentatively or nearly steadily with bubbles. The sliding motion of a bubble permits the continuous formation of a liquid film beneath the bubble. The coalescence of bubbles induces a vigorous oscillatory motion of the liquid–vapor interface on and above the heater surface. The sliding and the coalescence of the bubbles as described above are considered to be the primary mechanisms to "wet," at least in part, the surface beneath the bubbles and maintain rather effective heat transfer in low heat flux boiling under reduced gravity.

With an increase in the heat flux, the coalescence of bubbles in the horizontal direction became increasingly frequent. In the vapor slug regime, the bubble coalescence occurred also in the vertical direction; i.e., the large coalesced bubbles attaching to the heater surface often coalesced with those that had been thrust away from the surface by the former bubbles.

In Fig. 4 a couple of side and rear views of boiling in the vapor slugs regime for CFC-113 are presented. It seems, from the side view, that the heater is almost completely blanketed with large vapor slugs, but the rear view shows that the heater surface is not completely covered by vapor slugs or bubbles but is covered with a "network" of wriggling "canals" of liquid, which partition the rest of the surface area into discrete "hollow patches." It was observed that as the heat flux increased, the number of such patches considerably increased while the size of each patch rather decreased, resulting in an increase in the total area of patches over the heater surface. We assume that the "hollow patches" are no more than the bases of individual "primary bubbles" lying on the heater surface, which occasionally merge into larger slugs mounted on the array of the "primary bubbles." Each "canal" is considered to be a liquid wall separating two



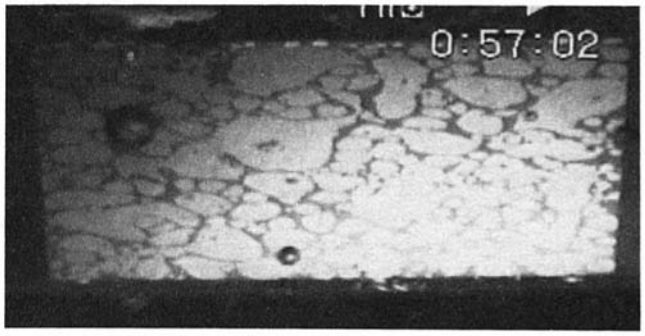
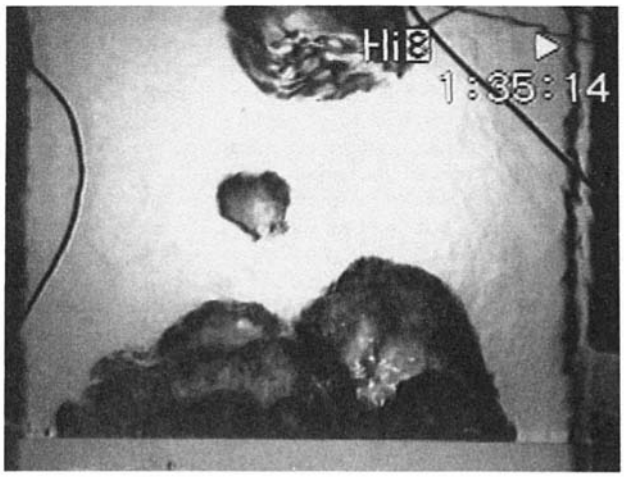




**Fig. 4 Boiling behavior of CFC-113 in vapor slug regime ($\Delta T_{sub}$ = 6 K, $q$ = 65 kW/m$^2$)**

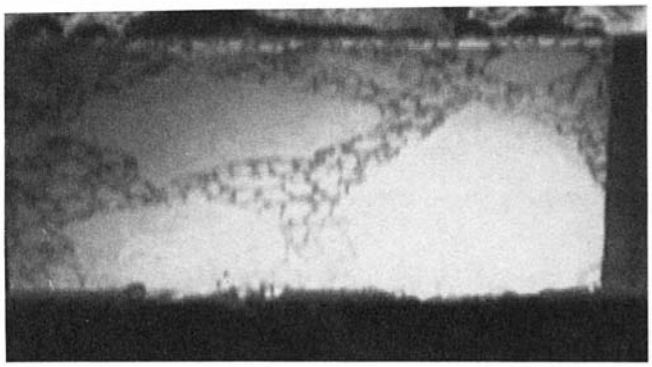
[2] Those photographs appearing in the present paper are all of steady-state boiling taken in a stable gravity condition during each parabola.



Downloaded 12 Dec 2010 to 193.140.21.150. Redistribution subject to ASME license or copyright; see http://www.asme.org/terms/Terms_Use.cfm




Side view



Rear view

**Fig. 5 Boiling behavior of *n*-pentane at the CHF ($\Delta T_{sub}$ = 17 K, $q$ = 108 kW/m$^2$)**

neighboring "primary bubbles," and hence its height above the heater surface may be comparable with the dimension of the "hollow patches." It is quite likely that the "network" of the "canals" connect with the bulk of the liquid at many places and thereby serves as the channels for supplying liquid from the bulk to the heater surface.

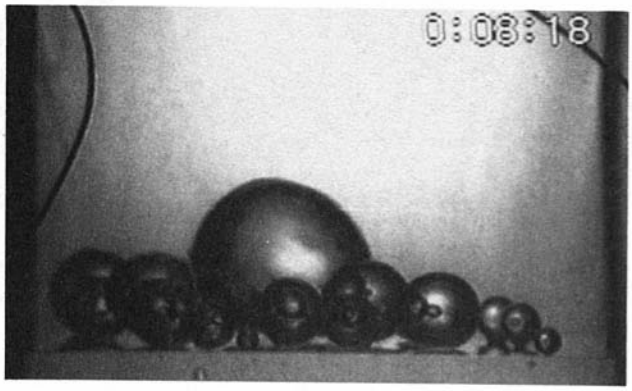
The question we should consider next is whether the "hollow patches" are "dried out" or are completely or partly covered with thin liquid films. The present observations provided no critical evidence for either possibility. Still we note a few circumstantial evidences of the former possibility. First, the contours of each "hollow patch" or the surrounding "canals" were substantially indented. The smallest scale of indentation recognized on the video recordings was the order of 10 $\mu$m or less. Such a lateral indentation on the vapor/liquid interface in the vicinity of the solid surface indicates the presence, on the surface, of an energy barrier resisting the capillary pressure generated by the strongly nonuniform curvature of the interface. The energy barrier of this kind could become explicit, if the vapor/liquid interface meets the solid surface, thereby forming a three-phase contact line on the surface. The irregular, somewhat jerky, motion of the canals over the heater surface may be ascribed at least in part to the stick-slip behavior of such contact lines (Fraaije et al., 1989).

Another evidence of dryout condition for the patches under vapor slugs is the appearance of "liquid islands" observed in some of the "hollow patches." These islands were considered to be the remnants of "canals" broken by the coalescence of the bubbles. Each island remained almost stationary irrespective of the motion of the contour of the "hollow patches" in which the island was confined. Such an immobility as well as noncircular shapes of the islands were quite unlikely unless they were bordered by three-phase contact lines beyond which dry areas spread.

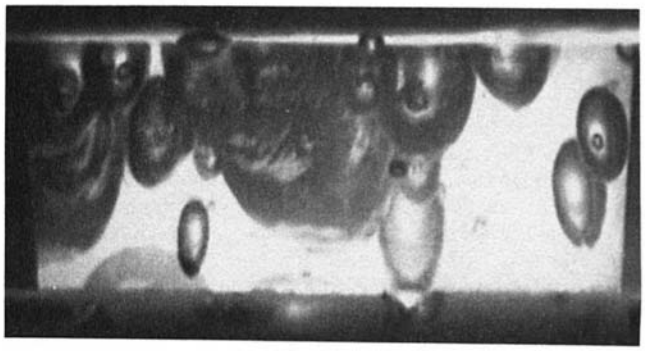
Figure 5 demonstrates an appearance of boiling regime transition at the CHF for *n*-pentane, which is defined here to be the heat flux at which a stationary "hollow area" first appeared on the heater surface. The rear view observations revealed that the formation of such a stationary "hollow area" resulted from a local break of the network of the "canals" due to their thinning. So far as the individual "hollow patches" bordered by the "canals" are, as we have assumed, dried out, the stationary "hollow area" is no more than an integrated dry area over which nucleate boiling no longer works.

It seems worthwhile to add that we observed the "canal network" structure also in the reference pool boiling experiments with the heater facing upward under the terrestrial condition, though the dimension of each "hollow patch" was substantially smaller than that in the reduced gravity boiling. We noticed no essential difference in the physical process toward the CHF between $10^{-2}g$ and the normal gravity.

*Water.* The boiling behavior observed with water was significantly different from the organic fluids described above. Figure 6 shows the boiling behavior in the isolated bubble regime. In contrast to the nearly hemispherical bubbles lying on the heater




Side view

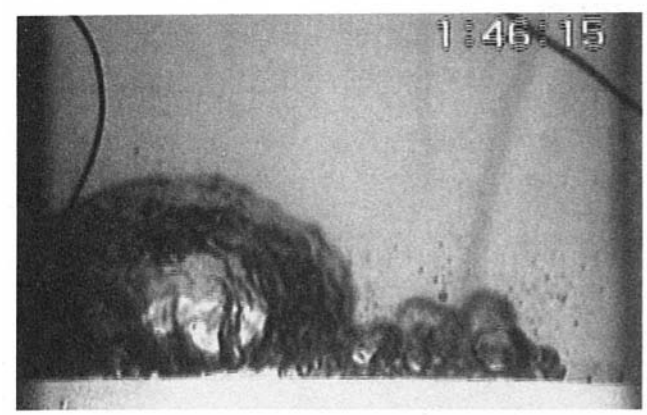


Rear view

**Fig. 6 Boiling behavior of water in isolated bubble regime ($\Delta T_{sub}$ = 2 K, $q$ = 14 kW/m$^2$)**



Downloaded 12 Dec 2010 to 193.140.21.150. Redistribution subject to ASME license or copyright; see http://www.asme.org/terms/Terms_Use.cfm




Side view



Rear view

**Fig. 7 Boiling behavior of water in bubble coalescence regime ($\Delta T_{sub}$ = 6 K, $q$ = 119 kW/m$^2$)**

surface in the organic fluids, bubbles generated in boiling water were generally quite spherical. They were little deformed by some $g$-jitter in the experimental environment or by mutual contact or collisions on the heater surface. The behavior of bubbles was strongly dependent upon the subcooling in the bulk of the liquid. When the subcooling was small, say less than 6 K, most of the bubbles attached themselves to the heater surface each with a very small contact area, or even detached from the surface and stayed very close to the heater surface. In the case of larger subcoolings, on the other hand, all the bubbles sprang off into the bulk of the liquid and condensed immediately just as in usual subcooled boiling under the normal gravity condition. This behavior still prevailed at the highest heat flux ($q$ = 119 kW/m$^2$) imposed in the present experiments, provided that a sufficiently large subcooling ($\Delta T_{sub} \geq$ 14 K) was maintained in the bulk of the liquid.

An appreciable bubble coalescence was observed only when a high heat flux ($q \geq$ 30 kW/m$^2$) was imposed to the heater and, at the same time, the bulk of the liquid was not greatly subcooled ($\Delta T_{sub} \leq$ 6 K). A typical configuration of the aggregate of bubbles in such a condition is shown in Fig. 7, where we find a large bubble slug covering a substantial part of the heater surface, and a number of smaller bubbles successively generated in the liquid layer beneath the slug and then engulfed in it. The vertical motion (relative to the heater surface) of coalescing bubbles illustrated above presents a striking contrast to the horizontal bubble motion characterizing the coalescence in the boiling of the organic fluids.

It should be noted that in a later part of the experiments a trace amount of silicone grease was accidentally leaked into the boiling chamber, and dispersed in the water in the form a cloud of tiny particles of the order of few microns. This contamination possibly had some influence on the physical and chemical nature of liquid/vapor interface. Closely inspecting the videotape record of the experiments, however, we found no grease particles adhering to the heater surface. Thus, we presume that such grease particles did not directly affect the boiling behavior for water.

The considerable differences found in bubble behavior between the organic fluids and water should be ascribed to some physical properties of water (or the water/heater pair) greatly deviating from the correspondents of the organic fluids. The large surface tension of water (about four times larger than those of the organic fluids) and such a poor wettability of the heater surface with water as to yield an advancing contact angle of some 40 deg are considered to be the primary factors relevant to the bubble behavior. It is reasonable to assume that the roles of these factors become even more important with the reduction of gravity effect, thereby contributing to extend the differences in bubble behavior. In addition to the primary factors listed above, the large liquid/vapor density difference for water (one order of magnitude larger than those for the organic fluids) and a rigidity or a viscoelasticity readily generated at water liquid/vapor interfaces as the result of adsorption of even a trace amount of contaminant (Mysels and Florence, 1970) might also have some influences on the bubble behavior. Straub et al. (1990a) reported that a considerable temperature gradient along the surface of isolated air bubbles in water did not yield any appreciable thermocapillary convection effect, such as was clearly observed for organic fluids. If the Marangoni effect is really weakened in water due to un-

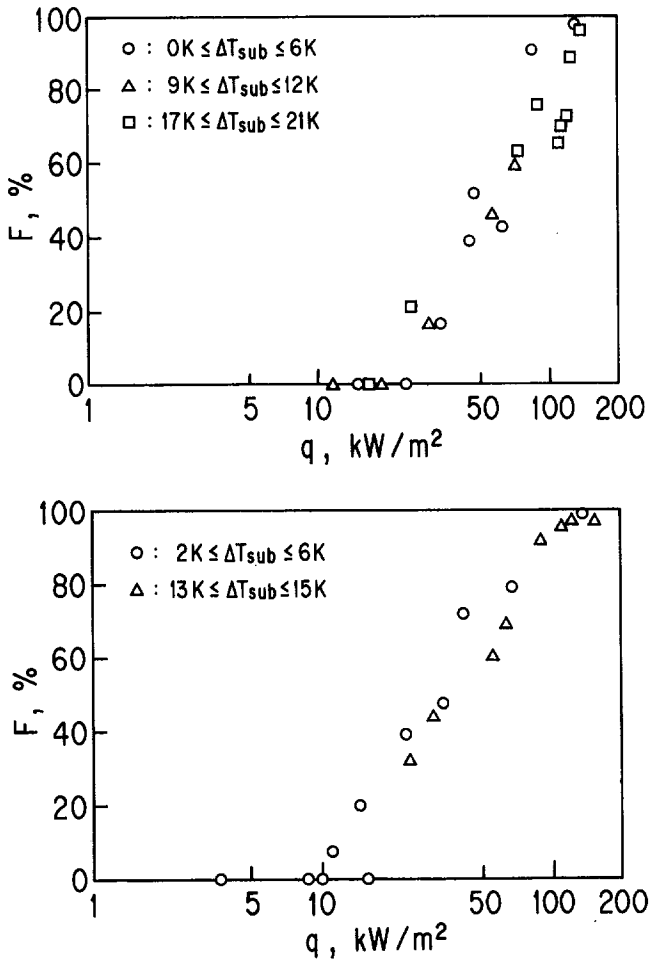



**Fig. 8 Fraction of bubble contact area versus heat flux in reduced gravity: (*a*) *n*-pentane; (*b*) CFC-113**



Downloaded 12 Dec 2010 to 193.140.21.150. Redistribution subject to ASME license or copyright; see http://www.asme.org/terms/Terms_Use.cfm

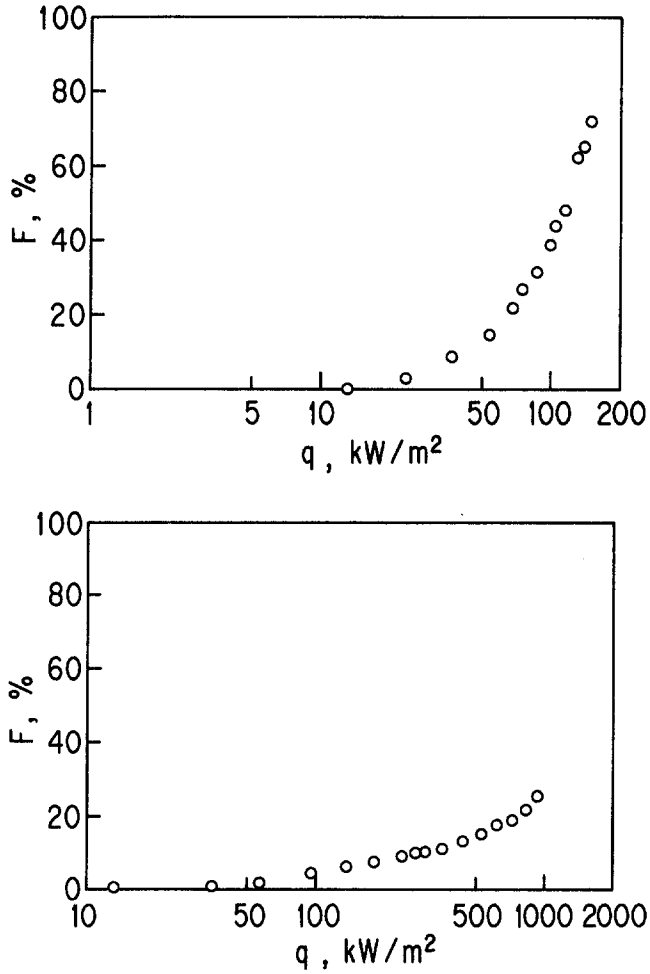



Fig. 9 Fraction of bubble contact area versus heat flux in normal gravity (saturation boiling): (*a*) CFC-113; (*b*) water

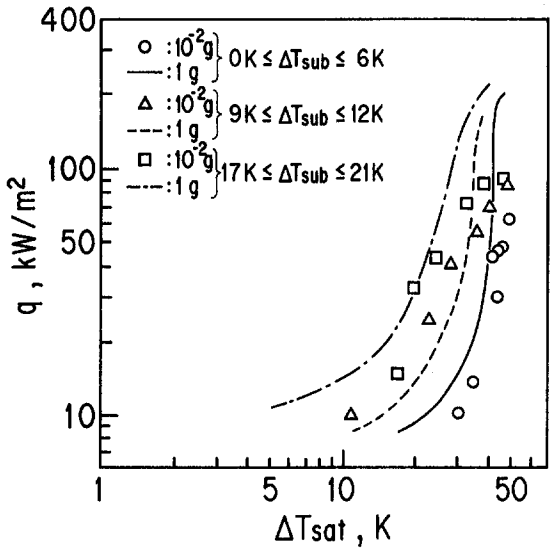



Fig. 10 Boiling curve for *n*-pentane

detectable amount of contaminant, this can be another factor that characterizes the particular behavior of water boiling under reduced gravity.

**2 Bubble/Heater Contact Area.** For both organic fluids in which vapor bubbles kept attaching themselves to the heater surface in the course of reduced gravity period, the surface area covered with the bubbles could be evaluated by analyzing the videotape despite rather low speed of recording (30 fps) in the present experiments. It should be noted here that "the surface area covered with bubbles" or "the bubble/heater contact area" does not necessarily mean the total dryout area on the heater surface. The former area may be the sum of the bases of isolated bubbles or the sum of the "hollow patches" separated from other by liquid canals, and thus it presumably includes a considerable "wet" area at a rather low heat flux, but it may well approximate the total dryout area at higher heat fluxes.

The variation of $F$, the fraction of the surface area covered with the bubbles, with the heat flux is plotted in Fig. 8 for each of the fluids. Since the bubble/heater contact is strongly dependent on the instantaneous gravity condition, particularly at low heat fluxes and small subcoolings, those surface area data compiled in Fig. 8 were collected exclusively from the periods in which the instantaneous gravity continuously fell in the range $-0.01g \sim +0.01g$. The uncertainty in determining the bubble/heater contact area was estimated to be about $\pm 10$ percent. Although the surface area in contact with each bubble tended to increase with the decrease in subcooling, the total contact area over the heater surface was, as Fig. 8 shows, found to change little with the subcooling.

In spite of a little scatter in the data for $n$-pentane, the graphic plot of those data in Fig. 8($a$) shows a monotonic increase of $F$ toward 100 percent with an increase in the heat flux, $q$. A much clearer trend is obtained in the $F$–$q$ plot for CFC-113 given in Fig. 8($b$). It is worth noting that a stationary "hollow area," which is considered to have been an integrated dry area as described before, formed at some location on the heater surface whenever $q$ corresponding to $F \geq 80$ percent (in the case of $n$-pentane) or $F \geq 70$ percent (in the case of CFC-113) was applied to the heater. Once a stationary "hollow area" formed, the surface temperature evaluated from the overall electric resistance of the ITO film exhibited a jump to a much higher level. So far as $q$ remained constant, the "hollow area" did not tend to spread over the heater surface with the lapse of time but was confined to a specific part of the surface throughout.

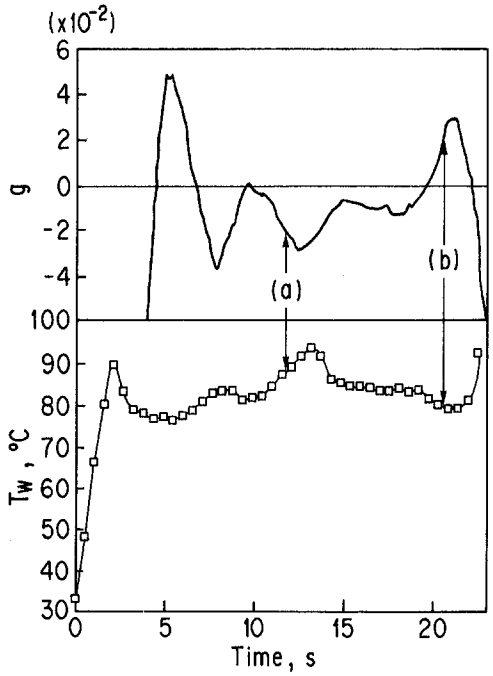



Fig. 11 Variation of acceleration and heater surface temperature during parabolic flight ($n$-pentane, $\Delta T_{sub} = 9$ K, $q = 70$ kW/m²)



Downloaded 12 Dec 2010 to 193.140.21.150. Redistribution subject to ASME license or copyright; see http://www.asme.org/terms/Terms_Use.cfm

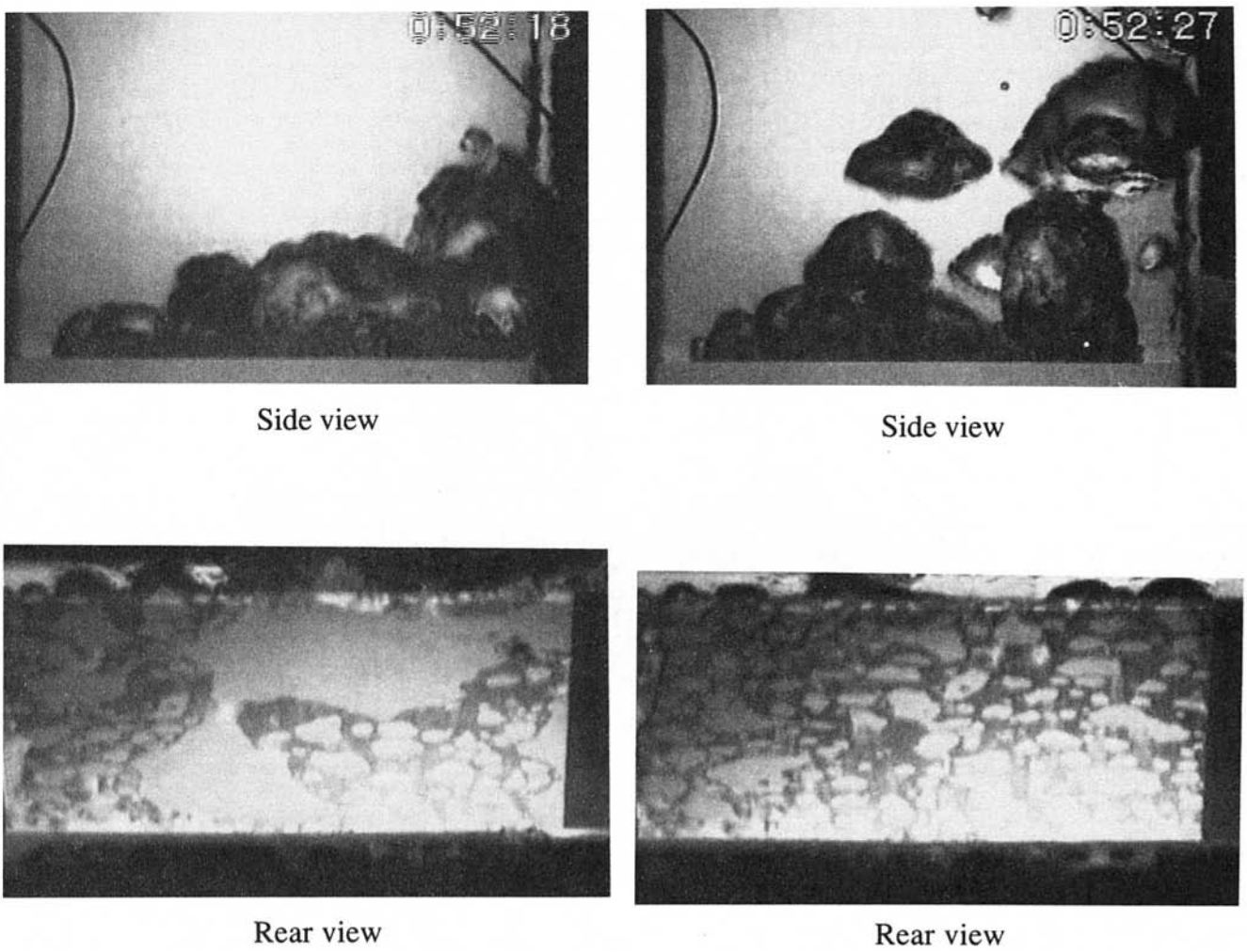



**Fig. 12 Boiling behaviors caused by residual acceleration (corresponding to Fig. 11): (*a*) residual acceleration upward to the heater ((*a*) in Fig. 11); (*b*) residual acceleration downward to the heater ((*b*) in Fig. 11)**

Further increase in $q$ resulted in the formation of two or more "hollow areas" and/or an enlargement of each "hollow area." As mentioned before, we define the CHF as the lowest heat flux that yielded a stationary "hollow area," still leaving the liquid canal network around the "hollow area." The complete drying of the heater surface ($F$ = 100 percent) was not achieved unless $q$ was raised beyond the CHF to some extent.

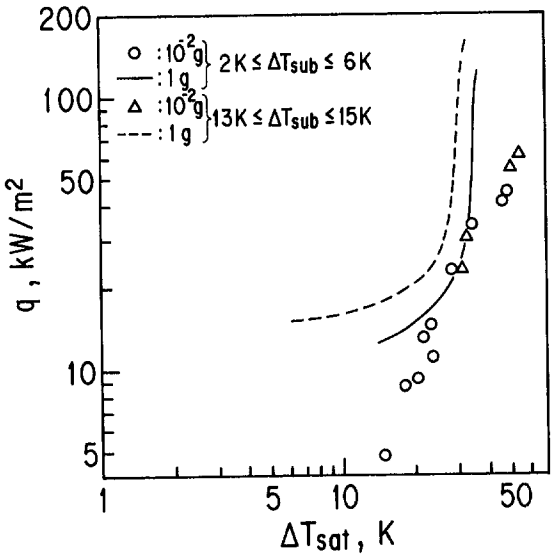



**Fig. 13 Boiling curve for CFC-113**

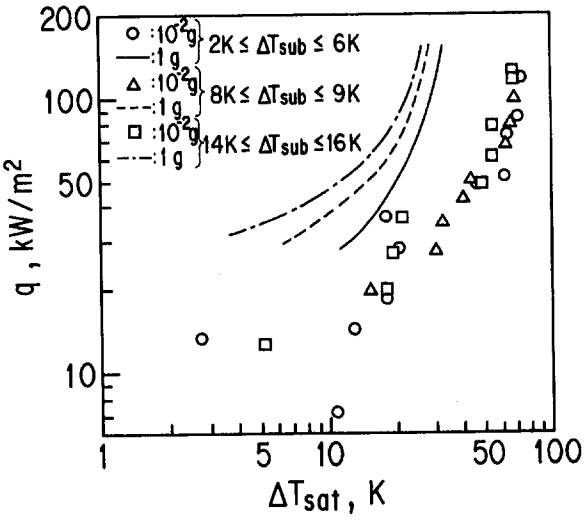



**Fig. 14 Boiling curve for water**



Downloaded 12 Dec 2010 to 193.140.21.150. Redistribution subject to ASME license or copyright; see http://www.asme.org/terms/Terms_Use.cfm

Preliminary experiments made with the same organic fluids under the terrestrial condition gave similar results to those of the parabolic flight experiments as far as the qualitative nature of the $F-q$ plot is concerned—a stationary dryout area formed at $F \sim 70$ percent or higher, when saturated CFC-113 was boiled under the terrestrial condition by the use of the same heater facing horizontal upward, though the CHF required to form the dryout area was about 40 percent higher than the CHF under the reduced gravity (Fig. 9*a*). The major difference of the terrestrial $F-q$ relation from the reduced gravity one lies in that an increase in $q$ up to the CHF caused a sudden increase in $F$; this is in contrast to rather gradual increase in $F$ with an increase in $q$ exceeding the CHF under the reduced gravity condition. Despite such a difference, as we mentioned in Sec. (1) we observed no appreciable difference in the physical process of the dryout due to gravity as far as $10^{-2}g$ of gravity level is concerned—the CHF resulted from thinning the "canal network" structure under the vapor slugs.

Although a similar analysis could not be done for reduced gravity water boiling, the CHF for saturated water under the terrestrial condition was perceived when about 30 percent of the heater surface was occupied with the vapor (Fig. 9*b*). It may be interesting to compare this finding with the results reported under the normal gravity water boiling (Torikai and Yamazaki, 1965) that the bubble/heater contact area on a tin oxide-coated glass plate heater was about 50 percent when the CHF was achieved. The roughness of Torikai and Yamazaki's heater surface was estimated to be $1 \sim 2$ $\mu$m, which was much larger than that in the present heater surface (about 0.1 $\mu$m). The difference in the fraction of bubble/heater contact area at the CHF might be relevant to the difference in the surface roughness, though no satisfactory interpretation on this matter can be provided at present.

**3 Boiling Curves.** With any of the three test fluids, the heater surface temperature became nearly constant in a later part of each reduced gravity period ($20 \sim 25$ s) as far as the nucleate boiling took place. As $4 \sim 5$ seconds had lapsed after the initiation of heating, we no longer observed any change in $T_w$ except some fluctuation corresponding to $g$-jitter. When no boiling took place or the film boiling substituted for the nucleate boiling, the surface temperature continued to increase in the course of the reduced gravity period and never approached some constant level. Since the quality of gravity also greatly influences the average heater surface temperature, especially in the high heat flux region, the heat flux versus surface superheat data shown later were obtained at a sufficiently later stage in each stable reduced gravity period preceded by a duration of reduced gravity within $\pm 0.02g$ for over 5 seconds. Thus, the data are assumed to represent, with a reasonable approximation, the steady-state heat transfer characteristics in nucleate boiling regime, though this is not the case with the nonboiling and the film boiling regimes. The uncertainty of heat flux in the present experiments was estimated about $\pm 5$ percent except at the vicinity of the CHFs where the uncertainty was $\pm 10$ percent.

Figure 10 collects the heat transfer data for reduced gravity nucleate boiling of $n$-pentane. Each data point was corrected by subtracting from the imposed electricity the backward heat flux calculated by assuming one-dimensional transient heat conduction. The three boiling curves drawn for comparison were based on the reference experiments under the terrestrial condition with the same apparatus with the same heater facing horizontal upward. An important point to be stressed here is that the heat transfer deterioration due to the reduction in gravity is insignificant in a low heat flux region characterized by isolated bubbles, and that some of the data even indicate some promotion of the heat transfer with the reduction in gravity. The heat transfer deterioration, however, becomes more significant with an increase in the heat flux. This tendency is already recognized in the results of the present authors' previous experiments (Oka et al., 1992), but it is opposed to Lienhard's inference (Lienhard, 1985) to which we already referred in the introduction of this paper.

With the reduction in gravity, the CHF was reduced to some 40 percent of that obtained in the normal gravity condition. In more detail, the magnitude of the reduction in the CHF seems to increase with the decrease in the subcooling. If we evaluate the typical gravity level in the present experiments to be $\sim 10^{-2}g$, the conventional one-fourth power relationship (Siegel, 1967) predicts the CHF reduced to 32 percent of that in the normal gravity condition. In view of the uncertainty in the experiments, however, the deviation of the observed CHF values from the one-fourth power relationship is not said to be significant.[3]

As far as the influence of the disturbance in the acceleration ($g$-jitter) during parabolic flight is concerned, the influence did not appear in a low heat flux region, but it was remarkable in a high heat flux region. Figure 11 depicts a typical example of the time variations of the acceleration data normal to the heater and the surface temperature data, and Fig. 12 presents how the resultant boiling behavior differs from each other. When the residual acceleration of $0.03g$ was in the upward direction to the heater surface ((*a*) in Fig. 11), the bubbles were pressed to the heater and the surface temperature increased, and a large bubble/heater contact (probably dryout) area was developed on the heater at this moment (Fig. 12*a*). After about 10 s when the residual acceleration of $0.03g$ functioned in the downward direction to the heater ((*b*) in Fig. 11), the surface temperature was cooled down about 15 K, and well developed nucleate boiling was maintained as shown in Fig. 12(*b*).

The results for CFC-113 are plotted in Fig. 13. The general tendency of heat transfer deterioration due to the reduction in gravity is similar to that for $n$-pentane except that much less dependency on the subcooling is found in CFC-113. We do not assume, however, this feature to be intrinsic to CFC-113. Instead, we presume the feature to be ascribed to the residual acceleration during the parabolic flights in the first day assigned to the experiments with CFC-113, which was negative, on the average, and was of larger magnitude than those in the other two days. Under such a negative acceleration, bubbles were pressed against the heater surface, thus hindering the conductive sensible heat transport from the heater to the liquid bulk. The depression of the role of this heat transport mode should have weakened the apparent subcooling dependency of the overall heat transfer. Again the CHF was reduced, with the reduction in gravity, to some 40 percent of that in the normal gravity.

Consistently with the large difference in bubble behavior between the organic fluids and water, we find the heat transfer behavior for water considerably different from those for the organic fluids. Figure 14 plots the heat transfer data for water under reduced gravity together with the boiling curves obtained under normal gravity. It is obvious that the heat transfer deterioration is significant in the entire nucleate boiling regime in the present experiments. Siegel (1967) cited some of the results of Schwartz and Mannes's parabolic flight experiments, which indicated no more than a slight influence of gravity on the nucleate boiling heat transfer from a metal ribbon heater to saturated water over the range up to about 190 kW/m$^2$ in heat flux on the ribbon. At present we do not have any particular explanation for this inconsistency.[4]

[3] Nevertheless, we are skeptical of one-fourth power relationship. Our latest experiments under $10^{-5}g$ (Oka et al., 1994) showed that the CHFs for CFC-113 were $15 \sim 50$ percent (strongly dependent on subcooling) of the terrestrial CHFs and that nucleate boiling was still maintained in saturated water at heat flux of 50 percent of the terrestrial CHF. These CHF values are significantly higher than those predicted by the one-fourth power relationship.

[4] In the latest experiments with subcooled and saturated water boiling on a small-capacity plate heater under microgravity of the order of $10^{-5}g$ lasting for 10 seconds, an extensive heat transfer deterioration was again observed (Oka et al., 1994).



Downloaded 12 Dec 2010 to 193.140.21.150. Redistribution subject to ASME license or copyright; see http://www.asme.org/terms/Terms_Use.cfm

## Concluding Remarks

Pool boiling experiments under reduced gravity ($\sim 10^{-2} g$) were conducted with three different fluids, viz., $n$-pentane, CFC113, and water. A considerable difference was observed in boiling behavior between the organic fluids and water. In the boiling of either organic fluid, most of the bubbles attached themselves to the heater surface, each with a large contact area throughout the duration of reduced gravity, and some of these bubbles coalesced each other on the heater surface even at low heat fluxes. In contrast to this, bubbles generated in water were very spherical in shape, making a slight contact with the heater surface or being lifted off from the surface. In a high heat flux region, water bubble coalescence occurred not on the heater surface but at small distance away from the surface. Primary bubbles newly formed under coalesced bubbles were successively swallowed into the coalesced bubbles, resulting in their further growth. Such a particular behavior for water must be related to its exceptionally large surface tension and large contact angles with which liquid water wetted the surface.

Different behavior was also noticed in the heat transfer characteristics: The boiling heat transfer for water deteriorated in the entire nucleate boiling regime in the present experiments, though for organic fluids the heat transfer deterioration due to the reduction in gravity was appreciable only at high heat fluxes. For both organic fluids the CHF's were decreased, with the reduction in gravity, to about 40 percent of the corresponding terrestrial CHF values.

The present observation suggests that the bubble/heater contact behavior is a key factor in boiling heat transfer under reduced gravity. If the latent heat transport plays a primary role in reduced gravity boiling heat transfer mechanism as claimed by Straub and Vogel (1991), a larger contact area under bubbles, in other words a longer bubble/heater contact contour, can be a condition favorable to efficient heat transfer, since the liquid-to-vapor phase change should take place preferentially in the vicinity of the three-phase contact line. The sensible heat transfer, which depends on the free convection in the liquid phase and also the thermal wake motion induced by rising bubbles under the normal gravity condition, seems to be substituted, under reduced gravity, mostly by the agitation of the thermal boundary layer due to bubble sliding on the heater surface and/or making mutual coalescence.

## Acknowledgments

The present study was financially supported by the Science and Technology Agency, Japan. Novespace, CNES, CEV (Centre d'Essais en Vol de Bretigny) and JGC Corporation provided continuous efforts for the present parabolic flights campaign.

## References

Bland, T. J., Downing, R. S., and Rogers, D. P., 1984, "A Two-Phase Thermal Management System for Large Space Platform," Paper No. AIAA-84-1758.

Ervin, J. S., Merte, H., Jr., Keller, R. B., and Kirk, K., 1992, "Transient Pool Boiling in Microgravity," *Int. J. Heat Mass Transfer*, Vol. 35, pp. 659–674.

Fraaije, J. G. E. M., Cazabat, M., Hua, X., and Cazabat, A. M., 1989, "Dynamic of Stick-Slip Jumps," *Colloids and Surface*, Vol. 41, pp. 77–86.

Lienhard, J. H., 1985, "On the Two Regimes of Nucleate Boiling," ASME JOURNAL OF HEAT TRANSFER, Vol. 107, pp. 262–264.

Merte, H., Jr., 1990, "Nucleate Pool Boiling in Variable Gravity," *Low-Gravity Fluid Dynamics and Transport Phenomena*, Progress in Astronautics and Aeronautics Vol. 130, AIAA, Washington, DC, pp. 15–69.

Moissis, R., and Berenson, P. J., 1963, "On the Hydrodynamic Transitions in Nucleate Boiling," ASME JOURNAL OF HEAT TRANSFER, Vol. 85, pp. 221–229.

Mysels, K. J., and Florence, A. T., 1970, "Techniques and Criteria in the Purification of Aqueous Surfaces," *Clean Surfaces: Their Preparation and Characterization for Interfacial Studies*, Marcel Dekker, New York, pp. 227–268.

Nishikawa, K., Fujita, Y., Uchida, S., and Ohta, H., 1984, "Effect of Surface Configuration on Nucleate Boiling Heat Transfer," *Int. J. Heat Mass Transfer*, Vol. 27, pp. 1559–1571.

Oka, T., Abe, Y., Tanaka, K., Mori, Y. H., and Nagashima, A., 1992, "Observational Study of Pool Boiling under Microgravity," *JSME Int. J. Series II*, Vol. 35, pp. 280–286.

Oka, T., Abe, Y., Mori, Y. H., and Nagashima, A., 1994, "Pool Boiling Heat Transfer Under Microgravity," *Trans. JSME Ser. B*, Vol. 67, pp. 3093–3100 [in Japanese].

Siegel, R., 1967, "Effect of Reduced Gravity on Heat Transfer," *Advances in Heat Transfer*, Vol. IV, Academic Press Inc., New York, pp. 143–228.

Siegel, R., and Usiskin, C., 1959, "A Photographic Study of Boiling in the Absence of Gravity," ASME JOURNAL OF HEAT TRANSFER, Vol. 81, pp. 230–236.

Straub, J., Weinzierl, A., and Zell, M., 1990a, "Thermokapillare Grenzflächenkonvektion an Gasblasen in einem Temperaturgradientenfeld," *Wärme- und Stoffübertragung*, Vol. 25, pp. 281–288.

Straub, J., Zell, M., and Vogel, B., 1990b, "Pool Boiling in a Reduced Gravity Field," *Proc. 9th Int. Heat Transfer Conf.*, Vol. 1, pp. 91–112.

Straub, J., and Vogel, B., 1991, "Heat Transfer Mechanism at Single Bubbles," DFVLR-BPT 82/22.

Straub, J., Zell, M., and Vogel, B., 1992, "Boiling Under Microgravity Conditions," ESA SP-353, pp. 269–297.

Torikai, K., and Yamazaki, T., 1965, "Attaching Area of Boiling Bubbles," *Trans. Japan Soc. Mech. Eng.*, Vol. 31, pp. 440–449 [in Japanese].



Downloaded 12 Dec 2010 to 193.140.21.150. Redistribution subject to ASME license or copyright; see http://www.asme.org/terms/Terms_Use.cfm

# Condensation of a Vapor Flowing Inside a Horizontal Rectangular Duct

**Q. Lu**[1]
Graduate Student.

**N. V. Suryanarayana**
Professor.

Department of Mechanical Engineering
and Engineering Mechanics,
Michigan Technological University,
Houghton, MI 49931

*Condensation of a vapor flow inside a horizontal rectangular duct, using the bottom plate as the only condensing surface, was experimentally investigated. The experimental measurements included condensate film thickness and heat transfer coefficients with R-113 and FC-72. The condensate film thickness, measured with an ultrasonic transducer, was used to obtain the local heat transfer coefficient. The heat transfer coefficient increased with increasing inlet vapor velocity. The rate of increase was enhanced noticeably after the appearance of interfacial waves. Within the limited range of the experimental variables, a correlation between St and $Re_{gL}$ was developed by a linear regression analysis. However, because of the effect of the interfacial waves, instead of a single correlation for the entire range of $Re_{gL}$, two separate equations (one for the wave-free regime and another for the regime with waves) were found. Analytical predictions of heat transfer rates in the annular condensation regime require the proper modeling of the interfacial shear stress. A properly validated interfacial shear stress model with condensation is not yet available. The measurement of condensate film thickness at several axial locations opens the door for determining the local interfacial stress and, hence, a model for the interfacial shear stress.*

## Introduction

In many condensing applications, the condensate is drained by gravity. Condensate draining with vapor shear is encountered in many industrial applications. Also, in low-gravity applications, alternative mechanisms for draining the condensate, such as vapor shear, are needed. Hence, a study of condensation inside horizontal tubes is significant for both space and industrial applications. Many analytical and experimental studies on condensation horizontal tubes have been reported in the literature. For example, Akers et al. (1958) measured the average $h_t$ for R-12 and propane inside horizontal tubes. Increasing the vapor velocity increased the heat transfer coefficient. For condensation of R-113 flowing inside a horizontal tube Chato (1962) found that inclining the tube very slightly with the horizontal plane increased the heat flux; however, when the vapor velocity was high the orientation of the tube was not important. Rosson and Myer (1965) obtained the local $h_x$ during condensation of methanol and acetone inside a horizontal tube. The local heat flux was measured with a heat flux meter. Goodykoontz and Dorsch (1966) measured the temperature gradient of the coolant in the cooling jacket during condensation of R-113 and steam inside a tube. Neglecting axial conduction in the tube they equated the heat flux to the product of the mass rate of the coolant in the jacket, the temperature gradient in the flow direction, and the specific heat of the coolant. Azer et al. (1971) similarly measured local heat fluxes for condensation of R-12 inside horizontal tubes. The results showed that $h_x$ decreased in the direction of flow and increased with the vapor velocity. With steam in a steam–air mixture condensing inside a horizontal square duct, Barry and Corradini (1988) determined $h_x$ by measuring the temperature gradient in the condensing surface. Their conclusions supported those of Azer et al. Analytical results of condensation with vapor flow between parallel plates have been recently reported by Narain (1991), Narain and Kizilyalli (1991), and Narain and Kamath (1991).

During condensation of vapor in a horizontal duct, the smooth annular regime is followed by an annular wavy regime. Both analytical and experimental studies on wave initiation and the effect of interfacial waves on condensation heat transfer have been reported, among others, by Soliman and Berenson (1970), Soliman and Azer (1974), Dukler (1977), Hanratty (1982), Hirschburg and Florschuetz (1982), Jensen and Yuen (1982), and Kocamustafaogullari (1985).

One of the objectives of this research was to determine experimentally the local heat transfer during R-113 and FC-72 condensation in the smooth annular regime, and the incipience of interfacial waves; this paper reports those experimental results.

## Apparatus and Procedure

The schematic of the experimental apparatus is shown in Fig. 1. R-113 and Fluorinert Compound FC-72 were the condensing fluids. The two main parts of the apparatus were a condensation loop and a coolant loop. In the condensation loop vapor was generated in a boiler and admitted to the test section through a converging unit, which provided a uniform velocity profile at inlet to the test section. It consisted of a rectangular section 102 mm high, 102 mm deep, and 200 mm long and was reduced to a width of 40 mm and a height of 25 mm, the same dimensions as the inlet of the test section. The converging unit was packed with 3-mm-dia glass tubes. A diverging section was added at the exit of the test section to prevent disturbances at the exit of the rectangular channel to the circular tube. The condensate in the test section was drained through a measuring glass tube.

The vapor that was not condensed in the test section was condensed in an auxiliary condenser. The condensates from both the test section and the auxiliary condenser were collected and pumped into the boiler. In the coolant loop, the coolant was pumped from a constant temperature bath to the cooling channels in the test section via a set of rotameters and back to the bath.

The horizontal test section, shown in Figs. 2 and 3, was 40 mm wide, 25 mm high, and 1000 mm long. The bottom condensing surface, made of 6.4 mm thick copper plate, was 914 mm long and 40 mm wide. The side and top plates were made of polycarbonate plastic sheets, which permitted visual observation of the flowing condensate.

[1] Current address: Picker International—Dunlee Division, Bellwood, IL 60104.

Contributed by the Heat Transfer Division and based on a paper presented at the ASME Winter Annual Meeting, Anaheim, California, November 8–13, 1992. Manuscript received by the Heat Transfer Division April 1993; revision received June 1994. Keywords: Condensation, Forced Convection, Associate Technical Editor: L. C. Witte.



Copyright © 1995 by ASME

Downloaded 12 Dec 2010 to 193.140.21.150. Redistribution subject to ASME license or copyright; see http://www.asme.org/terms/Terms_Use.cfm

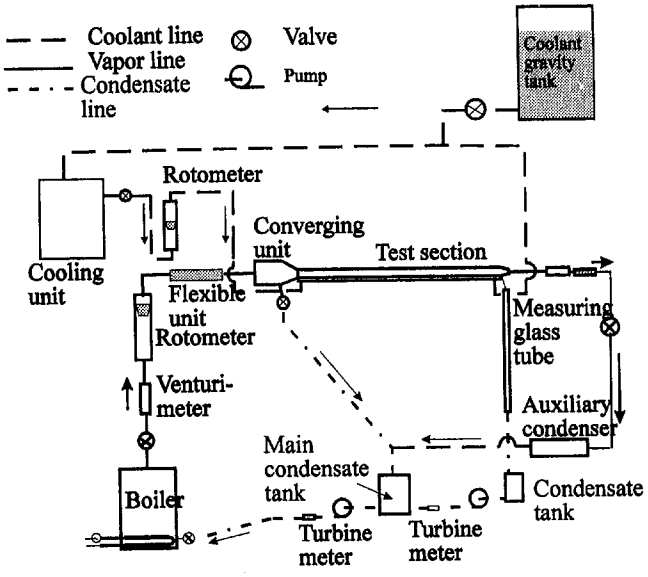



Fig. 1 Schematic of experimental apparatus

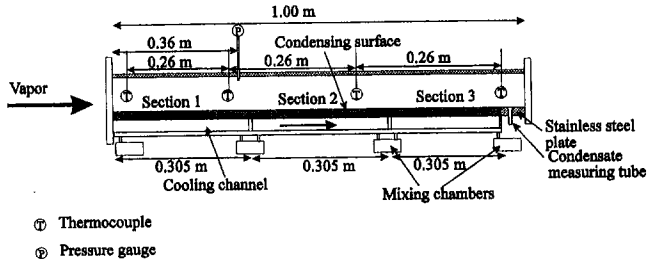



Fig. 2 Details of test section

The cooling channel underneath the condensing surface had sides of brass and the bottom was polycarbonate plastic. The channel was divided into three sections (in the direction of flow of the vapor) with plexiglass separators, each section being 305 mm long, 17.5 mm deep, and 40 mm wide. The coolant from the exit of each channel passed through a mixing chamber before it entered the next channel. The mixing chamber mixed the coolant so that the temperature measured in the chamber represented the bulk temperature of the coolant at the exit from a section of the channel.

The vapor flow at the inlet to the test section was measured by a rotameter. The condensate flow rate from the test section was found by measuring the time required to collect a known volume of the condensate in the measuring gage glass at the end of the test section.

The temperature of vapor in the test section was measured by four thermocouples equally spaced along the centerline of the test section (Fig. 2). The temperature of the condensing surface was measured by eight thermocouples embedded in the condensing plate (Fig. 3). Each thermocouple junction was placed near the condensing surface through a 1.2 mm I.D. hole in the copper plate and soldered to the condensing surface. The temperature difference of the coolant across each section of the cooling channel was measured with a differential thermocouple placed inside each mixing chamber. The total temperature difference was also measured with a differential thermocouple placed at the inlet and the outlet of the coolant to the test section. The vapor pressure, measured with a Bourdon-type pressure gage, yielded the saturation temperature of the vapor.

The film thickness was measured at five locations by an ultrasonic transducer. As the signal from the transducer was significantly attenuated through the copper plate, aluminum plugs were inserted into the condensing surface at those locations where the film thickness was to be measured. The attenuation of the signal through the aluminum plug was much less than through the copper plate. To measure the film thickness, the sonic velocity of the two fluids was determined in a separate calibration device. In the device the time delay between the reflections of the ultrasonic signal at the liquid–solid interface and the liquid–vapor interface was measured with an oscilloscope. The sonic velocities determined from the device were compared to published values and were found to be within 7 percent for R-113 and 1.5 percent for FC-72. By measuring the time delay with an oscilloscope between the signals reflected at condensing surface–condensate interface and condensate–vapor interface in the test section and relating it to the sonic velocity, the film thickness was computed.

The total heat transfer rate in the test section was determined from the measured mass flow rate of the coolant and its temperature rise across the whole cooling channel. This was compared to the heat transfer rate obtained from the computed value of the net enthalpy flow into the test section (the difference between the enthalpy associated with the vapor into the test section and the enthalpy associated with the vapor and the condensate at the exit of the test section). The difference between the two measured values was usually within 5 percent. If the difference between the two values was greater than 10 percent, the experimental data were discarded and the experiment repeated. The heat transfer rate to the coolant was used in processing the data. The heat transfer rate across each section was computed from the mass flow rate of the coolant and the temperature rise of the coolant across each section.

The air in the condensation loop was removed using a vacuum pump. The walls of the test section, the converging unit, and the vapor line were heated to about 5°C above the expected vapor saturation temperature using heating elements wrapped around the tubes leading to the test section. An additional heating ele-

## Nomenclature

$C_{pl}$ = specific heat of condensate
$D_H$ = hydraulic diameter of duct
$G$ = vapor mass velocity
$h_{fg}$ = enthalpy of vaporization
$h_s$ = sectional heat transfer coefficient
$h_t$ = average heat transfer coefficient
$h_x$ = local heat transfer coefficient
Ja = Jakob number = $C_{pl}\Delta T/h_{fg}$
$k_l$ = thermal conductivity of condensate
$L$ = total length of condensing surface
$\dot{m}_t$ = mass flow rate of the vapor at the inlet of the test section
$\mathrm{Nu}_i$ = Nusselt number with the average heat transfer coefficient from the leading edge to the trailing edge of section $i$
$\mathrm{Nu}_t$ = average Nusselt number for the entire condensing surface = $h_t L/k_l$
$\mathrm{Pr}_l$ = condensate Prandtl number
$q''$ = average heat flux to the coolant
$\mathrm{Re}_{gL}$ = inlet vapor Reynolds number = $v_{gi}L/\nu_g$
St = Stanton number = $\mathrm{Nu}_t/(\mathrm{Re}_{gL}\mathrm{Pr}_l)$
$\Delta T$ = difference between saturation temperature of vapor and condensing surface temperature
$v_{gi}$ = vapor velocity at the inlet of the test section
$x$ = axial distance from the leading edge of the condensing surface
$\delta$ = condensate film thickness
$\mu_g$ = dynamic viscosity of gas
$\mu_l$ = dynamic viscosity of condensate
$\nu_g$ = kinematic viscosity of gas
$\rho_g$ = density of vapor
$\rho_l$ = density of condensate



Downloaded 12 Dec 2010 to 193.140.21.150. Redistribution subject to ASME license or copyright; see http://www.asme.org/terms/Terms_Use.cfm

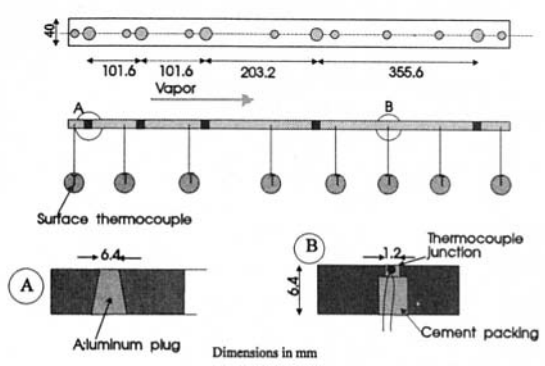



**Fig. 3 Details of condensing surface**

ment was placed on top of the test section to prevent condensation on the upper surface of the test section. The vapor flow rate to the test section was adjusted by regulating the power supply to the heating element in the boiler. The vapor temperature at inlet to the test section was maintained approximately 3°C above the saturation temperature by controlling the power supply to the heating element wrapped around the tubes between the boiler and the test section. A desired average condensing surface temperature was achieved by regulating the flow rate and the temperature of coolant to the cooling channel. The variation of the surface temperature along the test section from its average value was usually within 1.25°C. The total rise of the temperature of the coolant across the cooling channel was maintained at about 5°C. Steady state was assumed when the changes in the vapor flow rate, the condensate flow rate from the test section, the condensing surface temperature, and the total temperature difference in the temperature of the coolant across the cooling channel were within 1.5 percent over a period of 45 minutes to 1 hour.

A data acquisition system (consisting of a DT-100 data logger, made by ZiTech, and a PC computer) was used to collect the thermocouple voltages. The properties of R-113 and FC-72 were taken from the *ASHRAE Handbook* (1985) and the 3M Product Manual for Fluorinert™ Electronic Liquids (1989). Relevant properties of R-113 and FC-72 are given in Table 1.

Uncertainties were estimated by the method suggested by Kline and McClintock (1953). They are ±14 percent for the heat transfer coefficient, Nusselt and Stanton numbers, and ±2 percent for the inlet vapor velocity and inlet Reynolds number. The main causes of the uncertainties in the heat transfer coefficient were the uncertainties in the heat transfer rates and the surface temperature.

Details of the experimental setup and data are available in Lu (1992).

## Results and Discussion

There were 118 valid runs of experimental data with R-113 and 75 runs with FC-72. The two main variables in the experiment were the inlet vapor velocity to the test section ($v_{gi}$) and the difference between the saturation vapor temperature and the condensing surface temperature ($\Delta T$). Table 2 lists the range of the values of $v_{gi}$ and $\Delta T$ in the experiment. The ratio of the mass rate of condensation in the test section to the mass flow rate of vapor into the test section varied from 5 percent to 42 percent.

**Table 1 Thermodynamic properties of R-113 and FC-72**

| | R-113 | FC-72 |
|---|---|---|
| Saturation temperature, °C | 50 | 60 |
| Saturation pressure, kPa | 109.3 | 112.4 |
| Density of condensate, kg/m$^3$ | 1501.7 | 1604.2 |
| Density of vapor, kg/m$^3$ | 8.0 | 14.7 |
| Enthalpy of vaporization, kJ/kg | 142.8 | 84.1 |
| Liquid thermal conductivity, mW/m K | 70.1 | 54.4 |
| Specific heat, J/kg K | 986 | 1101 |
| Prandtl number of liquid | 7.1 | 5.4 |

**Table 2 Ranges of variables**

| Fluid | $v_{gi}$, m/s | $\Delta T$, °C |
|---|---|---|
| R-113 | 0.3–4.4 | 10–40 |
| FC-72 | 0.4–3.1 | 10–50 |

The condensate flow patterns along the condensing surface were observed visually. The flow of the condensate was either smooth or wavy, depending on the magnitudes of $v_{gi}$ and $\Delta T$. The conditions at which the wavy flow appeared are given in Table 3. In the wavy regime, both two-dimensional (2-D) and three-dimensional (3-D) interfacial waves were observed. The 2-D waves had a well-defined wavelength, while the 3-D waves were rather randomly shaped (having a pebble shape). At low values of $v_{gi}$ (less than about 1.5 m/s with R-113 and less than 1.1 m/s with FC-72) the condensate film was smooth. As the velocity was increased 2-D waves appeared near the exit of the test section and moved towards the inlet. At higher velocities, 3-D waves appeared after the 2-D waves along the condensing surface. At higher values of the inlet vapor velocity, 3-D waves occurred all along the condensing surface. Table 4 gives the values of $v_{gi}$ at which the 3-D waves covered the entire condensing surface.

To represent the data in dimensionless form, an appropriate characteristic length is needed to form the Reynolds and Nusselt numbers. If the velocity and temperature profiles are fully developed an appropriate characteristic length is the height or the hydraulic mean diameter of the duct. But, in the experiments the velocity at the test section inlet from the converging unit was close to a uniform velocity profile and the temperature profile was uniform. Hence the vapor flows as a boundary layer over the condensate; thus unless the boundary layer thickness is equal to half the height of the duct, an appropriate length is the axial distance from the leading edge. Boundary layer thickness estimates showed that even at the lowest flow rate, the boundary layer thickness at the exit was less than half the height of the test section. Hence the distance from the leading edge was chosen to form the Reynolds and Nusselt numbers.

The film thickness $\delta$ was measured when the vapor–condensate interface was smooth or wavy with small amplitude waves. As shown in Figs. 4($a$) and 4($b$) the film thickness increased rapidly near the leading edge of the condensing surface; but the rate of increase decreased with the axial distance from the leading edge. With increasing $v_{gi}$, $\delta$ decreased, but near the trailing edge of the condensing surface, the effect of $v_{gi}$ on $\delta$ became very small. With an increase in $v_{gi}$ higher momentum and interfacial stress leads to a thinning of the condensate film, which, in turn, results in a higher $h_x$ and an increase in the condensation rate. The higher condensate flow is accommodated in a thinner condensate film with an increase in the average velocity of the condensate (and a higher interfacial shear stress). The film thicknesses of both R-113 and FC-72 had the same trends.

**Table 3 Inlet velocities (m/s) for wave initiation**

| $\Delta T$, °C | R-113 | FC-72 |
|---|---|---|
| 10 | 1.59 | 1.13 |
| 20 | 1.40 | 1.09 |
| 30 | 1.27 | 0.9 |
| 40 | 1.27 | 0.84 |
| 50 | | 0.81 |



Downloaded 12 Dec 2010 to 193.140.21.150. Redistribution subject to ASME license or copyright; see http://www.asme.org/terms/Terms_Use.cfm

**Table 4 Inlet velocities (m/s) for 3-D waves**

| $\Delta T$, °C | R-113 | FC-72 |
|---|---|---|
| 10 | 2.20 | 1.8 |
| 20 | 1.78 | 1.60 |
| 30 | 1.73 | 1.38 |
| 40 | 1.52 | 1.34 |
| 50 | | 1.3 |

The variation of $h_t$ with $v_{gi}$ is shown in Fig. 5. At low values of $v_{gi}$, $h_t$ increased slightly with the vapor velocity. Beyond a certain value of $v_{gi}$ the increase in $h_t$ with $v_{gi}$ was much greater.

Figures 6($a$) and 6($b$) show typical distributions of the sectional heat transfer coefficients ($h_s$ over a particular section of the condensing surface). For both R-113 and FC-72, $h_s$ decreased along the condensing surface and $h_s$ in section 1 was much higher than in other sections. For equal values of $\Delta T$, for lower $\dot{m}_t$, $h_s$ with R-113 was higher than with FC-72; for higher $\dot{m}_t$, the reverse happened. This is consistent with the results shown in Fig. 5. With R-113 $h_t$ was slightly higher than with FC-72 when $v_{gi}$ was lower (lower $\dot{m}_t$). However, at higher $v_{gi}$, $h_t$ with R-113 was lower than with FC-72. At higher $v_{gi}$ interfacial waves appeared on the condensing surface. The interfacial waves affect the heat transfer process, but the extent of the effect may vary for different condensing fluids. The noticeable change of the heat transfer coefficients with R-113 and FC-72 at higher $v_{gi}$ is due to the effect of the interfacial waves on the heat transfer rates.

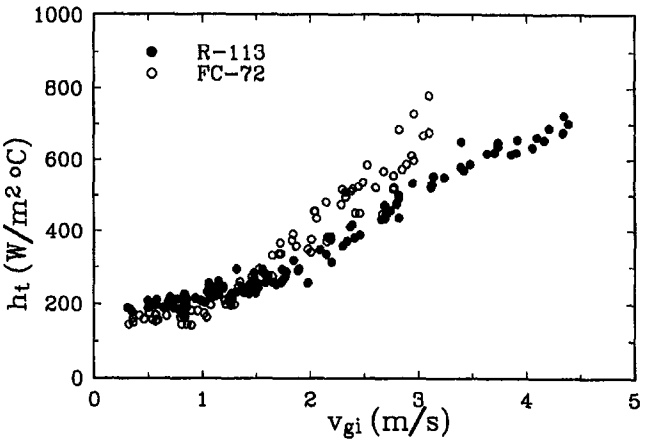
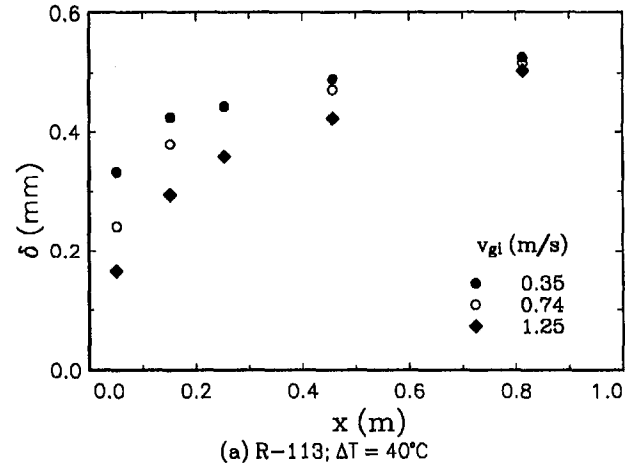


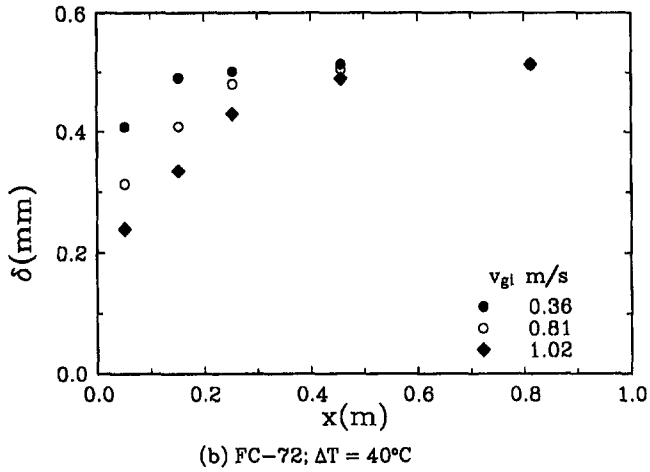

**Fig. 5 Average heat transfer coefficient**

Using the measured values of $\delta$, $h_x$ was determined. In the experiments, it was found that $\delta$ was less than 0.6 mm. As in most analyses on film condensation, when the film thickness is small, the temperature distribution within the condensate film is assumed to be linear. Hence, the local heat transfer coefficient can be expressed as

$$h_x = \frac{k_l}{\delta} \tag{1}$$

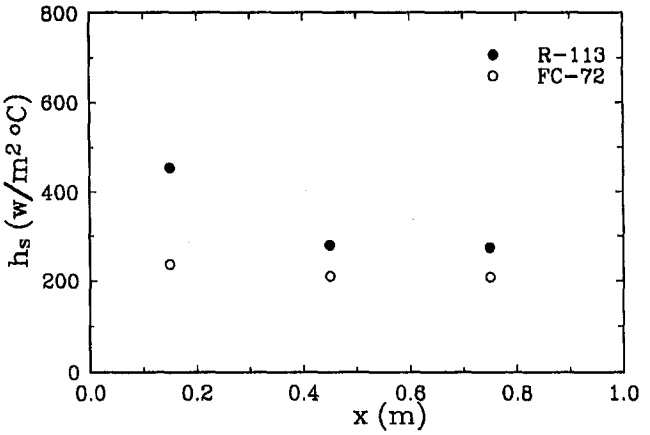



(a) R−113; ΔT = 40°C

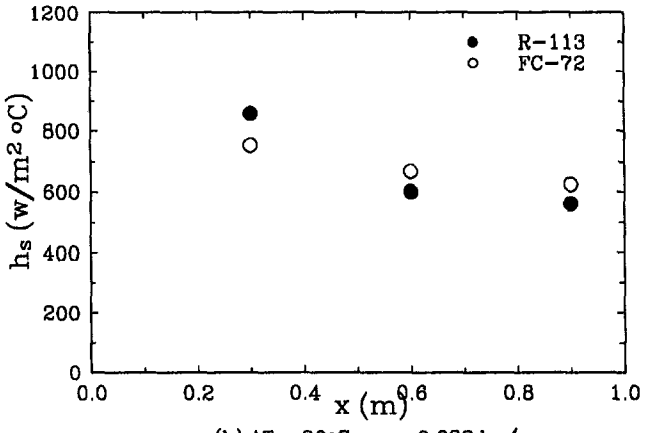



(b) FC−72; ΔT = 40°C

**Fig. 4 Condensate film thickness**




(a) ΔT = 20°C, $m_t$ = 0.016 kg/s

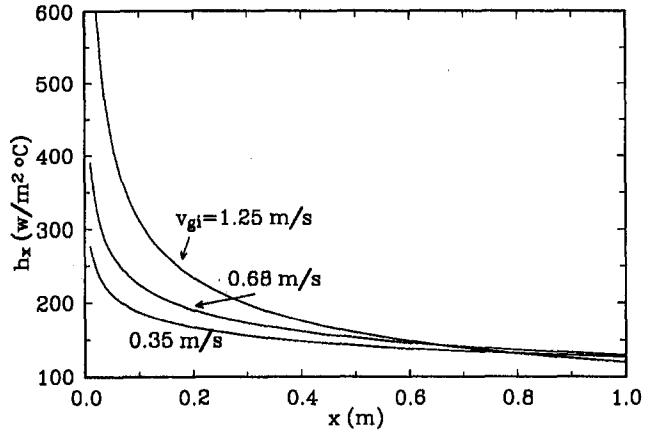



(b) ΔT = 20°C; $m_t$ = 0.032 kg/s

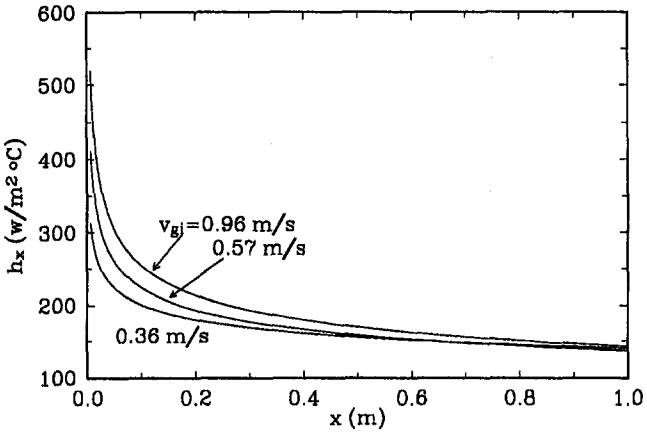
**Fig. 6 Sectional heat transfer coefficient**



Downloaded 12 Dec 2010 to 193.140.21.150. Redistribution subject to ASME license or copyright; see http://www.asme.org/terms/Terms_Use.cfm




(a) R−113; Δ T=20°C




(b) FC−72, ΔT = 20°C

**Fig. 7 Local heat transfer coefficient**

Assuming a power law relation between $\delta$ and $x$

$$\delta = c_1 x^{c_2} \tag{2}$$

where $c_1$ and $c_2$ are constants determined by a regression analysis from the measured values of $\delta$. Substituting Eq. (2) into Eq. (1) yields

$$h_x = \frac{k_l}{c_1} x^{-c_2} \tag{3}$$

Figures 7(*a*) and 7(*b*) show some typical trends of variation of $h_x$ with $x$. $h_x$ increased with $v_{gi}$. The effect of $v_{gi}$ decreased with increasing $x$. Close to the trailing edge of the surface, the effect of the vapor velocity became negligible.

There is a substantial amount of experimental results with steam. The main difficulties in comparing our results to many of the reported results are the difference in the geometry and the manner in which the results are reported. Instead of comparing individual results, we compared our results with the correlations proposed by Soliman et al. (1968), Azer et al. (1971), Traviss et al. (1973), and Shah (1979). The correlations are curve fits of a large number of the reported results for circular tubes.

The correlation of Traviss et al. followed the same trend for $h_x$. The correlations by Azer et al. and Soliman et al. predict much lower $h_x$ near the trailing edge. Shah's correlation is not suitable near the leading edge; at the leading edge the quality is close to 1 and it predicts very low values of $h_x$. The trends of $h_x$ in the present experiment were quite similar to those in the experiments

**Table 5 Average deviations of sectional and total heat transfer coefficients**

| | Deviation, percent | | | |
|---|---|---|---|---|
| | Section 1 | Section 2 | Section 3 | Total |
| Soliman | 22.2 | 237.0 | 31.9 | 22.2 |
| Azer | 30.3 | 39.9 | 37.8 | 29.9 |
| Traviss | 50.8 | 27.2 | 24.6 | 36.7 |
| Shah | 27.9 | 30.3 | 29.5 | 20.7 |

of Barry and Corradini (1988) and Traviss et al. (1973). Azer et al. (1971) also reported that $h_x$ decreased along the condensing surface and increased with the vapor velocity. However, their results showed that $h_x$ varied nearly linearly along the condensing surface, which was not the case in the present experiments. A comparison of the sectional and total average heat transfer coefficients with the predictions is given in Table 5. The comparisons are not an indication of either the accuracy of our data or the validity of the correlations but merely show how well the correlations predict $h_s$ and $h_t$ in a different geometry.

A comparison of the present experimental data with those of Akers and Rosson (1960) with a 9.5-mm-I.D. tube is shown in Fig. 8. Akers and Rosson used the hydraulic mean diameter as the characteristic dimension. With only the bottom surface as the condensing surface, a very small condensate film thickness, and a top adiabatic surface in our experiments, we used twice the height of the duct as the characteristic dimension. The trend in the two sets of data is similar at low values of the parameter $[D_H G/I_l(\rho_l/\rho_g)^{1/2}]$ but at higher values the slopes are different. The change in the slope of our data is clearly attributable to the onset of waves. Although there is no such break in data of Akers and Rosson (1960), a break was found in the data of Akers et al. (1958).

As a check of the validity of the method of using measured $\delta$ to obtain $h_x$, Eq. (3) was integrated (with the assumption of uniform $\Delta T$) to calculate $h_s$ and $h_t$. The calculated values were then compared with those measured from the heat balance on the coolant. The difference between the two values was within 15 percent with an average deviation of 12 percent.

A dimensional analysis showed that the parameters that describe the condensation process included the Nusselt number (or the Stanton number) and the Reynolds number. From the experimental data, values of $h_t$ from the leading edge to the trailing edge of each section were determined. The Nusselt numbers formed with the average heat transfer coefficients are represented by $\mathrm{Nu}_t$; as the trailing edge of section 3 is also the trailing edge of the condensing surface, $\mathrm{Nu}_t$ and represents $\mathrm{Nu}_3$. The effect of

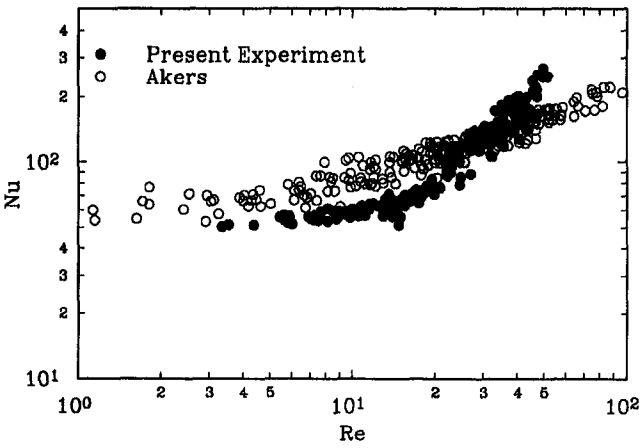



**Fig. 8 Comparison of present data with those of Akers and Rosson**



Downloaded 12 Dec 2010 to 193.140.21.150. Redistribution subject to ASME license or copyright; see http://www.asme.org/terms/Terms_Use.cfm

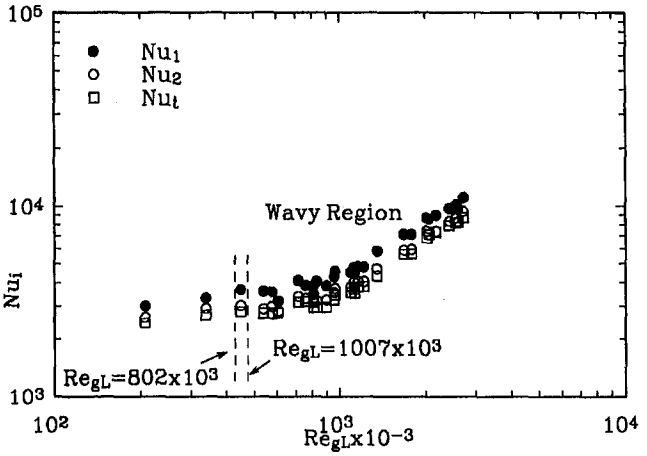
$Re_{gL}$ on $Nu_i$, the Nusselt number based on the average heat transfer coefficient up to the trailing edge of section $i$, is shown in Figs. 9(*a*) and 9(*b*). In the figures, $Re_{gL}$ at which interfacial waves appeared is denoted by a pair of dashed lines. Before the initiation of the interfacial waves, $Nu_i$ increased slightly with an increase in $Re_{gL}$. After the onset of interfacial waves, the increase in $Nu_i$ is much more significant. The influence of the interfacial waves is also demonstrated in Fig. 10 of St as a function of $Re_{gL}$. In the smooth flow region St decreases sharply with $Re_{gL}$; in the wavy flow region St is nearly constant.

Figure 10 clearly shows that, for the geometry considered, St correlates with $Re_{gL}$. However, because of the effect of the interfacial waves, which set in at $Re_{gL} \approx 10^6$, two distinct trends (before and after the onset of the waves) are observed. Therefore, instead of finding a single correlating equation over the entire range of $Re_{gL}$, two equations were found from a regression analysis.

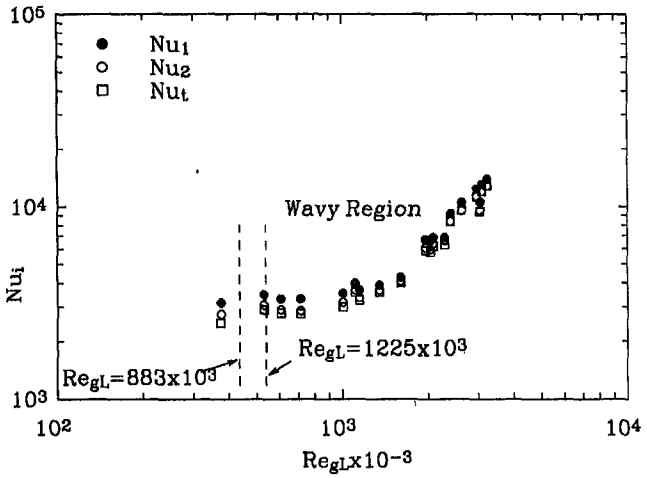
$$Re_{gL} < 10^6 \text{ (smooth regime)} \quad St = 4.63\ Re_{gL}^{-0.77} \qquad (4)$$

$$Re_{gL} > 10^6 \text{ (wavy regime)} \quad St = 2.38 \times 10^{-5}\ Re_{gL}^{0.11} \qquad (5)$$

The average deviation between the values predicted by Eqs. (4) and (5) and experimental values is ±8.8 percent. An examination of Eq. (5) shows that St is practically constant in the wavy regime, increasing very slightly with $Re_{gL}$.




(a) R−113; ΔT = 20°C




(b)FC−72; ΔT = 20°C

**Fig. 9 Average Nusselt number as a function of Reynolds number**

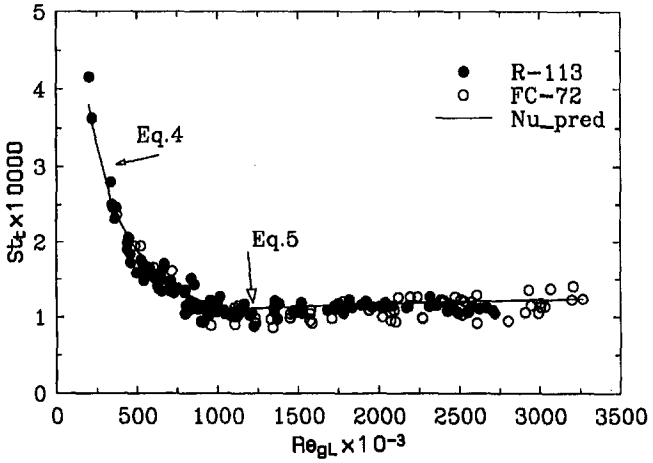



**Fig. 10 Stanton number as a function of Reynolds number**

## Conclusions

1 The condensate film thickness was thin (less than 0.6 mm). The film thickness increased rapidly at the leading edge of the condensing surface and was almost constant at the trailing edge. The film thickness decreased with increasing inlet vapor velocity.

2 The average heat transfer coefficients increased with increasing inlet vapor velocity. After interfacial waves appeared, the heat transfer coefficients increased significantly. It appears that the effect of interfacial waves became significant when $Re_{gL} > 1{,}000{,}000$.

3 Within the limited range of variables in the experiments, the Stanton number was correlated with the inlet vapor Reynolds number by a power law relation. However, to accommodate the effect of the interfacial waves two different correlating equations were found.

4 The effect of $\Delta T$ on the heat transfer of the condensation was also investigated. However, the trends are not yet conclusive. From a dimensional analysis Nu should depend on $Pr_l$, $\rho_g/\rho_l$, $\mu_g/\mu_l$, and Ja. In their analysis of a similar situation Narain and Kizilyalli (1991) confirm such a dependence. In the experiments there was either a very limited variation or no variation of the parameters listed. Further studies are necessary to establish the influence of all the parameters.

## Acknowledgments

The paper reports a part of the results of a project on condensation heat transfer. The support of the project by NASA-Lewis under grant No. NAG 3-711 and of Mr. John McQuillen, monitor, is gratefully acknowledged. The donation of FC-72 liquid by the 3-M Company is sincerely appreciated.

## References

Akers, W. W., Dean, H. A., and Crosser, O., 1958, "Condensing Heat Transfer Within Horizontal Tubes," *Chem. Engg. Prog.*, Vol. 54, No. 10, pp. 89–90.

Akers, W. W., and Rosson, H. E., 1960, "Condensation Inside a Horizontal Tube," *Chem. Eng. Prog. Symp. Series, Heat Transfer Storrs,* Vol. 56, No. 30, pp. 145–149.

*ASHRAE Handbook of Fundamentals,* 1985, ASHRAE, Atlanta, GA.

Azer, N. Z., Abis, L. V., and Swearingen, T. B., 1971, "Local Heat Transfer Coefficients During Forced Convection Condensation Inside Horizontal Tubes," *Trans. ASHRAE,* Vol. 77, pp. 182–201.

Barry, J. J., and Corradini, M. L., 1988, "Film Condensation in the Presence of Interfacial Waves," *Proceedings, National Heat Transfer Conference,* Houston, TX, Vol. 2.

Chato, J. C., 1962, "Condensation Inside Horizontal and Inclined Tubes," *ASHRAE Journal,* Vol. 4, pp. 52–60.

Dukler, A. E., 1977, "The Role of Waves in Two-Phase Flow: Some New Understandings," *Chem. Eng. Education,* Summer, pp. 108–117.

Fluorinert Electronic Liquids Product Manual, 1989, 3M Industrial Chemicals Products Division, St. Paul, MN.



Downloaded 12 Dec 2010 to 193.140.21.150. Redistribution subject to ASME license or copyright; see http://www.asme.org/terms/Terms_Use.cfm

Goodykoontz, J. H., and Dorsch, R. G., 1966, "Local Heat Transfer for Condensation of Steam in Vertical Downflow Within a 5/8 Inch-Diameter Tube," NASA-TN-D-3952.

Hanratty, T. J., 1982, "Interfacial Instabilities Caused by Air Flow Over a Thin Liquid Layer," in: *Waves on Fluid Interface, Proc. Symp. Math. Rec. Center,* The University of Wisconsin, Madison, R. E. Meyer, ed., Academic Press.

Hirschburg, R. I., and Florschuetz, L. W., 1982, "Laminar Wavy-Film Flow: Part II, Condensation and Evaporation," ASME JOURNAL OF HEAT TRANSFER, Vol. 104, pp. 459–464.

Jensen, R. J., and Yuen, M. C., 1982, "Local Heat and Mass Transfer Correlation in Horizontal Stratified Concurrent Flow," *Proc. 7th Int. Heat Transfer Conf.,* Munich, pp. 95–100.

Kline, S. J., and McClintock, F. A., 1953, "Description of Uncertainties in Single Sample Experiments," *Mech. Eng.,* Vol. 75, Jan., pp. 3–8.

Kocamustafaogullari, G., 1985, "Two-Fluid Modeling in Analyzing the Interfacial Stability of Liquid Film Flows," *Int. J. Multiphase Flow,* Vol. 11, p. 63.

Lu, Q., 1992, "An Experimental Investigation of Heat Transfer With Condensation in a Horizontal Rectangular Duct," Ph.D. Thesis, Michigan Technological University, Houghton, MI.

Narain, A., 1991, "Condensing Vapor Flows and the Case of Flow Between Parallel Plates," *Recent Advances in Mechanics of Structured Continua,* ASME AMD-Vol. 117, pp. 47–53.

Narain, A., and Kamath, R., 1991, "Internal Flows of Vapor Undergoing Film Condensation," *Proceedings of the Twenty Second Midwestern Mechanical Conf., Development in Mechanics,* Vol. 16, University of Missouri, Rolla, pp. 411–412.

Narain, A., and Kizilyalli, Y., 1991, "Pressure Driven Flow of Pure Vapor Undergoing Laminar Film Condensation Between Parallel Plates," *International Journal of Non-linear Mechanics,* Vol. 26, pp. 501–520.

Rosson, H. E., and Myer, J. A., 1965, "Point Values of Condensing Film Coefficient Inside a Horizontal Pipe," *Chem. Engg. Prog. Symp. Series,* Vol. 59, No. 61, pp. 190–199.

Shah, R. M., 1979, "A General Correlation for Heat Transfer During Film Condensation Inside Pipes," *Int. J. Heat Mass Transfer,* Vol. 22, pp. 547–556.

Soliman, M., Schuster, J. R., and Berenson, P. J., 1968, "A General Heat Transfer Correlation for Annular Condensation," ASME JOURNAL OF HEAT TRANSFER, Vol. 90, pp. 267–276.

Soliman, M., and Berenson, P. J., 1970, "Flow Stability and Gravitational Effects in Condenser Tubes," *Proc. 4th Int. Heat Transfer Conf.,* Vol. 6, Paris.

Soliman, H. M., and Azer, N. Z., 1974, "Visual Studies of Flow Patterns During Condensation Inside Horizontal Tubes," *5th Int. Heat Transfer Conference,* Tokyo, Vol. III, 241–245.

Traviss, D. P., Rohsenow, W. M., and Baron, A. B., 1973, "Forced-Convection Condensation Inside Tubes: A Heat Transfer Equation for Condenser Design," *ASHRAE Trans.,* Vol. 79, Part 1, pp. 157–165.



Downloaded 12 Dec 2010 to 193.140.21.150. Redistribution subject to ASME license or copyright; see http://www.asme.org/terms/Terms_Use.cfm

# Exact Solution to the One-Dimensional Inverse-Stefan Problem in Nonideal Biological Tissues

**Y. Rabin**

**A. Shitzer**

Department of Mechanical Engineering,
Technion - Israel Institute of Technology,
Haifa 32000, Israel

*A new analytic solution of the inverse-Stefan problem in biological tissues is presented. The solution, which is based on the enthalpy method, assumes that phase change occurs over a temperature range and includes the thermal effects of metabolic heat generation, blood perfusion, and density changes. As a first stage a quasi-steady-state solution is derived, defined by uniform velocities of the freezing fronts and thus by constant cooling rates at those interfaces. Next, the fixed boundary condition leading to the quasi-steady state is calculated. It is shown that the inverse-Stefan problem may not be solved exactly for a uniform initial condition, but rather for a very closely approximating exponential initial condition. Very good agreement is obtained between the new solution and an earlier one assuming biological tissues to behave as pure materials in which phase change occurs at a single temperature. A parametric study of the new solution is presented taking into account property values of biological tissues at low freezing rates typical of cryosurgical treatments.*

## Introduction

The freezing response of most biological tissues can be generalized by a theory known as the "two-factor hypothesis" of freezing damage (Mazur et al., 1972). The recovery of frozen biological tissue reveals an optimum cooling rate, which suggests this hypothesis. Tissue destruction at low cooling rates is linked to the "solution effect" whereas tissue destruction at high cooling rates is linked to the formation of intracellular ice (Mazur, 1963; Fahy, 1981; McGrath 1993). It is generally accepted that at those widely different cooling rates maximal destruction of biological tissues is achievable (Farrant, 1971; Akhtar et al., 1979; Gage et al., 1985; Miller and Mazur, 1976; Augustynowicz and Gage, 1985). These cooling rates, of the order of a few or hundreds of degrees Centigrade per minute, respectively, may vary among different tissues (Rubinsky and Onik, 1991).

Freezing at low cooling rates is better suited for cryosurgical applications as it allows deeper penetration of the cryotreatment. Therefore, one of the most important criteria for the success of a cryosurgical treatment is the maintenance of a desired low cooling rate at the freezing front during phase change (Orpwood, 1981).

In typical cryosurgical processes, the cooling rates vary throughout the tissue. An appropriate analysis of this problem, termed the Stefan problem, would facilitate the prediction of these variable cooling rates, and the location of the freezing front, e.g., Carslaw and Jaeger (1959). In these processes the variation of the temperature forcing function as effected by the cryoprobe, is specified as a boundary condition in the solution.

There also exists another family of solutions for phase change problems known as the inverse-Stefan problems. In this class of problems the desired cooling rate at the freezing front is the required boundary condition, whereas the temperature forcing function, at the interface with the cryoprobe, is calculated by the analysis. In this paper, we address this class of inverse-Stefan problems, namely, calculate the temperature forcing function, which is required to achieve certain desired cooling rates at the phase-change front in the tissue.

Phase change in a biological tissue, which is a nonideal material, occurs over a relatively wide temperature range. The upper limit of this range may be between −0.5°C and −1°C, whereas the lower limit may be between −5°C and −8°C (Altman and Dittmer, 1971; Wessling and Blackshear, 1973). This range of temperatures within which phase transition occurs excludes the application of existing analytic solutions to the inverse-Stefan problems, which assume phase change to occur at a single temperature (Carslaw and Jaeger, 1959; Rubinsky and Shitzer, 1976; Alexiades and Solomon, 1993). The only existing approximate analytic solution by Budman et al. (1993), which treats the biological tissue as a nonideal material, does not include heating due to metabolic processes nor does it account for the effects of blood perfusion. Rubinsky (1989) developed a microscopic scale model describing the relationship between heat and mass transfer and the response of the cells and blood vessels. The analysis is limited to cases without blood perfusion.

This paper presents an exact analytic solution to the inverse-Stefan problem in a biological tissue. The tissue is treated as a nonideal substance, freezing over a range of temperatures, which includes both metabolic heat and blood perfusion effects. The solution presented is based on the enthalpy method, which assumes that the latent heat of solidification is incorporated into the specific heat. Initially, the solution to the quasi-steady-state inverse-Stefan problem is presented. Based on this solution, a boundary condition that yields this quasi-steady state, is calculated.

The solution presented is general and is applicable to nonbiological materials by simply setting metabolic heat and blood perfusion to zero. Applications are numerous, including calculation of optimal cooling rates in food processing, prevention of thermal stresses in metal casting processes, etc.

## Problem Definition

The peak phase-change temperature $T_{m1}$ is defined as that at which the specific heat function attains a maximal value, Fig. 1. Enclosing this temperature are two regions undergoing phase transition: region [1] in which the temperature is below the upper limit of the phase-change temperature range, $T_{m1} \leq T \leq T_{ml}$, and

Contributed by the Heat Transfer Division for publication in the JOURNAL OF HEAT TRANSFER. Manuscript received by the Heat Transfer Division November 1993; revision received July 1994. Keywords: Phase-Change Phenomena, Transient and Unsteady Heat Transfer. Associate Technical Editor: R. Viskanta.



Copyright © 1995 by ASME

Downloaded 12 Dec 2010 to 193.140.21.150. Redistribution subject to ASME license or copyright; see http://www.asme.org/terms/Terms_Use.cfm

region [2] in which the temperature is above the lower limit of the phase-change temperature range, $T_{mf} \leq T \leq T_{m1}$. All in all, we identify four regions in the medium: unfrozen, frozen, and the two regions in the phase transition range. These regions are separated by three freezing fronts, $s_f$, $s_1$ and $s_l$, defined by the isotherms $T_{mf}$, $T_{m1}$, and $T_{ml}$, respectively, Fig. 1.

It is noted that the division of the domain into four regions and the definition of freezing front $s_1$ is due to mathematical considerations and does not bear any physiological significance. This division facilitates the inclusion of the variations of the thermophysical properties in the solution as assumed in Fig. 1.

The one-dimensional, analytic solution is developed for the following conditions:

($a$) The thermal conductivity is assumed to behave like a three-step temperature dependent function, Fig. 1. Previous solutions treated this property as a one-step (Rubinsky and Shitzer, 1976) or a two-step function (Budman et al., 1993). The present assumption moderates heat fluxes at the various boundaries and further provides for a more realistic depiction of the realistic conditions.

($b$) The volumetric specific heat is assumed to vary linearly throughout regions [1] and [2], Fig. 1. According to the enthalpy method, or the "weak solution" (Goodman, 1958; Voller, 1986), the coefficients of the specific heat function in these regions may be calculated by the known peak phase-change temperature and the latent heat.

($c$) During phase change there is a volume change, while the density is assumed constant in each region. This volume change is included in the volumetric specific heat discussed in section ($b$) above.

($d$) Blood perfusion in the unfrozen region is constant and uniform. This condition approximates closely peripheral tissues, which are supplied by a dense network of capillaries at relatively low blood perfusion rates.

($e$) Metabolic heat generation in the unfrozen region is constant and uniform.

($f$) The tissue is assumed to be depicted by a semi-infinite, thermally homogeneous medium.

($g$) Initially the temperature is uniform throughout the tissue.

In contrast to the existing analytic solutions of closely related problems (Carslaw and Jaeger, 1959; Rubinsky and Shitzer, 1976; Alexiades and Solomon, 1993; Budman et al., 1995), the quasi-steady-state problem is treated first. Subsequently, a forcing function is calculated at the interface between the tissue and the cryoprobe. A quasi-steady state is defined as a full steady state in a system of coordinates that follows the three freezing fronts, Fig. 2. Thus, at this state all freezing fronts advance at a constant and equal velocity and there is no change in the extent of the frozen region. It follows that in a quasi-steady state the cooling rates at the various freezing fronts are constant but may be different from one front to the other. Moreover, there may be a difference in the cooling rates on either side of any front due to the change in the thermophysical properties.

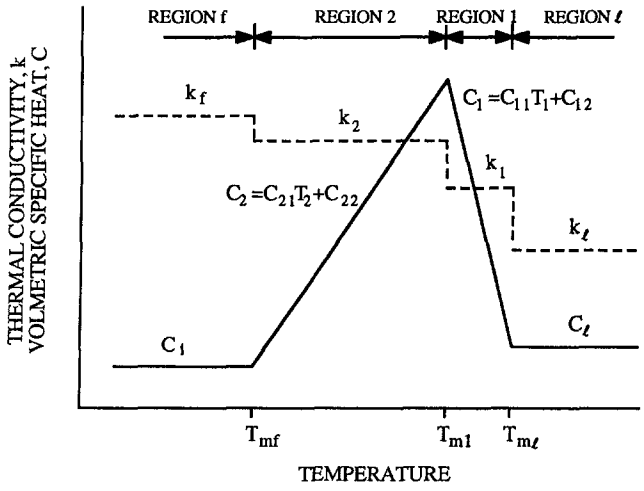



**Fig. 1 Schematic presentation of the temperature-dependent thermal conductivity and specific heat functions applied in this study**

## Analysis

It is customary to assume that in biological tissues characterized by low blood perfusion supplied by a dense capillary network, as is the case for peripheral tissues, the heat balance is given by the classical bioheat equation (Pennes, 1948):

$$C_l \frac{\partial T}{\partial t} = k_l \frac{\partial^2 T}{\partial x^2} + \dot{w}_b C_b (T_b - T) + \dot{q}_{\text{met}} \qquad (1)$$

## Nomenclature

$a$ = constant defined in Eqs. (25) and (27) in regions [1] and [2], respectively, 1/m$^2$
$b$ = constant defined in Eqs. (26) and (28) in regions [1] and [2], respectively, 1/m
$C_{ij}$ = volumetric specific heat coefficients in region $i$, J/m$^3$-°C$^2$ for $j$ = 1 and J/m$^3$-°C for $j$ = 2
$C_l$ = volumetric specific heat, J/m$^3$-°C
$D$ = constant of the solution in the unfrozen region, Eq. (3), 1/m
$g_{12}$ = integration constant in Eq. (12), m
$g_{11}$, $g_{21}$ = integration constants in Eqs. (12) and (15), respectively, 1/m
$h$ = volumetric specific enthalpy, J/m$^3$
$k$ = thermal conductivity, W/m-°C
$L$ = latent heat, J/m$^3$
$\dot{q}$ = volumetric heat source, W/m$^3$
$s$ = interface location, m
$t$ = time, s
$T$ = temperature, °C
$\dot{w}_b$ = volumetric blood perfusion per unit volume of tissue, 1/s
$x$ = coordinate, m
$\alpha$ = thermal diffusivity, m$^2$/s
$\epsilon$ = initial condition parameter defined in Eq. (18)
$\kappa_{ij}$ = $C_{ij}\dot{s}/k_i$ = ratio of freezing front velocity and thermal diffusivity, defined in Eq. (11), 1/m-°C for $j$ = 1 and 1/m for $j$ = 2
$\eta$ = transformed coordinate, m
$\xi$ = transformed coordinate, m
$\tau$ = time required for freezing front formation, s

**Subscripts**

0 = initial
1 = of region [1]
2 = of region [2]
$i1$ = slope of a temperature-dependent property in region [$i$]
$i2$ = constant of a property in region [$i$]
$b$ = blood
$f$ = frozen
$i, j$ = indices
$l$ = unfrozen
met = metabolic
$m1$ = peak value of specific heat in the phase transition region
$mf$ = lower phase transition temperature boundary
$ml$ = upper phase transition temperature boundary



Downloaded 12 Dec 2010 to 193.140.21.150. Redistribution subject to ASME license or copyright; see http://www.asme.org/terms/Terms_Use.cfm

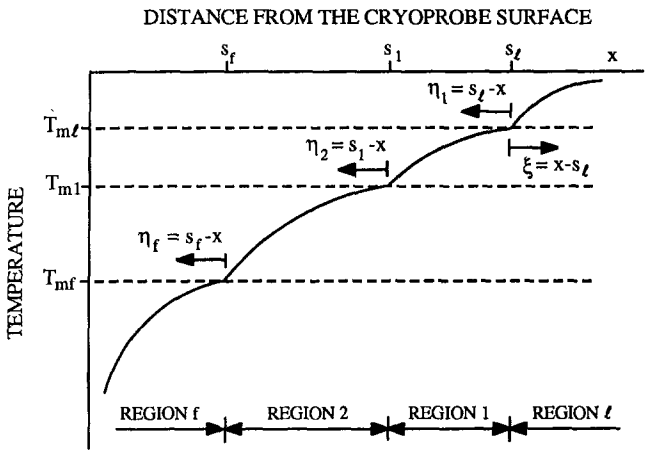



**Fig. 2 Schematic presentation of the various coordinate systems tracing the freezing fronts**

In the present analysis we distinguish between two main regions in the tissue: frozen and unfrozen. The cooling process in the unfrozen region in a quasi-steady state is well defined mathematically by the temperatures specified on its two boundaries. Thus, the bioheat equation may be solved for this region, independent of the other regions. As suggested by Rubinsky and Shitzer (1976), the temperature distribution in the unfrozen region is given by:

$$T_l = \left(T_b + \frac{\dot{q}_{\text{met}}}{\dot{w}_b C_b}\right)\cdot[1 - \exp(-D\xi)] + T_{ml}\exp(-D\xi) \quad (2)$$

$$D = \frac{\dot{s} + (\dot{s}^2 + 4\dot{w}_b C_b \alpha_l^2/k_l)^{1/2}}{2\alpha_l} \quad (3)$$

Equations (2) and (3) apply to a coordinate system moving with isotherm $T_{ml}$, Fig. 2. The variable $\dot{s}$ designates the interface velocity, which is identical at all moving fronts in a quasy-steady state.

Once freezing of the tissue is initiated, we assume that both blood perfusion and all metabolic activities cease. This assumption reduces the bioheat equation to a conventional heat diffusion equation, which applies in regions [1], [2], and [$f$], including the linear dependence of specific heat on the temperature:

$$\frac{C_{i1}T_i + C_{i2}}{k_i}\frac{\partial T_i}{\partial t} = \frac{\partial^2 T_i}{\partial x^2} \quad (4)$$

where the index $i$ can be 1, 2 or $f$.

Solution of this equation is subject to the following boundary conditions:

$$T_i|_{x=s_j} = T_{mj} \quad (5)$$

$$-k_i \left.\frac{\partial T_i}{\partial x}\right|^{+}_{x=s_j} = -k_j \left.\frac{\partial T_j}{\partial x}\right|^{-}_{x=s_j} \quad (6)$$

where the index $i$ is as in Eq. (4), and the index $j$ relates to regions [$l$], [1], or [2].

Equations (4)–(6) are transformed to the coordinate systems $\eta_i$, to yield:

$$\frac{\partial^2 T_i}{\partial \eta_i^2} = \frac{C_{i1}T_i + C_{i2}}{k_i}\left(\frac{\partial T_i}{\partial t} + \dot{s}\frac{\partial T_i}{\partial \eta_i}\right) \quad (7)$$

$$T_i|_{\eta_i=0} = T_{mi} \quad (8)$$

$$k_i \left.\frac{\partial T_i}{\partial \eta_i}\right|_{\eta_i=0} = \begin{cases} -k_l \left.\dfrac{\partial T_l}{\partial \xi}\right|_{\xi=0} & \text{for} \quad (i=1) \\ k_j \left.\dfrac{\partial T_j}{\partial \eta_j}\right|_{\eta_j=\eta_{sj}} & \text{for} \quad (i=2, j=1) \\ & \text{or} \quad (i=f, j=2) \end{cases} \quad (9)$$

In a quasi-steady state the temperature distribution in the $\eta_i$ coordinate system is independent of time. Thus, the time derivative in Eq. (7) may be omitted and the partial derivatives may be replaced by ordinary ones to yield:

$$\frac{d^2 T_i}{d\eta_i^2} = (\kappa_{i1}T_i + \kappa_{i2})\frac{dT_i}{d\eta_i} \quad (10)$$

where:

$$\kappa_{ij} \equiv \frac{C_{ij}\dot{s}}{k_i} \quad (11)$$

Equation (10) is integrated in two steps. The first step involves the substitution of the derivative $dT_i/d\eta_i$ by a dummy variable. This yields a first-order differential equation the solution of which is straightforward. In the second step the dummy variable is replaced by its defining derivative and the resulting equation is integrated again, to yield:

$$T_1 = \frac{1}{\kappa_{11}}\left\{g_{11}\tan\left[\frac{g_{11}}{2}(\eta_1 + g_{12})\right] - \kappa_{12}\right\} \quad (12)$$

where $g_{11}$ and $g_{12}$ are the integration coefficients in region [1]. It follows from Eq. (12) that $k_{11} \neq 0$ implying that the specific heat may not be constant in region [1]. Substitution of boundary condition (8) into Eq. (12) yields the functional relationship between $g_{12}$ and $g_{11}$. This leaves only one integration coefficient, $g_{11}$, in the expression for $T_1$:

$$T_1 = \frac{1}{\kappa_{11}}\left[g_{11}\frac{(\kappa_{11}T_{ml} + \kappa_{12}) + g_{11}\tan(g_{11}\eta_1/2)}{g_{11} - (\kappa_{11}T_{ml} + \kappa_{12})\tan(g_{11}\eta_1/2)} - \kappa_{12}\right] \quad (13)$$

The remaining boundary condition, Eq. (9), is now used to obtain an implicit expression for coefficient $g_{11}$:

$$k_l D\left(T_{ml} - T_b - \frac{\dot{q}_{\text{met}}}{\dot{w}_b C_b}\right) = \frac{k_l g_{11}^2}{2\kappa_{11}}\sec^2\left[\tan^{-1}\left(\frac{\kappa_{11}T_{ml} + \kappa_{12}}{g_{11}}\right)\right] \quad (14)$$

A similar procedure is applied to region [2] for a coordinate system located on isotherm $T_{m1}$. The resulting temperature distribution in region [2], using boundary condition (8), is given by:

$$T_2 = \frac{1}{\kappa_{21}}\left[g_{21}\frac{(\kappa_{21}T_{m1} + \kappa_{22}) + g_{21}\tanh(-g_{21}\eta_2/2)}{g_{21} + (\kappa_{21}T_{m1} + \kappa_{22})\tanh(-g_{21}\eta_2/2)} - \kappa_{22}\right] \quad (15)$$

where $g_{21}$ is given by the implicit expression which was obtained by substitution of Eq. (9) into Eq. (15):

$$\frac{k_1 g_{11}^2}{\kappa_{11}}\sec^2\left[\tan^{-1}\left(\frac{\kappa_{11}T_{m1} + \kappa_{12}}{g_{11}}\right)\right] = -\frac{k_2 g_{21}^2}{\kappa_{21}}\operatorname{sech}^2\left[\tanh^{-1}\left(\frac{\kappa_{21}T_{m1} + \kappa_{22}}{g_{21}}\right)\right] \quad (16)$$

The frozen region, [$f$], is treated next to complete the computation procedure for the quasi-steady state. It is noted that the specific heat in this region is constant and thus $\kappa_{f1} = 0$. Upon integration of Eq. (10), using boundary conditions (8) and (9),



Downloaded 12 Dec 2010 to 193.140.21.150. Redistribution subject to ASME license or copyright; see http://www.asme.org/terms/Terms_Use.cfm

**Table 1 Typical thermophysical properties of a peripheral biological tissue; data compiled from Chato (1985)**

| | |
|---|---|
| Initial Temperature, °C | 37 |
| Blood Temperature, °C | 37 |
| Thermal Conductivity in the unfrozen region W/m°C | 0.5 |
| Thermal Conductivity in region [1], W/m°C | 1.7 |
| Thermal Conductivity in region [2], W/m°C | 1.9 |
| Thermal Conductivity in the frozen region, W/m°C | 2.0 |
| Volumetric Specific Heat in the unfrozen region, MJ/m³ °C | 3.6 |
| Volumetric Specific Heat in the frozen region, MJ/m³ °C | 1.8 |
| Latent Heat of solidification, MJ/m³ | 233.4 |
| Volumetric Specific Heat Source of Blood, $\dot{w}_b C_b$, kW/m³ °C | 2.5 |
| Metabolic Heat Generation, kW/m³ | 2.5 |

an explicit temperature distribution for the frozen region is obtained:

$$T_f = \frac{k_2}{k_f}\frac{g_{21}^2}{2\kappa_{f2}\kappa_{21}}\operatorname{sech}^2\left[\tanh^{-1}\left(\frac{\kappa_{21}T_{mf}+\kappa_{22}}{g_{21}}\right)\right] \times [1-\exp(\kappa_{f2}\eta_f)] + T_{mf} \quad (17)$$

We now turn to finding the boundary condition, or the forcing function, at the interface between the cryoprobe and the phase changing medium. This boundary condition may be visualized as the temperature variations obtained by an observer moving at a constant velocity from $+\infty$ in the $-x$ direction relative to the quasi-steady-state solution. The boundary condition obtained by this method is precise but is impractical since infinite time is required to travel from $x = \infty$ to $x = 0$. We, therefore, turn to seeking an approximate solution to the forcing function at $x = 0$.

It is first noted that the temperature distribution in the unfrozen region decays exponentially to a constant value, Fig. 2. We can now place the observer, who is moving at a constant velocity in the negative $x$ direction, on point $x_0$. The location of this point can be selected such that the exponential in Eq. (2) would be of an arbitrarily small value, $\epsilon$:

$$\epsilon = \exp(-Dx_0) \quad (18)$$

This amounts to replacing the uniform initial condition with an exponential condition. The maximal difference between these two conditions appears at the interface between the cryoprobe and the phase changing medium. The new approximate boundary condition, at the interface between the cryoprobe and the tissue, may now be expressed by:

$$T_l(0,t) = \left(T_b + \frac{\dot{q}_{met}}{\dot{w}_b C_b}\right)\cdot[1-\epsilon\exp(-D\dot{s}t)] + \epsilon T_{ml}\exp(-D\dot{s}t) \quad (19)$$

As discussed above, under quasi-steady state, wherein all freezing fronts are moving at a constant and identical velocity, the cooling rates on these fronts would also be invariable. This condition of fixed cooling rates at the freezing fronts is actually the desired Stefan's condition (1891). These cooling rates may now be evaluated by an inverse transformation from coordinate system $\xi$ back to $x$:

$$\frac{\partial T_l}{\partial t}(x,t) = \frac{\partial T_l}{\partial t}(\xi,t) - \dot{s}\frac{\partial T_l}{\partial \xi}(\xi,t) \quad (20)$$

Since in the coordinate system $\xi$ the medium is in a quasi-steady state, the cooling rate at the front $s_l$, as viewed from the unfrozen region, is given by:

$$\frac{\partial T_l}{\partial t}(s_l,t) = -\dot{s}\frac{dT_l}{d\xi}(\xi=0) = \dot{s}D\left(T_{ml} - T_b - \frac{\dot{q}_{met}}{\dot{w}_b C_b}\right) \quad (21)$$

By equating heat fluxes at both sides of freezing front $s_l$, the cooling rate, as viewed from the freezing region [1], is given by:

$$\frac{\partial T_1}{\partial t}(s_l,t) = \frac{k_l}{k_1}\frac{\partial T_l}{\partial t}(s_l,t) \quad (22)$$

Similar mathematical derivations may be applied at freezing fronts $s_1$ and $s_f$. This involves differentiation of the temperature distributions at the origins of the coordinate systems and equating the heat fluxes on both sides of each front. Since this method involves an iterative process of calculation of coefficients, an alternative integral procedure is proposed. This procedure allows the calculation of the cooling rates at the freezing fronts $s_1$ and $s_f$, based on the cooling rate at front $s_l$, Eq. (21).

We first define a control volume encompassing regions [1] and [2] in which phase change is occurring. In a quasi-steady state, the difference between the incoming and outgoing heat fluxes equals the change in enthalpy in the control volume:

$$\left(-k_l\frac{\partial T}{\partial x}\bigg|_{x=s_l}^{+}\right) - \left(-k_f\frac{\partial T}{\partial x}\bigg|_{x=s_f}^{-}\right) = (h|_{x=s_l} - h|_{x=s_f})\frac{ds}{dt} \quad (23)$$

where the superscripts (+) and (−) indicate calculation by the unfrozen and frozen regions, respectively. It is noted that the change in enthalpy inside the control volume due to sensible heat is about two orders of magnitude smaller than that due to latent heat. Thus, as a first approximation, the change in enthalpy may be taken as the latent heat of freezing. With this approximation and coordinate transformation in Eq. (23), substitution into Eq. (20) yields the cooling rate as viewed from the frozen region:

$$\frac{\partial T}{\partial t}\bigg|_{x=s_f}^{-} = \dot{s}\frac{dT}{d\eta_2}\bigg|_{\eta_2=0} = -\frac{k_l\dot{s}}{k_f}\frac{dT}{d\xi}\bigg|_{\xi=0} - \frac{\dot{s}^2}{k_f}(h|_{x=s_l} - h|_{x=s_f}) \cong \frac{k_l}{k_f}\frac{\partial T}{\partial t}\bigg|_{x=s_l}^{+} - \frac{\dot{s}^2 L}{k_f} \quad (24)$$

As noted above, the rate of change of temperature on $s_f$, viewed from region [2], is equal to the product of the change given by Eq. (24) and the ratio of thermal conductivities of region [2] and of the frozen region. Equation (24) reveals that, with the increase of the freezing front velocity, the cooling rate in the frozen region would also increase.

## Results and Discussion

The present solution is compared to an existing analytic solution to an inverse-Stefan problem in a pure material (Rubinsky and Shitzer, 1976). In this solution phase change is assumed to occur at a single temperature at which the thermophysical properties are assumed to change stepwise. Unlike the present solution, the previous one assumes that the entire latent heat of freezing is absorbed at the single freezing front. The two solutions are in complete agreement in the unfrozen region. Therefore, com-

**Table 2 Phase-change interface temperatures, in °C, used for the comparison of the present solution with an existing one of a pure material (Rubinsky and Shitzer, 1976)**

| | $T_{m\ell}$ | $T_{m1}$ | $T_{mf}$ |
|---|---|---|---|
| $\Delta T_1$ | -1.0 | -1.05 | -1.1 |
| $\Delta T_2$ | -1.0 | -1.5 | -2.0 |
| $\Delta T_3$ | -1.0 | -3.0 | -5.0 |
| $\Delta T_4$ | -1.0 | -3.0 | -8.0 |



Downloaded 12 Dec 2010 to 193.140.21.150. Redistribution subject to ASME license or copyright; see http://www.asme.org/terms/Terms_Use.cfm

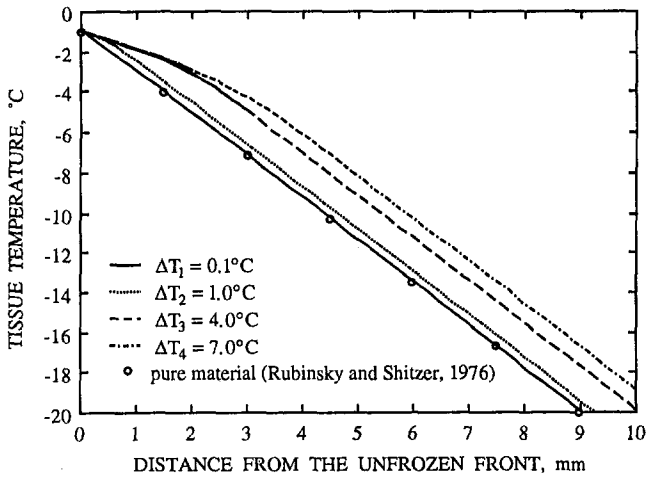



**Fig. 3 Comparison of a solution to an inverse-Stefan problem in a biological tissue behaving like a pure material (Rubinsky and Shitzer, 1976) with the present solution of a nonideal biological tissue. Parameter values are presented in Table 1**

parison is carried out in the frozen region and in the regions undergoing phase change. For comparison purposes we assume thermophysical properties typical to peripheral biological tissues, Table 1.

Comparison is presented for four cases differing in the temperature range in which phase change occurs, Table 2 and Fig. 3. The first case depicts a freezing process in pure materials in which phase change occurs at a single temperature. The second case depicts a real material that differs only slightly from a pure material. The third and fourth cases simulate typical biological materials in which phase change occurs gradually over a range of temperatures. These latter two cases demonstrate, among other things, the uncertainty relating to the precise temperatures that define the phase-change range. Thus, it is common to assume that peak phase change in a biological medium occurs at −3°C. The lower temperature bound, on the other hand, is less certain and ranges between −5°C and −8°C (Altman and Dittmer, 1971; Wessling and Blackshear, 1973).

Figure 3 shows the similarity in the temperature distributions in the frozen region for all cases studied. This similarity is retained even in the fourth case wherein an asymmetric specific heat function was assumed. Practically, all four temperature distributions may be considered to be identical following adjustments of the different temperature ranges in which phase change occurs. This similarity of solutions could be expected since the resulting temperature distributions in the phase-changing range are functionally dependent on the specific heat. Figure 3 indicates, clearly, that the various cases evaluated by the present solution conform closer to the existing solution as the phase-change temperature range is narrowed down.

The functional behavior of the solution coefficients, $g_{11}$ and $g_{21}$, is discussed next. These coefficients are obtained, through an iterative process, by Eqs. (14) and (16) for regions [1] and [2], respectively. It is noted that although the solutions, as presented by Eqs. (13) and (15), are straightforward, their actual computation requires the values of the $g_{i1}$ coefficients. These are obtainable by a trial and error process. Results for $g_{11}$ are presented graphically in Fig. 4 by means of the following two coefficients:

$$a_1 \equiv 2\kappa_{11}\frac{k_l}{k_1}D\left(T_{ml} - T_b - \frac{\dot{q}_{\text{met}}}{\dot{w}_b C_b}\right) \tag{25}$$

$$b_1 \equiv \kappa_{11}T_{ml} + \kappa_{12} \tag{26}$$

It is noted that for fixed values of the coefficient $b_1$, there is a similarity in the behavior of $g_{11}$ over a wide range of physiologically relevant values. At large values of the coefficient $a_1$, values of $g_{11}$ converge asymptotically to the same function, and become independent of $b_1$, Fig. 4.

Coefficients $g_{21}$ are presented in Fig. 5. Here, too, we define two new coefficients to facilitate the graphic presentation of $g_{21}$:

$$a_2 \equiv -\frac{\kappa_{21}k_l g_{11}^2}{\kappa_{11}k_2}\sec^2\left[\tan^{-1}\left(\frac{\kappa_{11}T_{ml} + \kappa_{12}}{g_{11}}\right)\right] \tag{27}$$

$$b_2 \equiv \kappa_{21}T_{ml} + \kappa_{22} \tag{28}$$

It is seen that for a range of low values of $a_2$ and for $b_2 > 0$, $g_{21}$ assumes constant values, which are dependent on $b_2$. At high values of $a_2$, $g_{21}$ converges to a log-linear function, independent of $b_2$, Fig. 5.

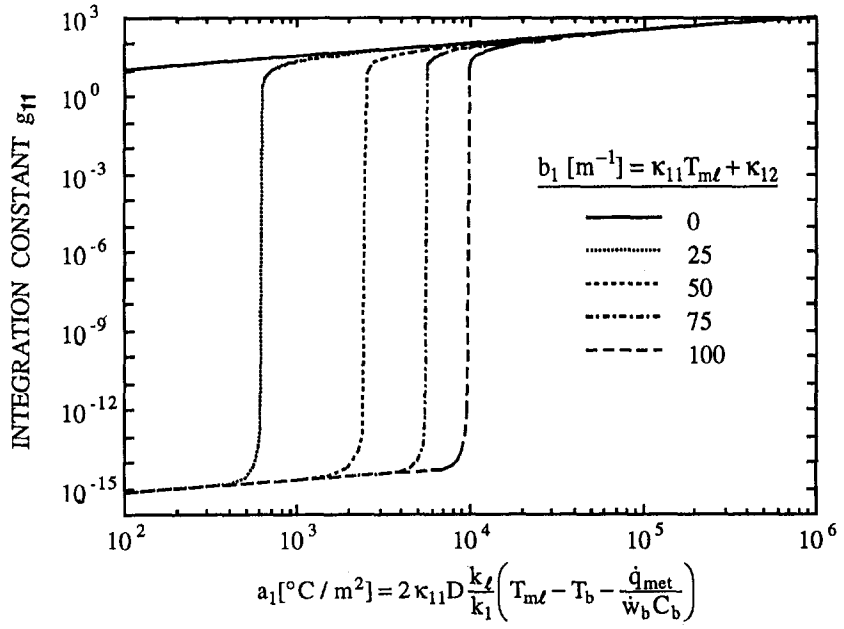



**Fig. 4 Computed values of the integration constant $g_{11}$, Eq. (14), versus the coefficients $a_1$ and $b_1$, defined by Eqs. (25) and (26), respectively**



Downloaded 12 Dec 2010 to 193.140.21.150. Redistribution subject to ASME license or copyright; see http://www.asme.org/terms/Terms_Use.cfm

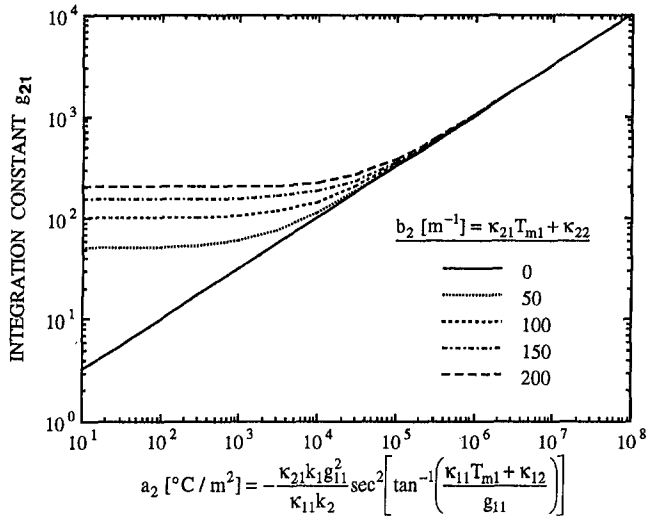



**Fig. 5 Computed values of the integration constant $g_{21}$, Eq. (16), versus the coefficients $a_2$ and $b_2$, defined by Eqs. (27) and (28), respectively**

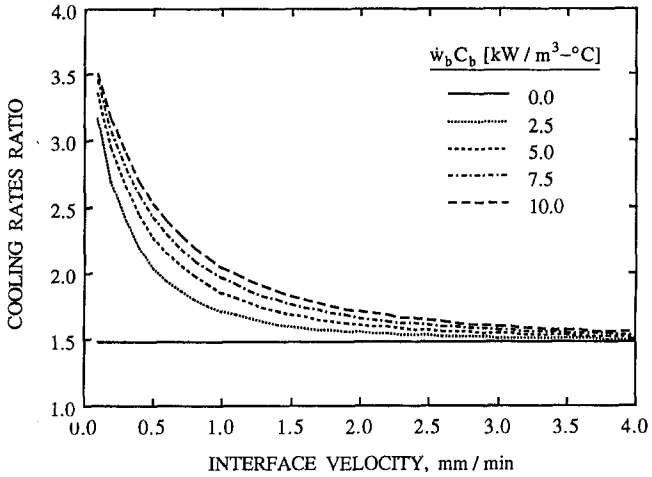



**Fig. 7 Cooling rates ratio of the unfrozen to frozen region at the freezing fronts versus the interface velocity**

We now turn to the cryosurgical process. In this study it is assumed that enhanced success of this process may be achieved by maintaining a prespecified cooling rate on the freezing front. In this case the freezing rates of interest are those existing at fronts $s_f$ and $s_t$, as calculated in the frozen and unfrozen regions, respectively. Figure 6 shows the relationship between the velocity of propagation and the cooling rate at freezing front $s_f$. It is seen that these two parameters are exponentially dependent for a case of zero blood flow. As blood perfusion increases, acting essentially as a heat source in the medium, cooling rate must also increase to maintain any desired constant velocity of propagation of the freezing front.

The relationship between cooling rate ratio and the velocity of propagation of freezing fronts is shown in Fig. 7. The cooling rate ratio is taken as the one between the unfrozen and frozen regions, as viewed from those regions, respectively. It is seen that as the velocity of propagation increases, the effect of blood perfusion on the cooling rate ratio diminishes. Actually, at very high velocities of propagation of the freezing front, which may not be attainable in practice, the cooling rate ratio equals that of the in-vitro case of no blood flow. As can be seen from Eq. (24), the cooling rate ratio depends linearly on the thermal conductivity ratio and on the enthalpy changes. The thermal conductivity values in the frozen and unfrozen regions bound the values in regions [1] and [2] while the enthalpy changes monotonically with temperature across these regions. Thus, the cooling rates within the regions undergoing phase change are between the cooling rates at the frozen and the unfrozen interfaces.

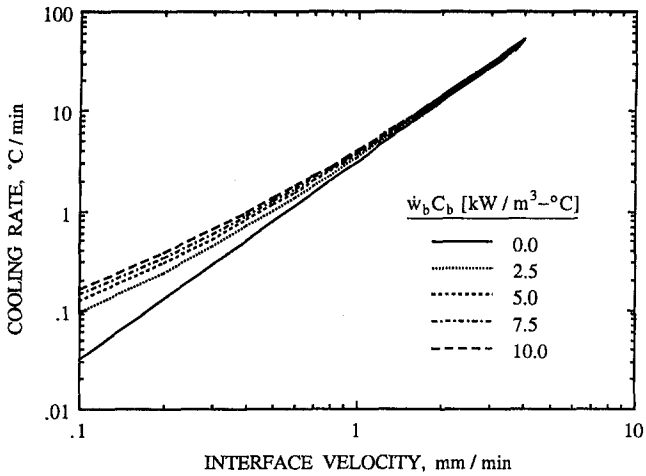



**Fig. 6 Cooling rate at the freezing front $s_f$ as viewed from the frozen region, versus the freezing front velocity**

The forcing function solution of the inverse-Stefan problem is studied next. This function is evaluated for five cases of various combinations of metabolic heat generation and specific heat source of the blood, Table 3, and for thermophysical properties listed in Table 1. A freezing rate of 10°C/min was assumed in the frozen region at the freezing front, which leads to freezing fronts velocities of about 1.6 mm/min, as can be seen in Fig. 6.

The expression for the forcing function for the condition in which the unfrozen region is in contact with the cryoprobe was obtained by Eq. (19), using an initial parameter value of $\epsilon = 0.05$. The forcing functions relating to regions [1] and [2] were calculated next, by replacing $\eta_1$ and $\eta_2$ with $\dot{s}t$, in Eqs. (13) and (15), respectively. The integration constants $g_{11}$ and $g_{21}$ were evaluated from Eqs. (14) and (16), as presented in Figs. 4 and 5, respectively. It is noted that for typical thermophysical properties of biological tissues and for cooling rates above 4°C/min in the frozen region at the freezing front, the integration constants $g_{11}$ and $g_{21}$ are almost log-linearly dependent on $a_1$ and $a_2$, respectively, and are independent of $b_1$ and $b_2$. These simplified relations are: $g_{i1} = a_i^{1/2}$. The forcing function relating to the frozen region was calculated last by a similar procedure, replacing $\eta_f$ with $\dot{s}t$ in Eq. (17), following the formation of all of the freezing fronts. The liquid nitrogen boiling temperature, −196°C, was taken as the lowest temperature bound of the forcing functions.

The results obtained for the forcing functions for the five cases studied, for a cooling rate of 10°C/min at $s_f$, are presented in Fig.

**Table 3 Duration and depth of penetration of cryotreatments, for a cooling rate of 10°C/min at the frozen front $s_f$, for five cases of various combinations of metabolic heat generation and specific heat source of the blood**

| Case No. | $\dot{w}_bC_b$ kW/m$^3$-°C | $\dot{q}_{met}$ kW/m$^3$ | Duration of cryotreatment, min | Depth of freezing penetration - $s_f$ front, mm | Phase transition width (regions [1] and [2], mm |
|---|---|---|---|---|---|
| 1 | 0.0 | 0.0 | 37.1 | 40.1 | 3.8 |
| 2 | 5.0 | 0.0 | 32.7 | 36.7 | 2.9 |
| 3 | 5.0 | 10.0 | 32.1 | 35.8 | 2.8 |
| 4 | 10.0 | 0.0 | 30.1 | 34.5 | 2.5 |
| 5 | 10.0 | 10.0 | 29.8 | 34.1 | 2.4 |



Downloaded 12 Dec 2010 to 193.140.21.150. Redistribution subject to ASME license or copyright; see http://www.asme.org/terms/Terms_Use.cfm

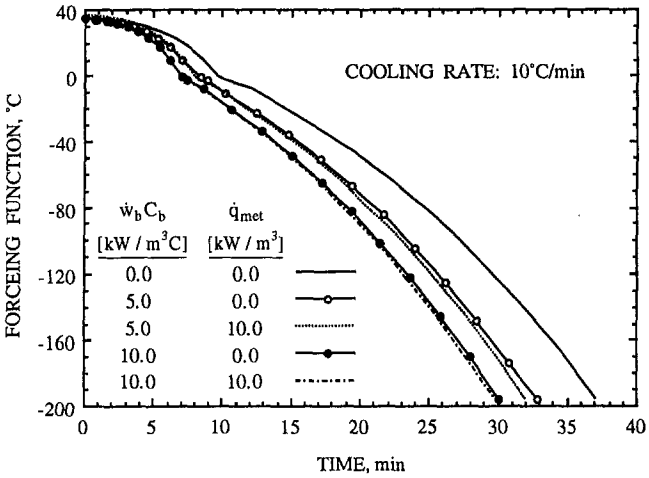



**Fig. 8 Forcing functions of the inverse-Stefan problem for various combinations of heat sources and a cooling rate of 10°C/min at the frozen front $s_f$. Parameter values are presented in Tables 1 and 3.**

8. Numerical results of the duration of the cryotreatment, depth, and freezing penetration (defined by $s_f$), and the phase transition width (defined by the distance between the freezing fronts $s_l$ and $s_f$) are all presented in Table 3. It is seen that the dependence of the forcing function on the relatively high metabolic heat generation, with respect to blood perfusion, is relatively weak. It can also be seen that with the increasing of blood perfusion, the slope of the forcing function increases, the depth of freezing penetration decreases, and the phase transition widens. Maximal blood perfusion and metabolic heat generation (Case 5) reduce the duration of cryotreatment by 20 percent, reduce the depth of freezing penetration by 15 percent, and reduce the phase transition width by 37 percent, all with respect to a tissue devoid of heat sources (Case 1).

The proposed exact solution of the inverse Stefan problem is one dimensional and is presented for Cartesian coordinates. It can be shown mathematically that a solution to the multidimensional inverse Stefan problem may not exist except for unique cases. However, observing that cell destruction increases with the decreasing of the freezing rates, in the range of low freezing rates, the present solution can be used as an upper bound forcing function for the multidimensional problem. By applying the proposed forcing function solution to a multidimensional cryotreatment one can ensure that the actual freezing rates would be equal to, or lower than, the defined freezing rate of the one-dimensional solution at all times. It can be expected that in superficial cryotreatments, and in cases of low depth of freezing penetration with respect to a typical cryoprobe dimension, the one-dimensional case will be close to the multidimensional one. Accordingly, the depth of freezing penetration in the one-dimensional case can be taken as the maximal bound for the multidimensional case.

## Conclusion

An analytic solution to the inverse-Stefan problem in a biological tissue, in which a constant cooling rate is maintained at the freezing front, is presented. The solution is derived for a nonideal material and is based on the enthalpy method applied in the range of phase-change temperatures. Thermal effects of blood perfusion as well as metabolic heat and density changes are accounted for. Results are compared to an existing solution derived for a pure material. The comparison was facilitated by assuming that phase change occurs over a very narrow temperature range, essentially simulating the behavior of a pure material. Conformity of the results of the two solutions is very good.

The solution is studied for a range of parameters, which are applicable to biological tissues undergoing cryosurgical processes. The relationship between the velocity of propagation of the freezing front and the constant cooling rates maintained at the freezing fronts is presented graphically. Results indicate the possibility to control the cooling rate at the freezing front for a range of phase-change temperatures, thermophysical and physiological properties and parameters.

## Acknowledgments

This work was supported in part by the James H. Belfer Chair in Mechanical Engineering and by the Technion Vice President for Research Fund, Sam Rose Research Fund.

## References

Akhtar, T., Pegg, D. E., and Foreman, J., 1979, "The Effect of Cooling and Warming Rates on the Survival of Cryopreserved L-Cells," *Cryobiology*, Vol. 16, pp. 424–429.

Alexiades, V., and Solomon, A. D., 1993, *Mathematical Modeling of Melting and Freezing Processes*, Hemisphere Publishing Corporation, Washington, DC.

Altman, P. L., and Dittmer, D. S., 1971, *Respiration and Circulation*, Federation of American Societies for Experimental Biology (Data Handbook), Bethesda, MD.

Augustynowicz, S. D., and Gage, A. A., 1985, "Temperature and Cooling Rate Variations During Cryosurgical Probe Testing," *International Journal of Refrigeration*, Vol. 8, No. 4, pp. 198–208.

Budman, H. M., Shitzer, A., and Dayan, J., 1995, "Analysis of the Inverse Problem of Freezing and Thawing of a Binary Solution During Cryosurgical Processes," ASME *Journal of Biomechanical Engineering*, in press.

Carslaw, H., and Jaeger, J., 1959, *Conduction of Heat in Solids*, Oxford, Chap. 11, pp. 282–286.

Chato, J. C., 1985, "Selected Thermophysical Properties of Biological Materials," in: *Heat Transfer in Medicine and Biology*, A. Shitzer and R. C. Eberhart, eds., Plenum Press, New York, Vol. 2, pp. 413–418.

Fahy, G. M., 1981, "Analysis of Solution Effect Injury: Cooling Rate Dependence of the Functional and Morphological Sequellae of Freezing in Rabbit Renal Cortex Protected With Dimethyl Sulfoxide," *Cryobiology*, Vol. 18, pp. 550–570.

Farrant, J., 1971, "Cryobiology: The Basis of Cryosurgery," in: *Cryogenics in Surgery*, H. von Leden and W. G. Cahan, eds., Lewis, London, pp. 15–42.

Gage, A. A., Guest, K., Montes, M., Caruna, J. A., and Whalen, D. A., Jr., 1985, "Effect of Varying Freezing and Thawing Rates in Experimental Cryosurgery," *Cryobiology*, Vol. 22, pp. 175–182.

Goodman, T. R., 1958, "The Heat Balance Integral and Its Application to Problems Involving a Change of Phase," *Transactions of the ASME*, Vol. 80, pp. 335–342.

McGrath, J. J., 1993, "Low Temperature Injury Processes," in: *Advances in Bioheat and Mass Transfer*, ASME HTD-Vol. 268, pp. 125–132.

Mazur, P., 1963, "Kinetics of Water Loss From Cells at Subzero Temperatures and the Likelihood of Intracellular Freezing," *The Journal of General Physiology*, Vol. 47, pp. 347–369.

Mazur, P., Leibo, S., and Chu, E. H. Y., 1972, "A Two-Factor Hypothesis of Freezing Injury," *Experimental Cell Research*, Vol. 71, pp. 345–355.

Miller, R. H., and Mazur, P., 1976, "Survival of Frozen-Thawed Human Red Cells as a Function of Cooling and Warming Velocities," *Cryobiology*, Vol. 13, pp. 404–414.

Orpwood, R. D., 1981, "Biophysical and Engineering Aspects of Cryosurgery," *Physical and Medical Biology*, Vol. 26, No. 4, pp. 555–575.

Pennes, H. H., 1948, "Analysis of Tissue and Arterial Blood Temperature in the Resting Human Forearm," *Journal of Applied Physiology*, Vol. 1, pp. 93–122.

Rubinsky, B., and Shitzer, A., 1976, "Analysis of a Stefan-Like Problem in a Biological Tissue Around a Cryosurgical Probe," ASME JOURNAL OF HEAT TRANSFER, Vol. 98, pp. 514–519.

Rubinsky, B., and Onik, G., 1991, "Cryosurgery: Advances in the Application of Low Temperatures to Medicine," *International Journal of Refrigeration*, Vol. 14, pp. 190–199.

Stefan, J., 1891, "Über die Theorie der Eisbildung, Insbesondere über die Eisbildung in Polarmeere," *Annals Physical Chemistry*, Vol. 42, pp. 269–286.

Voller, V. R., 1986, "A Heat Balance Integral Based on the Enthalpy Formulation," *International Journal of Heat and Mass Transfer*, Vol. 30, pp. 604–606.

Wessling, F. C., and Blackshear, P. L., 1973, "The Thermal Properties of Human Blood During the Freezing Process," ASME JOURNAL OF HEAT TRANSFER, Vol. 95, pp. 246–249.



Downloaded 12 Dec 2010 to 193.140.21.150. Redistribution subject to ASME license or copyright; see http://www.asme.org/terms/Terms_Use.cfm

# Stochastic Modeling of Molecular Transport to an Evaporating Microdroplet in a Superheated Gas

V. P. Carey

N. E. Hawks

Mechanical Engineering Department,
University of California,
Berkeley, CA 94720

*The investigation summarized in this paper explored the use of a stochastic, direct-simulation Monte-Carlo scheme to model heat and mass transfer associated with the vaporization of liquid nitrogen microdroplets in superheated nitrogen gas. Two different stochastic models of the molecule–surface interactions were used in the particle simulation scheme. The first, which imposes conservation of mass at the droplet surface, is appropriate for a heated or cooled solid sphere. The second models the net generation of vapor at the surface of an evaporating droplet by allowing the molecular flux to adjust itself dynamically to balance the energy exchange. Predictions of the particle simulation model with the mass conservation surface treatment are found to agree favorably with heat transfer data for a solid sphere in a rarefied gas. The effects of noncontinuum behavior and interface vapor generation on transport during microdroplet evaporation are explored and a closed-form relation for the heat transfer coefficient is developed, which closely matches all our simulation heat transfer predictions for evaporating microdroplets. This relation apparently is the first to account for the simultaneous effects of interface vapor generation and noncontinuum behavior on heat transfer controlled microdroplet evaporation.*

## Introduction

In a number of technological applications, a vaporizing liquid breaks up into droplets, some of which may be as small as 0.5 $\mu$m in diameter. It is well known, for example, that the final stages of convective evaporation in tubes at low wall superheat levels may be a mist flow evaporation process in which vaporization of small droplets is driven by heat transfer from the surrounding slightly superheated vapor to the droplets. Clearly the final stage of this process must involve vaporization of droplets less than 1.0 $\mu$m in diameter. In the atmosphere, embryonic water droplets frequently include droplets with diameters as small as 0.2 $\mu$m. For the smallest droplets in such circumstances, the size of the droplets approaches the mean free path of the surrounding gas molecules and the heat transfer process to the droplets, which drives the evaporation, is in the transition regime between free molecular and continuum transport. Because neither free molecular theory nor continuum theory is accurate in the transition regime, prediction of the evaporation rate of microdroplets in this size range is particularly challenging.

Investigations of the related problem of heat transfer from a sphere to a surrounding rarefied gas have been conducted by Takao (1963), Kavanau (1955), and Kyte et al (1953). Evaporation of liquid droplets in a hotter surrounding gas has been the subject of numerous studies, spanning a variety of applications. Most of these studies have focused on relatively large droplets, with diameters greater than 5 $\mu$m, surrounded by a gas at moderate to high pressures. The transport in such circumstances can be predicted by continuum theory.

There have been relatively few investigations of noncontinuum effects on droplet evaporation. Lou (1978), Chernayak and Margilevskiy (1989), and Young (1991) explored analytical extensions of kinetic theory as means to develop predictions of the heat and mass transfer between an evaporating droplet and a surrounding gas at arbitrary Knudsen number. Sone and Sugimoto (1993) numerically solved governing equations for the variation of the velocity distribution function adjacent to a liquid or solid sphere vaporizing into a vacuum ambient, but the specific case of droplet evaporation driven by molecular transport of thermal energy from a surrounding superheated vapor was not considered.

Our investigation differed from the above-mentioned studies of noncontinuum effects on droplet evaporation in that we explored the use of a stochastic, Monte-Carlo direct-simulation scheme as a method for predicting the molecular transport to an evaporating microdroplet under transition regime conditions. We are aware of no previous attempt to apply this type of simulation to evaporating microdroplets for circumstances where noncontinuum effects are important.

Vaporization of a droplet is fundamentally different from heat transfer to a solid cooled sphere in that vaporization at the surface of the droplet produces a net outward flux of vapor molecules. Some insight into the importance of the interface vapor generation effect on droplet vaporization can be obtained by considering continuum conduction-driven evaporation of a droplet. The governing equations and boundary conditions for heat and momentum transfer in such circumstances are

$$r^{-2}\frac{d}{dr}(r^2u_r) = 0 \tag{1}$$

$$u_r\frac{du_r}{dr} = -\frac{1}{\rho_v}\frac{dP}{dr} + \left(\frac{\nu}{r^2}\right)\frac{d}{dr}\left(r^2\frac{du_r}{dr}\right) - \left(\frac{2\nu u_r}{r^2}\right) \tag{2}$$

$$\rho_v c_p u_r\frac{dT}{dr} = r^{-2}\frac{d}{dr}\left(r^2k_v\frac{dT}{dr}\right) \tag{3}$$

$$\text{at}\quad r = r_s\text{:}\quad u_r = u_s,\quad T = T_s = T_{\text{sat}}(P_\infty) \tag{4}$$

$$\text{as}\quad r\to\infty\text{:}\quad u_r\to 0,\quad T\to T_\infty \tag{5}$$

where

$$u_s = q_s''/(\rho_v h_{lv}),\quad q_s'' = -k_v\left(\frac{dT}{dr}\right)_{r=r_s} \tag{6}$$

Contributed by the Heat Transfer Division for publication in the JOURNAL OF HEAT TRANSFER. Manuscript received by the Heat Transfer Division February 1994; revision received August 1994. Keywords: Evaporation, Phase-Change Phenomena, Sprays/Droplets. Associate Technical Editor: W. L. Grosshandler.



Copyright © 1995 by ASME

Downloaded 12 Dec 2010 to 193.140.21.150. Redistribution subject to ASME license or copyright; see http://www.asme.org/terms/Terms_Use.cfm

This formulation embodies the assumptions that the pressure at the droplet surface is only slightly different than that in the ambient and that the specified value of $T_{sat}$ properly accounts for any dependence of $T_{sat}$ on droplet size due to surface tension effects. For these circumstances, the continuity equation dictates that the radial velocity decays from its value at the droplet surface proportional to $1/r^2$. The continuity and energy transport equations can be solved together with the boundary conditions to obtain the velocity and temperature fields and the heat transfer to the droplet. The momentum equation can then be solved for the pressure field if desired. Using the temperature field result, the following relation for the Nusselt number can be obtained:

$$\mathrm{Nu}_D = \frac{2 \ln \{\mathrm{Ja} + 1\}}{\mathrm{Ja}} \tag{7}$$

where

$$\mathrm{Ja} = \frac{c_{pv}(T_\infty - T_s)}{h_{lv}} \tag{8}$$

For this continuum solution, it can be shown that

$$r_s u_s/\alpha_v = \ln \{\mathrm{Ja} + 1\} \tag{9}$$

Thus, the Jakob number Ja is a direct indicator of the magnitude of vapor velocity at the droplet surface. Note that in the limit of $\mathrm{Ja} \to 0$, $\mathrm{Nu}_D \to 2$, and the well-known case of heat transfer to a solid sphere (with no evaporation) is recovered. Equation (7) predicts that for $\mathrm{Ja} > 1.0$, $\mathrm{Nu}_D$ is reduced by more than 30 percent. Conditions corresponding to $\mathrm{Ja} > 1.0$ may be achieved in many droplet evaporation circumstances. It is therefore expected that, in general, the effects of the finite mass flux at the interface must be incorporated into models of droplet evaporation in a continuum gas. It further suggests that such effects may also be important when microdroplets evaporate under conditions where noncontinuum effects play an important role.

The particle simulation model used in this study was first validated against heat transfer data and a dimensionless correlation for heat transfer from a sphere in a rarefied gas. The simulation model was then used to explore the manner in which vapor generation at the interface and noncontinuum behavior influence the transport associated with droplets of liquid nitrogen evaporating in superheated, low-pressure nitrogen gas.

## Application of the Particle Simulation Method

The particle simulation method used here is a derivative of the direct-simulation Monte-Carlo (DSMC) technique pioneered by Bird (1976). Some of the refinements developed by McDonald (1989) and Baganoff and McDonald (1990) have also been incorporated into the scheme used here. The main features of the particle simulation method are described briefly in the appendix. The special features added in our investigation to model the evaporation of a spherical droplet in a superheated gas are described in detail below.

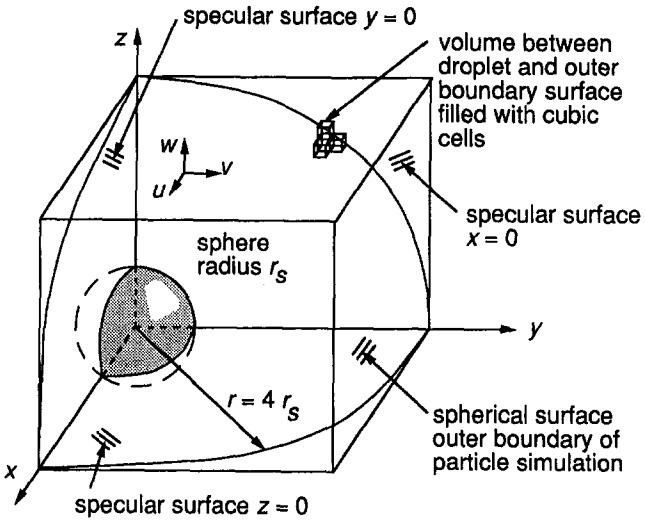



**Fig. 1 Boundaries and cell grid for the simulation domain**

To minimize memory requirements and computational time, the simulation domain was limited to one octant around the sphere, as shown in Fig. 1. In addition, to avoid the computational costs of extending the simulation out to large radial distances, in this study the simulation domain was limited to a radial distance of four sphere radii, and the simulation boundary condition was matched to the continuum transport solution beyond $r = 4r_s$.

The temperature gradient decreases rapidly with distance from the sphere, approximately proportional to $r^{-2}$. Consequently, while the temperature may drop significantly over a few mean free paths near the sphere, beyond $r = 4r_s$, it will take many free paths for the temperature to change significantly. The local Knudsen number $\mathrm{Kn}_r = \lambda(dT/dr)/(T_\infty - T_s)$ decreases rapidly with distance from the sphere, causing the temperature profile to approach that for continuum transport at large $r$. This line of reasoning, which divides the region near the sphere into a noncontinuum region close to the body and a continuum transport region farther away, apparently was first used by Langmuir (1915) to facilitate the analysis of noncontinuum transport to a cylindrical body. The matching process proposed as part of our simulation

## Nomenclature

$c_p$ = specific heat at constant pressure
$c_v$ = specific heat at constant volume
$D$ = diameter of sphere
$D_m$ = effective diameter of molecules
$h$ = heat transfer coefficient = $q''_{r=r_s}/(T_\infty - T_s)$
$h_{lv}$ = latent heat of vaporization
$k_v$ = gas thermal conductivity
$k_B$ = Boltzmann constant
$m$ = mass of a molecule
$n_m$ = number density of molecules
$\mathrm{Nu}_D$ = Nusselt number = $hD/k_v$
$q''$ = energy flux
$r_s$ = radius of sphere
$\Re$ = a random number uniformly distributed on [0, 1]
$T$ = absolute temperature
$T_0$ = temperature in the gas adjacent to the sphere surface
$u_{lv}$ = change in internal energy due to vaporization
$\vec{v}_r$ = relative velocity vector for collision pair
$\alpha$ = thermal diffusivity = $k/\rho c_p$
$\gamma$ = ratio of specific heats for vapor = $c_p/c_v$
$\Delta t$ = time interval for one time step of simulation
$\epsilon$ = molecular energy component
$\lambda$ = molecular mean free path
$\mu$ = absolute viscosity
$\nu$ = kinematic viscosity
$\rho_v$ = vapor density
$\sigma_t$ = energy accommodation coefficient

### Subscripts

$l$ = liquid
rot = rotational
$s$ = corresponding to the sphere surface
$tr$ = translation
$v$ = vapor
$\infty$ = corresponding to free-stream conditions
4 = corresponding to $r/r_s = 4$



Downloaded 12 Dec 2010 to 193.140.21.150. Redistribution subject to ASME license or copyright; see http://www.asme.org/terms/Terms_Use.cfm

scheme is therefore consistent with Langmuir's model, which has been widely used for problems of this type.

The octant simulation region shown in Fig. 1 was bounded by the surface of the sphere at $r = r_s$, the outer boundary at $r = 4r_s$, and specularly reflecting planar surfaces at $x = 0$, $y = 0$, and $z = 0$. The specular surfaces that lie along planes of symmetry have the effect of giving the octant the same statistical behavior as a complete sphere surrounded by particles. The region bounded by these surfaces was filled with cubic cells, which were used to collect collision candidate pairs and define regions over which particle properties were averaged to obtain macroscopic thermodynamic characteristics of the gas adjacent to the droplet.

Particles that move beyond the outer boundary when the particles are advanced along their trajectory are simply removed from the simulation. During each time step, particles are added to the simulation just inside the $r = 4r_s$ boundary. The rate of this particle addition $\dot{n}_p$ is computed as

$$\dot{n}_p = (\pi/2)(4r_s)^2 j_{in} \tag{10}$$

where $j_{in}$ is the molecular flux across a surface predicted by kinetic theory

$$j_{in} = \left(\frac{k_B T_4}{2\pi m}\right)^{1/2}\left(\frac{P_\infty}{k_B T_4}\right) \tag{11}$$

In the relation above, $T_4$ is the temperature specified at $r/r_s = 4$, and the pressure at this location is taken to be equal to that in the far ambient, $P_\infty$. This treatment allows the simulation domain to establish whatever mean particle density is necessary to balance the inward and outward fluxes at the outer boundary.

At the sphere surface, two different stochastic models of the molecule–surface interactions were used. One was based solely on a mass flux balance (the zero mass flux model) while the other (the zero energy flux model) allowed the mass flux to adjust itself so as to balance the energy exchange at the surface. The first approach is appropriate for a solid heated or cooled sphere, whereas the second more correctly models the interaction at the surface of an evaporating droplet. For both models, if a particle strikes the sphere surface during the time step, a random number $\Re$ uniformly distributed on [0, 1] is compared to the specified accommodation coefficient $\sigma_t$. If $\sigma_t \leq \Re$, the particle is diffusely scattered from the surface. Its speed and rotational energy are left unchanged, but its direction is randomly set by sampling a distribution that, in the mean, isotropically scatters particles from the surface. If $\sigma_t > \Re$, the particle thermally interacts with the surface. This interaction is treated differently by the two models. The zero mass flux model treats each interacting particle as if it is briefly adsorbed, and then leaves the surface, fully accommodated, after a short residence time. Computationally, such particles are removed from the simulation. The number of thermally interacting particles is counted and the energy delivered to the sphere by these particles is summed. As a subsequent calculation, particles are added to the simulation domain just beyond $r = r_s$ until the number added exactly equals the number of interacting particles during the time step. In this manner a zero net mass flux condition is imposed at the sphere surface. The net difference between the energy added to the sphere by incoming particles and the energy removed from the sphere by leaving particles is summed over the entire duration of the simulation. The heat transfer rate between the surrounding gas and the sphere is then computed as the total net energy exchange divided by the time length of the simulation.

For the zero energy flux model, each thermally interacting particle is treated as if it merges into the liquid droplet, delivering its energy, including an energy of vaporization, to the droplet. Computationally, particles that merge into the droplet are removed from the simulation. The number of particles absorbed in this manner is counted, and the energy delivered to the droplet by these particles is summed. In a subsequent portion of the time step calculations, particles are added to the simulation domain just beyond $r = r_s$. Each time a particle is added in this way, the energy carried away from the sphere by the particle is added to a cumulative total for the time step. When this total just exceeds the amount delivered to the sphere during the time step, the particle addition process is stopped. The amount by which the energy for the added particles exceeds that for the incoming particles is subtracted from the energy of the incoming particles in the next time step. This imposes a zero net energy flux condition on the sphere interface. However, the number of emitted particles will exceed the number of incident particles, resulting in a finite net mass flux from the droplet surface.

For both models, the location at which a particle is added to the simulation is determined by randomly sampling a distribution function that produces a uniform flux of particles over the surface of the sphere. The velocity components and rotational energy were randomly sampled from appropriate Boltzmann distributions for molecules crossing a fixed surface in a gas at the specified sphere temperature $T_s$. The distributions used are described in the appendix.

In the mean, the energy of saturated vapor molecules exceeds that of saturated liquid molecules by $mu_{lv}$. At temperature $T_s$, the mean energy of a diatomic vapor molecule is $(5/2)k_B T_s$. The energy of an arbitrary molecule in the gas with translational energy $\epsilon_{tr}$ and rotational energy $\epsilon_{\text{rot}}$ thus exceeds the mean energy of the liquid molecules in the droplet by $\epsilon_{tr} + \epsilon_{\text{rot}} - (5/2)k_B T_s + mu_{lv}$. In invoking the energy balance at the droplet interface, the mean energy of the saturated liquid molecules was taken as the level of zero energy. The energy delivered to the droplet by one interacting particle from the surrounding gas is therefore given by

$$\Delta E_g = N_{mpp}(\epsilon_{tr} + \epsilon_{\text{rot}} - (5/2)k_B T_s + mu_{lv}) \tag{12}$$

where $N_{mpp}$ is the number of molecules per particle in the simulation. This relation was used to compute the energy delivered to the droplet by a particle striking and interacting with the droplet. Based on similar reasoning, the following relation was used to compute the energy removed from the droplet by an emitted particle:

$$\Delta E_s = N_{mpp}(\epsilon_{tr} + \epsilon_{\text{rot}} - (5/2)k_B T_s + mu_{lv}) \tag{13}$$

In using this relation, $\epsilon_{tr}$ and $\epsilon_{\text{rot}}$ were first obtained by sampling the appropriate Boltzmann distributions at $T_s$.

An alternative approach to treating the droplet boundary would be to specify the emitted molecular flux from the droplet surface using the following relation obtained from kinetic theory for an interface at equilibrium (see, for example, Carey, 1992):

$$j_e = \frac{\sigma_t P_{\text{sat}}(T_s)}{\sqrt{2\pi m k_B T_s}} \tag{14}$$

In this treatment, the emitted particle flux is $j_e/N_{mpp}$ and the droplet surface temperature $T_s$ must be iteratively adjusted to match the energy transported by incident and emitted molecules at the droplet surface. The zero energy flux model was used for the calculations reported here because its accuracy is comparable to the flux specification model and it is somewhat simpler to implement computationally. We have run simulation calculations using the flux specification method described above. The results of those simulation runs differed only slightly from simulation results obtained with the zero energy flux model for the same conditions. The droplet surface temperature for the flux specification method agreed with that for the zero energy flux model within 0.3 K and the predicted heat transfer to the droplet for the two models agreed to within 1 percent. Using the zero energy flux model described here effectively neglects the slight shift in $T_s$ required to balance the inward and outward transport of energy at the droplet surface. As noted above, our calculations indicate that neglecting this effect has negligible impact on the predicted heat transfer.



Downloaded 12 Dec 2010 to 193.140.21.150. Redistribution subject to ASME license or copyright; see http://www.asme.org/terms/Terms_Use.cfm

In the simulation calculations in this study, the simulation domain shown in Fig. 1 was filled with cubic cells, which formed a uniform Cartesian mesh. Depending on the size of the droplet in the simulation, the side of the cell ranged from 0.0125 $\mu$m to 0.09375 $\mu$m. The number of cells used was a compromise between accuracy and computational effort. The ratio of the number of molecules per particle $N_{mpp}$ was chosen in each simulation to compromise between computational accuracy and storage limitations on the computer. The values used typically ranged from 2.70 to 1140 in the calculations reported here. Simulations were typically run for 5000 to 10,000 time steps, with a time step typically in the range of 25–50 picoseconds.

After running the simulation for a sufficiently long time, the simulation predicts the equilibrium temperature and density fields adjacent to the surface of the sphere for arbitrarily specified values of the sphere temperature $T_s$ and $T_4$. The matching procedure described in the previous section can then be used to determine the corresponding value of $T_\infty$ and the heat transfer coefficient. To do so, the heat flux from the sphere surface is first computed from the simulation results. For the zero mass flux surface interaction model, this is done as

$$q_s'' = \frac{\Delta E_{\text{net}}}{4\pi r_s^2 N_{\text{steps}} \Delta t/8} \tag{15}$$

where $N_{\text{steps}}$ is the number of time steps in the simulation and $\Delta E_{\text{net}}$ is the total net energy transferred to the surface due to particle interactions for the simulation. For the zero energy flux surface interaction model, $q_s''$ is computed as

$$q_s'' = \frac{\Delta N_{\text{net}} m u_{lv} N_{mpp}}{4\pi r_s^2 N_{\text{steps}} \Delta t/8} \tag{16}$$

where $\Delta N_{\text{net}}$ is the difference between the total number of incident particles that interacted with the surface and the total number emitted during the simulation. Conservation of energy requires that at steady state, the heat flux through the spherical surface at $r/r_s = 4$ must be given by

$$q_4'' = (4)^{-2} q_s'' = q_s''/16 \tag{17}$$

Transport of energy beyond $r = 4r_s$ is treated as continuum transport from an evaporating sphere with radius $4r_s$ for a surface temperature of $T_4$ and a heat flux of $q_s''/16$. Inverting the Nusselt number relation (7) for such circumstances yields

$$T_\infty = T_4 + \left(\frac{h_{lv}}{c_{pv}}\right)[e^{r_s q_s'' c_{pv}/4k_v h_{lv}} - 1] \tag{18}$$

The limit of $h_{lv} \to \infty$ corresponds to a sphere with no evaporation. In that case Eq. (18) reduces to

$$T_\infty = T_4 + \frac{r_s q_s''}{4k_v} \tag{19}$$

Equation (16) with Eq. (18) or Eq. (15) with Eq. (19) can be used to determine $T_\infty$, and $h$ can then be found as $h = q_s''/(T_\infty - T_s)$.

## Validation of the Simulation Model

The capability of the simulation scheme described in the previous section to accurately predict heat transfer was tested by comparing the variation of Nusselt number with Knudsen number indicated by available data with the variation predicted by the simulation. A series of six simulation computations were done for small-diameter cooled spheres with an accommodation coefficient $\sigma_t$ of 0.8 surrounded by low-pressure nitrogen gas. These calculations were done at a pressure of 20.6 kPa with $T_s$ = 66 K and $T_4$ = 120 K for sphere diameters of 0.15, 0.2, 0.36, 0.5, 1.0, and 1.5 $\mu$m. These correspond to $\text{Kn}_D$ values ranging from 0.86 to 0.0924, where $\text{Kn}_D = \lambda_\infty/D$ is the Knudsen number based on ambient mean free path and sphere diameter. The far ambient mean free path in this definition was evaluated using the following well-known result of simple kinetic theory

$$\lambda_\infty = \frac{1}{\sqrt{2}\pi n_{m,\infty} D_m^2} = \frac{k_B T_\infty}{\sqrt{2}\pi P_\infty D_m^2} \tag{20}$$

Since we wished to compare the simulation with heat transfer data for a heated solid sphere, the zero mass flux treatment of the particle–surface interactions was used in these calculations. The simulation was run for 5000 time steps to achieve the results presented here. Extension of the runs to 10,000 time steps was found to produce negligible difference in the statistics from the run.

In their study of free convection effects on heat transfer from a sphere to a rarefied gas, Kyte et al. (1953) recommended evaluating $k_v$ at the average of the far ambient temperature and the temperature just inside the gas near the surface of the sphere. Based on their recommendation, we also evaluated $k_v$ at the average of the far ambient temperature and the temperature just inside the gas near the surface of the sphere in our computations of $\text{Nu}_D = hD/k_v$. The variation of $\text{Nu}_D$ with $\text{Kn}_D$ indicated by the simulation calculations is compared to that indicated by the heat transfer data of Takao (1963) in Fig. 2. The data were obtained for a heated sphere with a diameter of 15 mm in low pressure air. It can be seen that the trend in the simulation results is in close agreement with the data.

Clift et al. (1978) have proposed the following correlation for heat transfer from small spherical bodies subject to noncontinuum effects:

$$\text{Nu}_D = \frac{2\sigma_t(1+\gamma)}{(9\gamma - 5)\,\text{Kn}_D + \sigma_t(1+\gamma)} \tag{21}$$

where $\gamma$ is the ratio of specific heats. These authors have stated that this correlation provides a good fit to the data of Takao (1963) if the accommodation coefficient is taken to be 0.8. Their comment to this effect was the basis for our selection of $\sigma_t = 0.8$ in the simulation calculations to be compared with the data. Using $\gamma = 1.40$ for nitrogen, the variation of $\text{Nu}_D$ with $\text{Kn}_D$ predicted by Eq. (21) for $\sigma_t = 0.8$ is also plotted as the solid curve in Fig. 2. It can be seen that the simulation results for $\sigma_t = 0.8$ also agree well with the prediction of this correlation.

## Simulation of Microdroplet Evaporation

To explore the interaction of vapor generation and noncontinuum effects, a series of simulation computations were done to

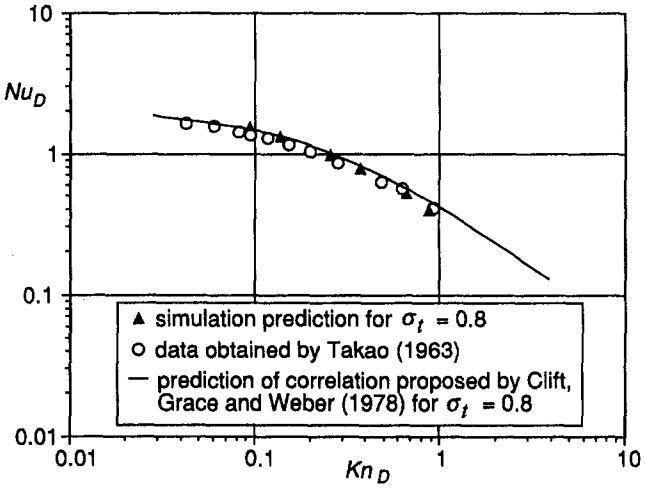



**Fig. 2 Comparison of the variation of $\text{Nu}_D$ with $\text{Kn}_D$ predicted by the simulation with data for a heated 15-mm-dia sphere obtained by Takao (1963) and the correlation proposed by Clift et al. (1978)**



Downloaded 12 Dec 2010 to 193.140.21.150. Redistribution subject to ASME license or copyright; see http://www.asme.org/terms/Terms_Use.cfm

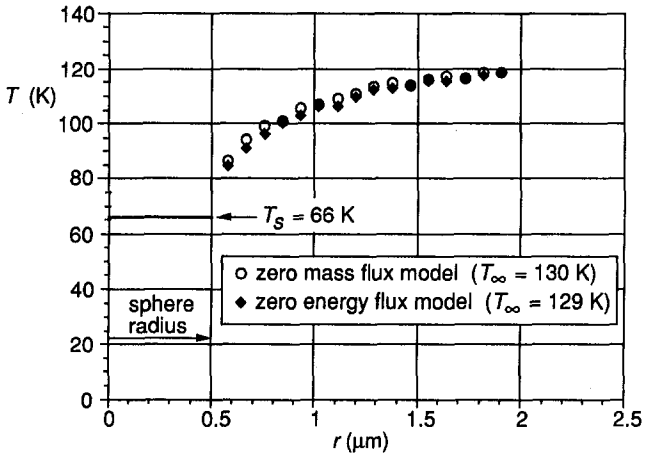



**Fig. 3 Comparison of predicted temperature fields for a solid cooled sphere (zero mass flux model) and an evaporating droplet of liquid nitrogen (zero energy flux model) having diameters of 1 $\mu$m. Both calculations were done for an ambient pressure of 20.6 kPa with $T_s$ = 66 K and $T_4$ = 120 K.**

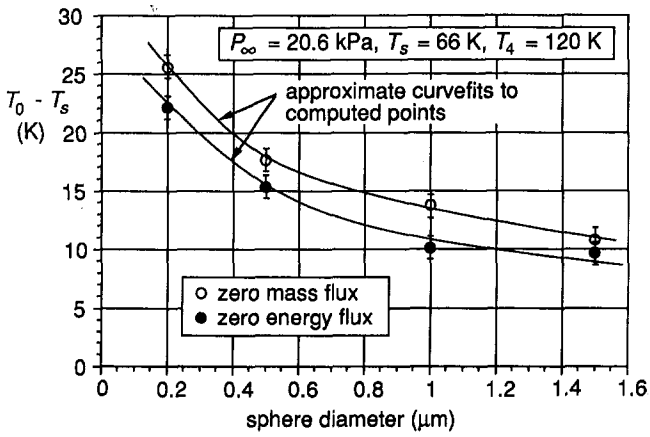



**Fig. 4 Predicted temperature slip at the surface for a solid cooled sphere (zero mass flux model) and an evaporating droplet of liquid nitrogen (zero energy flux model)**

model the thermal transport to a spherical nitrogen microdroplet surrounded by low-pressure superheated nitrogen gas. For all these calculations, the ambient pressure was taken to be 20.6 kPa with $T_s$ = 66 K. The value of the accommodation coefficient $\sigma_t$ for an evaporating interface has been the subject of much debate. The tabulation of $\sigma_t$ values assembled by Paul (1962) lists values ranging from 0.02 to 0.04 for some liquids to values very near 1.0 for others. Mills (1965) has suggested that molecular accommodation should be imperfect only when the interface is impure. Paul (1962) notes that in almost every case where $\sigma_t$ was found to be appreciably less than one, the average condition of the vapor molecules was different from that for the liquid phase because of association, disassociation, or polymerization. Based on these observations, we selected $\sigma_t$ = 0.9 for our evaluation of the surface interaction models, with the implicit assumptions that the liquid nitrogen is virtually pure and that association, disassociation, and polymerization do not occur to any significant degree. The simulation scheme can, of course, be used with lower accommodation coefficients for systems when low values of $\sigma_t$ are appropriate.

Simulation results were first obtained for sphere diameters of 0.2, 0.5, 1.0, and 1.5 $\mu$m for $T_4$ = 120 K using both the zero mass flux model and the zero energy flux model. The zero mass flux model is equivalent to the zero energy flux model in the limit Ja $\rightarrow$ 0. The results for these two models were compared to assess the effects of interface vapor generation on transport. Using relations given in Carey (1992), it is easy to show that for this range of droplet diameters, the shift in the saturation conditions due to interfacial tension effects is very small. The effect of droplet diameter on the saturation conditions was therefore neglected in these calculations, and the surface temperature of the droplet $T_s$ was kept constant at the normal saturation temperature, 66 K.

Figure 3 shows the temperature profile near the sphere predicted by the simulation with the two surface interaction models. Overall, the temperature profiles predicted by the two interaction models are very nearly the same. Near the sphere the profiles diverge somewhat, however, with the temperature for the zero energy flux model being lower. This was observed in varying degrees for all droplet sizes considered in our calculations.

Figure 4 shows the predicted variation of the temperature slip at the droplet surface with droplet size for the two surface interaction models considered in this study. The error bars on the computed points have been added to emphasize that the statistical uncertainty in the averaged quantities in the simulation translates to about $\pm$1 K uncertainty in the computed gas temperatures. The consistently lower slip for the zero energy flux model is apparently a consequence of injection of mass near the interface, which biases the temperature toward that of the interface. This tends to surround the droplet with molecules that have, on the average, lower energy than molecules near the sphere would if no net evaporation occurred. For lower mean energy, the molecules will transfer less energy to the interface when they strike it, resulting in a lower rate of heat transfer to the interface. This conclusion regarding the effect of net vapor generation at the interface on heat transfer is further verified by trends in Fig. 5, which shows the variation of $Nu_D$ with $Kn_D$ predicted by the simulation with $\sigma_t$ = 0.9 for the two different surface interaction models.

To explore further the effect of varying Ja, a series of simulation calculations were done for droplet diameters of 0.36 $\mu$m and 1.0 $\mu$m with $T_4$ set to values ranging from 120 to 400 K. This resulted in ambient temperatures ranging from 125 to 416 K. The ambient pressure and accommodation coefficient were again taken to be 20.64 kPa and 0.9, respectively. One effect of relatively large Ja is illustrated in Fig. 6. In this figure the $w$ velocity distribution is shown at two cell locations along the $z$ axis. One location is adjacent to the droplet surface ($r = r_s$) and the other is near $r = 4r_s$. Note that along the $z$ axis $w$ is the velocity component in the radial direction. The points in Fig. 6 are based on statistics collected for a bin size $\Delta w$ equal to $0.05\sqrt{k_B T/m}$, where $T$ is the local temperature in the cell. The $w$ velocity distribution exhibits a shift to positive values near the

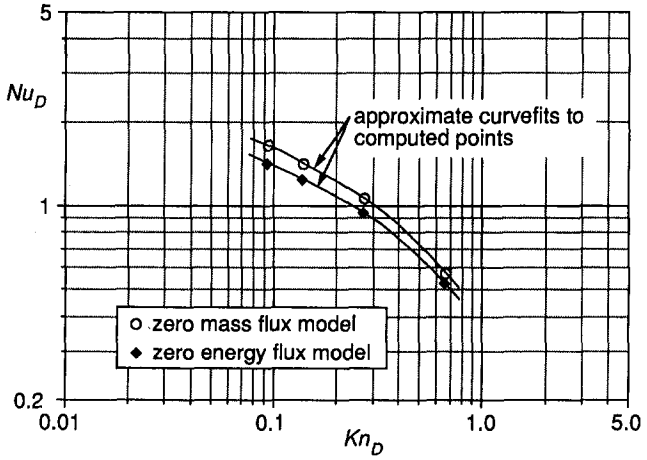



**Fig. 5 Comparison of predicted variations of $Nu_D$ with $Kn_D$ for a solid cooled sphere (zero mass flux model) and an evaporating droplet of liquid nitrogen (zero energy flux model). All calculations were done for an ambient pressure of 20.6 kPa with $T_s$ = 66 K and $T_4$ = 120 K.**



Downloaded 12 Dec 2010 to 193.140.21.150. Redistribution subject to ASME license or copyright; see http://www.asme.org/terms/Terms_Use.cfm

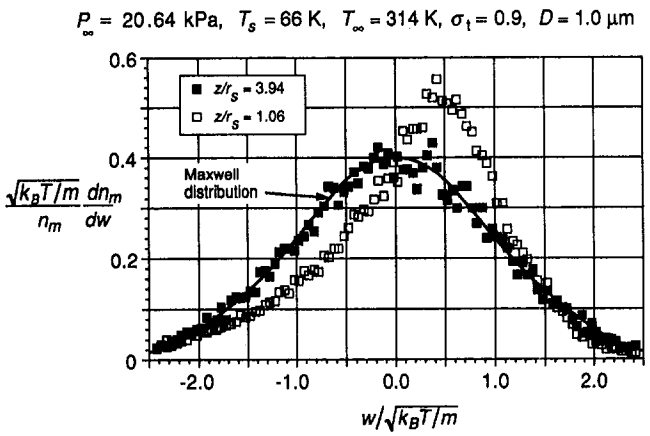



**Fig. 6 Distributions of the $w$ component of velocity obtained from the simulation at cells along the $z$ axis. The conditions indicated correspond to Ja = 1.22.**

droplet surface as a consequence of the net radial velocity associated with evaporation at the surface of the droplet. However, by the time the vapor reaches the outer edge of the simulation, the mean radial velocity has virtually dropped to zero and the $w$ velocity distribution is in good agreement with the well-known Maxwell distribution. At lower Ja values, the surface normal velocity distribution near the droplet surface is shifted to a lesser degree and more closely matches the Maxwell distribution. At both locations indicated in Fig. 6, the $u$ and $v$ velocity distributions from the simulation were found to agree well with the Maxwell distribution at the local temperature. The rotational energy distribution differed from the Boltzmann distribution by as much as 20 percent in the cell adjacent to the droplet surface. At $r = 3.96r_s$, the rotational energy distribution agreed with the Boltzmann distribution to within 3 percent.

In Fig. 7($a$), it can be seen that increasing the ambient temperature increases both Ja and $\mathrm{Kn}_D$. The combined effect of increasing both of these parameters is to reduce the Nusselt number, which explains the reduction of $\mathrm{Nu}_D$ with increasing ambient temperature indicated in Fig. 7($b$). Figure 7($c$) shows the computed variation of the fractional temperature slip with increasing ambient temperature. Even though $\mathrm{Kn}_D$ increases by a large amount over this temperature range, the fractional temperature slip at the surface of the droplet actually decreases because of the increased generation of vapor at the droplet surface associated with the increased vaporization rate at high ambient temperatures.

To assess the effect of Jakob number variation on heat transfer separately, Nusselt numbers corresponding to the points in Figs. 5 and 7 were normalized with values predicted by the correlation of Clift et al. (1978). The resulting ratios $\mathrm{Nu}_D/(\mathrm{Nu}_D)_{\mathrm{corr}}$ are plotted as a function of Ja in Fig. 8. In the continuum limit $(\mathrm{Nu}_D)_{\mathrm{corr}}$ is equal to 2, and from Eq. (7) this ratio is given by

$$\left(\frac{\mathrm{Nu}_D}{(\mathrm{Nu}_D)_{\mathrm{corr}}}\right)_{\mathrm{continuum}} = \frac{\ln\{\mathrm{Ja}+1\}}{\mathrm{Ja}} \tag{22}$$

It can be seen in this plot that although the computed points span a wide range of $\mathrm{Kn}_D$ values, they all lie close to the variation predicted by the continuum solution. The computed points lie within about 9 percent of the line corresponding to the continuum relation (22). These results imply that the heat transfer to an evaporating droplet at arbitrary $\mathrm{Kn}_D$ and Ja values is predicted reasonably well by the following relation, which is obtained by combining the correlation of Clift et al. (1978) with Eq. (22):

$$\mathrm{Nu}_D = \frac{2\sigma_t(1+\gamma)}{(9\gamma-5)\,\mathrm{Kn}_D + \sigma_t(1+\gamma)}\left[\frac{\ln\{\mathrm{Ja}+1\}}{\mathrm{Ja}}\right] \tag{23}$$

This relation does not provide a best fit to the points in Fig. 8, however. The imperfect fit suggests that simple superposition of the noncontinuum and interface vapor generation effects does not provide a completely accurate prediction of their effect on heat transfer and that it may be appropriate to introduce a correction factor to Eq. (23) to account for interactions between the mechanisms. Equation (23) was therefore empirically modified to the form below:

$$\left(\frac{\mathrm{Nu}_D}{(\mathrm{Nu}_D)_{\mathrm{corr}}}\right) = \frac{\ln\{\mathrm{Ja}+1\}}{\mathrm{Ja}} \times\left[1+\left(\frac{0.40\,\mathrm{Ja}}{1+10\,\mathrm{Ja}^2}\right)\left(\frac{\mathrm{Kn}_D}{0.001+\mathrm{Kn}_D}\right)\right] \tag{24}$$

This relation, plotted as the heavy curve in Fig. 8, fits all the points shown to within about 5 percent. By combining the correlation of Clift et al. (1978) with Eq. (24), the following improved correlation is obtained, which matches the computed heat transfer for evaporating nitrogen droplets to within 5 percent and reduces to the appropriate limits for $\mathrm{Ja}\to 0$ and $\mathrm{Kn}_D \to 0$:

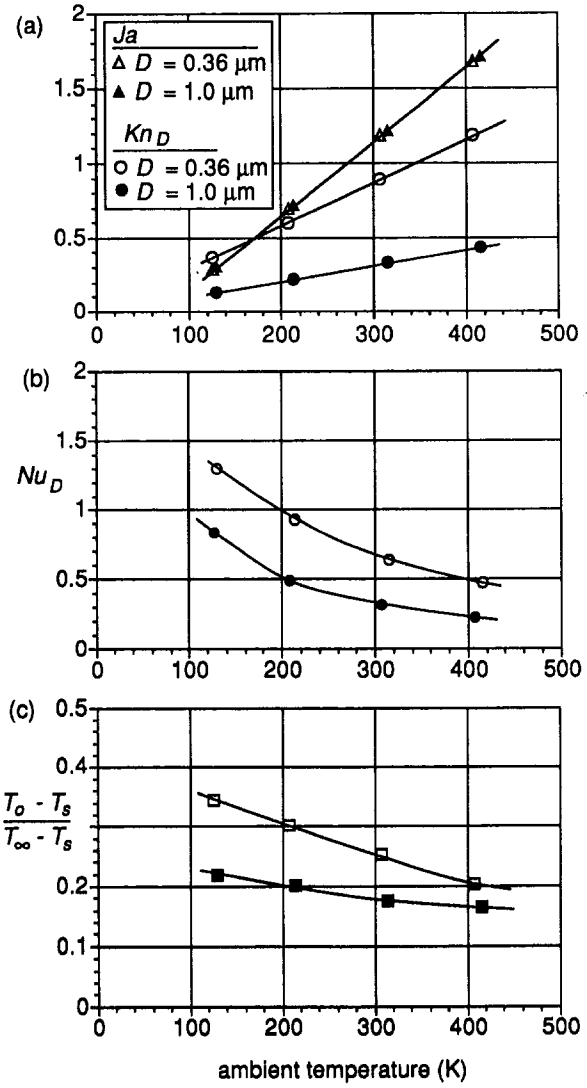



**Fig. 7 Variation of Ja, $\mathrm{Kn}_D$, $\mathrm{Nu}_D$, and temperature slip ratio with ambient temperature for liquid nitrogen droplets evaporating in superheated nitrogen gas at 20.6 kPa. The curves are approximate fits to points computed with the simulation scheme for $\sigma_t$ = 0.9.**



Downloaded 12 Dec 2010 to 193.140.21.150. Redistribution subject to ASME license or copyright; see http://www.asme.org/terms/Terms_Use.cfm

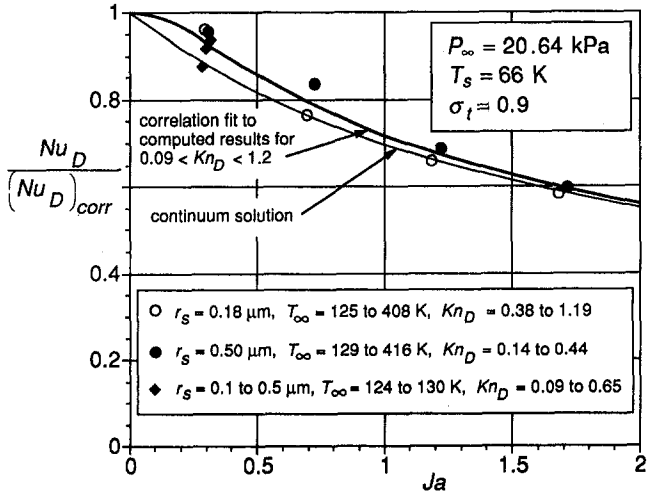



**Fig. 8 Predicted effect of varying Ja on heat transfer for nitrogen droplets evaporating in superheated nitrogen gas**

$$\mathrm{Nu}_D = \frac{2\sigma_t(1+\gamma)}{(9\gamma-5)\,\mathrm{Kn}_D + \sigma_t(1+\gamma)}\left[\frac{\ln\{\mathrm{Ja}+1\}}{\mathrm{Ja}}\right] \times\left[1+\left(\frac{0.40\,\mathrm{Ja}}{1+10\,\mathrm{Ja}^2}\right)\left(\frac{\mathrm{Kn}_D}{0.001+\mathrm{Kn}_D}\right)\right] \quad (25)$$

Although the computed results presented in this paper are specifically for an accommodation coefficient of 0.9, additional calculations have been done for accommodation coefficients ranging from 0.5 to 0.9. In general, the heat transfer variation with accommodation coefficient was found to be in good agreement with that predicted by Eq. (25).

## Prediction of Droplet Size Variation With Time

It is easy to show from an elementary energy balance that the time rate of change of the diameter of an evaporating droplet is related to the instantaneous heat transfer coefficient as

$$\frac{dD}{dt} = -\frac{2h(T_\infty - T_s)}{h_{lv}\rho_l} \quad (26)$$

For the diameter range of interest here, the droplet shrinking will have negligible effect on the equilibrium interface temperature at fixed pressure. This relation can be integrated if the variation of the heat transfer coefficient is known. Solving the correlation (25) for the heat transfer coefficient $h$, substituting into Eq. (26), and integrating from an initial diameter $D_0$ at $t = 0$ to $D = 0$ at $t = t_0$, the following the relation can be obtained for the time required to completely evaporate the droplet:

$$\frac{\alpha_v t_0}{D_0^2} = \frac{(\rho_l/\rho_v)}{8\ln\{\mathrm{Ja}+1\}}\left\{1+2\left[\frac{9\gamma-5}{\sigma_t(1+\gamma)}\right]\mathrm{Kn}_0 - \frac{800\,\mathrm{Ja}\,\mathrm{Kn}_0}{1+10\,\mathrm{Ja}^2}\left[1-\mathrm{Kn}_0\left(1000-\frac{9\gamma-5}{\sigma_t(1+\gamma)}\right)\times\ln\left\{\frac{\mathrm{Kn}_0+0.001}{\mathrm{Kn}_0}\right\}\right]\right\} \quad (27)$$

where

$$\mathrm{Kn}_0 = \lambda_\infty/D_0 \quad (28)$$

It is worth noting that Eq. (27) fully accounts for the effects of surface accommodation, interface vapor generation, and noncontinuum behavior on the total evaporation time for a microdroplet. Equation (27) reduces to the continuum evaporation time $t_{0,c}$ in the limit $\mathrm{Kn}_0 \to 0$. It can be shown that

$$\frac{t_0}{t_{0,c}} = 1+2\left[\frac{9\gamma-5}{\sigma_t(1+\gamma)}\right]\mathrm{Kn}_0 - \frac{800\,\mathrm{Ja}\,\mathrm{Kn}_0}{1+10\,\mathrm{Ja}^2}\left[1-\mathrm{Kn}_0\left(1000-\frac{9\gamma-5}{\sigma_t(1+\gamma)}\right)\ln\left\{\frac{\mathrm{Kn}_0+0.001}{\mathrm{Kn}_0}\right\}\right] \quad (29)$$

For the conditions considered in this study, $t_0/t_{0,c}$ is as large as 3, indicating that noncontinuum effects increase the total evaporation time by as much as a factor of three.

## Concluding Remarks

The stochastic model of the molecular transport between a microsphere and a surrounding gas proposed in this paper has the advantage that it directly calculates the temperature and density profiles in the region adjacent to the sphere, as well as the overall thermal energy transfer to the sphere. Incorporating a zero mass flux surface interaction model into the simulation and using an accommodation factor of 0.8, good agreement was found between the experimental heat transfer data for a heated sphere and the predictions of the simulation. This appears to support the validity of the modified simulation scheme proposed here, which includes matching to an outer continuum solution.

The results of this study indicate that use of a zero energy flux surface interaction model within the simulation appropriately accounts for the net generation of mass at the interface of an evaporating droplet. The results confirm the expectation that increased vapor generation reduces the temperature slip at the droplet surface for noncontinuum conditions.

The unique capability of the simulation methodology described here to treat noncontinuum and interface vapor generation effects in a very fundamental way has illuminated the microphysics of droplet evaporation and made it possible to develop a quasi-theoretical closed-form relation that can be used to predict evaporation rates of droplets when both these effects are important. In our survey of the prior literature we could find no Nusselt number relations for heat transfer controlled droplet evaporation that simultaneously account for these effects. It therefore appears that the relation reported in this paper is the first to permit explicit prediction of both noncontinuum and interface vapor generation effects on heat transfer for this type of droplet vaporization process. For the microdroplets considered here, noncontinuum effects increase the total droplet evaporation time by as much as a factor of three above that predicted for continuum transport under the same conditions.

It is also noteworthy that Eq. (27) quantifies the time scale of the microdroplet shrinkage as being on the order of about 0.1 ms for the conditions of interest here. The simulations indicate that for these conditions, it takes less than 0.1 μs for the system to establish temperature and density profiles close to the equilibrium variations. In hindsight we can therefore fully justify using a steady-state simulation to predict heat transfer for the dynamic process of droplet evaporation because the molecular gas transport adjusts much more rapidly than variations in the boundary conditions resulting from the decreasing size of the droplet.

## Acknowledgments

Support for this research was provided by the National Science Foundation under grant No. CTS-9024862. The comments and suggestions of the reviewers are also greatly appreciated.

## References

Baganoff, D., and McDonald, J. D., 1990, "A Collision-Selection Rule for a Particle Simulation Method Suited to Vector Computers," *Phys. Fluids A*, Vol. 2, pp. 1248–1259.

Bird, G. A., 1976, *Molecular Gas Dynamics*, Clarendon, Oxford, United Kingdom.

Borgnakke, C., and Larsen, P. S., 1975, "Statistical Collision Model for Monte Carlo Simulation of a Polyatomic Gas Mixture," *J. Computational Physics*, Vol. 18, pp. 405–420.



Downloaded 12 Dec 2010 to 193.140.21.150. Redistribution subject to ASME license or copyright; see http://www.asme.org/terms/Terms_Use.cfm

Carey, V. P., 1992, *Liquid–Vapor Phase-Change Phenomena,* Taylor and Francis, New York.

Chernyak, V. G., and Margilevskiy, A. Y., 1989, "The Kinetic Theory of Heat and Mass Transfer From a Spherical Particle in a Rarefied Gas," *Int. J. Heat Mass Transfer,* Vol. 32, pp. 2127–2134.

Clift, R., Grace, J. R., and Weber, M. E., 1978, *Bubbles, Drops, and Particles,* Academic Press, New York.

Kavanau, L. L., 1955, "Heat Transfer From Spheres to a Rarefied Gas in Subsonic Flow," *Transactions of the ASME,* Vol. 77, pp. 617–623.

Kyte, J. R., Madden, A. J., and Piret, E. L., 1953, "Natural Convection Heat Transfer at Reduced Pressure," *Chemical Engineering Progress,* Vol. 49, No. 12, pp. 653–662.

Langmuir, I., 1915, "The Dissociation of Hydrogen Into Atoms, Part II," *J. Am. Chem. Soc.,* Vol. 37, pp. 417–458.

Lou, Y. S., 1978, "On the Nonlinear Droplet Condensation and Evaporation Problem," *J. Appl. Physics,* Vol. 49, pp. 2350–2356.

McDonald, J. D., 1989, "A Computationally Efficient Particle Simulation Method Suited to Vector Computer Architecture," Report SUDAAR 589, Department of Aeronautics and Astronautics, Stanford University.

Mills, A. F., 1965, "The Condensation of Steam at Low Pressures," Technical Report on NSF GP-2520, series No. 6, issue No. 39, Space Sciences Laboratory, Univ. of California at Berkeley.

Paul, B., 1962, "Compilation of Evaporation Coefficients," *ARS Journal,* Vol. 32, pp. 1321–1328.

Sone, Y., and Sugimoto, H., 1993, "Kinetic Theory Analysis of Steady Evaporating Flows From a Spherical Condensed Phase Into a Vacuum," *Phys. Fluids A,* Vol. 5, pp. 1491–1511.

Takao, K., 1963, "Heat Transfer From a Sphere in a Rarefied Gas," *Rarefied Gas Dynamics, Proc. Third Int. Symp.,* Vol. II, Academic Press, New York, pp. 102–111.

Young, J. B., 1991, "The Condensation and Evaporation of Liquid Droplets in a Pure Vapour at Arbitrary Knudsen Number," *Int. J. Heat Mass Transfer,* Vol. 34, pp. 1649–1661.

## APPENDIX

To initiate the particle simulation calculation, the cells in the simulation domain are initially loaded with particles, each of which represents a fixed number of molecules of a given type. The number of particles initially loaded into the cells is arbitrarily set to correspond to the ambient number density of molecules. The mean number of particles in each cell is subsequently determined as the calculation is marched forward in time.

The particles initially loaded into the cells are randomly given translational and internal (rotational) energies by randomly sampling values from the Boltzmann distribution for the gas (at equilibrium) at the outer boundary temperature. The particle simulation method marches the computation forward in time. For each time step $\Delta t$, the following operations were executed:

1 Statistical information on particles in each cell was gathered at the beginning of each time step.
2 All particles were transported in space at constant velocity along their current velocity vectors for time $\Delta t$, ignoring possible collisions.
3 Each particle was checked to determine if it hit the sphere or hit a boundary of the simulation domain. If it had, appropriate actions were taken, based on the nature of the boundary. Specular surfaces only reverse the normal component of velocity of the particles that strike them. Particles striking the sphere or going beyond the outer boundary were removed from the simulation.
4 Particles were randomly added to cells along the outer boundary surface $r = 4r_s$ to simulate the molecular flux across this surface. The velocities and rotational energies were sampled from appropriate Boltzmann distributions for the outer boundary temperature.
5 Particles were randomly added to cells along the droplet surface $r = r_s$ using the appropriate surface interaction model.
6 Candidate collisions pairs were randomly selected in each cell until approximately $n_p/2$ candidate collision pairs were formed per cell, where $n_p$ is the particle number density in each cell. A selection rule (based on the statistical probability of collision) was used to determine whether the pair actually executed a collision.
7 For each of the candidate pairs accepted for collision, the collision is executed, conserving energy and momentum. The orientation of the post-collision relative velocity vector was chosen randomly.

For particles added to the domain at the sphere surface or at the outer boundary, the surface normal velocity component ($c_\perp$), the tangential velocity components ($c_=$) and the rotational energy were sampled from the distributions

$$\mathcal{J}(c_\perp)dc_\perp = \frac{mc_\perp}{k_BT}\, e^{-mc_\perp^2/2k_BT}dc_\perp \qquad \text{(A1)}$$

$$\mathcal{J}(c_=)dc_= = \left(\frac{m}{2\pi k_BT}\right)^{1/2} e^{-mc_=^2/2k_BT}dc_= \qquad \text{(A2)}$$

$$\mathcal{J}(\epsilon_{\text{rot}})d\epsilon_{\text{rot}} = \frac{1}{k_BT}\, e^{-\epsilon_{\text{rot}}/k_BT}d\epsilon_{\text{rot}} \qquad \text{(A3)}$$

In using the distributions above, $T$ was set equal to either $T_s$ or $T_4$, as appropriate. At the sphere surface $c_\perp$ was taken to be an outward normal velocity whereas at the outer boundary it was taken to be an inward normal velocity. Sampled velocity components were subsequently converted to $u$, $v$ and $w$ components associated with the $x$–$y$–$z$ coordinate system.

The selection rule used in step (6) above was essentially that recommended by Baganoff and McDonald (1990). For the hard-sphere interaction model used in this study, this amounts to picking the number of potential collision pairs $S$ for the cell equal to $\langle n_p\rangle/2$, where $\langle n_p\rangle$ is the mean particle number density per cell, and selecting collision pairs with probability $P_S$ given by

$$P_S = 1.5\,\frac{\langle n_p\rangle |\vec{v}_r|\,\Delta t}{\sqrt{2}\bar{n}_{p,\text{ref}}\,\lambda_{\text{ref}}} \qquad \text{(A4)}$$

where $\bar{n}_{p,\text{ref}}$ and $\lambda_{\text{ref}}$ are the mean particle density and mean free path for the reference condition at $r = 4\ r_s$, and $|\vec{v}_r|$ is the magnitude of the precollision relative velocity of the particles being considered as a possible collision pair. The value of the multiplier 1.5 in Eq. (A4) was chosen to match simulation collision frequencies with collision frequency predictions of kinetic theory for the conditions considered in this study.

Molecular collisions within the vapor were modeled with a simple hard-sphere interaction model. For hard-sphere collisions, post-collision relative velocities must be isotropically scattered. The method used in this study to randomly select postcollision velocities with isotropic scattering has been widely used in direct molecular simulation calculations. A detailed description of this methodology can be found in Bird (1976) or McDonald (1989).

If the collision is elastic (no exchange of energy in internal modes), the magnitude of the postcollision relative velocity vector is set equal to the value dictated by the precollision velocities of the particles. If the collision is inelastic, however, the postcollision fraction of relative translational energy to total collision energy is sampled from the distribution for an equilibrium gas. For diatomic molecules obeying a hard-sphere potential and having rotational internal storage only, Borgnakke and Larsen (1975) have shown that this fraction $f_{rt}$ obeys the distribution $\mathcal{J}(f_{rt})$ given by

$$\mathcal{J}(f_{rt})df_{rt} = 6f_{rt}(1 - f_{rt})df_{rt} \quad (\text{for } 0 \le f_{rt} \le 1) \qquad \text{(A5)}$$

In our calculations, this distribution was randomly sampled to determine $f_{rt}$ values for each collision.

Following McDonald (1989), an effective rotational collision number of 5 was used in our calculations with the result that one in five collisions was treated as inelastic. The method used to partition the collision energy in the postcollision state using the stochastically determined $f_{rt}$ value is similar to that used by McDonald (1989) for high-speed rarefied gas flows.



Downloaded 12 Dec 2010 to 193.140.21.150. Redistribution subject to ASME license or copyright; see http://www.asme.org/terms/Terms_Use.cfm

# Flow and Cold Heat-Storage Characteristics of Phase-Change Emulsion in a Coiled Double-Tube Heat Exchanger

**H. Inaba**
Professor.

**S. Morita**
Graduate Student.

Department of Mechanical Engineering,
Faculty of Engineering,
Okayama University,
Tsushimanaka 3-1-1, Okayama, Japan

*This paper dealt with the flow and cold heat-storage characteristics of the oil (tetradecane, $C_{14}H_{30}$, freezing point 278.9 K)/water emulsion as a latent heat-storage material having a low melting point. A coiled double-tube heat exchanger was used for the cold heat-storage experiment. The pressure drop, the heat transfer coefficient, and the finishing time of cold heat storage in the coiled tube were measured as experimental parameters. It was understood that the flow behavior of the emulsion as a non-Newtonian fluid had an important role in the present cold heat storage. The useful nondimensional correlation equations for the additional pressure loss coefficient, the heat transfer coefficient, and the cold heat storage time were derived in terms of modified Dean number and heat capacity ratio.*

## 1 Introduction

A slurry-type latent heat storage (phase-change material) system is one of the available cooling systems that can take the place of the sensible (water) heat-storage system. The latent heat-storage system can scale down the pipe size due to the augmentation of the transported heat. It also can increase the heat transfer coefficient by the churning effect and high thermal conductivity of the dispersion materials.

Some studies of clathrate (Mori et al., 1975), ice (Takahashi et al., 1990) and snow (Shirakashi et al., 1990) as a cold latent heat-storage material have been reported. These latent heat-storage materials prove to have problems of grain sintering and separation between water and the dispersion material. The microencapsulated latent heat-storage materials (Yoshida, 1990) can prevent grain sintering; however, the stable homogeneous flow of the materials cannot be obtained if the microcapsules don't have very small diameter and flexibility.

The present phase-change emulsion consists of the latent heat-storage material particles dispersed into water, which flows stably and homogeneously. The phase-change emulsion is passed through the heat exchanger in order to store the latent cold heat. This can be done on account of the homogeneous dispersion of the small-size latent heat-storage material into the continuous liquid phase. However, this type of phase-change emulsion has a complex construction, non-Newtonian behavior, and the phase segregation. This study selects the oil (tetradecane, $C_{14}H_{30}$, freezing point $T_f = 278.9$ K, latent heat $L = 229$ kJ/kg as the phase-change material)/water (continuous phase) emulsion. The authors (Inaba et al., 1993) have already reported the physical properties (thermal conductivity, specific heat, viscosity, etc.) of the phase-change emulsion.

In the present study, a comparatively simple coiled double tube heat exchanger is used for evaluating the heat transfer and cold heat storage characteristics of the phase-change emulsions. The initial temperature, the concentration and the velocity of the phase-change emulsion are selected as the experimental parameters so that the pressure loss, the heat-transfer coefficient and the finishing time of the cold heat-storage from the liquid to the solid phase change are measured. Moreover, the nondimensional correlation equations of these factors are derived. The obtained results of the cold heat-storage experiment will contribute to the development of this type of latent heat-storage system.

## 2 Characteristics of Phase-Change Emulsion

Figure 1 shows the external appearance of the present phase-change (O/W-type) emulsion ($C' = 50.7$ wt%). The emulsion has a white color and fluidity. Figure 2 shows the microphotograph (2000 magnifications) of the test emulsion ($C' = 50.7$ wt%), which is diluted 5 times with water. Figure 2 shows the spherical-shaped latent heat-storage materials (tetradecane), which are dispersed homogeneously in water.

The composition ratio of the present phase-change emulsions are indicated in Table 1. The flow and the cold heat-storage characteristics are influenced by the concentrations of the surfactant $C_s$ and the tetradecane $C_t$. Therefore, the concentration of the emulsion $C'$ is defined as the amount of the concentrations of the surfactant $C_s$ and the tetradecane $C_t$. The dispersion diameter of the latent heat storage material is measured using a microvideo system with magnification 1000. Its dispersion diameter distribution is determined by the number of samples $N = 164$ of the spherical dispersion materials. The diameter of the dispersion material varies from $d = 0.1$ to 9 $\mu$m, and the arithmetic mean diameter is $d_m = 3.4$ $\mu$m within $\pm 20.4$ percent on a standard deviation. The test emulsion, which fills the test tube, has kept the stable dispersion mixing condition over one year. Moreover, the dispersion diameter distribution of the tetradecane after the cold latent heat storage experiment was similar to that before the experiment. From these facts, it is concluded that the stability of the emulsion is enough. The supercooling phenomenon does not appear in this cold latent heat storage experiment, judging from the experimental results of the variation of the phase change rate mentioned in section 4.3. Therefore, the freezing point of the dispersion material is estimated at $T_f = 278.9$ K, the same as that of pure tetradecane. The specific heat, density, and latent heat of the emulsion are estimated by the mixing ratio of the emulsion constituents (Inaba et al., 1993).

Eurcken's model (Inaba et al., 1993) for the dispersion material is applied in calculating the thermal conductivity of the present emulsion. A rotary viscous meter is utilized for the viscosity measurement since the emulsion shows generally a non-Newtonian behavior. The relationship between the shearing stress of the non-Newtonian fluid $\tau$ and the shear rate $u_\tau$ is derived by using a power-law function as follows:

$$\tau = \mu \cdot u_\tau^{n_e} \tag{1}$$

Contributed by the Heat Transfer Division for publication in the JOURNAL OF HEAT TRANSFER. Manuscript received by the Heat Transfer Division February 1994; revision received July 1994. Keywords: Forced Convection, Non-Newtonian, Flows and Systems, Thermal Energy Storage.



Copyright © 1995 by ASME

Downloaded 12 Dec 2010 to 193.140.21.150. Redistribution subject to ASME license or copyright; see http://www.asme.org/terms/Terms_Use.cfm

Figure 3 indicates the variation of the emulsion viscosity coefficient $\mu$ (defined by Eq. (1)) with temperature $T$ on each emulsion concentration $C'(=C_t + C_s)$. The obtained viscosity coefficient $\mu$ decreases with an increase in temperature $T$. On the other hand, the $\mu$ shows a little difference between the top and the bottom temperature range of the freezing point $T_f = 278.9$ K. The experimental data of viscosity coefficient are correlated by the following equation within ±5 percent on a standard deviation:

$$\mu = a \times \exp(b/T) \tag{2}$$

The coefficients $a$, $b$ are shown in Table 1. The values calculated from Eq. (2) are indicated by the solid lines for each concentration of the emulsion as shown in Fig. 3. The power-law value $n_e$ has a little dependence on concentration $C'$ and temperature $T$, and subsequently, the $n_e$ is estimated to be 0.894 within ±5 percent on a standard deviation. The above-mentioned properties (density, specific heat, latent heat, thermal conductivity, coefficient of viscosity, and power-law value) of the phase-change emulsion are used for nondimentionarization of heat-transfer and fluid flow resistance data as described in section 4.

## 3 Experimental Apparatus and Procedures

Figure 4 shows the experimental apparatus for the latent heat storage of the flowing emulsion. The experimental apparatus is constructed mainly by the emulsion and the brine conduits. The emulsion flow line consists of a tube pump, a surge tank as an absorber for the pulsatory flow motion by the tube pump, a coiled double tube heat exchanger (made of copper), an inlet emulsion tank, and a magnetic flow meter. A coiled double tube heat exchanger (coiled diameter $D$ = 280 mm, inner tube diameter $D_i$ = 20.0 mm, outer tube diameter $D_o$ = 32.0 mm, length $l$ = 10.3 m, and each tube thickness $\delta$ = 1.0 mm) is covered by a thermal insulating material of urethane foam in thickness of 100 mm. The dispersion material (tetradecane) of the test emulsion (total volume $V_0 = 5.1 \times 10^{-3}$ m$^3$ of the pipe except for the inlet tank flowing in the inner tube) is solidified by circulating the cold brine in the annular space in a coiled double tube heat exchanger. The emulsion flow line, except for part of the heat exchanger, is constructed of acryl tube (inner diameter $D_i$ = 20.0 mm and

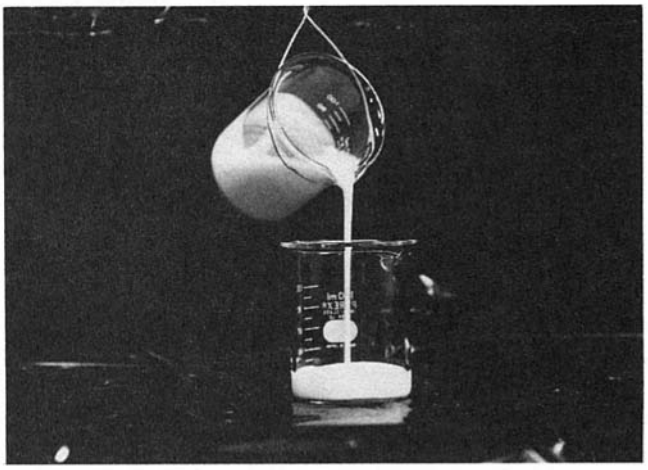


**Fig. 1 External appearance of emulsion (C′ = 50.7 wt%)**

## Nomenclature

$a, b$ = coefficient defined by Eq. (2)
$a_l, b_l$ = coefficient defined by Eq. (24)
$a_s, b_s$ = coefficient defined by Eq. (21)
$a_N, b_N$ = coefficient defined by Eq. (17)
$a_\phi, b_\phi$ = coefficient defined by Eq. (8)
$A$ = area of heat transfer surface, m$^2$
$C_t, C_s, C_w$ = concentration of tetradecane, surfactant and water, wt%
$Cp_{el}, Cp_{es}$ = specific heat of emulsion on liquid and solid phase, kJ/(kg·K)
$Cp$ = specific heat, kJ/(kg·K)
$C' = C_t + C_s$ = concentration of emulsion, wt%
$d$ = diameter of dispersion material, $\mu$m
$D$ = coiled diameter, m
$D_i, D_o$ = inner and outer tube diameter, m
De′ = modified Dean number
$f_c, f_s$ = friction coefficient of curved and straight tube
Fo = Fourier number
$h$ = heat transfer coefficient, W/(m$^2$·K)
$H$ = pressure loss, Pa
$i_e, i_w$ = hydraulic pressure gradient of emulsion and water, m
$k$ = thermal conductivity, W/(m·K)
$l$ = length, m
$L$ = latent heat, kJ/kg
$m$ = mass, kg
$\dot{m}$ = mass flow rate, kg/s
$n$ = power-law function
Nu = Nusselt number
Pr = Prandtl number
$P_{cr}$ = phase change rate defined by Eq. (23), percent
$q$ = quantity of release heat of emulsion, kJ
$\dot{q}_{ex}$ = quantity of release heat of emulsion per a second, kJ/s
$q_{le}$ = heat loss of a heat exchanger, yield by the temperature difference between a heat exchanger and the air, kJ
$q_{ls}$ = sensible heat loss of emulsion, as flow in a pipe except for the heat exchanger, kJ
$q_{ll}$ = latent heat loss of emulsion, as flow in a pipe except for the heat exchanger, kJ
$Q^*$ = heat capacity rate defined by Eq. (20)
Re′ = Reynolds number
Ste = Stefan number
$t$ = time, s
$T$ = temperature, K
$T_b, T_e$ = temperature of brine and emulsion, K
$T_f$ = freezing point, K
$\Delta T_m$ = logarithmic mean temperature difference, K
$u$ = mean velocity of inner tube, m/s
$u_\tau$ = shear rate, s$^{-1}$
$U$ = overall heat transfer coefficient, W/(m$^2$·K)
$V_0$ = volume of emulsion, m$^3$
$\alpha$ = thermal diffusivity, m$^2$/s
$\delta$ = thickness, mm
$\mu$ = viscosity coefficient defined by Eq. (1), Pa·s$^n$
$\rho$ = density, kg/m$^3$
$\tau$ = shearing stress, Pa
$\phi$ = additional pressure loss coefficient

### Subscripts

1 = inlet
2 = outlet
$b$ = brine
$c$ = copper or curved tube
$e$ = emulsion or heat exchanger
$f$ = freezing point
$l$ = latent heat
$l$ = heat loss or liquid phase
$m$ = mean
$s$ = sensible heat or solid phase



Downloaded 12 Dec 2010 to 193.140.21.150. Redistribution subject to ASME license or copyright; see http://www.asme.org/terms/Terms_Use.cfm

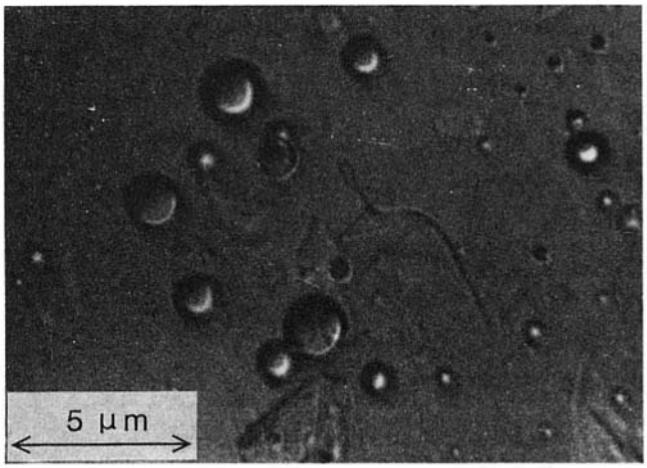



**Fig. 2 Microphotograph (magnified 2000 times) of emulsion ($C'$ = 50.7 wt% diluted five times with water)**

thickness $\delta$ = 2.0 mm), and it is insulated thermally by the urethane foam insulating material (50 mm in thickness).

The loop of cooling brine consists of two constant low temperature baths. The ethylene glycol 30 wt% solution is selected as the brine, which flows in the outside annular tube in the counterdirection against the emulsion flow in the inside tube of the coiled double tube heat exchanger. The temperature measurements are carried out at the inlet and outlet of the heat exchanger for the flowing emulsion and cooling brine by the thermopiles, which consist of five T-type thermocouples 0.1 mm in diameter. The flow mixers in the tube are set at the upstream side of the thermopiles in order to measure the average temperature of the emulsion and the brine. The thermocouples are calibrated by a standard thermometer within ±0.05 K. The amount of cold heat storage of the emulsion $q$ is calculated from the time integration of the transmitted heat of cooling brine $dq$, which is estimated from the measured temperature difference between inlet and outlet of the double tube heat exchanger, since it is impossible to measure directly the temperature of the dispersion material in the emulsion. The amount of the cold latent heat storage of the emulsion is derived as follows:

$$q = \int_0^t dqdt = \int_0^t (Cp_b \cdot \dot{m}_b \cdot \Delta(T_{b2} - T_{b1}) - dq_{te} - dq_{ts} - dq_{tl})dt \quad (3)$$

in which the $q_{te}$ is the heat loss from the heat exchanger, which is based on the temperature difference between the heat exchanger and the environment. The $q_{ts}$ is the sensible heat loss of the emulsion as flowing in a tube of experimental apparatus except for the coiled double tube heat exchanger. These heat losses of $q_{te}$ and $q_{ts}$ are measured at the preliminary experiments by using water as the test fluid. The $q_{te}$ and $q_{ts}$ account for 2 and 5 percent of the total heat (sensible heat + latent heat) of the emulsion, respectively. The $q_{tl}$ indicates the latent heat loss of the

**Table 1 Composition ratio of phase-change emulsion**

| $C_l$, wt% | $C_w$, wt% | $C_s$, wt% | $C'$ ($=C_l + C_s$), wt% | $a$ | $b$ |
|---|---|---|---|---|---|
| 40.0 | 49.3 | 10.7 | 50.7 | $5.78 \times 10^{-2}$ | $1.05 \times 10^{3}$ |
| 35.0 | 56.0 | 9.0 | 44.0 | $9.73 \times 10^{-3}$ | $9.52 \times 10^{2}$ |
| 25.0 | 66.7 | 8.3 | 33.3 | $9.00 \times 10^{-9}$ | $4.41 \times 10^{3}$ |
| 15.0 | 78.5 | 6.5 | 21.5 | $1.71 \times 10^{-7}$ | $3.55 \times 10^{3}$ |
| 5.0 | 92.8 | 2.2 | 7.2 | $3.49 \times 10^{-6}$ | $2.53 \times 10^{3}$ |

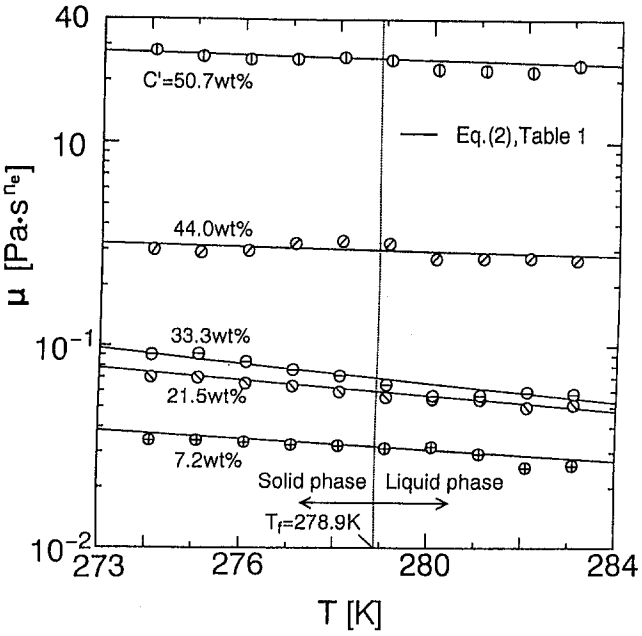



**Fig. 3 Variation of viscosity coefficient $\mu$ with temperature $T$**

emulsion and accounts for 3 percent of the total heat of the emulsion. The sum total of heat loss ($q_{te} + q_{ts} + q_{tl}$) accounts for about 10 percent of the total heat of the emulsion.

The temperature histories of the emulsion and cooling brine at the inlet and outlet of the heat exchanger are shown in Fig. 5. The emulsion temperatures $T_{e1}$ and $T_{e2}$ decrease rapidly at the beginning of the experiment with the large transfer rate due to the large temperature difference between the brine and the emulsion. Subsequently, these emulsion temperatures decrease gradually. The phase-change rate $P_{cr}$ is shown by the solid line in Fig. 6. $P_{cr}$ is derived by the heat balance from Eq. (3). As $P_{cr}$ approaches the value of 100 percent, the increasing rate of $P_{cr}$ decreases. The open circles in Fig. 6 indicate the phase-change

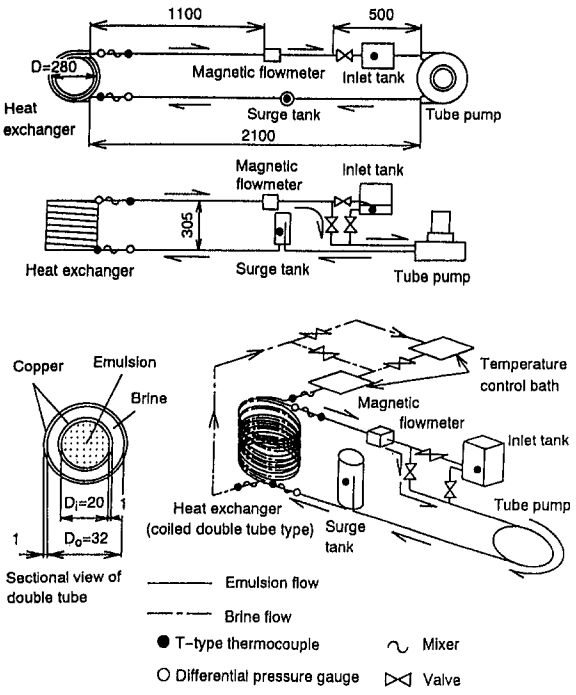



**Fig. 4 Experimental apparatus**



Downloaded 12 Dec 2010 to 193.140.21.150. Redistribution subject to ASME license or copyright; see http://www.asme.org/terms/Terms_Use.cfm

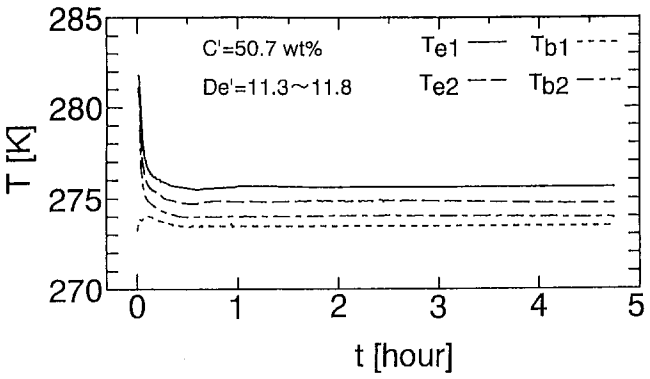



Fig. 5 Relationship between temperatures $T_{e1}$, $T_{e2}$, $T_{b1}$, $T_{b2}$, and time $t$

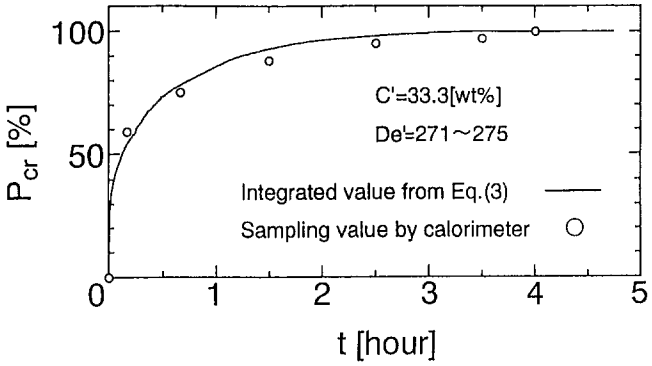



Fig. 6 Variation of phase-change rate $P_{cr}$ with time $t$

rate measured by using a water calorimeter (Inaba et al., 1993). The values calculated from Eq. (3) agree with those obtained data by the water calorimeter within ±5 percent.

The measurement of pressure loss in a coiled tube is carried out by a diffusion semiconductor differential pressure gage. The maximum differential pressure of the differential pressure gage used is 98.1 kPa, and the accuracy of the differential pressure gage is ±1.0 percent. The following experimental parameters are ranged in order to clarify the fundamental heat-storage characteristics of the emulsion:

- Inlet brine temperature $T_{b1} = 273.6 \pm 0.5$ K.
- Average velocity of the flowing brine in the annulus tube $u_b = 0.330 \pm 6.6 \times 10^{-3}$ m/s.
- Average velocity of the flowing emulsion $u_e = 0.25 \sim 1.10 \pm 5.0 \times 10^{-3}$ m/s.
- Initial inlet temperature of the emulsion $T_{e1i} = 281 \sim 298$ K.
- Concentration of the emulsion $(C_l + C_s)\,C' = 7.2 \sim 50.7 \pm 0.1$ wt%.

## 4 Experimental Results and Discussion

**4.1 Pressure Loss in a Coiled Tube.** Figure 7 shows the relationship between the pressure loss $H$ and average velocity of the water $u_w$ and the emulsion $u_e$ in the coiled tube. The solid line of Fig. 7 indicates the values calculated from the theoretical Eq. (4), which was developed by Mori and Nakayama (1964) as follows:

$$\frac{f_c}{f_s} = \frac{0.1080\ \mathrm{De}'^{1/2}}{1 - 3.2527\ \mathrm{De}'^{-1/2}} \tag{4}$$

Equation (4) agrees with the experimental data proposed by Ito (1959) within ±7 percent. The present measurement data of water agree well with the value of Eq. (4), so that the accuracy of the present measurement system is enough satisfied. The pressure loss of the emulsion demonstrates a higher value than that of water due to the existence of the dispersion material (tetradecane) and the viscous surfactant in the emulsion. Moreover, the pressure loss of the emulsion without phase change (liquid condition of dispersion latent heat storage material) is lower than that with phase change (solid condition). The relative velocity of the interface between the dispersion material on the liquid condition and the continuum phase decreases with the occurrence of the internal circulation of the dispersion material. Therefore, the value of pressure loss on the liquid phase of the dispersion material is smaller than that on the solid phase. Figure 8 shows the variation of the additional pressure loss coefficient $\phi$ (Shirakashi et al., 1990) with modified Dean number De′ on various concentrations of the emulsion related to both liquid ($T_{e1} = 281$ K) and solid phase ($T_{e1} = 275$ K) of the dispersion material.

The additional pressure loss coefficient $\phi$ is defined as follows:

$$\phi = \frac{i_e - i_w}{C' \times i_w} \tag{5}$$

Modified Dean number De′ is calculated by using the modified Reynolds number Re′ for the non-Newtonian fluid as follows:

$$\mathrm{De}' = \mathrm{Re}'\left(\frac{D_i}{D}\right)^{1/2} \tag{6}$$

in which

$$\mathrm{Re}' = 8^{1-n_e}\left[\frac{3n_e + 1}{4n_e}\right]^{-n_e}\left[\frac{\rho \cdot u_e^{2-n_e} \cdot D_i^{n_e}}{\mu}\right] \tag{7}$$

The additional pressure loss coefficient $\phi$ has the increasing tendency with an increase in the concentration $C'$ as shown in Fig. 8. The values of $\phi$ for the solid phase of the dispersion material are higher than these for the liquid phase at a given De′. It can be seen that the difference of $\phi$ values between the solid and liquid phase increases with on increase in the concentration $C'$. The relationship between $\phi$ and De′ is derived by the next power-law function:

$$\phi = a_\phi\ \mathrm{De}'^{\,b_\phi} \tag{8}$$

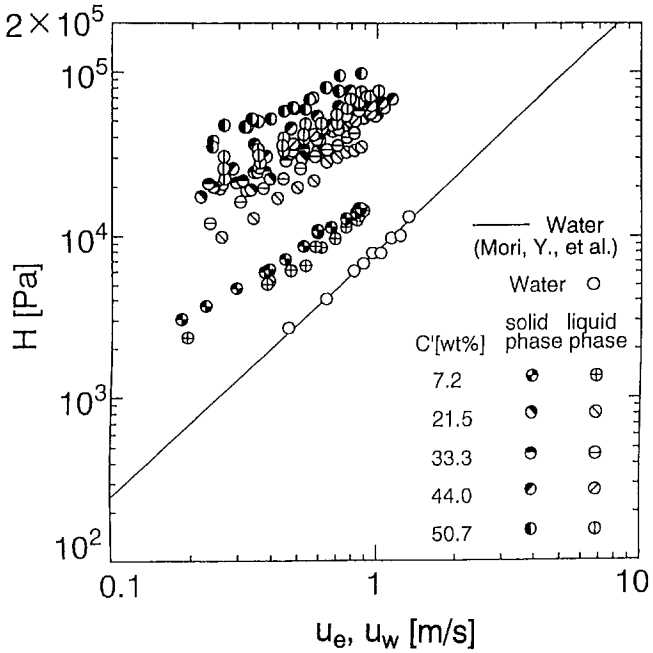



Fig. 7 Relationship between pressure loss $H$ and mean velocity $u_e$, $u_w$



Downloaded 12 Dec 2010 to 193.140.21.150. Redistribution subject to ASME license or copyright; see http://www.asme.org/terms/Terms_Use.cfm

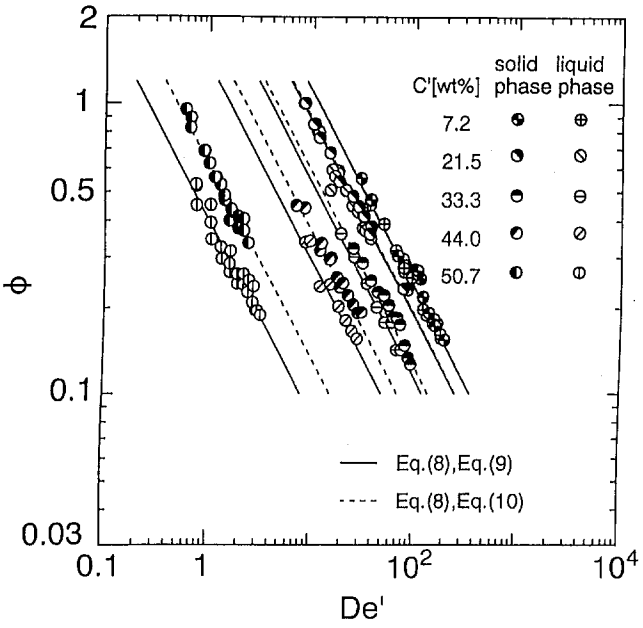



**Fig. 8 Variation of additional pressure loss coefficient $\phi$ with modified Dean number De'**

It is seen that the power-law value $b_\phi$ is a constant value of $-0.666$ for each concentration $C'$. The absolute value of additional pressure loss coefficient $\phi$ is affected by the concentration of the emulsion based on the amount of difference of dispersion material. Therefore, the coefficient $a_\phi$ is expressed as the function of the emulsion concentration $C'$. The coefficient $a_\phi$ is represented by Eqs. (9) and (10) for the liquid and solid phase, respectively, within $\pm 1.0$ percent on a standard deviation:

*Liquid phase ($T > 278.9$ K)*

$$a_\phi = -1.61 \times 10^{-3} C'^2 - 1.94 \times 10^{-2} C' + 5.25 \quad (9)$$

*Solid phase ($T < 278.9$ K)*

$$a_\phi = -1.66 \times 10^{-3} C'^2 - 9.89 \times 10^{-3} C' + 5.25 \quad (10)$$

The values calculated from Eqs. (9) and (10) are shown in Fig. 8 as solid and broken lines, respectively.

**4.2 Heat Transfer of the Emulsion in Coiled Tube.** The heat transfer coefficient of the test flowing emulsion is calculated by Eq. (11). Equation (11) represents an overall heat transfer $U$, which is introduced by the heat transfered $\dot{q}_{ex}$, through the coiled double tube heat exchanger:

$$U = \dot{q}_{ex} \cdot \Delta T_m^{-1} \cdot A^{-1} \quad (11)$$

The Nusselt number $Nu_b$ in the annulus coiled tube of the cooling brine is estimated by Eq. (12) proposed by Garimella et al. (1988):

$$Nu_b = 0.027\, De'^{0.94} Pr^{0.69} \left(\frac{D_i}{D}\right) \quad (12)$$

The heat transfer coefficient of the brine $h_b$ is calculated from

$$h_b = \frac{Nu_b \cdot k_b}{D_i} \quad (13)$$

The Nusselt number $Nu_e$ of the emulsion in a coiled tube is estimated by Eqs. (14) and (15):

$$U = \frac{1}{\frac{1}{h_b} + \frac{\delta}{k_c} + \frac{1}{h_e}} \quad (14)$$

Equation (14) is derived from the approximation of the overall heat transfer coefficient for a flat plate; the ratio of the inner diameter to the outer diameter of the inner tube of the coiled double tube heat exchanger is close to unity.

$$Nu_e = \frac{h_e \cdot D_i}{k_e} \quad (15)$$

The variation of the Nusselt number for the emulsion $Nu_e$ with the Dean number De' is presented in Fig. 9. The broken line in Fig. 9 shows the Nusselt number ($T = 275$ K) of the laminar water flow in a coiled tube. It is derived by Seban's equation (Mori and Nakayama, 1964) as follows:

$$Nu = 0.023\, De'^{0.85} Pr \left(\frac{D_i}{D}\right)^{-0.325} \quad (16)$$

The broken line agrees with the obtained data within $\pm 5$ percent on a standard deviation, so that the accuracy of the data obtained in the present experimental apparatus is satisfied. The gradient of $Nu_e$ against De' for the emulsion is a constant value of $b_N = 0.85$, which is almost equal to that for water. On the other hand, the value of $Nu_e$ increases with an increase in the concentration $C'$. From these results of $Nu_e$, it is understood that the mixing effect of the dispersion material brings the increase of heat transfer rate in the thermal boundary layer (Yoshida, 1990). The Nusselt number $Nu_e$ on the solid phase ($T < 278.9$ K) of the dispersion material is higher than that of the liquid phase ($T > 278.9$ K). This difference of $Nu_e$ between the solid phase and liquid phase of the dispersion material would be brought by the increase of the thermal conductivity with the solidification (Inaba et al., 1993) of latent heat-storage material and the decrease of the relative surface velocity on the dispersion material surface due to the above-mentioned internal circulation effect of the liquid phase.

The relationship between $Nu_e$ and Dean number De' is approximated by the following power-law function:

$$Nu_e = a_N \cdot De'^{b_N} \quad (17)$$

where the power-law value $b_N$ has a constant value of 0.85.

Equations (18) and (19) show the coefficient $a_N$ on solid and liquid phase, whose equations agree with the experimental data within $\pm 1.0$ percent on the range of De' = $1.5 \sim 10^3$.

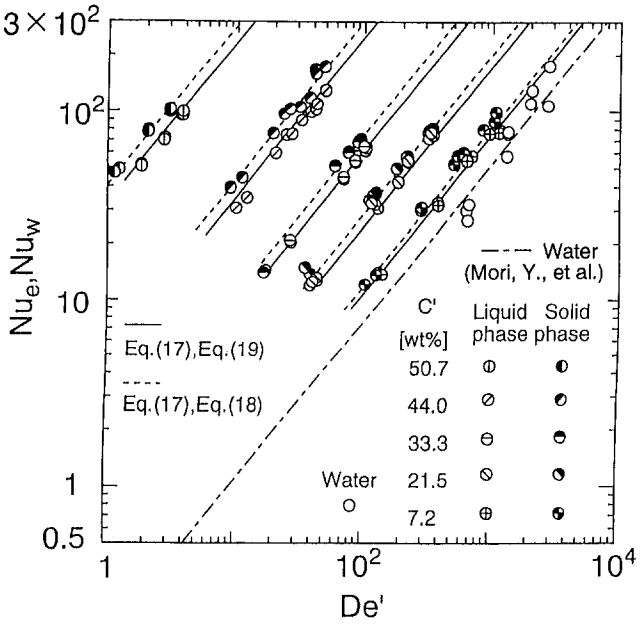



**Fig. 9 Variation of Nusselt number Nu with modified Dean number De'**



Downloaded 12 Dec 2010 to 193.140.21.150. Redistribution subject to ASME license or copyright; see http://www.asme.org/terms/Terms_Use.cfm

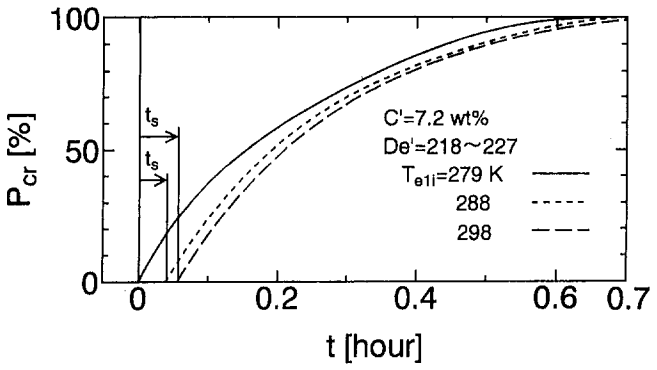



**Fig. 10 Variation of $P_{cr}$ with time $t$ on initial emulsion temperature $T_{e1i}$ = 279, 288, 298 K**

*Solid phase ($T < 278.9$ K)*

$$a_N = 7.51 \times 10^2/(55 - C')^2 - 9.66 \times 10^{-2} \quad (18)$$

*Liquid phase ($T > 278.9$ K)*

$$a_N = 7.10 \times 10^2/(55 - C')^2 - 5.37 \times 10^{-2} \quad (19)$$

The coefficient $a_N$ is indicated as a function of the concentration of the emulsion $C'$ in Eqs. (18) and (19). Because the value of Nusselt number is affected by the concentration of the emulsion based on the difference of the amount of the tetradecane as the dispersion material. The values estimated by Eq. (17) are also drawn by the broken line for the solid phase and by the solid line for the liquid phase in Fig. 9. These correlation equations agree well with the data within ±9.5 percent on a standard deviation.

**4.3 Time History of the Cold Heat-Storage Process.** Figure 10 shows the variation of the phase change rate $P_{cr}$ with the elapsing time $t$ from the start of the cooling for the emulsion concentration $C'$ = 7.2 wt%, Dean number De' = 218 ~ 227, three initial emulsion temperatures $T_{e1i}$ = 279, 288, and 298 K. The sensible heat is accumulated in the emulsion for the time period from the initial temperature of emulsion $T_{e1i}$ to the freezing point $T_f$. The delay at the beginning of solidification of the dispersion phase-change material increases with an increase in the initial emulsion temperature $T_{e1i}$ as shown in Fig. 10.

In the present study, the starting time for the phase change (solidification) of the dispersion latent heat storage material is defined when the sensible heat storage of the emulsion from the initial temperature of emulsion $T_{e1i}$ to the solidification temperature $T_f$ finishes, that is, that time is estimated by the total heat absorbed in the cooling brine. Figure 11 indicates the variation of the Fourier number $\mathrm{Fo}_s$ ($=\alpha \cdot t_s/D_i^2$) of the sensible heat-storage time $t_s$ with the heat capacity ratio $Q^*$ for each initial emulsion temperature $T_{e1i}$. The heat capacity ratio $Q^*$ is defined by

$$Q^* = \frac{\dot{m}_e \cdot Cp_e(T_{e1i} - T_f)}{\dot{m}_b \cdot Cp_b(T_{e1i} - T_{b1})} \quad (20)$$

The sensible heat-storage time of $\mathrm{Fo}_s$ increases with an increase of the initial emulsion temperature $T_{e1i}$, because the sensible heat-storage time $t_s$ increases with an increase of the initial emulsion temperature $T_{e1i}$. The relationship between $\mathrm{Fo}_s$ and $Q^*$ is derived by a power-law function as follows:

$$\mathrm{Fo}_s = a_s \cdot Q^{*b_s} \quad (21)$$

The constant value in Eq. (21) becomes $b_s = -0.297$ from experimental data reductions. The relationship between $a_s$ and $T_{e1i}$ is derived by the least-squares method as follows:

$$a_s = 5.30 \times 10^{-2} - 1.78/(T_{e1i} - 273.15)^2 \quad (22)$$

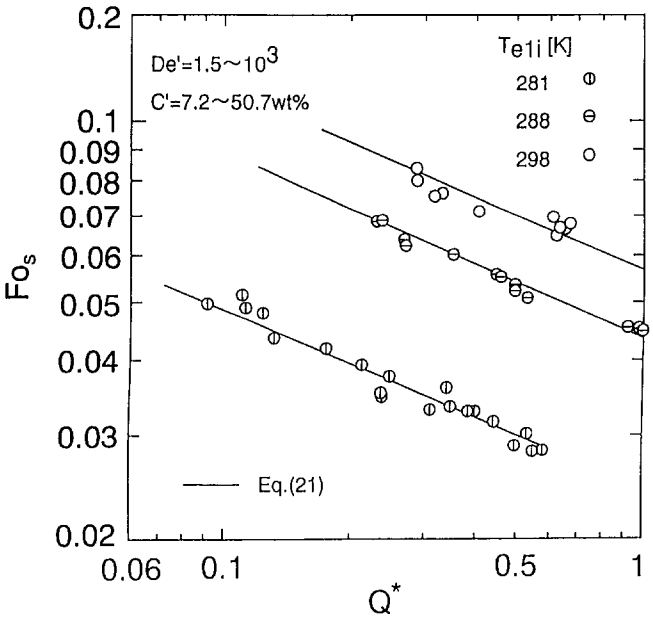



**Fig. 11 Relationship between sensible heat-storage time of Fourier number $\mathrm{Fo}_s$ and heat capacity ratio $Q^*$**

Since the sensible heat storage time $t_s$ is influenced by the temperature difference between the initial emulsion and the cooling brine, the coefficient $a_s$ in the case of constant cooling brine temperature is expressed as the function of the initial emulsion temperature $T_{e1i}$. The values of $\mathrm{Fo}_s$ calculated by Eq. (21) agree well with the experimental data within ±9.8 percent on a standard deviation as shown in Fig. 11.

Figure 12 presents the variation of the phase change rate $P_{cr}$ with time $t_l$ for the latent heat storage for each concentration $C'$ = 33.3, 44.0, and 50.7 wt%. The phase change rate $P_{cr}$ is estimated as the ratio of the amount of actual latent heat storage, which is calculated by subtracting the sensible heat storage from the total heat storage of the emulsion, to the amount of whole latent heat of the emulsion ($C_t/100 \times L$) as follows:

$$P_{cr} = [q/[(C_t/100) \times L] - \mathrm{Ste}] \times 100 \quad (23)$$

in which Stefan number Ste is defined as $\mathrm{Ste} = Cpes(T_f - T_{e2})/[(C_t/100) \times L]$.

Figure 13 indicates the relationship between Fourier number $\mathrm{Fo}_l$ and modified Dean number De' for the phase change rate $P_{cr}$ = 10, 50, and 100 percent. $\mathrm{Fo}_l$ decreases linearly with De' without the dependence of $C'$ on each $P_{cr}$, since the De' is included indirectly with the effect of the concentration $C'$.

$$\mathrm{Fo}_l = a_l \cdot \mathrm{De}'^{b_l} \quad (24)$$

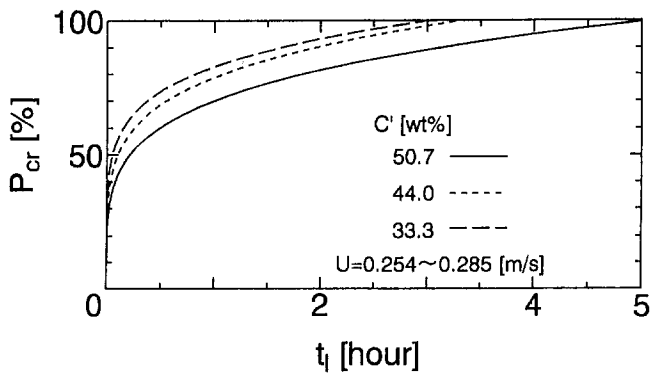



**Fig. 12 Relationship between phase-change rate $P_{cr}$ and time $t$**



Downloaded 12 Dec 2010 to 193.140.21.150. Redistribution subject to ASME license or copyright; see http://www.asme.org/terms/Terms_Use.cfm

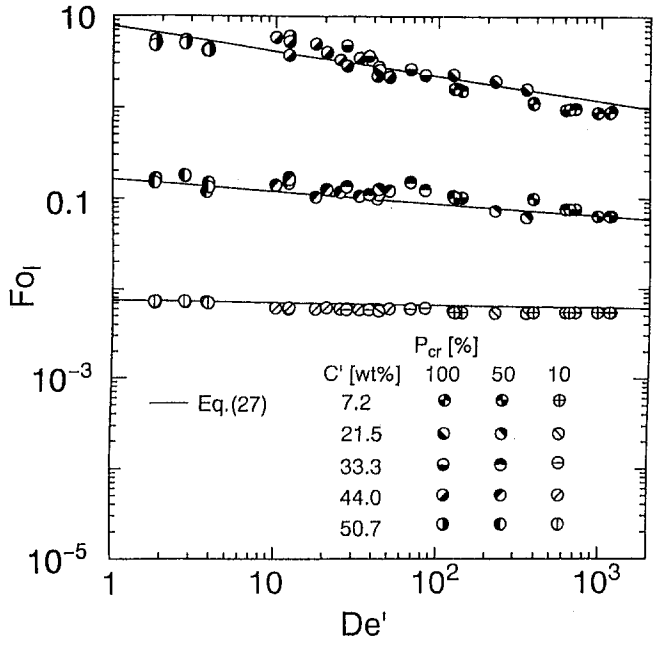



**Fig. 13 Variation of Fourier number Fo$_l$ with modified Dean number De'**

Fourier number Fo$_l$ increases with increasing of the phase change rate $P_{cr}$. The gradient of Fourier number Fo$_l$ against the modified Dean number De′ increases with an increase in the phase change rate $P_{cr}$, since the decrease of the temperature difference between the emulsion $T_e$ and cooling brine $T_b$ brings the predominance of the heat transfer of the emulsion, which increases with an increase in the Dean number De′. As a results, the coefficients $a_l$ and $b_l$ are expressed as the function of the phase change rate $P_{cr}$ in Eqs. (25) and (26). The coefficients $a_l$ and $b_l$ are determined by the least-squares method within ±4.0 percent.

$$a_l = 3.46 \times 10^{-3} \exp(7.72 \times 10^{-2} P_{cr}) \quad (25)$$

$$b_l = -1.82 \times 10^{-3} P_{cr} \quad (26)$$

The values calculated by Eq. (24) provide a good fit to the experimental data within ±3.5 percent as shown by the solid line in Fig. 13.

The Fourier numbers Fo$_s$, Fo$_l$ for the sensible and the latent heat storage, respectively, have been derived by the above-mentioned Eqs. (21) and (24). The overall Fourier number Fo (=Fo$_s$ + Fo$_l$) of the whole cold heat-storage time is represented by following Eq. (27). The measured experimental data reduction is carried out in the range of initial emulsion temperature $T_{e1i}$ = 281 ~ 298 K and phase change rate $P_{cr}$ = 10 ~ 100 percent. The values calculated by Eq. (27) agree well with the experimental results within ±11 percent on a standard deviation:

$$\mathrm{Fo} = a_s \cdot Q^{*b_s} + a_l \cdot \mathrm{De}'^{b_l} \quad (27)$$

in which the application ranges of parameters in Eq. (27) are $T_{e1i}$ = 281 ~ 298 K, De′ = 1.5 ~ $10^3$, $Q^*$ = 0.08 ~ 1.0, and $C'$ = 7.2 ~ 50.7 wt%.

## 5 Concluding Remarks

The cold heat-storage experiments of the emulsion including the phase-change material as a dispersion medium have been carried out by using the basic coiled double-tube heat exchanger. The fluid flow and heat transfer characteristics of the proposed latent cold heat storage system have been expressed in terms of the pressure loss, the heat transfer coefficient, and the heat-storage time. Consequently, some conclusions are obtained as follows:

The pressure loss of the emulsion in the coiled tube heat exchanger increases with an increase in the concentration of the dispersion phase change materials $C'$ at a given modified Dean number De′. The relationship between the additional pressure loss coefficient $\phi$ and De′ is derived by the power-law function, and the value of $\phi$ in the solid phase of the dispersion material is higher than that of the liquid phase.

It is noticed by the measurement that the Nusselt number Nu$_e$ of the flowing emulsion in a coiled tube heat exchanger increases with an increase in $C'$. The Nu$_e$ on the solid phase condition of the dispersion material is higher than that on the liquid phase condition. The relationship between Nu$_e$ and De′ is approximated by the power-law function.

The useful correlation equations of Fourier number Fo as the nondimensional heat-storage time, are proposed in terms of the phase-change rate, modified Dean number, and heat capacity ratio.

The above-mentioned correlation equations of the pressure loss, the heat transfer coefficient, and the cold heat storage time would be useful to design this type of latent cold heat storage system.

## References


Garimella, S., Richards, D. E., and Christensen, R. N., 1988, "Experimental Investigation of Heat Transfer in Coiled Annular Ducts," ASME JOURNAL OF HEAT TRANSFER, Vol. 110, pp. 329–336.

Inaba, H., Morita, S., and Nozu, S., 1993, "Fundamental Study of Cold Heat-Storage System of Phase-Change-Type Emulsion Having Cold Latent Heat Dispersion Material," *Trans. JSME*, Vol. 59, No. 565, pp. 2882–2889.

Inaba, H., Morita, S., and Nozu, S., 1993, "Viscosity Evaluation of Phase-Change Emulsion as a Low Temperature Heat-Storage Material," *Trans. JSTP*, Vol. 7, No. 4, pp. 239–244.

Ito, E., 1959, "Friction Factors for Turbulent Flow in Curved Pipes," *The Memoirs of the Institute of High Speed Mechanics, Tohoku University*, Vol. 14, No. 138, pp. 1–31.

Mori, S., Kato, K., Sakitani, K., and Arai, Y., 1975, "Pipeline Transport of Energy With Latent Heat of Gas-Hydrate Crystals in Cold Water at a Low Temperature," *Trans. JAR*, Vol. 50, No. 572, pp. 3–8.

Mori, Y., and Nakayama, W., 1964, "Study of Forced Convective Heat Transfer in Curved Pipes," *Trans. JSME*, Vol. 30, No. 216, pp. 977–988.

Shirakashi, M., Tokunaga, Y., and Hashimoto, T., 1987, "Pressure Loss Reduction Due to Mixing of Coarse Particles in a Pipe Flow," *Trans. of JSME*, Vol. 53–490, pp. 1672–1676.

Shirakashi, M., Takahashi, M., and Uchikura, A., 1990, "Hydraulic Conveying of Snow," *J. Multiphase Flow*, Vol. 4, No. 1, pp. 61–71.

Takahashi, H., Masuyama, T., and Kawashima, T., 1990, "Fundamental Study on Hydraulic Transport of Snow and Ice Particles," *J. Resources and Material*, Vol. 106, No. 9, pp. 514–520.

Winnikow, S., and Chao, B. T., 1966, "Droplet Motion in Purified Systems," *The Physics of Fluids*, Vol. 9, pp. 50–61.

Yoshida, M., 1990, "High-Efficiency Heat Transport Fluid Containing Microencapsulated Phase Change Material: (1) Flow Characteristics," *Chem. Eng. Symposium Series*, Vol. 23, pp. 32–36.




Downloaded 12 Dec 2010 to 193.140.21.150. Redistribution subject to ASME license or copyright; see http://www.asme.org/terms/Terms_Use.cfm

P. Adnani

I. Catton

M. A. Abdou

Mechanical, Aerospace, and Nuclear Engineering Department, University of California, Los Angeles, Los Angeles, CA 90024

# Non-Darcian Forced Convection in Porous Media With Anisotropic Dispersion

*Convective heat transfer in a particle packed tube is modeled in this paper. Axial and radial dispersion are both included in the governing equations. Results are compared with experimental data, and with previously developed models that did not include axial dispersion. It is shown that heat transfer in the thermally developing region is affected by axial dispersion when Peclet number is smaller than 10. Graphic results are provided to show the importance of axial dispersion for various Peclet numbers.*

## Introduction

Forced convection heat transfer in a particle packed tube is of great importance in the design of catalytic reactors and packed particle heat exchangers. Experimental data for flow in packed beds of spheres (Yagi and Wakao, 1959; Kwong and Smith, 1957; Plautz and Johnstone, 1955; Yagi and Kunii, 1960), and packed cylinders (Bunnell et al., 1949; Coberly and Marshall, 1951) are available for a wide range of flow rates and material properties. Some of these authors have also attempted to formulate a mathematical model for this problem by assuming slug flow and uniform thermal conductivity across the tube. These restrictive assumptions were shown some time ago to be invalid. (see Vafai, 1984).

Recent analyses of this problem by Cheng and Vortmeyer (1988) and Hunt and Tien (1988) have focused on the impact of non-Darcian effects on heat transfer. These non-Darcian effects include: (1) porosity variation near solid boundaries, (2) inertial forces in the momentum equation, (3) local dependence of effective medium conductivity on the superficial velocity, and (4) damping of hydrodynamic dispersion near solid boundaries. The existence of these effects in porous media has been verified to a certain extent by various experimental data.

While incorporation of non-Darcian effects in the governing equations has greatly improved the porous media models in the past few years, these models still do not account for all of the physical phenomena that exist in porous media. Our objective here is to look at one of these effects: the importance of axial dispersion. Previous models have always neglected the axial dispersion because the advective term in the axial direction have always been assumed to be larger than the axial dispersion term in this direction. It should be noted that the effective medium conductivity in porous media has two separate components: (1) a stagnant component that represents the medium conductivity when the fluid is not moving, and (2) a dispersive component that depends on the fluid superficial velocity. Therefore, neglecting the axial dispersion may not yield correct results at all Peclet numbers.

To check the validity of this assumption, axial dispersion will be included in the energy equation here. Results will first be compared with experimental data to check the model validity. Then results will be compared with the case with no axial dispersion. Heat transfer in the thermally developing region will be shown to be influenced by axial dispersion in a certain flow regime (Pe $< 10$).

Contributed by the Heat Transfer Division and presented at the ASME Winter Annual Meeting, Atlanta, Georgia, December 1–6, 1991. Manuscript received by the Heat Transfer Division March 1992; revision received July 1994. Keywords: Environmental Heat Transfer, Numerical Methods, Porous Media. Associate Technical Editor: C. E. Hickox, Jr.

## Governing Equations

The flow geometry under investigation here is shown in Fig. 1. Flow enters the tube at a uniform temperature $T_{in}$, the wall temperature is kept constant at another temperature $T_w$. The volume-averaged governing equations for an incompressible fluid are

$$\nabla \cdot \vec{V} = 0 \tag{1}$$

$$-\nabla P + \rho \vec{g} - \mu \frac{\vec{V}}{\gamma} - \rho \frac{F}{\gamma} |\vec{V}| \vec{V} + \mu \nabla^2 \vec{V} = 0 \tag{2}$$

$$(\rho C_p)_0 \frac{\partial T}{\partial t} + (\rho C_p)_f \vec{V} \cdot \nabla T = \nabla \cdot (k_e \nabla T) \tag{3}$$

The permeability $\gamma$ and inertia resistance coefficient $F$ were determined empirically by Ergun (1952) for sphere-pac beds to be

$$\gamma = \frac{d^2 \epsilon^3}{150(1-\epsilon)^2}, \quad F = \frac{1.75d}{150(1-\epsilon)} \tag{4}$$

It should be noted that these quantities depend on the porosity of the packed bed, which is not uniform across the tube. Experimental measurements of Benenati and Brosilow (1962) and Roblee et al. (1958) showed that the porosity of a sphere-pac bed varies sinusoidally from the free-stream value ($\epsilon_\infty$) of 0.4 to a value of 1 at solid boundaries. Hunt and Tien (1988) have suggested the following relationship for porosity variation in sphere-pac beds:

$$\epsilon = \epsilon_\infty \left[ 1 + 1.5 \exp\left( -\frac{6y}{d} \right) \right] \tag{5}$$

where $y$ is the distance from side walls. This porosity variation allows for channeling of flow near solid boundaries. After combining the gravity term with the hydrostatic pressure in the momentum equation, one can nondimensionalize the governing equations using $R_t, \upsilon/R_t, (T - T_w)/(T_{in} - T_w), \rho\upsilon^2/R_t^2$ for length, velocity, temperature, and pressure, respectively, to get

$$\frac{\partial u'}{\partial z'} = 0 \tag{6}$$

$$-\frac{\partial P'}{\partial z'} - \frac{1}{\mathrm{Da}} u' - \omega |u'| u' + \frac{1}{\epsilon} \frac{1}{r'} \frac{\partial}{\partial r'} \left( r' \frac{\partial u'}{\partial r'} \right) = 0 \tag{7}$$

$$\Omega \, \mathrm{Pr}_f \frac{\partial T'}{\partial t'} + \mathrm{Pr}_f u' \frac{\partial T'}{\partial z'} = \frac{1}{r'} \frac{\partial}{\partial r'} \left( r' k_r' \frac{\partial T'}{\partial r'} \right) + \frac{\partial}{\partial z'} \left( k_a' \frac{\partial T'}{\partial z'} \right) \tag{8}$$

The primes denote dimensionless quantities. The subscripts $r$ and $a$ denote radial and axial direction, respectively. The velocity



Copyright © 1995 by ASME

Downloaded 12 Dec 2010 to 193.140.21.150. Redistribution subject to ASME license or copyright; see http://www.asme.org/terms/Terms_Use.cfm

profile inside the tube is assumed to be hydrodynamically developed because studies such as Vafai (1984) have shown the size of entrance region for a packed bed to be very small. Within the solution domain, the flow is initially thermally developing and becomes nearly thermally developed with axial distance. The tube is long enough for the flow to become close enough to being thermally developed for the assumption of a zero axial temperature gradient to have little effect on the inlet region where axial dispersion is important. This was tested by increasing the computational length of the tube until no effect on the inlet region was found. The $M/R_t$ found that met this criterion was about 40 and that used in the computation was 45. The following boundary conditions were utilized:

$$T' = 1 \quad @ \quad z' = 0$$

$$\frac{\partial T'}{\partial z'} = 0 \quad @ \quad z' = \frac{M}{R_t}$$

$$\frac{\partial T'}{\partial r'} = 0 \quad @ \quad r' = 0$$

$$T' = 0 \quad @ \quad r' = 1 \tag{9}$$

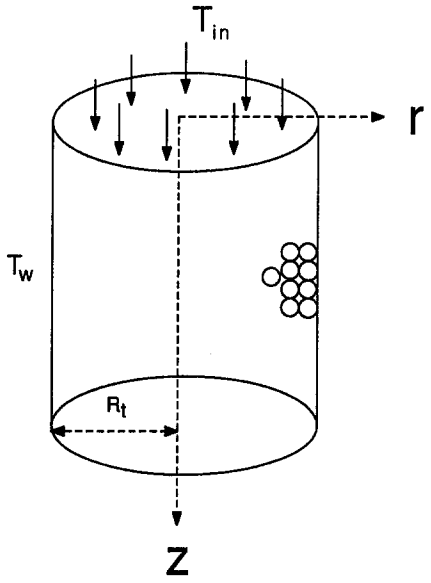



**Fig. 1 Forced convection in a packed tube**

## Radial and Axial Dispersion

Results from experiments of Levec and Carbonell (1985) and Yagi et al. (1960) show the effective thermal conductivities in the axial and radial directions to be different. Both studies suggest the axial component is larger than the radial component. Physically, this makes sense because interstitial velocities in the axial direction are larger than the interstitial velocities in the radial direction. To account for this anisotropy, different models will be used at each direction. In the radial direction, a modified version of the model by Cheng and Vortmeyer (1988) will be utilized. They suggest a linear relation between the dispersive component and the filtration velocity:

$$k_r' = \frac{k_0}{k_f} + D_T \xi \, \mathrm{Pr}_f \, \mathrm{Re} \tag{10}$$

where

$$\xi = \begin{cases} \left(\dfrac{y}{\tau d}\right)^m & \text{if } 0 \le y \le \tau d \\ 1 & \text{if } y > \tau d \end{cases} \tag{11}$$

Cheng and Vortmeyer (1988) suggest that the magnitudes of $D_T$, $\tau$, and $m$ are 0.25, 2.5 and 1 correspondingly. Since their model was derived assuming the flow has no inertia, it will be modified here by choosing $D_T$ to be 0.14 so that the results match the experimental data when flow has inertia. The conductivity $k_0$ is the effective medium conductivity when the fluid is stagnant. Its value is determined by using the two-dimensional unit cell model developed by Adnani et al. (1989). $\xi$ is a wall function that dampens hydrodynamic dispersion near solid boundaries. It is included here because, as the porosity is increased near solid boundaries, the path of fluid particles becomes less tortuous and dispersion becomes weaker. Combining $\xi$ and Re yields

$$\xi \, \mathrm{Re} = \begin{cases} \dfrac{y}{\tau d}\dfrac{ud}{\upsilon} = \dfrac{u}{\upsilon}\left(\dfrac{y}{\tau}\right) & 0 \le y \le \tau d \\ \dfrac{u}{\upsilon}(d) & y > \tau d \end{cases} \tag{12}$$

## Nomenclature

$C_p$ = specific heat at constant pressure
$d$ = diameter of particles in a packed bed
Da = Darcy number = $\gamma/L^2$
$D_T$ = empirical coefficient of dispersivity (Eq. (10))
$F$ = inertia resistance coefficient (Eq. (4))
$g$ = gravitational constant
$h$ = local heat transfer coefficient (Eq. (16))
$k$ = thermal conductivity
$m$ = parameter in Eq. (11)
$M$ = tube length
Nu = bulk Nusselt number (Eq. (15))
$P$ = pressure
Pe = Peclet number = $\mathrm{Pr}_f \times \mathrm{Re}$
$\mathrm{Pr}_f$ = fluid Prandtl number = $(\mu C_p)_f/k_f$
$r$ = radial coordinate
$R_t$ = tube radius
Re = particle Reynolds number = $ud/\upsilon$
$T$ = temperature
$t$ = time
$u, \upsilon, w$ = velocity components
$\vec{V}$ = velocity vector
$x, y, z$ = coordinate axes
$\gamma$ = permeability (Eq. (4))
$\epsilon$ = porosity
$\mu$ = dynamic viscosity
$\nu$ = kinematic viscosity
$\xi$ = wall damping parameter (Eq. (11))
$\rho$ = density
$\tau$ = empirical damping parameter (Eq. (11))
$\omega$ = dimensionless inertial coefficient = $FL/\gamma$
$\Omega$ = $(\rho C_p)_0/(\rho C_p)_f$

**Subscripts**

$a$ = axial
avg = averaged in the radial direction
$b$ = bulk value
$e$ = effective value with flow
$f$ = fluid
$in$ = inlet condition
$r$ = radial
$w$ = wall
$wi$ = with axial dispersion
$wo$ = without axial dispersion
0 = effective value with stagnant fluid
$\infty$ = far away from walls (free stream)

**Superscripts**

$'$ = dimensionless



Downloaded 12 Dec 2010 to 193.140.21.150. Redistribution subject to ASME license or copyright; see http://www.asme.org/terms/Terms_Use.cfm

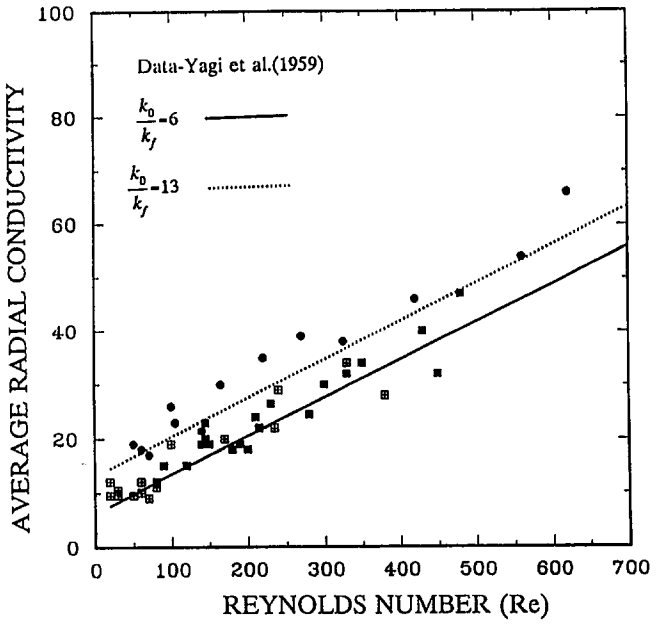



**Fig. 2 Comparison of effective conductivity with data of Yagi and Wakao (1959)**

The term inside the parentheses can be regarded as a mixing length. In the core region this mixing length is equivalent to the bead diameter because dispersivity is proportional to the bead diameter. Near the walls, mixing length has a value smaller than $d$ because the path of fluid particles is less tortuous. To account for this variation, the mixing length is assumed to vary linearly from 0 at the wall to $d$ at 2.5 particle diameters away from the wall. Note that near the wall, the value of the mixing length is bounded between 0 and $d$; therefore, even in this region the mixing length still depends on the particle size in a porous medium.

To estimate the axial dispersion coefficient ($k_a$) a modified version of the model suggested by Georgiadis (1987) will be used

$$k_a' = \frac{k_0}{k_f} + \frac{0.43}{1-\epsilon_\infty}\,\xi\,\mathrm{Pr}_f\mathrm{Re} \tag{13}$$

This model is modified to account for damping of hydrodynamic dispersion near solid walls by introducing the function $\xi$. Although this is done in an ad-hoc fashion, one must keep in mind that the same idea has been applied successfully to the radial component. The primes (denoting dimensionless quantities) will be dropped from here on for simplicity.

## Method of Solution

As an approximation, material properties for the fluid and solid phases will be assumed constant here. This is a reasonable assumption if the temperature and pressure do not change significantly inside the tube and the properties are evaluated at an average pressure and temperature. To model the sharp gradients and the channeling of flow near solid surfaces, a nonuniform grid is formed in the radial direction. For most calculations approximately 50 points were used in the radial direction and 600 points in the axial direction. In the radial direction 30 grid points were positioned within 4 bead diameters from the wall and the rest were spaced equally inside the tube. The momentum equation (Eq. (7)) is discretized in the radial direction, and is solved in an iterative fashion after specifying the axial pressure gradient.

Once the material properties and gas pressure are known, the effective medium conductivity with stagnant gas ($k_0$) can be determined from the unit cell model developed by Adnani et al. (1989). After solving the momentum equation and determining the velocity field, one can calculate the effective conductivities ($k_a$, $k_r$) from Eqs. (10) and (13). Note that these quantities change in the radial direction ($r$) but, because the flow is assumed to be hydrodynamically developed, there is no variation of conductivity in the axial direction ($z$). The energy equation (Eq. (8)) is solved using a two-dimensional time-dependent ADI scheme. The advective term in the energy equation was discretized using upwind differencing to avoid problems at high Peclet numbers.

## Comparison With Experimental Results

It was mentioned earlier that the radial conductivity model of Cheng and Vortmeyer (1988) was derived after assuming the flow has no inertia. Although this assumption is reasonable for cases where Re is less than 10, it is not so good at higher flow rates (see Georgiadis, 1987). Therefore, the empirical coefficient ($D_T$) of Cheng and Vortmeyer (1988) will be modified here so that good agreement with experimental results is obtained when flow has inertia.

To demonstrate the adequacy of the thermal model, the momentum and energy equations were integrated for the flow conditions corresponding to the experimental measurements in air by Yagi and Wakao (1959). Their data show some scattering at all Re (Fig. 2); this requires an explanation. Yagi and Wakao (1959) used various types of particle in their experiments. Some of these (i.e., cement clinkers) are not perfectly spherical. Additionally, results for different Re were obtained by either changing the flow rate or by changing the particle size. This means effective medium properties may have been changed, inadvertently, during the experiments. In spite of this, the predicted average conductivity ($k_{\mathrm{avg}}$) defined by

$$k_{\mathrm{avg}} = \frac{\int_0^1 2\pi k_r r dr}{\int_0^1 2\pi r dr} \tag{14}$$

is well within the experimental uncertainty range of Yagi and Wakao (1959) when $D_T$ is chosen to be 0.14.

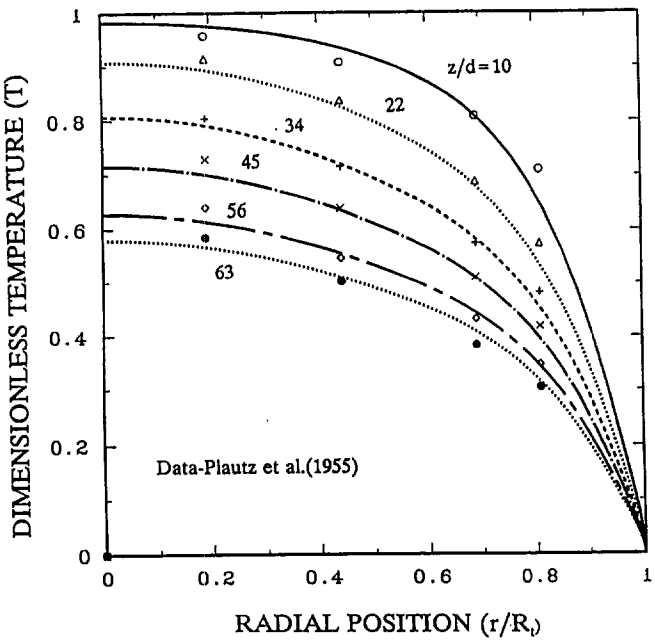



**Fig. 3 Comparison of temperature profile with data of Plautz and Johnstone (1955)**



Downloaded 12 Dec 2010 to 193.140.21.150. Redistribution subject to ASME license or copyright; see http://www.asme.org/terms/Terms_Use.cfm

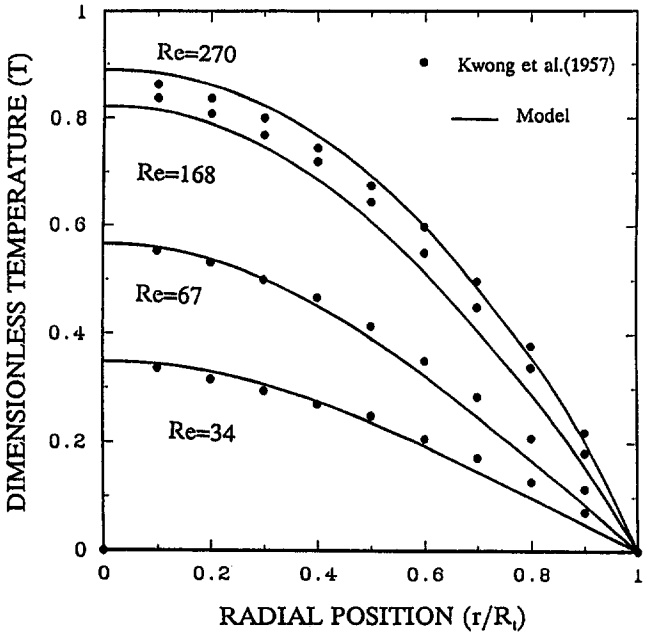



**Fig. 4 Comparison of temperature profile with data of Kwong and Smith (1957)**

A better set of data was obtained from the experiments of Plautz and Johnstone (1955). They performed their experiments with spherical glass particles at various air flow rates. Figure 3 shows the model prediction and the experimental results at different axial locations. Excellent agreements are obtained at all locations. Note that Re for this case is approximately 1000, meaning dispersion is the dominant mechanism influencing the heat transfer. To check the validity of our model at other Re, results were compared with the data of Kwong and Smith (1957). They were actually the first people who suggested that the radial conductivity is nonuniform across the tube. Figure 4 shows the model predictions and Kwong and Smith's data (1957) for a range of Re. All of the data were taken at 26 bead diameters downstream of the inlet. Considering the fact that the experimental uncertainty in these measurements was roughly ±10 percent, excellent agreement is obtained at all Re.

## Influence of Axial Dispersion

The objective in the previous section was to check the validity of the thermal conductivity models. It has been known for a long time that the axial diffusion term in the equivalent of this problem in a nonporous tube can be neglected for most cases (the only exception is liquid metals at low Pe). In porous media, however, the axial dispersion term depends on the filtration velocity. This means that neglecting the axial dispersion term might not be a correct assumption at all Pe. In this section, we test the validity of this hypothesis. We consider flow at several Pe to see whether the axial advective term is always larger than the axial dispersive term. In order to carry out a nondimensional analysis, ratio of Nu with axial dispersion over Nu without axial dispersion ($Nu_{wi}/Nu_{wo}$) will be plotted as a function of axial position. Nu is defined to be

$$\mathrm{Nu} = \frac{2hR_t}{k_f} \tag{15}$$

where $h$ is the local heat transfer coefficient

$$h = \frac{1}{T_b - T_w}\left(k_r \frac{\partial T}{\partial r}\right)_w \tag{16}$$

and $T_b$ is the bulk mean temperature

$$T_b = \frac{2\pi \int_0^1 uTrdr}{2\pi \int_0^1 urdr} \tag{17}$$

Figure 5 shows the results in the thermally developing region of the tube for Pe ranging from 0.7 to 14. Note that axial dispersion enhances the heat transfer (increased Nu) in the thermally developing region of the pipe. This effect disappears at some location downstream, and the location depends on Pe. It can be observed that at low Pe (Pe $<$ 10), the axial dispersion term does play a role on determining the heat transfer in the pipe. As Pe is increased, the advective term in the axial direction becomes larger and the presence of axial dispersion does not affect the results significantly.

## Conclusions

The influence of axial dispersion on heat transfer in a packed tube was investigated by incorporating a term to represent the axial dispersion in the energy equation. Previous studies in this area neglect axial dispersion in all flow regimes. Non-Darcian effects, i.e., flow inertia, porosity variation near walls, and dispersion damping near walls were also incorporated in the governing equations. Dispersion was assumed to be anisotropic in the radial and axial directions as suggested by the experimental evidence in the literature. Results in the radial direction were shown to be in good agreement with data of Yagi and Wakao (1959), and the accuracy of the axial dispersion model has been tested by Georgiadis (1987). Excellent agreement with the data of Plautz and Johnstone (1955) and Kwong and Smith (1957) was achieved when the combined axial and radial dispersivity models were used.

The analysis in this paper was done to determine whether the axial dispersion can be neglected at all Pe while studying convective heat transfer processes in porous media. It was shown that heat transfer results for Pe $<$ 10 can be underestimated if axial dispersion is not included in the analysis. The smaller the Pe, the larger the influence of axial dispersion. A set of dimensionless graphs is developed to show the importance of axial dispersion at various Pe. For Pe $>$ 10 the axial advective term

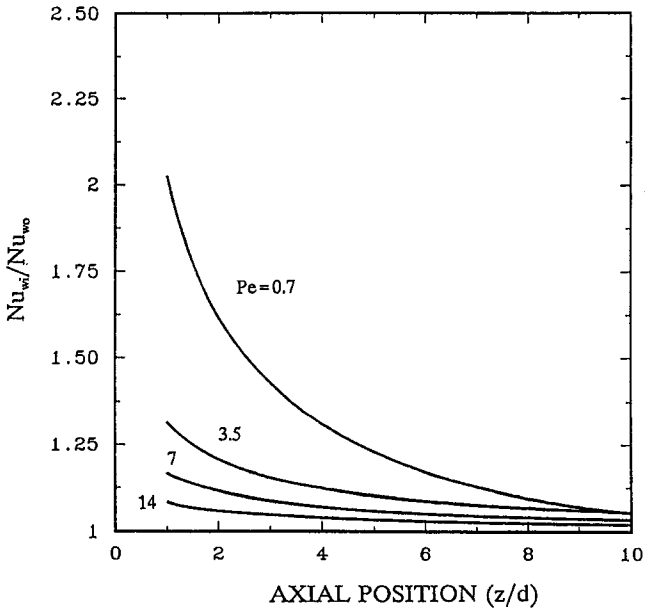



**Fig. 5 Influence of axial dispersion on axial heat transfer**



Downloaded 12 Dec 2010 to 193.140.21.150. Redistribution subject to ASME license or copyright; see http://www.asme.org/terms/Terms_Use.cfm

becomes large enough that axial dispersion can be neglected without affecting the result in a significant manner. Therefore, previous studies in this area are correct only in the flow regime $Pe > 10$. At smaller Pe, one must either include axial dispersion in the analysis or use information similar to what was shown in Fig. 5 to correct for the heat transfer results.

## Acknowledgments

This work was supported by the U.S. Department of Energy under contracts #DE-FG03-86ER52123 and #DE-FG03-86ER14033. We would like to thank one of the reviewers for calling our attention to the interesting and informative paper by Sozen and Vafai (1993). Unfortunately, it was called to our attention too late in the review process to exploit fully what it contained.

## References

Adnani, P., Raffray, A. R., Abdou, M. A., and Catton, I., 1989, "Modeling of Effective Thermal Conductivity for a Packed Bed," Report No. UCLA-FNT-29, University of California, Los Angeles.

Benenati, R. E., and Brosilow, C. B., 1962, "Void Fraction Distribution in Beds of Spheres," *AIChE Journal,* Vol. 8, No. 3, pp. 359–361.

Bunnell, D. G., Irvin, H. B., Olson, R. W., and Smith, J. M., 1949, "Effective Thermal Conductivities in Gas–Solid Systems," *Ind. Eng. Chem.,* Vol. 41, No. 9, pp. 1977–1981.

Cheng, P., and Vortmeyer, D., 1988, "Transverse Thermal Dispersion and Wall Channelling in a Packed Bed With Forced Convective Flow," *Chem. Eng. Sci.,* Vol. 43, No. 9, 2523–2532.

Coberly, C. A., and Marshall, W. R., 1951, "Temperature Gradients in Gas Streams Flowing Through Fixed Granular Beds," *Chem. Eng. Prog.,* Vol. 47, No. 3, pp. 141–150.

Ergun, S., 1952, "Fluid Flow Through Packed Columns," *Chem. Engng. Prog.,* Vol. 48, No. 2, pp. 89–94.

Georgiadis, J. G., 1987, "Nonlinear Convective Transport in Packed Beds," Ph.D. Dissertation, University of California, Los Angeles, CA.

Hunt, M. L., and Tien, C. L., 1988, "Non-Darcian Convection in Cylindrical Packed Beds," ASME JOURNAL OF HEAT TRANSFER, Vol. 110, pp. 378–384.

Kwong, S. S., and Smith, J. M., 1957, "Radial Heat Transfer in Packed Beds," *Ind. and Eng. Chem.,* Vol. 49, No. 5, pp. 894–903.

Levec, J., and Carbonell, R. G., 1985, "Longitudinal and Lateral Thermal Dispersion in Packed Beds. Part II: Comparison Between Theory and Experiment," *AIChE Journal,* Vol. 31, No. 4, pp. 591–602.

Plautz, D. A., and Johnstone, H. F., 1955, "Heat and Mass Transfer in Packed Beds," *AIChE Journal,* Vol. 1, No. 2, pp. 193–199.

Roblee, L. H. S., Baird, R. M., and Tierney, J. W., 1958, "Radial Porosity Variations in Packed Beds," *AIChE Journal,* Vol. 4, pp. 460–464.

Sozen, X. X., and Vafai, K., 1993, "Longitudinal Heat Dispersion in Porous Beds With Real Gas Flow," *AIAA Journal of Thermophysics and Heat Transfer,* Vol. 7, No. 1.

Vafai, K., 1984, "Convective Flow and Heat Transfer in Variable-Porosity Media," *J. Fluid Mech.,* Vol. 147, pp. 233–259.

Yagi, S., and Wakao, N., 1959, "Heat and Mass Transfer From Wall to Fluid in Packed Beds," *AIChE Journal,* Vol. 5, No. 1, pp. 79–85.

Yagi, S., and Kunii, D., 1960, "Studies on Heat Transfer Near Wall Surface in Packed Beds," *AIChE Journal,* Vol. 6, No. 1, pp. 97–104.

Yagi, S., Kunii, D., and Wakao, N., 1960, "Studies on Axial Effective Thermal Conductivities in Packed Beds," *AIChE Journal,* Vol. 6, No. 4, pp. 543–546.



Downloaded 12 Dec 2010 to 193.140.21.150. Redistribution subject to ASME license or copyright; see http://www.asme.org/terms/Terms_Use.cfm

# Direct Contact Melting of a Packed Bed

**D. A. Kearns**
Graduate Student.

**O. A. Plumb**
Professor.

Department of Mechanical and Materials Engineering,
Washington State University,
Pullman, WA 99164-2920

*Direct contact melting of a packed bed is studied experimentally. The effect of several parameters, including material properties, particle size, bed loading (applied external force), and thermal boundary conditions, is examined. Two types of melting are observed. If the load on the bed is small and the top of the bed is maintained at a temperature below the melting temperature, then crusting can occur. During this type of melting liquid flows away from the heated surface due to capillary action, and resolidifies forming a crust. The crust prevents downward movement of the packed bed, and melting of the solids below the crust results from convection and conduction. Eventually the crust is melted and the process repeats itself, resulting in a highly unsteady melting rate. If the bed load and the temperature at the top of the bed are sufficiently high, then direct contact melting persists. In this case the melting rate is steady and the parametric behavior can be predicted using a modification of an available theory for direct contact melting of monolithic solids. Although this theory accurately predicts the parametric behavior, the prediction of the actual melting rate is more than an order of magnitude higher than the experimental results.*

## Introduction

Phase-change phenomena have long been recognized as important engineering processes. In most cases, however, studies of phase-change phenomena have focused on melting of monolithic solids of various geometries. Melting of granular or porous materials has not been addressed, although work has been done on melting of materials in a nonmelting porous matrix by convection (Chellaiah and Viskanta, 1990; Kazmierczak et al., 1986). Understanding the transport phenomena that occur during melting in porous media is critical to modeling a wide range of processes. Applications include melting of snow and ice, melting of frozen soil, in situ vitrification of hazardous wastes, nuclear reactor accidents (Wang and Dhir, 1988), and a number of materials processing technologies (German, 1985; Yan, 1982; Anton et al., 1989), including liquid-enhanced sintering, hot isostatic processing, and a number of relatively new processes for the manufacture of metal–ceramic composites.

Moallemi et al. (1986) investigated direct contact melting of free-standing cylinders and blocks of $n$-octadecane (paraffin) exposed to a constant temperature surface. Heat transfer to the phase-change material was by conduction through a thin liquid film at the hot surface. This work indicated that melting rates decrease as the height of the solid, and hence the weight of the body is decreased, lowering the pressure in the liquid film. In addition, Moallemi demonstrated the conditions for which the liquid film can be assumed to be of constant thickness and derived both theoretical and empirical models for the velocity of the solid (melting rate) as a function of instantaneous solid height, $H(t)$. The theoretical analysis is based on the Nusselt thin film theory. Equation (1) is a dimensional form of Moallemi's theoretical melting rate written for a cylinder where $\alpha$ is the thermal diffusivity, Ste is the Stefan number, $\mu$ the dynamic viscosity, $R_0$ the radius of the circular contact area, $\rho$ is the solid density, $g$ the gravitational constant, and $A$ is the cross-sectional area.

$$V_{\text{melt}} = \left[\frac{2\alpha^3 \text{Ste}^3}{3\pi\mu R_0^4}\right]^{1/4} (\rho g A H(t))^{1/4} \qquad (1)$$

This result overpredicted the measured velocities by 12 to 25 percent. It was concluded that some of the model assumptions (uniform surface temperature, homogeneity, etc.) were at fault.

Hirata et al. (1991) investigated direct contact melting of rectangular blocks of $n$-octadecane and ice for various aspect ratios where the sides of the rectangular melting enclosures were held at constant temperature. The liquid produced by direct contact melting remained in contact with the solid and, depending on the aspect ratio, caused convection induced melting at the sides and top. Hirata's theoretical result for melting velocity can be shown to be identical to Eq. (1). Hirata points out that the thin film theory should be applicable only for Ste $\ll 1$ and notes that the accumulation of air bubbles in the thin liquid film can cause the predicted analytical melting velocity to be greater than the experimental results.

Bejan (1989) and Bejan and Tyvand (1992) have more recently presented a theoretical solution to the problem of pressure melting. In this case the effect of pressure on thermodynamic properties is included in the analysis.

In this paper the first experimental results for direct contact melting of packed beds will be presented. Experimental geometries were chosen so that conductive heat transfer mechanisms were dominant (direct contact melting). During the experiments, a constant force was applied to the top of a rectangular volume containing the packed bed while heat was applied through the lower boundary, resulting in one-dimensional vertical melting from below. Effects of several parameters including material properties, particle size, bed loading, and the thermal boundary condition at the top of the bed were studied. A comparison of experimental melting rates with those of Moallemi's model modified for application to the packed bed is also offered for direct contact melting. Results for conditions for which the melting process is unsteady are also presented and discussed.

## Experimental Apparatus and Procedure

A chamber having sidewalls fabricated from polyvinyladine fluoride sheeting (PVDF) 0.64 cm thick and top and bottom plates made from copper is shown in Fig. 1. PVDF was selected for its thermal and chemical properties as well as its low gamma absorption. A copper plate formed the bottom of the chamber, which is approximately 5 cm square. A custom-built ceramic wafer resistive heating element (5 ohms) is held against the copper plate by glass insulation packing. A thermopile type heat flux sensor 0.030 cm (0.012 in.) thick with integral thermocouple is sandwiched between the heater and the copper plate.

Contributed by the Heat Transfer Division and presented at the 29th National Heat Transfer Conference, Atlanta, Georgia, August 8–11, 1993. Manuscript received by the Heat Transfer Division September 1993: revision received April 1994. Keywords: Packed and Fluidized Beds, Phase-Change Phenomena, Porous Media. Associate Technical Editor: C. E. Hickox, Jr.

 Copyright © 1995 by ASME 

Downloaded 12 Dec 2010 to 193.140.21.150. Redistribution subject to ASME license or copyright; see http://www.asme.org/terms/Terms_Use.cfm

The upper surface of the melting volume is formed by a movable multipass water jacket (cooling lid) made of copper. This jacket could be maintained at a prescribed temperature by circulating water from a constant-temperature bath. A support arm and bearing allowed the cooling lid to move vertically inside the chamber opening on a guide rod such that only the weight of the water jacket/guide rod assembly (and any added weights) is supported by the packed bed. Instantaneous changes in bed height were measured with a linear variable differential transformer (LVDT) actuated by an arm from the top of the guide rod. The chamber was insulated with polystyrene foam and placed in an environment where the ambient air temperature was controlled to minimize heat losses from the vertical walls of the chamber. The melting chamber was mounted on a base plate so that the entire insulated unit could be removed for cleaning and replaced while maintaining precise alignment with the cooling lid. Temperatures at the inlet to the cooling lid, center bottom of the cooling lid, ambient, and chamber bottom (hot surface) were monitored using thermocouples. A gamma attenuation system (Am 241) allowed the liquid saturation front to be tracked during an experiment. A stepper motor moved the gamma source/detector assembly to recording stations vertically spaced 2 mm apart, projecting a collimated gamma beam 0.5 mm × 2.5 cm parallel with the heated surface. The overall size of the experiment was limited by gamma source/detector spacing and the enclosure used to provide an elevated ambient temperature.

The materials studied were selected on the basis of low melting point and availability of property data. Thymol, an organic crystalline solid (98 percent pure), was chosen because of its 50°C melting point. Quantities were screened to yield two particle sizes of 0.081 and 0.044 cm nominal diameters, with porosities measured at approximately 29 percent. Thermal conductivity was measured in the test cell to be 0.13 W/mK. This compares well with a published value of 0.15 W/mK (*International Critical Tables,* 1929). The thermal conductivity of liquid thymol is not available, hence, 0.13 W/mK is used in analyzing and interpreting the results. The viscosity of thymol liquid was also measured. The values are reported in Table 1 along with other properties. Ground ice (from tap water) was chosen as a second porous material with readily available properties and large heat of fusion. Experiments were conducted with one particle size having nominal diameter of 0.36 cm (0.14 in.) and a porosity of 49 percent.

Prior to initiation of an experiment with Thymol, air was circulated around the experimental apparatus at 50–52°C while the bed was heated from below with the heating element on low power. The water jacket was heated to the desired temperature (typically 48°C). When the copper plate reached the melting temperature, power to the heater was turned up to the desired level (4–10 W) and a computer data acquisition/step motor control algorithm was started. Prior to an ice melting experiment, the chamber and ice were cooled to −2°C. The cooling jacket

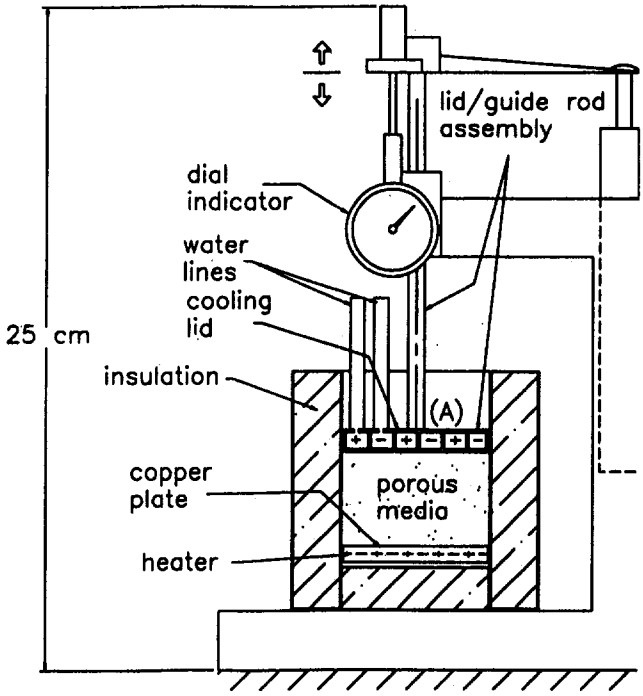



**Fig. 1 Experimental melting chamber**

was also cooled to −1 to −2°C. Just before a run, the ground ice particles were screened directly into the chamber. The chamber was then transferred to the apparatus and power-up and data acquisition commenced immediately with the ambient air at 24°C. In all experiments the top of the bed was carefully leveled to insure good contact with the cooling lid.

Five cm (2 in.) initial bed depths were set by either a leveling tool or calculated from bulk density and weighing. Gamma count data were not taken for high melting rates (all ice experiments) to allow more temperature, heat flux, and LVDT data to be recorded. Different bed loads were obtained by adding weights to the cooling jacket/guide-rod assembly. Four loads were used: base (250 g) (weight of lid/guide-rod assembly) and 1.5, 2.0, and 3.0 times the base load (375, 500, and 750 g, respectively).

## Results and Discussion

Two distinct melting phenomena were observed for the Thymol particles. In the first, which we believe to be direct contact melting, the solid particles remain in close contact with the heated surface and the load applied to the bed continues to act on the particles. Heat transfer, in this case, is likely dominated

## Nomenclature

$A$ = cross-sectional area of melting solid
$c$ = specific heat
$D$ = particle diameter
$F$ = applied load
$g$ = gravitational constant
$H$ = time-dependent bed height
$h_{sl}$ = latent heat of fusion
$k$ = thermal conductivity
$L$ = length of side of square melting surface (chamber bottom)
$\dot{m}$ = mass rate of liquid production during crusting
$M$ = mass of liquid accumulated in a pool during crusting cycle
$N$ = estimated number of particles in contact with hot surface
$Q$ = heat transfer to liquid pool
$R$ = radius of melting solid
Ste = Stefan number $= c_l(T_w - T_m)/h_{sl}$
$T$ = local temperature
$t$ = time
$T_m$ = melting temperature of solid
$T_w$ = heated surface temperature
$T_{\text{lid}}$ = cooling lid temperature
$T_T$ = ambient temperature
$V$ = volume
$V_{\text{melt}}$ = melting rate (velocity)
$z$ = coordinate direction
$\alpha$ = thermal diffusivity
$\beta$ = coefficient of thermal expansion
$\delta$ = film thickness
$\nu$ = kinematic viscosity
$\rho$ = density
$\phi$ = porosity of packed bed

### Subscripts

eff = effective
$l$ = liquid phase
$s$ = solid phase
0 = mean or initial



Downloaded 12 Dec 2010 to 193.140.21.150. Redistribution subject to ASME license or copyright; see http://www.asme.org/terms/Terms_Use.cfm

**Table 1 Material properties**

| Property | Symbol | Value | Units |
|---|---|---|---|
| *Thymol* | | | |
| Melting point | m.p. | 50.0 ± 1°C | °C |
| Density—solid | $\rho_s$ | 0.969 @ 24.4°C | g/cm$^3$ |
| Density—liquid | $\rho_l$ | 0.92 ± 9 percent @ 60°C | g/cm$^3$ |
| Specific heat—solid | $c_s$ | 1.32 + 0.013$T$ ± 3 percent, 0 < $T$ < 49°C | J/g K |
| Specific heat—liquid | $c_l$ | 2.371 ± 0.5 percent @ 50°C | J/g K |
| Heat of fusion | $h_{sl}$ | 114.93 | J/g |
| Solid thermal conductivity | $k_s$ | 0.13 ± 10 percent @ 23°C | W/m K |
| Liquid thermal conductivity | $k_l$ | 0.13 | W/m K |
| Kinematic viscosity | $\nu$ | 0.007654 $(T)^{-1.891}$, ± 1 percent $T$ in °C | m$^2$/s |
| Ice/water | | | |
| Melting point | m.p. | 0 | °C |
| Density—solid | $\rho_s$ | 0.917 @ 0°C | g/cm$^3$ |
| Specific heat—liquid | $c_l$ | 4.217 @ 0°C | J/g K |
| Heat of fusion | $h_{sl}$ | 333.43 @ 0°C | J/g |
| Liquid thermal conductivity | $k_l$ | 0.569 @ 0°C | W/m K |
| Kinematic viscosity | $\nu$ | $1.60 \times 10^{-6}$ | m$^2$/s |

by conduction across the thin film between the particles and the hot surface. Melting rates were constant when this type of melting phenomenon was observed. The second type of melting observed is one that we will call "crusting." Crusting involves the cessation of bed motion due to the formation of a solid layer of refrozen melt that was wicked away from the hot surface and adhered to the inside wall of the chamber. In this mode, heat transfer from the hot surface occurred by convection and/or conduction through a liquid pool that formed due to the blockage by the crust. For melting in ice, only direct contact melting was observed.

*Crusting.* During the first melting experiments involving thymol, an initial power level (5 W) was selected based on the heat required theoretically to melt the volume in a period of one hour. The load applied to the bed was that due only to the weight of the basic cooling jacket/guide-rod assembly (250 g). Lid and air temperatures were set to 40°C and 45°C, respectively. During these runs, crusting was pervasive and unrepeatable. In some cases crusting would occur immediately; in other cases there would be an initial period of direct contact melting. Cycles of crusting and releasing were observed as illustrated in Fig. 2, which shows bed depth as measured using the LVDT as a function of time.

The onset of crusting was immediately evident because it resulted in a sudden increase in base temperature. Particles near the hot surface were no longer subject to a load, allowing the liquid film to increase in thickness. Inspection of the chamber after such a run confirmed the existence of a solidified layer. Gamma count scans indicated the presence of an air pocket forming due to the fixing of the volume below the crust. Figure 3 shows a typical set of gamma data for such a case where the asymptote at approximately 2200 counts is through the liquid, or liquid-saturated bed, the asymptote at approximately 2800 counts is through the dry bed. Counts through the empty chamber were approximately 4800 over the five second counting time used in these experiments. Each S-shaped line between the asymptotes locates the liquid saturation front in the bed at a given time, with the melt progressing from left to right. From this figure we surmise that crusting occurred twice and a pocket of air built up in each case. Air pockets are indicated by the peaks in gamma counts that rise above 2800. As melting erodes the surface of the crust facing the heat source, the liquid produced takes up less volume than the crust material, and since the crust "lid" cannot

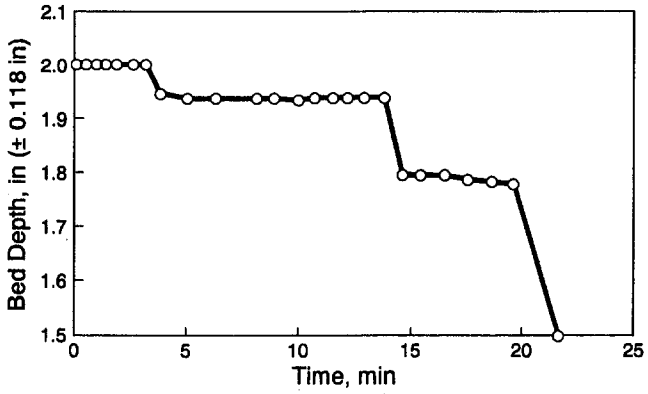



**Fig. 2 Measurement of bed depth as a function of time for crusting-type melting of thymol**

move down, an air pocket is formed. The time elapsed between the count profiles in Fig. 3 is approximately 12 minutes. It was assumed that crusting occurred because of the low initial bed temperature, the water jacket temperature, and lateral heat losses due to an ambient temperature 5°C below the melting point. The small load on the bed was also a possible factor.

The second experiment was run with the water jacket and ambient air temperatures set to 48°C with power and load at base levels. Crusting still occurred, but only after an initial period of constant melting. The next experiment was run with all parameters the same except that the bed load was doubled. In this case a constant melting rate was observed (as in Fig. 6). It was decided that, due to the unpredictable nature of the crusting phenomenon, future experiments in Thymol would concentrate on constant melting rates at the higher bed loads. Water jacket and air temperatures were maintained just below the melting point,

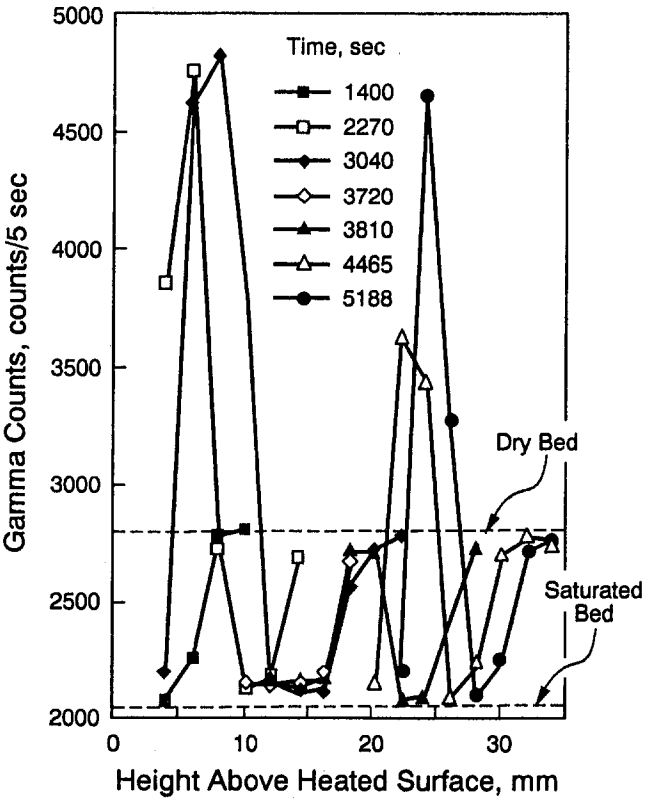



**Fig. 3 Gamma counts showing density distribution as a function of time for crusting-type melting of thymol**



Downloaded 12 Dec 2010 to 193.140.21.150. Redistribution subject to ASME license or copyright; see http://www.asme.org/terms/Terms_Use.cfm

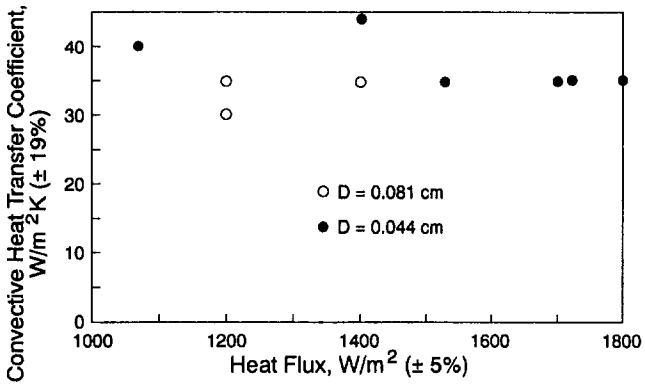



**Fig. 4 Experimental results for the effective convective heat transfer coefficients for crusting**

and power input was the principal independent variable along with the particle size and bed load. Different water jacket temperatures were effectively ruled out, although when crusting persisted, particularly at low loads, the ambient air temperature was raised to 51–52°C.

We surmise that when a crust is formed a liquid pool laden with unmelted particles exists beneath the crust. In this case the dominant heat transfer mode would be natural convection in a horizontal pool. Convective heat transfer coefficients during periods of crusting can be calculated from the experimental measurements. These are shown in Fig. 4. For the range of parameters studied the resulting convective heat transfer coefficients are nearly constant at 35 W/m$^2$ K (±19 percent). For natural convection in the absence of solids the Globe and Dropkin correlation (Incropera and DeWitt, 1990) predicts a convective heat transfer coefficient of 116 W/m$^2$ K for an excess temperature of 20°C, which is typical for the results shown in Fig. 4. The coefficient of thermal expansion was assumed to be 0.0009 K$^{-1}$ for these calculations. If the layer beneath the crust is assumed to be a packed bed with initial porosity of 0.3 and the initial particle size, then the layer is stable (Nield and Bejan, 1992). In this case the unit conductance is approximately 5 W/m$^2$ K. Because our results fall between these two limits, we assume that convection plays a factor in the heat transfer across the layer beneath the crust, but that it is damped by the presence of solid particles.

A simple energy balance was utilized to predict the pool depth (or crust height) for comparison with experimental observations. The power input is equated to the rate heat is transferred to the liquid plus the energy being consumed by melting of the crust and solids in the liquid pool.

$$Q = \frac{dM}{dt} h_{sl} + Mc_l \frac{dT}{dt} \tag{2}$$

In Eq. (2), $dM/dt$ is the rate of liquid production from melting of the crust and from melting of solids in the pool, $M$ is the mass of the liquid in the pool and $dT/dt$ is the average temperature gradient in the pool during the time period in question. Now writing

$$M = \rho_l AH \tag{3}$$

where $H$ is the accumulated depth of the liquid pool measured by the LVDT in experiments at the end of the crusting cycle over time $dt$, we can solve for the approximate depth $H_{th}$ and compare it to $H$. Combining Eqs. (2) and (3) results in

$$\frac{dH_{th}}{dt} = \frac{Q}{\rho_l A h_{sl}} - \frac{c_l H}{h_{sl}\rho_l A} \frac{dT}{dt} \tag{4}$$

Predictions using Eq. (4) are in good agreement with the measured drop in bed height after a crusting cycle. In some crusting experiments, temperatures were seen to fluctuate, indicating that clumps of the blockage released and sank to the bottom of the liquid pool. The Rayleigh numbers calculated for these results indicate both convective and conductive heat transfer modes were present depending on the liquid pool depth and temperature difference.

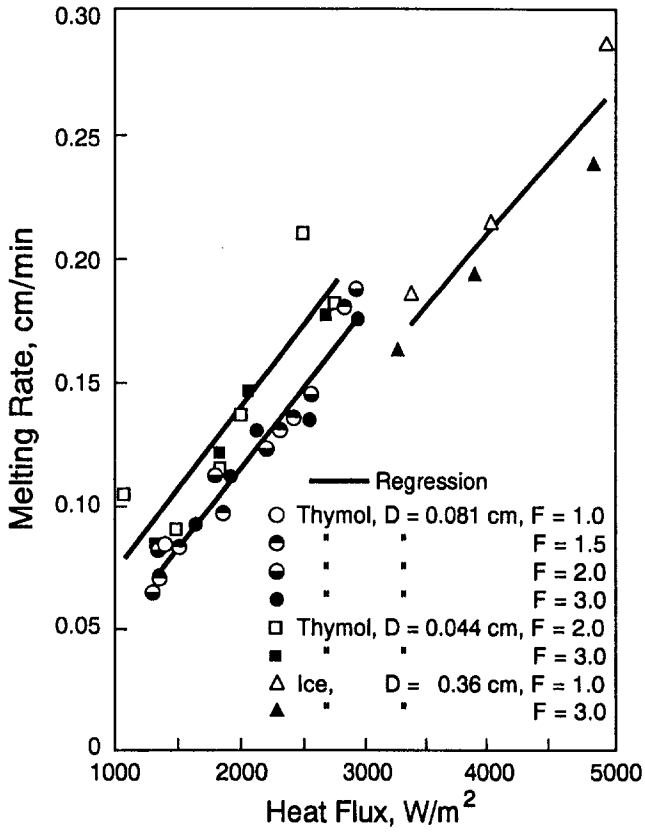



**Fig. 5 Experimental results for melting velocity as a function of heat flux for direct contact melting**

*Direct Contact Melting.* Experiments in which direct contact melting was observed showed similar results for Thymol and ice. The melting rates were constant, varied linearly with heat input, and showed little sensitivity to bed load. Figure 5 shows the measured melting velocity or rate at which the bed height decreased as a function of heat flux for all experiments. Regression lines for the two different Thymol particle sizes and the ice data are shown. Standard deviations range from 0.038 for the 0.081 cm thymol to 0.044 for the ice (0.36 cm).

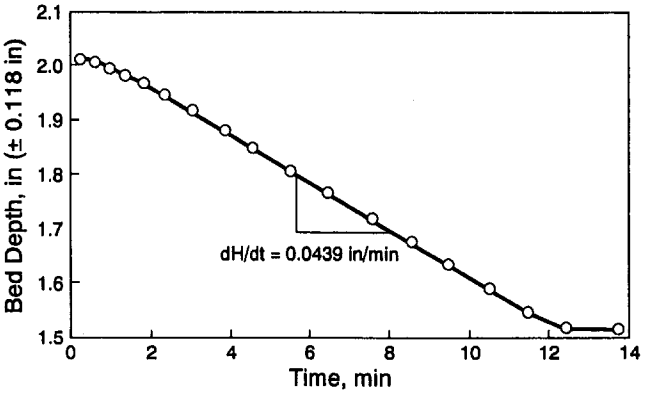



**Fig. 6 Measured bed depth as a function of time for direct contact melting**



Downloaded 12 Dec 2010 to 193.140.21.150. Redistribution subject to ASME license or copyright; see http://www.asme.org/terms/Terms_Use.cfm

This figure illustrates higher melting rates for smaller particles at a fixed heat flux. This result is at least qualitatively consistent with Eq. (1). Figure 6 shows a typical LVDT trace for direct contact melting. In this case the melting process is very steady as compared to the crusting-type melting discussed above.

An attempt was made to extract the unit surface conductance for direct contact melting from the experimental data. The results are shown in Fig. 7. These data indicate a weak dependence on load, particle size, and heat flux. The unit conductance appears to decrease with increased load, decrease with particle size, and decrease as heat flux is increased. The uncertainty in these results is estimated to be ±19 percent. Gamma counts taken during direct contact melting are shown in Fig. 8. In this case saturation fronts move up the bed uniformly as would be expected. The last trace in this figure was recorded about one minute after the cooling jacket hit stops preventing it from going below the approximate liquid volume. This trace shows the existence of an air pocket when melting was completed. The unsaturated zone can be seen to be on the order of 5 mm in thickness for this particular case.

While the bulk of the experiments exhibited constant melting rates, many of the runs with Thymol showed a combination of crusting and releasing, or initial constant melting followed by crusting. Crusting was more likely to occur at low heat flux or low bed load. It also occurred more readily for the smaller thymol particles presumably due to the higher capillary potential. All of the experiments with ice exhibited constant melting rates.

*Comparison With Theory.* In developing a modification to the Moallemi theory discussed above, it is assumed that the packed bed can be modeled as a series of vertical cylinders having a diameter and porosity consistent with the physical properties of the experimental bed. The Moallemi theory is then assumed to be valid for each individual particle (cylinder). The force term in Eq. (1) can be written

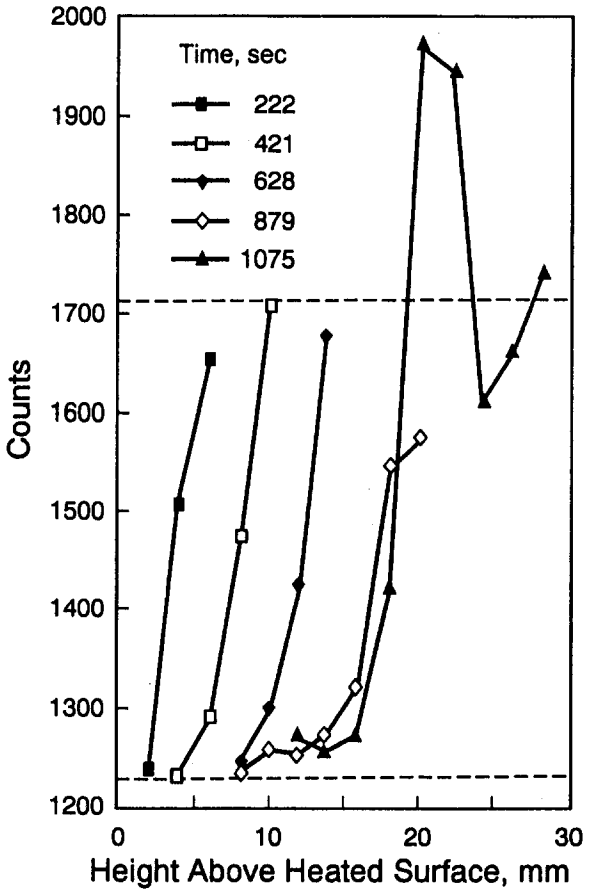



**Fig. 8 Density distribution near the melting front for direct contact melting of 0.081 cm thymol**

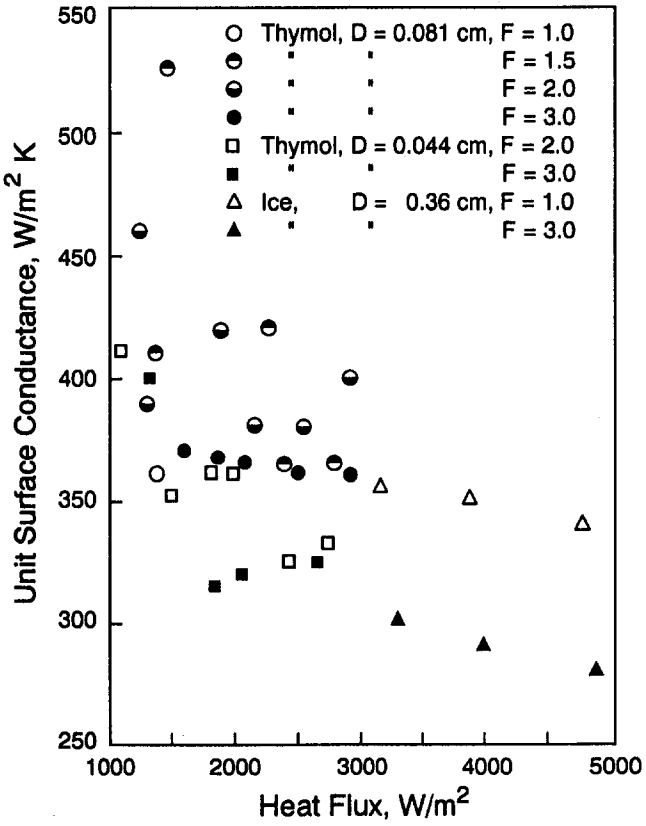



**Fig. 7 Unit surface conductance for direct contact melting**

$$F = \rho g A H(t) + F_{\text{ext}}, \tag{5}$$

where $A$ is the cross-sectional area of the bed and $F_{\text{ext}}$ is the externally applied load. For our experiments the external load is three to twelve times greater than the weight of the solids even with buoyancy forces due to melted liquid neglected. Thus, we assume $F \approx F_{\text{ext}}$ and take $F$ to be the total force acting on the bed. The force acting on an individual particle can be estimated by dividing $F$ by the total number of particles ($N$) in contact with the hot surface. Beginning with the definition of porosity for the bed,

$$\phi = \frac{\text{pore volume}}{\text{total volume}} = \frac{V_T - V_s}{V_T} = \frac{HL^2 - NH\frac{\pi}{4}D_0^2}{HL^2}, \tag{6}$$

where $V_T$ is the total volume of the chamber, $V_S$ is the solid volume, $H$ is the bed depth, $L$ is the length of one side of the square chamber bottom, and $D_0$ is the average particle diameter. The number of particles can be approximated as

$$N = \frac{4L^2(1-\phi)}{\pi D_0^2}. \tag{7}$$

The average particle area in contact with the surface must also be estimated. For a large number of particles, the average diameter in contact with the surface can be approximated as the average chord length for a sphere taken parallel to the melting surface. This results in an effective diameter of $\pi D_0/4$. This effective diameter or the corresponding radius has been used in the following comparison between theory and experimental results. Replacing the body force in Eq. (1) with $F = F_{\text{ext}}$ and recognizing



Downloaded 12 Dec 2010 to 193.140.21.150. Redistribution subject to ASME license or copyright; see http://www.asme.org/terms/Terms_Use.cfm

that this force is applied over $N$ particles having radius $R_0 = D_{\text{eff}}/2$ results in

$$V_{\text{melt}} = \left[\frac{2\alpha^3 \text{Ste}^3}{3\pi\mu R_0^4}\right]^{1/4}\left(\frac{F}{N}\right)^{1/4} \quad (8)$$

Equation (8) and the experimental results are compared in Fig. 9. Uncertainties in the experimental results are estimated to be ±20 percent. This figure demonstrates that the experimental results are well correlated by the theory, in that the melting velocity varies as the 1/4 power of the parameter that represents the right-hand side of Eq. (8). However, the theory overpredicts the results by a factor of 40. Moallemi noted a 12 to 25 percent overprediction in his comparisons between the same theory and experiments using monolithic solids. It should also be noted that in adapting the theory to a packed bed we assume that melting occurs only over the area given by $N\pi D_{\text{eff}}^2/4$, the solid fraction at the melting surface. This reduces $V_{\text{melt}}$ in Eq. (8) by 43.1 percent, far short of the factor of 40 necessary to obtain good agreement.

Part of the discrepancy between theory and experiment may lie in the estimation of the number of particles in direct contact with the hot surface. The difference between the number of particles in contact with the hot surface and the number of particles actually bearing the load at the hot surface could help explain why the theory overpredicts melting rates. It is possible that the larger particles carry the load, bridging over smaller particles, increasing the effective mean diameter. However, the effective particle size would have to increase 1000-fold to obtain good agreement between theory and experiment. In fact, if the packed bed were treated as a monolithic solid, the theory would still be approximately one order of magnitude above the experimental results. This causes us to question the applicability of the thin film based theory to our results. The Moallemi theory predicts film thicknesses of the order $10^{-4}$ m for our experimental conditions. Our particle sizes are of the order $10^{-4}$ m to $10^{-3}$ m. Thus, the necessary condition that $\delta \ll D_{\text{eff}}$ is not satisfied implying that a theory that does not rely on the thin film assumption may be necessary. It is also possible that entrapped air near the heated surface has a significant effect on the results.

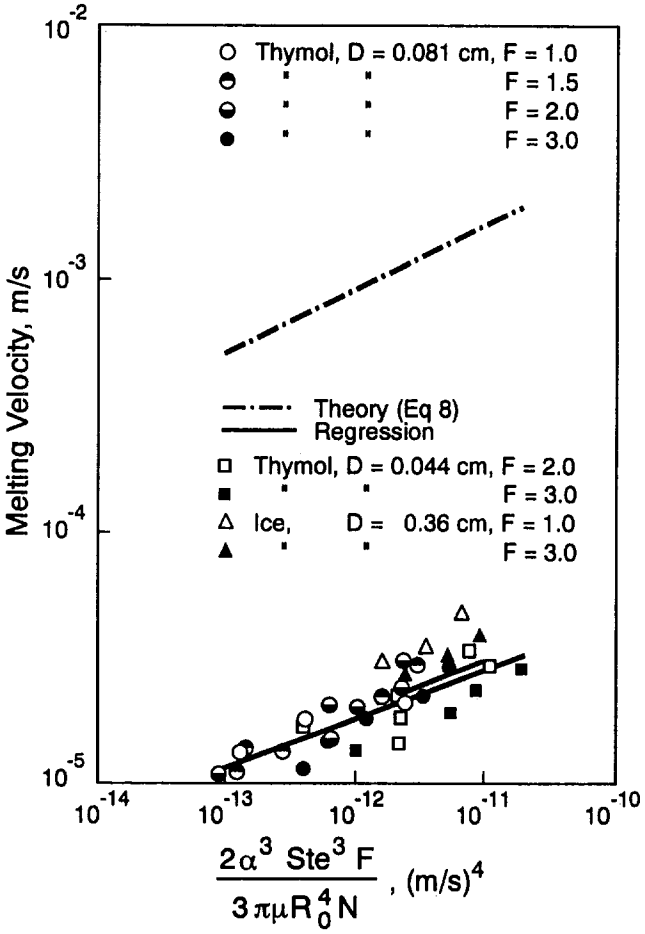



**Fig. 9 Comparison between experimental results and the modified theory given by Eq. (8)**

## Conclusions

Experimental results for one-dimensional melting of packed beds subjected to a constant external force are presented. Two distinct melting regimes were observed. Under certain conditions, a blockage or crust of refrozen melt formed in the packed bed above the hot surface, adhering to the inside of the chamber and preventing the downward motion of the bed. Combined conductive and convective heat transfer modes occurred with continued melting of the crust and of solids in the liquid pool that accumulated below the crust. Under other conditions melting rates were constant and the packed bed remained in direct contact with the hot surface. The experimental results for this direct contact regime were compared to a model developed by Moallemi for monolithic solids that was modified for application to the packed bed. Based on experimental results and comparison with the theory, the following conclusions are drawn:

1 Two modes of melting are possible: If there are significant lateral or vertical heat losses from the melt, crusting will occur; otherwise direct contact melting results.
2 With a bed very near the melting temperature and no lateral heat losses, direct contact melting occurs. This is not strongly affected by bed load and is correlated well parametrically by the Moallemi theory modified for packed beds. However, the actual melting rate is more than an order of magnitude less than that predicted by the theory.
3 The unit surface conductance approaches a constant value as heat flux and load increase for direct contact melting.
4 Crusting type melting is an unsteady and, at least at this point, unpredictable process.


## Acknowledgment

This material is based upon work supported by the National Science Foundation under Grant No. CTS-9016104.


## References


Anton, D. L., Shah, D. M., Duhl, D. N., and Gramer, A. F., 1989, "Selecting High-Temperature Structural Intermetallic Compounds: The Engineering Approach," *JOM*, Sept., p. 12.

Bejan, A., 1989, "The Fundamentals of Sliding Contact Melting and Friction," ASME JOURNAL OF HEAT TRANSFER, Vol. 111, pp. 13–20.

Bejan, A., and Tyvand, P. A., 1992, "Pressure Melting of Ice Under a Body With a Flat Base," ASME JOURNAL OF HEAT TRANSFER, Vol. 114, pp. 529–531.

Chellaiah, S., and Viskanta, R., 1990, "Natural Convection Melting of a Frozen Porous Medium," *Int. J. of Heat and Mass Transfer*, Vol. 33, No. 5, pp. 887–899.

German, R. M., 1985, *Liquid Phase Sintering*, Plenum Press, New York.

Hirata, T., Makino, Y., and Kaneko, Y., 1991, "Analysis of Close-Contact Melting for Octadecane and Ice Inside Isothermally Heated Horizontal Rectangular Capsule," *Int. J. of Heat and Mass Transfer*, Vol. 34, No. 12, pp. 3097–3106.

Incropera, F. P., and DeWitt, D. P., 1990, *Introduction to Heat Transfer*, 2nd ed., Wiley, New York, p. 518.

*International Critical Tables of Numerical Data, Physics, Chemistry and Technology*, 1929, Vols. III, IV, and V, NRC, McGraw-Hill, New York.

Kazmierczak, M., Poulikakos, D., and Pop, I., 1986, "Melting From a Flat Plate Embedded in a Porous Medium in the Presence of Steady Natural Convection," *Numerical Heat Transfer*, Vol. 10, pp. 571–581.

Moallemi, M. K., Webb, B. W., and Viskanta, R., 1986, "An Experimental and Analytical Study of Close-Contact Melting," ASME JOURNAL OF HEAT TRANSFER, Vol. 108, pp. 894–899.

Nield, D. A., and Bejan, A., 1992, *Convection in Porous Media*, Springer-Verlag, New York, pp. 141–168.

Yan, M. F., 1982, "Sintering of Ceramics and Metals," *Advances in Powder Technology*, G. Y. Chin, ed., ASM, Metals Park, OH.

Wang, C. H., and Dhir, V. K., 1988, "An Experimental Investigation of Multidimensional Quenching of a Simulated Core Debris Bed," *Proc. of the 1988 National Heat Transfer Conf.*, H. R. Jacobs, ed., Vol. 2, ASME HTD-Vol. 96, pp. 219–228.





Downloaded 12 Dec 2010 to 193.140.21.150. Redistribution subject to ASME license or copyright; see http://www.asme.org/terms/Terms_Use.cfm

# Finite Difference Modeling of Anisotropic Flows

**M. Keyhani**
Associate Professor.

**R. A. Polehn**
Graduate Student.

Mechanical and Aerospace Engineering Department,
University of Tennessee,
Knoxville, TN 37996-2210

*A modification to the finite difference equations is proposed in modeling multidimensional flows in an anisotropic material. The method is compared to the control volume version of the Taylor expansion and the finite element formulation derived from the Galerkin weak statement. For the same number of nodes, the proposed finite difference formulation approaches the accuracy of the finite element method. For the two-dimensional case, the effect on accuracy and solution stability is approximately the same as quadrupling the number of nodes for the Taylor expansion with only a proportionately small increase in the number of computations. Excellent comparisons are made with a new limiting case exact solution modeling anisotropic heat conduction and a transient, anisotropic conduction experiment from the literature.*

## Introduction

Previous finite difference and finite element modeling efforts for anisotropic diffusion range from solidification, such as the work by Weaver and Viskanta (1989) and Sinha et al. (1992), to the sacrificial liners of rocket nozzles, such as the work by Friedman and McFarland (1968). Because of the increasing use of composite materials, decomposing polymers, and fibrous media, the development of more efficient analysis tools for solving anisotropic conduction and porous media flow problems would improve their cost effectiveness.

The anisotropic (off-diagonal) part of the diffusion term has been modeled in several ways via the finite difference method. The oldest method is a Taylor expansion involving the use of diagonal neighbors, which can be found in Forsythe and Wasow (1960). Friedman and McFarland (1968) developed a finite difference method for anisotropic heat conduction in a decomposing solid, applying the anisotropic computations at odd time steps. Their formulation of the anisotropic portion raises questions concerning conservation of energy, because the amount of energy leaving one control volume is not equivalent to that entering the next (energy disappears during the computation). Fillo et al. (1975) applied the finite difference method to the graphite blanket of a fusion reactor. The method developed, using the concept of thermal resistances, was said to support directional thermal conductivities, although the exact method of application was unclear.

Katayama et al. (1974) proposed a method of stretching the material based on the ratio of the with-ply and across-ply conductivities and thus avoided consideration of the off-diagonal terms. Application of this technique would be difficult if the ratio of the conductivities varied with time or position. Another method of avoiding the off-diagonal terms would be to align the nodes with the principal planes of the material. This method would exclude nonorthotropic materials and stacked orthotropic materials would cause meshing difficulties.

The finite control volume technique was applied to anisotropic conduction by Banaszek (1984). In a comparison with a steady-state solution by Chang et al. (1973), the maximum relative error compared favorably to the finite element weak statement prediction. A detailed development of the finite volume equations for anisotropic conduction is given by Blackwell and Hogan (1993). Padovan (1974) has applied the finite element method to heat conduction and Sinha et al. (1992) have applied the finite element method to diffusion in porous media. For a given nodal spacing and approximation basis (assumed trial function), the Galerkin weak statement finite element formulation is considered the standard for comparison at this time. However, the matrices for the finite element formulation are less diagonally dominant than an equivalent finite difference formulation, and successful solution for finite elements often require the use of time-consuming elimination methods. For the bilinear basis, a uniform rectangular mesh, and element-averaged data, the anisotropic components of this finite element formulation reduce to the Taylor expansion method discussed above. Thus, in comparing a linear basis finite difference formulation plus the Taylor expansion to the bilinear basis weak statement formulation, the improvement in accuracy comes from the improved two-dimensional handling furnished by the bilinear basis rather than an improved way of computing the anisotropic components.

The Taylor expansion as presented by Forsythe and Wasow is restricted in applicability. For this study, a more general algebraic approximation to the anisotropic flow term, suitable for a variable mesh and variable properties, will be derived using the control volume method, as defined by Patankar (1980).

## Anisotropic Heat Conduction

For Cartesian coordinates, the conduction of heat within an anisotropic material is expressed by

$$\rho c \frac{\partial T}{\partial t} = \frac{\partial}{\partial x_i}\left(k_{ij}\frac{\partial T}{\partial x_j}\right) \tag{1}$$

For the purposes of discussion in this section, we will concentrate on the anisotropic flow term in Eq. (1) and consider a material that is orthotropic. For this material, the diffusive coefficient ($k_{ij}$) depends on the with-ply and across-ply (principal) conductivities and the rotational angle between the plies of the material and the computational axis. We define the case when the computational axes are aligned with the principal conductivities as the orthotropic case and define the case when the computational axes are rotated as the anisotropic case. For the anisotropic case, the components of the diffusive tensor are found by applying the usual transformation for second order tensors to the orthotropic principal values. In two dimensions, the heat conduction term, re-expressed in terms of heat fluxes, is

$$\frac{\partial}{\partial x_i}\left(k_{ij}\frac{\partial T}{\partial x_j}\right) = -\frac{\partial}{\partial x}(q''_{x_d} + q''_{x_o}) - \frac{\partial}{\partial y}(q''_{y_o} + q''_{y_o}) \tag{2}$$

where subscripts $d$ and $o$ represent the diagonal and off-diagonal terms, respectively. Since the off-diagonal terms in Eq. (2) are not zero, then nominally a temperature difference in the $y$ direction can cause conduction in the $x$ direction. As an example, the

Contributed by the Heat Transfer Division for publication in the JOURNAL OF HEAT TRANSFER. Manuscript received by the Heat Transfer Division September 1993; revision received July 1994. Keywords: Conduction, Porous Media. Associate Technical Editor: C. E. Hickox, Jr.



Copyright © 1995 by ASME

Downloaded 12 Dec 2010 to 193.140.21.150. Redistribution subject to ASME license or copyright; see http://www.asme.org/terms/Terms_Use.cfm

heat fluxes in the $x$ direction due to the diagonal and off-diagonal terms are

$$q''_{x_d} = -k_{11}\frac{\partial T}{\partial x} \quad q''_{x_o} = -k_{12}\frac{\partial T}{\partial y} \tag{3}$$

## Anisotropic Mass Flow in Porous Media

The pore pressure equation is obtained by combining the conservation of mass and an empirical momentum equation for low flow rates in porous media, Darcy's equation. Darcy's equation for anisotropic flow is

$$-\frac{K_{ij}}{\mu}\frac{\partial P}{\partial x_j} = v_i \tag{4}$$

Scheideggar (1954) analyzed experimental data to show that the permeability can be treated as a second order tensor and Gray and O'Neil (1976) showed that Eq. (4) also applies to compressible flow by the use of volume averaging of the general flow equations. The conservation of mass for compressible flow in porous media is

$$\frac{\partial}{\partial t}(\epsilon\rho) + \frac{\partial}{\partial x_i}(\rho v_i) = 0 \tag{5}$$

Multiplying Eq. (4) by the fluid density and substituting into Eq. (5), we obtain the pore pressure equation

$$\frac{\partial}{\partial t}(\epsilon\rho) = \frac{\partial}{\partial x_i}\left(\rho\frac{K_{ij}}{\mu}\frac{\partial P}{\partial x_j}\right) \tag{6}$$

The coefficient in the right-hand term in Eq. (6) is the equivalent to the thermal conductivity in Eq. (1). For the finite difference approximation, the choice of the proper effective diffusive coefficient was analyzed and discussed by Polehn (1994). To summarize, for continuously varying properties, the recommended method is to evaluate the coefficient using the properties at the interpolated temperature and pressure at the control volume face. The determination of the effective diffusive coefficient for the case of a change in material is avoided by placement of computational nodes at those discontinuities.

## Algebraic Approximation for Anisotropic Flows

Both Eq. (6) and Eq. (1) can be solved with the same general method. For easier presentation, the finite difference equations will be given and discussed in terms of the conservation of energy. The mass flow finite difference equations are the same as those shown, except that pressure is substituted for temperature and the mass flow diffusive tensor ($\rho K_{ij}/\mu$) is substituted for the thermal conductivity tensor ($k_{ij}$). Finite difference approximation of the anisotropic terms in Eq. (2) is easy for the control volume method, where the properties and temperature differences are evaluated relative to the control volume boundary. Figure 1($a$) shows a variable mesh two-dimensional control volume and the associated anisotropic conduction flows. The east face diagonal flow term is due to the temperature difference ($T_E - T_P$) and the off-diagonal term is due to the temperature difference ($T_{ne} - T_{se}$). The discretized version of the heat conduction term is obtained by integrating the diffusion terms in Eq. (2) over the volume of the control volume. For the two-dimensional case, the discretized version for a control volume is

$$\begin{aligned}\iint \frac{\partial}{\partial x_i}\left(k_{ij}\frac{\partial T}{\partial x_j}\right)dxdy &= \left[\frac{\Delta y k_{11}}{\delta x}\right]_e (T_E - T_P) \\ &+ [k_{12}]_e(T_{ne} - T_{se}) + \left[\frac{\Delta x k_{22}}{\delta y}\right]_n (T_N - T_P) \\ &+ [k_{21}]_n(T_{ne} - T_{nw}) - \left[\frac{\Delta y k_{11}}{\delta x}\right]_W (T_P - T_W) \\ &- [k_{12}]_W(T_{nw} - T_{sw}) - \left[\frac{\Delta x k_{22}}{\delta y}\right]_S (T_P - T_S) \\ &- [k_{21}]_S(T_{se} - T_{sw})\end{aligned} \tag{7}$$

In the right-hand side of Eq. (7), the right-hand column terms are similar to the usual finite difference approximations and the left-hand column terms are required to adjust the equation for the off-diagonal heat fluxes. Note that the control volume corners are not computational nodes and thus these corner temperatures must be estimated. This study proposes to improve the estimate of the main control volume corner temperatures by forcing them to obey the steady-state conservation principle of anisotropic flow of heat for a staggered control volume, shown in Fig. 1($b$). Note that in a given time step, the transient aspects of the transport phenomena (storage and volumetric generation) are fully accounted for through the solution of the full governing equation for the main control volume. Therefore, by forcing the temperature at the corner of a given main control volume (staggered control volume with time frozen) to obey the steady-state conservation equation, one has not lost the transient effect. It is fully accounted for in the main control volume, and indeed the inclusion of the transient effects in the solution of the staggered control volume would be double counting of the transient effects.

The staggered control volume midpoint temperature, $T^c_{ne}$, can

## Nomenclature

$c$ = specific heat
$e$ = error in the prediction
$f$ = anisotropic computational weighting factor
Fo = Fourier number
$k$ = thermal conductivity
$K$ = permeability
$P$ = pressure
$q''$ = heat flux
$t$ = time
$T$ = temperature
$v$ = velocity
$x$ = coordinate length
$X$ = normalized length
$y$ = coordinate length
$Y$ = normalized length
$\alpha$ = thermal diffusivity
$\gamma$ = across-ply coordinate direction
$\Gamma$ = diffusive coefficient for the generalized diffusive problem
$\Delta$ = distance between nodes
$\Delta t$ = time step size
$\delta x$ = distance between nodes, $x$ direction
$\Delta x$ = width of control volume
$\delta y$ = distance between nodes, $y$ direction
$\Delta y$ = height of control volume
$\epsilon$ = porosity
$\zeta$ = with-ply coordinate direction
$\theta$ = angle from computational $x$ axis to with-ply direction
$\mu$ = viscosity
$\rho$ = density
$\phi$ = general variable for diffusive problem
$\Omega$ = anisotropic computational adjustment, defined by Eq. (9)

### Subscripts

$d$ = tensor diagonal term
$e$, etc. = control volume surface locations defined in Fig. 1($a$)
$E$, etc. = nodal locations defined in Fig. 1($a$)
$i, j$ = tensor indices
$I$ = initial value
$o$ = tensor off-diagonal term
SURF = surface value

### Superscripts

$c$ = midpoint of staggered control volume defined in Fig. 1 ($b$)



Downloaded 12 Dec 2010 to 193.140.21.150. Redistribution subject to ASME license or copyright; see http://www.asme.org/terms/Terms_Use.cfm

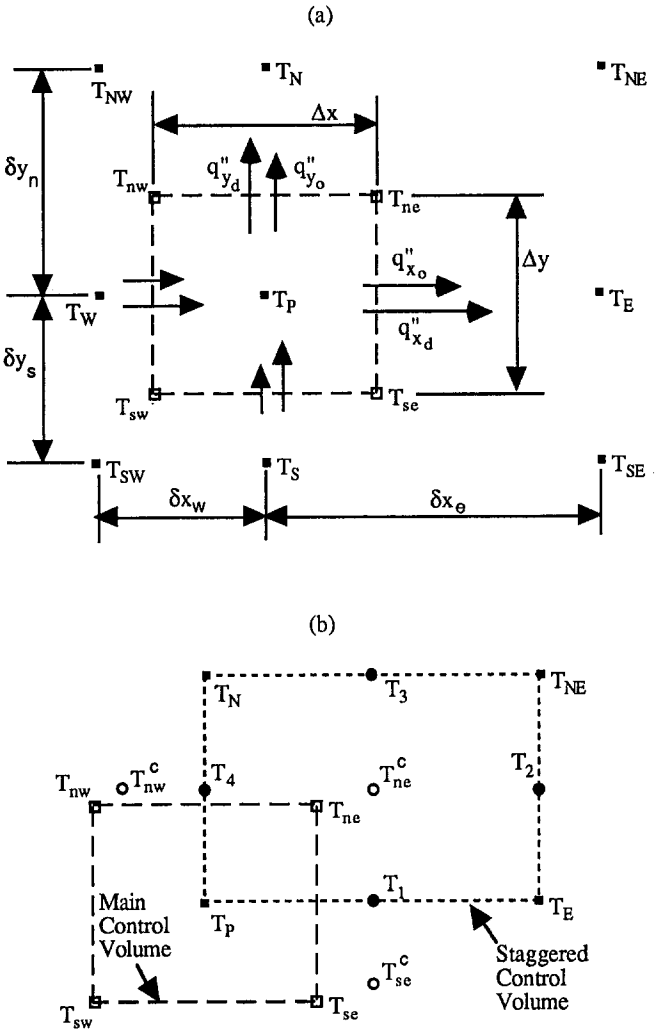



**Fig. 1 Sample control volumes in a nonuniform mesh: (*a*) anisotropic heat conduction through the main control volume; (*b*) northeast staggered control volume for derivation of the proposed method**

be expressed in terms of the side midpoint temperatures ($T_1$, $T_2$, $T_3$, and $T_4$) and the surrounding nodal temperatures ($T_P$, $T_E$, $T_{NE}$, and $T_N$), which are the corner values for this staggered control volume. Noting from reciprocity that $k_{21} = k_{12}$, this steady-state conservation relation is

$$\left(\frac{4k_{22}\delta x_e}{\delta y_n} + \frac{4k_{11}\delta y_n}{\delta x_e}\right) T^c_{ne} = \frac{2k_{22}\delta x_e}{\delta y_n} T_1 + \frac{2k_{11}\delta y_n}{\delta x_e} T_2 + \frac{2k_{22}\delta x_e}{\delta y_n} T_3 + \frac{2k_{11}\delta y_n}{\delta x_e} T_4 + fk_{12}(T_P - T_E + T_{NE} - T_N) \quad (8)$$

where $f$ is the computational weighting factor that is a function of the method of estimation. The value $f = 2$ will ensure that the last term in Eq. (8) is equivalent to the four off-diagonal terms in Eq. (7). Because of the piecewise linear profile assumption, these side midpoint temperatures ($T_1$, $T_2$, $T_3$, and $T_4$) can in turn be expressed in terms of the nodal temperatures. Substituting and gathering terms, the approximation for $T^c_{ne}$ is

$$T^c_{ne} = \tfrac{1}{4}[(1 + \Omega)T_P + (1 - \Omega)T_E + (1 + \Omega)T_{NE} + (1 - \Omega)T_N] \quad (9)$$

where

$$\Omega = \frac{fk_{12}}{k_{ne}} \quad \text{and} \quad k_{ne} = \frac{k_{11}\delta y_n}{\delta x_e} + \frac{k_{22}\delta x_e}{\delta y_n}$$

We will consider two weighting factors for the finite difference method, $f = 0$ and $f = 2$. A weighting factor of $f = 0$ assumes that for the staggered control volume, the off-diagonal components of the conductivity tensor are ignored and the midpoint temperature, $T^c_{ne}$, becomes the average of the four surrounding nodes. This relation produces the control volume equivalent of the Taylor expansion as found in Forsythe and Wasow (1960).

A weighting factor of $f = 2$ is obtained by direct application of the anisotropic finite difference scheme used in Eq. (7) to the staggered control volume. This weighting factor attempts to model the anisotropic effect that skews the temperature profile between computational nodes and thus results in an improved estimate of $T^c_{ne}$. The better this temperature estimate, the better the estimate of the heat transfer for the off-diagonal portion of the heat conduction term and in turn the better the global temperature predictions. Note that both methods of $f = 0$ and $f = 2$ are based on interpolations of the surrounding four nodal temperatures, but $f = 2$ results in an interpolation that accounts for the influence of $k_{12}$, the anisotropic component of the thermal conductivity. For the rectangular mesh case, a formulation for the finite element method, equivalent to Eq. (9), was suggested by Polehn (1994).

The southeast midpoint temperature, $T^c_{se}$, and the northwest midpoint temperature, $T^c_{nw}$, can be obtained in a similar manner as for the northeast midpoint temperature. For a moderately nonuniform mesh, the actual control volume face temperature differences can be reasonably estimated by scaling, based on distance. As two examples, the north and east face temperature differences are

$$T_{ne} - T_{se} = \frac{2\Delta y}{(\delta y_n + \delta y_s)}(T^c_{ne} - T^c_{se})$$

$$T_{ne} - T_{nw} = \frac{2\Delta x}{(\delta x_e + \delta x_w)}(T^c_{ne} - T^c_{nw}) \quad (10)$$

This scaling is reasonable because analysts typically distribute mesh nonuniformity in a gradual manner, especially in regions where gradients are significant. Note that this proposed approximation is used for communication between two adjacent control volumes, where the mesh size change is small. Equation (10) is a compromise that partially accounts for nonuniformity of the mesh and the accuracy does decrease if there are abrupt changes in mesh size. The complex anisotropic interpolation required to obtain a better estimate of the corner temperatures was judged by us as not worth the extra computational effort.

## Steady Flow Anisotropic Exact Solution

Exact solutions for anisotropic flows are limited in the literature. Ozisik (1980) presents a selection of anisotropic heat conduction solutions. In addition, Chang et al. (1973) applied Green's functions to obtain numerically generated steady-state and transient exact solutions for anisotropic heat conduction. For this study, we will contrive an easy-to-verify anisotropic solution by solving a "one-dimensional" segmented test problem in which the computational axis is not aligned with the plies of the material. To contrive an exact solution, an extreme case for conductivity (permeability) is chosen, where the conductivity (permeability) in the across-ply direction is zero and the conductivity (permeability) in the with-ply direction is a finite value. Note that a very large family of anisotropic exact solutions can be generated in this way using transient or steady state one-dimensional solutions.

Actually, this test problem is not as unrealistic as it seems for flow in a porous composite. As measured by Stokes and Koenig (1991), the across-ply permeability of a carbon phenolic may be larger than the with-ply permeability by a factor of 500 or more. Because the diffusion terms for Eqs. (1) and (6) are of the same form, the normalized solutions are identical for steady flow. We



Downloaded 12 Dec 2010 to 193.140.21.150. Redistribution subject to ASME license or copyright; see http://www.asme.org/terms/Terms_Use.cfm

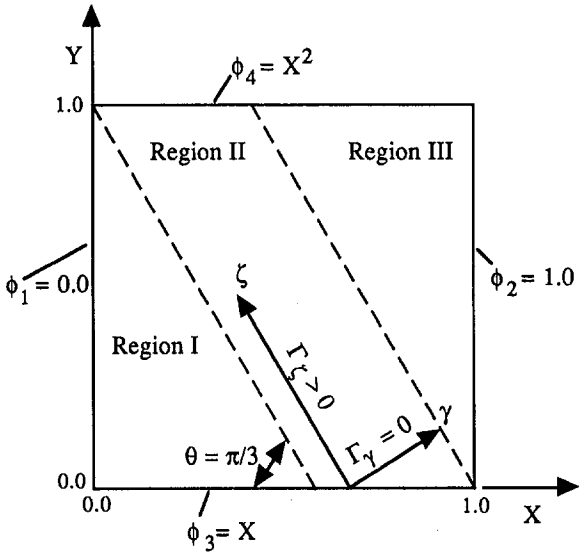



**Fig. 2 Schematic of the two-dimensional steady state anisotropic flow problem; for conduction heat transfer $\phi = T$ and for incompressible flow through porous media $\phi = P$**

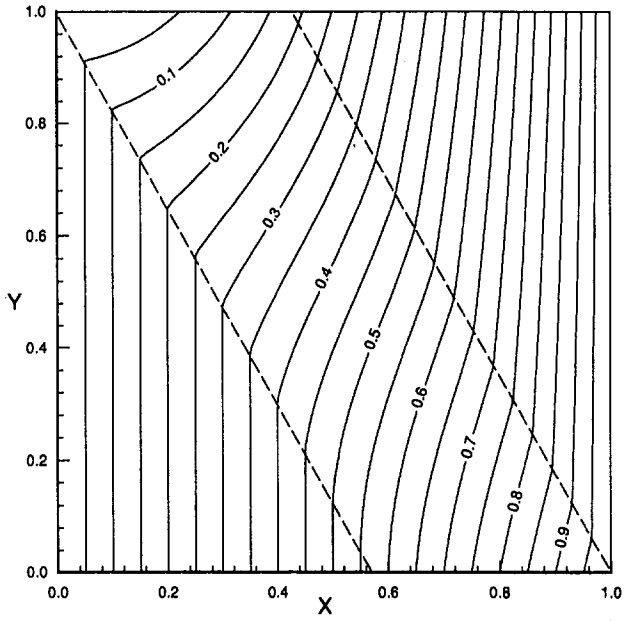



**Fig. 3 Exact solution of the steady-state anisotropic flow problem**

will represent the steady flow problem with the general diffusion equation

$$\frac{d}{dx_i}\left(\Gamma_{ij}\frac{d\phi}{dx_j}\right) = 0 \tag{11}$$

The schematic of the steady flow test problem and the boundary conditions are shown in Fig. 2. Thus, in the with-ply direction, which for our test problem lies at an angle of $\pi/3$ from the computational $x$ axis, the flow is one dimensional and easily computed. For constant property steady flow in the with-ply direction, Eq. (11) can be normalized and simplified to

$$\frac{d^2\phi}{d\zeta^2} = 0 \tag{12}$$

where $\zeta$ is the coordinate in the with-ply direction. Thus, the solution $\phi$ is a family of linear curves that depend on the boundary values for each of the four sides of the analysis region. For convenience of discussion, the analysis region is subdivided into three regions. The exact solution is

Region I

$$\phi = X$$

Region II

$$\phi = X + \frac{Y}{\tan\theta} + Y\left[\left(X - \frac{1-Y}{\tan\theta}\right)^2 - \left(X + \frac{Y}{\tan\theta}\right)\right]$$

Region III

$$\phi = \left[\frac{1-Y}{1-Y+(1-X)\tan\theta}\right] \times \left[1 + \frac{(1-X)\tan\theta}{1-Y}\left(X - \frac{1-Y}{\tan\theta}\right)^2\right] \tag{13}$$

The exact solution $\phi$ representing the isobars of the constant density anisotropic flow or the isotherms for anisotropic heat conduction is shown in Fig. 3. It can be seen that the solution is highly two dimensional even though the solution $\phi$ is constructed with a set of one-dimensional solutions. Note that in Region I the solution $\phi$ varies linearly with $X$ only because the boundary value $\phi_1$ is constant and the adjacent boundary value $\phi_3$ varies linearly with $X$. Because there are no discontinuities in the specified boundary values for $\phi$, there are no discontinuities in the solution anywhere in the analysis region. However, note that there are discontinuities in the slope of the solution $\phi$ at the boundaries between Regions I, II, and III, which is due to the change in the boundary conditions from region to region. This exact solution was used to verify the proposed finite difference model for anisotropic flows. Because the intent was to model the problem successfully without alignment of the nodes to the plies of the material, the computational plane was aligned to the sides of the analysis region.

Figure 4 shows the normalized maximum prediction error ($\infty$ norm) for each method as a function of the mesh refinement. The error is normalized with respect to the exact solution. For this test problem, the accuracy of the proposed method is somewhat better than the prediction of the accepted standard, the Galerkin weak statement finite element method. The largest prediction errors are found near the sharp discontinuity in slope between Regions I and II, in the area enclosed by $X = 0.175$ to 0.3 and $Y = 0.5$ to 0.8. Although the largest change in slope is near $(X, Y)$

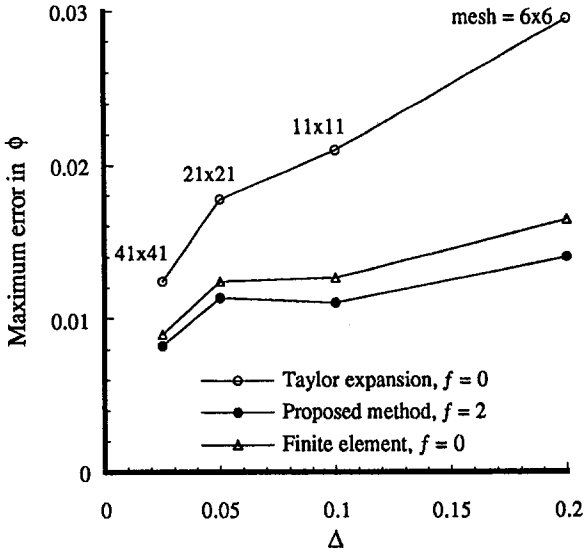



**Fig. 4 Normalized maximum error in the prediction as a function of mesh size**



Downloaded 12 Dec 2010 to 193.140.21.150. Redistribution subject to ASME license or copyright; see http://www.asme.org/terms/Terms_Use.cfm

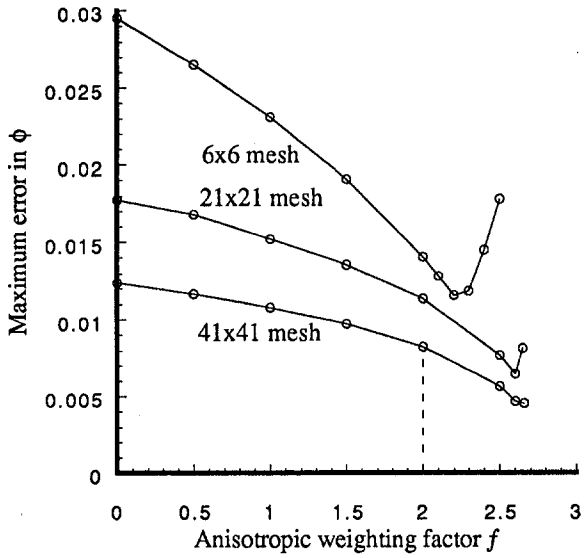



**Fig. 5 Effect of the anisotropic weighting factor on the maximum error in the prediction**

= (0.0, 1.0), the adjacent boundary conditions control the prediction error near that point. The 2 norm for the prediction error is

$$\|e\|_2 = [\sum_i (\phi - \phi_{\text{Exact}})_i^2]^{1/2} \qquad (14)$$

For every mesh size considered in Fig. 4, the 2 norm for the prediction error showed the same relative ranking between schemes as for the ∞ norm for the prediction error.

For the finite difference method, a positive anisotropic weighting factor $f$ can improve the prediction. For this particular test problem, Fig. 5 shows that an apparent optimum weighting factor can be found that minimizes the prediction error for each mesh size chosen. Unfortunately, the solution error was found to rise very rapidly for those weighting factors just higher than the apparent optimum. As the weighting factor rises beyond $f = 2.5$, solution divergence causes the computational time to increase rapidly with $f$. Because of the tendency toward divergence and the rapid rise in error near the apparent optimum, for the finite difference method, the theoretical value of $f = 2$ is preferable. The additional accuracy attained from the proposed finite difference modification, Eq. (9) with $f = 2$, comes at the expense of extra computations associated with the equation itself plus the increased iterations to achieve convergence. In exchange for this additional work, for a given number of computational nodes, the method improves accuracy and will be shown to reduce the magnitude of the second law violation that is routinely observed in anisotropic computations.

## Comparison With an Anisotropic Conduction Heat Transfer Experiment

We will now use our proposed method to model the transient anisotropic conduction heat transfer experiment performed by Katayama et al. (1974). Figure 6 shows a schematic of the experimental setup of Katayama et al. The material properties reported by Katayama et al. were: with-ply thermal conductivity = 0.8 W/m-K; across-ply thermal conductivity = 0.1 W/m-K; $\rho$ = 987 kg/m$^3$; and $c$ = 1404 J/kg-K. The anisotropic test material was formed with stacked paper cut at a 45° angle to the plies of the paper. The material was placed in an evacuated chamber to insulate the bottom and sides, and a time-dependent surface temperature boundary condition was imposed at the top surface. Eight thermocouples were installed at the numbered locations 1 to 8 as shown in Fig. 6.

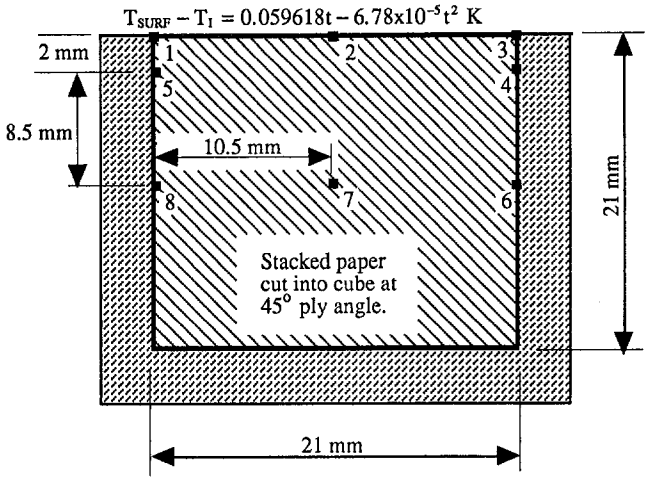



**Fig. 6 Schematic of the anisotropic heat conduction experiment performed by Katayama et al.**

Unfortunately, the original data for the experiment of Katayama et al. were not available, and our attempts at communicating with the authors were not successful. As a last resort, the data points were carefully measured from an enlargement of the graph in his paper and transcribed to Fig. 7. From now, a reference to the measured temperature will refer to these transcribed values. The measured temperatures by thermocouples 1, 2, and 3 show that the applied boundary condition at the top surface was close to uniform at a given time. Despite the application of a one-dimensional boundary condition, the predicted isotherms assume a highly two-dimensional character. Even at small distances into the material, the anisotropic (directional) conductivities cause proportionately large two-dimensional temperature variations. For example, thermocouples 4 and 5 are at the same distance from the heated surface, yet thermocouple 4 indicates a much higher temperature. Because the plies of the paper furnish an easy path for heat transfer to thermocouple 4, the temperature at this location follows the surface temperature closely. On the other hand, there is a much larger time lag for the temperature at ther-

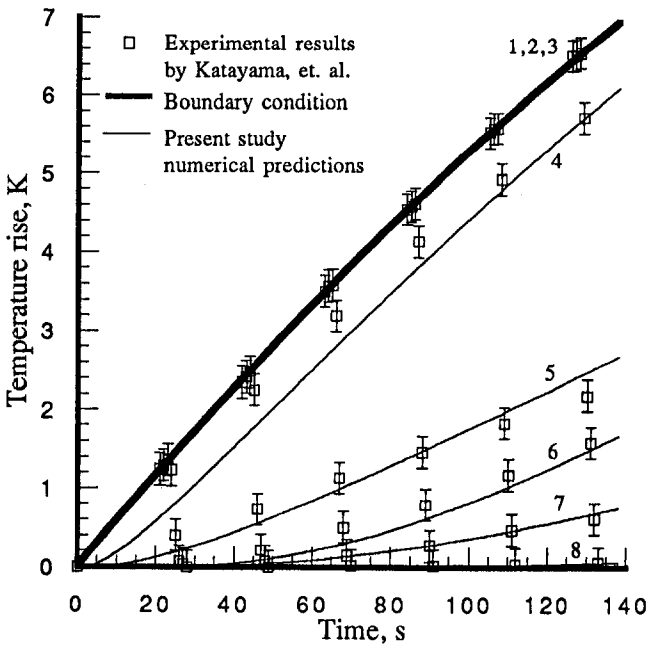



**Fig. 7 Comparison of the predicted temperatures by the proposed method ($f$ = 2) with the measured values by Katayama et al.**



Downloaded 12 Dec 2010 to 193.140.21.150. Redistribution subject to ASME license or copyright; see http://www.asme.org/terms/Terms_Use.cfm

mocouple 5 because heat must cross the gaps between the sheets of paper. The error bars show that the temperature measurement accuracy, as reported by Katayama et al., was 0.2 K.

The numerical predictions were obtained with a uniform mesh of 43 × 43 nodes and a time step size of 0.5 second. The predicted temperatures, obtained using the proposed finite difference modification $f = 2$, are also shown in Fig. 7. Note that the predicted temperatures follow the same trend as the experimental data and that a reasonable agreement is achieved. Additional experimental uncertainties (not specified by Katayama et al.), such as thermocouple location, uncertainty in thermophysical properties, coupled with computational error does place the prediction outside the temperature error bars for some data points. Another complicating factor for the comparison is the unknown extent of imperfection in the "adiabatic" boundary condition in the experiment. The predicted temperatures for thermocouple 4 follow a trend close to that of the surface ramp temperature change, while the measured values are unreasonably close to the surface conditions for $t < 90$ s. It is suspected that the deviation here is due to an imperfect adiabatic boundary condition and/or uncertainty in the thermocouple location in the experimental setup.

The temperature prediction for the thermocouple 5 location, near the insulated surface with no direct ply path to the heated surface, was found to be relatively sensitive to the time step and mesh size. Thus, computations for the location $(x, y) = (0, 18.9$ mm), adjacent to thermocouple 5, were used for comparison and convergence studies. The estimated errors at 120 s for the various models are shown in Fig. 8. Richardson extrapolation was used for each scheme to estimate the converged solution and in turn the error. Figure 8 shows that the prediction error of the proposed method is substantially lower than the Taylor expansion method. A comparison of Fig. 8 and Fig. 4 also shows that the weak statement finite element prediction has changed places relative to that of the proposed method $f = 2$. Note that the ratio of the with-ply to across-ply diffusive coefficient is 8 to 1 for the thermal experiment, while the diffusive coefficients for the exact solution are finite and zero in the principal material directions. As the material becomes less anisotropic, the proposed finite difference method, $f = 2$, will lose its slight advantage in accuracy over the weak statement version of the finite element method. Although fully implicit schemes are stable and thus an advantage for anisotropic problems, there is a tendency of the prediction to drift as the time step is refined. Figure 8 shows that as the time step size is reduced, the proposed and the finite element predictions change in a very similar way. Thus, the proposed method does not accentuate the drift due to the implicit computational scheme.

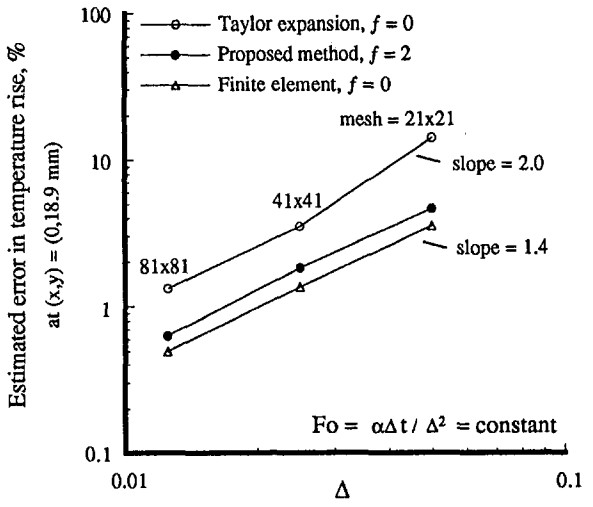



**Fig. 8 Estimated error in the prediction at $t = 120$ s**

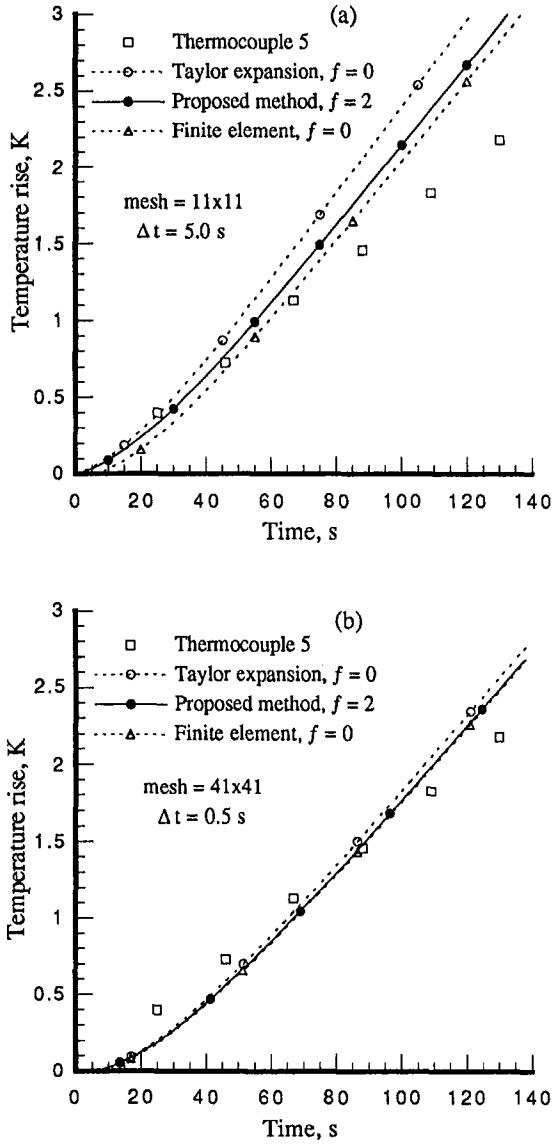



**Fig. 9 Comparison of temperature predictions by various methods with thermocouple 5: (*a*) the coarse-mesh results; (*b*) the refined-mesh results**

Figure 9($a$) compares the coarse mesh predictions of the three methods for the thermocouple 5 location. It can be seen that the finite element prediction is the most accurate for the number of nodes, but as usual for the finite element method, this is accomplished at the expense of increased computations. As $f$ increases, the prediction for thermocouple 5 drops, moving closer to the finite element prediction. In fact, a hybrid scheme of applying the finite element recursion relation to the staggered control volume yields $f = 1.5$, with a prediction that falls between those of the Taylor expansion and the proposed method. Refined mesh predictions for the thermocouple 5 location are shown in Fig. 9($b$). Note that the predictions for the proposed method and for the weak statement finite element method are practically the same. However, the Taylor expansion prediction still lags the other methods.

For highly anisotropic flows, Fig. 4 and Figs. 9($a$, $b$) show that a method comparable in accuracy to the weak statement finite element method is now available for the finite difference method. The Galerkin weak statement minimizes the energy norm for a given mesh distribution and approximation basis (this does not necessarily minimize local error, but tends to produce a smaller effective error on a global basis). For the finite difference method, the proposed modification changes the approximation



Downloaded 12 Dec 2010 to 193.140.21.150. Redistribution subject to ASME license or copyright; see http://www.asme.org/terms/Terms_Use.cfm

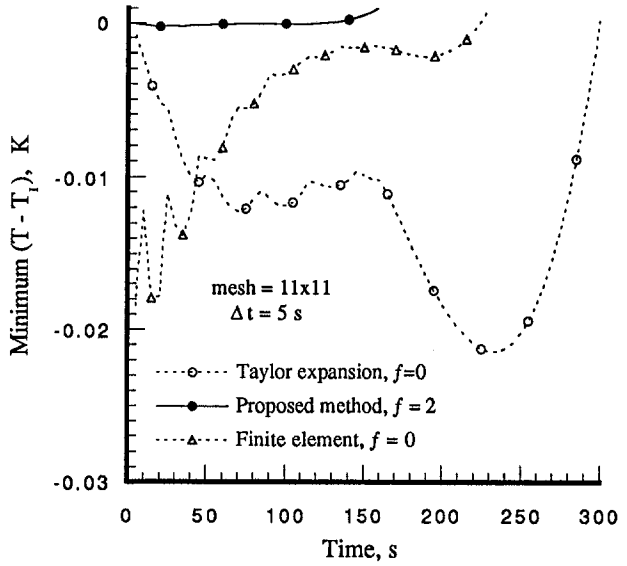



**Fig. 10 Minimum predicted temperature (undershoot) in the domain**

basis for the off-diagonal terms and thus allows the otherwise less-accurate finite difference method to approach and in extreme cases to surpass the finite element accuracy.

When the predicted temperature ($T - T_I$) is less than zero, the magnitude of the prediction is an indication of the extent of the second law violation. The time history of the minimum predicted temperature ($T - T_I$) in the domain is presented in Fig. 10. The Taylor expansion method displays an unstable tendency in that the magnitude of the negative numbers generated increase with time until the heatup seems to push the region of undershoot off of the analysis region. The predicted minimum temperatures for the proposed method $f = 2$ are still negative, but much closer to zero, and are even slightly better than the values obtained via a quadrupled Taylor expansion prediction (not shown). Because orthotropic finite difference computations do not produce this undershoot, we believe that the negative numbers generated are due to an inability to estimate the corner temperatures for the control volumes accurately. In going from the Taylor expansion to the proposed method, a much better estimate of the control volume corner temperature is achieved, therefore the undershoot is less and the prediction is more accurate. Note that the large undershoot seen in the finite element solution in Fig. 10 is a result of the Galerkin weak statement optimization process on the energy storage term. As discussed by Baker (1983), this causes the coarse-mesh prediction to oscillate about the true temperature.

## Conclusions

A versatile method of adapting one-dimensional solutions to create two-dimensional anisotropic exact solutions was presented. To create these complex two-dimensional solutions, the diffusive coefficient in one principal plane is assumed to be zero, known one-dimensional solutions are rotated in the computational plane, and boundary conditions are judiciously chosen. This method can produce anisotropic exact solutions that are suitable as benchmark cases for numerical codes. If a code is capable of producing accurate predictions for the case when the ratio of the diffusive coefficients is infinity, then it should have no difficulty in predicting anisotropic flows when the ratio of the diffusive coefficients has a realistic magnitude.

An improved finite difference scheme has been presented for the modeling of anisotropic diffusion and is shown to approach (and for extreme cases to exceed) the accuracy of the Galerkin weak statement finite element formulation. This is accomplished by "forcing" the estimates of the corner temperatures for the main control volume to obey the governing equation for steady-state anisotropic conduction heat transfer. The computational cost of this improvement is small in that fewer computational nodes are required to achieve a given accuracy.

An anisotropic exact solution was created to model heat conduction (or constant density flow in porous media) and in a benchmark comparison, the proposed finite difference scheme was shown to improve the prediction significantly. To attain the same accuracy with the Taylor expansion, the number of computational nodes must be increased by a factor of four to sixteen. In comparison to the finite element method, in the case of the test problem the accuracy of the proposed method was shown to slightly exceed that of the finite element formulation. The accuracy of the proposed method was also verified via comparison with an anisotropic experiment from the literature.

## Acknowledgments

Financial support of this work under NASA grant No. NAG8-862 is gratefully acknowledged.

## References

Baker, A. J., 1983, *Finite Element Computational Mechanics,* 1st ed., Hemisphere Publishing, New York.

Banaszek, J., 1984, "A Conservative Finite Element Method for Heat Conduction Problems," *International Journal for Numerical Methods in Engineering,* Vol. 20, pp. 2033–2050.

Blackwell, B. F., and Hogan, R. E., 1993, "Numerical Solution of Axisymmetric Heat Conduction Problems Using Finite Control Volume Technique," *Journal of Thermophysics and Heat Transfer,* Vol. 7, No. 3, pp. 462–471.

Chang, Y. P., Kang, C. S., and Chen, D. J., 1973, "The Use of Fundamental Green's Functions for the Solution of Problems of Heat Conduction in Anisotropic Media," *International Journal of Heat and Mass Transfer,* Vol. 16, pp. 1905–1918.

Fillo, J. A., Powell, J., and Benenati, R., 1975, "A Nonsteady Heat Conduction Code With Radiation Boundary Conditions," ASME Paper No. 75-WA-HT-91.

Forsythe, G. E., and Wasow, W. R., 1960, *Finite Difference Methods for Partial Differential Equations,* 1st ed., Wiley, New York.

Friedman, H. A., and McFarland, B. L., 1968, "Two-Dimensional Ablation and Heat Conduction Analysis for Multimaterial Thrust Chamber Walls," *Journal of Spacecraft and Rockets,* Vol. 5, No. 7, pp. 753–761.

Gray, G. G., and O'Neill, K., 1976, "On the General Equations for Flow in Porous Media and Their Reduction to Darcy's Law," *Water Resources Research,* Vol. 12, No. 2, pp. 148–154.

Katayama, K., Saito, A., and Kobayashi, N., 1974, "Transient Heat Conduction in Anisotropic Solids," *1974 International Heat Transfer Conference,* Vol. I, pp. 137–141.

Ozisik, M. N., 1980, *Heat Conduction,* 1st ed., Wiley, New York.

Padovan, J., 1974, "Steady Conduction of Heat in Linear and Nonlinear Fully Anisotropic Media by Finite Elements," ASME JOURNAL of HEAT TRANSFER, Vol. 96, pp. 313–317.

Patankar, S. V., 1980, *Numerical Heat Transfer and Fluid Flow,* 1st ed., Hemisphere Publishing, New York.

Polehn, R. A., 1994, "Thermal Response of an Axisymmetric, Charring-Decomposing Polymer," Ph.D. Dissertation, University of Tennessee at Knoxville, TN.

Scheideggar, A. E., 1954, "Directional Permeability of Porous Media to Homogenous Fluids," *Geofisica pura e Applicata,* Vol. 28, pp. 75–90.

Sinha, S. K., Sundararajan, T., and Garg, V. K., 1992, "Anisotropic Porous Medium Model for Alloy Solidification," *Transport Phenomena in Materials Processing and Manufacturing,* ASME HTD-Vol. 196, pp. 193–200.

Stokes, E. H., and Koenig, J. R., 1991, "Gas Permeability of FM 5055 (Pre-Avtex Shutdown) Carbon Phenolic Composite in the Fill Direction as a Function of Across-Ply Compressive Load and Temperature," SRI-MME-91-056-6672-003, Southern Research Institute, Birmingham, AL.

Weaver, J. A., and Viskanta, R., 1989, "Effects of Anisotropic Heat Conduction on Solidification," *Numerical Heat Transfer, Part A,* Vol. 15, pp. 181–195.



Downloaded 12 Dec 2010 to 193.140.21.150. Redistribution subject to ASME license or copyright; see http://www.asme.org/terms/Terms_Use.cfm

# Deterministic Chaotic Behavior of Heat Transfer in Gas Fluidized Beds

**D. V. Pence**

**D. E. Beasley**

**J. B. Riester**

Thermal-Fluid Sciences
Research Laboratory,
Department of Mechanical Engineering,
Clemson University,
Clemson, SC 29634

*Instantaneous heat transfer signals acquired in the bubble flow regime in a gas fluidized bed were examined for evidence of deterministic chaotic behavior. Signals were acquired using a heat flux sensor mounted on the surface of a horizontal, heated cylinder. Both standard statistical measures and nonlinear analysis techniques were employed to provide qualitative as well as quantitative information regarding dynamic behavior of heat transfer in such a facility. Power spectra provided preliminary evidence that heat transfer in fluidized beds may be chaotic in nature. Positive finite estimates of the Kolmogorov entropy provide further evidence of behavior consistent with chaos. Mutual information has a dual purpose in this work. It was used to evaluate a time delay in which to embed the time series heat transfer signal, and as a qualitative measure of the degree of chaos inherent in the signals. The quantitative information derived from mutual information allows the system dynamics to be represented as phase trajectories in a pseudo-phase space created by embedding a measured discrete signal in the space defined by time-delay coordinate axes. Embedding dimensions determined via the correlation integral suggest that four degrees of freedom quantify the system dynamics for the fluidizing conditions investigated in this work. Embedding dimensions were found to be independent of the fluidization velocity. This is a consequence of maintaining operating conditions within the bubble flow regime. The Kolmogorov entropy was shown to delineate fundamental changes in hydrodynamics conditions at the surface of the cylinder. Phase plots provide a means of analyzing the dynamics of heat transfer occurring at the surface of the cylinder. Two distinct characteristic emulsion phase contacts were identified using phase space trajectories. Phase space trajectories that result from particles remaining motionless at the heat transfer surface are distinctly different from those that result from particles actively mixing at the surface of the cylinder.*

## Introduction

Heat transfer between submerged surfaces and bubbling gas fluidized beds presents unique challenges in developing fundamental physical understanding of the processes that govern the transport, and in predicting the rates of heat transfer. Heat transfer at a submerged surface is largely determined by surface renewal mechanisms resulting from bubble and emulsion phase interaction. These interactions are a result of the bed hydrodynamics, which include both small and large-scale motion in the bed. In the present study, the methods of deterministic chaos are used to examine the instantaneous nature of heat transfer at a submerged surface in a bubbling fluidized bed.

Investigations of time series measurements of void fraction and pressure drop by several researchers (Skrzycke et al., 1993; Schouten et al., 1992; Fuller et al., 1993; Daw and Halow, 1991, 1993) reveal that the hydrodynamics in gas fluidized beds exhibit characteristics associated with deterministic chaotic behavior. The coupled nature of heat transfer and hydrodynamics underlies convective heat transfer processes in single-phase systems. This is also true of the convective processes associated with gas fluidized beds. In conjunction with the newly acquired information regarding the hydrodynamics, investigation of heat transfer using nonlinear analysis techniques is expected to provide further insight into the underlying physics of heat transfer phenomena in gas fluidized beds. In addition to providing physical insight, processes exhibiting chaotic behavior present opportunities for control using recently developed control methods for nonlinear systems.

Chaotic behavior is characterized by extreme sensitivity to initial conditions, which makes system behavior unpredictable. Although such system behaviors may appear to be random, deterministic chaos is a result of many underlying ordered behaviors. This fundamental nature of chaotic systems presents the possibility of control, and makes chaotic systems unusually flexible because they can move rapidly among operating conditions. This flexibility allows small perturbations of appropriate system parameters to accomplish control objectives. Recent efforts at modeling chaotic behavior using nonlinear model equations and learning neural networks have exhibited the capability of describing deterministic chaotic behavior. Using real-time chaos control algorithms, Ditto et al. (1990) demonstrated the first control of a chaotic system. Since that time, these efforts have been extended to a variety of physical systems including biological and medical applications.

While analyses of time series measurements using standard statistical means of evaluation provide some information, it is rather limited. For instance, Fourier power spectra quantify the power associated with each frequency inherent in a signal. However, in the case of chaotic time series signals, the information available from power spectra is generally qualitative, i.e., chaotic time series signals tend to be broad-band in nature. More important quantitative information, such as a description of the degree of chaos inherent in the signal, requires use of relatively new concepts.

Most of these concepts were developed as a result of the work of Packard et al. (1980) and Takens (1980). According to Packard et al. and Takens, the multidimensional physical phenomena occurring within a system can be equivalently represented in phase space using a single measurement time series. The two

Contributed by the Heat Transfer Division and presented at the 6th AIAA/ASME Joint Thermophysics and Heat Transfer Conference, Colorado Springs, Colorado, June 19–23, 1994. Manuscript received by the Heat Transfer Division February 1994; revision received August 1994. Keywords: Packed and Fluidized Beds, Transient and Unsteady Heat Transfer. Associate Technical Editor: B. W. Webb.



Copyright © 1995 by ASME

Downloaded 12 Dec 2010 to 193.140.21.150. Redistribution subject to ASME license or copyright; see http://www.asme.org/terms/Terms_Use.cfm

approaches are different in that Packard et al. reconstruct the physical phenomena in phase space using time derivatives of the original signal, whereas Takens suggests using a time delay of the original measurement. Following the convention of Moon (1993), pseudo-phase space is designated to represent the trajectory when constructed using time-delay coordinates, while phase space is reserved for trajectories constructed in time derivative coordinate axes.

In the present study, both standard statistical means and nonlinear techniques were employed in the evaluation of instantaneous heat transfer coefficients (a single measurement time series) for the presence of deterministic chaotic behavior. Power spectra were used as standard statistical measures, whereas techniques developed from deterministic chaos theory were employed as nonlinear techniques. These include mutual information, correlation dimension, Kolmogorov entropy, and phase space projections. The correlation dimension and Kolmogorov entropy provided quantitative measures of the degree of chaos whereas mutual information and phase plots yielded qualitative information regarding the nature of the system dynamics.

In addition to providing information regarding the nature of chaos exhibited by a time series measurement, mutual information allows the determination of an appropriate time delay necessary for time-delay embedding. The concept, suggested by Shannon and Weaver (1949), is employed in the manner proposed by Fraser and Swinney (1986). The correlation integral provides a means for characterizing the fractal nature of a time series via the correlation dimension. It is also used to assess the number of degrees of freedom necessary to characterize the dynamics of the signal (Grassberger and Procaccia, 1983a, b). Consequently, knowledge of the number of degrees of freedom (or minimum embedding dimension) is expected to facilitate dimensionless scaling.

Kolmogorov entropy provides a measure of the relative degree of chaos exhibited by a system. Time derivative phase portraits are used to distinguish between various cylinder to bed interactions, including bubble and emulsion phase contact. Recent studies (Pence et al., 1993) indicate that bed hydrodynamics at the surface of a submerged object leads to two distinct types of emulsion phase contact. These include stationary and mixing particle behavior, which have distinctively different heat transfer trajectories in phase space.

## Experimental Facilities and Measurements

Heat transfer in gas fluidized beds occurs primarily between the fluidized media within the bed and an immersed object, such as a horizontal steam tube for gas fluidized coal combustors. To simulate this condition, a 5-cm-dia cylinder was positioned horizontally in a gas fluidized bed test facility with the axis located 30 cm above the distributor plate. To provide a means of measuring heat transfer from the surface, the cylinder was internally heated to a temperature 35°C above the bed temperature. Internal heating was accomplished using a cartridge heater. A platinum film heat flux probe was mounted flush with the surface of the cylinder and maintained at a constant temperature slightly higher (approximately 0.5°C) than that of the cylinder. The platinum film was connected to a constant temperature anemometer bridge circuit so that recordings of the instantaneous bridge voltage variations, required to maintain a constant probe temperature, provided a single measurement time series representative of the instantaneous heat transfer rate.

The probe, a 6 by 0.635 mm strip of platinum deposited on a 6-mm-dia, 850-$\mu$m-thick Pyrex substrate disk, was covered with a thin layer of aluminum oxide to protect it from the harsh environment in the fluidized bed. The probe response time was determined experimentally to be less than 1 ms, which is much faster than the measured dynamic frequencies occurring within the bed. Further descriptions of the characteristics of film probes employed for heat flux measurement are found in Beasley and Figliola (1988) and Figliola et al. (1993).

The 76-cm-square fluidized bed test facility was charged with 275 kg of 85 percent spheroidal glass particles with a mean diameter of 715 $\mu$m and a density of 2500 kg/m$^3$. The resultant slumped bed height was 34 cm. The particles correspond to Geldart's (1973) Group D and have an experimentally determined

## Nomenclature

$a$ = point on trajectory in pseudo-phase space
$b$ = point on trajectory in pseudo-phase space
$c$ = argument in the Heaviside function
$C_d(\epsilon)$ = correlation integral for dimension $d$ and radius $\epsilon$
$d$ = dimension in which a single measurement time series is embedded for the purpose of analysis
$f$ = frequency, Hz
$h$ = instantaneous heat transfer coefficient, W/m$^2$-K
$H(\mathbf{q})$ = average unconditional uncertainty associated with making measurement $q$
$H(\mathbf{s})$ = average unconditional uncertainty associated with making measurement $s$
$H(\mathbf{s}, \mathbf{q})$ = average conditional uncertainty associated with making measurement $s$ and measurement $q$ time lagging $s$ by $k$ points
$I(k)$ = mutual information, in binary number system, bits
$k$ = integer time delay (number of points series is delayed)
$K_2$ = order-2 Renyi entropy, bits/s
$m$ = embedding dimension
$N$ = number of data points in a single measurement time series
$N_{\text{bins}}$ = number of bins used to evaluate mutual information = $I(k)$
$P(i)$ = probability of finding measurement $s$ in bin $i$
$P(j)$ = probability of finding measurement $q$ in bin $j$
$P(i, j)$ = probability of finding measurement $s$ in bin $i$ and measurement $q$ in bin $j$
$q$ = future discrete measurement
$s$ = current or present discrete measurement
$t$ = time, s
$u$ = fluidization velocity, m/s
$\mathbf{x}(n)$ = original single measurement time series
$\mathbf{x}(n + (m - 1)k)$ = single measurement time series delayed $(m - 1)k$ points
$\mathbf{X}_{a,i}$ = $i$th dimensional component of point $a$ on pseudo-phase space trajectory
$\mathbf{X}_{b,i}$ = $i$th dimensional component of point $b$ on pseudo-phase space trajectory
$\delta$ = minimum embedding dimension or degrees of freedom
$\epsilon$ = radius of sphere used to determine correlation integral = $C_d(\epsilon)$
$\theta$ = circumferential or angular position of probe in relation to stagnation region, deg
$\phi$ = Heaviside function
$\tau$ = actual time delay = $k$/sample frequency, s
$\nu$ = correlation exponent or correlation dimension



Downloaded 12 Dec 2010 to 193.140.21.150. Redistribution subject to ASME license or copyright; see http://www.asme.org/terms/Terms_Use.cfm

minimum fluidization velocity of 0.34 m/s when fluidized with air at room temperature. This value of minimum fluidization velocity agrees within the experimental uncertainty with the correlation of Wen and Yu (1966).

The cylinder was heated and allowed to reach a steady-state condition for a fixed fluidization velocity, and a constant temperature bridge circuit employed to maintain a constant sensor temperature. A total of 24,000 data points of bridge voltage were acquired at a sample rate of 800 Hz using an analog to digital converter with 12 bit nominal resolution. Operation of the fluidized bed was limited to the bubbling flow regime, with fluidization velocities of 0.5, 0.7 and 1.0 m/s. Measurements were acquired at several circumferential positions about the axis of the cylinder for each fluidization velocity. Angular positions of the probe varied from the stagnation region at the bottom of the cylinder (0 deg) to 180 deg at 45 deg increments. In order to eliminate high-frequency line noise, signals were filtered using a low-pass filter with a threshold of 40 Hz.

## Data Analysis

**Statistical Analysis Techniques: Power Spectra.** Power spectra of time series measurements represent the energy content corresponding to each frequency inherent in the sampled signal. As expected, for periodic and multiperiodic signals the power spectra exhibit significant energy content only at discrete frequencies. When plotted on semi-logarithmic axes, purely random signals display broad-band frequency characteristics with energy fluctuations about a mean value. Chaotic signals tend to exhibit broad-band frequency spectra as well; however, the magnitude of the energy content tends to vary with frequency. Since both chaotic and random signals exhibit broad-band characteristics, power spectra cannot be used as the sole mechanism for identifying chaotic behavior from single variable time series data.

### Nonlinear Analysis Techniques—Quantitative

*Time-Delay Embedding.* According to Takens' embedding theorem (1980), a single measurement time series contains sufficient information regarding the system dynamics to define its state. A time series of $N$ data points is represented by $\mathbf{x}(n)$, where $n = 1, 2, 3, \ldots, N$. If the same time series were to begin $k$ points later, the new series would be expressed as $\mathbf{x}(n + k)$, where $n = 1, 2, 3, \ldots, N - k$. The value $k$ is an integer representation of the number of time steps the signal is delayed. If $\mathbf{x}(n)$ is plotted against $\mathbf{x}(n + k)$, a two-dimensional pseudo-phase space trajectory results. Similarly, an $m$-dimensional phase-space trajectory can be constructed using $\mathbf{x}(n)$, $\mathbf{x}(n + k)$, $\mathbf{x}(n + 2k)$, $\ldots$, $\mathbf{x}(n + (m - 1)k)$. This pseudo-phase space representation of the original time series is often denoted as time-delay embedding, where $k$ is referred to as the integer time delay and $m$ as the embedding dimension.

The actual number of degrees of freedom necessary to represent the dynamic state of the system is referred to as the minimum embedding dimension, $\delta$. This is the minimum dimension in which the attractor, if one exists, is expected to be reproducible. Its value is the next highest integer value of the fractal dimension of the attractor, an estimate of which is provided by the correlation dimension, $\nu$. The relationship between $\nu$ and $m$ was determined by Takens (1980) to be $m > 2\nu$.

Daw and Halow (1991) have found embedding dimensions, $m$, to be of the order of 6 or 7 for pressure drop measurements in gas fluidized beds, suggesting that three degrees of freedom represent the dynamics of their system. Of the several methods available for evaluating the embedding dimension, the correlation integral is employed in this work. The correlation integral estimates the average number of points within a sphere of radius $\epsilon$, as it moves to each point on a trajectory in pseudo-phase space. Knowledge of a time delay sufficient for reproducing the characteristics of the attractor is necessary. A method for determining such a time delay is presented first.

*Mutual Information.* The time delay necessary to construct a pseudo-phase space trajectory from a discrete, noise-free signal can in principle be chosen arbitrarily (Takens, 1980). However, this is not the case for noise distorted data.

Fraser and Swinney (1986) have shown that time delays derived from mutual information are more appropriate for nonlinear systems than the first minimum of the autocorrelation; the mutual information function does not have an underlying linear relationship as does the autocorrelation function. They recommend using the time that corresponds to the first minimum of the mutual information function as the time delay for embedding. Using the time delay obtained from the mutual information function allows for the details of the stretching and folding of the attractor to be observed visually in phase space.

The procedure is based upon the concept of uncertainty explained by Shannon and Weaver (1949). Uncertainties associated with measurements are dependent upon the probabilities of certain outcomes. Creating a histogram of the time series measurement results in an unconditional uncertainty (or probability) associated with making any measurement $s$. In the present study, the method is applied to a scalar time series in order to evaluate a time delay by reconstructing a two-dimensional trajectory in time-delay coordinates.

The mutual information function is a measure of the surprise that a measurement will yield given knowledge of the previous measurement. In other words, mutual information is a quantitative measure of the amount that knowledge of measurement $s$ reduces the uncertainty of a future measurement $q$. Mutual information is based on entropy as defined in information theory.

Consider mutual information of a two-dimensional phase space trajectory. Entropy is a term that describes the rate of memory loss due to the chaotic nature of the system, and according to

$$H(\mathbf{s}) = -\sum_{i}^{N} P(i) \log_2 [P(i)] \tag{1}$$

is directly related to the probability of finding measurement $s$ in bin $i$, $P(i)$. $H(\mathbf{s})$ is also referred to as the average unconditional uncertainty associated with making measurement $s$. Similarly, $H(\mathbf{q})$ is the average unconditional uncertainty in making measurement $q$ time lagged $k$ points after measurement. Both are used to calculate the mutual information of a time series, which is found from

$$I(k) = H(\mathbf{s}) + H(\mathbf{q}) - H(\mathbf{s}, \mathbf{q}) \tag{2}$$

With $P(i, j)$ being the joint probability that measurement $s$ falls in bin $i$ and measurement $q$ after $k$ time lags falls in bin $j$, the average conditional uncertainty $H(\mathbf{s}, \mathbf{q})$ is defined in accordance with Eq. (1). Using the base 2 logarithm, the uncertainty and mutual information are represented in bits.

According to Fraser and Swinney (1986) the bin size can either remain fixed or adjust to the local conditions. Ideally the bin size should result in a flat histogram of data points from the original signal.

*Correlation Dimension.* Several methods for estimating the fractal dimension of an attractor from a single measurement time series exist (Grassberger and Procaccia, 1983a). The correlation integral, which also provides a means for determining the embedding dimension, is employed in this work. According to Grassberger and Procaccia (1983b), the correlation integral for $d$-dimensional space is defined by

$$C_d(\epsilon) = \lim_{N\to\infty} \frac{1}{N^2} \sum_{a}^{N} \sum_{b}^{N} \phi \left[ \epsilon - \left( \sum_{i=1}^{d} |\mathbf{X}_{a,i} - \mathbf{X}_{b,i}|^2 \right)^{1/2} \right] \tag{3}$$

where $\phi(c)$ is the Heaviside function yielding values of one or zero depending on the sign of the argument $c$. $\mathbf{X}_{a,i}$ and $\mathbf{X}_{b,i}$ represent the $i$th dimensional component of points $a$ and $b$, respec-



Downloaded 12 Dec 2010 to 193.140.21.150. Redistribution subject to ASME license or copyright; see http://www.asme.org/terms/Terms_Use.cfm

tively, in pseudo-phase space on a $d$-dimensional attractor. $N$ represents the total number of points evaluated. For large values of $N$, the correlation integral provides an estimate of the average fraction of points within a sphere of radius $\epsilon$ as the sphere moves to each point on the trajectory.

The correlation exponent or dimension, $\nu$, is a quantitative measure used for characterizing the local structure of an attractor. Estimates of $\nu$ can be determined from the relationship

$$C_d(\epsilon) \sim \epsilon^{\nu} \exp(-d\tau K_2) \tag{4}$$

by plotting ln $C_d(\epsilon)$ versus ln $\epsilon$ for values of $d$ equal to 2 or greater. Each curve exhibits a region of linearity, the slope of which corresponds to $\nu$. As the dimension, $d$, is increased beyond the embedding dimension, the linear region of the curves yield consistent values of $\nu$ and are displaced from each other by a factor of $\exp(-d\tau K_2)$. The value of $m$ alone is not of fundamental importance, but rather ensures that the slope of the curve of ln $C_d(\epsilon)$ versus ln $\epsilon$ is sufficiently converged to determine $\nu$ and $\delta$. Here $d$ represents the dimension in which the trajectory is embedded for evaluation of $C_d(\epsilon)$, $\tau$ the actual time delay of the embedding, and $K_2$ the order-2 Renyi entropy.

*Kolmogorov Entropy.* Kolmogorov entropy is a measure of the surprise that a measurement will yield given knowledge of the history of all previous measurements. In other words, Kolmogorov entropy represents the rate of memory loss of the system dynamics. It is similar to the mutual information; however, mutual information only incorporates knowledge of the previous measurement as opposed to all previous measurements. Purely periodic signals show no loss of memory and yield Kolmogorov entropy values equal to zero. On the other hand, random signals are completely unpredictable, yielding infinite values of Kolmogorov entropy. For a signal to be considered chaotic in nature, its Kolmogorov entropy must be noninfinite and positive. For discrete data sets, infinity corresponds to very large values; approximately 5000 bits/s or greater for the present study.

Grassberger and Procaccia (1983a, b) provide a means for estimating the Kolmogorov entropy using the correlation integral, which was also used for estimating the embedding dimension. In the limit as $d$ tends to infinity and $\epsilon$ tends to zero, the following equation:

$$K_{2,d}(\epsilon) = \frac{1}{\tau} \ln \frac{C_d(\epsilon)}{C_{d+1}(\epsilon)} \tag{5}$$

yields the order-2 Renyi-entropy, $K_2$. According to Grassberger and Procaccia (1983a, b), estimates obtained using this method are slightly lower than the actual values of the Kolmogorov entropy.

### Nonlinear Analysis Techniques—Qualitative

*Phase Plots.* Phase space trajectories are constructed using the time series signal, $\mathbf{x}(n)$, and the time derivatives, $\partial\mathbf{x}(n)/\partial t$, of the signal. Pseudo-phase space trajectories result from plotting $\mathbf{x}(n)$, $\mathbf{x}(n + k)$, $\mathbf{x}(n + 2k)$, . . . , $\mathbf{x}(n + (\delta - 1)k)$ where $\delta$ is the minimum embedding dimension. To investigate the qualitative nature of the system dynamics, the trajectories are generally projected onto the coordinate axes. These projections are termed phase plots or phase portraits. According to several investigators, phase plots using time derivatives are proportional to pseudo-phase plots, which have been orthogonalized using principal component analysis. In the present study, phase space portraits from time derivative phase space trajectories are employed as a means of extracting qualitative information regarding the dynamics of the signal. Quantitative aspects regarding the chaotic nature of the signal are investigated using pseudo-phase space trajectories.

## Results and Discussion

The single measurement time series analyzed in this work are instantaneous records of the rate of heat transfer from a constant temperature probe to the media in the fluidized bed. Figure 1 shows three seconds of data chosen to illustrate the difference between bubble phase contact, mixing emulsion phase contact, and stationary emulsion phase contact. When bubbles make contact with the surface of the cylinder, heat transfer from the cylinder is at its lowest. This condition is denoted by (*a*) in Fig. 1. Contact (*b*) represents the condition where the emulsion phase adjacent to the cylinder is essentially motionless. Initial contact of the emulsion phase with the cylinder results in a dramatic increase in the value of heat transfer over that of the bubble phase. As long as the particles remain essentially motionless at the surface, heat is transferred from the cylinder to the particles via conduction. As the temperature of the particles increases with time, the instantaneous rate of heat transfer decays. If the particles in the emulsion phase are in a state of continual mixing at the surface of the cylinder, the heat transfer fluctuates about a constant mean value, as represented by contact (*c*). The mean duration of contact for each condition varies with fluidization velocity and angular position of the sensor. Further details regarding these parametric effects are available from Pence et al. (1993).

The previous discussion provides some physical interpretation of the measured heat transfer signals. The present study examined heat transfer signals for chaotic behavior; both qualitative and quantitative measures were employed to determine whether the behavior is consistent with chaos and to characterize the nonlinear structure. Since chaotic signals are known to have broad-band frequency spectra, Fourier power spectra were employed to investigate the nature of the frequency distribution in the heat transfer signals. Power spectra provide clear evidence that heat transfer in gas fluidized beds is not periodic. On the other hand, power levels in the spectrum of the heat transfer signal do not fluctuate about a mean value as they do for random signals, providing preliminary evidence that fluidized bed heat transfer may be chaotic as opposed to random. Further investigation was warranted.

While system dynamics are not clearly defined from power spectra, limited insight into the dynamics of the system is available from such analyses. Figure 2 illustrates the variations in the frequency of the system dynamics, which occur as the fluidization velocity is varied. Spectra for the three fluidization velocities at an angular position of 45 deg were normalized by their maximum power to emphasize the shift in the dominant frequencies. At the highest fluidization velocity, 1.0 m/s, the power is concentrated at the lower frequencies. This is in agreement with the original time series data. Low frequencies correspond to longer bubble and emulsion phase contacts, which are evident in signals acquired at this velocity. The duration of both bubble and emulsion phase contacts decreases with decreases in fluidization velocity for this angular position. The result is a redistribution of the power content to a wider range of frequencies. Visual con-

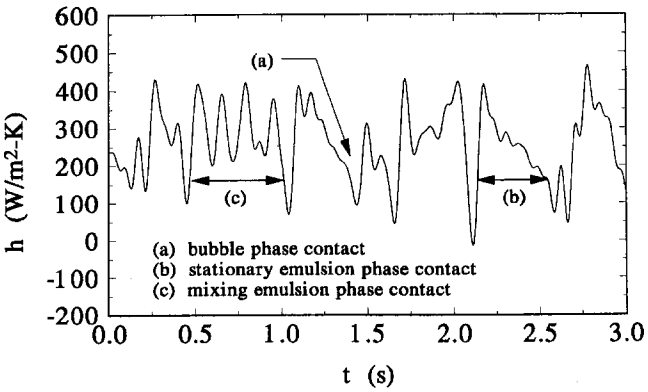



**Fig. 1 Representative instantaneous heat transfer signal**



Downloaded 12 Dec 2010 to 193.140.21.150. Redistribution subject to ASME license or copyright; see http://www.asme.org/terms/Terms_Use.cfm

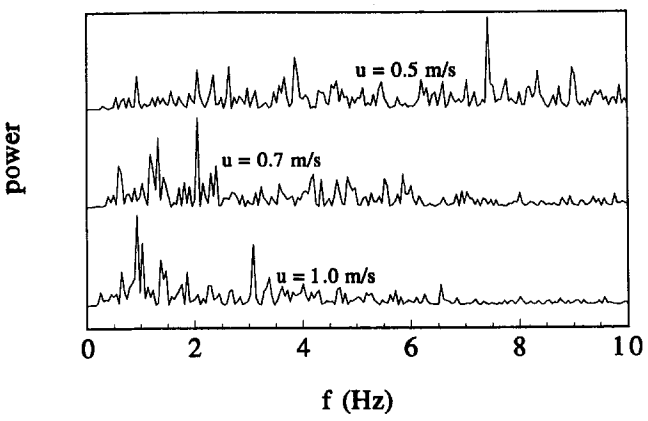



Fig. 2 Frequency variations in normalized power spectra as a function of fluidization velocity (offset for clarity)

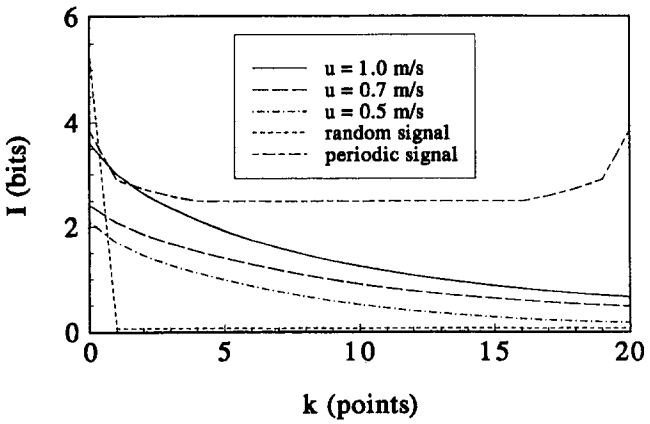



Fig. 3 Mutual information as a function of integer value time delay ($\theta$ = 45 deg)

firmation of this trend is available from Fig. 2. Comparisons of the frequency spectra variations with angular position for a fixed fluidization velocity were also conducted. The results indicate that frequency spectra are significantly less dependent on the angular position of the sensor than on the fluidization velocity.

**Chaotic Signal Analysis.** For time-delay embedding of a single measurement time series, information derived from the time series may be used to determine the number of time steps in which to embed the signal. In the present study this value is determined using the mutual information function. Values of mutual information calculated for a two-dimensional pseudo-phase space trajectory are plotted as a function of integer time delay in Fig. 3. The abscissa, $k$, represents the integral number of time steps the signal is delayed. For the current work, the bin sizes remained fixed such that $(N_{\text{bins}})^2 < 0.1\ N$, where $N_{\text{bins}}$ is the number of bins and $N$ is the total number of data points (Daw and Halow, 1993). Using $2^{14}$ data points and the restriction on the number of bins, the flattest histograms (Fraser and Swinney, 1986) corresponded to approximately 40 bins. For comparative purposes, the mutual information for each signal was determined using 40 equal sized bins. It is evident from Figure 3 that no first minimum exists; rather the mutual information decays continually. Daw and Halow (1993) found similar behavior for some of their pressure drop measurements, and employ 10 to 50 percent of the maximum value of the mutual information to set their time delay. However, for the signals analyzed in this work a consistent value of 40 percent of the maximum value was found to yield time delays that resulted in pseudo-phase trajectories that qualitatively agree with trajectories in time-derivative phase space. In the present case, signals are embedded in pseudo-phase space for the evaluation of correlation dimensions, time-delay values, and entropy estimates. Time-derivative phase space is used to gain qualitative information from phase portraits because the physical nature of the hydrodynamics has been previously identified in terms of the derivative of the signal (Pence et al., 1993).

In addition to time-delay information, the mutual information function provides an estimate of the degree of predictability of the phase space trajectory. In Fig. 3, comparisons are made for variations in fluidization velocity at a fixed sensor position of 45 deg. Mutual information of a random signal and a periodic signal are provided as a comparative tool. Random signals show a complete loss of mutual information between measurements of a signal delayed one or more points. Periodic signals display a high degree of mutual information shared between measurements of the signal regardless of the time delay. Heat transfer signals obtained in the present study lie between the two extremes, as is expected of signals exhibiting chaotic behavior. Values of mutual information tend to be dependent on fluidization velocity. For the particle size investigated, higher fluidization velocities result in higher mutual information. As the fluidization velocity was increased for the 715 $\mu$m particles investigated in this work, the contribution of gas convection increased. The effect of emulsion phase contact is thus reduced, which reduces the peak-to-peak heat transfer variations. Reduced peak-to-peak variations are expected to be the cause for increases in the mutual information.

Caution must be used in generalizing these results. Comparing the work of Skrzycke et al. (1993) and Daw and Halow (1993), it is apparent that trends in mutual information of pressure drop signals are a function of particle size, and possibly a function of particle density. Skrzycke et al. performed mutual information analyses on pressure drop signals acquired by fluidizing 175-$\mu$m-dia stainless steel particles with air and reported a trend opposite in nature to that of Daw and Halow. The latter investigators fluidized 3175 $\mu$m nylon spheres with air.

Variations in mutual information as a function of the circumferential position around the cylinder were also investigated for a fixed fluidization velocity of 1.0 m/s. The top half of the cylinder, 135 and 180 deg positions, is more highly correlated in terms of mutual information than the bottom of the cylinder at 0 and 45 deg. Mutual information tendencies for the 90 deg location lie between these two extremes.

The correlation dimension for a signal can be determined given knowledge of a time delay for pseudo-phase space reconstruction of the trajectory. Natural logarithmic plots of the correlation integral, $C_d(\epsilon)$, versus radii, $\epsilon$, provide the necessary information for calculating the correlation exponent, $\nu$, which is the slope of the linear region of the curve. A plot of this type is represented in Fig. 4 for an angular position of the sensor corresponding to 45 deg from the stagnation region and a fluidization velocity of 1.0 m/s. Values of $d$ from 2 through 10 represent the dimension

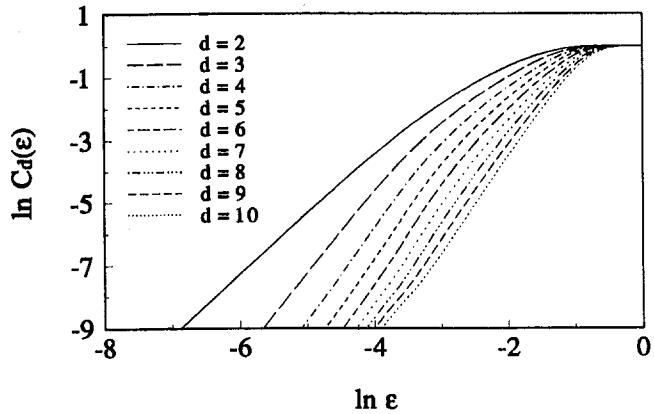



Fig. 4 Correlation integral variations with radius ($u$ = 1.0 m/s, $\theta$ = 45 deg)



Downloaded 12 Dec 2010 to 193.140.21.150. Redistribution subject to ASME license or copyright; see http://www.asme.org/terms/Terms_Use.cfm

in which 10,000 consecutive points of the filtered signal are embedded using time-delay coordinate axes. The minimum value of $d$ (dimension) for which the slope no longer changes is considered an appropriate embedding dimension.

The correlation exponent corresponding to Fig. 4 was found to be 3.04. Having a fractal value rather than an integral value is a good indication that the signal may be chaotic in nature. For the signal represented in Fig. 4, invariance of the slope beyond a dimension of 7 indicates that the attractor should be completely unfolded when embedded in seven-dimensional phase space. A good approximation to the minimum embedding dimension is the next larger integral value of the correlation exponent. For this case, the minimum embedding dimension or number of degrees of freedom would equal four. A similar analysis for the remaining signals yielded the results provided in Table 1. Values of 7 for the embedding dimension correspond well with results reported by Daw and Halow (1993).

Fractal values of the correlation exponent $\nu$, such as those reported in Table 1, suggest that the signals may be chaotic. However, the Kolmogorov entropy provides stronger evidence regarding the chaotic nature of a signal. Estimates of the Kolmogorov entropy using the second-order Renyi entropy, $K_2$, are also available in Table 1. In the present context, $K_2$ would range from 0 for a periodic signal to approximately 5000 bits/s for a random signal. The positive, noninfinite (i.e., <5000 bits/s) values of entropy strongly suggest that the signals are chaotic in nature.

The uncertainties in both correlation dimensions and Kolmogorov entropy estimates are subject to errors in estimating the correlation integral. However, evaluating a large number (i.e., 10,000) of consecutive data points minimizes uncertainties encountered if only subsets of the data series are evaluated. Uncertainties are also introduced when inconsistencies in quantitative values exist for data acquired under identical operating conditions. We found both $\nu$ and $K_2$ to be reproducible to within 6 percent for different data sets taken under the same operating conditions. Finally, uncertainty levels associated with the linearity of the scaling region can be quantified using the standard error of the curve fit to this linear region. Such a measure provides an indication of the data scatter and the length of the scaling region. The 95 percent confidence interval in $\nu$ was determined from the standard error of the fit for each case in Table 1; this yielded an average value of $\pm 0.06$.

The variations of the entropy with angular position are shown in Fig. 5. Daw and Halow (1993) attributed significant changes in entropy to changes in fluidization conditions. This is also believed to be the case for the present data. Although fluidization velocities were limited to the bubble flow regime, fluidization conditions vary with angular position. When a bubble makes contact with a cylinder, it does so at the bottom half of the cylinder. It then rises, adjacent to the surface of the cylinder, and detaches somewhere before the angular position of 135 deg. Bubbles rarely make direct contact with the cylinder at this particular location, and the emulsion phase is replaced via another mechanism. This is unlike the hydrodynamic behavior at 0, 45, and 90 deg where surface renewal of the emulsion phase is primarily a result of actual bubble contact with the surface of the cylinder. This provides a reasonable explanation as to the difference in the entropy at 135 from those at 0 through 90. Similarly, the entropy value at 180 deg indicates that the particle–cylinder interaction is once again different at this location than at any other. Further investigation of these phenomena and their relation to chaotic behavior are currently under way.

**Table 1 Quantitative information regarding the chaotic nature of heat transfer in gas fluidized beds**

| u | θ | ν | m | δ | k | $K_2$ |
|---|---|---|---|---|---|---|
| m/s | degrees | | | | points | bits/s |
| | | | | | | |
| 1.0 | 0 | 3.13 | 7 | 4 | 9 | 37 |
| | 45 | 3.04 | 7 | 4 | 8 | 42 |
| | 90 | 3.10 | 7 | 4 | 9 | 41 |
| | 135 | 3.10 | 7 | 4 | 17 | 17 |
| | 180 | 3.55 | 8 | 4 | 11 | 30 |
| | | | | | | |
| 1.0 | 45 | 3.04 | 7 | 4 | 8 | 42 |
| 0.7 | | 3.18 | 7 | 4 | 9 | 38 |
| 0.5 | | 3.18 | 7 | 4 | 7 | 54 |
| | | | | | | |

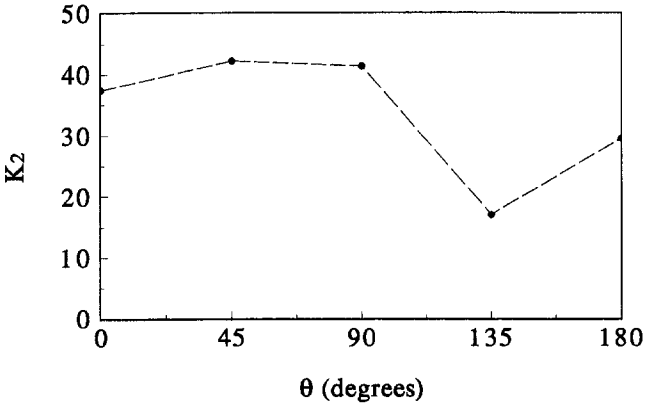



**Fig. 5 Kolmogorov entropy as a function of angular position ($u$ = 1.0 m/s)**

Since the flow regime was restricted to bubbling flow for each data set acquired, the estimates of Kolmogorov entropy are not expected to vary significantly with the fluidization velocity for a fixed angular position. However, the entropy value reported for a fluidization velocity of 0.5 m/s fixed at 45 deg from the stagnation position is 40 percent higher than the value reported for 0.7 m/s at the same position. The calculated values are available in Table 1. Skrzycke et al. (1993) and Daw and Halow (1993) both report significant increases in the Kolmogorov entropy near minimum fluidization for pressure drop signals. This behavior appears to be confirmed in the present study; however, further investigation is clearly warranted.

**Qualitative Analysis of Phase Plots.** Considerable information regarding the dynamic behavior of a system is assessable from phase portraits. As a first step to characterizing entire trajectories, phase portraits are constructed for individual emulsion phase contacts. This allows for detailed investigation of the difference in trajectory patterns for stationary versus mixing particles at the heat transfer surface. The emulsion phase contact represented by ($b$) in Fig. 1 is shown in phase space in Fig. 6($a$). This type of contact represents stationary particles at the heat transfer surface, which explains the transient decay in the heat transfer coefficient with time. Following the trajectory in the figure, point 1 corresponds a bubble in full contact with the heat transfer surface. As the trajectory evolves in a clockwise direction, an increase in the heat transfer coefficient is indicative of the passage of the bubble as particles in the bubble wake begin to make contact with the surface. Point 2 is the maximum value of heat transfer, corresponding to the onset of emulsion phase contact. Since the particles are essentially motionless, the heat transfer coefficient decays with no significant recurrence of high heat transfer rates. The decay process continues until a bubble once again makes contact with the cylinder. This corresponds to point 3 on the phase space trajectory.

In a similar manner, the contact represented by ($c$) in Fig. 1 is shown in Fig. 6($b$). This type of contact represents particles that are actively mixing at the heat transfer surface. If the trajectory in Fig. 6($b$) is followed in the same manner that was done for Fig. 6($a$), the top of the loop once again corresponds to the passage of a bubble. The farthest point on the right of the trajec-



Downloaded 12 Dec 2010 to 193.140.21.150. Redistribution subject to ASME license or copyright; see http://www.asme.org/terms/Terms_Use.cfm

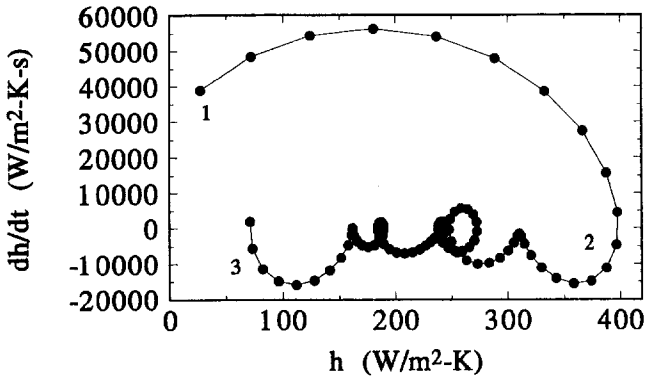



**Fig. 6(*a*) Transient: (1) bubble contact; (2) initial emulsion contact; (3) bubble contact**

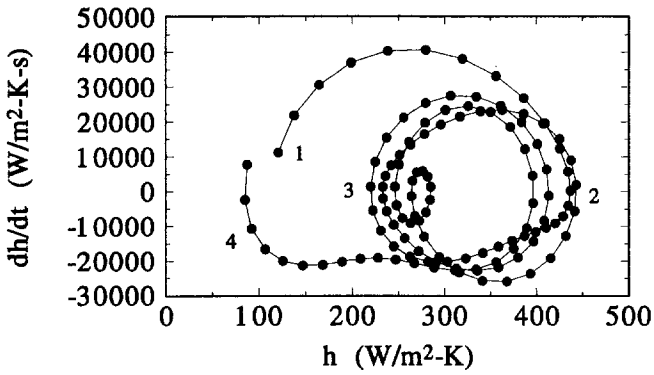



**Fig. 6(*b*) Steady state: (1) bubble contact; (2) initial emulsion contact; (3) emulsion renewal without direct bubble contact; (4) bubble contact**

tory, point 2, indicates the onset of emulsion phase contact. However, for this trajectory there are recurrences of the high values of heat transfer. Emulsion phase that has been heated by the cylinder causes a decrease in the rate of heat transfer from the probe, resulting in point 3 of the trajectory. The passage of a bubble near, but not adjacent to, the cylinder causes the replacement of the heated particles with cooler particles. This causes the trajectory to revisit point 2, a process that is repeated until the emulsion phase is replaced by a bubble, indicated by point 4 on the trajectory.

The single measurement time series corresponding to a probe position of 0 deg and a fluidization velocity of 0.5 m/s is represented in Fig. 7($a$). As shown in Table 1, the minimum embedding dimension corresponding to this signal is four. Therefore, if an attractor is present, it should be essentially unfolded when embedded in four-dimensional phase space. In addition to the original signal, Fig. 7 contains time derivative phase portraits. Using analysis techniques developed by Pence et al. (1993), it was determined that the emulsion phase contacts for this signal were predominantly transient in nature. Figure 7($b$) represents a plot of the original signal versus the first time derivative. Its characteristic shape, reminiscent of an insect wing, is typical of other phase trajectories from predominantly transient signals. The farthest point to the left corresponds to bubble phase contacts, as was concluded from Fig. 6. Bubbles in gas fluidized beds do not yield consistent void fractions equal to 1.0, therefore bubbles containing particles tend to increase the heat transfer activity during bubble phase contact. This accounts for the concentration of the trajectory at the far left region of the portrait. The first time derivative versus the second time derivative of the signal (Fig. 7$c$) also highlights characteristics that are indicative of transient contact. Projections onto these axes show a tendency for the trajectory to pass through a central point, resulting in a "figure 8" appearance. Figure 7($d$) represents the original signal versus the second time derivative of the signal.

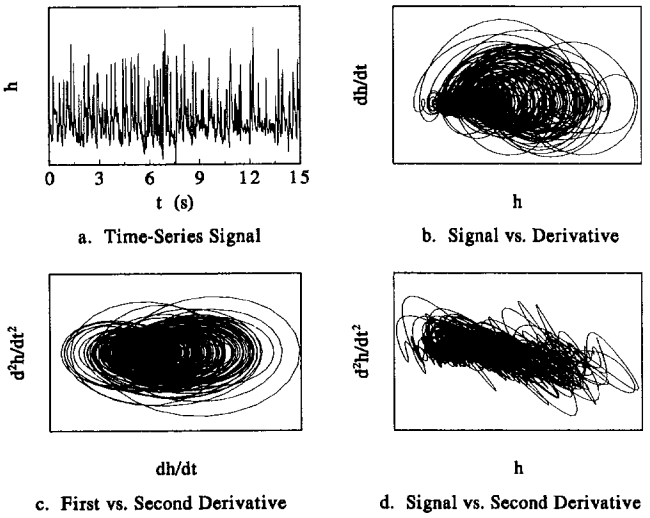



**Fig. 7 Phase space representation of a heat transfer signal ($\theta$ = 0 deg, $u$ = 0.5 m/s)**

Figures 8($a$–$d$) represent the original signal and its respective three-dimensional phase space portraits for the signal acquired at an angular position of 180 deg for fluidization velocity of 0.5 m/s. During the entire 15 seconds of the signal, only three bubbles make actual contact with the surface. These are assumed to have occurred when a large bubble eclipsed the entire cylinder, eliminating the particles that were actively mixing at the top of the cylinder. As was identified in Fig. 6($b$), trajectories for mixing conditions tend to focus near the right side of the phase plot. This is confirmed in Fig. 8($b$). The three visits to the left-hand side of the plot indicate the bubble contacts. In comparing Fig. 8($c$) to Fig. 7($c$), it is evident that mixing conditions do not exhibit the "figure 8" appearance typical of transient contacts when plotted on the first derivative versus second derivative axes.

## Conclusions

Standard statistical methods such as power spectra provide limited information regarding the frequency distribution of a heat transfer signal acquired in a gas fluidized bed operating in the bubbling flow regime. More robust nonlinear techniques developed to describe deterministic chaos provide means for assessing additional details of the qualitative and quantitative structure of

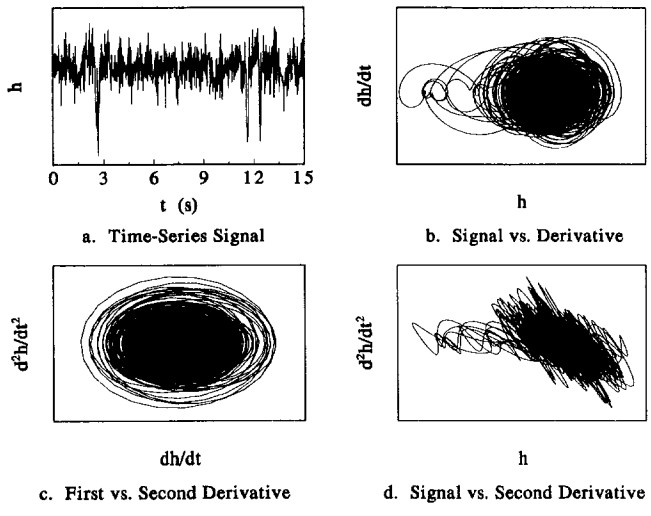



**Fig. 8 Phase space representation of a heat transfer signal ($\theta$ = 180 deg, $u$ = 0.5 m/s)**



Downloaded 12 Dec 2010 to 193.140.21.150. Redistribution subject to ASME license or copyright; see http://www.asme.org/terms/Terms_Use.cfm

such time series. Qualitative techniques provide an indication that instantaneous heat transfer signals exhibit chaotic behavior. Quantitative techniques provide useful measures of the inherent complexity in the signal, as well as indicators of specific physical phenomena.

Correlation dimensions provide an indication of the local fractal nature of a system. For the signals investigated in this work, these values ranged from 3.04 to 3.55. Embedding dimensions remained fairly consistent for most conditions investigated. A positive, non-infinite estimate of the Kolmogorov entropy provides further evidence that heat transfer signals behave chaotically. Estimates using the second-order Renyi entropy ranged from 17 to 54 bits/s, where an infinite value for the discrete signals in this work corresponds to approximately 5000 bits/s. As reported by previous investigators, changes in Kolmogorov entropy are also indicative of changes in the fluidization conditions. Such variations were clearly evident in this work, both with angular position of the heat flux sensor as well as with fluidization velocities.

Having demonstrated that heat transfer in gas fluidized beds behave in a manner consistent with deterministic chaos provides the incentive to investigate the possibilities of control and simulation using chaos-based algorithms.

## Acknowledgments

The authors would like to express their appreciation to Jack Halow, Mark Spano, and Bill Ditto for their encouragement in pursuing this research and their fruitful discussions regarding chaos analysis. Thanks are also extended to Andrew Fraser for providing us with a copy of his mutual information code with variable bin size, which provided us a means for checking our fixed bin size code. Finally, we would like to thank Brian Mueller, a devoted and determined graduate student, for his persistence in getting the fluidized bed facility in working order so that data could be obtained for analyses.

## References

Beasley, D. E., and Figliola, R. S., 1988, "A Generalized Analysis of a Local Heat Flux Probe," *J. Physics E: Sci. Instru.*, Vol. 21, pp. 316–322.

Daw, C. S., and Halow, J. S., 1991, "Characterization of Voidage and Pressure Signals From Fluidized Beds Using Deterministic Chaos Theory," *Proceedings of the 11th International Conference on Fluidized Bed Combustion*, ASME, Montreal, Vol. 2, pp. 777–786.

Daw, C. S., and Halow, J. S., 1993, "Evaluation and Control of Fluidization Quality Through Chaotic Time Series Analysis of Pressure-Drop Measurements," *AIChE Symposium Series*, Vol. 89, No. 296, pp. 103–122.

Ditto, W. L., Rauseo, S. N., and Spano, M. L., 1990, "Experimental Control of Chaos," *Physical Review Letters*, Vol. 65, No. 26, pp. 3211–3214.

Figliola, R. S., Swaminathan, M., and Beasley, D. E., 1993, "A Study of the Dynamic Response of a Local Heat Flux Probe," *Meas. Sci. Technol.*, Vol. 4.

Fraser, A. M., and Swinney, H. L., 1986, "Independent Coordinates for Strange Attractors From Mutual Information," *Physical Review A*, Vol. 33, No. 2, pp. 1134–1140.

Fuller, T. A., Flynn, T. J., Daw, C. S., and Halow, J. S., 1993, "Interpretation of Pilot-Scale, Fluidized Bed Behavior Using Chaotic Time Series Analysis," *Proceedings of the 12th International Conference on Fluidized Bed Combustion*, ASME, San Diego, Vol. 1, pp. 126–140.

Geldart, D., 1973, "Types of Fluidization," *Powder Technology*, Vol. 7, pp. 285–292.

Grassberger, P., and Procaccia, I., 1983a, "Measuring the Strangeness of Strange Attractors," *Physica D*, Vol. 9, pp. 189–208.

Grassberger, P., and Procaccia, I., 1983b, "Estimation of the Kolmogorov Entropy From a Chaotic Signal," *Physical Review A*, Vol. 28, No. 4, pp. 2591–2593.

Moon, F. C., 1993, *Chaotic and Fractal Dynamics: An Introduction for Applied Scientists and Engineers*, Wiley, New York, pp. 53–55.

Packard, N. H., Crutchfield, J. P., Farmer, J. D., and Shaw, R. S., 1980, "Geometry From a Time Series," *Physical Review Letters*, Vol. 45, No. 9, pp. 712–716.

Pence, D. V., Beasley, D. E., and Figliola, R. S., 1993, "Heat Transfer and Surface Renewal Dynamics in Gas Fluidized Beds," ASME JOURNAL OF HEAT TRANSFER, accepted for publication.

Schouten, J. C., and van den Bleek, C. M., 1992, "Chaotic Hydrodynamics of Fluidization: Consequences for Scaling and Modeling of Fluid Bed Reactors," *AIChE Symposium Series*, Vol. 88, No. 289, pp. 70–84.

Schouten, J. C., van der Stappen, M. L. M., and van den Bleek, C. M., 1992, "Deterministic Chaos Analysis of Gas–Solids Fluidization," *Proceedings of the 7th International Conference on Fluidization*, Engineering Foundation, New York, Vol. 7, pp. 103–111.

Shannon, C. E., and Weaver, W., 1949, *The Mathematical Theory of Communication*, The University of Illinois Press, Urbana, IL.

Skrzycke, D. P., Nguyen, K., and Daw, C. S., 1993, "Characterization of the Fluidization Behavior of Different Solid Types Based on Chaotic Time Series Analysis of Pressure Signals," *12th International Conference on Fluidized Bed Combustion*, ASME, San Diego, Vol. 1, pp. 155–166.

Takens, F., 1980, "Detecting Strange Attractors in Turbulence," *Lecture Notes in Mathematics*, D. A. Rand and L. S. Young, eds., Springer-Verlag, Berlin, Vol. 898, pp. 366–381.

Wen, C. Y., and Yu, Y. H., 1966, "A Generalized Method of Predicting the Minimum Fluidization Velocity," *AIChE Journal*, Vol. 12, pp. 610–612.



Downloaded 12 Dec 2010 to 193.140.21.150. Redistribution subject to ASME license or copyright; see http://www.asme.org/terms/Terms_Use.cfm

# A Variable Heat Flux Model of Heat Transfer in Grinding: Model Development

T.-C. Jen

A. S. Lavine

Mechanical, Aerospace, and Nuclear Engineering Department, University of California, Los Angeles, Los Angeles, CA 90095-1597

*In any grinding process, thermal damage is one of the main limitations to accelerating the completion of the product while maintaining high quality. Therefore, the objective of the present study is to understand the thermal behavior in the grinding process and possibly achieve the ultimate goal of avoiding thermal damage in the grinding process. A model previously developed is improved to analyze the heat transfer mechanisms in the grinding process. Heat generated at the interface between the abrasive grains and workpiece (i.e., the wear flat area) is considered. A conjugate heat transfer problem is then solved to predict the temperature in the grinding zone. In the previous model, all the heat fluxes were assumed to be uniformly distributed along the grinding zone. This led to a contradiction in the temperature matching condition. This reveals that the heat fluxes into each of the various materials are not uniform along the grinding zone. An improved model, accounting for the variation of the heat fluxes along the grinding zone, is presented. The temperature and heat flux distributions along the grinding zone are presented, along with comparisons to previous theoretical results.*

## Introduction

The grinding process is an important precision machining process, which requires high accuracy. It is well known that this process requires a very high energy input in comparison to other machining processes (e.g., milling and turning). In any grinding process, virtually all the grinding energy is dissipated as heat in the grinding zone (Outwater and Shaw, 1952). Most of the heat generation in the grinding zone is due to friction and plastic deformation. This heat can cause the workpiece temperature to become elevated. Sufficiently high temperatures can cause various forms of thermal damage to the workpiece and wheel. Therefore, understanding the heat generation mechanism and the heat transfer paths are crucial in attaining the objective of avoiding thermal damage.

A substantial amount of research has been conducted on heat transfer in grinding. The interested readers are referred to Snoeys et al. (1978) and Malkin (1984) for detailed literature reviews. Some particularly relevant papers are reviewed here. A model was developed by Lavine and Jen (1991a), based on a series of previous studies (e.g., Lavine et al., 1989). The advantage of this model over earlier ones was that, by considering coupled heat transfer to the workpiece, wheel, and fluid, it eliminated the need to specify a priori the fraction of grinding energy entering the workpiece or the convective heat transfer coefficient of the grinding fluid. This model assumed that the heat fluxes into the workpiece, wheel, grains, and fluid were uniformly distributed in the grinding zone. However, an apparent contradiction for the temperature matching condition was found, as shown in Lavine and Jen (1991a). More recently, this model was modified (Jen and Lavine, 1992a) to allow the heat fluxes to vary with location (i.e., to allow $x$ dependence), while the heat transfer coefficients for the various materials used were for uniform heat fluxes. For the case of uniform grinding power input, as was used in that study, this may not cause significant error. However, for the case of a triangular grinding power input, which may be more realistic for the grinding process (see, e.g., Kohli, 1993), this may cause significant error in the workpiece temperature prediction. This will be shown later. An improved model is developed in the present study (also, see a preliminary study by Jen and Lavine, 1992b), which accounts for the effect of the heat flux variation along the grinding zone. With the aid of Duhamel's Theorem, the correct heat flux variations along the grinding zone are obtained numerically. The temperature and heat flux distributions along the grinding zone, and comparisons with previous theoretical results are presented.

## Theoretical Analysis

The physical configuration and coordinate system for a typical grinding wheel and workpiece are shown in Fig. 1. The grinding zone is the region of length $l$ and width $b$ over which the wheel contacts the workpiece. The wheel and workpiece are shown moving in the same direction. This is termed "down" grinding. "Up" grinding, in which the wheel and workpiece are moving in different directions, is beyond the scope of the present study. However, with appropriate modifications, the present model could be used for up grinding. Some typical grinding parameters are shown in Table 1. There are two basic types of grinding: conventional and creep feed grinding. The major distinguishing features of creep feed grinding are the larger depth of cut and the lower workpiece speed.

It is helpful to recognize that there are many grains on the grinding wheel, which cut into the workpiece with very high speed. Heat is generated in the vicinity of each grain as it moves through the grinding zone. Consider an individual grain moving through the grinding zone. Heat is generated at three locations: the grain/workpiece interface, the grain/chip interface, and the shear plane between the workpiece and chip. Generally speaking, the frictional heat generated at the grain/chip interface is relatively small in comparison to the total grinding power. This was implicitly indicated by Malkin and Anderson (1974). Hahn (1956) argued that most of the heat is generated at grain/workpiece interfaces due to the larger frictional rubbing force than the cutting force (which is responsible for heat generation at the shear plane). This is especially true when the depth of cut of an individual grain is small. However, when this depth of cut is larger, the heat generated at the shear plane may not be negligible. In the present model, due to the significant complexity of including the effect of the heat generated at the shear planes, all the heat is assumed to be generated at the grain/workpiece interface.

Contributed by the Heat Transfer Division for publication in the JOURNAL OF HEAT TRANSFER. Manuscript received by the Heat Transfer Division November 1993; revision received July 1994. Keywords: Conjugate Heat Transfer, Materials Processing and Manufacturing Processes, Moving Boundaries. Associate Technical Editor: Y. Jaluria.

 Copyright © 1995 by ASME 

Downloaded 12 Dec 2010 to 193.140.21.150. Redistribution subject to ASME license or copyright; see http://www.asme.org/terms/Terms_Use.cfm

The heat generated at a grain/workpiece interface ($q''_{\text{grind}}$) conducts into either the workpiece or the abrasive grain. Thus,

$$q''_{\text{grind}}(x) = q''_{wg}(x) + q''_{g}(x) \tag{1}$$

where $q''_{wg}(x)$ is the heat flux into the workpiece at the grain location and $q''_{g}(x)$ is the heat flux into the grain.

Of the heat that conducts into the workpiece, (i.e., $q''_{wg}$), some remains in the workpiece and some is removed by convection to the grinding fluid. If it is assumed that the heat that conducts into the workpiece at a particular $x$ location ($q''_{wg}(x)$) either remains in the workpiece or is removed by the fluid in the vicinity of that same location (see Jen, 1993, for detail), then:

$$q''_{wg}(x)A = q''_{wb}(x) + q''_{f}(x)(1 - A) \tag{2}$$

Here $A$ is the fractional grain/workpiece contact area, $q''_{wb}(x)$ is the heat flux that remains in the workpiece, and $q''_{f}(x)$ is the heat flux into the fluid.

The basic approach used in the present study is first to develop thermal models for each heat transfer path (i.e., workpiece, grain and fluid) based on the assumption of uniform heat flux. (This assumption is later relaxed.) One result is a relationship between heat flux and temperature rise for each heat transfer path, of the form $h = q''/\theta$. The function $h$ will be called a local heat transfer coefficient. These heat transfer coefficients were previously presented in Lavine and Jen (1991a, b), and will be briefly summarized here. Then the "conjugate" heat transfer problem, with varying heat fluxes, will be solved using Duhamel's Theorem.

**Heat Transfer to Abrasive Grain, Workpiece, and Fluid.** In order to solve the true problem with varying heat fluxes, the heat transfer coefficients for uniform heat fluxes are needed as a building block. The local grain, workpiece, and grinding fluid heat transfer coefficients due to a uniform heat flux input are given by (Lavine and Jen, 1991b):

$$h_g = \sqrt{\pi(k\rho c_p)_g v_s/4x}\, f(\zeta) \tag{3}$$

where $\zeta(x) = (\pi\alpha_g x/A_0 v_s)^{1/2}$,

$$f(\zeta) = \frac{2\zeta}{\pi^{1/2}[1 - \exp(\zeta^2)\,\text{erfc}\,(\zeta)]} \tag{4}$$

$$h_{wb}(x) = \sqrt{\frac{\pi(k\rho c_p)_w v_w}{4x}} \tag{5}$$

$$\bar{h}_{wg} = \frac{3}{4}\sqrt{\frac{\pi(k\rho c_p)_w v_s}{l_g}} \tag{6}$$

$$h_f(x) = \sqrt{\frac{\pi(k\rho c_p)_f v_s}{4x}} \tag{7}$$

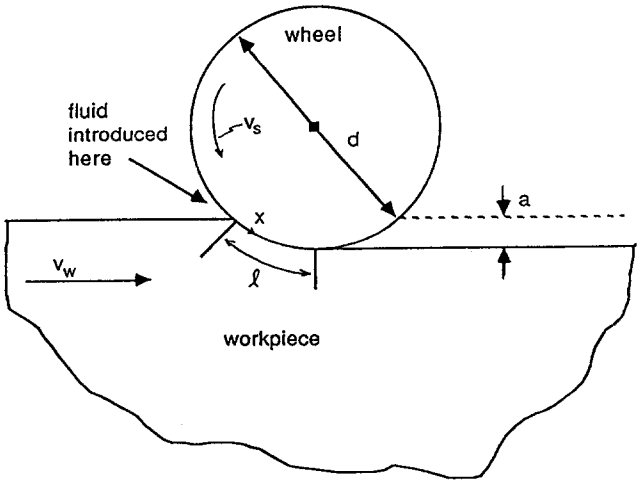



**Fig. 1 Grinding geometry**

For the grinding fluid heat transfer coefficient, slug flow is used throughout the present study rather than boundary layer flow, because it yields temperature predictions which agree better with experimental data. Note that this solution for $h_f$ assumes that the fluid remains liquid. In reality, the fluid may boil under some conditions. This is discussed in more detail by Jen (1993).

**Duhamel's Theorem.** In early works (e.g., Malkin, 1974; Lavine and Jen, 1991a), a uniformly distributed heat flux into each component is assumed. However, as demonstrated in Lavine and Jen (1991a), the heat flux that enters each material is *not* uniform. A remedy is proposed by Jen and Lavine (1992a), in which they allowed the heat fluxes to vary with location while using the heat transfer coefficient for the uniform heat flux case. It will be demonstrated later that this approach does give a very good approximation of the temperature distribution when the grinding power input is uniformly distributed. However, this approach gives a very bad temperature prediction when the grinding power input is triangular. Very recently, a combined analytical and experimental study (Kohli, 1993) showed that a triangular grinding power input is more realistic under actual grinding conditions.

In order to allow the heat fluxes in the various models to vary with location, Duhamel's Theorem is applied. The general form of Duhamel's Theorem (Wylie and Barrett, 1982) for the surface temperature distribution is as follows:

$$\theta_s(x) = \int_0^x \frac{dq''(\xi)}{d\xi}\,\frac{1}{h(x-\xi)}\,d\xi\,\Big|_{\text{St.}} \tag{8}$$

## Nomenclature

$a$ = depth of cut
$A$ = fractional grain/workpiece contact area = $A_g/A_{\text{tot}}$
$A_0$ = individual grain/workpiece contact area
$A_{\text{tot}}$ = grinding zone area = $lb$
$b$ = grinding zone depth
$C$ = a constant defined by Eq. (21)
$c_p$ = specific heat
$d$ = wheel diameter
$f(\zeta)$ = function defined by Eq. (4)
$h$ = heat transfer coefficient for uniform heat flux
$k$ = thermal conductivity
$l$ = grinding zone length
$l_g$ = width of individual grain heat source
$q''$ = heat flux
$T_i$ = temperature before encountering grinding zone
$v_s$ = wheel velocity
$v_w$ = workpiece velocity
$x$ = distance from beginning of grinding zone
$\alpha$ = thermal diffusivity
$\zeta$ = $(\pi\alpha_g x/A_0 v_s)^{1/2}$
$\theta$ = surface temperature rise relative to ambient temperature, i.e., $T - T_i$ (except for $\bar{\theta}_{wg} = \bar{T}_{wg} - T_{wb}$)
$\xi$ = dummy variable
$\rho$ = density

**Subscripts**

$f$ = fluid
$i$ = nodal point index in the grinding zone
$g$ = grain
grind = grinding power
$s$ = surface (except in $v_s$)
St. = Stieltjes integral
$w$ = workpiece
$wb$ = workpiece background
$wg$ = workpiece under grain



Downloaded 12 Dec 2010 to 193.140.21.150. Redistribution subject to ASME license or copyright; see http://www.asme.org/terms/Terms_Use.cfm

**Table 1 Typical grinding conditions ($v_s$ = 30 m/s, $d$ = 200 mm, $A$ = 0.01, $l_g$ = 110 $\mu$m)**

| | $v_w$ (mm/s) | a (mm) | $\ell = \sqrt{ad}$ (mm) |
|---|---|---|---|
| Conventional | 100 | 0.005 | 1 |
| Creep Feed | 1 | 0.5 | 10 |

where St. means the Stieltjes integral, which incorporates the discontinuities of heat fluxes. The detailed formulations of temperature distributions for the different models are written below, with the assumption of discontinuities in heat fluxes only at $x = 0$. This assumption is modified in Jen (1993) to account for the occurrence of film boiling.

$$\theta_{wb,s}(x) = \int_0^x \frac{dq''_{wb}(\xi)}{d\xi} \frac{1}{h_{wb}(x-\xi)}\, d\xi + \frac{q''_{wb}(0)}{h_{wb}(x)} \tag{9}$$

$$\theta_{f,s}(x) = \int_0^x \frac{dq''_{f}(\xi)}{d\xi} \frac{1}{h_{f}(x-\xi)}\, d\xi + \frac{q''_{f}(0)}{h_{f}(x)} \tag{10}$$

$$\bar{\theta}_{wg,s}(x) = \int_0^x \frac{dq''_{wg}(\xi)}{d\xi} \frac{1}{\bar{h}_{wg}}\, d\xi + \frac{q''_{wg}(0)}{\bar{h}_{wg}(x)} = \frac{q''_{wg}(x)}{\bar{h}_{wg}} \tag{11}$$

$$\bar{\theta}_{g,s}(x) = \int_0^x \frac{dq''_{g}(\xi)}{d\xi} \frac{1}{h_{g}(x-\xi)}\, d\xi + \frac{q''_{g}(0)}{h_{g}(x)} \tag{12}$$

where the overbars denote averages underneath a single grain.

Note that all temperature rises must be zero at $x = 0$, from the boundary condition that the wheel, workpiece, and fluid temperatures are all equal to $T_i$ at $x = 0$. This is automatically satisfied for $\bar{\theta}_{g,s}$, $\theta_{wb,s}$ and $\theta_{f,s}$, since $h_g(0)$, $h_{wb}(0)$, and $h_f(0)$ are all infinite. The requirement $\bar{\theta}_{wg,s}(0) = 0$ implies $q''_{wg}(0) = 0$. Then Eqs. (1) and (2) yield:

$$q''_{g}(0) = q''_{\text{grind}}(0) \tag{13}$$

$$q''_{wb}(0) + (1-A)q''_{f}(0) = 0. \tag{14}$$

**Coupling the Models.** The models for the wheel, fluid, and workpiece are now coupled by requiring that the surface temperatures match.

At a point on the workpiece surface that is not underneath a grain, the temperature rise is equal to the workpiece background temperature rise, $\theta_{wb,s}$, which must equal the fluid temperature rise, $\theta_{f,s}$:

$$\theta_{wb,s}(x) = \theta_{f,s}(x) \tag{15}$$

This leads to:

$$\int_0^x \frac{dq''_{wb}(\xi)}{d\xi} \frac{1}{h_{wb}(x-\xi)}\, d\xi + \frac{q''_{wb}(0)}{h_{wb}(x)} = \int_0^x \frac{dq''_{f}(\xi)}{d\xi} \frac{1}{h_{f}(x-\xi)}\, d\xi + \frac{q''_{f}(0)}{h_{f}(x)} \tag{16}$$

Now if $q''_{wb}(0)$ and $q''_f(0)$ are assumed to be nonzero, it can be shown that as $x \to 0$, the two integral terms in Eq. (16) approach zero faster than the other two terms. This implies $q''_{wb}(0)/h_{wb}(x) = q''_f(0)/h_f(x)$ for small $x$. The interested readers are referred to Jen (1993) for detailed derivations. In combination with Eq. (14) this yields $q''_{wb}(0) = q''_f(0) = 0$, so that the initial assumption of nonzero values is false. Then Eq. (16) becomes:

$$\int_0^x \frac{dq''_{wb}(\xi)}{d\xi} \frac{1}{h_{wb}(x-\xi)}\, d\xi = \int_0^x \frac{dq''_{f}(\xi)}{d\xi} \frac{1}{h_{f}(x-\xi)}\, d\xi \tag{17}$$

At a point on the workpiece surface that is beneath a grain, the grain temperature rise, $\bar{\theta}_{g,s}$, must equal the sum of the workpiece background temperature rise and the individual grain temperature rise relative to the workpiece background temperature:

$$\bar{\theta}_{g,s}(x) = \theta_{wb,s}(x) + \bar{\theta}_{wg,s}(x) \tag{18}$$

Similarly, this can be expressed as:

$$\int_0^x \frac{dq''_{g}(\xi)}{d\xi} \frac{1}{h_{g}(x-\xi)}\, d\xi + \frac{q''_{\text{grind}}(0)}{h_g(x)} = \int_0^x \frac{dq''_{wb}(\xi)}{d\xi} \frac{1}{h_{wb}(x-\xi)}\, d\xi + \frac{q''_{wg}(x)}{\bar{h}_{wg}} \tag{19}$$

If $q''_{\text{grind}}(x)$ is assumed to be known, then Eqs. (1), (2), (17) and (19) are four equations that can be solved for the four unknown heat fluxes. In particular, these four equations can be combined into one integral equation for $q''_{wb}(x)$:

$$q''_{wb}(x) = \frac{A\bar{h}_{wg}}{1+(1-A)C}\left\{\int_0^x \left(\left[\frac{dq''_{\text{grind}}(\xi)}{d\xi} - \frac{1}{A}\frac{dq''_{wb}(\xi)}{d\xi}(1+(1-A)C)\right]\frac{1}{h_g(x-\xi)} - \frac{dq''_{wb}(\xi)}{d\xi}\frac{1}{h_{wb}(x-\xi)}\right)d\xi + \frac{q''_{\text{grind}}(0)}{h_g(x)}\right\} \tag{20}$$

where:

$$C = \frac{h_f(x)}{h_{wb}(x)} = \frac{q''_f(x)}{q''_{wb}(x)} \tag{21}$$

where $C$ is a constant. Note that Eq. (21) can be verified by using Eq. (17). It is worth noting that Eq. (20) is only valid when flow boiling doesn't occur. The readers are referred to Jen (1993) for detailed derivations when film boiling occurs.

Before giving details of the numerical procedure, a brief discussion of the differences between the present model and the previous models are discussed. It was pointed out by Lavine and Jen (1991a) that the true solution of this coupled heat transfer problem does not have uniform heat fluxes into each of the various materials. With some modifications, Jen and Lavine (1992a) allowed all the heat fluxes to vary with $x$, but they still used the heat transfer coefficients for uniform heat fluxes. It will be shown later that this approximate solution is quite accurate when $q''_{\text{grind}}(x)$ is uniform, but it is highly inaccurate when $q''_{\text{grind}}(x)$ is triangular. With the aid of Duhamel's Theorem, the present model correctly handles arbitrary heat flux variations. It is also worth noting that the triangular grinding power input may be more appropriate for the grinding process than the uniform grinding power input used previously (e.g., Kohli, 1993, and Ohishi and Furukawa, 1985). Therefore, this new model is more accurate and flexible, because it imposes less restrictive assumptions.

**Numerical Procedure.** It can be seen that the final expression of the governing equations, Eq. (20), is in the form of a Volterra integral equation. An attempt was made to solve it using a fixed point iteration method. However, the iterations did not always converge. An alternative method is employed that will now be described.

It is helpful first to recognize that all the heat transfer coefficients for the uniform heat flux case approach infinity as $x \to 0$. Thus, all kernels of the integral terms in Eq. (20) approach zero as $\xi \to x$. This reveals that we do not need information at $\xi = x$ for all integral terms. Therefore, if we use backward differences for the derivative $dq''_{wb}/d\xi$, we can march through the grinding zone, in the direction of increasing $x$, and solve explicitly for $q''_{wb}(x)$ from the left-hand side of Eq. (20). The only difficulty is that we cannot use backward differences at $x = 0$. But if we can determine the values of $q''_{wb}$ at the first three discretized points after $x = 0$, we can solve this governing equation beyond these points without iteration. Bearing this concept in mind, the numerical procedure will now be presented as follows:



Downloaded 12 Dec 2010 to 193.140.21.150. Redistribution subject to ASME license or copyright; see http://www.asme.org/terms/Terms_Use.cfm

Table 2 Material properties and nondimensional parameters

| | water-based | oil | $Al_2O_3$ | steel |
|---|---|---|---|---|
| k (W/m-K) | 0.68 | 0.15 | 46 | 60.5 |
| $\rho$ (kg/m$^3$) | 1000 | 820 | 4000 | 7854 |
| $c_p$ (J/kg-K) | 4180 | 2000 | 770 | 434 |

1 In order to accelerate the convergence at the first three points, the first guess of $q''^{0}_{wb}(x)$ for these points is adopted from the previous approach (see Jen and Lavine, 1992a).

2 If we move the two terms on the right-hand side that are $q''_{wb}(x)$ dependent to the left-hand side, then the left-hand side of Eq. (20) is a function of $q''_{wb}(x)$ only and the right-hand side of the equation can be evaluated exactly. For the first three points, an iterative procedure is used (Jen and Lavine, 1992a) to solve for $q''_{wb}$, until the following convergence criterion is satisfied for the workpiece background temperature:

$$\epsilon = \frac{\max\ |\theta^{n+1}_{wb,i} - \theta^{n}_{wb,i}|}{\max\ |\theta^{n+1}_{wb,i}|} < 10^{-6} \qquad (22)$$

where $i$ is the nodal point index in the grinding zone, and $n$ is the iteration number.

3 With the values of $q''_{wb}(x)$ at these three points known, a second-order accuracy backward difference can be used for $dq''_{wb}/d\xi$ beyond those three points, so that Eq. (20) only has one unknown (i.e., $q''_{wb}(x)$). By marching along the grinding zone, all $q''_{wb}(x)$ can be calculated without further iteration.

4 With calculated $q''_{wb}(x)$, the other heat fluxes and temperatures can be calculated easily from Eqs. (1), (2), (21), and (9)–(12).

Grid convergence tests have been performed using three different grids for a case of creep feed grinding conditions, which is adopted from Ohishi and Furukawa (1985). As the grid size varies from 20001 to 40001, the maximum change in workpiece background temperature is less than 1.2 percent everywhere and less than 0.3 percent after $x = 3.58 \times 10^{-4}$ m. When the grid size varies from 40001 to 80001, the maximum change is less than 1 percent everywhere and less than 0.3 percent after $x = 1.57 \times 10^{-4}$ m, which is less than 1 percent of the total grinding zone. The error becomes smaller farther downstream. From the tests described above, 40001 grid points are sufficient for the present study.

Before giving the detailed results of the present model, an average grinding power is defined, for convenience, as follows:

$$q''_{\text{tot}} = \frac{1}{l}\int_0^l A q''_{\text{grind}}(x)\,dx \qquad (23)$$

The reason for introducing Eq. (23) is that experimental results are usually reported in terms of $q''_{\text{tot}}$, that is, the total grinding power divided by the total grinding area.

## Results and Discussion

In this section, this newly improved model will be used to give predictions of various temperatures and heat fluxes. The physical properties of abrasive grains ($Al_2O_3$), workpiece (steel), and grinding fluids (water-based or oil) are listed in Table 2. The grinding conditions, unless specifically stated, are the conditions listed in Table 1. The triangular grinding power input is used (unless otherwise stated). The average grinding powers used here are in the normal ranges of typical conventional and creep feed grinding conditions (Andrew et al., 1985). The workpiece material properties are taken to be those of plain carbon steel (see Table 2). The ambient temperature is taken to be 25°C for water based grinding fluid and 40°C for oil, as explained in Lavine and Jen (1991a).

**Comparison to Previous Results.** The results of the present model will first be compared to the previous model (Jen and Lavine, 1992a) for creep feed grinding, using an aluminum oxide wheel and water-based grinding fluid. Figure 2 demonstrates the workpiece background temperature variation through the grinding zone, for the cases of uniform and triangular grinding power input. It can be seen from the figure that for the case of uniform grinding power input, the workpiece background temperature distribution for the present model is almost the same as the previous model. The maximum workpiece background temperature difference is less than 2°C. This close agreement is typical of all cases considered, which confirms the earlier statement that the approximate solutions presented by the previous model are quite accurate when $q''_{\text{grind}}(x)$ is uniformly distributed along the grinding zone. However, when the triangular grinding power input is used, the workpiece background temperatures predicted by these two models do not agree for $x$ greater than about 2.0 mm. Furthermore, the previous model predicts that $T_{wb}$ approaches $T_i$ at the end of the grinding zone. This clearly unrealistic result indicates that the previous model cannot be used with a triangular grinding power input. This creates a problem in using the previous model, in light of the experimental observations by Kohli (1993) that a triangular grinding power input appears more accurately to simulate real grinding conditions.

It can be seen from the figure that the maximum workpiece background temperatures of the present model are approximately the same when using the two different grinding power inputs. This was true of all cases investigated. However, the workpiece background temperature distributions are vastly different for the two different shapes of grinding power input. For the uniform grinding power input case, the workpiece background temperature increases monotonically, and the maximum temperature always occurs at the end of the grinding zone. For the triangular grinding power input case, the temperature does not increase monotonically, and the maximum temperature occurs somewhere in the middle portion of the grinding zone. In this case, the maximum temperature occurs at about $x = 8$ mm (for a grinding zone length of 17.5 mm).

A comparison between the previous theoretical results and experimental measurements of the maximum workpiece background temperature was presented in Lavine and Jen (1991a). Since the present model agrees well with the previous model for prediction of the maximum workpiece background temperature, the comparison to experimental data would be essentially the

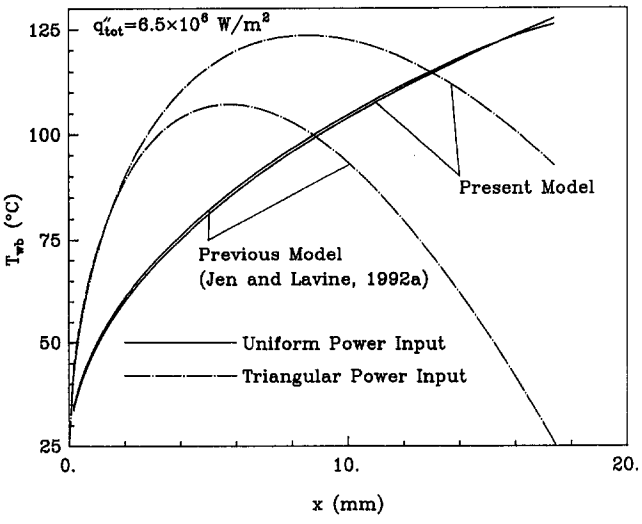



Fig. 2 Comparison to previous results: workpiece background temperature distribution



Downloaded 12 Dec 2010 to 193.140.21.150. Redistribution subject to ASME license or copyright; see http://www.asme.org/terms/Terms_Use.cfm

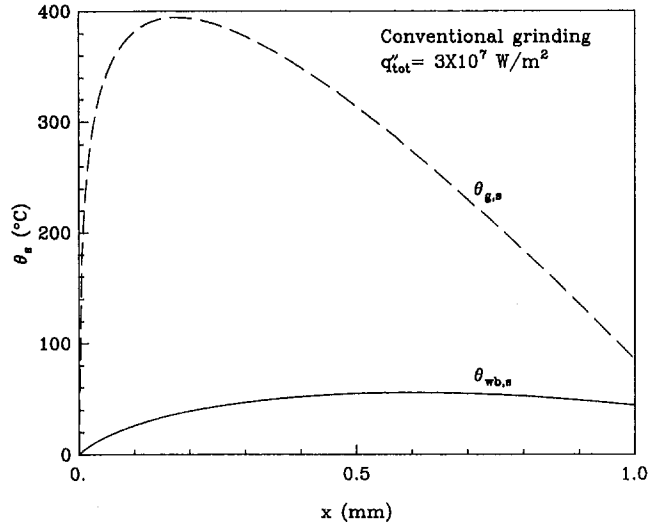



**Fig. 3(a) Temperature distributions (triangular grinding power input, $q''_{tot} = 3 \times 10^7$ W/m$^2$, conventional grinding with water-based grinding fluid)**

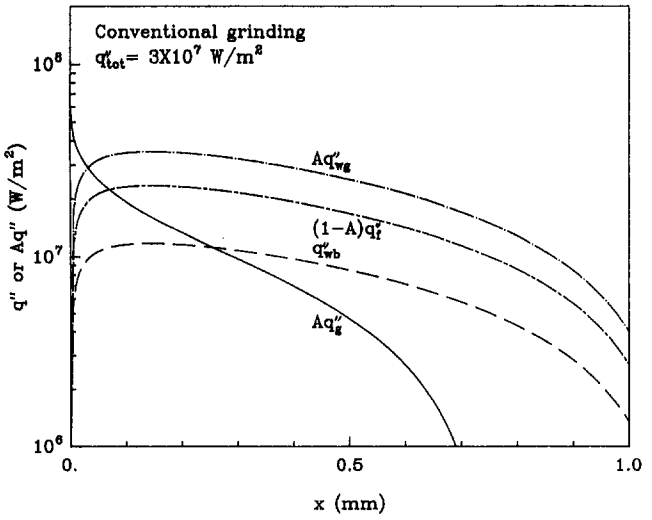



**Fig. 3(b) Heat flux distributions (triangular grinding power input, $q''_{tot} = 3 \times 10^7$ W/m$^2$, conventional grinding with water-based grinding fluid)**

same as in that earlier paper. To summarize, the theoretical model gives excellent agreement with experimental measurements for conventional grinding conditions (Yasui and Tsukuda, 1983). For creep feed grinding conditions (Ohishi and Furukawa, 1985), the model agrees well with experimental data when oil is used as the grinding fluid. However, the agreement is worse when water-based grinding fluid is used. There are several possible reasons for this discrepancy, for example, the effect of conduction in the direction of motion and the effect of shear plane heat generation. However, these will affect the temperature prediction for both water-based grinding fluid and oil. The true reasons for this discrepancy are still unresolved. Interested readers are referred to Jen (1993) for a detailed discussion.

**Conventional Grinding Conditions.** One example will be given to demonstrate the temperature and heat flux distributions along the grinding zone under conventional grinding conditions (see Table 1).

Figure 3($a$) demonstrates the temperature distributions along the grinding zone for a case where film boiling does not occur. A triangular grinding power input with the average grinding power input of $3 \times 10^7$ W/m$^2$ is used, which is specially chosen so that film boiling does not occur. It is clearly seen from the figure that the grain surface temperature rise, $\theta_{g,s}$, increases very rapidly near the beginning of the grinding zone, and reaches its maximum value of 392°C at $x = 0.18$ mm. The grain temperature rise decreases smoothly after the maximum temperature is reached. The workpiece background surface temperature rise, $\theta_{wb,s}$, is much lower than the grain surface temperature rise, $\theta_{g,s}$, throughout the grinding zone. A maximum workpiece background temperature rise of 56°C is reached at $x = 0.6$ mm. Experiments by Yasui (1984) show that the workpiece background temperature peaks in the middle of the grinding zone, which agrees qualitatively with the present model.

Figure 3($b$) shows the heat flux distributions along the grinding zone. The heat fluxes $q''_g$ and $q''_{wg}$ are usually two orders of magnitude larger than $q''_{wb}$ and $q''_f$. This is because these heat fluxes occur over the small contact area of a grain (see Eqs. (1) and (2)). In order to give a clearer picture of the energy partition, two curves for $Aq''_{wg}$ and $Aq''_g$ are demonstrated instead of $q''_{wg}$ and $q''_g$. These two heat fluxes ($Aq''_{wg}$ and $Aq''_g$) are per unit area of the grinding zone, rather than per unit area of actual contact. Similarly, $(1 - A)q''_f$ is used instead of $q''_f$.

It can be noted from Eq. (2) that the curve for $Aq''_{wg}$ is equal to the sum of the curves of $q''_{wb}$ and $(1 - A)q''_f$. A triangular grinding power input is used with its maximum at the beginning of the grinding zone. It has been shown in Eq. (13) that the grain

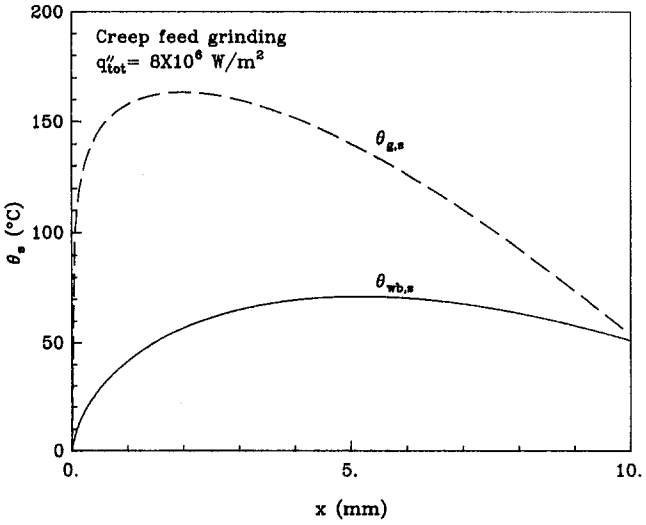



**Fig. 4(a) Temperature distributions (triangular grinding power input, $q''_{tot} = 8 \times 10^6$ W/m$^2$, creep feed grinding with water-based grinding fluid)**

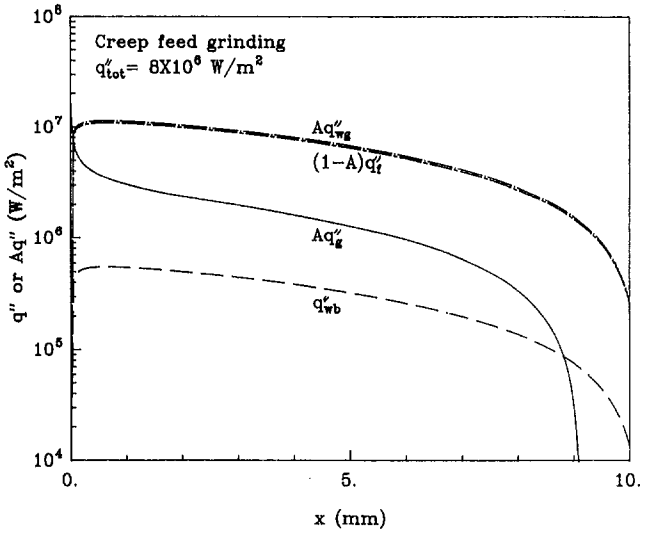



**Fig. 4(b) Heat flux distributions (triangular grinding power input, $q''_{tot} = 8 \times 10^6$ W/m$^2$, creep feed grinding with water-based grinding fluid)**



Downloaded 12 Dec 2010 to 193.140.21.150. Redistribution subject to ASME license or copyright; see http://www.asme.org/terms/Terms_Use.cfm

heat flux ($q''_g$) is equal to the grinding power input at $x = 0$. It can be seen that $Aq''_g = 6 \times 10^7$ W/m$^2$ at $x = 0$ (two times the average grinding power input), and smoothly decreases. The grain heat flux, $Aq''_g$, becomes negative after about $x = 0.75$ mm, which is not shown in the figure. This means that the heat generated at the grain/workpiece interface is totally removed by the workpiece along with additional heat from the grain. This can be explained as follows. The temperature underneath a grain reaches a maximum early in the grinding zone (see Fig. 3($a$)) and then decreases. At some distance from the surface, the grain remains hot and therefore heat is transferred toward the surface. The workpiece cools faster than the grain due to such effects as convection to the fluid and its larger volume for heat diffusion. Therefore, the workpiece heat flux remains positive from the surface into the cooler region of the workpiece. Similar behavior was also found in an analysis presented by Guo and Malkin (1995). It can be seen that the heat that enters the workpiece ($Aq''_{wg}$) increases very rapidly near the beginning of the grinding zone, and reaches its maximum of $3 \times 10^7$ W/m$^2$ at $x = 0.1$ mm. After the maximum temperature point, $Aq''_{wg}$ decreases throughout the grinding zone. Note that the heat that enters the workpiece ($Aq''_{wg}$) is either removed by the workpiece ($q''_{wb}$) or the grinding fluid ($(1 - A)q''_f$). It can be seen that the heat removed by the grinding fluid is about two times larger than the heat removed by the workpiece. In fact, 67 percent of the heat that enters the workpiece (or about 52 percent of $q_{tot}$) is removed by the grinding fluid. It should be noted that the grinding fluid often undergoes film boiling under conventional grinding conditions, which greatly reduces the percentage of the heat removed by the grinding fluid (Lavine and Malkin, 1990).

**Creep Feed Grinding Conditions.** One example will be given here to show the temperatures and heat flux distributions along the grinding zone under creep feed grinding conditions. The grinding conditions are the typical creep feed conditions given in Table 1.

Figure 4($a$) demonstrates the temperature distributions along the grinding zone for a case without film boiling. The average grinding power input is $8 \times 10^6$ W/m$^2$. A triangular grinding power input is used with its maximum at the beginning of the grinding zone. The shapes of the temperature curves are similar to the conventional case shown in Fig. 3($a$). Figure 4($b$) shows the heat flux distributions along the grinding zone. In comparison to the example shown in Fig. 3($b$) for conventional grinding conditions, the heat that enters the workpiece ($Aq''_{wg}$) is almost totally removed by the grinding fluid ($(1 - A)q''_f$) under creep feed grinding conditions, while a significant portion of the heat remained in the workpiece ($q''_{wb}$) under conventional grinding conditions. This was also confirmed experimentally by Shafto et al. (1975), in which they showed that most of the heat that enters the workpiece is removed by the grinding fluid.

## Conclusions

A theoretical model has been developed to predict the temperature and heat flux distributions along the grinding zone. This model is developed successively by improving the earlier models (Lavine and Jen, 1991a, b; Jen and Lavine, 1992a), and eliminates many deficiencies encountered in the previous studies by many researchers. Several major conclusions can be made as follows:

1 Instead of assuming uniform heat flux into the workpiece, wheel, and fluid, the heat fluxes are allowed to vary with $x$ by using Duhamel's Theorem.

2 As shown by Kohli (1993), a triangular grinding power input may be more appropriate under real grinding conditions. With triangular grinding power input, the present model demonstrates that the workpiece temperature distribution is distinctly different from the workpiece temperature distribution when a uniform grinding power input is used.

3 For the case of triangular grinding power input, the maximum temperature is located somewhere in the middle, which agrees with experimental results (e.g., Kohli, 1993; Yasui, 1984), but the maximum temperature is located at the end of the grinding zone when a uniform grinding power is used. It is worth noting that if the maximum temperature occurs at the end of the grinding zone, this temperature could possibly be easily reduced by injecting grinding fluid at the end of the grinding zone.

4 The maximum workpiece temperature calculated for the uniform grinding power input case agrees very well with the same temperature predicted when a triangular grinding power is used.

5 In comparison to conventional grinding conditions, the heat removed by the grinding fluid is dominant under creep feed grinding conditions. This is in agreement with the results presented by Shafto et al. (1975).

## Acknowledgments

The support of the National Science Foundation, General Motors, and General Electric is gratefully acknowledged.

## References

Andrew, C., Howes, T. D., and Pearce, T. R. A., 1985, *Creep Feed Grinding*, Holt, Rinehart, and Winston, New York, pp. 12–15.

Carslaw, H. S., and Jaeger, J. C., 1947, *Conduction of Heat in Solids*, Oxford University Press, London, United Kingdom.

DesRuisseaux, N. R., and Zerkle, R. D., 1970a, "Thermal Analysis of the Grinding Process," ASME *Journal of Engineering for Industry*, Vol. 92, pp. 428–434.

DesRuisseaux, N. R., and Zerkle, R. D., 1970b, "Temperature in Semi-infinite and Cylindrical Bodies Subjected to Moving Heat Sources and Surface Cooling," ASME JOURNAL OF HEAT TRANSFER, Vol. 92, pp. 456–464.

Guo, C., and Malkin, S., 1995, "Analysis of Energy Partition in Grinding," ASME *Journal of Engineering for Industry*, Vol. 117, pp. 55–61.

Hahn, R. S., 1956, "The Relation Between Grinding Conditions and Thermal Damage in the Workpiece," *Transactions of the ASME*, Vol. 78, pp. 807–812.

Jen, T. C., and Lavine, A. S., 1992a, "Thermal Aspects of Grinding: The Effect of Flow Boiling," in: *Transport Phenomena in Materials Processing and Manufacturing*, ASME HTD-Vol. 196, pp. 91–98.

Jen, T. C., and Lavine, A. S., 1992b, "Thermal Aspects of Grinding: An Improved Model of Heat Transfer to Workpiece, Wheel and Fluid," in: *Heat Transfer in Material Processing*, ASME HTD-Vol. 224, pp. 1–7.

Jen, T. C., 1993, "Thermal Aspects of Grinding: Heat Transfer to Workpiece, Wheel and Fluid," Ph.D. Dissertation, MANE Department, UCLA.

Kohli, S., 1993, "Energy Partition for Grinding With Aluminum Oxide and Cubic Boron Nitride Abrasive Wheels," Master's Thesis, Department of Mechanical Engineering, University of Massachusetts.

Lavine, A. S., Malkin, S., and Jen, T. C., 1989, "Thermal Aspects of Grinding With CBN Wheels," *CIRP Annals*, Vol. 38, No. 1, pp. 557–560.

Lavine, A. S., and Malkin, S., 1990, "The Role of Cooling in Creep Feed Grinding," *Int. J. Adv. Manuf. Technol.*, Vol. 5, pp. 97–111.

Lavine, A. S., and Jen, T. C., 1991a, "Thermal Aspects of Grinding: Heat Transfer to Workpiece, Wheel, and Fluid," ASME JOURNAL OF HEAT TRANSFER, Vol. 113, pp. 296–303.

Lavine, A. S., and Jen, T. C., 1991b, "Coupled Heat Transfer to Workpiece, Wheel, and Fluid in Grinding, and the Occurrence of Workpiece Burn," *Int. J. Heat Mass Transfer*, Vol. 34, No. 4/5, pp. 983–992.

Lavine, A. S., 1991, "Thermal Aspects of Grinding: The Effect of Heat Generation at the Shear Planes," *Annals of the CIRP*, Vol. 40, No. 1, pp. 343–345.

Malkin, S., and Anderson, R. B., 1974, "Thermal Aspects of Grinding. Part 1—Energy Partition," ASME *Journal of Engineering for Industry*, Vol. 96, pp. 1177–1183.

Malkin, S., 1974, "Thermal Aspects of Grinding. Part 2—Surface Temperatures and Workpiece Burn," ASME *Journal of Engineering for Industry*, Vol. 96, pp. 1184–1191.

Malkin, S., 1984, "Grinding of Metals: Theory and Application," *J. Applied Metalworking*, Vol. 3, No. 2, pp. 95–109.

Ohishi, S., and Furukawa, Y., 1985, "Analysis of Workpiece Temperature and Grinding Burn in Creep Feed Grinding," *Bulletin of JSME*, Vol. 28, No. 242, pp. 1775–1781.

Outwater, J. O., and Shaw, M. C., 1952, "Surface Temperatures in Grinding," *Transactions of ASME*, Vol. 74, pp. 73–86.

Shafto, G. R., Howes, T. D., and Andrew, C., 1975, "Thermal Aspects of Creep Feed Grinding," *16th MTDR Conf.*, Manchester, United Kingdom, pp. 31–37.

Snoeys, R., Maris, M., and Peters, J., 1978, "Thermally Induced Damage in Grinding," *CIRP Annals*, Vol. 27, No. 2, pp. 571–581.

Wylie, C. R., and Barrett, L. C., 1982, *Advanced Engineering Mathematics*, McGraw-Hill, pp. 454–455.

Yasui, H., and Tsukuda, S., 1983, "Influence of Fluid Type on Wet Grinding Temperature," *Bull. Japan Soc. of Prec. Engg.*, Vol. 17, No. 2, pp. 133–134.

Yasui, H., 1984, "On Limiting Grinding Condition for Fluid Supply Effect," *Proceedings of 5th International Conference on Production Engineering*, Tokyo, pp. 58–63.



Downloaded 12 Dec 2010 to 193.140.21.150. Redistribution subject to ASME license or copyright; see http://www.asme.org/terms/Terms_Use.cfm

# Predicting the Impact of Quenching on Mechanical Properties of Complex-Shaped Aluminum Alloy Parts

**D. D. Hall**
Graduate Research Assistant.

**I. Mudawar**
Professor and Director.

Boiling and Two-Phase Flow Laboratory,
School of Mechanical Engineering,
Purdue University,
West Lafayette, IN 47907

*The mechanical properties of age-hardenable aluminum alloy extrusions are critically dependent on the rate at which the part is cooled (quenched) after the forming operation. The present study continues the development of an intelligent spray quenching system, which selects the optimal nozzle configuration based on part geometry and composition such that the magnitude and uniformity of hardness (or yield strength) is maximized while residual stresses are minimized. The quenching of a complex-shaped part with multiple, overlapping sprays was successfully modeled using spray heat transfer correlations as boundary conditions within a finite element program. The hardness distribution of the heat-treated part was accurately predicted using the quench factor technique; that is, the metallurgical transformations that occur within the part were linked to the cooling history predicted by the finite element program. This study represents the first successful attempt at systematically predicting the mechanical properties of a quenched metallic part from knowledge of only the spray boundary conditions.*

## Introduction

Aluminum alloys are used for a wide range of applications, from common household products such as storm-screen window frames to structural members in military and commercial aircraft. The competitiveness of the global marketplace requires that heat-treated alloys satisfy stringent metallurgical requirements. The mechanical and metallurgical properties of extrusions and forgings of age-hardenable aluminum alloys are critically dependent on the rate at which the part is cooled (quenched) after the forming operation. If the final product does not meet the required specifications, a costly posttreatment operation is required, consisting of additional heat treatment and mechanical straightening of warped sections. In addition, the effect of posttreatment operations on the final metallurgical properties can seldom be predicted with accuracy. Thus, an intelligent spray quenching system is proposed that will optimize the quenching process to achieve superior part quality and consistency between production runs with minimal cost.

Spray quenching involves directing high-pressure sprays of liquid onto areas of the part where higher cooling rates are required. The droplets within the spray impact the part surface and remove heat very efficiently. Fairly uniform cooling of the part can be achieved by proper location and operation of the spray nozzles. Currently, the initial nozzle placement and operating pressure is one of trial and error, guided by the visual appearance of the part and the experience of the operator. Improper placement and operation of the nozzles may result in high residual stresses, nonuniform properties, low corrosion resistance, warping, soft spots, and cracking, all of which may lead to low strength and premature part failure. The nozzle configuration is subsequently modified until post-heat treatment tests reveal that the required mechanical and metallurgical properties were obtained.

The present study is part of an ongoing cross-disciplinary initiative at the Purdue University Boiling and Two-Phase Flow Laboratory involving several engineering departments, whose primary goal is the development of the CAD-based intelligent spray quenching system proposed by Deiters and Mudawar (1989) and illustrated in Fig. 1. The operator would input the composition and geometry of the extrusion or forging into the CAD system and, after consulting its extensive data bases, the system would output the nozzle configuration (type, placement, and pressure) required to achieve optimum cooling and the desired mechanical and metallurgical properties, thus eliminating the need for costly posttreatment operations. The specific objective of the present study is the following: predict the hardness distribution of a heat-treated Al 2024-T6 extrusion using the finite element method and compare with measurements in order to demonstrate that it is possible to configure a quenching system that would yield the desired product specifications without costly testing.

**Metallurgical Aspects of Heat Treatment.** The present study deals with heat-treatable aluminum–copper alloys, specifically Al 2024, which is composed of 93.5 percent aluminum, 4.4 percent copper, 1.5 percent magnesium, and 0.6 percent manganese. The development of the alloy microstructure during the heat treatment process can be more easily described by considering a two-component alloy consisting of aluminum and copper. Figure 2 shows the aluminum-rich region of the aluminum-copper phase diagram and the approximate composition range of the 2××× series of aluminum alloys (indicated by the shaded region), which are characterized by their ability to be significantly strengthened by artificial aging (precipitation hardening). The evolution of the alloy microstructure during slow cooling can be analyzed using phase diagrams, which represent the equilibrium phases associated with various combinations of temperature and composition. However, during the quenching process, phase transformations are time dependent and phase diagrams only serve as a general guide to understanding the heat treatment process.

The heat treatment process begins by heating the alloy to the solution heat treatment temperature, which is above the solvus temperature (the point where copper becomes soluble within aluminum) but below the solidus temperature (the point where the alloy begins to melt, complete melting occurs at the liquidus

Contributed by the Heat Transfer Division for publication in the JOURNAL OF HEAT TRANSFER. Manuscript received by the Heat Transfer Division March 1994; revision received July 1994. Keywords: Boiling, Materials Processing and Manufacturing Processes, Sprays/Droplets. Associate Technical Editor: A. Faghri.



Copyright © 1995 by ASME

Downloaded 12 Dec 2010 to 193.140.21.150. Redistribution subject to ASME license or copyright; see http://www.asme.org/terms/Terms_Use.cfm

temperature). When held above the solvus temperature for sufficient time, the copper (solute) will diffuse completely into the aluminum (solvent) to form a solid solution. Subsequent cooling of the alloy below the solvus temperature causes the solid solution to become supersaturated and the alloy seeks equilibrium by precipitating the $\theta$-phase, $CuAl_2$. As illustrated in Fig. 2, rapid cooling suppresses precipitation, preserving the homogeneous supersaturated solid solution, and results in an alloy that is age-hardenable. Conversely, slow cooling causes coarse precipitates to form at the grain boundaries and produces an alloy that cannot be age-hardened. Aging the alloy at an intermediate temperature allows the formation of a fine dispersion of precipitates within the aluminum grains, which hinders deformations and consequently increases the strength and hardness of the alloy. If the precipitates begin to coalesce into a more coarse dispersion, the alloy is overaged and there will be a smaller number of dislocation barriers, thus reducing strength and hardness.

From an age-hardenability viewpoint, it seems desirable to cool the entire part as quickly as possible from the solution heat treatment temperature. However, very rapid quenching of the exterior of a part having a cross section with large variations in thickness causes the interior of thin sections to cool much quicker than the interior of thick sections. Large spatial temperature gradients will exist during cooling, which lead to high thermal stresses and, hence, residual stresses and possible warping (if the part is relatively thin and the gradients are severe). If the part is cooled too slowly, uniform cooling may exist, but the desired strength or hardness cannot be obtained in the subsequent age-hardening heat treatment. Consequently, an optimum cooling strategy exists within a window of acceptable cooling rates such that the part is cooled as quickly and uniformly as possible (Chevrier et al., 1981). The proper placement and operation of spray nozzles allows the local surface heat flux to be controlled such that all locations within the part cool at an optimum rate. Before the tradeoff between maximizing strength and minimizing residual stresses can be analyzed, the quality of the quenching process must be quantified.

**C-Curve.** Fink and Willey (1948) pioneered the attempt to describe the relationship between cooling rate (quenching rate) and final alloy strength by identifying the temperature range over which the cooling rate has its most critical influence on the mechanical properties of the aged material. Their research resulted in the development of the C-curve, which represents the time required at different temperatures to precipitate a sufficient amount of solute to reduce the maximum attainable strength or hardness by a given percentage. Fink and Willey used a delayed quenching technique to determine the C-curve for rolled and extruded Al 7075-T6. Small samples, which could be considered isothermal at any given time, were rapidly quenched from the solution heat treatment temperature to intermediate temperatures where they were held for a given time and then rapidly quenched to room temperature. The samples were then artificially aged as specified by the temper designation and their yield strength, tensile strength, or hardness were measured. This procedure was repeated using different intermediate temperatures and different holding times. The locus of points on temperature–time coordinates with a particular hardness or strength defines a C-curve for the alloy. Evancho and Staley (1974) and Staley (1987) used transformation rate equations developed by Cahn (1956a) to derive a theoretical equation for the C-curve,

$$C_t = -k_1 k_2 \exp\left(\frac{k_3 k_4^2}{RT(k_4 - T)^2}\right) \exp\left(\frac{k_5}{RT}\right), \qquad (1)$$

where $C_t$ is the critical time required at a temperature, $T$, to precipitate a sufficient amount of solute to reduce the maximum attainable strength or hardness by the percentage represented by the C-curve. $k_1$ is the natural logarithm of the fraction of solute not precipitated or, as will be seen later, the yield-strength ratio or hardness ratio. The C-curve constants for Al 2024-T6 are $k_2 = 2.38 \times 10^{-12}$, $k_3 = 1.31 \times 10^3$, $k_4 = 8.40 \times 10^2$, and $k_5 = 1.47 \times 10^5$ (Kim, 1989).

The shape of the C-curve can be explained on the basis of the variation of nucleation and growth rates with temperature. At relatively high temperatures, the driving force for transformation is very small so that both nucleation rates (rate at which nuclei of a critical size or larger appear) and subsequent growth rates (rate of continued precipitation at nuclei above the critical size) are slow and a long time is required for transformation. At relatively low temperatures, slow diffusion rates (rate at which atoms cluster to form a nucleus) limit the rate of transformation. Therefore, a maximum precipitation rate is obtained at intermediate temperatures where diffusion rates remain high and the instability of the supersaturated solid solution causes high nucleation and growth rates.

Fink and Willey (1948) used average quenching rates through this critical temperature range to assess the quality of a quenching process. However, when cooling rates vary considerably during the quench (e.g., complex-shaped part), quantitative predictions of the final mechanical properties using average quenching rates were not possible. The quench factor technique developed by Evancho and Staley (1974) uses information from the entire C-curve to predict how the thermal history affects the final mechanical properties of wrought alloys.

**Quench Factor Technique.** A quench factor analysis of a transient nonisothermal quench is only valid if the internal re-

## Nomenclature

$c_p$ = specific heat at constant pressure
$C_t$ = critical time defined in Eq. (1)
$d_{32}$ = Sauter mean diameter (SMD)
$h$ = convection heat transfer coefficient
$h_{fg}$ = latent heat of vaporization
$H$ = Rockwell B hardness
$k$ = thermal conductivity
$k_1$ = natural logarithm of hardness ratio (or fraction of solute not precipitated) used to define the C-curve
$k_i$ = empirical constant in Eq. (1), $i$ = 2, 3, 4, or 5
$Nu_{32}$ = Nusselt number = $h\, d_{32}/k_f$
Pr = Prandtl number
$q''$ = heat flux
$Q''$ = volumetric spray flux
$R$ = universal gas constant = 8.314 J/gmol·K
$Re_{32}$ = Reynolds number = $\rho_f Q'' d_{32}/\mu_f$
$t$ = time
$T$ = temperature
$\Delta T$ = $T_s - T_f$
$\Delta T_{sub}$ = liquid subcooling = $T_{sat} - T_f$
$U_m$ = mean drop velocity
$x$ = coordinate along spray major axis
$y$ = coordinate along spray minor axis
$\zeta$ = fraction of solute precipitated during the quench
$\mu$ = dynamic viscosity
$\rho$ = density
$\sigma$ = yield strength; surface tension
$\tau$ = quench factor

**Subscripts**

CHF = critical heat flux
DFB = departure from film boiling
$f$ = saturated liquid; final condition
$g$ = saturated vapor
$i$ = initial condition
max = maximum
min = minimum
MIN = minimum heat flux
OSP = onset of single-phase cooling
$s$ = surface condition
sat = saturated condition



/ asme v2439 0541 Mp 2 Monday Apr 10 10:22 AM LP-J Heat (May) 0541

Downloaded 12 Dec 2010 to 193.140.21.150. Redistribution subject to ASME license or copyright; see http://www.asme.org/terms/Terms_Use.cfm

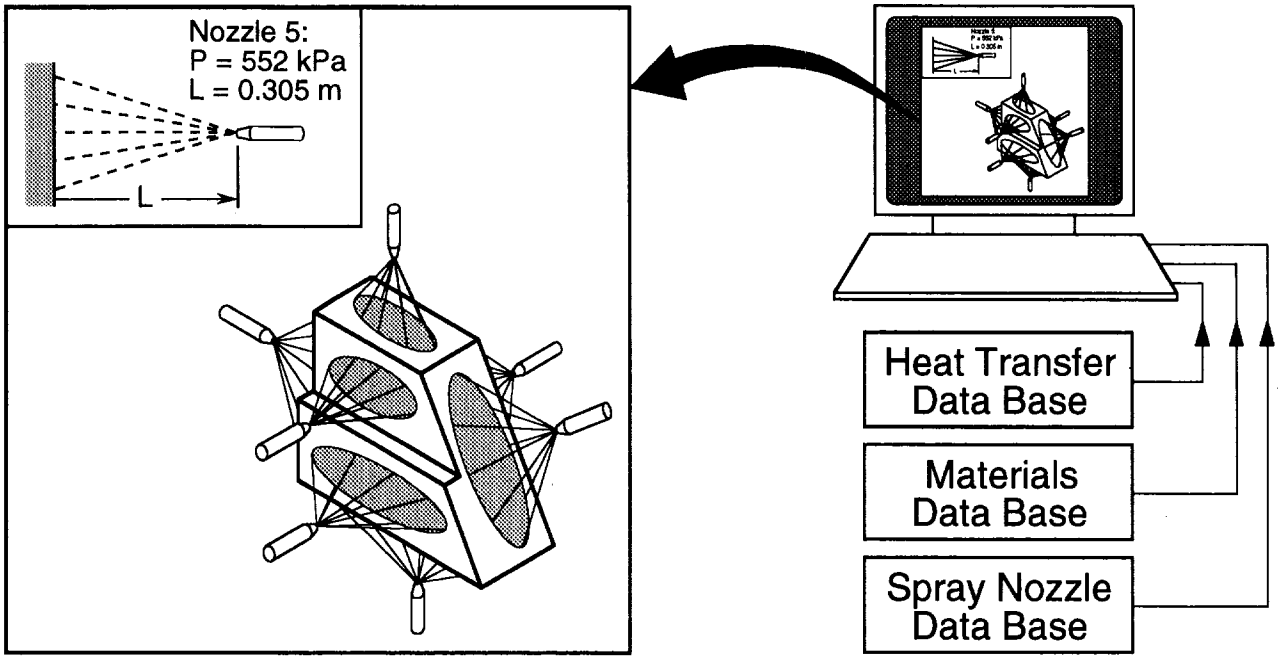



**Fig. 1 CAD-based intelligent spray-quenching system**

action (precipitation of solute), which occurs during cooling below the solvus temperature, is additive (Evancho and Staley, 1974). Avrami (1940) determined that a reaction is additive when the nucleation rate is proportional to the growth rate over the range of temperatures experienced during the reaction (i.e., precipitation kinetics remain unchanged). Cahn (1956b) demonstrated that additivity, as defined by Avrami, is observed in a reaction where the precipitation rate is only a function of temperature and amount of phase transformation previously completed. Furthermore, Cahn showed that a measure of the amount transformed during continuous cooling is given by

$$\tau = \int_{t_i}^{t_f} \frac{dt}{C_t}, \tag{2}$$

where $\tau$ was later referred to as the quench factor by Evancho and Staley (1974). Quench factors of zero and infinity correspond to suppression of precipitation and complete precipitation, respectively. The integral in Eq. (2) can be numerically calculated, as shown in Fig. 3, by discretizing the temperature–time cooling curve into small time increments. Each incremental quench factor represents the ratio of the amount of time the alloy was at a specific temperature to the amount of time required to obtain a specified amount of transformation at that temperature. As the time increment is decreased, the nonisothermal quench will essentially become a series of isothermal quenches, which are additive if the alloy obeys the rule of additivity over the entire range of transformation temperatures. In the process of determining the C-curve for Al 2024, Kim (1989) verified the assumption of additivity for this alloy.

Evancho and Staley (1974) developed the following equation to describe the precipitation kinetics of aluminum alloys during continuous cooling:

$$\zeta = 1 - \exp(k_1\tau), \tag{3}$$

where $\zeta$ equals the fraction of solute precipitated and $k_1$ corresponds to the C-curve from which the quench factor was calculated. Evancho and Staley (1974) and Staley (1987) developed the following equation to predict yield strength, $\sigma$, using Eq. (3) under the premise that the relative strength of age-hardenable aluminum alloys is directly related to the amount of solute remaining in solid solution $(1 - \zeta)$ after the quench (Conserva and Fiorini, 1973),

$$\frac{\sigma - \sigma_{\min}}{\sigma_{\max} - \sigma_{\min}} = \exp(k_1\tau), \tag{4}$$

where $\sigma_{\max}$ and $\sigma_{\min}$ are the maximum and minimum yield strengths of age-hardened specimens, which have been cooled from the solution heat treatment temperature at a near-infinite and extremely slow rate, respectively.

Axter (1980) performed various quenching experiments and concluded that the resistance to indentation, hardness, was proportional to yield strength for high strength aluminum alloys. The relative ease of measuring hardness prompted Bates (1988) and Kim (1989) to define a hardness ratio that would replace the yield strength ratio in Eq. (4),

$$\frac{H - H_{\min}}{H_{\max} - H_{\min}} = \exp(k_1\tau). \tag{5}$$

where $H_{\max}$ = 78.4 HRB and $H_{\min}$ = 2.2 HRB (Kim, 1989).

Thus, given the temperature–time history and C-curve of a wrought alloy, the final mechanical properties (strength or hardness) of the part can be determined using the quench factor technique. The quench factor technique has been successfully used to predict the yield strength and hardness of small (i.e., isothermal) aluminum alloy parts (Evancho, 1973; Evancho and Staley, 1974; Sawtell, 1984; Bates, 1987; Bates and Totten, 1988; Kim, 1989) and steel parts (Bates, 1988; Bates and Totten, 1992).

## Experimental Methods

**Materials Processing Test Bed.** The materials processing test bed shown in Fig. 4(*a*) was used to simulate the heat treatment process (solution heat treating, spray quenching, and artificial aging) of aluminum alloys in an industrial environment. The testpiece was heated in a Lindberg model 54857-V tube furnace having a cylindrical heating length of 60 cm and diameter of 15 cm. A three-zone programmable controller was used to control temperature of the three independent heating zones, thus ensuring uniform heating of the test piece. The furnace was mounted above the quench tank to allow the test piece to be



Downloaded 12 Dec 2010 to 193.140.21.150. Redistribution subject to ASME license or copyright; see http://www.asme.org/terms/Terms_Use.cfm

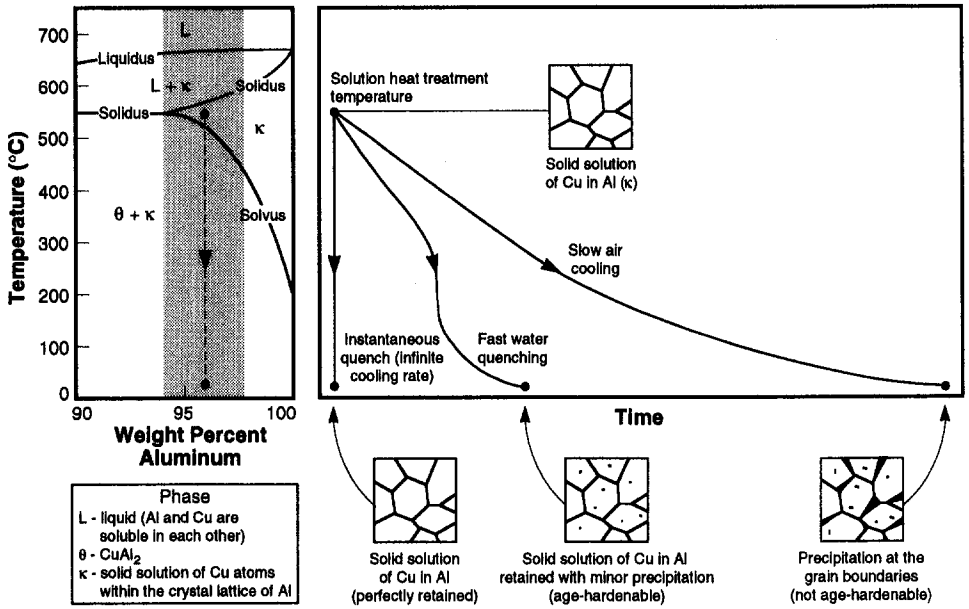
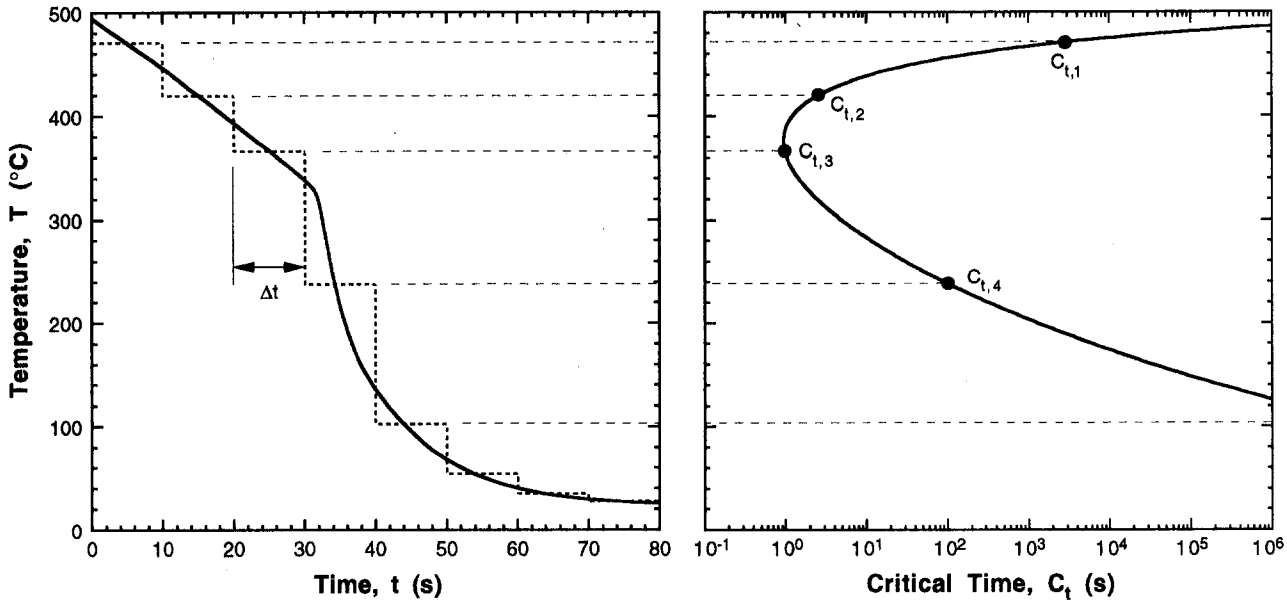



**Fig. 2 Aluminum-rich region of the Al–Cu phase diagram and the microstructure that develops following quenching of an Al–Cu (4.4 wt%) alloy**

lowered into the spray chamber using a vertical translation system. The spray chamber was fabricated from optical grade Lexan sheet to permit observation of the spray quenching process. Steam produced by the quench was removed by an exhaust system connected to the back of the test chamber. The lower quench tank served as a storage reservoir for recirculation of water during the quench. The fluid delivery loop contained a fan-cooled centrifugal pump, rated to deliver $25.2 \times 10^{-3}$ m$^3$/s (40 gpm) at 690 kPa (100 psi), and a 5 $\mu$m filter. The large capacity of the pump required a bypass line back into the quench tank to maintain flow stability.

Water was delivered to the spray nozzles using four nozzle arrays, one on each side of the spray chamber. The nozzle arrays, which consisted of three nozzles vertically separated by 11.4 cm (4.5 in.), allowed some flexibility of nozzle positioning relative to the test piece. The operating pressure of each nozzle array was independently controlled using four globe valves connected to four steel-reinforced flexible rubber hoses. Pressure was moni-




$$\tau = \int_{t_i}^{t_f} \frac{dt}{C_t} \approx \frac{\Delta t_1}{C_{t,1}} + \frac{\Delta t_2}{C_{t,2}} + \cdots + \frac{\Delta t_n}{C_{t,n}} = \sum_{m=1}^{n} \frac{\Delta t_m}{C_{t,m}} \quad \text{where} \quad C_t = -k_1 k_2 \exp\left(\frac{k_3 k_4^2}{RT(k_4 - T)^2}\right) \exp\left(\frac{k_5}{RT}\right), \ T \text{ in Kelvins}$$

$$H = H_{min} + (H_{max} - H_{min}) \exp(k_1 \tau)$$

**Fig. 3 Numerical calculation of the quench factor and hardness using a temperature–time curve and the C-curve**



Downloaded 12 Dec 2010 to 193.140.21.150. Redistribution subject to ASME license or copyright; see http://www.asme.org/terms/Terms_Use.cfm

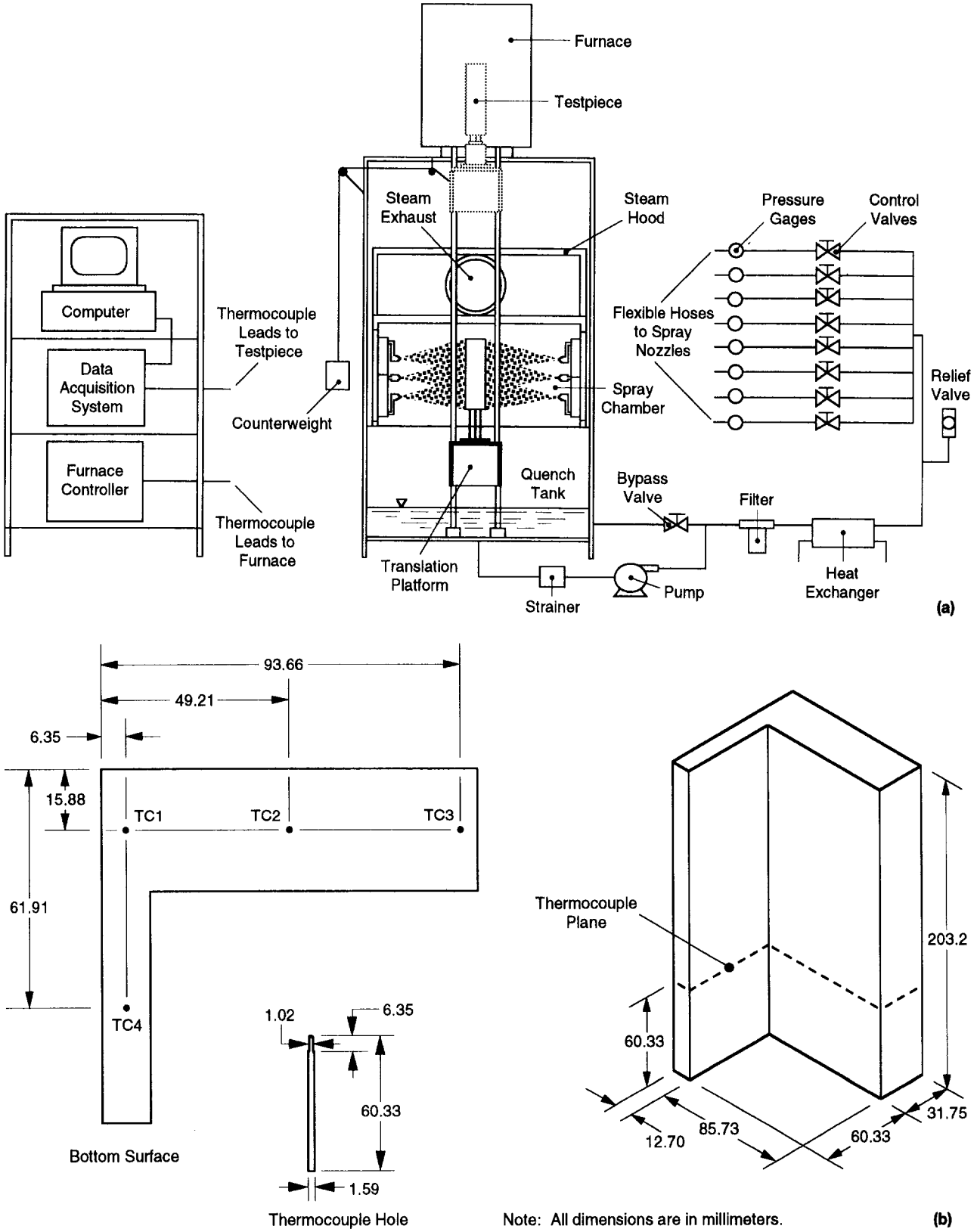



**Fig. 4** *(a)* **Schematic of the materials processing test bed;** *(b)* **Al 2024 L-shape dimensions and thermocouple placement**

tored using glycerin-filled stainless steel pressure gages with a range of 0–1.10 MPa (0–160 psi). The flat spray nozzles used in the present study were operated at a pressure of 552 kPa (80 psig) and a distance of 0.305 m (12 in.) from the test piece surface.

**L-Shaped Test Piece.** The L-shaped test piece shown in Fig. 4(*b*) was machined from an Al 2024 extrusion obtained from the Aluminum Company of America (ALCOA). The dimensions were chosen such that the effects of section thickness on cooling uniformity could be investigated both experimentally and nu-



Downloaded 12 Dec 2010 to 193.140.21.150. Redistribution subject to ASME license or copyright; see http://www.asme.org/terms/Terms_Use.cfm

merically. The thick and thin protruding sections had a thermal mass ratio of 4:1. The L-shape was instrumented with four chromel-alumel (type K) thermocouples, which consisted of 0.13 mm (0.005 in.) wire within a 0.81 mm (0.032 in.) diameter Inconel 600 sheathing with magnesium oxide insulation. The thermocouples were located such that the thermal history of the interior of both the thick and thin sections was fully characterized. Boron nitride powder, which has a thermal conductivity comparable to aluminum, was used to fill the void surrounding the thermocouple bead, thus ensuring excellent thermal contact with the alloy. Type K thermocouples were chosen for their high-temperature capabilities and adequate transient response. All thermocouples were placed in a plane three-tenths the length of the L-shape above the lower surface.

Surface roughness effects on the temperature-time history of spray quenched parts were observed by Rozzi (1991). Furthermore, Mudawar and Valentine (1989) and Klinzing et al. (1992) used polished surfaces to obtain the spray quenching heat transfer correlations used in the present numerical study (see Table 1). Therefore, the surface of the testpiece was carefully polished before each test to ensure uniform surface roughness and repeatability between quenches.

**Procedure.** The time the alloy is held at the solution heat treatment temperature depends upon the type of product, alloy composition, fabricating procedure, and section thickness. The extruded Al 2024 L-shape was heated to the solution heat treatment temperature of 495°C and held for 160 min before rapid quenching to room temperature. The subsequent artificial aging process resulting in the T6 temper consisted of 16 hr at 190°C (ASM, 1991).

Testing commenced with the raising of the test piece into the furnace using the vertical translation system. Accurate control of the furnace temperature was essential since the solution heat treatment temperature was only 7°C below the solidus temperature. When the test piece reached the solution heat treatment temperature (or artificial aging temperature), its temperature was constantly monitored to avoid overheating. The spray quenching process was initiated by engaging the pump and allowing the sprays to reach hydrodynamic equilibrium. The test piece was quickly lowered into the spray chamber using the translation system and thermocouple temperatures were recorded every 0.1 seconds throughout the quench.

A Goko Seiki Works model 3R hardness tester was used to measure Rockwell B hardness according to ASTM Standard E

**Table 1 Spray-quenching heat transfer correlations**

| Quenching (Boiling) Regime | Correlation |
|---|---|
| Film Boiling Regime (Klinzing et al., 1992) | $q'' = 6.325\times10^{1}\,\Delta T^{1.691}\,Q''^{0.264}\,d_{32}^{-0.062}$ |
| Point of Departure from Film Boiling (Klinzing et al., 1992) | $q''_{DFB} = 6.100\times10^{6}\,Q''^{0.588}\,U_m^{0.244}$<br>$\Delta T_{DFB} = 2.808\times10^{2}\,Q''^{0.087}\,U_m^{0.110}\,d_{32}^{-0.035}$ |
| Film-Wetting Regime (Klinzing et al., 1992) | $q'' = q''_{MIN} + \left(q''_{DFB} - q''_{MIN}\right)\left(\frac{\Delta T - \Delta T_{MIN}}{\Delta T_{DFB} - \Delta T_{MIN}}\right)^2$ |
| Point of Minimum Heat Flux (Klinzing et al., 1992) | $q''_{MIN} = 3.324\times10^{6}\,Q''^{0.544}\,U_m^{0.324}$<br>$\Delta T_{MIN} = 2.049\times10^{2}\,Q''^{0.066}\,U_m^{0.138}\,d_{32}^{-0.035}$ |
| Transition Boiling Regime (Klinzing et al., 1992) | $q'' = q''_{CHF} - \frac{q''_{CHF} - q''_{MIN}}{\left(\Delta T_{CHF} - \Delta T_{MIN}\right)^3}\left[\Delta T_{CHF}^3 - 3\,\Delta T_{CHF}^2\,\Delta T_{MIN} + 6\,\Delta T_{CHF}\,\Delta T_{MIN}\,\Delta T - 3\left(\Delta T_{CHF} + \Delta T_{MIN}\right)\Delta T^2 + 2\,\Delta T^3\right]$ |
| Point of Critical Heat Flux (Mudawar and Valentine, 1989) | $\frac{q''_{CHF}}{\rho_g\,h_{fg}\,Q''} = 122.4\left[1 + 0.0118\left(\frac{\rho_g}{\rho_f}\right)^{1/4}\left(\frac{\rho_f\,c_{p,f}\,\Delta T_{sub}}{\rho_g\,h_{fg}}\right)\right]\left(\frac{\sigma}{\rho_f\,Q''^2\,d_{32}}\right)^{0.198}$<br>$\Delta T_{CHF} = 18.0\left[\left(\rho_g\,h_{fg}\,Q''\right)\left(\frac{\sigma}{\rho_f\,Q''^2\,d_{32}}\right)^{0.198}\right]^{1/5.55}$ |
| Nucleate Boiling Regime (Mudawar and Valentine, 1989) | $q'' = 1.87\times10^{-5}\left(\Delta T\right)^{5.55}$ |
| Onset of Single-Phase Cooling (Mudawar and Valentine, 1989) | $\Delta T_{OSP} = 13.43\,Re_{32}^{0.167}\,Pr_f^{0.123}\left(\frac{k_f}{d_{32}}\right)^{0.220}$ |
| Single-Phase Regime (Mudawar and Valentine, 1989) | $Nu_{32} = 2.512\,Re_{32}^{0.76}\,Pr_f^{0.56}$ |

Units of the parameters: $q''$ (W/m$^2$), $\Delta T = T_s - T_f$ (°C), $Q''$ (m$^3$·s$^{-1}$/m$^2$), $U_m$ (m/s), $d_{32}$ (m), $h$ (W/m$^2$·K), $\rho_f$ (kg/m$^3$), $\rho_g$ (kg/m$^3$), $h_{fg}$ (J/kg), $c_{p,f}$ (J/kg·K), $k_f$ (W/m·K), $\mu_f$ (N·s/m$^2$), $\sigma$ (N/m)

Dimensionless parameters: $Nu_{32} = h\,d_{32}/k_f$, $Pr_f = c_{p,f}\,\mu_f/k_f$, $Re_{32} = \rho_f\,Q''\,d_{32}/\mu_f$

Range of validity of the correlations:

$T_f = 23$ °C, $Q'' = 0.58\times10^{-3} - 9.96\times10^{-3}$ m$^3$·s$^{-1}$/m$^2$, $U_m = 10.1 - 29.9$ m/s, $d_{32} = 0.137\times10^{-3} - 1.35\times10^{-3}$ m

Properties: The fluid properties used in the correlations for the point of incipient boiling and the single-phase regime are evaluated at the film temperature, $T_{film} = 0.5\,(T_s + T_f)$. The fluid properties used in the CHF correlation are evaluated at the fluid saturation temperature (Mudawar and Valentine, 1989).



Downloaded 12 Dec 2010 to 193.140.21.150. Redistribution subject to ASME license or copyright; see http://www.asme.org/terms/Terms_Use.cfm

18-93 (ASTM, 1993). Several external hardness measurements were conducted on the heat-treated test piece. Internal hardness measurements were subsequently obtained by cutting the test piece near the thermocouple plane using a wet band saw. The exposed surface was lightly milled, sanded, and polished to provide a smooth measurement surface. Lubricating oil was used during the milling process to eliminate heating of the test piece, which would possibly invalidate the measurements. The sanding and polishing processes removed material on the surface that was worked beyond its yield strength during the milling process.

## Numerical Methods

**Determination of the Heat Transfer Boundary Condition.** The spray quenching heat transfer correlations developed by Mudawar and Valentine (1989) and Klinzing et al. (1992), shown in Table 1, depend on values of the spray hydrodynamic parameters (volumetric spray flux, mean drop diameter, and mean drop velocity) just prior to impingement upon the surface. Hence, accurate knowledge of the spatial distribution of the spray hydrodynamic parameters was essential if the spray quenching process was to be numerically modeled. The spray hydrodynamic parameters of the nozzles used in the materials processing test bed were measured at discrete locations within the spray field and mathematical models of the spatial distributions were developed.

Flat spray nozzles are commonly used in spray quenching since they can provide relatively even spray coverage when several nozzles with overlapping spray patterns are utilized. The elliptical spray pattern generated by the flat spray nozzles facilitated the identification of major ($x$ axis) and minor ($y$ axis) spray axes. Visual examination of a typical flat spray nozzle revealed a uniform spray pattern, which was fairly symmetric about the major and minor axes.

The volumetric spray flux, $Q''$, was defined as the local volume flow rate per unit surface area. Measurements revealed that the volumetric spray flux exhibited a maximum value near the center of the spray and decayed exponentially away from the center. Thus, the spatial distribution of the volumetric spray flux was modeled by

$$Q'' = A_0 \exp(A_1 x^2 + A_2 y^2), \qquad (6)$$

where $A_0$ is the volumetric spray flux measured at the nozzle centerline and $A_1$ and $A_2$ are constants determined using a least-squares curve fit. The volumetric spray flux model for the flat spray nozzles used in the present study is illustrated in Fig. 5. A repeatability study was also conducted to verify that the models developed using a single nozzle were applicable to all nozzles of that type (Hall, 1993).

The spray quenching heat transfer correlations contain mean drop diameters and velocities instead of the complete drop size and velocity distributions of the spray. Sauter mean diameter, SMD or $d_{32}$, is the diameter of the drop whose ratio of volume to surface area is the same as that of the entire spray. The mean drop velocity, $U_m$, is simply the average of measured individual drop velocities. A phase-Doppler particle analyzer, manufactured by Aerometrics, Inc., was used to measure drop size and velocity simultaneously at discrete locations within the spray field. Multiple tests were conducted at each location to ensure repeatability. Several locations within the spray field were targeted in order to obtain a result that was representative of the entire spray. $d_{32}$ and $U_m$ did not appear to vary considerably, or predictably, between measurement locations. Hence, an average $d_{32}$ (286 $\mu$m) and an average $U_m$ (13.5 m/s) were used as the mathematical models for the spray field at a distance of 0.305 m (12 in.) from the nozzle orifice.

Typically, the quenching phase of a heat treatment operation consists of either a stationary part or a long extrusion moving through an array of overlapping sprays. The nozzle spacing

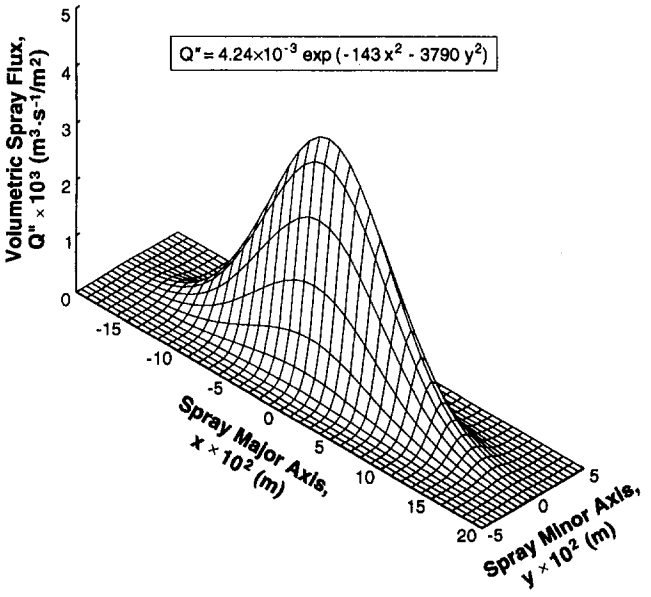



**Fig. 5 Spatial distribution model of volumetric spray flux for the flat spray nozzles used in the present study**

should be optimized to eliminate undesired axial nonuniformity in the heat transfer coefficient. Volumetric spray flux appeared to be the primary spray hydrodynamic parameter controlling the spatial variation of the heat transfer coefficient since $d_{32}$ and $U_m$ were insensitive to location. Thus, an optimal nozzle configuration should produce a uniform spray field as well. The spray interaction between adjacent nozzles whose major axes coincide was investigated and a methodology was developed for optimizing nozzle spacing and adapting the single nozzle models for use with nozzle arrays having overlapping spray patterns (Hall, 1993). Figure 6 compares the nonoptimized nozzle configuration used in past studies to the nozzle configuration used in the present study, which eliminates the majority of axial temperature gradients in a stationary test piece and permits the quenching process to be analyzed using a two-dimensional numerical model.

**Numerical Procedure.** Numerical simulation of the spray quenching process involves the solution of the transient heat diffusion equation with temperature dependent thermophysical properties and temperature and spatially dependent boundary conditions. The ability of the commercial finite element program ABAQUS (Hibbitt, Karlsson, and Sorensen, Inc., 1989) to define the heat transfer coefficient easily as a function of location and surface temperature made it ideal for the present study. The efficient nonlinear equation solver and self-adaptive time stepping scheme were additional benefits.

The spray quenching process will be optimized in future studies by adjusting the nozzle configuration; hence, locations on the surface of the extrusion may or may not be experiencing convection due to the water spray. Thus, the ABAQUS input file (Hall, 1993) was generalized to permit a convection boundary condition for all surface elements. A FORTRAN subroutine was written within the input file to determine the heat transfer coefficient as a function of surface temperature and surface location relative to the spray nozzles. The subroutine was consulted for each surface node at every iteration of every time increment. If the location was being sprayed, the subroutine performed the following tasks: (1) local spray hydrodynamic parameters were determined, (2) quenching regime experienced at this location, and (3) corresponding local surface heat flux were calculated using the spray quenching heat transfer correlations, and (4) convection heat transfer coefficient was defined as $h = q''/\Delta T$. Radiation heat transfer from sprayed surfaces was neglected since



Downloaded 12 Dec 2010 to 193.140.21.150. Redistribution subject to ASME license or copyright; see http://www.asme.org/terms/Terms_Use.cfm

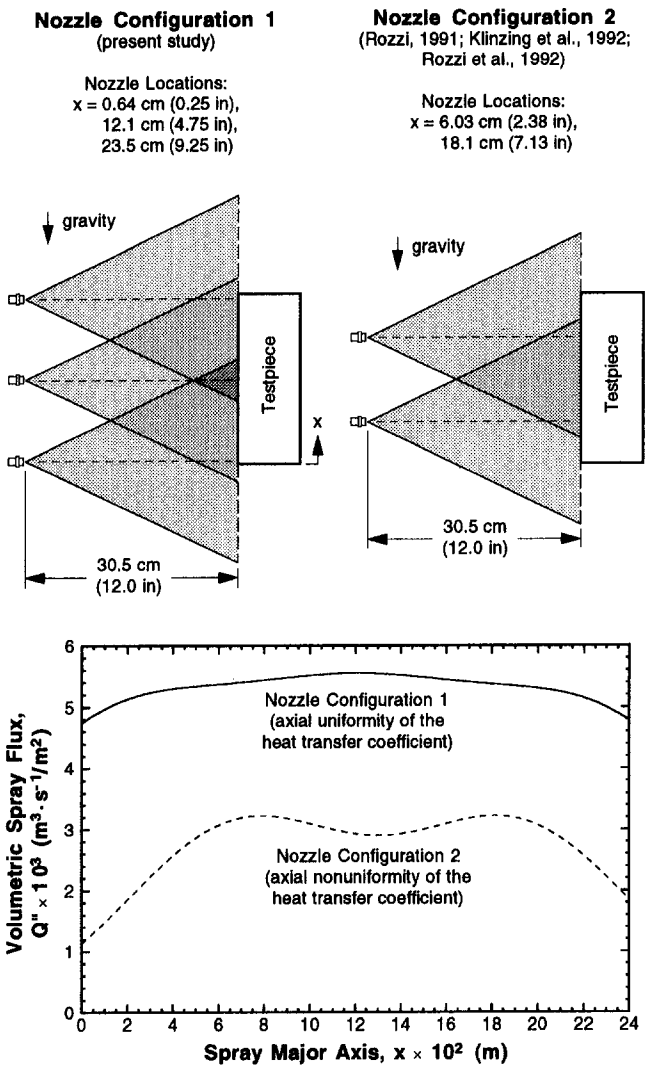



**Fig. 6 Spatial distribution of volumetric spray flux on the major axis of the nozzle configurations used in the materials processing test bed**

the heat transfer coefficient due to radiation alone (based on a surface temperature of 495°C and an emissivity of 0.15 (Gubareff et al., 1960)) was less than 0.6 percent of the lowest value of the heat transfer coefficient due to spray convection (determined using the film boiling correlation listed in Table 1 for a location near the edge of the spray field). Free convection and radiation from unsprayed surfaces were found to have a negligible effect on the numerical results. ABAQUS iterated each time increment until the solution at each node differed by less than 0.01°C between iterations. A nearly continuous temperature–time history was obtained by defining a maximum allowable time increment of 0.1 seconds. Solution convergence was investigated to determine the appropriate element type and size required by the present problem.

## Results and Discussion

**Experimental Results.** The nozzle configuration used in the quenching process was chosen such that axial uniformity and in-plane variations of hardness would be obtained in the heat treated part. The in-plane variations of hardness were necessary to verify that the quench factor technique accurately predicts the trends in hardness throughout the part cross section. Previous experiments indicated that a single nozzle array (consisting of three optimally spaced nozzles whose major axes coincide) impinging the thin section yielded the largest possible variation of in-plane hardness using this type nozzle and operating pressure (Hall, 1993). This realistic nozzle configuration was justified by viewing the L-shape as the symmetric fourth of an I-beam extrusion as shown in Fig. 7. The web thickness of an I-beam is usually less than the flange thickness. However, the thicker web used in the present study was necessary to promote in-plane hardness variations. The thermocouples were located within the L-shape such that relatively different cooling histories would be obtained and, hence, a wide range of hardness values would be predicted using the quench factor technique.

The L-shape was solution heat treated, spray quenched, and artificially aged to achieve the T6 temper. Rockwell B hardnesses predicted using the quench factor technique and temperatures measured during the spray quenching process are indicated in Fig. 8(*a*). Following artificial aging, several hardness measurements were made on the surface of the test piece near the thermocouple plane. The L-shape was subsequently cut open and the exposed surface carefully prepared for additional hardness measurements near the thermocouple locations. The measurements shown in Fig. 8(*a*) represent an average hardness rounded to the nearest 0.5 HRB. External measurements made near thermocouple locations were in good agreement with the quench factor predictions. The percent differences between predicted and externally measured hardness were 0.6, 3.3, and 0.7 percent for the surface locations near TC 1, TC 3, and TC 4, respectively. Additional measurements conducted on other planes parallel to the thermocouple plane confirmed the axial uniformity of hardness. The percent differences between predicted and internally measured hardness were 0.1, 1.0, 1.2, and 2.8 percent at TC 1, TC 2, TC 3, and TC 4, respectively.

The maximum attainable hardness for Al 2024-T6, $H_{max}$ in Eq. (5), may be approximately 2 HRB higher than the value used to predict hardness in the present study (Kim, 1989). Thus, hardness predicted using the quench factor technique has an uncertainty of approximately 2.5 percent. This uncertainty combined with the uncertainty associated with the calibration of the hardness tester explains any differences in magnitude between measured and predicted hardness. Furthermore, these uncertainties do not affect the hardness trends (measured or predicted) observed within the L-shape. Thus, the experimental hardness measurements verify that the quench factor technique accurately predicts the hardness distribution of a heat-treated part from its measured temperature-time history. This confirmation paves the way for the next phase leading to the development of the CAD-based intelligent spray quenching system: combine the quench factor technique and the finite element prediction of temperature history to predict hardness without any experimental data.

**Numerical Predictions.** The ability of the numerical methods developed in the present study to predict the temperature–time history of a spray-quenched part accurately was verified in a related study (Hall, 1993). The quench factor technique was

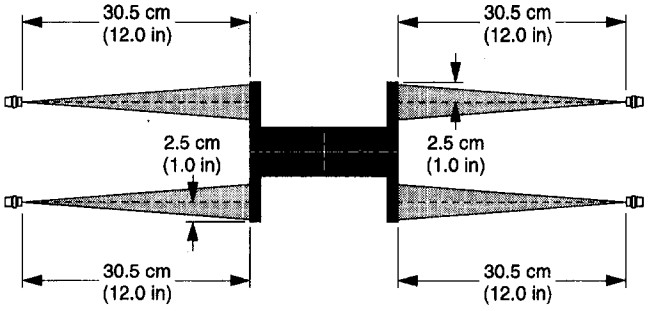



**Fig. 7 I-beam extrusion and possible nozzle configuration used in industry. The L-shape used in the present study represents the symmetric fourth of the I-beam.**



Downloaded 12 Dec 2010 to 193.140.21.150. Redistribution subject to ASME license or copyright; see http://www.asme.org/terms/Terms_Use.cfm

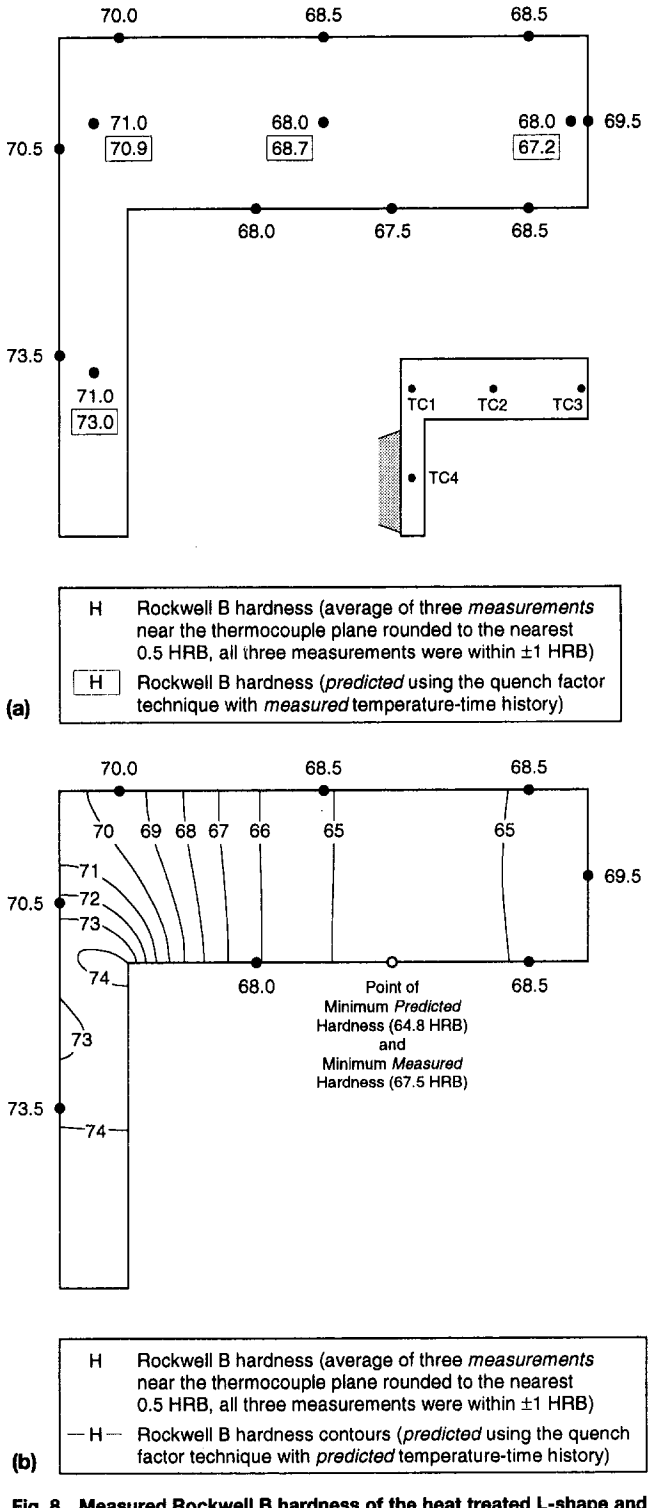



**Fig. 8 Measured Rockwell B hardness of the heat treated L-shape and hardness predicted using the quench factor technique with (*a*) measured and (*b*) predicted temperature–time history**

used in the current study to predict the hardness distribution from this temperature–time history. Figure 8(*b*) shows that external hardness measurements made on the surface of the test piece near the thermocouple plane were in good agreement with the numerical predictions. The predicted hardness distribution accurately represented the trends in hardness observed throughout the L-shape. Furthermore, the point of minimum predicted hardness and minimum measured hardness coincided. The difference between measured and predicted hardness was a maximum in the thick section. This was attributed to significant forced convection from unsprayed surfaces of the testpiece to mist and air currents inside the spray chamber. The methodology developed in the current study accounted only for free convection from unsprayed surfaces and, hence, the thick section cooled quicker and had a slightly higher hardness than predicted. This phenomenon did not affect the ability of the method to predict trends in hardness accurately. Furthermore, this error should decrease when a larger portion of the surface is being sprayed (i.e., as the quench is improved by adding sprays to the thick section).

The experimental hardness measurements verify that the quench factor technique accurately predicts the hardness of a heat-treated part from the temperature history predicted using the methodology developed in this study. This additional confirmation paves the way for the final phase leading to the development of the CAD-based intelligent spray-quenching system: optimization of the spray quenching process by predicting and testing more appropriate nozzle configurations to maximize the magnitude and uniformity of hardness. This issue will be addressed in future studies.

## Conclusions

This study continues the development of the CAD-based intelligent spray-quenching system, originally proposed by Deiters and Mudawar (1989), which, once completed, will optimize the quenching of aluminum alloys to achieve superior part quality. The primary goal of the present study was to develop a method for predicting the hardness distribution within heat-treated aluminum alloy extrusions. Key conclusions from this study are as follows:

1 Previously, the quench factor technique was applied only to small isothermal samples having simple geometries (e.g., spheres, sheet). This study has shown that the quench factor technique accurately predicts the hardness distribution of non-isothermal, complex-shaped aluminum alloy parts from the measured temperature–time history.

2 The spray quenching of a complex-shaped part with multiple, overlapping spray nozzles was successfully modeled using the methodology developed in the current study and the spray-quenching heat transfer correlations developed by Mudawar and Valentine (1989) and Klinzing et al. (1992). The hardness distribution of a heat-treated Al 2024-T6 extrusion was successfully predicted using the quench factor technique and the numerically predicted temperature–time history.

3 Since the quench factor technique has been validated for both strength and hardness, the methodology developed in this study should also give accurate yield strength predictions.

4 The coupling of the quench factor technique with the finite element method and spray-quenching heat transfer correlations enables the determination of the final mechanical properties a priori; hence, the performance of a spray quenching system can be judged prior to operation. Once perfected, the CAD-based intelligent spray quenching system will significantly reduce cost and increase productivity.

## Acknowledgments

The authors gratefully acknowledge the financial support of the Purdue University Engineering Research Center for Intelligent Manufacturing Systems. Financial support for the first author was provided in the form of the United States Department of Energy Predoctoral Integrated Manufacturing Fellowship. The authors also thank Jerry Hagers, Rudolf Schick, and Chris Schaffer of Spraying Systems Company and Gerry Dail of ALCOA for their valuable technical assistance.

## References

ASM, 1991, *ASM Handbook*, Vol. 4, 10th ed., ASM International, Materials Park, OH.



Downloaded 12 Dec 2010 to 193.140.21.150. Redistribution subject to ASME license or copyright; see http://www.asme.org/terms/Terms_Use.cfm

ASTM, 1993, *Annual Book of ASTM Standards,* Vol. 03.01, American Society for Testing and Materials, Philadelphia, PA.

Avrami, M., 1940, "Kinetics of Phase Change II—Transformation-Time Relations for Random Distribution of Nuclei," *Journal of Chemical Physics,* Vol. 8, pp. 212–224.

Axter, S. E., 1980, "Effects of Interrupted Quenches on the Properties of Aluminum," Society of Manufacturing Engineers Technical Paper CM80-409.

Bates, C. E., 1987, "Selecting Quenchants to Maximize Tensile Properties and Minimize Distortion in Aluminum Parts," *Journal of Heat Treating,* Vol. 5, pp. 27–40.

Bates, C. E., 1988, "Predicting Properties and Minimizing Residual Stress in Quenched Steel Parts," *Journal of Heat Treating,* Vol. 6, pp. 27–45.

Bates, C. E. and Totten, G. E., 1988, "Procedure for Quenching Media Selection to Maximize Tensile Properties and Minimize Distortion in Aluminum Alloy Parts," *Heat Treatment of Metals,* Vol. 15, pp. 89–97.

Bates, C. E., and Totten, G. E., 1992, "Application of Quench Factor Analysis to Predict Hardness Under Laboratory and Production Conditions," *Proceedings of the First International Conference on Quenching and Control of Distortion,* Chicago, IL, pp. 33–39.

Cahn, J. W., 1956a, "The Kinetics of Grain Boundary Nucleated Reactions," *Acta Metallurgica,* Vol. 4, pp. 449–459.

Cahn, J. W., 1956b, "Transformation Kinetics During Continuous Cooling," *Acta Metallurgica,* Vol. 4, pp. 572–575.

Chevrier, J. C., Simon, A., and Beck, G., 1981, "Optimal Cooling Rate and Process Control in Metallic Parts Heat Treatment," *Heat and Mass Transfer in Metallurgical Systems,* D. B. Spalding and N. H. Afgan, eds., Hemisphere Publishing Corp., Washington, DC, pp. 535–544.

Conserva, M., and Fiorini, P., 1973, "Interpretation of Quench-Sensitivity in Al-Zn-Mg-Cu Alloys," *Metallurgical Transactions,* Vol. 4, pp. 857–862.

Deiters, T. A., and Mudawar, I., 1989, "Optimization of Spray Quenching for Aluminum Extrusion, Forging, or Continuous Casting," *Journal of Heat Treating,* Vol. 7, pp. 9–18.

Evancho, J. W., 1973, "Effects of Quenching on Strength and Toughness of 6351 Extrusions," Alcoa Laboratories Report 13-73-HQ40, Alcoa Center, PA.

Evancho, J. W., and Staley, J. T., 1974, "Kinetics of Precipitation in Aluminum Alloys During Continuous Cooling," *Metallurgical Transactions,* Vol. 5, pp. 43–47.

Fink, W. L., and Willey, L. A., 1948, "Quenching of 75S Aluminum Alloy," *Transactions AIME,* Vol. 175, pp. 414–427.

Gubareff, G. G., Janssen, J. E., and Torborg, R. H., 1960, *Thermal Radiation Properties Survey,* 2nd ed., Honeywell Research Center, Minneapolis, MN.

Hall, D. D., 1993, "A Method of Predicting and Optimizing the Thermal History and Resulting Mechanical Properties of Aluminum Alloy Parts Subjected to Spray Quenching," M.S. Thesis, Purdue University, West Lafayette, IN.

Hibbitt, Karlsson and Sorensen, Inc., 1989, *ABAQUS User's Manual, Ver. 4.8,* Providence, RI.

Kim, J. S., 1989, "Prediction of the Influence of Water Spray Quenching on the Age-Hardenability of Aluminum Alloy 2024," M.S. Thesis, Purdue University, West Lafayette, IN.

Klinzing, W. P., Rozzi, J. C., and Mudawar, I., 1992, "Film and Transition Boiling Correlations for Quenching of Hot Surfaces With Water Sprays," *Journal of Heat Treating,* Vol. 9, pp. 91–103.

Mudawar, I., and Valentine, W. S., 1989, "Determination of the Local Quench Curve for Spray-Cooled Metallic Surfaces," *Journal of Heat Treating,* Vol. 7, pp. 107–121.

Rozzi, J. C., 1991, "Quenching of Aluminum Parts Having Irregular Geometries Using Multiple Water Sprays," M.S. Thesis, Purdue University, West Lafayette, IN.

Rozzi, J. C., Klinzing, W. P., and Mudawar, I., 1992, "Effects of Spray Configuration on the Uniformity of Cooling Rate and Hardness in the Quenching of Aluminum Parts With Nonuniform Shapes," *Journal of Materials Engineering and Performance,* Vol. 1, pp. 49–60.

Sawtell, R. R., 1984, "Effects of Quenching Path in Aluminum Alloy 7075," *Aluminum,* Vol. 60, pp. 198–202.

Staley, J. T., 1987, "Quench Factor Analysis of Aluminum Alloys," *Materials Science and Technology,* Vol. 3, pp. 923–935.



Downloaded 12 Dec 2010 to 193.140.21.150. Redistribution subject to ASME license or copyright; see http://www.asme.org/terms/Terms_Use.cfm

# Assessing Halon Alternatives for Aircraft Engine Nacelle Fire Suppression

W. Grosshandler

C. Presser

D. Lowe

W. Rinkinen

National Institute of Standards and Technology, Gaithersburg, MD 20899

*A coaxial turbulent spray burner was built to evaluate the relative effectiveness of different chemicals for suppressing fires in a jet engine nacelle. The fire suppressant of current choice, halon 1301 ($CF_3Br$), must be replaced because of its detrimental effect on the ozone layer. The alternatives being considered lack the chemical activity of $CF_3Br$, so that the ability of the agents to mix into the flame convectively and to absorb heat is critical to their success. An agent delivery system was designed to inject the desired amount of material into the air upstream of a fuel nozzle and to control the agent injection rate through variation of the storage pressure and the duration of time that a solenoid valve remains open. The influence of air velocity, fuel flow, and injection period on the amount of nitrogen required to extinguish a jet fuel spray flame is discussed. The effectiveness of eleven different fluorocarbons, hydrofluorocarbons, and hydrochlorofluorocarbons is compared to that of halon 1301. The alternatives required 1.7 to 2.3 times the amount (on a mass basis) of $CF_3Br$ to extinguish the spray flame, with HCFC-22 being the most efficient and FC-31-10 the least.*

## Introduction

Chlorinated and brominated hydrocarbons as a class of chemicals have come under close scrutiny because they have been implicated in the depletion of stratospheric ozone (Anderson, 1987). Under the auspices of an international agreement, commonly known as the Montreal Protocol, halon 1301 has been singled out as being particularly effective at scavenging ozone, and its manufacture has been eliminated starting in 1994 (Harrington, 1993).

Halon 1301, or trifluorobromomethane ($CF_3Br$), is used as a fire extinguishing agent in aircraft engine nacelles (the structure encasing the compressor, combustor and turbine) because of the chemical's many positive attributes; viz., it can be stored in a small volume as a liquid at room temperature and pressures greater than 1.61 MPa; it is a gas at atmospheric conditions, allowing it to be dispersed quickly leaving no residue; it has low toxicity in pure form; it can be produced at a reasonable price in high quantity; and, most important, very little agent is required to extinguish the fire.

A fire resulting from a leaking fuel line in the engine nacelle is often detected with a thermal sensor after the temperature exceeds a threshold value. The agent is released manually by the crew within seconds after confirming that a fire is present. Suppression is normally successful if the flow of fuel can be eliminated and the agent concentration can be maintained above a minimum level (6 percent by volume for halon 1301) throughout the nacelle for a minimum of a half second.

Alternatives to halon 1301 are sought (Grosshandler et al., 1994) that do not create unacceptable safety, environmental, or systems compatibility problems. This article describes the features of a turbulent spray burner used to predict the performance of alternative agents in simulated full-scale engine nacelle fires. A systematic study of the facility using nitrogen as the suppressant, and the measured suppression effectiveness of eleven low-ozone-depleting agents (listed in Table 1) are presented.

Contributed by the Heat Transfer Division for publication in the JOURNAL OF HEAT TRANSFER. Manuscript received by the Heat Transfer Division September 1993; revision received May 1994. Keywords: Combustion, Fire/Flames, Reacting Flows. Associate Technical Editor: R. Viskanta.

## Background on Flame Suppression

A flame will be extinguished when the time required for the chemical chain reaction, $t_{chem}$ (estimated from the inverse of a global kinetic rate coefficient), exceeds the time it takes to replenish the necessary heat and reactants, $t_{flow}$ (given by the ratio of a characteristic length scale and convective flow velocity). Liñan (1974) showed that as the maximum flame temperature and the fuel burning rate decrease, a critical value of the Damköhler number ($D_a \equiv t_{flow}/t_{chem}$) is reached where the flame is abruptly extinguished. This suggests two strategies for suppressing fires: (1) decreasing $t_{flow}$ by increasing the flow velocity (or strain rate); and (2) increasing $t_{chem}$ by reactant removal, cooling the flame, or chemical inhibition.

Fundamental studies have shown that the character of the fluid mechanical flow field is a key parameter in controlling flame extinction (Williams, 1974). As the strain rate increases, $t_{flow}$ decreases and a flame becomes weaker and easier to extinguish by agent addition. If the flame is strained at a high enough rate, the flame will self-extinguish. Reactant removal is accomplished by actively eliminating or by simply consuming the fuel and/or air. Under sufficiently rich or lean conditions flame extinction will again occur without the aid of a fire suppressing agent. Cooling the flame reduces the rate of energy release due to the exponential temperature dependence in the Arrhenius rate coefficient. This can be accomplished by reducing the heat feedback from the surroundings, by cooling the fuel and air, or by increasing the heat capacity of the material entering the flame. A gaseous agent with higher specific heat (higher molecular weight and number of atoms) will generally be more effective in this situation.

Halon 1301 contains bromine, which inhibits the combustion reaction by tying up the chain-branching hydrogen radicals in a catalytic cycle involving HBr. Chlorine interacts with the flame in a similar manner but to a much lesser degree. Fluorine also reacts with hydrogen to form HF, but the hydrogen–fluorine bond is so strong that the F atom is not recycled. Hence, the agents investigated in this study rely primarily on a physical cooling mechanism rather than chemical inhibition to suppress a fire. Tucker et al. (1981) and Sheinson et al. (1989) further discuss the chemical and physical aspects of fire suppression.

Pitts et al. (1990) present a comprehensive review of the literature relevant to fire suppression by various gaseous agents, and discuss the role of different suppression mechanisms and


Copyright © 1995 by ASME


Downloaded 12 Dec 2010 to 193.140.21.150. Redistribution subject to ASME license or copyright; see http://www.asme.org/terms/Terms_Use.cfm

various test procedures. The conventional method to determine the amount of agent necessary for suppression of a liquid fuel fire is to increase the concentration slowly in a low-velocity air stream flowing concentrically over a small (≈25 mm diameter) burning pool. This apparatus, referred to as a cup burner, has been used for evaluating halon 1301 and other flame extinguishants (e.g., Booth et al., 1973). The cup burner cannot simulate the combined droplet evaporation and turbulent mixing that might occur in a realistic engine nacelle fire.

Hamins et al. (1994) looked at suppression mechanisms for the specific application of aircraft protection, and described different facilities used to cover a wide range of possible fire conditions. A description by Bennett (1992) of full-scale engine nacelle fires indicates that the fires of interest are turbulent and characterized by a range of strain rates. The turbulent spray burner, designed for the current study, produces a complicated flame structure in which fuel droplets vaporize and react with an oxidizer that can be composed of either pure air, or air mixed with combustion products and/or fuel vapor. Because of the inherent differences in the structure of the combustion zone between the turbulent spray burner and the more traditional cup burner apparatus, different suppression behavior in the two facilities would not be unexpected.

## Experimental Facility

An objective of this investigation was to develop a laboratory apparatus that captures the critical elements that exist within an engine nacelle fire as an alternative to difficult and costly experiments on a full-scale facility. In addition to the flexibility offered by a reduced-scale facility, the turbulent spray burner minimizes the influence of agent transport and vaporization on flame suppression effectiveness, and allows independent control of the rate at which the agent enters the flame.

The spray burner facility, shown in Fig. 1, consists of an air delivery system, a fuel delivery system, and an agent injection system. Air at atmospheric pressure coflows around a 6-mm-dia fuel supply passage within a 0.5-m-long, 50-mm-dia stainless steel pipe. A pyrex tube with a 65 mm ID, supported on a Teflon ring, confines the flame for an additional 75 mm beyond the outer steel casing. This pyrex tube is used to observe the mixing of the agent with the flame front. The fuel is injected along the centerline through a pressure-jet nozzle that forms a 45 deg solid-cone spray. The exit of the nozzle is flush with the open end of the surrounding air passage. The flame is stabilized on a 35-mm-dia steel disk attached to the nozzle body. The air is supplied by a high-capacity compressor at 800 kPa, and the flow is monitored with a sonic orifice. The air temperature varied between 19 and 24°C as measured with a type-K thermocouple that was positioned 1.1 m upstream of the nozzle exit. The average air velocity, measured over the burner cross section, is adjustable to a maximum of 50 m/s. The fuel, JP-8, is stored in an 18 liter tank and delivered to the burner with an electric gear pump at pressures controllable to 1.0 MPa-g. The nozzle is designed to deliver fuel at a rate of 0.5 ml/s when the gage pressure is 687 kPa.

The gaseous agents were injected impulsively into the air stream at a position 0.54 m upstream of the nozzle. Uniform

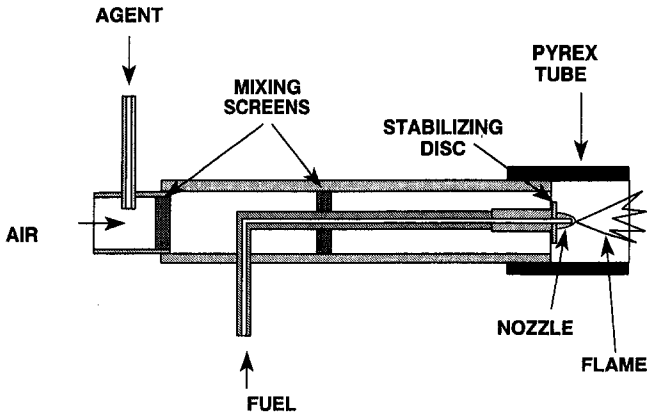



**Fig. 1 Cross-sectional view of turbulent spray burner**

dispersion across the air stream was enhanced by injecting the gas in a radial direction into a reduced diameter (25 mm) section of the air passage through two 6 mm diameter tubes. Screens with a 50 percent open area were placed 40 and 80 mm downstream of the injection point to ensure complete mixing between the air and agent prior to encountering the flame zone.

The injection mechanism, shown in Fig. 2, consists of the agent supply bottle connected to a stainless steel storage vessel through a metering valve, and to the burner through a computer-controlled solenoid valve. The storage volume, including the one liter pressure vessel and associated plumbing, is 1040 ± 10 ml and the agent pressure is adjustable up to 687 kPa-g. The agent temperature and pressure in the storage vessel are monitored with a type-K thermocouple and a pressure transducer, respectively, located upstream of the solenoid valve. The amount of agent injected is controlled by varying the initial pressure, the time that the solenoid valve is open, and the size of a metering orifice located just upstream of the solenoid valve. The actual mass delivered is computed from the difference between the initial and final pressures in the storage vessel. The rate of injection is determined primarily by the initial pressure and the size of the metering orifice (4.8 and 6.4-mm-dia orifices were used in the reported investigation).

## Experimental Methodology

The flow of air and JP-8 was varied to ascertain how flame stability was affected by these parameters. The fuel pressure was first fixed at 687 ± 10 kPa-g (corresponding to a mass flow rate of around 0.42 g/s). The spray is ignited with a relatively low air flow using a propane torch. The flame extends well beyond the exit of the pyrex tube and is highly luminous under these conditions. As the air flow is increased, the flame attaches itself to the stabilizing disk and the plume length decreases until the flame is stationed within the pyrex tube. At high air flows, little soot radiation is observed beyond the exit plane, although the flame itself maintains some luminosity. A moderate amount of

## Nomenclature

$a$ = Redlich–Kwong interaction constant
$b$ = Redlich-Kwong covolume
$C_p$ = constant pressure specific heat
$D_n$ = Damköhler number
FSN = flame suppression number
$m$ = mass
$\dot{m}$ = rate of mass flow
$P$ = pressure
$R$ = universal gas constant
$T$ = temperature
$t_{chem}$ = characteristic chemical reaction time
$t_{flow}$ = characteristic flow time
$V$ = volume
$VF$ = volume factor
$\beta$ = mass fraction of agent in air stream
$\gamma$ = specific heat ratio
$\rho_L$ = saturated liquid density

**Subscripts**

air = pertaining to air
halon = pertaining to halon
$f$ = final state
$i$ = pertaining to agent $i$, or initial state



Downloaded 12 Dec 2010 to 193.140.21.150. Redistribution subject to ASME license or copyright; see http://www.asme.org/terms/Terms_Use.cfm

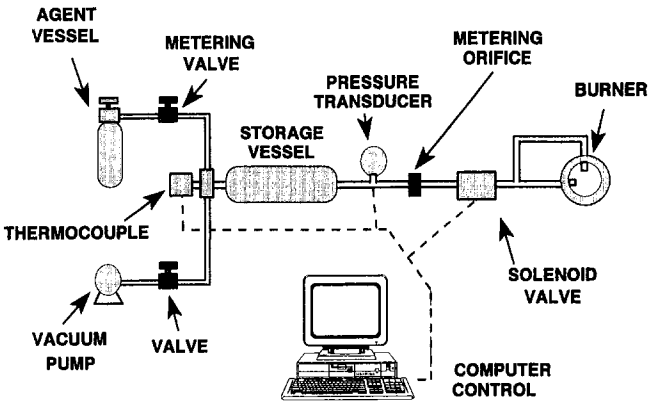



**Fig. 2 Schematic of gaseous agent injection system**

soot forms on the nozzle face in a matter of minutes. A stable flame is sustainable until the air flow rate exceeds 73 g/s, at which point the flame blows out. The average gas velocity across the air duct is about 33 m/s at the above-mentioned mass flow rate, which translates to an estimated residence time in the recirculation zone downstream of the stabilizing disk of 5 ms. Blowout experiments were repeated for fuel nozzle pressures of 515 and 858 kPa-g. At the reduced pressure, the fuel flow rate decreases by about 14 percent, which results in an equivalent decrease in the amount of air necessary to extinguish the flame. The higher fuel line pressure has no appreciable affect on the blowout limit. The operating conditions chosen as the baseline measurements were a mass flow rate of JP-8 of 0.42 g/s and an air flow rate of 33 g/s at atmospheric pressure (resulting in an average inlet air velocity of 14 m/s). This produced an 18 kW flame with an overall equivalence ratio of about 0.17. The temperatures of the fuel and air, and the initial temperature of the agent, were ambient (19–24°C).

The injection system, under idealized conditions (incompressible flow, massless valves, no pressure losses), is designed to deliver a square-wave pulse of agent to the burner for the amount of time programmed by the computer controller. The actual flow deviates substantially from this scenario. There is a 15 ms delay from when the solenoid is triggered to the actual initiation of agent flow. When the valve starts to close, pressure waves are created which reverberate in the injection system at the acoustic velocity, causing the flow to modulate (Grosshandler et al., 1993).

The critical temperatures of the agents listed in Table 1 vary from a low of 19.7°C for FC-116 to a high of 130.6°C for HFC-236fa. To account for possible nonideal gas behavior in the storage vessel, the Redlich–Kwong equation of state (Van Wylen and Sonntag, 1978) was used to determine the mass of agent, $m$, contained in the vessel of volume $V$, at pressure $P$ and temperature $T$; i.e.,

$$m = \frac{PVM}{RT}\left[\frac{1}{1-bm/V} - \frac{am/(VRT^{3/2})}{1+bm/V}\right]^{-1}, \qquad (1)$$

where $M$ is the molecular weight of the gaseous agent, $a$ and $b$ are constants dependent upon the critical properties of the agent, and $R$ is the universal gas constant (8.314 kJ/kmol-°C). The maximum difference in mass calculated by the ideal gas equation of state and Eq. (1) was 7 percent. The initial temperature is measured, and the final temperature is determined by assuming that the expansion occurs isentropically; i.e.,

$$\frac{T_f}{T_i} = \left(\frac{P_f}{P_i}\right)^{\gamma-1/\gamma}. \qquad (2)$$

Gamma is the specific heat ratio for the gas, defined as $(M \cdot C_p + R)/M \cdot C_p$, using the values for $M$ and $C_p$ from Table 1. By measuring the change in pressure, Eq. (1) can be used to determine the total amount of mass injected into the burner. The uncertainty in mass created by using Eq. (2) for temperature is small since the temperature changes less than 20°C during injection. The vessel pressure was recorded at a rate of 700 Hz, with the initial and final conditions obtained from the average of at least 100 points measured one-half second prior to the release of the agent, and for one second after the solenoid valve closes, respectively. The uncertainty in the total mass calculated is estimated to be less than ±8 percent.

The mass fraction of agent required to extinguish the flame, $\beta$, is defined in terms of the mass flow of agent, $\dot{m}_i$, and air, $\dot{m}_{air}$:

$$\beta \equiv \frac{\dot{m}_i}{\dot{m}_i + \dot{m}_{air}}. \qquad (3)$$

**Table 1 Thermodynamic properties of chemicals being evaluated (based on references in Yang and Breuel, 1994)**

| Formula | Compound | Boiling Point @ 101 kPa, °C | Critical Temp., °C | Molec. Wt., kg/kmol | $C_p$ (gas) @ 25°C & 101 kPa, kJ/kg-K | $\rho_L$ (sat.) @ 25°C, kg/m3 |
|---|---|---|---|---|---|---|
| $N_2$ | Nitrogen | -196 | -147.0 | 28 | 1.042 | 52[1] |
| $C_2F_6$ | FC-116 | -78.2 | 19.7 | 138 | 0.772 | 608[1] |
| $CF_3Br$ | Halon 1301 | -57.8 | 67.0 | 149 | 0.466 | 1551 |
| $CH_2F_2/C_2HF_5$ | HFC-32/125 | -52.5 | 73.2 | 67 | 0.830 | 1040 |
| $C_2HF_5$ | HFC-125 | -48.6 | 66.3 | 120 | 0.798 | 1190 |
| $CHF_2Cl$ | HCFC-22 | -40.9 | 96.2 | 87 | 0.795 | 1192 |
| $C_3F_8$ | FC-218 | -36.8 | 72.0 | 188 | 0.781 | 1321 |
| $C_2H_2F_4$ | HFC-134a | -26.2 | 101.2 | 102 | 0.852 | 1209 |
| $C_3HF_7$ | HFC-227ea | -16.4 | 101.7 | 170 | 0.769 | 1395 |
| $C_2HF_4Cl$ | HCFC-124 | -13.2 | 122.5 | 137 | 0.714 | 1357 |
| cyclo-$C_4F_8$ | FC-318 | -7.0 | 115.2 | 200 | 0.776 | 1499 |
| $C_3H_2F_6$ | HFC-236fa | -1.5 | 130.6 | 152 | 0.804 | 1356 |
| $C_4F_{10}$ | FC-31-10 | -2.0 | 113.2 | 238 | 0.755 | 1497 |

[1] gas density computed at storage bottle conditions, 25 °C and 4.1 MPa



Downloaded 12 Dec 2010 to 193.140.21.150. Redistribution subject to ASME license or copyright; see http://www.asme.org/terms/Terms_Use.cfm

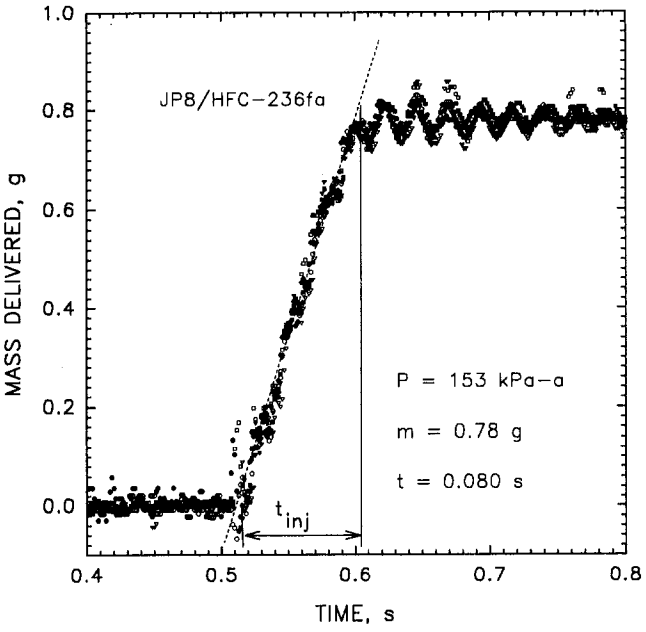



**Fig. 3 Mass–time trace for injection of HFC-236fa. The different symbols correspond to six successive runs in which amount of agent is just enough to extinguish JP-8 spray flame.**

The mass flow rate of air is measured directly. The parameter $\dot{m}_i$ is the ratio of the mass of agent added to the flame, as determined from Eq. (1), and the actual time interval of agent injection into the burner. The variation of mass of agent with time for a typical discharge is shown in Fig. 3, with each symbol representing a different injection event for the same initial conditions. The injection time interval is estimated from where the line drawn tangent to the rapidly increasing portion of the pressure trace intersects zero and the final value of mass in the vessel. The pressure oscillations shown in Fig. 3 at the end of the event were present in all cases and are due to the impulsive operation of the solenoid valve. The frequency is determined by the acoustic velocity and the size of the storage tank.

The mass of nitrogen delivered from the storage vessel to the burner as a function of injection time interval was measured for a fixed initial vessel pressure of 687 kPa-g (Grosshandler et al., 1993). The results indicate that the delivered mass of nitrogen increases almost linearly with time in the range between about 25 and 250 ms. Deviations from linear behavior occur for shorter periods because the valve does not have enough time to open fully, and for longer periods due to the finite amount of agent ($\approx$10 g for $N_2$) initially contained in the storage vessel.

A number of experiments were carried out with the burner operating at baseline conditions and with air as the extinguishing agent to ensure that the flame could not be suppressed simply by blowing it out. When air was injected into the burner, the flame fluctuated momentarily, but was never extinguished even when the storage pressure and injection period were at their maximum values (viz., 687 kPa-g and 910 ms).

The protocol used in the experiments was first to ignite the fuel spray and set the air and fuel flows to the desired level. The flame was allowed to burn for several minutes to ensure steady operation. The storage vessel was pumped down and then flushed several times with the agent being tested to purge contaminating gases from the system. The pressure in the vessel was adjusted with the solenoid valve closed using the inlet metering valve. Initially, a pressure was chosen that was expected to be insufficient to extinguish the flame. The computer-controlled data acquisition system was initiated, and the response of the flame to the injection process was observed. If the flame was not extinguished, the pressure in the agent vessel was increased and the experiment was repeated immediately. Eventually, a pressure was found that was sufficient to suppress the flame. This procedure was normally repeated four times for each agent.

## Characterization With Nitrogen

The influence of air velocity, injection period, and injection pressure on the amount of $N_2$ required to extinguish the JP-8 spray flame and on the value of $\beta$ was investigated to characterize the operation of the experimental facility. The turbulent burner was set to deliver air at 33 g/s and fuel at 0.42 g/s, and the storage vessel was pressurized with nitrogen to 113 kPa-g. The injection interval was then increased one millisecond at a time until the flame was suppressed. Flame extinguishment occurred between 23 and 26 ms for five different runs, delivering an average of 0.33 $\pm$ 0.03 g nitrogen at a mean flow rate of 11.2 $\pm$ 0.5 g/s. The extinguishing mass fraction ($\beta$) varied between 0.24 and 0.26. This value compares to a mass fraction for nitrogen of 0.28 measured in the cup burner apparatus with JP-8 as the fuel (Hamins et al., 1994).

Additional experiments were carried out with the fuel flow fixed and with air flows of 22 and 44 g/s. The amount of nitrogen required to extinguish the lower air velocity flame was 0.32 g, or $\beta$ = 0.33. The higher air flow rate required an average total nitrogen mass of 0.29 g and $\beta$ = 0.21 to suppress the flame. In this case, doubling the air flow (which increased the amount of excess air) reduced the mass of nitrogen required by 10 percent. This observation is consistent with Liñan's (1974) explanation for extinction because increasing the air flow both decreases $t_{flow}$ (through higher strain rate) and increases $t_{chem}$ (through dilution), driving the Damköhler down toward its critical value.

A series of experiments was carried out with the air and fuel flow rates at baseline conditions, and with the time interval fixed at 79 ms ($\pm$5 ms) as the nitrogen pressure was increased. Figure 4 presents the variation of the mass of nitrogen delivered to the burner as a function of initial vessel pressure. The open squares indicate that the flame remained lit after agent delivery; the solid squares correspond to successful extinguishment. The minimum vessel pressure necessary to extinguish the flame was 167 kPa-g. The amount of nitrogen injected at this pressure and time interval was 0.58 $\pm$ 0.03 g. The variations in mass delivered for a

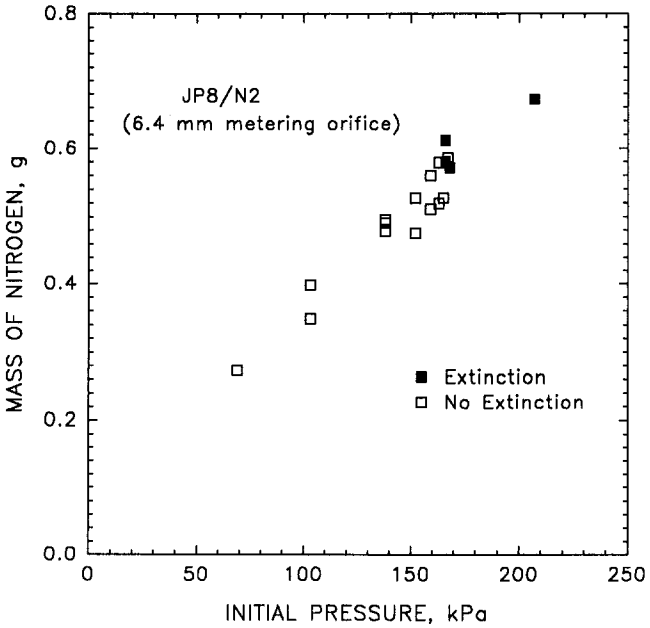



**Fig. 4 Effect of vessel pressure on extinguishment of JP-8 spray flame by nitrogen. Solid symbols indicate extinction; open squares indicate no extinction.**



Downloaded 12 Dec 2010 to 193.140.21.150. Redistribution subject to ASME license or copyright; see http://www.asme.org/terms/Terms_Use.cfm

fixed pressure are caused by run-to-run variations in the rate of injection.

The injection time interval has an effect on the minimum mass of nitrogen required to extinguish the flame. The open squares presented in Fig. 5 illustrate this effect. For these experiments, the initial pressure was fixed at 167 kPa-g and the injection time interval was gradually increased until extinction occurred. The minimum mass of nitrogen is about 0.32 g, for a set injection period of 23 ms. Reducing the set time to 6 ms has no impact on the amount of nitrogen required to quench the flame because the actual period of injection does not change appreciably (being a function of the time required to open the solenoid valve). Injection times longer than 23 ms resulted in the delivery of greater amounts of $N_2$, with more than three times as much $N_2$ required when the injection time is set to 260 ms.

At long injection time intervals, a limit for $\beta$ is reached below which the flame cannot be extinguished no matter how long the nitrogen is allowed to flow (even if the nitrogen reservoir were not finite). Nitrogen flowed continuously in one experiment, and the concentration was increased until the flame was suppressed. The extinguishing mass fraction was found to be 0.11, and is indicated by the arrow (labeled "continuous flow limit") in Fig. 5. This compares to a $\beta$ of 0.28 found in the cup burner with the same fuel/agent combination. Less nitrogen may be required to extinguish the spray flame because regions of greater strain rate exist (i.e., $t_{flow}$ is reduced). The solid squares also shown in the figure are values of $\beta$ that correspond to the different injection time intervals. As the time is shortened, $\beta$ increases, reaching a limiting mass fraction of 0.28.

If the value of $\beta$ were the sole criterion for evaluating an extinguishing strategy, one would chose to inject the agent over an extended period of time. However, as seen in Fig. 5, this has the undesirable effect of greatly increasing the amount of agent required to put out the flame. For an agent that is to be used in a transient manner, the total mass must also be considered. This is distinct from the quasi-steady state measurements taken with the cup burner apparatus, for which $\beta$ is a reasonable measure of performance.

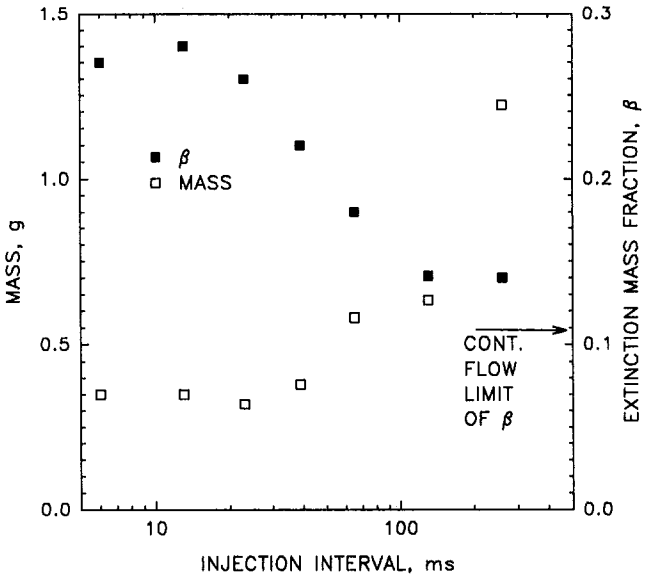



**Fig. 5 Effect of injection time interval on mass of nitrogen (open squares) required to extinguish JP-8 spray flame. Solid squares are the corresponding mass fractions, $\beta$. The arrow indicates the limiting value for $\beta$ when nitrogen flows continuously.**

## Performance of the Alternative Agents

A fixed injection time of 65 ms was chosen to compare the performance of the alternative agents. This value is intermediate between the estimated residence time in the spray flame and a typical time interval for injection in an actual engine nacelle. At this setting, an initial pressure of 167 kPa-g is necessary to extinguish the flame with nitrogen. Nitrogen is considered chemically inert during suppression, and has a much lower molecular weight than halon 1301 and the alternative gaseous agents that were evaluated. As a result, a lower pressure is required in the vessel to deliver the equivalent mass of the heavier molecular weight compounds. The 6.4-mm-dia flow-metering orifice (see Fig. 2) was replaced with a 4.8 mm orifice to increase the pressure drop. The flow remained unchoked for all gases other than $N_2$. Extinguishment experiments were performed using halon 1301 to establish a performance reference (Hamins et al., 1994). An average over five experiments led to a required initial $CF_3Br$ pressure of 24 kPa-g to suppress the flame, which translates to a mass of 0.44 ± .04 g and a mass fraction, $\beta$, of 0.15.

The repeatability of the experimental technique is demonstrated in Fig. 3, for one typical case where the mass of the agent, HFC-236fa, is just above the extinction threshold. This figure presents the mass of agent delivered to the burner with respect to time for six different trials (each represented with a different symbol). The average mass injected is 0.78 g with a range of ±0.02 g. The initial pressure needed to cause extinction is 52 ± 2 kPa-g, and the calculated injection interval is 80 ± 8 ms.

Expressing the results in terms of the flame suppression number (FSN) is a convenient way to compare the performance of the different agents. The FSN is defined as the mass of agent relative to the mass of halon 1301 used to suppress an identical flame; i.e.,

$$\mathrm{FSN} \equiv \frac{m_i}{m_{\mathrm{halon}}}. \tag{4}$$

The volume factor ($VF$) accounts for the differences in saturated liquid densities of the agents, and is defined as follows:

$$VF \equiv \frac{\dot{m}_i}{\dot{m}_{\mathrm{halon}}} \frac{\rho_{L,\mathrm{halon}}}{\rho_{L,i}} = \frac{\beta_i}{(1-\beta_i)} \frac{(1-\beta_{\mathrm{halon}})}{\beta_{\mathrm{halon}}} \frac{\rho_{L,\mathrm{halon}}}{\rho_{L,i}}. \tag{5}$$

The volume factor provides a logical conversion from the mass fraction required to the storage volume because the saturated liquid condition at ambient temperature is close to the condition maintained when the storage vessel is filled (assuming negligible solubility of the pressurizing gas).

Figure 6 compares the mass fractions of thirteen different agents required to suppress the spray flame, and their respective flame suppression numbers and volume factors. The agents are arranged according to increasing boiling point, so as to provide a gross indication of their ability to quickly flood a unit volume. (Pitts et al., 1994, discuss in detail the important role of agent dispersion on suppression effectiveness.) Nitrogen requires a mass fraction of 0.18 to extinguish the flame, compared to 0.15 for $CF_3Br$. The mass fractions of the alternatives increase approximately in the order of HCFCs, HFCs, and FCs, with the least effective agent, FC-31-10, requiring a $\beta$ of 0.27 for suppression. The FSN rankings are in the same order, with HCFC-22 the best alternative on a mass basis (other than $N_2$) requiring 50 percent more mass than halon 1301. Of the alternatives examined, nitrogen has the highest specific heat at 25°C (see Table 1) and the highest effectiveness on a mass basis. The differences among the fluorinated alternatives are not large, and all have similar values for $C_p$. These results suggest that the suppression mechanism for the fluorinated compounds is primarily physical.

Nitrogen and FC-116 are not liquids at 25°C and 4.1 MPa (the conditions used to define VF). Neither are viable candidates when ranked according to volume factor (see Fig. 6) unless a very high pressure storage container is available. The HFC-32/125 mixture has the next highest volume factor, with a value of 2.7. The remaining agents have values of VF between 1.8 and 2.3, with HCFC-124 requiring the least storage volume as defined here.



Downloaded 12 Dec 2010 to 193.140.21.150. Redistribution subject to ASME license or copyright; see http://www.asme.org/terms/Terms_Use.cfm

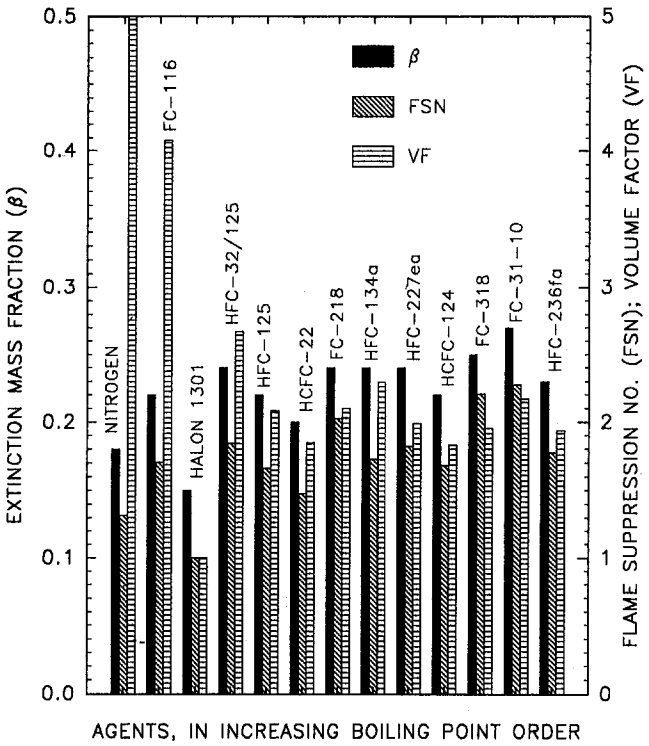



**Fig. 6 Comparison of mass fraction ($\beta$), flame suppression number (FSN), and volume factor (*VF*) for gaseous agents evaluated in this study.**

## Experimental Uncertainty

The data assembled during this investigation provide a quantitative measure of the effectiveness of different compounds for suppressing a laboratory scale, fuel lean, JP-8 turbulent spray flame. The injection time interval for a fixed set of conditions varied by as much as 8.3 ms (1/120 s) because the solenoid valve operates on 60 Hz AC power. This does not add to the uncertainty in the mass nor rate of injection since both of these parameters are determined from the actual pressure trace independent of the initial time interval setting. The reported values of mass and $\beta$ vary less than $\pm 8$ percent between experiments taken on different days for the same actual injection interval. Undiscovered systematic errors increase the uncertainty in the absolute values of pressure, injection times and flow rates of the fuel and air. The uncertainty in relative values, however, remains less than $\pm 10$ percent since the systematic errors are greatly reduced by the normalization procedure. This level of certainty in $\beta$, FSN, and VF is sufficient to rank the agents and to identify the best choices for full-scale testing.

## Conclusions

It is concluded that the turbulent spray burner facility produces a stable flame over a range of air and fuel flows, and that the agent delivery system is able to control accurately the injection period between about 20 and 900 ms. The bench-scale spray burner is suitable for comparing the performance of gaseous extinguishing agents in transient operation, but full-scale engine nacelle trials are required to verify if the results can be reliably scaled up by the needed factor of 100.

The mass fraction, total mass, and minimum volume of agent required to extinguish a given flame must all be considered when ranking the performance of different fire fighting agents. Of the twelve alternatives to halon 1301 evaluated in the turbulent spray burner, nitrogen required the least mass to extinguish the flame, followed by HCFC-22; FC-31-10 required the most. The spread between the most and least effective fluorinated alternatives (on a mass basis) is not large, but is greater than the uncertainty of the results ($\pm 10$ percent).

On a volume basis, the two HCFCs were the best and nitrogen the poorest performer. The mixture of HFC-32 and HFC-125 had the largest volume factor of the chemicals with critical temperatures greater than 25°C.

The alternative agents performed better in the turbulent spray burner relative to halon 1301 than was predicted from cup burner measurements. It is suspected that this is due to the higher strain rates present in the spray burner and the reduced amount of time for the bromine atom in halon 1301 to chemically inhibit the combustion process. The chlorine containing compounds, overall, appeared to be the most effective alternatives. Generally speaking, about twice as much mass and volume were needed to suppress the spray flame using these alternative agents when compared to halon 1301.

## Acknowledgments

The authors wish to acknowledge the U.S. Air Force, Army, and Navy and the Federal Aviation Administration for funding the Agent Screening for Halon 1301 Aviation Replacement program. The project was under the direction of Mr. Michael Bennett at the Flight Dynamics Laboratory, Vehicle Subsystems Division, Survivability Enhancement Branch, Wright Patterson AFB.

## References

Anderson, S. O., 1987, "Halons and the Stratospheric Ozone Issue," *Fire Journal,* Vol. 81, pp. 56–62, 118–125.

Bennett, M., 1992, "Halon Replacement for Aviation Systems," *Proceedings of the 1992 International CFC and Halon Alternatives Conference,* The Alliance for Responsible CFC Policy, Fredrick, MD, Sept., p. 667.

Booth, K., Melia, B. J., and Hirst, R., 1973, "Critical Concentration Measurements for Flame Extinguishment Using a Laboratory 'Cup Burner' Apparatus," ICI Mond Division, Wilmington Laboratory, Aug. 31.

Grosshandler, W., Lowe, D., Rinkinen, W., and Presser, C., 1993, "A Turbulent Spray Burner for Assessing Halon Alternative Fire Suppressants," ASME Paper No. 93-WA/HT-23.

Grosshandler, W. L., Gann, R. G., and Pitts, W. M., eds., 1994, *Evaluation of Alternative In-Flight Fire Suppressants for Full-Scale Testing in Simulated Aircraft Engine Nacelles and Dry Bays,* NIST SP-861, Apr.

Hamins, A., Gmurczyk, G., Grosshandler, W., Rehwoldt, R., Vázquez, I., Cleary, T., Presser, C., and Seshadri, K., 1994, "Flame Suppression Effectiveness," in: *Evaluation of Alternative In-Flight Fire Suppressants for Full-Scale Testing in Simulated Aircraft Engine Nacelles and Dry Bays,* W. L. Grosshandler, R. G. Gann, and W. M. Pitts, eds., NIST SP-861, Apr., Sec. 4.

Harrington, J. L., 1993, "The Halon Phaseout Speeds Up," *NFPA Journal,* Vol. 87, No. 2, pp. 38–42.

Liñan, A., 1974, "The Asymptotic Structure of Counterflow Diffusion Flames for Large Activation Energies," *Acta Astronautica,* Vol. 1, p. 1007.

Pitts, W. M., Nyden, M. R., Gann, R. G., Mallard, W. G., and Tsang, W., 1990, "Construction of an Exploratory List of Chemicals to Initiate the Search for Halon Alternatives," NIST Technical Note 1279, Aug.

Sheinson, R. S., Penner-Hahn, J. E., and Indritz, D., 1989, "The Physical and Chemical Action of Fire Suppressants," *Fire Safety Journal,* Vol. 15, pp. 437–450.

Tucker, D. M., Drysdale, D. D., and Rasbash, D. J., 1981, "The Extinction of Diffusion Flames Burning in Various Oxygen Concentrations by Inert Gases and Bromotrifluormethane," *Combustion and Flame,* Vol. 41, p. 293.

Van Wylen, G. J., and Sonntag, R. E., 1978, *Fundamentals of Classical Thermodynamics,* 2nd ed., Wiley, New York, p. 400.

Williams, F. A., 1974, "A Unified View of Fire Suppression," *Journal of Fire and Flammability,* Vol. 5, p. 54.

Yang, J., and Breuel, B., 1994, "Thermodynamic Properties of Alternative Agents," in: *Evaluation of Alternative In-Flight Fire Suppressants for Full-Scale Testing in Simulated Aircraft Engine Nacelles and Dry Bays,* W. L. Grosshandler, R. G. Gann, and W. M. Pitts, eds., NIST SP-861, Apr., Sec. 2.



Downloaded 12 Dec 2010 to 193.140.21.150. Redistribution subject to ASME license or copyright; see http://www.asme.org/terms/Terms_Use.cfm

**O. Deutschmann**
Graduate Student.

**U. Riedel**
Postdoctoral Fellow.

**J. Warnatz**
Professor.

Institut für Technische Verbrennung,
Universität Stuttgart,
70550 Stuttgart,
Federal Republic of Germany

# Modeling of Nitrogen and Oxygen Recombination on Partial Catalytic Surfaces

*In connection with recombination coefficients derived from experimental data described in the literature, a reaction scheme including detailed rate expressions for O and N atom recombination on the surface of re-entry vehicles is established, consisting of elementary reaction steps. To validate the reaction mechanism derived, surface chemistry and fluid mechanical processes are coupled assuming a one-dimensional stagnation flow field. A quantitative agreement is achieved between recombination coefficients resulting from the numerical computations and those calculated from experiments. The temperature dependence of the recombination coefficient is explained by elementary reaction steps. Furthermore, the reaction scheme established is implemented in a two-dimensional Navier–Stokes code computing the re-entry flow around a simple geometry to show the importance of a detailed modeling of surface reactions.*

## Introduction

Nitrogen and oxygen atom recombination on partial catalytic surfaces has gained new attention during the last years in connection with heat transfer problems of hypersonic vehicles. During re-entry of a reusable space vehicle, like the Space Shuttle in the upper atmosphere, a shock wave forms in front of the vehicle and leads to a very high translational temperature in the flow field. A large amount of nitrogen and oxygen molecules are dissociated under these conditions and a nonnegligible part of the O and N atoms produced strike the surface of the orbiter and recombine catalytically to molecules, generating heat. This heat of recombination is responsible for a considerable part of the increase of the orbiter surface temperature and, hence, affects the performance of heat shields of these hypersonic vehicles.

This paper focuses on the development of a model to describe atom recombination using a detailed surface reaction mechanism. This mechanism is established in connection with recombination coefficients calculated from experiments described in the literature. The model is validated by a stagnation flow field simulation.

Finally, the reaction scheme is implemented in a two-dimensional Navier–Stokes code to simulate the flow around a simple half-cylinder showing the influence of partial catalytic surfaces in flow field regions close to the surface.

## Recombination Experiments and Models

In the last two decades, several experiments were performed to study the recombination processes occurring on materials which can be used for thermal protection systems. The coating of the high-temperature reusable surface insulation (HRSI) of the Space Shuttle is called "reaction cured glass (RCG)." RCG is made of silica (94 percent), $B_2O_3$ (4 percent), and $SiB_4$ (2 percent) (Kim and Boudart, 1991) and shows a low probability of atom recombination. However, some recombination occurs and has to be taken into account in order to calculate the surface heat flux.

The first flight experiment that clearly demonstrated the effect of surface catalysis on the surface heat flux to a space vehicle during re-entry was conducted by Stewart et al. (1981, 1982, 1983). Further experiments to investigate the atom recombination on RCG-coated HRSI surfaces were done by Scott (1981), Kolodziej and Stewart (1987), Willey (1988), and Stewart et al. (1991). They used arc plasma test facilities where the recombination data are inferred from stagnation point heat flux measurements in a high-temperature dissociated arc jet flow. In contrast to that, Breen and Rosner (1973) as well as Marinelli and Campbell (1986) and Marinelli (1988) used measurements of atom concentrations before and after passing the surface. The only data available from the Marinelli experiments are for RCG at 300 K. Breen and Rosner (1973) used Lockheed's LI-0042 coating for their experiments.

The fraction of the chemical energy transferred to the surface by atom recombination depends on the rate at which atoms are recombining and releasing their dissociation energy on the surface. Two coefficients are defined to describe the global recombination process, the recombination coefficient $\gamma$, and the chemical energy accommodation coefficient $\beta$. The fraction of incident atoms impinging on the surface that recombine is defined as the recombination coefficient

$$\gamma \equiv \frac{m}{m_\downarrow}, \tag{1}$$

where $m_\downarrow$ is the mass flux of the incident atoms and $m$ is the mass flux of recombining atoms.

The chemical energy accommodation coefficient $\beta$ is defined as

$$\beta \equiv \frac{q_c}{m h_D}, \tag{2}$$

where $q_c$ is the chemical energy flux to the surface by recombination and $h_D$ is the enthalpy of dissociation per unit mass. The net energy transferred to the surface depends on the product of the recombination coefficient and the chemical energy accommodation coefficient. This product $\gamma\beta$ is also called energy transfer recombination coefficient and is a function of temperature.

The experimental data show the general trend that the recombination coefficients ($\gamma$ as well as $\gamma\beta$) reach a maximum at about 1600 K. But we must distinguish between two kinds of experiments: Data derived from heat flux measurements correspond to the energy transfer recombination coefficient, while experiments considering atom concentrations correspond to the recombination coefficient. $\gamma$ as well as $\gamma\beta$ have to be considered in order to describe exactly the flow around a hypersonic vehicle and the heat transfer to its surface.

Different models were developed to predict those recombination coefficients. Here, only some main ideas of these models can

Contributed by the Heat Transfer Division for publication in the JOURNAL OF HEAT TRANSFER. Manuscript received by the Heat Transfer Division September 1993; revision received May 1994. Keywords: High-Temperature Phenomena, Reacting Flows, Space Power Systems. Associate Technical Editor: W. L. Grosshandler.



Copyright © 1995 by ASME

Downloaded 12 Dec 2010 to 193.140.21.150. Redistribution subject to ASME license or copyright; see http://www.asme.org/terms/Terms_Use.cfm

be mentioned. Recently, Willey (1993) compared five kinetic models for atom recombination in detail, so we can refer to his work.

In principle, there are two reaction paths possible for recombination of atoms on a surface: Considering the first path, an atom near the surface reacts with an adsorbed surface atom to form a molecule which desorbs immediately. This mechanism is called the Eley–Rideal mechanism (ER). In contrast to that, the Langmuir–Hinshelwood mechanism (LH) describes the reaction of two neighboring adsorbed surface atoms to a molecule that can desorb into the gas phase. Willey (1993) derived four models for the energy transfer catalytic recombination coefficient on the basis of either the ER or the LH mechanism. The most appropriate model was shown to be a four-parameter model depending on temperature only. It includes adsorption equilibrium and is based on the ER mechanism.

Seward and Jumper (1991) derived a model for oxygen recombination on silicon-dioxide surfaces, the basic material the Space Shuttle thermal protection tiles are made of. The model is based on the ER mechanism and takes into account adsorption and desorption of atoms and the recombination reaction of a gas-phase oxygen atom with an adsorbed surface atom.

## A Detailed Model Based on Elementary Reactions

The models described in the literature either use a global one-step mechanism or involve only one of the two possible recombination processes (e.g., LH or ER mechanism). The use of global one-step mechanisms (e.g., using recombination and accommodation coefficients for surface reactions) obtained by empirical fitting is limited to conditions very similar to that of the fit process. Extrapolation in this case is a risky procedure and can lead to a breakdown of the model used, due to the strong nonlinearities included in the rate laws describing chemistry.

Therefore, the necessity of extrapolation to conditions far beyond the limits of validation of a chemistry model (density and temperature can differ by orders of magnitude between measurement and application for hypersonic problems) leads to the need for a more sophisticated concept as it is offered by use of detailed reaction mechanisms consisting of elementary steps. This use of elementary reactions has the advantage that their rate coefficients depending exclusively on temperature (the so-called "pressure dependence" of rate coefficients results from missing resolution in elementary steps, i.e., interaction of several elementary reactions). This temperature dependence can be described in a rather simple manner by a modified Arrhenius expression

$$k = AT^b \exp(-E_A/RT), \tag{3}$$

**Table 1 Gas-phase reaction mechanism**

| Reaction | $A$ (cm, mole, s) | $b$ | $E_A$ (kJ/mole) |
|---|---|---|---|
| *Dissociation:* | | | |
| $O_2 + M_1 \rightarrow O + O + M_1$ | $2.70 \times 10^{19}$ | −1.00 | 494.00 |
| $N_2 + M_2 \rightarrow N + N + M_2$ | $3.70 \times 10^{21}$ | −1.60 | 941.00 |
| $NO + M_3 \rightarrow N + O + M_3$ | $2.90 \times 10^{15}$ | 0.00 | 621.00 |
| *Exchange:* | | | |
| $O + N_2 \rightarrow NO + N$ | $1.82 \times 10^{14}$ | 0.00 | 319.00 |
| $NO + O \rightarrow O_2 + N$ | $3.80 \times 10^{09}$ | 1.00 | 173.00 |

*Collision efficiencies of third bodies:*

| | $O_2$ | $N_2$ | O | N | NO |
|---|---|---|---|---|---|
| $M_1$ | 1.00 | 0.10 | 2.80 | 0.10 | 0.10 |
| $M_2$ | 0.10 | 1.00 | 0.10 | 2.80 | 0.10 |
| $M_3$ | 0.05 | 0.05 | 1.00 | 1.00 | 1.00 |

with the pre-exponential factor $A$, the temperature coefficient $b$, and the activation energy $E_A$ with a well-defined physical or chemical meaning.

The concept of elementary reactions is well tested and commonly accepted in homogeneous gas phase reacting systems (e.g., in gas phase combustion as a rather complicated and challenging case of a reacting flow), and has recently been extended to other reacting flows (hypersonic problems, chemical vapor deposition, etc.). Applications of this concept to heterogeneous reacting flow additionally demand knowledge of surface chemistry in terms of elementary reaction rate coefficients (Warnatz, 1992). Unfortunately, in contrast to the state of the art in gas phase chemistry, there is a nearly complete lack of these rate data in the literature.

The atom recombination model proposed in this paper uses the concept of elementary reactions and involves the LH as well as the ER mechanism. The probability of recombination depends on the gas properties as well as on surface properties. Therefore, the processes in both phases have to be coupled and cannot be considered to be independent of each other.

## Gas-Phase Chemistry

The gas-phase reaction scheme is taken directly from models of air dissociation chemistry by Riedel et al. (1993a) without modification. The mechanism used and the associated rate expressions are shown in Table 1. For some of the reactions, a modified Arrhenius expression, Eq. (3), has to be considered.

## Nomenclature

$A$ = pre-exponential factor
$[A]$ = concentration of species $A$
$A_{\text{eff}}$ = effective surface site area
$b$ = temperature coefficient
$D$ = molecular diameter of surface species
$E_A$ = activation energy
$E_D$ = desorption energy
$h_D$ = enthalpy of dissociation per unit mass
$h_k$ = specific enthalpy of species $k$
$j_k$ = gas-phase mass flux of species $k$ to the surface
$k$ = rate coefficient
$k_{\text{ads}}$ = adsorption rate coefficient
$k_{\text{des}}$ = desorption rate coefficient
$K_g$ = number of gas phase species
$K_s$ = number of surface species
$L$ = distance from reactor inlet to disk
$m$ = mass flux of recombining atoms
$m_1$ = mass flux of the incident atoms
$M_k$ = molecular mass of species $k$
$M_\infty$ = free-stream Mach number
$q_c$ = chemical energy flux to the surface by recombination
$R$ = universal gas constant
$S$ = initial sticking coefficient
$\dot{s}_k$ = chemical molar production rate by surface reaction
$T$ = temperature
$T_w$ = wall temperature
$u$ = bulk normal fluid velocity at the surface
$V_k$ = diffusion velocities
$x$ = distance normal to the disk surface
$Y_k$ = gas-phase species mass fractions
$\beta$ = energy accommodation coefficient
$\gamma$ = recombination coefficient
$\Gamma$ = surface site density
$\epsilon$ = surface emissivity
$\lambda$ = thermal conductivity
$\nu$ = vibrational frequency
$\rho$ = mass density
$\sigma$ = Stefan–Boltzmann constant
$\tau$ = sum of surface reactants' stoichiometric coefficients



Downloaded 12 Dec 2010 to 193.140.21.150. Redistribution subject to ASME license or copyright; see http://www.asme.org/terms/Terms_Use.cfm

In some reactions, a third body is required for the reaction to proceed. When this is the case, the concentration of the third body must appear in the expression for the rate-of-progress variable. Some species often act more efficiently as third bodies than others do. Therefore, collision efficiencies are used to describe this behavior, see Table 1.

## Gas-Surface Interaction

Multistep treatment of oxygen and nitrogen atom surface recombination in terms of elementary reactions has to include the following processes (see Fig. 1):

1 adsorption of O and N atoms
2 desorption of adsorbed atoms
3 Eley–Rideal recombination
4 Langmuir–Hinshelwood recombination
5 desorption of recombination products like $N_2$, $O_2$

The adsorption of $N_2$ and $O_2$ is neglected in the following discussion due to the high temperatures encountered during re-entry.

All of the processes (1)–(5) are included in the reaction scheme established in Table 2, as a result of comparison between experimental data and data extracted from our stagnation flow field computations. Therefore, in the remainder of this section we discuss the different rate laws needed to model each elementary reaction step, whereas in the next section the boundary conditions imposed in the numerical computations and the solution methods are presented.

In Table 2 the symbol "(s)" denotes a free surface site and species with a label "(s)" are adsorbed at the surface. The rate coefficients $k$ are assumed to have an Arrhenius temperature dependence where the pre-exponential factor $A$ and the activation energy $E_A$ are specified; see Eq. (3). The temperature exponent $b$ is always assumed to be zero. For adsorption processes, sticking coefficients are given. Sticking coefficients describe the fraction of incident atoms impinging on a surface that are really adsorbed. Considering a clean surface, the term initial sticking coefficient is used. To convert initial sticking coefficients $S$ to usual kinetic rate coefficient, there is the relation (Motz and Wise, 1960)

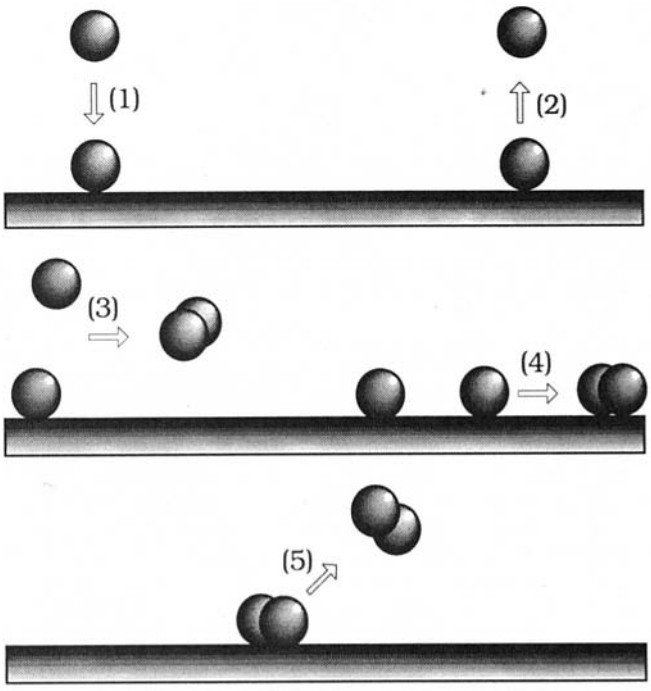



**Fig. 1 Elementary steps during surface recombination of atoms**

**Table 2 Surface reaction mechanism**

| Reaction | $A$ (cm, mole, s) | $E_A$ (kJ/mole) |
|---|---|---|
| *Adsorption:* | | |
| O + (s) → O(s) | 0.1 (sticking coefficient) | |
| N + (s) → N(s) | 0.1 (sticking coefficient) | |
| *Desorption:* | | |
| O(s) → O + (s) | $5.0*10^{11}$ | 200 |
| N(s) → N + (s) | $7.3*10^{11}$ | 215 |
| $O_2$(s) → $O_2$ + (s) | $1.0*10^{12}$ | 10 |
| $N_2$(s) → $N_2$ + (s) | $1.0*10^{12}$ | 10 |
| *Eley–Rideal Mechanism (low energy accommodation):* | | |
| O + O(s) → $O_2$ + (s) | $6.0*10^{13}$ | 60 |
| N + N(s) → $N_2$ + (s) | $2.5*10^{13}$ | 40 |
| *Langmuir–Hinshelwood Mechanism (high energy accommodation):* | | |
| O(s) + O(s) → $O_2$(s) + (s) | $2.0*10^{19}$ | 160 |
| N(s) + N(s) → $N_2$(s) + (s) | $7.0*10^{17}$ | 130 |

$$k_{\text{ads}} = \frac{S}{1 - S/2}\frac{1}{\Gamma^{\tau}}\sqrt{\frac{RT}{2\pi M_k}} \tag{4}$$

with $\Gamma$ = total surface site concentration, $\tau$ = sum of surface reactants' stoichiometric coefficients, $T$ = gas temperature, and $M_k$ = molecular mass. $\tau$ is equal to unity for all adsorption reactions given in Table 2.

Considering a surface reaction with species $A$, $B$, and $C$ (see Table 2)

$$A + B \rightarrow C \tag{5}$$

the chemical production rate $\dot{s}_k$ of species $C$ is calculated from the concentrations $[A]$ and $[B]$ and the rate coefficient $k$ as

$$\dot{s}_k = k[A][B], \tag{6}$$

where gas-phase concentrations are given in mole $cm^{-3}$, concentrations for adsorbed species in mole $cm^{-2}$, and the production rate in mole $cm^{-2}\,s^{-1}$.

In the literature, there are only few rate data for reactions on silicon-dioxide-like surfaces. Sticking coefficients for such materials vary between $10^{-3}$ and $10^{-1}$. Seward and Jumper (1991) suggested for their recombination model a temperature dependent initial sticking coefficient of $S = 0.05\ \exp(-T/500\ \text{K})$ based on experiments of $O_2$ adsorption on silica and a fit to experimental recombination coefficients. We used the relatively large initial sticking coefficient of 0.1 for atomic oxygen and nitrogen, because no bond has to be broken before adsorption.

Rate coefficients for desorption can be approximately estimated from (Christmann, 1991)

$$k_{\text{des}} = \nu \exp(-E_D/RT) \tag{7}$$

with $\nu$ = vibrational frequencies of the bond considered, $E_D$ = desorption energy. Experimentally determined frequency factors for first-order desorption reactions range usually between $10^{11}$ $s^{-1}$ and $10^{14}$ $s^{-1}$. A half-bond strength of a Si–O bond in a $SiO_2$ molecule is about 225 kJ $mole^{-1}$ (Wells, 1962). We used these values as a initial set of coefficients ($\nu$, $E_D$) for our computations. Molecular oxygen and nitrogen can be regarded to be in an intermediate state on the surface after recombination and desorb after a very short residence time, and therefore, the activation energy is very small.

Surface reaction rate coefficients for the LH mechanism can be estimated from the frequency of surface collisions (Ljungström et al., 1989)



Downloaded 12 Dec 2010 to 193.140.21.150. Redistribution subject to ASME license or copyright; see http://www.asme.org/terms/Terms_Use.cfm

$$\nu_{\text{surf}} = \frac{D}{A_{\text{eff}}}\sqrt{\frac{\pi RT}{2M_k}} \tag{8}$$

with $D$ = molecular diameter of surface species and $A_{\text{eff}}$ = effective surface site area, and $M_k$ the molecular mass. We estimated a value of about $10^{+18}$ cm$^2$ mole$^{-1}$ s$^{-1}$ for oxygen in a $SiO_2$ surface structure. In this simple picture, the exponential term of $k$ can be regarded as the number of successful collisions (having the necessary activation energy). Hence, $\nu_{\text{surf}}$ is a maximum value for the rate coefficient $k$. The surface site density used is $1.35 \times 10^{19}$ m$^{-2}$, estimated from the density of silica.

Experimental results of recombination coefficient measurements have been used for a more detailed determination of rate coefficients. A stagnation flow field was simulated (see below) to compare recombination coefficients determined from experiments with those coming from the model proposed here.

The location of the inflection of the temperature dependence of the recombination coefficient serves as fitting parameter for the ratio of atom desorption reactions and the recombination reactions. Heat balances during recombination are used to get proper heat accommodation coefficients by a fit of the reaction of the two surface recombination mechanisms (see discussion below).

## Stagnation Flow Field

To validate the model, a stagnation flow field is considered as shown in Fig. 2. At a distance $x = L$ away from the stagnation point of a flat-faced configuration, a uniform velocity distribution flow is imposed. By confining the attention to the center of the surface, edge effects can be neglected, permitting use of a one-dimensional analysis (Warnatz et al., 1994). The variables are independent of radius. The boundary-value problem that has to be solved is stated by Evans and Greif (1987) and by Kee et al. (1988).

The solution of the gas-phase problem is coupled with the surface properties and the reaction scheme associated. Therefore, the surface boundary conditions become more complex. The gas-phase mass flux of each species $k$ to the surface, $j_k$, is a combination of diffusive and convective processes and is balanced by the creation or depletion rate of that species, $\dot{s}_k$, by surface reactions, i.e.,

$$j_k = \rho Y_k u + \rho Y_k V_k = \dot{s}_k M_k \quad (k = 1, \ldots, K_g), \tag{9}$$

where $u$ is the bulk normal fluid velocity at the surface (Stefan velocity) and $V_k$ is the diffusion velocity, $Y_k$ the mass fraction, and $M_k$ the molecular mass of the $k$th species. $\rho$ is the density and $K_g$ is the number of gas-phase species.

The temperature boundary condition is derived from an energy balance at the interface: The conductive, convective, and diffusive energy transport in the gas phase is balanced by thermal radiative and chemical heat release at the surface,

$$\lambda\frac{\partial T}{\partial x} - \sum_{k=1}^{K_g}\rho Y_k(V_k + u)h_k = \sigma\epsilon(T^4 - T_w^4) + \sum_{k=K_g+1}^{K_g+K_s}\dot{s}_k M_k h_k. \tag{10}$$

Here, $\lambda$ is the thermal conductivity and $h_k$ the specific enthalpy of species $k$. In the radiation term, $\sigma$ is the Stefan–Boltzmann constant, $\epsilon$ is the surface emissivity, and $T_w$ is the wall temperature to which the surface radiates. The sum on the right-hand side runs over all surface species.

We used the code SPIN developed by Coltrin et al. (1991a) for the computational solution of the stagnation flow problem. SPIN computes species, temperature, and velocity profiles, and fluxes at the gas-surface interface as well as surface coverages. The program accounts for finite-rate gas-phase, surface chemical kinetics, and multicomponent molecular transport. SPIN is designed to run in conjunction with the CHEMKIN (Kee et al., 1989), SURFACE CHEMKIN (Coltrin et al., 1991b), and TRANSPORT (Kee et al., 1983, 1986) packages, where the details of the chemical reaction rate and transport property formulation can be found. SPIN uses the TWOPNT solver (Grcar, 1991) that implements a Newton/time step algorithm (Grcar et al., 1986) to obtain the steady-state solution.

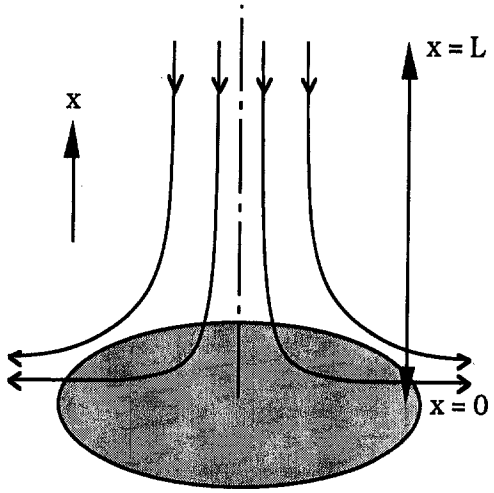



**Fig. 2 Sketch of stagnation flow field**

The initial conditions for the simulation are chosen to be similar to that in the experiments of Scott (1981) and Kolodziej and Stewart (1987), which are used for the fit of kinetic data in the model. The inlet velocity was 2000 m s$^{-1}$ and the distance between the inlet and the surface is set to be $L$ = 10 cm. The initial gas temperatures varied in the computation to obtain surface temperatures in the region of 800 K to 2000 K. Air or nitrogen is chosen as the initial gas. The inlet pressure and the initial gas composition (the relation of O to $O_2$ and N to $N_2$) is chosen according to the experimental pressure values and the atom concentration at the surface. The total pressure used ranges from 500 Pa to 3000 Pa, and the atom mass fractions are varied between 0.1 and 0.8. A summary of the experimental data used is given by Willey (1993). A surface emissivity of silica of $\epsilon$ = 0.8 (Weast, 1987) is assumed in all computations.

## Results and Discussion

The number of atoms striking the surface can be derived from the kinetic theory of gases, using the temperature and the partial pressure at the surface. SPIN computes the species mass fluxes at the gas-surface interface as well as the contribution of surface reactions to the species destruction rates. That allows us to distinguish between the recombination due to LH or ER mechanism, respectively, and to calculate recombination coefficients according Eq. 1.

A key question is whether the ER or the LH mechanism dominates. For the purpose of predicting thermal load on a surface exposed to dissociated gas, these mechanisms differ considerably: Melin and Madix (1971) and Halpern and Rosner (1978) have measured recombination and energy transfer coefficients independently and found that the energy transferred per molecule to many materials is much less than the dissociation energy.

Here, it is assumed that the molecules, formed due to LH recombination, loose all their heat of dissociation to the surface ($\beta$ = 1), but $\beta$ for the ER mechanism is less than unity. This implies that the molecules formed at the surface due to the ER mechanism must leave the surface in exited states. They may be quenched in the boundary layer or restrike to the wall and give up their excitation energy as described by Rosner and Feng (1974).



Downloaded 12 Dec 2010 to 193.140.21.150. Redistribution subject to ASME license or copyright; see http://www.asme.org/terms/Terms_Use.cfm

The calculated temperature dependence of the recombination coefficients $\gamma$ for oxygen (Fig. 3) and nitrogen (Fig. 4) are compared with values calculated from arc-jet heat flux data and data extracted from an atom density measurement. Curves are shown for two simulation cases: The first one denotes the total recombination coefficients due to both recombination processes; the second one takes only the LH recombination into account. Thus, comparison of simulated data and data calculated from experiments is easier.

The measurements of Breen and Rosner (1973) in which numbers of atoms recombining were measured correspond to the simulated total recombination coefficients. In contrast to that, Scott (1981) as well as Kolodziej and Stewart (1987) determined the recombination coefficient from stagnation point heat flux measurements in a high-temperature dissociated arc jet flow. Therefore, they consider an energy transfer recombination coefficient, i.e., $\gamma\beta$ instead of $\gamma$. It can be seen from the comparison of the recombination coefficients that the recombination based on number of atoms is about a factor of five larger than that based on heat flux. This implies that $\beta$ is much less than unity and has a value of about 0.2 for the tile materials used.

The ER mechanism is assumed to have a low-energy accommodation on the surface ($\beta < 1$) in contrast to LH mechanism ($\beta = 1$), see above. Hence, the total recombination coefficients have to be larger than the recombination coefficients measured by the heat flux method. On the other hand, these heat flux measured recombination coefficients must be larger than coefficients provided only by the LH mechanism simulation only. This fact was used for a more detailed determination of rate coefficients for the LH and ER reactions, respectively.

Both experimental and simulated recombination coefficients show a strong temperature dependence. They rise with increasing temperature up to a value of almost $10^{-1}$ for a temperature of about 1600 K. Further temperature increase yields a fall-off of $\gamma$. This high-temperature effect on the recombination coefficient for RCG was first reported by Stewart and Leiser (1976) using arc-jet data.

At low temperatures, the surface is well covered by adsorbed N and O atoms having a low thermal energy. The surface diffusion and the recombination of two adsorbed atoms (LH mechanism) require a certain thermal activation energy. Hence, the recombination is almost only realized when a gaseous atom strikes the surface with sufficient energy (ER mechanism) and the recombination rate is limited by the flux of atoms to the surface. This behavior results in very small energy transfer recombination coefficients (see values derived from heat flux measurements) and a low $\gamma$ due to LH recombination (computations), respectively, whereas the total recombination coefficient has a considerable value (see Figs. 3 and 4).

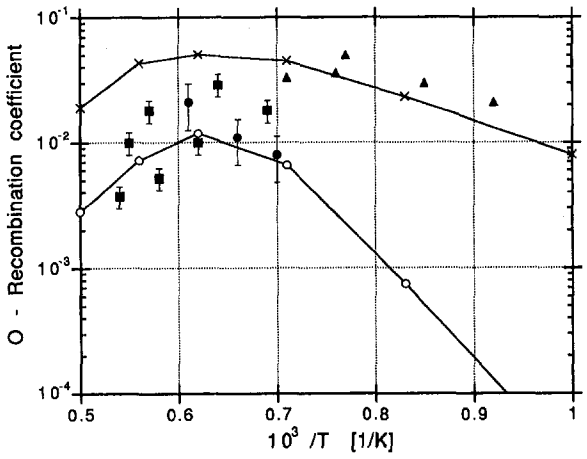



**Fig. 3 Comparison of experimental and simulated data for the temperature dependence of the oxygen recombination coefficient; experiment: ▲ atom density measurements by Breen and Rosner (1973), ■ heat flux measurements by Kolodziej and Stewart (1987), ● heat flux measurements by Scott (1981); simulation: × total recombination coefficient, ○ Langmuir-Hinshelwood recombination coefficient**

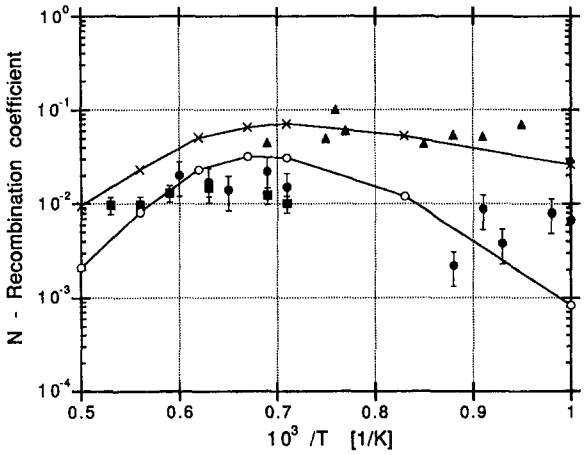



**Fig. 4 Comparison of experimental and simulated data for the temperature dependence of the nitrogen recombination coefficient; experiment: ▲ atom density measurements by Breen and Rosner (1973), ■ heat flux measurements by Kolodziej and Stewart (1987), ● heat flux measurements by Scott (1981); simulation: × total recombination coefficient, ○ Langmuir-Hinshelwood recombination coefficient**

For increasing temperature, the importance of the LH recombination rises rapidly, leading to high recombination coefficients and heat flux. The maximum of recombination is achieved for about 1600 K. At this temperature, the shift of the adsorption–desorption equilibrium of oxygen and nitrogen atoms towards desorption leads to a more and more empty surface. The probability that gaseous atoms strike an adsorbed atom becomes very low and, on the other hand, the low surface coverage yields substantially less neighboring sites placed by O or N atoms, respectively. Both processes together result in a decrease of energy transfer as well as the total recombination coefficient.

## Two-Dimensional Computation With Detailed Surface Chemistry

The model for atom recombination was implemented into a two-dimensional Navier–Stokes code calculating the hypersonic flow around a half-cylinder in order to take catalytic wall effects into account.

Whereas very often mathematical modeling is simplified for two-dimensional geometries by neglecting second-order effects like molecular transport and thus solving the Euler equations, gas-surface interactions require the solution of the full set of Navier–Stokes equations. The detailed nonequilibrium surface reaction scheme described above has been implemented in a two-dimensional Navier–Stokes code solving fluid mechanical equations, gas-phase chemistry, and surface chemistry together with a detailed transport model in a fully coupled approach.

## Governing Equations and Solution Procedure

The solution algorithm is based on a fully conservative formulation of the conservation equations and uses a first-order flux splitting scheme (Fletcher, 1988) for the convective terms. All second-order derivatives are approximated by central differences. The system of ordinary differential-algebraic equations resulting after spatial discretization is solved using the semi-implicit extrapolation code LIMEX (Deuflhard et al., 1987), which integrates the equations in time until the steady state is reached. On the boundaries, all time-dependent equations are replaced by algebraic equations containing no time derivatives.



Downloaded 12 Dec 2010 to 193.140.21.150. Redistribution subject to ASME license or copyright; see http://www.asme.org/terms/Terms_Use.cfm

A detailed discussion of the numerical algorithm and the discretization techniques to capture the strong shock wave in front of the re-entry body can be found in Riedel (1993a, b). The transport model implemented to calculate the mixture viscosity, the thermal conductivity, and the binary diffusion coefficients is documented in Kee et al. (1986).

## Results

The numerical method described above has been used to calculate the nonequilibrium hypersonic flow around a half-cylinder (infinite in the third direction) with a radius of 1 m. Free-stream conditions are taken to correspond approximately to the *standard atmosphere* (U.S. Standard Atmosphere, 1976) at a geometric altitude of 75 km ($p_\infty = 2.52$ Pa, $\rho_\infty = 0.43 * 10^{-4}$ kg m$^{-3}$, $T_\infty = 205.3$ K). The free-stream Mach number is $M_\infty = 25.0$.

The computational domain is depicted in Fig. 5. It shows a sketch of the half cylinder in the $(x, y)$ plane. $(x, y) = (-1.0$ m, 0.0 m) is the body surface on the symmetry line. All profiles are plotted as a function of the $x$ coordinate: in the region $-1.5$ m $\leq x < -1.0$ m along the symmetry line in front of the body and for $x \geq -1.0$ m along the body surface.

Two models have been compared: In a first calculation a fully noncatalytic wall has been assumed, whereas in the second case the processes on the surface have been modeled on the basis of the detailed surface reaction scheme. Concerning the surface boundary conditions for species and energy, Eqs. (9) and (10) were implemented together with the no-slip condition for the velocity and a zero gradient of pressure normal to the body surface.

Figure 6 clearly indicates that catalytic effects have an important influence on the surface temperature as well as on the concentrations near and at the surface itself. The stagnation point temperature of 1920 K computed with the detailed surface reaction model is increased by 80 K if compared to the result for a fully noncatalytic wall (1840 K). The mass fraction of atomic oxygen found in the stagnation point is 0.19, a significant difference to the value of 0.23 we get when catalytic effects are ignored.

The temperature in the region close to the body is decreasing from the stagnation point to the outflow boundary in both cases. But, including detailed surface chemistry in the model, as a result of the interaction of surface and gas phase chemistry we have an increase of oxygen molecules and decrease of atomic oxygen in this region.

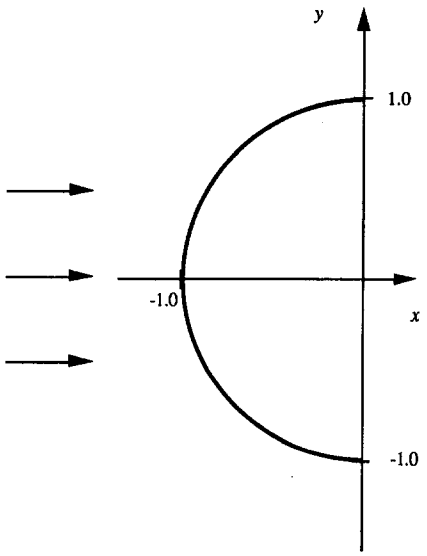



**Fig. 5 Sketch of the half-cylinder in the $(x, y)$ plane. $(x, y) = (-1.0$ m, 0.0 m) is the body surface on the symmetry line. The flow is coming from the left with a Mach number of 25.0; for other inflow conditions see text.**

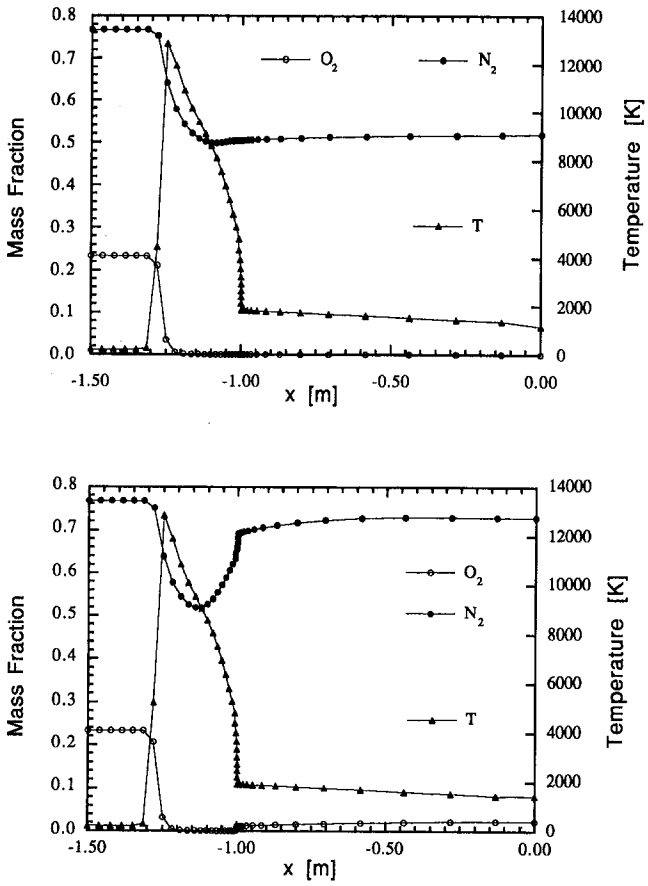



**Fig. 6 Comparison of temperature, molecular oxygen, and molecular nitrogen profiles along the symmetry line and along the body surface. Upper part: noncatalytic wall. Lower part: partial catalytic wall with finite rate surface chemistry.**

## Conclusion

The consideration of heat flux measurements as well as atom density measurements for oxygen and nitrogen atom recombination on a re-entry vehicle wall (RCG coated) allows us to study two recombination processes (LH and ER mechanisms). On that basis, a detailed surface reaction mechanism including rate expressions for O and N atom recombination on the surfaces is established. To test the model and for a more detailed determination of rate coefficients, the computer code SPIN simulating a stagnation flow field is used. A quantitative agreement could be achieved between simulated recombination coefficients and those calculated from experiments. The complex temperature dependence of the recombination coefficients are explained by elementary reaction processes.

The surface reaction scheme proposed was implemented in a two-dimensional Navier–Stokes code solving a re-entry problem. The oxygen and nitrogen profiles as well as the wall temperature were changed considerably in the region close to the body due to partial catalytic effects. Therefore, a finite rate surface chemistry should be included in the numerical prediction of hypersonic flow fields.

Possible extensions of the atom recombination model are:

Temperature has a strong effect on the energy accommodation coefficient $\beta$ for some materials. Halpern and Rosner (1978) showed for N recombination on iridium that $\beta$ increases with temperature up to 1600 K, then drops sharply. Stewart and Leiser (1976) pointed out that probably $\beta < 1$ and decreases at high temperature for RCG coating.

Decomposition and ablation of the insulation material itself could also be occurring under high temperature conditions and



Downloaded 12 Dec 2010 to 193.140.21.150. Redistribution subject to ASME license or copyright; see http://www.asme.org/terms/Terms_Use.cfm

influence the recombination process. Decomposition has been observed for several low-viscosity borosilicate glasses near 1480 K by Stewart and Leiser (1976). For higher viscosity glasses, like the RCG, this decomposition occurs at higher temperatures.

It was shown that the concept of elementary surface chemistry can be used to explain the observed temperature dependence of nitrogen and oxygen atom recombination on high temperature partial catalytic surfaces. However, more experimental work is recommended in order to determine the rate coefficients in more detail and substitute experimental results for some intuitive work.

## References


Breen, J., and Rosner, D. E., 1973, "Catalysis Study for Space Shuttle Vehicle Thermal Protection Systems," NASA Contract Report CR-134124.

Christmann, K., 1991, *Introduction to Surface Physical Chemistry,* Springer, New York.

Coltrin, M. E., Kee, R. J., Evans, G. H., Meeks, E., Rupley, F. M., and Grcar, J. F., 1991a, "SPIN: A Fortran Program for Modeling One-Dimensional Rotating Disk/Stagnation-Flow Chemical Vapor Deposition Reactors," Sandia National Laboratories Report SAND91-8003.

Coltrin, M. E., Kee, R. J., and Rupley, F. M., 1991b, "SURFACE CHEMKIN (Version 4.0): A Fortran Package for Analyzing Heterogeneous Chemical Kinetics at a Solid-Surface–Gas-Phase Interface," Sandia National Laboratories Report SAND90-8003B.

Deuflhard, P., Hairer, E., and Zugck, J., 1987, "One-Step and Extrapolation Methods for Differential-Algebraic Systems," *Numer. Math.,* Vol. 51, pp. 501–516.

Evans, G., and Greif, R., 1987, "A Numerical Model of the Flow and Heat Transfer in a Rotating Disk Chemical Vapor Deposition Reactor," ASME JOURNAL OF HEAT TRANSFER, Vol. 109, pp. 928–935.

Fletcher, C. A. J., 1988, *Computational Techniques for Fluid Dynamics,* Vol. II—*Specific Techniques for Different Flow Categories,* Springer, Berlin.

Grcar, J. F., Kee, R. J., Smooke, M. D., and Miller, J. A., 1986, "A Hybrid Newton/Time-Integration Procedure for the Solution of Steady, Laminar, One-Dimensional, Premixed Flames," *Twenty-First Symposium (International) on Combustion,* The Combustion Institute, Pittsburgh, pp. 1773–1782.

Grcar, J. F., 1991, "The TWOPNT Program for Boundary Value Problems," Sandia National Laboratories Report SAND91-8230.

Halpern, B., and Rosner, D. E., 1978, "Chemical Energy Accommodation at Catalyst Surfaces," *J.C.S. Faraday I.,* Vol. 74, pp. 1883–1912.

Kee, R. J., Warnatz, J., and Miller, J. A., 1983, "A FORTRAN Computer Code Package for the Evaluation of Gas Phase Viscosities, Heat Conductivities, and Diffusion Coefficients," Sandia National Laboratories Report SAND83-8209.

Kee, R. J., Dixon-Lewis, G., Warnatz, J., Coltrin, M. E., and Miller, J. A., 1986, "A Fortran Computer Code Package for the Evaluation of Gas-Phase Multicomponent Transport Properties," Sandia National Laboratories Report SAND86-8246.

Kee, R. J., Miller, J. A., Evans, G. H., and Dixon-Lewis, G., 1988, "A Computational Model of the Structure and Extinction of Strained Opposed Flow, Premixed Methane-Air Flame," *Twenty-Second Symposium (International) on Combustion,* The Combustion Institute, Pittsburgh, pp. 1479–1494.

Kee, R. J., Rupley, F. M., and Miller, J. A., 1989, "CHEMKIN-II: A Fortran Chemical Kinetics Package for the Analysis of Gas-Phase Chemical Kinetics," Sandia National Laboratories Report SAND89-8009.

Kim, Y. C., and Boudart, M., 1991, "Recombination of O, N, and H Atoms on Silica: Kinetics and Mechanism," *Langmuir,* Vol. 7, pp. 2999–3005.

Kolodziej, P., and Stewart, D. A., 1987, "Nitrogen Recombination on High-Temperature Reusable Surface Insulation and the Analysis of Its Effect on Surface Catalysis," AIAA-87-1637.

Ljungström, S., Kasemo, B., Rosén, A., Wahnström, T., and Fridell, E., 1989, "An Experimental Study of OH and $H_2O$ Formation on Pt in the $H_2+O_2$ Reaction," *Surf. Sci.,* Vol. 216, pp. 63–92.

Marinelli, W. J., and Campbell, J. P., 1986, "Spacecraft-Metastable Energy Transfer Studies: Final Report," NAS9-17565.

Marinelli, W. J., 1988, "Collisional Quenching of Atoms and Molecules on Spacecraft Thermal Protection Surfaces," Paper No. AIAA-88-2667.

Melin, G. A., and Madix, R. J., 1971, "Energy Accommodation During Oxygen Atom Recombination on Metal Surfaces," *Trans. Faraday Soc.,* Vol. 67, pp. 198–211.

Motz, H., and Wise, H., 1960, "Diffusion and Heterogeneous Reaction. III. Atom Recombination at a Catalytic Boundary," *J. Chem. Phys.,* Vol. 32, pp. 1893–1894.

Riedel, U., Maas, U., and Warnatz, J., 1993a, "Detailed Numerical Modeling of Chemical and Thermal Nonequilibrium in Hypersonic Flows," *IMPACT Comput. Sci. Eng.,* Vol. 5, pp. 20–52.

Riedel, U., Maas, U., and Warnatz, J., 1993b, "Simulation of Nonequilibrium Hypersonic Flows," *Comp. & Fluids,* Vol. 22, pp. 285–294.

Rosner, D. E., and Feng, H., 1974, "Energy Transfer Effects of Excited Molecule Production by Surface-Catalyzed Atom Recombination," *Trans. Faraday Soc.,* Vol. 70, pp. 884–907.

Scott, C. D., 1981, "Catalytic Recombination of Nitrogen and Oxygen on High Temperature Reusable Surface Insulation," *Progr. Astronaut. Aeronaut.,* Vol. 77, pp. 192–212.

Seward, W. A., and Jumper, E. J., 1991, "Model for Oxygen Recombination on Silicon-Dioxide Surfaces," *Journal of Thermophysics and Heat Transfer,* Vol. 5, No. 3, pp. 284–291.

Stewart, D. A., and Leiser, D. B., 1976, "Effect of Radiant and Convective Heating on the Optical and Thermochemical Properties of Reusable Surface Insulation," Paper No. AIAA-76-444.

Stewart, D. A., Rakich, J. V., and Lanfranco, M. J., 1981, "Catalytic Surface Effects Experiment on the Space Shuttle," Paper No. AIAA-81-1143.

Stewart, D. A., Rakich, J. V., and Lanfranco, M. J., 1982, "Catalytic Surface Effects Experiment on the Space Shuttle," *Progr. Astronaut. and Aeronaut.,* Vol. 82, pp. 248–272.

Stewart, D. A., Rakich, J. V., and Lanfranco, M. J., 1983, "Catalytic Surface Effects on the Space Shuttle Thermal Protection System During Earth Entry of Flights STS-2 Trough STS-5," NASA CP 2283.

Stewart, D. A., Chen, Y. K., and Henline, W. D., 1991, "Effect of Nonequilibrium Flow Chemistry and Surface Catalysis on Surface Heating to AFE," Paper No. AIAA-91-1371.

U.S. Standard Atmosphere, 1976, U.S. Government Printing Office, Washington, DC.

Warnatz, J., 1992, "Resolution of Gas Phase and Surface Chemistry Into Elementary Reactions. Plenary Lecture," *Twenty-Fourth Symposium (International) on Combustion,* The Combustion Institute, Pittsburgh, pp. 553–579.

Warnatz, J., Allendorf, M., Kee, R. J., and Coltrin, M. E., 1994, "A Model of Elementary Chemistry and Fluid Mechanics in the Combustion of Hydrogen on Platinum Surfaces," *Combust. Flame,* Vol. 96, pp. 393–406.

Weast, R. C., ed., 1987, *Handbook of Chemistry and Physics,* 68th ed., CRC Press, Boca Raton, FL.

Wells, A. F., 1962, "Structural Inorganic Chemistry," 3rd ed., Oxford University Press, London.

Willey, R. J., 1988, "Arc Jet Diagnostics Tests, Final Report," NASA-JSC/ASEE SFFP.

Willey, R. J., 1993, "Comparison of Kinetic Models for Atom Recombination on High-Temperature Reusable Surface Insulation," *Journal of Thermophysics and Heat Transfer,* Vol. 7, No. 1, pp. 55–62.




Downloaded 12 Dec 2010 to 193.140.21.150. Redistribution subject to ASME license or copyright; see http://www.asme.org/terms/Terms_Use.cfm

**W. Luangdilok**
Senior Nuclear Engineer,
Fauske & Associates, Inc.,
16W070 West 83rd St.,
Burr Ridge, IL 60521
Assoc. Mem. ASME

**R. B. Bennett**
Senior Engineer,
Nuclear Operations Division,
American Electric Power Service
Corporation,
1 Riverside Plaza,
Columbus, OH 43216-6631

# Fog Inerting Effects on Hydrogen Combustion in a PWR Ice Condenser Containment

*A mechanistic fog inerting model has been developed to account for the effects of fog on the upward lean flammability limits of a combustible mixture based on the thermal theory of flame propagation. Benchmarking of this model with test data shows reasonably good agreement between the theory and the experiment. Applications of the model and available fog data to determine the upward lean flammability limits of the $H_2$–air–steam mixture in the ice condenser upper plenum region of a pressurized water reactor (PWR) ice condenser containment during postulated large loss of coolant accident (LOCA) conditions indicate that combustion may be suppressed beyond the downward flammability limit (8 percent $H_2$ by volume).*

## Introduction

Steam condensation within the ice condenser of a pressurized water reactor (PWR) containment designed with an ice condenser, generates small water droplets (i.e., fog) in the micrometer size range within the bulk of the gas stream. These small water droplets are carried by the gas stream into the upper plenum of the ice condenser (Fig. 1) where igniters are present to control hydrogen concentrations below the lean flammability limits (normally ~4.5 vol. percent without the presence of fog).

If high fog concentrations exist in the upper plenum, the minimum hydrogen concentration required for ignition would be higher to compensate for heat loss to droplet vaporization. This would result in no burns in the upper plenum and transport to and the accumulation of hydrogen in the upper compartment. Depending on the differences between the flammability limits in the upper plenum and in the upper compartment, and on the hydrogen evolution rates during postulated loss of coolant accidents (LOCAs), ignition in the upper plenum may or may not occur at all. The consequence of hydrogen bypassing burns in the upper plenum would likely lead to burns in the upper compartment where fog inerting is negligible. Due to the large volume of the upper compartment (~55 percent of containment volume for a typical ice condenser containment), any burns in the upper compartment will involve a large amount of mass and energy, and the pressure effects will be felt through the whole containment.

On the other hand, the volume of the upper plenum is typically only 4 ~ 5 percent of the containment. Burns in the upper plenum normally result in negligible effects on the overall containment pressures and temperatures. Therefore, it is important to know the effects of fog on the flammability limits so that good assessments of combustion phenomena during postulated accidents can be performed.

The purpose of this paper is to develop a fog inerting model and the fog inerting map covering a wide range of fog droplet sizes and to apply the model to predict the flammability limits of the gas stream in the ice condenser upper plenum during accident conditions.

The effects of water droplets on flame quenching were discussed by Hertzberg (1981), who established the fundamental knowledge of the flammability behavior of hydrogen–air mixtures under the influence of added water vapor. Research on utilizing fogs to suppress combustion or mitigate combustion pressure was carried out at Sandia National Laboratories in the early 1980s (Sherman et al., 1981; Baer et al., 1984). Past efforts on fog inerting analysis at Westinghouse (Tsai and Liparulo, 1982) showed, except for some discrepancies, general agreement with test data of droplet size > 20 $\mu$m. The Westinghouse analysis did not extend down to droplet diameters as small as 1 $\mu$m, which is more typical of fog in the upper plenum. The model developed in this paper agrees well with available experiments. The model can also predict fog inerting in the range of 1 $\mu$m or smaller.

## Flammability Limits With Heat Losses

The problem of flammability limits of a combustible gaseous mixture is discussed thoroughly by Williams (1985) where the thermal theory of flame propagation with heat losses was developed to address the quenching of premixed flames. If a flame quenches due to heat losses, the mixture that supplies gases to the flame can be considered nonflammable under the condition being considered. For this reason, the limits of flammability due to the presence of fog (water aerosols of small droplet sizes) in the gaseous mixture can be addressed using Williams' theory.

The thermal theory of flame propagation with heat losses involves solving a differential equation representing a simplified model of a plane, one-dimensional, nonadiabatic flame for a burning velocity. The equation is a steady-state energy equation determining a temperature distribution of the flame region and is solved by the activation-energy asymptotics method. Under certain conditions, it is found that no solution for the burning velocity exists, thus indicating the presence of flammability limits. Under other conditions, two burning velocities are obtained, one of which presumably corresponds to an unstable flame.

The major result of the simplified theory is that flame propagation will not be sustained or the mixture is not flammable if

$$T_f < T_{af}\left(\frac{RT_{af}}{E} + 1\right)^{-1} \tag{1}$$

where $T_f$ is the flame temperature in the presence of heat loss, $T_{af}$ is the adiabatic flame temperature, $R$ is the universal gas constant, and $E$ is the global (i.e., single step kinetics) activation energy of the reaction. To apply the criterion of Eq. (1), one needs to evaluate the actual flame temperature dictated by the environment and the adiabatic flame temperature of a given mixture. The mixture is flammable if heat losses do not result in flame temperatures less than the right-hand side of Eq. (1).

The temperature required for flame propagation approaches the adiabatic flame temperature $T_{af}$ as the activation energy $E$ increases. The global activation energy is an empirical value dependent upon among the many radical reactions involved in the

Contributed by the Heat Transfer Division for publication in the JOURNAL OF HEAT TRANSFER. Manuscript received by the Heat Transfer Division June 1993; revision received October 1994. Keywords: Combustion, Fire/Flames, Modeling and Scaling. Associate Technical Editor: W. L. Grosshandler.



Copyright © 1995 by ASME

Downloaded 12 Dec 2010 to 193.140.21.150. Redistribution subject to ASME license or copyright; see http://www.asme.org/terms/Terms_Use.cfm

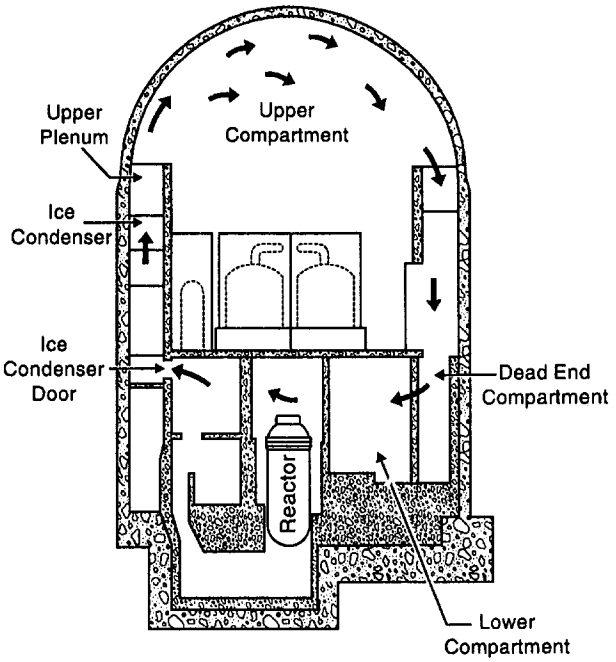



**Fig. 1 Typical PWR ice condenser containment**

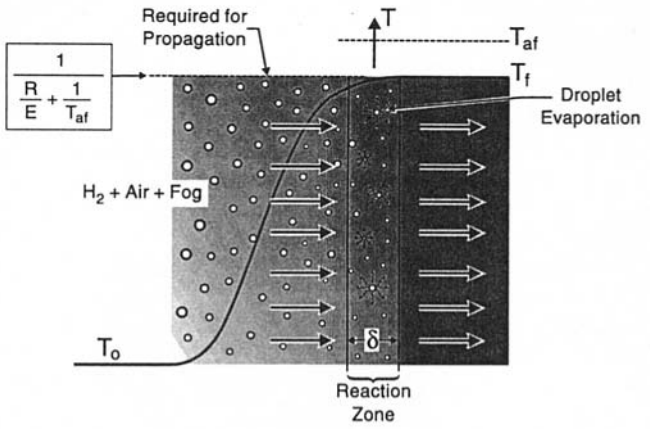



**Fig. 2 Schematic of thermal theory of flame propagation with heat losses**

combustion processes, and changes with the composition, temperature and pressure. For hydrogen oxidation, the process proceeds through several radical reactions (Dryer, 1991). The global activation energy for $H_2/O_2/N_2$ mixtures near flammability limits at 1 atm and 298 K was estimated to be 100.4 kJ/mol by Mitani and Williams (1979). Similar global activation energy values were also obtained numerically by detailed modeling of the reaction mechanism (He and Clavin, 1993).

The flame propagation criterion in Eq. (1) can be readily applied to a combustible mixture in the presence of fog. Due to the very small droplets (micrometer range) of fog, the available heat transfer area of the droplets is very large. Heat absorption due to fog evaporation in the reaction zone is significant. If the fog concentration is sufficiently high, the resulting flame temperature may go below the temperature required for flame propagation. Evaluations of flame temperatures due to fog evaporation are considered in the following section.

**Heat Loss Due to Fog Evaporation.** To calculate flame temperatures ($T_f$) in the presence of fog, the flame cooling due to fog evaporation within the reaction zone must be considered. Let $Y_d$ be the volumetric ratio of fog to gas mixture flowing into the reaction zone of a one-dimensional flame, $d$ the fog mean diameter, and $\delta$ the reaction zone thickness as illustrated in Fig. 2. The number of fog droplets per unit reaction zone area ($N$) can be written as

$$N = Y_d \delta \Big/ \left(\frac{\pi}{6} d^3\right) \tag{2}$$

Let $\dot{m}_d$ be the fog evaporation rate (kg/s) per droplet, $h_{fg}$ the heat of evaporation (J/kg), and $c_s\Delta T$ the vapor sensible heat (J/kg) acquired by the vaporized mass during combustion in a flame front. Then, the rate of heat loss ($L$) due to droplet evaporation per unit flow area of the reaction zone becomes

$$L = (h_{fg} + c_s\Delta T)\dot{m}_d N \tag{3}$$

For hydrogen–air flames, the flame speed is relatively high compared to most other fuel gases. This results in a very thin flame thickness, and, consequently, a short residence time for droplets to remain in the flame front. For example, for a 0.2 m/s flame speed, the corresponding flame thickness is about 270 $\mu$m and the time required to propagate through this thickness is only 1.3 ms.

Utilizing the definition of $N$ from Eq. (2), Eq. (3) becomes

$$L = \frac{(h_{fg} + c_s\Delta T)\dot{m}_d Y_d \delta}{\frac{\pi}{6} d^3} \tag{4}$$

If the gas mass flux ($\dot{m}$) of temperature $T_o$ and of hydrogen mass fraction $F_H$ enters the reaction zone, then the energy balance of the reaction zone can be written as

$$\dot{m}c_p(T_f - T_o) = \dot{m}QF_H - L \tag{5}$$

## Nomenclature

$c_p$ = specific heat of gaseous mixture evaluated at $T_o + \frac{1}{3}(T_{af} - T_o)$, J/kg·K
$c_s$ = specific heat capacity of water vapor, J/kg·K
$d$ = fog mean diameter, m
$E$ = global activation energy of reactions, J/mol
$D$ = tube diameter, m
$F_H$ = initial mass fraction of hydrogen
$h_{fg}$ = latent heat of vaporization of water, J/kg
$j$ = fractional thickness factor for fog inerting
$k$ = thermal conductivity of gaseous product mixture, W/m·K
$L$ = rate of heat loss per unit area, J/m·s
$\dot{m}_d$ = fog (water aerosol) evaporation rate per drop, kg/s
$Q$ = heat of reaction, J/kg
$R$ = universal gas constant = 8.314 J/mol·K
$S_u$ = laminar flame speed, m/s
$T_{af}$ = adiabatic flame temperature, K
$T_f$ = actual flame temperature, K
$T_o$ = preburn gas temperature, K
$V_b$ = flame speed due to buoyancy effects
$Y_d$ = average volumetric ratio of fog to gaseous mixture
$\alpha$ = thermal diffusivity of gaseous product mixture evaluated at $T_o + \frac{1}{3}(T_{af} - T_o)$, m²/s
$\delta$ = flame reaction zone thickness, m
$\rho_b$ = burned gas density, kg/m³
$\rho_g$ = gaseous mixture density evaluated at $T_o$, kg/m³
$\rho_w$ = water density evaluated at $T_o$, kg/m³



Downloaded 12 Dec 2010 to 193.140.21.150. Redistribution subject to ASME license or copyright; see http://www.asme.org/terms/Terms_Use.cfm

where $c_p$ is heat capacity of the gaseous mixture, $T_f$ is flame temperature, and $Q$ is heat released in the chemical reaction per unit mass of hydrogen converted. Solving Eq. (5), with $\Delta T = T_f - T_o$ in the heat loss term, yields the following expression for the flame temperature:

$$T_f = T_o + \frac{1}{c_p + c_s\left(\frac{\dot{m}_d N}{\dot{m}}\right)}\left[QF_H - h_{fg}\left(\frac{\dot{m}_d N}{\dot{m}}\right)\right] \quad (6)$$

The calculation of droplet evaporation rate ($\dot{m}_d$) is well formulated in the area of combustion of atomized liquid fuel droplets and is available from several standard textbooks (such as Rosner, 1986, and Lefebvre, 1991). The quasi-steady droplet evaporation rate based on diffusion-controlled processes can be expressed as

$$\dot{m}_d = 2\pi d\left(\frac{k}{c_p}\right)_g \ln\left[1 + c_p \frac{\left(\frac{T_{af} + T_f}{2} - T_o\right)}{h_{fg}}\right] \quad (7)$$

where $k$ is thermal conductivity and the subscript $g$ refers to the surrounding gaseous product mixture properties (namely, the postburn properties). Equation (7) is not applicable to droplet sizes comparable to the gas mean free path ($\sim$0.1 $\mu$m). For very small droplets, a separate treatment is needed; and this is discussed later. According to Lefebvre (1991) and Hubbard et al. (1975), best results are obtained using the one-third rule of Sparrow and Gregg (1958) where average properties are evaluated at $T_o + \frac{1}{3}(T_{af} - T_o)$. The droplet surface temperature is assumed to be the same as the initial temperature of the gaseous mixture.

For a one-dimensional, planar flame the mass flux ($\dot{m}$) through the flame front can be written in terms of its laminar flame speed, $S_u$, as $\dot{m} = \rho S_u$. By substituting this and the expression for $\dot{m}_d$ into Eq. (6), and using the resulting expression for the flame temperature in the flame propagation criterion Eq. (1), one obtains the maximum diameter of the fog droplets for inerting, $d_{crit}$. After several algebraic manipulations, this critical diameter can be shown to be $d_{crit} = j\delta$, where the dimensionless term $j$ is a fractional thickness factor:

$$j \equiv \left[ Y_d \frac{12[h_{fg} + c_s(T_{ig} - T_o)]}{c_p(T_{af} - T_{ig})} \times \ln\left\{1 + \frac{c_p\left(\frac{T_{af} + T_{ig}}{2} - T_o\right)}{h_{fg}}\right\}\right]^{1/2} \quad (8)$$

where $T_{ig} = T_{af}(1 + (R/E)T_{af})^{-1}$ is the minimum flame temperature required for propagation (i.e., the right hand side of Eq. (1)), and $T_{af} \equiv T_o + QF_H/c_p$ by definition.

The reaction zone thickness $\delta$, as typically derived in the thermal theory of flame propagation (Glassman, 1987; Strehlow, 1991), is approximately equal to thermal diffusivity divided by the flame speed; i.e., $\delta \cong \alpha/S_u$. The laminar flame speed $S_u$ for hydrogen–steam–air mixtures at temperature $T_o$ is given by the correlation of Liu and MacFarlane (1983):

$$S_u = 0.01[A_1 + A_2(0.42 - X_H) + A_3(0.42 - X_H)^2]e^{A_6X_sT_o^{A_4 + A_5(0.42 - X_H)}} \quad (9)$$

where $X_H$ is hydrogen mole fraction, $X_S$ is steam mole fraction and, for $X_H < 0.42$, $A_1 = 0.0464$, $A_2 = -0.212$, $A_3 = 0.234$, $A_4 = 1.57$, $A_5 = 0.38$, and $A_6 = -2.21$.

The correlation of Eq. (9) was constructed based on data at high concentration of hydrogen (18 to 63 vol. percent $H_2$). To extrapolate data to the lower limits, Liu and MacFarlane (1983) assumed that $S_u = 0$ at 0.5 vol. percent $H_2$. Iijima and Takeno (1986) also predict zero flame speed at the limiting conditions, which leads to $\delta$ becoming infinitely large. With a very large reaction zone thickness, large heat losses would be unavoidable. If this is so, flame propagation would be very unlikely. Since the lean flammability limits do exist at finite flame speed, the reaction zone thickness at the lean flammability limits cannot be predicted using such laminar flame speed correlations.

A finite flame speed and reaction zone thickness are supported by the early work of Hertzberg (1976, 1981) and others. In lean "quiescent" mixture tests, the flame speeds generated as the flame front propagated away from the ignition source were observed to be augmented by the buoyant rise of the hot gas plume. Furthermore, as discussed by Lovachev (1973, 1979), it is generally accepted that buoyancy favors upward flame propagation. Therefore, the reaction zone thickness at the lean flammability limits should be determined by $\delta = \alpha/U$ where $U = V_b + S_u$ and $V_b$ is the buoyancy-induced flow velocity. For weak combustible mixtures of different fuels in small tubes of various diameters $D$, the measured flame speeds have been shown (Levy, 1950) to agree well with the upward translation velocity, obtained theoretically (Davies and Taylor, 1950) for an air column rising in a vertical tube filled with water, sealed at the top and open to the atmosphere at the bottom. The flame speed approximated by the upward translation velocity (Ural and Zalosh, 1988), is written as

$$U = 0.48[gD(\rho_g - \rho_b)/2\rho_g]^{1/2} \quad (10)$$

Equation (10) is useful in interpretation of small-scale experimental data, to be discussed later. However, the applicability of Eq. (10) is questionable in a large-scale nuclear reactor containment building where $D$ is not easy to define. Theoretically, under the condition of our interest, i.e., near the flammability limits in a large vessel, the buoyancy effects on flame speed should not depend on the diameter of the vessel. Since initially the flames may propagate from an ignition source at far distance from the walls. For this situation $V_b$ can be approximated from the inviscid Bernoulli equation,

$$V_b = \left(4\alpha g \frac{\rho_g - \rho_b}{\rho_g + \rho_b}\right)^{1/3} \quad (11)$$

where $g$ is the acceleration due to gravity and $\rho_b$ is the burned gas density.

With the flame velocity and, hence, flame thickness known, the critical fog diameter for inerting, $d_{crit}$, can be found by evaluating the fractional thickness factor from Eq. (8).

For a fixed volumetric ratio $Y_d$, as droplet size decreases to a very small value, the number per unit volume, $N$, increases. In this limit Eq. (6) predicts a flame temperature below the entering temperature, $T_o$. Hence, a limit on the droplet size must be found. This limit is considered in the following section.

**Small Droplet Limit.** To determine the critical fog diameter as the droplet sizes approach the submicrometer range, we may assume that the droplet is so small that the heat transfer rate approaches infinity. Hence, the heat absorbed by evaporation can be assumed to be instantaneous and the energy loss term written as

$$L = \dot{m}Y_d\left(\frac{\rho_w}{\rho_g}\right)[h_{fg} + c_s\Delta T] \quad (12)$$

where $\Delta T = T_f - T_o$. Since $Y_d(\rho_w/\rho_g)$ in Eq. (12) represents a mass fraction of water droplets, $\rho_w$ and $\rho_g$ should be evaluated at $T_o$ to preserve the original mass fraction. It is noted that droplet size is no longer relevant under this condition.



Downloaded 12 Dec 2010 to 193.140.21.150. Redistribution subject to ASME license or copyright; see http://www.asme.org/terms/Terms_Use.cfm

Using Eq. (12) in Eq. (5) and solving for $T_f$, we obtain an expression for the flame temperature due to the assumed instantaneous evaporation of fog as

$$T_f = \frac{T_{af} - \left(\frac{h_{fg}}{c_s} - T_o\right)X}{1 + X} \tag{13}$$

where

$$X = \frac{c_s}{c_p}\frac{\rho_w}{\rho_g} Y_d$$

Applying Eq. (13) in the flame propagation criterion Eq. (1), we obtain the critical volume fraction for fog inerting in the small droplet limit:

$$Y_{d,\text{crit}} \equiv c_p\left(\frac{T_{af} - T_{ig}}{h_{fg} + c_s(T_{ig} - T_o)}\right)\frac{\rho_g}{\rho_w} \tag{14}$$

Equation (14) implies that for very small droplets fog inerting is a function of neither droplet size nor flame speed. This expression yields a conservative lower-bound value (for the small droplet limit) of the critical fog volume fraction. Since it does not contain any flame parameters, the uncertainties in flame speeds as encountered for larger droplets do not exist in this case.

**Fog Inerting Map.** Based upon the concepts of critical fog diameter and critical fog volume fraction, a fog inerting map can be constructed, identifying the flammability limits of a mixture. The boundaries between the flammable zone and the nonflammable zone are formed by the expressions derived for $d_{\text{crit}}$ and $Y_{d,\text{crit}}$ as shown in Fig. 3. The nonflammable zone is the region above or to the left of the boundary lines. The two boundary lines intersect each other at a limiting point where further reduction in fog mean diameter is no longer valid. For fog mean diameters smaller than the limiting point, the inerting criterion is bounded by $Y_{d,\text{crit}}$. The limiting point is obtained by substituting $Y_{d,\text{crit}}$ into Eq. (8), i.e.,

$$d_{\text{crit,limit}} = \delta\left[12\frac{c_p}{c_s}\frac{\rho_g}{\rho_w}\frac{T_{af} - T_{ig}}{T_{ig} - T_o + \frac{h_{fg}}{c_s}}\frac{h_{fg} + c_s(T_{ig} - T_o)}{c_p(T_{af} - T_{ig})} \times \ln\left\{1 + \frac{c_p\left(\frac{T_{af} + T_{ig}}{2} - T_o\right)}{h_{fg}}\right\}\right]^{1/2} \tag{15}$$

It is noted that for a given gas temperature the location of the boundary lines is a function of hydrogen mole fraction through $T_{af}$. The boundary lines move upward with increasing hydrogen mole fraction resulting in a smaller nonflammable zone.

Limited experimental data are available to compare with the theoretical predictions in Fig. 3. Some fog-related work was also carried out at Sandia National Laboratory (Baer et al., 1984), which focused on the mitigating effects of fog on hydrogen combustion pressures at high hydrogen concentration (up to 40 vol. percent $H_2$). These data are not applicable to the lower flammability limits, which are the focus of this paper.

The effects of water fog on the upward lean flammability limit of hydrogen–air mixtures were experimentally examined in a 0.15-m-dia, 1-m-long tube by Zalosh and Bajpai (1982). Ignition was initiated with an electrode, and thermocouples were used as an indication of flame propagation. In this test scries, fogs of various mean droplet sizes and concentrations were generated using five different microfog nozzles. The minimum volume mean droplet diameter generated in the tests was 20 $\mu$m while

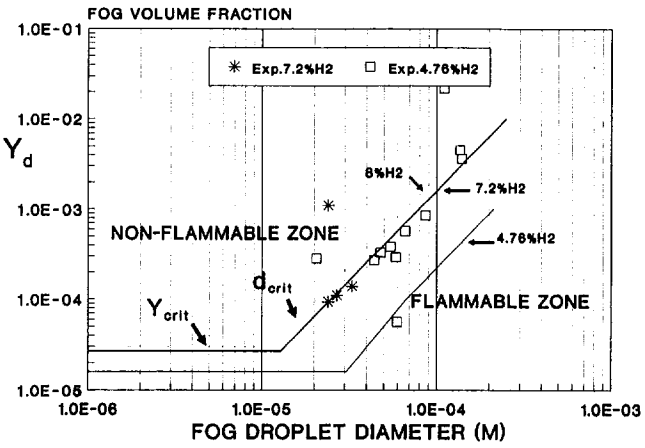



**Fig. 3 Fog inerting map for hydrogen–air mixtures: comparisons of theoretical predictions with FMRC experiments**

the maximum was about 140 $\mu$m. Measurements of droplet size and their distribution were based on the reduction in electrical resistance of a hot-wire probe upon contact with the droplets. They assumed an average gas velocity with the droplet size distribution and then used the number density data to calculate the fog volume fraction.

The data consist of two sets: one with 4.76 percent $H_2$ at 293 K and another one with 7.2 percent $H_2$ at 323 K. These data are plotted in Fig. 3. The data points are sufficient to indicate the trend in spite of some scatter due to inherent inaccuracy in the experiments. In all experiments, only the thermocouple above the igniter actually sensed the presence of flame. Thus, flame propagation was upward only. Since the combustion tube was aligned vertically and hydrogen–air mixtures were fed from above, the motion of gas was in the downward direction. This downward gas velocity was about 1 ~ 2 cm/s. The observations that only upward flame propagation occurred imply buoyancy effects and flame speeds greater than 1 ~ 2 cm/s.

As discussed in the previous section, in order to apply the theory to the data at the upward lean flammability limits the appropriate value for the flame speed is $U$ and not $S_u$. The value of $U$ given by Eq. (10) for 7.2 percent $H_2$ is 0.288 m/s, while that given by Eqs. (9) and (11) is 0.298 m/s. These results are plotted in Fig. 3, where the asterisk represents experimental measurements of ignition.

For the data set with 4.76 percent $H_2$, it is found that $U = 0.27$ m/s using Eq. (10), and only 0.085 m/s using Eqs. (9) and (11). A value of 0.27 m/s yields a $d_{\text{crit}}$ line almost identical for the 4.76 and 7.6 percent $H_2$ cases. The line marked 4.76 percent $H_2$ in Fig. 3 represents the situation for $U = 0.085$ m/s, which should be compared to the experimental data plotted at open squares. Note that since the experimental data points for 4.76 and 7.2 percent $H_2$ appear to lie on the same line; this supports the choice of the higher velocity for the 4.76 percent $H_2$ case. This leads to similar flame thickness and critical fog diameter for the two concentrations.

To demonstrate the prediction for high $H_2$ concentrations in an actual containment building (where no experimental data are available), an 8 percent hydrogen calculation is shown in Fig. 3. In this case, Eqs. (9) and (11) are used to calculate the flame speed to reflect that this is an application to a large-scale vessel.

The critical volume fractions, $Y_{d,\text{crit}}$, are also shown in Fig. 3 for the small diameter limit. No experimental data are available for the small droplets to support or refute the theoretical predictions. However, the values are more conservative than one would predict if no limit existed.

**Expected Fog Concentration in PWR Ice Condenser Plant.** As steam and air pass through the ice condenser, the heat



Downloaded 12 Dec 2010 to 193.140.21.150. Redistribution subject to ASME license or copyright; see http://www.asme.org/terms/Terms_Use.cfm

transfer is dominated by condensation of the steam onto cold surfaces. At least some of the water vapor will condense in the flowstream, generating fog. In the complex geometry of the ice condenser, it is difficult to predict the amount of fog generated in the flow stream accurately. Although fog generation has been predicted in a simple geometry (Epstein and Hauser, 1991), the ice geometry changes as the ice melts, and the ice baskets provide an obstruction between the flowstream and the ice.

One experiment has been performed that measures the fog concentration at the outlet of a full-scale section of an ice condenser (Ligotke et al., 1991). Although the measurement of fog concentration was not the primary goal of this experiment, some general observations can be made from the data presented. When little ice has melted from the test section, such as in the early phases of a transient, little or no fog concentration exits the test section ($Y_d = 10^{-5}$ or less). As the ice depletes, the fog volume fraction raises to the $10^{-5}$ range, although this appears to be dependent on the steam flow rate. When there is very little ice left, $Y_d$ can reach $3 \times 10^{-4}$ for high steam flow rates.

Since this set of experiments was not designed primarily for fog concentration measurements, the test conditions are not directly related to accident conditions of interest. The steam flow was not varied as the ice melted, as would be expected in a severe accident. Cases with low steam flows, which would be representative of the latter stages of an accident, were not continued until most of the ice had melted. From a review of the data presented, it can be concluded that little or no fog would be expected until approximately one third of the ice had melted. For the moderate steam flow rates expected in the later stages of an accident when ice is still available, fog volume fractions in the range of $5 \times 10^{-5}$ can be expected. Proprietary data available to one author (Bennett) support this conclusion.

According to the fog inerting map (Fig. 3), the flammability limits are divided into two regions: one that depends on the droplet size and another one that does not. To establish the fog inerting criteria for the upper plenum, one needs to determine first the range of the fog droplet size expected in the upper plenum. To do this we will rely on the work of Strum and Toor (1992), which characterized fog produced by water vapor condensation (the same mechanism as in the ice condenser during postulated reactor accidents). In their work, water fog produced by condensation outside an insulated 1.1-cm-dia tube was characterized by optical instruments. The measured fog possessed a centerline mean droplet size from 1.6 to 4 $\mu$m for a 62°C jet, and 3 to 7 $\mu$m for an 85°C jet. The surrounding room temperature was about 20°C or lower. The mean droplet size as well as fog concentration increased with axial distance from the tube exit. Fog concentrations reached a maximum value at 15 diameter distance from the outlet (due to entrainment of the surrounding air) and declined thereafter. This measurement indicates that a minimum mean droplet size of fog expected from condensation would be bounded by 1 or 2 $\mu$m.

Considering the measurements given above, the fog inerting criteria for the upper plenum should be determined by the critical fog volume fraction of $Y_{d,\text{crit}}$. Sample calculations using the conditions (i.e., gas temperatures and compositions) predicted by the MAAP code (Fauske and Associates, 1990), a nuclear reactor accident analysis program, of a large LOCA event for a typical PWR ice condenser containment yield the critical fog volume fraction of $3 \times 10^{-5}$ for 8 percent $H_2$ concentration at which downward flame propagation resulting in complete burn (Sherman et al., 1981) can be expected.

Comparing the calculated value for the fog volume fraction to the maximum expected fog volume fraction ($5 \times 10^{-5}$) in the upper plenum, discussed previously, indicates that for a large LOCA condition, combustion may be suppressed above 8 percent hydrogen concentration due to fog inerting as compared to the minimum required hydrogen mole fraction of 4.5 percent in the absence of fog.

## Conclusion

The fog inerting model predicts the flammability limits as a function of fog aerosol size, fog volume fraction, hydrogen volume fraction, and mixture temperature. The model analytical results can be summarized as follows:

1 The *critical fog volume fraction,* $Y_{d,\text{crit}}$, is defined as a fog volume fraction below which fog inerting does not occur regardless of the mean drop size of fog aerosol. The critical fog volume fraction is mainly a function of hydrogen concentration.
2 The *critical fog mean diameter,* $d_{\text{crit}}$, is defined as a fog mean diameter below which fog inerting occurs. The critical fog mean diameter is a function of fog volume fraction and hydrogen concentration.

These results form a basis for constructing a fog-inerting-criteria map. The model may be generalizable to other types of fog and gaseous mixtures not considered in this paper.

When applied to the upper plenum of the typical PWR ice condenser containment during postulated accidents, only the critical fog volume fraction criterion should be used due to the small droplet sizes in the range of 1 to 2 $\mu$m expected in the upper plenum. For large LOCA conditions, it is estimated that hydrogen combustion in the upper plenum may be suppressed beyond 8 percent hydrogen concentration during a period of maximum fog volume fraction ($\sim 5 \times 10^{-5}$).

## Acknowledgments

The comments on this work during its early phase of development from Dr. R. E. Henry, Dr. M. Epstein, and Dr. C. D. Wu of FAI are acknowledged.

## References

Baer, M. R., Griffiths, S. K., and Shepherd, J. E., 1984, "Hydrogen Combustion in Aqueous Foams," *Nuclear Sci. & Eng.*, Vol. 88, pp. 436–444.

Davies, R. M., and Taylor, G. I., 1950, "The Mechanics of Large Bubbles Rising Through Extended Liquids and Through Liquids in Tubes," *Proc. Roy. Soc. London,* Vol. 200A, p. 385.

Dryer, F. L., 1991, "The Phenomenology of Modeling Combustion Chemistry," in: *Fossil Fuel Combustion,* W. Bartok and A. F. Sarofim, eds., Wiley, pp. 126, 166–167.

Epstein, M., and Hauser, G. M., 1991, "Simultaneous Formation and Thermophoretic Droplet Deposition in a Turbulent Pipe Flow," ASME JOURNAL OF HEAT TRANSFER, Vol. 113, pp. 224–231.

Fauske and Associates, 1990, "MAAP 3.0B Complete Code Manual," EPRI NP-777-1 CCML, Electric Power Research Institute.

Glassman, I., 1987, *Combustion,* Academic Press, New York, pp. 117–118.

He, L., and Clavin, P., 1993, "Premixed Hydrogen-Oxygen Flames. Part I: Flame Structure Near the Flammability Limits," *Combustion and Flame,* Vol. 93, pp. 391–407.

Hertzberg, M., 1976, "The Theory of Flammability Limits: Natural Convection," Bureau of Mines Report of Investigation, RI-8127.

Hertzberg, M., 1981, "Flammability Limits and Pressure Development in Hydrogen–Air Mixtures," *Proc. Workshop on the Impact of Hydrogen on Water Reactor Safety,* Albuquerque, NM, Vol. III of IV, NUREG/CR-2017, SAND 81-0661, pp. 17–65.

Hubbard, G. L., Denny, V. E., and Mills, A. F., 1975, "Droplet Evaporation: Effects of Transients and Variable Properties," *Int. J. Heat Mass Transfer,* Vol. 18, pp. 1003–1008.

Iijima, T., and Takeno, T., 1986, "Effects of Temperature and Pressure on Burning Velocity," *Combustion and Flame,* Vol. 65, pp. 35–43.

Lefebvre, A. H., 1991, "Fuel Atomization, Droplet Evaporation, and Spray Combustion," in: *Fossil Fuel Combustion,* W. Bartok and A. F. Sarofim, eds., Wiley, New York, pp. 601–602.

Levy, A., 1950, *Proc. Roy. Soc. London,* Vol. 283A, p. 134.

Ligotke, M. W., Eschbach, E. J., and Winegardner, W. K., 1991, "Ice Condenser Aerosol Tests," NUREG/CR-5768.

Liu, D., and MacFarlane, R., 1983, "Laminar Burning Velocities of Hydrogen–Air and Hydrogen–Air–Steam Flames," *Combustion and Flame,* Vol. 49, pp. 59–71.

Lovachev, L. A., 1973, "Flammability Limits: An Invited Review," *Combustion & Flame,* Vol. 20, pp. 259–289.

Lovachev, L. A., 1979, "Flammability Limits—A Review," *Comb. Science & Tech.,* Vol. 20, pp. 209–224.

Marshall, B. W., 1986, "Hydrogen: Air: Steam Flammability Limits and Combustion Characteristics in the FITS Vessel," NUREG/CR-3468, SAND84-0383, Sandia National Laboratories.



Downloaded 12 Dec 2010 to 193.140.21.150. Redistribution subject to ASME license or copyright; see http://www.asme.org/terms/Terms_Use.cfm

Mitani, T., and Williams, F. A., 1979, "Studies of Premixed Hydrogen Flames," Ph.D. Dissertation, U. of Calif. at San Diego; also, *Combustion and Flame,* Vol. 39, 1980, pp. 169–190.

Rosner, D. E., 1986, *Transport Processes in Chemically Reacting Flow Systems,* Butterworth-Heineman, p. 332.

Sherman, M. P., Baer, M. R., and Griffiths, S. K., 1981, "Deliberate Ignition and Water Fogs as $H_2$ Control Measures for Sequoyah," Workshop on the Impact of Hydrogen on Water Reactor Safety, Albuquerque, NM.

Sparrow, E. M., and Gregg, J. L., 1958, "The Variable Property Problem in Free Convection," *Trans. ASME,* Vol. 80, pp. 879–886.

Strehlow, R. A., 1991, "Premixed Flames and Detonations: Combustion Safety and Explosions," in: *Fossil Fuel Combustion,* W. Bartok and A. F. Sarofim, eds., Wiley, New York, pp. 346.

Strum, M. L., and Toor, H. L., 1992, "Microphysical Measurements of Fog Formed in a Turbulent Jet," *Aerosol Sci. and Technology,* Vol. 16, pp. 151–165.

Tsai, S. S., and Liparulo, N. J., 1982, "Fog Inerting Criteria for Hydrogen/Air Mixtures," 2nd Int. Workshop on the Impact of Hydrogen on Water Reactor Safety, Albuquerque, NM.

Ural, E. A., and Zalosh, R. G., 1988, "HICCUP: A Computer Code for Hydrogen Injection, Combustion, and Cooldown Using Phenomenological Models," EPRI NP-5721-CCM, Mar.

Williams, F. A., 1985, *Combustion Theory,* Benjamin/Cummings, pp. 271–276.

Zalosh, R. G., and Bajpai, S. N., 1982, "The Effect of Water Fogs on the Deliberate Ignition of Hydrogen," EPRI NP-2637.



Downloaded 12 Dec 2010 to 193.140.21.150. Redistribution subject to ASME license or copyright; see http://www.asme.org/terms/Terms_Use.cfm

# ERRATA

To the technical note "Determination of the Reaction Function in a Reaction-Diffusion Parabolic Problem," by H. R. B. Orlande and M. N. Özişik, published in the November 1994 issue of the ASME JOURNAL OF HEAT TRANSFER, Vol. 116, pp. 1041–1044:

Figures 1–3, shown below, were inadvertently omitted from the published version of this note. ASME sincerely regrets the error.

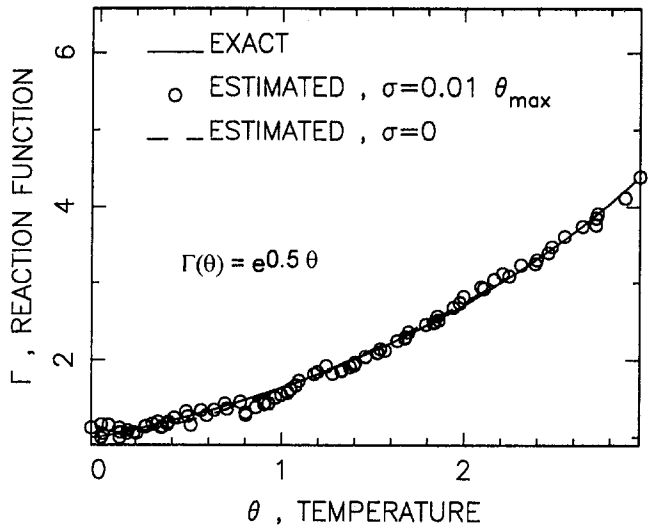



Fig. 1 Inverse solution with exponential variation of the reaction function in the form $\Gamma(\theta) = e^{0.5\theta}$

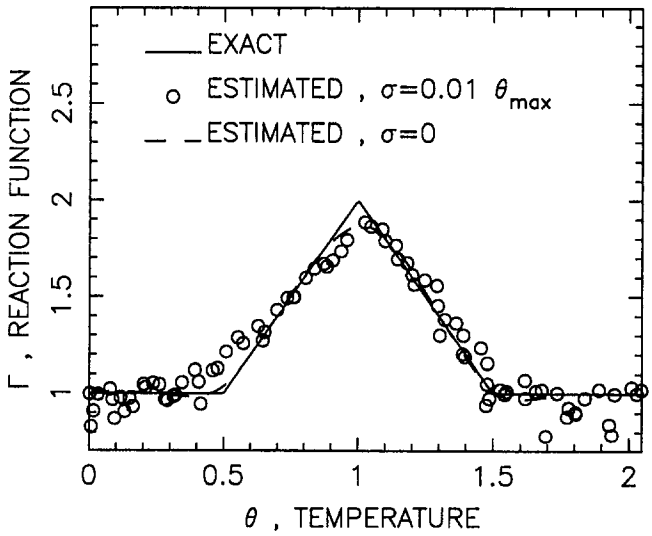



Fig. 2 Inverse solution with triangular variation of the reaction function

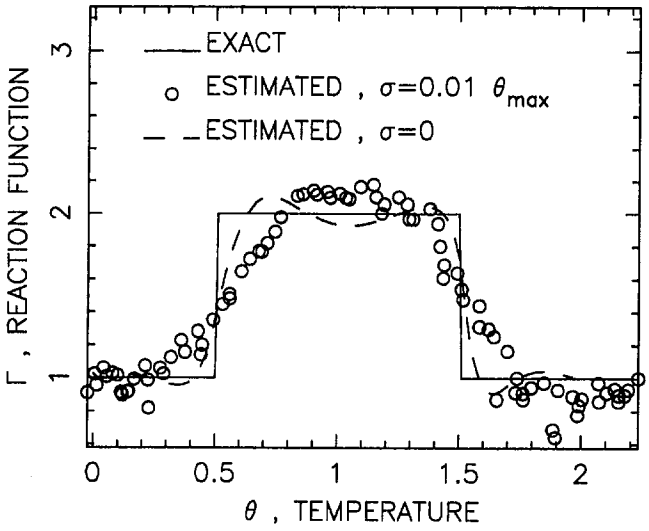



Fig. 3 Inverse solution with step variation of the reaction function



Copyright © 1995 by ASME

Downloaded 12 Dec 2010 to 193.140.21.150. Redistribution subject to ASME license or copyright; see http://www.asme.org/terms/Terms_Use.cfm

Journal of Heat Transfer

# Technical Notes

This section contains shorter technical papers. These shorter papers will be subjected to the same review process as that for full papers.

## Thermal Contact Conductance of Ceramic Substrate Junctions

**K. C. Chung,[1] H. K. Benson,[2,4] and J. W. Sheffield[3,4]**

### Nomenclature

$H$ = microhardness, Pa
$h$ = thermal contact conductance with a coating layer, W/m$^2$K
$k$ = harmonic mean thermal conductivity, W/mK
$m$ = asperity slope
$P$ = contact pressure, Pa
$r$ = surface roughness, m
Ra = average surface roughness, m

### Introduction

Ceramics have been present within microelectronic packaging since the first integrated circuitry. Ceramics possess an unmatched range of mechanical, electrical, and thermal properties. Due to their low coefficient of thermal expansion and high-temperature stability, metallic oxides, including aluminum oxide and aluminum nitride, have been used as semiconductor substrates within microelectronic devices. Fletcher and Sparks (1992) conducted an experimental investigation to determine the overall thermal conductance, the thermal contact conductance, and the thermal conductivity of selected porous ceramic materials, including alumina, partially stabilized zirconia, and mullite bonded silicon carbide. At nominal contact pressure, the overall conductance ranged from 15 to 50 W/m$^2$K while the thermal contact conductance data varied from 50 to 110 W/m$^2$K. As the need for more compact integrated circuitry increases, elaborate designs combining ceramic, metallic, and composite materials have been developed. In order to control the thermal dissipation of such devices, the thermal contact conductance of these metallic and ceramic interfaces must be determined. A review of the literature (Chung et al., 1993; O'Callaghan et al., 1983; Ochterbeck et al., 1990) showed that most investigations of thermal contact conductance of metallic coated contacts are related to the metal substrate junctions. Peterson and Fletcher (1988) conducted an experiment to investigate the thermal contact conductance between four mold compounds and heat spreader materials. A bare junction using three different substrate materials, Invar, Kovar, and Alloy 42, and four mold compounds, MG25F-LMP, MG45F-04, Polyset 410B, and Polyset 410C, were studied. However, no coated substrate samples are discussed in their experimental work. Hence, a study of ceramic substrates coated with different materials was needed.

The interface between aluminum 6061-T651 and alumina substrates with four different types of coating materials, Al plus Cu, iron carbide, Cu, and Al, were the focus of this investigation. The alumina, which is the predominant material used in dual-in-line package (DIP) semiconductor devices, was coated with four different materials including both metals and nonmetals and contacted with aluminum samples having two different surface roughnesses to provide a wide range of thermophysical and mechanical properties. Measurements of the thermal contact conductance were made at an average interface temperature of 60 ± 2°C and over a range of interface pressures from 0.1 MPa to 0.5 MPa, which are pressures comparable to those used in electronic packaging.

### Experimental Investigation

The details of the experimental facilities used in this investigation, along with their construction, operation, and accuracy, have been previously reported by Chung (1992). A series of thermal contact conductance tests were conducted to determine the effects of contact pressure for various surface coatings and surface roughnesses.

Due to its low electrical conductivity, alumina, $Al_2O_3$, has been considered as a semiconductor candidate and it has exhibited better structural and thermal capabilities than metallic materials for high-temperature applications. The alumina substrates specimens were fabricated via a process of mixing, milling, dry pressing, prefiring, and finally firing at 1600°C for 60 minutes. The specimens were 1.27 cm in length and 2.54 cm in diameter. The thermal conductivity of the $Al_2O_3$ substrate specimens was measured by thermal conductivity data generated from the vacuum tests. A stainless steel 304 specimen of known thermal conductivity was used as a standard reference for the measurement of the thermal conductivity of the $Al_2O_3$ (5.3 ± 0.2 W/mK) at constant interface temperature, 60 ± 2°C. Microhardness of the $Al_2O_3$ flat surfaces was measured using a LECO microhardness tester at room temperature. An average Vickers microhardness value, 3.1 ± 0.2 GPa, was measured for the $Al_2O_3$ substrates.

[1] Associate Professor, Department of Mechanical Engineering, National Yunlin Institute of Technology, Touliu, Yunlin 640, Taiwan.
[2] Undergraduate student.
[3] Professor; Mem. ASME.
[4] Department of Mechanical and Aerospace Engineering and Engineering Mechanics, University of Missouri—Rolla, Rolla, MO 65401.

Contributed by the Heat Transfer Division of THE AMERICAN SOCIETY OF MECHANICAL ENGINEERS. Manuscript received by the Heat Transfer Division September 1993; revision received August 1994. Keywords: Conduction, Thermal Packaging. Associate Technical Editor: L. S. Fletcher.



Copyright © 1995 by ASME
Downloaded 12 Dec 2010 to 193.140.21.150. Redistribution subject to ASME license or copyright; see http://www.asme.org/terms/Terms_Use.cfm

**Table 1 Experimental specimen characteristics**

| Sample No. | Substrate Material | Coating Material | Coating Thickness ($\mu$m) | Contact Sample | Average Surface Roughness ($\mu$m) |
|---|---|---|---|---|---|
| 1A | $Al_2O_3$ | Al+Cu | 0.2+0.3 | Al 6061-T651 | 0.08 |
| 1B | $Al_2O_3$ | Al+Cu | 0.2+0.3 | Al 6061-T651 | 5.2 |
| 2A | $Al_2O_3$ | iron carbide | 0.3 | Al 6061-T651 | 0.08 |
| 2B | $Al_2O_3$ | iron carbide | 0.3 | Al 6061-T651 | 5.2 |
| 3A | $Al_2O_3$ | Cu | 0.3 | Al 6061-T651 | 0.08 |
| 3B | $Al_2O_3$ | Cu | 0.3 | Al 6061-T651 | 5.2 |
| 4A | $Al_2O_3$ | Al | 0.2 | Al 6061-T651 | 0.08 |
| 4B | $Al_2O_3$ | Al | 0.2 | Al 6061-T651 | 5.2 |

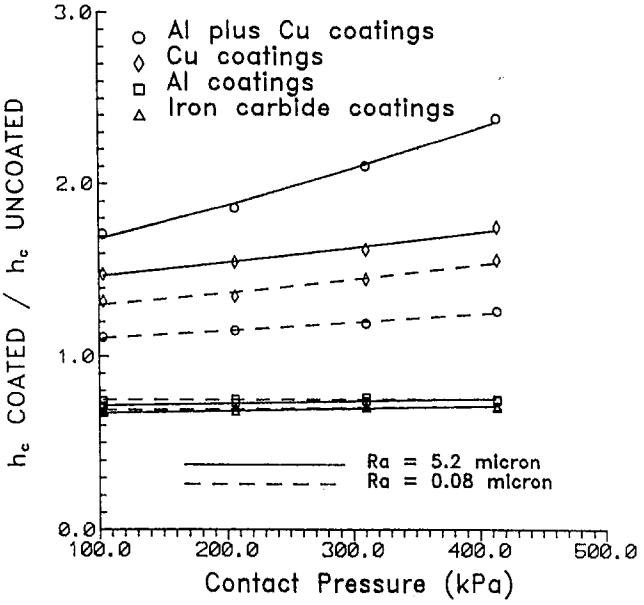



**Fig. 2 Improvement in the thermal contact conductance for different coating materials**

Each specimen was coated on one contact surface with a thin layer of metal or nonmetal. Four different coating materials, Al plus Cu, iron carbide, Cu, and Al, were used to produce coatings on $Al_2O_3$ substrates by a glow discharge plasma technique. The upper contact surfaces of the aluminum 6061-T651 samples were prepared with two different surface roughnesses. The characteristic test specimens are shown in Table 1.

## Results and Discussion

The thermal contact conductance was determined experimentally from the temperature drop and the heat flow rate across the interface. The heat flux through the interface was considered to be the mean of the thermal fluxes through the heat flowmeters. The uncertainty in the temperature drop across the interface is the result of the uncertainties associated with the thermocouple readings and the extrapolated temperature. An estimate of the total uncertainty in the interfacial temperature drop is obtained from the square root of the sum of the squares of the individual uncertainties, which the probable error will be approximately ± 8 percent. The uncertainty in the microhardness of the alumina substrate material used in the investigation was determined to be ±4.5 percent. The uncertainty in the thermal conductivity was ±2 percent for the alumina substrate.

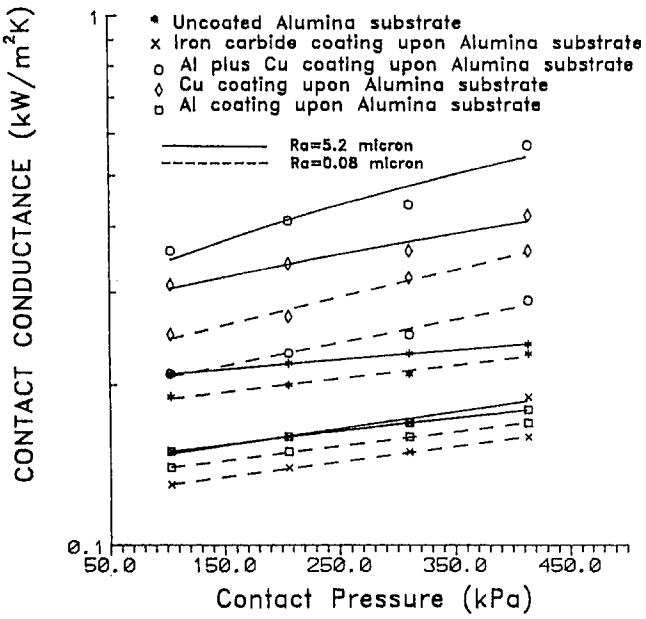



**Fig. 1 Thermal contact conductance of different coating materials upon Al 6061-T651 in contact with alumina substrate**

Figure 1 portrays the data of thermal contact conductance of all coating substrates and compares the values with the control samples (uncoated substrates) at same contact pressures. The iron carbide and Al coatings produced thermal contact conductances approximately 30 percent lower than uncoated substrates.

The ratio of the coated thermal contact conductance to the uncoated thermal contact conductance was plotted as a function of the contact pressure in Fig. 2. The enhancement of the thermal contact conductance for surface roughness of Ra = 5.2 $\mu$m varied from 1.7 to 2.4 times increase for Al plus Cu coatings and 1.5 to 1.8 times increase for Cu coatings. For a surface roughness of Ra = 0.08 $\mu$m, the thermal contact conductance varied from 1.1 to 1.3 times increase for Al plus Cu coatings and 1.4 to 1.6 times increase for Cu coatings. It can be seen that the iron carbide and Al coatings did not obtain thermal contact conductance enhancement. The results also indicated that higher thermal contact conductance for Cu and Al plus Cu coatings were obtained for rougher surfaces. The 5.2 $\mu$m average surface roughness contacts resulted in higher dimensionless thermal contact conductance than 0.08 $\mu$m average surface roughness contacts by 9.5 percent for Cu coatings and 39.7 percent for Al plus Cu coatings. For a surface roughness of 0.08 $\mu$m, the copper coatings gave higher dimensionless thermal contact conductance values than aluminum plus copper coating, whereas for the 5.2 $\mu$m surface roughness the opposite result was observed.

## Conclusions

An experimental determination was made of thermal contact conductance using copper, aluminum, iron carbide, and copper plus aluminum coatings on alumina substrates in contact with aluminum. The thermal contact conductances between ceramic substrates and aluminum contact surfaces were measured. The effect of surface roughness on thermal contact conductance of metal-to-ceramic contacts was examined. The most significant improvements in thermal contact conductance were observed for



Downloaded 12 Dec 2010 to 193.140.21.150. Redistribution subject to ASME license or copyright; see http://www.asme.org/terms/Terms_Use.cfm

Al plus Cu coating specimens. In general, ceramics exhibit good structural and thermal capability at high temperature. They are more resistant to oxidation, corrosion erosion, and wear than most metals. Through the use of modern deposition techniques, high-quality metallic coatings on ceramic substrates or ceramic coatings on metallic substrates can be achieved for specific applications.

## References


Chung, K. C., 1992, "Thermal Contact Conductance of a Phase-Mixed Coating Layer by Transitional Buffering Interface," Ph.D. Dissertation, Department of Mechanical and Aerospace Engineering and Engineering Mechanics, University of Missouri—Rolla.

Chung, K. C., Sheffield, J. W., Sauer, H. J., Jr., O'Keefe, T. J., and Williams, A., 1993, "Thermal Contact Conductance of a Phase-Mixed Coating Layer by Transitional Buffering Interface," *AIAA Journal of Thermophysics and Heat Transfer*, Vol. 7, No. 6, pp. 326–333.

Fletcher, L. S., and Sparks, T. H., 1992, "Thermal Contact Conductance of Porous Ceramic Materials," *Proceedings of the NSF/DITAC Workshop on Thermal Conduction Enhancement in Microelectronics*, A. Williams, ed., Melbourne, Australia, pp. 71–77.

O'Callaghan, P. W., Snaith, B., Probert, S. D., and Al-Astrabadi, F. R., 1983, "Prediction of Interfacial Filler Thickness for Minimum Thermal Contact Resistance," *AIAA Journal*, Vol. 21, No. 9, pp. 1325–1330.

Ochterbeck, J. M., Fletcher, L. S., and Peterson, G. P., 1990, "Evaluation of Thermal Enhancement Films for Electronic Packages," *Proceedings of the 9th International Heat Transfer Conference*, Israel, pp. 445–450.

Peterson, G. P., and Fletcher, L. S., 1988, "Evaluation of Thermal Contact Conductance Between Mold Compound and Heat Spreader Materials," ASME JOURNAL OF HEAT TRANSFER, Vol. 110, pp. 996–999.


# Analytical Solution for Balanced Symmetric Counterflow Regenerator


## J. J. Saastamoinen[1]


## Nomenclature

$C_1$ = heat capacity, J/K
$\dot{C}_1$ = heat capacity flow rate of the gas, W/K
$h$ = effective heat transfer coefficient, W/m$^2$ K
$L$ = length of regenerator, m
$S_1$ = heat transfer area, m$^2$
$t$ = time, s
$y$ = coordinate along the gas flow, m
$\epsilon$ = thermal efficiency
$\eta$ = dimensionless time = $\Pi t/t_1$
$\theta$ = dimensionless temperature of the solid
$\vartheta$ = dimensionless temperature of the gas
$\Lambda$ = dimensionless length of the regenerator = $hS_1/\dot{C}$
$\xi$ = dimensionless coordinate along the gas flow = $\Lambda y/L$
$\Pi$ = dimensionless heating or cooling period = $hSt_1/C$

### Subscripts

1 = cooling or heating period, half period

## Introduction

Several methods of calculating the efficiency of regenerators have been presented in the literature. Some methods are based on numerical evaluation of the governing partial differential equations. One of the earliest and still most powerful numerical methods is presented by Lambertson (1958). The method can easily be extended to include nonlinearities caused by temperature. The local gas properties and local flow gas velocities depend on the local temperature and have an effect on the local heat transfer coefficient inside the regenerator. Direct numerical evaluation of the governing partial differential equation has the advantage that the temperature dependence of the local heat transfer coefficient can easily be included in the calculations.

Other methods, often called closed methods, are based on solving the integral equation for the temperature distribution of the solid at the switching instant. Different calculation methods have been presented and reviewed by Jakob (1957), Hausen (1976), Schmidt and Willmott (1981), and recently Willmott and Knight (1993). These methods are difficult to apply in practice, since they require the programming of the numerical calculation method or involve complicated functions. Simple formulas for engineering calculations that could be applied in the rapid estimation of the regenerator operation are required.

## Equations Describing Heat Transfer

The heat transfer in the gas and in the solid is described by the partial differential equations

$$\frac{\partial \vartheta}{\partial \xi} = \theta - \vartheta \qquad \frac{\partial \theta}{\partial \eta} = \vartheta - \theta \tag{1}$$

in dimensionless form. The dimensionless temperature scale is chosen so that the dimensionless fluid inlet temperatures become 0 and 1. The temperature distribution of the solid at the start of the cooling period is related to the temperature at the end of the cooling period

$$F(\xi) = \theta(0, \xi) = 1 - \theta(\Pi, \Lambda - \xi) \tag{2}$$

due to the symmetry in the cyclic operation. Equations (1) and the symmetry relation, Eq. (2), lead to the classical integral equation of the regenerator theory

$$e^{-\Pi}F(\xi) + F(\Lambda - \xi) + \int_0^{\xi} F(u)\sqrt{\frac{\Pi}{\xi - u}}\, e^{-\Pi - \xi + u} I_1[2\sqrt{\Pi(\xi - u)}]\, du = 1 \tag{3}$$

for the temperature distribution, $F(\xi)$, in the solid at the start of the cooling period. This integral equation is complicated due to the variable $\Lambda - \xi$ in the function $F(\Lambda - \xi)$. $I_n(x)$ is the modified Bessel function. The thermal efficiency of the balanced symmetric regenerator can be related to the temperature distribution at the start of the cooling period by the equation

$$\epsilon = \frac{2}{\Pi}\int_0^{\Lambda} F(\xi)\, d\xi - \frac{\Lambda}{\Pi} \tag{4}$$

Nahavandi and Weinstein (1961) have presented an approximate calculation method by expressing the solid temperature distribution $F(\xi)$ in the integral Eq. (3) as a polynomial of $\xi$. Similar methods and refinements have been presented by Romie (1979), Willmott and Duggan (1980), and Willmott and Knight (1993). These methods lead in principle to an infinite number of equations with an infinite number of unknown coefficients. Finite numbers of equations and unknown coefficients are obtained, when the degree of the polynomial is restricted to some specific value. The calculation method is considered to converge when an increase in the degree of the polynomial no longer has an effect on the calculated efficiency. Baclic (1985) presents an improved method applying the well-known Galerkin method. High accuracy is obtained with only three equations. The integrals are calculated analytically and an analytical approximate explicit solution for the regenerator efficiency is derived. Romie


[1] Technical Research Centre of Finland, VTT Energy, Box 1603, 40100 Jyväskylä, Finland.



Contributed by the Heat Transfer Division of THE AMERICAN SOCIETY OF MECHANICAL ENGINEERS. Manuscript received by the Heat Transfer Division January 1994; revision received June 1994. Keywords: Heat Exchangers, Packed and Fluidized Beds, Transient and Unsteady Heat Transfer. Associate Technical Editor: T. Rabas.





Downloaded 12 Dec 2010 to 193.140.21.150. Redistribution subject to ASME license or copyright; see http://www.asme.org/terms/Terms_Use.cfm

Al plus Cu coating specimens. In general, ceramics exhibit good structural and thermal capability at high temperature. They are more resistant to oxidation, corrosion erosion, and wear than most metals. Through the use of modern deposition techniques, high-quality metallic coatings on ceramic substrates or ceramic coatings on metallic substrates can be achieved for specific applications.

## References


Chung, K. C., 1992, "Thermal Contact Conductance of a Phase-Mixed Coating Layer by Transitional Buffering Interface," Ph.D. Dissertation, Department of Mechanical and Aerospace Engineering and Engineering Mechanics, University of Missouri—Rolla.

Chung, K. C., Sheffield, J. W., Sauer, H. J., Jr., O'Keefe, T. J., and Williams, A., 1993, "Thermal Contact Conductance of a Phase-Mixed Coating Layer by Transitional Buffering Interface," *AIAA Journal of Thermophysics and Heat Transfer*, Vol. 7, No. 6, pp. 326–333.

Fletcher, L. S., and Sparks, T. H., 1992, "Thermal Contact Conductance of Porous Ceramic Materials," *Proceedings of the NSF/DITAC Workshop on Thermal Conduction Enhancement in Microelectronics*, A. Williams, ed., Melbourne, Australia, pp. 71–77.

O'Callaghan, P. W., Snaith, B., Probert, S. D., and Al-Astrabadi, F. R., 1983, "Prediction of Interfacial Filler Thickness for Minimum Thermal Contact Resistance," *AIAA Journal*, Vol. 21, No. 9, pp. 1325–1330.

Ochterbeck, J. M., Fletcher, L. S., and Peterson, G. P., 1990, "Evaluation of Thermal Enhancement Films for Electronic Packages," *Proceedings of the 9th International Heat Transfer Conference*, Israel, pp. 445–450.

Peterson, G. P., and Fletcher, L. S., 1988, "Evaluation of Thermal Contact Conductance Between Mold Compound and Heat Spreader Materials," ASME JOURNAL OF HEAT TRANSFER, Vol. 110, pp. 996–999.


# Analytical Solution for Balanced Symmetric Counterflow Regenerator


**J. J. Saastamoinen**[1]


## Nomenclature

$C_1$ = heat capacity, J/K
$\dot{C}_1$ = heat capacity flow rate of the gas, W/K
$h$ = effective heat transfer coefficient, W/m$^2$ K
$L$ = length of regenerator, m
$S_1$ = heat transfer area, m$^2$
$t$ = time, s
$y$ = coordinate along the gas flow, m
$\epsilon$ = thermal efficiency
$\eta$ = dimensionless time = $\Pi t/t_1$
$\theta$ = dimensionless temperature of the solid
$\vartheta$ = dimensionless temperature of the gas
$\Lambda$ = dimensionless length of the regenerator = $hS_1/\dot{C}$
$\xi$ = dimensionless coordinate along the gas flow = $\Lambda y/L$
$\Pi$ = dimensionless heating or cooling period = $hSt_1/C$

### Subscripts

1 = cooling or heating period, half period

## Introduction

Several methods of calculating the efficiency of regenerators have been presented in the literature. Some methods are based on numerical evaluation of the governing partial differential equations. One of the earliest and still most powerful numerical methods is presented by Lambertson (1958). The method can easily be extended to include nonlinearities caused by temperature. The local gas properties and local flow gas velocities depend on the local temperature and have an effect on the local heat transfer coefficient inside the regenerator. Direct numerical evaluation of the governing partial differential equation has the advantage that the temperature dependence of the local heat transfer coefficient can easily be included in the calculations.

Other methods, often called closed methods, are based on solving the integral equation for the temperature distribution of the solid at the switching instant. Different calculation methods have been presented and reviewed by Jakob (1957), Hausen (1976), Schmidt and Willmott (1981), and recently Willmott and Knight (1993). These methods are difficult to apply in practice, since they require the programming of the numerical calculation method or involve complicated functions. Simple formulas for engineering calculations that could be applied in the rapid estimation of the regenerator operation are required.

## Equations Describing Heat Transfer

The heat transfer in the gas and in the solid is described by the partial differential equations

$$\frac{\partial \vartheta}{\partial \xi} = \theta - \vartheta \qquad \frac{\partial \theta}{\partial \eta} = \vartheta - \theta \tag{1}$$

in dimensionless form. The dimensionless temperature scale is chosen so that the dimensionless fluid inlet temperatures become 0 and 1. The temperature distribution of the solid at the start of the cooling period is related to the temperature at the end of the cooling period

$$F(\xi) = \theta(0, \xi) = 1 - \theta(\Pi, \Lambda - \xi) \tag{2}$$

due to the symmetry in the cyclic operation. Equations (1) and the symmetry relation, Eq. (2), lead to the classical integral equation of the regenerator theory

$$e^{-\Pi}F(\xi) + F(\Lambda - \xi) + \int_0^{\xi} F(u)\sqrt{\frac{\Pi}{\xi - u}}\, e^{-\Pi - \xi + u} I_1[2\sqrt{\Pi(\xi - u)}]\, du = 1 \tag{3}$$

for the temperature distribution, $F(\xi)$, in the solid at the start of the cooling period. This integral equation is complicated due to the variable $\Lambda - \xi$ in the function $F(\Lambda - \xi)$. $I_n(x)$ is the modified Bessel function. The thermal efficiency of the balanced symmetric regenerator can be related to the temperature distribution at the start of the cooling period by the equation

$$\epsilon = \frac{2}{\Pi}\int_0^{\Lambda} F(\xi)\, d\xi - \frac{\Lambda}{\Pi} \tag{4}$$

Nahavandi and Weinstein (1961) have presented an approximate calculation method by expressing the solid temperature distribution $F(\xi)$ in the integral Eq. (3) as a polynomial of $\xi$. Similar methods and refinements have been presented by Romie (1979), Willmott and Duggan (1980), and Willmott and Knight (1993). These methods lead in principle to an infinite number of equations with an infinite number of unknown coefficients. Finite numbers of equations and unknown coefficients are obtained, when the degree of the polynomial is restricted to some specific value. The calculation method is considered to converge when an increase in the degree of the polynomial no longer has an effect on the calculated efficiency. Baclic (1985) presents an improved method applying the well-known Galerkin method. High accuracy is obtained with only three equations. The integrals are calculated analytically and an analytical approximate explicit solution for the regenerator efficiency is derived. Romie


[1] Technical Research Centre of Finland, VTT Energy, Box 1603, 40100 Jyväskylä, Finland.



Contributed by the Heat Transfer Division of THE AMERICAN SOCIETY OF MECHANICAL ENGINEERS. Manuscript received by the Heat Transfer Division January 1994; revision received June 1994. Keywords: Heat Exchangers, Packed and Fluidized Beds, Transient and Unsteady Heat Transfer. Associate Technical Editor: T. Rabas.




Copyright © 1995 by ASME




Downloaded 12 Dec 2010 to 193.140.21.150. Redistribution subject to ASME license or copyright; see http://www.asme.org/terms/Terms_Use.cfm

and Baclic (1988) generalize the method for the asymmetric unbalanced regenerator.

Nusselt (1927) and Hausen (1976) have presented explicit analytical solutions, in which new terms in the solution can be generated in succession. Addition of new terms does not alter the terms already generated in these explicit solutions. These solutions are very complicated and direct numerical evaluation of the partial differential equations is more practical.

## Solution of Equations

In the following, a novel explicit exact analytical series solution, in which new terms can be generated in succession, is derived. The function $F(\xi)$ in the integral equation, Eq. (3), is presented as the Maclaurin series

$$F(\xi) = \sum_{n=0}^{\infty} F_n(\xi) \frac{\Pi^n}{n!} \tag{5}$$

The exponential function $e^{-\Pi}$ and the kernel function can be expanded in powers of $\Pi$, when noticing that it is of similar form as the generating function for the generalized Laguerre polynomials $L_n^{(k)}(x)$ (Abramowitz and Stegun, 1972). Equating the terms having equal powers, we obtain the equation

$$F_{n+1}(\xi) + F_{n+1}(\Lambda - \xi) = Y_n(\xi) = Y_n(\Lambda - \xi) \tag{6}$$

where

$$\frac{Y_n(\xi)}{n+1} = F_n(\xi) - e^{-\xi} \int_0^{\xi} e^u F_n(u) du - Z_{n-1}(\xi) \tag{7}$$

where

$$Z_{n-1}(\xi) = \sum_{k=0}^{n-1} \frac{(-1)^{n-k+1} n!}{k!(n-k+1)!} \times \left[ F_k(\xi) - e^{-\xi} \int_0^{\xi} e^u F_k(u) L_{n-k}^{(1)}(\xi - u) du \right] \tag{8}$$

The recurrence relation, Eq. (6), cannot directly be used to generate new functions from the previous ones. By differentiating Eq. (6) twice with respect to the coordinate $\xi$, the integrals and the function $F_n(\Lambda - \xi)$ can be removed. The result is a linear differential equation of second order, which can readily be solved by double integration. New functions $F_n(\xi)$ can be generated when the preceding functions $F_k(\xi)$, $k < n$ are known. The integrals are elementary involving powers and exponential functions. However, the integration is very tedious to do by hand. The integration was performed by a commercial program that integrates expressions in analytic form. The first eight functions $F_n(\xi)$ were generated by a computer. The first four are

$$F_0(\xi) = \frac{1+\xi}{2+\Lambda} = \frac{1}{2} + \frac{1}{2} \frac{\xi - (\Lambda - \xi)}{2+\Lambda}$$

$$F_1(\xi) = \frac{1}{2} \frac{1}{2+\Lambda}$$

$$F_2(\xi) = \frac{1}{12} \frac{1 - e^{-\Lambda}}{(2+\Lambda)^2} [\xi - (\Lambda - \xi)] + \frac{1}{6} \frac{1}{2+\Lambda} [e^{-\xi} - e^{-(\Lambda - \xi)}]$$

$$F_3(\xi) = \frac{1}{4} \frac{1 - e^{-\Lambda}}{(2+\Lambda)^2} - \frac{1}{8} \frac{1}{2+\Lambda} [e^{-\xi} + e^{-(\Lambda - \xi)}] \tag{9}$$

By using Eq. (9) the solid initial temperature, Eq. (5), can be presented in the form

$$F(\xi) = \sum_{n=0}^{\infty} (A_n + B_n e^{-\xi} + C_n e^{\xi}) \frac{\xi^n}{n!} \tag{10}$$

The analytical expressions for the solid and the gas temperature distributions in cyclic state are obtained by applying the Laplace transform to the partial differential equations (1) with the initial condition (10) and gas inlet temperature $\vartheta(\xi = 0, \eta) = 0$. The results are

$$\theta = \sum_{n=0}^{\infty} \left[ A_n G_n(\eta, \xi) + B_n e^{-\eta - \xi} (\xi/\eta)^{n/2} I_n(2\sqrt{\xi\eta}) + C_n \frac{1}{2^n} e^{-\eta/2 + \xi} G_n(\eta/2, 2\xi) \right]$$

$$\vartheta = \sum_{n=0}^{\infty} \left[ A_n H_n(\eta, \xi) + B_n e^{-\eta - \xi} (\xi/\eta)^{(n+1)/2} I_{n+1}(2\sqrt{\xi\eta}) + C_n \frac{1}{2^{n+1}} e^{-\eta/2 + \xi} H_n(\eta/2, 2\xi) \right] \tag{11}$$

where

$$G_n(\eta, \xi) = e^{-\eta} \xi^n \left( \frac{1}{n!} + \sum_{k=1}^{\infty} (-1)^k [L_k^{(0)}(\eta) - L_{k-1}^{(0)}(\eta)] \frac{\xi^k}{(n+k)!} \right)$$

$$H_n(\eta, \xi) = e^{-\eta} \xi^n \sum_{k=0}^{\infty} (-1)^k L_k^{(0)}(\eta) \frac{\xi^{k+1}}{(n+k+1)!} \tag{12}$$

## Concluding Remarks

In rotating regenerators, the cycle period is usually short. The dimensionless period, $\Pi$, is 2 or less in practical rotary air preheaters installed in power station boilers according to Atthey (1988). The use of the first four functions $F_n(\xi)$ gives the approximation

$$\epsilon \approx \frac{\Lambda}{2+\Lambda} \left( 1 - \frac{\Pi^2}{6\Lambda} \frac{1 - e^{-\Lambda}}{2+\Lambda} \right) \tag{13}$$

which gives good accuracy for the case $\Pi \leq 2$. The use of first eight functions gives

$$\epsilon = \frac{\Lambda}{2+\Lambda} - \frac{\Pi^2}{6} \frac{1 - e^{-\Lambda}}{(2+\Lambda)^2} + \frac{\Pi^4}{120(2+\Lambda)^2} \times \left[ \left( \frac{7}{6}\Lambda - \frac{1}{6}\Lambda^2 \right) e^{-\Lambda} + \frac{5}{12}(1 - e^{-2\Lambda}) - \frac{5}{3} \frac{(1 - e^{-\Lambda})^2}{2+\Lambda} \right] + \frac{\Pi^6}{5040(2+\Lambda)^4} \left[ -\frac{7\Lambda^2}{8} - \frac{7\Lambda}{12} - \frac{7}{2} + e^{-\Lambda} \left( \frac{\Lambda^6}{72} - \frac{11\Lambda^5}{36} + \frac{145\Lambda^4}{144} + \frac{473\Lambda^3}{144} + \frac{29\Lambda^2}{96} - \frac{805\Lambda}{288} + \frac{245}{24} \right) + \frac{1}{24} e^{-2\Lambda} (\Lambda^4 - 45\Lambda^2 - 86\Lambda - 68) + \frac{35}{96} e^{-3\Lambda} (\Lambda^2 + 12\Lambda + 36) \right] \tag{14}$$

The truncation error of Eq. (14) is of the order $\Pi^8/9!$. Calculated efficiency values are compared to published data in Table 1, which shows that the accuracy of the simple Eq. (13) is good. The comparison to additional data of Baclic shows that the accuracy of the Eq. (13) also remains quite good when $\Pi = 3$.

Equation (13) is very simple, but accurate enough, involving only an exponential function, which is advantageous in the rapid estimation of regenerator efficiency. Even the more complicated solution, Eq. (14) is easier to use than other methods or equations presented in the literature, which require the use of a computer or at least a programmable calculator. The formula presented by



Downloaded 12 Dec 2010 to 193.140.21.150. Redistribution subject to ASME license or copyright; see http://www.asme.org/terms/Terms_Use.cfm

**Table 1 Comparison of efficiencies: (a) Eq. (13), (b) Eq. (14) with three terms, (c) Eq. (14) with four terms**

| Method | Λ=5 | Λ=10 | Λ=20 |
|---|---|---|---|
| a | 0.7008 | 0.8287 | 0.9077 |
| b | 0.7013 | 0.8290 | 0.9078 |
| c | 0.7012 | 0.8289 | 0.9078 |
| Baclic, 1985 | 0.7011 | 0.8288 | 0.9077 |

Baclic is very accurate, but it involves the calculation of the values of some Bessel functions, which makes it difficult to be used in practice. The simple form is also useful in obtaining simple analytical solutions for economic optimization of a regenerator, where an economic target function that depends both on the efficiency and heat transfer area are maximized or minimized. It should be noted that these simple formulas are restricted to small values of Π. The more complicated formula presented by Baclic is valid for all values of Π.

## References


Abramowitz, M., and Stegun, I., 1972, *Handbook of Mathematical Functions*, Dover Publications, New York.

Atthey, D. R., 1988, "An Approximate Thermal Analysis for a Regenerative Heat Exchanger," *Int. J. Heat Mass Transfer*, Vol. 31, No. 7, pp. 1431–1441.

Baclic, B. S., 1985, "The Application of the Galerkin Method to the Solution of the Symmetric and Balanced Counterflow Regenerator Problem," ASME JOURNAL OF HEAT TRANSFER, Vol. 107, pp. 214–221.

Hausen, H., 1976, *Wärmeübertragung im Gegenstrom, Gleichstrom und Kreuzstrom*, Springer-Verlag, Berlin.

Jakob, M., 1957, *Heat Transfer*, Vol. II, Wiley, New York.

Lambertson, T. J., 1958, "Performance Factors of a Periodic Flow Heat Exchanger," *ASME Transactions*, Vol. 80, pp. 586–592.

Nahavandi, A. N., and Weinstein, A. S., 1961, "A Solution to the Periodic-Flow Regenerative Heat Exchanger Problem," *Appl. Sci. Res.*, Section A, Vol. 10, pp. 335–348.

Nusselt, W., 1927, "Die Theorie des Winderhitzer," *Z. Ver. Dt. Ing*, Vol. 71, pp. 85–91.

Romie, F. E., 1979, "Periodic Thermal Storage: The Regenerator," ASME JOURNAL OF HEAT TRANSFER, Vol. 101, pp. 726–731.

Romie, F. E., and Baclic, B. S., 1988, "Methods for Rapid Calculation of the Operation of Asymmetric Counterflow Regenerators," ASME JOURNAL OF HEAT TRANSFER, Vol. 110, pp. 785–788.

Schmidt, F. W., and Willmott, A. J., 1981, *Thermal Energy Storage and Regeneration*, McGraw-Hill, New York.

Willmott, A. J., and Duggan, R. C., 1980, "Refined Closed Methods for the Contra-flow Thermal Regenerator Problem," *Int. J. Heat Mass Transfer*, Vol. 23, pp. 655–662.

Willmott, A. J., and Knight, D. P., 1993, "Improved Collocation Methods for Thermal Regenerator Simulations," *Int. J. Heat Mass Transfer*, Vol. 36, No. 6, pp. 1663–1670.


# On the Effective Driving Force for Transport in Cooling Towers


**M. Sadasivam[1,2] and A. R. Balakrishnan[1,3]**


## Nomenclature

$a$ = interfacial area, $m^2/m^3$
$b_o$ = slope of saturated air enthalpy, J/(kg·°C)
$B''$ = defined in Eq. (4), J/(kg·°C)
$C_p$ = specific heat, J/(kg·°C)
$C_s$ = humid heat, J/(kg·°C)
$G$ = superficial gas mass velocity, $kg/(m^2 \cdot s)$
$h$ = convective heat transfer coefficient, $W/(m^2 \cdot °C)$
$H$ = enthalpy, J/kg; $H^*$: apparent enthalpy, J/kg
$k_y$ = gas phase mass transfer coefficient, $kg/(m^2 \cdot s)$
$L$ = superficial liquid mass velocity, $kg/(m^2 \cdot s)$
Le = Lewis number
NTU = number of transfer units
$q$ = heat flux, $W/m^2$
$r$ = convective Lewis number
$T$ = temperature, °C
$Y$ = absolute humidity, kg $H_2O$/kg dry air
$Z$ = height of tower, m
$\alpha$ = defined in Eq. (4), J/(kg·°C)
$\beta$ = defined in Eq. (4), J/(kg·°C)
$\epsilon$ = effectiveness
$\lambda$ = latent heat of vaporization, J/kg

### Subscripts

$A$ = component A, water vapor
$B$ = component B, dry air
$G$ = air
$H$ = heat transfer
$i$ = interface condition
$L$ = (liquid) water
$m$ = mass transfer
$o$ = reference point
$s$ = sensible heat transfer
$w$ = wet bulb

Since both heat and mass transfer take place in cooling towers, Merkel (1926) suggested that the driving force for heat transfer in cooling towers is the enthalpy difference of the wet air at the interface and in the bulk. Cooling tower design equations have been obtained analytically based on Merkel's (1926) approach and by expressing the saturated air enthalpy as a linear function of temperature ($\epsilon$–NTU method of Berman, 1961, and Jaber and Webb, 1989) or as a quadratic function of temperature (Foust et al., 1979; Fahim et al., 1985). In all these studies the Lewis relation has been assumed to be valid. In this study an apparent air enthalpy is defined, thereby obviating the need to invoke the Lewis relation, and the use of this apparent enthalpy in the $\epsilon$–NTU method of cooling tower design is demonstrated.

The so-called Lewis relation can be distinguished from the Lewis number by considering the following parameter:

$$r = \frac{h_G a_H}{C_s k_y a_m} \tag{1}$$

$r$ is related to the Lewis number, Le, defined as the ratio of the Schmidt number to the Prandtl number, by empirical correlations. For the air–water system, Lewis (after W. K. Lewis) showed that the ratio of the gas-phase heat transfer coefficient to the gas-phase mass transfer coefficient is approximately equal to the humid heat of the wet air. This implies that $r$ should be unity for the air–water system, and is commonly called the "Lewis relation." However, this is only approximately true, for as Hensel and Treybal (1952) have pointed out, $r$ can be as high as two at very low liquid flow rates. However, only when $r$ is unity, is it called the Lewis relation. Some investigators have called $r$ the convective Lewis number, $Le_c$, when $r$ takes on values other than unity. $r$ is also sometimes referred to as the psychrometric ratio (when $a_H = a_m$, which is quite common). Different authors have used different definitions for the Lewis number, Le. Webb (1990) compared all these definitions and concluded that the


[1] Department of Chemical Engineering, Indian Institute of Technology Madras, Madras 600 036 India.

[2] Research scholar; present address: International Development and Engineering Associates Ltd., Madras 600 034 India.

[3] Associate Professor; Mem. ASME.



Contributed by the Heat Transfer Division of THE AMERICAN SOCIETY OF MECHANICAL ENGINEERS. Manuscript received by the Heat Transfer Division February 1994; revision received August 1994. Keywords: Direct-Contact Heat Transfer, Heat Exchangers, Mass Transfer. Associate Technical Editor: T. J. Rabas.





Downloaded 12 Dec 2010 to 193.140.21.150. Redistribution subject to ASME license or copyright; see http://www.asme.org/terms/Terms_Use.cfm

**Table 1 Comparison of efficiencies: (a) Eq. (13), (b) Eq. (14) with three terms, (c) Eq. (14) with four terms**

| Method | Λ=5 | Λ=10 | Λ=20 |
|---|---|---|---|
| a | 0.7008 | 0.8287 | 0.9077 |
| b | 0.7013 | 0.8290 | 0.9078 |
| c | 0.7012 | 0.8289 | 0.9078 |
| Baclic, 1985 | 0.7011 | 0.8288 | 0.9077 |

Baclic is very accurate, but it involves the calculation of the values of some Bessel functions, which makes it difficult to be used in practice. The simple form is also useful in obtaining simple analytical solutions for economic optimization of a regenerator, where an economic target function that depends both on the efficiency and heat transfer area are maximized or minimized. It should be noted that these simple formulas are restricted to small values of Π. The more complicated formula presented by Baclic is valid for all values of Π.

## References


Abramowitz, M., and Stegun, I., 1972, *Handbook of Mathematical Functions*, Dover Publications, New York.

Atthey, D. R., 1988, "An Approximate Thermal Analysis for a Regenerative Heat Exchanger," *Int. J. Heat Mass Transfer*, Vol. 31, No. 7, pp. 1431–1441.

Baclic, B. S., 1985, "The Application of the Galerkin Method to the Solution of the Symmetric and Balanced Counterflow Regenerator Problem," ASME JOURNAL OF HEAT TRANSFER, Vol. 107, pp. 214–221.

Hausen, H., 1976, *Wärmeübertragung im Gegenstrom, Gleichstrom und Kreuzstrom*, Springer-Verlag, Berlin.

Jakob, M., 1957, *Heat Transfer*, Vol. II, Wiley, New York.

Lambertson, T. J., 1958, "Performance Factors of a Periodic Flow Heat Exchanger," *ASME Transactions*, Vol. 80, pp. 586–592.

Nahavandi, A. N., and Weinstein, A. S., 1961, "A Solution to the Periodic-Flow Regenerative Heat Exchanger Problem," *Appl. Sci. Res.*, Section A, Vol. 10, pp. 335–348.

Nusselt, W., 1927, "Die Theorie des Winderhitzer," *Z. Ver. Dt. Ing*, Vol. 71, pp. 85–91.

Romie, F. E., 1979, "Periodic Thermal Storage: The Regenerator," ASME JOURNAL OF HEAT TRANSFER, Vol. 101, pp. 726–731.

Romie, F. E., and Baclic, B. S., 1988, "Methods for Rapid Calculation of the Operation of Asymmetric Counterflow Regenerators," ASME JOURNAL OF HEAT TRANSFER, Vol. 110, pp. 785–788.

Schmidt, F. W., and Willmott, A. J., 1981, *Thermal Energy Storage and Regeneration*, McGraw-Hill, New York.

Willmott, A. J., and Duggan, R. C., 1980, "Refined Closed Methods for the Contra-flow Thermal Regenerator Problem," *Int. J. Heat Mass Transfer*, Vol. 23, pp. 655–662.

Willmott, A. J., and Knight, D. P., 1993, "Improved Collocation Methods for Thermal Regenerator Simulations," *Int. J. Heat Mass Transfer*, Vol. 36, No. 6, pp. 1663–1670.


# On the Effective Driving Force for Transport in Cooling Towers


**M. Sadasivam[1,2] and A. R. Balakrishnan[1,3]**


## Nomenclature

$a$ = interfacial area, $m^2/m^3$
$b_o$ = slope of saturated air enthalpy, J/(kg·°C)
$B''$ = defined in Eq. (4), J/(kg·°C)
$C_p$ = specific heat, J/(kg·°C)
$C_s$ = humid heat, J/(kg·°C)
$G$ = superficial gas mass velocity, $kg/(m^2 \cdot s)$
$h$ = convective heat transfer coefficient, $W/(m^2 \cdot °C)$
$H$ = enthalpy, J/kg; $H^*$: apparent enthalpy, J/kg
$k_y$ = gas phase mass transfer coefficient, $kg/(m^2 \cdot s)$
$L$ = superficial liquid mass velocity, $kg/(m^2 \cdot s)$
Le = Lewis number
NTU = number of transfer units
$q$ = heat flux, $W/m^2$
$r$ = convective Lewis number
$T$ = temperature, °C
$Y$ = absolute humidity, kg $H_2O$/kg dry air
$Z$ = height of tower, m
$\alpha$ = defined in Eq. (4), J/(kg·°C)
$\beta$ = defined in Eq. (4), J/(kg·°C)
$\epsilon$ = effectiveness
$\lambda$ = latent heat of vaporization, J/kg

### Subscripts

$A$ = component A, water vapor
$B$ = component B, dry air
$G$ = air
$H$ = heat transfer
$i$ = interface condition
$L$ = (liquid) water
$m$ = mass transfer
$o$ = reference point
$s$ = sensible heat transfer
$w$ = wet bulb

Since both heat and mass transfer take place in cooling towers, Merkel (1926) suggested that the driving force for heat transfer in cooling towers is the enthalpy difference of the wet air at the interface and in the bulk. Cooling tower design equations have been obtained analytically based on Merkel's (1926) approach and by expressing the saturated air enthalpy as a linear function of temperature ($\epsilon$–NTU method of Berman, 1961, and Jaber and Webb, 1989) or as a quadratic function of temperature (Foust et al., 1979; Fahim et al., 1985). In all these studies the Lewis relation has been assumed to be valid. In this study an apparent air enthalpy is defined, thereby obviating the need to invoke the Lewis relation, and the use of this apparent enthalpy in the $\epsilon$–NTU method of cooling tower design is demonstrated.

The so-called Lewis relation can be distinguished from the Lewis number by considering the following parameter:

$$r = \frac{h_G a_H}{C_s k_y a_m} \tag{1}$$

$r$ is related to the Lewis number, Le, defined as the ratio of the Schmidt number to the Prandtl number, by empirical correlations. For the air–water system, Lewis (after W. K. Lewis) showed that the ratio of the gas-phase heat transfer coefficient to the gas-phase mass transfer coefficient is approximately equal to the humid heat of the wet air. This implies that $r$ should be unity for the air–water system, and is commonly called the "Lewis relation." However, this is only approximately true, for as Hensel and Treybal (1952) have pointed out, $r$ can be as high as two at very low liquid flow rates. However, only when $r$ is unity, is it called the Lewis relation. Some investigators have called $r$ the convective Lewis number, $Le_c$, when $r$ takes on values other than unity. $r$ is also sometimes referred to as the psychrometric ratio (when $a_H = a_m$, which is quite common). Different authors have used different definitions for the Lewis number, Le. Webb (1990) compared all these definitions and concluded that the


[1] Department of Chemical Engineering, Indian Institute of Technology Madras, Madras 600 036 India.

[2] Research scholar; present address: International Development and Engineering Associates Ltd., Madras 600 034 India.

[3] Associate Professor; Mem. ASME.



Contributed by the Heat Transfer Division of THE AMERICAN SOCIETY OF MECHANICAL ENGINEERS. Manuscript received by the Heat Transfer Division February 1994; revision received August 1994. Keywords: Direct-Contact Heat Transfer, Heat Exchangers, Mass Transfer. Associate Technical Editor: T. J. Rabas.





Copyright © 1995 by ASME

Downloaded 12 Dec 2010 to 193.140.21.150. Redistribution subject to ASME license or copyright; see http://www.asme.org/terms/Terms_Use.cfm

ratio of thermal diffusivity to mass diffusivity is the most meaningful one. Webb (1988) has described the magnitude of the possible errors associated with cooling tower design procedures. It may be concluded from the above that the introduction of the Lewis relation into the balance equations results in error. This is because even for air–water systems, the convective Lewis number varies widely.

## Analysis

A mass and energy balance over a differential segment in the cooling tower gives

$$G_B dH_G = k_y a_m (H^*_{Gi} - H^*_G) dZ = dq \qquad (2)$$

where $H^*_G$, the apparent enthalpy, is given by

$$H^*_G = C_s r T_G + \lambda_{A0} Y_A \qquad (3)$$

Assuming the Lewis relation is valid for the air–water system, i.e., $r = 1.0$, results in the apparent enthalpy collapsing to the absolute enthalpy, which is the Merkel approach, i.e., the driving potential for heat transfer in cooling towers is the enthalpy difference of the wet air at the interface and at the bulk. This is true if, and only if, $r$ is unity, i.e., the Lewis relation is satisfied. On the other hand Eq. (2) is based on the effective or apparent enthalpy driving potential, $H^*_G$. This effective or apparent enthalpy differs from the actual enthalpy in that it has included in it the

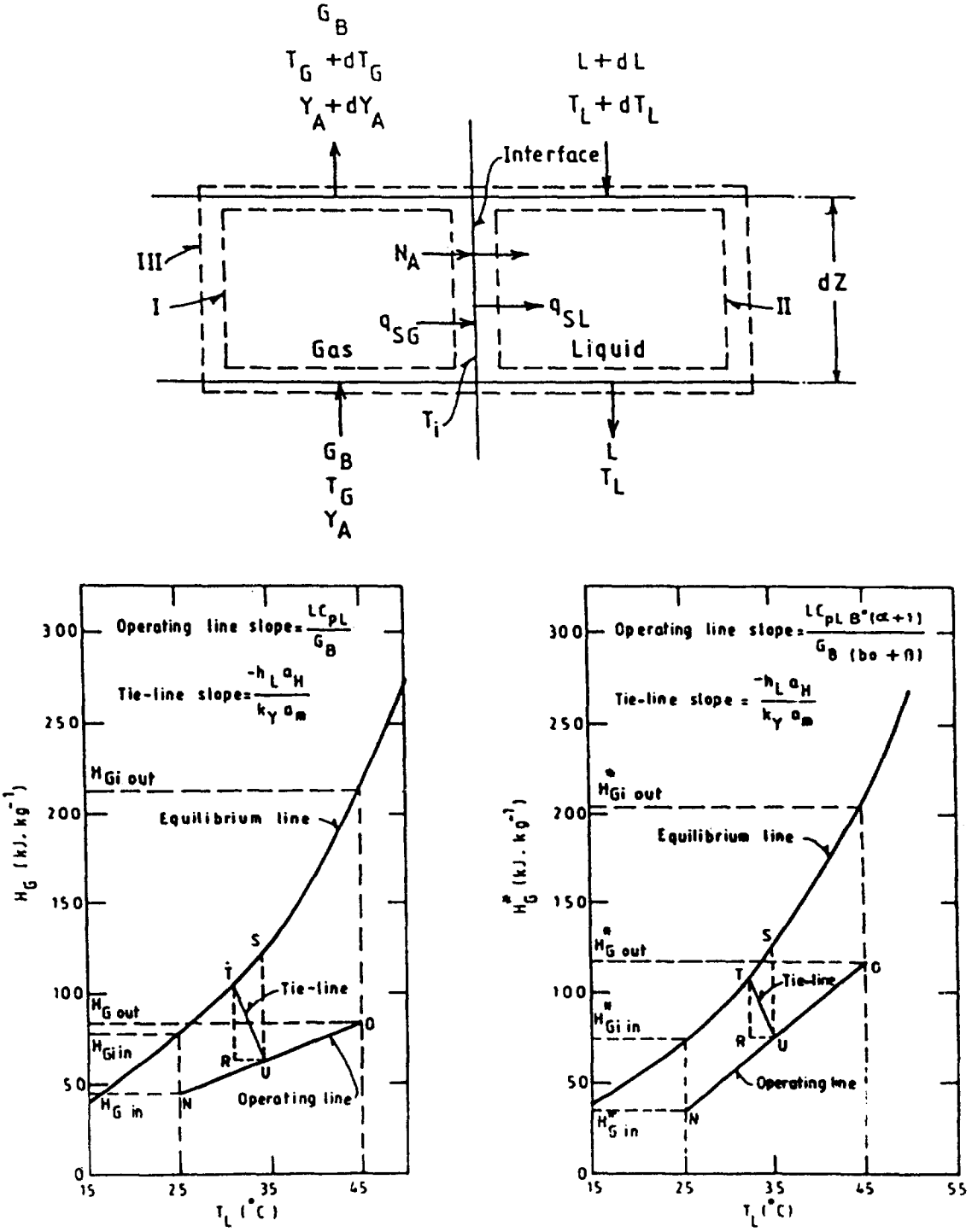



**Fig. 1 Operating diagram of the cooling tower: (*a*) on the air enthalpy versus liquid temperature diagram; (*b*) on the air apparent enthalpy versus liquid temperature diagram; (*c*) schematic of a differential segment of a cooling tower**



Downloaded 12 Dec 2010 to 193.140.21.150. Redistribution subject to ASME license or copyright; see http://www.asme.org/terms/Terms_Use.cfm

convective Lewis number, $r$. From Eq. (3) it is seen that the apparent enthalpy is less than the actual enthalpy when $r$ is less than one and vice versa.

Figure 1 shows the operating diagram of cooling towers in terms of the actual enthalpy and the apparent enthalpy. It is seen that when the apparent enthalpy is used the equilibrium line gets shifted closer to the operating line, i.e., driving potential is reduced. All the previous studies on cooling towers have indeed shown that using absolute enthalpies results in underestimation of the cooling tower height. The cooling tower design problem can best be handled on an operating diagram drawn on the apparent enthalpy ($H_G^*$) versus temperature chart (Fig. 1). This requires a relationship between the apparent and actual enthalpies of the air. This can be obtained using the tie-line relationship (see Fig. 1). Point $U$ on the operating line corresponds to any position in the column, and point $T$ (on the equilibrium line) represents the interface conditions. The distance $TR$ is the enthalpy driving force ($H_{Gi} - H_G$) within the gas phase. Point $S$ corresponds to a position where the heat transfer resistance is neglected on the liquid side, i.e., $T_i = T_L$ (or the slope of $h_L a_H / k_y a_m$ is infinite). However, as Marseille et al. (1991) have shown, the liquid side heat transfer cannot be neglected in cooling tower design without incurring error. The slope of the operating line is $L.C_{pL}/G_B$ (from the overall enthalpy balance). The slope of the tie-line is obtained from the liquid side enthalpy balance. If the operating diagram is constructed in terms of the saturated apparent enthalpy ($H_{Gi}^*$) versus temperature, Fig. 1($b$), the slope of the tie-line will remain the same as for $H_{Gi}$ versus $T_L$. Using the liquid side and overall enthalpy balance and representing the saturated enthalpy $H_{Gi}$ and the saturated apparent enthalpy $H_{Gi}^*$, as a linear function of $T_i$, it can be shown

$$dH_G = \frac{(b_0 + \beta)}{(\alpha + 1)B''} dH_G^* \tag{4}$$

where $\beta = h_L a_H / k_y a_m$; $\alpha = \beta.G_B/L.C_{pL}$; $B'' = f' - \{\alpha/(\alpha + 1)\}\cdot(b_0 + \beta) + \beta$; and $b_0$ and $f'$ are the slopes of the $H_{Gi}$ versus $T$ and $H_{Gi}^*$ versus $T$ curves, respectively. Introducing Eq. (4) in the overall enthalpy balance gives

$$dq = G_B \frac{(b_0 + \beta)}{(\alpha + 1)B''} dH_G^* = LC_{pL} dT_L \tag{5}$$

Following an approach similar to the $\epsilon$–NTU method of Jaber and Webb (1989), it can be shown that $L\cdot C_{pL}/f'$ is the water capacity rate and $G_B(b_0 + \beta)/(\alpha + 1)B''$ is the air capacity rate. These water and air capacity rates differ from the definitions of Jaber and Webb (1989), in that while $f'$ in the present study is the slope of the apparent saturated air enthalpy versus temperature curve ($H_{Gi}^*$ versus $T$), Jaber and Webb (1989) used the true saturated air enthalpy versus temperature curve ($H_{Gi}$ versus $T$). Furthermore, in the present study, the capacity rate of the fluid is a function of the convective Lewis number. However, if the Lewis relation is invoked, i.e., $r = 1$, the present definitions of water and air capacity rate collapse to the definitions used by Jaber and Webb (1989).

**Table 1 Comparison of cooling tower heights estimated by present method and rigorous method**

| $T_{Gin}$ | $Z_s$ | | $Z$ | | | | | |
|---|---|---|---|---|---|---|---|---|
| | | | r = 1.0 | | r = 0.9 | | r = 0.8 | |
| | $T_{Lin1}$ | $T_{Lin2}$ | $T_{Lin1}$ | $T_{Lin2}$ | $T_{Lin1}$ | $T_{Lin2}$ | $T_{Lin1}$ | $T_{Lin2}$ |
| 27 | 0.464 | 0.785 | 0.422 | 0.762 | 0.428 | 0.772 | 0.434 | 0.782 |
| 29 | 0.498 | 0.849 | 0.463 | 0.832 | 0.465 | 0.845 | 0.468 | 0.838 |
| 31 | 0.557 | 0.926 | 0.513 | 0.918 | 0.512 | 0.911 | 0.507 | 0.904 |
| 33 | 0.619 | 1.021 | 0.575 | 1.026 | 0.564 | 1.004 | 0.554 | 0.984 |
| 35 | 0.707 | 1.143 | 0.655 | 1.168 | 0.632 | 1.123 | 0.610 | 1.081 |

$T_{Lin1}$ = 35°C; $T_{Lin2}$ = 40°C; L = 1.0 kg/(m²s); G = 1.0 kg/(m²s); $h_G$ = 47.09 W/(m²C); $h_L$ = 3975 W/(m²C); a = 42 m²/m³; $K_y$ = 0.054 kg/(m²s).

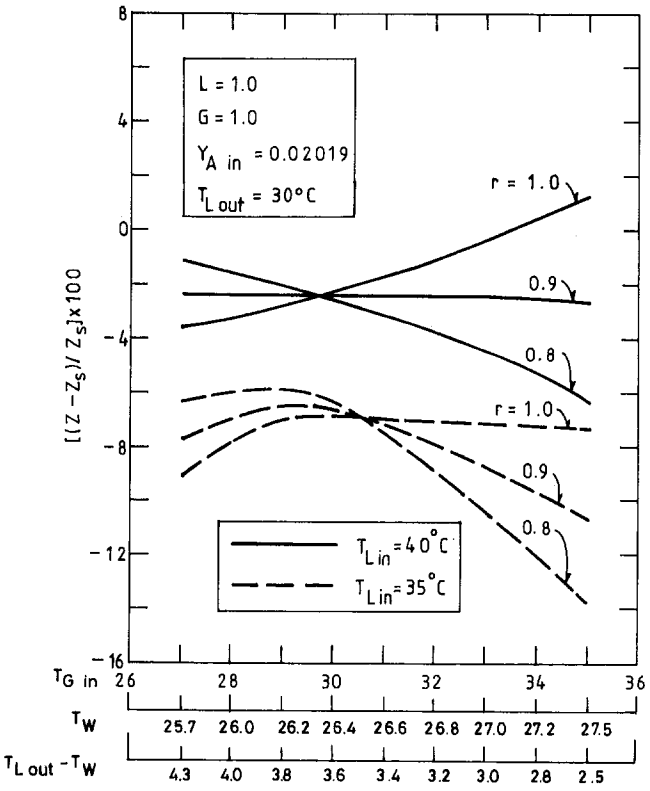



**Fig. 2 Effect of inlet air temperature on required height**

From the operating diagram of the cooling tower, Fig. 1, it is obvious that the maximum heat that can be transferred without violating the Second Law of Thermodynamics is

$$q_{max} = m_{min}(H_{Giout}^* - H_{Gin}^*) \tag{6}$$

The effectiveness $\epsilon$ can now be defined as $\epsilon = q_{actual}/q_{max}$ and related to the NTU (number of transfer units) by (as described by Jaber and Webb, 1989)

$$\epsilon = \frac{1 - \exp[-\text{NTU}(1 - C_R)]}{1 - C_R \exp[-\text{NTU}(1 - C_R)]} \tag{7}$$

where NTU = $k_y \cdot a_m / m_{min}$; $C_R$ (capacity rate ratio) = $m_{min}/m_{max}$ $m_{min}$ and $m_{max}$: minimum and maximum of $L\cdot C_{pL}/f'$ and $\{G_B(b_0 + \beta)\}/\{(\alpha + 1)B''\}$.

## Results and Discussion

Numerical results were obtained for different inlet conditions for a countercurrent flow cooling tower using the modified $\epsilon$–NTU method described above. The height of the column required to accomplish a prescribed cooling duty was determined at different liquid to air ratios ($L/G$), at various values of $r$. The height ($Z$) obtained from the modified $\epsilon$–NTU method is compared with the height ($Z_s$) obtained from a rigorous method described by Treybal (1984), which is used as a benchmark. This is shown in Table 1 and also in Fig. 2. The rigorous method requires the tower to be divided into a very large number of segments over which the mass and energy balance equations coupled with the rate equations have to be solved over each differential segment sequentially. This procedure obviously requires the use of a computer. The heat and mass transfer coefficients of the 1 in. Berl saddles packing (fill) required for the computations were obtained using the procedures described by Treybal (1984). The $\epsilon$–NTU method requires the assumption that the saturated enthalpy (or apparent enthalpy) versus temperature relation is linear, which is not strictly true. Jaber and Webb (1989) have shown that if the tower is divided into up to three segments and



Downloaded 12 Dec 2010 to 193.140.21.150. Redistribution subject to ASME license or copyright; see http://www.asme.org/terms/Terms_Use.cfm

the $\epsilon$–NTU method applied over each segment, the linearity assumption is not violated.

In Fig. 2, the effect of air inlet temperature on the height obtained by the present method when compared with the rigorous method is shown. It is seen from the figure that up to a particular air inlet temperature, the underprediction of the column height decreases at all $r$ values at the lower cooling range and at the lower values of $r$ at the higher cooling range. However, in both cases, the curves for different values of $r$ meet at a particular point when the trend is reversed. This indicates that at this point $r$ does not have any significant effect. This can be explained by examining the definition of $r$, which has the gas side heat transfer coefficient in the numerator and the mass transfer coefficient in the denominator. These coefficients are obtained from the hydrodynamic conditions in the tower and the type of tower internals. At the point where the curves meet, even though $h_G$ has a finite value, the temperature driving force approaches zero and therefore all the cooling takes place only due to mass transfer. Beyond this point the trend is reversed as the contribution of the sensible heat transfer to the net cooling may be in the reverse direction. This can be observed from the rigorous method.

From a thermodynamic point of view it is possible to cool water of a temperature less than the entering air dry bulb temperature. This is because the actual or apparent enthalpy is for most practical purposes a function of adiabatic saturation temperature, or for air–water systems, the wet bulb temperature. It is also possible to operate a tower with entering air saturated, so long as its temperature is less than the water outlet temperature when the driving force is the wet bulb temperature approach. In Fig. 2 as the air inlet temperature increases, keeping its humidity constant, the wet bulb temperature of the air increases. Since the air inlet temperature is less than the water outlet temperature, cooling takes place.

Computations indicate that the $L/G$ ratio does not have any effect on the change in heights obtained from the rigorous method and the $\epsilon$–NTU method at all values of $r$. This is in accordance with the results of Sutherland (1983) and Jaber and Webb (1989).

## Summary

The driving potential available for net heat transfer in countercurrent cooling towers has been expressed in terms of an apparent enthalpy. This apparent enthalpy is not limited by the Lewis relation, i.e., $r$ need not necessarily be one. While this apparent enthalpy driving potential can be used in graphic methods as well as analytical methods of solution for cooling tower design, the present study has demonstrated its application in the $\epsilon$–NTU method of design.

## References


Berman, L. D., 1961, *Evaporative Cooling of Circulating Water,* H. Sawistowski, ed., 2nd ed., Pergamon Press, New York, Chap. 2, pp. 94–99.

Fahim, M. A., Al-Ameeri, R. S., and Wakao, N., 1985, "Equations for Calculating Temperatures in Adiabatic Air Water Contact Towers," *Chemical Engineering Communications,* Vol. 36, pp. 1–8.

Foust, A. S., Wenzel, L. A., Clump, C. W., Maus, L., and Anderson, L. B., 1979, *Principles of Unit Operations,* 2nd ed., Wiley, New York, Part 3, Chap. 17, pp. 437–443.

Hensel, S. L., Jr., and Treybal, R. E., 1952, "Air Water Contact, Adiabatic Humidification of Air With Water in a Packed Tower," *Chemical Engineering Progress,* Vol. 48, pp. 362–370.

Jaber, H., and Webb, R. L., 1989, "Design of Cooling Towers by the Effectiveness–NTU method," ASME JOURNAL OF HEAT TRANSFER, Vol. 111, pp. 837–843.

Marseille, T. J., Schliesing, J. S., and Bell, D. M., 1991, "Extending Cooling Tower Thermal Performance Prediction Using a Liquid Side Film Resistance Model," *Heat Transfer Engineering,* Vol. 12, pp. 19–30.

Merkel, F., 1926, "Verdunstungskuhlung," *VDI Zeitschriff Deutscher Ingenieure,* Vol. 70, pp. 123–128.

Treybal, R. E., 1984, *Mass Transfer Operations,* 3rd ed. McGraw-Hill, New York.

Sutherland, J. W., 1983, "Analysis of Mechanical Draft Counterflow Air/Water Cooling Towers," ASME JOURNAL OF HEAT TRANSFER, Vol. 105, pp. 576–583.

Webb, R. L., 1988, "A Critical Review of Cooling Tower Design Methods," in: *Heat Transfer Equipment Design,* R. K. Shah, E. C. Subba Rao, and R. A. Mashelkar, eds., Hemisphere Publishing Corp., Washington, DC, pp. 547–558.

Webb, R. L., 1990, "Standard Nomenclature for Mass Transfer Processes," *International Communications in Heat and Mass Transfer,* Vol. 17, pp. 529–535.


# Unsteady Buoyancy Exchange Flow Through a Horizontal Partition


**M. Singhal[1] and R. Kumar[2]**


## Nomenclature

$A = L/D$ = vent aspect ratio
$D$ = width of the vent
$g$ = acceleration due to gravity
$H_1$ = width of the enclosure
$H_2$ = height of the enclosure
$L$ = height of the vent
Pr = Prandtl number
$Q_{nd}$ = nondimensional total heat transfer across the vent
$Q^*$ = normalized form of $Q_{nd}$
$\mathrm{Ra} = g\beta\Delta T_i D^3/\alpha\nu$ = Rayleigh number
$\mathrm{Ra}_{cr}$ = critical value of Rayleigh number for onset of flow through the vent
$T_{\mathrm{cold}}$ = initial temperature of fluid in upper chamber
$T_{\mathrm{hot}}$ = initial temperature of fluid in the lower chamber
$T_{\mathrm{ref}}$ = reference temperature
$\Delta T_i = T_{\mathrm{hot}} - T_{\mathrm{cold}}$ = initial reference temperature difference between upper and lower chamber
$U = uL/\alpha$ = dimensionless component of velocity in $x$ direction
$V = vL/\alpha$ = dimensionless component of velocity in $y$ direction
$X, Y$ = dimensionless horizontal and vertical coordinates
$\alpha$ = thermal diffusivity of the fluid
$\beta$ = coefficient of thermal expansion
$\nu$ = kinematic viscosity of the fluid
$\theta = \dfrac{T - T_{\mathrm{ref}}}{\Delta T_i}$ = dimensionless temperature
$\tau = t\alpha/D^2$ = dimensionless time

## Introduction

Flow through apertures connecting two enclosures has been a subject of study for the last thirty years. Early studies were limited to openings in vertical partitions. The fundamental difference between flow through a vent in vertical partition and the flow through a horizontal partition is the stable stratification of the fluid in the former case while the configuration is unstable for the latter. As a result, in flows through a vertical partition, the lighter fluid layers move over heavy fluid layers with minimal interaction.

Brown (1962) was the first to study the flow through square openings in a horizontal partition with the heavier fluid above


[1] Dept. of Mechanical Engineering, Clemson University, Clemson, SC 29631.
[2] Knolls Atomic Power Laboratory, P.O. Box 1072, Schenectady, NY 12301.



Contributed by the Heat Transfer Division of THE AMERICAN SOCIETY OF MECHANICAL ENGINEERS. Manuscript received by the Heat Transfer Division July 1993; revision received July 1994. Keywords: Enclosure Flows, Mixed Convection, Natural Convection. Associate Technical Editor: Y. Jaluria.





Downloaded 12 Dec 2010 to 193.140.21.150. Redistribution subject to ASME license or copyright; see http://www.asme.org/terms/Terms_Use.cfm

the $\epsilon$–NTU method applied over each segment, the linearity assumption is not violated.

In Fig. 2, the effect of air inlet temperature on the height obtained by the present method when compared with the rigorous method is shown. It is seen from the figure that up to a particular air inlet temperature, the underprediction of the column height decreases at all $r$ values at the lower cooling range and at the lower values of $r$ at the higher cooling range. However, in both cases, the curves for different values of $r$ meet at a particular point when the trend is reversed. This indicates that at this point $r$ does not have any significant effect. This can be explained by examining the definition of $r$, which has the gas side heat transfer coefficient in the numerator and the mass transfer coefficient in the denominator. These coefficients are obtained from the hydrodynamic conditions in the tower and the type of tower internals. At the point where the curves meet, even though $h_G$ has a finite value, the temperature driving force approaches zero and therefore all the cooling takes place only due to mass transfer. Beyond this point the trend is reversed as the contribution of the sensible heat transfer to the net cooling may be in the reverse direction. This can be observed from the rigorous method.

From a thermodynamic point of view it is possible to cool water of a temperature less than the entering air dry bulb temperature. This is because the actual or apparent enthalpy is for most practical purposes a function of adiabatic saturation temperature, or for air–water systems, the wet bulb temperature. It is also possible to operate a tower with entering air saturated, so long as its temperature is less than the water outlet temperature when the driving force is the wet bulb temperature approach. In Fig. 2 as the air inlet temperature increases, keeping its humidity constant, the wet bulb temperature of the air increases. Since the air inlet temperature is less than the water outlet temperature, cooling takes place.

Computations indicate that the $L/G$ ratio does not have any effect on the change in heights obtained from the rigorous method and the $\epsilon$–NTU method at all values of $r$. This is in accordance with the results of Sutherland (1983) and Jaber and Webb (1989).

## Summary

The driving potential available for net heat transfer in countercurrent cooling towers has been expressed in terms of an apparent enthalpy. This apparent enthalpy is not limited by the Lewis relation, i.e., $r$ need not necessarily be one. While this apparent enthalpy driving potential can be used in graphic methods as well as analytical methods of solution for cooling tower design, the present study has demonstrated its application in the $\epsilon$–NTU method of design.

## References

Berman, L. D., 1961, *Evaporative Cooling of Circulating Water,* H. Sawistowski, ed., 2nd ed., Pergamon Press, New York, Chap. 2, pp. 94–99.

Fahim, M. A., Al-Ameeri, R. S., and Wakao, N., 1985, "Equations for Calculating Temperatures in Adiabatic Air Water Contact Towers," *Chemical Engineering Communications,* Vol. 36, pp. 1–8.

Foust, A. S., Wenzel, L. A., Clump, C. W., Maus, L., and Anderson, L. B., 1979, *Principles of Unit Operations,* 2nd ed., Wiley, New York, Part 3, Chap. 17, pp. 437–443.

Hensel, S. L., Jr., and Treybal, R. E., 1952, "Air Water Contact, Adiabatic Humidification of Air With Water in a Packed Tower," *Chemical Engineering Progress,* Vol. 48, pp. 362–370.

Jaber, H., and Webb, R. L., 1989, "Design of Cooling Towers by the Effectiveness–NTU method," ASME JOURNAL OF HEAT TRANSFER, Vol. 111, pp. 837–843.

Marseille, T. J., Schliesing, J. S., and Bell, D. M., 1991, "Extending Cooling Tower Thermal Performance Prediction Using a Liquid Side Film Resistance Model," *Heat Transfer Engineering,* Vol. 12, pp. 19–30.

Merkel, F., 1926, "Verdunstungskuhlung," *VDI Zeitschriff Deutscher Ingenieure,* Vol. 70, pp. 123–128.

Treybal, R. E., 1984, *Mass Transfer Operations,* 3rd ed. McGraw-Hill, New York.

Sutherland, J. W., 1983, "Analysis of Mechanical Draft Counterflow Air/Water Cooling Towers," ASME JOURNAL OF HEAT TRANSFER, Vol. 105, pp. 576–583.

Webb, R. L., 1988, "A Critical Review of Cooling Tower Design Methods," in: *Heat Transfer Equipment Design,* R. K. Shah, E. C. Subba Rao, and R. A. Mashelkar, eds., Hemisphere Publishing Corp., Washington, DC, pp. 547–558.

Webb, R. L., 1990, "Standard Nomenclature for Mass Transfer Processes," *International Communications in Heat and Mass Transfer,* Vol. 17, pp. 529–535.

# Unsteady Buoyancy Exchange Flow Through a Horizontal Partition

**M. Singhal[1] and R. Kumar[2]**

## Nomenclature

$A = L/D$ = vent aspect ratio
$D$ = width of the vent
$g$ = acceleration due to gravity
$H_1$ = width of the enclosure
$H_2$ = height of the enclosure
$L$ = height of the vent
Pr = Prandtl number
$Q_{nd}$ = nondimensional total heat transfer across the vent
$Q^*$ = normalized form of $Q_{nd}$
$\mathrm{Ra} = g\beta\Delta T_i D^3/\alpha\nu$ = Rayleigh number
$\mathrm{Ra}_{cr}$ = critical value of Rayleigh number for onset of flow through the vent
$T_{\mathrm{cold}}$ = initial temperature of fluid in upper chamber
$T_{\mathrm{hot}}$ = initial temperature of fluid in the lower chamber
$T_{\mathrm{ref}}$ = reference temperature
$\Delta T_i = T_{\mathrm{hot}} - T_{\mathrm{cold}}$ = initial reference temperature difference between upper and lower chamber
$U = uL/\alpha$ = dimensionless component of velocity in $x$ direction
$V = vL/\alpha$ = dimensionless component of velocity in $y$ direction
$X, Y$ = dimensionless horizontal and vertical coordinates
$\alpha$ = thermal diffusivity of the fluid
$\beta$ = coefficient of thermal expansion
$\nu$ = kinematic viscosity of the fluid
$\theta = \dfrac{T - T_{\mathrm{ref}}}{\Delta T_i}$ = dimensionless temperature
$\tau = t\alpha/D^2$ = dimensionless time

## Introduction

Flow through apertures connecting two enclosures has been a subject of study for the last thirty years. Early studies were limited to openings in vertical partitions. The fundamental difference between flow through a vent in vertical partition and the flow through a horizontal partition is the stable stratification of the fluid in the former case while the configuration is unstable for the latter. As a result, in flows through a vertical partition, the lighter fluid layers move over heavy fluid layers with minimal interaction.

Brown (1962) was the first to study the flow through square openings in a horizontal partition with the heavier fluid above

[1] Dept. of Mechanical Engineering, Clemson University, Clemson, SC 29631.
[2] Knolls Atomic Power Laboratory, P.O. Box 1072, Schenectady, NY 12301.

Contributed by the Heat Transfer Division of THE AMERICAN SOCIETY OF MECHANICAL ENGINEERS. Manuscript received by the Heat Transfer Division July 1993; revision received July 1994. Keywords: Enclosure Flows, Mixed Convection, Natural Convection. Associate Technical Editor: Y. Jaluria.



Copyright © 1995 by ASME

Downloaded 12 Dec 2010 to 193.140.21.150. Redistribution subject to ASME license or copyright; see http://www.asme.org/terms/Terms_Use.cfm

the partition both analytically and experimentally. In his analysis he assumed that all heat transfer is due to advection only and no mixing occurs within the vent. Assuming friction to be negligible, he invoked the Bernoulli equation to predict that Nusselt number is proportional to the product of the square root of Grashof number and Prandtl number, using the height of the vent as the reference length. The partition was considered to be impermeable to heat. The experiments were conducted using air as the fluid medium to cover a range of $3 \times 10^4 < \mathrm{Gr} < 4 \times 10^7$ and from 0.0825 to 0.66 for height to width ratio of the vent.

Recently, an experimental study was reported by Epstein (1988) on buoyancy-driven exchange flow through small openings in horizontal partitions for the same geometric configuration as in this study. The experimental apparatus consisted of two enclosures, one on top of the other, with brine and fresh water as working fluids. The study concentrated on finding the effect of height-to-diameter aspect ratio of the vent ($L/D$) on the dimensionless exchange flow rate as defined by Mercer and Thompson (1975). Four different flow regimes were identified as $L/D$ was varied from 0.01 to 10.0.

An experimental investigation was carried out by Conover (1992) to study the buoyant countercurrent exchange flow through a vented horizontal partition using a two-component laser-Doppler velocimeter. Detailed measurements of velocity were made a small distance above a circular tube with an aspect ratio of 1. Even for this aspect ratio and a Reynolds number ranging between 2400 and 7700, the mixing in the vent was found to be turbulent and unsteady. He also found that the flow coefficient was nearly constant for a Reynolds number as low as 2400. The work of Steckler et al. (1984, 1986) showed that exchange flow rate reached self-similarity only for Reynolds number greater than 10,000. Myrum (1990) conducted heat transfer experiments using water in a top-vented enclosure heated by a disk on the enclosure floor. He observed four modes of flow that were unstable and oscillated randomly from one to the next.

Jaluria and Tan (1992) performed an experimental study to show that the use of Bernoulli's equation is appropriate only at pressure differences that are larger than a critical value. Jaluria et al. (1993) presented a flow visualization study in water/brine and air/heated air systems, and showed that the transient effects were important for the air system in terms of bringing out the oscillatory nature of the transport processes.

The flow patterns and the mechanisms that change the flow from one regime to the other will be explored in this paper for a vent that is kept slightly off-center to induce asymmetry. Time traces of heat transfer are discussed for a vent aspect ratio of 1.0.

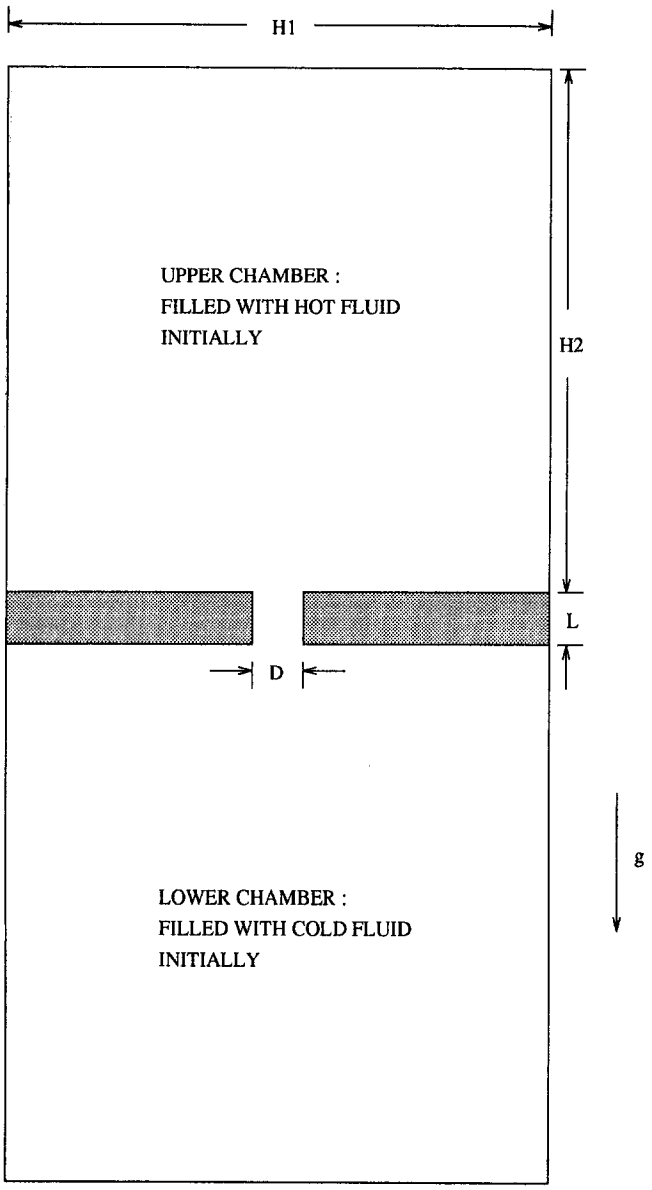



**Fig. 1 Schematic diagram of the model**

## Solution Methodology

The time-dependent governing equations for two-dimensional flow were derived from the fundamental laws of conservation of mass, momentum, and energy using the Boussinesq approximation for the body force term. No-slip conditions were used for velocity boundary conditions at the wall including the partition. Initially, the fluid is at rest everywhere in the domain; therefore velocity components were set equal to zero at nondimensionalized time $\tau = 0$. All the walls were treated as adiabatic and hence the normal gradients of temperature were set equal to zero at all fluid–wall interfaces. At $\tau = 0$, the lower chamber contains hot fluid with $\theta = 1$ and the upper chamber contains cold fluid with $\theta = 0$. The flow parameters of interest are Rayleigh number, Ra, and Prandtl number, Pr. Prandtl number is maintained constant at 0.7. Referring to Fig. 1, the geometric parameters are vent aspect ratio, $A$, $H_1/L$, and the enclosure aspect ratio, $H_1/H_2$. In this study these parameters are fixed at 1, 10, and 1, respectively.

The governing equations were discretized over the computational domain using a control volume approach as documented by Patankar (1980). The resulting algebraic equations for velocity components and temperature were solved using SIMPLE algorithm, which involves the use of pressure correction equations for enforcing mass conservation. The code thus developed was tested against certain benchmark solutions to validate it. For the enclosure under consideration, time step independence and grid size independence were tested prior to obtaining solution for the desired problem. A time increment was fixed at $10^{-3}$ and a nonuniform grid of $40 \times 60$ was used. A grid of $12 \times 12$ was selected for the vent through a separate grid independence study. One complete unsteady solution for one geometry and one Rayleigh number involved computations of up to 100,000 time steps with approximately 15 iterations for every time step.

Two cases were run for each Rayleigh number, one with the vent shifted to the right by one node and another left shifted, thereby inducing asymmetry to the solutions. The two shifted vents gave identical heat transfer results for all the cases. In the transition regime, the flow patterns were mirror images about the horizontal plane passing through the vent. Hence, only results for the right-shifted vents are presented here.

## Definitions

The nondimensional heat transfer at any instant is given by

$$Q_{nd} = \frac{Q}{k\Delta T_i} = \frac{hD}{k} = \left[ \int_{4.6}^{5.6} V\theta dX - \int_{4.6}^{5.6} \frac{\partial \theta}{\partial Y} dX \right]. \quad (1)$$



Downloaded 12 Dec 2010 to 193.140.21.150. Redistribution subject to ASME license or copyright; see http://www.asme.org/terms/Terms_Use.cfm

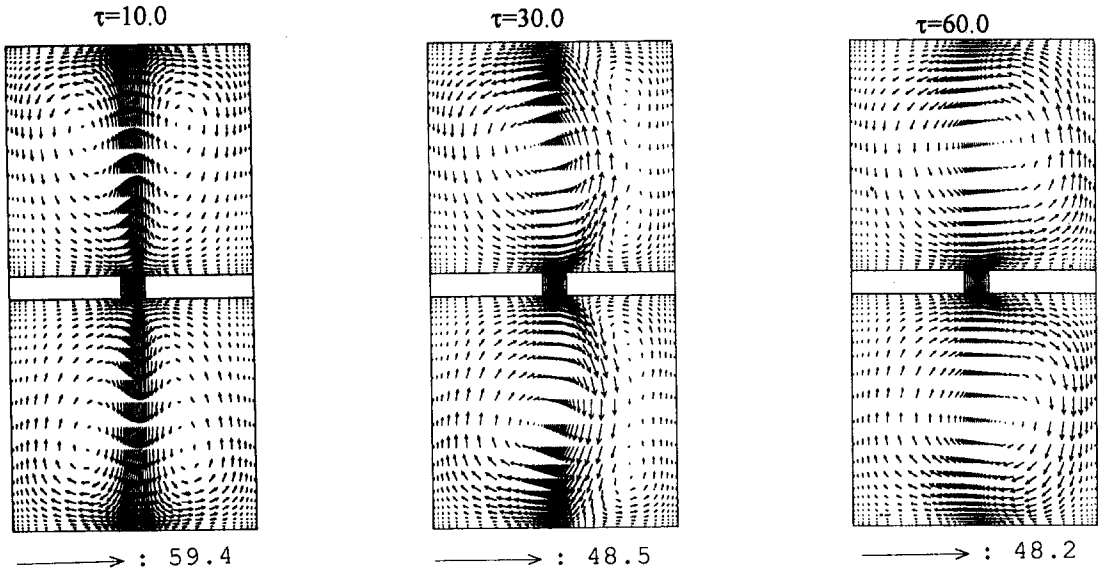



Fig. 2(*a*) Overall velocity field for Ra = 1200

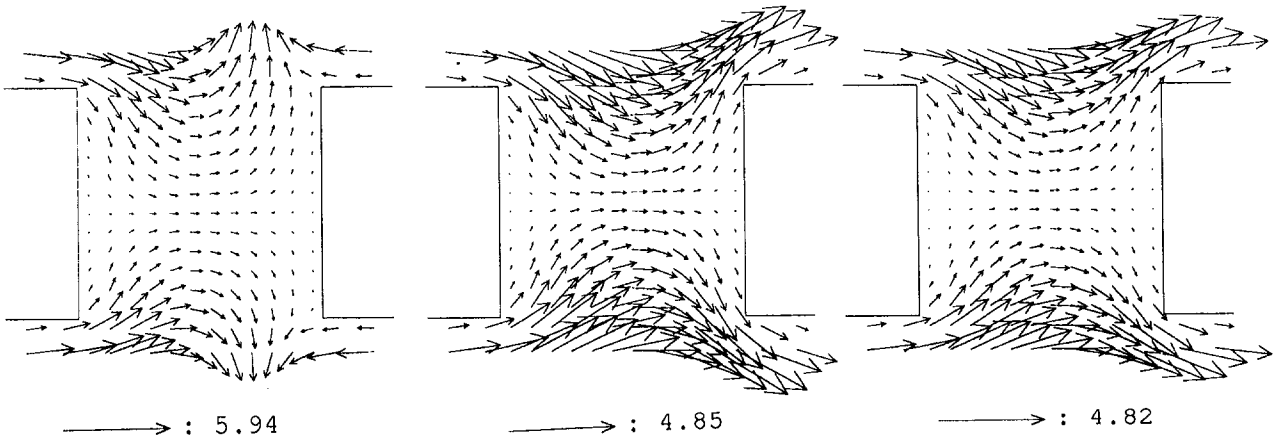



Fig. 2(*b*) Magnified view of the velocity field in the vent for Ra = 1200

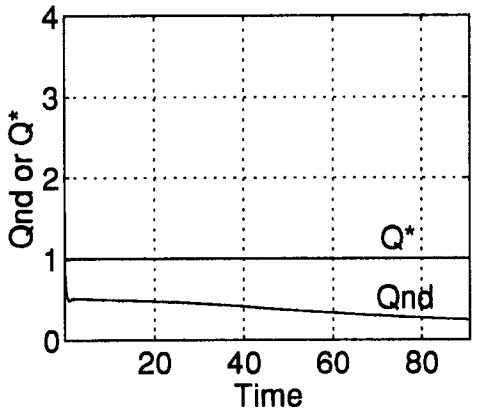



Fig. 2(*c*) Time trace of nondimensional heat transfer rates for Ra = 1200

This may be further normalized as

$$Q^* = \left[\int_{4.6}^{5.6} V\theta dX - \int_{4.6}^{5.6} \frac{\partial\theta}{\partial Y} dX\right] \Big/ -\int_{4.6}^{5.6} \frac{\partial\theta}{\partial Y} dX \quad (2)$$

$Q^*$, as defined above, will be approximately equal to 1.0 if heat transfer by advection is negligible as compared to that by conduction. Both $Q_{nd}$ and $Q^*$ were then calculated at the midplane of the vent at an interval of 10 time steps throughout the simulation.

## Results and Discussion

Based on the mode of heat transfer and the associated flow characteristics, three categories have been identified for an aspect ratio of 1.0. These are the conduction regime, the countercurrent



Downloaded 12 Dec 2010 to 193.140.21.150. Redistribution subject to ASME license or copyright; see http://www.asme.org/terms/Terms_Use.cfm

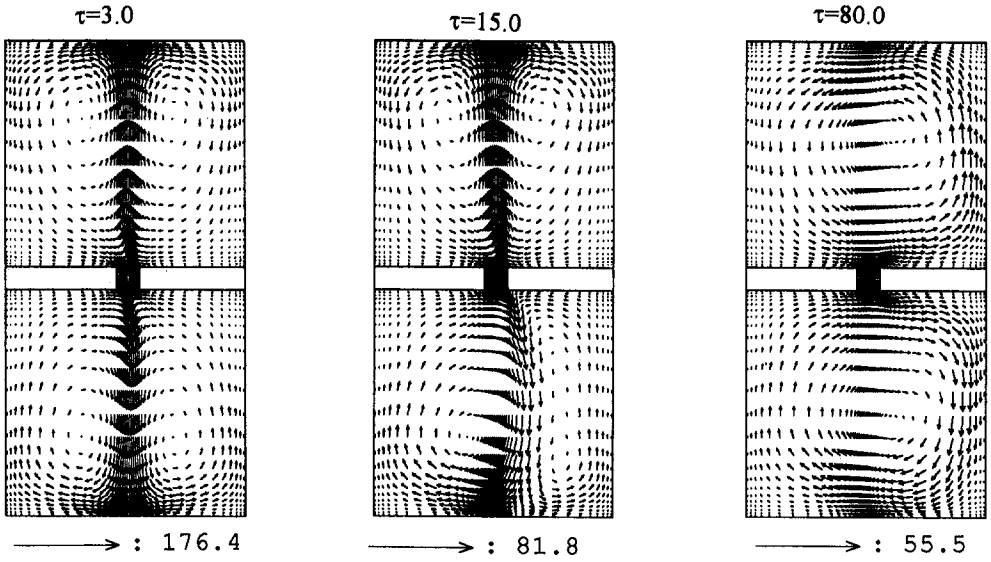



Fig. 3(*a*) Overall velocity field for Ra = 2500

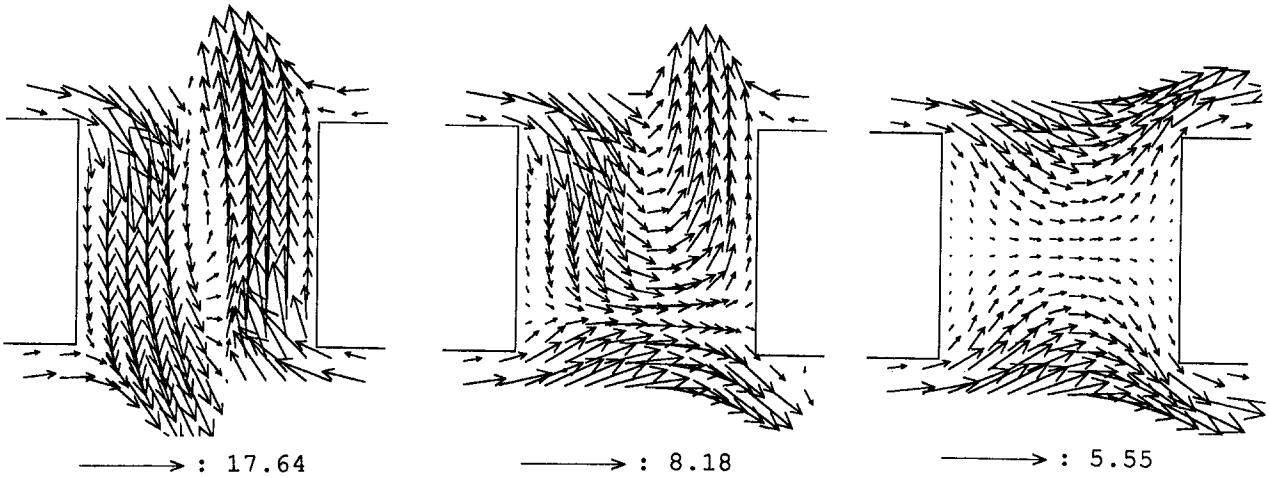



Fig. 3(*b*) Magnified view of the velocity field in the vent for Ra = 2500

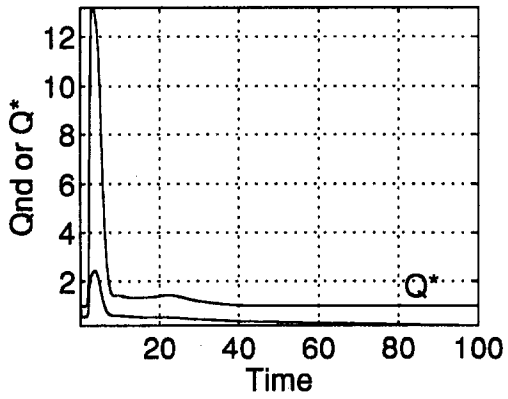



Fig. 3(*c*) Time trace of nondimensional heat transfer rates for Ra = 2500

regime, and the oscillatory regime. These are largely governed by the Rayleigh number as explained below.

**Conduction Regime.** For Ra $\leq$ 1200, there is no bulk fluid motion within the vent and all the heat transfer is primarily by conduction. Flow patterns for this Rayleigh number at different time steps are given in Figs. 2($a$) and 2($b$). In the enclosures, bulk fluid motion ensues immediately after the initial establishment of a temperature gradient in the vent. A plume rises steadily into the upper chamber, forcing the colder fluid to move along the side wall to replace the rising fluid forming two cells of equal strength on either side of it. From the start, the cells are asymmetric and become more pronounced in each chamber. Then the cells in the lower chamber become more asymmetric before merging into a single cell. There is a time delay before the upper chamber behaves exactly like the upper one exhibiting a single cell. At large $\tau$, the fluid in the chambers has accelerated enough to drive the fluid in the vent by entrainment and shear.



Downloaded 12 Dec 2010 to 193.140.21.150. Redistribution subject to ASME license or copyright; see http://www.asme.org/terms/Terms_Use.cfm

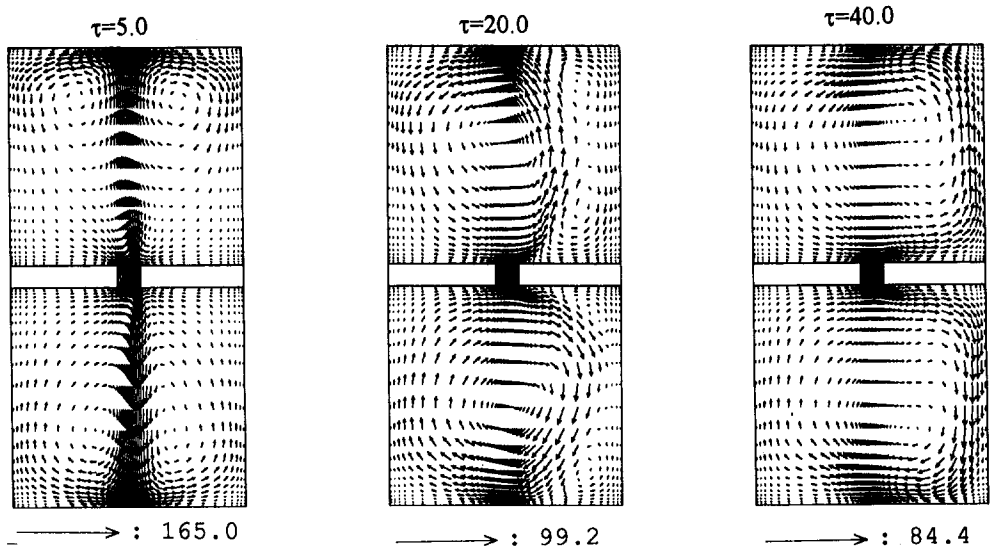



Fig. 4(*a*) Overall velocity field for Ra = 5000

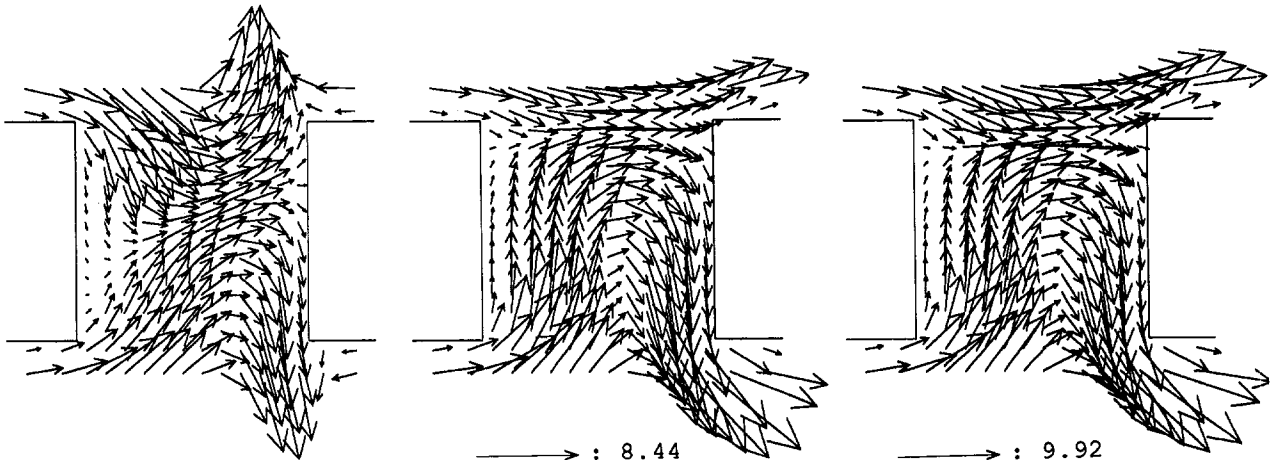



Fig. 4(*b*) Magnified view of the velocity field in the vent for Ra = 5000

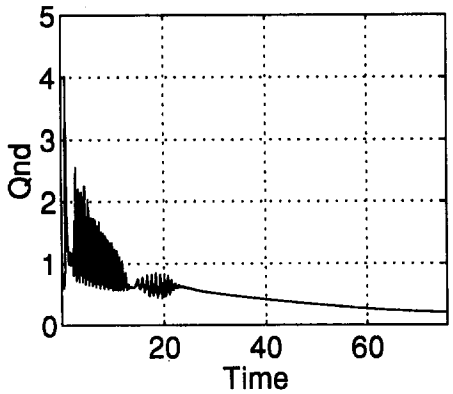



Fig. 4(*c*) Time trace of nondimensional heat transfer rates for Ra = 5000

Catton and Edwards (1967) performed an experimental study on the effects of side walls on natural convection. They were able to obtain $Ra_{cr}$ as a function of height-to-width ratio for insulating as well as conducting lateral walls. For an aspect ratio of 1.0 and insulating lateral walls, they reported that $Ra_{cr}$ was in the range of $1 \times 10^4$ to $2 \times 10^4$. They also developed a heat transfer correlation.

$Q^*$ is close to 1.0 for all $\tau$'s as shown in Fig. 2($c$). Thus, in the conduction flow regime the net flow in the vertical direction is negligible, as can be seen from velocity vector plots.

**Countercurrent Regime.** This regime is characterized by a downflow along approximately one half of the vent and an upflow along the rest to satisfy continuity. If the flow pattern is as



Downloaded 12 Dec 2010 to 193.140.21.150. Redistribution subject to ASME license or copyright; see http://www.asme.org/terms/Terms_Use.cfm

described above, one of the criteria that can be used to identify and describe the countercurrent regime is that the normalized heat transfer, $Q^*$, is at least 5 percent above that for conduction. This occurs for Ra > 1200. With time, the flow gradually reverts to the conduction regime with one large cell in each chamber for Ra = 1200.

As the Rayleigh number is increased in this flow regime to Ra = 2500, the countercurrent velocities increase and peak at $\tau >$ 3.0 (Fig. 3*a*). For $\tau > 3.0$, the flow tends to slow down at the vent and also everywhere in the enclosure. The downward flow on the left side of the vent is unable to penetrate the bottom enclosure and reverts itself within the vent. This flow characteristic is evident in Fig. 3(*b*) for $\tau = 15.0$. For the left-shifted vent not shown in the figure, a mirror image of this flow pattern was observed. In that case, the upward flow on the right side of the vent reverted following its inability to penetrate into the upper compartment. In either case, a complete recirculation pattern does not appear at the vent, due to the asymmetry imposed in the vent location. The heat transfer results in Fig. 3(*c*) show that at $\tau = 3.0$, a peak appears and drops to the conduction flow regime close to $\tau = 80.0$.

**Oscillatory Regime.** As the Rayleigh number is further increased, the velocity at the vent in each of the two streams moving in opposite directions increases. Consequently, the boundary layer thickness decreases while the shear layer grows. This reduces the effective area for the fluid to move through, eventually leading to choking conditions at a critical Rayleigh number of Ra ~ 4000. Beyond this Rayleigh number, two distinct streams at the vent can no longer be sustained and a transition to oscillatory flow occurs (Figs. 4*a*, 4*b*). An exchange flow takes place between the two enclosures around what appears to be a cell. This cell is not completely formed, once again possibly because of the asymmetry in the vent location.

This regime is characterized as oscillatory and is identified by the varying amplitude in the $Q_{nd}$ time trace (Fig. 4*c*). The heat transfer results suggest that there are varying amplitude oscillations in a narrow frequency range that eventually die out and essentially reproduce the flow behavior quantified in the countercurrent and conduction regimes. The average heat transfer rates are lower for oscillatory regime compared to those for countercurrent regime. A temperature–time trace obtained by Mitchell and Quinn (1966) in a confined layer heated from below showed that the fluid oscillated in a narrow frequency band, as found in the current study. They also noted that the oscillations were stable over a large Rayleigh number range. A direct comparison of our results with those of Mitchell and Quinn (1966) cannot be made since their mean flow was steady.

## Conclusions

A numerical study of unsteady, laminar, buoyant flow through a horizontal rectangular vent placed slightly asymmetrically between two large enclosures was performed. Based on the flow patterns in the vent and the corresponding modes of heat transfer through it, three flow regimes were identified: the conduction regime (Ra ≤ 1200), the countercurrent flow regime (1300 ≤ Ra ≤ 4000), and the oscillatory flow regime (Ra > 4000). In the countercurrent flow regime, the fluid moves through the vent in two distinct but opposite streams and show a peak in heat transfer rate quickly followed by a conduction flow regime. Heat transfer results associated with the oscillatory flow display interesting characteristics of increasing amplitudes in a narrow frequency range. The average heat transfer for this regime was lower compared to the countercurrent regime.

## References


Brown, W., 1962, "Natural Convection Through Rectangular Openings in Partitions—2: Horizontal Partitions," *Int. J. Heat and Mass Transfer*, Vol. 5, pp. 869–878.

Catton, I., and Edwards, D. K., 1967, "Effects of Side Walls on Natural Convection Between Horizontal Plates Heated From Below," ASME JOURNAL OF HEAT TRANSFER, Vol. 89, pp. 295–299.

Conover, T. A., 1992, "Laser Doppler Velocimetry Study of Buoyant Countercurrent Exchange Flow Through a Vented Horizontal Partition," M.S. Thesis, Clemson University, Clemson, SC.

Epstein, M., 1988, "Buoyancy Driven Exchange Flow Through Small Openings in Horizontal Partitions," ASME JOURNAL OF HEAT TRANSFER, Vol. 110, pp. 885–893.

Jaluria, Y., and Tan, Q., 1992, "Flow Through a Horizontal Vent in an Enclosure Fire," ASME HTD-Vol. 199, pp. 115–122.

Jaluria, Y., Lee, S. H.-K., Mercier, G. P., and Tan, Q., 1993, "Visualization of Transport Across a Horizontal Vent Due to Density and Pressure Differences," ASME HTD-Vol. 252, pp. 65–81.

Mercer, A., and Thompson, H., 1975, "An Experimental Investigation of Some Further Aspects of the Buoyancy-Driven Exchange Flow Between Carbon Dioxide and Air Following a Depressurization Accident in a Magnox Reactor, Part 1: The Exchange Flow in Inclined Ducts," *J. Br. Nucl. Energy Soc.*, Vol. 14, No. 4, pp. 327–334.

Mitchell, W. T., and Quinn, J. A., 1966, "Thermal Convection in a Completely Confined Fluid Layer," *AIChE Journal*, Vol. 12, No. 6, pp. 1116–1124.

Myrum, T., 1990, "Natural Convection From a Heat Source in a Top-Vented Enclosure," ASME JOURNAL OF HEAT TRANSFER, Vol. 112, pp. 632–639.

Patankar, S. V., 1980, *Numerical Heat Transfer and Fluid Flow*, Hemisphere Publ. Corp., New York.

Steckler, K., Baum, H., and Quintiere, J., 1984, "Fire Induced Flows Through Room Openings—Flow Coefficients," *Twentieth Symposium (International) on Combustion*, The Combustion Institute, pp. 1591–1600.

Steckler, K., Baum, H., and Quintiere, J., 1986, "Salt Water Modelling of Fire Induced Flows in Multicompartment Enclosures," *Twenty-First Symposium (International) on Combustion*, The Combustion Institute, pp. 143–149.


# Generalized Zoning Method in One-Dimensional Participating Media


**A. K. Ma**[1]


## Nomenclature

$A$ = area

$D$ = slab thickness

$d^3g_i d^3g_j$ = differential direct-exchange area from volume zone $i$ to volume zone $j$

$d^3g_k d^3g_i$ = differential direct-exchange area from volume zone $k$ to volume zone $i$

$d^3g_k d^3g_i \Phi(\theta_{k,i,j}) d^3g_i d^3g_j$ = differential scattering-exchange area as defined in Eq. (3)

$E_b$ = blackbody emissive power of the medium

$E_{b1}$ = blackbody emissive power of surface 1

$g$ = volume zone

$g_i g_j$ = direct-exchange area from volume zone $i$ to zone $j$

$g_i s_1$ = direct-exchange area from volume zone $i$ to surface 1

$g_j g_i \Phi g_i s_1$ = scattering-exchange area as defined in Eq. (8)

$g_k g_i \Phi g_i g_j$ = scattering-exchange area as defined in Eq. (5)

$K_t$ = extinction coefficient of the medium


[1] Hong Kong Polytechnic, Department of Building Services Engineering, Kowloon, Hong Kong.



Contributed by the Heat Transfer Division of THE AMERICAN SOCIETY OF MECHANICAL ENGINEERS. Manuscript received by the Heat Transfer Division July 1993; revision received April 1994. Keywords: Radiation. Associate Technical Editor: M. F. Modest.





Downloaded 12 Dec 2010 to 193.140.21.150. Redistribution subject to ASME license or copyright; see http://www.asme.org/terms/Terms_Use.cfm

described above, one of the criteria that can be used to identify and describe the countercurrent regime is that the normalized heat transfer, $Q^*$, is at least 5 percent above that for conduction. This occurs for Ra > 1200. With time, the flow gradually reverts to the conduction regime with one large cell in each chamber for Ra = 1200.

As the Rayleigh number is increased in this flow regime to Ra = 2500, the countercurrent velocities increase and peak at $\tau >$ 3.0 (Fig. 3*a*). For $\tau > 3.0$, the flow tends to slow down at the vent and also everywhere in the enclosure. The downward flow on the left side of the vent is unable to penetrate the bottom enclosure and reverts itself within the vent. This flow characteristic is evident in Fig. 3(*b*) for $\tau = 15.0$. For the left-shifted vent not shown in the figure, a mirror image of this flow pattern was observed. In that case, the upward flow on the right side of the vent reverted following its inability to penetrate into the upper compartment. In either case, a complete recirculation pattern does not appear at the vent, due to the asymmetry imposed in the vent location. The heat transfer results in Fig. 3(*c*) show that at $\tau = 3.0$, a peak appears and drops to the conduction flow regime close to $\tau = 80.0$.

**Oscillatory Regime.** As the Rayleigh number is further increased, the velocity at the vent in each of the two streams moving in opposite directions increases. Consequently, the boundary layer thickness decreases while the shear layer grows. This reduces the effective area for the fluid to move through, eventually leading to choking conditions at a critical Rayleigh number of Ra ~ 4000. Beyond this Rayleigh number, two distinct streams at the vent can no longer be sustained and a transition to oscillatory flow occurs (Figs. 4*a*, 4*b*). An exchange flow takes place between the two enclosures around what appears to be a cell. This cell is not completely formed, once again possibly because of the asymmetry in the vent location.

This regime is characterized as oscillatory and is identified by the varying amplitude in the $Q_{nd}$ time trace (Fig. 4*c*). The heat transfer results suggest that there are varying amplitude oscillations in a narrow frequency range that eventually die out and essentially reproduce the flow behavior quantified in the countercurrent and conduction regimes. The average heat transfer rates are lower for oscillatory regime compared to those for countercurrent regime. A temperature–time trace obtained by Mitchell and Quinn (1966) in a confined layer heated from below showed that the fluid oscillated in a narrow frequency band, as found in the current study. They also noted that the oscillations were stable over a large Rayleigh number range. A direct comparison of our results with those of Mitchell and Quinn (1966) cannot be made since their mean flow was steady.

## Conclusions

A numerical study of unsteady, laminar, buoyant flow through a horizontal rectangular vent placed slightly asymmetrically between two large enclosures was performed. Based on the flow patterns in the vent and the corresponding modes of heat transfer through it, three flow regimes were identified: the conduction regime (Ra ≤ 1200), the countercurrent flow regime (1300 ≤ Ra ≤ 4000), and the oscillatory flow regime (Ra > 4000). In the countercurrent flow regime, the fluid moves through the vent in two distinct but opposite streams and show a peak in heat transfer rate quickly followed by a conduction flow regime. Heat transfer results associated with the oscillatory flow display interesting characteristics of increasing amplitudes in a narrow frequency range. The average heat transfer for this regime was lower compared to the countercurrent regime.

## References


Brown, W., 1962, "Natural Convection Through Rectangular Openings in Partitions—2: Horizontal Partitions," *Int. J. Heat and Mass Transfer*, Vol. 5, pp. 869–878.

Catton, I., and Edwards, D. K., 1967, "Effects of Side Walls on Natural Convection Between Horizontal Plates Heated From Below," ASME JOURNAL OF HEAT TRANSFER, Vol. 89, pp. 295–299.

Conover, T. A., 1992, "Laser Doppler Velocimetry Study of Buoyant Countercurrent Exchange Flow Through a Vented Horizontal Partition," M.S. Thesis, Clemson University, Clemson, SC.

Epstein, M., 1988, "Buoyancy Driven Exchange Flow Through Small Openings in Horizontal Partitions," ASME JOURNAL OF HEAT TRANSFER, Vol. 110, pp. 885–893.

Jaluria, Y., and Tan, Q., 1992, "Flow Through a Horizontal Vent in an Enclosure Fire," ASME HTD-Vol. 199, pp. 115–122.

Jaluria, Y., Lee, S. H.-K., Mercier, G. P., and Tan, Q., 1993, "Visualization of Transport Across a Horizontal Vent Due to Density and Pressure Differences," ASME HTD-Vol. 252, pp. 65–81.

Mercer, A., and Thompson, H., 1975, "An Experimental Investigation of Some Further Aspects of the Buoyancy-Driven Exchange Flow Between Carbon Dioxide and Air Following a Depressurization Accident in a Magnox Reactor, Part 1: The Exchange Flow in Inclined Ducts," *J. Br. Nucl. Energy Soc.*, Vol. 14, No. 4, pp. 327–334.

Mitchell, W. T., and Quinn, J. A., 1966, "Thermal Convection in a Completely Confined Fluid Layer," *AIChE Journal*, Vol. 12, No. 6, pp. 1116–1124.

Myrum, T., 1990, "Natural Convection From a Heat Source in a Top-Vented Enclosure," ASME JOURNAL OF HEAT TRANSFER, Vol. 112, pp. 632–639.

Patankar, S. V., 1980, *Numerical Heat Transfer and Fluid Flow*, Hemisphere Publ. Corp., New York.

Steckler, K., Baum, H., and Quintiere, J., 1984, "Fire Induced Flows Through Room Openings—Flow Coefficients," *Twentieth Symposium (International) on Combustion*, The Combustion Institute, pp. 1591–1600.

Steckler, K., Baum, H., and Quintiere, J., 1986, "Salt Water Modelling of Fire Induced Flows in Multicompartment Enclosures," *Twenty-First Symposium (International) on Combustion*, The Combustion Institute, pp. 143–149.


# Generalized Zoning Method in One-Dimensional Participating Media


**A. K. Ma**[1]


## Nomenclature

$A$ = area

$D$ = slab thickness

$d^3g_i d^3g_j$ = differential direct-exchange area from volume zone $i$ to volume zone $j$

$d^3g_k d^3g_i$ = differential direct-exchange area from volume zone $k$ to volume zone $i$

$d^3g_k d^3g_i \Phi(\theta_{k,i,j}) d^3g_i d^3g_j$ = differential scattering-exchange area as defined in Eq. (3)

$E_b$ = blackbody emissive power of the medium

$E_{b1}$ = blackbody emissive power of surface 1

$g$ = volume zone

$g_i g_j$ = direct-exchange area from volume zone $i$ to zone $j$

$g_i s_1$ = direct-exchange area from volume zone $i$ to surface 1

$g_j g_i \Phi g_i s_1$ = scattering-exchange area as defined in Eq. (8)

$g_k g_i \Phi g_i g_j$ = scattering-exchange area as defined in Eq. (5)

$K_t$ = extinction coefficient of the medium


[1] Hong Kong Polytechnic, Department of Building Services Engineering, Kowloon, Hong Kong.



Contributed by the Heat Transfer Division of THE AMERICAN SOCIETY OF MECHANICAL ENGINEERS. Manuscript received by the Heat Transfer Division July 1993; revision received April 1994. Keywords: Radiation. Associate Technical Editor: M. F. Modest.





Copyright © 1995 by ASME

Downloaded 12 Dec 2010 to 193.140.21.150. Redistribution subject to ASME license or copyright; see http://www.asme.org/terms/Terms_Use.cfm

$Q_1$ = net radiative energy loss for surface 1
$s$ = surface
$W_{dgi,dgj}$ = directional radiosity from differential zone $i$ to zone $j$
$W_{dgk,dgj}$ = directional radiosity from differential zone $k$ to zone $j$
$W_{gi,1}$ = radiosity from zone $i$ to surface 1
$W_{gi,gj}$ = radiosity from zone $i$ to zone $j$
$x$ = axial distance
$\beta$ = anisotropic coefficient
$\theta_{k,i,j}$ = phase angle as defined in Fig. 1
$\Phi(\theta_{k,i,j})$ = phase function as defined in Eq. (4)
$\omega_0$ = scattering albedo

**Subscripts**

$i$ = zone index
$j$ = zone index
$k$ = zone index
$m$ = zone index
1 = zone or surface index
2 = zone or surface index

## 1 Introduction

The governing equation in thermal radiation is the Radiative Transfer Equation (RTE). This equation has the form of an integro-differential equation, and as such is difficult to solve analytically; hence, many numerical methods have been proposed. Some of them transform RTE into a set of differential equations by assuming the intensity can be discretized into a finite number of directions. Examples of this type of method are the Discrete Ordinate method, Multi-Flux method, and Discrete Intensity Method (Chan, 1987). Another method, using a similar approach, is the P-N Differential Approximation, in which the angular distribution of intensity is approximated by a finite series of spherical harmonics. All these methods utilize either an assumption or an approximation in simplifying the RTE. Nevertheless, some solutions for simple geometries have been obtained by direct numerical integration of the RTE and energy equations (Siegel and Howell, 1992).

Hottel's zoning method (Hottel and Sarofim, 1967) and Monte Carlo method (Howell and Perlmutter, 1964), on the other hand, make no approximation or assumption to simplify the RTE. Utilizing the concept of radiosity and the principle of conservation of energy, the Hottel zoning method (CZM) transforms the RTE into a set of algebraic equations. Hottel's method has been shown to compare exceptionally well with a few exact solutions (Yuen and Ma, 1991). Besides having difficulties in handling nonhomogeneous radiative properties, the isotropic assumption used in this method limits its applications. Recently, this assumption was alleviated by the Generalized Zoning Method (GZM) proposed by Yuen and Takara (1990). They had applied GZM to calculate radiative transfer in a cubic enclosure with linear anisotropic scattering material. Due to the lack of benchmark solution for thermal radiation in three-dimensional systems, the GZM formulation had not been verified. In this paper, the GZM formulation is applied to one-dimensional systems and compared with existing solutions to verify the validity of the GZM formulation.

## 2 Mathematical Formulation

The basic formulation of GZM resembles the CZM; the only exception is the introduction of scattering-exchange areas in the GZM formulation. The scattering-exchange area, unlike the direct-exchange area defined by Hottel, enables one to calculate radiative transfer in an anisotropic scattering medium.

Consider three differential zones, $dV_k$, $dV_i$, and $dV_j$, in a one-dimensional and anisotropic scattering system as shown in Fig. 1. The energy coming from differential volume $dV_i$ in the direction of $dV_j$ is the product of radiosity and the differential direct-exchange area $d^3g_i d^3g_j$. This energy, under local thermodynamic equilibrium, is equal to the emission from the differential volume $dV_i$ and the scattering of all incoming radiation to $dV_i$ into the direction of $dV_j$. Mathematically,

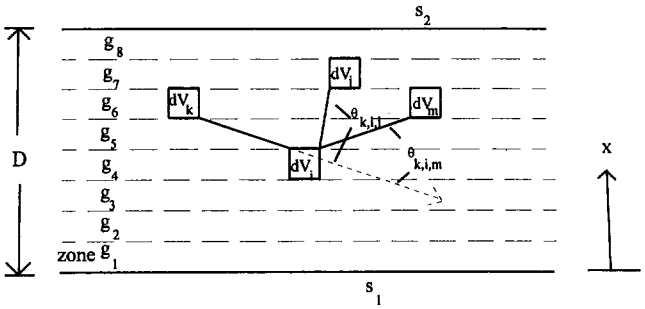



**Fig. 1 Geometry of a one-dimensional system, typical zonal arrangement, and depiction of differential volume zones**

$$W_{dg_i dg_j} d^3g_i d^3g_j = (1-\omega_0)E_{dgi} d^3g_i d^3g_j + \frac{\omega_0}{4K_t dV_i} W_{dg_k dg_i} d^3g_k d^3g_i \Phi(\theta_{k,i,j}) d^3g_i d^3g_j \quad (1)$$

where

$$d^3g_i d^3g_j = \frac{K_t^2 dV_j e^{-K_t r_{ij}} dV_i}{\pi r_{ij}^2} \quad (2)$$

and

$$d^3g_k d^3g_i \Phi(\theta_{k,i,j}) d^3g_i d^3g_j = \frac{K_t^2 dV_k e^{-K_t r_{ik}} dV_i}{\pi r_{ik}^2} \Phi(\theta_{k,i,j}) \frac{K_t^2 dV_j e^{-K_t r_{ij}} dV_i}{\pi r_{ij}^2} \quad (3)$$

$d^3g_k d^3g_i \Phi(\theta_{k,i,j}) d^3g_i d^3g_j$, a differential scattering-exchange area, represents the fraction of energy coming from the differential volume $dV_k$ to the differential volume $dV_i$, and then being scattered through a phase function $\Phi(\theta_{k,i,j})$ into the direction of $dV_j$. The linear anisotropic phase function is given by:

$$\Phi(\theta_{k,i,j}) = 1 + \beta \cos(\theta_{k,i,j}) \quad (4)$$

$\beta$ is the anisotropic coefficient with value ranging from $-1$ to $+1$, and $\theta$ is the phase angle. It should be emphasized that the energy scattered from $dV_i$ into the direction of $dV_j$ is different from that into the direction of $dV_m$ (shown in Fig. 1). Obviously, this distinction is caused by different phase angles. Therefore, it is necessary to designate the radiosity $W_{dgi,dgj}$ to distinguish it from $W_{dgi,dgm}$. The first subscript in each radiosity term denotes the location of the radiosity in a medium, and the second subscript denotes the location to which the radiosity is going. Through this distinction, radiosity becomes a vector quantity.

The linear anisotropic scattering medium as shown in Fig. 1 is divided into $N$ zones for numerical computation. The radiosity equation for the finite-sized zone can be written in a similar way as:

$$W_{gi,gj} = (1-\omega_0)E_{gi} + \frac{\omega_0}{g_i g_j} \sum_{k=1}^{N} g_k g_i \Phi g_i g_j W_{gk,gi} \quad (5)$$

with $i = 1$ to $N$, and $j = 1$ to $N$. $E_{gi}$ is the emissive power of zone $g_i$. $g_k g_i \Phi g_i g_j$ denotes the scattering-exchange area from volume zone $k$, through zone $i$, and finally arrives at zone $j$. $g_i g_j$ is the direct-exchange area from zone $i$ to zone $j$. For the sake of clarity, mathematical expressions for all scattering-exchange



Downloaded 12 Dec 2010 to 193.140.21.150. Redistribution subject to ASME license or copyright; see http://www.asme.org/terms/Terms_Use.cfm

**Table 1 Comparison of solutions between CZM and GZM in an isotropic scattering medium**

| | CZM | | | GZM | | |
|---|---|---|---|---|---|---|
| $K_tD \setminus \omega_0$ | 0.1 | 0.5 | 0.8 | 0.1 | 0.5 | 0.8 |
| 0.1 | 0.153 [a] | 0.091 [a] | 0.039 [a] | 0.153 [a] | 0.091 [a] | 0.039 [a] |
| 1.0 | 0.747 [c] | 0.559 [c] | 0.304 [c] | 0.747 [a] | 0.559 [a] | 0.304 [a] |
| 10.0 | 0.979 [d] | 0.855 [e] | 0.658 [e] | 0.979 [a] | 0.854 [b] | 0.657 [b] |

(a) = 4 zones, (b) = 8 zones, (c) = 16 zones, (d) = 32 zones, (e) = 64 zones.

areas are omitted. Interested readers are referred to Ma (1992) for the derivations of these scattering-exchange areas. It can be shown that they can be expressed in the form of functions of standard exponential integrals. Mathematical expression of all direct-exchange areas can be found in Hottel and Sarofim (1967).

Two different cases are used here to verify the GZM formulation in a one-dimensional medium. The first case considers an isothermal medium enclosed by two black and cold walls (at zero degree). The second case considers a medium at radiative equilibrium with unequal wall temperatures (bottom black wall at $E_{b1}$, and top black wall at zero).

**2.1 Isothermal Medium.** Using conservation of energy and the radiosity equation, the normalized heat flux for the bottom wall $s_1$ is given by:

$$\frac{Q_1}{E_bA} = (1-\omega_0)\sum_{i=1}^{N}\frac{g_is_1}{A} + \omega_0\sum_{i=1}^{N}\sum_{k=1}^{N}\frac{g_kg_i\Phi g_is_1}{A}\frac{W_{gk,gi}}{E_b} \quad (6)$$

$E_b$ is the blackbody emissive power of the medium, and it is a known quantity for an isothermal medium. Equation (5) can be rewritten into a set of simultaneous linear algebraic equations with the unknowns being the radiosities $W_{gk,gi}$. $W_{gk,gi}$ can then be solved easily by standard matrix inversion techniques. In this work, a Gauss–Siedel iteration is utilized, and the convergence criterion is set at 0.1 percent. Substituting the solution for $W_{gk,gi}$ into Eq. (6) results in the solution of the normalized surface heat flux $Q_1/E_bA$.

If the medium is isotropic, the normalized surface heat flux can be calculated by the CZM. Hence, a comparison between CZM and GZM will demonstrate the accuracy of GZM in an isotropic scattering medium. The normalized surface heat flux in an anisotropic scattering medium can be calculated by the Monte Carlo method (Love et al., 1967). The accuracy of GZM in this type of medium can be assessed with a direct comparison.

**2.2 Radiative Equilibrium.** In this case, the medium is at radiative equilibrium with the bottom surface $s_1$ kept at $E_{b1}$ and the top surface $s_2$ at zero (see Fig. 1). Using conservation of energy again, the net total energy loss for the bottom surface is given by:

$$Q_1 = E_{b1}A_1 - \sum_{i=1}^{N} W_{gi,1}g_is_1 \quad (7)$$

In addition, $W_{gi,1}$ is given by:

$$W_{gi,1} = (1-\omega_0)E_{gi} + \frac{\omega_0}{g_is_1}\left[\sum_{j=1}^{N} W_{gj,gi}g_jg_i\Phi g_is_1 + E_{b1}s_1g_i\Phi g_is_1\right] \quad (8)$$

with $s_1g_i\Phi g_is_1$ denoting the surface-volume-surface scattering-exchange area, and $g_jg_i\Phi g_is_1$ being the volume-volume-surface scattering-exchange area. $E_{gi}$, which represents the emissive power in the volume zone $g_i$, is not known. However, using an energy balance, $E_{gi}$ can be replaced by radiosities. Therefore, Eq. (8) can be rewritten as:

$$W_{gi,1} = (1-\omega_0)\left[\sum_{j=1}^{N} W_{gj,gi}\frac{g_jg_i}{4K_tV_i} + E_{b1}\frac{s_1g_i}{4K_tV_i}\right] + \frac{\omega_0}{g_is_1}\left[\sum_{j=1}^{N} W_{gj,gi}g_jg_i\Phi g_is_1 + E_{b1}s_1g_i\Phi g_is_1\right] \quad (9)$$

The radiosity $W_{gj,gi}$ in this equation must be known before the evaluation of $W_{gi,1}$ can be made. This can be accomplished by solving a set of radiosity equations as shown below:

$$W_{gj,gi} = (1-\omega_0)\left[\sum_{k=1}^{N} W_{gk,gj}\frac{g_kg_j}{4K_tV_i} + E_{b1}\frac{s_1g_j}{4K_tV_i}\right] + \frac{\omega_0}{g_jg_i}\left[\sum_{k=1}^{N} W_{gk,gj}g_kg_j\Phi g_jg_i + E_{b1}s_1g_j\Phi g_jg_i\right] \quad (10)$$

with $i = 1$ to $N$, and $j = 1, N$. Again, $W_{gj,gi}$ are solved by the Gauss–Siedel iteration method; hence, $W_{gi,1}$ is determined. Substituting the value of $W_{gi,1}$ into Eq. (7) results in the solution of $Q_1$.

## 3 Results and Discussion

In this section, the results obtained for an isothermal medium are displayed and discussed first, followed by the results obtained for a medium at radiative equilibrium.

### 3.1 Isothermal Medium

*3.1.1 Isotropic Scattering Medium.* Normalized surface heat fluxes in an isotropic scattering medium calculated by GZM and CZM are shown in Table 1.

Excellent agreements are obtained for all optical thicknesses and scattering albedos. These results verify the correctness of the GZM formulation in an isotropic scattering medium. Additionally, an interesting result is observed from this comparison. As shown in Table 1, the number of zones required in the GZM method to achieve the same accuracy (relative error of 1 percent) is tremendously reduced. This unexpected result can be attributed to the more complete description of scattering using the scattering-exchange area, which includes the incoming component, the scattering component, and the outgoing component. For the same number of zones, the energy scattered into a volume zone in the GZM formulation is more accurately described than in the CZM formulation; consequently, GZM can achieve a faster convergence (fewer number of zones) than CZM.

*3.1.2 Linear Anisotropic Scattering Medium* The normalized energy to the bottom surface $Q_1/E_bA$ for the linear anisotropic scattering medium is calculated by GZM and Monte Carlo, and shown in Tables 2 and 3. Exceptionally good agreements are obtained for all optical thicknesses and scattering albedos. From this comparison, it is seen that GZM can accurately calculate radiative transfer in an isothermal and linear anisotropic scattering medium.

**Table 2 Comparison of GZM with Monte Carlo for a strongly forward anisotropic ($\beta = 1$) scattering medium**

| | GZM | | | Monte Carlo | | |
|---|---|---|---|---|---|---|
| $K_tD \setminus \omega_0$ | 0.1 | 0.5 | 0.8 | 0.1 | 0.5 | 0.8 |
| 0.1 | 0.153 [a] | 0.091 [a] | 0.039 [a] | 0.152 [a] | 0.092 [a] | 0.038 [a] |
| 1.0 | 0.749 [a] | 0.565 [a] | 0.307 [b] | 0.749 [a] | 0.564 [a] | 0.306 [b] |
| 10.0 | 0.986 [b] | 0.892 [c] | 0.711 [c] | 0.986 [b] | 0.896 [c] | 0.717 [c] |

(a) = 4 zones, (b) = 8 zones, (c) = 16 zones.



Downloaded 12 Dec 2010 to 193.140.21.150. Redistribution subject to ASME license or copyright; see http://www.asme.org/terms/Terms_Use.cfm

Table 3 Comparison of GZM with Monte Carlo for a strongly backward anisotropic ($\beta = -1$) scattering medium

| | GZM | | | Monte Carlo | | |
|---|---|---|---|---|---|---|
| $K_tD \setminus \omega_0$ | 0.1 | 0.5 | 0.8 | 0.1 | 0.5 | 0.8 |
| 0.1 | 0.153 [a] | 0.091[a] | 0.039[a] | 0.152[a] | 0.091[a] | 0.038[a] |
| 1.0 | 0.745[a] | 0.553[a] | 0.301[b] | 0.744[a] | 0.554[a] | 0.300[b] |
| 10.0 | 0.971[b] | 0.818[c] | 0.608[c] | 0.971[b] | 0.818[c] | 0.609[c] |

(a) = 4 zones, (b) = 8 zones, (c) = 16 zones.

**3.2 Radiative Equilibrium.** A comparison of solutions between GZM and Dayan and Tien (1975) for normalized surface heat flux $Q_1/E_{b1}A$ in a linear anisotropic scattering medium is shown in Table 4. An excellent agreement is again obtained. In addition, typical temperature distributions $\sigma T^4/\sigma T_1^4$ calculated by GZM compare very well with those obtained from Dayan and Tien (1975) as shown in Table 5.

## 4 Conclusion

The Generalized Zoning Method is shown to predict radiative quantities in one-dimensional, isotropic and linear anisotropic scattering media accurately. For media with a uniform temperature, excellent agreement between CZM and GZM in an isotropic scattering medium, and Monte Carlo and GZM in a linear anisotropic scattering medium, are obtained. For a linear anisotropic scattering medium at radiative equilibrium, the GZM solutions compare very well with the solutions obtained by Dayan and Tien.

In an isothermal and isotropic scattering medium, the GZM method can achieve the same converged solution (relative error of 1 percent) with fewer zones than CZM. This result suggests that GZM is more accurate than CZM. The primary difference between CZM and GZM is the scattering-exchange areas introduced in the GZM formulation. The scattering-exchange areas enable one to compute radiative transfer in an anisotropic scattering medium, and are responsible for the improved accuracy achieved by GZM in an isotropic scattering medium.

The formulation of GZM in one-dimensional media is identical to the formulation in three-dimensional systems. The only difference is the mathematical expression for the scattering-exchange areas. Interested readers are referred to Yuen and Takara (1990) for the derivation of three-dimensional scattering-exchange areas. Because the formulation of GZM remains unchanged for multidimensional systems, and the GZM solutions agree exceptionally well with well-established solutions in one-dimensional media, the GZM formulation is valid for multidimensional media.

Table 4 Normalized heat flux comparison for a one-dimensional planar problem with linear anisotropic scattering (radiative equilibrium case)

| | $\omega_0\beta = -0.7$ | | $\omega_0\beta = 0.7$ | |
|---|---|---|---|---|
| $K_tD$ | D&T | GZM | D&T | GZM |
| 0.1 | 0.901 | 0.901[a] | 0.931 | 0.930[a] |
| 0.5 | 0.661 | 0.662[b] | 0.750 | 0.749[b] |
| 1.0 | 0.505 | 0.503[b] | 0.611 | 0.610[b] |
| 3.0 | 0.260 | 0.259[c] | 0.358 | 0.355[c] |

(a) = 4 zones, (b) = 8 zones, (c) = 16 zones

Table 5 Temperature distribution comparison for a medium at radiative equilibrium with $K_tD = 0.5$

| | $\omega_0\beta = -0.7$ | | $\omega_0\beta = 0.7$ | |
|---|---|---|---|---|
| x / D | D&T | GZM | D&T | GZM |
| 0.06 | 0.63 | 0.63[a] | 0.68 | 0.67[a] |
| 0.2 | 0.60 | 0.59[a] | 0.62 | 0.62[a] |
| 0.3 | 0.55 | 0.56[a] | 0.57 | 0.58[a] |
| 0.4 | 0.52 | 0.52[a] | 0.54 | 0.55[a] |
| 0.5 | 0.5 | 0.5[a] | 0.5 | 0.5[a] |
| 0.7 | 0.44 | 0.44[a] | 0.42 | 0.42[a] |
| 0.8 | 0.415 | 0.415[a] | 0.37 | 0.37[a] |
| 0.9 | 0.38 | 0.38[a] | 0.35 | 0.35[a] |

(a) = 8 zones

Hottel's zoning method is a powerful numerical method in solving practical problems in thermal radiation. Unfortunately, the assumption of isotropic scattering employed in his formulation imposes restriction on its applications. This restriction is finally alleviated by the GZM formulation but the basic principle of Hottel's method remains intact. Hence, the effectiveness of the zoning formulation is extended. Since scattering in most insulation materials and in combustion chambers are anisotropic (Viskanta and Menguc, 1987), GZM is a valuable tool to analyze these systems.


## Acknowledgments

The author would like to express his gratitude to Professor Walter Yuen at University of California, Santa Barbara for the introduction of Generalization Zoning Method to him, and the helpful discussions on the mathematical derivations of one-dimensional scattering-exchange areas.


## References


Chan, S. H., 1987, "Numerical Methods for Multidimensional Radiative Transfer Analysis in Participating Media," *Annual Review of Numerical Fluid Mechanics and Heat Transfer,* Vol. 1, pp. 305–350.

Dayan, A., and Tien, C. L., 1975, "Heat Transfer in Gray Planar Medium With Linear Anisotropic Scattering," ASME JOURNAL OF HEAT TRANSFER, Vol. 97, pp. 391–396.

Hottel, H. C., and Sarofim, A. F., 1967, *Radiative Transfer,* McGraw-Hill, New York.

Howell, J. R., and Perlmutter, M., 1964, "Monte Carlo Solution of Radiant Heat Transfer in a Nongrey Nonisothermal Gas With Temperature Dependent Properties," *AIChE J.,* Vol. 10, No. 4, pp. 562–567.

Love, T. J., Stockham, L. W., Lee, F. C., Munter, W. A., and Tsai, Y. W., 1967, "Radiative Heat Transfer in Absorbing, Emitting and Scattering media," University of Oklahoma Report, ARL 67-0210.

Ma, A. K., 1992, "Turbulence/Radiation Interaction in a Nongray and Anisotropic Scattering Medium," Ph.D. Dissertation, University of California at Santa Barbara.

Siegel, R., and Howell, J. R., 1992, *Thermal Radiation Heat Transfer,* 3rd ed., McGraw-Hill, New York.

Viskanta, R., and Menguc, M. P., 1987, "Radiative Heat Transfer in Combustion Systems," *Progress in Energy and Combustion Science,* Vol. 13, pp. 97–160.

Yuen, W. W., and Takara, E. E., 1990, "Development of a Generalization Zonal Method for the Analysis of Radiative Heat Transfer in Absorbing and Anisotropically Scattering Media," ASME HTD-Vol. 130, pp. 123–132.

Yuen, W. W., and Ma, A., 1991, "On the Development of Approximation Methods for Radiative Heat Transfer—A Fundamental Limitation and the Utilization of the Radiation-Length Concept," *Numerical Methods in Thermal Problems,* Vol. VII, Part 1, pp. 729–739.





Downloaded 12 Dec 2010 to 193.140.21.150. Redistribution subject to ASME license or copyright; see http://www.asme.org/terms/Terms_Use.cfm

# Smoothing Monte Carlo Exchange Factors

**R. I. Loehrke,[1] J. S. Dolaghan,[1] and P. J. Burns[1]**

## Nomenclature

$A_i$ = area of surface $i$, $m^2$
$A_r$ = array rms error (Eq. (9))
$C_i$ = convergence measure (Eq. (8))
$C_{ij}$ = error bound (Eq. (6))
$E_{ij}$ = exchange factor estimate = $\epsilon_i F_{ij}$
$F_{ij}$ = exchange fraction estimate = $N_{ij}/N_i$
$\mathcal{F}^k_{b,i}$ = fraction of blackbody emission from surface $i$ in wavelength band $k$
$K$ = confidence measure (Eq. (6))
$N_i$ = number of photons released from surface $i$
$N_{ij}$ = number of photons released from surface $i$ and absorbed by surface $j$
$N_e$ = total number of photons released in the enclosure = $N_i$ summed over all surfaces
$N_s$ = number of surfaces in enclosure
$\dot{Q}$ = heat flow rate, W
$T$ = temperature, K
$\epsilon$ = emittance
$\sigma$ = Stefan–Boltzmann constant, $\mathrm{Wm^{-2}\,K^{-4}}$

### Superscripts and Subscripts

$i$ = surface number
$j$ = surface number
$k$ = wavelength band

## Introduction

In order to obtain a complete set of radiant heat exchange factors using Monte Carlo methods, photon bundles must be released from each surface in an enclosure (except for at most one). The exchange factors so obtained satisfy the restrictions imposed by the first law of thermodynamics, but not those due to the second law. This note describes a method for improving the accuracy of the exchange factor estimates by forcing second-law compliance.

The radiation emitted from surface $i$ and absorbed by surface $j$ in wavelength band $k$ may be written as

$$\dot{Q}^k_{i\to j} = \epsilon^k_i F^k_{ij} A_i\, \sigma T^4_i \mathcal{F}^k_{b,i} \tag{1}$$

The exchange fractions are estimated in the Monte Carlo approach by

$$F^k_{ij} = \frac{N^k_{ij}}{N^k_i} \tag{2}$$

By the nature of the simulation

$$\sum_{j=1}^{N_s} F^k_{ij} = 1 \tag{3}$$

which ensures conservation of energy since all photons must be absorbed by some surface in an enclosure.

The second-law restriction that there must be zero net heat flow between surfaces at the same temperature leads to the reciprocity relation

$$E^k_{ij} A_i = E^k_{ji} A_j \tag{4}$$

where $E^k_{ij} = \epsilon^k_i F^k_{ij} = \epsilon^k_i\,(N^k_{ij}/N^k_i)$ is the exchange factor. The net radiative transfer in wavelength band $k$ from surface $i$ to surface $j$ is then

$$\dot{Q}^k_{ij} = E^k_{ij} A_i \sigma (\mathcal{F}^k_{b,i} T^4_i - \mathcal{F}^k_{b,j} T^4_j) \tag{5}$$

While Eq. (3) is satisfied for any number of photon emissions, Eq. (4) is satisfied only asymptotically as the number of emissions goes to infinity. Consequently, Eq. (4) may be used to assess convergence and to manipulate the values in the exchange factor matrix with the aim of improving the accuracy of the estimate. This latter process, referred to here as smoothing, is done separately in each wavelength band $k$. Thus, hereinafter, we drop the superscript $k$.

## Analysis

The twin objectives of smoothing are: (1) to make use of reciprocity to reduce the error in the exchange factor estimate (or reduce the number of emissions required to achieve a given error level) and (2) to yield a symmetric matrix $A_i E_{ij}$ for more compact storage. This is done by averaging the pairs of terms related by Eq. (4). However, the estimates obtained from Eq. (2) for exchange fractions between different pairs of surfaces are not, in general, of the same quality, as $F_{ij}$ and $F_{ji}$ are obtained from parent populations having different means and variances. It can be shown (Parzen, 1960) that, for large $N_i$, the fractional error in the exchange fraction predicted by the Monte Carlo simulation $|(F_{ij,\mathrm{exact}} - F_{ij})/F_{ij}|$ is bounded by

$$C_{ij} = K\sqrt{\frac{1 - F_{ij}}{N_i F_{ij}}} \tag{6}$$

with a confidence level determined by the constant $K$ (for 95 percent confidence, $K$ is 1.96). Consequently, an average that weights more heavily the estimate with the smaller error bound is adopted. New estimates $F'_{ij}$ of the exchange fractions that satisfy reciprocity are obtained from

$$A_i \epsilon_i F'_{ij} = A_i E'_{ij} = \left(\frac{C^2_{ji}}{C^2_{ij} + C^2_{ji}}\right) A_i E_{ij} + \left(1 - \frac{C^2_{ji}}{C^2_{ij} + C^2_{ji}}\right) A_j E_{ji} \tag{7}$$

These weights are based on the minimum variance linear estimator for a pair of samples (see appendix).

Smoothing is carried out in two steps. First, reciprocity is satisfied by the weighted averaging Eq. (7). Then, energy conservation, which is undermined by the first operation, is re-established. This second step could be done by using Eq. (3) directly to alter the diagonal terms, which are unaffected by reciprocity. However, when the diagonal elements are small, such alteration can lead to problems such as negative exchange fractions. Instead, the least-squares method of Larsen and Howell (1986), developed to correct a system that satisfies reciprocity but not conservation, is used. In this final step, $N_s$ simultaneous equations are solved for new estimates of the exchange factors $E''_{ij}$, which satisfy both conservation and reciprocity and which minimize the square of the weighted correction summed over all surfaces $\sum_{i=1}^{N_s}\sum_{j=1}^{N_s} (E''_{ij} - E'_{ij})^2/2E'^2_{ij}$. With this approach, corrections are distributed over the entire exchange factor matrix; larger exchange factors tend to receive larger corrections and estimates of $F_{ij} = 0$ are unaltered.

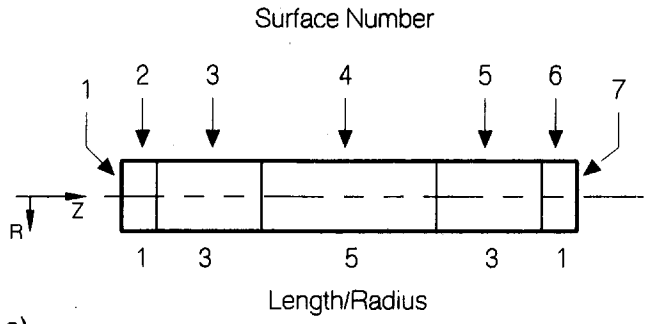
[1] Colorado State University, Fort Collins, CO 80523.

Contributed by the Heat Transfer Division of THE AMERICAN SOCIETY OF MECHANICAL ENGINEERS. Manuscript received by the Heat Transfer Division January 1994; revision received August 1994. Keywords: Radiation. Associate Technical Editor: S. H. Chan.

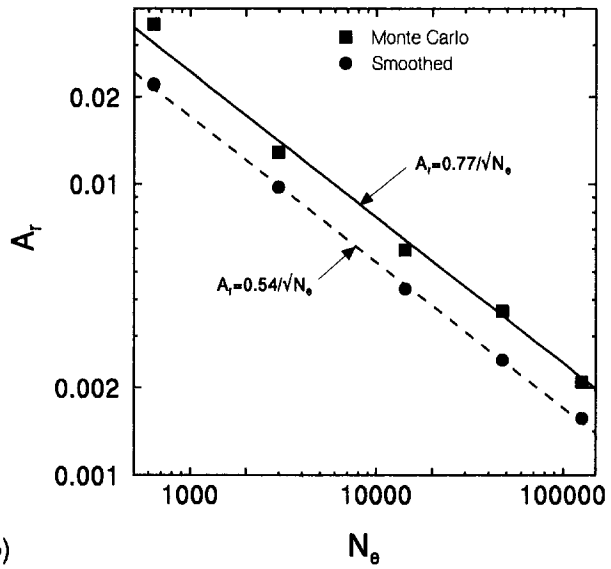


Copyright © 1995 by ASME

Downloaded 12 Dec 2010 to 193.140.21.150. Redistribution subject to ASME license or copyright; see http://www.asme.org/terms/Terms_Use.cfm




a)




b)

**Fig. 1** *(a)* **Test geometry: right circular cylinder partitioned into seven surfaces; *(b)* matrix rms error: each point represents the average of 20 simulations**

## Results

The smoothing procedure has been implemented as a post-processing program (Dolaghan et al., 1992) and tested using a Monte Carlo code in which the number of photon bundles emitted from each surface in a given wavelength band is chosen on the basis of a convergence criterion stemming from the error bound Eq. (6) (Maltby and Burns, 1991). Bundles are emitted from a specified surface $i$ and the convergence measure

$$C_i = \frac{1}{N_s}\sum_{j=1}^{N_s} C_{ij}F_{ij} = \frac{K}{N_s}\sum_{j=1}^{N_s}\sqrt{\frac{F_{ij}(1-F_{ij})}{N_i}} \qquad (8)$$

is calculated periodically. Emissions from surface $i$ are terminated when $C_i$ falls below a prescribed limit $C_{i,\max}$.

The test geometry, shown in Fig. 1($a$), is a right, circular cylinder with an aspect ratio, length/diameter = 6.5. The side is divided, as shown, into five rings of unequal lengths. These rings, together with the top and bottom, form an enclosure with $N_s$ = 7. The exchange fraction predictions for black surfaces from a typical simulation are compared with the exact values in Table 1. In a black enclosure, the exchange fractions are identical to the shape factors. A set of three rows is given for each surface, $i$. The first row shows the exact shape factors, the second shows the raw Monte Carlo estimates and the third presents the results of smoothing these estimates. A convergence limit $C_{i,\max}$ = 0.01 was prescribed for this Monte Carlo run, and applied uniformly to each surface. This resulted in the release of about 2000 photons from each of the seven surfaces.

An analysis of the data summarized in Table 1 shows that smoothing resulted in improved estimates for 35 of the 49 exchange factors with two estimates unchanged. Also shown in Table 1 is one measure of the overall error in the exchange fraction estimates. The matrix rms error

$$A_r = \left[\frac{1}{N_s^2}\sum_{i=1}^{N_s}\sum_{j=1}^{N_s}|F_{ij,\text{exact}} - F_{ij}|^2\right]^{1/2} \qquad (9)$$

is reduced by about 30 percent in this simulation. The results are, of course, subject to statistical variation. A sense for the typical improvement can be obtained from Fig. 1($b$) where the matrix rms error is plotted as a function of the total number of photons released. Each point represents the average of 20 differently seeded Monte Carlo simulations, each made with the same $C_{i,\max}$. The variation in $N_e$ was obtained by changing the specified $C_{i,\max}$. Slight differences in the total number of photons required at a given error level for each simulation have been averaged out. These data show that reciprocity smoothing provides roughly a factor of two reduction in the number of photons emissions required for a given error level, compared with the raw Monte Carlo results.

## Conclusion

A complete radiation heat transfer analysis of all of the surfaces in an enclosure requires a full set of exchange factors. Photon bundles must be released from each surface of the enclosure to generate this set. Many of the photon journeys from a surface

**Table 1 Exchange fractions before and after smoothing results from a single simulation; exact/Monte Carlo/smoothed**

Notation: aaa-b = aaa x $10^{-b}$

| i | $F_{i1}$ | $F_{i2}$ | $F_{i3}$ | $F_{i4}$ | $F_{i5}$ | $F_{i6}$ | $F_{i7}$ |
|---|---|---|---|---|---|---|---|
| 1 | 000-0 | 618-3 | 326-3 | 437-4 | 520-5 | 100-5 | 585-5 |
| | 000-0 | 631-3 | 313-3 | 410-4 | 700-5 | 100-5 | 700-5 |
| | 000-0 | 629-3 | 316-3 | 407-4 | 674-5 | 100-5 | 726-5 |
| 2 | 309-3 | 382-3 | 291-3 | 164-4 | 912-6 | 140-6 | 501-6 |
| | 302-3 | 378-3 | 305-3 | 137-4 | 667-6 | 333-6 | 100-5 |
| | 314-3 | 369-3 | 301-3 | 135-4 | 944-6 | 333-6 | 100-5 |
| 3 | 544-4 | 970-4 | 697-3 | 148-3 | 248-5 | 304-6 | 867-6 |
| | 520-4 | 985-4 | 691-3 | 155-3 | 200-5 | 000-0 | 150-5 |
| | 526-4 | 100-3 | 691-3 | 153-3 | 200-5 | 667-6 | 833-4 |
| 4 | 437-5 | 328-5 | 886-4 | 807-3 | 886-4 | 328-5 | 437-5 |
| | 100-5 | 200-5 | 860-4 | 827-3 | 790-4 | 200-5 | 300-5 |
| | 407-5 | 270-5 | 917-4 | 807-3 | 876-4 | 275-5 | 450-5 |
| 5 | 867-6 | 304-6 | 248-5 | 148-3 | 697-3 | 970-4 | 544-4 |
| | 500-6 | 500-6 | 200-5 | 149-3 | 696-3 | 950-4 | 565-4 |
| | 112-5 | 315-6 | 200-5 | 146-3 | 704-3 | 926-4 | 536-4 |
| 6 | 501-6 | 140-6 | 912-6 | 164-4 | 291-3 | 382-3 | 309-3 |
| | 500-6 | 000-0 | 200-5 | 140-4 | 278-3 | 405-3 | 300-3 |
| | 500-6 | 333-6 | 200-5 | 137-4 | 278-3 | 396-3 | 310-3 |
| 7 | 585-5 | 100-5 | 520-5 | 437-4 | 326-3 | 618-3 | 000-0 |
| | 750-5 | 000-0 | 200-5 | 455-4 | 318-3 | 627-3 | 000-0 |
| | 726-5 | 200-5 | 500-5 | 450-4 | 321-3 | 619-3 | 000-0 |

Array-averaged RMS error
$A_r$ = 6.682 x $10^{-3}$ (Monte Carlo)
$A_r$ = 4.723 x $10^{-3}$ (Smoothed)



Downloaded 12 Dec 2010 to 193.140.21.150. Redistribution subject to ASME license or copyright; see http://www.asme.org/terms/Terms_Use.cfm

yield redundant information, exchange factors that could have been obtained, using reciprocity, from bundles released from other surfaces. The smoothing technique described here uses this redundant information to improve the exchange factor estimates. The technique was evaluated with the results of a simulation where the number of photon bundles released from each surface was set by an accuracy criterion. This evaluation showed that the accuracy improvement due to smoothing was comparable to that obtained by doubling the total number of photons released in the simulation. This translates, for equal accuracy, into a CPU time savings of a factor of two for problems involving large numbers of surfaces and high accuracy, since the time to perform the smoothing is small compared to the simulation time.

## References


Dolaghan, J. S., Loehrke, R. I., and Burns, P. J., 1992, "User's Manual for SMOOTH—Version 1.0," Department of Mechanical Engineering, Colorado State University.

Hammersley, J. M., and Handscomb, D. C., 1964, *Monte Carlo Methods*, Methuen, 1964, Sec. 2.4.

Larsen, M. E., and Howell, J. R., 1986, "Least-Squares Smoothing of Direct-Exchange Areas in Zonal Analysis," ASME JOURNAL OF HEAT TRANSFER, Vol. 108, pp. 239–242.

Maltby, J. D., and Burns, P. J., 1991, "Performance, Accuracy and Convergence in a Three-Dimensional Monte Carlo Radiative Heat Transfer Simulation," *Numerical Heat Transfer*, Part B, Fundamentals, Vol. 19, pp. 191–209.

Parzen, E., 1960, *Modern Probability Theory and Its Application*, Wiley, New York, p. 231.

Walpole, R. E., and Myers, R. H., 1978, *Probability and Statistics for Engineers and Scientists*, 2nd ed., Macmillan, p. 71.


## APPENDIX

The estimate

$$F_{ij} = \frac{N_{ij}}{N_i} \tag{A-1}$$

has an expected value of $F_{ij,\text{exact}}$ and a variance $\text{var}(F_{ij}) = F_{ij,\text{exact}}(1 - F_{ij,\text{exact}})/N_i$ (Hammersley and Handscomb, 1964). Each complete Monte Carlo simulation for an enclosure yields a pair of independent, jointly distributed, random variables, $F_{ij}$ and $F_{ji}$, for each pair of surfaces. According to reciprocity, $F_{ji}$ is also an estimator $\hat{F}_{ij}$ of $F_{ij,\text{exact}}$ given by

$$\hat{F}_{ij} = aF_{ji} = a\frac{N_{ji}}{N_j} \tag{A-2}$$

where $a = \epsilon_j A_j/\epsilon_i A_i$. The linear combination of Eqs. (A-1) and (A-2), $F'_{ij} = wF_{ij} + (1 - w)\hat{F}_{ij}$, provides a third unbiased estimate of $F_{ij,\text{exact}}$. The variance of this estimate is $\text{var}(F'_{ij}) = w^2\,\text{var}(F_{ij}) + a^2(1 - w)^2\,\text{var}(F_{ji})$ (Walpole and Myers, 1978). The weighting factor $w$, which minimizes $\text{var}(F'_{ij})$, is given by

$$w = \frac{1}{1 + \dfrac{\text{var}(F_{ij})}{a^2\,\text{var}(F_{ji})}}$$

This can be written, using reciprocity, as

$$w = \frac{1}{1 + \dfrac{(1 - F_{ij,\text{exact}})/(F_{ij,\text{exact}}N_i)}{(1 - F_{ji,\text{exact}})/(F_{ji,\text{exact}}N_j)}}$$

In those cases where the true exchange fractions are known to be identical, e.g., due to geometric symmetry, the weighting factor reduces to $w = N_i/(N_i + N_j)$. In general, the exchange fractions must be estimated and this leads to $w = C_{ji}^2/(C_{ij}^2 + C_{ji}^2)$.

# Enhancement of Nucleate Boiling Heat Transfer and Depression of Surface Tension by Surfactant Additives


**Wuu-Tsann Wu,[1] Yu-Min Yang,[1] and Jer-Ru Maa[1]**


## Nomenclature

$C$ = bulk concentration of solution, ppm
$h$ = boiling heat transfer coefficient, kW m$^{-2}$ K$^{-1}$
$\Delta h$ = boiling heat transfer coefficient enhancement by surfactant, kW m$^{-2}$ K$^{-1}$
$n$ = const
$q$ = heat flux, kW m$^{-2}$
$t$ = time, min
$\Delta T_{\text{sat}}$ = superheat, K
$Y$ = $C(d\sigma/dC)^2$, mN$^2$ m$^{-2}$
$\sigma$ = surface tension, mN m$^{-1}$
$\Delta\sigma$ = equilibrium surface tension depression by surfactant, mN m$^{-1}$

### Subscripts

$w$ = water

## Introduction

Theoretically, surface tension is an important variable for boiling. The rate of nucleus formation is proportional to $e^{-\sigma^3}$. Thus, small decreases in $\sigma$ should cause large increases in the number of nuclei. The cavitation theory predicts that the force required to rupture a liquid in tension is proportional to $\sigma^{3/2}$. Thus, liquid with large surface tensions should be difficult to fracture. Detailed discussions of these theories are available (Westwater, 1956). On the other hand, considering the equation of state only, no reason is apparent why a surfactant should affect the metastable state. Therefore, on nucleation theoretical grounds only, a decrease in $\sigma$ by surfactant additive may have no effect or it may increase the rate of heat transfer. It cannot decrease the heat flow. Surface tension also affects different fundamental processes in nucleate boiling differently, such as bubble growth, bubble departure, bubble shape, etc. However, the way through which nucleate boiling heat transfer may be varied by the changes in these processes is not so obvious.

In the meantime, it is known that due to diffusion-controlled adsorption of surfactant molecules, the surface tension of a surfactant solution is dependent on the history of the system. As a new surface is created, the time necessary to achieve equilibrium may be from seconds to hours depending on surfactant species and concentration. Because the formation of bubbles in a boiling system is an extremely rapid process, sometimes requiring only a few milliseconds, it would seem that if surface tension has any effect on boiling solutions it would be the dynamic surface tension that would apply and not the static (or equilibrium) surface tension. Unfortunately, experimental evidence gathered to date has not proved the existence of such an effect.

Morgan et al. (1949) were able to measure, with a du Nouy tensiometer, the surface tension of a fresh surface of aqueous Drene solution in about 20 seconds at 72°F. Data were taken for


[1] Department of Chemical Engineering, National Cheng Kung University, Tainan, Taiwan 701.



Contributed by the Heat Transfer Division of THE AMERICAN SOCIETY OF MECHANICAL ENGINEERS. Manuscript received by the Heat Transfer Division September 1993, revision received June 1994. Keywords: Augmentation and Enhancement, Boiling, Phase-Change Phenomena. Associate Technical Editor: V. K. Dhir.





Downloaded 12 Dec 2010 to 193.140.21.150. Redistribution subject to ASME license or copyright; see http://www.asme.org/terms/Terms_Use.cfm

yield redundant information, exchange factors that could have been obtained, using reciprocity, from bundles released from other surfaces. The smoothing technique described here uses this redundant information to improve the exchange factor estimates. The technique was evaluated with the results of a simulation where the number of photon bundles released from each surface was set by an accuracy criterion. This evaluation showed that the accuracy improvement due to smoothing was comparable to that obtained by doubling the total number of photons released in the simulation. This translates, for equal accuracy, into a CPU time savings of a factor of two for problems involving large numbers of surfaces and high accuracy, since the time to perform the smoothing is small compared to the simulation time.

## References


Dolaghan, J. S., Loehrke, R. I., and Burns, P. J., 1992, "User's Manual for SMOOTH—Version 1.0," Department of Mechanical Engineering, Colorado State University.

Hammersley, J. M., and Handscomb, D. C., 1964, *Monte Carlo Methods*, Methuen, 1964, Sec. 2.4.

Larsen, M. E., and Howell, J. R., 1986, "Least-Squares Smoothing of Direct-Exchange Areas in Zonal Analysis," ASME JOURNAL OF HEAT TRANSFER, Vol. 108, pp. 239–242.

Maltby, J. D., and Burns, P. J., 1991, "Performance, Accuracy and Convergence in a Three-Dimensional Monte Carlo Radiative Heat Transfer Simulation," *Numerical Heat Transfer*, Part B, Fundamentals, Vol. 19, pp. 191–209.

Parzen, E., 1960, *Modern Probability Theory and Its Application*, Wiley, New York, p. 231.

Walpole, R. E., and Myers, R. H., 1978, *Probability and Statistics for Engineers and Scientists*, 2nd ed., Macmillan, p. 71.


## APPENDIX

The estimate

$$F_{ij} = \frac{N_{ij}}{N_i} \tag{A-1}$$

has an expected value of $F_{ij,\text{exact}}$ and a variance $\text{var}(F_{ij}) = F_{ij,\text{exact}}(1 - F_{ij,\text{exact}})/N_i$ (Hammersley and Handscomb, 1964). Each complete Monte Carlo simulation for an enclosure yields a pair of independent, jointly distributed, random variables, $F_{ij}$ and $F_{ji}$, for each pair of surfaces. According to reciprocity, $F_{ji}$ is also an estimator $\hat{F}_{ij}$ of $F_{ij,\text{exact}}$ given by

$$\hat{F}_{ij} = aF_{ji} = a\frac{N_{ji}}{N_j} \tag{A-2}$$

where $a = \epsilon_j A_j/\epsilon_i A_i$. The linear combination of Eqs. (A-1) and (A-2), $F'_{ij} = wF_{ij} + (1 - w)\hat{F}_{ij}$, provides a third unbiased estimate of $F_{ij,\text{exact}}$. The variance of this estimate is $\text{var}(F'_{ij}) = w^2\,\text{var}(F_{ij}) + a^2(1 - w)^2\,\text{var}(F_{ji})$ (Walpole and Myers, 1978). The weighting factor $w$, which minimizes $\text{var}(F'_{ij})$, is given by

$$w = \frac{1}{1 + \dfrac{\text{var}(F_{ij})}{a^2\,\text{var}(F_{ji})}}$$

This can be written, using reciprocity, as

$$w = \frac{1}{1 + \dfrac{(1 - F_{ij,\text{exact}})/(F_{ij,\text{exact}}N_i)}{(1 - F_{ji,\text{exact}})/(F_{ji,\text{exact}}N_j)}}$$

In those cases where the true exchange fractions are known to be identical, e.g., due to geometric symmetry, the weighting factor reduces to $w = N_i/(N_i + N_j)$. In general, the exchange fractions must be estimated and this leads to $w = C_{ji}^2/(C_{ij}^2 + C_{ji}^2)$.

# Enhancement of Nucleate Boiling Heat Transfer and Depression of Surface Tension by Surfactant Additives


**Wuu-Tsann Wu,[1] Yu-Min Yang,[1] and Jer-Ru Maa[1]**


## Nomenclature

$C$ = bulk concentration of solution, ppm
$h$ = boiling heat transfer coefficient, kW m$^{-2}$ K$^{-1}$
$\Delta h$ = boiling heat transfer coefficient enhancement by surfactant, kW m$^{-2}$ K$^{-1}$
$n$ = const
$q$ = heat flux, kW m$^{-2}$
$t$ = time, min
$\Delta T_{\text{sat}}$ = superheat, K
$Y$ = $C(d\sigma/dC)^2$, mN$^2$ m$^{-2}$
$\sigma$ = surface tension, mN m$^{-1}$
$\Delta\sigma$ = equilibrium surface tension depression by surfactant, mN m$^{-1}$

### Subscripts

$w$ = water

## Introduction

Theoretically, surface tension is an important variable for boiling. The rate of nucleus formation is proportional to $e^{-\sigma^3}$. Thus, small decreases in $\sigma$ should cause large increases in the number of nuclei. The cavitation theory predicts that the force required to rupture a liquid in tension is proportional to $\sigma^{3/2}$. Thus, liquid with large surface tensions should be difficult to fracture. Detailed discussions of these theories are available (Westwater, 1956). On the other hand, considering the equation of state only, no reason is apparent why a surfactant should affect the metastable state. Therefore, on nucleation theoretical grounds only, a decrease in $\sigma$ by surfactant additive may have no effect or it may increase the rate of heat transfer. It cannot decrease the heat flow. Surface tension also affects different fundamental processes in nucleate boiling differently, such as bubble growth, bubble departure, bubble shape, etc. However, the way through which nucleate boiling heat transfer may be varied by the changes in these processes is not so obvious.

In the meantime, it is known that due to diffusion-controlled adsorption of surfactant molecules, the surface tension of a surfactant solution is dependent on the history of the system. As a new surface is created, the time necessary to achieve equilibrium may be from seconds to hours depending on surfactant species and concentration. Because the formation of bubbles in a boiling system is an extremely rapid process, sometimes requiring only a few milliseconds, it would seem that if surface tension has any effect on boiling solutions it would be the dynamic surface tension that would apply and not the static (or equilibrium) surface tension. Unfortunately, experimental evidence gathered to date has not proved the existence of such an effect.

Morgan et al. (1949) were able to measure, with a du Nouy tensiometer, the surface tension of a fresh surface of aqueous Drene solution in about 20 seconds at 72°F. Data were taken for


[1] Department of Chemical Engineering, National Cheng Kung University, Tainan, Taiwan 701.



Contributed by the Heat Transfer Division of THE AMERICAN SOCIETY OF MECHANICAL ENGINEERS. Manuscript received by the Heat Transfer Division September 1993, revision received June 1994. Keywords: Augmentation and Enhancement, Boiling, Phase-Change Phenomena. Associate Technical Editor: V. K. Dhir.





Copyright © 1995 by ASME

Downloaded 12 Dec 2010 to 193.140.21.150. Redistribution subject to ASME license or copyright; see http://www.asme.org/terms/Terms_Use.cfm

the more concentrated solution, 1 percent, and the dilute one, 0.1 percent. Although these two solutions have essentially the same equilibrium surface tension, the 0.1 percent solution exhibits a higher effective (dynamic) surface tension than does the 1 percent solution. It is worthy to note that this dynamic behavior of Drene surfactant solutions has also been confirmed later by a method, which approximated the boiling process, based on determining the bubble volume during gas bubble formation at horizontal circular orifices (Benzing and Myers, 1955). Morgan et al. attributed the much higher heat transfer coefficient of 1 percent Drene solution to rapidity of the solution to establish its equilibrium surface tension at the fresh interface formed in the boiling process. They concluded that the surface tension of a "young" surface controls the heat transfer coefficient.

Jontz and Myers (1960) reached the same conclusion, that the boiling coefficient of the Tergitol–water solution varied inversely with dynamic surface tension, which was measured by the method based on the work of Benzing and Myers (1955). However, the presence of aerosol in water was found to have no effect on the dynamic surface tension. Thus the dynamic surface tension in this case is the same as the surface tension of pure water and, as far as surface tension can affect boiling, it would seem that the boiling coefficients of these solutions should be the same as for water. Nevertheless, a fourfold increase resulted in the boiling coefficient. They suggested that a pluralistic explanation (effect of dynamic surface tension and effect of the surfactant molecules serving as nuclei for the formation of bubbles) may be necessary to explain the extreme divergence of results obtained by previous workers in this field.

The effect of surfactant additive on boiling has been attributed to the departure from equilibrium surface tension, which is produced by rapid extension of the vapor–liquid interface during growth and coalescence of vapor bubbles in the vicinity of the boiling surface (Yang, 1990). The surface tension of a rapidly extending interface in surfactant solution is higher than the static value because the surfactant component cannot diffuse to the adsorbed layer promptly. This may result in an interfacial flow driven by the surface tension gradient (known as Marangoni flow). This Marangoni effect (dynamic surface effect) can be expressed, in a simplified form, by the $Y(\equiv C(d\sigma/dC)^2)$ value, which is shown to be a representation of the elasticity of an adsorbed film. $Y$ always has a maximum at a specific concentration for a particular surfactant. The theoretical prediction has been shown to be consistent qualitatively with the experimental results of Tzan and Yang (1990). While surfactant additives generally depress surface tension, the primary effect may thus be due to factors that may be at best only indirectly related to changes in surface tension. It is reasonable, however, to doubt if an exceedingly complex phenomenon like boiling of surfactant solution can be explained simply by a function such as $Y$. In fact, absence of a vapor–liquid mass transfer and uniform stretching rate of plane vapor–liquid interface should be assumed in the theoretical derivation of the Marangoni effect, and the diffusion coefficient of surfactant in the bulk solution should be known. The situation is that although the Marangoni effect approach seems to be promising, comprehensive analysis of it is impossible for the present.

Table 1 lists chronologically some investigations of surfactant effect on boiling water from literature. Because changes in physical properties, such as viscosity and density, were usually too slight for significance, static surface tension alone has been correlated with nucleate boiling heat transfer coefficient, so that $h \propto \sigma^n$. The results are contradictory. "At least a dozen values are published for $n$" (Lowery and Westwater, 1957). As may be seen in Table 1, liquid status (pool or flow), heating surface (tube or plate), and even orientation (vertical or horizontal, not shown in the table) were diversely different from one reference to the other. It is possible that the lack of correlation between $h$ and $\sigma$ is, at least partly, due to the diversity of different experimental systems. In order that surfactant effect can be elucidated, thus, results obtained in the exactly same apparatus are desirable.

The objective of this work is to report the new systematically obtained experimental data of surfactant effect on nucleate boiling heat transfer in water by nine additives. Anionic, cationic, and nonionic surfactants were studied with highest concentration up to 400 ppm. Static and dynamic surface tensions of aqueous solution of surfactants were also measured at room temperature. The enhancement of heat transfer coefficient is related to the depression of static surface tension. The suitability of this correlation is also discussed.

## Experimental

The pool boiling apparatus used in this work was basically that which was constructed by Tzan and Yang (1990). That reference may be consulted for the details of the apparatus and the experimental data uncertainty. Saturated boiling took place on the outer surface of a horizontal seamless stainless steel tube (5.28 mm o.d., 4.8 mm i.d., and 100 mm long). The heat flux released from the electric heating element to the liquid was controlled by adjusting the current supplied by a rectifier with a capacity of 20 V and 500 A. The boiling surface temperature could be calculated from the inner tube surface temperature, which was measured by

**Table 1 Surfactants that affect the rate of nucleate boiling heat transfer of water**

| References | Liquid status | Heating surfaces | Surfactants |
|---|---|---|---|
| Strobe et al. (1939) | Flow | Tube | Duponol |
| Morgan et al. (1949) | Pool | Tube | Drene; Sodium lauryl sulfonate |
| Jontz and Myers (1960) | Pool | Plate | Tergitol; Aerosol-22 |
| Roll and Myers (1964) | Pool | Plate | Aerosol OT; Aerosol AY; Aerosol IB; Aerosol MA; Hyonic PE-200; Hyonic PE-300 |
| Frost and Kippenhan (1967) | Flow | Tube | Ultra Wet 60L |
| Huplik and Raithby (1972) | Pool | Plate | FC-176 |
| Shah and Darby (1973) | Flow | Plate | Joy |
| Shibayama et al. (1980) | Flow | Plate | Sodium oleate; Rapisool B80; Puluronic type F98, F88, F208 |
| Filippov and Saltanov (1982) | Pool | Tube | Octadecylamine |
| Yang and Maa (1983) | Pool | Plate | Sodium lauryl sulfate; Sodium lauryl benzene sulfonate |
| Saltanov et al. (1986) | Pool | Tube | Octadecylamine |
| Chang et al. (1987) | Flow | Tube | Sodium lauryl sulfate |
| Tzan and Yang (1990) | Pool | Tube | Sodium lauryl sulfate |
| Yang (1990) | — | — | — |
| Chou and Yang (1991) | Pool | Plate | Sodium lauryl sulfate |
| Wu et al. (1993) | Pool | Tube | Sodium lauryl sulfate |
| Wu et al. (this work) | Pool | Tube | Sodium lauryl sulfate; Aerosol-22 Tergitol; Dodecyl trimethylammonium chloride; Tween 20; Tween 40; Tween 80; *n*-Octanol; Triton X-100 |



Downloaded 12 Dec 2010 to 193.140.21.150. Redistribution subject to ASME license or copyright; see http://www.asme.org/terms/Terms_Use.cfm

**Table 2 Surfactant additives**

| Types | Surfactants | Molecular weight | Sources |
|---|---|---|---|
| Anionic | SLS (sodium lauryl sulfate) | 288 | Sigma |
| | Tergitol | 334 | Sigma |
| | Aerosol-22 | 412 | Sigma |
| Cationic | DTMAC (dodecyl trimethyl ammonium chloride) | 264 | TCI |
| Nonionic | Triton X-100 | ~770 | Aldrich |
| | *n*-Octanol | 130 | Wako |
| | Tween 20 | ~580 | Merck |
| | Tween 40 | ~640 | Merck |
| | Tween 80 | ~670 | Merck |

a chromel-alumel thermocouple placed at the central position in the tube, and the heat flux values. Surfactant effect on boiling hysteresis was also examined. It was found that incipient superheat and boiling curve determined by increasing heat flux make no difference with those determined by reducing heat flux for all surfactants studied in this work. The boiling data reported below are those determined by decreasing heat flux. Furthermore boiling of surfactant solutions more or less suffered from foaming problem.

Nine additives—including three anionic, one cationic, and five nonionic surfactants—were used as received without further purification. They are summarized in Table 2. Aqueous solutions of various concentrations for each surfactant were prepared by diluting a concentrated mother liquid solution of known concentration.

Surface tensions of the aqueous surfactant solutions were measured at room temperature (25 ± 1°C) with commercial equipment (CBVP-A3 Type, Kyowa Interface Science Co., Ltd., Japan) by the Wilhelmy plate method. As new fresh surface has been suddenly formed during measurement, the variation of surface tension with time, if it prevails, could be traced by a recorder. Dynamic surface tension of surfactant solution can be measured, and the equilibrium (static) values may be obtained from the long-time asymptote.

## Experimental Uncertainty

In the present experiment, the surface tension of distilled water, which is the solvent of all surfactant solutions, was measured nine times. The measurement of surface tension of water was followed by aqueous solutions with various amounts of each surfactant. Experimental mean value for water surface tension was 72.5 mN/m and the corresponding standard deviation was 0.1 mN/m. The tabulated surface tension of water at 25°C is 71.97 mN/m. From these results we can confidently estimate that the measurement uncertainty for surface tension was well within 1 percent.

The uncertainty due to measurement errors in the determination of surface temperature was analyzed and found to be about 1.5 percent at a $\Delta T_{sat}$ of 23 K and 2.8 percent at a $\Delta T_{sat}$ of 18 K. On the other hand, those values for uncertainty in the determination of heat flux were 1.4 percent at a $q$ of 450 kW/m$^2$ and 2.7 percent at a $q$ of 100 kW/m$^2$. Before and after a series of runs for aqueous solutions of a particular surfactant had been conducted, runs using pure water were always made to check whether there is any significant change of surface condition during this set of experiments. The data revealed that they were inconsistent with each other within about 8 percent.

## Results and Discussion

Nucleate boiling curves for aqueous solutions of nine surfactants with various concentrations were obtained. To the knowledge of the authors, these experimental boiling heat transfer data for aqueous solutions of surfactants are original ones in literature, except that those of SLS, Tergitol, and Aerosol-22 have been reported by other authors as shown in Table 1. Three types of surfactant exert different degrees of effect on boiling heat transfer. In general, the enhancement increases in the order: anionic > nonionic > cationic. This tentative conclusion, however, cannot be verified in different geometry or geometric scale of boiling surface and in other surfactants for lack of systematic experimental data in literature.

The dynamic surface tension profiles for the corresponding surfactant solutions were traced. It was found that the dynamic interfacial behavior of these surfactants might be of minor significance. The role the dynamic surface tension may play in boiling of surfactant solution seem to be still in a bewildering status. While it has been recognized that the vapor–liquid interface may not be in equilibrium during boiling, the surface tension measurements by the Wilhelmy plate method of this work indicated insignificant interfacial dynamics of surfactant solution. It follows that the promptness of diffusion and adsorption may be assumed for nine surfactants used in this work. Nothing exact, however, has been obtained at the very beginning. On the other hand, even if a proper device (e.g., gas bubbling apparatus as mentioned above) is available to measure the dynamic surface tension for surfactant solution, Jontz and Myers (1960) showed that slowness of diffusion and adsorption of Aerosol-22 does not inhibit the drastic enhancing effect on heat transfer coefficient.

The equilibrium surface tensions for various surfactant solutions are shown in Fig. 1. It was found that the depression of equilibrium surface tension increases in the order: nonionic > anionic > cationic. For nonionic surfactants: Triton X-100 > Tween 20, 40, 80 > *n*-octanol; and for anionic surfactants: SLS > Aerosol-22 > Tergitol.

In order that the experimental results of this work can be compared consistently with the data available in literature, the ratios of heat transfer coefficient enhancement, $\Delta h/h_w$, and equilibrium surface tension depression, $\Delta\sigma/\sigma_w$, by surfactant additive were evaluated. Figure 2 shows the data of nine surfactant additives of this work by correlating $\Delta h/h_w$ to $\Delta\sigma/\sigma_w$ for $q$ = 300 kW/

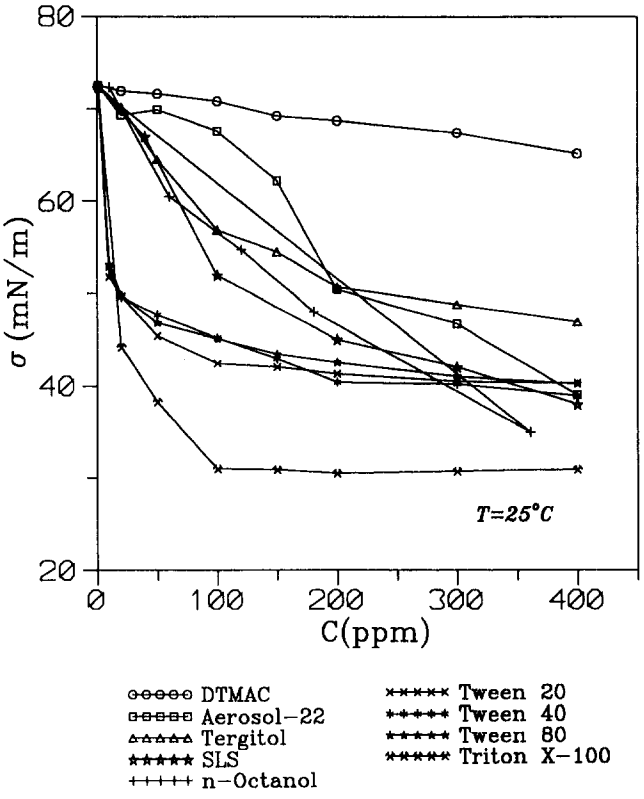



**Fig. 1 The static (equilibrium) surface tension for various surfactant solutions**



Downloaded 12 Dec 2010 to 193.140.21.150. Redistribution subject to ASME license or copyright; see http://www.asme.org/terms/Terms_Use.cfm

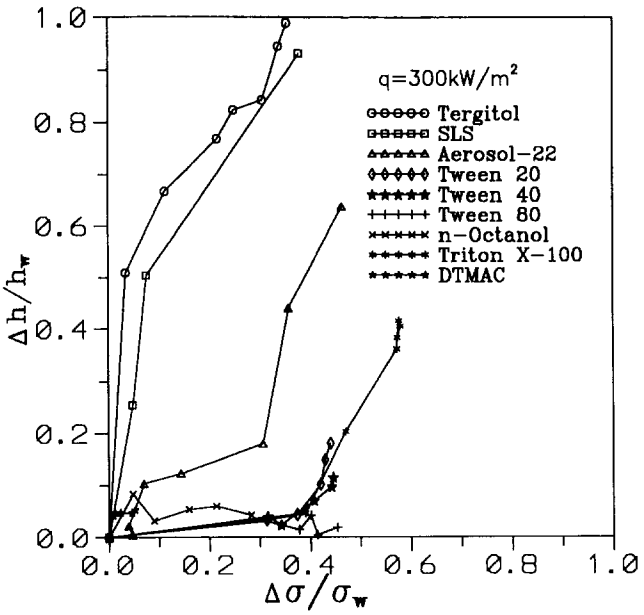



**Fig. 2 The correlation between heat transfer coefficient enhancement and equilibrium surface tension depression: $q$ = 300 kW/m²**

$m^2$. As shown in this figure, the effect of equilibrium surface tension on boiling heat transfer is still experimentally unproved. It also tried to correlate some experimental results available in literature in the same manner. Unfortunately, all the evidence reveals that the possibility of the existence of a universal correlation between heat transfer coefficient enhancement and equilibrium surface tension depression should be excluded. Besides concentration and type of surfactant, heat flux (or superheat) and geometry and geometric scale of boiling surface were all found to play roles in boiling characteristics of surfactant solutions.

From an engineering design point of view, it is most desirable that the results of surfactant effect on boiling heat transfer can be analyzed, generalized, and formulated in a more convenient form for calculations. Unfortunately, it seems to be impossible to achieve the ambitions for the present in view of the diversity of the experimental results as shown in Fig. 2, as obtained with the exact same apparatus in this work.

## Conclusions

Surfactant effects on nucleate boiling heat transfer and surface tension of water were systematically demonstrated in this work by nine additives—including three anionic, one cationic, and five nonionic surfactants. The present experimental results and those available in the literature reveal that neither equilibrium nor dynamic surface tension may be the explanation of the surfactant effect on boiling to the best of the present knowledge in this field. The possibility of the existence of a universal correlation between heat transfer coefficient enhancement and equilibrium surface tension depression by surfactant additive should be excluded.

Although comprehensive analysis of it seems to be very difficult for the present, the dynamic surface effect (which was proposed by Yang, 1990) on boiling turns out to be one of the possible approaches to the problem.

No convincing experimental evidence, however, can be due to nucleation theory (which was proposed by Lowery and Westwater, 1957; Jontz and Myers, 1966) as a possible explanation for surfactant effect on boiling of water.

## Acknowledgments

This study was supported by the National Science Council of the Republic of China through grant No. NSC 82-0402-E006-176.

## References

Benzing, R. L., and Myers, J. E., 1955, "Low Frequency Bubble Formation at Horizontal Circular Orifices," *Industrial and Engineering Chemistry,* Vol. 47, No. 10, pp. 2089–2090.

Chang, C. S., Maa, J. R., and Yang, Y. M., 1987, "Dynamic Surface Effect and Nucleate Flow Boiling of Dilute Surfactant Solutions," *Journal of the Chinese Institute of Chemical Engineers,* Vol. 18, No. 1, pp. 125–130.

Chou, C. C., and Yang, Y. M., 1991, "Surfactant Effect on the Temperature Profile Within the Superheated Boundary Layer and the Mechanism of Nucleate Pool Boiling," *Journal of the Chinese Institute of Chemical Engineers,* Vol. 22, No. 2, pp. 71–80.

Filippov, G. A., and Saltanov, G. A., 1982, "Steam-Liquid Media Heat-Mass Transfer and Hydrodynamics With Surface-Active Substance Additives," *Proceedings, 7th International Heat Transfer Conference,* Vol. 4, Hemisphere, New York, pp. 443–447.

Frost, W., and Kippenhan, C. J., 1967, "Bubble Growth and Heat Transfer Mechanisms in the Forced Convection Boiling of Water Containing a Surface Active Agent," *International Journal of Heat and Mass Transfer,* Vol. 10, pp. 931–949.

Huplik, V., and Raithby, G. D., 1972, "Surface-Tension Effects in Boiling From a Downward-Facing Surface," ASME JOURNAL OF HEAT TRANSFER, Vol. 94, pp. 403–409.

Jontz, P. D., and Myers, J. E., 1960, "The Effect of Dynamic Surface Tension on Nucleate Boiling Coefficients," *AIChE Journal,* Vol. 6, No. 1, pp. 34–38.

Lowery, A. J., and Westwater, J. W., 1957, "Heat Transfer to Boiling Methanol—Effect of Added Agents," *Industrial and Engineering Chemistry,* Vol. 49, pp. 1445–1448.

Morgan, A. I., Bromley, L. A., and Wilke, C. R., 1949, "Effect of Surface Tension on Heat Transfer in Boiling," *Industrial and Engineering Chemistry,* Vol. 41, No. 12, pp. 2767–2769.

Roll, J. B., and Myers, J. E., 1964, "The Effect of Surface Tension on Factors in Boiling Heat Transfer," *AIChE Journal,* Vol. 10, No. 4, pp. 530–534.

Saltanov, G. A., Kukushkin, A. N., Solodov, A. P., Sotskov, S. A., Jakusheva, E. V., and Chempik, E., 1986, "Surfactant Influence on Heat Transfer at Boiling and Condensation," *Proceedings, 8th International Heat Transfer Conference,* Vol. 5, Hemisphere, New York, pp. 2245–2250.

Shah, B. H., and Darby, R., 1973, "The Effect of Surfactant on Evaporative Heat Transfer in Vertical Film Flow," *International Journal of Heat and Mass Transfer,* Vol. 16, pp. 1889–1903.

Shibayama, S., Katsuta, M., Suzuki, K., Kurose, T., and Hatano, Y., 1980, "A Study on Boiling Heat Transfer in a Thin Liquid Film," *Heat Transfer (Japan Research),* Vol. 9, No. 4, pp. 12–40.

Strobe, G. W., Baker, E. M., and Badger, W. L., 1939, "Boiling-Film Heat Transfer Coefficients in a Long-Tube Vertical Evaporator," *Industrial and Engineering Chemistry,* Vol. 31, No. 2, pp. 200–206.

Tzan, Y. L., and Yang, Y. M., 1990, "Experimental Study of Surfactant Effects on Pool Boiling Heat Transfer," ASME JOURNAL OF HEAT TRANSFER, Vol. 112, pp. 207–212.

Westwater, J. W., 1956, "Boiling of Liquids," *Advances in Chemical Engineering,* Vol. 1, T. B. Drew and J. W. Hoopes, Jr., eds, Academic Press, New York.

Wu, W. T., Hu, C. L., and Yang, Y. M., 1993, "Surfactant Effect on Boiling Incipience and Bubble Growth Dynamics of Surface Boiling in Water," *Journal of the Chinese Institute of Chemical Engineers,* Vol. 24, No. 2, pp. 111–118.

Yang, Y. M., and Maa, J. R., 1983, "Pool Boiling of Dilute Surfactant Solutions," ASME JOURNAL OF HEAT TRANSFER, Vol. 105, pp. 190–192.

Yang, Y. M., 1990, "Dynamic Surface Effect on Boiling of Aqueous Surfactant Solutions," *International Communications in Heat and Mass Transfer,* Vol. 17, No. 6, pp. 711–727.

# Forced Convection Film Condensation on a Horizontal Tube—Influence of Vapor Boundary-Layer Separation

**S. B. Memory[1] and J. W. Rose[2]**

## Nomenclature

$d$ = diameter of condenser tube

$F$ = dimensionless parameter = $(gd\mu h_{fg})/(k\Delta TU_\infty^2)$

[1] Department of Mechanical Engineering, University of Miami, Coral Gables, Miami, FL.

[2] Department of Mechanical Engineering, Queen Mary and Westfield College, University of London, London, United Kingdom.

Contributed by the Heat Transfer Division and presented at the National Heat Transfer Conference, San Diego, California, August 9–12, 1992. Manuscript received by the Heat Transfer Division May 1993; revision received May 1994. Keywords: Condensation, Flow Separation, Forced Convection. Associate Technical Editor: V. K. Dhir.



Downloaded 12 Dec 2010 to 193.140.21.150. Redistribution subject to ASME license or copyright; see http://www.asme.org/terms/Terms_Use.cfm

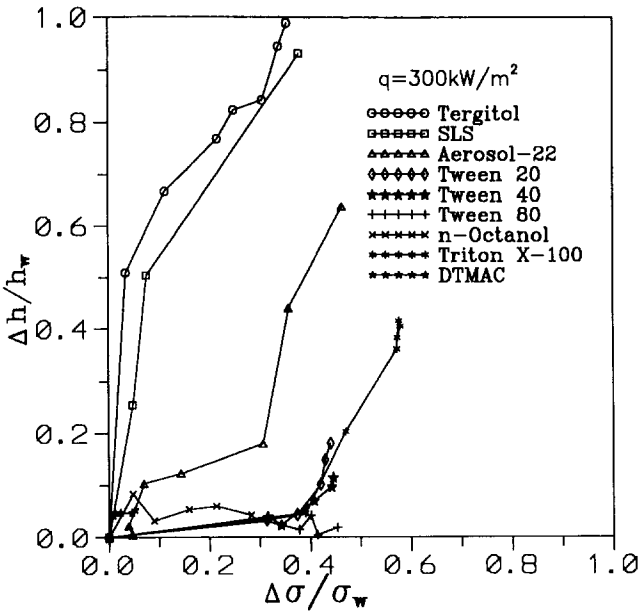



**Fig. 2 The correlation between heat transfer coefficient enhancement and equilibrium surface tension depression: $q$ = 300 kW/m²**

$m^2$. As shown in this figure, the effect of equilibrium surface tension on boiling heat transfer is still experimentally unproved. It also tried to correlate some experimental results available in literature in the same manner. Unfortunately, all the evidence reveals that the possibility of the existence of a universal correlation between heat transfer coefficient enhancement and equilibrium surface tension depression should be excluded. Besides concentration and type of surfactant, heat flux (or superheat) and geometry and geometric scale of boiling surface were all found to play roles in boiling characteristics of surfactant solutions.

From an engineering design point of view, it is most desirable that the results of surfactant effect on boiling heat transfer can be analyzed, generalized, and formulated in a more convenient form for calculations. Unfortunately, it seems to be impossible to achieve the ambitions for the present in view of the diversity of the experimental results as shown in Fig. 2, as obtained with the exact same apparatus in this work.

## Conclusions

Surfactant effects on nucleate boiling heat transfer and surface tension of water were systematically demonstrated in this work by nine additives—including three anionic, one cationic, and five nonionic surfactants. The present experimental results and those available in the literature reveal that neither equilibrium nor dynamic surface tension may be the explanation of the surfactant effect on boiling to the best of the present knowledge in this field. The possibility of the existence of a universal correlation between heat transfer coefficient enhancement and equilibrium surface tension depression by surfactant additive should be excluded.

Although comprehensive analysis of it seems to be very difficult for the present, the dynamic surface effect (which was proposed by Yang, 1990) on boiling turns out to be one of the possible approaches to the problem.

No convincing experimental evidence, however, can be due to nucleation theory (which was proposed by Lowery and Westwater, 1957; Jontz and Myers, 1966) as a possible explanation for surfactant effect on boiling of water.

## Acknowledgments

This study was supported by the National Science Council of the Republic of China through grant No. NSC 82-0402-E006-176.

## References

Benzing, R. L., and Myers, J. E., 1955, "Low Frequency Bubble Formation at Horizontal Circular Orifices," *Industrial and Engineering Chemistry,* Vol. 47, No. 10, pp. 2089–2090.

Chang, C. S., Maa, J. R., and Yang, Y. M., 1987, "Dynamic Surface Effect and Nucleate Flow Boiling of Dilute Surfactant Solutions," *Journal of the Chinese Institute of Chemical Engineers,* Vol. 18, No. 1, pp. 125–130.

Chou, C. C., and Yang, Y. M., 1991, "Surfactant Effect on the Temperature Profile Within the Superheated Boundary Layer and the Mechanism of Nucleate Pool Boiling," *Journal of the Chinese Institute of Chemical Engineers,* Vol. 22, No. 2, pp. 71–80.

Filippov, G. A., and Saltanov, G. A., 1982, "Steam-Liquid Media Heat-Mass Transfer and Hydrodynamics With Surface-Active Substance Additives," *Proceedings, 7th International Heat Transfer Conference,* Vol. 4, Hemisphere, New York, pp. 443–447.

Frost, W., and Kippenhan, C. J., 1967, "Bubble Growth and Heat Transfer Mechanisms in the Forced Convection Boiling of Water Containing a Surface Active Agent," *International Journal of Heat and Mass Transfer,* Vol. 10, pp. 931–949.

Huplik, V., and Raithby, G. D., 1972, "Surface-Tension Effects in Boiling From a Downward-Facing Surface," ASME JOURNAL OF HEAT TRANSFER, Vol. 94, pp. 403–409.

Jontz, P. D., and Myers, J. E., 1960, "The Effect of Dynamic Surface Tension on Nucleate Boiling Coefficients," *AIChE Journal,* Vol. 6, No. 1, pp. 34–38.

Lowery, A. J., and Westwater, J. W., 1957, "Heat Transfer to Boiling Methanol—Effect of Added Agents," *Industrial and Engineering Chemistry,* Vol. 49, pp. 1445–1448.

Morgan, A. I., Bromley, L. A., and Wilke, C. R., 1949, "Effect of Surface Tension on Heat Transfer in Boiling," *Industrial and Engineering Chemistry,* Vol. 41, No. 12, pp. 2767–2769.

Roll, J. B., and Myers, J. E., 1964, "The Effect of Surface Tension on Factors in Boiling Heat Transfer," *AIChE Journal,* Vol. 10, No. 4, pp. 530–534.

Saltanov, G. A., Kukushkin, A. N., Solodov, A. P., Sotskov, S. A., Jakusheva, E. V., and Chempik, E., 1986, "Surfactant Influence on Heat Transfer at Boiling and Condensation," *Proceedings, 8th International Heat Transfer Conference,* Vol. 5, Hemisphere, New York, pp. 2245–2250.

Shah, B. H., and Darby, R., 1973, "The Effect of Surfactant on Evaporative Heat Transfer in Vertical Film Flow," *International Journal of Heat and Mass Transfer,* Vol. 16, pp. 1889–1903.

Shibayama, S., Katsuta, M., Suzuki, K., Kurose, T., and Hatano, Y., 1980, "A Study on Boiling Heat Transfer in a Thin Liquid Film," *Heat Transfer (Japan Research),* Vol. 9, No. 4, pp. 12–40.

Strobe, G. W., Baker, E. M., and Badger, W. L., 1939, "Boiling-Film Heat Transfer Coefficients in a Long-Tube Vertical Evaporator," *Industrial and Engineering Chemistry,* Vol. 31, No. 2, pp. 200–206.

Tzan, Y. L., and Yang, Y. M., 1990, "Experimental Study of Surfactant Effects on Pool Boiling Heat Transfer," ASME JOURNAL OF HEAT TRANSFER, Vol. 112, pp. 207–212.

Westwater, J. W., 1956, "Boiling of Liquids," *Advances in Chemical Engineering,* Vol. 1, T. B. Drew and J. W. Hoopes, Jr., eds, Academic Press, New York.

Wu, W. T., Hu, C. L., and Yang, Y. M., 1993, "Surfactant Effect on Boiling Incipience and Bubble Growth Dynamics of Surface Boiling in Water," *Journal of the Chinese Institute of Chemical Engineers,* Vol. 24, No. 2, pp. 111–118.

Yang, Y. M., and Maa, J. R., 1983, "Pool Boiling of Dilute Surfactant Solutions," ASME JOURNAL OF HEAT TRANSFER, Vol. 105, pp. 190–192.

Yang, Y. M., 1990, "Dynamic Surface Effect on Boiling of Aqueous Surfactant Solutions," *International Communications in Heat and Mass Transfer,* Vol. 17, No. 6, pp. 711–727.

# Forced Convection Film Condensation on a Horizontal Tube—Influence of Vapor Boundary-Layer Separation

**S. B. Memory[1] and J. W. Rose[2]**

## Nomenclature

$d$ = diameter of condenser tube

$F$ = dimensionless parameter = $(gd\mu h_{fg})/(k\Delta TU_\infty^2)$

[1] Department of Mechanical Engineering, University of Miami, Coral Gables, Miami, FL.

[2] Department of Mechanical Engineering, Queen Mary and Westfield College, University of London, London, United Kingdom.

Contributed by the Heat Transfer Division and presented at the National Heat Transfer Conference, San Diego, California, August 9–12, 1992. Manuscript received by the Heat Transfer Division May 1993; revision received May 1994. Keywords: Condensation, Flow Separation, Forced Convection. Associate Technical Editor: V. K. Dhir.



Copyright © 1995 by ASME

Downloaded 12 Dec 2010 to 193.140.21.150. Redistribution subject to ASME license or copyright; see http://www.asme.org/terms/Terms_Use.cfm

$G$ = dimensionless parameter = $(k\Delta T/\mu h_{fg})(\rho\mu/\rho_v\mu_v)^{1/2}$
$g$ = acceleration due to gravity
$h_{fg}$ = latent heat of vaporization
$k$ = thermal conductivity of condensate
Nu = mean Nusselt number for a whole tube = $\alpha d/k$
$\mathrm{Nu}_{\pi/2}$ = mean Nusselt number for a half tube = $\alpha_{\pi/2} d/k$
$P$ = dimensionless parameter = $(\rho_v h_{fg}\mu/\rho k\Delta T)$
$P_\infty$ = saturation vapor pressure
$q$ = mean heat flux
Re = two-phase Reynolds number = $\rho U_\infty d/\mu$
$U_\infty$ = free-stream vapor velocity
$\alpha$ = mean heat transfer coefficient for a whole tube
$\alpha_{\pi/2}$ = mean heat transfer coefficient for a half tube
$\Delta T$ = mean temperature drop across the condensate film
$\xi$ = suction parameter = $(q/h_{fg})(d/\rho_v\mu_v U_\infty)^{1/2}$
$\mu$ = viscosity of condensate
$\mu_v$ = viscosity of vapor
$\rho$ = density of condensate
$\rho_v$ = density of vapor
$\varphi_s$ = angle around tube at which vapor boundary layer separates

## Introduction

For filmwise condensation on a horizontal tube at low vapor velocity, good agreement has been found between heat transfer measurements and laminar condensate flow theory. Based on the approach of Shekriladze and Gomelauri (1966) and Fujii et al. (1972), Rose (1984) gave the following equations for laminar condensate flow around a horizontal tube:

$$\mathrm{Nu}\,\mathrm{Re}^{-1/2} = \frac{0.9 + 0.728F^{1/2}}{(1 + 3.44F^{1/2} + F)^{1/4}} \tag{1}$$

$$\mathrm{Nu}\,\mathrm{Re}^{-1/2} = \frac{0.9(1 + G^{-1})^{1/3} + 0.728F^{1/2}}{(1 + 3.44F^{1/2} + F)^{1/4}} \tag{2}$$

where $F$ and $G$ are dimensionless parameters. In Eqs. (1) and (2), the effects of vapor boundary-layer separation and pressure variation in the condensate film are neglected. Equation (1) is a very accurate representation of numerical solutions first obtained by Shekriladze and Gomelauri (1966) who used the asymptotic (infinite suction) approximation for the shear stress at the vapor–condensate interface. Equation (2) incorporates a correction to account more accurately for the vapor shear stress based on the integral approach of Fujii et al. (1972).

In experiments with condensation of ethylene glycol with vertical vapor downflow over a horizontal tube at high vapor velocities, Memory and Rose (1986) found significant discrepancies between experiment and theory. An abrupt thickening of the condensate film on the lower half of the tube was also noted under certain conditions. This had been reported earlier by Nicol and Wallace (1976) for condensation of steam and attributed to separation of the vapor boundary-layer, which gives rise to an abrupt reduction in the tangential shear stress on the surface of the condensate film.

Fujii et al. (1979) obtained solutions (see also Lee and Rose, 1982) that included the effect of vapor boundary-layer separation. The vapor shear stress and vapor boundary-layer separation position were determined by an integral approach due to Truckenbrodt (1956) for uniform suction. Rose (1984) approximated the angle of separation given by this approach by:

$$\varphi_s = 1.76 + 0.164\xi + 0.00869\xi^2 \tag{3}$$

where $\xi$ is the suction parameter $(q/h_{fg})(d/\rho_v\mu_v U_\infty)^{1/2}$. By adopting the method of Truckenbrodt (1956) as modified by Fujii et al. (1979), Rose (1984) further obtained

$$\varphi_s = 2.93 - 1.02\exp(-0.147\xi - 0.0127\xi^2) \tag{4}$$

Mayhew et al. (1965), using an approximate analysis due to Prandtl (1935), gave an equation for the angle of vapor boundary-layer separation, again based on uniform suction, as

$$\varphi_s = \cos^{-1}(-(\xi/4.36)^2) \quad \text{for} \quad \xi < 4.36 \tag{5a}$$

$$\varphi_s = \pi \quad \text{for} \quad \xi > 4.36 \tag{5b}$$

Equations (3) and (5) predict that the vapor boundary layer does not separate for $\xi > 6.33$ and $\xi > 4.36$, respectively. Equation (4) predicts that the angle of separation approaches an asymptotic value of 168° with increasing $\xi$, i.e., that separation is not completely suppressed.

Rose (1984) included the effect of pressure variation in the condensate film in the presence of vapor flow around the tube and proposed the following conservative equation for the mean heat transfer coefficient:

$$\mathrm{Nu}\,\mathrm{Re}^{-1/2} = \frac{0.64(1 + 1.81P)^{0.209}(1 + G^{-1})^{1/3} + 0.728F^{1/2}}{(1 + 3.51F^{0.53} + F)^{1/4}} \tag{6}$$

In order to investigate uncertainties for the lower half of the tube, two types of experiment have been designed by the present authors to try and throw further light on the effects of separation; both were performed with vertical vapor downflow over a single horizontal tube. Measurements were first made for the upper half of the tube only where separation does not occur. The lower half of the tube was internally well insulated. In the second experiment a vertical "flap" was attached to the bottom of the tube to delay the point of separation (see Thwaites, 1947).

From the upper half of the tube only Eqs. (1), (2), and (6) become (see Memory, 1989)

$$\mathrm{Nu}_{\pi/2}\,\mathrm{Re}^{-1/2} = \frac{1.273 + 0.866F^{1/2}}{(1 + 3.51F^{0.53} + F)^{1/4}} \tag{7}$$

$$\mathrm{Nu}_{\pi/2}\,\mathrm{Re}^{-1/2} = \frac{1.273(1 + G^{-1})^{1/3} + 0.866F^{1/2}}{(1 + 3.51F^{0.53} + F)^{1/4}} \tag{8}$$

$$\mathrm{Nu}_{\pi/2}\,\mathrm{Re}^{-1/2} = \frac{1.273(1 + 1.81P)^{0.209}(1 + G^{-1})^{1/3} + 0.866F^{1/2}}{(1 + 3.51F^{0.53} + F)^{1/4}} \tag{9}$$

## Apparatus and Procedure

The apparatus is essentially the same as that used by Memory and Rose (1986). Ethylene glycol vapor flowed vertically downward over a horizontal copper test condenser tube through which cooling water passed. The vapor velocity was calculated from the precisely measured power input to the boilers with a small correction to account for the thermal loss from the apparatus. The coolant temperature rise was measured using a ten-junction thermopile, the measuring junctions being located after well-insulated mixing boxes. A second measurement of coolant temperature rise was taken from single thermocouples at inlet and exit from the condenser tube. The two values generally agreed to within 0.05 K. Great care was taken to ensure adequate isothermal immersion of the thermocouple leads and to prevent significant thermal conduction between the condenser tube and the body of the test section and the environment.

The vapor temperature was obtained from two thermocouples located in the test section 65 mm upstream of the condenser tube. The vapor pressure could be measured to within ±50 Pa using a mercury and ethylene glycol manometer fitted with a vernier scale. The highest estimated uncertainty in the experimental value of the heat transfer coefficient was approximately 8 percent and occurred at the lowest vapor pressure of 1 kPa and the lowest coolant flow rate of 0.4 l/min. At the highest vapor pressure of 15 kPa (with a similar coolant flow rate), the estimated uncertainty was always less than 2 percent.

Strenuous efforts were made to ensure that the apparatus was



Downloaded 12 Dec 2010 to 193.140.21.150. Redistribution subject to ASME license or copyright; see http://www.asme.org/terms/Terms_Use.cfm

leak-tight. With the boiler heaters off and the apparatus at ambient temperature at an absolute pressure of 500 Pa, the pressure rise in a 12 hour interval never exceeded 400 Pa (3 mm Hg). This "leak-rate" was checked frequently between test runs throughout the course of the investigation. The tube surfaces were also checked frequently through the viewing window during the tests to ensure complete wetting and film condensation.

Two methods were used to control the auxiliary condenser condensation rate so as to maintain steady pressures when operating with different vapor and coolant flow rates. One was to adjust the coolant temperature at inlet to the auxiliary condenser and the other was to admit air into the auxiliary condenser. Tests were carried out for several pressures in the range of 1–10 kPa. At each pressure tests were done for several vapor velocities.

The experimental condenser tubes are shown in Fig. 1. For the "half-tube" (Fig. 1*a*), copper was machined from the inside surface of the lower half of the tube to leave a wall thickness of only 0.5 mm. A half cylinder of PTFE ("teflon") was then inserted as shown. When calculating the heat transfer rate to the upper half of the tube, a small "fin" correction was made for heat transfer to and along the thin lower-side copper layer. The second tube (Fig. 1*b*) had a vertical strip of metal ("Thwaites (1947) flap") attached to the bottom of the tube parallel to the axis of the tube. The top of the strip fitted tightly into a slot 1.5 mm deep × 1.5 mm wide cut into the underside of the tube. Tests were conducted using both a copper and a stainless-steel strip to assess the fin contribution to the heat transfer due to the strip.

The wall temperature in each case was measured by thermocouples (three for the half-tube and six for the tube with flap) embedded in the tube wall at a diameter of 9.5 mm. The wall thermocouples were spaced evenly around the circumference of the tube, but offset from the top of the tube by 15 and 25 deg, respectively, for the half-tube and tube with flap as shown. The thermocouple junctions were located midway along the length of the tubes in longitudinally machined grooves (1.6 mm × 1.6 mm)

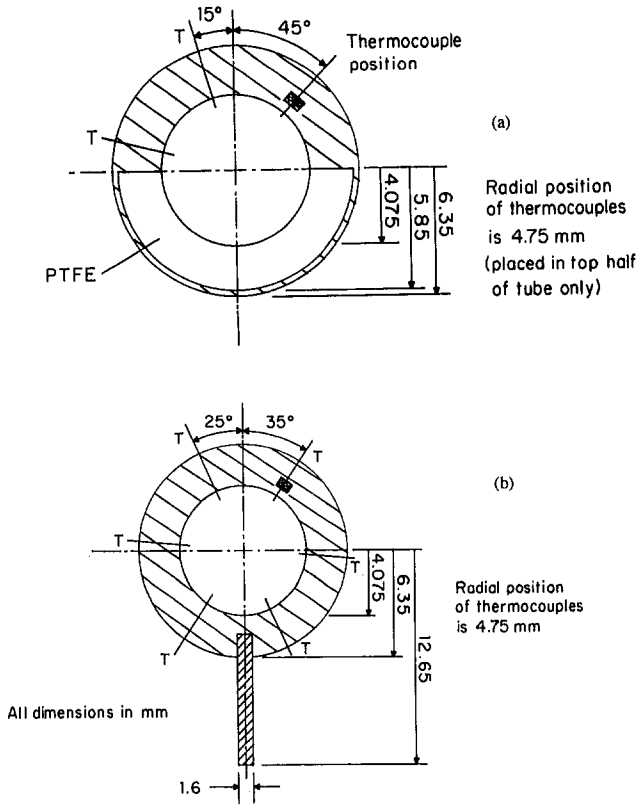



**Fig. 1 Test condenser tubes: (*a*) half tube; (*b*) tube fitted with Thwaites flap; *T* denotes position of wall thermocouple**

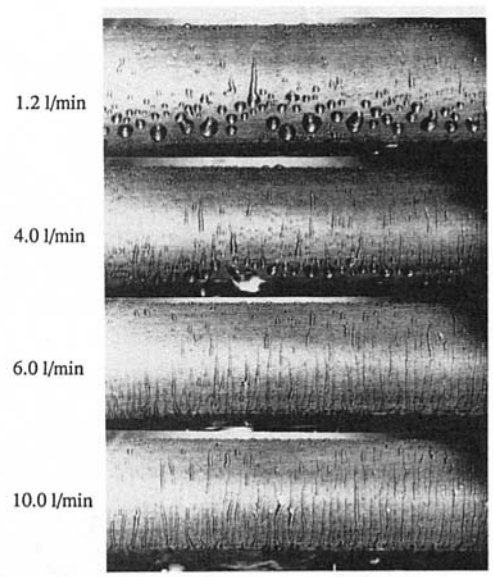



**Fig. 2 Dropwise condensation at a fixed vapor approach velocity ($U_\infty$ = 45 m/s) and four coolant flow rates (indicated to the left of the photograph)**

enclosed by tightly fitting soldered copper strips. The tubes were finished by copper plating and machining down to the required outside diameter. The wall outer surface temperature was taken as an arithmetic mean of the wall thermocouples, with a small correction to account for their depth below the surface.

## Dropwise Condensation Visual Investigation

During the course of the investigation, dropwise condensation occurred "fortuitously" due to contamination in the apparatus. Figure 2 shows a photograph of dropwise condensation during vapor downflow. During dropwise condensation, the position of vapor boundary-layer separation is indicated by the fact that below the separation point, the drops are almost stationary while higher on the tube, the droplets move rapidly down the surface under the influence of vapor shear stress. The angle of vapor boundary-layer separation from the top of the tube can thus be estimated from the photograph.

Photographs were taken at different vapor velocities, condensation rates and pressures. Values of $\varphi_s$ are compared with those calculated from Eqs. (3)–(5) in Fig. 3. It can be seen that the limited number of points are generally in fair agreement with

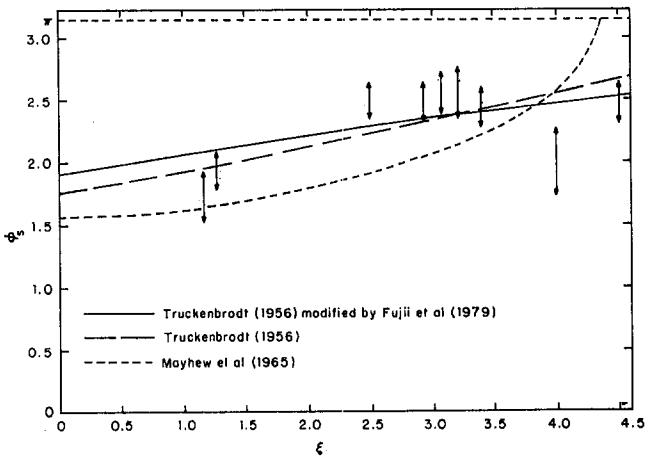



**Fig. 3 Comparison of separation angle estimated from photography with theory. Arrowheads denote limits of uncertainty.**



Downloaded 12 Dec 2010 to 193.140.21.150. Redistribution subject to ASME license or copyright; see http://www.asme.org/terms/Terms_Use.cfm

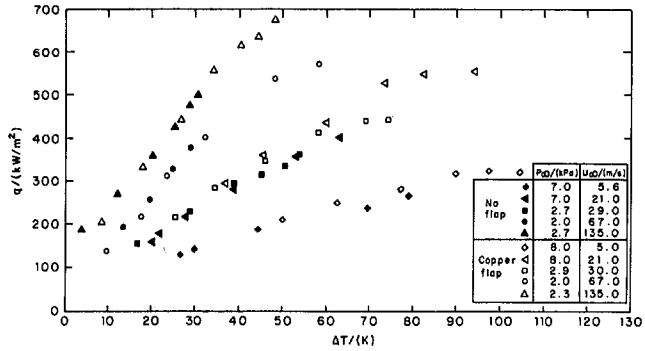



**Fig. 4 Dependence of heat flux on vapor-to-wall temperature difference for tubes with and without copper flap**

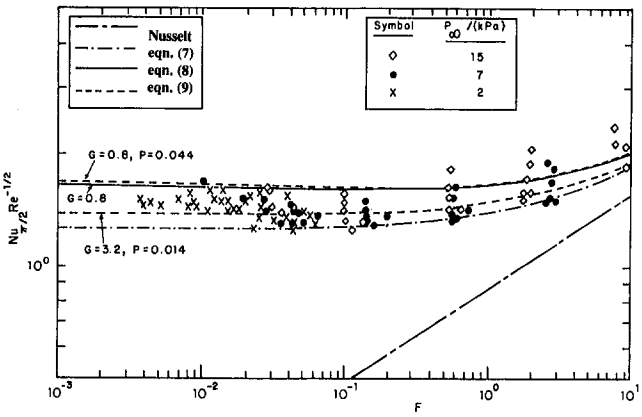



**Fig. 6 Comparison of corrected half-tube data with theory**

theory and are somewhat closer to Eqs. (3) and (4) than to Eq. (5).

## Results and Discussion

For the tube fitted with the Thwaites flap, it was expected that vapor boundary-layer separation would be delayed or suppressed and that maintenance of downward shear stress over a larger proportion of the surface would lead to higher heat transfer coefficients. Figure 4 shows the dependence of heat flux on mean vapor-to-wall temperature difference for the tube fitted with and without the copper flap under similar experimental conditions of vapor pressure and vapor velocity. It is clear that the Thwaites flap has little discernible effect on the mean heat transfer rate. However, below a vapor velocity of around 100 m/s, visual observation did indicate that the abrupt thickening of the condensate film (similar to that mentioned by Nicol and Wallace, 1976, and Fujii et al., 1979) moved back around the tube for increases in condensation rate. The fact that suppression of boundary-layer separation apparently has little effect on the heat transfer may in part be due to the smaller contribution from the lower (and thicker) part of the condensate film and also to the fact that vapor boundary-layer separation, with abrupt thickening of the condensate film, may lead to turbulence and enhanced heat transfer for the lower part of the tube.

Above 100 m/s, it was noted that the position of the abrupt thickening of the condensate film was insensitive to condensation rate and further increases in vapor velocity. This may be due to shock-induced boundary-layer separation (see Shapiro, 1953). For the present tube and duct dimensions, and for the vapor pressures used, it was estimated (see Memory, 1989) that local sonic conditions at the "edge" of the vapor boundary layer would occur at about the position of the abrupt thickening of the condensate film for a vapor approach velocity of around 110 m/s.

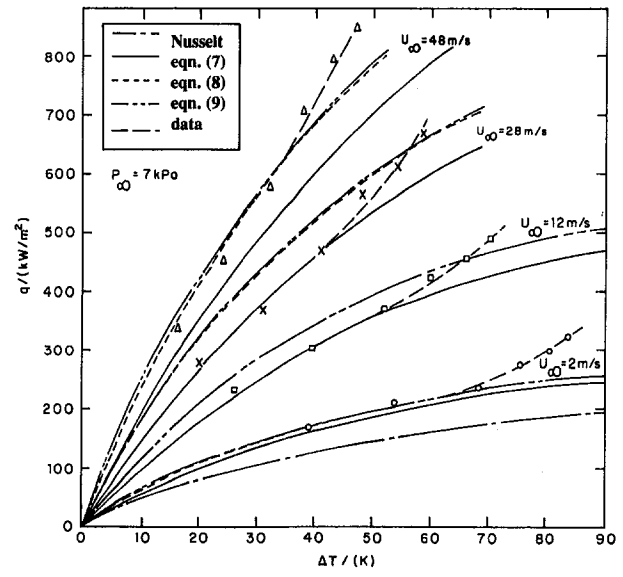



**Fig. 5 Dependence of heat flux on vapor-to-wall temperature difference for half-tube**

The half-tube experimental results are compared with Eqs. (7), (8), and (9) in Fig. 5. It may be seen that the data are in general agreement with theory except at the higher values of $\Delta T$ where the experimental data show an inflection, after which the heat flux increases more rapidly than indicated by laminar condensate flow theory. It is also seen that the inflection occurs at lower values of $\Delta T$ for higher vapor velocities. These facts are consistent with onset of turbulence in the condensate film at high vapor shear stress.

Figure 6 compares the half-tube data (for three vapor pressures) with theory on a dimensionless basis. Equation (9) is shown for the extreme combinations of $G$ and $P$ obtained from the data. The theoretical curves incorporate the interphase mass transfer correction discussed by Memory and Rose (1986). This correction was only significant at the lower pressures. [Note that the correction resulting from vapor boundary-layer separation (see Memory and Rose, 1986) is not required for the half-tube.] The agreement between experiment and theory is good and can be attributed to there being no uncertainties associated with the lower half of the tube.

The data in Fig. 6 indicate a slight upturn in the value of $\mathrm{Nu}\,\mathrm{Re}^{-1/2}$ for decreasing $F$ (increasing vapor velocity), similar to that reported by Memory and Rose (1986) for a whole tube. The minimum value of $\mathrm{Nu}\,\mathrm{Re}^{-1/2}$ for a whole tube was found to occur at a value of $F$ around 0.1 and was attributed by Memory and Rose to onset of turbulence in the condensate film. Figure 6 indicates that a minimum occurs at a similar value of $F$ for the half-tube and suggests onset of turbulence in the condensate film, prior to vapor boundary-layer separation, at high vapor shear stress.

## Conclusions

Evidence of vapor-boundary-layer separation has been seen in photographs of dropwise condensation. These indicate that vapor-boundary-layer separation occurs at locations broadly in agreement with theory.

For the tube fitted with the Thwaites flap, visual observation suggests that vapor-boundary-layer separation can be suppressed under conditions of strong suction for vapor approach velocities below about 100 m/s. However, no significant increase in the measured heat transfer was noted. This may be due to the presence of turbulence in the condensate film beyond the point of separation.

The half-tube data are in good agreement with laminar condensate film theory, with significantly less scatter than the data



Downloaded 12 Dec 2010 to 193.140.21.150. Redistribution subject to ASME license or copyright; see http://www.asme.org/terms/Terms_Use.cfm

for a whole tube. Discrepancies between experiment and theory for a whole tube are thought to be attributable to uncertainties (vapor-boundary-layer separation and turbulence) in the condensate film on the lower half of the tube.

## References


Fujii, T., Uehara, H., and Kurata, C., 1972, "Laminar Filmwise Condensation of Flowing Vapour on a Horizontal Cylinder," *Int. J. Heat Mass Transfer*, Vol. 5, pp. 235–246.

Fujii, T., Honda, H., and Oda, K., 1979, "Condensation of Steam on a Horizontal Tube—The Influence of Oncoming Vapor Velocity and Thermal Condition at the Tube Wall," *Condensation Heat Transfer*, 18th Nat. Heat Transfer Conf., San Diego, CA, pp. 35–43.

Lee, W. C., and Rose, J. W., 1982, "Filmwise Condensation on a Horizontal Tube—Effect of Vapour Velocity," *Proc. 7th Int. Heat Transfer Conf.*, Munich, Vol. 5, pp. 101–106.

Mayhew, Y. R., Griffiths, D. J., and Phillips, J. W., 1965, "Effect of Vapour Drag on Laminar Film Condensation on a Vertical Surface," *Proc. Inst. Mech. Eng.*, Vol. 180, pp. 280–289.

Memory, S. B., and Rose, J. W., 1986, "Filmwise Condensation of Ethylene Glycol on a Horizontal Tube at High Vapour Velocity," *Proc. 8th Int. Heat Transfer Conf.*, San Francisco, CA, Vol. 4, pp. 1607–1614.

Memory, S. B., 1989, "Forced Convection Film Condensation on a Horizontal Tube at High Vapour Velocity," PhD Thesis, University of London, United Kingdom.

Nicol, A. A., and Wallace, D. J., 1976, "Condensation With Appreciable Vapour Velocity and Variable Wall Temperature," *Symp. on Steam Turbine Condensers*, NEL Report No. 619, pp. 27–38.

Prandtl, L., 1935, "The Mechanics of Viscous Fluids," *Aerodynamic Theory*, W. F. Durand, ed., Vol. III, pp. 34–208.

Rose, J. W., 1984, "Effect of Pressure Gradient on Forced Convection Film Condensation on a Horizontal Tube," *Int. J. Heat Mass Transfer*, Vol. 27, pp. 39–47.

Shapiro, A. H., 1953, *The Dynamics and Thermodynamics of Compressible Fluid Flow*, Ronald Press Co., New York.

Shekriladze, I. G., and Gomelauri, V. I., 1966, "Theoretical Study of Laminar Film Condensation of Flowing Vapour," *Int. J. Heat Mass Transfer*, Vol. 9, pp. 581–591.

Thwaites, B., 1947, "The Production of Lift Independently of Incidence—The Thwaites Flap," R. & M. No. 2611, pp. 625–644.

Truckenbrodt, E., 1956, "Ein einfaches Naherungsverfahren zum Berechnen der Laminaren Riebungsicht mit Absangung," *Forschung Ing. Wes.*, Vol. 32, pp. 147–157.


# "Wrinkled" Film Boiling


## S. M. Lu[1] and D. J. Lee[1]


## Introduction

Low heat flux film boiling in a pool is noted for its smooth and regularly wavy vapor–liquid interface. Bubbles form and depart in an orderly manner. As the heat flux is increased, film boiling with very vigorous bubble formation and departure appears. The bubbles are considerably larger than those in the low-flux case. The low and high heat flux film boiling, by their appearances, will be respectively referred to as the laminar and turbulent film boiling.

Film boiling is also affected by the degree of subcooling. As the degree of subcooling increases, the vapor–liquid interface becomes more stable than that in saturated boiling and bubbles that depart from the interface are reduced in size quickly.

As both heat flux and subcooling are increased, a regime of film boiling with peculiar features is encountered. The smooth vapor–liquid interface becomes wrinkled and the film boiling is accompanied by noise and vibration. This film boiling will be called "wrinkled" film boiling in this paper.

The purpose of this paper is to report on the occurrence of wrinkled film boiling in pool. Zones in which wrinkled film boiling occurs are mapped experimentally. The effects of heating wire diameter, material, and degree of subcooling on the zone of wrinkled film boiling are investigated. A possible cause of wrinkled film boiling is suggested.

## Experimental

A parallelepiped pool of dimension 250 (W) × 200 (D) × 250 (H) mm was used. It was equipped with a cooling coil and an auxiliary heater for temperature regulation. The data acquisition system has been described by Lu and Lee (1991). Photographs were taken by a Strobo-Memo Drux C-2D1S camera. The sound generated in wrinkled film boiling was measured by a microphone attached to the pool wall and was recorded by an oscilloscope. The frequency of bubble departure in film boiling was measured by stroboscope and also by a He–Ne laser with a phototransducer (G1116, Kogen, Japan) as the light receiver. Methanol was used for boiling. The heating wires were: Kanthal A1 (a Fe–Al alloy) wire, 1.2 mm; Ni–Cr wire, 1.0 mm; DSD (a Fe–Al alloy) wire, 1.2, 1.0, 0.75, and 0.35 mm; and W wire, 0.60, 1.00, and 1.58 mm.

In the experiments, methanol was heated to the desired temperature. Then, a constant voltage (CV) heating method (Lu and Lee, 1991) was used to heat the test wire. The ends of the wires were not plated with copper so film boiling on the wire was obtained at a heat flux lower than the critical heat flux. The data recorded are total voltage, voltage drop across the test section of the wire, electric current, and the temperature of pool measured at a point 1 cm below the center of the wire. The estimated error for heat flux measurement was at most 2.7 percent, for bubble departure frequency, less than 1 Hz, and for liquid subcooling, less than 0.6 K.

## Results and Discussion

**1 Photographic Observation.** Figure 1(*a, b, c*) show photographs of laminar, wrinkled, and turbulent film boiling at 760 torr and $\Delta T_{sub}$ = 45°C, with 1.2 mm Kanthal A1 wire. Because of the logistics of mounting the background ruler, the numbers appear upside down.

Figure 1(*a*) shows that in laminar film boiling, the vapor–liquid interface is smooth. Wavelength is around 11 mm and bubble departure frequency is about 25.6 Hz. As the heat flux is increased, wrinkled film boiling occurs. This is shown in Fig. 1(*b*). The vapor–liquid interface wrinkles with noise and vibration. The heat flux in this case is about 57 percent more than that in Fig. 1(*a*); however, the brightness of the wire and the bubble size are not significantly different from Fig. 1(*a*). A portion of the input energy is thus dissipated in the form of noise and vibration. Bubbles form at wavelength around 17 mm, while the small wrinkles that are all over the vapor–liquid interface are at about 1 mm wavelength.

The sound generated in wrinkled film boiling was recorded. The sound wave is a series of wave clusters separated by a period of quiet time. An increase in heat flux increases the amplitude of the sound wave and decreases the quiet time. Over a large range of pool temperature, the frequency of sound in the wave clusters was found to be about 900 Hz for Kanthal A1 wire. Frequency is dependent on both wire material and wire diameter and independent of the degree of subcooling. For 0.6 mm tungsten wire, the frequency was found to be about 1350 Hz, which is close to the second natural frequency of 1200 Hz (Stokey, 1976).

Continued increase in heat flux intensifies wrinkling and noise. But then the phenomenon is taken over by a film boiling with distinctively subdued noise of different tone. The vapor–liquid interface regains smoothness. Bubbles are huge and boiling is


[1] Chemical Engineering Department, National Taiwan University, Taipei, Taiwan.



Contributed by the Heat Transfer Division of The American Society of Mechanical Engineers. Manuscript received by the Heat Transfer Division February 1994; revision received July 1994. Keywords: Boiling, Phase-Change Phenomena. Associate Technical Editor: V. K. Dhir.





Downloaded 12 Dec 2010 to 193.140.21.150. Redistribution subject to ASME license or copyright; see http://www.asme.org/terms/Terms_Use.cfm

for a whole tube. Discrepancies between experiment and theory for a whole tube are thought to be attributable to uncertainties (vapor-boundary-layer separation and turbulence) in the condensate film on the lower half of the tube.

## References


Fujii, T., Uehara, H., and Kurata, C., 1972, "Laminar Filmwise Condensation of Flowing Vapour on a Horizontal Cylinder," *Int. J. Heat Mass Transfer*, Vol. 5, pp. 235–246.

Fujii, T., Honda, H., and Oda, K., 1979, "Condensation of Steam on a Horizontal Tube—The Influence of Oncoming Vapor Velocity and Thermal Condition at the Tube Wall," *Condensation Heat Transfer*, 18th Nat. Heat Transfer Conf., San Diego, CA, pp. 35–43.

Lee, W. C., and Rose, J. W., 1982, "Filmwise Condensation on a Horizontal Tube—Effect of Vapour Velocity," *Proc. 7th Int. Heat Transfer Conf.*, Munich, Vol. 5, pp. 101–106.

Mayhew, Y. R., Griffiths, D. J., and Phillips, J. W., 1965, "Effect of Vapour Drag on Laminar Film Condensation on a Vertical Surface," *Proc. Inst. Mech. Eng.*, Vol. 180, pp. 280–289.

Memory, S. B., and Rose, J. W., 1986, "Filmwise Condensation of Ethylene Glycol on a Horizontal Tube at High Vapour Velocity," *Proc. 8th Int. Heat Transfer Conf.*, San Francisco, CA, Vol. 4, pp. 1607–1614.

Memory, S. B., 1989, "Forced Convection Film Condensation on a Horizontal Tube at High Vapour Velocity," PhD Thesis, University of London, United Kingdom.

Nicol, A. A., and Wallace, D. J., 1976, "Condensation With Appreciable Vapour Velocity and Variable Wall Temperature," *Symp. on Steam Turbine Condensers*, NEL Report No. 619, pp. 27–38.

Prandtl, L., 1935, "The Mechanics of Viscous Fluids," *Aerodynamic Theory*, W. F. Durand, ed., Vol. III, pp. 34–208.

Rose, J. W., 1984, "Effect of Pressure Gradient on Forced Convection Film Condensation on a Horizontal Tube," *Int. J. Heat Mass Transfer*, Vol. 27, pp. 39–47.

Shapiro, A. H., 1953, *The Dynamics and Thermodynamics of Compressible Fluid Flow*, Ronald Press Co., New York.

Shekriladze, I. G., and Gomelauri, V. I., 1966, "Theoretical Study of Laminar Film Condensation of Flowing Vapour," *Int. J. Heat Mass Transfer*, Vol. 9, pp. 581–591.

Thwaites, B., 1947, "The Production of Lift Independently of Incidence—The Thwaites Flap," R. & M. No. 2611, pp. 625–644.

Truckenbrodt, E., 1956, "Ein einfaches Naherungsverfahren zum Berechnen der Laminaren Riebungsicht mit Absangung," *Forschung Ing. Wes.*, Vol. 32, pp. 147–157.


# "Wrinkled" Film Boiling


## S. M. Lu[1] and D. J. Lee[1]


## Introduction

Low heat flux film boiling in a pool is noted for its smooth and regularly wavy vapor–liquid interface. Bubbles form and depart in an orderly manner. As the heat flux is increased, film boiling with very vigorous bubble formation and departure appears. The bubbles are considerably larger than those in the low-flux case. The low and high heat flux film boiling, by their appearances, will be respectively referred to as the laminar and turbulent film boiling.

Film boiling is also affected by the degree of subcooling. As the degree of subcooling increases, the vapor–liquid interface becomes more stable than that in saturated boiling and bubbles that depart from the interface are reduced in size quickly.

As both heat flux and subcooling are increased, a regime of film boiling with peculiar features is encountered. The smooth vapor–liquid interface becomes wrinkled and the film boiling is accompanied by noise and vibration. This film boiling will be called "wrinkled" film boiling in this paper.

The purpose of this paper is to report on the occurrence of wrinkled film boiling in pool. Zones in which wrinkled film boiling occurs are mapped experimentally. The effects of heating wire diameter, material, and degree of subcooling on the zone of wrinkled film boiling are investigated. A possible cause of wrinkled film boiling is suggested.

## Experimental

A parallelepiped pool of dimension 250 (W) × 200 (D) × 250 (H) mm was used. It was equipped with a cooling coil and an auxiliary heater for temperature regulation. The data acquisition system has been described by Lu and Lee (1991). Photographs were taken by a Strobo-Memo Drux C-2D1S camera. The sound generated in wrinkled film boiling was measured by a microphone attached to the pool wall and was recorded by an oscilloscope. The frequency of bubble departure in film boiling was measured by stroboscope and also by a He–Ne laser with a phototransducer (G1116, Kogen, Japan) as the light receiver. Methanol was used for boiling. The heating wires were: Kanthal A1 (a Fe–Al alloy) wire, 1.2 mm; Ni–Cr wire, 1.0 mm; DSD (a Fe–Al alloy) wire, 1.2, 1.0, 0.75, and 0.35 mm; and W wire, 0.60, 1.00, and 1.58 mm.

In the experiments, methanol was heated to the desired temperature. Then, a constant voltage (CV) heating method (Lu and Lee, 1991) was used to heat the test wire. The ends of the wires were not plated with copper so film boiling on the wire was obtained at a heat flux lower than the critical heat flux. The data recorded are total voltage, voltage drop across the test section of the wire, electric current, and the temperature of pool measured at a point 1 cm below the center of the wire. The estimated error for heat flux measurement was at most 2.7 percent, for bubble departure frequency, less than 1 Hz, and for liquid subcooling, less than 0.6 K.

## Results and Discussion

**1 Photographic Observation.** Figure 1(*a, b, c*) show photographs of laminar, wrinkled, and turbulent film boiling at 760 torr and $\Delta T_{sub}$ = 45°C, with 1.2 mm Kanthal A1 wire. Because of the logistics of mounting the background ruler, the numbers appear upside down.

Figure 1(*a*) shows that in laminar film boiling, the vapor–liquid interface is smooth. Wavelength is around 11 mm and bubble departure frequency is about 25.6 Hz. As the heat flux is increased, wrinkled film boiling occurs. This is shown in Fig. 1(*b*). The vapor–liquid interface wrinkles with noise and vibration. The heat flux in this case is about 57 percent more than that in Fig. 1(*a*); however, the brightness of the wire and the bubble size are not significantly different from Fig. 1(*a*). A portion of the input energy is thus dissipated in the form of noise and vibration. Bubbles form at wavelength around 17 mm, while the small wrinkles that are all over the vapor–liquid interface are at about 1 mm wavelength.

The sound generated in wrinkled film boiling was recorded. The sound wave is a series of wave clusters separated by a period of quiet time. An increase in heat flux increases the amplitude of the sound wave and decreases the quiet time. Over a large range of pool temperature, the frequency of sound in the wave clusters was found to be about 900 Hz for Kanthal A1 wire. Frequency is dependent on both wire material and wire diameter and independent of the degree of subcooling. For 0.6 mm tungsten wire, the frequency was found to be about 1350 Hz, which is close to the second natural frequency of 1200 Hz (Stokey, 1976).

Continued increase in heat flux intensifies wrinkling and noise. But then the phenomenon is taken over by a film boiling with distinctively subdued noise of different tone. The vapor–liquid interface regains smoothness. Bubbles are huge and boiling is


[1] Chemical Engineering Department, National Taiwan University, Taipei, Taiwan.



Contributed by the Heat Transfer Division of The American Society of Mechanical Engineers. Manuscript received by the Heat Transfer Division February 1994; revision received July 1994. Keywords: Boiling, Phase-Change Phenomena. Associate Technical Editor: V. K. Dhir.





Copyright © 1995 by ASME

Downloaded 12 Dec 2010 to 193.140.21.150. Redistribution subject to ASME license or copyright; see http://www.asme.org/terms/Terms_Use.cfm

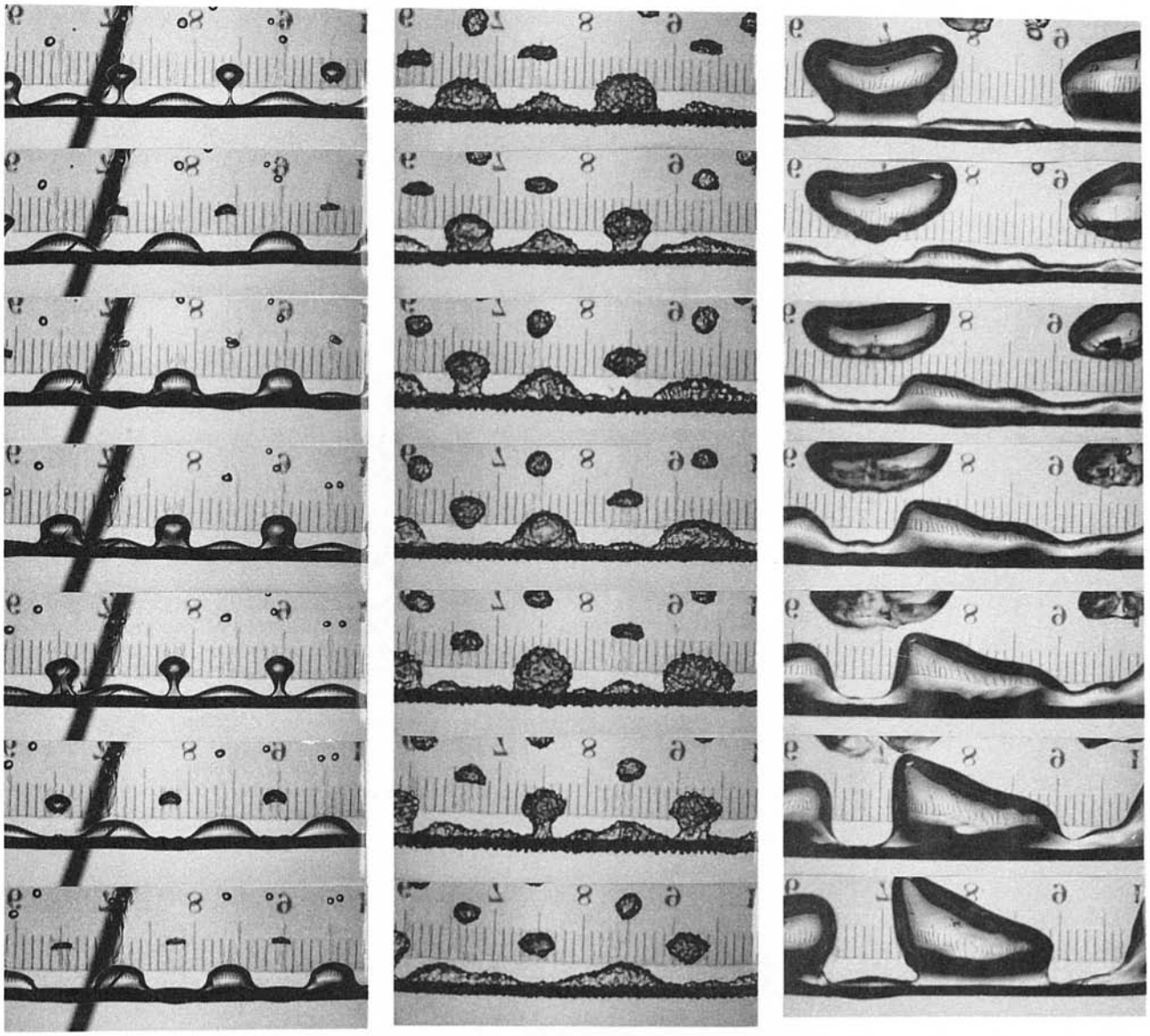


**Fig. 1 Photographs of film boiling, 760 torr, $\Delta T_{sub}$ = 45°C, Kanthal A1 wire, $D$ = 1.2 mm, $L$ = 133 mm. Film speed, 2.46 m/s, 12 mm slot, 4.88 ms per frame. Time sequence is from top to bottom: (*a*) laminar film boiling, $q$ = 600 kW/m²; (*b*) wrinkled film boiling, $q$ = 947 kW/m²; (*c*) turbulent film boiling, $q$ = 1150 kW/m²**

vigorous. This is shown in Fig. 1(*c*). Bubble sizes increased more than two times. Although the increase in heat flux was 21 percent of that in Fig. 2(*b*), the color of heating wire brightened up when boiling entered this region.

**2 Zones of Wrinkled Film Boiling.** Zones where wrinkled film boiling occurs are mapped on the plot of heat flux versus degree of subcooling. This is shown in Fig. 2 for 1.2 mm Kanthal A1 wire. Curves A and B are the lower and upper bounds of the zone of wrinkled film boiling obtained with increasing heat flux. Curves C and D are the upper and lower bounds of wrinkled film boiling obtained with decreasing heat flux. Thus, hysteresis exists. The frequency in sound clusters is not affected by hysteresis. In the following, the zone enveloped by curves B and D is taken as the zone of wrinkled film boiling. Figure 2 shows that the apex of the zone is at $\Delta T_{sub}$ = 32°C and $q$ = 800 kW/m². This minimum degree of subcooling is the critical subcooling to which the pool must be cooled for wrinkled film boiling to occur. For film boiling with the degree of subcooling smaller than the critical subcooling, changes from laminar to turbulent film boiling occurs without wrinkled film boiling. Such a zone is shown in Fig. 2 by the dotted lines bridged by the large letter I. The boundary, however, is fuzzy. The laminar and turbulent film boiling may, nevertheless, be distinguished by the frequency spectrum of the bubble departure described in the next section.

Figure 3 shows zones of wrinkled film boiling obtained for wires of different materials and diameters at 760 torr. Three points of interest should be noted. First, with the increase in wire diameter, the zone of wrinkled film boiling shifts toward the low heat flux region. Second, wires of different materials but the same diameter are in the same zone, like Ni–Cr and DSD wires of 1.0 mm, and Kanthal A1 and DSD wires of 1.2 mm. Third, for tungsten wire, a zone of wrinkled film boiling was found for the 0.6 mm wire, but not for the 1.0 and 1.58 mm wires. This last point will be discussed further later.

**3 Frequency Spectrum and Transition Film Boiling.** Visual observation shows that wrinkled film boiling, if it occurs, signals transition of laminar to turbulent film boiling. However, transition will occur irrespective of the existence of wrinkled film boiling if heat flux to film boiling is increased continuously.

Thus, in addition to visual observation, film boiling was also investigated by the frequency spectrum of bubble departure. The



Downloaded 12 Dec 2010 to 193.140.21.150. Redistribution subject to ASME license or copyright; see http://www.asme.org/terms/Terms_Use.cfm

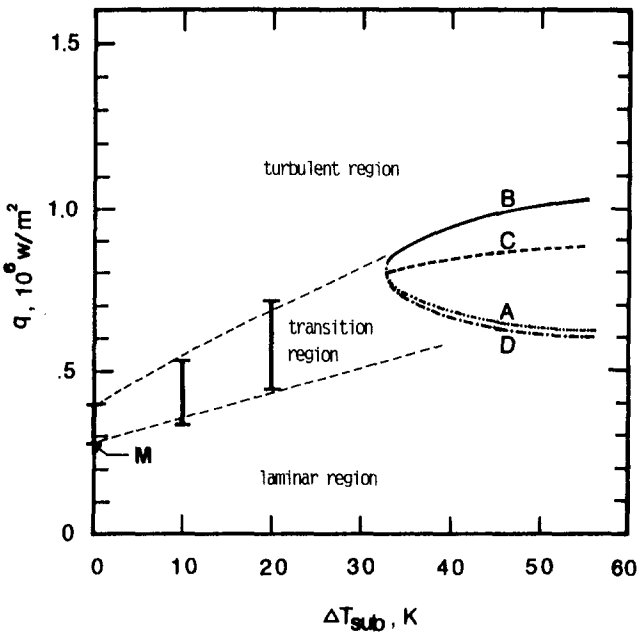



**Fig. 2 Zones of wrinkled film boiling, 760 torr, $\Delta T_{sub}$ = 45°C, Kanthal A1 wire, $D$ = 1.2 mm. Curves A and B and Curves C and D are envelopes of wrinkled film boiling obtained by increasing or decreasing heat flux. The region between the two dashed lines bridged by the large characters I is the estimated region of transition between laminar and turbulent film boiling at subcooling below the critical subcooling.**

presence of a vapor on the path of a laser beam causes the light to scatter and thus interrupt the signal to be received by the phototransducer. The voltage signals of the receiver were analyzed using fast Fourier transform to obtain the bubble departure frequency spectrum. Figures 4(*a, b, c*) show respectively the frequency spectrum of laminar, transition, and turbulent film boiling obtained under subcooling 25°C and 0.75 mm DSD wire. Figure 4(*a*) shows that for laminar film boiling at heat flux 805 kW/m$^2$, the frequency spectrum is monodispersed, with the major frequency at 22.7 Hz. This value is consistent with that measured by a stroboscope. Figure 4(*c*) shows that for turbulent film boiling at heat flux of 1290 kW/m$^2$, the frequency spectrum is flat, indicating random departure of bubbles. Figure 4(*b*) shows that for film boiling at the intermediate heat flux 934 kW/m$^2$, the frequency spectrum shows two peaks at 22 Hz and 23 Hz, respectively. These three film boiling may be located in Fig. 3 by using the heat flux and degree of subcooling given in Fig. 4. The results show that the film boiling shown by Figs. 4(*a, b, c*) are found near the curve that marks the zone of wrinkled film boiling for 0.75 mm DSD wire. Thus, both visual and spectral inspections point to the fact that wrinkled film boiling signals transition from laminar to turbulent film boiling.

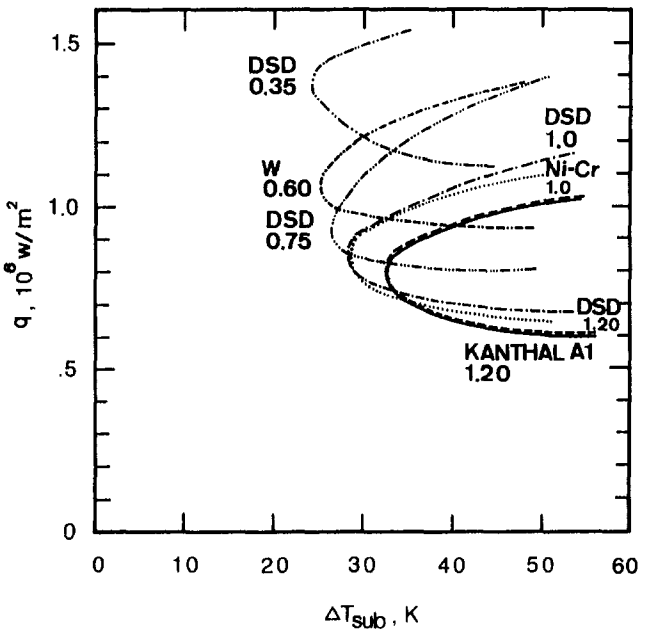



**Fig. 3 Zones of wrinkled film boiling for different wires, at 760 torr. Diameters are in mm.**

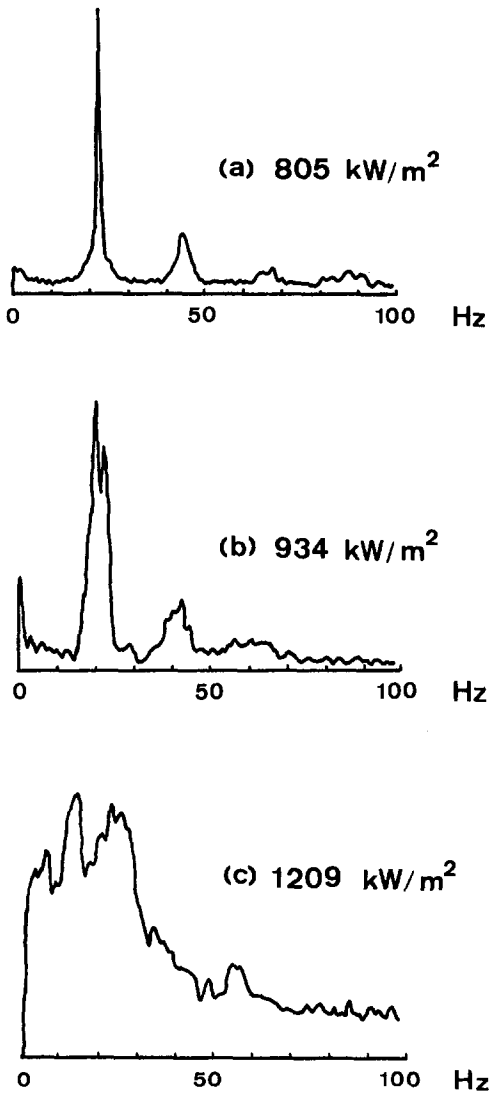



**Fig. 4 Frequency spectra of bubble departure, $\Delta T_{sub}$ = 25°C, DSD wire, 0.75 mm: (*a*) laminar film boiling, maximum amplitude 0.072; (*b*) wrinkled film boiling, maximum amplitude 0.031; (*c*) turbulent film boiling, maximum amplitude 0.020**

**4 Speculated Cause of Wrinkled Film Boiling.** It has already been noted that for tungsten wire with diameters 1.0 and 1.58 mm, wrinkled film boiling was not observed. As tungsten wire is stiffer than Kanthal A1 and DSD wires, the existence of wrinkled film boiling for the last two wires that have about the same diameter implies that wrinkled film boiling occurs when fluid–wire interaction satisfies certain conditions.

It is speculated here that wrinkled film boiling may be a manifestation of wire vibration induced by film boiling that satisfies some specific conditions. Manson (1967) reported that when bubbles depart periodically and uniformly from an infinitely long wire, the wire experiences an oscillatory force. As a result, in



Downloaded 12 Dec 2010 to 193.140.21.150. Redistribution subject to ASME license or copyright; see http://www.asme.org/terms/Terms_Use.cfm

laminar film boiling, the pressure along the wire oscillates harmonically at a major frequency $f_{max}$, which is usually much lower than the natural frequency of metal wire and no wrinkled film boiling occurs.

In transition film boiling, there are two or more frequencies of bubble departure. Experiments show that the frequency of bubble departure, and therefore the frequency of pressure impulse, is affected by the degree of subcooling. Figure 4($b$) shows that two frequencies were measured at 25°C of subcooling. The frequency of impulses exerted by the departure of bubbles may therefore be as high as $(f_{max})^2$. If the frequency of the impulse coincides with the natural frequency of the wire, "lock-in" vibration may occur and result in wrinkled film boiling. In turbulent film boiling, as shown in Fig. 4($c$), bubble departures occur at various frequencies. Interference of frequencies then occurs and as a result kills the chance for "lock in" and thus prevents wrinkled film boiling.

## Concluding Remarks

The effects of wire materials, diameters, and degrees of subcooling on wrinkled film boiling have been investigated experimentally. For a given wire material, the larger the diameter, the lower the heat flux of the zone of wrinkled film boiling. Wrinkled film boiling, if it occurs, signals the transition of laminar to turbulent film boiling. It is speculated that wrinkled film boiling is due to "lock in" in the frequency of pressure impulse imparted by the departing bubbles and the natural frequency of the wire.


## Acknowledgments

The authors are grateful to National Science Council for the support of project No. NSC79-0402-E002-04.


## References


Lu, S. M., and Lee, D. J. 1991, "The Effects of Heating Methods on Pool Boiling," *Int. J. Heat Mass Transfer*, Vol. 34, pp. 127–134.

Manson, L., 1967, "A Periodic Nonuniform Heat Transfer Mechanism in Film Boiling," ASME JOURNAL OF HEAT TRANSFER, Vol. 89, pp. 111–112.

Stokey, W. F., 1976, "Vibration of Systems Having Distributed Mass and Elasticity," in: *Shock and Vibration Handbook*, C. M. Harris, and C. E. Crede, ed., Chap. 7. pp. 13–15.


# The Effect of Inlet Subcooling on the Critical Heat Flux for Downward Flow With Upstream Compressibility


**X. C. Huang,[1] S. W. Ruan,[1] and G. Bartsch[1]**


## Introduction

Various systems involving two-phase flow and heat transfer, such as nuclear reactors, boilers, refineries, and refrigeration units are subject to thermohydraulic instability. A consequence is that the critical heat flux (CHF) may be much lower than under stable flow conditions. Mayinger et al. (1966) observed in a vertical test section for upflow with upstream compressibility two kinds of CHF conditions: a stable CHF and a pulsating CHF, with the latter being as much as 20 to 50 percent lower than the former. The pulsating CHF was preceded by low-frequency fluctuations of pressure, wall temperatures, and mass flux through the test section. An interesting fact is that below some specific inlet subcooling ($\Delta T_{sub}$), the pulsating flow condition did not lead to physical burnout of the test section and the pulsation could be suppressed by further increasing the heat flux until stable CHF occurred. As a result, the dependence of CHF on $\Delta T_{sub}$ showed a step function.

Recently, Ruan et al. (1992, 1993a, b, 1994) conducted systematic investigations on CHF for downward flow. It was found that the upstream devices, such as the plenum, preheater, and throttling valves have significant effects on the value and mechanism of the CHF. For stiff configurations without upstream compressibility the CHF could reach about the same value as for upflow. If, however, the upstream compressibility was present in the loop, the burnout occurred at much lower heat flux with the CHF being only about 20 percent of its stable value. This is much like the pulsating CHF observed by Mayinger et al. (1966) for upflow. Similarly, at very low $\Delta T_{sub}$, the large, low-frequency temperature fluctuations did not lead to physical burnout of the test section and could be suppressed by further increasing the heating power until CHF occurred for the second time. These two CHF conditions were called CHF 1 and CHF 2, respectively, and are illustrated in Fig. 1 for a mass flux of 200 kg/m$^2$s at atmospheric pressure. The dependence of CHF on $\Delta T_{sub}$ also displays a step function. It should be noted that due to the upstream compressibility CHF 2 is still much lower than stable CHF in a stiff system (Ruan et al., 1993b, 1994).

Because of the low value of the heat flux prior to CHF 1, bubbly flow occurs within the flow channel (the thermodynamic vapor quality at the test section outlet is usually near zero). CHF 1 corresponds to transition from bubbly flow to slug flow. This can be inferred from the large wall temperature fluctuations with long period over the lower half (outlet) of the test section. At large $\Delta T_{sub}$, the pulsating CHF 1 is characterized by an increasing amplitude of the wall temperature fluctuation with the increase of heating power, which may cause a physical burnout of the test section. For lower $\Delta T_{sub}$, however, slug flow has only limited consequences. Although similar wall temperature fluctuation also occurs, its magnitude usually does not exceed 400°C. With further increase of the heat flux, the large-amplitude fluctuation of wall temperatures gradually disappears, indicating that a stable vapor core has formed within the flow channel. Annular flow prevails to the occurrence of CHF 2.

The flow patterns at different heat flux levels are also indicated in Fig. 1. It immediately suggests that the first boiling crisis CHF

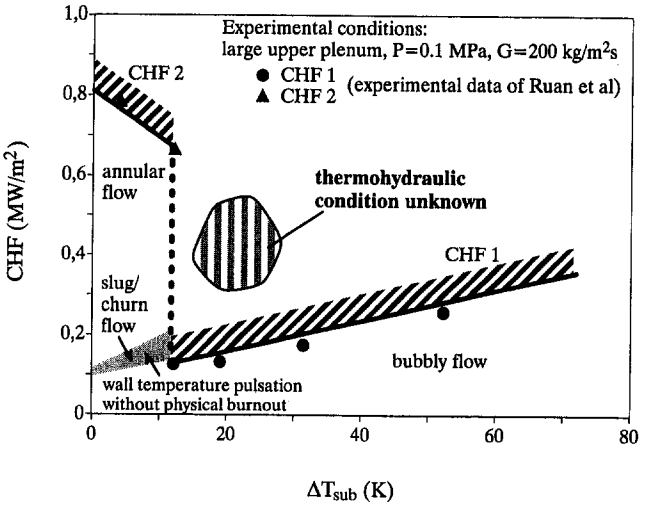



**Fig. 1 Two different critical heat flux conditions for downward flow with upstream compressibility observed by Ruan et al.**


[1] Institut für Energietechnik, TU Berlin, Marchstr. 18, 10587 Berlin, Federal Republic of Germany.



Contributed by the Heat Transfer Division of THE AMERICAN SOCIETY OF MECHANICAL ENGINEERS. Manuscript received by the Heat Transfer Division September 1993; revision received April 1994. Keywords: Boiling, Flow Instability, Phase-Change Phenomena. Associate Technical Editor: L. C. Witte.





Downloaded 12 Dec 2010 to 193.140.21.150. Redistribution subject to ASME license or copyright; see http://www.asme.org/terms/Terms_Use.cfm

laminar film boiling, the pressure along the wire oscillates harmonically at a major frequency $f_{max}$, which is usually much lower than the natural frequency of metal wire and no wrinkled film boiling occurs.

In transition film boiling, there are two or more frequencies of bubble departure. Experiments show that the frequency of bubble departure, and therefore the frequency of pressure impulse, is affected by the degree of subcooling. Figure 4($b$) shows that two frequencies were measured at 25°C of subcooling. The frequency of impulses exerted by the departure of bubbles may therefore be as high as $(f_{max})^2$. If the frequency of the impulse coincides with the natural frequency of the wire, "lock-in" vibration may occur and result in wrinkled film boiling. In turbulent film boiling, as shown in Fig. 4($c$), bubble departures occur at various frequencies. Interference of frequencies then occurs and as a result kills the chance for "lock in" and thus prevents wrinkled film boiling.

## Concluding Remarks

The effects of wire materials, diameters, and degrees of subcooling on wrinkled film boiling have been investigated experimentally. For a given wire material, the larger the diameter, the lower the heat flux of the zone of wrinkled film boiling. Wrinkled film boiling, if it occurs, signals the transition of laminar to turbulent film boiling. It is speculated that wrinkled film boiling is due to "lock in" in the frequency of pressure impulse imparted by the departing bubbles and the natural frequency of the wire.


## Acknowledgments

The authors are grateful to National Science Council for the support of project No. NSC79-0402-E002-04.


## References


Lu, S. M., and Lee, D. J. 1991, "The Effects of Heating Methods on Pool Boiling," *Int. J. Heat Mass Transfer*, Vol. 34, pp. 127–134.

Manson, L., 1967, "A Periodic Nonuniform Heat Transfer Mechanism in Film Boiling," ASME JOURNAL OF HEAT TRANSFER, Vol. 89, pp. 111–112.

Stokey, W. F., 1976, "Vibration of Systems Having Distributed Mass and Elasticity," in: *Shock and Vibration Handbook*, C. M. Harris, and C. E. Crede, ed., Chap. 7. pp. 13–15.


# The Effect of Inlet Subcooling on the Critical Heat Flux for Downward Flow With Upstream Compressibility


**X. C. Huang,[1] S. W. Ruan,[1] and G. Bartsch[1]**


## Introduction

Various systems involving two-phase flow and heat transfer, such as nuclear reactors, boilers, refineries, and refrigeration units are subject to thermohydraulic instability. A consequence is that the critical heat flux (CHF) may be much lower than under stable flow conditions. Mayinger et al. (1966) observed in a vertical test section for upflow with upstream compressibility two kinds of CHF conditions: a stable CHF and a pulsating CHF, with the latter being as much as 20 to 50 percent lower than the former. The pulsating CHF was preceded by low-frequency fluctuations of pressure, wall temperatures, and mass flux through the test section. An interesting fact is that below some specific inlet subcooling ($\Delta T_{sub}$), the pulsating flow condition did not lead to physical burnout of the test section and the pulsation could be suppressed by further increasing the heat flux until stable CHF occurred. As a result, the dependence of CHF on $\Delta T_{sub}$ showed a step function.

Recently, Ruan et al. (1992, 1993a, b, 1994) conducted systematic investigations on CHF for downward flow. It was found that the upstream devices, such as the plenum, preheater, and throttling valves have significant effects on the value and mechanism of the CHF. For stiff configurations without upstream compressibility the CHF could reach about the same value as for upflow. If, however, the upstream compressibility was present in the loop, the burnout occurred at much lower heat flux with the CHF being only about 20 percent of its stable value. This is much like the pulsating CHF observed by Mayinger et al. (1966) for upflow. Similarly, at very low $\Delta T_{sub}$, the large, low-frequency temperature fluctuations did not lead to physical burnout of the test section and could be suppressed by further increasing the heating power until CHF occurred for the second time. These two CHF conditions were called CHF 1 and CHF 2, respectively, and are illustrated in Fig. 1 for a mass flux of 200 kg/m$^2$s at atmospheric pressure. The dependence of CHF on $\Delta T_{sub}$ also displays a step function. It should be noted that due to the upstream compressibility CHF 2 is still much lower than stable CHF in a stiff system (Ruan et al., 1993b, 1994).

Because of the low value of the heat flux prior to CHF 1, bubbly flow occurs within the flow channel (the thermodynamic vapor quality at the test section outlet is usually near zero). CHF 1 corresponds to transition from bubbly flow to slug flow. This can be inferred from the large wall temperature fluctuations with long period over the lower half (outlet) of the test section. At large $\Delta T_{sub}$, the pulsating CHF 1 is characterized by an increasing amplitude of the wall temperature fluctuation with the increase of heating power, which may cause a physical burnout of the test section. For lower $\Delta T_{sub}$, however, slug flow has only limited consequences. Although similar wall temperature fluctuation also occurs, its magnitude usually does not exceed 400°C. With further increase of the heat flux, the large-amplitude fluctuation of wall temperatures gradually disappears, indicating that a stable vapor core has formed within the flow channel. Annular flow prevails to the occurrence of CHF 2.

The flow patterns at different heat flux levels are also indicated in Fig. 1. It immediately suggests that the first boiling crisis CHF

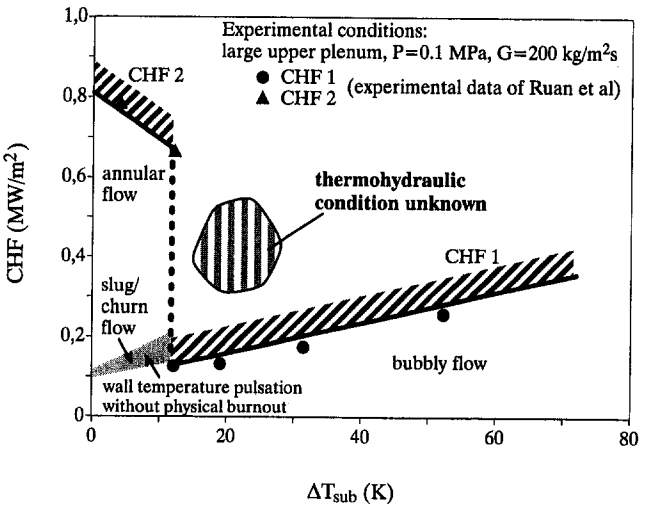



**Fig. 1 Two different critical heat flux conditions for downward flow with upstream compressibility observed by Ruan et al.**


[1] Institut für Energietechnik, TU Berlin, Marchstr. 18, 10587 Berlin, Federal Republic of Germany.



Contributed by the Heat Transfer Division of THE AMERICAN SOCIETY OF MECHANICAL ENGINEERS. Manuscript received by the Heat Transfer Division September 1993; revision received April 1994. Keywords: Boiling, Flow Instability, Phase-Change Phenomena. Associate Technical Editor: L. C. Witte.





Copyright © 1995 by ASME

Downloaded 12 Dec 2010 to 193.140.21.150. Redistribution subject to ASME license or copyright; see http://www.asme.org/terms/Terms_Use.cfm

1 represents an unoverridable barrier for transition from bubbly flow through slug/churn flow to the annular flow when the experiments are carried out in the conventional way, i.e., increasing the heating power with all inlet conditions being held constant. However, it does not exclude the possibility that annular flow exists behind the barrier, and can be reached in a special way. In the following, experimental verification of this idea will be described.

## Experimental Apparatus and Procedure

The experimental apparatus (Fig. 2) is the same as that used by Ruan et al. (1992, 1993a, b, 1994). The main components of the water loop are the pump, turbine flowmeters, preheaters, water-vapor separator, pressurizer, condenser, cooler, filters, and the ion-exchanger. Dual-distilled water is used as the test fluid, whose electrical conductivity is kept less than 0.1 $\mu$S/cm. The test section is an Inconel 600 tube 399 mm long with an outer diameter of 12 mm and a wall thickness of 1.5 mm. It was heated with a DC power supply (15 V, 2500 A). Sixteen chromel-alumel thermocouples were fixed with clamps on the outside surface of the test section to measure the wall temperature and to protect the test section from physical burnout. The power to the test section was automatically cut off when one of the thermocouple readings exceeded a preset value of about 600°C.

The uncertainty of heat flux and inlet subcooling were estimated to be within ±4 percent and ±1 K.

In the present work, a large upper plenum (Ruan et al., 1993b, 1994) consisting of the water-vapor separator, pressurizer, and condenser was used. Its compressibility can be taken as infinite due to the large compressible volume. The flow entered the test section via the water-vapor separator and was led to the cooler after leaving the test section (arrows in Fig. 2).

The inlet subcooling was adjusted using two preheaters. Preheater 1 (41.5 kW) can automatically maintain a constant outlet temperature. Preheater 2 (about 1 kW, only manually adjustable), located just before the entrance of the water-vapor separator, was used for very small inlet subcooling conditions, at which the wall temperature pulsations of CHF 1 dies down with the further increase of heat flux.

An experiment begins at a very small inlet subcooling with preheater 2 being switched on fully. The power to the test section is then increased slowly and continuously using a function generator. For small inlet subcooling, slug flow can be easily traversed without causing unacceptable overheating of the test section wall. The heat flux can then be further increased to a level sufficiently higher than that of the slug/churn flow, but lower than CHF 2. The small wall temperature fluctuations and strong vapor condensation in the cooler indicate the existence of annular flow in the test section.

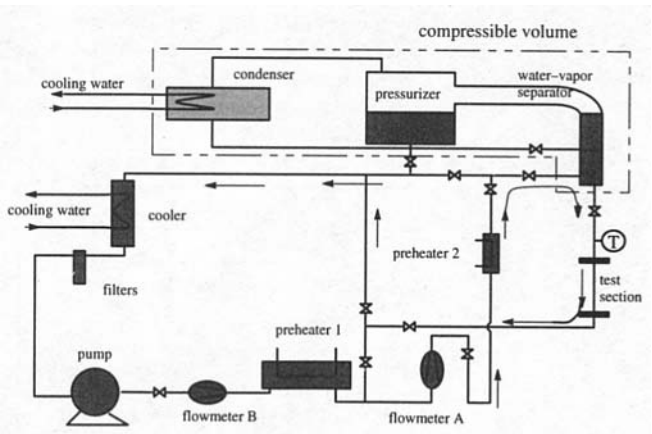



**Fig. 2 The experimental apparatus showing the water loop and the upper plenum**

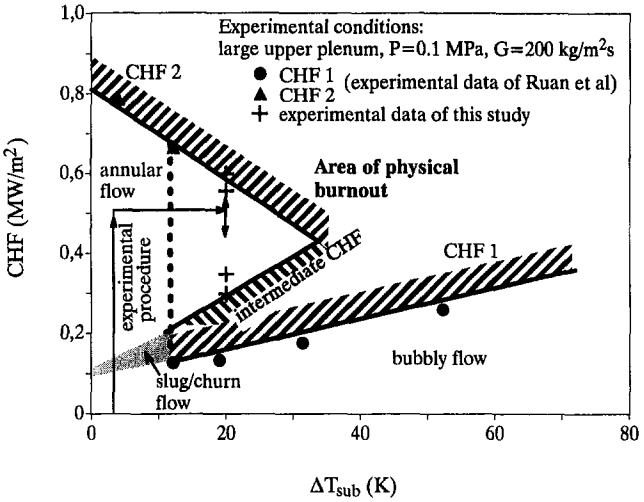



**Fig. 3 Experimental results of the three critical heat flux conditions**

## Experimental Results

All tests were conducted at atmospheric pressure with a mass flux of 200 kg/m$^2$-s, which corresponds approximately to the bubble rising velocity in a still pool, so that countercurrent flow of vapor and water is at its most critical condition. After the heat flux was increased to 51 MW/m$^2$ at a $\Delta T_{sub}$ of about 4 K, preheater 2 was shut down. It has been confirmed that annular flow does not break down despite the gradually increased $\Delta T_{sub}$. Annular flow still existed as $\Delta T_{sub}$ increased to about 20 K after 10 minutes; see Fig. 3. To check the stability of the annular flow at higher $\Delta T_{sub}$, this operating point was maintained for 40 minutes in our first experiment.

One of the characteristics of annular flow at large $\Delta T_{sub}$ is that condensation occurs not only downstream of the test section, but also just above the inlet of the test section, indicating that part of the vapor produced in the test section rises to the inlet. This causes a variation of the inlet temperature or $\Delta T_{sub}$ with the heat flux applied to the test section. For this reason, the steady-state $\Delta T_{sub}$ after the shutdown of the heating power, rather than $\Delta T_{sub}$ at CHF, was used for the presentation of our experimental results (Fig. 3) as practiced by Ruan et al. (1993b, 1994).

After annular flow has been established at large $\Delta T_{sub}$, an increase of heat flux should lead to dryout of the test section. However, it is not obvious what will happen if the heat flux is reduced, although in the normal sense a reduction of power should reduce the burnout danger. An increase of the heating power indeed led to a dryout condition, which is similar to CHF 2 at low subcoolings, but at lower heat flux as shown in Fig. 3. The reduction of heat flux with $\Delta T_{sub}$ = 20 K led to another critical condition at about 0.30 MW/m$^2$, which is higher than CHF 1 at the same $\Delta T_{sub}$. This critical condition represents a lower limit of the heat supply to the test section, below which annular flow cannot be sustained. Temporarily, we call this critical condition the intermediate CHF.

Figure 3 is an extension of Fig. 1 with the new CHF data obtained as described above. It shows three critical conditions represented by three independent straight lines. More experimental results will be required to verify the linear relationship for the intermediate CHF. The upper and lower margins of the slug/churn flow at low $\Delta T_{sub}$ (shaded in Figs. 1 and 3) represent the degenerated intermediate CHF and CHF 1 condition, so that fluctuation of the wall temperature does not lead to physical burnout of the test section.

## Conclusions

These results show that the dependence of CHF for downward flow on $\Delta T_{sub}$ in a loop with upstream compressibility is more



Downloaded 12 Dec 2010 to 193.140.21.150. Redistribution subject to ASME license or copyright; see http://www.asme.org/terms/Terms_Use.cfm

complicated than assumed up to now. Three different kinds of CHF may occur for a single $\Delta T_{sub}$, so that a single linear correlation for CHF versus $\Delta T_{sub}$ is far from sufficient. The existence of the intermediate CHF shows that the critical condition does not always occur as an upper limit of the local heat flux, but also as a lower limit. This may explain some special burnout phenomena encountered in complicated configurations such as in the rod bundle of a nuclear reactor core with downward flow. The "Z" form of the burnout boundary in Fig. 3 suggests that the specific CHF that occurs for a given $\Delta T_{sub}$ depends on the course of the process. If the boiling channel is directly heated under constant inlet conditions, only CHF 1 and part of CHF 2 can be observed. In practical situations with possible change of the local thermo-hydraulic conditions the operating point may be trapped in the dead corner in Fig. 3. In this case burnout cannot be avoided by simply reducing the heat flux to the boiling surface.

Some preliminary experiments show that for a mass flux higher than 1000 kg/m$^2$s, CHF 1 and the intermediate CHF do not occur at all, indicating that the behavior observed in this study might occur only at low mass fluxes. The complicated subcooling effect is believed to be caused by the compressibility-induced flow instability. A more detailed observation of the mechanism based on transient wall temperature measurements will be published soon.

## References


Mayinger, F., Schad, O., and Weiss, E., 1966, "Der Einfluss der hydrodynamischen Bedingungen auf die kritische Heizflächenbelastung beim Sieden," *Brennst.-Wärme-Kraft*, Vol. 18, pp. 288–294.

Ruan, S. W., Bartsch, G., Schreoder-Richter, G., and Yang, S. M., 1992, "Experimental Study of the Critical Heat Flux in Downflow Boiling With Upstream Compressibility," presented at the Joint Conference of 3rd ISHT and 5th ISTP (JCHTT), Beijing, Oct. 6–10.

Ruan, S. W., Bartsch, G., and Yang, S. M., 1993a, "Effects of Upper Plenum on the Critical Heat Flux of Downward Flow," presented at the 6th International Symposium on Transport Phenomena in Thermal Engineering, Seoul, May 9–13.

Ruan, S. W., Bartsch, G., and Yang, S. M., 1993b, "Characteristics of the Critical Heat Flux for Downward Flow in a Vertical Tube at Low Flow Rate and Low Pressure Conditions," presented at the 3rd World Conference on Experimental Heat Transfer, Fluid Mechanics and Thermodynamics, Honolulu, HI, Oct. 31–Nov. 5.

Ruan, S. W., Bartsch, G., and Yang, S. M., 1994, "Characteristics of the Critical Heat Flux for Downward Flow in a Vertical Tube at Low Flow Rate and Low Pressure Conditions," *Experimental Thermal and Fluid Science*, Vol. 7, No. 3.


# Condensation of Nonazeotropic Binary Refrigerant Mixtures Including R22 as a More Volatile Component Inside a Horizontal Tube


**M. Shizuya,[1] M. Itoh,[1] and K. Hijikata[2]**


## Nomenclature

$Cp_L$ = liquid isobaric specific heat of refrigerant
$g$ = gravitational acceleration
Ga = Galileo number = $gd^3/\upsilon_L^2$
$H$ = ratio of sensible to latent heat = $Cp_L(T_{sat} - T_w)/\Delta h_V$
$\Delta h_V$ = latent heat of refrigerant vaporization
$M$ = mass flow rate
$\bar{M}$ = nondimensional mass flow rate = $M/d\eta_L$
$\bar{M}_L$ = nondimensional liquid mass flow rate = $M(1 - X)/d\eta_L$
$Pr_L$ = liquid Prandtl number of refrigerant
$Re_L$ = liquid Reynolds number = $4M(1 - X)/\pi d\eta_L$
$\eta_L$ = liquid viscosity of refrigerant
$\nu_L$ = liquid kinematic viscosity of refrigerant
$\rho_L$ = liquid density of refrigerant
$\rho_v$ = vapor density of refrigerant

## Introduction

Optimal use of nonazeotropic refrigerant mixtures as working fluids in heat pump and refrigeration systems allows higher coefficients of performance and wider temperature ranges than pure refrigerants. However, these mixtures also have some disadvantages. The greatest problem is that performance is significantly reduced during phase change in heat exchangers compared to pure refrigerants.

Limited heat transfer has been reported for refrigerant mixture condensation inside a horizontal tube (Koyama et al., 1988, 1990; Mochizuki et al., 1988; Inoue et al., 1988). Thus, neither generalized correlations nor the conditions for heat transfer reduction when comparing mixtures with pure refrigerants, are well understood yet.

This paper reports local condensation heat transfer of refrigerant mixtures flowing inside a horizontal tube with smooth or grooved surfaces. Three binary mixtures of R22 and less volatile components, and their four pure refrigerants, are tested to clarify the effect of refrigerant properties on heat transfer. Smooth and grooved tube data are used to compare heat transfer improvement by surface grooving between refrigerant mixtures and their pure components.

## Experimental Apparatus and Procedure

**Tested Refrigerants.** For refrigerant mixtures, R22 was selected as a more volatile component and R142b, R114, and R123 were selected as less volatile components. Four pure refrigerants of these mixture components were also tested. The basic properties of each pure refrigerant are summarized in Table 1. Among the less volatile refrigerants, R142b and R123 are possible alternative refrigerants with very low ozone depletion potential. Although R114 is not such an alternative, it was selected because of its intermediate boiling temperature between R142b and R123, and also because similar heat transfer has been reported when it is mixed with R22 (Koyama et al., 1988, 1990).

Since our main objective was to clarify the basic heat transfer characteristics of refrigerant mixtures compared to pure refrigerants, mole fraction ratios were limited to almost even values for respective mixtures (R22 ratios: R22/142b—54 percent, R22/114 and R22/123—50 percent).

**Table 1 Thermophysical properties of single refrigerant**

| Refrigerant | R22 | R142b | R114 | R123 |
|---|---|---|---|---|
| Molecular formula | $CHClF_2$ | $CH_3CClF_2$ | $CClF_2CClF_2$ | $CHClCF_3$ |
| Molecular weight | 86.5 | 100.5 | 170.9 | 152.9 |
| Boiling temp. (K)* | 232.4 | 263.4 | 277.0 | 300.3 |
| Saturation pressure (MPa)** | 1.96 | 0.69 | 0.45 | 0.22 |
| Liq. viscosity (Pa·s)** | $0.13\times10^{-3}$ | $0.26\times10^{-3}$ | $0.27\times10^{-3}$ | $0.33\times10^{-3}$ |
| Liq. thermal conductivity (W/m·K)** | $74\times10^{-6}$ | $74\times10^{-6}$ | $60\times10^{-6}$ | $69\times10^{-6}$ |
| Latent heat (kJ/kg)** | 156.6 | 188.9 | 118.8 | 160.5 |

(* : at atmospheric pressure, ** : saturated state at 333 K)


[1] Mechanical Engineering Research Laboratory, Hitachi, Ltd., Tsuchiura, Ibaraki 300, Japan.

[2] Department of Mechanical Engineering Science, Tokyo Institute of Technology, Meguro, Tokyo 152, Japan.



Contributed by the Heat Transfer Division of THE AMERICAN SOCIETY OF MECHANICAL ENGINEERS. Manuscript received by the Heat Transfer Division May 1993, revision received July 1994. Keywords: Condensation. Associate Technical Editor: L. C. Witte.





Downloaded 12 Dec 2010 to 193.140.21.150. Redistribution subject to ASME license or copyright; see http://www.asme.org/terms/Terms_Use.cfm

complicated than assumed up to now. Three different kinds of CHF may occur for a single $\Delta T_{sub}$, so that a single linear correlation for CHF versus $\Delta T_{sub}$ is far from sufficient. The existence of the intermediate CHF shows that the critical condition does not always occur as an upper limit of the local heat flux, but also as a lower limit. This may explain some special burnout phenomena encountered in complicated configurations such as in the rod bundle of a nuclear reactor core with downward flow. The "Z" form of the burnout boundary in Fig. 3 suggests that the specific CHF that occurs for a given $\Delta T_{sub}$ depends on the course of the process. If the boiling channel is directly heated under constant inlet conditions, only CHF 1 and part of CHF 2 can be observed. In practical situations with possible change of the local thermo-hydraulic conditions the operating point may be trapped in the dead corner in Fig. 3. In this case burnout cannot be avoided by simply reducing the heat flux to the boiling surface.

Some preliminary experiments show that for a mass flux higher than 1000 kg/m$^2$s, CHF 1 and the intermediate CHF do not occur at all, indicating that the behavior observed in this study might occur only at low mass fluxes. The complicated subcooling effect is believed to be caused by the compressibility-induced flow instability. A more detailed observation of the mechanism based on transient wall temperature measurements will be published soon.

## References


Mayinger, F., Schad, O., and Weiss, E., 1966, "Der Einfluss der hydrodynamischen Bedingungen auf die kritische Heizflächenbelastung beim Sieden," *Brennst.-Wärme-Kraft*, Vol. 18, pp. 288–294.

Ruan, S. W., Bartsch, G., Schreoder-Richter, G., and Yang, S. M., 1992, "Experimental Study of the Critical Heat Flux in Downflow Boiling With Upstream Compressibility," presented at the Joint Conference of 3rd ISHT and 5th ISTP (JCHTT), Beijing, Oct. 6–10.

Ruan, S. W., Bartsch, G., and Yang, S. M., 1993a, "Effects of Upper Plenum on the Critical Heat Flux of Downward Flow," presented at the 6th International Symposium on Transport Phenomena in Thermal Engineering, Seoul, May 9–13.

Ruan, S. W., Bartsch, G., and Yang, S. M., 1993b, "Characteristics of the Critical Heat Flux for Downward Flow in a Vertical Tube at Low Flow Rate and Low Pressure Conditions," presented at the 3rd World Conference on Experimental Heat Transfer, Fluid Mechanics and Thermodynamics, Honolulu, HI, Oct. 31–Nov. 5.

Ruan, S. W., Bartsch, G., and Yang, S. M., 1994, "Characteristics of the Critical Heat Flux for Downward Flow in a Vertical Tube at Low Flow Rate and Low Pressure Conditions," *Experimental Thermal and Fluid Science*, Vol. 7, No. 3.


# Condensation of Nonazeotropic Binary Refrigerant Mixtures Including R22 as a More Volatile Component Inside a Horizontal Tube


**M. Shizuya,[1] M. Itoh,[1] and K. Hijikata[2]**


## Nomenclature

$Cp_L$ = liquid isobaric specific heat of refrigerant
$g$ = gravitational acceleration
Ga = Galileo number = $gd^3/\upsilon_L^2$
$H$ = ratio of sensible to latent heat = $Cp_L(T_{sat} - T_w)/\Delta h_V$
$\Delta h_V$ = latent heat of refrigerant vaporization
$M$ = mass flow rate
$\bar{M}$ = nondimensional mass flow rate = $M/d\eta_L$
$\bar{M}_L$ = nondimensional liquid mass flow rate = $M(1 - X)/d\eta_L$
$Pr_L$ = liquid Prandtl number of refrigerant
$Re_L$ = liquid Reynolds number = $4M(1 - X)/\pi d\eta_L$
$\eta_L$ = liquid viscosity of refrigerant
$\nu_L$ = liquid kinematic viscosity of refrigerant
$\rho_L$ = liquid density of refrigerant
$\rho_v$ = vapor density of refrigerant

## Introduction

Optimal use of nonazeotropic refrigerant mixtures as working fluids in heat pump and refrigeration systems allows higher coefficients of performance and wider temperature ranges than pure refrigerants. However, these mixtures also have some disadvantages. The greatest problem is that performance is significantly reduced during phase change in heat exchangers compared to pure refrigerants.

Limited heat transfer has been reported for refrigerant mixture condensation inside a horizontal tube (Koyama et al., 1988, 1990; Mochizuki et al., 1988; Inoue et al., 1988). Thus, neither generalized correlations nor the conditions for heat transfer reduction when comparing mixtures with pure refrigerants, are well understood yet.

This paper reports local condensation heat transfer of refrigerant mixtures flowing inside a horizontal tube with smooth or grooved surfaces. Three binary mixtures of R22 and less volatile components, and their four pure refrigerants, are tested to clarify the effect of refrigerant properties on heat transfer. Smooth and grooved tube data are used to compare heat transfer improvement by surface grooving between refrigerant mixtures and their pure components.

## Experimental Apparatus and Procedure

**Tested Refrigerants.** For refrigerant mixtures, R22 was selected as a more volatile component and R142b, R114, and R123 were selected as less volatile components. Four pure refrigerants of these mixture components were also tested. The basic properties of each pure refrigerant are summarized in Table 1. Among the less volatile refrigerants, R142b and R123 are possible alternative refrigerants with very low ozone depletion potential. Although R114 is not such an alternative, it was selected because of its intermediate boiling temperature between R142b and R123, and also because similar heat transfer has been reported when it is mixed with R22 (Koyama et al., 1988, 1990).

Since our main objective was to clarify the basic heat transfer characteristics of refrigerant mixtures compared to pure refrigerants, mole fraction ratios were limited to almost even values for respective mixtures (R22 ratios: R22/142b—54 percent, R22/114 and R22/123—50 percent).

**Table 1 Thermophysical properties of single refrigerant**

| Refrigerant | R22 | R142b | R114 | R123 |
|---|---|---|---|---|
| Molecular formula | $CHClF_2$ | $CH_3CClF_2$ | $CClF_2CClF_2$ | $CHClCF_3$ |
| Molecular weight | 86.5 | 100.5 | 170.9 | 152.9 |
| Boiling temp. (K)* | 232.4 | 263.4 | 277.0 | 300.3 |
| Saturation pressure (MPa)** | 1.96 | 0.69 | 0.45 | 0.22 |
| Liq. viscosity (Pa·s)** | $0.13\times10^{-3}$ | $0.26\times10^{-3}$ | $0.27\times10^{-3}$ | $0.33\times10^{-3}$ |
| Liq. thermal conductivity (W/m·K)** | $74\times10^{-6}$ | $74\times10^{-6}$ | $60\times10^{-6}$ | $69\times10^{-6}$ |
| Latent heat (kJ/kg)** | 156.6 | 188.9 | 118.8 | 160.5 |

(* : at atmospheric pressure, ** : saturated state at 333 K)


[1] Mechanical Engineering Research Laboratory, Hitachi, Ltd., Tsuchiura, Ibaraki 300, Japan.

[2] Department of Mechanical Engineering Science, Tokyo Institute of Technology, Meguro, Tokyo 152, Japan.



Contributed by the Heat Transfer Division of THE AMERICAN SOCIETY OF MECHANICAL ENGINEERS. Manuscript received by the Heat Transfer Division May 1993, revision received July 1994. Keywords: Condensation. Associate Technical Editor: L. C. Witte.





Copyright © 1995 by ASME

Downloaded 12 Dec 2010 to 193.140.21.150. Redistribution subject to ASME license or copyright; see http://www.asme.org/terms/Terms_Use.cfm

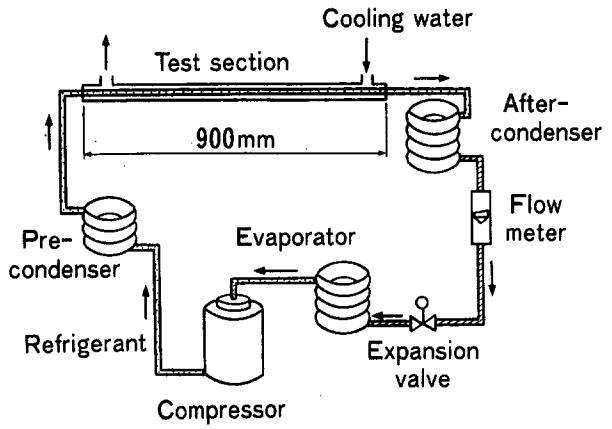



Fig. 1 Experimental apparatus

Table 2 Detailed dimensions of heat transfer tube

| Tube | Smooth | Grooved |
|---|---|---|
| Outer diam. (mm) | 7.0 | 7.0 |
| Av. wall thickness (mm) | 0.42 | 0.37 |
| Av. inner diam. (mm) | 6.16 | 6.26 |
| Groove depth (mm) | — | 0.19 |
| Groove pitch (mm) | — | 0.38 |
| Groove helical angle (deg) | — | 14 |
| Cross section of grooved tube | | |

**Experimental Apparatus.** A schematic of the experimental apparatus is shown in Fig. 1. The elements of the condensing section and the evaporator had separate cooling water loops, which enabled control of condensation or evaporation rates in those elements. Superheated vapor from the compressor was fed into the condensing section, where it partially condensed and was converted into wet saturated vapor in the precondenser. It then flowed into the test section, a tube-in-tube counterflow heat exchanger mounted horizontally (inside the inner tube as a refrigerant channel). The vapor condensed further, being maintained in a wet saturated state (decrease in vapor quality ranged from 0.1 to 0.4), and then flowed into the after-condenser and condensed completely. The vapor quality $X$, condensing temperature, and flow rate of the refrigerant at the test section were adjusted by controlling the flow rate of the cooling water loops of the precondenser and the test section, the bypass flow rate at the compressor, and the expansion valve. All parts and tubes in the condensing section were thermally insulated to minimize experimental errors.

Copper tubes with smooth or helically grooved inner surfaces were selected as test specimens (Table 2). These tubes had slightly smaller inner diameters, and the grooved tube had deeper grooves (the surface area ratio to the smooth tube was 1.6) than

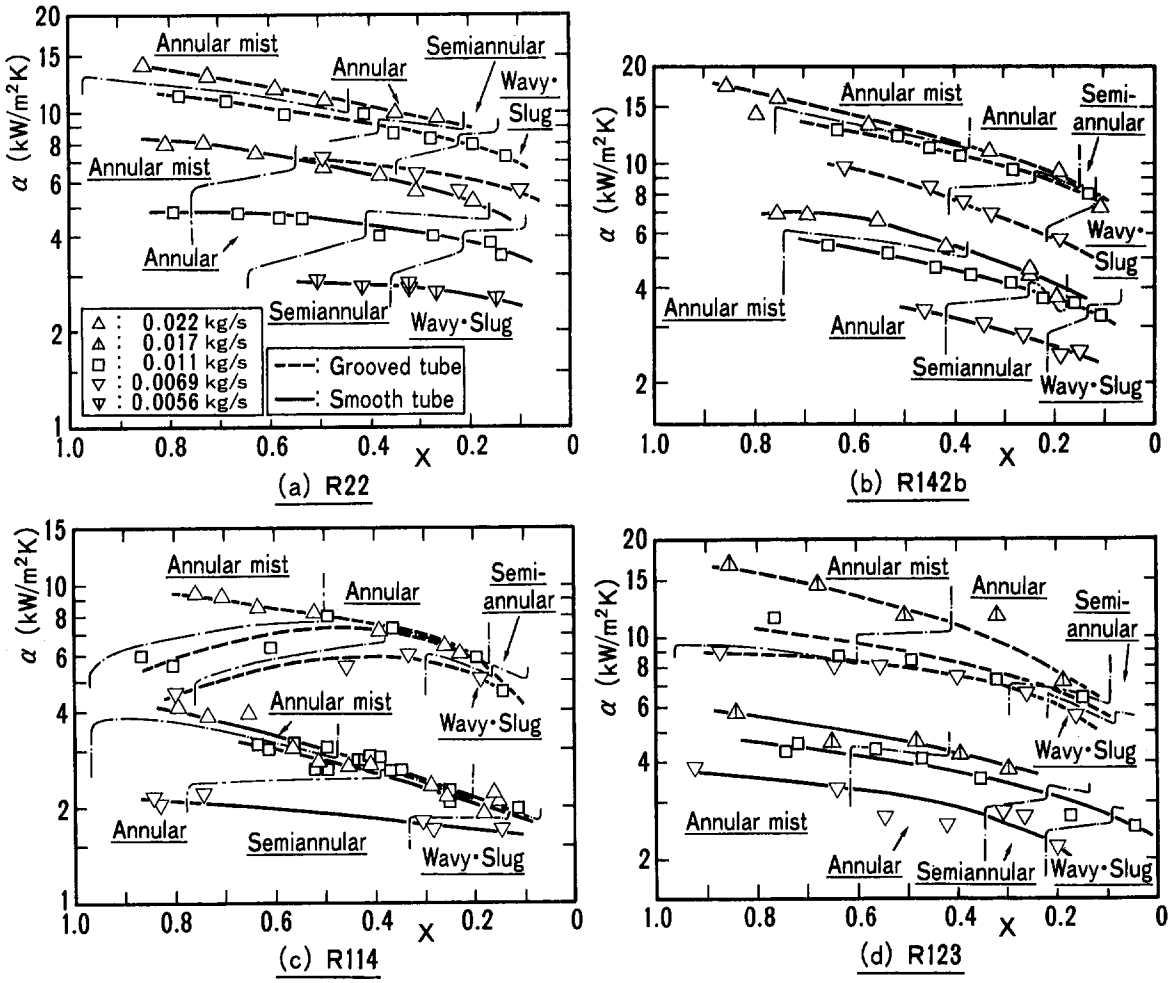



Fig. 2 Test results of all refrigerants



Downloaded 12 Dec 2010 to 193.140.21.150. Redistribution subject to ASME license or copyright; see http://www.asme.org/terms/Terms_Use.cfm

those now in use for heat exchangers of heat pumps. Their effective heat transfer length $l$ was 900 mm. Copper-constantan thermocouples were soldered to the outer surface to measure circumferential distributions of the tube wall temperature at 200, 450, and 700 mm from the tube inlet; vinyl chloride coating was also applied to the outermost surface to regulate heat flux normal to the tube surface to within the heat flux range in actual heat exchangers. Vapor temperature, refrigerant pressure, and cooling water temperature were measured at the inlet and outlet of both the precondenser and the test section by copper-constantan thermocouples and precision Bourdon-tube gages; flow rates of refrigerant and cooling water at both elements were measured by float-type flow meters. Mole fractions of refrigerant mixtures were determined directly by the amounts of both components introduced into the refrigerant channel, because separation and deposition of one or both components were unlikely to occur in such a simple channel.

During the experiment, the condensation temperature of the refrigerant and the heat flux normal to the tube inner surface were maintained at almost constant values in the range of 320 to 350 K (depending on the refrigerant) and of 10 kW/m$^2$. The flow rate and $X$ were varied from 0.0056 to 0.022 kg/s, and from 0.02 to 0.9, respectively.

**Data Reduction and Thermophysical Properties.** The heat transfer coefficient $\alpha$ on the tube inner surface in the test section was determined by applying the measured data to Eq. (1), and was transformed into the measured Nusselt number $Nu_{exp}$ by using Eq. (2):

$$\alpha = Q/\{\pi \cdot d \cdot l \cdot (T_{sat} - T_w)\} \quad (1)$$

$$Nu_{exp} = \alpha \cdot d/\lambda_L \quad (2)$$

where $Q$ is the heat flow rate in the test section derived from temperature increase and flow rate of the cooling water, $d$ is the tube inner diameter, $T_{sat}$ and $T_w$ are the refrigerant and wall temperatures averaged in the test section, and $\lambda_L$ is the liquid thermal conductivity of the refrigerant.

Using pressure-enthalpy diagrams for each refrigerant prepared in advance, $X$ was determined for the refrigerant in the test section. First, the specific enthalpy at the inlet of the precondenser, where the refrigerant was still in a superheated vapor state, was obtained by applying corresponding pressures and temperatures to the diagrams. Specific enthalpy drops in the precondenser and the test section were also calculated from the flow rate of the refrigerant and heat flow rate in each element. Subtracting the former and the latter enthalpy drops succeedingly from the above-mentioned specific enthalpy, specific enthalpies (mixed mean values of wet saturated vapor) at the inlet and outlet of the test section were obtained. Then $X$ at both positions was obtained by applying these specific enthalpies to the diagrams, and averaging these values yielded the final value.

Heat transfer data in the present study can be regarded as "local" in a general sense, because the refrigerant condenses partially in the test section. As the accuracies of $Q$, $T_{sat}$, and $T_w$ are 10 percent, 0.1°, and 0.1°, respectively, the total accuracy of $\alpha$ is thought to be 20 percent.

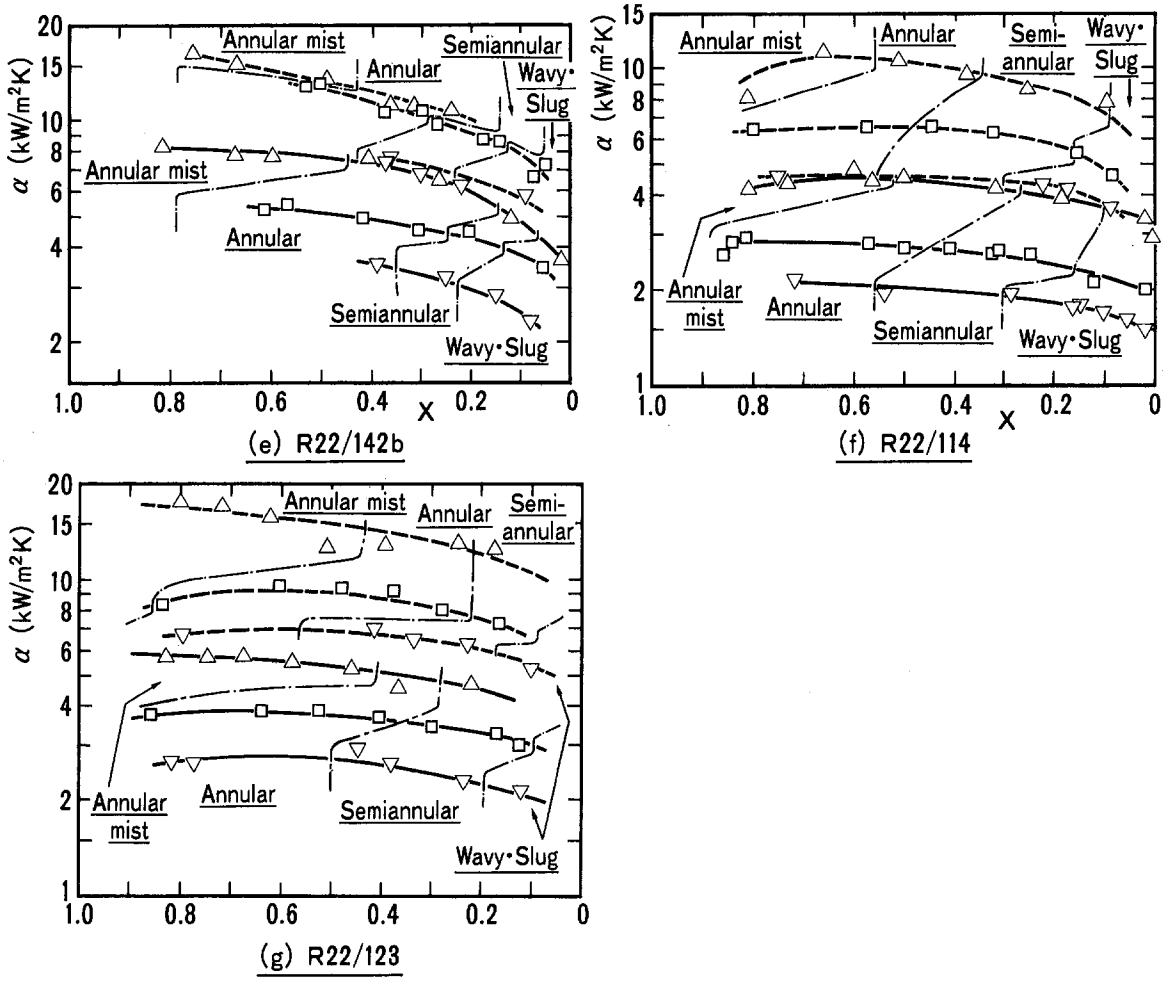



Fig. 2 (continued)



Downloaded 12 Dec 2010 to 193.140.21.150. Redistribution subject to ASME license or copyright; see http://www.asme.org/terms/Terms_Use.cfm

Thermodynamic properties, as well as the pressure-enthalpy diagrams of the refrigerant mixtures, were calculated using the Soave–Redlick–Kwong equation of state. Following Koyama et al. (1988, 1990), local liquid and vapor thermophysical properties of mixtures in a wet saturated vapor state were estimated from the saturated vapor and liquid values on the basis of their local fraction ratios of components.

## Results and Discussion

**Typical Results.** The relationships between $\alpha$ and $X$ for all pure refrigerants and mixtures are shown in Fig. 2. The flow patterns for all refrigerants estimated by the method proposed by Tandon et al. (1985) are also shown for reference. As indicated in previous studies (Koyama et al., 1988, 1990; Mochizuki et al.,

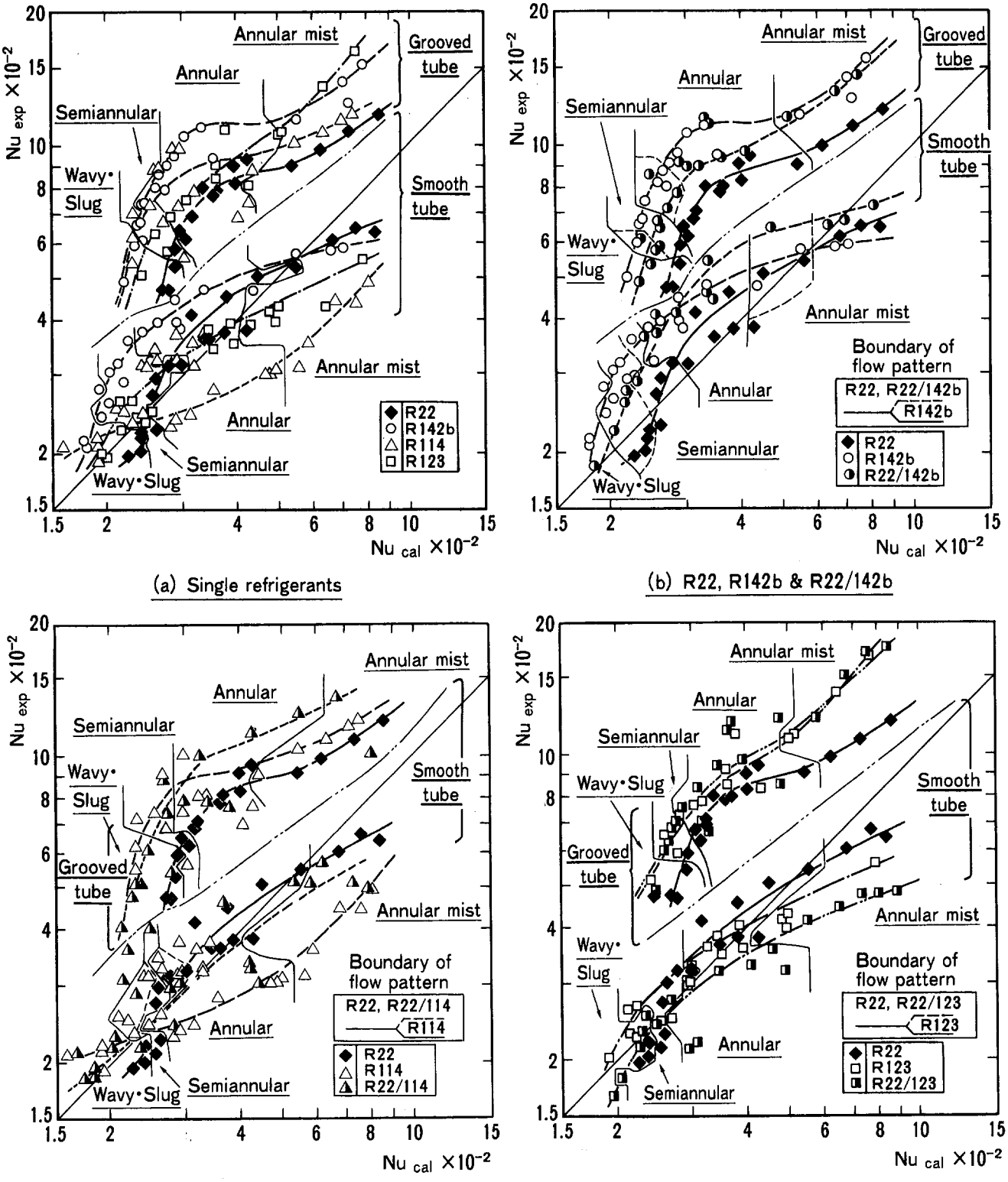



**Fig. 3 Nondimensional heat transfer characteristics**



Downloaded 12 Dec 2010 to 193.140.21.150. Redistribution subject to ASME license or copyright; see http://www.asme.org/terms/Terms_Use.cfm

1988), $\alpha$ decreases monotonically with decreases in $X$ for most refrigerants. On the other hand, in some cases of R114 and its mixture, such dependencies of $\alpha$ on $X$ are weak as indicated by Inoue et al. (1988). Heat transfer appears to be improved by grooving the tube inner surface for all refrigerants. In the above-mentioned practical evaluations based on measured data, generalized information on heat transfer characteristics cannot be derived because of the accompanying effects of differences in thermophysical properties. In the next section, therefore, nondimensional parameters are introduced for evaluating heat transfer.

**Nondimensional Characteristics and Discussion.** The semi-empirical equation of Fujii et al. (1980) for pure refrigerants flowing inside a smooth horizontal tube was thought to be the best among such correlation equations. Thus, data were transformed into nondimensional parameters based on Fujii's equation (see the appendix).

The relationships between $Nu_{exp}$ derived from measured data and the calculated Nusselt numbers by Fujii's equation $Nu_{cal}$, for all refrigerants, are shown in Fig. 3. As for flow pattern, the applicable ranges of Fujii's equation (the "forced convection condensation region" and "combined body force and forced convection condensation region"), correspond approximately to Tandon's annular and semi-annular regimes.

The data for pure refrigerants inside a smooth tube in Fig. 3($a$) show that $Nu_{cal}$ agrees well with $Nu_{exp}$ for R22 and R123 in annular and semi-annular flow, but that there can be large deviations (up to 50 percent relatively) between those parameters for R142b and R114. This means the estimation accuracy of Fujii's equation for pure refrigerants is not always satisfactory. However, the relative deviations for refrigerant mixtures are considered to be proportional to their fraction ratios of components when heat transfer is not reduced. Therefore, $Nu_{exp}/Nu_{cal}$ can be used for relative performance comparison of elements in each refrigerant group, that is, a mixture and its pure components. The data for respective refrigerant groups in Figs. 3($b \sim d$) show that heat transfer for the mixture R22/142b is equal to or slightly higher than the average of its pure components inside both smooth and grooved tubes. The heat transfer of both the mixture R22/114 and the mixture R22/123 is somewhat lower inside a smooth tube, and is equal to or slightly higher than the average of their pure components inside a grooved tube.

To clarify the performance trends discussed above, comparisons of $Nu_{exp}/Nu_{cal}$ between elements in respective refrigerant groups in annular flow regimes are shown in Fig. 4. Although somewhat large data dispersions are observed for some refrigerants, two basic heat transfer characteristics for refrigerant mixtures, in contrast with individual components, can be deduced. First, heat transfer is reduced when using mixtures in cases where the boiling temperatures of their components differ greatly. A qualitative explanation is that more volatile vapor near the vapor–liquid interface accumulates more quickly during condensation, and creates a thick vapor diffusion layer, which leads to greater heat transfer resistance. Second, heat transfer appears to be improved by grooving on the tube inner surface for mixtures as well as pure refrigerants, and compensates to a considerable degree for the above-mentioned heat transfer reduction. Heat transfer ratios of grooved tube to smooth tube exceed the corresponding inner surface area ratio of 1.6 for all refrigerants. This is because deep grooves enhance heat transfer in the vapor diffusion layer as well as in the liquid film near the tube surface, by the tops of the grooves protruding over the liquid film within most of the annular flow regime.

Finally, Table 3 summarizes heat transfer for refrigerant mixtures with nearly even mole fractions of components between the present and previous studies. Performance ratios for local Nu in the present study were calculated by averaging the data of $Nu_{exp}/Nu_{cal}$ in Fig. 4 for respective refrigerants. Because the data of the previous studies were obtained with a different definition of Nu and with a lower refrigerant mass velocity than in the present study, some deviations may appear in these performance results. With all such deviations, Table 3 shows that performance trends observed for mixtures other than those of the present study are also consistent with the above-mentioned characteristics.

## Conclusion

Experimental data have been presented for condensation heat transfer of several binary refrigerant mixtures and their pure components flowing inside a horizontal tube. The results are summarized as follows:

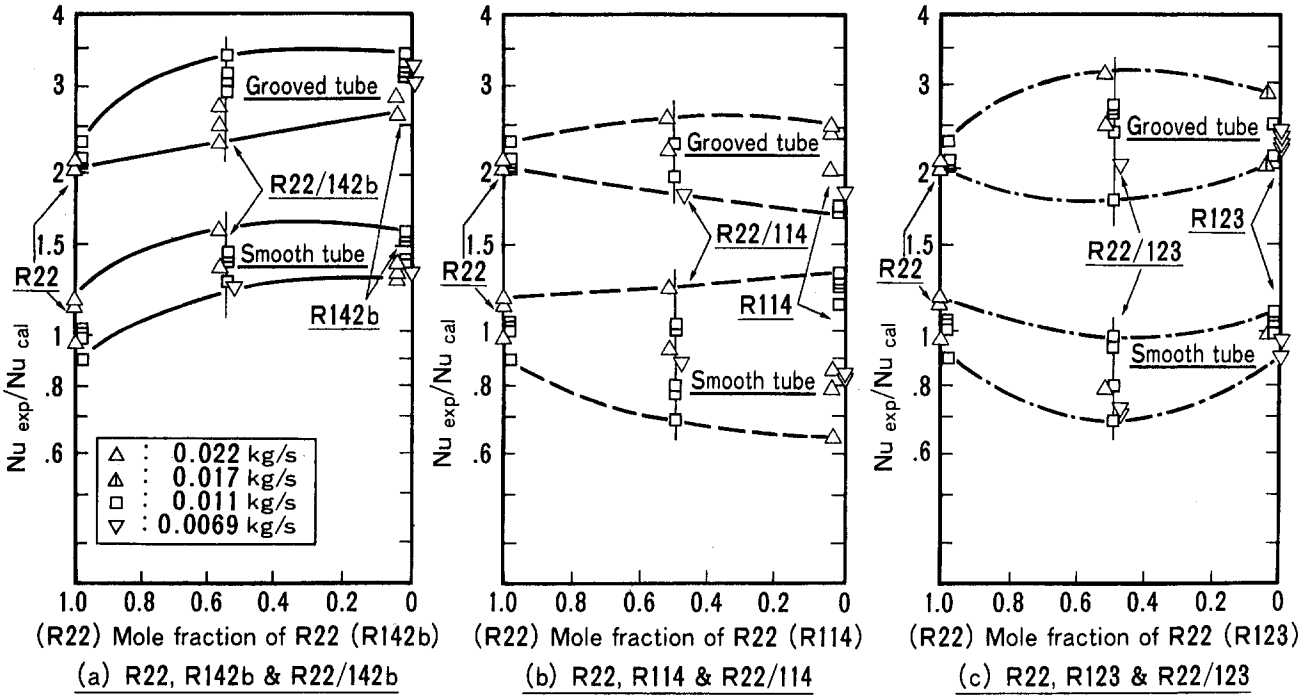



**Fig. 4 Comparison of heat transfer performance (in annular flow regime)**



Downloaded 12 Dec 2010 to 193.140.21.150. Redistribution subject to ASME license or copyright; see http://www.asme.org/terms/Terms_Use.cfm

**Table 3 Comparison of heat transfer performance for refrigerant mixtures in the present and previous studies**

| Reference | Refrigerant | Boiling temp. diff. (deg.) | Kind of tube | Kind of Nu | Performance ratio* |
|---|---|---|---|---|---|
| Mochizuki et al. (1988) | R11/113 | 23.8 | Smooth | Average | 1.0 |
| Pres. study | R22/142b | 31.0 | Grooved | Local | 1.09 |
| | | | Smooth | | 1.15 |
| Inoue et al. (1988) | R114/113 | 43.8 | Smooth | Average | 0.90 |
| Koyama et al. (1990) | R22/114 | 44.6 | Grooved | Average | 0.77 |
| Pres. study | | | Grooved | Local | 1.02 |
| | | | Smooth | | 0.90 |
| Pres. study | R22/123 | 67.9 | Grooved | Local | 1.08 |
| | | | Smooth | | 0.78 |

(* : Ratio of data for mixture to averaged data for pure components)

1 Heat transfer is reduced when using refrigerant mixtures in cases where the boiling temperatures of their components differ greatly.
2 Heat transfer appears to be improved for refrigerant mixtures by grooving the tube inner surface, and it also compensates to a considerable degree for this performance reduction.

## References


Fujii, T., Honda, H., and Nozu, S., 1980, "Condensation of Fluorocarbon Refrigerants Inside a Horizontal Tube," *Refrigeration*, Vol. 55, pp. 3–20 [in Japanese].

Inoue, T., Mochizuki, S., and Morita, A., 1988, "Condensation of Nonazeotropic Binary Mixtures in a Horizontal Tube (R113+R114)," *Proc. 25th Nat. Heat Transf. Symposium of Japan*, pp. 460–462 [in Japanese].

Koyama, S., Miyara, A., Fujii, T., Takamatsu, H., and Yonemoto, K., 1988, "Condensation of Refrigerant Mixtures R22+R114 Inside a Horizontal Tube," *Trans. JSME*, Ser. B, Vol. 54, pp. 1447–1452 [in Japanese].

Koyama, S., Miyara, A., Takamatsu, H., and Fujii, T., 1990, "Condensation Heat Transfer of Binary Refrigerant Mixtures of R22 and R114 Inside a Horizontal Tube With Internal Spiral Grooves," *Int. J. Refrig.*, Vol. 13, No. 4, pp. 256–263.

Mochizuki, S., Inoue, T., and Tominaga, M., 1988, "Condensation of Nonazeotropic Binary Mixtures in a Horizontal Tube (R113+R11)," *Trans. JSME*, Ser. B, Vol. 54, pp. 1796–1801 [in Japanese].

Tandon, T. N., Varma, H. K., and Gupta, C. P., 1985, "Prediction of Flow Patterns During Condensation of Binary Mixtures in a Horizontal Tube," ASME JOURNAL OF HEAT TRANSFER, Vol. 107, pp. 424–430.


## APPENDIX

### Semi-empirical Equation for Heat Transfer of Pure Refrigerant Inside a Horizontal Smooth Tube (Fujii et al., 1980)

The larger value of $Nu_F$ (for "forced convection condensation") and $Nu_B$ (for "combined body force and forced convection condensation") is applied to $Nu_{cal}$ (estimation):

$$\begin{cases} Nu_F = 0.018\{Re_L\sqrt{\rho_L/\rho_V}\}^{0.9}\left(\dfrac{X}{1-X}\right)^{0.1X+0.8} \times Pr_L^{1/3}(1 + AH/Pr_L) & \text{(A1)} \\ Nu_B = 0.725(GaPr_L/H)^{1/4} \times \dfrac{(1 + 3\times 10^{-3}\sqrt{Pr_L}C^{(3.1-0.5/Pr_L)})^{0.3}}{(1+DB)^{1/4}} & \text{(A2)} \end{cases}$$

where

$$A = 0.071\, Re_L^{0.1}(\rho_L/\rho_V)^{0.55}\left(\frac{X}{1-X}\right)^{0.2-0.1X} Pr_L^{1/3}$$

$$B = \frac{(1 + 1.6\times 10^{11}(H/Pr_L)^5)^{1/4}}{\sqrt{\rho_L/\rho_V}}\left\{\frac{(GaPr_L/H)^{1/4}}{\bar{M}_L\left(\dfrac{X}{1-X}\right)}\right\}^{1.8}$$

$$C = 0.47(\rho_L/\rho_V)^{0.5}(H/Pr_L)^{1/12}\left(Re_L\frac{X}{1-X}\right)^{0.9} \Big/ (GaPr_L/H)^{1.1/4}$$

$$D = 20\exp(-\bar{M}/3000)$$

# Onset of Natural Convection in a Horizontal Porous Medium With Mixed Thermal Boundary Conditions


## K. E. Wilkes[1]


### Nomenclature

$a$ = horizontal wavenumber = $kL$
$b$ = normalized horizontal wavenumber = $a/\pi$
$B$ = Biot number = $hL/\lambda$
$C$ = specific heat
$g$ = acceleration of gravity
$h$ = surface heat transfer coefficient
$k$ = horizontal wavenumber
$\mathbf{k}$ = unit vector in vertical direction
$K$ = fluid flow permeability, or, with a subscript, the analog of the Biot number for fluid velocity
$L$ = thickness of porous medium
$P$ = pressure
$R$ = normalized Rayleigh number = $Ra/\pi^2$
Ra = Rayleigh number, Eq. (11)
$t$ = time
$T$ = temperature
$\mathbf{u}$ = velocity vector
$z$ = vertical distance from bottom surface
$\alpha$ = thermal diffusivity, defined as thermal conductivity of porous medium, divided by the density and specific heat of the saturating fluid
$\beta$ = volume coefficient of thermal expansion of fluid
$\Delta T$ = temperature difference between bottom and top of porous medium
$\epsilon$ = porosity
$\eta$ = specific heat ratio, Eq. (4)
$\lambda$ = thermal conductivity of porous medium, including contributions of both the solid and fluid phases
$\mu$ = dynamic viscosity of fluid
$\nu$ = kinematic viscosity of fluid = $\mu/\rho$
$\rho$ = density of fluid
$\rho_0$ = fluid density at reference temperature

### Subscripts

0 = variable evaluated at reference temperature
$c$ = critical value
$f$ = fluid
$l$ = lower surface


[1] Oak Ridge National Laboratory, Oak Ridge, TN 37831-6070.



Contributed by the Heat Transfer Division of THE AMERICAN SOCIETY OF MECHANICAL ENGINEERS. Manuscript received by the Heat Transfer Division May 1992; revision received August 1993. Keywords: Building Heat Transfer, Natural Convection, Porous Media. Associate Technical Editor: C. E. Hickox, Jr.





Downloaded 12 Dec 2010 to 193.140.21.150. Redistribution subject to ASME license or copyright; see http://www.asme.org/terms/Terms_Use.cfm

**Table 3 Comparison of heat transfer performance for refrigerant mixtures in the present and previous studies**

| Reference | Refrigerant | Boiling temp. diff. (deg.) | Kind of tube | Kind of Nu | Performance ratio* |
|---|---|---|---|---|---|
| Mochizuki et al. (1988) | R11/113 | 23.8 | Smooth | Average | 1.0 |
| Pres. study | R22/142b | 31.0 | Grooved | Local | 1.09 |
| | | | Smooth | | 1.15 |
| Inoue et al. (1988) | R114/113 | 43.8 | Smooth | Average | 0.90 |
| Koyama et al. (1990) | R22/114 | 44.6 | Grooved | Average | 0.77 |
| Pres. study | | | Grooved | Local | 1.02 |
| | | | Smooth | | 0.90 |
| Pres. study | R22/123 | 67.9 | Grooved | Local | 1.08 |
| | | | Smooth | | 0.78 |

(* : Ratio of data for mixture to averaged data for pure components)

1 Heat transfer is reduced when using refrigerant mixtures in cases where the boiling temperatures of their components differ greatly.
2 Heat transfer appears to be improved for refrigerant mixtures by grooving the tube inner surface, and it also compensates to a considerable degree for this performance reduction.

## References


Fujii, T., Honda, H., and Nozu, S., 1980, "Condensation of Fluorocarbon Refrigerants Inside a Horizontal Tube," *Refrigeration*, Vol. 55, pp. 3–20 [in Japanese].

Inoue, T., Mochizuki, S., and Morita, A., 1988, "Condensation of Nonazeotropic Binary Mixtures in a Horizontal Tube (R113+R114)," *Proc. 25th Nat. Heat Transf. Symposium of Japan*, pp. 460–462 [in Japanese].

Koyama, S., Miyara, A., Fujii, T., Takamatsu, H., and Yonemoto, K., 1988, "Condensation of Refrigerant Mixtures R22+R114 Inside a Horizontal Tube," *Trans. JSME*, Ser. B, Vol. 54, pp. 1447–1452 [in Japanese].

Koyama, S., Miyara, A., Takamatsu, H., and Fujii, T., 1990, "Condensation Heat Transfer of Binary Refrigerant Mixtures of R22 and R114 Inside a Horizontal Tube With Internal Spiral Grooves," *Int. J. Refrig.*, Vol. 13, No. 4, pp. 256–263.

Mochizuki, S., Inoue, T., and Tominaga, M., 1988, "Condensation of Nonazeotropic Binary Mixtures in a Horizontal Tube (R113+R11)," *Trans. JSME*, Ser. B, Vol. 54, pp. 1796–1801 [in Japanese].

Tandon, T. N., Varma, H. K., and Gupta, C. P., 1985, "Prediction of Flow Patterns During Condensation of Binary Mixtures in a Horizontal Tube," ASME JOURNAL OF HEAT TRANSFER, Vol. 107, pp. 424–430.


## APPENDIX

### Semi-empirical Equation for Heat Transfer of Pure Refrigerant Inside a Horizontal Smooth Tube (Fujii et al., 1980)

The larger value of $Nu_F$ (for "forced convection condensation") and $Nu_B$ (for "combined body force and forced convection condensation") is applied to $Nu_{cal}$ (estimation):

$$\begin{cases} Nu_F = 0.018\{Re_L\sqrt{\rho_L/\rho_V}\}^{0.9}\left(\dfrac{X}{1-X}\right)^{0.1X+0.8} \times Pr_L^{1/3}(1 + AH/Pr_L) & \text{(A1)} \\ Nu_B = 0.725(GaPr_L/H)^{1/4} \times \dfrac{(1 + 3\times 10^{-3}\sqrt{Pr_L}C^{(3.1-0.5/Pr_L)})^{0.3}}{(1+DB)^{1/4}} & \text{(A2)} \end{cases}$$

where

$$A = 0.071\, Re_L^{0.1}(\rho_L/\rho_V)^{0.55}\left(\frac{X}{1-X}\right)^{0.2-0.1X} Pr_L^{1/3}$$

$$B = \frac{(1 + 1.6\times 10^{11}(H/Pr_L)^5)^{1/4}}{\sqrt{\rho_L/\rho_V}}\left\{\frac{(GaPr_L/H)^{1/4}}{\bar{M}_L\left(\dfrac{X}{1-X}\right)}\right\}^{1.8}$$

$$C = 0.47(\rho_L/\rho_V)^{0.5}(H/Pr_L)^{1/12}\left(Re_L\frac{X}{1-X}\right)^{0.9} \Big/ (GaPr_L/H)^{1.1/4}$$

$$D = 20\exp(-\bar{M}/3000)$$

# Onset of Natural Convection in a Horizontal Porous Medium With Mixed Thermal Boundary Conditions


**K. E. Wilkes**[1]


## Nomenclature

$a$ = horizontal wavenumber = $kL$
$b$ = normalized horizontal wavenumber = $a/\pi$
$B$ = Biot number = $hL/\lambda$
$C$ = specific heat
$g$ = acceleration of gravity
$h$ = surface heat transfer coefficient
$k$ = horizontal wavenumber
$\mathbf{k}$ = unit vector in vertical direction
$K$ = fluid flow permeability, or, with a subscript, the analog of the Biot number for fluid velocity
$L$ = thickness of porous medium
$P$ = pressure
$R$ = normalized Rayleigh number = $Ra/\pi^2$
Ra = Rayleigh number, Eq. (11)
$t$ = time
$T$ = temperature
$\mathbf{u}$ = velocity vector
$z$ = vertical distance from bottom surface
$\alpha$ = thermal diffusivity, defined as thermal conductivity of porous medium, divided by the density and specific heat of the saturating fluid
$\beta$ = volume coefficient of thermal expansion of fluid
$\Delta T$ = temperature difference between bottom and top of porous medium
$\epsilon$ = porosity
$\eta$ = specific heat ratio, Eq. (4)
$\lambda$ = thermal conductivity of porous medium, including contributions of both the solid and fluid phases
$\mu$ = dynamic viscosity of fluid
$\nu$ = kinematic viscosity of fluid = $\mu/\rho$
$\rho$ = density of fluid
$\rho_0$ = fluid density at reference temperature

### Subscripts

0 = variable evaluated at reference temperature
$c$ = critical value
$f$ = fluid
$l$ = lower surface


[1] Oak Ridge National Laboratory, Oak Ridge, TN 37831-6070.



Contributed by the Heat Transfer Division of THE AMERICAN SOCIETY OF MECHANICAL ENGINEERS. Manuscript received by the Heat Transfer Division May 1992; revision received August 1993. Keywords: Building Heat Transfer, Natural Convection, Porous Media. Associate Technical Editor: C. E. Hickox, Jr.





Copyright © 1995 by ASME

Downloaded 12 Dec 2010 to 193.140.21.150. Redistribution subject to ASME license or copyright; see http://www.asme.org/terms/Terms_Use.cfm

$s$ = solid
$u$ = upper surface

## Introduction

The conditions for the onset of natural convection in a horizontal fluid-saturated porous medium heated from below have been the subject of many analytical and experimental studies. The earliest of the analytical studies was performed by Horton and Rogers (1945), who studied the case of a porous medium bounded by two isothermal, impermeable planes. They obtained a critical Rayleigh number of $4\pi^2$. This result was also found by Lapwood (1948), who also studied the case of a porous medium with an isothermal, impermeable bottom surface and an isothermal, constant pressure top surface. For this latter case, Lapwood found a critical Rayleigh number of 27.1. Nield (1968) developed a formalism for calculating the critical Rayleigh number for thermohaline convection with a variety of thermal and mechanical boundary conditions, and obtained numerical values for various combinations of isothermal or constant heat flux thermal boundary conditions and impermeable or constant pressure mechanical boundary conditions. Nield and Bejan (1991) also summarize the same analysis. The purpose of this paper is to utilize Nield's formalism to calculate critical Rayleigh numbers for cases of mixed thermal boundary conditions for two sets of practically important mechanical boundary conditions: (1) impermeable top and bottom boundaries, and (2) impermeable bottom and constant pressure top boundaries.

The results of this investigation should apply to a number of porous medium systems. In particular they apply to the study of materials used to insulate attics of residential buildings. In this application, the insulation is bounded on the bottom side by gypsum board, which is exposed to the air in the interior of the house, while the top surface is open to the attic air space. For this application, experiments by Wilkes et al. (1991a, 1991b, 1992) have shown that heat transfer by natural convection can be an important heat transfer mechanism for at least one type of commonly used insulation material under frequently encountered weather conditions. However, measured critical Rayleigh numbers were found to be lower than literature values for isothermal surfaces. The calculations presented here were performed to assist in gaining a better understanding of these experimental results.

## Mathematical Analysis

Since the mathematical analysis follows that of Nield, only the salient features are presented here. As is usual in this type of analysis, the Boussinesq approximation is used, wherein density variations are ignored except for their buoyancy effect. Also, all thermal properties are taken to be constants. With these approximations, the governing (three-dimensional) continuity, momentum (Darcy's law), and energy equations are:

$$\nabla \cdot \mathbf{u} = 0 \tag{1}$$

$$\frac{\rho_0}{\epsilon}\left[\frac{\partial \mathbf{u}}{\partial t} + (\mathbf{u}\cdot\nabla)\mathbf{u}\right] = -\rho g\mathbf{k} - \nabla P - \frac{\mu}{K}\mathbf{u} \tag{2}$$

and

$$\eta\frac{\partial T}{\partial t} + \mathbf{u}\cdot\nabla T = \alpha\nabla^2 T \tag{3}$$

where

$$\eta = \frac{\epsilon\rho_f C_f + (1-\epsilon)\rho_s C_s}{\rho_f C_f} \tag{4}$$

These are augmented by the equation of state:

$$\rho = \rho_0[1 - \beta(T - T_0)] \tag{5}$$

The porous medium is taken to lie between planes $z = 0$ and $z = L$, and is infinite in the $x$ and $y$ directions. When internal convection is absent, the top and bottom planes are taken to be at temperatures of $T_0$ and $T_u$, with $T_0 > T_u$. Convection boundary conditions are applied at the top and bottom planes with heat transfer coefficients $h_u$ and $h_l$, with corresponding Biot numbers of $B_u$ and $B_l$, respectively. A Biot number of zero corresponds to a uniform heat flux at the boundary, while a Biot number approaching infinity corresponds to an isothermal boundary.

Nield performed a perturbation analysis for thermohaline convection, assuming periodic perturbations in the $x$ and $y$ directions. His final eigenvalue equation, specialized to the purely thermal case, is given by

$$\begin{vmatrix} R\Sigma_1 - f - K_l & R\Sigma_2 - g & R\Sigma_3 & R\Sigma_4 \\ R\Sigma_2 - g & R\Sigma_1 - f - K_u & R\Sigma_4 & R\Sigma_3 \\ \Sigma_3/b^2 & \Sigma_4/b^2 & R\Sigma_1 - f - B_l & R\Sigma_2 - g \\ \Sigma_4/b^2 & \Sigma_3/b^2 & R\Sigma_2 - g & R\Sigma_1 - f - B_u \end{vmatrix} = 0 \tag{6}$$

where $f = \pi b \coth \pi b$, $g = \pi b \operatorname{cosech} \pi b$,

$$\Sigma_1 = \sum_{n=1}^{\infty} \frac{2n^2b^2}{(n^2+b^2)[(n^2+b^2)^2 - Rb^2]} \tag{7}$$

$$\Sigma_2 = \sum_{n=1}^{\infty} \frac{(-1)^n 2n^2b^2}{(n^2+b^2)[(n^2+b^2)^2 - Rb^2]} \tag{8}$$

$$\Sigma_3 = \sum_{n=1}^{\infty} \frac{2n^2b^2}{(n^2+b^2)^2 - Rb^2} \tag{9}$$

$$\Sigma_4 = \sum_{n=1}^{\infty} \frac{(-1)^n 2n^2b^2}{(n^2+b^2)^2 - Rb^2} \tag{10}$$

$$R = \frac{\mathrm{Ra}}{\pi^2} = \frac{1}{\pi^2}\frac{g\beta\rho_f C_f \Delta T L K}{\nu\lambda} \tag{11}$$

and

$$b^2 = \frac{a^2}{\pi^2} = \frac{(k_x^2 + k_y^2)L^2}{\pi^2} \tag{12}$$

$K_l$ and $K_u$ are discrete parameters for the mechanical boundary conditions at the bottom and top planes. A value of 0 corresponds to an open boundary, while a value of $\infty$ corresponds to an impermeable boundary.

For a given set of mechanical and thermal boundary conditions, the minimum value of $R$ that is a solution of Eq. (6) defines the critical Rayleigh number at which convection commences. Equation (6) was solved numerically for arbitrary values of the upper and lower Biot numbers for the following two combinations of mechanical boundary conditions: (1) both boundaries impermeable (i.e., $K_u = K_l = \infty$), and (2) impermeable bottom boundary and open top boundary (i.e., $K_l = \infty$, $K_u = 0$). For cases where $K_u$ or $K_l$ was equal to infinity, the order of the determinant in Eq. (6) was reduced by eliminating the rows and columns that contained the infinite parameter. The periodic perturbations in the $x$ and $y$ directions have wavenumbers of $k_x$ and $k_y$. In order for the solutions to remain finite as $x$ or $y$ goes to $\infty$, $k_x$ and $k_y$ must be real numbers. Also, by definition, Ra is a positive real number. Because of these reasons, the numerical searches on $b$ and $R$ were confined to the positive real axis of the complex plane.



Downloaded 12 Dec 2010 to 193.140.21.150. Redistribution subject to ASME license or copyright; see http://www.asme.org/terms/Terms_Use.cfm

**Table 1 Comparison of numerical results for critical Rayleigh number and critical wavenumber with those obtained by Nield**

| | | | | Nield (1968) | | Present Results | |
|---|---|---|---|---|---|---|---|
| $K_l$ | $K_u$ | $B_l$ | $B_u$ | $Ra_c$ | $a_c$ | $Ra_c$ | $a_c$ |
| ∞ | ∞ | ∞ | ∞ | $4\pi^2 =$ 39.4784 | $\pi =$ 3.14159 | 39.4784 | 3.14160 |
| ∞ | ∞ | ∞ | 0 | 27.10 | 2.33 | 27.0976 | 2.32622 |
| ∞ | ∞ | 0 | 0 | 12 | 0 | 12.0000 | 0.00007 |
| ∞ | 0 | ∞ | ∞ | 27.10 | 2.33 | 27.0975 | 2.32622 |
| ∞ | 0 | 0 | ∞ | 17.65 | 1.75 | 17.6536 | 1.74987 |
| ∞ | 0 | ∞ | 0 | $\pi^2 =$ 9.86960 | $\pi/2 =$ 1.57080 | 9.8696 | 1.57081 |
| ∞ | 0 | 0 | 0 | 3 | 0 | 3.00000 | 0.00007 |

Note: $B = 10^6$ was taken to be equivalent to $B = \infty$. Other values of ∞ were handled numerically by reducing the order of the determinant in Eq. (6) by eliminating rows and columns containing the infinite parameter.

The accuracy of the numerical results was determined by comparison of calculated critical Rayleigh numbers and critical wavenumbers with those in the literature for the limiting cases of upper and lower Biot numbers of 0 or ∞. Table 1 shows a comparison of calculated critical Rayleigh numbers and wavenumbers with Nield's results. In all cases, the present results are essentially identical to those of Nield (1968). Based on these comparisons, the present Rayleigh numbers are accurate to five to six significant figures, and the wavenumbers are accurate to three to five significant figures.

## Numerical Results

Figure 1 shows the calculated critical Rayleigh number versus Biot number for the case of impermeable top and bottom surfaces. For curves 1 through 8, the Biot number at either the top or bottom is held at a fixed value of ∞, 10, 1 or 0, while the other Biot number is given on the abscissa. For curve 9, the Biot numbers at both the top and bottom are variables. Because of the symmetry of this problem, top and bottom Biot numbers may be interchanged without influencing the critical Rayleigh number. Decreasing the Biot number at either the top or bottom leads to lower critical Rayleigh numbers. Curves 1 through 8 have similar shapes and are roughly parallel, while curve 9 cuts across the other curves. The curves in Fig. 1 may be divided into three zones: (1) $B < 10^{-2}$, which corresponds to nearly uniform heat flux boundary conditions, (2) $B > 10^2$, which corresponds to nearly isothermal boundary conditions, and (3) $10^{-2} < B < 10^2$, which corresponds to mixed boundary conditions.

A similar plot of critical Rayleigh numbers for the case of an impermeable bottom and an open top is given in Fig. 2. Because of the asymmetry of this problem, interchanging the top and bottom Biot numbers leads to different critical Rayleigh numbers. Again, a decrease in the Biot number at either the top or bottom leads to a lower critical Rayleigh number. Curves 1, 3, and 5, for which the upper Biot number is a different constant for each curve, form one family of similarly shaped curves, and curves 2, 4, and 6, for which the lower Biot number is a different constant value for each curve, form another family of similarly shaped curves. Curve 7, for which neither Biot number is a constant, cuts

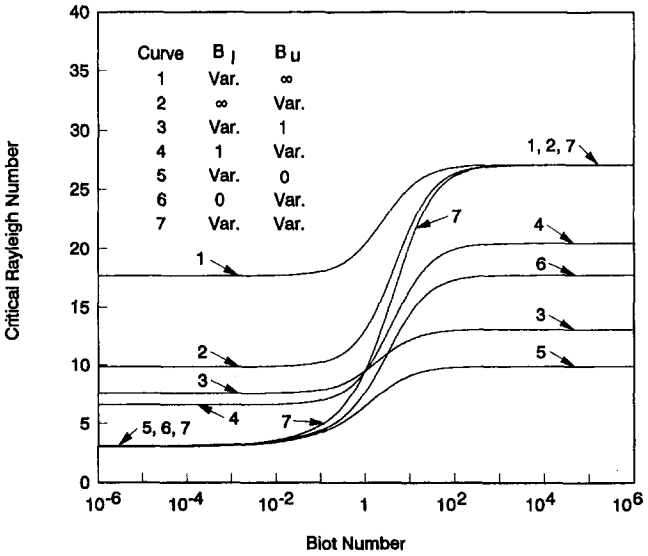



**Fig. 2 Critical Rayleigh number as a function of Biot number for impermeable bottom and open top boundaries. Biot numbers noted as "Var." are plotted on the abscissa.**

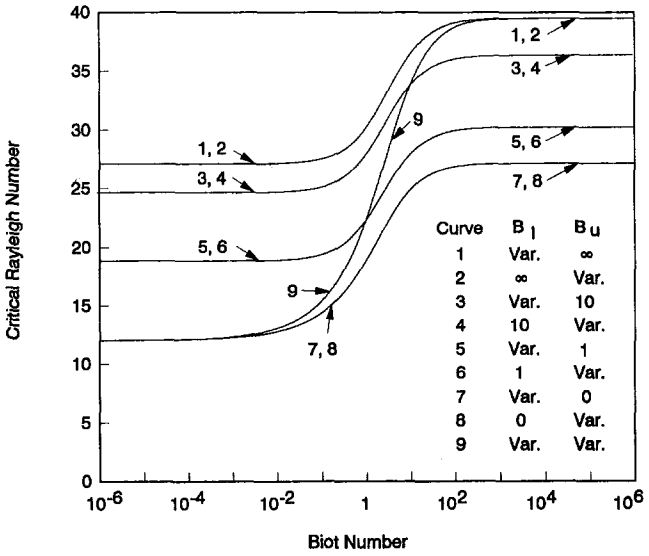



**Fig. 1 Critical Rayleigh number as a function of Biot number for impermeable top and bottom boundaries. Biot numbers noted as "Var." are plotted on the abscissa.**

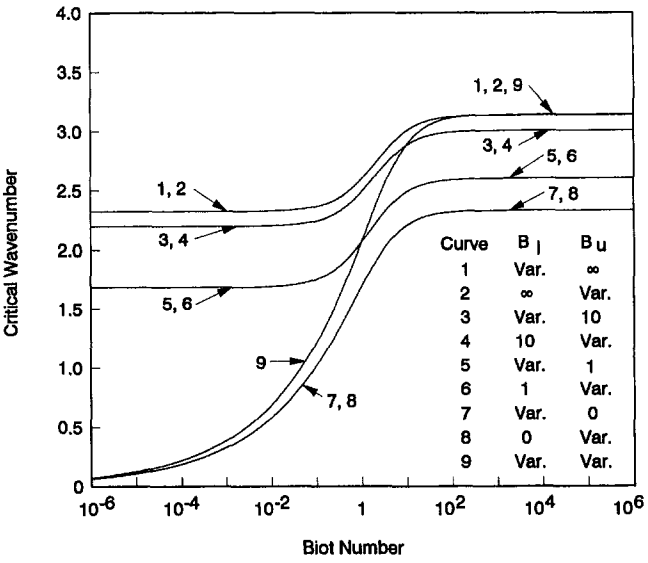



**Fig. 3 Critical wavenumber as a function of Biot number for impermeable top and bottom boundaries. Biot numbers noted as "Var." are plotted on the abscissa.**



Downloaded 12 Dec 2010 to 193.140.21.150. Redistribution subject to ASME license or copyright; see http://www.asme.org/terms/Terms_Use.cfm

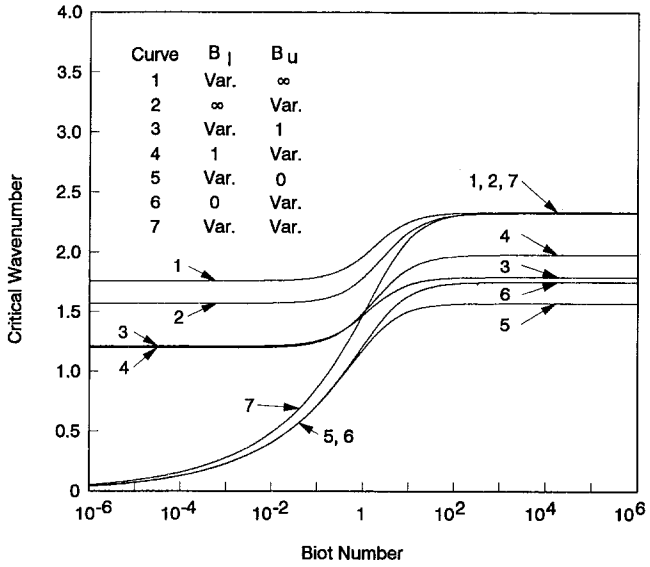



**Fig. 4 Critical wavenumber as a function of Biot number for impermeable bottom and open top boundaries. Biot numbers noted as "Var." are plotted on the abscissa.**

across the other curves. The curves in Fig. 2 may be divided into the same three zones as those in Fig. 1.

Critical wavenumbers for the two sets of mechanical boundary conditions are shown in Figs. 3 and 4. When either of the Biot numbers is decreased, the critical wavenumber decreases. When both Biot numbers approach zero, the critical wavenumber also approaches zero. When only one Biot number approaches zero, the critical wavenumber remains finite.

## Application to Experiments on Building Insulation

While the results presented here should have applicability to a number of physical and engineering systems, the work was undertaken to understand better the data obtained on low-density loose-fill fiberglass thermal insulation in a simulated residential attic (Wilkes et al., 1991a, 1991b, 1992). The insulation material is characterized by an apparent thermal conductivity, which is a term used in the insulation industry to represent the total of heat flows by conduction and radiation through the material. Low-density loose-fill fiberglass insulation has an apparent thermal conductivity of about 0.06 W/m·K, of which about 60 percent is attributed to radiation and most of the remainder is attributed to conduction through still air. This type of insulation has an average permeability of about $2 \times 10^{-8}$ to $8 \times 10^{-8}$ m$^2$, which varies strongly with installed density (Wilkes and Graves, 1993). In addition, there is a large gradient of permeability through the thickness of the insulation in the as-installed condition, due to the highly compressible nature of the material. The presence of a large amount of radiation, the inhomogeneity of insulation material properties, and the presence of wood ceiling joists within the insulation make the results of experiments on this material

**Table 2 Characteristics of loose-fill fiberglass insulations tested in simulated attic**

| Specimen | Thickness, mm | Density, kg/m$^3$ | Permeability, m$^2$ | Apparent Thermal Conductivity, W/m·K |
|---|---|---|---|---|
| 2 | 241 | 6.41 | $1.26 \times 10^{-7}$ | 0.079 |
| 3 | 241 | 7.21 | $7.18 \times 10^{-8}$ | 0.072 |
| 4 | 457 | 8.97 | $3.70 \times 10^{-8}$ | 0.064 |

**Table 3 Calculated Biot and critical Rayleigh numbers for simulated attic tests**

| Specimen | Critical Temperature Difference, K | Mean Temperature, °C | Experimental $Ra_c$ | $B_l$ | $B_u$ | Calculated $Ra_c$ |
|---|---|---|---|---|---|---|
| 2 | 17.8 | 11.2 | 20.7 | 15 | 34-76 | 23.8-24.8 |
| 3 | 17.8 | 11.2 | 13.0 | 17 | 37-84 | 24.0-25.0 |
| 4 | 18.7 | 11.2 | 14.8 | 36 | 79-178 | 25.5-26.0 |

unsuitable for a test of the validity of the theory presented above. However, it was hoped that the above theory would assist in understanding the results of these experiments.

The loose-fill insulation was installed in the simulated attic, with the bottom side of the insulation placed on gypsum board and the top side open to the attic air space. The gypsum board was heated by conduction–convection and radiation from air and surroundings at a temperature near 21°C. The temperature of the air in the attic space took on various values depending on the weather conditions that were simulated. Characteristics of the insulation materials are given in Table 2 (see Wilkes et al., 1992, 1993, for the source of these values). Boundary resistances obtained from attic experiments were about 0.20 m$^2$·K/W on the bottom side (including 0.08 m$^2$·K/W due to the gypsum board), and 0.04 to 0.09 m$^2$·K/W on the top side.

Table 3 gives the temperature difference across the insulation and the mean temperature at which convection started, along with Biot numbers and critical Rayleigh numbers. The experimental Rayleigh numbers were obtained from measured values, while the calculated Rayleigh numbers were obtained from Eq. (6) for the given Biot numbers. Table 3 shows that the experimental Rayleigh numbers range from 13.0 to 20.7, and are significantly lower than the calculated values of 23.8 to 26.0.

While the calculated critical Rayleigh numbers are slightly lower than the ideal value of 27.1 that applies to isothermal boundaries, the mixed thermal boundary conditions in these experiments do not appear to explain the magnitude of the experimental Rayleigh numbers. It is likely that the experimental Rayleigh numbers are lower than the classical value of 27.1 because of a number of factors, including (a) slightly nonisothermal boundaries, (b) the permeability gradient through the thickness of the insulation, (c) the fact that a substantial amount of the heat transfer in the absence of convection is due to radiation, (d) the presence of wood ceiling joists, and (e) inhomogeneities and variability of the material properties. Additional analyses would be required to determine which of these other factors are the most significant.

## Summary

The mathematical formalism developed by Nield (1968) has been used to calculate critical Rayleigh numbers and critical wavenumbers for the onset of natural convection in a horizontal porous medium subject to mixed thermal boundary conditions. Two practically important cases were examined. The first case corresponds to impermeable top and bottom boundaries, and the second corresponds to an impermeable bottom boundary and an open top boundary. It was found that at limiting Biot numbers of 0 and ∞, the calculated critical Rayleigh numbers and critical wavenumbers agreed very well with those given in the literature. Numerical values are given for a wide range of intermediate Biot numbers. The results of these analyses were applied to analysis of experimental data on the thermal performance of low-density loose-fill fiberglass insulation tested in a simulated attic with an open top boundary. Experimental critical Rayleigh numbers were substantially lower than the ideal value of 27.1. The mixed thermal boundary conditions were not sufficient to explain the difference between the experimental critical Rayleigh numbers and the ideal value.



Downloaded 12 Dec 2010 to 193.140.21.150. Redistribution subject to ASME license or copyright; see http://www.asme.org/terms/Terms_Use.cfm

## Acknowledgments

This work was supported by the Office of Buildings Energy Research, U.S. Department of Energy, as part of the National Program for Building Thermal Envelope Systems and Materials, managed by Martin Marietta Energy Systems, Inc. under Contract No. DE-AC05-84-OR21400.

## References

Horton, C. W., and Rogers, F. T., Jr., 1945, "Convection Currents in a Porous Medium," *Journal of Applied Physics,* Vol. 16, pp. 367–370.

Lapwood, E. R., 1948, "Convection of a Fluid in a Porous Medium," *Proceedings of the Cambridge Philosophical Society,* Vol. 44, pp. 508–521.

Nield, D. A., 1968, "Onset of Thermohaline Convection in a Porous Medium," *Water Resources Research,* Vol. 4, pp. 553–560.

Nield, D. A., and Bejan, A., 1991, *Convection in Porous Media,* Springer-Verlag, New York, pp. 141–147.

Wilkes, K. E., Wendt, R. L., Delmas, A., and Childs, P. W., 1991a, "Attic Testing at the Roof Research Center—Initial Results," *1991 International Symposium on Roofing Technology,* pp. 391–400, National Roofing Contractors Association, Rosemont, IL.

Wilkes, K. E., Wendt, R. L., Delmas, A., and Childs, P. W., 1991b, "Thermal Performance of One Loose-Fill Fiberglass Attic Insulation," *Insulation Materials: Testing and Applications,* Vol. 2, ASTM STP 1116, R. S. Graves and D. C. Wysocki, eds., American Society for Testing and Materials, Philadelphia.

Wilkes, K. E., and Childs, P. W., 1992, "Thermal Performance of Fiberglass and Cellulose Attic Insulations," *Proceedings of the ASHRAE/DOE/BTECC Conference on Thermal Performance of the Exterior Envelopes of Buildings V,* pp. 357–367, American Society of Heating, Refrigerating, and Air-Conditioning Engineers, Inc., Atlanta, GA.

Wilkes, K. E., and Graves, R. S., 1993, "Air-Flow Permeability of Attic Insulation Materials," ORNL/M-2646, Oak Ridge National Laboratory, Oak Ridge, TN.

# Free Convection Induced by a Vertical Wavy Surface With Uniform Heat Flux in a Porous Medium

**D. A. S. Rees[1] and I. Pop[2]**

## Nomenclature

$a$ = amplitude of the nonuniform surface = $\pi\bar{a}/l$
$f$ = reduced streamfunction
$g$ = acceleration due to gravity
$h$ = reduced temperature
$k$ = thermal conductivity
$K$ = permeability of the porous medium
$l$ = half-wavelength, or lengthscale, of the surface undulations
$\underline{n}$ = unit vector normal to the surface
$p$ = pressure
$q$ = heat flux
Ra = $g\beta K(q_w/k)l^2/\alpha\nu$, the Darcy–Rayleigh number based on $q_w$ and $l$
$s_t$ = shape function for the wavy surface
$T$ = dimensional temperature: $T - T_\infty = (q_w l/k)\theta$
$x, y$ = streamwise and cross-stream coordinates: $(x, y) = (\bar{x}/l, \bar{y}/l)$
$\alpha$ = thermal diffusivity of the saturated medium
$\beta$ = coefficient of thermal expansion
$\eta$ = pseudosimilarity variable
$\theta$ = dimensionless temperature
$\nu$ = kinematic viscosity
$\sigma$ = function associated with the surface undulations
$\psi$ = streamfunction = $\bar{\psi}/l$

### Superscripts

$\bar{}$ = dimensional variables
$\hat{}$ = boundary layer variables
$'$ = differentiation with respect to $\hat{x}$

### Subscripts

$c$ = denoting center of hump
$t$ = transverse variations
$w$ = condition at the wall
$\infty$ = condition at infinity

## 1 Introduction

The study of free convection heat transfer from uniform surfaces embedded in a saturated porous medium has attracted a great deal of interest for many investigators over the last two decades; see Nield and Bejan (1992) for a comprehensive review of this topic. Studies have centered on those cases where the thermal boundary conditions allow the use of similarity transformations to reduce the governing equations to a system of ordinary differential equations. In general, this means that the heated surface is plane. However, in practice, surfaces are sometimes roughened intentionally in order to enhance the heat transfer. Roughened surfaces are encountered in several heat transfer devices such as flat-plate solar collectors and flat-plate condensers in refrigerators. Larger scale surface nonuniformities are encountered in cavity wall insulating systems and grain storage containers. The only papers to date that study the effects of such nonuniformities on thermal boundary layer flow of a Newtonian fluid are those of Moulic and Yao (1989a, b) and Yao (1983). The present authors have very recently obtained similarity solutions for a vertical, sinusoidally wavy surface with a uniform *wall temperature* embedded in a porous medium (Rees and Pop, 1994a). However, the modeling of many practical configurations requires the imposition of a uniform *heat flux* from the bounding surface.

In this paper we consider the effects of transverse surface waves on the free convective boundary layer induced by a uniform heat flux vertical surface embedded in a porous medium. In this regard, the present study is akin to that of Moulic and Yao (1989b), who considered the Newtonian fluid analogue of this problem. Since the transformed boundary layer equations are nonsimilar, they are solved numerically using the Keller box method (see Keller and Cebeci, 1971). The distribution of the wall temperature along the wavy surface is presented and the accuracy is verified by comparing with previous results for a vertical flat plate embedded in a porous medium obtained by Kumari et al. (1990).

## 2 Analysis

Consider a vertical surface with transverse waves embedded in a porous medium with constant ambient temperature, $T_\infty$, as shown in Fig. 1. In particular, we assume that the surface profile is given by

$$\bar{y} = \bar{s}_t(\bar{x}) = \bar{a}\sin(\pi\bar{x}/l), \tag{1}$$

where $\bar{a}$ is the amplitude of the wavy surface and $2l$ is the wavelength. The local heat flux rate normal to the surface is maintained at a constant value, $q_w$. The flow is considered to be steady and two dimensional. All fluid and porous medium properties are considered to be constant except for the buoyancy term, and we

[1] School of Mechanical Engineering, University of Bath, Claverton Down, Bath, BA2 7AY, United Kingdom.

[2] Faculty of Mathematics, University of Cluj, R-3400, Cluj, CP 253, Romania.

Contributed by the Heat Transfer Division of THE AMERICAN SOCIETY OF MECHANICAL ENGINEERS. Manuscript received by the Heat Transfer Division September 1992; revision received March 1993. Keywords: Flow Nonuniformity, Natural Convection, Porous media. Associate Technical Editor: C. E. Hickox, Jr.



Downloaded 12 Dec 2010 to 193.140.21.150. Redistribution subject to ASME license or copyright; see http://www.asme.org/terms/Terms_Use.cfm

## Acknowledgments

This work was supported by the Office of Buildings Energy Research, U.S. Department of Energy, as part of the National Program for Building Thermal Envelope Systems and Materials, managed by Martin Marietta Energy Systems, Inc. under Contract No. DE-AC05-84-OR21400.

## References

Horton, C. W., and Rogers, F. T., Jr., 1945, "Convection Currents in a Porous Medium," *Journal of Applied Physics,* Vol. 16, pp. 367–370.

Lapwood, E. R., 1948, "Convection of a Fluid in a Porous Medium," *Proceedings of the Cambridge Philosophical Society,* Vol. 44, pp. 508–521.

Nield, D. A., 1968, "Onset of Thermohaline Convection in a Porous Medium," *Water Resources Research,* Vol. 4, pp. 553–560.

Nield, D. A., and Bejan, A., 1991, *Convection in Porous Media,* Springer-Verlag, New York, pp. 141–147.

Wilkes, K. E., Wendt, R. L., Delmas, A., and Childs, P. W., 1991a, "Attic Testing at the Roof Research Center—Initial Results," *1991 International Symposium on Roofing Technology,* pp. 391–400, National Roofing Contractors Association, Rosemont, IL.

Wilkes, K. E., Wendt, R. L., Delmas, A., and Childs, P. W., 1991b, "Thermal Performance of One Loose-Fill Fiberglass Attic Insulation," *Insulation Materials: Testing and Applications,* Vol. 2, ASTM STP 1116, R. S. Graves and D. C. Wysocki, eds., American Society for Testing and Materials, Philadelphia.

Wilkes, K. E., and Childs, P. W., 1992, "Thermal Performance of Fiberglass and Cellulose Attic Insulations," *Proceedings of the ASHRAE/DOE/BTECC Conference on Thermal Performance of the Exterior Envelopes of Buildings V,* pp. 357–367, American Society of Heating, Refrigerating, and Air-Conditioning Engineers, Inc., Atlanta, GA.

Wilkes, K. E., and Graves, R. S., 1993, "Air-Flow Permeability of Attic Insulation Materials," ORNL/M-2646, Oak Ridge National Laboratory, Oak Ridge, TN.

# Free Convection Induced by a Vertical Wavy Surface With Uniform Heat Flux in a Porous Medium

**D. A. S. Rees[1] and I. Pop[2]**

## Nomenclature

$a$ = amplitude of the nonuniform surface = $\pi\bar{a}/l$
$f$ = reduced streamfunction
$g$ = acceleration due to gravity
$h$ = reduced temperature
$k$ = thermal conductivity
$K$ = permeability of the porous medium
$l$ = half-wavelength, or lengthscale, of the surface undulations
$\underline{n}$ = unit vector normal to the surface
$p$ = pressure
$q$ = heat flux
Ra = $g\beta K(q_w/k)l^2/\alpha\nu$, the Darcy–Rayleigh number based on $q_w$ and $l$
$s_t$ = shape function for the wavy surface
$T$ = dimensional temperature: $T - T_\infty = (q_w l/k)\theta$
$x, y$ = streamwise and cross-stream coordinates: $(x, y) = (\bar{x}/l, \bar{y}/l)$
$\alpha$ = thermal diffusivity of the saturated medium
$\beta$ = coefficient of thermal expansion
$\eta$ = pseudosimilarity variable
$\theta$ = dimensionless temperature
$\nu$ = kinematic viscosity
$\sigma$ = function associated with the surface undulations
$\psi$ = streamfunction = $\bar{\psi}/l$

### Superscripts

$\bar{}$ = dimensional variables
$\hat{}$ = boundary layer variables
$'$ = differentiation with respect to $\hat{x}$

### Subscripts

$c$ = denoting center of hump
$t$ = transverse variations
$w$ = condition at the wall
$\infty$ = condition at infinity

## 1 Introduction

The study of free convection heat transfer from uniform surfaces embedded in a saturated porous medium has attracted a great deal of interest for many investigators over the last two decades; see Nield and Bejan (1992) for a comprehensive review of this topic. Studies have centered on those cases where the thermal boundary conditions allow the use of similarity transformations to reduce the governing equations to a system of ordinary differential equations. In general, this means that the heated surface is plane. However, in practice, surfaces are sometimes roughened intentionally in order to enhance the heat transfer. Roughened surfaces are encountered in several heat transfer devices such as flat-plate solar collectors and flat-plate condensers in refrigerators. Larger scale surface nonuniformities are encountered in cavity wall insulating systems and grain storage containers. The only papers to date that study the effects of such nonuniformities on thermal boundary layer flow of a Newtonian fluid are those of Moulic and Yao (1989a, b) and Yao (1983). The present authors have very recently obtained similarity solutions for a vertical, sinusoidally wavy surface with a uniform *wall temperature* embedded in a porous medium (Rees and Pop, 1994a). However, the modeling of many practical configurations requires the imposition of a uniform *heat flux* from the bounding surface.

In this paper we consider the effects of transverse surface waves on the free convective boundary layer induced by a uniform heat flux vertical surface embedded in a porous medium. In this regard, the present study is akin to that of Moulic and Yao (1989b), who considered the Newtonian fluid analogue of this problem. Since the transformed boundary layer equations are nonsimilar, they are solved numerically using the Keller box method (see Keller and Cebeci, 1971). The distribution of the wall temperature along the wavy surface is presented and the accuracy is verified by comparing with previous results for a vertical flat plate embedded in a porous medium obtained by Kumari et al. (1990).

## 2 Analysis

Consider a vertical surface with transverse waves embedded in a porous medium with constant ambient temperature, $T_\infty$, as shown in Fig. 1. In particular, we assume that the surface profile is given by

$$\bar{y} = \bar{s}_t(\bar{x}) = \bar{a}\sin(\pi\bar{x}/l), \tag{1}$$

where $\bar{a}$ is the amplitude of the wavy surface and $2l$ is the wavelength. The local heat flux rate normal to the surface is maintained at a constant value, $q_w$. The flow is considered to be steady and two dimensional. All fluid and porous medium properties are considered to be constant except for the buoyancy term, and we

[1] School of Mechanical Engineering, University of Bath, Claverton Down, Bath, BA2 7AY, United Kingdom.
[2] Faculty of Mathematics, University of Cluj, R-3400, Cluj, CP 253, Romania.
Contributed by the Heat Transfer Division of THE AMERICAN SOCIETY OF MECHANICAL ENGINEERS. Manuscript received by the Heat Transfer Division September 1992; revision received March 1993. Keywords: Flow Nonuniformity, Natural Convection, Porous media. Associate Technical Editor: C. E. Hickox, Jr.



Copyright © 1995 by ASME

Downloaded 12 Dec 2010 to 193.140.21.150. Redistribution subject to ASME license or copyright; see http://www.asme.org/terms/Terms_Use.cfm

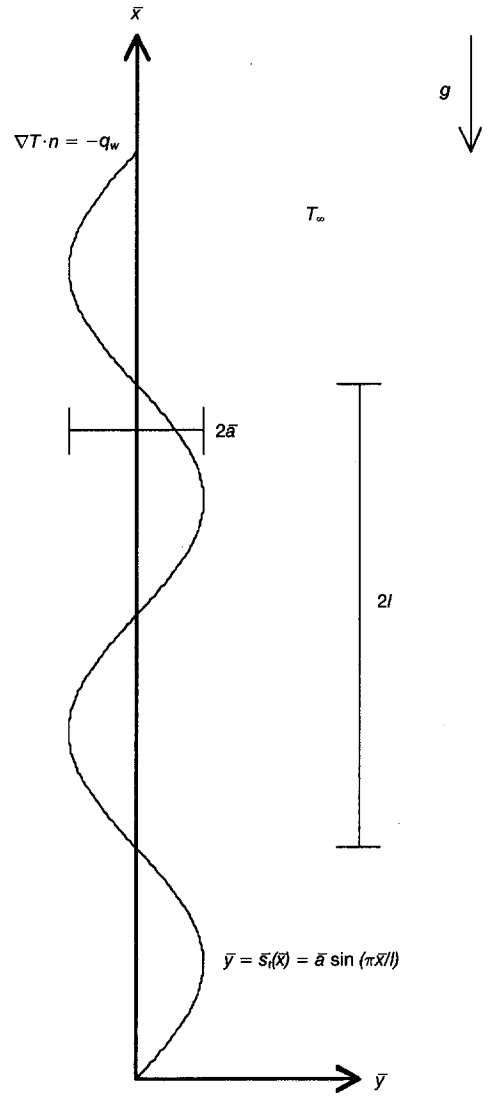



**Fig. 1 Physical model and coordinate system depicting transverse surface waves**

assume that the Boussinesq approximation is valid. In terms of dimensionless variables, the Darcy and energy equations can be written as

$$\frac{\partial^2\psi}{\partial x^2} + \frac{\partial^2\psi}{\partial y^2} = \mathrm{Ra}\,\frac{\partial\theta}{\partial y}, \tag{2}$$

$$\frac{\partial^2\theta}{\partial x^2} + \frac{\partial^2\theta}{\partial y^2} = \frac{\partial\psi}{\partial y}\frac{\partial\theta}{\partial x} - \frac{\partial\psi}{\partial x}\frac{\partial\theta}{\partial y}. \tag{3}$$

The boundary conditions that apply are the following:

$$\psi = 0, \quad \frac{\partial\theta}{\partial y} - a\cos\pi x\,\frac{\partial\theta}{\partial x} = -\sigma \quad \text{on}$$

$$y = s_t(x) = \frac{a}{\pi}\sin\pi x, \tag{4a}$$

$$\frac{\partial\psi}{\partial y} \to 0, \quad \theta \to 0 \quad \text{as} \quad y \to \infty, \tag{4b}$$

where $\sigma$, a function associated with the geometry of the surface, is given by

$$\sigma = \left(1 + \left(\frac{ds_t}{dx}\right)^2\right)^{1/2} = (1 + a^2\cos^2\pi x)^{1/2}, \tag{5}$$

and the dimensionless variables are defined in the nomenclature. In this paper we restrict attention to those cases for which the nondimensional wave amplitude remains $O(1)$ as $\mathrm{Ra} \to \infty$.

The effect of the wavy surface boundary conditions can be transferred to the governing equations by means of the transformation

$$\hat{x} = x, \quad \hat{y} = y - \frac{a}{\pi}\sin\pi x. \tag{6}$$

Equations (2) and (3) become

$$\nabla_1^2\psi = \mathrm{Ra}\,\frac{\partial\theta}{\partial\hat{y}}, \tag{7}$$

$$\nabla_1^2\theta = \frac{\partial\psi}{\partial\hat{y}}\frac{\partial\theta}{\partial\hat{x}} - \frac{\partial\psi}{\partial\hat{x}}\frac{\partial\theta}{\partial\hat{y}}, \tag{8}$$

and the boundary conditions are now

$$\psi = 0, \quad \frac{\partial\theta}{\partial\hat{y}} - a\cos\pi\hat{x}\,\frac{\partial\theta}{\partial\hat{x}} = -\sigma \quad \text{on} \quad \hat{y} = 0, \tag{9a}$$

$$\frac{\partial\psi}{\partial\hat{y}} \to 0, \quad \theta \to 0 \quad \text{as} \quad \hat{y} \to \infty, \tag{9b}$$

where

$$\nabla_1^2 = \frac{\partial^2}{\partial\hat{x}^2} + \sigma^2\frac{\partial^2}{\partial\hat{y}^2} - 2a\cos\pi\hat{x}\,\frac{\partial^2}{\partial\hat{x}\partial\hat{y}} + a\pi\sin\pi\hat{x}\,\frac{\partial}{\partial\hat{y}}. \tag{10}$$

Next, we introduce the boundary layer variables

$$\psi = \mathrm{Ra}^{1/3}\hat{x}^{2/3}f(\hat{x},\eta), \quad \theta = \mathrm{Ra}^{-1/3}\hat{x}^{1/3}h(\hat{x},\eta), \tag{11a}$$

here

$$\eta = \mathrm{Ra}^{1/3}\hat{y}/\hat{x}^{1/3}. \tag{11b}$$

Thus, on introducing Eq. (11) into Eqs. (7) and (8), and formally letting $\mathrm{Ra} \to \infty$, we obtain the following boundary layer equations at leading order:

$$\sigma^2 f_\eta = h, \tag{12}$$

$$\sigma^2 h_{\eta\eta} + \tfrac{2}{3}fh_\eta - \tfrac{1}{3}f_\eta h = \hat{x}(f_\eta h_{\hat{x}} - h_\eta f_{\hat{x}}) \tag{13}$$

and the corresponding boundary conditions are

$$f = 0, \quad h_\eta = -1/\sigma \quad \text{on} \quad \eta = 0, \tag{14a}$$

$$h \to 0 \quad \text{as} \quad \eta \to \infty. \tag{14b}$$

It is also convenient to introduce a third transformation to render the boundary conditions independent of $\hat{x}$:

$$f = \sigma^{1/3}\hat{f}(\hat{x},\hat{\eta}), \quad h = \sigma^{2/3}\hat{h}(\hat{x},\hat{\eta}), \tag{15a}$$

where

$$\eta = \sigma^{5/3}\hat{\eta}. \tag{15b}$$

Equations (12) and (13) become

$$\hat{f}_{\hat{\eta}} = \hat{h}, \tag{16}$$

$$\hat{h}_{\hat{\eta}\hat{\eta}} + \tfrac{1}{3}(2\hat{f}\hat{h}_{\hat{\eta}} - \hat{f}_{\hat{\eta}}\hat{h}) = \hat{x}(\hat{f}_{\hat{\eta}}\hat{h}_{\hat{x}} - \hat{h}_{\hat{\eta}}\hat{f}_{\hat{x}}) + \frac{\sigma'}{3\sigma}\hat{x}(2\hat{f}_{\hat{\eta}}\hat{h} - \hat{f}\hat{h}_{\hat{\eta}}), \tag{17}$$

and the boundary conditions transform to

$$\hat{f} = 0, \quad \hat{h}_{\hat{\eta}} = -1 \quad \text{on} \quad \hat{\eta} = 0, \tag{18a}$$

$$\hat{h} \to 0 \quad \text{as} \quad \hat{\eta} \to \infty, \tag{18b}$$

where the prime denotes differentiation with respect to $\hat{x}$.



Downloaded 12 Dec 2010 to 193.140.21.150. Redistribution subject to ASME license or copyright; see http://www.asme.org/terms/Terms_Use.cfm

## 3 Results and Discussion

Both the above-described systems of equations [i.e. (12, 13) and (16, 17)] were solved numerically by means of the Keller box method for different values of the wave amplitude, $a$. Integration in the $\eta$ or $\hat{\eta}$ direction was over a nonuniform grid from 0 to 30, a value well outside the boundary layer. The grid chosen gave a value of $h_w = 1.29612$ for the surface temperature for the boundary layer flow over a flat plate (i.e., $\sigma = 1$ or $a = 0$ in Eqs. (12, 13)); this compares very well with the value, $h_w = 1.29618$, which is correct to five decimal places and which we obtained by solving the resulting similarity equations using a combination of the fourth-order Runge–Kutta method and Richardson extrapolation. It is worth mentioning that this value of $h_w$ is in good agreement with the value $h_w = 1.29532$ obtained by Kumari et al. (1990) for a vertical plane surface with uniform surface heat flux embedded in a fluid-saturated porous medium.

Integration in $\hat{x}$ involved uniform steps of length 0.01, which generally gives very accurate results. At each step, convergence was assumed to have taken place when the maximum absolute change in any quantity was less than $10^{-10}$ and double precision arithmetic was used throughout. In general, convergence was increasingly difficult to achieve as $\hat{x}$ increased and as $a$ increased. We presume that this is caused by increasing ill-conditioning of the Jacobian matrix used in the Newton–Raphson scheme. However, values of $\hat{x}$ up to 40 and wave amplitudes up to 0.5 gave no numerical difficulties.

In our discussion of the results we will confine our comments primarily to the surface temperature distribution. Figure 2 shows the distribution of the surface temperature, $h_w = h(\hat{x}, 0)$, for different values of $a$. The main effect of the presence of surface undulations is to raise the temperature of the bounding surface above the value 1.29612, corresponding to that of a plane surface. This is a consequence of the fact that the component of the buoyancy force parallel to the wavy surface is less than or equal to that of a plane surface, as can be seen by the factor, $1/\sigma^2$, in Eq. (12). We find that the positions of maximum and minimum surface temperature correspond almost exactly to where $d\sigma/d\hat{x} = 0$, that is, at integer values of $\hat{x}$. A similar observation was made by Moulic and Yao (1989b).

The corresponding distributions of the scaled temperature, $\hat{h}(\hat{x}, 0)$, are not shown for the sake of brevity. However, the effect of the scalings, Eq. (15), is to shift the "mean" value of the temperature close to 1.29612. Whereas $h(\hat{x}, 0)$, shown in Fig. 2, exhibits decaying oscillations, the corresponding behavior of $\hat{h}(\hat{x}, 0)$ tends fairly quickly to what looks like a periodic function. This was investigated numerically by solving Eqs. (15) and (16) for $a = 0.5$, a particularly large amplitude wave. Figure 3(*a*) shows the evolution of $\hat{h}_w(\hat{x}, 0) - \hat{h}_w(\hat{x} - 2, 0)$ as $\hat{x}$ increases, where 2 is the nondimensional wavelength of the waves. The envelope of this function decays as $\hat{x}^{-3/2}$, as is demonstrated by the graph of $(\hat{h}_w(\hat{x}) - (\hat{h}_w(\hat{x} - 2))\hat{x}^{3/2}$ shown in Fig. 3(*b*). From our numerical evidence we conclude that the large-$\hat{x}$ behavior of the flow field is periodic, although we have been unable to prove this analytically. It is important to state that no numerical evidence was found that an inner boundary layer structure exists within the basic boundary layer as $\hat{x}$ increases; it was originally thought that such a structure might occur since the width of the surface wave decreases relative to the boundary layer thickness as $\hat{x}$ increases. Indeed, since the submission of the original draft of this manuscript we have found that such a structure does exist when the heated surface is horizontal (Rees and Pop, 1994b).

Finally, we considered the effect of a quite different form of boundary nonuniformity, namely that of a single smooth hump on an otherwise plane surface. In particular, the hump was of

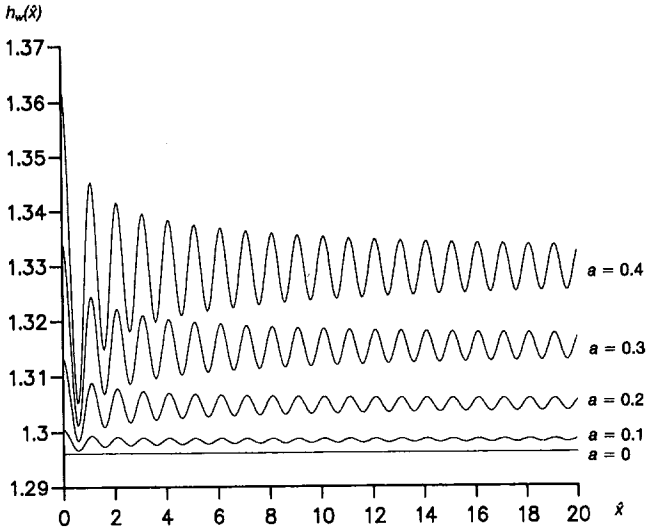



**Fig. 2 Variation of the surface temperature, $h_w(\hat{x})$, for $a = 0$, 0.1, 0.2, 0.3, and 0.4**

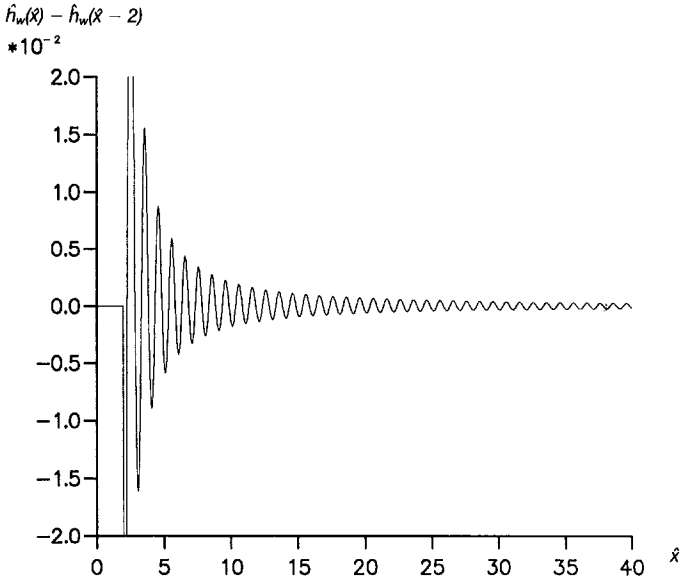



**Fig. 3(*a*) Variation of $\hat{h}_w(\hat{x}) - \hat{h}_w(\hat{x} - 2)$ for $a = 0.5$**

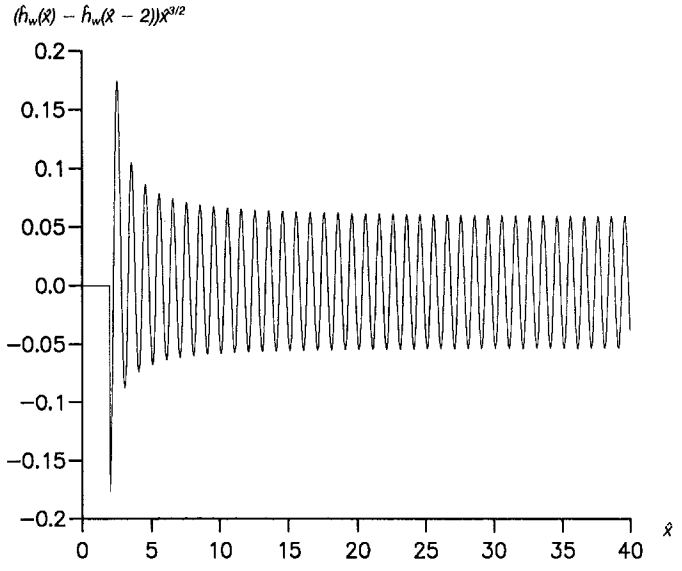



**Fig. 3(*b*) Variation of $(\hat{h}_w(\hat{x}) - \hat{h}_w(\hat{x} - 2))\hat{x}^{3/2}$ for $a = 0.5$**

Finally, we considered the effect of a quite different form of boundary nonuniformity, namely that of a single smooth hump on an otherwise plane surface. In particular, the hump was of



Downloaded 12 Dec 2010 to 193.140.21.150. Redistribution subject to ASME license or copyright; see http://www.asme.org/terms/Terms_Use.cfm

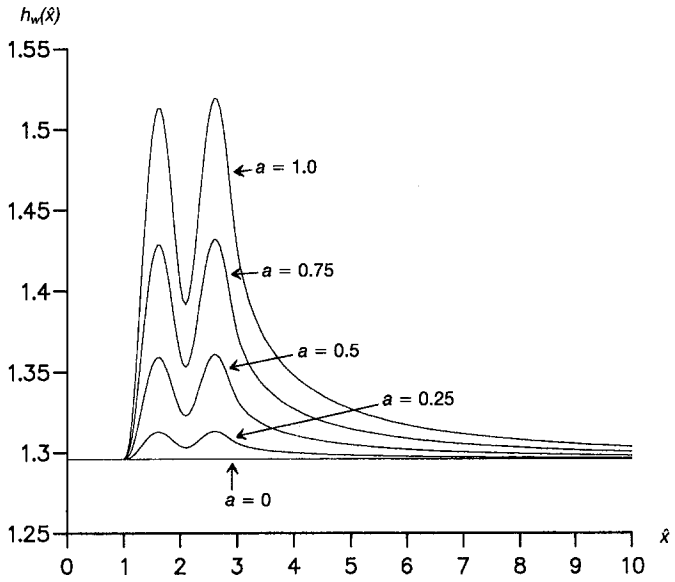



**Fig. 4 Variation in the surface temperature, $h_w(\hat{x})$, for a hump of length 2, centered at $\hat{x}_c = 2$, for $a = 0, 0.25, 0.5, 0.75$, and 1**

nondimensional length 2 and centered at $\hat{x} = \hat{x}_c = 2$. A surface profile having the form

$$s_t(\hat{x}) = 0, \quad 0 \le \hat{x} < 1$$

$$s_t(\hat{x}) = \frac{a}{\pi}(1 + \cos\pi\hat{x}), \quad 1 \le \hat{x} \le 3$$

$$s_t(\hat{x}) = 0, \quad 3 < \hat{x} \le 20. \tag{19}$$

was assumed and hence Eqs. (12) and (13) were solved with $\sigma$ given by

$$\sigma = 1, \quad 0 \le \hat{x} < 1$$

$$\sigma = (1 + a^2 \sin^2 \pi\hat{x})^{1/2}, \quad 1 \le \hat{x} \le 3$$

$$\sigma = 1, \quad 3 < \hat{x} \le 20. \tag{20}$$

The wall temperature distribution, $h_w(\hat{x})$, as a function of both $\hat{x}$ and $a$, is displayed in Fig. 4. Although the temperature is found to increase (decrease) whenever the slope of $\sigma$ increases (decreases), the presence of the boundary layer flow ensures that the positions of maximum temperature are shifted downstream of the positions of maximum slope. The two maxima in the surface temperature are caused by $\sigma$ having two maxima. The effect of having such a nonuniformity on the surface temperature can be seen to persist a substantial distance downstream of the hump.

## 4 Conclusions

We have investigated the effects of large-scale surface nonuniformities on the boundary layer flow induced by a constant heat flux, vertically aligned, semi-infinite surface embedded in a porous medium. The amplitude of the waves of the surface were assumed to have the same order of magnitude as their wavelength as the Rayleigh number becomes large. Assuming the validity of the boundary layer approximation, it was found that the flow could only be determined by solving a pair of parabolic partial differential equations. Local hot spots were found to correspond almost exactly to points at which the slope of the function $\sigma$ takes its maximum values. It was also found that the effect of an isolated hump on the surface persists a substantial distance downstream of the hump.

The analysis has been restricted to values of $x$ that take $O(1)$ values as $\mathrm{Ra} \to \infty$. In this range of values of $x$, the boundary layer thickness is $O(\mathrm{Ra}^{-1/3})$, which is much smaller than the $O(1)$ length scale associated with the waves of the surface. It is now of some interest to investigate the regime where $x = O(\mathrm{Ra}^{1/3})$ for within this regime the width of the boundary layer is $O(1)$, which is comparable with the surface wavelength and amplitude; we hope to address this problem in the near future.


## Acknowledgments

The first-named author would like to thank the SERC for providing a travel grant to enable this research to be undertaken, and the University of Cluj for their kind hospitality.


## References


Keller, H. B., and Cebeci, T., 1971, "Accurate Numerical Methods for Boundary Layer Flows. 1. Two Dimensional Flows," *Proc. Int. Conf. Numerical Methods in Fluid Dynamics*, Lecture Notes in Physics, Springer, New York.

Kumari, M., Pop, I., and Nath, G., 1990, "Natural Convection in Porous Media Above a Near Horizontal Uniform Heat Flux Surface," *Wärme- und Stoffübertr.*, Vol. 25, pp. 155–159.

Moulic, S. G., and Yao, L. S., 1989a, "Mixed Convection Along a Wavy Surface," ASME JOURNAL OF HEAT TRANSFER, Vol. 111, pp. 974–979.

Moulic, S. G., and Yao, L. S., 1989b, "Natural Convection Along a Vertical Wavy Surface With Uniform Heat Flux," ASME JOURNAL OF HEAT TRANSFER, Vol. 111, pp. 1106–1108.

Nield, D. A., and Bejan, A., 1992, *Convection in Porous Media*, Springer-Verlag, Berlin.

Rees, D. A. S., and Pop, I., 1994a, "A Note on Free Convection Along a Vertical Sinusoidally Wavy Surface in a Porous Medium," ASME JOURNAL OF HEAT TRANSFER, Vol. 116, pp. 505–508.

Rees, D. A. S., and Pop, I., 1994b, "Free Convection Induced by a Horizontal Sinusoidally Wavy Surface in a Porous Medium," accepted by *Fluid Dynamics Research*.

Yao, L. S., 1983, "Natural Convection Along a Vertical Wavy Surface," ASME JOURNAL OF HEAT TRANSFER, Vol. 105, pp. 465–468.


# Simulation of the Cyclic Injection Mold-Cooling Process Using Dual Reciprocity Boundary Element Method


**Shia Chung Chen[1,3] and Yung Chien Chung[2,3]**


## Nomenclature

$C_p$ = specific heat of polymer melt
$[C]$ = square matrix for coefficients associated with $\dot{T}$
$f_j$ = coordinate function at point $j$ to approximate $\dot{T}$
$[G]$ = square matrix for coefficients associated with $q$
$[H]$ = square matrix for coefficients associated with $T$
$h_{\mathrm{air}}$ = heat transfer coefficient of the ambient air
$h_c$ = heat transfer coefficient of the coolant
$\bar{J}_{\mathrm{avg}}$ = cycle-averaged heat flux at cavity surface
$K_m$ = thermal conductivity of mold
$K_p$ = thermal conductivity of polymer melt
$n$ = normal direction of mold boundary
$\{q^{n+1}\}$ = column matrix for heat flux at time $t = t_{n+1}$
$r$ = distance
$T$ = temperature field
$\dot{T}$ = time derivative of temperature


[1] Associate Professor.

[2] Research Assistant.

[3] Department of Mechanical Engineering, Chung Yuan University, Chung Li, Taiwan 32023.



Contributed by the Heat Transfer Division of THE AMERICAN SOCIETY OF MECHANICAL ENGINEERS. Manuscript received by the Heat Transfer Division October, 1993; revision received May 1994. Keywords: Materials Processing and Manufacturing Processes. Associate Technical Editor: Y. Jaluria.





Downloaded 12 Dec 2010 to 193.140.21.150. Redistribution subject to ASME license or copyright; see http://www.asme.org/terms/Terms_Use.cfm

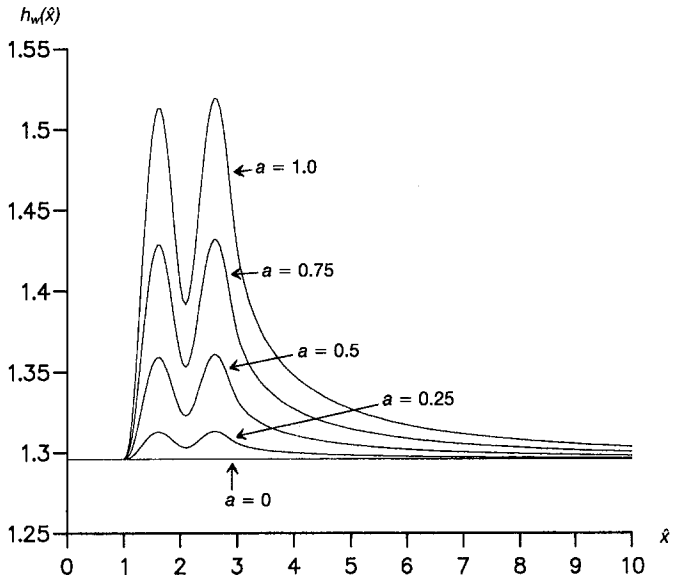



**Fig. 4 Variation in the surface temperature, $h_w(\hat{x})$, for a hump of length 2, centered at $\hat{x}_c = 2$, for $a = 0, 0.25, 0.5, 0.75$, and 1**

nondimensional length 2 and centered at $\hat{x} = \hat{x}_c = 2$. A surface profile having the form

$$s_t(\hat{x}) = 0, \quad 0 \le \hat{x} < 1$$

$$s_t(\hat{x}) = \frac{a}{\pi}(1 + \cos\pi\hat{x}), \quad 1 \le \hat{x} \le 3$$

$$s_t(\hat{x}) = 0, \quad 3 < \hat{x} \le 20. \tag{19}$$

was assumed and hence Eqs. (12) and (13) were solved with $\sigma$ given by

$$\sigma = 1, \quad 0 \le \hat{x} < 1$$

$$\sigma = (1 + a^2 \sin^2 \pi\hat{x})^{1/2}, \quad 1 \le \hat{x} \le 3$$

$$\sigma = 1, \quad 3 < \hat{x} \le 20. \tag{20}$$

The wall temperature distribution, $h_w(\hat{x})$, as a function of both $\hat{x}$ and $a$, is displayed in Fig. 4. Although the temperature is found to increase (decrease) whenever the slope of $\sigma$ increases (decreases), the presence of the boundary layer flow ensures that the positions of maximum temperature are shifted downstream of the positions of maximum slope. The two maxima in the surface temperature are caused by $\sigma$ having two maxima. The effect of having such a nonuniformity on the surface temperature can be seen to persist a substantial distance downstream of the hump.

## 4 Conclusions

We have investigated the effects of large-scale surface nonuniformities on the boundary layer flow induced by a constant heat flux, vertically aligned, semi-infinite surface embedded in a porous medium. The amplitude of the waves of the surface were assumed to have the same order of magnitude as their wavelength as the Rayleigh number becomes large. Assuming the validity of the boundary layer approximation, it was found that the flow could only be determined by solving a pair of parabolic partial differential equations. Local hot spots were found to correspond almost exactly to points at which the slope of the function $\sigma$ takes its maximum values. It was also found that the effect of an isolated hump on the surface persists a substantial distance downstream of the hump.

The analysis has been restricted to values of $x$ that take $O(1)$ values as $\mathrm{Ra} \to \infty$. In this range of values of $x$, the boundary layer thickness is $O(\mathrm{Ra}^{-1/3})$, which is much smaller than the $O(1)$ length scale associated with the waves of the surface. It is now of some interest to investigate the regime where $x = O(\mathrm{Ra}^{1/3})$ for within this regime the width of the boundary layer is $O(1)$, which is comparable with the surface wavelength and amplitude; we hope to address this problem in the near future.


## Acknowledgments

The first-named author would like to thank the SERC for providing a travel grant to enable this research to be undertaken, and the University of Cluj for their kind hospitality.


## References


Keller, H. B., and Cebeci, T., 1971, "Accurate Numerical Methods for Boundary Layer Flows. 1. Two Dimensional Flows," *Proc. Int. Conf. Numerical Methods in Fluid Dynamics*, Lecture Notes in Physics, Springer, New York.

Kumari, M., Pop, I., and Nath, G., 1990, "Natural Convection in Porous Media Above a Near Horizontal Uniform Heat Flux Surface," *Wärme- und Stoffübertr.*, Vol. 25, pp. 155–159.

Moulic, S. G., and Yao, L. S., 1989a, "Mixed Convection Along a Wavy Surface," ASME JOURNAL OF HEAT TRANSFER, Vol. 111, pp. 974–979.

Moulic, S. G., and Yao, L. S., 1989b, "Natural Convection Along a Vertical Wavy Surface With Uniform Heat Flux," ASME JOURNAL OF HEAT TRANSFER, Vol. 111, pp. 1106–1108.

Nield, D. A., and Bejan, A., 1992, *Convection in Porous Media*, Springer-Verlag, Berlin.

Rees, D. A. S., and Pop, I., 1994a, "A Note on Free Convection Along a Vertical Sinusoidally Wavy Surface in a Porous Medium," ASME JOURNAL OF HEAT TRANSFER, Vol. 116, pp. 505–508.

Rees, D. A. S., and Pop, I., 1994b, "Free Convection Induced by a Horizontal Sinusoidally Wavy Surface in a Porous Medium," accepted by *Fluid Dynamics Research*.

Yao, L. S., 1983, "Natural Convection Along a Vertical Wavy Surface," ASME JOURNAL OF HEAT TRANSFER, Vol. 105, pp. 465–468.


# Simulation of the Cyclic Injection Mold-Cooling Process Using Dual Reciprocity Boundary Element Method


**Shia Chung Chen[1,3] and Yung Chien Chung[2,3]**


## Nomenclature

$C_p$ = specific heat of polymer melt
$[C]$ = square matrix for coefficients associated with $\dot{T}$
$f_j$ = coordinate function at point $j$ to approximate $\dot{T}$
$[G]$ = square matrix for coefficients associated with $q$
$[H]$ = square matrix for coefficients associated with $T$
$h_{\mathrm{air}}$ = heat transfer coefficient of the ambient air
$h_c$ = heat transfer coefficient of the coolant
$\bar{J}_{\mathrm{avg}}$ = cycle-averaged heat flux at cavity surface
$K_m$ = thermal conductivity of mold
$K_p$ = thermal conductivity of polymer melt
$n$ = normal direction of mold boundary
$\{q^{n+1}\}$ = column matrix for heat flux at time $t = t_{n+1}$
$r$ = distance
$T$ = temperature field
$\dot{T}$ = time derivative of temperature


[1] Associate Professor.
[2] Research Assistant.
[3] Department of Mechanical Engineering, Chung Yuan University, Chung Li, Taiwan 32023.



Contributed by the Heat Transfer Division of THE AMERICAN SOCIETY OF MECHANICAL ENGINEERS. Manuscript received by the Heat Transfer Division October, 1993; revision received May 1994. Keywords: Materials Processing and Manufacturing Processes. Associate Technical Editor: Y. Jaluria.





Copyright © 1995 by ASME

Downloaded 12 Dec 2010 to 193.140.21.150. Redistribution subject to ASME license or copyright; see http://www.asme.org/terms/Terms_Use.cfm

$\{T^n\}$ = column matrix for temperature at time $t = t_n$
$\{T^{n+1}\}$ = column matrix for temperature at time $t = t_{n+1}$
$T_{air}$ = ambient air temperature
$T_C$ = coolant temperature
$T_m$ = cyclic transient mold temperature
$T_{m,s}$ = steady cyclic component of mold temperature
$T_{m,t}$ = cyclic time-varying component of mold temperature
$T_p$ = polymer melt temperature
$t$ = time
$z$ = direction across cavity thickness
$\Delta t$ = time interval during calculation
$\rho_m$ = density of mold
$\rho_p$ = density of polymer melt

## Introduction

The injection molding process consists of three major stages in a cycle: filling, packing, and cooling. The cooling stage lasts for about three-fourths of the cycle time in a typical cycle. Generally speaking, the cyclic cooling process is a three-dimensional transient heat conduction problem associated with derivative boundary conditions and complicated boundary geometry. Although to conduct a complete analysis for both transient temperature variations of the mold and polymer melt simultaneously is possible in principle, the computation cost is too expensive to be implemented during the actual design process. In recent years, attention has been focused on the development of a methodology that is computationally efficient and, at the same time, accurate enough for design purpose.

In most of the previous investigations of heat transfer phenomenon in injection molding, mold surface temperature is assumed to be constant. In the 1980s, efforts were put toward the influence of the cooling system on mold cavity surface temperature (Austin, 1985; Kwon et al., 1986). The most popular methodology is to use the steady-state boundary element method to avoid mold domain analysis and to introduce the cycle-averaged heat flux on the melt-mold interface as a boundary condition. In recent developments (Himasekhar et al., 1992; Chen and Chung, 1992), the transient variation of cavity temperature within a steady cycle is evaluated from the instantaneous heat flux at the mold cavity surface approximated by one-dimensional transient heat conduction analysis and imposed on the averaged cavity temperature obtained from a steady-state, cycle-averaged approach. Despite the fact that this method provides an efficient way to calculate cavity surface temperatures and is currently employed in CAE application, its limitations and accuracy have yet to be investigated and verified. On the other hand, when a complete transient analysis is performed, discretization of the mold domain is required. This needs more user time as well as large computer memory and time.

In this paper, transient heat conduction model is used for mold temperature calculation. In order to minimize the effort of mold domain discretization and the associated computations, dual reciprocity boundary element method is implemented to study the cyclic, transient characteristics of heat transfer in an injection mold for the first time. The analysis algorithm is developed and applied to a plate mold. Simulated results are illustrated and discussed.

## Formulation and Numerical Methodology

In previous studies (Himasekhar et al., 1992; Chen and Chung, 1992), the periodic transient mold temperature is separated into two components: (1) a steady cycle-averaged component and (2) a time-varying component within a typical cycle, i.e.,

$$T_m(\vec{r}, t) = T_{m,s}(\vec{r}) + T_{m,t}(z, t) \quad \text{for} \quad \vec{r} \in \Omega_m \tag{1}$$

The steady temperature component is obtained by the cycle-averaged boundary element analysis based on the steady-state heat conduction equation of Laplacian type:

$$\nabla^2 T_{m,s} = 0 \quad \text{for} \quad \vec{r} \in \Omega_m \tag{2}$$

Corresponding boundary conditions defined over the boundary surfaces of the mold are described in the following:

$$-K_m \frac{\partial T_{m,s}}{\partial n} = h_{air}(T_{m,s} - T_{air}) \quad \text{for} \quad \vec{r} \in S_e \tag{3}$$

$$-K_m \frac{\partial T_{m,s}}{\partial n} = h_c(T_{m,s} - T_C) \quad \text{for} \quad \vec{r} \in S_c \tag{4}$$

$$-K_m \frac{\partial T_{m,s}}{\partial n} = \bar{J}_{av} \quad \text{for} \quad \vec{r} \in S_p \tag{5}$$

where $S_e$, $S_c$, $S_p$, and $\Omega_m$ represent the exterior of the mold exterior boundary surface, cooling channel surface, melt-mold interface, and domain of the mold, respectively. The heat transfer coefficients for air and coolant are designated as $h_{air}$ and $h_c$. $\bar{J}_{avg}$ is the cycle-averaged heat flux transferring from polymer melt into cavity surface. The ambient environment temperatures, $T_{air}$ and $T_C$, with respect to the mold are defined for air and coolant correspondingly. $K_m$ is the thermal conductivity of the mold. The time-varying component within a typical cycle is approximated by one-dimensional transient heat conduction expressed as

$$\rho_m C_m \frac{\partial T_{m,t}(z, t)}{\partial t} = \frac{\partial}{\partial z}\left[K_m \frac{\partial T_{m,t}(z, t)}{\partial z}\right] \quad \text{for} \quad z \in S_p \tag{6}$$

under a periodic boundary condition specified by the time varying flux. Analysis as well as iteration algorithms were reported previously (Himasekhar et al., 1992; Chen and Chung, 1992).

In the present formulation, the mold temperature $T_m(\vec{r}, t)$ is directly solved by the transient heat conduction equation described as

$$\rho_m C_m \frac{\partial T_m(\vec{r}, t)}{\partial t} = K_m \nabla^2 T_m(\vec{r}, t) \quad \text{for} \quad \vec{r} \in \Omega_m \tag{7}$$

with the same boundary conditions defined over $S_e$ and $S_c$ as in Eqs. (3) and (4). However, within the mold cavity, $\Omega_p$, polymer melt also satisfies the transient heat conduction equation

$$\rho_p C_p \frac{\partial T_p}{\partial t} = \frac{\partial}{\partial z}\left(K_p \frac{\partial T_p}{\partial z}\right) \quad \text{for} \quad \vec{r} \in \Omega_p \tag{8}$$

where $\rho_p$ and $C_p$ are density and specific heat of the polymer melt, respectively. On the mold cavity surface $S_p$ compatible boundary conditions must be fulfilled. That is,

$$K_m \frac{\partial T_m}{\partial n} = -K_p \frac{\partial T_p}{\partial n} \quad \text{for} \quad \vec{r} \in S_p \tag{9}$$

$$T_m = T_p \quad \text{for} \quad \vec{r} \in S_p \tag{10}$$

Equation (7) for the heat conduction is then transformed into an integral equation using Green's second identity, fundamental solution, and dual reciprocity method (Brebbia and Wrobel,

**Table 1 Materials properties and processing parameters**

Thermal properties of polymer melt:
$K_p$ = 0.30 W/m K, $C_p$ = 1850 J/kg K, and $\rho$ = 1192 kg/m$^3$
Thermal properties of mold:
$K_m$ = 36.5 W/m K, $C_m$ = 462 J/kg K, and $\rho_m$ = 7820 kg/m$^3$
Part thickness: 4 mm
Coolant temperature of core side and cavity side: 30°C
Ambient air temperature: 30°C
Heat transfer coefficient of core coolant and cavity coolant: 5475 W/m$^2$ °C
Heat transfer coefficient of air: 10 W/m$^2$ °C
Initial polymer melt temperature: 220°C
Mold cycle time: 15 seconds



Downloaded 12 Dec 2010 to 193.140.21.150. Redistribution subject to ASME license or copyright; see http://www.asme.org/terms/Terms_Use.cfm

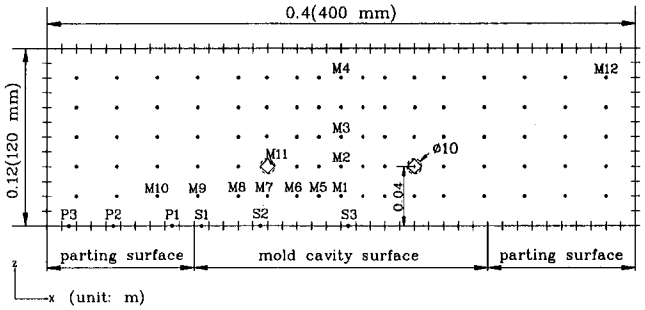



**Fig. 1 Boundary element mesh and chosen interior points for a plate mold. Geometry for mold dimension, cooling channels, mold cavity, and parting surface are also shown.**

1987). The approximation function for the transient term of heat conduction equation is chosen to be

$$f_j(\vec{r}) = r(\vec{r}, \vec{r}_j) \tag{11}$$

After discretization over the boundary and choosing some interior points in the domain of the mold and using the explicit scheme for $\dot{T}$, the Crank–Nicolson formulation for $T$, and the implicit scheme for $q$, Eq. (7) can be finally formulated into a linear matrix form of

$$\left(\frac{2}{\Delta t}[C] + [H]\right)\{T^{n+1}\} - 2[G]\{q^{n+1}\} = \left(\frac{2}{\Delta t}[C] - [H]\right)\{T^n\} \tag{12}$$

Detailed formulae are described elsewhere (Brebbia and Wrobel, 1987).

A rectangular plate was used to verify the applicability and accuracy of dual reciprocity boundary element method (DRBEM). The plate has a uniform initial temperature of 70°C. All the boundaries are subjected to a temperature of 0°C at time $t \geq 0$. The calculated temperatures at the center and near one corner of the plate using DRBEM are compared with values obtained from analytical solutions. In the first few seconds, the numerical results exhibit a maximum error of about 7 percent. Afterwards, the discrepancy decreases and the calculated values show good consistency with analytical ones with an error less than 1 percent.

By introducing boundary values and solving Eq. (12), transient mold temperatures including cavity surface temperature are obtained. For the first cycle, the initial mold temperature is same as coolant temperature. Mold temperatures at the end of the first cycle are used as initial mold temperatures for the second cycle. Before the analysis for the next cycle, obtained cavity surface temperatures are used to evaluate heat flux along cavity surface from Eq. (8) using finite difference method. The heat flux at cavity surface is then used to recalculate mold temperatures for the next analysis. Iteration is continued until temperature variation between the present cycle and the previous cycle is less than 0.1°C. A $\Delta t$ of 0.5 seconds is used for the analysis.

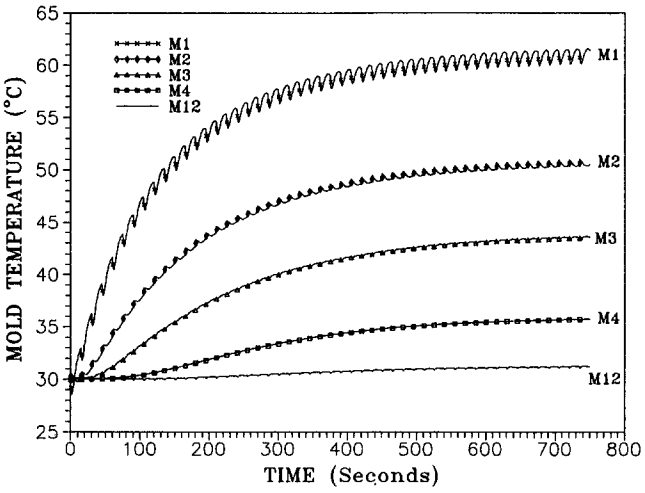



**Fig. 3 Cyclic, transient variations of mold temperatures at location M1, M2, M3, M4, and M12 versus injection cycles**

## Results and Discussions

Material properties and process parameters required for analysis are listed in Table 1.

A simple plate mold, with cooling channel arrangement as indicated in Fig. 1, is analyzed. Due to the symmetry, only the upper half of the mold is analyzed. Both boundary element mesh and chosen internal mold points are also shown. In Fig. 2, cyclic, transient variation of mold cavity surface temperatures located at S1, S2, and S3 for the first fifty cycles are illustrated. The cyclic mold temperatures for the parting surfaces labeled P1, P2, and P3 and for the cooling channel surface located at M11 are also shown. Mold temperature variation for locations (along vertical direction and between two cooling channels) designated M1, M2,

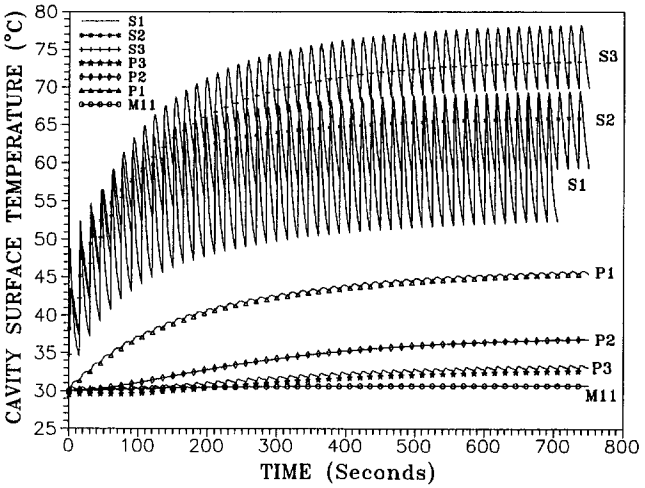



**Fig. 2 Cyclic, transient variations of mold cavity surface temperatures located at S1, S2, S3, P1, P2, P3, and M11 versus injection cycles**

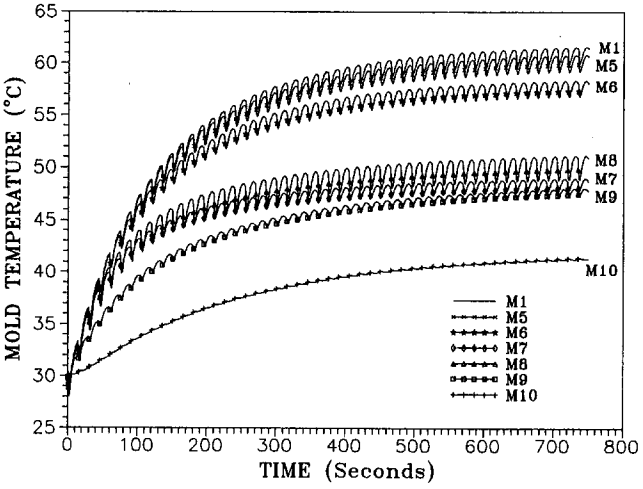



**Fig. 4 Cyclic, transient variations of mold temperatures at location M1, M5, M6, M7, M8, M9, and M10 versus injection cycles**



Downloaded 12 Dec 2010 to 193.140.21.150. Redistribution subject to ASME license or copyright; see http://www.asme.org/terms/Terms_Use.cfm

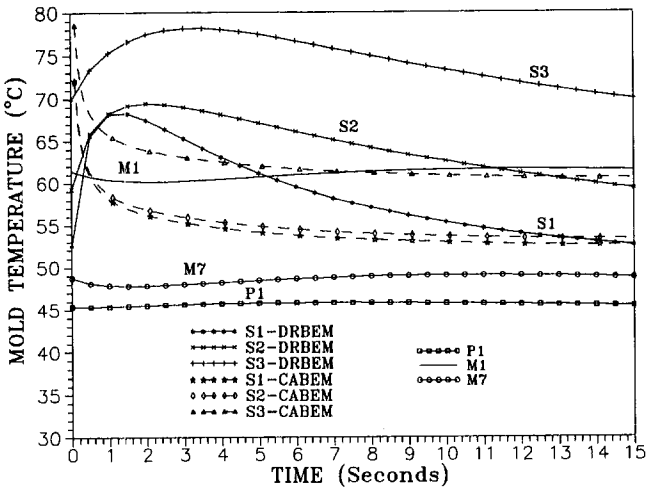



**Fig. 5 Transient temperature variation for locations S1, S2, S3, P1, M1, and M7 within a steady cyclic period. Results obtained from cycle-averaged boundary element approach for S1, S2, and S3 are also indicated for comparison.**

M3, and M4, as well as for M12 located near the mold exterior, are given in Fig. 3. On the other hand, cyclic mold temperatures for locations between the cooling channel and cavity surface and along the horizontal direction labeled M1, M5, M6, M7, M8, M9, and M10 are described in Fig. 4. It is found that within a steady cycle the transient temperature fluctuations at the mold cavity surface are much larger than those farther away from it. Along the cavity surface, the temperature at S3 is higher than that at S1 by about 10°C despite the fact that they are the same distance from the cooling channel. This is because more heat is transferred through the mold exterior at S1 than at S3. On the parting surface, location P1, which took more heat from the mold cavity, results in the highest temperature value as compared with those of P2 and P3. Among M1, M2, M3, and M4, the mold temperature and its cyclic transient variation decrease with increasing distance from the mold cavity. Near the mold exterior (M12), the temperature is almost the same as the ambient temperature. From Fig. 4 it can be seen that mold temperature decreases in a direction toward mold exterior except at location M7, which lies directly beneath the cooling channel and has a slightly lower temperature than that of M8. The transient temperature variations in a typical cycle during steady cyclic period for S1, S2, S3, M1, M7, and P1 are displayed in detail in Fig. 5. The transient variations of mold cavity surface temperatures analyzed using transient heat conduction model and DRBEM are also compared with those calculated on a cycle-averaged basis imposed by a transient variation as illustrated in Fig. 5. The present formulation results in higher mold temperature and slower temperature variation rate. The average difference in predicted temperatures may be as high as 15°C. This indicates that using a steady-state heat conduction model and the cycle-averaged approach underestimates mold temperature and overestimates the variation rate of heat transfer within a mold.

## Conclusions

The cyclic, transient heat transfer within an injection mold is analyzed using iterative DRBEM/FDM based on transient heat conduction model in a decoupled sequence. It is found that the transient temperature fluctuation at mold cavity surface is much larger than that away from it. Simulated results from the present method are also compared with those calculated by a modified boundary element method based on a cycle-averaged approach and combined with a one-dimensional transient analysis. The latter can predict only the temperature variation for cavity surface within a steady cyclic period. Also, it results in lower value and higher variation rate of cavity surface temperature due to the exclusion of the transient term in the heat conduction equation.

## References

Austin, C., 1985, "Mold Cooling," *SPE Technical Papers,* Vol. 31, pp. 764–766.

Brebbia, C. A., and Wrobel, L. C., 1987, "The Solution of Parabolic Problems Using the Dual Reciprocity Boundary Element," in: *Advanced Boundary Element Methods,* IUTAM Symposium, San Antonio, Springer-Verlag, New York, pp. 55–71.

Chen, S. C., and Chung, Y. C., 1992, "Simulation of Cyclic Transient Mold Cavity Surface in Injection Mold-Cooling Process," *Int. Comm. Heat Mass Transfer,* Vol. 19, pp. 559–568.

Himasekhar, K., Lottey, L., and Wang, K. K., 1992, "CAE of Mold Cooling in Injection Molding Using a Three-Dimensional Numerical Solution," ASME *Journal of Engineering for Industry,* Vol. 114, pp. 213–221.

Kwon, T. H., Shen, S. F., and Wang, K. K., 1986, "Computer-Aided Cooling System Design for Injection Molding," *SPE Technical Papers,* Vol. 32, pp. 110–115.



Downloaded 12 Dec 2010 to 193.140.21.150. Redistribution subject to ASME license or copyright; see http://www.asme.org/terms/Terms_Use.cfm

Journal of Heat Transfer

# Discussion

## Analysis of Heat Transfer Regulation and Modification Employing Intermittently Emplaced Porous Cavities[1]

## Analysis of Flow and Heat Transfer Over an External Boundary Covered With a Porous Substrate[2]

**D. A. Nield.**[3] In each of these papers the authors have modeled flow in a porous medium by a Brinkman–Forchheimer–extended Darcy equation (Eq. (5) of the first paper, Eq. (2) of the second) in which the coefficient of the Darcy term $\mathbf{v}/K$ is the same as the coefficient of the Brinkman term $\nabla^2\mathbf{v}$, and each is denoted by $\nu_{\text{eff}}$. In the past it has been common practice not to distinguish between these coefficients, but recent work (see, for example, Givler and Altobelli, 1994) has demonstrated that in some situations it is important to make the distinction. The permeability $K$ is defined so that the coefficient of the Darcy term is the kinematic viscosity of the fluid saturating the medium, which is appropriately denoted by $\nu$. The coefficient of the Brinkman term depends on the nature of the porous medium, and is appropriately denoted by $\nu_{\text{eff}}$.

The inclusion of derivatives of the Darcy number and inertial coefficient in Eq. (17) of the first paper is potentially misleading to the reader, because it is inconsistent with the authors' statement on p. 605 that the porous medium is considered homogeneous.

In the second paper, the authors have used the same matching conditions as those presented by Vafai and Kim (1990), and have taken no account of the critique of that paper by Nield (1991). In particular, in Eq. (12*b*), they have matched both the pressure and the viscous portion of the normal stress, and thus have overdetermined the system of equations by imposing an inappropriate additional constraint (see p. 270 of Nield, 1991). (In their paper the number of imposed boundary conditions is one more than the order of the differential equation system.) The effect on the flow field and heat transfer is probably small.

### References

Givler, R. C., and Altobelli, S. A., 1994, "A Determination of the Effective Viscosity for the Brinkman–Forchheimer Flow Model," *J. Fluid Mech.*, Vol. 258, pp. 355–370.

Nield, D. A., 1991, "The Limitations of the Brinkman–Forchheimer Equation in Modeling Flow in a Saturated Porous Medium and at an Interface," *Int. J. Heat Fluid Flow*, Vol. 12, pp. 269–272.

Vafai, K., and Kim, S. J., 1990, "Analysis of Surface Enhancement by a Porous Substrate," ASME JOURNAL OF HEAT TRANSFER, Vol. 112, pp. 700–706.

### Authors' Closure

**K. Vafai**[4] **and S. J. Kim.**[5] Much of the discussion given by Prof. Nield results from incorrect understanding of the assumptions made in our work. In what follows each point raised by Professor Nield is clarified.

1 In general the coefficient of the Darcy term $\mathbf{v}/K$ is $\mu_f$ and the coefficient of the Brinkman term $\nabla^2\mathbf{v}$ is $\mu_{\text{eff}}$ as shown in Eq. (5) of Vafai and Kim (1990). We are well aware that there are some situations where it is important to make a distinction, as shown and discussed for example in works of Vafai and Kim (1990), Ettefagh et al. (1991), and Huang and Vafai (1994). But Lundgren (1972) and Neale and Nader (1974) have shown that setting the effective viscosity of the fluid-saturated porous medium equal to the fluid viscosity provides good agreement with experimental data. Hence lacking definitive information on $\mu_{\text{eff}}$ it has become a common practice to set the effective viscosity equal to the fluid viscosity.

2 Here, it appears that there is misunderstanding of the numerical procedure for handling a porous/fluid composite layer. As pointed out in Vafai and Kim (1990) one can use separate calculation schemes for the porous and fluid regions, which would require an involved iterative procedure for matching the interface conditions. A more efficient approach is to combine the two sets of governing equations for the fluid region and the porous region into one set of conservation equations. In other words the porous substrate and the fluid region can be modeled as a single domain governed by one set of equations, the solution of which satisfies the continuity of the velocities, stresses, temperature, and the heat fluxes across the porous/fluid interface. Hence the inclusion of derivatives of the Darcy number and inertial coefficient in Eq. (17) of the first paper plays a role only across the interface. The same approach has been used by other investigators, for example, Beckerman et al. (1987) and Poulikakos (1986). It should be noted that in Vafai and Huang (1994), the $S^*$ for the fluid region at the interface will also include the derivatives of the Darcy number and inertial coefficients as shown and discussed in detail in the works of Huang and Vafai (1994a, b, c).

3 Vafai and Kim (1990) have used the same boundary conditions as for example used in Beckerman et al. (1987). Equation (10b) of Vafai and Kim (1990) implies matching of the total normal stress at the interface. This equation can be written as

$$-P_{\text{I}} + 2\mu_{\text{I}}\left[\frac{\partial v_y}{\partial y}\right]_{\text{I}} = -P_{\text{II}} + 2\mu_{\text{II}}\left[\frac{\partial v_y}{\partial y}\right]_{\text{II}}$$

It can be shown that this equation can be reduced to

$$P_{\text{I}} = P_{\text{II}}$$

because at the interface

$$\mu_{\text{I}}\left[\frac{\partial v_y}{\partial y}\right]_{\text{I}} = \mu_{\text{II}}\left[\frac{\partial v_y}{\partial y}\right]_{\text{II}}$$

for a two-dimensional configuration (Chen and Chen, 1992). Therefore both forms of the normal stress boundary conditions cited in Vafai and Kim (1990) or Vafai and Huang (1994) are correct. These points are also discussed in Vafai and Kim (1995). Furthermore, there appears to be a total misunderstanding on the part of Professor Nield since we did not even directly

[1] By K. Vafai and P. C. Huang, published in the August 1994 issue of the ASME JOURNAL OF HEAT TRANSFER, Vol. 116, pp. 604–613.

[2] P. C. Huang and K. Vafai, published in the August 1994 issue of the ASME JOURNAL OF HEAT TRANSFER, Vol. 116, pp. 768–771.

[3] Department of Engineering Science, University of Auckland, Private Bag 92019, Auckland, New Zealand.

[4] Department of Mechanical Engineering, The Ohio State University, Columbus, Ohio 43210.

[5] Thermal Engineering Center, Storage Systems Division, IBM Corporation, Tucson, AZ 85744.



Copyright © 1995 by ASME

Downloaded 12 Dec 2010 to 193.140.21.150. Redistribution subject to ASME license or copyright; see http://www.asme.org/terms/Terms_Use.cfm